PREFACE

Karl A. GSCHNEIDNER, Jr., and LeRoy EYRING

These elements perplex us in our rearches [sic], *baffle us in our speculations, and haunt us in our very dreams. They stretch like an unknown sea before us – mocking, mystifying, and murmuring strange revelations and possibilities.*

Sir William Crookes (February 16, 1887)

Today, about a decade short of two centuries after Lt. C.A. Arrhenius discovered the rare earths, we are witnessing a rapid growth in our knowledge of this family of 17 elements. In the five years, 1971 through 1975, we have learned as much about the rare earths as in the previous 25 years. In an attempt to assess the current state of the art (1976) the editors, with the encouragement of the publishers and other fellow scientists, have invited experts in various areas to write comprehensive, broad, up-to-date, and critical reviews. Some of the subjects were chosen because they are mature and still quite active; others because they are essential as background information and for reference; and some topics because they are relatively new and exciting areas of research. Unfortunately there are a few areas which have not been included in the four volumes either because they could not be covered adequately at present or because the appropriate authors were unavailable. Perhaps a future volume could remedy this and bring other rapidly expanding topics up-to-date.

A goal of these volumes is to attempt to combine and integrate as far as practical the physics and the chemistry of these elements. The strategy has been to divide the work into four volumes, the first two dealing primarily with metallic materials and the other two with non-metallic substances. The interaction of these disciplines is important if our knowledge and understanding is to advance quickly and broadly. Historically there are several important instances where one discipline had a great influence on the advancement of the science of rare earths. From the time of Arrhenius' discovery in Ytterby, Sweden until the last naturally occurring rare earth was discovered (lutetium in 1907) the chemistry of the rare earths was hopelessly confused, but the theoretical work of Niels Bohr and the experimental studies of H.G.J. Moseley (both physicists) in 1913–1914 showed that there were 15 lanthanide elements to be expected plus the two closely related metals scandium and yttrium. The discovery of ferromagnetism in gadolinium by G. Urbain,

P. Weiss and F. Trombe in 1935 stirred much excitement and was a foreshadow of the activities of the past twenty years. All of this, however, might not have been were it not for the efforts of two groups of chemists headed by G.E. Boyd at the Oak Ridge National Laboratory and F.H. Spedding at the Ames Laboratory who in the late 1940's developed the ion exchange techniques for separating rare earths. The method developed by the latter group is still being utilized by many industrial firms for preparing high purity rare earth materials. In the 1960's and 1970's several important discoveries—rare earth phosphors, cracking catalysts, rare earth-cobalt permanent magnets, etc. have made significant practical impacts and stimulated much research, but the extent of these are difficult to judge and put into their proper perspective at this time. Hopefully, these four volumes, and any which may follow will make a major contribution to our progress in understanding these exotic and fascinating elements.

In writing these chapters the authors have been asked to use the term "rare earths" to include Sc, Y and the elements La through Lu, and the term "lanthanides" when referring to only the elements La through Lu. The editors have attempted to enforce this usage rigorously when editing the various chapters. Furthermore, we have encouraged the authors to use the SI units as far as practicable to bring the subject matter into accord with current scientific and technical practice.

CONTENTS

VOLUME 1: METALS

PROLOGUE*

F.H. SPEDDING
Ames Laboratory – US DOE and Departments of Chemistry, Physics, and Materials Science and Engineering, Iowa State University, Ames, Iowa 50011, USA

The rare earths are a group of 17 metallic elements which occur in the third column, elements 21, 39, and 57, and elements 58 through 71 which appear in the extended sixth row of the periodic table. They all form trivalent compounds with three electrons in their valency shell, and in the metals most of them have three electrons in their conduction bands. They all exist in dilute aqueous solutions as trivalent positive ions. Since these elements represent about $\frac{1}{6}$ of the total elements in the periodic table and about $\frac{1}{5}$ of the elements that are reasonably available in the earth's crust, they are bound to play an important role in our future technology. Further, in the metallic form, they comprise about $\frac{1}{4}$ of the metals which are sufficiently available to be used in making useful alloys.

The rare earths are not really rare in nature. Cerium is reported to be more abundant in the earth's crust than lead and tin, and even the rarer elements, europium and lutetium are much more abundant than the platinum group elements. Except for scandium, these rare earths have never been found in nature as individual rare earths, but wherever they are found, they occur as mixtures of these elements in some combined form. The relative abundance of the individual rare earths can, however, vary considerably in these mixtures, depending on where they are found. In general, the even atomic numbered elements are from three to ten times as abundant as the odd numbered adjacent elements in the lanthanide series, and in the earth's crust, the light (lower atomic number) lanthanides are more abundant than the heavies.

The first of the rare earths, yttrium, was discovered just before the beginning of the Nineteenth Century (1794) in a rare Swedish ore, and separated in the form of an impure oxide. At that time, the more active metals such as magnesium, calcium, aluminum and barium had been isolated only in their oxide form. These oxides were believed to be elements and were referred to as "common earths". The ancient Greeks taught that all matter was made up of

*This work was supported by the US Department of Energy, Division of Basic Energy Sciences.

four elements: air, earth, fire and water, and the earths were those compounds which could not be split further by the sources of heat then available in the laboratory. Since yttrium oxide, called yttria, resembled the "common earths", it subsequently became known as a "rare earth". Not until 1808 did Sir Humphry Davy demonstrate that the "earths" as a class were not elements themselves, but were compounds of oxygen and metallic elements.

During the next 110 years, all the naturally occurring rare earths were discovered and isolated; however, they proved to be a very difficult group of elements to discover, to isolate, and to obtain their compounds in pure form. Much of the chemistry investigated in the Nineteenth Century was done in aqueous solutions and we now know that the trivalent ions of the rare earths strongly attract the water dipoles around them so as to form a sheath around the rare earth ions. These early chemists were, therefore, working with trivalent ions which were shielded by a water envelope and the properties of the rare earths in solution or in the hydrated crystals were much alike. As a result, the rare earth salts readily formed solid solutions with each other, and when a rare earth was precipitated, the crystals always contained a mixture of rare earths. At best, the rare earth desired was only slightly enriched in a single chemical operation.

The property that one rare earth ion can readily be substituted for another in the lattice of almost any rare earth crystal with very little strain resulted in the development of many fractional separation methods being devised to separate one rare earth from another. A typical process would be to dissolve a large amount of the mixed rare earth oxides using some acid and then to precipitate half of the rare earths present as some salt. The liquid would be separated from the crystals and the crystals redissolved. The operation was then repeated on both fractions, although the amount of rare earth precipitated in each batch would be only one-half of the amount precipitated in the original operation. This process would be repeated many times and the heavy rare earths would concentrate at one end of the series and the light rare earths at the other. All the natural lanthanide elements were discovered and isolated from each other by such methods, although in almost all cases, it required hundreds, or occasionally even thousands of fractionations to obtain an individual rare earth in a highly pure form. This enormous amount of labor could be shortened somewhat by procedures such as combining adjacent inner fractions and treating them as one unit, or by starting simultaneously several large batches of the same mixed oxide. As the fractionation proceeded and the rare earth salts became spread over too many units so as to make the amount of rare earth salt in any one unit rather small, corresponding units from all the simultaneous batches could be combined and the fractionation continued on the combined samples. Often these early rare earth chemists would start the process using one fractionational method and then proceed on various sections of the original series, using a different fractional method, because it would work better on the changed oxide mixtures whose composition would differ greatly from that of the original mixed oxide. However, in spite of these modifications, the amount of "pure" rare earth coming out of each end of the series was usually quite small and in most cases,

rather impure. Due to the enormous amount of labor involved for the rare earth chemist, it was extremely difficult for the average chemist to get any of the heavier rare earths to experiment with, and when available, they were extremely expensive. This resulted in the general impression among chemists that they were rare elements. The separation problem was still further complicated by the fact that the usual analytical methods available for determining the quantity of ordinary elements present in a sample did not work at all well for these rare earth elements. For a large part of this historical period, the various fractions had to be analyzed by atomic weight determinations, although the process could be aided somewhat by observing the color of the precipitants, since a few of the rare earths are colored. By observing color changes along the series as the fractionational process continued, the rate of progress of the method could be estimated.

It was not until 1859 that Bunsen first applied the spectrograph to analytical chemistry determinations, and this development proved useful in the case of the rare earths. The nature of the spectra of the various rare earths was not understood until well into the Twentieth century, so the analytical methods were empirical and not always dependable. The uncertainty was due to the fact that the transition elements also separated along with the rare earths in the fractionation process, and tended to complicate the various spectra obtained. As a result of these complications, the discovery of over 70 new rare earths was reported in the literature. Many of the "new" elements were based on spectra differences in the fractions obtained, and no one knew how many rare earths should exist. It was not until 1869 that Mendeleyev published his first periodic chart. Incidentally, in doing so, he had to leave a blank where scandium now occurs, and he predicted a new element would be found which would have the general properties now attributed to the rare earths. Shortly afterwards (1879) scandium was discovered, and its discovery greatly aided in the general acceptance of Mendeleyev's ideas. While the chart had a place for lanthanum, there was no place in his chart for the other rare earths, since they also seemed to fall in the space reserved for lanthanum. The early chemists seemed to think they were discovering a new type of element with properties very similar to the properties which we now ascribe to isotopes, and some even speculated that these other rare earths were different modifications of lanthanum.

After Moseley published his work relating X-ray spectra to atomic number in 1912, it became known for the first time how many rare earth elements should exist, and it became possible to eliminate many of the elements which had been falsely reported in the literature. The anomaly that 14 elements with properties similar to lanthanum existed, intrigued the theorists, and the existence of these elements proved an important clue in developing our present theories of atomic structure.

In whatever form the lanthanides are found in nature, they always occur as mixtures containing considerable amounts of either lanthanum or yttrium or both. Lanthanum and yttrium from the beginning were always considered by the chemists to be members of the rare earth group, and this classification continues

to this day. However, with the development of the modern theories of atomic structure, the physicists preferred to include only the elements 58 through 71 in this category. When it was discovered that the new synthetic elements in the seventh row of the periodic table also occurred in a region which an inner 5f subshell was filling and that many of these elements resembled rare earths, they also were called rare earths belonging to a second series. However, shortly, many scientists started calling the elements 58 through 71 lanthanides and the elements 90 through 103 actinides. During this period there developed some confusion in the literature as to just what was a rare earth. Fortunately, this matter was somewhat clarified when the International Union for Pure and Applied Chemistry recommended in 1968 that the elements 58 through 71 be referred to as "lanthanides" and that the name rare earth be reserved for the elements scandium, yttrium, lanthanum and the lanthanides.

It is now known that at element 57, a change takes place in the way the electrons are added to the atoms as the atomic number increases. As the charge on the nucleus increases with increasing atomic number, the extra electron which balances this increased positive charge starts entering an inner 4f shell in the atom, leaving the number of valency electrons undisturbed. Since this inner shell is shielded by the completed $5s^2$–$5s^6$ subshells, they play a very little role in determining the chemical properties of the elements, and atomic theory states that this inner shell can hold up to 14 electrons. This gives rise to the 14 elements of atomic number 58 through 71. Also as the positive charge on the nucleus increases with atomic number, the extra charge pulls all the electrons in somewhat. The presence of the balancing 4f electrons greatly influences this contraction because of the way they modify how much positive charge the other electrons, particularly the valency electrons, see. This contraction is known as the lanthanide contraction. In most compounds this contraction permits the neighboring atoms to approach closer to the center of the rare earth ion so that the lattice parameters of the crystal change in a predictable way across the series. The crystal structure of many compounds and alloys remain similar across the series, but the smaller lattice parameters cause their properties to change in a predictable manner. In other cases, at some point in the series, the crystal structure can change abruptly to a different crystal structure possessing different properties. The new structure can continue along the lanthanide series with its decreasing lattice parameters.

Theorists who are relating one property of a substance to another, or who are developing relationships between the properties of a material and its crystal structure and composition find in the properties of the lanthanide elements a powerful tool in their work. By observing how the properties change across the lanthanide series for a given material, they can see whether the relationships they have developed are likely to be real or whether they are essentially curve fitting.

It has been known for some time that the valency electrons are the electrons which are usually easiest to remove from the rare earth ion and which overlap the neighboring atoms in the condensed state. They are, therefore, responsible

for most of the chemical binding and in theory, if one knew the location and magnitude of the electric and magnetic fields which they set up, one could predict most of the properties of the materials. It takes considerably more energy to remove electrons from the inner shells and therefore, they play almost no part in the valency forces. Since the rare earths usually have three electrons in their valency shell, this accounts for all of them exhibiting trivalent behavior. The 4f electrons are electrically well shielded from their neighboring atoms by the completed 5s and 5p subshells so they only slightly influence the valency forces; however, in some of the rare earths, there is not much energy difference in the binding between the 4f and the 5d electrons which act as a valency electron. By changing the environment around a rare earth ion, and therefore the crystal fields which act upon it, it is possible to promote a 4f electron to the valency shell making the rare earth 4-valent, or to demote the 5d valency electron into the 4f shell, thereby making the ion divalent. It was early found that, in aqueous solutions, the 4f electron of cerium, under special conditions could be promoted to give a 4-valent cerium and later, in the case of europium and ytterbium, that a 5d valency electron could be changed to a 4f electron so as to give divalent compounds. It was therefore possible to separate cerium, europium and ytterbium from the other lanthanides by first putting them in their tetra- or divalent state and then removing them with a simple chemical operation. It should also be pointed out that in the fractionation process, if these elements could be removed at some point in the procedure, the process became much more rapid. In media other than water, such as fused salts, or in the solid state, praseodymium and terbium could be made tetravalent while europium, samarium, thulium, neodymium and perhaps others could exist in the divalent form.

The mixed rare earths are found rather widely distributed in nature. They are found in most rocks in concentrations of from $\frac{1}{10}$ to 100 parts per million. When molten acid silicate rocks come in contact with the molten basalt, rare earths are extracted into the silicates at a somewhat higher concentration, and the extraction is a little bit more efficient for lanthanum than lutetium. In recent years, accurate analytical methods have been developed for determining the relative abundance of the rare earths when they are present in such low concentrations. This is done by means of the mass spectrograph and by activation analysis. The rare earths are, therefore, of great interest to the theorists and geochemists, because if these workers can get good analytical results of the relative abundances of these elements across the rare earth series, they can work backwards to see whether the rocks at any time have been above a certain temperature or if they have been molten. Further, information can be obtained as to whether the environment in which the extraction took place was a reducing or oxidizing environment. Since europium can be reduced to the divalent form and therefore separates rapidly from the other rare earths, it will be in low abundance in the series, while if the extraction takes place in an oxidizing atmosphere, cerium will be oxidized to the 4-valent state, and again get depleted from the system. For these reasons, there was great interest in the rare earth content of the moon

rocks. The results showed that the thermal history of these rocks was much more complicated than had been originally believed.

The rare earths can also occur as minerals rich in rare earth content. We find deposits of such minerals as monazite, xenotime, bastnaesite, gadolinite, samarskite and many others, although many of them only occur in small pockets in the massive rocks. These minerals were probably precipitated from either the molten rocks or from superheated brines under pressure. It is known that the molten magma is welling up under the mid-ocean mountain ranges, and comes in contact with sea water at high pressures and temperatures. Brines also come in contact with the hot rocks under pressure deep in volcanos and in the deep ocean trenches where the ocean plates reenter the molten magma. In these areas, the rare earths are extracted from the molten rocks and at other temperatures and pressures are redeposited. While information concerning the properties of these materials under these conditions at present is sketchy, the presence of rare earth minerals can tell us something about the earth's earlier history, although we can already draw some conclusions from the information now available. As we learn more about the phase systems and solubilities of these rare earth compounds under conditions of high temperatures and pressure, much more precise information can be deduced as to previous history of the rock formations in which they occurred.

When organic matter derived from many living specimens is calcined, the ashes contain rare earths at a concentration of a few parts per million. This phenomenon is widespread, but it is not known whether these trace elements play an essential role in the living process. Further research in this area should be interesting.

The nuclear properties of the rare earths are of great interest to nuclear scientists. The even numbered rare earths are rich in stable isotopes, possessing from three to seven each; while the odd numbered rare earths have few: Pm has no stable isotopes, five have 1 isotope and two have 2 isotopes. Radioactive rare earths are formed in fission in considerable abundance, and this is not only true for uranium, but for the heavier actinides in general. They can also be formed by accelerators and by radioactive decay from other radioactive isotopes. The lanthanide elements appear in that part of the periodic table where the number of radioactive isotopes are the most numerous. Already, from 10 to 20 radioactive isotopes for each element have been identified. It is also in this part of the periodic table where the nuclei show anomalies, some of them being quite ellipsoidal. Several of the isotopes belong to the "magic number" group, where all the neutrons are in completed shells. A careful study of the nuclear properties of the rare earths has already played an important role in helping establish the shell model of the nucleus, and I am sure that in the future, as the properties of these isotopes are better known and understood, a great deal more will be learned about nuclei. The relative abundance of the rare earths, elements and isotopes is of great interest to the cosmologists in developing the theories of how the universe, galaxies and stars formed; how the various celestial bodies obtain their energy, and how they decay in cosmic time.

Some of the rare earth nuclei have small capture cross-sections for neutrons, and some have extremely large capture cross-sections. From the practical viewpoint, since the rare earths are formed in fission, such information plays an important role in nuclear energy technology. A knowledge of the cross-section, lifetimes and chemical behavior of the isotopes is extremely important in the design of reactors, control rods, "nuclear poisons" and reactor waste disposal processes.

The preparation of the pure rare earth metals from their salts or oxides also proved to be a very difficult problem. Rare earth molten metals react strongly with the light elements: hydrogen, nitrogen, carbon, oxygen, phosphorus, sulphur and the halides. In fact, in a molten mixture of rare earths and other metals, the rare earths will take these elements away from most of the other metals, and either collect them in the slag or into nodules clustered about the rare earth ions in the metal. Even if the other metal is still solid, the rare earth will remove such impurities from its surface and even to some extent extract them from the solid. The rare earths should never be melted in air or even in a poor vacuum. The molten rare earths will rapidly become a rich rare earth alloy of hydrogen, oxygen, nitrogen and carbon. Many of the properties of the rare earth metal can rapidly shift as the impurity content increases. The problem is further enhanced by the fact that these impurities have the values of the low atomic weights, so that there is a considerable difference between impurity concentrations as expressed in atomic per cent and in weight per cent. The worst case would be hydrogen in lutetium metal, where the ratio of their weights is 1:175, thus for each 1 ppm H by weight in Lu, the atomic concentration is 175 ppm H. The rare earths also readily alloy with most of the other metals of the periodic table, and as is well known, such alloys can have properties different from that of either one of the pure metals. In fact, in the author's opinion, the molten rare earths come as close to being the universal solvent which the ancient alchemists sought so diligently as is likely to be found. These properties make it extremely difficult to find crucibles in which to melt the metal, and the early crucibles available were particularly bad for this purpose.

The second difficulty was that it was difficult to obtain pure metal reductants, so that as the metal was reduced with potassium or calcium, all the impurities in these materials would end up in the rare earth metal, and finally it was difficult to get pure rare earth salts. The laborious process needed to isolate these elements meant that except for cerium and lanthanum, usually only small samples could be obtained. They were almost certain to contain several rare earths. As a result of these difficulties, most of the metal made in the earlier years was extremely impure and many of the properties reported for a particular rare earth were likely to be in error.

Well over 100 years ago, Mosander produced the first rare earth metal. It was extremely impure and certainly contained several rare earths and considerable quantities of carbon and oxygen. Prior to World War II, the apparatus available for making rare earth metals was inadequate for such studies. Good crucibles were not available. High temperature sources and good high vacuum equipment

were not available in most laboratories, and frequently the materials used in the reduction were very impure, particularly with regard to the light elements. This situation was marked in the early years of rare earth development, and even in the first half of the Twentieth Century, when many of these difficulties had been minimized, those materials that were produced were much less pure than they were thought to be at the time. Except for cerium and lanthanum, due to the above difficulties, only small amounts of rare earth metals were made and they were expensive. Only a few properties were determined and almost no work was done with regard to alloys. It was not until the 1950's after the band displacement method of ion exchange, which was capable of producing extremely pure individual rare earths had been developed at Iowa State College that widespread intensive research on the individual rare earths got under way. Industry adopted these methods and started producing them in any quantity desired at reasonable prices. Later, as the industrial demand for certain rare earths became important, liquid-liquid extraction methods were developed which were even less expensive for example, for obtaining yttrium and europium. Also, during the 1950's, processes for producing pure rare earth metals were developed after sheet tantalum and tungsten became readily available commercially, as did ultra-high vacuum equipment. As the pure rare earth metals were produced and their properties explored, considerable research on the rare earth alloys commenced in many laboratories, so that today, there is a rather extensive literature on the properties of many of these alloys, as is evident in many chapters of this volume. In spite of this effort, the author feels that the field has barely been scratched, and that an enormous amount of work still remains to be done.

The history of the mixed rare earths is another story. Towards the end of the Nineteenth Century, industrial uses began to appear for these mixtures. During this period, Carl Auer invented the Welsbach gas mantle and the lighter flint. A sizable industry developed for producing these materials and considerable amounts of mixed rare earths were needed in their manufacture. While it is relatively easy to separate the mixed rare earths from their minerals, prior to this time, most of these mixtures had been obtained from rare minerals. With the development of the industry, cheaper sources were sought. It was found that certain minerals such as monazite occurred concentrated in the earth's crust in considerable quantities and scientists became aware that the rare earths were not really rare. Carl Auer, for his scientific achievements and his development of the sizable rare earth industry, was made a Count by the Austrian Emperor, and since that time he is now better known as Count Carl Auer von Welsbach. This industry has continued to grow to this day, and many other uses for the mixed rare earths and for the easily separated cerium and lanthanum were found. These mixed rare earths were found to be excellent catalysts for certain organic reactions and considerable quantities of them are used by the petroleum industry in the cracking of petroleum. They are also used as catalysts in other organic reactions but it is difficult to estimate to what extent they are used, since many industries impose proprietary secrecy on their use and do not publish figures. However, the author believes that this is a very important field, and that as more

research is done on varying the composition of the mixtures and on the effect of individual rare earths on various organic reactions, a considerably greater market should develop for these elements.

Lanthanum oxide has a very high refractive index, and it has found considerable use in the glass industry for optical equipment. Lanthanum, cerium and didymium (a mixture of praseodymium and neodymium) have found applications in the glass and ceramic industry for decolorizing glasses, getting rid of glare, and for ceramic coatings. Cerium oxide proved to be a better polishing powder than rouge in polishing glass.

Extremely intense white light can be obtained by coring carbon arcs with mixed rare earths. Such arcs have been widely used in the movie industry and in searchlights.

When the mixed rare earths as they are extracted from the various ores are reduced to the metal, the alloy produced is known as misch metal. This alloy, as well as metallic cerium, have found wide applications in the metallurgical industries. They are used as "getters" to remove or localize impurities in other metals, e.g., steel and ductile iron. They are also used in the manufacture of "flints" in cigarette lighters and have found use as pyrophoric materials in many military applications. This, of course, is only a partial list of the applications which have been found for the mixed rare earths, but the total sales of these materials account for about one-half of the dollar value and more than 90% of the tonnage volume of the rare earths consumed in the world.

While the 4f electrons play only a minor role in the valency forces which determine the chemical properties of the rare earths, they can play a major role in certain physical properties. As the electrons enter the 4f shell, their orbital angular momentum and their spin momentum are not balanced, so that most of the lanthanide elements are strongly paramagnetic and in the case of the metals and certain solid compounds as their temperature is lowered, they can become antiferromagnetic with various spin arrangements, ferrimagnetic, and in some cases, even strongly ferromagnetic. Some of them have ferromagnetism stronger than the iron group elements. It has been found that some alloys, particularly the Co_5Sm alloy, form stronger and longer-lasting permanent magnets than the common ones now in use and an appreciable market is now developing for these materials.

In recent years, there has been a large amount of research carried out on the magnetic properties of the rare earth metals, alloys, and solid compounds. The great sensitivity of these properties to changes in temperature and pressure as well as presence of impurities, makes such data of great value to the theorists. Already, they have played an important role in developing our present understanding of magnetism and as more data is accumulated, I am sure that it will continue to help guide the improvements which the theorists will make in this area.

The presence of these unbalanced electrons result in the rare earth materials possessing extremely complex spectra. The unbalanced angular momentum of the inner 4f shell can combine in many ways with the unbalanced moments of

the valency shell or conduction bands, and this gives rise to many metastable states, particularly in the condensed state of matter, where the energy levels of the rare earths are subject to the crystal fields of the surrounding atoms. As the temperature is raised or the pressure increased, many of these low-lying levels can be populated or have their population changed. Each state results in the rare earth material having different magnetic properties and if the material is made up of a mixture of a given rare earth ion existing in these various states, the magnetic properties of the material will be a weighted average of the relative population and magnetic property of the various occupied states in the material. Such behavior accounts for the sensitivity of the rare earths to temperature and pressure.

The spectra of the rare earths are now beginning to be understood theoretically, and the richness of the possible excited states make these materials a rich source for laser materials, fluorescent screens such as television screens, intense sources of light such as street lights, and perhaps in the future even to the invention of intense panel lighting, where an entire wall will fluoresce brilliantly in any shade desired by the application of an electric potential.

While the properties of the aqueous solutions and the hydrate crystals change only slowly as one progresses across the lanthanide series, as the water envelope surrounding the rare earth ions is removed, the difference in properties between adjacent elements become much more marked. If the rare earth ions are complexed with organic molecules which replace some of the water molecules, such as chelates, (organic molecules which wrap themselves around the rare earth ion), the difference between the properties of adjacent elements becomes much more marked. Advantage of these phenomena has been utilized in developing the ion exchange and liquid-liquid extraction methods for separating the rare earths in high purity. If the water envelope is completely removed, as in anhydrous salts, the difference in properties becomes still more marked and finally in the metals and alloys, the difference in properties can be quite appreciable. While the difference in properties between adjacent rare earth metals may not be too great, the difference in properties across the series from lanthanum to lutetium is as great as for many of the other series which occur in the periodic table, such as copper, silver and gold; sodium, potassium, rubidium and cesium; calcium, strontium and barium; and iron, cobalt and nickel. For example, the melting point of lutetium is almost twice that of lanthanum. Even for the small changes in properties across the series, exhibited by the aqueous solutions, these small differences can play an important role in scientists getting a better understanding of electrolytic solutions, since all the rare earth salts are strong electrolytes.

Good, precise data on the thermodynamic and other properties of such solutions can give the theorists material for understanding the nature of electrolytes and this is extremely important, since the ocean is an electrolyte and electrolytes play a very important role in most life processes. To sum up, the properties of the various rare earth metals, alloys and compounds can vary widely so that it is possible to pick one of these materials which possesses almost

any property one desires. The rare earths should, therefore, play an ever increasing role in finding substitutes for scarce materials. While the properties of the rare earth material which could be used in such substitutions will not be exactly the same as those of the scarce material, it will possess the properties which that material possessed that made it important in its industrial applications. Unfortunately, while it is possible to find a rare earth material which will perform equally as well as many of the more common materials in some applications, they are seldom used for this purpose, because the common materials are much cheaper. But, as some materials become scarce and more expensive, then the rare earths will be more widely used. Their uses will also increase as the rare earths become cheaper. This can be brought about as quantity uses for several of the rare earths can be found, since the additional operations of getting three or four of the rare earths is not much more complicated than getting the one now desired, and which at the present time has to bear the entire cost. At the present time, if a rare earth material is to be used, it must possess some unique properties which are much better than those of the more common materials. Unfortunately from the commercial viewpoint, many of these uses require only very small amounts of the rare earths to bring about the desired results. Nevertheless, I am confident that as time goes on, the specific uses of the individual rare earths will steadily increase and the industry will continue to grow both in volume and total dollar sales.

Handbook on the Physics and Chemistry of Rare Earths, edited by K.A. Gschneidner, Jr. and L. Eyring

Chapter 1

ATOMIC PROPERTIES (FREE ATOM)

Zipora B. GOLDSCHMIDT
Racah Institute of Physics, The Hebrew University of Jerusalem, Jerusalem, Israel

Contents

Symbols

A_d = energies of 5d electrons in the field of the nucleus and of the closed inner shells
A_f = energies of 4f electrons in the field of the nucleus and of the closer inner shells
A, B, C = Racah parameters for d^N configurations
$C^{(k)}$ = spherical harmonic tensor operator
CI = configuration interaction
E, E^0, E_{nl} = energy eigenvalues
E^i = Racah parameters for f^N configurations
$-e$ = electronic charge
f, F = single-electron operators
F^k, F_k = "direct" Slater parameters
g, G = two-electron operators
G^k, G_k = "exchange" Slater parameters
G_2 = one of the special Cartan's groups
$\hbar$ = Planck's constant $/2\pi$
H, H_0 = hamiltonian
H_1 = electrostatic interaction
H_2 = spin–orbit interaction
H_{ss} = spin–spin interaction
H_{soo} = spin–other-orbit interaction
H_A = effective electrostatic interaction
$H_B, H_{EL\text{-}SO}$ = effective electrostatic–spin–orbit interaction
HF = Hartree–Fock
j, J = total angular momenta
l, L = orbital angular momenta
m = electronic mass
$M_l, M_L, m_s, M_S, m_j, M_J$ = magnetic quantum numbers
$M^k, N^k, K^{k\pm}$ = mutual magnetic interaction parameters
n = principal quantum number
p = electronic linear momentum
$P_k(\cos \omega_{ij})$ = Legendre polynomial
q, Q = seniority operator
Q = quadrupole interaction
Q^k = effective EL–SO parameters for f^N configurations
r = vector pointing from nucleus to electron
$r = |r|$
r_{ij} = distance between electrons i and j
$R^k, H, J, K, L_2, L_4,$
$M, N, P_2, R_1, R_2,$
R_3, R_4, T_1, T_2, T_3 = configuration interaction parameters
R_n = rotation group in n dimensions
R_{nl}/r = radial factor of the energy eigenfunction
s, S = spin angular momenta
S^k, T^k = effective EL–SO parameters for 4f–5d electrons
SCF = self-consistent field
SDI = spin-dependent interactions
ss = spin–spin

soo = spin–other-orbit
T^i = three-electron effective electrostatic parameters
$t^{(11)k}$, $T^{(11)k}$ = coupled tensor operators
$U \equiv (u_1, u_2)$ = set of integers characterizing the irreducible representations of G_2
$u^{(k)}$, $U^{(k)}$ = unit tensor operators
$U(r_i)$ = central field potential
$v^{(\kappa k)}$, $V^{(\kappa k)}$ = double tensor operators
v = seniority quantum number
$W \equiv (w_1, w_2, w_3)$ = set of integers characterizing the irreducible representations of the rotation group in seven dimensions R_7
W_m = electrostatic energy for terms of maximum multiplicity
Y_{lm_l} = spherical harmonics
Z = atomic number
α, β = spin factors of the energy eigenfunctions
α, β, γ = two-electron effective electrostatic parameters for f^N configurations
β = Bohr magneton
Δ = mean error
Ψ, ψ = energy eigenfunctions
$\xi(r_i)$ = radial part of the operator representing the spin–orbit interaction
ω_{ij} = angle between r_i and r_j
$\zeta_{nl}, \zeta_{nl,n'l'}$ = spin–orbit parameters

Introduction

The analysis of rare earth spectra, especially those of the very complex lanthanides, started in the early fifties, with the publication of the four papers by Racah (1942–1949), entitled "Theory of Complex Spectra". In these papers Racah developed a powerful and elegant technique for calculating the energy levels of configurations comprising two or more electrons by defining the concepts of tensor operators, recoupling coefficients, seniority and coefficients of fractional parentage. This technique has since become the basis for all modern energy level calculations. In particular, in his fourth paper, Racah applied the theory of continuous groups to the problem of characterizing the states of f^N configurations and calculating their energy levels.

The interpretation of the lanthanide spectra was further enhanced through the simultaneous developments of new experimental methods and instrumentation on the one hand, and the introduction of electronic computers for the performance of complex calculations, on the other hand.

As far as the energy-level calculations are concerned, it has been concluded, already in the first stages of the calculations, that electrostatic interaction between neighbouring configurations, as well as effective electrostatic interactions (which represent, to second order of perturbation theory, interactions with distant configurations) should be taken into account in order to obtain reliable and meaningful results. Since very little was known at that time concerning the strengths of the various interactions, especially of those between

configurations, the "comparison method" has been developed and used. According to this method, the interpretation of several neighbouring spectra, both along an isoionic sequence and of different degrees of ionization of the same element, is carried out simultaneously, and the values of the parameters representing the same interactions in the various spectra are continuously compared. Simple spectra, especially two-electron ones, at both ends of the lanthanide group, are especially suitable for such a comparison.

The following results were obtained:

(a) In most investigated spectra, good agreement between theory and experiment was obtained, concerning both the energy levels and their g-factors.

(b) Reliable and consistent values were obtained for the parameters representing the various interactions within and between configurations.

(c) A complete understanding of the effects of the separate interactions on the energy level structure was achieved.

(d) The stage has been reached where it is possible to make detailed predictions about the structure of these spectra, even in those cases where the experimental material is scant.

In recent calculations, the agreement between theory and experiment was further improved by including in the calculations additional interactions, namely, the spin-dependent spin–spin, spin–other-orbit and effective electrostatic–spin–orbit (effective EL–SO) interactions.

This chapter comprises two parts. In part 1 the theoretical methods for the energy-level calculations are discussed. Part 2 deals with the energy-level structure of the lanthanide spectra, as affected by their electronic properties and the strengths of the various interactions. The results and conclusions are obtained mainly through the use of the semiempirical method; results of ab initio calculations are sometimes given for comparison.

PART 1. THE THEORY OF COMPLEX SPECTRA – ASSUMPTIONS AND APPROXIMATIONS

1. The central field approximation (Slater, 1929; Condon et al., 1951)

Energy level calculations of atomic systems are based on the Schrödinger equation

$$H\psi = E\psi. \tag{1.1}$$

At the outset the investigated atom or ion is regarded as made up of a point nucleus of infinite mass and charge Ze, surrounded by N electrons, each of mass m and charge $-e$. The nonrelativistic Hamiltonian of such a system is

$$H = \sum_{i=1}^{N} p_i^2/2m - \sum_{i=1}^{N} Ze^2/r_i + \sum_{i>j=1}^{N} e^2/r_{ij}, \tag{1.2a}$$

where $p_i^2/2m$ is the kinetic energy of the electron i, Ze^2/r_i its potential energy in

the field produced by the nucleus, and e^2/r_{ij} is the electrostatic interaction between the electrons i and j.

A better description of the energy level structure of the atomic system is obtained, by adding to (1.2a) terms of relativistic origin, which represent the magnetic interactions of the electronic orbits and spins. Among these, the spin–orbit interaction described by a term of the form (Condon et al., 1951)

$$\sum_i \xi(r_i)\boldsymbol{l}_i \cdot \boldsymbol{s}_i \tag{1.3}$$

is by far the dominant one. The approximate Hamiltonian, capable of reproducing with reasonable precision, the various features connected with the energy-level structure, is thus given by the following formula

$$H = \sum_{i=1}^{N} [p_i^2/2m - Ze^2/r_i + \xi(r_i)\boldsymbol{l}_i \cdot \boldsymbol{s}_i] + \sum_{i>j=1}^{N} e^2/r_{ij}. \tag{1.2b}$$

A more adequate description is obtained by including additional terms in the Hamiltonian, as will be discussed below.

Exact solutions of Schrödinger's equation are impossible for atoms containing more than one electron. The most common approximation used for solving Schrödinger's equation for complex atoms is "the central field approximation". In this approximation, each electron is considered to move in the field of the nucleus and a mean central field due to the charge distribution of the other electrons. If electron i moves in the spherically symmetric potential $-U(r_i)/e$, the Hamiltonian H_0 for the central field approximation will be

$$H_0 = \sum_{i=1}^{N} [p_i^2/2m + U(r_i)]. \tag{1.4}$$

The difference $V = H - H_0$ may now be treated as a perturbation potential. Schrödinger's equation

$$\sum_{i=1}^{N} [(-\hbar^2/2m)\nabla_i^2 + U(r_i)]\boldsymbol{\psi} = E^0\boldsymbol{\psi} \tag{1.5}$$

for the central field approximation, can be separated by choosing a solution such that

$$\boldsymbol{\psi} = \prod_{i=1}^{N} \psi_i(k_i) \qquad \text{and} \qquad E^0 = \sum_{i=1}^{N} E_i^0(k_i). \tag{1.6}$$

The equation satisfied by each $\psi(k)$ is

$$[(-\hbar^2/2m)\nabla^2 + U(r)]\psi(k) = E^0(k)\psi(k), \tag{1.7}$$

where k represents the set of quantum numbers (nlm_l). Physically this means that in the central field approximation each electron moves in the central field $U(r)$ exactly as it would move if the other electrons were absent. The normalized solutions of (1.7) for bound states may be written as

$$\psi(k) = r^{-1}R_{nl}(r)Y_{lm_l}(\theta, \phi), \tag{1.8}$$

where Y_{lm_l} are the spherical harmonics defined by Condon et al. (1951). The radial function $R_{nl}(r)$ depends on the central potential $U(r)$ and, as in the case of the hydrogen atom, its number of nodes (not including the origin) is $n - l - 1$. In the general central potential $U(r)$, the allowed energy values $E^0(k)$ are degenerate only with respect to m_l but not with respect to l. The degeneracy of the energy eigenvalues with respect to l is a property of the coulomb potential energy e^2/r and is therefore a characteristic property of the hydrogen atom only.

The spin of the electron is taken into account by multiplying $\psi(k)$ by α or β according to the two possible spin orientations $m_s = \pm\frac{1}{2}$ along the z axis. Although the substitution

$$\boldsymbol{\psi} = \psi_1(k_1)\psi_2(k_2)\ldots\psi_N(k_N)$$

has been made, it is clear that any permutation of the N electron indices with respect to the N sets of quantum numbers also leads to a solution of Schrödinger's equation belonging to the same eigenvalue E^0. Each of the $N!$ Ψ-functions thus obtained should be multiplied by N spin functions, one for each electron. Of all possible linear combinations of the resulting functions, only those which are totally antisymmetric with respect to a simultaneous permutation of the spin and spatial coordinates of any pair of electrons can serve as eigenfunctions for an atomic system. This is the mathematical formulation of the Pauli exclusion principle. The normalized antisymmetric functions of an N electron system can, therefore, be written as "determinantal product states"

$$\boldsymbol{\psi}(K_1K_2\ldots K_N) = \frac{1}{\sqrt{N!}}\begin{vmatrix} \psi_1(K_1)\psi_2(K_1)\ldots\psi_N(K_1) \\ \vdots \\ \psi_1(K_N)\psi_2(K_N)\ldots\psi_N(K_N) \end{vmatrix}, \tag{1.9}$$

where $K = (nlm_sm_l)$. These functions are known as zero-order wave functions. Since the eigenvalues $E^0(K)$ are degenerate with respect to m_s and m_l, the eigenvalues E^0 in the central field approximation are characterized by the symbols

$$(n_1l_1)(n_2l_2)\ldots(n_Nl_N).$$

This sequence of quantum numbers specifies the *electronic configuration* of the system. The energy levels E^0 themselves are called *configurations.*

2. Electrostatic and spin–orbit interactions as first-order perturbations

Once the zero-order wave functions are known, they can be used for calculating the first-order corrections to the energies due to the perturbation potential

$$V = H - H_0 = \sum_{i=1}^{N}[-Ze^2/r_i - U(r_i)] + \sum_{i>j=1}^{N} e^2/r_{ij} + \sum_{i=1}^{N}\xi(r_i)\boldsymbol{l}_i\cdot\boldsymbol{s}_i. \tag{1.10}$$

The first term on the right is purely radial and causes only a displacement of each configuration as a whole. Each of the two other terms, namely the

electrostatic interaction $H_1 = \Sigma_{i>j} e^2/r_{ij}$ and the spin–orbit interaction $H_2 = \Sigma_i \xi(r_i)\boldsymbol{l}_i \cdot \boldsymbol{s}_i$, is different for different states of the same configuration, thus serving to partly remove the degeneracies of the configurations; that is, under the influence of these two interactions each configuration splits into *levels*. In the first order of perturbation theory each configuration is treated separately, assuming that the distances between the configurations are much greater than the splittings caused by $H_1 + H_2$. Therefore, only $H_1 + H_2$ will be considered as the perturbation potential.

The first-order energy corrections E^1 are obtained by first calculating the matrix elements

$$(\Gamma|H_1 + H_2|\Gamma') = \int \psi^*(\Gamma)(H_1 + H_2)\psi(\Gamma')\,d\tau \tag{1.11}$$

where $\Gamma \equiv (K_1 K_2 \ldots K_N)$ and $\Psi(\Gamma)$, $\psi(\Gamma')$ run over all determinantal product states belonging to the same configuration, and then solving the secular equation

$$\det|(\Gamma|H_1 + H_2|\Gamma') - E^1\delta_{\Gamma\Gamma'}| = 0. \tag{1.12}$$

The methods for calculating integrals of the type (1.11) are described by Condon et al. (1951), both for H_2 which is a single-electron operator of the form $F = \Sigma_{i=1}^N f(i)$ and for H_1 which is a two-electron operator of the form $G = \Sigma_{i>j=1}^N g(i, j)$. The results are summarized below:

(1) The matrix element $(\Gamma|F|\Gamma')$

(a) vanishes if $\Gamma'(\equiv K_1' \ldots K_N')$ differs from $\Gamma(\equiv K_1 \ldots K_N)$ by more than one individual set of quantum numbers;

(b) has the value

$$(\Gamma|F|\Gamma') = \pm(K_t|f|K_t') \tag{1.13}$$

if all sets in Γ agree with all those in Γ' except that $K_t \neq K_t'$. The sign is positive or negative according to the parity of the permutation which changes the conventional order of Γ' so as to match each of its $(N-1)$ remaining sets with the identical set in Γ.

(c) if $\Gamma' = \Gamma$

$$(\Gamma|F|\Gamma) = \sum_{i=1}^{N} (K_i|f|K_i). \tag{1.14}$$

(d) For the spin–orbit interaction

$$f \equiv \xi(r)\boldsymbol{l} \cdot \boldsymbol{s},$$

on calculating the matrix elements $(K_t|f|K_t')$ or $(K_i|f|K_i)$, the integrations over the radial and angular variables may be separated. The integration over the radial variables results in the factor

$$\zeta_{nl,n'l'} = \int_0^\infty R_{nl}(r)\xi(r)R_{n'l'}(r)\,dr \tag{1.15a}$$

for case (b) or

$$\zeta_{nl} = \int_0^\infty R_{nl}^2(r)\xi(r)\,dr \tag{1.15b}$$

for case (c).

ζ_{nl} is known as the spin–orbit parameter of the electron *nl*. The spin–orbit interaction of each electron can thus be written in the form

$$\zeta_{nl}\boldsymbol{l}\cdot\boldsymbol{s}; \tag{1.16}$$

it is considered as an interaction between the electron's spin and orbital angular momenta and is represented by the parameter ζ_{nl}.

(2) The matrix element $(\Gamma|G|\Gamma')$

(a) vanishes if Γ' differs from Γ by more than two individual sets of quantum numbers.

(b) has the value

$$(\Gamma|G|\Gamma') = \pm[(K_rK_t|g|K_r'K_t') - (K_rK_t|g|K_t'K_r')] \tag{1.17}$$

if all sets in Γ reappear in Γ' with the exception of $K_r \neq K_r'$ and $K_t \neq K_t'$; the $\pm$ sign is determined by the parity of the permutation required to match the remaining $(N-2)$ sets of Γ' with the identical ones in Γ.

(c)

$$(\Gamma|G|\Gamma') = \pm \sum_{K_t} [(K_rK_t|g|K_r'K_t) - (K_rK_t|g|K_tK_r')] \tag{1.18}$$

if Γ' differs from Γ by but one set $K_r \neq K_r'$; K_t runs over the $(N-1)$ individual sets that are common to Γ and Γ'.

(d) if $\Gamma = \Gamma'$

$$(\Gamma|G|\Gamma) = \sum_{r>t=1}^{N} [(K_rK_t|g|K_rK_t) - (K_rK_t|g|K_tK_r)]; \tag{1.19}$$

in (1.19) the matrix elements with positive sign are called *direct matrix elements* and those with negative sign *exchange matrix elements*. Thus the electrostatic interaction breaks up into a *direct part* and an *exchange part*. The direct part describes, classically speaking, the Coulomb interaction between the charge distributions of the electron pairs involved, whereas the exchange part has no classical analog.

(e) if $g(i,j)$ is independent of the spin, a property held by the electrostatic interaction H_1, then the sum over the spin coordinates implied by the $(\ |\ |\ )$ sign in (1.19), gives a factor unity for the direct matrix element and a factor $\delta(m_s^r, m_s^t)$ in the exchange matrix element, so that the exchange matrix elements are different from zero only for electrons of like spins. *Thus the "exchange interaction" depends on the relative orientation of the spins of the interacting electrons. It is, therefore, considered as an interaction between the spins of the electrons.*

(f) it can be shown that both the direct and exchange parts of the electrostatic interaction may be considered as interactions between the orbital angular

momenta $\boldsymbol{l}_i$ and $\boldsymbol{l}_j$ of the electrons. To this end, e^2/r_{ij} is separated into a sum of products of a radial factor and an angular factor, expanding it in a series of Legendre polynomials of the angle ω_{ij} between the vectors $\boldsymbol{r}_i$ and $\boldsymbol{r}_j$ pointing from the nucleus to the electrons i and j:

$$e^2/r_{ij} = e^2 \sum_k (r_<^k/r_>^{k+1}) P_k(\cos \omega_{ij}) \tag{1.20}$$

where $r_<$ and $r_>$ are respectively the smaller and the larger of the magnitudes of $\boldsymbol{r}_i$ and $\boldsymbol{r}_j$. Each Legendre polynomial P_k in this expansion can be expressed as a scalar product $\boldsymbol{C}^{(k)}(i) \cdot \boldsymbol{C}^{(k)}(j)$ of spherical harmonic tensor operators of degree k (Racah, 1942b), the matrix elements of which depend on the relative orientation of the orbital angular momenta of the interacting electrons. Thus

$$e^2/r_{ij} = e^2 \sum_k (r_<^k/r_>^{k+1})(\boldsymbol{C}^{(k)}(i) \cdot \boldsymbol{C}^{(k)}(j)). \tag{1.21}$$

On inserting this expression in (1.19), integrating over the radial variables, and remembering that the exchange interaction was already found to depend also on the relative orientation of the spins, the following result is obtained:

$$H_1(\text{direct}) = \sum_{\substack{\text{all} \\ \text{electron} \\ \text{pairs}}} \sum_k a_k(\boldsymbol{l}_a \cdot \boldsymbol{l}_b) F^k(n_a l_a, n_b l_b), \tag{1.22}$$

$$H_1(\text{exchange}) = \sum_{\substack{\text{all} \\ \text{electron} \\ \text{pairs}}} \sum_k b_k(\boldsymbol{s}_a \cdot \boldsymbol{s}_b, \boldsymbol{l}_a \cdot \boldsymbol{l}_b) G^k(n_a l_a, n_b l_b), \tag{1.23}$$

where

$$F^k(n_a l_a, n_b l_b) = R^k(n_a l_a n_b l_b, n_a l_a n_b l_b) \tag{1.24}$$

$$G^k(n_a l_a, n_b l_b) = R^k(n_a l_a n_b l_b, n_b l_b n_a l_a) \tag{1.25}$$

and

$$R^k(n_a l_a n_b l_b, n_c l_c n_d l_d) = e^2 \times \int_0^\infty \int_0^\infty (r_<^k/r_>^{k+1}) R_{n_a l_a}(r_1) R_{n_b l_b}(r_2) R_{n_c l_c}(r_1) R_{n_d l_d}(r_2)\, \mathrm{d}r_1\, \mathrm{d}r_2, \tag{1.26}$$

F^k, G^k and R^k are known as the "Slater integrals" or "Slater parameters".

The properties of the electrostatic interaction specified in paragraphs (e) and (f) above and given in formulae (1.22) through (1.26) can be summarized as follows: *the direct and exchange parts of the electrostatic interaction within a configuration are respectively represented by the Slater integrals F^k and G^k. The direct interaction is considered as an interaction between the orbital angular momenta of the electrons, whereas the exchange part is considered as an interaction both between the orbital and the spin angular momenta of the electrons.*

3. Classification of the states. Couplings

The procedure for finding the first-order energy corrections, through the use of formulae (1.11), (1.12) etc., can be greatly simplified by finding in advance linear combinations $\Psi(\Delta)$ of the determinantal product states, such that

$$(\Delta|H_1 + H_2|\Delta') = 0 \tag{1.27}$$

where Δ and Δ' characterize eigenstates of the same configuration and $\Delta \neq \Delta'$. Under these conditions, the energy corrections to first order are given by

$$E^1 = (\Delta|H_1 + H_2|\Delta). \tag{1.28}$$

The problem is, therefore, to find the functions $\Psi(\Delta)$ fulfilling the condition (1.27), namely, functions for which the energy matrix is diagonal.

Only in very simple cases can such functions be found in advance. However, in many cases it is relatively easy to find functions for which the energy matrices are "almost" diagonal, that is, they are split into submatrices whose orders are relatively small. These functions are eigenfunctions of the various angular momentum operators characterizing the investigated atomic system, as will be discussed in the following subsections.

3.1. *Two-electron configurations (outside closed shells)*

In treating two-electron configurations, four angular momenta are involved: these are the spins $\boldsymbol{s}_1$ and $\boldsymbol{s}_2$ and the orbits $\boldsymbol{l}_1$ and $\boldsymbol{l}_2$ of the two electrons. In order to establish the two-electron functions for which the energy matrices are as diagonal as possible, four cases should be considered.

3.1.1. $H_1 \gg H_2$ – *Russell–Saunders (LS) coupling*

In this case only H_1 is taken into account in first-order perturbation theory. H_1 commutes with $\boldsymbol{S}$ and $\boldsymbol{L}$ where

$$\boldsymbol{S} = \boldsymbol{s}_1 + \boldsymbol{s}_2, \qquad \boldsymbol{L} = \boldsymbol{l}_1 + \boldsymbol{l}_2.$$

Therefore its matrices are diagonal with respect to S, L, M_S, M_L and are independent of M_S and M_L. Consequently, in this case, functions $\Psi(\Delta)$ fulfilling the condition (1.27) exist, with $\Delta = (n_1 l_1 n_2 l_2 S L M_S M_L)$. These functions, which have the form $|n_1 l_1 n_2 l_2 S L M_S M_L)$ or $|(s_1, s_2)S, (n_1 l_1, n_2 l_2)L, M_S, M_L)$ in Dirac's notation, are simultaneous eigenfunctions of the five operators S^2, L^2, S_z, L_z and H_1. The first-order energy corrections in LS coupling are therefore given by the eigenvalues of H_1, namely by

$$E^1_{LS} = (\Delta|H_1|\Delta). \tag{1.29}$$

These are characterized by the quantum numbers γSL (where γ stands for the configuration quantum numbers), and since they are independent of M_S and M_L they are $(2S+1)(2L+1)$-fold degenerate. The set of $(2S+1)(2L+1)$ states

$|\gamma SLM_S M_L)$ belonging to the eigenvalue γSL is called a *term*. The last results can be summarized as follows: *in LS coupling, under the influence of the electrostatic interaction, each configuration splits into terms.* Table 1.1 comprises the lists of terms for the various two-electron configurations characteristic of rare earth spectra.

H_1 commutes also with the total angular momentum $\boldsymbol{J} = \boldsymbol{S} + \boldsymbol{L}$. Consequently its matrices are diagonal with respect to J and M_J and independent of M_J. Since the states $|\gamma SLJM_J)$ are linear combinations of $|\gamma SLM_S M_L)$ with the same γSL, and since in the scheme $\gamma SLM_S M_L$ the energy is independent of M_S and M_L, it follows that in the scheme $\gamma SLJM$ the energy is also independent of J. There exist, therefore, two complete systems of functions in which H_1 is diagonal and has eigenvalues characterized by γSL. These systems are respectively described by the $\gamma SLM_S M_L$ and $\gamma SLJM$ sets of quantum numbers. Any function belonging to one of these systems is a simultaneous eigenfunction of S^2 and L^2. A complete system of functions, each of which is a simultaneous eigenfunction of S^2 and L^2 is referred to as an *LS-coupling scheme.*

If the spin–orbit interaction is also allowed for, the scheme $SLJM_J$ is preferable to the scheme $SLM_S M_L$. This is so because H_2 commutes with $\boldsymbol{J} = \boldsymbol{S} + \boldsymbol{L}$, but not with $\boldsymbol{S}$ or with $\boldsymbol{L}$ separately. Consequently the matrices of H_2 are diagonal with respect to J and M_J and independent of M_J. This means that J and M_J remain rigorous quantum numbers even when the spin–orbit interaction is included in the calculations; this is not true for S and L.

In LS coupling $H_2 \ll H_1$; therefore H_2 affects the energy levels only in second-order perturbation theory. The energy corrections E^2_{LS} due to the spin–orbit interaction are given, in this approximation, by the diagonal matrix ele-

TABLE 1.1.
Russell–Saunders terms for two-electron configurations.

Configuration	Terms: $S = 0, 1; \lvert l_1 - l_2 \rvert \leq L \leq l_1 + l_2$ For equivalent electrons: also $S + L$ even							
s^2	^1S							
sp		$^{1,3}P$						
ds			$^{1,3}D$					
fs				$^{1,3}F$				
pp′	$^{1,3}S$	P	D					
p^2	^1S	^3P	^1D					
dp		$^{1,3}P$	D	F				
fp			$^{1,3}D$	F	G			
dd′	$^{1,3}S$	P	D	F	G			
d^2	^1S	^3P	^1D	^3F	^1G			
fd		$^{1,3}P$	D	F	G	H		
ff′	$^{1,3}S$	P	D	F	G	H	I	
f^2	^1S	^3P	^1D	^3F	^1G	^3H	^1I	
fg		$^{1,3}P$	D	F	G	H	I	K

ments of H_2 in the scheme $\gamma SLJM_J$

$$E^2_{LS} = (\gamma SLJM|H_2|\gamma SLJM). \tag{1.30}$$

In this manner, a given term γSL is split by the spin–orbit interaction into a close group of *levels*, still characterized by S and L, to a good approximation, and distinguished by different values of J. For each individual level the standard notation $^{2S+1}L_J$ is used. The group as a whole is called a *multiplet*. The removal of the degeneracy of the terms due to H_2 is generally not complete: each level is still $(2J + 1)$-fold degenerate. This degeneracy is a result of the spherical symmetry of the hamiltonian (1.2b) and its removal is possible only by adding perturbations possessing lower symmetry, such as an external magnetic field.

Whenever H_2 is small enough relative to H_1 so that its matrix elements non-diagonal with respect to S and L are negligible, it is said that there exists an *LS coupling* in the investigated configuration. *The term LS coupling means that the energy levels are characterized by the quantum numbers γSLJ, namely, the states $|\gamma SLJM)$ are approximate eigenstates of the hamiltonian.* A characteristic property of a configuration with LS coupling is that the splitting of the multiplets is much smaller than the distances between them. In two-electron configurations the multiplets are singlets ($S = 0$) and triplets ($S = 1$).

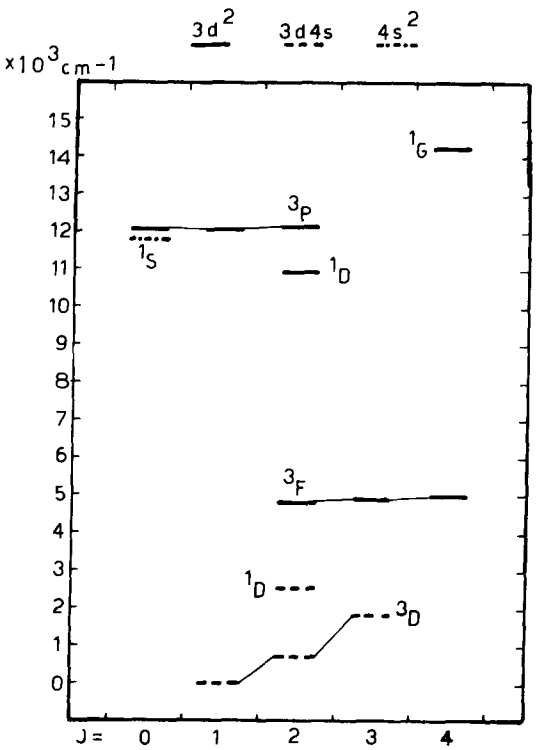

Fig. 1.1. Energy levels of ScII $3d^2 + 3d4s + 4s^2$ (LS coupling).

LS coupling exists in many spectra of the light and medium elements, and also in some simple spectra of heavy elements including the rare earths. It is, therefore, the best known coupling. The Grotrian diagram of ScII $3d^2 + 3d4s + 4s^2$, given in fig. 1.1 constitutes a characteristic example of *LS* coupling.

3.1.2. $H_2 \gg H_1 - jj$ *coupling*

In this case only H_2 is taken into account in first-order perturbation theory. H_2 commutes with the total angular momenta $\boldsymbol{j}_i = \boldsymbol{s}_i + \boldsymbol{l}_i$ of the individual electrons; therefore, its matrices are diagonal with respect to j_i and m_{j_i} and independent of m_{j_i}. Consequently H_2 is totally diagonal in the zero-order scheme

$$\Delta = (n_1 l_1 j_1 m_{j_1} n_2 l_2 j_2 m_{j_2}).$$

The energy corrections in *jj* coupling are given, to first-order perturbation theory, by

$$E^1_{jj} = (\Delta | H_2 | \Delta). \tag{1.31}$$

The configurations split into levels characterized by $\gamma j_1 j_2$, each level being $(2j_1 + 1)(2j_2 + 1)$-fold degenerate. Table 1.2 comprises the lists of *jj*-levels for various two-electron configurations of the lanthanide spectra. Since the matrices of H_2 are independent of m_{j_i}, they will be diagonal in any scheme characterized by $\gamma j_1 j_2$. In particular they will be diagonal in the scheme $\gamma j_1 j_2 J M_J$, where $\boldsymbol{J} = \boldsymbol{j}_1 + \boldsymbol{j}_2$, and independent of J and M_J. The last scheme is referred to as the *jj coupling scheme*. Its importance lies in the fact that it is adapted to the perturbation H_1 which commutes with $\boldsymbol{J}$ but not with $\boldsymbol{j}_i$. H_1 is diagonal in J and M_J and independent of M_J. J and M_J thus remain rigorous quantum numbers even when the electrostatic interaction is included in the calculations; this is not true for j_i.

When $H_1 \ll H_2$, H_1 is taken into account only in second-order perturbation theory. The energy corrections due to the electrostatic interaction are then given by the diagonal matrix elements of H_1 in the scheme $\gamma j_1 j_2 JM$:

$$E^2_{jj} = (\gamma j_1 j_2 JM | H_1 | \gamma j_1 j_2 JM) \tag{1.32}$$

and each $\gamma j_1 j_2$ level (of the first order) splits into a close group of levels characterized by $\gamma j_1 j_2 J$. The number of levels in each group is even and equals $2j_< + 1$, where $j_<$ is the smaller of j_1 and j_2.

TABLE 1.2.
jj levels for two-electron configurations.

Configuration	*jj*-level: $j_i = l_i \pm \frac{1}{2}$
fs	$(\frac{5}{2}\ \frac{1}{2})$ $(\frac{7}{2}\ \frac{1}{2})$
fp	$(\frac{5}{2}\ \frac{1}{2})$ $(\frac{7}{2}\ \frac{1}{2})$ $(\frac{5}{2}\ \frac{3}{2})$ $(\frac{7}{2}\ \frac{3}{2})$
fd	$(\frac{5}{2}\ \frac{3}{2})$ $(\frac{7}{2}\ \frac{3}{2})$ $(\frac{5}{2}\ \frac{5}{2})$ $(\frac{7}{2}\ \frac{5}{2})$

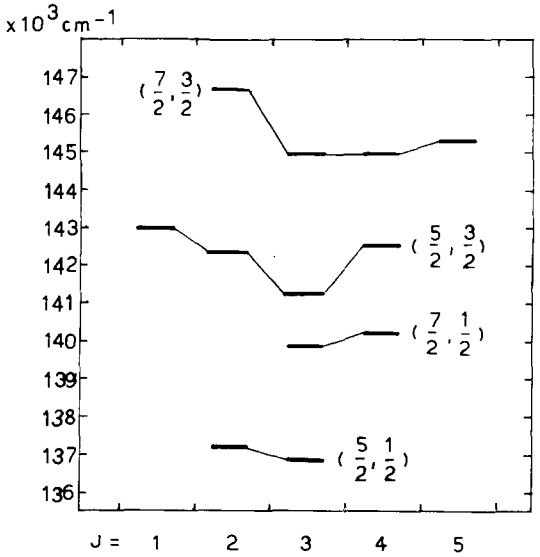

Fig. 1.2. Energy levels of PrIV 4f6p (*jj* coupling).

Whenever H_1 is small enough relative to H_2 so that its matrix elements non-diagonal in j_i can be neglected, it is said that there exists a *jj* coupling in the investigated configuration. *In jj coupling the states* $|\gamma j_1 j_2 JM)$, *namely* $|(s_1, n_1 l_1) j_1, (s_2, n_2 l_2) j_2, JM)$ *are approximate eigenstates of* H. In this coupling, the spin–orbit interaction first couples the spin and the orbital angular momenta of each electron into its total angular momentum $\boldsymbol{j}_i = \boldsymbol{s}_i + \boldsymbol{l}_i$. The electrostatic interaction then couples the individual $\boldsymbol{j}_i$ into the total angular momentum $\boldsymbol{J} = \boldsymbol{j}_1 + \boldsymbol{j}_2$. The energy level structure of a two-electron configuration in *jj* coupling is a group structure, each group comprising an even number of levels. Figure 1.2 shows the Grotrian diagram of PrIV 4f6p as an example of *jj* coupling. The groups of adjacent levels appearing in the diagram are composed of two or four levels in correspondence with the values $\frac{1}{2}$ and $\frac{3}{2}$ taken by j_p.

3.1.3. H_2 (*electron* 1) $\gg$ H_1 (*direct part*) $\gg$ H_1 (*exchange part*), H_2 (*electron* 2) – *jK* (*known also as jl*) *coupling*

In some excited configurations of two-electron spectra, one electron is tightly bound to the atom and the other much more loosely. It may then happen that the electrostatic interaction between the two electrons is weaker than the spin–orbit interaction of the inner electron, but stronger than that of the outer one. In this case the approximate eigenstates of the hamiltonian are the eigenstates of $\boldsymbol{j}_1^2 = (\boldsymbol{s}_1 + \boldsymbol{l}_1)^2$, $\boldsymbol{K}^2 = (\boldsymbol{j}_1 + \boldsymbol{l}_2)^2$, $\boldsymbol{J}^2 = (\boldsymbol{K} + \boldsymbol{s}_2)^2$ and J_z, namely $|[s_1, n_1 l_1) j_1, n_2 l_2] K_1, s_2, JM_J)$. A complete system of such states is referred to as a *jK* (*or jl*) *coupling scheme*. It must be emphasized that a necessary condition for K to be a good quantum number is that all interactions which couple the spin s_2 of the outer electron to the other angular momenta characterizing the system, should be

TABLE 1.3.
jK levels for two electron configurations.

Configuration	*jK* levels: $j_1 = l_1 \pm \frac{1}{2}$; $\lvert j_1 - l_2 \rvert \leq K \leq j_1 + l_2$ In the list below K appears in the brackets
fd	$^5_2[\frac{1}{2}]$ $^5_2[\frac{3}{2}]$ $^5_2[\frac{5}{2}]$ $^5_2[\frac{7}{2}]$ $^5_2[\frac{9}{2}]$ $^7_2[\frac{3}{2}]$ $^7_2[\frac{5}{2}]$ $^7_2[\frac{7}{2}]$ $^7_2[\frac{9}{2}]$ $^7_2[\frac{11}{2}]$
ff	$^5_2[\frac{1}{2}]$ $^5_2[\frac{3}{2}]$ $^5_2[\frac{5}{2}]$ $^5_2[\frac{7}{2}]$ $^5_2[\frac{9}{2}]$ $^5_2[\frac{11}{2}]$ $^7_2[\frac{1}{2}]$ $^7_2[\frac{3}{2}]$ $^7_2[\frac{5}{2}]$ $^7_2[\frac{7}{2}]$ $^7_2[\frac{9}{2}]$ $^7_2[\frac{11}{2}]$ $^7_2[\frac{13}{2}]$
fg	$^5_2[\frac{3}{2}]$ $^5_2[\frac{5}{2}]$ $^5_2[\frac{7}{2}]$ $^5_2[\frac{9}{2}]$ $^5_2[\frac{11}{2}]$ $^5_2[\frac{13}{2}]$ $^7_2[\frac{1}{2}]$ $^7_2[\frac{3}{2}]$ $^7_2[\frac{5}{2}]$ $^7_2[\frac{7}{2}]$ $^7_2[\frac{9}{2}]$ $^7_2[\frac{11}{2}]$ $^7_2[\frac{13}{2}]$ $^7_2[\frac{15}{2}]$

weak, that is, *jK* coupling requires the exchange part of the electrostatic interaction between the two electrons to be weak, in addition to the spin–orbit interaction of the outer electron.

Due to the spin–orbit interaction of the inner electron and the direct electrostatic interaction, each configuration splits into levels, characterized by the quantum numbers $\gamma j_1 K$; these levels are $2(2K + 1)$-fold degenerate. On account of the s_2-dependent interactions, each of these levels splits into two adjacent levels having the consecutive J values

$$J = K \pm s_2 = K \pm \tfrac{1}{2}.$$

Consequently, the characteristic energy level structure of a two-electron configuration in *jK* coupling is a pair structure. Table 1.3 comprises the list of *jK* levels for the configurations fd, ff and fg. Figure 1.3 exhibits the Grotrian diagram of CeIII 4f5g as an example of *jK* coupling.

3.1.4. $H_1 \sim H_2$ – *intermediate coupling*

When the electrostatic and the spin–orbit interactions are of the same order of magnitude, both should be included in first-order perturbation theory. In this case the energy matrices are diagonal only in J and M_J and are independent of M_J, and it is impossible to find in advance a system of states $\psi(\Delta)$ for which the energy matrices are completely diagonal. In particular, neither of the three coupling schemes

$$|\gamma SLJM_J) \qquad |\gamma j_1 j_2 JM_J) \qquad |\gamma j_1 KJM_J)$$

mentioned above is an approximate system of eigenstates of the hamiltonian. Consequently, it is impossible to define a coupling in the configuration under discussion. The lack of a definite coupling is referred to as *intermediate coupling.*

In order to calculate the energy levels of a configuration where intermediate coupling prevails, the matrix elements of the perturbation $H_1 + H_2$ are calculated in one of the above mentioned coupling schemes. Because of the diagonality of $H_1 + H_2$ in JM_J and its independence of M_J the energy matrix breaks up into

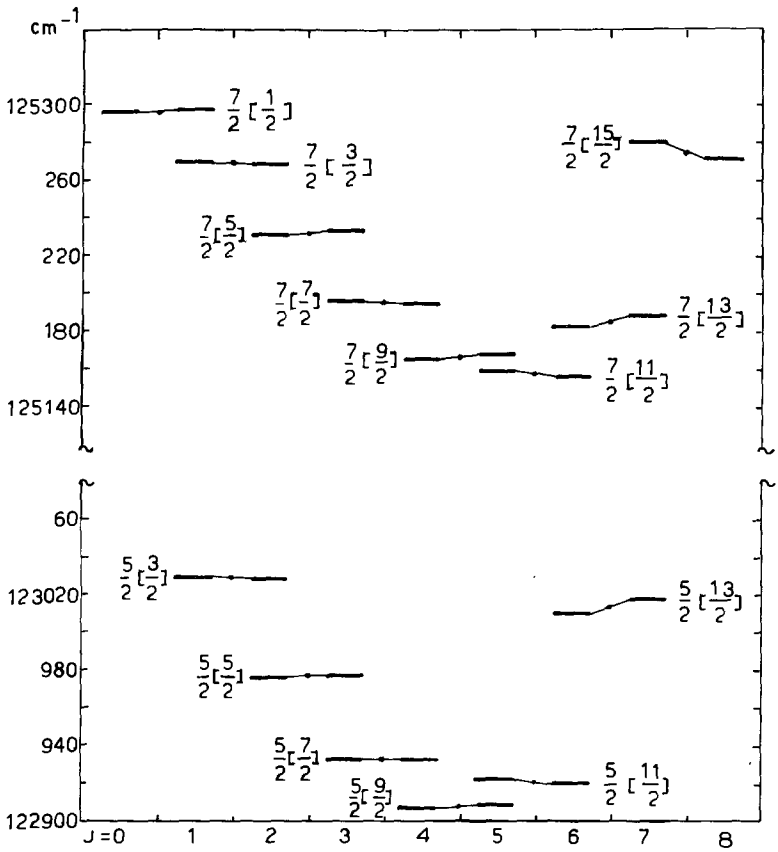

Fig. 1.3. Energy levels of CeIII 4f5g (*jK* coupling).

submatrices of relatively small orders – one for each J. These matrices are then numerically diagonalized. The energy eigenstates obtained in the diagonalization process are linear combinations of the states used for calculating the energy matrices.* For example, if the energy matrices were calculated in the LS scheme, the energy eigenstates belonging to the eigenvalue E^i are given by

$$|\gamma E^i J M_J) = \sum_{SL} |\gamma SLJM_J)(\gamma SLJ|\gamma E^i J). \tag{1.33}$$

In the Heisenberg approach, the transformation coefficients $(\gamma SLJ|\gamma E^i J)$ (which are independent of M_J) are referred to as the components of the eigenvector $|\gamma E^i J M_J)$ in the scheme $|\gamma SLJM_J)$. The squares of these components measure the amount of γSL-term mixtures due to the off-diagonal elements of the spin–orbit

*See footnote on p. 30 of this article.

interaction. The eigenvectors of a configuration with intermediate coupling generally comprise several components of the same order of magnitude, in any coupling scheme.

3.1.5. *Couplings in two-electron configurations – conclusion*

It was shown in the above discussion that the possibility of defining a coupling in a given configuration is conditioned by the fact that one or several interactions are much stronger than others. A definition of a coupling means a determination of the order in which the angular momenta of the individual electrons are coupled to each other. This determination defines the scheme for which the energy matrices are diagonal to first-order of perturbation theory, namely the scheme which should be used for characterizing the energy levels. The type of coupling prevailing in a given configuration is reflected in its Grotrian diagram, and also through the Landé g factors of the energy levels and the intensities of the spectral lines. Table 1.4 summarizes the physical conditions for the various couplings, in two-electron configurations.

3.1.6. *Intermediate coupling calculation*

Quantitatively, the extent of prevalence of a definite coupling is established by examining the components of the eigenvectors obtained in the diagonalization of the matrices of $H_1 + H_2$, these matrices being calculated in the appropriate coupling scheme. Thus, it is customary, always, to take into account the complete perturbation $H_1 + H_2$ already in first-order perturbation theory, to calculate its matrix elements in the coupling scheme corresponding to the physical coupling and then to diagonalize these matrices. This method of calculation is referred to as "Intermediate coupling calculation".

3.2. *Many-electron configurations*

The low configurations of the lanthanide spectra comprise, at most, four types of electrons, $n_i l_i$ (= 4f, 5d, 6s, 6p), outside closed shells. These configurations are of the following types: l^N, $l^N l_1$, $l^N l_1 l_2$, $l^N l_1 l_2 l_3$, $l^N l_1^2 l_2$, $l^N l_1^3$, or generally $l_1^{N_1} l_2^{N_2} l_3^{N_3} l_4^{N_4}$. In order to understand the couplings in many-electron configurations, it is, therefore, sufficient to understand the couplings in l^N ($N \geqslant 3$) configurations on the one hand and in three-electron $l_1 l_2 l_3$ configurations on the other hand.

3.2.1. *LS coupling*

This coupling prevails in a many-electron configuration when the electrostatic interactions between all electron pairs are much stronger than all spin–orbit interactions of the individual electrons. Therefore, as before, H_1 alone can be taken into account in first-order perturbation theory, and the most appropriate quantum numbers for characterizing the energy eigenstates are

$$n_i l_i S L M_S M_L \quad \text{or} \quad n_i l_i S L J M.$$

TABLE 1.4.
Physical conditions for various couplings in two-electron configurations.

Coupling	Conditions in terms of interactions	Conditions in terms of parameters	Order of coupling of angular momenta	Coupling scheme for characterizing the energy eigenstates	Characteristic energy-level structure
LS	$H_1 \gg H_2$	$F^k, G^k \gg \zeta_{n_1l_1}, \zeta_{n_2l_2}$	$s_1 + s_2 = S \quad l_1 + l_2 = L \quad S + L = J$ or in short notation $[(s_1s_2)S, (l_1l_2)L]J$	$\gamma SLJM$	Multiplets (singlets and triplets)
jj	$H_2 \gg H_1$	$\zeta_{n_1l_1}, \zeta_{n_2l_2} \gg F^k, G^k$	$s_1 + l_1 = j_1 \quad s_2 + l_2 = j_2, \quad j_1 + j_2 = J$ or in short notation $[(s_1l_1)j_1, (s_2l_2)j_2]J$	$\gamma j_1 j_2 JM$	Groups comprising an even number of levels
jK	H_2(el.1) $\gg H_1$(direct) $\gg$ $\gg H_1$(exchange), H_2(el.2)	$\zeta_{n_1l_1} \gg F^k \gg G^k, \zeta_{n_2l_2}$	$s_1 + l_1 = j_1 \quad j_1 + l_2 = K, \quad K + s_2 = J$ or in short notation $[((S_1l_1)j_1, l_2)K_1s_2]J$	$\gamma j_1 KJM$	Pairs

But contrary to the two-electron case, neither of these sets of quantum numbers is sufficient for an unambiguous characterization of the states, since, generally, states with the same SLM_SM_L or $SLJM$ appear more than once in a given configuration.

3.2.1.1. *Three-electron configuration of the type* $n_al_an_bl_bn_cl_c$ ($n_al_a \neq n_bl_b \neq n_cl_c$)

In order to distinguish terms with the same γSL, the concept of a "parent" was introduced. The use of this concept indicates the order in which the individual $\boldsymbol{s}_i$ and $\boldsymbol{l}_i$ are coupled to $\boldsymbol{S}$ and $\boldsymbol{L}$. If the first two angular momenta $\boldsymbol{s}_a\boldsymbol{l}_a$ and $\boldsymbol{s}_b\boldsymbol{l}_b$ are coupled first, then the terms will be characterized by

(I) $\quad n_al_an_bl_bS_{ab}L_{ab}n_cl_c\,SL$

where $\boldsymbol{S}_{ab} = \boldsymbol{s}_a + \boldsymbol{s}_b$ and $\boldsymbol{L}_{ab} = \boldsymbol{l}_a + \boldsymbol{l}_b$. The terms $S_{ab}L_{ab}$ of the two-electron configuration $n_al_an_bl_b$ are called *parents* of the terms $\gamma S_{ab}L_{ab}SL$ of the three-electron configuration since

$$\boldsymbol{S} = \boldsymbol{S}_{ab} + \boldsymbol{s}_c \qquad \text{and} \qquad \boldsymbol{L} = \boldsymbol{L}_{ab} + \boldsymbol{l}_c.$$

On adding the two quantum numbers of the parent, the total number of quantum numbers characterizing the states of the three non-equivalent electron configuration is 12, which is the same as the number required for characterizing the determinantal product states.

If the last two angular momenta are coupled first, the terms will be characterized by

(II) $\quad n_al_an_bl_bn_cl_cS_{bc}L_{bc}SL$

In this case the parents $S_{bc}L_{bc}$ are terms of the two-electron configuration $n_bl_bn_cl_c$.

The first angular momentum $\boldsymbol{s}_a\boldsymbol{l}_a$ can also be coupled with the third one $\boldsymbol{s}_c\boldsymbol{l}_c$; in this case the terms are characterized by

(III) $\quad n_al_an_cl_cS_{ac}L_{ac}n_bl_bSL.$

From the mathematical point of view, the three coupling schemes are completely equivalent. The eigenstates of each scheme constitute a complete set of orthogonal states, which can be expressed as linear combinations of the eigenstates of another scheme.

From the physical point of view the three coupling schemes are not equivalent, but describe different situations. States of three-electron configurations, which are eigenstates of the energy, do not in general belong to any of these coupling schemes, since H_1 is not diagonal in any of them (H_1 does not commute with S_{ab}^2, L_{ab}^2 etc.). However, if the interaction between the electrons in the states a and b is much stronger than their interactions with the electron c, then the scheme (I) is preferable to the two other schemes: the energy eigenstates will be very close to the states of (I). It is then common to say that the coupling in this configuration is characterized by scheme (I).

3.2.1.2. *Three-electron configuration of the type* $(n_a l_a)^2 n_c l_c$

In this case only $(n_a l_a)^2 S_a L_a$ can serve as parents and the terms are characterized by

(Ia) $(n_a l_a)^2 S_a L_a n_c l_c SL.$

It is worthwhile to point out that the electrostatic interaction $n_a l_a$–$n_c l_c$ is generally not diagonal in the quantum numbers $S_a L_a$. Consequently, when this interaction is strong, $S_a L_a$ are not good quantum numbers, and the states characterized by the scheme (Ia) are not approximate eigenstates of the energy.

3.2.1.3. l^N $(N \geq 3)$ *configurations*

Configurations of these types appear in rare earth spectra with $l = 2, 3$, namely d^N and f^N. Classifications of the states of these configurations have been carried out by Racah (1943, 1949, 1951, [illegible], [illegible]); these are based on group theoretical considerations. Each of these types of configurations will be treated here separately.

d^N *configurations*

According to Racah, a unique characterization of the terms of these configurations is achieved by introducing only one quantum number in addition to the set $(nd)^N SL$. For this purpose the irreducible representations of the rotation group in five dimensions R_5 can be used, but it is more common to use the seniority number v. In the latter case the states are classified according to the eigenvalues of the seniority operator

$$Q = \sum_{i>j=1}^{N} q_{ij} \tag{1.34}$$

where q_{ij} is a scalar operator defined by its matrix elements

$$(l^2 LM_L | q_{ij} | l^2 LM_L) = (2l + 1)\delta(L, 0) \tag{1.35}$$

Racah has shown that each term of l^N belonging to a non-zero eigenvalue of Q has already appeared in the configuration l^{N-2}. A quantum number v is thus assigned to each term, where v equals the smallest N for which this term first appeared. The eigenvalues of the seniority operator depend only on N and v, and are given by

$$Q(N, v) = \tfrac{1}{4}(N - v)(4l + 4 - N - v). \tag{1.36}$$

The terms of d^N are, therefore, uniquely characterized by $(nd)^N vSL$. The configuration d^3 comprises only the ^2D term twice. A term of this type has already appeared in the configuration d^1; thus, one of the ^2D terms of d^3 has seniority $v = 1$. The second ^2D and all the other terms of d^3 appear for the first time in this configuration and therefore have $v = N = 3$ $(Q(N, v) = 0)$.

f^N *configurations*

For the purpose of characterizing the terms of f^N, Racah used the irreducible representations of the rotation group in seven dimensions, R_7, and of the special

group G_2. The irreducible representations of R_7 are characterized by three integers $W \equiv (w_1, w_2, w_3)$ such that $2 \geqslant w_1 \geqslant w_2 \geqslant w_3 \geqslant 0$; the irreducible representations of G_2 are characterized by two integers $U \equiv (u_1, u_2)$. By introducing the quantum numbers WU in addition to $(n\mathrm{f})^N SL$, the terms of f^N can be uniquely characterized, with the exception of some terms belonging to f^5, f^6 and f^7, for which $U \equiv (31)$ or $U \equiv (40)$. These terms are arbitrarily distinguished through the use of an additional label τ. The classification of the f^N terms by means of the irreducible representations of R_7 is equivalent to their classification by means of the seniority number v. If two integers a and b are defined such that

$$w_1 = \cdots = w_a = 2, \qquad w_{a+1} = \cdots = w_{a+b} = 1, \qquad w_{a+b+1} = \cdots = w_3 = 0$$

then v and W are related by

$$a = \tfrac{1}{2}v - S, \qquad b = \min(2S, 2l + 1 - v).$$

Thus, the terms of f^N are uniquely characterized by one of the following sets of quantum numbers

(I) $(n\mathrm{f})^N \tau WUSL$ (II) $(n\mathrm{f})^N \tau vUSL$.

The classification of the terms of f^N for $N \leqslant 7$ is given in table 1.5. The terms of f^{14-N} are identical to those of f^N.

It is worthwhile to notice that the matrices of H_1 between states belonging to $(n\mathrm{d})^N$ are not diagonal in v, neither are the matrices of H_1 between $(n\mathrm{f})^N$ states diagonal in WU or vU.

The Grotrian diagram of PrIII $4\mathrm{f}^3$ is given in fig. 1.4. This is one of the exceptional cases in the lanthanide spectra where a $4\mathrm{f}^N$ configuration is almost completely known.

3.2.1.4. *The configurations $l^N l_1$ and $l^N l_1 l_2$*

Having classified the terms of the configurations l^N, $l_a^2 l_c$ and $l_a l_b l_c$, it is a simple task to classify the terms of $l^N l_1$ and $l^N l_1 l_2$. The terms of the $l^N l_1$ configuration can be uniquely classified by giving the set of quantum numbers

$$l^N(\alpha \bar{S}\bar{L}),\ l_1,\ SL$$

where $\alpha \equiv v$ for d^N configurations and $\alpha \equiv \tau WU$ or $\alpha \equiv \tau vU$ for f^N configurations. The Grotrian diagram of PrIII $4\mathrm{f}^2 5\mathrm{d}$, given in fig. 1.5 is an example of LS coupling in $l_a^2 l_c$ configurations. The terms of $l^N l_1 l_2$ can be uniquely classified by giving one of the following sets of quantum numbers:

(I) $l^N(\alpha \bar{S}\bar{L}), l_1(S_1 L_1), l_2, SL$, (II) $l^N(\alpha \bar{S}\bar{L}), l_1 l_2(S_2 L_2), SL$,

(III) $l^N(\alpha \bar{S}\bar{L}), l_2(S_3 L_3), l_1, SL$.

3.2.1.5. *The configuration $l_1^{N_1} l_2^{N_2} l_3^{N_3} l_4^{N_4}$*

These configurations can be classified by giving four quantum numbers in addition to $(n_1 l_1)^{N_1}(\alpha_1 S_1 L_1)$, $(n_2 l_2)^{N_2}(\alpha_2 S_2 L_2)$, $(n_3 l_3)^{N_3}(\alpha_3 S_3 L_3)$, $(n_4 l_4)^{N_4}(\alpha_4 S_4 L_4)$, SL

TABLE 1.5.
Classification of the terms of f^N.

N	v	W	U	SL
0	0	(000)	(00)	^{1}S
1	1	(100)	(10)	^{2}F
2	2	(110)	(10)	^{3}F
			(11)	^{3}PH
	2	(200)	(20)	^{1}DGI
	0	(000)	(00)	^{1}S
3	3	(111)	(00)	^{4}S
			(10)	^{4}F
			(20)	^{4}DGI
	3	(210)	(11)	^{2}PH
			(20)	^{2}DGI
			(21)	^{2}DFGHKL
	1	(100)	(10)	^{2}F
4	4	(111)	(00)	^{5}S
			(10)	^{5}F
			(20)	^{5}DGI
	4	(211)	(10)	^{3}F
			(11)	^{3}PH
			(20)	^{3}DGI
			(21)	^{3}DFGHKL
			(30)	^{3}PFGHIKM
	2	(110)	(10)	^{3}F
			(11)	^{3}PH
	4	(220)	(20)	^{1}DGI
			(21)	^{1}DFGHKL
			(22)	^{1}SDGHILN
	2	(200)	(20)	^{1}DGI
	0	(000)	(00)	^{1}S
5	5	(110)	(10)	^{6}F
			(11)	^{6}PH
	5	(211)	(10)	^{4}F
			(11)	^{4}PH
			(20)	^{4}DGI
			(21)	^{4}DFGHKL
			(30)	^{4}PFGHIKM
	3	(111)	(00)	^{4}S
			(10)	^{4}F
			(20)	^{4}DGI
	5	(221)	(10)	^{2}F
			(11)	^{2}PH
			(20)	^{2}DGI
			(21)	^{2}DFGHKL
			(30)	^{2}PFGHIKM
			(31)	^{2}PDFFGHHIIKKLMNO
	3	(210)	(11)	^{2}PH
			(20)	^{2}DGI
			(21)	^{2}DFGHKL
	1	(100)	(10)	^{2}F

TABLE 1.5. (*Contd.*).

N	*v*	*W*	*U*	*SL*
6	6	(100)	(10)	^{7}F
	6	(210)	(11)	^{5}PH
			(20)	^{5}DGI
			(21)	^{5}DFGHKL
	4	(111)	(00)	^{5}S
			(10)	^{5}F
			(20)	^{5}DGI
	6	(221)	(10)	^{3}F
			(11)	^{3}PH
			(20)	^{3}DGI
			(21)	^{3}DFGHKL
			(30)	^{3}PFGHIKM
			(31)	^{3}PDFFGHHIIKKLMNO
	4	(211)	(10)	^{3}F
			(11)	^{3}PH
			(20)	^{3}DGI
			(21)	^{3}DFGHKL
			(30)	^{3}PFGHIKM
	2	(110)	(10)	^{3}F
			(11)	^{3}PH
	6	(222)	(00)	^{1}S
			(10)	^{1}F
			(20)	^{1}DGI
			(30)	^{1}PFGHIKM
			(40)	^{1}SDFGGHIIKLLMNQ
	4	(220)	(20)	^{1}DGI
			(21)	^{1}DFGHKL
			(22)	^{1}SDGHILN
	2	(200)	(20)	^{1}DGI
	0	(000)	(00)	^{1}S
7	7	(000)	(00)	^{8}S
	7	(200)	(20)	^{6}DGI
	5	(110)	(10)	^{6}F
			(11)	^{6}PH
	7	(220)	(20)	^{4}DGI
			(21)	^{4}DFGHKL
			(22)	^{4}SDGHILN
	5	(211)	(10)	^{4}F
			(11)	^{4}PH
			(20)	^{4}DGI
			(21)	^{4}DFGHKL
			(30)	^{4}PFGHIKM
	3	(111)	(00)	^{4}S
			(10)	^{4}F
			(20)	^{4}DGI
	7	(222)	(00)	^{2}S
			(10)	^{2}F
			(20)	^{2}DGI
			(30)	^{2}PFGHIKM

TABLE 1.5. (*Contd.*)

N	v	W	U	SL
			(40)	^{2}SDFGGHIIKLLMNQ
	5	(221)	(10)	^{2}F
			(11)	^{2}PH
			(20)	^{2}DGI
			(21)	^{2}DFGHKL
			(30)	^{2}PFGHIKM
			(31)	^{2}PDFFGHHIIKKLMNO
	3	(210)	(11)	^{2}PH
			(20)	^{2}DGI
			(21)	^{2}DFGHKL
	1	(100)	(10)	^{2}F

according to the order in which the angular momenta S_iL_i of the four sub-configurations $l_i^{N_i}$ are coupled to each other. For example, the terms of the configuration 4f5d6s6p of CeI are uniquely classified as follows

$$4f5d(S_{fd}L_{fd}),\ 6s6p(S_{sp}L_{sp}),\ SL.$$

3.2.2. *jj coupling*

This coupling prevails in a many-electron configuration when the spin–orbit interaction of each electron is stronger than its electrostatic interaction with other electrons. Since this coupling does not exist in the many-electron configurations of the rare earth spectra, it will not be discussed here.

3.2.3. J_1j *or* J_1J_2 *coupling*

These couplings are generalizations of *jj* coupling in two-electron configurations. J_1j coupling is widespread in the configurations

$4f^N6s$ ($N = 1, 2, 3, 4, 9, 10, 11, 12, 13$), $4f^N6p$ ($N = 1, 2, \ldots, 13$), $4f^N5d$ (on the right-hand side)

of the lanthanide group. In these configurations the order of the interactions according to their strength is

Electrostatic interaction of the $4f^N$ core $>$ spin–orbit interaction of the $4f^N$ core

$\gg$ electrostatic interaction $4f^N - nl$ ($=6s, 6p, 5d$) $\ll$ spin–orbit interaction of nl ($=6p, 5d$)*.

Therefore the most appropriate coupling scheme for characterizing the states of

*For a 6s electron the extreme inequality on the right is meaningless; however, in this case $s = j$ and a J_1j coupling exists because of the two other inequalities.

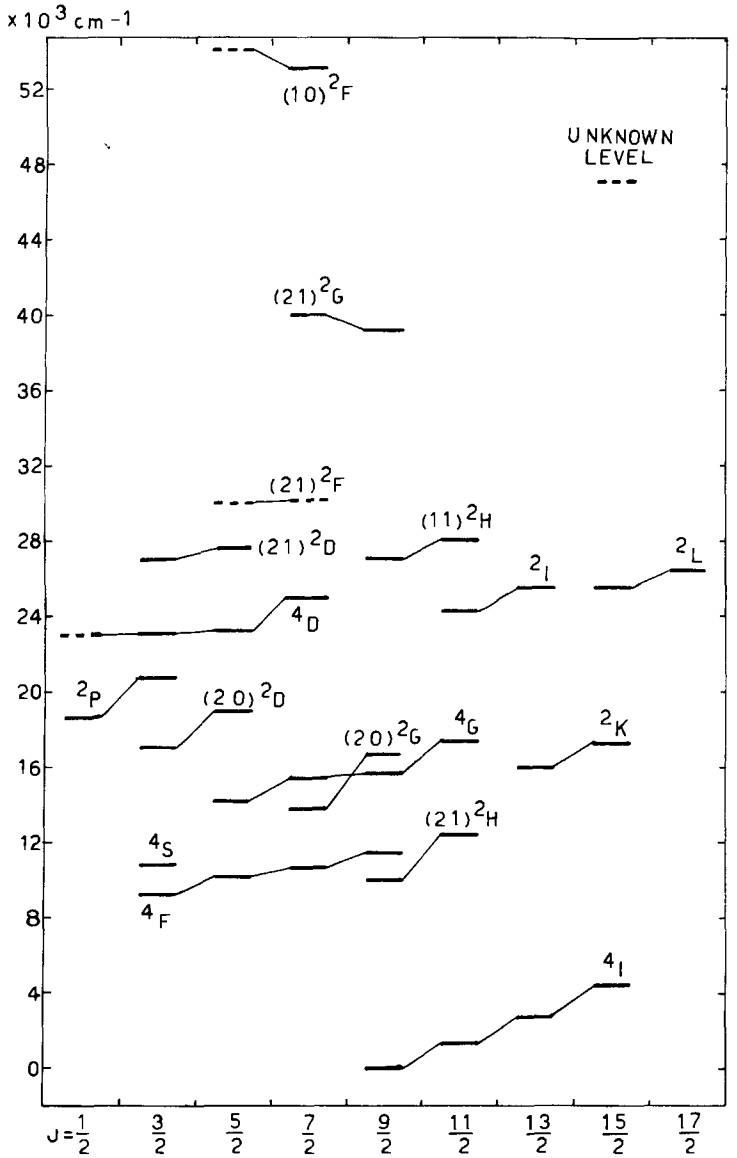

Fig. 1.4. Energy levels of PrIII $4f^3$ (*LS* coupling).

these configurations is

$$(4f)^N(\tau WUS_1L_1J_1), nlj, JM_J$$

Figure 1.6 exhibits the Grotrian diagram of PrIII $4f^26p$ as an example of J_1j coupling.

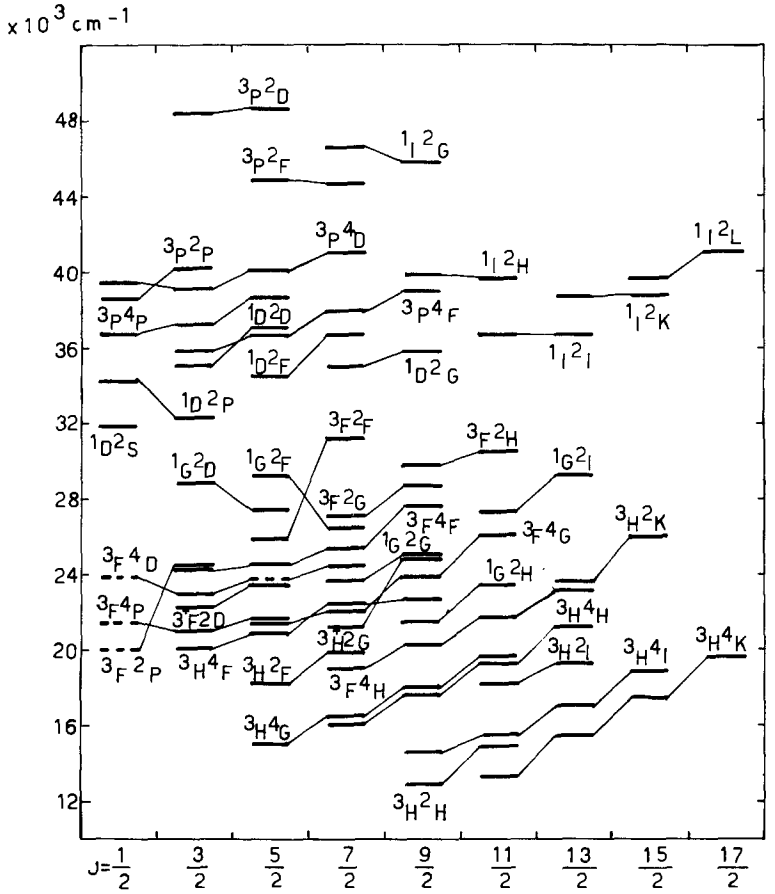

Fig. 1.5. Energy levels of PrIII $4f^2 5d$ (*LS* coupling).

J_1J_2 coupling prevails in the configurations $4f^N 6s6p$, and in $4f^N 5d6p$ on the right-hand side of the lanthanide group. Here the order of interactions according to their strength is

$$H_1(f^N) > H_2(f^N) \gg H_1(f^N - l_1 l_2) \ll H_2(l_1, l_2) < H_1(l_1 - l_2)$$

and the most appropriate coupling scheme for characterizing the states of these configurations is

$$(4f)^N(\tau WUS_1L_1J_1),\ n_1l_1n_2l_2(S_2L_2J_2),\ JM_J$$

J_1J_2 coupling exists also in the configurations $4f^N 5d^2 6p$ and $4f^N 5d6s6p$ on the right-hand side of the lanthanide group, their states being respectively characterized by the following sets of quantum numbers:

$$(4f)^N(\tau UWS_1L_1J_1),\ [5d^2(\bar{S}\bar{L})6p](S_2L_2J_2),\ JM_J,$$

$$(4f)^N(\tau UWS_1L_1J_1),\ [5d, 6s6p\ (\bar{S}\bar{L})](S_2L_2J_2),\ JM_J.$$

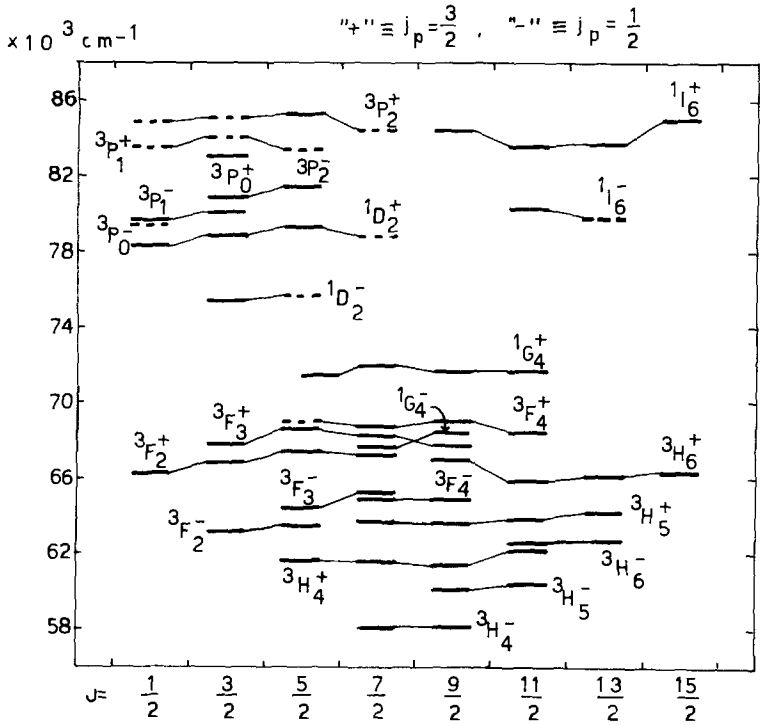

Fig. 1.6. Energy levels of PrIII $4f^26p$ (J_1j coupling).

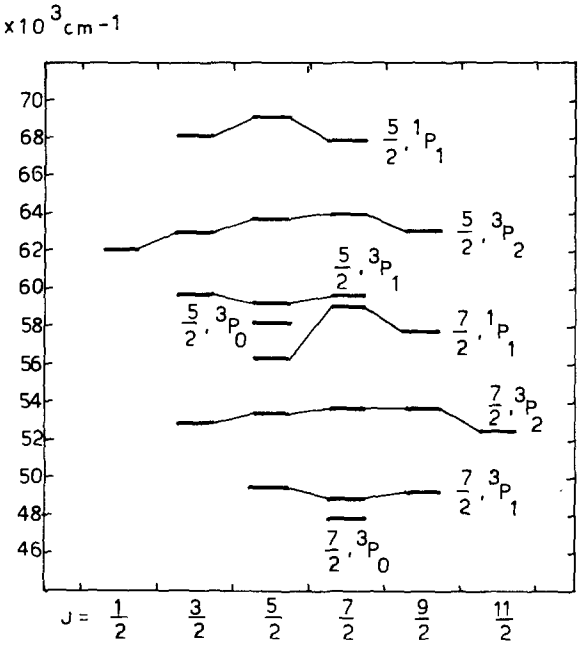

Fig. 1.7. Energy levels of YbII $4f^{13}6s6p$ (J_1J_2 coupling).

Figure 1.7 shows the Grotrian diagram of YbII $4f^{13}_{J_1}6s6p(^{1,3}P_{J_2})$, J as an example of J_1J_2 coupling.

3.2.4. *J_1L_2 coupling*

This coupling is a generalization of *jK* (or *jl*) coupling in two-electron configurations. It prevails in configurations of the type $4f^N5d^2$ and $4f^N5d6s$, on the right-hand side of the lanthanide group. The order of interactions in these configurations is

$$\left.\begin{array}{l} H_1(f^N) \gg H_2(f^N) \\ \qquad\qquad \gg \\ H_1(l_1 - l_2) \gg \end{array}\right\} \text{direct part of } H_1(f^N - l_1l_2) \gg \left\{\begin{array}{l} H_2(l_1, l_2) \\ \text{exchange part of } H_1(f^N - l_1l_2) \end{array}\right.$$

and the most appropriate coupling scheme for characterizing the states of these configurations is

$$[(4f)^N(\tau UWS_1L_1J_1),\ l_1l_2(L_2)]K,\ S_2,\ JM_J.$$

The characteristic energy-level structure of these configurations is that of singlets or triplets, in accordance with the value 0 or 1 taken by S_2. This structure is exhibited in the Grotrian diagram of YbII $4f^{13}_{7/2}4d6s(^{1,3}D)$, KJ given in fig. 1.8.

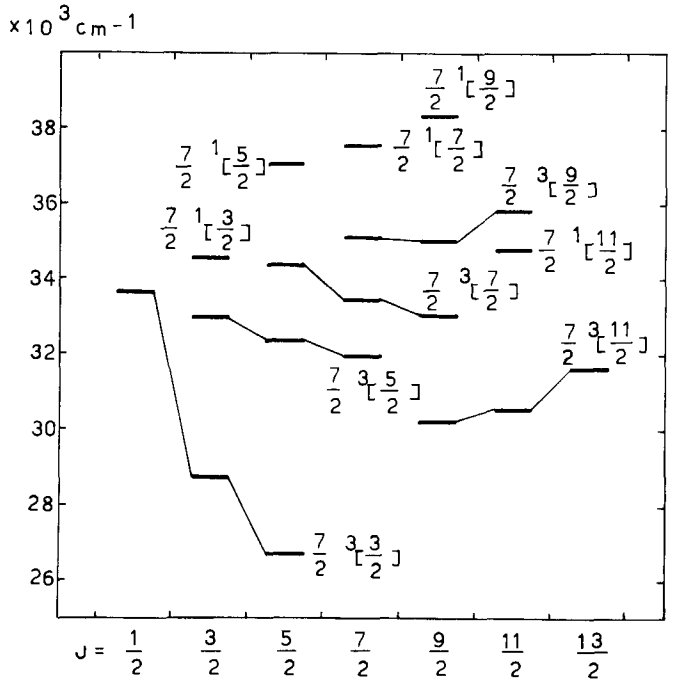

Fig. 1.8. Energy levels of YbII $4f^{13}_{7/2}5d6s$ (J_1L_2 coupling).

3.2.5. *Intermediate coupling*

When many interactions in the configuration under discussion are of the same order of magnitude, it is impossible to define a coupling in this configuration. As was mentioned in the two-electron case, the lack of a coupling is referred to as intermediate coupling. Energy-level calculations of such configurations, and their characterization in the scheme for which the energy matrices were calculated, are carried out as described in section 3.1.4.* As already stated in the two-electron case, it is customary always to take into account the complete perturbation $H_1 + H_2$ already in first order perturbation theory. The squares of the eigenvectors in a desired coupling scheme, obtained during the diagonalization of the energy matrices, serve as means of identification of the energy levels.

3.3. *Configuration interaction (CI) between neighbouring configurations*

One of the characteristic properties of rare earth spectra is that several configurations of the same parity overlap or are energetically close to each other. Consequently, in these spectra, the energy level problem cannot be treated configuration by configuration, but electrostatic interaction *between* configurations must be included in the calculations in addition to the electrostatic and spin–orbit interactions within the configurations.† The energy eigenstates of this group of configurations are then described as linear combinations of states of the individual interacting configurations; the quantum numbers characterizing the configurations cease to be rigorous quantum numbers, and in cases of strong CI they are no longer even good quantum numbers. In such cases the concept of a configuration becomes meaningless. For complex configurations of the lanthanide spectra, the inclusion of CI in the energy-level calculations entails the construction of large matrices and the evaluation of a large number of radial integrals (parameters) which represent the various interactions.

4. Calculation of the algebraic matrices (the angular parts of the energy matrices)

The explicit calculation of the energy levels of a given configuration (or group of configurations) is carried out as summarized in the following steps:
(1) each term in the Hamiltonian is expressed as a sum of products of two factors, one of which comprises only the angular variables and the second only the radial variables.

*See footnote on page 30.

†The spin–orbit one-electron interaction is diagonal in the l_i quantum numbers of the individual electrons. Consequently the spin–orbit interaction between configurations is different from zero when the interacting configurations differ only by the principal quantum number of one electron ($nl \leftrightarrow n'l$). Since such pairs of configurations are generally very remote from each other energetically, spin–orbit interaction between configurations can be neglected in first-order perturbation theory.

(2) the factors which comprise the angular variables are expressed in terms of tensor-operators.
(3) the angular parts of the energy matrices are rigorously calculated through the use of "Racah algebra" (Racah, 1942b, 1943, 1949; Fano et al., 1959). The matrices thus obtained are known as the "algebraic matrices."
(4) The radial parts of the energy matrices can either be treated as adjustable parameters, the values of which are determined by comparing the theoretical formulae to the experimental energy levels, or be found by performing abinitio calculations.

For the electrostatic and spin–orbit interaction, steps 1 and 2 have already been carried out; the appropriate expressions are given in formulae 1.21 and 1.3 respectively.

In this section formulae are given for the algebraic matrix elements of the electrostatic and spin–orbit interactions between antisymmetric functions of various electronic configurations characteristic of the rare earth spectra. All these formulae were constructed in the $\gamma SLJM$ coupling scheme.*

4.1. *Antisymmetric functions*

4.1.1. *Two-electron configurations*

An eigenfunction of a two-electron configuration in the LS coupling scheme will be written in the form $(12|n_a l_a n_b l_b SLM_S M_L)$. This function is a linear combination of products of the one-electron eigenfunctions $(1|n_a l_a m_{s_a} m_{l_a})(2|n_b l_b m_{s_b} m_{l_b})$, with Wigner coefficients as the expansion coefficients. Following Fano et al. (1959) an antisymmetric eigenfunction of a system of two electrons will be indicated with the notation $(12|\}n_a l_a n_b l_b SLM_S M_L)$.

For $(n_a l_a) \neq (n_b l_b)$

$$(12|\}n_a l_a n_b l_b SLM_S M_L) = \frac{1}{\sqrt{2}}[(12|n_a l_a n_b l_b SLM_S M_L) - (21|n_a l_a n_b l_b SLM_S M_L)]$$

$$= \frac{1}{\sqrt{2}}[(12|n_a l_a n_b l_b SLM_S M_L) - (-1)^{s_a+s_b-S+l_a+l_b-L} \quad (1.37)$$

$$\times (12|n_b l_b n_a l_a SLM_S M_L)]. \quad (1.38)$$

In the same manner, $(12|n_a l_a n_b l_b SLJM)$ is a linear combination of $(12|n_a l_a n_b l_b SLM_S M_L)$, and the antisymmetric eigenfunction in the $SLJM$ coupling

*Generally, the choice of the coupling scheme in which the algebraic matrices are calculated is of no importance, since the available computer programs for diagonalizing the energy matrices can be used for obtaining the components of the eigenvectors in any desired coupling scheme. This fact is particularly relevant for complex configurations. However, for simple configurations in which a definite coupling prevails, it is worthwhile to calculate the algebraic matrices in the appropriate coupling scheme, in order to achieve a better understanding of the energy level structure.

scheme is given by

$$(12|\}n_a l_a n_b l_b SLJM) = \frac{1}{\sqrt{2}}[(12|n_a l_a n_b l_b SLJM) - (21|n_a l_a n_b l_b SLJM)]$$

$$= \frac{1}{\sqrt{2}}[(12|n_a l_a n_b l_b SLJM) - (-1)^{s_a+s_b-S+l_a+l_b-L} \times (12|n_b l_b n_a l_a SLJM)]. \quad (1.39)$$

For $(n_a l_a) = (n_b l_b) = (nl)$, the antisymmetric function is given by

$$(12|\}(nl)^2 SLM_S M_L) = (12|(nl)^2 SLM_S M_L)$$

or

$$(12|\}(nl)^2 SLJM) = (12|(nl)^2 SLJM) \quad (1.40)$$

for $S + L$ even. An antisymmetric function does not exist for $S + L$ odd. From now on the notation $(12|n_a l_a n_b l_b SL\}$ will be used for representing the group of $(2S + 1)(2L + 1)$ functions $(12|n_a l_a n_b l_b SLM_S M_L)$ and the notation $(12|n_a l_a n_b l_b SLJ\}$ for representing the group of $2J + 1$ functions $(12|n_a l_a n_b l_b SLJM)$.

4.1.2. *Three-electron configurations*

For non-equivalent electrons

$$(n_a l_a) \neq (n_b l_b) \neq (n_c l_c),$$

the analog of (1.37) is

$$(123|\}n_a l_a n_b l_b (S_{ab} L_{ab}),\ n_c l_c,\ SL\}$$

$$= \frac{1}{\sqrt{6}}[(123|n_a l_a n_b l_b (S_{ab} L_{ab}),\ n_c l_c,\ SL\} - (213|n_a l_a n_b l_b (S_{ab} L_{ab}),\ n_c l_c,\ SL\}$$

$$+ (231|n_a l_a n_b l_b (S_{ab} L_{ab}),\ n_c l_c,\ SL\} - (321|n_a l_a n_b l_b (S_{ab} L_{ab}),\ n_c l_c,\ SL\}$$

$$+ (312|n_a l_a n_b l_b (S_{ab} L_{ab}),\ n_c l_c,\ SL\} - (132|n_a l_a n_b l_b (S_{ab} L_{ab}),\ n_c l_c,\ SL\}] \quad (1.41)$$

The analog of (1.38) is more complicated here, because a permutation of the factors in the three electron case involves also a recoupling instead of a simple reordering. This was obtained by Z.B. Goldschmidt (1968a), but will not be repeated here.

For $(n_a l_a) = (n_b l_b) = (nl)$, $(n_c l_c) = (n'l')$

$$(123|\}(nl)^2 (S_1 L_1),\ n'l',\ SL\} = \frac{1}{\sqrt{3}}[(123|(nl)^2 (S_1 L_1),\ n'l',\ SL\}$$

$$+ (231|(nl)^2 (S_1 L_1),\ n'l',\ SL\} + (312|(nl)^2 (S_1 L_1),\ n'l',\ SL\}], \qquad S_1 + L_1 \text{ even.} \quad (1.42)$$

For three equivalent electrons

$$(n_a l_a) = (n_b l_b) = (n_c l_c) = (nl),$$

the three terms on the right-hand side of (1.42) are not orthogonal and therefore (1.42) is not normalized. In order to construct normalized antisymmetric functions for $N \geqslant 3$ equivalent electrons Racah (1943) introduced the concept of "fractional parentage coefficients". By means of these coefficients, the antisymmetric function of three equivalent electrons is given by

$$(123|\}(nl)^3 \alpha SL\} = \sum_{S'L'} (123|(nl)^2(S'L'), nl, SL\}(l^2(S'L')lSL|\}l^3 \alpha SL) \tag{1.43}$$

where α denotes the set of quantum numbers needed, in addition to S and L, for an unambiguous characterization of the terms of $(nl)^3$. The terms $(nl)^2 S'L'$ are referred to as fractional parents and the expansion coefficients $(l^2(S'L')lSL|\}l^3 \alpha SL)$ are known as "coefficients of fractional parentage."

4.1.3. $(nl)^N$ *configurations*

The antisymmetric function for a configuration $(nl)^N$ of N equivalent electrons is given by a formula similar to (1.43):

$$(12 \ldots n|\}(nl)^N \alpha SL\} = \sum_{\alpha' S' L'} (12 \ldots (n-1)|\}(nl)^{N-1}(\alpha' S' L'), nl, SL\} \times (l^{N-1}(\alpha' S' L')lSL|\}l^N \alpha SL) \tag{1.44}$$

with $(nl)^{N-1} \alpha' S' L'$ as fractional parents and $(l^{N-1}(\alpha' S' L')lSL|\}l^N \alpha SL)$ the coefficients of fractional parentage of l^N. These coefficients obey the condition of orthonormalization

$$\sum_{\alpha' S' L'} (l^N \alpha SL\{|l^{N-1}(\alpha' S' L')lSL)(l^{N-1}(\alpha' S' L')lSL|\}l^N \alpha'' SL) = \delta_{\alpha\alpha''} \tag{1.45}$$

They were tabulated by Racah (1943) for p^N and d^N configurations and by Racah (1949) and Judd (1963) for f^N configurations, for $3 \leqslant N \leqslant 2l+1$, and also by Nielson et al. (1964). Formula 19 of Racah (1943) gives the coefficients of fractional parentage of the almost closed shell l^{4l+2-N} in terms of those of l^{N+1}:

$$(l^{4l+1-N}(\alpha' S' L')lSL|\}l^{4l+2-N} \alpha SL) = (-1)^{S+S'+L+L'-l-1/2} \times \sqrt{(N+1)[S'][L']/[(4l+2-N)[S][L]]}\,(l^N(\alpha SL)lS'L'|\}l^{N+1} \alpha' S' L').^* \tag{1.46}$$

Rosenzweig (1952) used the last formula for tabulating the coefficients of fractional parentage for d^N with $N = 6, 7, 8$.

4.1.4. $(nl)^N n'l'$ *configurations.*

Antisymmetric functions of more complicated configurations are obtained through the use of similar methods to those listed above. Only one example will

*$[S']$ stands for $2S'+1$, etc.

be given here – that of the configuration $(nl)^N n'l'$ (formula 26 of Racah, 1943):

$$(12\ldots(N+1)|\}l^N(\alpha_1 S_1 L_1)l'SL\} = (N+1)^{-1/2}\sum_{i=1}^{N+1}(-1)^{P_i} \times \hat{(}12\ldots(i\mp 1)(i+1)\ldots(N+1)i|l^N(\alpha_1 S_1 L_1)l'SL\} \tag{1.47}$$

where each function on the right-hand side is an antisymmetric function of the electrons $1, 2, \ldots, (i-1)(i+1)\ldots(N+1)$ and P_i is the parity of the permutation which exchanges i with $N+1$. This formula is a generalization of formula (1.42) given above for the configuration $(nl)^2 n'l'$.

4.2. *Matrix elements of the electrostatic interaction*

The starting point for the calculation of the matrix elements of the electrostatic interaction H_1 is its tensor-operator expression

$$H_1 = e^2\sum_k (r_<^k/r_>^{k+1})\sum_{i>j}(C_i^{(k)}\cdot C_j^{(k)}). \tag{1.48}$$

The matrix elements of H_1 between two antisymmetric eigenfunctions ψ and ψ' of the electronic system will be written in the form $(\psi\{|H_1|\}\psi')$. Integration over the radial variables results in the Slater integrals (parameters) defined in formulae (1.24)–(1.26). The calculations of the angular parts involve matrix elements of the type

$$\{l_a l_b SL|C_i^{(k)}\cdot C_j^{(k)}|l_c l_d SL\}$$

which, according to Racah's algebra, are expressed in terms of the reduced matrix elements $(l\|C^{(k)}\|l')$ of the $C^{(k)}$'s and $6j$-symbols $\begin{Bmatrix} abc \\ def \end{Bmatrix}$ (Judd, 1963; Rotenberg et al., 1959):

$$\{l_a l_b SL|C_i^{(k)}\cdot C_j^{(k)}|l_c l_d SL\} = (-1)^{l_b+l_c+L}(l_a\|C^{(k)}\|l_c)(l_b\|C^{(k)}\|l_d)\begin{Bmatrix} l_a l_c k \\ l_d l_b L \end{Bmatrix}. \tag{1.49}$$

The reduced matrix elements of the $C^{(k)}$'s can, in turn, be expressed in terms of $3j$-symbols $\begin{pmatrix} abc \\ \alpha\beta\gamma \end{pmatrix}$: (Judd, 1963; Rotenberg et al., 1959):

$$(l\|C^k\|l') = (-1)^l\{[l][l']\}^{1/2}\begin{pmatrix} lkl' \\ 000 \end{pmatrix}. \tag{1.50}$$

$\begin{pmatrix} lkl' \\ 000 \end{pmatrix}$ vanishes unless l, k and l' satisfy the triangular condition and also the condition $l + l' + k$ even. These properties of $\begin{pmatrix} lkl' \\ 000 \end{pmatrix}$ limit the range of k to a small number of values; therefore the number of terms in (1.48) is small.

4.2.1. *Two-electron configurations*

For the case $\psi \equiv n_a l_a n_b l_b$ $\psi' \equiv n_c l_c n_d l_d$, one obtains, because of the antisymmetry

of the eigenfunctions:

$$\{n_a l_a n_b l_b SL\{|H_1|\}n_c l_c n_d l_d SL\}$$
$$= \frac{1}{2}\{n_a l_a n_b l_b SL|H_1|n_c l_c n_d l_d SL\}$$
$$- \frac{1}{2}(-1)^{1/2+1/2-S+l_c+l_d-L}\{n_a l_a n_b l_b SL|H_1|n_d l_d n_c l_c SL\}$$
$$- \frac{1}{2}(-1)^{1/2+1/2-S+l_a+l_b-L}\{n_b l_b n_a l_a SL|H_1|n_c l_c n_d l_d SL\}$$
$$+ \frac{1}{2}(-1)^{1/2+1/2+1/2+1/2-2S+l_a+l_b+l_c+l_d-2L}\{n_b l_b n_a l_a SL|H_1|n_d l_d n_c l_c SL\}. \quad (1.51)$$

Owing to the symmetry of H_1 and to the fact that H_1 is diagonal in the parity of the eigenfunctions, the last expression reduces to:

$$\{n_a l_a n_b l_b SL\{|H_1|\}n_c l_c n_d l_d SL\} = \{n_a l_a n_b l_b SL|H_1|n_c l_c n_d l_d SL\}$$
$$+ (-1)^{l_c+l_d-L-S}\{n_a l_a n_b l_b SL|H_1|n_d l_d n_c l_c SL\}. \quad (1.52)$$

For the special case $(n_a l_a) = (n_b l_b) = (nl)$, $(n_c l_c) = (n_d l_d) = (n'l')$, the following equality holds:

$$\{(nl)^2 SL\{|H_1|\}(n'l')^2 SL\} = \{(nl)^2 SL|H_1|(n'l')^2 SL\}. \quad (1.53)$$

If $(n_a l_a) = (n_b l_b) = nl$ but $(n_c l_c) \neq n_d l_d$ one obtains

$$\{(nl)^2 SL\{|H_1|\}n_c l_c n_d l_d SL\} = \sqrt{2}\{(nl)^2 SL|H_1|n_c l_c n_d l_d SL\}. \quad (1.54)$$

On writing each of the above matrix elements of H_1 as a sum of products of the radial and the angular factors, for example:

$$\{n_a l_a n_b l_b SL|H_1|n_c l_c n_d l_d SL\} = \sum_k R^k(n_a l_a n_b l_b, n_c l_c n_d l_d)\{l_a l_b SL|C_i^{(k)} \cdot C_j^{(k)}|l_c l_d SL\} \quad (1.55)$$

and using formula (1.49), explicit expressions are obtained for the various matrix elements of the electrostatic interaction:

$$\{n_a l_a n_b l_b SL\{|e^2/r_{12}|\}n_c l_c n_d l_d SL\}$$
$$= \sum_k R^k(n_a l_a n_b l_b, n_c l_c n_d l_d)(-1)^{l_b+l_c+L}(l_a\|C^{(k)}\|l_c)(l_b\|C^{(k)}\|l_d)\begin{Bmatrix} l_a & l_c & k \\ l_d & l_b & L \end{Bmatrix}$$
$$+ (-1)^S \sum_k R^k(n_a l_a n_b l_b, n_d l_d n_c l_c)(-1)^{l_b+l_c}(l_a\|C^{(k)}\|l_d)(l_b\|C^{(k)}\|l_c)\begin{Bmatrix} l_a & l_d & k \\ l_c & l_b & L \end{Bmatrix}, \quad (1.56)$$

$$\{(nl)^2 SL\{|e^2/r_{12}|\}(n'l')^2 SL\} = \sum_k R^k(nlnl, n'l'n'l')(-1)^{l+l'+L}(l\|C^{(k)}\|l')^2\begin{Bmatrix} ll' & k \\ l'l & k \end{Bmatrix}, \quad (1.57)$$

$$\{(nl)^2 SL\{|e^2/r_{12}|\}n_c l_c n_d l_d SL\} = \sqrt{2}\sum_k R^k(nlnl, n_c l_c n_d l_d)(-1)^{l+l_c+L}$$
$$\times (l\|C^{(k)}\|l_c)(l|C^{(k)}\|l_d)\begin{Bmatrix} l & l_c & k \\ l_d & l & L \end{Bmatrix}. \quad (1.58)$$

A use of formula (1.56) for the special case $(n_a l_a) = (n_c l_c)$, $(n_b l_b) = (n_d l_d)$ results in a formula for the matrix elements of the electrostatic interaction within a configuration which comprises two non-equivalent electrons:

$$\{n_a l_a n_b l_b SL\{|e^2/r_{12}|\}n_a l_a n_b l_b SL\} = \sum_k f_k F^k + (-1)^S \sum_k g_k G^k$$
$$= \sum_k F^k(n_a l_a, n_b l_b)(-1)^{l_a+l_b+L}(l_a\|C^{(k)}\|l_a)(l_b\|C^{(k)}\|l_b)\begin{Bmatrix} l_a & l_a & k \\ l_b & l_b & L \end{Bmatrix}$$
$$+ (-1)^S \sum_k G^k(n_a l_a, n_b l_b)(l_a\|C^{(k)}\|l_b)^2\begin{Bmatrix} l_a & l_b & k \\ l_a & l_b & L \end{Bmatrix}. \quad (1.59)$$

The first term on the right-hand side of (1.59) represents the *direct interaction* whereas the second term represents the *exchange interaction*. It is sometimes convenient to replace the factor $(-1)^S$ with the Dirac operator

$$-\frac{1}{2}[1 + 4(s_1 \cdot s_2)]. \quad (1.60)$$

A use of formula (1.57) for the special case $(nl) = (n'l')$ results in a formula for the matrix elements of the electrostatic interaction within a configuration comprising two equivalent electrons:

$$\{(nl)^2 SL\{|e^2/r_{12}|\}(nl)^2 SL\} = \sum_k f_k F^k = \sum_k F^k(nl, nl)(-1)^L(l\|C^{(k)}\|l)^2\begin{Bmatrix} l & l & k \\ l & l & L \end{Bmatrix} \quad (1.61)$$

F^k and $G^k/[k]$ are positive and decreasing functions of k (Condon et al., 1951; Racah, 1942b).

By means of formulae (1.56)–(1.61), the matrix elements of the electrostatic interaction within and between configurations are expressed as linear combinations of a small number of Slater integrals – electrostatic parameters. The coefficients of the parameters comprise products of nj-symbols. To avoid the occurrence of fractional coefficients for the electrostatic parameters in the evaluation of the matrix elements, new parameters are defined (Condon et al., 1951):

$$F_k = F^k/D_k, \qquad G_k = G^k/D_k, \qquad R_k = R^k/D_k \quad (1.62)$$

The values of the D_k's connecting the F^k's and the G^k's with the corresponding F_k's and G_k's are given in tables 1^6 and 2^6 of Condon et al. (1951). The definitions of the R_k's will be given below (see also Z.B. Goldschmidt 1968a, b). The explicit expressions for the matrix elements of the electrostatic interaction in terms of the F_k's and the G_k's *within* two-electron configurations comprising s, p, d and f electrons are given by Condon et al. (1951). The explicit expressions for the matrix elements of the electrostatic interaction *between* two-electron configurations comprising the above mentioned electrons are given below (see also Z.B. Goldschmidt, 1968a).

For the configurations d^2 and f^2 it is customary to replace the Slater parameters F_k by the Racah parameters A, B, C and E^0, E^1, E^2, E^3 respectively (Racah, 1942b, 1949).

4.2.1.1. *Electrostatic parameters and matrix elements for the configuration* d^2

Racah defined the electrostatic parameters A, B, C for the configuration d^2 through the following formulae:

$$A = F_0 - 49F_4 = F^0 - F^4/9 \qquad B = F_2 - 5F_4 = (9F^2 - 5F^4)/441$$
$$C = 35F_4 = 5F^4/63 \tag{1.63}$$

In terms of these "new" parameters the terms of d^2 are expressed in the simple form

$$^1S = A + 14B + 7C$$
$$^3P = A + 7B$$
$$^1D = A - 3B + 2C$$
$$^3F = A - 8B$$
$$^1G = A + 4B + 2C \tag{1.64}$$

where the triplets are expressed only in terms of A and B and the parameter C contributes only to the singlets.

4.2.1.2. *Electrostatic parameters and matrix elements for the configuration* f^2

The electrostatic parameters for f^2 are defined through the following formulae:

$$E^0 = F_0 - 10F_2 - 33F_4 - 286F_6 \qquad E^1 = (70F_2 + 231F_4 + 2002F_6)/9$$
$$E^2 = (F_2 - 3F_4 + 7F_6)/9 \qquad E^3 = (5F_2 + 6F_4 - 91F_6)/3 \tag{1.65}$$

In terms of these parameters the terms of f^2 are expressed as follows:

$$^1S = E^0 + 9E^1$$
$$^3P = E^0 + 33E^3$$
$$^1D = E^0 + 2E^1 + 286E^2 - 11E^3$$
$$^3F = E^0$$
$$^1G = E^0 + 2E - 260E^2 - 4E^3$$
$$^3H = E^0 - 9E^3$$
$$^1I = E^0 + 2E^1 + 70E^2 + 7E^3 \tag{1.66}$$

4.2.1.3. *Definitions of the electrostatic CI parameters*

f^2–d^2 *configurations*

$$G_1(\mathrm{ff, dd}) = \frac{1}{35} R^1(\mathrm{ff, dd}) = G_1(\mathrm{fd})$$

$$G_3(\mathrm{ff, dd}) = \frac{1}{315} R^3(\mathrm{ff, dd}) = G_3(\mathrm{fd})$$

$$G_5(\mathrm{ff, dd}) = \frac{1}{1524.6} R^5(\mathrm{ff, dd}) = G_5(\mathrm{fd})$$

f^2–p^2 *configurations*

$$G_2(\mathrm{ff, pp}) = \frac{1}{175} R^2(\mathrm{ff, pp}) = G_2(\mathrm{fp})$$

$$G_4(\mathrm{ff, pp}) = \frac{1}{189} R^4(\mathrm{ff, pp}) = G_4(\mathrm{fp})$$

f^2–s^2 *configurations*

$$G_3(\mathrm{ff, ss}) = \frac{1}{7} R^3(\mathrm{ff, ss}) = G_3(\mathrm{fs})$$

d^2–p^2*configurations*

$$G_1(\mathrm{dd, pp}) = \frac{1}{15} R^1(\mathrm{dd, pp}) = G_1(\mathrm{dp})$$

$$G_3(\mathrm{dd, pp}) = \frac{1}{245} R^3(\mathrm{dd, pp}) = G_3(\mathrm{dp})$$

d^2–s^2 *configurations*

$$G_2(\mathrm{dd, ss}) = \frac{1}{5} R^2(\mathrm{dd, ss}) = G_2(\mathrm{ds})$$

p^2–s^2 *configurations*

$$G_1(\mathrm{pp, ss}) = \frac{1}{3} R^1(\mathrm{pp, ss}) = G_1(\mathrm{sp})$$

f^2–fp *configurations*

$$L_2 = \frac{1}{525} R^2(\mathrm{ff, fp})$$

$$L_4 = \frac{1}{693} R^4(\mathrm{ff, fp})$$

f^2–ds *configurations*

$$N = \frac{1}{21} R^3(\mathrm{ff, ds}) = \frac{1}{21} R^3(\mathrm{fd, sf})$$

fp–d^2 *configurations*

$$R_1 = \frac{1}{35} R^1(\mathrm{fp, dd}) = \frac{1}{35} R^1(\mathrm{fd, dp})$$

$$R_3 = \frac{1}{735} R^3(\mathrm{fp, dd}) = \frac{1}{735} R^3(\mathrm{fd, dp})$$

fp–ds *configurations*

$$T_1 = \frac{1}{5} R^1(\mathrm{fp}, \mathrm{ds}) = \frac{1}{5} R^1(\mathrm{fs}, \mathrm{dp})$$

$$T_3 = \frac{1}{35} R^3(\mathrm{fp}, \mathrm{sd}) = \frac{1}{35} R^3(\mathrm{fd}, \mathrm{sp})$$

fp–p^2 *configurations*

$$P_2 = \frac{1}{25} R^2(\mathrm{fp}, \mathrm{pp})$$

d^2–ds *configurations*

$$H = \frac{1}{35} R^2(\mathrm{dd}, \mathrm{ds})$$

p^2–ds *configurations*

$$K = \frac{1}{3} R^1(\mathrm{pp}, \mathrm{ds}) = \frac{1}{3} R^1(\mathrm{dp}, \mathrm{ps})$$

fd–fs *configurations*

$$M = \frac{1}{15} R^2(\mathrm{fd}, \mathrm{fs})$$

$$N = \frac{1}{21} R^3(\mathrm{fd}, \mathrm{sf}) = \frac{1}{21} R^3(\mathrm{ff}, \mathrm{ds})$$

fd–dp *configurations*

$$R_1 = \frac{1}{35} R^1(\mathrm{fd}, \mathrm{dp}) = \frac{1}{35} R^1(\mathrm{fp}, \mathrm{dd})$$

$$R_3 = \frac{1}{735} R^3(\mathrm{fd}, \mathrm{dp}) = \frac{1}{735} R^3(\mathrm{fp}, \mathrm{dd})$$

$$R_2 = \frac{1}{245} R^2(\mathrm{fd}, \mathrm{pd})$$

$$R_4 = \frac{1}{441} R^4(\mathrm{fd}, \mathrm{pd})$$

fd–sp *configurations*

$$T_3 = \frac{1}{35} R^3(\mathrm{fd}, \mathrm{sp}) = \frac{1}{35} R^3(\mathrm{fp}, \mathrm{sd})$$

$$T_2 = \frac{1}{35} R^2(\mathrm{fd}, \mathrm{ps}) = \frac{1}{35} R^2(\mathrm{fs}, \mathrm{pd})$$

fs–dp *configurations*

$$T_1 = \frac{1}{5} R^1(\mathrm{fs}, \mathrm{dp}) = \frac{1}{5} R^1(\mathrm{fp}, \mathrm{ds})$$

$$T_2 = \frac{1}{35} R^2(\mathrm{fs}, \mathrm{pd}) = \frac{1}{35} R^2(\mathrm{fd}, \mathrm{ps})$$

dp–sp *configurations*

$$J = \frac{1}{5} R^2(\mathrm{dp}, \mathrm{sp})$$

$$K = \frac{1}{3} R^1(\mathrm{dp}, \mathrm{ps}) = \frac{1}{3} R^1(\mathrm{pp}, \mathrm{ds})$$

4.2.1.4. *Matrix elements of the electrostatic interaction between two-electron configurations*

$$\{\mathrm{f}^2\,{}^1\mathrm{D}\{|e^2/r_{12}|\}\mathrm{fp}\,{}^1\mathrm{D}\} = -12\sqrt{42}\,L_2 - 22\sqrt{42}\,L_4$$
$$\{\mathrm{f}^2\,{}^3\mathrm{F}\{|e^2/r_{12}|\}\mathrm{fp}\,{}^3\mathrm{F}\} = -30\sqrt{21}\,L_2 + 22\sqrt{21}\,L_4$$
$$\{\mathrm{f}^2\,{}^1\mathrm{G}\{|e^2/r_{12}|\}\mathrm{fp}\,{}^1\mathrm{G}\} = -10\sqrt{231}\,L_2 - 2\sqrt{231}\,L_4$$
$$\{\mathrm{f}^2\,{}^1\mathrm{S}\{|e^2/r_{12}|\}\mathrm{p}^2\,{}^1\mathrm{S}\} = 15\sqrt{21}\,G_2(\mathrm{fp}) + 12\sqrt{21}\,G_4(\mathrm{fp})$$
$$\{\mathrm{f}^2\,{}^3\mathrm{P}\{|e^2/r_{12}|\}\mathrm{p}^2\,{}^3\mathrm{P}\} = 15\sqrt{14}\,G_2(\mathrm{fp}) - 9\sqrt{14}\,G_4(\mathrm{fp})$$
$$\{\mathrm{f}^2\,{}^1\mathrm{D}\{|e^2/r_{12}|\}\mathrm{p}^2\,{}^1\mathrm{D}\} = 9\sqrt{14}\,G_2(\mathrm{fp}) + 3\sqrt{14}\,G_4(\mathrm{fp})$$
$$\{\mathrm{f}^2\,{}^1\mathrm{S}\{|e^2/r_{12}|\}\mathrm{d}^2\,{}^1\mathrm{S}\} = -3\sqrt{35}\,G_1(\mathrm{fd}) - 12\sqrt{35}\,G_3(\mathrm{fd}) - 66\sqrt{35}\,G_5(\mathrm{fd})$$
$$\{\mathrm{f}^2\,{}^3\mathrm{P}\{|e^2/r_{12}|\}\mathrm{d}^2\,{}^3\mathrm{P}\} = -2\sqrt{70}\,G_1(\mathrm{fd}) - 3\sqrt{70}\,G_3(\mathrm{fd}) + 33\sqrt{70}\,G_5(\mathrm{fd})$$
$$\{\mathrm{f}^2\,{}^1\mathrm{D}\{|e^2/r_{12}|\}\mathrm{d}^2\,{}^1\mathrm{D}\} = -6\sqrt{6}\,G_1(\mathrm{fd}) + 11\sqrt{6}\,G_3(\mathrm{fd}) - 55\sqrt{6}\,G_5(\mathrm{fd})$$
$$\{\mathrm{f}^2\,{}^3\mathrm{F}\{|e^2/r_{12}|\}\mathrm{d}^2\,{}^3\mathrm{F}\} = -3\sqrt{15}\,G_1(\mathrm{fd}) + 8\sqrt{15}\,G_3(\mathrm{fd}) + 11\sqrt{15}\,G_5(\mathrm{fd})$$
$$\{\mathrm{f}^2\,{}^1\mathrm{G}\{|e^2/r_{12}|\}\mathrm{d}^2\,{}^1\mathrm{G}\} = -\sqrt{55}\,G_1(\mathrm{fd}) - 4\sqrt{55}\,G_3(\mathrm{fd}) - \sqrt{55}\,G_5(\mathrm{fd})$$
$$\{\mathrm{f}^2\,{}^1\mathrm{D}\{|e^2/r_{12}|\}\mathrm{ds}\,{}^1\mathrm{D}\} = \frac{2}{5}\sqrt{210}\,N$$
$$\{\mathrm{f}^2\,{}^1\mathrm{S}\{|e^2/r_{12}|\}\mathrm{s}^2\,{}^1\mathrm{S}\} = -\sqrt{7}\,G_3(\mathrm{fs})$$
$$\{\mathrm{fp}\,{}^1\mathrm{D}\{|e^2/r_{12}|\}\mathrm{p}^2\,{}^1\mathrm{D}\} = -6\sqrt{3}\,P_2$$
$$\{\mathrm{fp}\,{}^1\mathrm{D}\{|e^2/r_{12}|\}\mathrm{d}^2\,{}^1\mathrm{D}\} = 2\sqrt{7}\,R_1 + 72\sqrt{7}\,R_3$$
$$\{\mathrm{fp}\,{}^3\mathrm{F}\{|e^2/r_{12}|\}\mathrm{d}^2\,{}^3\mathrm{F}\} = 2\sqrt{35}\,R_1 - 18\sqrt{35}\,R_3$$
$$\{\mathrm{fp}\,{}^1\mathrm{G}\{|e^2/r_{12}|\}\mathrm{d}^2\,{}^1\mathrm{G}\} = 2\sqrt{105}\,R_1 + 2\sqrt{105}\,R_3$$
$$\{\mathrm{fp}\,{}^{1,3}\mathrm{D}\{|e^2/r_{12}|\}\mathrm{ds}\,{}^{1,3}\mathrm{D}\} = -\sqrt{5}\,T_1 \mp 3\sqrt{5}\,T_3$$
$$\{\mathrm{p}^2\,{}^1\mathrm{S}\{|e^2/r_{12}|\}\mathrm{d}^2\,{}^1\mathrm{S}\} = -2\sqrt{15}\,G_1(\mathrm{dp}) - 21\sqrt{15}\,G_3(\mathrm{dp})$$
$$\{\mathrm{p}^2\,{}^3\mathrm{P}\{|e^2/r_{12}|\}\mathrm{d}^2\,{}^3\mathrm{P}\} = -3\sqrt{5}\,G_1(\mathrm{dp}) + 21\sqrt{5}\,G_3(\mathrm{dp})$$
$$\{\mathrm{p}^2\,{}^1\mathrm{D}\{|e^2/r_{12}|\}\mathrm{d}^2\,{}^1\mathrm{D}\} = -\sqrt{21}\,G_1(\mathrm{dp}) - 3\sqrt{21}\,G_3(\mathrm{dp})$$

$$\{p^2\ ^1D\{|e^2/r_{12}|\}ds\ ^1D\} = \frac{2}{5}\sqrt{15}\ K$$

$$\{p^2\ ^1S\{|e^2/r_{12}|\}s^2\ ^1S\} = -\sqrt{3}\ G_1(sp)$$

$$\{d^2\ ^1D\{|e^2/r_{12}|\}ds\ ^1D\} = -2\sqrt{35}\ H$$

$$\{d^2\ ^1S\{|e^2/r_{12}|\}s^2\ ^1S\} = \sqrt{5}\ G_2(ds)$$

$$\{fd\ ^{1,3}F\{|e^2/r_{12}|\}fs\ ^{1,3}F\} = -2\sqrt{3}\ M \mp 2\sqrt{3}\ N$$

$$\{fd\ ^{1,3}P\{|e^2/r_{12}|\}dp\ ^{1,3}P\} = -7\sqrt{6}\ R_1 - 42\sqrt{6}\ R_3 \mp (7\sqrt{6}\ R_2 + 42\sqrt{6}\ R_4)$$

$$\{fd\ ^{1,3}D\{|e^2/r_{12}|\}dp\ ^{1,3}D\} = -14R_1 + 126R_3 \pm (42R_2 - 42R_4)$$

$$\{fd\ ^{1,3}F\{|e^2/r_{12}|\}dp\ ^{1,3}F\} = -2\sqrt{21}\ R_1 - 12\sqrt{21}\ R_3 \mp (12\sqrt{21}\ R_2 + 2\sqrt{21}\ R_4)$$

$$\{fd\ ^{1,3}P\{|e^2/r_{12}|\}sp\ ^{1,3}P\} = 5\sqrt{3}\ T_3 \pm 7\sqrt{3}\ T_2$$

$$\{fs\ ^{1,3}F\{|e^2/r_{12}|\}dp\ ^{1,3}F\} = \frac{5}{7}\sqrt{7}\ T_1 \pm 3\sqrt{7}\ T_2$$

$$\{dp\ ^{1,3}P\{|e^2/r_{12}|\}sp\ ^{1,3}P\} = -\sqrt{2}\ J \mp \sqrt{2}\ K$$

4.2.2. *Three-electron configurations*

Theoretical formulae for the matrix elements of the electrostatic interaction *within* and *between* all possible types of three-electron configurations were constructed by Z.B. Goldschmidt, both in explicit form (Z.B. Goldschmidt, 1968a; Fano et al., 1963) and as linear combinations of two-electron matrix elements (Z.B. Goldschmidt, 1968a, 1971). These quite lengthy formulae will not be included here.

4.2.3. $(nl)^N$ *configurations*

Two general methods, both of which are due to Racah (1943, 1949) can be used for obtaining the matrix elements of the electrostatic interaction within l^N configurations. According to the first method, one uses the electrostatic matrix elements within the configuration l^2 and the "two-electron" coefficients of fractional parentage which connect antisymmetric states of l^N with those of l^{N-2} and l^2. These can be expressed in terms of the "one-electron" coefficients of fractional parentage, which respectively connect the antisymmetric states of l^N and l^{N-1} with those of l^{N-1} and l^{N-2}.

$$\{l^N\alpha SL\{|H_1|\}l^N\alpha' SL\} = \frac{1}{2}N(N-1)\sum_{\substack{\alpha_1 S_1 L_1 \\ S_2 L_2}} (l^N\alpha SL\{|l^{N-2}(\alpha_1 S_1 L_1), l^2(S_2 L_2), SL)$$

$$\times \{l^2 S_2 L_2|e^2/r|l^2 S_2 L_2\}(l^{N-2}(\alpha_1 S_1 L_1), l^2(S_2 L_2), SL|\}l^N\alpha' \mathrm{SL}) \qquad (1.67)$$

where

$$(l^{N-2}(\alpha_1 S_1 L_1), l^2(S_2 L_2), SL|\}l^N\alpha SL) = \sum_{\alpha' S' L'} (S_1 L_1, l^2(S_2 L_2) SL|S_1 L_1 l(S' L')lSL)$$

$$\times (l^{N-2}(\alpha_1 S_1 L_1)l, S' L'|\}l^{N-1}\alpha' S' L')\ (l^{N-1}(\alpha' S' L')l, SL|\}l^N\alpha SL) \qquad (1.68)$$

and

$$(S_1L_1, l^2(S_2L_2)SL|S_1L_1l(S'L')lSL) = (-1)^{1+S_1+S+L_1+L}\{[S_2][S'][L_2][L']\}^{1/2}\begin{Bmatrix} S_1 & \frac{1}{2} & S' \\ \frac{1}{2} & S & S_2 \end{Bmatrix}\begin{Bmatrix} L_1 & l & L' \\ l & L & L_2 \end{Bmatrix}. \tag{1.69}$$

In the second method the electrostatic matrix elements for l^N are related to those for l^{N-1}:

$$(l^N\alpha SL\{|H_1|\}l^N\alpha' SL) = N(N-2)^{-1}\sum_{\alpha_1\alpha_1' S_1L_1}(l^N\alpha SL\{|l^{N-1}(\alpha_1S_1L_1)lSL) \times (l^{N-1}\alpha_1S_1L_1\{|H_1|\}l^{N-1}\alpha_1'S_1L_1)(l^{N-1}(\alpha_1'S_1L_1)lSL|\}l^N\alpha' SL). \tag{1.70}$$

The use of this method necessitates a chain calculation starting from $N = 2$. However, its advantage over the first method lies in the fact that the use of the coefficients (1.68) can be avoided.

Although the use of any one of these two methods completely solves the problem of calculating the matrix elements of H_1 for l^N configurations, several short-cuts can be achieved corresponding to various special cases. These also are due to Racah (1943, 1949). He defined unit tensor-operators $\boldsymbol{u}^{(k)}$ such that

$$(nl\|\boldsymbol{u}^{(k)}\|n'l') = \delta(n, n')\delta(l, l') \tag{1.71}$$

For a system of N electrons the following unit operators can be defined

$$\boldsymbol{U}^{(k)} = \sum_{i=1}^{N}\boldsymbol{u}_i^{(k)}, \tag{1.72}$$

the reduced matrix elements of which between states of l^N are given by the following formula:

$$(l^N\alpha SL\|\boldsymbol{U}^{(k)}\|l^N\alpha' S'L') = N\delta(S, S')\{[L][L']\}^{1/2}\sum_{\alpha_1S_1L_1}(l^N\alpha SL\{|l^{N-1}(\alpha_1S_1L_1)lSL) \times (l^{N-1}(\alpha_1S_1L_1)lSL|\}l^N\alpha' S'L')(-1)^{L_1+l+L+k}\begin{Bmatrix} L & k & L' \\ l & L_1 & l \end{Bmatrix}. \tag{1.73}$$

The matrix elements of H_1 for the configuration l^N can now be expressed (up to an additive constant) in terms of the matrix elements of the scalar product $\boldsymbol{U}^{(k)} \cdot \boldsymbol{U}^{(k)}$:

$$\{(nl)^N\alpha SL\{|H_1|\}(nl)^N\alpha' SL\} = \frac{1}{2}\sum_{k\,\text{even}}F^k(nl, nl)(l\|\boldsymbol{C}^{(k)}\|l)^2\{l^N\alpha SL|\boldsymbol{U}^{(k)} \cdot \boldsymbol{U}^{(k)}|l^N\alpha' SL\} = \frac{1}{2}\sum_{k\,\text{even}}F^k(nl, nl)(l\|\boldsymbol{C}^{(k)}\|l)^2\sum_{\alpha''S''L''}(-1)^{L+L''}(2L+1)^{-1}(l^N\alpha SL\|\boldsymbol{U}^{(k)}\|l^N\alpha'' S''L'') \times (l^N\alpha'' S''L''\|\boldsymbol{U}^{(k)}\|l^N\alpha' SL). \tag{1.74}$$

(The additive constant equals $-\frac{1}{2}\delta(\alpha, \alpha')(l\|\boldsymbol{C}^{(k)}\|l)^2N(2l+1)^{-1}$).

On investigating the structure of l^N configurations on the basis of the theory of seniority, Racah (1943) obtained the following relations between the reduced

matrix elements of $\boldsymbol{U}^{(k)}$ (k even) for l^N configurations and the corresponding ones for l^v configurations:

$$(l^N\alpha vSL\|\boldsymbol{U}^{(k)}\|l^N\alpha' vS'L') = [(2l+1-N)/(2l+1-v)] \times (l^v\alpha vSL\|\boldsymbol{U}^k\|l^v\alpha' vS'L'), \tag{1.75}$$

$$(l^N\alpha vSL\|\boldsymbol{U}^k\|l^N\alpha' v-2\,S'L') = \{(N+2-v)(4l+4-N-v)/4(2l+2-v)\}^{1/2} \times (l^v\alpha vSL\|\boldsymbol{U}^k\|l^v\alpha' v-2\,S'L') \tag{1.76}$$

matrix elements with $\Delta v \neq 0, \pm 2$ vanish. These relations greatly simplify the calculations of the desired matrix elements for l^N if those for l^v are known.

4.2.3.1. $(nl)^N$ *configurations comprising almost closed shells*

The matrix elements of the electrostatic interaction for $(nl)^{4l+2-N}$ are equal to the corresponding ones of $(nl)^N$. This conclusion is obtained through the use of the following relation, also obtained by Racah (1942b)

$$(l^{4l+2-N}\alpha SL\|\boldsymbol{U}^{(k)}\|l^{4l+2-N}\alpha' S'L') = -(-1)^k(l^N\alpha SL\|\boldsymbol{U}^{(k)}\|l^N\alpha' S'L')^* \tag{1.77}$$

and as a result of the fact that each of the coefficients of F^k comprises a product of two reduced matrix elements of $\boldsymbol{U}^k$.

4.2.3.2. *The case of the half-filled shell* $(nl)^{2l+1}$

The configuration $(nl)^{2l+1}$ can be looked upon as a configuration comprising $2l+1$ electrons or $2l+1$ holes. The eigenfunctions corresponding to $2l+1$ electrons and to $2l+1$ holes will be designated respectively as

$$\psi_L(l^{2l+1}\alpha vSL) \quad \text{and} \quad \psi_R(l^{2l+1}\alpha vSL).$$

The following relation holds between these eigenfunctions (formula 65 of Racah 1943):

$$\psi_R(l^{2l+1}\alpha vSL) = (-1)^{(v-1)/2}\psi_L(l^{2l+1}\alpha vSL) \tag{1.78}$$

Substitution of (1.78) in (1.77) for $N = 2l+1$ results in

$$(l_R^{2l+1}\alpha vSL\|\boldsymbol{U}^{(k)}\|l_R^{2l+1}\alpha' v'S'L') = (-1)^{(v+v'-2)/2}(l_L^{2l+1}\alpha vSL\|\boldsymbol{U}^{(k)}\|l_L^{2l+1}\alpha' v'S'L') = -(-1)^k(l_L^{2l+1}\alpha vSL\|\boldsymbol{U}^{(k)}\|l_L^{2l+1}\alpha' v'S'L'). \tag{1.79}$$

Therefore

$$(l^{2l+1}\alpha vSL\|\boldsymbol{U}^{(k)}\|l^{2l+1}\alpha' v'S'L') = (-1)^{k+(v+v')/2}(l^{2l+1}\alpha vSL\|\boldsymbol{U}^{(k)}\|l^{2l+1}\alpha' v'S'L') \tag{1.80}$$

*This relation holds for any value of k except for $k = 0$ in which case the relation holds apart from a constant diagonal term.

for $2l+1$ electrons or holes. In our case k is even and v and v' are odd; therefore $(l^{2l+1}\alpha vSL\|U^{(k)}\|l^{2l+1}\alpha' v'S'L')$ vanishes in case $v' = v$ ($\Delta v = 0$), and may be different from zero for $\Delta v = \pm 2$. Hence the matrix elements of the electrostatic interaction, which comprise products of two reduced matrix elements of $U^{(k)}$ satisfy, for half-filled shells, the selection rule $\Delta v = 0, \pm 4$.

4.2.3.3. f^N *configurations. The choice of the electrostatic parameters*

In section 3.2.1.3 a description has been given of the classification of the states of the configurations f^N in terms of the irreducible representations W and U of the groups R_7 and G_2. For the purpose of studying the properties of the matrix elements of H_1 for f^N configurations, it is necessary to express also H_1 as a sum of terms, each of which corresponds to the irreducible representations W and U of R_7 and G_2. This was done by Racah (1949), when he expressed H_1 in terms of

$$e_0E^0 + e_1E^1 + e_2E^2 + e_3E^3 \tag{1.81}$$

instead of

$$f^0F_0 + f^2F_2 + f^4F_4 + f^6F_6 \quad \text{or} \quad f_0F^0 + f_2F^2 + f_4F^4 + f_6F^6 \tag{1.82}$$

where

$$f^k = D_k f_k. \tag{1.83}$$

The definition of the parameters E^i was given in formula (1.65). The coefficients e_i of E^i are given below in terms of the f^k's

$$\begin{aligned} e_0 &= f^0 = N(N-1)/2 \\ e_1 &= 9f^0/7 + f^2/42 + f^4/77 + f^6/462 \\ e_2 &= 143f^2/42 - 130f^4/77 + 35f^6/462 \\ e_3 &= 11f^2/42 + 4f^4/77 - 7f^6/462 \end{aligned} \tag{1.84}$$

and correspond to

$$WUL = (000)(00)0,\ (000)(00)0,\ (400)(40)0,\ (220)(22)0,$$

respectively.

The eigenvalues of e_0 and e_1 are easily obtained for all terms of f^N since they are both scalars also with respect to R_7 and G_2. The eigenvalues of e_0 equal $\frac{1}{2}N(N-1)$ for all terms of f^N. e_1 is diagonal in the scheme $vUSL$ and its eigenvalues are independent of U and L. It follows from formula (1.66) that

$$e_1(f^2SL) = q_{12} + \frac{1}{2} - 2(s_1 \cdot s_2) \tag{1.85}$$

where q_{12} is the seniority operator for f^2. Using formula (1.36) and the relation

$$\sum_{i>j} 2(s_i \cdot s_j) = S(S+1) - \frac{3}{4}N \tag{1.86}$$

one obtains the eigenvalues of e_1

$$e_1(\mathrm{f}^N v U S L) = \frac{9}{2}(N - v) + \frac{1}{4} v(v+2) - S(S+1). \tag{1.87}$$

This means that e_1 vanishes for terms of highest multiplicity of f^N for which $N = v = 2S$. The calculation of the matrix elements of e_2 and e_3 is somewhat more complicated. The appropriate formulae for these matrix elements were given by Racah (1949), including tables for the quantities appearing in these formulae, for all terms of f^N. It is worthwhile to mention the following properties of e_2 and e_3: e_2 is diagonal with respect to v and vanishes for $v = 2S$; therefore e_2 does not contribute to the terms of highest multiplicity of f^N. For these terms the matrix elements of e_3 are given by the following formula (Judd, 1963):

$$\{\mathrm{f}^N, v = N, U, {}^{N+1}L | e_3 | \mathrm{f}^N, v = N, U, {}^{N+1}L\}$$
$$= 3(u_1^2 + u_2^2 + u_1 u_2 + u_1 u_2 + 5u_1 + 4u_2) - \frac{3}{2} L(L+1) \tag{1.88}$$

where $(u_1 u_2) = U$. The spacings among terms of highest multiplicity can, therefore, be expressed in terms of the parameter E^3 only. Since terms of highest multiplicity for f^N, f^{7-N}, f^{7+N} and f^{14-N} (where $0 \leqslant N \leqslant 7$) belong to the same irreducible representations WU of R_7 and G_2 respectively, they all have the same energy spacings. Their positions in terms of E^3 are given in fig. 1.9 for $0 \leqslant N \leqslant 7$, assuming that E^3 is the same for all configurations. The explicit calculations of the matrices of H_1 for all f^N configurations has been carried out by Racah (1942b), Z.B. Goldschmidt (1968a), Reilly (1953), Wybourne (1961) and Runciman (1962).

4.2.4. *$(nl)^N n'l'$ configurations* (Judd, 1962; Fano et al., 1963; Wybourne, 1965; Z.B. Goldschmidt, 1971)

The matrix elements of the electrostatic interaction within $l^N l'$ configurations can be written as a sum of two parts: (1) matrix elements within the l^N core; these are the same as the matrix elements for l^N configurations and are diagonal in all quantum numbers of the electrons outside the core. (2) Matrix elements between l^N and l'; these are given by the following formula:

$$\{(nl)^N(\alpha_1 S_1 L_1) n'l' SL \{|H_1|\} (nl)^N(\alpha_1' S_1' L_1') n'l' SL\}$$
$$= \sum_k f_k F^k(nl, n'l') + \sum_k g_k G^k(nl, n'l') \tag{1.89}$$

where

$$f_k = \delta(S_1, S_1')(-1)^{L_1' + L + l}[l][l']$$
$$\times \begin{pmatrix} l & k & l \\ 0 & 0 & 0 \end{pmatrix} \begin{pmatrix} l' & k & l' \\ 0 & 0 & 0 \end{pmatrix} \begin{Bmatrix} L_1 & k & L_1' \\ l' & L & l' \end{Bmatrix} (l^N \alpha_1 S_1 L_1 \| U^{(k)} \| l^N \alpha_1' S_1' L_1') \tag{1.90}$$

or

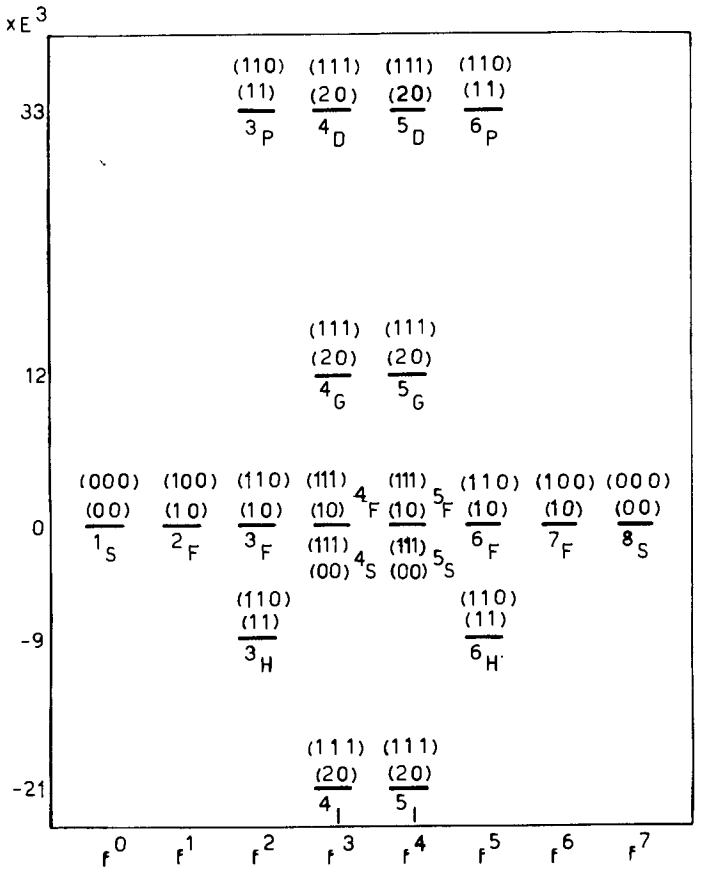

Fig. 1.9. The energies of the terms of maximum multiplicity of f^N as multiples of E^3.

$$f_k = N \sum_{\bar{\alpha}\bar{S}\bar{L}} \delta(S_1, S_1')(-1)^{\bar{L}+L_1+L_1'+L}(l^N(\alpha_1 S_1 L_1)\{|l^{N-1}(\bar{\alpha}\bar{S}\bar{L})lS_1L_1)$$
$$\times (l^{N-1}(\bar{\alpha}\bar{S}\bar{L})lS_1'L_1'|\}l^N(\alpha_1'S_1'L_1'))\{[L_1][L_1']\}^{1/2}[l][l']$$
$$\times \begin{pmatrix} l & k & l \\ 0 & 0 & 0 \end{pmatrix}\begin{pmatrix} l' & k & l' \\ 0 & 0 & 0 \end{pmatrix}\begin{Bmatrix} L_1 & k & L_1' \\ l & \bar{L} & l \end{Bmatrix}\begin{Bmatrix} L_1 & k & L_1' \\ l' & L & l' \end{Bmatrix} \tag{1.91}$$

and

$$g_k = N \sum_{\bar{\alpha}\bar{S}\bar{L}} (-1)^{S_1+S_1'}(l^N(\alpha_1 S_1 L_1)\{|l^{N-1}(\bar{\alpha}\bar{S}\bar{L})lS_1L_1)(l^{N-1}(\bar{\alpha}\bar{S}\bar{L})lS_1'L_1'|\}l^N(\alpha_1'S_1'L_1'))$$
$$\times \{[S_1][L_1][S_1'][L_1']\}^{1/2}[l][l']\begin{pmatrix} l & k & l' \\ 0 & 0 & 0 \end{pmatrix}^2\begin{Bmatrix} \frac{1}{2} & S & S_1 \\ \frac{1}{2} & \bar{S} & S_1' \end{Bmatrix}\begin{pmatrix} \bar{L} & l & L_1 \\ l & k & l' \\ L_1' & l' & L \end{pmatrix}. \tag{1.92}$$

4.2.4.1. *Conjugate configurations of the type* $(nl)^{4l+2-N}n'l'$

(*a*) *Direct part*

For $(nl)^{4l+2-N}n'l'$, the direct part of the electrostatic interaction between the core electrons $(nl)^{4l+2-N}$ and the outer electron $n'l'$ is equal in magnitude and opposite in sign to the direct part of this interaction for $(nl)^N n'l'$. This conclusion follows immediately from formulae (1.90) and (1.77).

(*b*) *Exchange part*

For configurations of the type $(nl)^{4l+1}n'l'$ comprising an electron and a hole, the following results have been obtained (Condon et al., 1951; Racah, 1942b; Z.B. Goldschmidt, 1971):

(1) For a given SL term the exchange interaction is given (up to an additive constant common to all terms) by the formula

$$\sum_k g_k G^k(nl, n'l') = \sum_k 2[l][l']\begin{pmatrix} l & k & l' \\ 0 & 0 & 0 \end{pmatrix}^2 \delta(S, 0)\delta(k, L)G^k(nl, n'l')/(2k+1) \tag{1.93}$$

This means that the exchange interaction is different from zero only for singlets, and among the singlets, only for those having $L = k$.

(2) The total sum of the splittings between singlets and triplets remains invariant on passing from the two-electron configuration ll' to the configuration $l^{4l+1}l'$ comprising an electron and a hole. This result can be proved by starting out from that part of formula (1.59) which represents the exchange interaction $l - l'$, and disregarding the $(-1)^{S+l+l'+L}$ phase factor which is responsible for the alternation rule. For a given SL term one has

$$\begin{aligned} \sum_k g_k G^k(-1)^{S+l+l'+L} &= \sum_k (-1)^{l+l'+L}(l\|C^{(k)}\|l')^2 \begin{Bmatrix} l & l' & k \\ l & l' & L \end{Bmatrix} G^k \\ &= \sum_k (-1)^{L+k}[l][l']\begin{pmatrix} l & k & l' \\ 0 & 0 & 0 \end{pmatrix}^2 \begin{Bmatrix} l & l' & k \\ l & l' & L \end{Bmatrix} G^k. \end{aligned} \tag{1.94}$$

The expression representing the totality of the singlet–triplet splittings, obtained by multiplying formula (1.94) by two and summing over L, is

$$\sum_k 2[l][l']\begin{pmatrix} l & k & l' \\ 0 & 0 & 0 \end{pmatrix}^2 G^k(nl, n'l')/(2k+1). \tag{1.95}$$

The last expression is identical with (1.93).

The results and conclusions obtained in this paragraph can easily be generalized to the electrostatic interaction between the configurations $(nl)^N n'l'$ and $(nl)^N n''l''$ (Z.B. Goldschmidt, 1971).

Formulae for the matrix elements of the electrostatic interaction for more complicated configurations have been constructed by various authors (Rosenzweig, 1952; Wybourne, 1963; Nir, 1969) and will not be given here.

Recently, several types of computer programs have been constructed, for obtaining the numerical values of the algebraic matrix elements. Some of them use, as input data, formulae of the types given in the last and the following

paragraphs (Stein, 1967; Bordarier, 1966), whereas others use only the tensor-operator form of the desired interaction together with lists of the interacting configurations (Bordarier, 1970; Oreg, 1973a, b).

4.3. *Matrix elements of the spin–orbit interaction*

Since

$$H_2 = \sum_i \xi_{n_i l_i}(\boldsymbol{l}_i \cdot \boldsymbol{s}_i)$$

is an operator of the type F, its matrix elements $(\psi\{|H_2|\}\psi')$ between two antisymmetric functions ψ and ψ' of the electronic system are more easily calculated than those of H_1. As was already stated in section 2, integration over the radial variables results in the following formula:

$$H_2 = \sum_i \zeta_{n_i l_i} \boldsymbol{l}_i \cdot \boldsymbol{s}_i, \tag{1.96}$$

the definition of the spin–orbit parameter $\zeta_{n_i l_i}$ was given in formula (1.15b). According to this definition $\zeta_{n_i l_i}$ are positive numbers.

4.3.1. *One-electron configurations*

Since

$$\boldsymbol{l} \cdot \boldsymbol{s} = \frac{1}{2}(\boldsymbol{j}^2 - \boldsymbol{l}^2 - \boldsymbol{s}^2)^*, \tag{1.97}$$

the matrix elements of H_2 for one electron configurations are given by the elementary formula

$$\zeta_{nl}(sljm|\boldsymbol{l} \cdot \boldsymbol{s}|sljm) = \frac{1}{2}\zeta_{nl}[j(j+1) - l(l+1) - s(s+1)]$$

$$= \begin{cases} \frac{1}{2}l\zeta_{nl} & \text{for} \quad j = l + \frac{1}{2} \\ -\frac{1}{2}(l+1)\zeta_{nl} & \text{for} \quad j = l - \frac{1}{2} \end{cases} \tag{1.98}$$

Hence all except s configurations split into two levels having the following properties:

(1) The level of the higher j lies above that of the lower.

(2) The splitting between the levels equals $\frac{1}{2}(2l+1)\zeta_{nl}$.

(3) The center of gravity of the levels remains unchanged on including H_2, when the levels are weighted according to their degeneracy.

*The property of H_2 to be diagonal in l follows from this formula; see footnote on page 29.

4.3.2. *Two-electron configurations*

In this case

$$H_2 = \zeta_{n_1 l_1}(\boldsymbol{l}_1 \cdot \boldsymbol{s}_1) + \zeta_{n_2 l_2}(\boldsymbol{l}_2 \cdot \boldsymbol{s}_2)$$

and the angular parts of the matrix elements are given by (Fano et al., 1959):

$$\begin{aligned}
&(\tfrac{1}{2} l_1 \tfrac{1}{2} l_2\, SLJM\{|\boldsymbol{l}_1 \cdot \boldsymbol{s}_1|\}\tfrac{1}{2} l_1 \tfrac{1}{2} l_2\, S'L'JM) \\
&\quad = (-1)^{l_1+l_2+L+L'+J+1}\{\tfrac{3}{2} l_1(l_1+1)(2l_1+1)[S][S'][L][L']\}^{1/2} \\
&\qquad \times \begin{Bmatrix} S & S' & 1 \\ \frac{1}{2} & \frac{1}{2} & \frac{1}{2} \end{Bmatrix} \begin{Bmatrix} L & L' & 1 \\ l_1 & l_1 & l_2 \end{Bmatrix} \begin{Bmatrix} S & S' & 1 \\ L' & L & J \end{Bmatrix}, \qquad (1.99)
\end{aligned}$$

$$\begin{aligned}
&(\tfrac{1}{2} l_1 \tfrac{1}{2} l_2\, SLJM\{|\boldsymbol{l}_2 \cdot \boldsymbol{s}_2|\}\tfrac{1}{2} l_1 \tfrac{1}{2} l_2\, S'L'JM) \\
&\quad = (-1)^{l_1+l_2+S+S'+J+1}\{\tfrac{3}{2} l_2(l_2+1)(2l_2+1)[S][S'][L][L']\}^{1/2} \\
&\qquad \times \begin{Bmatrix} S & S' & 1 \\ \frac{1}{2} & \frac{1}{2} & \frac{1}{2} \end{Bmatrix} \begin{Bmatrix} L & L' & 1 \\ l_2 & l_2 & l_1 \end{Bmatrix} \begin{Bmatrix} S & S' & 1 \\ L' & L & J \end{Bmatrix} \qquad (1.100)
\end{aligned}$$

In the particular case $l_1 = l_2$ the expressions (1.99) and (1.100) are equal if $S + L$ and $S' + L'$ have the same parity and differ in sign if $S + L$ and $S' + L'$ have opposite parities. For a configuration comprising two equivalent electrons $(n_1 l_1) = (n_2 l_2) = (nl)$ only terms with $S + L$ even are allowed. In this case it is enough to calculate only one of the expressions (1.99) or (1.100) and multiply the result by a factor of 2.

4.3.3. $(nl)^N$ *configurations*

In this case the angular part of the matrix elements is given by

$$\begin{aligned}
&\left(l^N \alpha SLJM \left\{\left|\sum_i \boldsymbol{l}_i \cdot \boldsymbol{s}_i\right|\right\} l^N \alpha' S'L'JM\right) \\
&\quad = (-1)^{S'+L+J}\{\tfrac{3}{2} l(l+1)(2l+1)\}^{1/2} \begin{Bmatrix} S & S' & 1 \\ L' & L & J \end{Bmatrix} \\
&\qquad \times (l^N \alpha SL \| \boldsymbol{V}^{(11)} \| l^N \alpha' S'L') \qquad (1.101)
\end{aligned}$$

where $\boldsymbol{V}^{(11)}$ is the double tensor

$$\boldsymbol{V}^{(11)} = \sum_i \boldsymbol{s}_i \boldsymbol{u}_i^{(1)} \qquad (1.102)$$

defined by Racah (1942b), and

$$\begin{aligned}
&(l^N \alpha SL \| \boldsymbol{V}^{(11)} \| l^N \alpha' S'L') = N(-1)^{1/2+l+S+L}\{[S][S'][L][L']\}^{1/2} \\
&\quad \times \sum_{\bar{\alpha}\bar{S}\bar{L}} (l^N \alpha SL\{|^{N-1}(\bar{\alpha}\bar{S}\bar{L})lSL)(l^{N-1}(\bar{\alpha}\bar{S}\bar{L})lS'L')\} l^N \alpha' S'L')(-1)^{\bar{S}+\bar{L}} \\
&\quad \times \begin{Bmatrix} S & 1 & S' \\ \frac{1}{2} & \bar{S} & \frac{1}{2} \end{Bmatrix} \begin{Bmatrix} L & 1 & L' \\ l & \bar{L} & l \end{Bmatrix}. \qquad (1.103)
\end{aligned}$$

For $S = S'$ and $L = L'$ one has

$$(-1)^{S'+L+J}\begin{Bmatrix} S & S' & 1 \\ L' & L & J \end{Bmatrix} = \tfrac{1}{2}[J(J+1) - L(L+1) - S(S+1)]$$
$$\times [S(S+1)(2S+1)L(L+1)(2L+1)]^{-1/2} \tag{1.104}$$

Since the matrix elements of $\boldsymbol{L} \cdot \boldsymbol{S}$ are given by $\frac{1}{2}[J(J+1) - L(L+1) - S(S+1)]$, the matrix elements of H_2 diagonal in L and S can be expressed as $\lambda \boldsymbol{L} \cdot \boldsymbol{S}$ where λ is a constant for a given (empirical) term. This is the mathematical expression of the *Landé interval rule* which states that within a Russell–Saunders multiplet the interval between two levels having consecutive J values is proportional to the higher J value of the pair.

For terms of maximum multiplicity and $N \leqslant 2l + 1$ all spins are "parallel" and H_2 can be written in the following form:

$$\zeta_{nl} \sum_i \boldsymbol{l}_i \cdot \boldsymbol{s}_i = \zeta_{nl} \left(\sum_i \boldsymbol{l}_i \right) \cdot \boldsymbol{s} = \zeta_{nl}(\boldsymbol{L} \cdot \boldsymbol{S})/N = \zeta_{nl}(\boldsymbol{L} \cdot \boldsymbol{S})/2S \tag{1.105}$$

Consequently, for terms of maximum multiplicity

$$\lambda = \zeta_{nl}/2S \tag{1.106}$$

and the matrix elements of H_2 for the levels belonging to these terms are given by the simple formula

$$(l^n \alpha S(=\tfrac{1}{2}N) LJM | \boldsymbol{L} \cdot \boldsymbol{S} | l^N \alpha S(=\tfrac{1}{2}N) LJM) \zeta_{nl}/2S$$
$$= \tfrac{1}{2}(J(J+1) - L(L+1) - S(S+1))\zeta_{nl}/2S \tag{1.107}$$

In this case, the interval between two adjacent levels belonging to a given term equals

$$J\zeta_{nl}/2S \tag{1.108}$$

where J is the higher J value of the pair, and is thus *independent of* L. Consequently, levels belonging to different terms of maximum multiplicity, and having the same J value, can thus be made to coincide, by displacing the centers of gravity of these terms. This property is illustrated in fig. 1.10 for the quintets of f^4.

The total splitting of terms of maximum multiplicity due to the spin–orbit interaction can also be calculated through the use of formula (1.107). It is found to be equal to

$$\tfrac{1}{2}(2L+1)\zeta_{nl} \text{ for terms with } L \geqslant S \tag{1.109}$$

and

$$L(2S+1)\zeta_{nl}/2S \text{ for terms with } L < S. \tag{1.110}$$

Judd (1963) has carried out a thorough analysis of the properties of the matrix elements of the spin–orbit interaction for f^N configurations through the use of the theory of continuous groups; he thus succeeded in explaining the vanishing of various matrix elements of this interaction.

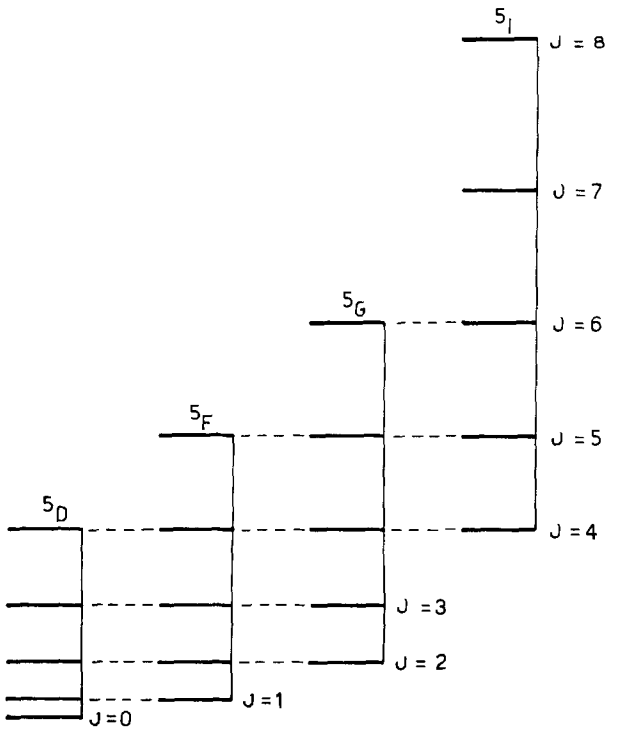

Fig. 1.10. The quintets of f^4; in the limit of LS coupling, these can be displaced so that all levels with the same J coincide.

4.3.3.1. $(nl)^N$ *configurations comprising almost closed shells*

The matrix elements of the spin–orbit interaction for $(nl)^{4l+2-N}$ are equal in magnitude but opposite in sign as compared to the corresponding ones in $(nl)^N$. This conclusion follows from formula (1.77) which is valid also when $\boldsymbol{V}^{(11)}$ is substituted for $\boldsymbol{U}^{(k)}$ and $2 = 1 + 1$ is substituted for k in the phase factor. The following formula holds for the reduced matrix elements of $\boldsymbol{V}^{(\kappa k)}$ (Racah, 1942b):

$$(l^{4l+2-N}\alpha SL\|\boldsymbol{V}^{(\kappa k)}\|l^{4l+2-N}\alpha' S'L') = -(-1)^{\kappa+k}(l^N\alpha SL\|\boldsymbol{V}^{(\kappa k)}\|l^N\alpha' S'L'). \qquad (1.111)$$

4.3.3.2. *The case of the half-filled shell*

All reduced matrix elements of $\boldsymbol{V}^{(11)}$ diagonal in v vanish for $(nl)^{2l+1}$ configurations; consequently all diagonal matrix elements of the spin–orbit interaction are zero. This conclusion follows immediately through the use of formula (1.111) and the relation (1.78) between the eigenfunctions corresponding to $2l + 1$ electrons and $2l + 1$ holes (see discussion in section 4.2.3.2) resulting in the following relation:

$$(l^{2l+1}\alpha vSL\|\boldsymbol{V}^{(\kappa k)}\|l^{2l+1}\alpha' v'S'L') = (-1)^{\kappa+k+(v+v')/2}(l^{2l+1}\alpha vSL\|\boldsymbol{V}^{(\kappa k)}\|l^{2l+1}\alpha' v'S'L') \qquad (1.112)$$

4.3.4. $(nl)^N n'l'$ *configurations*

The matrix elements of the spin–orbit interaction for $(nl)^N n'l'$ can be cal-

culated by using the following formula (Wybourne, 1965):

$$\{(nl)^N(\alpha_1 S_1 L_1)n'l'SLJ\{|H_2|\}(nl)^N(\alpha_1' S_1' L_1')n'l'S'L'J\}$$
$$= (-1)^{S'+L+J+S_1+L_1+l'+1/2}\{[S][L][S'][L']\}^{1/2}\begin{Bmatrix} S & S' & 1 \\ L' & L & J \end{Bmatrix}$$
$$\times\left[[l(l+1)(2l+1)]^{1/2}(-1)^{S'+L'}\begin{Bmatrix} S & S' & 1 \\ S_1' & S_1 & \frac{1}{2} \end{Bmatrix}\right.$$
$$\times\begin{Bmatrix} L & L' & 1 \\ L_1' & L_1 & l \end{Bmatrix}(l^N\alpha_1 S_1 L_1\|\boldsymbol{V}^{(11)}\|l^N\alpha_1' S_1' L_1')\zeta_{nl}$$
$$+[l'(l'+1)(2l'+1)]^{1/2}(-1)^{S+L}\delta(\alpha_1 S_1 L_1, \alpha_1' S_1' L_1')\begin{Bmatrix} S & S' & 1 \\ \frac{1}{2} & \frac{1}{2} & S_1 \end{Bmatrix}\begin{Bmatrix} L & L' & 1 \\ l' & l' & L_1 \end{Bmatrix}$$
$$\left.\times(\tfrac{1}{2}l'\|\boldsymbol{v}^{(11)}\|\tfrac{1}{2}l')\zeta_{n'l'}\right] \qquad (1.113)$$

In the conjugation process $(nl)^N n'l' \rightarrow (nl)^{4l+2-N}n'l'$, the coefficient of ζ_{nl} changes sign. For $N = 2l+1$, all coefficients of ζ_{nl} diagonal in the seniority quantum number v (characterizing the core states) vanish. These results follow immediately from formulae (1.111) and (1.112).

5. "Weak" interactions

Energy-level calculations conducted to first-order perturbation theory and based on the hamiltonian (1.2b), which comprises (only) the electrostatic and spin–orbit interactions, do indeed reproduce the energy level structure qualitatively; however, the quantitative agreement obtained between calculated and observed energy levels and other related properties is rather poor, even when all the radial integrals F^k, G^k, R^k and ζ are considered as adjustable parameters.

The fit between theory and experiment can be improved by adding two types of terms to the hamiltonian (1.2b). Terms of the first type represent the "mutual magnetic interactions." These interactions, which are of relativistic origin, are provided by the Breit equation (Bethe et al., 1957), which, in the nonrelativistic limit, breaks up into terms which can be given a simple physical interpretation (Bethe et al., 1957; Slater, 1960). All of these terms that are spin-independent (such as the orbit–orbit interaction, the retardation of the Coulomb interaction, and the relativistic correction due to the mass variation with velocity) are absorbed by the electrostatic parameters (real and effective*, including the additive constant). Into this category also falls the spin–spin contact term which is diagonal with respect to the total spin angular momentum of the electrons. The terms which are not absorbed are the spin–spin (ss) and the spin–other-orbit (soo) interactions, which, respectively represent the mutual interaction between the magnetic dipole moments of the electrons and between the dipole moment of one electron and the orbital motion of another. These will be discussed in

*See definition and explanation below.

section 6. Terms of the second type are known as "effective interactions", and represent, to second order perturbation theory, interactions with distant configurations. These will be discussed in section 7.

6. The mutual magnetic interactions

6.1. *Introduction*

Investigations of the effects of the mutual magnetic interactions on the energy level structure of atomic spectra date from the work of Breit on the $1snp\ ^3P$ terms of He I and Li II (Breit, 1930; Condon et al., 1951). Marvin (1947) computed the matrix elements of these interactions for two-electron configurations comprising s, p and d electrons. These, except for matrix elements involving equivalent electrons, were found to be in error. Jucys and his collaborators (1961) investigated, from a theoretical standpoint, the properties of these interactions in various complex configurations, thereby correcting and extending Marvin's results. Trees (1951) computed the matrix elements of the ss interaction for d^N configurations. Horie (1963) derived formulae in which the matrix elements of the ss and soo interactions for l^N configurations were expressed in terms of the unit tensor operators and double tensors defined by Racah. These formulae will be cited below. Blume, Freeman and Watson (1962, 1963, 1964) obtained Hartree–Fock values for the radial integrals describing the mutual magnetic interactions for various d^N and f^N configurations in transition-element and lanthanide ions, respectively. They also calculated the contribution of the two-electron soo interaction to the spin–orbit parameter ζ_{nl}, including exchange effects. Recently, systematic and thorough investigations on the effects of the mutual magnetic interactions on the energy level structure of various configurations of heavy atoms have been conducted by various authors (Z.H. Goldschmidt, 1967; Z.B. Goldschmidt et al., 1968; Judd et al., 1968; Crosswhite et al., 1968; Z.B. Goldschmidt, 1970; Judd, 1970; Pasternak et al., 1972; Z.B. Goldschmidt, 1973; Pasternak et al., 1974; Z.B. Goldschmidt and Ben-Ezra, 1975; Z.B. Goldschmidt and Cohen, 1975). The results of these investigations concerning the lanthanide spectra will be cited in the appropriate sections below.

6.2. *Expressions for the operators. Definitions of the parameters*

The spin–spin (ss) interaction can be included in the hamiltonian of an atomic system by adding the following term to expression (1.2b):

$$H_{ss} = 2\beta^2 \sum_{\substack{i,j \\ i \neq j}} [(\boldsymbol{s}_i \cdot \boldsymbol{s}_j) r_{ij}^2 - 3(\boldsymbol{r}_{ij} \cdot \boldsymbol{s}_i)(\boldsymbol{r}_{ij} \cdot \boldsymbol{s}_j)]/r_{ij}^5 \qquad (1.114)$$

where $\beta = e\hbar/2mc$. The tensor-operator form of this interaction can be written as (Judd, 1963; Innes, 1953)

$$H_{ss} = -\beta^2(5)^{-1/2}\sum_k (-1)^k\{(2k+5)!/(2k)!\}^{1/2}$$
$$\times\sum_{i\neq j}[(r_j^k/r_i^{k+3})([\boldsymbol{C}_i^{(k+2)}\times\boldsymbol{C}_j^{(k)}]^{(2)}\cdot[\boldsymbol{s}_i\times\boldsymbol{s}_j]^{(2)})$$
$$+(r_i^k/r_j^{k+3})([\boldsymbol{C}_i^{(k)}\times\boldsymbol{C}_j^{(k+2)}]^{(2)}\cdot[\boldsymbol{s}_i\times\boldsymbol{s}_j]^{(2)})] \tag{1.115}$$

On integrating over the radial variables r_i and r_j, either the first or the second term in the brackets will be included, in accordance with the fulfillment of $r_j < r_i$ or $r_i < r_j$ respectively.

The term in the hamiltonian representing the spin–other-orbit (soo) interaction can be expressed as

$$H_{soo} = 2\beta^2\sum_{i\neq j}[\nabla_i(1/r_{ij})\times\boldsymbol{p}_i]\cdot(\boldsymbol{s}_i+2\boldsymbol{s}_j) \tag{1.116}$$

its tensor operator form being

$$H_{soo} = \beta^2 2(3)^{-1/2}\sum_k(-1)^k$$
$$\times\sum_{i\neq j}\{(r_i^{k-2}/r_j^{k+1})(2k+1)(2k-1)^{1/2}[\boldsymbol{C}_j^{(k)}\times[\boldsymbol{C}^{(k)}\times\boldsymbol{l}]_i^{(k-1)}]^{(1)}$$
$$-(r_j^k/r_i^{k+3})(2k+1)(2k+3)^{1/2}[\boldsymbol{C}_j^{(k)}\times[\boldsymbol{C}^{(k)}\times\boldsymbol{l}]_i^{(k+1)}]^{(1)}$$
$$-(r_i^{k-2}/r_j^{k+1})(k+1)(2k+1)^{1/2}[\boldsymbol{C}_j^{(k)}\times[\boldsymbol{C}^{(k)}\times\boldsymbol{l}]_i^{(k)}]^{(1)}$$
$$+(r_j^k/r_i^{k+3})k(2k+1)^{1/2}[\boldsymbol{C}_j^{(k)}\times[\boldsymbol{C}^{(k)}\times\boldsymbol{l}]_i^{(k)}]^{(1)}$$
$$+(r_i^{k-1}/r_j^{k+1})(\partial/\partial r_i)[k(k+1)(2k+1)]^{1/2}[\boldsymbol{C}_j^{(k)}\times\boldsymbol{C}_i^{(k)}]^{(1)}$$
$$+(r_j^k/r_i^{k+2})(\partial/\partial r_i)[k(k+1)(2k+1)]^{1/2}[\boldsymbol{C}_j^{(k)}\times\boldsymbol{C}_i^{(k)}]^{(1)}\}\cdot(\boldsymbol{s}_i+2\boldsymbol{s}_j) \tag{1.117}$$

Since the ss and the soo interactions are represented by two-electron operators, they comprise, in analogy with the electrostatic interaction, both a direct and an exchange part. For the spin–spin interaction, these parts are described in terms of the radial integrals $M^k(nl, n'l')$, $M^k(n'l', nl)$ – and $N^k(nl, n'l')$ respectively. The definitions of these parameters are given below (Marvin, 1947).

$$M^k(nl, n'l') = \beta^2\int_0^\infty\int_{r_j}^\infty(r_j^k/r_i^{k+3})R_{nl}^2(r_i)R_{n'l'}^2(r_j)\,\mathrm{d}r_i\mathrm{d}r_j,$$
$$M^k(n'l', nl) = \beta^2\int_0^\infty\int_0^{r_j}(r_i^k/r_j^{k+3})R_{nl}^2(r_i)R_{n'l'}^2(r_j)\,\mathrm{d}r_i\mathrm{d}r_j,$$
$$N^k(nl, n'l') = \beta^2\int_0^\infty\int_0^{r_j}(r_i^k/r_j^{k+3})R_{nl}(r_i)R_{n'l'}(r_j)R_{n'l'}(r_i)R_{nl}(r_j)\,\mathrm{d}r_i\mathrm{d}r_j$$
$$= N^k(n'l', nl) \tag{1.118}$$

It follows from these definitions that

$$N^k(nl, nl) = M^k(nl, nl) \tag{1.119}$$

The exchange part of the spin–other-orbit interaction includes, in addition, radial

integrals $K^{k\pm}$ (Jucys et al., 1961) in which derivatives of the one-electron radial function appear under the integral sign (see the last two terms in formula (1.117)):

$$K^{k\pm}(nl, n'l') = A \pm B + C \pm D \tag{1.120}$$

where

$$A = \beta^2 \int_0^\infty \int_0^{r_i} (\partial/\partial r_i)(R_{nl}(r_i)/r_i) R_{n'l'}(r_j)(r_j^k/r_i^{k+1}) R_{n'l'}(r_i) R_{nl}(r_j)\, \mathrm{d}r_i \mathrm{d}r_j,$$

$$B = \beta^2 \int_0^\infty \int_0^{r_i} R_{nl}(r_i) R_{n'l'}(r_j)(r_j^k/r_i^{k+1})(\partial/\partial r_i)(R_{n'l'}(r_i)/r_i) R_{nl}(r_j)\, \mathrm{d}r_i \mathrm{d}r_j,$$

$$C = \beta^2 \int_0^\infty \int_{r_i}^\infty (\partial/\partial r_i)(R_{nl}(r_i)/r_i) R_{n'l'}(r_j)(r_i^k/r_j^{k+1}) R_{n'l'}(r_i) R_{nl}(r_j)\, \mathrm{d}r_i \mathrm{d}r_j,$$

$$D = \beta^2 \int_0^\infty \int_{r_i}^\infty R_{nl}(r_i) R_{n'l'}(r_j)(r_i^k/r_j^{k+1})(\partial/\partial r_i)(R_{n'l'}(r_i)/r_i) R_{nl}(r_j)\, \mathrm{d}r_i \mathrm{d}r_j. \tag{1.121}$$

The K^{k+} integrals can be integrated by parts and expressed as linear combinations of the N^k's:

$$K^{k+}(nl, n'l') = kN^k(nl, n'l') - (k+1)N^{k-2}(nl, n'l'). \tag{1.122}$$

For K^{k-}, it is easy to see that

$$K^{k-}(nl, n'l') = -K^{k-}(n'l', nl), \qquad K^{k-}(nl, nl) = 0. \tag{1.123, 1.124}$$

6.3. *J-dependence of the matrix elements and their contribution to the multiplet structure* (Z.B. Goldschmidt, Mallow and Starkand, 1971)

The operator representing the ss interaction is of rank $\kappa = 2$ in the spin space and $k = 2$ in the orbital space. Therefore, its matrix elements are proportional to the 6j-symbol $\begin{Bmatrix} S & S' & 2 \\ L' & L & J \end{Bmatrix}$. The matrix elements of the soo interaction are proportional to $\begin{Bmatrix} S & S' & 1 \\ L' & L & J \end{Bmatrix}$, since the operator describing this interaction has $\kappa = 1$ and $k = 1$. Consequently, for the soo interaction the Landé interval rule is still valid in the approximation of LS coupling, whereas the second rank character of the ss operator introduces deviations from this rule.

6.4. *Spin selection rules*

(a) *Spin–spin interaction*: For configurations comprising an even number of electrons, the matrix elements connecting two singlets or a singlet and a triplet vanish. For configurations comprising an odd number of electrons, the matrix elements connecting two doublets vanish. These conclusions follow immediately on remembering that each matrix element of the ss interaction is proportional to $\begin{Bmatrix} S & S' & 2 \\ L' & L & J \end{Bmatrix}$.

(b) *Spin–other-orbit interaction*: Because of the factor $\begin{Bmatrix} S & S' & 1 \\ L' & L & J \end{Bmatrix}$ included in each matrix element of the soo interaction, these matrix elements vanish between two singlets.

6.5. *Matrix elements for* $(nl)^N$ *configurations* (Horie, 1953; Pasternak et al., 1972)

$$(l^N\alpha SLJM|H_{ss}|l^N\alpha'S'L'JM) = (-1)^{S'+L+J}\begin{Bmatrix} S & S' & 2 \\ L' & L & J \end{Bmatrix}(l^N\alpha SL\|H_{ss}\|l^N\alpha'S'L') \tag{1.125}$$

where

$$\begin{aligned}(l^N\alpha SL\|H_{ss}\|l^N\alpha'S'L') &= (-1)^{S+S'+L+L'+1}\sum_k 2\{5(2k+5)!/(2k)!\}^{1/2} \\ &\times (l\|\boldsymbol{C}^{(k)}\|l)(l\|\boldsymbol{C}^{(k+2)}\|l)M^k \\ &\times \sum_{\alpha''S''L''}(l^N\alpha SL\|\boldsymbol{V}^{(1k)}\|l^N\alpha''S''L'')(l^N\alpha''S''L''\|\boldsymbol{V}^{(1k+2)}\|l^N\alpha'S'L') \\ &\times \begin{Bmatrix} S & S' & 2 \\ 1 & 1 & S'' \end{Bmatrix}\begin{Bmatrix} L & L' & 2 \\ k+2 & k & L'' \end{Bmatrix}\end{aligned} \tag{1.126}$$

and k may take the values 0, 2 or 0, 2, 4 for d^N and f^N configurations respectively.

Concerning the soo interaction, only the first two terms of (1.117) make non-vanishing contributions to the matrix elements for $(nl)^N$ configurations. In this case it is both analytically and computationally convenient to express the soo operator in the following form:

$$\begin{aligned}H'_{soo} = 2\sum_{k,K} M^k &(l\|\boldsymbol{C}^{(K)}\|l)(l\|\boldsymbol{U}^{(K;k+1}\|l)[(-1)^K 3^{1/2}(2K+1)^{-1/2}(\boldsymbol{U}^{(K)}\cdot\boldsymbol{T}^{(1k+1)K}) \\ &+ 2(-1)^{k+1}3^{1/2}(2k+3)^{-1/2}(\boldsymbol{U}^{(k+1)}\cdot\boldsymbol{T}^{(1K)k+1})]\end{aligned} \tag{1.127}$$

where $K = k, k+2$

$$\boldsymbol{T}^{(1t)k} = \sum_i \boldsymbol{t}_i^{(1t)k} = \sum_i [\boldsymbol{s}_i \times \boldsymbol{u}_i^{(t)}]^{(k)} \tag{1.128}$$

and

$$\begin{aligned}\boldsymbol{U}^{(k;k+1)} &= 3^{-1/2}(2k+1)(2k+3)^{1/2}[\boldsymbol{C}^{(k)}\times\boldsymbol{l}]^{(k+1)} \\ \boldsymbol{U}^{(k+2;k+1)} &= -3^{-1/2}(2k+5)(2k+3)^{1/2}[\boldsymbol{C}^{(k+2)}\times\boldsymbol{l}]^{(k+1)}.\end{aligned}$$

The prime over the H_{soo} in the left-hand side of eq. (1.127) indicates that a term proportional to the spin–orbit interaction has been omitted from the first two terms of equation (1.117). The matrix elements of H'_{soo} are given by

$$\begin{aligned}&(l^N\alpha SLJM|H'_{soo}|l^N\alpha'S'L'JM) \\ &= (-1)^{S'+L+J}\begin{Bmatrix} S & S' & 1 \\ L' & L & J \end{Bmatrix}(l^N\alpha SL\|H'_{soo}\|l^N\alpha'S'L'),\end{aligned} \tag{1.129}$$

where

$$(l^N\alpha SL\|H'_{\text{soo}}\|l^N\alpha'S'L') = 2(3)^{1/2}(-1)^{L+L'}\sum_{k,K} M^k(l\|\boldsymbol{U}^{(K;k+1)}\|l)(l\|\boldsymbol{C}^{(K)}\|l)$$
$$\times\Big[\sum_{\alpha''S''L''}(l^N\alpha SL\|\boldsymbol{U}^{(K)}\|l^N\alpha''S''L'')(l^N\alpha''S''L''\|\boldsymbol{V}^{(1k+1)}\|l^N\alpha'S'L')\begin{Bmatrix} L & K & L'' \\ k+1 & L' & 1\end{Bmatrix}$$
$$\times 2\sum_{\alpha''S''L''}(l^N\alpha SL\|\boldsymbol{U}^{(k+1)}\|l^N\alpha''S''L'')$$
$$\times(l^N\alpha''S''L''\|\boldsymbol{V}^{(1K)}\|l^N\alpha'S'L')\begin{Bmatrix} L & k+1 & L'' \\ K & L' & 1\end{Bmatrix}\Big] \qquad (1.130)$$

The first sum in the square brackets of (1.130) yields, for $k = 0$, matrix elements which are proportional to those of the spin–orbit interaction and is therefore omitted in a semiempirical calculation.

6.5.1. *Conjugate configurations of the type* $(nl)^{4l+2-N}$

The matrix elements of H_{ss} and H'_{soo} remain invariant under the conjugation process $(nl)^N \rightarrow (nl)^{4l+2-N}$. This conclusion follows immediately on inspecting formulae (1.126) and (1.130), (1.77) and (1.111).

6.6. *Matrix elements for* $(nl)^N n'l'$ *configurations*

Recently, Z.B. Goldschmidt, Mallow and Starkand (1971) have obtained closed formulae for the matrix elements of the ss and soo interactions between the non-equivalent $nln'l'$ electrons in configurations of the type $(nl)^N n'l'$, including the special cases of $N = 1$ and $N = 4l + 1$. Only various general properties of these matrix elements will be summarized below, the explicit formulae will be published elsewhere.

6.6.1. *Conjugate configurations of the type* $(nl)^{4l+2-N}n'l'$ *– direct part*

In the configurations $(nl)^{4l+2-N}n'l'$ conjugate to $(nl)^N n'l'$ it is possible to predict at the outset the properties of the direct part of the mutual magnetic interactions, by expressing them in terms of the symmetrical double tensors $\boldsymbol{T}^{(\kappa k)} = \sum_{i=1}^{N} \boldsymbol{t}_i^{(\kappa k)}$ operating on the $(nl)^N$ core.

For the ss interaction, the reduced matrix elements between the core states comprise an odd symmetrical double tensor ($\kappa + k$ odd) and are therefore the same for $(nl)^{4l+2-N}n'l'$ and $(nl)^N n'l'$. The soo interaction is composed of two parts: The first, comprising the factors $\boldsymbol{l}_i$ and $\boldsymbol{s}_i$, behaves under conjugation like the spin–orbit interaction. It is represented by an even symmetrical double tensor ($\kappa + k$ even) and therefore changes sign; the second part, comprising $\boldsymbol{l}_i$ and $\boldsymbol{s}_j$, is represented by an odd symmetrical operator, and therefore remains invariant under conjugation.

6.6.2. *Conjugate configurations of the type* $(nl)^{4l+1}n'l'$ *comprising an electron and a hole-exchange part*

In configurations comprising an electron and a hole, most exchange matrix elements vanish, as in the analogous case of the electrostatic interaction (see

TABLE 1.6.
Allowed values of the spin and orbital quantum numbers for non-vanishing matrix elements in $nln'l'$ and $(nl)^{4l+1}n'l'$.*,a

Interaction	$nln'l'$ spin	$nln'l'$ orbit	$(nl)^{4l+1}n'l'$ spin	$(nl)^{4l+1}n'l'$ orbit
ss	$S = S' = 1$	No limitations	$S = S' = 1$	$\delta(L,k)\delta(L',t) + \delta(L,t)\delta(L',k)$
soo and Effective EL–SO**	$\left\{\begin{matrix} S=S'=1 \\ S=0 \quad S'=1 \\ S=1 \quad S'=0 \end{matrix}\right\}$	No limitations	$\left\{\begin{matrix} - \\ S=0 \quad S'=1 \\ S=1 \quad S'=0 \end{matrix}\right\}$	$\delta(L,k)\delta(L',t) + \delta(L,t)\delta(L',k)$
Electrostatic	$\left\{\begin{matrix} S=S'=1 \\ S=S'=0 \end{matrix}\right\}$	No limitations	$S = S' = 0$	$\delta(L,k)\delta(L',k)$

*For the ss interaction $t = k+2$; for the soo interaction $t = k-1, k, k+1$. **See section 7.4. [a]Z.B. Goldschmidt, Mallow and Starkand (1971).

section 4.2.4). This is a result of particularly strong spin and orbital selection rules.

(a) *Spin selection rules.* Of the non-vanishing matrix elements allowed for $nln'l'$, only those matrix elements with lowest multiplicities survive for the conjugate $(nl)^{4l+1}n'l'$, as summarized in table 1.6.

(b) *Orbital selection rules.* As shown in table 1.6, most of the matrix elements which appear for $nln'l'$ vanish for $(nl)^{4l+1}n'l'$, due to the delta functions relating the total angular momentum quantum numbers L and L' to the ranks k and t* of the tensors operating on the orbital parts of the wave functions of each pair of interacting electrons.

7. Configuration interaction with distant configurations to second order of perturbation theory – Effective interactions

Even when CI between neighbouring configurations has been included in first-order perturbation theory, CI with all distant configurations has still been neglected. Although CI with each distant configuration may be small, the over-all effects of these configurations may be quite large, since their density increases as the continuum is approached. It is of course impossible to construct energy matrices including CI with all configurations. Rather, following Bacher and Goudsmit (1934), CI with distant configurations can be taken into account, in second-order perturbation theory, by adding effective interactions to the hamiltonian of the perturbed configuration (group of configurations). In this approximation the effective interactions are generally described by two, three or

*For the ss interaction $t = k+2$; for the soo interaction $t = k-1, k, k+1$.

four-electron operators, the character of which depends on the perturbed and perturbing configurations. This approach has several advantages: In the first place, no increase in the dimensions of the energy matrices is involved, and the number of additional (radial) parameters is relatively small. Furthermore, the effects of various classes of perturbing configurations can be studied separately.

On remembering that the two-dominant interactions for many-electron atoms are the electrostatic interaction $H_1 = \Sigma_{i>j} e^2/r_{ij}$ and the spin–orbit interaction $H_2 = \Sigma_i \zeta_i(\boldsymbol{l}_i \cdot \boldsymbol{s}_i)$, the effective interactions have the form

$$H_{\text{eff}} = -(H_1 + H_2)(H_1 + H_2)/\Delta E \tag{1.131}$$

ΔE being the (positive) energy separation between the perturbing and the perturbed configurations. H_{eff} decomposes into three parts:

$$\text{(I)} \qquad H_{\text{A}} = -H_1 H_1/\Delta E \tag{1.132}$$

known as "effective electrostatic interaction"

$$\text{(II)} \qquad H_{\text{B}} = -(H_1 H_2 + H_2 H_1)/\Delta E \tag{1.133}$$

which is referred to as "effective electrostatic–spin–orbit (effective EL–SO)" interaction

$$\text{(III)} \qquad H_{\text{C}} = -H_2 H_2/\Delta E \tag{1.134}$$

which turns out to have the same angular dependence as the usual spin–orbit interaction (Rajnak et al., 1964; Stein, 1967) and therefore does not constitute an independent interaction.

Generally, $H_{\text{A}} \gg H_{\text{B}}$; this relation is to be expected on considering the origin of these two interactions. An additional property of these interactions which is connected with their origin is the following: H_{A}, when expressed in tensor-operator form is *spin-independent*, in analogy with the real electrostatic interaction, whereas H_{B} is *spin-dependent*, in analogy with the magnetic interactions.

The effective interactions have been investigated by various authors, both from the theoretical and from the semiempirical points of view, as will be specified below.

7.1. *Effective electrostatic interaction in* $(nl)^N$ *configurations*

The properties of this interaction, from the theoretical point of view, were extensively studied by Rajnak and Wybourne (1963) and by Racah and Stein (1967) for the following types of perturbing configurations:

(1) $l^{N-2}l'^2$ and $l^{N-2}l'l''$, (2) $l'^{4l'}l^{N+2}$ and $l'^{4l'+1}l''^{4l''+1}l^{N+2}$

(3) $l'^{4l'+1}l^N l''$, (4) $l^{N-1}l'$, (5) $l'^{4l'+1}l^{N+1}$.

The following results were obtained:

(1) For perturbing configurations having two "new electronic states" as compared to the perturbed configuration, H_{A} is a two-electron interaction. An electron $n'l'$ belonging to the perturbing configuration is said to occupy "a new

electronic state" if no electronic state with the same $n'l'$ is included in the perturbed configuration. For these results "a new hole state" plays the same role as "a new electronic state." For example, the perturbing configuration $l'^{4l'+1}l^N l''$ (see type (3) above) comprises one "new electron", namely l'', and one new hole, namely l'^{-1}, as compared to the perturbed configuration $l'^{4l'+2}l^N$; the corresponding H_A is therefore a two-electron interaction. The same result holds for perturbing configurations of the types (1) and (2).

(2) If the perturbing configuration comprises only one "new electronic state" as compared to the perturbed configuration, then H_A is a three electron interaction. This result holds for perturbing configurations of the types (4) and (5).

These results can be explained in the following way:

H_A includes the factor $H_1 H_1$. Due to the first H_1 two electrons jump from l^N to the perturbing configuration, due to the second H_1 two electrons jump back to l^N. Therefore, in general, four electrons are involved in the effective interaction process. But if an electron jumps from l^N into a "new electronic state" of the perturbing configuration, the *same* electron must jump back to l^N. In this case the effective interaction is represented by a three-electron operator (result no. 2). If two electrons jump from l^N into "new electronic states" of the perturbing configuration, the same two electrons must jump back to l^N, and the effective interaction is represented by a two-electron operator (result no. 1). A graphic explanation is given in fig. 1.11. Consequently, H_A in its tensor operator form can be written as a sum of two terms: the two-electron term H_A^2 and the three-electron term H_A^3.

$$H_A^2 = -\sum_{t>0}[t]P^t \sum_{i\neq j}(\boldsymbol{u}_i^{(t)} \cdot \boldsymbol{u}_j^{(t)}) = \sum_{t>0} P^t y_t \tag{1.135}$$

$$H_A^3 = -\sum_{\substack{k,k',k'' \\ \text{even and positive}}} \sqrt{[k][k'][k'']}P(k,k',k'') \sum_{i\neq j\neq h} [\boldsymbol{u}_i^{(k)} \cdot \boldsymbol{u}_j^{(k')} \cdot \boldsymbol{u}_h^{(k'')}]^{(0)}$$

$$= \sum_{\substack{k,k',k'' \\ \text{even and positive}}} P(k,k',k'')V(k,k',k'') \tag{1.136}$$

The quantities P^t and $P(k,k',k'')$ contain the Slater integrals describing the "real" electrostatic interaction between the perturbing and the perturbed

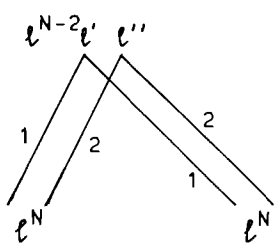

Fig. 1.11a. $H_A^2 \equiv$ two-electron effective electrostatic interaction. An example: $l^N \rightarrow l^{N-2}l'l'' \rightarrow l^N$.

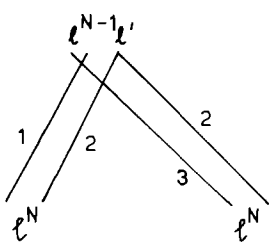

Fig. 1.11b. $H_A^3 \equiv$ three-electron effective electrostatic interaction. An example: $l^N \rightarrow l^{N-1}l' \rightarrow l^N$.

configurations, as well as the energy separation between them. They may be treated as adjustable parameters on carrying out semi-empirical calculations. Since the contributions to the effective interaction of all perturbing configurations of the same type (namely, having the same l_i and differing from each other only in n_i) have the same angular expressions y_t or $V(k, k', k'')$, the parameters P^t and $P(k, k', k'')$, on performing a semi-empirical calculation, absorb the (radial) contributions of all these configurations.

The allowed values of t in (1.135) are $0 < t \leqslant 2l$. However, for even values of t, the coefficients of the P^t's have the same angular dependence as the coefficients of the Slater parameters F^t describing the "real" electrostatic interaction within the l^N configuration. Therefore, only P^t's with odd t constitute independent parameters*. The number of these parameters in the range $0 < t \leqslant 2l$ is l, as compared to $l+1$, the number of the "real" Slater parameters. For d^N configurations, H_A^2 takes the form

$$H_A^2 = -\sum_{i \neq j} [P^1(\boldsymbol{u}_i^{(1)} \cdot \boldsymbol{u}_j^{(1)}) + P^3(\boldsymbol{u}_i^{(3)} \cdot \boldsymbol{u}_j^{(3)})] \tag{1.137}$$

and for f^N configurations

$$H_A^2 = -\sum_{i \neq j} [P^1(\boldsymbol{u}_i^{(1)} \cdot \boldsymbol{u}_j^{(1)}) + P^3(\boldsymbol{u}_i^{(3)} \cdot \boldsymbol{u}_j^{(3)}) + P^5(\boldsymbol{u}_i^{(5)} \cdot \boldsymbol{u}_j^{(5)})]. \tag{1.138}$$

On the whole, the electrostatic interaction, real and two-electron effective, is described by a number of parameters $(2l + 1)$ which equals the number of terms of the l^2 configuration. This means that on including the two-electron effective electrostatic interaction in the calculations

(1) the experimental terms of the l^2 configuration can be exactly fitted to the theoretical formulae of this configuration;

(2) the agreement between the observed and calculated terms of the l^N configurations is greatly improved.

The last result can also be understood through the use of Bacher and Goudsmit's approach (1934). These authors expressed the energies of the terms of the l^N configurations as sums of one-electron, two-electron, three-electron interactions etc.

$$E(l^N) = \sum_{\substack{\text{all} \\ \text{electrons}}} E(l) + \sum_{\substack{\text{all} \\ \text{pairs}}} E(l^2) + \sum_{\substack{\text{all} \\ \text{triples}}} E(l^3) + \cdots \tag{1.139}$$

They also compared their approximation method with the usual perturbation theory. This comparison is repeated in table 1.7. Bacher and Goudsmit immediately concluded from the table that if the approximation used was a pair-approximation or better, and if the exact energies of the two-particle problem were used in that approximation, then all the higher orders of the pair interaction have been included. This conclusion of Bacher and Goudsmit very clearly explains the result (2) above. It also appears from table 1.7 that the triple

*In a semiempirical treatment, the effects of the effective electrostatic interactions described by P^t's with even values of t are absorbed by the "real" Slater parameters.

TABLE 1.7.
Relation between the n-particle approximation and perturbation theory.[a]

Perturbation theory \ n-particle corrections	Pairs	Triples	Quadruples	Quintuples	etc.
1st order	x				
2nd order	x	x			
3rd order	x	x	x		
4th order	x	x	x	x	
etc.					

[a]Bacher and Goudsmit (1934).

energy enters for the first time in the second order of the perturbation theory. This is in complete agreement with the results obtained above for the effective electrostatic interaction.

Returning now to H_A^3 (formula 1.136) and remembering that k, k', k'' may take only even values in the range $0 < k, k', k'' \leq 2l$ and fulfill the triangular condition among themselves, it follows that for d^N configurations the only allowed $P(kk'k'')$ are characterized by the four triads (222)(224)(244)(444), and for f^N configurations, the allowed $P(kk'k'')$ are characterized by the nine triads (222)(224)(244)(444)(246)(446)(266)(466)(666). Judd (1967) and Feneuille (1966) have shown that for d^N configurations only two out of the four parameters mentioned above constitute independent parameters. For f^N configurations Judd (1966) has shown that only six of these parameters are independent.

7.1.1. *The choice of the effective electrostatic parameters for* f^N *configurations*

As was already shown in section 4.2.1.2 and 4.2.3.3, Racah, in his analysis of the "real" electrostatic interaction within f^N configurations, has constructed linear combinations of the operators $\Sigma_{i>j}(\boldsymbol{C}_i^{(k)} \cdot \boldsymbol{C}_j^{(k)})$, which correspond to the irreducible representations W and U of the groups R_7 and G_2 respectively. Judd (1966) has used the same approach for the parametrization of the effective electrostatic two and three-electron operators. From the two-electron effective operators y_t of formula (1.135), he constructed the three linear combinations

$$e_4 = y_1 + y_3 + y_5, \qquad e_5 = y_1 - 2y_3 + y_5, \qquad e_6 = 11y_1 - 3y_5 \tag{1.140}$$

for which $WU = (000)(00)$, $(111)(00)$ and $(220)(22)$, respectively. The operator e_6 is identical to Ω of Racah (1949). The eigenvalues of e_4, e_5 and e_6 can easily be expressed in terms of the eigenvalues $G(R_7)$, $G(G_2)$ and $G(R_3)$ of Casimir's operators for the groups R_7, G_2 and R_3. They are $5G(R_7) - 3N$, $12G(G_2) - 10G(R_7)$ and $\frac{1}{2}L(L+1) - 12G(G_2)$ for e_4, e_5 and e_6 respectively. $5G(R_7)$ and $12G(G_2)$ are given in tables 1.8 and 1.9. Thus, the two-electron effective electrostatic interaction for f^N configurations is given by the following formula:

$$[5G(R_7) - 3N]E^4 + [12G(G_2) - 10G(R_7)]E^5 + [\tfrac{1}{2}L(L+1) - 12G(G_2)]E^6 \tag{1.141}$$

TABLE 1.8.
Eigenvalues of the Casimir operator for the group R_7.[a]

$W \equiv (w_1 w_2 w_3)$	$5G(R_7)$
(000)	0
(100)	3
(110)	5
(111)	6
(200)	7
(210)	9
(211)	10
(220)	12
(221)	13
(222)	15

[a]Racah (1951).

TABLE 1.9.
Eigenvalues of the Casimir operator for the group G_2.[a]

$U \equiv (u_1 u_2)$	$12G(G_2)$
(00)	0
(10)	6
(11)	12
(20)	14
(21)	21
(30)	24
(22)	30
(31)	32
(40)	36

[a]Racah (1949).

and the total two-electron electrostatic interaction, real and effective, is represented by the sum

$$\sum_{i=0}^{6} e_i E^i \tag{1.142}$$

where E^i are the parameters representing this interaction.

It should be mentioned that Rajnak and Wybourne (1963) have used the expression

$$\alpha L(L+1) + \beta G(G_2) + \gamma G(R_7) \tag{1.143}$$

as a representative of the two-electron effective interaction instead of the sum $\Sigma_{i=4}^{6} e_i E^i$. Racah (1964), Trees (1964) and Z.B. Goldschmidt (1968a, b) have used a third three-parameter expression:

$$\alpha L(L+1) + \beta Q + 12\gamma G(G_2), \tag{1.144}$$

in which the eigenvalues of the seniority operator Q have replaced $G(R_7)$. This expression can be looked on as a generalization of the two-parameter expression $\alpha L(L+1) + \beta Q$ used by Racah (1952) for d^N configurations.

TABLE 1.10.
Description of the three-electron operators.[a]

t_i	WU
t_2	(220)(22)
t_3	(222)(00)
t_4	(222)(40)
t_6	(420)(22)
t_7	(420)(40)
t_8	(420)(42)

[a]Judd (1966).

For the three-electron effective electrostatic interaction, Judd (1966) has constructed the six-parameter expression

$$t_2T^2 + t_3T^3 + t_4T^4 + t_6T^6 + t_7T^7 + t_8T^8 \tag{1.145}$$

The operators t_i are identified with the operators $t(WU)$ as listed in table 1.10, and $t(WU)$ are linear combinations of $V(kk'k'')$ according to the formula

$$t(WU) = \sum V(kk'k'')(kk'k''|WU). \tag{1.146}$$

The coefficients $(kk'k''|WU)$ as well as the matrix elements of t_i for the f^3 configuration were calculated by Judd (1966) (see tables VI and VIII there). That part of table VIII which comprises the matrix elements of the six independent operators $t_i (i = 2, 3, 4, 6, 7, 8)$ is repeated here in table 1.11.

7.1.2. *The N dependence of the matrix elements*

The straightforward way to calculate the matrix elements of H^2_A and H^3_A for l^N configurations is to take the matrix elements of l^2 and l^3 respectively as starting points, and perform chain calculations through the use of formula 1.70 (with H^2_A substituted for H_1) and the following formula (Judd, 1966):

$$\{l^N\alpha SL\{|H^3_A|\}l^N\alpha' SL\} = [N/(N-3)] \sum_{\bar{\alpha}\bar{\alpha}'\bar{S}\bar{L}} (l^N\alpha SL\{|l^{N-1}(\bar{\alpha}\bar{S}\bar{L})lSL)$$
$$\times \{l^{N-1}\bar{\alpha}\bar{S}\bar{L}\{|H^3_A|\}l^{N-1}\bar{\alpha}'\bar{S}\bar{L}\}(l^{N-1}(\bar{\alpha}'\bar{S}\bar{L})lSL|\}l^N\alpha' SL) \tag{1.147}$$

As in the case of the electrostatic interaction, although these equations completely solve the problem of calculating the desired matrix elements for any l^N configuration, several short-cuts can be taken, corresponding to the various special cases.

7.1.3. *The two-electron effective electrostatic interaction in f^N configurations*

The coefficients of the two-electron effective parameters E^4, E^5 and E^6 listed in formula (1.141) are already given for any f^N configuration, since they depend only on the number N and on the eigenvalues of Casimir's operators G for the groups R_7, G_2 and R_3, the irreducible representations of which characterize the states of f^N. The special case of the configurations f^{14-N} conjugate to f^N should be mentioned: Since the states of f^{14-N} are identical with those of f^N, the coefficients of E^i $(i = 4, 5, 6)$ for the terms of f^{14-N} are the same as those for the correlated terms of f^N, apart from a constant term. The same result holds for the other sets of two-electron effective terms mentioned above (formulae 1.143 and 1.144).

7.1.4. *The three-electron effective interaction in f^N configurations*

If one would use, as coefficients of $P(k, k', k'')$ in formula (1.136), the operators $\boldsymbol{U}^{(k)} = \Sigma_i \boldsymbol{u}_i^{(k)}$ instead of $\boldsymbol{u}_i^{(k)}$, these coefficients would be proportional to the

TABLE 1.11.
The matrix elements $(f^3 WUSL|t_i|f^3 W'U'SL)$.[a]

$WUSL$	$W'U'SL$	t_i F^*	t_2 $(2)^{1/2}/2156$	t_3 $(6720)^{-1/2}$	t_4 $1/56(15015)^{1/2}$	t_6 $1/924(455)^{1/2}$	t_7 $1/168(5005)^{1/2}$	t_8 $(16336320)^{-1/2}$
$(111)(00)^4S$	$(111)(00)^4S$		0	288	0	0	0	0
$(111)(20)^4D$	$(111)(20)^4D$		1694	8	−8008	0	0	0
$(111)(10)^4F$	$(111)(10)^4F$		0	−72	0	0	0	0
$(111)(20)^4G$	$(111)(20)^4G$		616	8	7280	0	0	0
$(111)(20)^4I$	$(111)(20)^4I$		−1078	8	−1960	0	0	0
$(210)(11)^2P$	$(210)(11)^2P$		−385	−48	0	−30030	0	0
$(210)(20)^2D$	$(210)(20)^2D$		−319	32	−1144	12870	10296	0
$(210)(20)^2D$	$(210)(21)^2D$		$36(33)^{1/2}$	0	$468(33)^{1/2}$	$-624(33)^{1/2}$	$156(33)^{1/2}$	0
$(210)(21)^2D$	$(210)(21)^2D$		−423	−3	3237	−1677	−1833	4641
$(100)(10)^2F$	$(100)(10)^2F$		0	0	0	0	0	0
$(100)(10)^2F$	$(210)(21)^2F$		$231(22)^{1/2}$	0	0	0	0	0
$(210)(21)^2F$	$(210)(21)^2F$		−21	−3	1365	1365	−1365	−3315
$(210)(20)^2G$	$(210)(20)^2G$		−116	32	1040	4680	−9360	0
$(210)(20)^2G$	$(210)(21)^2G$		$3(4290)^{1/2}$	0	$-24(4290)^{1/2}$	$-52(4290)^{1/2}$	$-8(4290)^{1/2}$	0
$(210)(21)^2G$	$(210)(21)^2G$		11	−3	−2475	1221	1947	1309
$(210)(11)^2H$	$(210)(11)^2H$		105	−48	0	8190	0	0
$(210)(11)^2H$	$(210)(21)^2H$		0	0	$84(455)^{1/2}$	0	$252(455)^{1/2}$	0
$(210)(21)^2H$	$(210)(21)^2H$		−399	−3	−1995	−2709	567	−1071
$(210)(20)^2I$	$(210)(20)^2I$		203	32	−280	−8190	2520	0
$(210)(21)^2K$	$(210)(21)^2K$		56	−3	1827	−252	21	−1071
$(210)(21)^2L$	$(210)(21)^2L$		336	−3	−525	1260	−315	945

[a]Judd (1966).
*The numbers F are multiplicative constants common to all members of a column.

triple product

$$[\boldsymbol{U}^{(k)} \cdot \boldsymbol{U}^{(k')}) \cdot \boldsymbol{U}^{(k'')}]^{(0)} \tag{1.148}$$

(k, k' and k'' even), apart from two and one-electron terms. One could then use formulae (1.75)–(1.80) in order to simplify the calculation of the matrix elements of H_A^3 for l^N configurations. It is worthwhile to mention the following conclusions obtained through the use of these formulae:

(1) Conjugate configurations of the type l^{4l+2-N}: the matrix elements of H_A^3 between terms of l^{4l+2-N} are equal in value and opposite in sign to the matrix elements between the correlated terms of l^N. This conclusion is a direct result of formula (1.77) and the fact that all k's are even.

(2) For a half filled shell l^{4l+1}, the reduced matrix elements of $\boldsymbol{U}^{(k)}$ with even k satisfy the selection rule $\Delta v = \pm 2$; therefore the triple product (1.148) also satisfies the selection rule $\Delta v = \pm 2$ (whereas the electrostatic energy matrices satisfy the selection rule $\Delta v = 0, \pm 4$). Hence, all diagonal elements of H_A^3 vanish, and all second-order effects are well represented by two-electron effective interactions.

As mentioned above, Judd (1966) used the three-electron effective operators t_i, instead of $\boldsymbol{u}_i^{(k)}$ or $\boldsymbol{U}^{(k)}$. In order to find the N-dependence of their matrix elements, he again used the powerful and elegant apparatus of group theory, as well as the formalism of second quantization and the theories of quasi-spin and seniority. For t_6, t_7 and t_8 he obtained the following formulae, which are identical to formulae (1.75) and (1.76) above:

$$\{\mathrm{f}^N \alpha v SL | t_i | \mathrm{f}^N \alpha' v SL\} = [(7-N)/(7-v)]\{\mathrm{f}^v \alpha v SL | t_i | \mathrm{f}^v \alpha' v SL\}, \tag{1.149}$$

$$\{\mathrm{f}^N \alpha v SL | t_i | \mathrm{f}^N \alpha' v - 2SL\}$$
$$= \{(N+2-v)(16-N-v)/4(8-v)\}^{1/2}\{\mathrm{f}^v \alpha v SL | t_i | \mathrm{f}^v \alpha' v - 2SL\}. \tag{1.150}$$

For t_2, t_3 and t_4 the process of finding the N dependence of the matrix elements as well as the relations obtained are somewhat more complicated and the interested reader is referred to Judd's original paper (1966) for a complete study of this subject.

7.2. *Effective electrostatic interaction in $(nl)^N n'l'$ configurations: two-electron operators*

For perturbed configurations of the type $(nl)^N n'l'$, the effective electrostatic interaction can be represented by two, three and four-electron operators. A four-electron operator is obtained when the perturbing configuration comprises no "new electronic state" as compared to the perturbed configuration. For example: the perturbed configuration is $(nl)^N n'l'$ and the perturbing configuration is $(nl)^{N+1}$. For $(nl)^N n'l'$ configurations of rare earth spectra, only the effects of the two-electron nl–$n'l'$ effective operators have been investigated. On including these operators in the energy level calculations, in addition to the complete effective interaction of the $(nl)^N$ $(=4\mathrm{f}^N)$ core, the fit between observed and

calculated levels improved to such an extent, that at present there seems to be no need for the inclusion of additional effective electrostatic interactions in these configurations. Consequently, only the two-electron nl–$n'l'$ effective operators will be discussed here. The tensor-operator form of these operators is given by the following formula (Stein, 1967; Z.B. Goldschmidt and Starkand, 1970; Z.B. Goldschmidt, 1973):

$$H^2_{\mathrm{A}}(nl-n'l') = -\sum_t F^t \sum_{i\neq j} (\boldsymbol{u}_i^{(t)} \cdot \boldsymbol{v}_j^{(t)}) - \sum_t G^t \sum_{i\neq j} (\boldsymbol{z}_i^{(t)} \cdot \tilde{\boldsymbol{z}}_j^{(t)}) \tag{1.151}$$

where $\boldsymbol{u}^{(t)}$, $\boldsymbol{v}^{(t)}$, $\boldsymbol{z}^{(t)}$, $\tilde{\boldsymbol{z}}^{(t)}$ are unit tensor-operators, defined by their reduced matrix elements as follows:

$$\begin{aligned} &(nl\|\boldsymbol{u}^{(t)}\|nl) = 1, \qquad (n'l'\|\boldsymbol{v}^{(t)}\|n'l') = 1, \\ &(nl\|\boldsymbol{z}^{(t)}\|n'l') = 1, \qquad (n'l'\|\tilde{\boldsymbol{z}}^{(t)}\|nl) = 1. \end{aligned} \tag{1.152}$$

The first term, described by the parameters F^t, represents the *direct* part of the two-electron effective interaction, whereas the second term, described by the parameters G^t, represents the *exchange* part of this interaction. F^t and G^t are referred to as "effective Slater parameters." The allowed values of t for the direct part range from zero to the smaller of $2l$ and $2l'$, but since the "real" Slater parameters, with the even t's contained in this list, have already been included in the calculations, only the F^t's having odd t constitute independent parameters. The allowed values of t for the exchange part are $|l-l'| \leqslant t \leqslant l+l'$. Here again, only G^t's with t having the same parity as $l+l'+1$ are to be added as new parameters; those with t having the opposite parity have already been included as "real" exchange Slater parameters. Table 1.12 comprises the lists of effective Slater parameters for the configurations ls, dp, dd', fp, fd, ff' and fg. On the whole, on adding the effective interactions to the energy matrices, the number of Slater parameters, real and effective, is equal to the number of terms in the ll' two-electron configuration. In a least squares calculation including all these interactions the "even" direct and the "$l+l'$ parity" exchange effective interactions are absorbed by the original Slater parameters.

TABLE 1.12.
Effective non-equivalent two-electron Slater parameters.

Configuration	Direct part	Exchange part
ls	–	–
dp	F^1	G^2
dd'	F^1, F^3	G^1, G^3
fp	F^1	G^3
fd	F^1, F^3	G^2, G^4
ff'	F^1, F^3, F^5	G^1, G^3, G^5
fg	F^1, F^3, F^5	G^2, G^4, G^6

7.2.1. *Matrix elements*

7.2.1.1. *nln'l' configurations*

The matrix elements of $H^2_A(nl - n'l')$ for $nln'l'$ configurations are given by the following formula:

$$\{nln'l'SL\{|H^2_A(nl - n'l')|\}nln'l'SL\} = \sum_t f_t F^t + (-1)^S \sum_t g_t G^t$$

$$= \sum_t F^t (-1)^{1+l+l'+L} \begin{Bmatrix} l & l & t \\ l' & l' & L \end{Bmatrix} + (-1)^S \sum_t G^t (-1)^{1+l+l'} \begin{Bmatrix} l & l' & t \\ l & l' & L \end{Bmatrix}. \quad (1.153)$$

7.2.1.2. $(nl)^N n'l'$ *configurations*

The formulae for the matrix elements of $H^2_A(nl - n'l')$ for $(nl)^N n'l'$ configurations are obtained by the same methods as those for the matrix elements of the electrostatic interaction. These will not be given explicitly here.

7.2.1.3. *Conjugate configurations of the type* $(nl)^{4l+2-N}n'l'$

The conclusions cited in this paragraph are obtained in the same manner as those for the "real" electrostatic interaction; therefore, they will be stated without proof.

(a) *Direct part*

The direct part of the two-electron effective electrostatic interaction $nl - n'l'$ remains invariant under the conjugation process $(nl)^N n'l' \rightarrow (nl)^{4l+2-N}n'l'$.

(b) *Exchange part for* $(nl)^{4l+1}n'l'$ *configurations*

(1) The coefficient of G^t is given (up to an additive constant common to all terms) by the formula

$$g_t = 2(-1)^t(2t + 1)^{-1}\delta(S, 0)\delta(t, L). \quad (1.154)$$

That means that the effective electrostatic exchange interaction (like the "real" electrostatic interaction) is different from zero only for singlets; furthermore, each specific coefficient g_t is different from zero only for one singlet characterized by $L = t$.

(2) The total singlet–triplet splitting, given by the following expression for $nln'l'$,

$$2(-1)^{t+1}(2t + 1)^{-1}G^t \quad (1.155)$$

remains constant in magnitude but changes sign under the conjugation process $nln'l' \rightarrow (nl)^{4l+1}n'l'$, as seen by comparing formulae (1.155) and (1.154).

7.3. *Effective EL–SO interaction in* $(nl)^N$ *configurations*

Since the spin–orbit operator is a sum of one-electron operators each of which is diagonal with respect to the orbital quantum number l, the perturbing configurations can differ from the perturbed configuration $(nl)^N$ by the principal quantum number n of one electron state only. Three kinds of perturbing configurations can thus occur:

(1) $(nl)^{N-1}n'l$, (2) $(n'l)^{4l+1}(nl)^{N+1}$, (3) $(n'l')^{4l'+1}(nl)^N n''l'$.

The contributions to the effective EL–SO operator due to these kinds of perturbing configurations have been obtained by Pasternak et al. (1972). These authors have shown that after omitting terms proportional to the spin–orbit interaction, the contributions of the configurations $(nl)^{N-1}n'l$ and $(n'l)^{4l+1}(nl)^{N+1}$ have the same angular dependence, whereas that of $(n'l')^{4l'+1}(nl)^N n''l'$ vanishes.

The expression for the effective EL–SO operator is

$$H_{\text{EL–SO}} = -2 \sum_{k \text{ even}} Q^k [l(l+1)(2l+1)/(2k+1)]^{1/2} \sum_{t \text{ odd}} [t] \begin{Bmatrix} 1 & k & t \\ l & l & l \end{Bmatrix} (\boldsymbol{U}^{(k)} \cdot \boldsymbol{T}^{(1t)k}), \tag{1.156}$$

where the parameters Q^k are defined as follows:

$$Q^k = (l \| \boldsymbol{C}^{(k)} \| l)^2 \sum_{n'} R^k(nlnl, nln'l) \zeta_{nl,n'l} / \Delta E_{nn'} \tag{1.157}$$

with $R^k(nlnl, nln'l)$ and $\zeta_{nl,n'l}$, respectively, a Slater and a spin–orbit parameter. The first kind of perturbing configuration has also been studied by Stein (1967). Eq. (1.156) agrees with formula (E23) of Stein, except for his double tensor $\boldsymbol{V}^{(t,1)}$, which should be replaced by the coupled tensor $\boldsymbol{T}^{(1t)k}$.

The matrix elements of the effective EL–SO interaction are given by

$$(l^N \alpha SLJM | H_{\text{EL–SO}} | l^N \alpha' S'L'JM) = (-1)^{S'+L+J} \begin{Bmatrix} S & S' & 1 \\ L' & L & J \end{Bmatrix} \times (l^N \alpha SL \| H_{\text{EL–SO}} \| l^N \alpha' S'L'), \tag{1.158}$$

where

$$(l^N \alpha SL \| H_{\text{EL–SO}} \| l^N \alpha' S'L') = -2 \sum_{\substack{k \text{ even} \\ t \text{ odd}}} Q^k [l(l+1)(2l+1)]^{1/2} [t] \begin{Bmatrix} 1 & k & t \\ l & l & l \end{Bmatrix} \times \sum_{\alpha'' S'' L''} (-1)^{L+L'} \begin{Bmatrix} L & L' & 1 \\ t & k & L'' \end{Bmatrix} (l^N \alpha SL \| \boldsymbol{U}^{(k)} \| l^N \alpha'' S'' L'') (l^N \alpha'' S'' L'' \| \boldsymbol{V}^{(1t)} \| l^N \alpha' S'L'). \tag{1.159}$$

The last expression remains invariant under the conjugation process $l^N \to l^{4l+2-N}$. For a half-filled shell, the matrix elements satisfy the selection rule $\Delta v = 0, \pm 4$.

7.4. *Effective* EL–SO *interaction in* $(nl)^N n'l'$ *configurations*

The effective EL–SO interaction in $(nl)^N n'l'$ configurations has been investigated by Z.B. Goldschmidt, Mallow and Starkand (1971) from a theoretical point of view. In this case, the possible types of perturbing configurations are:

(1) $(nl)^N n''l'$, (2) $(nl)^{N-1}n'''ln'l'$, (3) $(n^*l')^{4l'+1}(nl)^N(n'l')^2$,

(4) $(n^{**}l)^{4l+1}(nl)^{N+1}n'l'$, (5) $(n^+l^+)^{4l^++1}(nl)^N n'l'n^{++}l^+$.

On considering only the $(nl)^N$–$n'l'$ part of the effective EL–SO interaction, it was found that the contributions of configurations of the types (1) and (3) have

the same angular dependence; the same holds for the configurations (2) and (4); furthermore, the contributions of perturbing configurations of type (5) vanish.

For perturbed configurations of the type $(nl)^N n'l'$, the effective EL–SO interaction is generally a two-electron interaction; therefore, it comprises both a direct and an exchange part. The expression for the effective EL–SO operator in this case is:

$$H_{\text{EL-SO}}(nl - n'l') = \sum_{\substack{k \text{ even} \\ t \text{ odd} \\ i \neq j}} 2(3)^{-1/2}[t]\Big\{ S^k(nln'l', nln''l')[l'(l'+1)(2l'+1)]^{1/2}$$

$$\times \begin{Bmatrix} 1 & k & t \\ l' & l' & l' \end{Bmatrix} ([\boldsymbol{u}_i^{(k)} \times \boldsymbol{v}_j^{(t)}]^{(1)} \cdot \boldsymbol{s}_j) + S^k(nln'l', n'''ln'l')[l(l+1)(2l+1)]^{1/2}$$

$$\times \begin{Bmatrix} 1 & k & t \\ l & l & l \end{Bmatrix} (\boldsymbol{s}_i \cdot [\boldsymbol{u}_i^{(t)} \times \boldsymbol{v}_j^{(k)}]^{(1)}) \Big\} + \sum_{\substack{k,t \\ i \neq j}} (3)^{-1/2}[t] \Big\{ T^k(nln'l', n''l'nl)$$

$$\times (-1)^{t+1}[l'(l'+1)(2l'+1)]^{1/2} \begin{Bmatrix} 1 & k & t \\ l & l' & l' \end{Bmatrix} + T^k(nln'l', n'l'n'''l)(-1)^k[l(l+1)$$

$$\times (2l+1)]^{1/2} \begin{Bmatrix} 1 & k & t \\ l' & l & l \end{Bmatrix} \Big\} \{(\boldsymbol{s}_i \cdot [\boldsymbol{z}_i^{(t)} \times \tilde{\boldsymbol{z}}_j^{(k)}]^{(1)}) + ([\boldsymbol{z}_i^{(k)} \times \tilde{\boldsymbol{z}}_j^{(t)}]^{(1)} \cdot \boldsymbol{s}_j)\}, \qquad (1.160)$$

where $\boldsymbol{u}^{(k)}$, $\boldsymbol{v}^{(k)}$, $\boldsymbol{z}^{(k)}$ and $\tilde{\boldsymbol{z}}^{(k)}$ are the unit tensor-operators defined in (1.152). The parameters S^k and T^k, which represent respectively the direct and exchange part of this interaction are special cases of

$$Q^k(n_a l_a n_b l_b, n_c l_c n_d l_d) = (l_a \| \boldsymbol{C}^{(k)} \| l_c)(l_b \| \boldsymbol{C}^k \| l_d)$$
$$\times \mathrm{R}^k(\mathrm{n_a l_a n_b l_b, n_c l_c n_d l_d}) \zeta_{\mathrm{n_x l_x, n_y l_y}} / \Delta \mathrm{E}, \qquad (1.161)$$

where R^k and ζ are respectively Slater and spin–orbit parameters, and x, y stand for b, d or a, c for the direct part and for b, c or a, d for the exchange part of the interaction. Formulae for the matrix elements of the effective EL–SO interaction for $(nl)^N n'l'$ configurations will not be given explicitly here. The matrix elements of this interaction have been calculated by several authors, for sp (Z.B. Goldschmidt, 1973a) dp (Z.B. Goldschmidt and Ben-Ezra, 1975) and fd (Z.B. Goldschmidt and Cohen, 1975) configurations. The general properties of the matrix elements of this interaction have been summarized by Z.B. Goldschmidt, Mallow and Starkand (1971), and will be repeated here briefly.

(1) J-dependence and contribution to multiplet structure: Since the operator representing this interaction is of ranks $\kappa = 1$ and $K = 1$ in the spin and orbital spaces respectively, its matrix elements are proportional to $\begin{Bmatrix} S & S' & 1 \\ L' & L & J \end{Bmatrix}$. That means that the Landé interval rule is still valid in the approximation of LS coupling.

(2) Spin selection rules: matrix elements between two singlets vanish.

(3) Conjugate configurations of the type $(nl)^{4l+2-N} n'l'$.

*In this sum k can only have the parity of $l + l'$, as follows from the definition of the T^k's.

(a) direct part: since that part of the direct interaction related to the $(nl)^N$ core can be represented by an even symmetrical operator $T^{(\kappa K)} = \Sigma_t t_i^{(\kappa K)}$, the matrix elements change sign on passing from $(nl)^N n'l'$ to $(nl)^{4l+2-N} n'l'$.
(b) exchange part – the configuration $(nl)^{4l+1} n'l'$: the properties of the exchange part of the effective EL–SO interaction, for configurations comprising an electron and a hole are summarized in table 1.6.

PART 2. PROPERTIES AND METHODS OF INTERPRETATION OF THE LANTHANIDE SPECTRA

8. Electronic structure; competition between electrons

The group of elements known as lanthanides comprises fifteen elements in which a progressive filling of the 4f shell occurs. The group starts with lanthanum ($Z = 57$) and ends with lutecium ($Z = 71$).

All neutral lanthanides, in their ground configuration, comprise the closed shell electronic structure of the noble gas xenon

$$1s^2 2s^2 2p^6 3s^2 3p^6 3d^{10} 4s^2 4p^6 4d^{10} 5s^2 5p^6,$$

and two or three external electrons ($6s^2$ or $5d6s^2$), in addition to a group of $4f^N$ electrons.

The lanthanide spectra, especially in low ionizations, are characterized by a high abundance of spectral lines and a high density of energy levels, both even and odd, in which no apparent regularity, such as a multiplet structure, may be discerned. Consequently, these spectra are classified as "very complex", and their successful interpretation has only recently been accomplished.

The characteristic structure of the lanthanide spectra, to be described below, is mainly determined by the special properties of the 4f eigenfunctions; these, in turn, arise from the special nature of the 4f effective potential-energy function, U_{eff} (4f), for these elements. The investigation of these properties dates back to Mayer (1941); they are also discussed by Cowan (1973). On using self-consistent field methods these authors have shown that, for small values of the atomic number Z, U_{eff} (4f) has only a single minimum, such that the 4f electron is only weakly bound to the atom, in an orbit of rather large radius r, which is essentially hydrogenic – *external* 4f *electron.* For larger values of Z, a second minimum of U_{eff}(4f) develops at small radii. At first this second minimum is very shallow ($U_{\text{eff}} > 0$) (see fig. 1.12a for indium ($Z = 49$)). As Z increases, the second minimum becomes deeper and wider, but, up to barium ($Z = 56$), the 4f eigenfunction is still mainly localized in the hydrogenic outer well, as shown in fig. 1.12b. For lanthanum ($Z = 57$), a sudden change in the properties of the 4f eigenfunction occurs, the second minimum has become sufficiently deep and wide, so that the 4f eigenfunction is entirely contained therein (fig. 1.12c). Consequently, both the spatial extension and the binding energy of the 4f eigenfunction drop suddenly at the beginning of the lanthanide group – *internal*

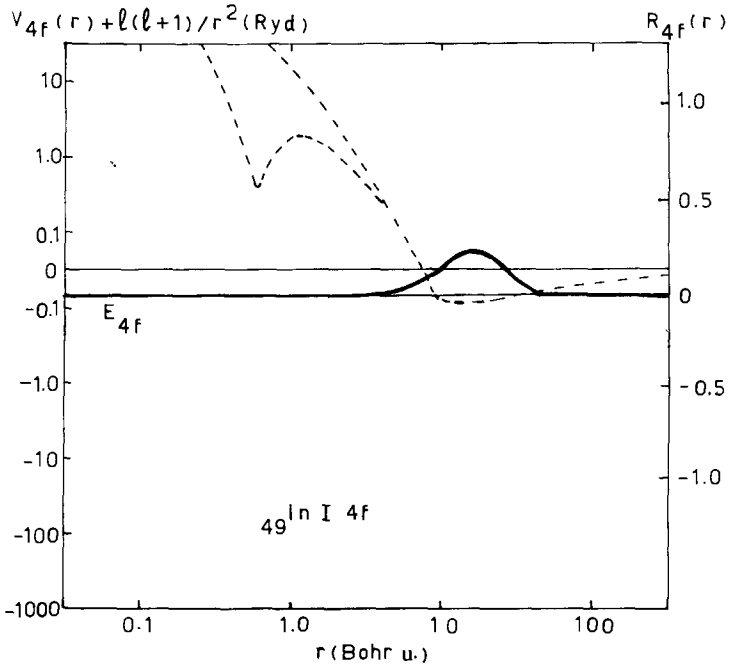

Fig. 1.12a. Dashed curves: Hydrogenic and "true"* effective potentials for a 4f electron in In I ($Z = 49$). Solid curve: The radial wave function for 4f electrons.

*Computed by Cowan (1973) via the Hartree-plus-statistical exchange (HX) approximation.

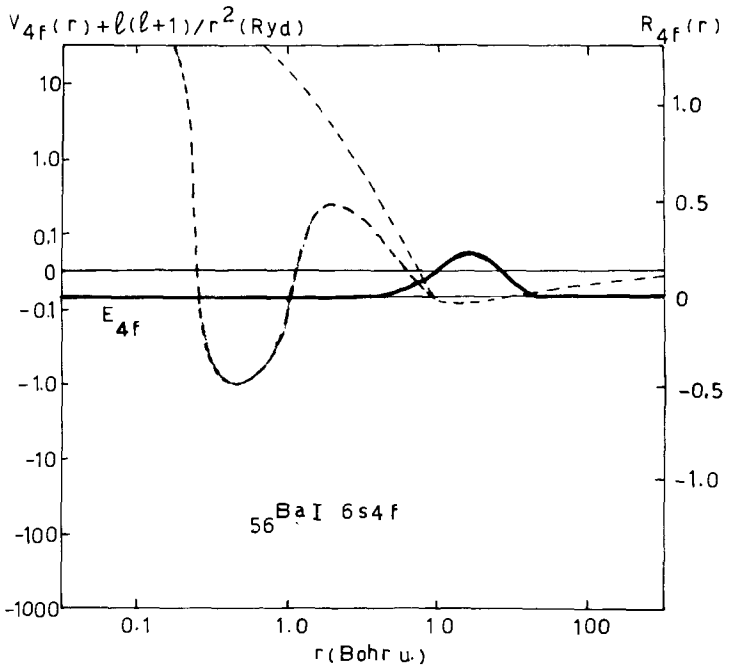

Fig. 1.12b. Similar to fig. 1.12a, but drawn for BaI($Z = 56$). (Cowan, 1973).

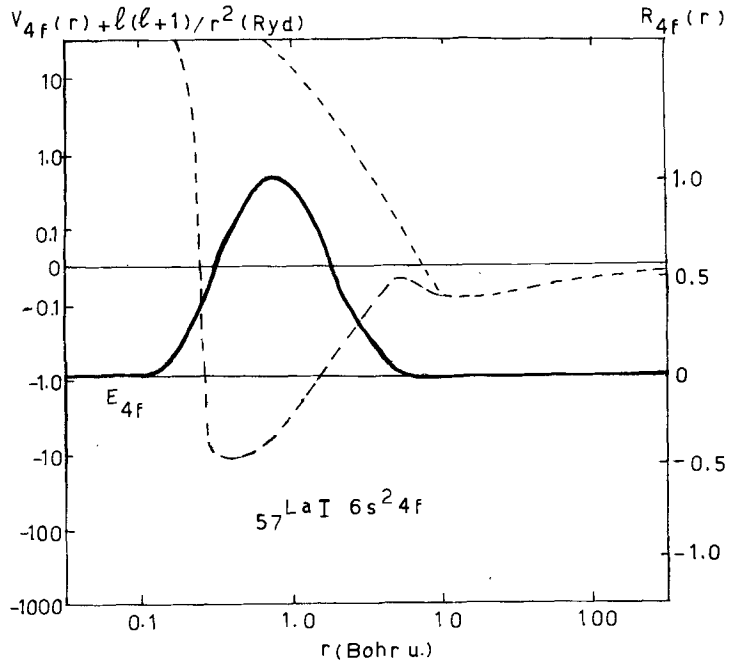

Fig. 1.12c. Similar to fig. 1.12a, but drawn for LaI(Z = 57).(Cowan, 1973).

4f *electron.* On moving from left to right along the group, the nuclear charge and the number of 4f electrons increase by one on each step. Since the mutual screening of the 4f electrons is incomplete, a further diminuation of the 4f radii and binding energies occurs accompanied by smaller contractions of the 5d and 6s shells. This phenomenon is referred to as the "lanthanide contraction." All of these properties are illustrated in figs. 1.13 and 1.14. Figure 1.13 demonstrates that, for the lanthanides, the radii of the 4f electrons are appreciably smaller than those of the $n = 5$ and $n = 6$ electrons. In fig. 1.14, the one-electron energy eigenvalues E_{nl} are given as functions of Z. The sudden drop of E_{4f} at $Z = 57$ is clearly seen. However, it should be noticed that $|E_{4f}| < |E_{5s}|$, $|E_{5p}|$, meaning that the 4f electrons are not too strongly bound in the inner well of $U_{\text{eff}}(4f)$. Actually, the eigenvalue E_{nl} serves as a good measure of the binding energy only when removal of the nl electron would result in a small rearrangement of the remaining electrons (Koopmans' theorem, 1934). Clearly, one would expect that the removal of a 4f internal electron would result in greater changes of the charge distributions of the remaining electrons than the removal of an external 5d, 6s or 6p electron. Consequently, the 4f electrons are less tightly bound than would appear from fig. 1.14, and one could conclude by saying that for the lanthanides, the binding energies of the 4f, 5d, 6s and 6p electrons are roughly equal. This property will be referred to as the *competition between electrons.* The competition between electrons is manifested in the structure of the lanthanide

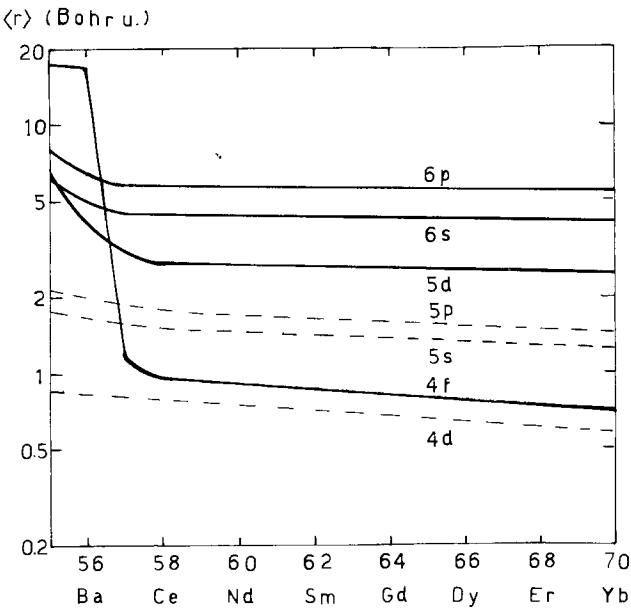

Fig. 1.13. Computed expectation values of r for various orbitals in excited $4f^{n-3}5d6s6p$ configurations of neutral lanthanides (For LaI the 4f6s6p and 5d6s6p configurations were considered, etc.) (Cowan, 1973, HX approximation).

spectra through two other competitions, to be discussed below, which are known as (Z.B. Goldschmidt, 1968a, 1968b):

(1) Competition between configurations.

(2) Competition between interactions.

The effects of the sudden drop of the energy and spatial extension of the 4f

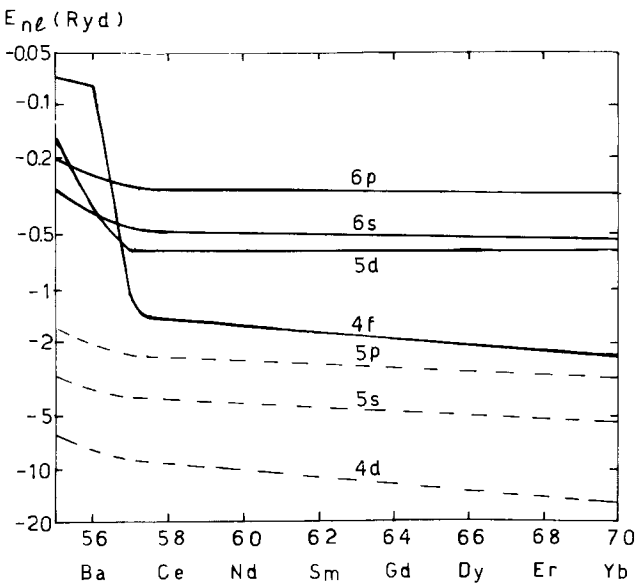

Fig. 1.14. One electron energy eigenvalues E_{nl} for the same configurations considered in fig. 1.13 (Cowan, 1973, HX approximation).

eigenfunctions on the lanthanide spectra have already been noticed by Russell and Meggers in 1932. On investigating the first three spectra of lanthanum, these authors wrote: "Lanthanum is a chemical analogue of scandium and yttrium, but, although the corresponding spectra are strikingly similar, some interesting differences are noted ... the first two spectra of La exhibit a large number of (additional) middle-set terms ascribed to the binding of a 4f electron .... In BaI, the 4f electron is much more loosely bound than the 6p .... In LaII, the terms produced by the 4f electrons lie lower than those arising from the 6p." It follows that the lanthanide group commences with lanthanum (in accord with the chemists' categorization) and not with cerium (according to spectroscopists categorization), although cerium is the first member of the group the ground configuration of which comprises a 4f electron. This conclusion will be confirmed below in a systematic discussion of the lanthanides' energy-level structure.

9. The characteristic structure of the lanthanide spectra

9.1. *Competition between configurations*

By this term we refer to the accumulation of many configurations, both even and odd, at about the same height, thus leading to a high density of energy levels. This competition is a direct result of the above mentioned competition between electrons. In order to describe the structure of the lanthanide spectra in terms of these competitions, each lanthanide, characterized by its atomic number Z, has been assigned an ordinal number

$$N = Z - 57;$$

that is, $N = 0$ for lanthanum ($Z = 57$), $N = 1$ for cerium ($Z = 58$), etc. In this way, the number of electrons outside closed shells will be $N + K$, where K equals 3, 2, 1 or 0 for first, second, third or fourth spectra respectively.

9.1.1. *First and second spectra*

The characteristic structure of the first and second lanthanide spectra is given in fig. 1.15. Each spectrum consists of two systems of configurations A and B based on the cores $4f^N$ and $4f^{N+1}$ respectively, where N is the ordinal number defined above. Each system comprises one group of low configurations and two groups of high ones, the parity of the high configurations being opposite to that of the low ones.

System A
- low-parity of N
- $4f^N(5d + 6s)^K \equiv 4f^N 5d^K + 4f^N 5d^{K-1}6s + 4f^N 5d^{K-2}6s^2$
- high I-parity of $N + 1$
- $4f^N(5d + 6s)^{K-1}6p \equiv 4f^N 5d^{K-1}6p + 4f^N 5d^{K-2}6s6p + 4f^N 5d^{K-3}6s^2 6p$
- high II-parity of $N + 1$
- $4f^{N-1}(5d + 6s)^{K+1} \equiv 4f^{N-1}5d^{K+1} + 4f^{N-1}5d^K 6s + 4f^{N-1}5d^{K-1}6s^2$

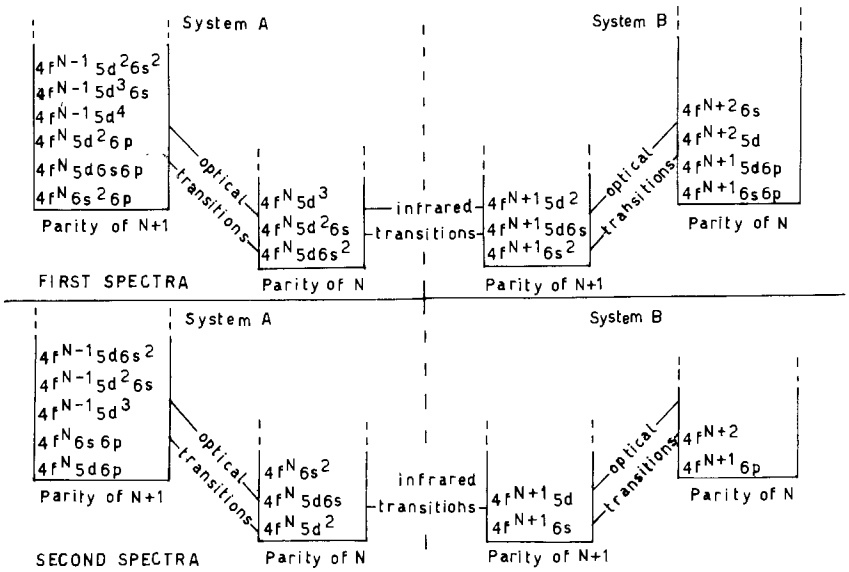

Fig. 1.15. Characteristic structure of first and second lanthanide spectra.

$$\text{System B}\begin{cases}\text{low-parity of } N+1\\ 4f^{N+1}(5d+6s)^{K-1} \equiv 4f^{N+1}5d^{K-1} + 4f^{N+1}5d^{K-2}6s + 4f^{N+1}5d^{K-3}6s^2\\ \text{high I-parity of } N\\ 4f^{N+1}(5d+6s)^{K-2}6p \equiv 4f^{N+1}5d^{K-2}6p + 4f^{N+1}5d^{K-3}6s6p + 4f^{N+1}5d^{K-4}6s^26p\\ \text{high II-parity of } N\\ 4f^{N+2}(5d+6s)^{K-2} \equiv 4f^{N+2}5d^{K-2} + 4f^{N+2}5d^{K-3}6s + 4f^{N+2}5d^{K-4}6s^2\end{cases}$$

The following facts should be noted:

(1) In each system all configurations of the same parity overlap or are close to each other.

(2) In each system there exist spectral transitions in the optical region between *high* and *low* configurations. Since the optical transitions which connect the two systems are very few (see next paragraph), each of the systems effectively generates a separate spectrum. The overlap of these two spectra is one of the reasons for the abundance of lines in lanthanide spectra.

(3) The low configurations of the systems A and B lie at about the same height, and since they have opposite parities, there exist spectral transitions between them in the infra-red region. The same also holds for the high configurations of A and B. These transitions, which are usually difficult to detect, are very important for determining the relative height of the two systems, and, in particular, for establishing the system which contains the ground level of the ion under investigation.

(4) The three competing configurations in each of the six groups "low A", "high I-A", "high II-A", "low B", "high I-B" and "high II-B", are obtained from each

other by interchanging 5d and 6s electrons. The overlap of the configurations in each group demonstrates *the competition between the 5d and 6s electrons.*
(5) The group of "low A" configurations is obtained from the group "low B" by replacing a 4f by a 5d or 6s electron. The same applied to the groups "high I-A" and "high I-B". Since the low as well as the high I configurations of the two systems lie at about the same height, we deduce *the competition 4f–5d, 6s.* This competition leads to the existence of two stable cores $4f^N$ and $4f^{N+1}$, in such a way that the lowest configurations of the groups $4f^N(5d+6s)^K$ and $4f^{N+1}(5d+6s)^{K-1}$ compete for the title "ground configuration" of the ion. On the other hand, a configuration obtained from $4f^N(5d+6s)^K$ by replacing an additional 4f electron by a 5d or 6s electron is an excited configuration. The same applies to $4f^{N+1}(5d+6s)^{K-1}$ when one of its 5d or 6s electrons is replaced by a 4f electron.
(6) The groups of configurations "high I-A" and "high II-A" overlap. This shows that an excitation of a 4f electron from the $4f^N$ core into a 5d or 6s state is energetically equivalent to an excitation of a 5d or 6s electron into 6p. The two groups of configruations differ in the two electrons 4f6p compared with $(5d+6s)^2 \equiv 5d^2+5d6s+6s^2$. We can summarize this situation by stating that *in the high configurations of system A there exists a competition between the pairs of electrons 4f6p, $5d^2$, 5d6s and $6s^2$.*
(7) The groups of configurations "high I-B" and "high II-B" overlap. This shows that an excitation of an electron from a 5d or 6s state into 6p is energetically equivalent to its excitation from the same initial state into a 4f state, thus transforming the $4f^{N+1}$ core into $4f^{N+2}$. *In the high configurations of the system B there exists a competition between 4f and 6p electrons.*

9.1.2. *Third and fourth spectra*

The characteristic structure of the third and fourth spectra is shown in fig. 1.16. In the third spectra the system A comprises, as before, three groups of configurations.

$$\text{System A} \begin{cases} \text{low} & 4f^N(5d+6s) \\ \text{high I} & 4f^N 6p \\ \text{high II} & 4f^{N-1}(5d+6s)^2 \end{cases} (K=1).$$

The competitions described above between the separate configurations of the "low A" group on the one hand and between those of the "high A" groups on the other hand, exist also here, although a stabilization of the 5d shell with respect to the 6s is recognized.

The system B degenerates, in the third spectra, into the single configuration $4f^{N+1}$.

Contrary to the situation in the first and second spectra, where the lowest configurations of the A and B systems compete for the title ground configuration, the configuration $4f^{N+1}$ ("low B") in the third spectra is lower than $4f^N(5d+6s)$ ("low A") by such an amount that most of the transitions between

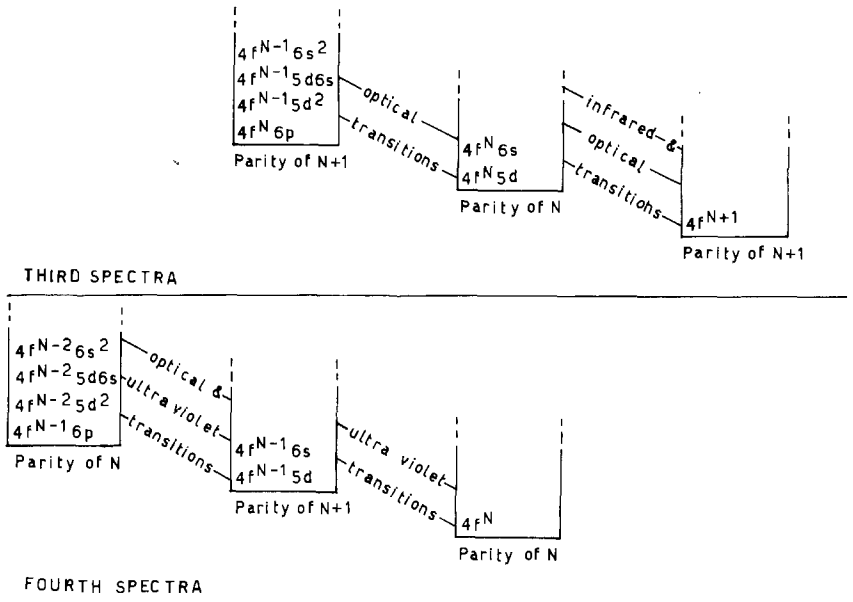

Fig. 1.16. Characteristic structure of third and fourth lanthanide spectra.

them fall in the optical region*. We can therefore conclude that in the third spectra the two systems A and B have degenerated into one system consisting of three stories with optical transitions between the first and second stories as well as between the second and third ones.

The above-mentioned structural differences between the third spectra and those belonging to lower degrees of ionization may be explained as follows: On raising the degree of ionization, the effective charge seen by the electrons outside closed shells increases; this increase is greatest for the internal 4f electrons, smaller for the "half internal" 5d electrons, and smallest for the outer 6s electrons. Consequently in the third spectra the binding energies of these electrons satisfy the inequalities

$$E_{4f} < E_{5d} < E_{6s}.$$

In the fourth spectra the system B does not exist at all. The system A has degenerated into two groups of configurations: "low", $4f^N$, which forms the ground configuration in each of these spectra, and "high II", $4f^{N-1}(5d+6s)$. These groups constitute the first and second stories of the fourth spectra respectively. A third story comprises the two additional groups of configurations $4f^{N-1}6p$ and $4f^{N-2}(5d+6s)^2$. These three stories are analogous to those of the third spectra with the difference that here $N-1$ takes the place of N in the third spectra. The separations of the stories are greater in the fourth spectra, which indicates a further stabilization of the 4f and 5d shells.

*La III and Gd III form exceptions to this rule (see table 1.13b).

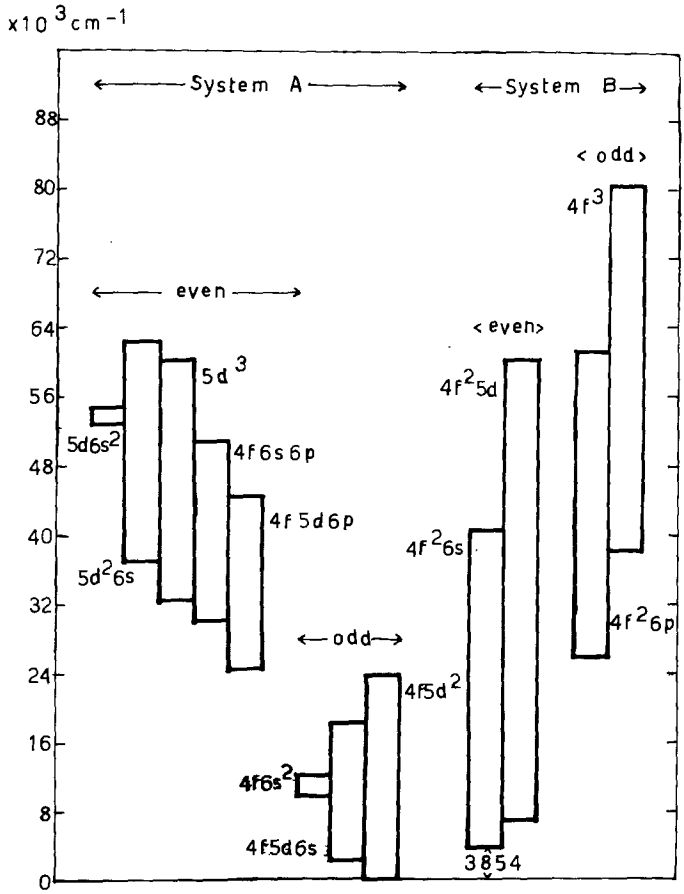

Fig. 1.17. Block diagram for CeII.

The Block diagrams of Ce II and Ce III, given in figs. 1.17 and 1.18, constitute concrete examples of the structure of a second and a third lanthanide spectrum.

Tables 1.13a and 1.13b comprise the ground levels and ionization potentials of the neutral through triply ionized lanthanides (Martin et al., 1974).

9.1.3. *Quantitative results*

Lately, several successful attempts have been made, to reach quantitative conclusions about the energy differences between the lowest levels of systems A and B for first, second and third lanthanide spectra (Brewer, 1971a,b; Nugent and Vander Sluis, 1971; Martin, 1971, 1972; Vander Sluis and Nugent, 1972, 1974; the methods used by these authors are based on the ideas of Racah, 1960–1963; Jørgensen, 1962). For most of these spectra, the lowest configurations of systems A and B are $4f^N5d6s^K$ and $4f^{N+1}6s^K$ respectively. The energy differences between the lowest levels of these configurations have, therefore,

TABLE 1.13a.

Ground levels and ionization potentials for the neutral and singly ionized lanthanide atoms. The designation of the ground level of Tb II is enclosed in braces because the indicated level has not yet been experimentally established as lowest.[b]*

			Neutral, I			Singly ionized, II		
Z	N	Element	Ground level	System	I.P.[a] (V)	Ground level	System	I.P.[a] (V)
57	0	La	$5d6s^2\ ^2D_{3/2}$	A	5.5770(6)	$5d^2\ ^3F_2$	A	11.060(10)
58	1	Ce	$4f5d6s^2\ ^1G_4$	A	5.466(20)	$4f5d^2\ ^4H_{7/2}$	A	10.85(8)
59	2	Pr	$4f^36s^2\ ^4I_{9/2}$	B	5.422(20)	$4f^3(^4I_{9/2})6s\ (9/2, 1/2)_4$	B	10.55(8)
60	3	Nd	$4f^46s^2\ ^5I_4$	B	5.489(20)	$4f^4(^5I_4)6s\ (4, 1/2)_{7/2}$	B	10.73(8)
61	4	Pm	$4f^56s^2\ ^6H_{5/2}$	B	5.554(20)	$4f^56s\ ^7H_2$	B	10.90(8)
62	5	Sm	$4f^66s^2\ ^7F_0$	B	5.631(20)	$4f^66s\ ^8F_{1/2}$	B	11.07(8)
63	6	Eu	$4f^76s^2\ ^8S_{7/2}$	B	5.666(7)	$4f^76s\ ^9S_4$	B	11.241(6)
64	7	Gd	$4f^75d6s^2\ ^9D_2$	A	6.141(20)	$4f^75d6s\ ^{10}D_{5/2}$	A	12.09(8)
65	8	Tb	$4f^96s^2\ ^6H_{15/2}$	B	5.852(20)	$\{4f^9(^6H_{15/2})6s(15/2, 1/2)_8\}$	B	11.52(8)
66	9	Dy	$4f^{10}6s^2\ ^5I_8$	B	5.927(8)	$4f^{10}(^5I_8)6s\ (8, 1/2)_{17/2}$	B	11.67(8)
67	10	Ho	$4f^{11}6s^2\ ^4I_{15/2}$	B	6.018(20)	$4f^{11}(^4I_{15/2})6s\ (15/2, 1/2)_8$	B	11.80(8)
68	11	Er	$4f^{12}6s^2\ ^3H_6$	B	6.101(20)	$4f^{12}(^3H_6)6s\ (6, 1/2)_{13/2}$	B	11.93(8)
69	12	Tm	$4f^{13}6s^2\ ^2F_{7/2}$	B	6.18436(6)	$4f^{13}(^2F_{7/2})6s\ (7/2, 1/2)_4$	B	12.05(8)
70	13	Yb	$4f^{14}6s^2\ ^1S_0$	B	6.25394(2)	$4f^{14}6s\ ^2S_{1/2}$	B	12.184(6)
71	14	Lu	$4f^{14}5d6s^2\ ^2D_{3/2}$	A	5.42589(2)	$4f^{14}6s^2\ ^1S_0$	A	13.9(4)

[a]The number in parentheses is the estimated standard-deviation error in the last digit of the quoted value. [b]Martin et al. (1974).

**Added in proof*: More accurate values for several first ionization potentials were recently determined by Worden, Solarz, Paisner and Conway (to be published in J. Opt. Soc. Amer. 1978).

TABLE 1.13b.

Ground levels and ionization potentials for the doubly and triply ionized lanthanide atoms. The designations of the ground levels of Pm III, and Dy III are enclosed in braces because the indicated levels have not yet been experimentally established as lowest.[b]

			Doubly ionized, III		Triply ionized, IV	
Z	N	Element	Ground level	I.P.[a] (V)	Ground level	I.P.[a] (V)
57	0	La	$5d\ ^2D_{3/2}$	19.1774(6)	$5p^6\ ^1S_0$	49.95(6)
58	1	Ce	$4f^2\ ^3H_4$	20.198(3)	$4f\ ^2F_{5/2}$	36.758(5)
59	2	Pr	$4f^3\ ^4I_{9/2}$	21.624(3)	$4f^2\ ^3H_4$	38.98(2)
60	3	Nd	$4f^4\ ^5I_4$	22.1(3)	$4f^3\ ^4I_{9/2}$	40.41(20)
61	4	Pm	$\{4f^5\ ^6H_{5/2}\}$	22.3(4)	$4f^4\ ^5I_4$	41.1(3)
62	5	Sm	$4f^6\ ^7F_0$	23.4(3)	$4f^5\ ^6H_{5/2}$	41.4(4)
63	6	Eu	$4f^7\ ^8S_{7/2}$	24.92(10)	$4f^6\ ^7F_0$	42.6(3)
64	7	Gd	$4f^7 5d\ ^9D_2$	20.63(10)	$4f^7\ ^8S_{7/2}$	44.0(3)
65	8	Tb	$4f^9\ ^6H_{15/2}$	21.91(10)	$4f^8\ ^7F_6$	39.79(20)
66	9	Dy	$\{4f^{10}\ ^5I_8\}$	22.8(3)	$4f^9\ ^6H_{15/2}$	41.47(20)
67	10	Ho	$4f^{11}\ ^4I_{15/2}$	22.84(10)	$4f^{10}\ ^5I_8$	42.5(3)
68	11	Er	$4f^{12}\ ^3H_6$	22.74(10)	$4f^{11}\ ^4I_{15/2}$	42.65(20)
69	12	Tm	$4f^{13}\ ^2F_{7/2}$	23.68(10)	$4f^{12}\ ^3H_6$	42.69(20)
70	13	Yb	$4f^{14}\ ^1S_0$	25.03(2)	$4f^{13}\ ^2F_{7/2}$	43.74(20)
71	14	Lu	$4f^{14}6s\ ^2S_{1/2}$	20.9596(10)	$4f^{14}\ ^1S_0$	45.19(2)

[a]The number in parentheses is the estimated standard-deviation error in the last digit of the quoted value. [b]Martin et al. (1974).

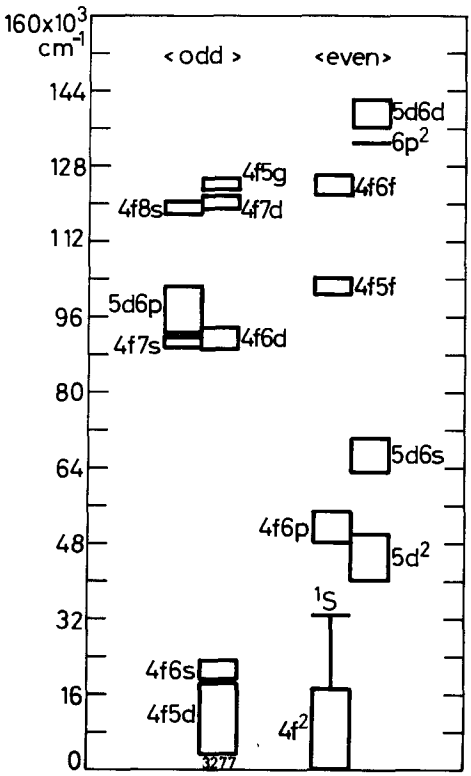

Fig. 1.18. Block diagram for CeIII.

been compared, for a fixed ionization degree. The results obtained are given in table 1.14 and represented as functions of N by broken lines in fig. 1.19. It can be seen from this figure that the broken lines show striking regularities, which are repeated almost exactly for different degrees of ionization (see also columns 4, 6 and 8 in table 1.14). These regularities can be well understood, by considering the formulae obtained for the electrostatic energies of the f^N configurations in terms of the Racah parameters E^i. From formula (1.66) of section 4.2.1.2 for the electrostatic energies of f^2, it follows that E^0 is the baricenter of the triplets and therefore the mean value of the interaction of two f electrons with parallel spins; $2E^1$ is the distance between the baricenter of ^{1}DGI and the baricenter of the triplets; $9E^1$ is the distance of ^{1}S from the baricenter of the triplets. The distances of the individual terms from the baricenters of their group are expressed in terms of E^3 for the triplets and in terms of E^2 and E^3 for the singlets. For f^N configurations, it follows from the discussion in section 4.2.3.3 and from formulae (1.87), (1.88), that for $0 \leq N \leq 7$ and for terms of maximum multiplicity, $S = \frac{1}{2}N$, the electrostatic energy W_m is given by

$$W_m(f^N) = \tfrac{1}{2}N(N-1)E^0 + [3(u_1^2 + u_2^2 + u_1u_2 + 5u_1 + 4u_2) - \tfrac{3}{2}L(L+1)]E^3. \quad (1.162)$$

The coefficient of E^3 depends only on L and $U \equiv (u_1u_2)$ and is independent of v or $W \equiv (w_1w_2w_3)$; it vanishes for $N = 0$, 1, 6, 7, that is, for f^N configurations having only one term of maximum multiplicity, and generally for terms of maximum multiplicity characterized by S(00) and F(10); it is different from zero

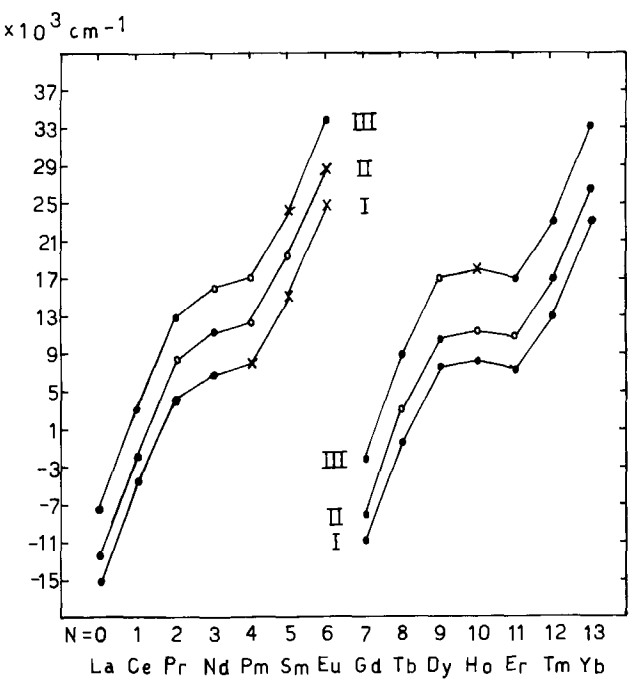

Fig. 1.19. Energy differences between the lowest levels of $4f^N 5d6s^K$ (system A) and $4f^{N+1}6s^K$ (system B), as functions of N. ● – observed value, × – based on calculations carried out with higher observed levels, ○ – predicted value.

TABLE 1.14.
Energy differences between the lowest levels of $4f^N 5d6s^K$ and $4f^{N+1}6s^K$ for first, second and third lanthanide spectra.*,**

		First spectra		Second spectra		Third spectra	
Element	N	$4f^N 5d6s^2$–$4f^{N+1}6s^2$	Δ(II, I)	$4f^N 5d6s$–$4f^{N+1}6s$	Δ(III, II)	$4f^N 5d$–$4f^{N+1}$	Δ(III, I)
La	0	−15.197	2.944	−12.253	5.058	−7.195	8.002
Ce	1	−4.763	3.291	−1.472	4.749	3.277	8.040
Pr	2	4.432[a])	3.8	(8.2)	4.6	12.847	8.415
Nd	3	6.764	4.546	11.310	4.7	(16.0)	9.2
Pm	4	8.0	4.3	(12.3)	4.8	(17.1)	9.1
Sm	5	15.5	4.1	(19.6)	4.9	24.5	9.0
Eu	6	25.1	3.9	29.0	4.9	33.856[b])	8.8
Gd	7	−10.947	2.955	−7.992	5.611	−2.381[c])	8.566
Tb	8	0.286	3.1	(3.4)	5.6	8.972	8.686
Dy	9	7.565	3.029	10.594	5.6	(17.2)	9.6
Ho	10	8.379	3.2	(11.6)	6.5	18.1	9.7
Er	11	7.177	3.4	(10.6)	6.4	16.976	9.799
Tm	12	13.120	3.447	16.567	6.330	22.897	9.777
Yb	13	23.188	3.571	26.759	6.627	33.386	10.198

*This table is mainly based on tables compiled by Martin (Table I, 1971, Table III, 1972) which contain the references to the various differences. References to more recent data also included in this table are given below.

[a])Blaise et al. (1973a).

[b])Sugar and Spector (1974).

[c])Johansson and Litzen (1973).

**The energy differences are given in thousands of cm^{-1}.

for other terms of maximum multiplicity; for the P, H(11) terms appearing in f^2 and f^5, the coefficient of E^3 takes the values 33 and -9 respectively; for D, G, I(20) appearing in f^3 and f^4, the coefficient of E^3 takes the values 33, 12 and -21 (see fig. 1.9).

For each f^N, $0 \leqslant N \leqslant 7$, the baricenter of the terms with maximum multiplicity is given by $\frac{1}{2}N(N-1)E^0$. For $N > 7$ there are no terms with $S = \frac{1}{2}N$ and the maximal spin is given by

$$S_m = \tfrac{1}{2}(14 - N)$$

The electrostatic interaction for such f^N configurations can be calculated according to the following rule due to Condon et al. (1951), chap. XIII: $W(f^{14-\epsilon})$ is obtained from $W(f^\epsilon)$ by adding to it $(7-\epsilon)$ times the expression $9^6 11$ with $nl = n'l'$. This last expression has the value $13E^0 + 9E^1$ and, since

$$7 - \epsilon = 7 - (14 - N) = N - 7,$$

it follows that

$$W_m(f^N, N > 7) = \tfrac{1}{2}N(N-1)E^0 + 9(N-7)E^1 + [3(u_1^2 + u_2^2 + u_1u_2 + 5u_1 + 4u_2) - \tfrac{3}{2}L(L+1)]E^3. \quad (1.163)$$

Equations (1.162) and (1.163) can be written as one equation in the following manner:

$$W_m(f^N) = NA_f + \tfrac{1}{2}N(N-1)E^0 + \tfrac{9}{2}(N - 2S)E^1 + [3(u_1^2 + u_2^2 + u_1 + 5u_1 + 4u_2) - \tfrac{3}{2}L(L+1)]E^3 \quad (1.164)$$

where the first term added on the right-hand side represents the energies of the f electrons in the field of the nucleus and of the closed inner shells.

On calculating the energy differences $4f^N 5d6s^K - 4f^{N+1}6s^K$, only those contributions due to the 5d or $6s^K$ electrons, which are constant or linear in N, are taken into account, assuming that the nonlinear contributions can be neglected*. The energy difference between the lowest terms of $4f^N 5d6s^K$ and $4f^{N+1}6s^K$ are then given by the expression:

$$W_m(4f^N 5d6s^K) - W_m(4f^{N+1}6s^K) \approx \{A_d - A_f + x(\text{fds}) - 9(S_N - S_{N+1} + \tfrac{1}{2})E^1\} + N(y(\text{fds}) - E^0) + [z(U, L)_N - z(U, L)_{N+1}]E^3 \quad (1.165)$$

where A_d is defined in the same manner as A_f, $x(\text{fds})$ and $Ny(\text{fds})$ represent respectively the constant and the linear (in N) contributions due to the 5d and $6s^K$ electrons, and $z(U, L)_N$ stands for the square brackets in (1.164). In obtaining (1.165) from (1.164), the approximation has been made that the electrostatic parameters do not change on passing from $f^N ds^K$ to $f^{N+1}s^K$.

Expression (1.165) consists essentially of three parts: the first part is independent of N, but has a strong discontinuity in the middle of the group, as $S_N - S_{N+1} + \frac{1}{2}$ vanishes on the left half of the group and equals one on the right

*This assumption will be justified by the results of the comparison between theory and experiment (see also Nugent et al., 1971; Martin, 1972).

half. The second part increases linearly with N. The last part is an oscillating function of N: $z(U, L)_N - z(U, L)_{N+1}$ takes the values 0, 9, 12, 0, −12, −9, 0 on the left half, and again the same values on the right half, if the UL values of the lowest terms of f^N and f^{N+1} are considered.

It has thus been shown that the expression (1.165), as a function of N, describes the broken lines of fig. 1.19 very well qualitatively.

In order to make a quantitative comparison between theory and experiment, it is convenient to get rid of the oscillating term. As was mentioned above, this can be achieved by comparing the baricenters of the terms of maximum multiplicity instead of comparing the energies of the lowest terms of $f^N ds^K$ and $f^{N+1}s^K$. The differences between these baricenters are given by expression (1.165) without the last term. For each degree of ionization, the fourteen points, representing these differences as functions of N, lie (in two groups of seven) on two straight lines. This quantitative comparison has been carried out by Nugent et al. (1971) and by Vander Sluis et al. (1972, 1974). In their works they used a formula similar to (1.165) above, from which they omitted not only the last term but also the term represented by E^1, thus bringing all points onto one line. In addition, they included in their formula a term proportional to the spin–orbit parameter ζ_{4f}.

The theory described above was used to predict unknown $f^N ds^K - f^{N+1}s^K$ energy differences for the various lanthanides as seen in table 1.14. This theory is also applicable for studying energy differences between $4f^N nl6s^K$ and $4f^{N+1}6s^K$ and between various configurations involving the same number of 4f electrons (Vander Sluis et al., 1972, 1974; Brewer, 1971a,b).

The results obtained are also useful in correlating the thermodynamic properties of the chemical compounds of the lanthanides (Brewer, 1971a,b).

9.1.4. *Configuration interaction* (CI)

Read again section 3.3. It is worthwhile to add here that the experience gained in the course of studying the lanthanide spectra has shown that CI between *all* configurations of the same parity should be included in the energy-level calculations and it cannot be limited to one system only.

9.2. *Competition between interactions*

9.2.1. *The large number of interactions*

The number of interactions (parameters) included in the energy matrices of a group of competing configurations is large. This property is attributable to two factors:

(1) These configurations may comprise four types of electrons – 4f, 5d, 6s and 6p. This fact, and especially the presence of 4f electrons (large l), cause the number of interactions *within* the configuration to be large.

(2) The competition between a large number of such configurations results in a large number of interactions between the configurations. As an example, tables 1.15 and 1.16 are given, which contain, respectively, the electrostatic parameters

TABLE 1.15.
Parameters for the even configurations of CeII.

	$4f^25d$	$4f6s$	$4f5d6p$	$4f6s6p$	$5d^3$	$5d^26s$	$5d6s^2$
$4f^25d$	$E^0, E^1, E^2, E^3(f^2)$ F_2, F_4, G_1, G_3, G_5(fd)						
$4f^26s$	M(fd, fs) N(fd, sf)	$E^0, E^1, E^2, E^3(f^2)$ G_3(fs)					
$4f5d6p$	$L_2, L_4(f^2, fp)$ R_1, R_3(fd, dp) R_2, R_4(fd, pd)	T_1(fs, dp) T_2(fs, pd)	$F_0, F_2, F_4, G_1, G_3, G_5$(fd) F_2, G_2, G_4(fp) F_2, G_1, G_3(dp)				
$4f6s6p$	T_3(fd, sp) T_2(fd, ps)	$L_2, L_4(f^2, fp)$	J(dp, sp) K(dp, ps)	F_0, G_3(fs) F_2, G_2, G_4(fp) G_1(sp)			
$5d^3$	$G_1, G_3, G_5(f^2, d^2)$	–	$R_1, R_3(fp, d^2)$	–	$A, B, C(d^2)$		
$5d^26s$	$N(f^2, ds)$	$G_1, G_3, G_5(f^2, d^2)$	T_1(fp, ds) T_3(fp, sd)	$R_1, R_3(fp, d^2)$	$H(d^2, ds)$	$A, B, C(d^2)$ G_2(ds)	
$5d\,6s^2$	$G_3(f^2, s^2)$	$N(f^2, ds)$	–	T_1(fp, ds) T_3(fp, sd)	$G_2(d^2, s^2)$	$H(d^2, ds)$	A

TABLE 1.16.
Parameters for the odd configurations of CeII.

	$4f^3$	$4f^26p$	$4f5d^2$	4f5d6s	$4f6s^2$
$4f^3$	$E^0, E^1, E^2, E^3(f^2)$				
$4f^26p$	$L_2, L_4(f^2, fp)$	$E^0, E^1, E^2, E^3(f^2)$ $F_2, G_2, G_4(fp)$			
$4f5d^2$	$G_1, G_3, G_5(f^2, d^2)$	$R_1, R_3(fp, d^2)$	$A, B, C(d^2)$ $F_2, F_4, G_1, G_3, G_5(fd)$		
4f5d6s	$N(f^2, ds)$	$T_1(fp, ds)$ $T_3(fp, sd)$	$H(d^2, ds)$ $M(fd, fs)$ $N(fd, sf)$	$F_0, F_2, F_4, G_1, G_3, G_5(fd)$ $G_3(fs)$ $G_2(ds)$	
$4f6s^2$	$G_3(f^2, s^2)$		$G_2(d^2, s^2)$	$M(fd, fs)$ $N(fd, sf)$	F_0

between the various electron pairs within and between configurations, for the groups of even and odd configurations of CeII. By also adding the spin–orbit, effective and mutual-magnetic parameters to the squares located along the diagonal, the totality of interactions included in the energy matrices is obtained. Similar tables can be prepared for first, third and fourth spectra.

9.2.2. *Classification of the* CI

It is interesting to point out the correspondence between the various CI parameters and the competitions between electrons mentioned in section 9.1.1. This correspondence is summarized in table 1.17.

9.2.3. *The competition between interactions and its effects on the characteristic structure of the lanthanide spectra*

As discussed in part 1, the relative strengths of the various interactions determine the special characteristics of the spectrum under consideration, such as the structure of the energy level scheme, the composition of the eigenstates, the values of the g-factors, intensities and selection rules. In particular, the existence of a coupling depends on some of the interactions being much stronger than the remaining ones. It is a characteristic property of the lanthanides, that a large number of interactions, CI included, are of the same order of magnitude. In such cases it may become impossible to define a coupling and/or to characterize the levels according to configuration quantum numbers. This is referred to as *competition between interactions*. This competition explains the lack of apparent regularity in the energy-level structure, and the breakdown of the selection rules for the spectral transitions. This is an additional reason for the extreme richness in spectral lines of the lanthanide spectra.

TABLE 1.17.
The correspondence between CI parameters and the competitions between electrons.

Competition between electrons	CI parameters
5d–6s	H(dd, ds), G_2(dd, ss), J(dp, sp), K(dp, ps) M(fd, fs), N(fd, sf)
4f–5d, 6s	G_1(ff, dd), G_3(ff, dd), G_5(ff, dd), N(ff, ds), G_3(ff, ss)
4f6p–5d^2, 5d6s	R_1(fp, dd), R_3(fp, dd), T_1(fp, ds), T_3(fp, sd)
4f–6p	L_2(ff, fp), L_4(ff, fp), R_1(fd, dp), R_3(fd, dp), R_2(fd, pd), R_4(fd, pd), T_1(fs, dp), T_2(fs, pd), T_2(fd, ps), T_3(fd, sp)

9.2.4. *Classification of the various interactions according to their strengths. A qualitative discussion.*

It is worthwhile to demonstrate the competition between interactions by means of a qualitative evaluation of the strengths of the various interactions. This evaluation is based on the properties of the radial wavefunctions $R_{nl}(r)$ of the 4f, 5d, 6s and 6p electrons. In fig. 1.20 the radial charge densities $R^2_{nl}(r)$ are plotted as functions of r for the 4f, 5s, 5p, 5d, 6s and 6p electrons of Ce I 4f5d6s6p. These charge distributions, which are characteristic of all lanthanides were obtained by Z.B. Goldschmidt (1972) by performing Hartree–Fock calculations.

The following facts should be noticed:

(1) This plot clearly demonstrates that the 4f electron is located inside the 5s and 5p closed shells – internal electron.

(2) The 6s and 6p are external electrons; their charge distributions largely overlap.

(3) The 5d is an external electron with respect to the 4f electron and an internal electron with respect to the 6s and 6p electrons.

(4) There is almost no overlapping of the charge distribution of the 4f electron and those of the 6s and 6p electrons.

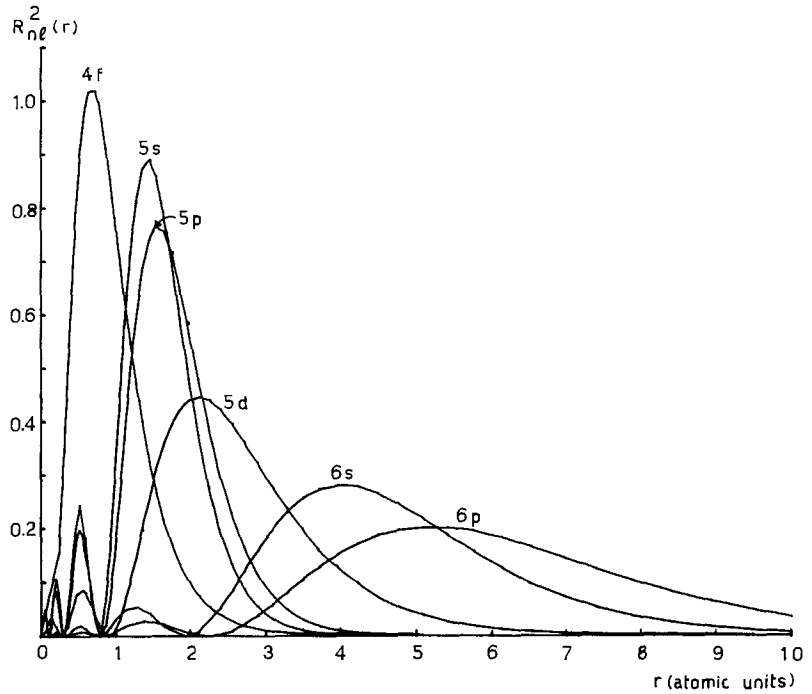

Fig. 1.20. Radial charge density $R^2_{nl}(r)$ as a function of r for the 4f, 5s, 5p, 5d, 6s and 6p electrons of CeI.

(5) On moving to the right hand side of the lanthanide group, the charge distributions under discussion, especially that of the 4f electron, contract ("the lanthanide contraction" – see section 8).

From these facts, qualitative conclusions will now be drawn, concerning the relative strengths of the various interactions, both the spin–orbit interactions and the electrostatic interactions within and between configurations, including their mode of change along the lanthanide group for a definite degree of ionization.

(1) The strongest electrostatic interactions within configurations are:

(i) The interaction between the internal 4f–4f electrons – this results from the fact that $\langle r_{ij}^{-1} \rangle$ is very large for these electrons. This interaction strengthens considerably on moving to the right hand side of the lanthanide group, because of the lanthanide contraction.

(ii) The exchange interaction between the external 6s and 6p electrons – this interaction is very strong because of the almost complete overlap of the charge distributions of these electrons,. A strengthening of this interaction on moving towards the right hand side of group is to be expected, because of the lanthanide contraction.

(2) Strong electrostatic interactions within configurations are the interactions between the 5d–5d, 4f–5d, 5d–6s and 5d–6p electrons. The direct part of these interactions is strong, since $\langle r_{ij}^{-1} \rangle$ is large, although smaller than that for 4f–4f. The exchange part of these interactions is strong, because of the overlapping of the charge distributions of 5d with the internal 4f electron on the one hand and with the external 6s and 6p electrons on the other hand. Since the contraction of the 4f shell, on moving to the right hand side of the group, is greater than the contraction of the other shells, a weakening of the 4f–5d interaction is to be expected, especially of its exchange part. On the other hand, the 5d–5d interaction is expected to strengthen. It is difficult to predict the mode of change of the 5d–6s and 5d–6p interactions*.

(3) The following electrostatic interactions are expected to be very weak:

(i) The direct interaction between the 4f internal electron and the 6p external electron: $\langle r_{ij}^{-1} \rangle$ is relatively small.

(ii) The exchange interactions 4f–6s and 4f–6p.

(4) Electrostatic interactions *between* the configurations $l_a l_b$–$l_c l_d$ are stronger, the larger the overlap of the charge distributions of the l_a and l_c electrons on the one hand and that of the l_b and l_d electrons on the other hand, and also the smaller the distance between the overlapping parts of l_a, l_c and l_b, l_d. J(dp, sp), K(dp, ps), H(dd, ds), G_1(ff, dd) and R_1(fp, dd) are examples of strong CI, which are expected to compete with the dominant interactions within the configurations. M(fd, fs), N(fd, sf), L_2(ff, fp), L_4(ff, fp) are examples of weak CI.

(5) Since the lanthanides belong to the group of heavy elements, it is to be expected that the spin–orbit interactions of the 4f, 5d and 6p electrons will be strong and compete, in many cases, with strong electrostatic interactions.

*From the quantitative results of the energy-level calculations given below, it is known that the 5d–6s and 5d–6p interactions strengthen on moving to the right-hand side of the group.

Qualitative conclusions on the relative strengths of the various spin–orbit interactions can be deduced from the expression obtained for ζ_{nl} through the use of the Coulomb potential energy, $U = -Z_{\text{eff}}e^2/r$, and hydrogenic eigenfunctions:

$$\zeta_{nl} \in Z_{\text{eff}} \int_0^\infty r^{-3} R_{nl}^2(r)\, \mathrm{d}r = 2Z_{\text{eff}}^4/n^3 l(l+1)(2l+1). \tag{1.166}$$

On assuming that the electrons 4f, 5d and 6p "see" the same effective charge, the following ratios between the various ζ_{nl} are derived from (1.166)

$$\zeta_{6p} : \zeta_{4f} = 4.15 \qquad \zeta_{6p} : \zeta_{5d} = 2.89 \qquad \zeta_{5d} : \zeta_{4f} = 1.43$$

The ratios between these parameters, as calculated from the experimental splittings of the doublets of the one-electron spectrum of Ce IV, are

$$\zeta_{6p} : \zeta_{4f} = 4.87 \qquad \zeta_{6p} : \zeta_{5d} = 3.15 \qquad \zeta_{5d} : \zeta_{4f} = 1.55$$

that is, they are not far from the hydrogenic ratios.

On lowering the degree of ionization and moving from Ce IV to Ce III and then to Ce II and Ce I, the values of ζ_{6p} and ζ_{5d} decrease considerably, whereas the value of ζ_{4f} remains almost unchanged. The weakening of the spin–orbit interactions of the 6p and 5d electrons follows from the decrease of the effective charge seen by these electrons due to the screening by inner electrons. The spin–orbit interaction of the 4f electron does not change when the added electrons are external – 6p, 6s or 5d – since their screening effect is negligible; it does decrease to some extent when 4f electrons are added. On moving towards the right hand side of the group, the effective charge seen by the electrons outside close shells increases, resulting in an increase of the values of all parameters ζ_{nl}. The increase of the effective charge is greatest for 4f electrons because of their incomplete screening; therefore the increase of ζ_{4f} is the greatest.

Since, on assuming a Coulomb potential and hydrogenic eigenfunctions, the electrostatic parameters are proportional to Z_{eff}, whereas, the spin–orbit parameters are proportional to Z_{eff}^4, the increase of the spin–orbit parameters, on moving to the right hand side of the group is much greater than the increase of the electrostatic parameters.

The qualitative evaluation of the strengths of the various interactions was confirmed through the quantitative determination of the values of the parameters representing these interactions. Both the qualitative and the quantitative evaluations point to competitions between many interactions of the same relative strength.

10. Methods of interpretation of the lanthanide spectra

The interpretation of a given spectrum is achieved while calculating its energy levels. For this purpose, the energy matrices are constructed, which include all the relevant interactions within and between configurations, and these are

subsequently diagonalized. It is a tradition in theoretical spectroscopy to calculate exactly only the angular part of the energy matrices, whereas the radial integrals are regarded as adjustable parameters. This method of calculation is known as "*the semiempirical method*". As aforesaid, the knowledge of the strengths of the various interactions (parameters) *within* the configurations enables the establishment of the couplings in the individual configurations, that is the choice of the most appropriate coupling scheme for characterizing the states of these configurations. The knowledge of the strengths of the interactions (parameters) *between* configurations enables the evaluation of the repulsions they induce on the energy levels. This helps in understanding the deviations of the energy level schemes from the characteristic structure of the individual configurations.

For simple spectra, the various interaction parameters are evaluated by a direct comparison of the theoretical formulae for the energy levels with their experimental values. Since in most cases the number of parameters is much smaller than the number of levels, the energy level calculation is based on an iterative diagonalization-least-squares process. This process comprises four parts:

(1) Approximate evaluation of the various interaction parameters.

(2) Diagonalization of the energy matrices. The results of the diagonalization include, in addition to the calculated values of the energy levels, also their g-factors, the components of their eigenvectors in any desired coupling scheme, and their derivatives with respect to the parameters.

(3) Comparison of the theoretical results with experimental data. This is based on the heights of the levels, their "names" and their g-factors.

(4) Improvement of the initial values of the parameters, and of the fit between the calculated and observed levels, by means of a least-squares calculation.

For complex spectra, like those of most of the lanthanides, the situation is completely different, since in these spectra we usually have:

(1) High-order energy matrices, which possess many large off-diagonal elements.

(2) A dense list of observed energy levels, most of which are not identified by the experimentalist – only their J and g values are given.

These features complicate the evaluation of the initial parameters directly from the experimental data of a single spectrum and lead to uncertainties in the proper fit of experimental levels to calculated ones, thereby preventing the straightforward application of the iterative process.

In order to get complete and meaningful information about the values of the various parameters, it is necessary to carry out simultaneously the interpretation of several neighbouring spectra, both along an isoionic sequence and of different ions of the same element, in such a way that the values of parameters representing the same interactions in the various spectra are continuously compared. This method, referred to as the "comparison method" is based on the fact, known also in simpler spectra, that the values of the parameters change systematically while moving along an isoionic row or along different degrees of ionization of the same element.

For the purpose of obtaining initial values of unknown parameters, it is

convenient to start with simple spectra, especially two-electron ones, at both ends of the lanthanide group, since in these spectra the orders of the energy matrices are relatively small, and the identity of the experimental levels is usually certain. Also, in these spectra, a detailed analysis of the role played by the individual interactions can be performed, which facilitates the interpretation of more complex spectra.

However, the information about the values of the parameters obtained from two-electron spectra is incomplete; in particular, the relative phases of the CI parameters cannot be established.

Complete, unambiguous and reliable information concerning *all* parameters relevant to lanthanide spectra can be gained through the interpretation of three electron spectra. In the first stage of this interpretation, initial values of the parameters are established, both by using the results of the interpretation of all available two-electron neighbouring spectra, and by direct comparison of the theoretical formulae of "isolated levels" of the investigated three-electron spectrum to their experimental values. Several diagonalizations are then performed, using various possible values for the still doubtful parameters. The results of these diagonalizations are compared with the experimental data. This comparison is best done in several steps, starting with extreme J values, for which the density of energy levels is relatively low, so that many of them may be regarded as isolated; in addition, the number of competing interactions (parameters) for these levels is comparatively small since they belong to only a part of the competing configurations. The proper choice of initial values for many of the parameters guarantees in advance a proper fit between many observed levels and calculated ones. Ambiguities in the fit are resolved by means of additional criteria such as observed g-factors. Of special use are g-factors having extreme values, since their corresponding calculated values can easily be traced in the various stages of the calculations. In cases of disagreement between calculated and observed levels and/or their g-factors, examination of the derivatives of these levels with respect to the various parameters often points out the parameters responsible for this discrepancy, and also leads to the establishment of improved values for these parameters. In this way the correct values of all doubtful parameters which enter into the determination of extreme J energy levels are determined. After a satisfactory fit for most levels included in the first step of the calculations has been obtained, the process is repeated for intermediate J values, until a rough, but over-all, fit of all levels has been achieved. This fit is subsequently improved, and still better values for the parameters are obtained, by a straightforward application of the iterative diagonalization-least-squares process.

Two points should be particularly stressed:

(1) In each stage of the calculations, conclusions concerning corrected values for the various parameters should be reached only after comparing these corrected values with those of the corresponding parameters in neighbouring spectra.

(2) In order to achieve a good agreement between all calculated and observed

levels, in particular in intermediate J values, it is always necessary to include CI with all neighbouring configurations, and generally also effective interactions, which represent CI with distant configurations.

It is worthwhile to point out that rough estimates of the values of the various parameters can be obtained by performing ab-initio calculations such as Hartree self-consistent field (SCF) calculations, or Hartree–Fock (HF) calculations. As will be seen in subsequent sections, the values of the parameters thus obtained are generally considerably *greater* than the corresponding semiempirical parameters. A diagonalization of the energy matrices obtained by the substitution of the SCF or HF parameters results in a calculated energy level scheme in which both the spacings between and within multiplets are greater than the experimental ones. The use of the smaller semiempirical parameter values reproduces the experimental energy level scheme more accurately, since they have absorbed a part of the CI with distant configurations (see section 7). It should, however, be emphasized that the information obtained from the ab-initio calculations about ratios between values of various parameters and about the relative phases of the CI parameters can be quite valuable.

11. Results

The application of the methods described above resulted in a complete understanding of many first, second, third and fourth lanthanide spectra. In these spectra, excellent agreement between theory and experiment has been achieved, and consistent values for the parameters representing the various interactions have been obtained. The stage has been reached where it is possible to make detailed predictions about the structure of lanthanide spectra, even in those cases where the experimental data are still poor.

Table 1.18 includes a list of references for various investigations conducted on the lanthanide spectra.

12. "Isolated" configurations of the types $4f^n$ and $4f^{n-1}n'l'$

In this section we summarize the results of investigations of several types of configurations characteristic of the lanthanide spectra, which, in the first approximation, may be considered as "isolated" and therefore treated separately. In this case, the electrostatic interaction with other configurations is introduced only to second order perturbation theory, namely, by including in the hamiltonian of the investigated configuration effective electrostatic interactions in addition to the "real" electrostatic and spin–orbit interactions. It is shown that further improvement between calculated and observed levels can be obtained through the inclusion of the spin-dependent interactions (SDI), i.e. ss, soo and effective EL–SO.

The results described here include information concerning the *strengths* of the various interactions (Z.B. Goldschmidt, 1968a; Z.B. Goldschmidt and Nir, 1971)

TABLE 1.18.
Table of references for investigations conducted on lanthanide spectra.

			First spectra		Second spectra		Third spectra		Fourth spectra	
Z	N	Element	analysis	I.P.	analysis	I.P.	analysis	I.P.	analysis	I.P.
57	0	La	1–6	7	1, 2, 8–15	16	1, 17–19	20	21	22
58	1	Ce	23–27	28	10, 12, 13, 29–31	16	8–13, 30, 32–36	20	37	20
59	2	Pr	38–40	41	42, 43	16	10–12, 44–54	20	10–13, 15, 47, 48, 51–53, 55–60	20
60	3	Nd	61–64	41	43, 61–66	16	67	20	66	20
61	4	Pm	68	41	69	16	–	20	–	20
62	5	Sm	70, 71	41	71	16	72	20	–	20
63	6	Eu	73–77	41, 78	79	80	81, 82	82	–	20
64	7	Gd	83–89	28	77, 83, 87, 88, 90–94	20	95, 96	20	97	20
65	8	Tb	98–105	41	106	16	107	20	–	20
66	9	Dy	108–111	110	108–110	16	–	20	–	20
67	10	Ho	112–114	41	115, 116	16	117	20	–	20
68	11	Er	118–126	41	126–131	16	132	20	133	20
69	12	Tm	134–136	137	137–140	16	141	20	–	20
70	13	Yb	86, 142–145	146	10, 147–151	151	10–13, 15, 152, 153	20	–	20
71	14	Lu	154–158	158	10, 11, 35, 159, 160	16	161	161	162	162

[1]Russell and Meggers (1932); [2]Moore (1958); [3]Stein (1967a); [4]Stein (1967b); [5]Ben Ahmed, Blaise, Verges and Wyart (1973); [6]Ben Ahmed, Verges, Wilson and Giacchetti (1976); [7]Garton and Wilson (1966); [8]Amiel (1955); [9]Stern (1955); [10]Goldschmidt, Z.B. (1968a); [11]Goldschmidt, Z.B. (1968b); [12]Goldschmidt, Z.B. (1973a); [13]Goldschmidt, Z.B. (1973b); [14]Goldschmidt, Z.B. (1976a); [15]Goldschmidt, Z.B., Salomon and Starkland (1971); [16]Sugar and Reader (1965); [17]Sugar and

Kaufman (1965); [18]Odabasi (1967); [19]Johansson and Litzen (1971); [20]Sugar and Reader (1973); [21]Reader and Epstein (1975); [22]Epstein and Reader (1971); [23]Martin (1971); [24]Goldschmidt, Z.B. and Salomon (1970); [25]Oreg, Salomon and Z.B. Goldschmidt (1973); [26]Oreg (1973); [27]Salomon (1973); [28]Reader and Sugar (1970); [29]Harrison, Albertson and Hosford (1941); [30]Goldschmidt, Z.B. (1972); [31]Corliss (1973); [32]Russell et al. (1937); [33]Sugar (1965a); [34]Spector (1965a); [35]Goldschmidt, Z.B. (1966); [36]Johansson and Litzén (1972); [37]Lang (1936); [38]Zalubas and Borchardt (1973); [39]Blaise et al. (1973a); [40]Blaise et al. (1973b); [41]Reader and Sugar (1966); [42]Rosen et al. (1941); [43]Racah, Z.B. Goldschmidt and Lonka (1960); [44]Sugar (1963); [45]Trees (1964); [46]Feneuille and Pelletier-Allard (1968); [47]Goldschmidt, Z.B., Pasternak and Z.H. Goldschmidt (1968); [48]Goldschmidt, Z.B. and Pasternak (1970); [49]Crosswhite, Crosswhite and Judd (1968); [50]Sugar (1969); [51]Newman and Taylor (1971); [52]Copland, Newman and Taylor (1971a); [53]Copland, Newman and Taylor (1971b); [54]Sugar (1974); [55]Sugar (1965b); [56]Judd, Crosswhite and Crosswhite (1968); [57]Wilson and Fred (1968); [58]Sugar (1971); [59]Morrison and Rajnak (1971); [60]Goldschmidt, Z.B. and Cohen (1975); [61]Schuurmans (1946); [62]Blaise, Chevillard, Verges and Wyart (1970); [63]Morillon (1970); [64]Blaise, Wyart, Hoekstra and Kruiver (1971); [65]Albertson, Harison and McNally (1942); [66]Wyart (1970); [67]Crosswhite and Crosswhite (1970); [68]Reader and Davis (1967); [69]Davis and Reader (1972); [70]Albertson (1937); [71]Blaise, Morillon, Schweighofer and Verges (1969); [72]Dupont (1967); [73]Russell and King (1939); [74]Smith and Wybourne (1965); [75]Smith and Collins (1970); [76]Smith and Wilson (1970); [77]Goldschmidt, Z.B. and Nir (1971); [78]Parr (1971); [79]Russell, Albertson and Davis (1941); [80]Reader (1973); [81]Martin and Sugar (1973); [82]Sugar and Spector (1974); [83]Russell (1950); [84]Pinnington (1967); [85]Nir and Z.B. Goldschmidt (1969); [86]Nir (1969a); [87]Wyart (1970); [88]Blaise, Chevillard, Verges, Wyart and van Kleef (1971); [89]van Kleef, Blaise, Wyart (1971); [90]Zeldes (1953); [91]Smith and Wybourne (1965); [92]Spector (1970a); [93]Spector (1970b); [94]Blaise, van Kleef and Wyart (1971); [95]Callahan (1963); [96]Johansson and Litzén (1973); [97]Kielkopf and Crosswhite (1970); [98]Klinkenberg (1966); [99]Klinkenberg and Meinders (1966); [100]Klinkenberg (1967); [101]Meinders and Klinkenberg (1968); [102]Klinkenberg and van Kleef (1970); [103]Klinkenberg (1972); [104]Racah and Z.B. Goldschmidt (1964); [105]Arnoult and Gerstenkorn (1966); [106]Meinders (1969); [107]Meinders, van Kleef and Wyart (1972); [108]Conway and Worden (1971); [109]Wyart (1971); [110]Wyart (1973); [111]Griffin, Ross and Cowan (1972); [112]Blaise, Camus, Guelachvili, Verges and Wyart (1972a); [113]Blaise, Camus, Guelachvili, Verges and Wyart (1972b); [114]Wyart, Blaise, Verges, Camus and Fred (1973); [115]Sugar (1968); [116]Livingston and Pinnington (1971); [117]McElaney (1967); [118]Marquet and Davis (1965); [119]Marquet and Behring (1965); [120]Spector (1965b); [121]Racah, Z.B. Goldschmidt and Toaff (1966); [122]Spector (1966); [123]Spector (1967a); [124]Spector (1971a); [125]Held (1971); [126]van Kleef and Koot (1973); [127]McNally and Vander Sluis (1959); [128]Judd and Marquet (1962); [129]Goldschmidt, Z.B. (1963); [130]Vander Sluis and McNally (1970); [131]Spector (1971b); [132]Spector (1973); [133]Carter (1966); [134]Camus (1966); [135]Camus (1970); [136]Sugar, Meggers and Camus (1973); [137]Camus (1971); [138]Spector (1967b); [139]Camus and Sugar (1971a); [140]Camus and Sugar (1971b); [141]Sugar (1970a); [142]Meggers and Corliss (1966); [143]Goldschmidt, Z.B. and Nir (1967); [144]Nir (1969b); [145]Nir and Z.B. Goldschmidt (1976); [146]Camus and Tomkins (1969); [147]Racah (1954); [148]Racah (1960); [149]Racah, Z.B. Goldschmidt and Bordarier (1965); [150]Meggers (1967); [151]Kaufman and Sugar (1973); [152]Bryant (1965); [153]Sugar (1970b); [154]Klinkenberg (1954); [155]Bovey, Steers and Wise (1960); [156]Pinnington (1963); [157]Camus and Masoudi (1972); [158]Camus and Tomkins (1972); [159]Meggers and Scribner (1930); [160]Bovey and Pearse (1956); [161]Kaufman and Sugar (1971); [162]Sugar and Kaufman (1972).

within the investigated configurations, and the separate effects of these interactions on the energy level schemes. Couplings are defined in the various configurations, and correlated in each case with the strong interactions. Finer structural details of the energy level schemes are discussed in terms of the weak interactions.

12.1. *The* $4f^n$ *configurations*

The $4f^n$ configuration forms the ground configuration of the third and fourth lanthanide spectra. In the second spectra it belongs to the "high II-B" group and in the first spectra it is so high that it has not yet been discovered in any known spectrum. On the other hand, the low configurations characteristic of the first and second lanthanide spectra are of the types $4f^{n-1}n'l'$, $4f^{n-2}n'l'n''l''$ and $4f^{n-3}n'l'n''l''n'''l'''$ ($n'l'$, $n''l''$, $n'''l'''$ may be equivalent) for which the $4f^x$ core forms the parent or the grandparent configuration; of these, the $4f^{n-2}6s^2$ configuration should especially be mentioned here, since (1) it forms the ground configuration of most first lanthanide spectra, (2) it can theoretically be treated as if it were a $4f^{n-2}$ configuration, $6s^2$ being a closed shell. Levels belonging to $4f^n$ and $4f^{n-2}6s^2$ configurations of various lanthanide ions have been experimentally discovered and theoretically analysed as will be specified below. A summary of the results obtained is given in this section. This summary includes quantitative information on the values of the following parameters and (where possible) also on their mode of change along the lanthanide group, both for a definite ionization stage and for different ions of the same element:

(1) The electrostatic parameters E^0, E^1, E^2, E^3.
(2) The spin–orbit parameter ζ_{4f}.
(3) The effective electrostatic parameters α, β, γ, T^i.
(4) The mutual magnetic ss and soo parameters M^0, M^2, M^4.
(5) The effective EL–SO parameters Q^2, Q^4, Q^6.

It has been found that the coupling in $4f^n$ and $4f^{n-2}6s^2$ is close to LS coupling on the left hand side of the lanthanide group and approaches intermediate coupling on moving towards the middle and right hand side of the group.

The detailed understanding of the spectroscopic properties of the $4f^n$ configurations greatly facilitates the theoretical interpretation of the more complicated configurations $4f^{n-1}n'l'$, $4f^{n-2}n'l'n''l''$ and $4f^{n-3}n'l'n''l''n'''l'''$ in free ions and of the configurations $4f^n$ of the lanthanide ions in crystals, solutions and intermetallic compounds.

12.1.1. *The* $4f^2$ *configurations*

The $4f^2$ configuration comprises, theoretically, the seven terms

$$^1S_0,\ ^3P_{0,1,2},\ ^1D_2,\ ^3F_{2,3,4},\ ^1G_4,\ ^3H_{4,5,6},\ ^1I_6$$

which split into 13 levels. The matrices of the electrostatic interaction are given in formula 1.66; those of the spin–orbit interaction were calculated by Spedding (1940); the matrices of additional SDI were calculated by Z.H. Goldschmidt

(1967), and Pasternak and Z.B. Goldschmidt (1968) and independently by Judd et al. (1968). When all the levels are experimentally known, information (with some limitations) can be obtained on all parameters of types (1)–(5) mentioned above, except for the three-electron T^{i}'s.

The configuration $4f^2$ is known experimentally in the three ions PrIV (Sugar, 1965b), CeIII (Sugar, 1965a; Johansson and Litzen, 1972) and LaII (Meggers, 1932; Russell and Meggers, 1932). In the first two ions it forms the ground configuration, whereas in LaII it starts at 55107 cm^{-1} above the ground level $5d^2\ ^3F_2$. The lowest of all $4f^2$ levels is $^3H_4$ as can be expected from Hund's rule and from the properties of the spin–orbit interaction. $4f^2(^3H_4)$ is, therefore, the ground level of both PrIV and CeIII.

12.1.1.1. PrIV $4f^2$

Only 12 out of the 13 expected levels are experimentally known. The missing level is $^1S_0$. The Grotrian diagram of PrIV $4f^2$ is given in fig. 1.21. As seen from the diagram, the coupling in this configuration is close to *LS* coupling, although deviations from the Landé interval rule occur due to the off-diagonal spin–orbit matrix elements. The most conspicuous deviation occurs for the levels belonging to the ^3F term due to the mutual repulsion between $^3F_4$ and $^1G_4$. The energy levels of this configuration were calculated (using the semiempirical method) by several authors, to various degrees of approximation:

(1) Sugar (1965b) used the conventional hamiltonian (including only the electrostatic and spin–orbit interactions within the $4f^2$ configuration) and added to it

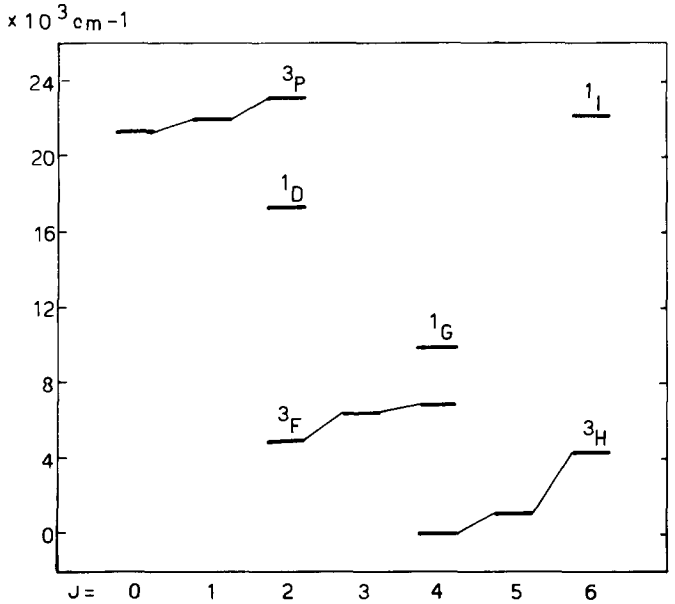

Fig. 1.21. Energy levels of PrIV $4f^2$.

only that part of the effective electrostatic interaction described by $L(L+1)\alpha$ (see formula (1.144) above). He obtained a moderate agreement between observed and calculated levels with a mean error of 125 cm^{-1}.
(2) Z.B. Goldschmidt (1968a) recalculated the energy levels of this configuration with the additional effective electrostatic term $12G(G_2)\gamma$. The term $Q\beta$ could not be included in this calculation since the matrix elements of Q differ from zero only for the missing term ^1S. The mean error reduced to 34 cm^{-1}. In order to determine the importance of the effective electrostatic interactions Goldschmidt also carried out a calculation in which α and γ were fixed on zero values. The mean error increased to 264 cm^{-1}. The values obtained for the parameters in the various

TABLE 1.19.
Parameter values for PrIV $4f^2(cm^{-1})$.

Parameter	Calc(1)[a] H_1+H_2	Calc(2)[a] $+\alpha,\gamma$ of H^2_A but $\beta=0$	Calc(3)[b,c] $+\beta=-620$	Calc(4)[b,c] +SDI	ab initio calculations	
E^0	6705 ± 108	6799 ± 53	6791 ± 62	6792 ± 3		
E^1	5040 ± 103	5011 ± 17	5011 ± 20	5009.6 ± 0.9	6568[d]	
E^2	22.1 ± 0.9	23.15 ± 14	23.12 ± 0.16	23.154 ± 0.007	36.34[d]	
E^3	475 ± 5	488 ± 1	488 ± 1	487.54 ± 0.05	696.9[d]	
α	[0]	24 ± 1	24 ± 1	23.88 ± 0.06	28[e]	47[f]
β	[0]	[0]	[−620]	[−620]	−645[e]	−345[f]
γ	[0]	−49 ± 6	−48 ± 7	−49.05 ± 0.29	−51.3[e]	−49.8[f]
ζ	737 ± 48	760 ± 6	758 ± 8	799.5 ± 1.8	878[g]	1097[f]
M^0	[0]	[0]	[0]	2.45 ± 0.10	2.24[g]	2.275[h]
M^2	[0]	[0]	[0]	0.85 ± 0.13	1.26[g]	1.270[h]
M^4	[0]	[0]	[0]	0.67 ± 0.08	0.85[g]	0.861[h]
Q^2	[0]	[0]	[0]	88.3 ± 5.0		39.9[h]
Q^4	[0]	[0]	[0]	[88.3]		18.2[h]
Q^6	[0]	[0]	[0]	[88.3]		17.1[h]
Δ	264	34	39	1.67		

[a]Z.B. Goldschmidt (1968a); [b]Z.B. Goldschmidt, A. Pasternak and Z.H. Goldschmidt (1968); [c]Z.B. Goldschmidt, A. Pasternak and Z.H. Goldschmidt (1970); [d]Wilson and Fred (1969); [e]Morrison and Rajnak (1971)*; [f]Copland, Newman and Taylor (1971b)*; [g]Blume, Freeman and Watson (1964); [h]Copland, Newman and Taylor (1971a).

*The relations between the parameters α, β and γ defined by Rajnak and Wybourne (1963) (see formula (1.143 above), and those defined by Racah (1964), Trees (1964) and Z.B. Goldschmidt (1968a, 1968b) and also used in this chapter (formula 1.144 above) are:

$$\alpha_{RW}=\alpha_{RTG} \qquad \tfrac{1}{12}\beta_{RW}=\gamma_{RTG} \qquad -\tfrac{2}{5}\gamma_{RW}=\beta_{RTG}.$$

It should also be pointed out that on comparing the results of semiempirical calculations performed, respectively, with the two sets of $\alpha\beta\gamma$ parameters, the following equalities are to be expected:

$$(E^0+\tfrac{1}{5}\gamma(7-n)/(n-1))_{RW}=E^0_{RTG} \qquad (E^1+\tfrac{1}{5}\gamma)_{RW}=E^1_{RTG}.$$

These equalities follow from the following relation (formula 6–16 of Judd (1963) and formulae 1.36 and 1.87 above):

$$5G(R_7)=\tfrac{1}{4}v(16-v)-S(S+1)=\tfrac{1}{2}n(7-n)-2Q+e_1$$

where n designates the number of 4f electrons in the configuration $4f^n$.

approximations are given in table 1.19. The results concerning the observed and calculated levels and the composition percentages of the eigenvectors are given in table 1.20.

(3) Inspection of column 7 of table 1.20 shows that after including second order electrostatic effects, the remaining deviations between observed and calculated levels were of "magnetic" character, namely, they differed in magnitude and in sign for levels belonging to the same (triplet) term*.For this reason, Z.H. Goldschmidt (1967) and Z.B. Goldschmidt et al. (1968, 1970) have repeated the energy-level calculations of PrIV $4f^2$, including additional terms in the hamiltonian, which represent the spin-dependent interactions (SDI), namely the ss, soo and effective EL–SO interactions. For the $4f^2$ configuration, the values of the parameters M^0, M^2, M^4, Q^2, Q^4, Q^6 describing these interactions, as well as the value of the spin–orbit parameter ζ_{4f}, are to be determined from the six splittings of the three triplet terms ^3P, ^3F, ^3H. It follows that not all of these parameters may be allowed to vary freely in a least-squares calculation. Since a systematic investigation of the properties of the spin-dependent interactions for all $3d^n$ configurations of the third and fourth spectra of the iron group resulted in the conclusion that the Q^k's were approximately independent of k (Z.B. Goldschmidt et al., 1968; Z.B. Goldschmidt, 1973a), all Q^k's were constrained to be equal to each other also for PrIV $4f^2$. This property of the Q^k's was also confirmed in the energy-level calculations of PrIII $4f^3$ (Z.B. Goldschmidt et al., 1968, 1970; see also section 12.1.2 below). In Z.B. Goldschmidt's calculation (1968a) described in (2) above, β was fixed on the value zero, since the level $^1S_0$ was missing. The authors of the work described in this paragraph arrived at the conclusion that the βQ correction should nevertheless be included in the calculations, because of its contribution to the $^3P_0$ level (which includes 1% of $^1S_0$ in the composition percentages of its eigenvector). Assuming (α/β) CeIII $4f^2$ (Z.B. Goldschmidt et al., 1968; Z.B. Goldschmidt, 1973a), all Q^k's were constrained to least-squares calculations of PrIV $4f^2$ were carried out with β fixed on this value. The parameters obtained in this calculation are given in columns 4 and 5 of table 1.19. The M^k's, representing the mutual magnetic interactions were found to be positive decreasing functions of k, as required by their definition. The Q^k's, representing the effective EL–SO interaction, were also found to be positive.

The results concerning the energy levels are given in columns 8–13 of table 1.20. On including the additional SDI, the mean error reduced to $2\,cm^{-1}$(!), meaning that these interactions indeed improve the fit between observed and calculated *multiplet splittings*. This improvement is graphically demonstrated in fig. 1.22.

It must be emphasized that the above results crucially depend on the simultaneous introduction of all three SDI. The omission of any of these interactions leads to absurd values for the remaining parameters. The strengths of the additional SDI, that is, their contributions to the various multiplet splittings can

*It should be remembered that for this calculation the electrostatic problem is completely solved, since the number of electrostatic parameters (real and effective) equals the number of terms.

TABLE 1.20.
Energy levels of PrIV $4f^2(cm^{-1})$.

Term	J	Obs	Calc(1)[a] H_1+H_2	O–C(1)	Calc(2)[a] α, γ of H_A^2 but $\beta=0$	O–C(2)	Calc(3)[b,c] $+\beta=$ $-620\,cm^{-1}$	O–C(3)	Calc(4)[b,c] +SDI	O–C(4)	g-calc (4)	Composition percentage (4)
^3H	4	0.0	12	−12	17	−17	23	−23	0	0	0.806	97% + ^1G 3%
	5	2 152.2	2 062	90	2 147	5	2 146	6	2 151	1	1.033	100%
	6	4 389.1	4 228	161	4 377	12	4 370	19	4 390	−1	1.166	100%
^3F	2	4 996.7	4 978	19	4 989	8	4 991	6	4 997	0	0.674	98% + ^1D 2%
	3	6 415.4	6 340	75	6 408	7	6 405	10	6 415	0	1.083	100%
	4	6 854.9	6 984	−129	6 888	−33	6 890	−35	6 855	0	1.161	65% + ^1G 33% + ^3H 2%
^1G	4	9 921.4	10 152	−231	9 904	17	9 903	18	9 921	0	1.083	64% + ^3F 34% + ^3H 1%
^1D	2	17 334.5	17 669	−334	17 330	5	17 330	5	17 334	1	1.033	90% + ^3P 8% + ^3F 2%
^3P	0	21 390.1	21 443	−53	21 372	18	21 351	39	21 389	1	0/0	99% + ^1S 1%
	1	22 007.6	22 026	−18	21 979	29	21 993	15	22 008	0	1.500	100%
	2	23 160.9	23 238	−77	23 211	−50	23 219	−58	23 160	1	1.459	92% + ^1D 8%
^1I	6	22 211.6	21 703	509	22 212	0	22 213	−1	22 212	0	1.000	100%
^1S	0	–	52 233	–	52 125	–	47 811	–	47 778	–	0/0	99% + ^3P 1%

[a]Z.B. Goldschmidt (1968a); [b]Z.B. Goldschmidt, A. Pasternak and Z.H. Goldschmidt (1968); [c]Z.B. Goldschmidt, A. Pasternak and Z.H. Goldschmidt, unpublished material (1970).

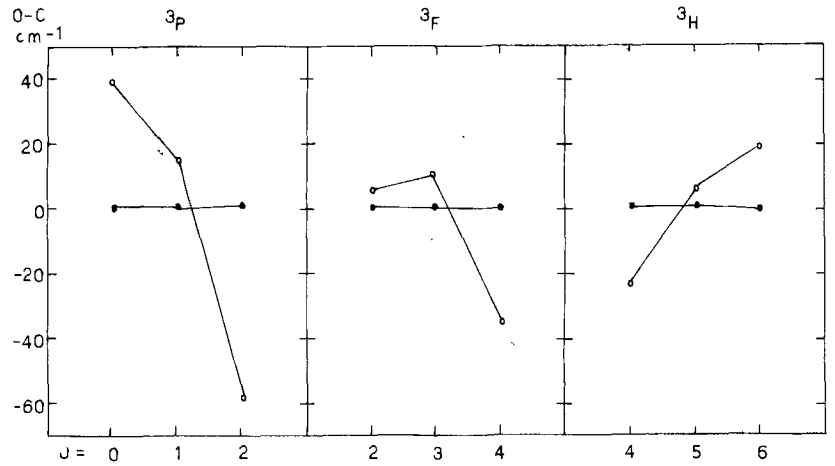

Fig. 1.22. PrIV $4f^2$: improvement in the multiplet splittings due to the spin-dependent interactions (SDI). ○ – without SDI, ● – including SDI.

be calculated by multiplying the derivatives of the energy levels with respect to the SDI parameters – by the corresponding parameter values. It was thus found that the strength of the ss interaction is several cm^{-1}, whereas the strengths of the soo and the effective EL–SO interactions amount to several tens of cm^{-1}.
(4) Judd et al. (1968) have also examined the effects of the SDI on the energy level structure of PrIV $4f^2$. However, they included only the parameters M^0, M^2, M^4 and Q^6* in their least-squares calculations. Consequently, the values they obtained for the M^k's ($M^0 = 1.560$, $M^2 = 0.537$, $M^4 = 0.249\,cm^{-1}$) were too small as compared to both the values obtained by Z.B. Goldschmidt et al. (1968) (see table 1.19) and to the values obtained in Hartree–Fock calculations, as will be specified below. Furthermore, they obtained for Q^6 a negative value ($Q^6 = -252\,cm^{-1}$). This is in contrast with their own evaluation, obtained with the aid of Rajnak (1962) eigenfunctions, that the value of Q^6 due to the single configuration 4f5f should be about 11 cm^{-1}, and that negative contributions could hardly be expected until perturbing configurations that are well into the continuum are reached. The negative value of Q^6 is also in contrast with the results of ab-initio calculations performed by Copland et al. (1971a) as described below, and in contrast with the results of Z.B. Goldschmidt et al. (1968, 1970) (see tables 1.19 and 1.27), who obtained positive values for the Q^k's in PrIV $4f^2$, PrIII $4f^3$, and in all $3d^n$ configurations of the third and fourth spectra of the iron group (see also Z.B. Goldschmidt, 1970; Pasternak et al., 1972, 1974; Z.B. Goldschmidt, 1973a).

*Judd et al. chose parameters P^k to describe the effective EL–SO interaction, which differ by multiplicative factors from the Q^k's used in this chapter. The following relation holds between P^k and Q^k: $Q^k = \frac{1}{6}(3\|C^{(k)}\|3)^2 P^k$.

Ab-initio calculations of PrIV $4f^2$ have been carried out by several authors. Blume et al. (1964) have calculated the spin–orbit parameter ζ_{4f} within the Hartree–Fock description; their calculations are based on a theory in which the contribution of the two-electron spin–other-orbit interaction to ζ_{4f} is taken into account and exchange effects are included. Their results therefore include also Hartree–Fock values for the mutual-magnetic interaction parameters M^k for $4f^n$ configurations of various lanthanide ions; the values they obtained for PrIV $4f^2$ are included in table 1.19. This table also includes (average) Hartree–Fock values for the "real" electrostatic parameters E^i, as presented by Wilson and Fred (1969). Morrison and Rajnak (1971) have performed ab initio calculations for PrIV $4f^2$, in order to evaluate the contributions of various perturbing configurations to the effective electrostatic parameters α, β and γ. They found that (i) it was not sufficient to consider only excitations to bound excited states, but that the continuum excited states also give significant contributions to these parameters; these contributions are of opposite signs, depending upon whether the excitation is of a one-electron or a two-electron type; (ii) among all bound states, the contribution of the $4d^8\ 4f^4$ configuration is by far the dominant contribution. Copland et al. (1971b) also reported numerical estimates for the effective electrostatic parameters α, β and γ in PrIV $4f^2$. These were obtained through the use of the modified version of the Herman and Skillman (1963) Hartree–Fock–Slater computer program. These authors showed that bound state excitations alone grossly overestimate the parameters, and introduced a screening factor of $\frac{1}{5}$ for the two-electron excitations $nd \rightarrow 4f$. In a second paper (1971a), these authors used the same computer program to determine the SDI parameters M^k and Q^k (due to the perturbing configurations 4f5f, 4f6f, 4f7f) for PrIV $4f^2$. No screening was introduced in this case.

The parameter values obtained in the last three works are also included in table 1.19 for comparison with the values of the corresponding parameters obtained in the semiempirical method. It is seen that there is a good agreement between the parameter values obtained in both methods as far as magnitudes and signs are concerned; as already mentioned and explained in section 10, the magnitudes of the parameters obtained in the ab initio calculations are generally greater than those obtained in the semiempirical calculations.

12.1.1.2. CeIII $4f^2$

Ten out of the thirteen levels belonging to this configuration were discovered by Sugar (1965a). The three missing levels $^3P_{0,1,2}$ were found by Johansson and Litzen (1972). The theoretical analysis of this configuration was carried out by Z.B. Goldschmidt (1968a, 1972). The first stage of this analysis was based on Sugar's ten levels, whereas in the final stage all thirteen levels were included. The results obtained concerning the values of the various parameters and energy levels are given in tables 1.21 and 1.22 respectively. Three variations were performed: the first one included only the "real" electrostatic and spin–orbit interactions; in the second variation the effective electrostatic parameters $\alpha\ \beta\ \gamma$ were added (since the $^1S_0$ level of this configuration is experimentally known, the

TABLE 1.21.
Parameter values for CeIII $4f^2(cm^{-1})$.[a]

Parameters	Calc(1) H_1+H_2	Calc(2) $+H_A^2$	Calc(3) +SDI	HF
E^0	5338 ± 272	5052 ± 45	5049 ± 1	–
E^1	3080 ± 101	3906 ± 14	3906.9 ± 0.4	5631
E^2	20 ± 2	18.49 ± 12	18.491 ± 0.003	31.38
E^3	355 ± 15	384.9 ± 0.8	384.45 ± 0.02	601
α	[0]	42.0 ± 1.0	42.17 ± 0.02	–
β	[0]	−1082 ± 20	−1079.5 ± 0.5	–
γ	[0]	−87.6 ± 4.9	−87.9 ± 0.1	–
ζ	612 ± 136	539 ± 5	571.1 ± 0.7	681
M^0	[0]	[0]	3.00 ± 0.09	1.633
M^2	[0]	[0]	0.78 ± 0.10	0.905
M^4	[0]	[0]	0.79 ± 0.07	0.612
$Q^2=Q^4=Q^6$	[0]	[0]	75 ± 2	–
Δ	810	28	0.7	

[a]Z.B. Goldschmidt (1972).

value of β could be determined in the least-squares calculation); the third variation included also the additional SDI, namely, the ss, the soo and the effective EL–SO interactions. The reduction of the mean error, from 810 cm^{-1} through 28 cm^{-1} to 0.6 cm^{-1}, on improving the approximation is shown in table 1.21; the improvement of the fit between the individual observed and calculated levels can be seen by comparing the O_i–C_i values in columns 5, 7 and 9 of table 1.22. The improvements of the calculated triplet splittings due to the inclusion of the additional SDI are also illustrated in fig. 1.23. For comparison, the values of

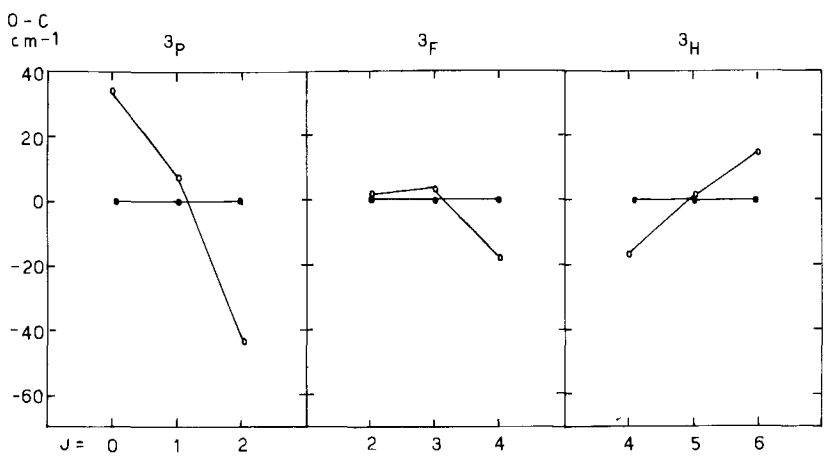

Fig. 1.23. CeIII $4f^2$: improvement in the multiplet splittings due to the SDI. ○ – without SDI, ● – including SDI.

TABLE 1.22.
Energy levels of CeIII $4f^2(cm^{-1})$.[a]

Term	J	Obs	Calc (1) H_1+H_2	O–C (1)	Calc (2) $+H_A^2$	O–C (2)	Calc (3) +SDI	O–C (3)	g-calc (3)	Composition percentage (3)
^3H	4	0	67	−67	17	−17	0	0	0.806	97% + ^1G 3%
	5	1 528	1 841	−313	1 527	1	1 528	0	1.033	100%
	6	3 127	3 634	−507	3 112	15	3 127	0	1.166	100%
^3F	2	3 763	3 871	−108	3 761	2	3 763	0	0.674	98% + ^1D 2%
	3	4 765	5 032	−267	4 761	4	4 765	0	1.083	100%
	4	5 006	4 741	265	5 024	−18	5 006	0	1.149	61% + ^1G 37% + ^3H 2%
^1G	4	7 120	6 765	355	7 108	12	7 120	0	1.095	60% + ^3F 39% + ^3H 1%
^1D	2	12 835	13 038	−203	12 832	3	12 835	0	1.027	91% + ^3P 7% + ^3F 2%
^3P	0	16 072	16 166	−94	16 038	34	16 072	0	$\frac{0}{0}$	100%
	1	16 524	16 732	−208	16 517	7	16 524	0	1.500	100%
	2	17 317	17 726	−409	17 361	−44	17 317	0	1.465	93% + ^1D 7%
^1I	6	17 421	15 389	2 032	17 421	0	17 421	0	1.000	100%
^1S	0	32 839	33 314	−475	32 839	0	32 839	0	$\frac{0}{0}$	100%

[a]Z.B. Goldschmidt (1972).

E^i, ζ and M^k obtained by performing Hartree–Fock calculations (Z.B. Goldschmidt, 1972) are also given (column 5 of table 1.21). As concluded in the case of PrIV $4f^2$, the orders of magnitude obtained for the parameters in both methods of calculation are the same; except for M^0 and M^4, the values of the parameters obtained in the HF method are greater than those obtained in the semiempirical method.

The results of the calculations confirm the conclusion stated above, that the coupling in this configuration is close to *LS* coupling, the only conspicuous mixture is the one occurring between the levels $^3F_4$ and $^1G_4$.

12.1.1.3. LaII $4f^2$

In the spectrum of LaII, the $4f^2$ configuration, belonging to the group High II-B, overlaps the $6p^2$ and 6s6d configurations, which belong to a third floor of system A (not given in fig. 1.15). The Grotrian diagram of these configurations is given in fig. 1.24. The terms of $4f^2$ and $6p^2$ were first calculated by Condon and Shortley (1951). Their results presented two puzzles:

(1) $4f^2$: The ratios obtained in their work for the electrostatic parameters E^i differ considerably from those obtained for other $4f^n$ configurations in neighbouring lanthanide spectra, and also from the ratios calculated with 4f hydrogenic functions (see table 1.23).

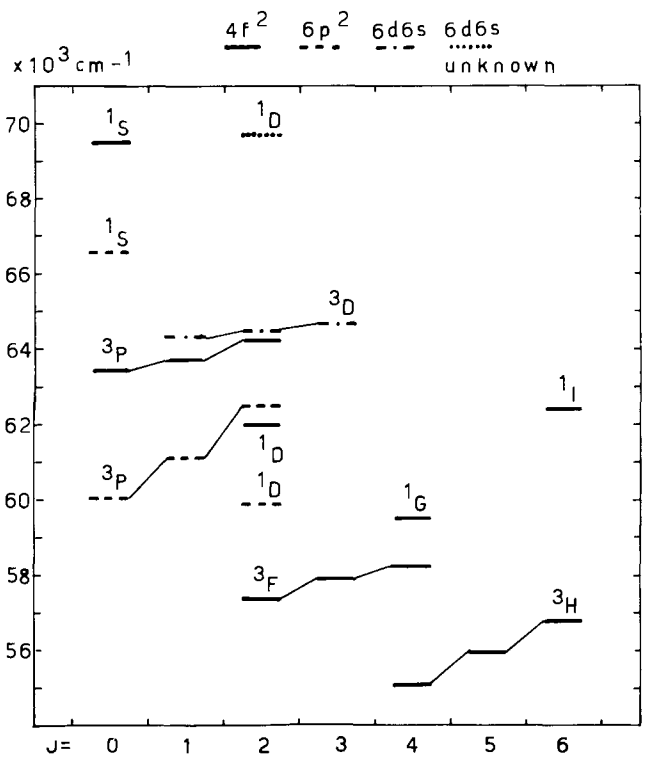

Fig. 1.24. Energy levels of LaII $4f^2 + 6p^2 + 6s6d$.

TABLE 1.23.
Ratios between the electrostatic parameters E^i for various $4f^n$ configurations of the lanthanide spectra.

	E^1	E^2	E^3
Hydrogenic functions	14.68	0.077	1.49
PrIV $4f^{2a}$	14.68	0.068	1.43
CeIII $4f^{2b}$	14.68	0.069	1.44
PrIII $4f^{3c}$	14.68	0.069	1.42
CeII $4f^{3b}$	14.68	0.078	1.32
CeII $4f^3(+CI)^b$	14.68	0.077	1.40
LaII $4f^{2d}$	14.68	0.037	2.09
LaII $4f^{2e}$	14.68	0.055	1.34
LaII $4f^2(+CI)^f$	14.68	0.054	1.30

[a]Z.B. Goldschmidt, Pasternak and Z.H. Goldschmidt (1970); [b]Z.B. Goldschmidt (1972); [c]Z.B. Goldschmidt and Pasternak (1970); [d]Condon and Shortley (1951); [e]Z.B. Goldschmidt (1968a); [f]Z.B. Goldschmidt (1976a).

(2) $6p^2$: The interval ratio $(^1S - {}^1D)/(^1D - {}^3P)$ should, to first order theory, have the value $\frac{3}{2}$, whereas its experimental value in LaII is 18.43!

These puzzles were resolved by Z.B. Goldschmidt (1968a, 1976a) who found that:

(1) the designations given by Russell and Meggers (1932) to the two levels at 59 900.08 cm^{-1} and 63 026.27 cm^{-1} should be interchanged:

Level (cm^{-1})	Identified by Russell & Meggers as	Should be identified as
59 900.08	$4f^2\ {}^1D_2$	$6p^2\ {}^1D_2$
62 026.27	$6p^2\ {}^1D_2$	$4f^2\ {}^1D_2$

(2) configuration interaction, especially between $6p^2$ and 6s6d, should be included in the first order energy-level calculations.

These conclusions were arrived at through the following considerations:

(1) The (upward) repulsions of the LaII $4f^2$ levels by the lower configurations $5d^2$, 5d6s, and 4f6p were calculated and compared with the (downward) calculated repulsions of the CeIII $4f^2$ levels, due to the higher $5d^2$, 5d6s and 4f6p configurations. It was found, for both ions, that among all these repulsions, those originating from $5d^2$ are the dominant ones. The repulsions $4f^2$–$5d^2$ are given in table 1.24 for both ions. On comparing the magnitudes of these repulsions, the following deductions can be made:

(i) The repulsions are greatest for the ^1S's of both ions; next, according to the orders of magnitude of the repulsions, come the ^3P's and the ^1D's.

TABLE 1.24.
Electrostatic repulsions between the corresponding terms of the configurations $4f^2$ and $5d^2$ in CeIII and LaII.*

Term	CeIII[a] (cm^{-1})	LaII[b] (cm^{-1})
^1S	−4740	2800
^3P	−1280	900
^1D	−920	620
^3F	−245	215
^1G	−375	365

*The sign indicates the direction of the repulsion of the $4f^2$ terms; [a]Z.B. Goldschmidt (1972); [b]Z.B. Goldschmidt (1976a).

(ii) For CeIII $4f^2$, ^3P is lower than ^1I by approximately 500 cm^{-1} – this after being pushed down by $5d^2(^3P)$ by about 1300 cm^{-1} (see table 1.24). In LaII $4f^2$, ^3P is pushed up by $5d^2(^3P)$ by about 900 cm^{-1}. Therefore, in LaII $4f^2$, ^3P should be higher than ^1I by 1500–2000 cm^{-1}. A glance at fig. 1.24 and table 1.26 shows that this is indeed the case.

(iii) For the purpose of evaluating the energetic height of LaII $4f^2\,^1D_2$, the value of the interval ratio $(^1D - {}^1G)/(^1I - {}^1G)$ has been compared in PrIV $4f^2$, CeIII $4f^2$ and LaII $4f^2$.

It was found that

$$(^1D - {}^1G)/(^1I - {}^1G) = 0.6 \text{ for PrIV } 4f^2 \qquad (^1D - {}^1G)/(^1I - {}^1G) = 0.56 \text{ for CeIII } 4f^2$$

Since the repulsion of $4f^2(^1D)$ by $5d^2$ is greater than that of $4f^2(^1G)$, and $4f^2(^1I)$ is not affected at all by $5d^2$, it follows that the value of this interval ratio for LaII should be greater than its value for PrIV or CeIII; that is, the relative height of ^1D with respect to ^1G and ^1I should be greater in LaII. For the level 59 900 cm^{-1} identified by Russell and Meggers as $4f^2\,^1D$, the interval ratio has the value $(^1D - {}^1G)/(^1I - {}^1G) = 0.13$. It is clear that this identification is false. For the level 62 026 cm^{-1}

$$(^1D - {}^1G)/(^1I - {}^1G) = 0.86$$

This level was, therefore, identified by Z.B. Goldschmidt (1968a, 1976a) as $4f^2\,^1D_2$.

(2) As for the $6p^2$ configuration: in order to obtain the predicted value for the interval ratio $(^1S - {}^1D)/(^1D - {}^3P)$, one would expect the $6p^2\,^1D_2$ level to lie at about 64 000 cm^{-1}. But the only available experimental level lies at 59 900 cm^{-1}. There should, therefore, exist some configuration, having its $^1D_2$ level higher than $6p^2\,^1D_2$, which is responsible for the downward repulsion of the last level from its predicted position at about 64 000 cm^{-1} to the experimental value 59 900 cm^{-1}.

TABLE 1.25.
Parameter values for LaII $4f^2(cm^{-1})$.[a]

Parameter	Calc $H_1 + H_2 + H_A^2$	HF
E^0	58 463 ± 76	
E^1	1 783 ± 25	2 018
E^2	6.73 ± 0.20	11.43
E^3	163 ± 1	164
α	−33 ± 2	
β	−725 ± 36	
γ	9 ± 8	
ζ	314 ± 8	415
Δ	50	

[a]Z.B. Goldschmidt (1968a).

Indeed, Russell and Meggers identified the ^3D term of the 6s6d configuration, its center of gravity lying at 64 572 cm^{-1} (the ^1D term of this configuration is missing, but its unperturbed value is higher than 64 572 cm^{-1}). Since the configurations $6p^2$ and 6s6d comprise electrons all of which have the same principal quantum number $n = 6$, they are expected to interact strongly with each other. That this is indeed the case was shown by Z.B. Goldschmidt (1976a), who calculated the energy levels of the seven even configurations

$$5d^2 + 5d6s + 6s^2 + 4f6p + 4f^2 + 6p^2 + 6s6d$$

of LaII in intermediate coupling, including configuration interaction and effective electrostatic interaction for the $4f^2$ configuration.

The results of this calculation will be discussed in section 13.2. In this paragraph only the results of the calculation of $4f^2$ as an isolated configuration will be included. Such a calculation is justified because of the facts that (i) the interactions of $4f^2$ with the configurations $6p^2$ and 6s6d overlapping it are small. (ii) the interactions with the low distant configurations are taken into account to second order perturbation theory on including the effective parameters $\alpha\ \beta\ \gamma$ in the energy matrices of $4f^2$. The results obtained are included in tables 1.25 and 1.26. The mean error is 50 cm^{-1}. The "new" relations obtained for E^i are also included in table 1.23.

12.1.2. *The* $4f^3$ *configurations*

12.1.2.1. PrIII $4f^3$

The $4f^3$ configuration comprises 17 terms which split into 41 levels. 38 levels belonging to PrIII $4f^3$ were found by Sugar (1963). The missing levels were $(10)^2F_{5/2,7/2}$ and $(21)^2F_{7/2}$. The energy levels of this configuration were calculated by various authors, to various degrees of approximation:

(1) Trees (1964) performed two variations:

TABLE 1.26.
Energy levels of LaII $4f^2$ (cm^{-1}).[a]

Term	J	Obs	Calc	O–C	g-obs	g-calc	Composition percentage
^3H	4	55 107	55 092	15	0.883	0.805	97%
	5	55 982	55 960	22	1.033	1.033	100%
	6	56 838	56 875	−37	1.14	1.166	99%
^3F	2	57 400	57 368	32	0.675	0.675	98%
	3	57 919	57 965	−46	1.085	1.083	100%
	4	58 259	58 228	31	1.196	1.164	67% + ^1G 32%
^1G	4	59 528	59 544	−16	1.046	1.081	66% + ^1G 33%
^1D	2	62 026	62 042	−16	1.054	1.084	80% + ^3P 18%
^1I	6	62 408	62 408	0	1.003	1.001	99%
^3P	0	63 464	63 497	−33		$\frac{0}{0}$	94% + ^1S 6%
	1	63 703	63 723	−20	1.471	1.500	100%
	2	64 279	64 214	65	1.414	1.408	82% + ^1D 18%
^1S	0	69 505	69 501	4		$\frac{0}{0}$	94% + ^3P 6%

[a]Z.B. Goldschmidt (1968a).

in the first one he included the conventional hamiltonian (electrostatic and spin–orbit interactions within the $4f^3$ configuration) only; in this case the values of the five parameters E^i ($i = 0$, 1, 2, 3) and ζ_{4f} were determined by 37 experimentally known levels.* The mean error obtained was 484 cm^{-1}. In the second variation Trees added the effective electrostatic interaction represented by the parameters α and γ. He did not include the correction term $Q\beta$ in this variation, since both ^2F terms, the matrix elements of which comprise this correction (one directly and the second through a mixture with the first), were missing. The introduction of α and γ reduced the mean error to 168 cm^{-1}, which is about a third of its former value.

(2) Z.H. Goldschmidt (1966) recalculated the energy levels of PrIII $4f^3$, including, in addition to all parameters mentioned above, also the parameter β† and the effective electrostatic three-electron parameters T^i ($i = 2$, 3, 4, 6, 7, 8) introduced by Judd (1966). The mean error reduced to 37 cm^{-1}.

(3) Crosswhite, Crosswhite and Judd (1968) identified the levels $(21)^2F_{7/2}$ and $(10)^2F_{5/2,7/2}$, substituted for Sugar's level $(11)^2H_{9/2}$ at 26 979 cm^{-1} a "new" level at 27 179 cm^{-1} and repeated the energy-level calculations of this configuration, with all the parameters mentioned in (2) above. The mean error obtained was 31 cm^{-1}.

*The level at 34 193 cm^{-1} designated by Sugar as $(21)^2F_{5/2}$ was rejected by Trees and also by the other authors who investigated this configuration.

†The inclusion, in the least-squares calculation, of the correction term βQ was indeed possible, since the eigenvector of the level at 27 597 cm^{-1} ($J = \frac{5}{2}$) was found to include non-negligible components of both ^2F terms, in addition to its main component $(21)^2D$; therefore, the derivative of the corresponding calculated energy level with respect to β was large enough to permit a reliable determination of β.

(4) Z.B. Goldschmidt, Pasternak and Z.H. Goldschmidt (1968) identified independently the level $(10)^2F_{7/2}$, rejected Sugar's level $^4D_{1/2}$ at 23 465 cm^{-1}, and identified a third level at 27 089.66 cm^{-1} as $(11)^2H_{9/2}$. They calculated the energy levels of PrIII $4f^3$, once as an isolated configuration, including also the SDI, namely the ss, soo and effective EL–SO interactions; the mean error reduced to 16 cm^{-1}. In a second calculation they also included in first order perturbation theory, configuration interaction with $4f^26p$, $4f5d^2$ and 4f5d6s. Although the mean error within the $4f^3$ configuration hardly changed, the inclusion of configuration interaction is reflected in the values of the various parameters and, of course, in the compositions of the eigenvectors.
(5) Crosswhite, Crosswhite and Judd (1968) performed a second variation of their calculation mentioned above, in which they included all possible Hermitian two-electron scalar operators and the six three-electron T^i's. This collection of operators allows for the effective electrostatic and EL–SO interactions as well as for the mutual magnetic ss and soo interactions. The mean error reduced to 11 cm^{-1}.

The parameters obtained in the various approximations described above are given in table 1.27, which includes also the corresponding mean errors. The large reductions of the mean error at each stage of the calculations shows the

TABLE 1.27.
Parameter values for PrIII $4f^3(cm^{-1})$.

Parameter	Calc(1)[a] H_1+H_2	Calc(2)[a] $+\alpha, \gamma$ of H^2_A but $\beta=0$	Calc(3)[b] $+\beta$ of $H^2_A+T^i$ of H^3_A	Calc(4)[c] +SDI	ab initio calculations	
E^0	11 024 ± 130	11 182 ± 110	11 172 ± 26	11 172 ± 12		
E^1	4 212 ± 60	4 265 ± 30	4 246 ± 7	4 249 ± 3		
E^2	20.82 ± 0.80	20.57 ± 0.30	19.95 ± 0.12	20.04 ± 0.05		
E^3	401 ± 5	417 ± 3	410 ± 1	409.4 ± 0.4		
α	[0]	29 ± 2	31.4 ± 0.6	31.1 ± 0.3		83[e]
β	[0]	[0]	−834 ± 80	−898 ± 10		−1278[e]
γ	[0]	−64 ± 10	−68 ± 2.8	−67.6 ± 1.2		−102[e]
T^2	[0]	[0]	410 ± 32	427 ± 12		456[f]
T^3	[0]	[0]	36 ± 10	35 ± 5		41[f]
T^4	[0]	[0]	84 ± 14	77 ± 7		68[f]
T^6	[0]	[0]	−263 ± 24	−246 ± 10		−204[f]
T^7	[0]	[0]	328 ± 37	331 ± 16		327[f]
T^8	[0]	[0]	303 ± 43	296 ± 19		286[f]
ζ	643 ± 45	660 ± 20	663 ± 4	692 ± 10	838[d]	959[g]
M^0	[0]	[0]	[0]	1.83 ± 0.58	2.08[d]	1.840[g]
M^2	[0]	[0]	[0]	1.28 ± 0.82	1.17[d]	1.018[g]
M^4	[0]	[0]	[0]	0.10 ± 0.62	0.79[d]	0.688[g]
Q^2	[0]	[0]	[0]	95.7 ± 36.8		114[g]
Q^4	[0]	[0]	[0]	[95.7]		50[g]
Q^6	[0]	[0]	[0]	[95.7]		47[g]
Δ	484	168	37	16		

[a]Trees (1964); [b]Z.H. Goldschmidt (1966); [c]Z.B. Goldschmidt, Pasternak and Z.H. Goldschmidt (1968); [d]Blume, Freeman and Watson (1964); [e]Copland, Newman and Taylor (1971b); [f]Newman and Taylor (1971); [g]Copland, Newman and Taylor (1971a).

importance of the effective electrostatic and the SDI interactions. For comparison, the values of the various parameters obtained through the performance of ab-initio calculations (Blume et al., 1964; Newman and Taylor, 1971; Copland et al., 1971a, b) are also included in this table.

The Grotrian diagram of this configuration is given in fig. 1.4. The observed and calculated energy levels obtained in the calculations described in (4) above, are given in table 1.28, which includes also the composition percentages of the eigenvectors. For comparison, the observed minus calculated values of a varia-

TABLE 1.28.
Energy levels of PrIII $4f^3(cm^{-1})^a$.

Assignment	J	Obs.	Calc.	O–C	Calc. g	O–C without SDI
^4I 97% + $(21)^2H$ 2%	9/2	0.0	−13	13	0.733	1
^4I 99%	11/2	1 398.34	1 396	2	0.966	3
^4I 100%	13/2	2 893.14	2 901	−8	1.107	−1
^4I 99% + ^2K 1%	15/2	4 453.76	4 472	−18	1.199	−11
^4F 95% + $(20)^2D$ 4%	3/2	9 370.66	9 363	8	0.425	15
^4F 98% + $(20)^2D$ 2%	5/2	10 138.18	10 135	3	1.032	8
^4F 93% + $(20)^2G$ 4% + $(21)^2G$ 3%	7/2	10 859.06	10 869	−3	1.215	−6
^4F 78% + $(21)^2H$ 16% + $(20)^2G$ 2%	9/2	11 761.69	11 759	2	1.248	−11
$(21)^2H$ 60% + ^4F 10% + $(20)^2G$ 10%	9/2	10032.92	10 035	2	0.988	−21
$(21)^2H$ 82% + $(11)^2H$ 13% + ^4G 4%	11/2	12 494.63	12 505	−10	1.097	0
^4S 95% + ^2P 4%	3/2	10 950.24	10 948	2	1.963	1
$(20)^2G$ 41% + $(21)^2G$ 30% + ^4G 24%	7/2	13 887.6	13 880	8	0.932	17
$(20)^2G$ 29% + ^4G 45% + $(21)^2G$ 18%	9/2	16 763.98	16 759	5	1.144	13
^4G 99%	5/2	14 187.35	14 189	−2	0.575	19
^4G 76% + $(20)^2G$ 14% + $(21)^2G$ 9%	7/2	15 443.48	15 443	0	0.966	21
^4G 53% + $(20)^2G$ 18% + $(21)^2G$ 14%	9/2	15 705.13	15 707	−2	1.138	−8
^4G 95% + $(11)^2H$ 3% + $(21)^2H$ 2%	11/2	17 409.58	17 406	4	1.263	−33
^2K 99%	13/2	16 089.14	16 097	−8	0.935	−17
^2K 96% + ^2L 3% + ^4I 1%	15/2	17 642.06	17 639	3	1.064	6
$(20)^2D$ 49% + ^2P 41% + ^4F 4%	3/2	17 095.63	17 089	7	1.048	6
$(20)^2D$ 98% + ^4F 2%	5/2	19 046.09	19 033	13	1.196	20
^2P 95% + ^4D 5%	1/2	18 693.65	18 683	11	0.633	19
^2P 53% + $(20)^2D$ 41% + $(21)^2D$ 3%	3/2	20 856.86	20 847	10	1.095	6
^4D 95% + ^2P 5%	1/2		23 498		0.032	
^4D 82% + $(21)^2D$ 15%	3/2	23 091.7	23 108	−16	1.136	−52
^4D 79% + $(21)^2D$ 19%	5/2	23 245.99	23 252	−6	1.326	−2
^4D 98% + $(10)^2F$ 1%	7/2	24 886.51	24 873	14	1.424	39
^2I 84% + $(11)^2H$ 14% + $(21)^2H$ 1%	11/2	24 357.98	24 387	−29	0.950	−16
^2I 99%	13/2	25 391.75	25 403	−11	1.076	−23

TABLE 1.28 (*Contd.*)

Assignment	J	Obs.	Calc.	O–C	Calc. g	O–C without SDI
^{2}L 97% + ^{2}K 3%	15/2	25 244.61	25 239	6	0.945	8
^{2}L 100%	17/2	26 447.88	26 414	34	1.059	38
(21)^{2}D 88% + ^{4}D 16% + (20)^{2}D 3%	3/2	26 921.49	26 930	−9	0.867	−11
(21)^{2}D 58% + ^{4}D 20% + (21)^{2}F 12%	5/2	27 597.13	27 605	−8	1.161	−6
(11)^{2}H 87% + (21)^{2}H 11%	9/2	27 089.66	27 108	−18	0.912	−12
(11)^{2}H 69% + ^{2}I 16% + (21)^{2}H 14%	11/2	28 101.77	28 107	−5	1.066	−20
(21)^{2}F 41% + (10)^{2}F 34% + (21)^{2}D 23%	5/2		30 490		0.938	
(21)^{2}F 61% + (10)^{2}F 37% + ^{4}D 1%	7/2		31 614		1.145	
(21)^{2}G 58% + (20)^{2}G 41%	9/2	39 225.6	39 210	16	1.110	−14
(21)^{2}G 59% + (20)^{2}G 40%	7/2	39 940.72	39 946	−5	0.891	28
(10)^{2}F 61% + (21)^{2}F 38%	7/2	53 092.8	53 092	1	1.141	0
(10)^{2}F 55% + (21)^{2}F 45%	5/2		54 026		0.857	

[a]Z.B. Goldschmidt, Pasternak and Z.H. Goldschmidt (1968).

tion which did not include the SDI are also given. The improvement of the multiplet splittings due to the inclusion of the SDI is illustrated in fig. 1.25.

12.1.2.2. CeII $4f^3$

In CeII, the configuration $4f^3$ belongs to the group High II-B, its lowest level $^4I_{9/2}$ being located 38 195 cm^{-1} above the ground level of this spectrum. Only six out of the theoretically expected seventeen terms have been experimentally

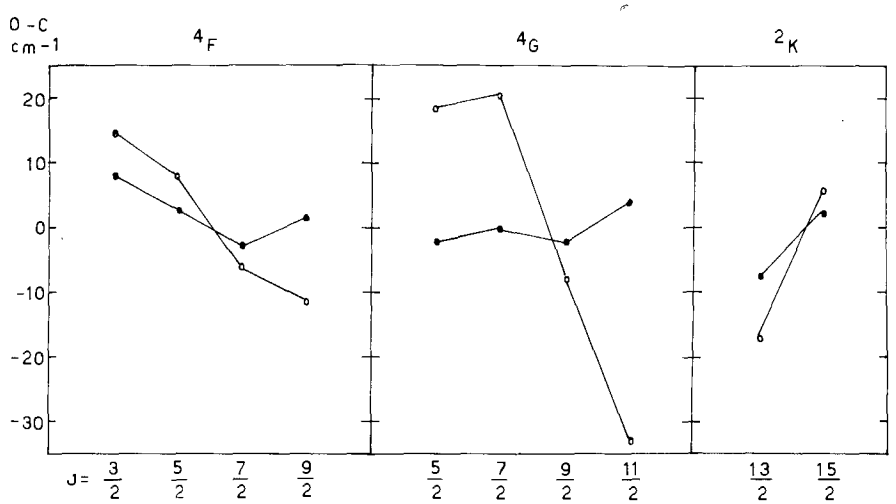

Fig. 1.25. PrIII $4f^3$: improvement in the multiplet splittings due to the SDI. ○ – without SDI, ● – including SDI.

located (Harrison et al., 1941, Z.B. Goldschmidt, 1968a, Corliss, 1973, and Corliss and Z.B. Goldschmidt as also specified in Corliss, 1973). The six experimentally known terms ^{4}I, ^{4}F, (21)^{2}H, (20)^{2}G, ^{4}G, ^{2}K comprise 18 levels (out of the expected 41).

A preliminary calculation of the energy levels of this configuration has been carried out by Z.B. Goldschmidt (1968a), being based on the 10 experimental levels known at that time. In 1972, Z.B. Goldschmidt recalculated the energy-levels of this configuration, including CI with other odd known configurations, namely, 4f5d^2, 4f5d6s, 4f6s^2, and 4f^{2}6p. The results of this calculation will be discussed in section 14.

12.1.3. *Other* 4f^n *configurations*

The experimental data available on other 4f^n configurations in free lanthanide ions are rather scant, as summarized below:

(1) The 4f configuration was discovered in CeIV (Lang, 1936) and in LaIII (Sugar and Kaufman, 1965; Odabasi, 1967; Johansson and Litzen, 1971). The 4f^{13} configuration is known in Yb IV (Bryant, 1965) and in Tm III (Sugar, 1970). The knowledge of these configurations makes it possible to determine the values of the spin–orbit parameter ζ_{4f} at both ends of the lanthanide group. These are given in table 1.29 and in fig. 1.26.

(2) Dupont (1967) identified the seven levels of SmIII 4f^6 ^{7}F; Johansson and Litzen (1973) discovered the five levels GdIII 4f^8 ^{7}F$_{2-6}$. The values of ζ_{4f} obtained from these levels are also given in table 1.29 and in fig. 1.26.

(3) The nine levels ^{8}S$_{7/2}$, ^{6}P$_{5/2,7/2}$ and ^{6}I$_{7/2-17/2}$ of EuIII 4f^7 were identified by Sugar and Spector (1974). No calculation of the energy levels of this configuration has been carried out.

(4) Meinders et al. (1972) discovered the 10 levels ^{6}H$_{15/2-5/2}$ and ^{6}F$_{11/2-5/2}$ of TbIII 4f^9. They also performed a preliminary calculation of these levels, based only on the conventional hamiltonian $H_1 + H_2$. The values obtained for the parameters are also included in table 1.29 and in fig. 1.26. As seen from the figure, the points representing the values of the E^i for TbIII 4f^9 are not located on the smooth (straight) lines drawn for the purpose of describing the mode of change of these parameters on moving along the group for a fixed degree of ionization. The reason for this phenomenon seems to be the omission of the effective electrostatic interaction in their calculation. Indeed, the authors point out that a calculation including α ($=21\,\mathrm{cm}^{-1}$) results in a value of $550\,\mathrm{cm}^{-1}$ for E^3, which is in complete agreement with the value of $545\,\mathrm{cm}^{-1}$ obtained from fig. 1.26.

(5) McElaney (1967) discovered the 6 levels ^{4}I$_{15/2-9/2}$ and ^{4}F$_{9/2}$, ^{4}H$_{11/2}$ of HoIII 4f^{11}. No calculation of this configuration has been carried out. However, the parameter values can be deduced from fig. 1.26; they are also included in table 1.29.

(6) Spector (1973) located the 3 levels ^{3}H$_{6,5}$ and ^{3}F$_4$ of ErIII 4f^{12}. Predicted values for the parameters of this configuration have been obtained by Z.B. Goldschmidt (1976b), on comparing the experimental data and the results of the calculations

TABLE 1.29.
Parameter values for $4f^n$ configurations in lanthanide ions (cm^{-1}).

Ion	Configuration	Ref.	E^1	E^2	E^3	α	β	γ	ζ
CeIV	4f	a,b							644
PrIV	$4f^2$	c,d	5011 ± 17	23.15 ± 0.14	488 ± 1	24 ± 1	[−620]	−49 ± 6	760 ± 6
YbIV	$4f^{13}$	a,b							2883
LaIII	4f	a,b							429
CeIII	$4f^2$	e	3906 ± 14	18.49 ± 0.12	385 ± 1	42 ± 1	−1082 ± 20	−88 ± 5	539 ± 5
PrIII	$4f^3$	f,c	4246 ± 7	19.95 ± 0.12	410 ± 1	31.4 ± 0.6	−834 ± 80	−68 ± 2.8	663 ± 4
SmIII	$4f^6(^7F)$	g							1150
GdIII	$4f^8(^7F)$	g							1306 ± 63
TbIII	$4f^9$	h	5404 ± 140	27.6 ± 2	507.8 ± 2	[0]	[0]	[0]	1555.6 ± 7
HoIII	$4f^{11}$	g	6100	29.0	590	[0]	[0]	[0]	1940
ErIII	$4f^{12}$	g	6339	30.40	609	[0]	[0]	[0]	2237
TmIII	$4f^{13}$	i							2507
LaII	$4f^2$	a	1783 ± 25	6.73 ± 20	163 ± 1	−33 ± 2	−725 ± 36	9 ± 8	314 ± 8
CeII	$4f^3$	e	3044 ± 85	16.94 ± 1.27	272 ± 3	7 ± 3	[−600]	[−50]	429 ± 8

[a]Z.B. Goldschmidt (1968a); [b]Z.B. Goldschmidt (1968b); [c]Z.B. Goldschmidt, Pasternak and Z.H. Goldschmidt (1968); [d]Z.B. Goldschmidt, Pasternak and Z.H. Goldschmidt (1970); [e]Z.B. Goldschmidt (1972); [f]Z.H. Goldschmidt (1966); [g]Z.B. Goldschmidt (1976b); [h]Meinders, van Kleef and Wyart (1972); [i]Sugar (1970a).

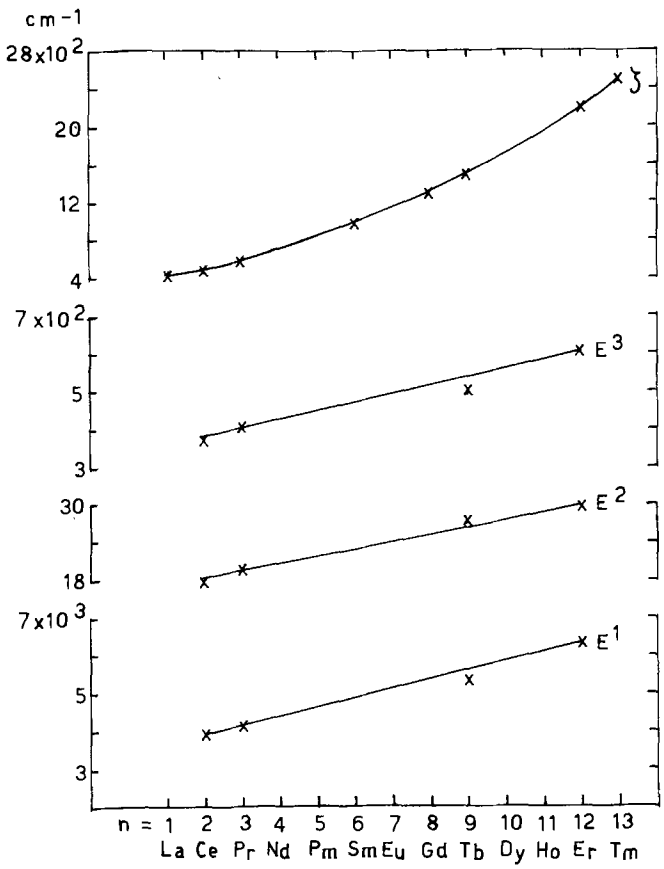

Fig. 1.26. $4f^n$ configurations: values of the various interaction parameters as functions of n, for third lanthanide spectra.

TABLE 1.30.
Low energy levels of ErI $4f^{12}6s^2$, ErII $4f^{12}6s$ and ErIII $4f^{12}$(cm^{-1}).

Level	ErI $4f^{12}6s^{2a,b}$	ErII $4f^{12}6s^{b,c,d}$ core levels	ErIII $4f^{12e}$
$^3H_6$	0	0	0
$^3H_5$	6 958	6 968	6 970
$^3H_4$	10 751	10 774	
$^3F_4$	5 035	5 051	5 082
$^3F_3$	12 378	12 390	
$^3F_2$	13 098	13 206	

[a]Marguet and Davis (1965). [b]Z.B. Goldschmidt (1968a).
[c]McNally and Vander Sluis (1959). [d]Vander Sluis and McNally (1970). [e]Spector (1973).

TABLE 1.31.
Parameter values for ErI $4f^{12}6s^2$, ErII $4f^{12}6s$ and ErIII $4f^{12}$(cm^{-1}).

Parameter	ErI $4f^{12}6s^2$[a]	ErII $4f^{12}6s$[a] (core parameters)	ErIII $4f^{12}$[b]
E^1	6291	6307	6339
E^2	30.04	30.26	30.40
E^3	602	606	609
ζ_{4f}	2235	2237	2238

[a]Z.B. Goldschmidt (1968a); [b]Z.B. Goldschmidt (1976b).

of ErI $4f^{12}6s^2$ (Z.B. Goldschmidt, 1968a), ErII $4f^{12}6s$ (Z.B. Goldschmidt, 1963, 1968a) and ErIII $4f^{12}$, and on referring to the fact that, on the right hand side of the lanthanide group, the energy levels of the $4f^n$ core are approximately independent of the number of 6s outer electrons surrounding it. The low energy levels and the parameter values of these configurations are given in tables 1.30 and 1.31 respectively. The parameter values are also included in table 1.29.

12.1.4. *Conclusion*

The $4f^2$ and $4f^3$ configurations have been thoroughly and profoundly investigated. Information has been obtained on the strengths of the various interactions, and on the coupling being close to *LS* coupling. In particular, the importance of the effective electrostatic and the spin-dependent interactions in reproducing the energy-level structure of these configurations has been established. Furthermore, a comparison has been made between the values of the interaction parameters obtained through the use of the semiempirical method on the one hand, and as a result of ab initio calculations on the other hand. It was found that the values of the parameters obtained in both methods agree as far as orders of magnitudes and signs are concerned; however, the values of the parameters obtained as a result of the ab-initio calculations are generally greater than the corresponding values obtained in the semiempirical method.

Information has been obtained on the mode of change of the various parameters on moving along the group for a fixed degree of ionization, and in some cases (Ce, Pr) also on moving between various ions of the same element. For $4f^n$ configurations belonging to the third spectra of the lanthanide group, both qualitative and quantitative information on this mode of change can be obtained on inspecting table 1.29 and fig. 1.26; it is seen that the electrostatic parameters change approximately linearly with n, and therefore with Z_{eff}, as expected from the theory, whereas ζ_{4f} is not a linear function of $n(Z_{eff})$, but of some power of $n(Z_{eff})$, with an exponent greater than 1. The quantitative information concerning the mode of change of these parameters is obtained on considering the following ratios:

$$E^1(\text{ErIII } 4f^{12})/E^1(\text{CeIII } 4f^2) = 6339/3906 = 1.62$$

$$E^2(\mathrm{ErIII}\ 4f^{12})/E^2(\mathrm{CeIII}\ 4f^2) = 30.40/18.49 = 1.64$$
$$E^3(\mathrm{ErIII}\ 4f^{12})/E^3(\mathrm{CeIII}\ 4f^2) = 609/385 = 1.58$$

i.e.

$$E^i(\mathrm{ErIII}\ 4f^{12})/E^i(\mathrm{CeIII}\ 4f^2) \approx 1.61 \qquad i = 1, 2, 3$$

also

$$\zeta(\mathrm{ErIII}\ 4f^{12})/\zeta(\mathrm{CeIII}\ 4f^2) = 2237/539 = 4.15 \approx 1.61^3$$

On assuming that the E^i increase as Z_{eff}, ζ increases as Z_{eff}^3 and not as Z_{eff}^4, as in the case of the Coulomb potential energy and hydrogenic eigenfunctions. It is interesting also to calculate the amount of increase of ζ, starting with LaIII 4f and ending with TmIII $4f^{13}$:

$$\zeta(\mathrm{TmIII}\ 4f^{13})/\zeta(\mathrm{LaIII}\ 4f) = 2507/429 = 5.84$$

As a result of the increase in the parameter values, the level spacings of the $4f^n$ configurations also increase; for example, the (energy) width of TmIII $4f^{13}$ is greater than the width of the conjugate configuration LaIII 4f, the width of ErIII $4f^{12}$ is greater than that of CeIII $4f^2$, etc.

Since the increase of the spin–orbit parameter ζ is much greater than the increase of the E^i, the coupling in the $4f^n$ configurations changes from a good LS coupling on the left hand side of the group to intermediate coupling as one moves towards the right hand side of the group.

12.2. *The* $4f^{n-1}6s$ *configurations*

The $4f^{n-1}6s$ configurations are the simplest of the $4f^{n-1}n'l'(n'l' = 5d, 6s, 6p, \ldots)$ configurations which are common in the lanthanide spectra. They are found among the low lying configurations of these spectra; in the second spectra they belong to the group "Low B", and compete with the $4f^{n-2}5d^2$, $4f^{n-2}5d6s$ and $4f^{n-2}6s^2$ configurations, for the title "Ground configuration" (see table 1.13a). In the third and fourth lanthanide spectra, the ground configuration is generally $4f^n$, and following it, in this order of height, are the configurations $4f^{n-1}5d$ and $4f^{n-1}6s$. Levels belonging to $f^{n-1}s$ configurations have been experimentally identified in many lanthanide ions, as shown below. The properties of these configurations, concerning the energy-level structure, the strengths of the various interactions, including the values of the parameters representing them, and the prevailing coupling, were discussed by Wybourne (1965) and by Z.B. Goldschmidt (1968a, b), making use of the experimental data available at that time. Since then many more lanthanide spectra have been analysed and a more complete picture of the structure of the $f^{n-1}s$ configurations can now be drawn.

The characteristic structure of these configurations can be understood by inspecting their Grotrian diagrams, several typical examples of which are given in figs. 1.27–1.31. It can be seen that for $(n-1) = 1, 2, 3, 4, 9, 10, 11, 12, 13$ the

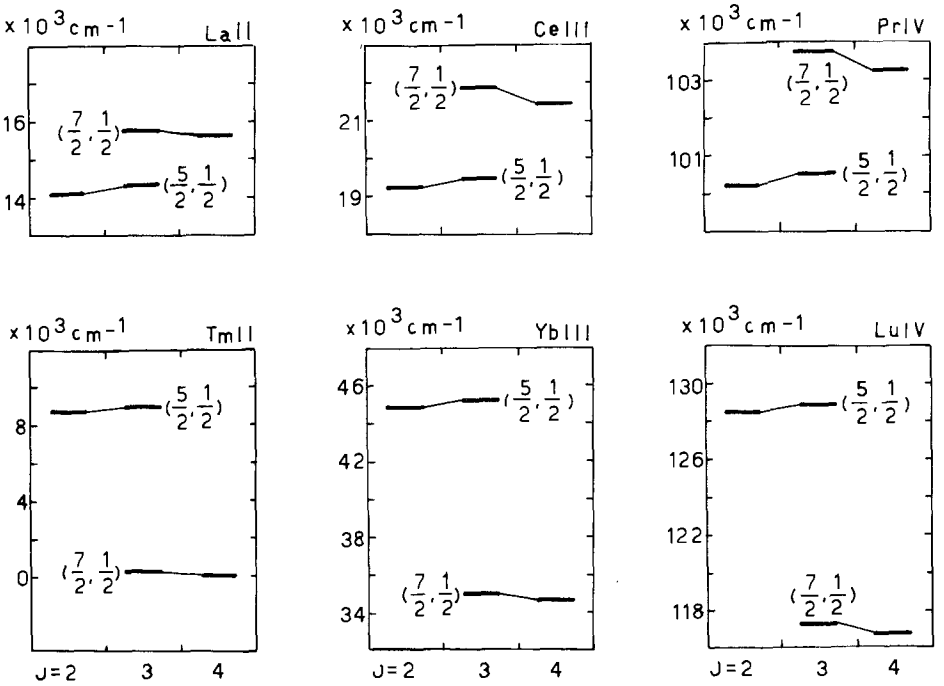

Fig. 1.27. Energy levels of the 4f6s configuration in LaII, CeIII and PrIV and of the $4f^{13}6s$ configuration in TmII, YbIII and LuIV.

energy levels are grouped into pairs, where each pair consists of two adjacent levels having consecutive J values. The centers of gravity of the pairs constitute level diagrams which are analogous to those describing the corresponding $4f^{n-1}$ cores, (see for example, figs. 1.28 and 1.21 above). These facts lead to the immediate conclusion that the coupling prevailing in these configurations is a J_1j coupling, where J_1 is the total angular momentum of the core $4f^{n-1}$ and j is the total angular momentum of the 6s electron. In order to convince the reader, the Grotrian diagram of ErII $4f^{12}6s$ is also drawn in LS coupling – see fig. 1.31b. The existence of J_1j coupling in these configurations is due to the fact that the interactions among the $4f^{n-1}$ core electrons are much stronger than the electrostatic interaction $4f^{n-1}$–6s. Within the $4f^{n-1}$ core, the electrostatic interaction is stronger than the spin–orbit interaction (see section 12.1). The relative strengths of the various interactions are, therefore, given by the first multiple inequality of section 3.2.3, and the most appropriate coupling scheme for characterizing the energy levels of these configurations is:

$$4f^{n-1}(\alpha S_1 L_1 J_1)6sj;\ JM\ (n-1=1,2,3,4,9,10,11,12,13).$$

Since $j=\frac{1}{2}$, it follows that $J=J_1\pm\frac{1}{2}$. Therefore, each core level, characterized by $\alpha S_1 L_1 J_1$, splits into a pair of levels having the J values $J=J_1\pm\frac{1}{2}$ (for $J_1=0$, J

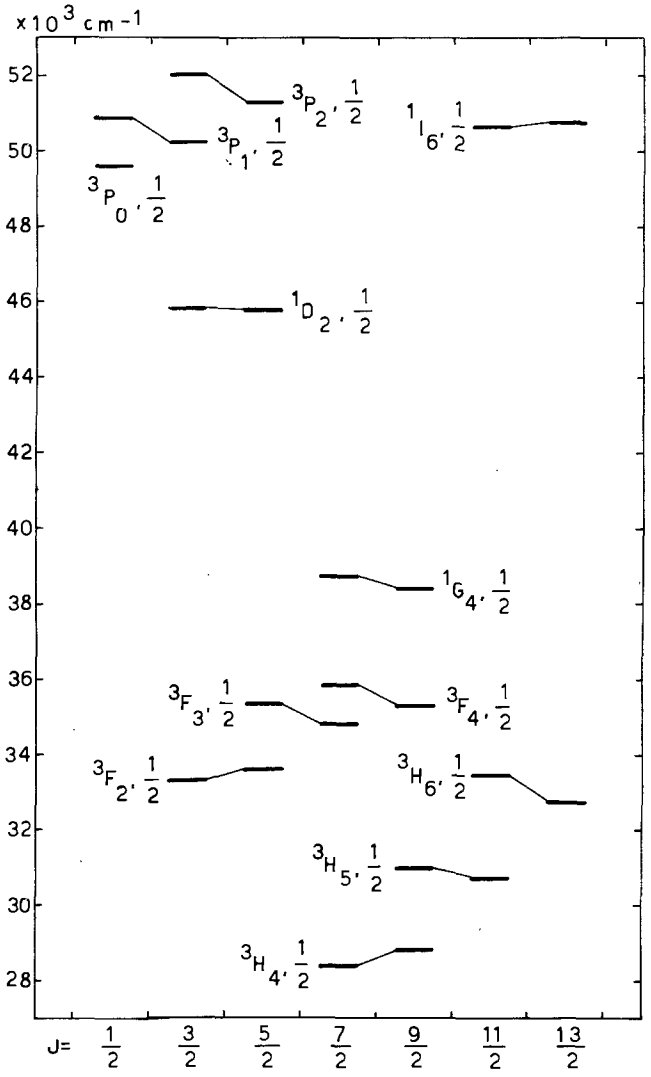

Fig. 1.28. Energy levels of PrIII $4f^2 6s$.

assumes only the single value $J = \frac{1}{2}$). The smallness of pair splittings reflects the weakness of the 4f–6s interaction.

It has been pointed out by Z.B. Goldschmidt, (1968a, b) that the pair structure exhibits a definite regularity: for each term $\alpha S_1 L_1$ of the $4f^{n-1}$ core having $S_1 \neq 0$, the pair associated with the maximal $J_1 (= S_1 + L_1)$ core level is inverted; as J_1 decreases, the splittings of the pairs belonging to the same $\alpha S_1 L_1$ decrease. For a core term with $S_1 > L_1$, the pair associated with the minimal $J_1 (= S_1 - L_1)$ core level is still inverted; for a core term having $S_1 = L_1$, the smallest $J_1 (= L_1 - S_1)$ value is zero, and the pair has degenerated into a single level with $J = \frac{1}{2}$; for the case $L_1 > S_1$, as J_1 decreases, the decrease of the pair splittings continues, until,

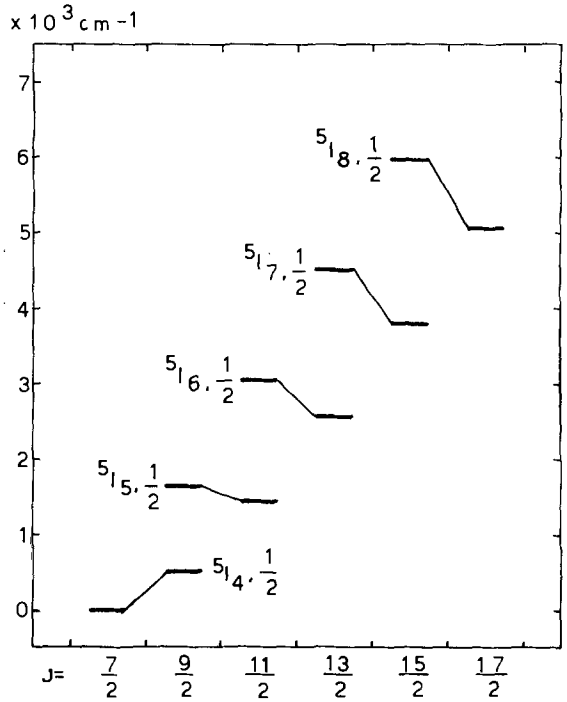

Fig. 1.29. Energy levels of NdII $4f^4(^5I)6s$.

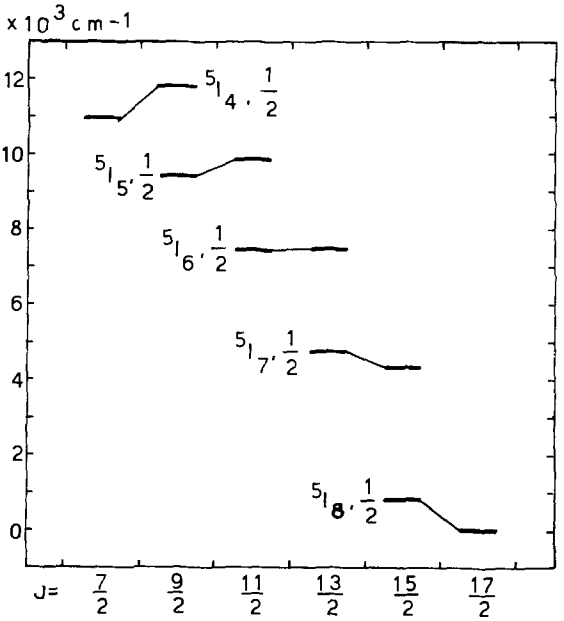

Fig. 1.30. Energy levels of DyII $4f^{10}(^5I)6s$.

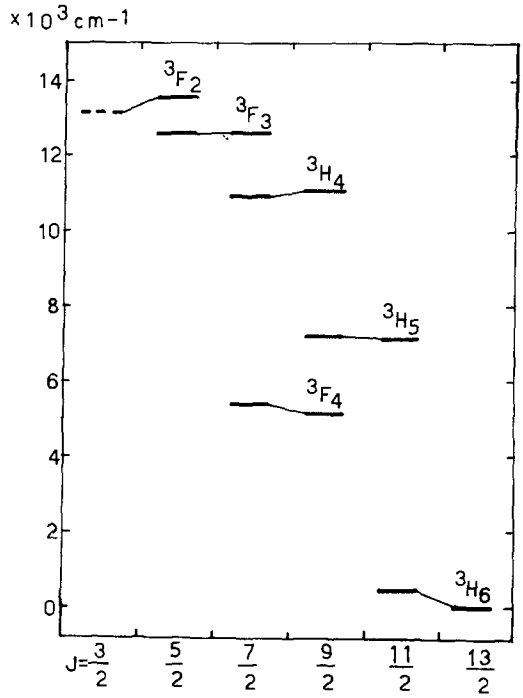

Fig. 1.31a. Energy levels of ErII $4f^{12}6s$ (J_1j coupling).

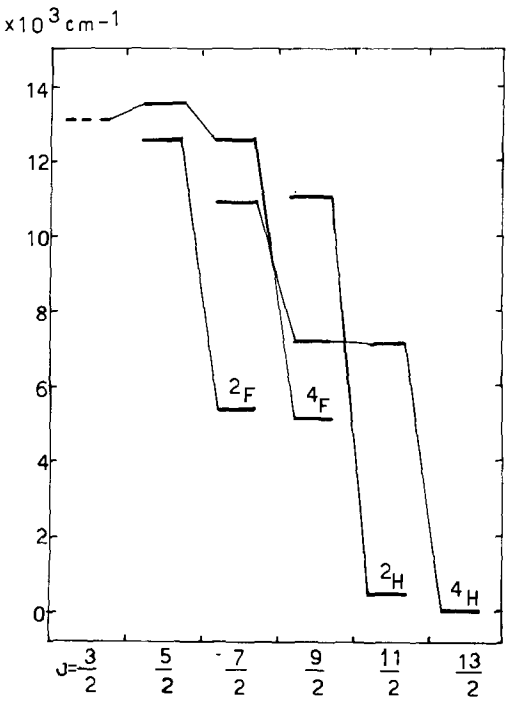

Fig. 1.31b. Energy levels of ErII $4f^{12}6s$ (drawn in *LS* coupling).

for a certain J_1 value, the pairs become normal. The pair arising from the core level $J_1 = L_1 - S_1$ is always normal. This regularity of the pair structure was explained (Z.B. Goldschmidt, 1968a, b) by studying the formulae of the matrix elements of the 4f–6s exchange interaction in the J_1j coupling scheme. The elements diagonal in J_1 are given by (Judd, 1962) (up to an additive constant which depends only on n – see footnote on p. 128):

$$\begin{aligned}&(4f^{n-1}(\alpha S_1 L_1 J_1), 6sj; JM|H_{\text{exch}}|4f^{n-1}(\alpha' S_1' L_1' J_1'), 6sj; JM)\\ &\quad = \pm G_3(4f, 6s)\delta(\alpha, \alpha')\delta(S_1, S_1')\delta(L_1, L_1')\\ &\qquad \times [L_1(L_1+1) - S_1(S_1+1) - J_1(J_1+1)]/(2J+1)\end{aligned} \tag{1.167}$$

where the $\pm$ signs correspond to $J = J_1 \pm \frac{1}{2}$ respectively. The off diagonal elements are given by (Judd, 1962):

$$\begin{aligned}&(4f^{n-1}(\alpha S_1 L_1 J_1[= J \pm \tfrac{1}{2}]), 6sj; JM|H_{\text{exch}}|4f^{n-1}(\alpha' S_1' L_1' J_1'[= J \mp \tfrac{1}{2}]), 6sj; JM)\\ &\quad = G_3(4f, 6s)\delta(\alpha, \alpha')\delta(S_1, S_1')\delta(L_1, L_1')[(S_1 + L_1 + J + \tfrac{3}{2})(S_1 + L_1 + \tfrac{1}{2} - J)\\ &\qquad \times (L_1 + J + \tfrac{1}{2} - S_1)(S_1 + J + \tfrac{1}{2} - L_1)]^{1/2}/(2J+1).\end{aligned} \tag{1.168}$$

From the first of these formulae, we get the theoretical splitting of the pair $\alpha S_1 L_1 J_1$ in J_1j coupling

$$\begin{aligned}\Delta T(\alpha_1 S_1 L_1 J_1) = T_{J_1+1/2} - T_{J_1-1/2} = [(2J_1' + 1)/2J_1(J_1+1)][L_1(L_1+1)\\ - S_1(S_1+1) - J_1(J_1+1)]G_3(4f, 6s).\end{aligned} \tag{1.169}$$

Since $G_3(4f, 6s)$ is always positive (Racah, 1942b), the property of a pair to be normal or inverted depends on the sign of the second brackets:

$[\cdots] > 0$ normal pair $\qquad [\cdots] < 0$ inverted pair

The regularities in the pair structure cited above follow immediately by substituting the appropriate J_1 values in the last formula.

For core singlet terms, $S_1 = 0$, $J_1 = L_1$, the last formula gives $\Delta T(\alpha_1 S_1 L_1 J_1) = 0$, that is to say, pairs arising from singlet parent terms should have zero splitting.

Looking at the Grotrian diagrams given in figs. 1.27–1.31a, one can see that the experimental splittings generally confirm the theory. Two exceptions will be mentioned here. (1) For NdII $4f^4(^5I)6s$, the theory predicts the pairs

$$J_1 = L_1 - S_1 = 4, \qquad J_1 = L_1 - S_1 + 1 = 5$$

to be normal. A glance at fig. 1.29 shows that the pair $^5I_4$ is indeed normal, whereas the pair $^5I_5$ is inverted, the last phenomenon resulting from the effect of the electrostatic matrix elements not diagonal in J_1. (2) for PrIII $4f^26s$ the splitting of the $^1G_4$ pair is finite, in disagreement with the zero splitting predicted by the theory. This finite splitting reflects the strong admixture of the core levels $^1G_4$ and $^3F_4$ due to the spin–orbit interaction of the 4f electrons.

The energy levels of the $4f^{n-1}6s$ configuration were calculated for all known second, third and fourth lanthanide spectra. In some of the calculations the complete energy matrices of the investigated configurations were diagonalized, whereas in others use was made only of partial energy matrices, based on the lowest core term (or terms). The parameters obtained in these calculations are

given in table 1.32. The last two columns of this table contain, wherever available, the smallest (percentage) value of all leading components of the eigenvectors of levels originating from the lowest (physical) core term, both in J_1j and in LS coupling. A glance at these columns confirms our initial assumption that the coupling prevailing in the $4f^{n-1}6s$ configurations is J_1j coupling for

TABLE 1.32.
Parameter values for $4f^{n-1}6s$ configurations in lanthanide ions (cm^{-1}).

Parameters / Ion configuration	ζ_{4f}	$G_3(4f, 6s)$	Smallest J_1j leading component (%)	Smallest LS leading component (%)
LaII $4f6s^{a,b}$	444	151	92	68
CeII $4f^26s^{a,b,c}$	534.9 ± 8.7	190 ± 35	97	60
PrII $4f^3(^4I)6s^d$	659 ± 3	190 ± 5	89	
NdII $4f^4(^5I)6s^d$	780 ± 2	203 ± 3	77	
PmII $4f^5(^6H)6s^e$	991 ± 23	205 ± 11	57	90
SmII $4f^6(^7F)6s^f$	1135	217		97
EuII $4f^7(^8S)6s^g$		209	100	100
GdII $4f^8(^7F)6s^e$	1231 ± 26	222 ± 10	51	81
DyII $4f^{10}(^5I)6s^h$	1772	211		50
HoII $4f^{11}(^4I)6s^i$	2028	210		
ErII $4f^{12}6s^{a,b,j}$	2237 ± 1	214 ± 3	100	65
TmII $4f^{13}6s^a$	2506	212	100	57
CeIII $4f6s^a$	635	299	99	69
PrIII $4f^26s^a$	757 ± 6	305 ± 11	95	64
EuIII $4f^6(^7F)6s^e$	1412 ± 48	295 ± 16	51	87
GdIII $4f^7(^8S)6s^g$		294	100	100
TbIII $4f^8(^7F)6s^e$	1547 ± 49	315 ± 18	63	98
TmIII $4f^{12}6s^k$	2632 ± 10	274 ± 30	100	66
YbIII $4f^{13}6s^a$	2914	337	100	54
PrIV $4f6s^l$	861	384	99	69
LuIV $4f^{13}6s^m$	3355 ± 9	437 ± 33	100	61

Parameters / Ion configuration	E^1	E^2	E^3	α	β	γ
CeII $4f^26s^{a,b,c}$	3792 ± 24	18.10 ± 0.19	383.5 ± 1.6	20.5 ± 1.7	−652 ± 46	−38.2 ± 8.2
PrII $4f^3(^4I)6s^d$	[4212]	[20.8]	[400]	[0]	[0]	[0]
NdII $4f^4(^5I)6s^d$	[4450]	[21.5]	[440]	[0]	[0]	[0]
ErII $4f^{12}6s^{a,b,j}$	6307 ± 16	30.26 ± 0.9	606 ± 1	[0]	[0]	[0]
PrIII $4f^26s^a$	4954 ± 16	22.8 ± 0.1	481 ± 1	24 ± 1	[0]	−52 ± 5
TmIII $4f^{12}6s^k$	6995 ± 98	33.75 ± 0.6	676.4 ± 7	[0]	[0]	[0]

[a]Z.B. Goldschmidt (1968a); [b]Z.B. Goldschmidt (1968b); [c]Z.B. Goldschmidt (1972); [d]Racah, Z.B. Goldschmidt and Lonka (1960); [e]Z.B. Goldschmidt (1976b); [f]Carlier (1967); [g]Wyborne (1965); [h]Conway and Worden (1971); [i]Sugar (1968); [j]Z.B. Goldschmidt (1963); [k]Sugar (1970); [l]Sugar (1965b); [m]Sugar and Kaufman (1972).

TABLE
Energy levels of

Term	J	Observed (cm^{-1})	$(E_j - E_{j-1})/J$	Calc (cm^{-1})	O–C (cm^{-1})	g-obs	g-calc. intermediate
^{8}F	13/2	7 992.268		8 161	−169	1.535	1.538
	11/2	9 092.491	169	9 151	−59	1.505	1.534
	9/2	10 292.567	218	10 138	155	1.555	1.558
	7/2	11 084.335	176	10 968	116	1.590	1.602
	5/2	11 669.863	167	11 622	48	1.700	1.698
	3/2	12 071.778	161	12 093	−21	1.990	1.983
	1/2	12 309.508	158	12 377	−67	3.980	3.980
^{6}F	11/2	9 943.779		9 958	−14	1.500	1.473
	9/2	11 343.525	255	11 228	116	1.450	1.452
	7/2	12 318.288	217	12 245	73	1.415	1.414
	5/2	13 030.786	204	13 027	4	1.325	1.331
	3/2	13 515.189	194	13 582	−67	1.085	1.083
	1/2	13 800.345	190	13 914	−114	−0.635	−0.646

[a]Blaise, van Kleef and Wyart (1971); [b]Z.B. Goldschmidt (1976b).

$n - 1 = 1$–4, 9–13. On considering in detail the percentages given in these columns, one can see that in the J_1j (LS) column the percentages decrease (increase) on going from 1 to 4 and from 13 to 10; namely, on approaching the center of the lanthanide group, the J_1j coupling weakens and the energy-level structure moves towards LS coupling.

The situation in the central region of the lanthanide group can be well understood by studying, for example, the $4f^8(^7F)6s$ sub-configuration of GdII (Blaise et al., 1971; Z.B. Goldschmidt, 1976b) (the same subconfiguration in TbIII – Meinders et al. (1972) – can also serve for the same purpose). All 13 levels belonging to this subconfiguration are experimentally known, and are given in table 1.33 together with their observed g-factors. Their Grotrian diagram is drawn twice: first in J_1j coupling (fig. 1.32a), according to the tradition as to the coupling existing in $4f^{n-1}6s$ configurations, and secondly in LS coupling (fig. 1.32b), continuing the line of thought of the last paragraph. A glance at fig. 1.32a shows that the pair structure has practically disappeared: the pair splittings are larger than the distances between their centers of gravity; also the regularity in the pair structure in J_1j coupling, predicted through formula 1.169 has disappeared: on substituting in this formula the values of $S_1(=3)$ and $L_1(=3)$ of the ^{7}F core, one obtains

$$\Delta T(^7F_{J_1}) = -\tfrac{1}{2}(2J_1 + 1)G_3(4f, 6s). \tag{1.170}$$

This dependence of the splittings on J_1 is clearly not obeyed by the experimental levels of GdII $4f^8(^7F)6s$. A comparison of the Landé g-factors calculated in J_1j coupling to their corresponding observed values (see table 1.33) reveals great

1.33.
GdII $4f^8(^7F)6s$[a,b]

g-calc. *LS*	g-calc. J_1j	Composition percentage. *LS* 1st component		2nd component		Composition percentage. J_1j 1st component		2nd component	
1.538	1.538	^8F	100			$^7F_6$	100		
1.552	1.545	^8F	81	^6F	19	$^7F_5$	56	$^7F_6$	44
1.576	1.556	^8F	88	^6F	12	$^7F_4$	54	$^7F_5$	46
1.619	1.571	^8F	92.5	^6F	7.5	$^7F_3$	53	$^7F_4$	47
1.714	1.600	^8F	96	^6F	4	$^7F_2$	52	$^7F_3$	48
2.000	1.667	^8F	98	^6F	2	$^7F_1$	51	$^7F_2$	49
4.000	2.000	^8F	99.6	^6F	0.4	$^7F_0$	50.5	$^7F_1$	49.5
1.455	1.462	^6F	81	^8F	19	$^7F_6$	56	$^7F_5$	44
1.434	1.455	^6F	88	^8F	12	$^7F_5$	54	$^7F_4$	46
1.397	1.444	^6F	92.5	^8F	7.5	$^7F_4$	53	$^7F_3$	47
1.314	1.429	^6F	96	^8F	4	$^7F_3$	52	$^7F_2$	48
1.067	1.400	^6F	98	^8F	2	$^7F_2$	51	$^7F_1$	49
−0.667	1.333	^6F	99.6	^8F	0.4	$^7F_1$	50.5	$^7F_0$	49.5

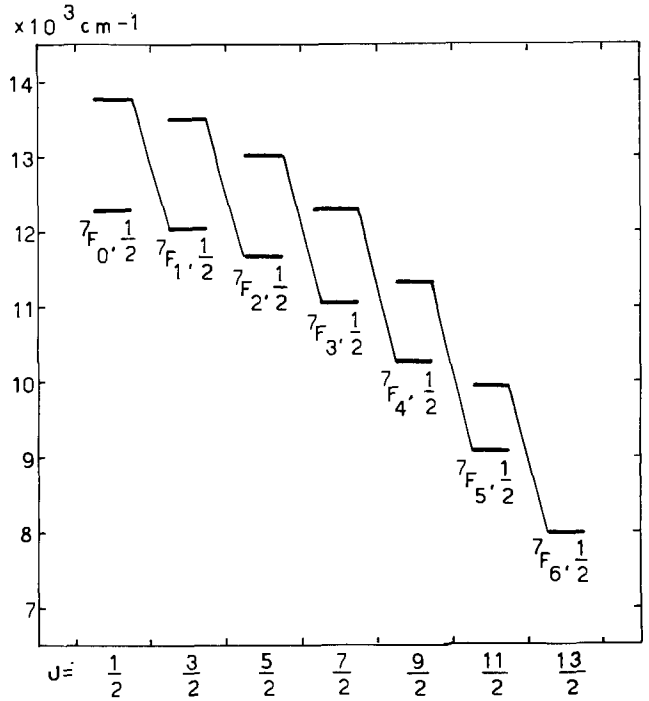

Fig. 1.32a. Energy levels of GdII $4f^8(^7F)6s$ (drawn in J_1j coupling).

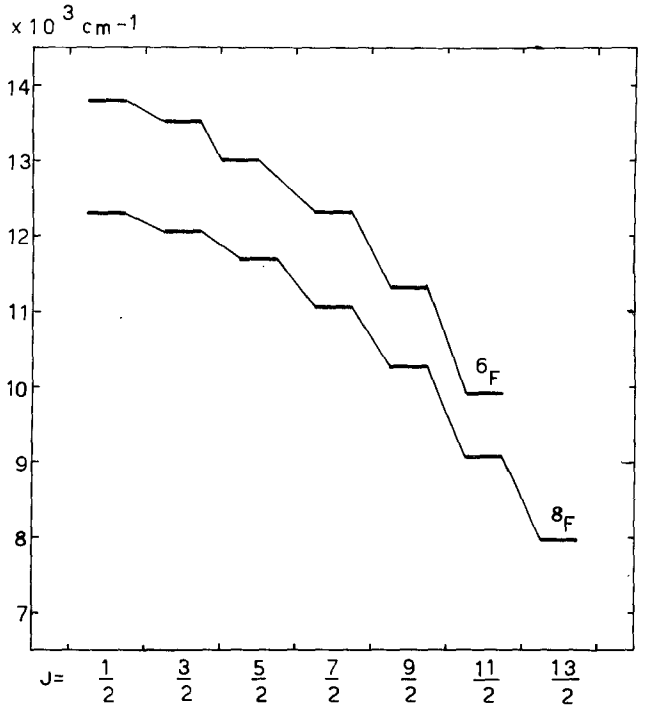

Fig. 1.32b. Energy levels of GdII $4f^8(^7F)6s$ (drawn in *LS* coupling).

discrepancies, especially for levels characterized by small J values. In conclusion, the levels of GdII $4f^8(^7F)6s$ do not obey J_1j coupling. On the other hand, if the experimental levels are characterized in *LS* coupling, the corresponding Grotrian diagram (fig. 1.32b) comprising the two multiplets ^8F and ^6F looks satisfactory in the sense that the distance between the two multiplets is greater than their splittings, especially for lower J values; the Landé interval rule is approximately obeyed (see also table 1.33) and the *LS* calculated g-values are in agreement with the observed values (table 1.33). Finally, a calculation of the energy levels and the components of the eigenvectors in both *LS* and J_1j coupling gives

	LS	J_1j
(1) for the smallest value (percentage) of all leading components of the eigenvectors	81%	50.5%
(2) for the mean value of all leading components of the eigenvectors	92.5%	52.8%

In conclusion the coupling prevailing in GdII $4f^8(^7F)6s$ is *LS* coupling. The same conclusion holds also for TbIII $4f^8(^7F)6s$ and for the configuration $4f^6(^7F)6s$ in

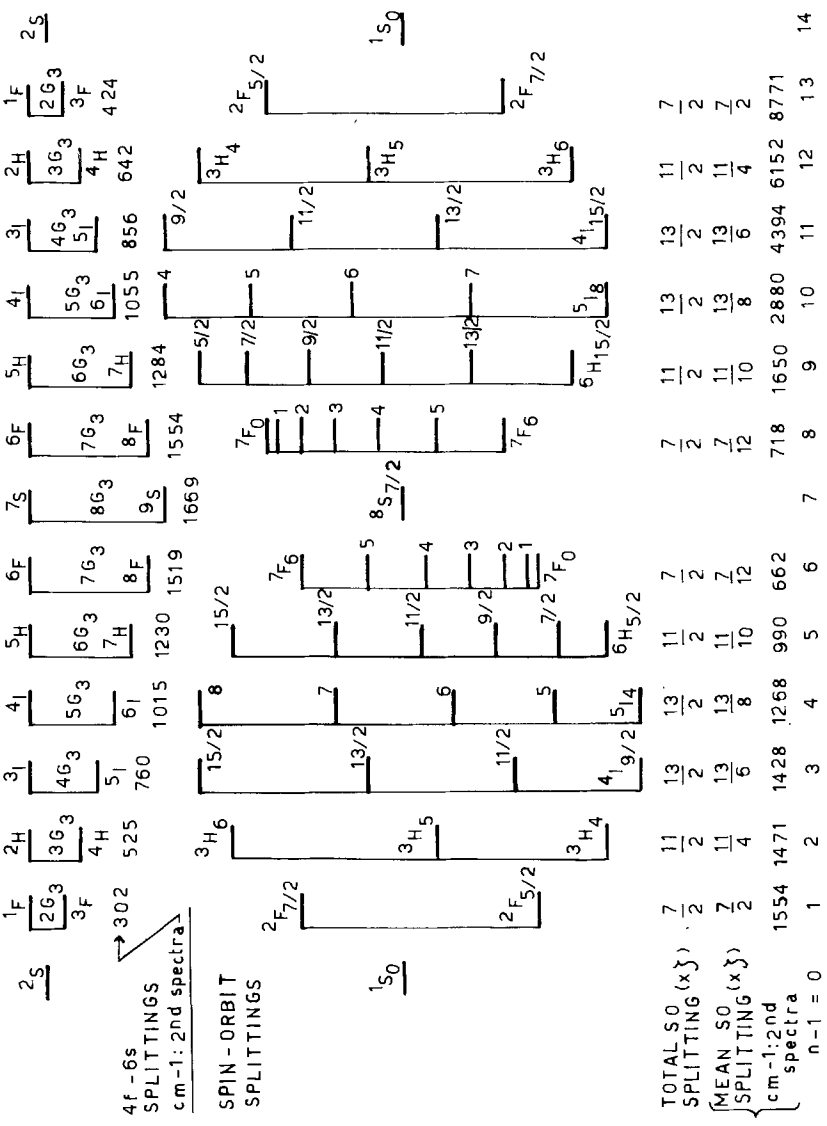

Fig. 1.33. $4f^{n-1}6s$ configurations: comparison of the splittings due to $G_3(4f6s)$ and ζ_{4f}.

SmII and EuIII. The transition from J_1j to LS coupling, on approaching the middle of the group from both sides occurs in PmII $4f^5(^6H)6s$ and GdII $4f^8(^7F)6s$ in the second lanthanide spectra and in SmIII $4f^5(^6H)6s$ and TbIII $4f^8(^7F)6s$ in the third spectra.

An examination of table 1.32 shows that the parameter $G_3(4f, 6s)$ describing the weak 4f–6s electrostatic interaction is constant along the lanthanide group, except for a small increase at the beginning of the group. On the other hand, the spin–orbit parameter ζ_{4f} increases to a large extent on advancing from left to right along the group. The question arises: what causes the change in coupling from J_1j (on the left-hand side) to LS (in the middle) and again to J_1j (on the right-hand side of the group)? In order to answer this question one should compare the *splittings* due to each of the two above mentioned interactions on moving from left to right along the lanthanide group. These are drawn in fig. 1.33 (for constant values of ζ_{4f} and $G_3(4f, 6s)$), for the lowest *core term* of each $4f^{n-1}6s$ configuration. A close examination of this figure shows that:

(1) it is symmetric with respect to the center of the group.

(2) two lowest core terms, which are equidistant, one from an end of the group and the other from its center, have the same L_1 value. This is a group theoretical property (see table 1.5).

(3) the splitting due to the 4f–6s exchange interaction, given by the expression $nG_3(4f, 6s)$, for $(n-1) \leqslant 7$*, greatly increase on approaching the middle of the group from both sides. The values of these splittings in cm^{-1} based on the semi-empirically determined values of G_3 for second lanthanide spectra are also included in fig. 1.33.

(4) Since the total splitting of a core term $4f^{n-1}(\alpha S_1 L_1)$, $L_1 \geqslant S_1$ due to the spin–orbit interaction is $\frac{1}{2}(2L_1+1)\zeta_{4f}$ (see formula 1.109), core terms with the same L_1 have equal total splittings. The total splittings of the core terms due to the spin–orbit interaction are given in the first row at the bottom of fig. 1.33, in terms of ζ_{4f}.

(5) the total spin S_1 of the $4f^{n-1}$ core lowest term equals $\frac{1}{2}(n-1)$(for $(n-1) \leqslant 7$) and $\frac{1}{2}(14-(n-1))$ (for $(n-1) > 7$); therefore the number of splittings $(= 2S_1)$, increases as one approaches the center of the group from both ends (not including, of course, the center itself). Consequently the individual splittings greatly decrease. The mean values of the individual splittings are given in the second row at the bottom of fig. 1.33 in terms of ζ_{4f}, and in the third row in cm^{-1}. The values written in the third row were obtained by substituting, in the expressions given in the second row, the semiempirical values of ζ_{4f} for the second lanthanide spectra, as given in table 1.32.

On comparing the individual splittings due to the core spin–orbit interaction to

*For the configuration $4f^{n-1}(\alpha S_1 L_1)$, 6s, $SL(= L_1)$, the coefficient g^3 of $G_3(4f, 6s)$ is given by the eigenvalues of $-\frac{1}{2}[n-1+4(S_1 \cdot s)]$ (Racah, 1942b). For the lowest core terms $S_1 = \frac{1}{2}(n-1)$, and S takes the values $\frac{1}{2}n$ or $\frac{1}{2}(n-2)$.

(a) $S = \frac{1}{2}n$: $g^3 = -(n-1)$ (b) $S = \frac{1}{2}(n-2)$: $g^3 = 1$

The splitting of the pair based on the lowest core term $\alpha S_1 L_1$ is, therefore, nG_3.

those due to the electrostatic exchange 4f–6s interaction, it can immediately be concluded that the coupling in LaII($n-1=1$)–NdII($n-1=4$) is J_1j, in PmII($n-1=5$)–GdII($n-1=8$) it is LS, and in TbII($n-1=9$)–TmII($n-1=13$) it is again J_1j coupling. This is in complete agreement with the physical situation in these configurations.

Similar conclusions can be drawn for the third and fourth spectra.

12.3. *The* $4f^{n-1}6p$ *configurations*

A systematic study of the $4f^{n-1}6p$ configurations, provides quantitative information on the parameters $F_2(4f, 6p)$, $G_2(4f, 6p)$ and $G_4(4f, 6p)$ which represent the electrostatic 4f–6p interaction, on the spin–orbit parameter ζ_{6p}, and yields additional values for the $4f^{n-1}$ core parameters mentioned above. Since 4f is an internal electron, whereas 6p is an external one, the electrostatic 4f–6p interaction is very weak, especially the exchange part which is represented by $G_2(4f, 6p)$ and $G_4(4f, 6p)$.

The relations between the various interactions are given by the first multiple inequality of section 3.2.3, thus leading to the conclusion that in the $4f^{n-1}6p$ configurations there exists a J_1j coupling, and the most appropriate coupling scheme for characterizing the levels of these configurations is:

$$(4f^{n-1}(\alpha S_1 L_1 J_1)6pj; JM)$$

Since the total angular momentum j of the 6p electron can assume the two values

$$j = \tfrac{1}{2}, \tfrac{3}{2}$$

each level of the $4f^{n-1}$ core characterized by $\alpha S_1 L_1 J_1$ splits, due to the 4f–6p electrostatic interaction, into two groups of levels: one group comprises a pair of adjacent levels (doublet) with the consecutive J values

$$J = J_1 \pm \tfrac{1}{2},$$

whereas the second group comprises four adjacent levels (quartet) with the consecutive J values

$$J = J_1 \pm \tfrac{3}{2}, J_1 \pm \tfrac{1}{2}.$$

The small separations between the levels belonging to each group indicate the weakness of the 4f–6p interaction. A typical example of an energy level diagram of a $4f^{n-1}6p$ configuration is that of PrIII $4f^2 6p$ given in fig. 1.6.

In this case too the regularities in the structure of the doublets and the quarters were investigated (Z.B. Goldschmidt, 1968a,b). Since the exchange interaction 4f–6p is very weak, the structure of these groups should mainly be determined by the direct 4f–6p interaction, which is a quadrupole interaction represented by $F_2(4f, 6p)$. The angular part of this interaction in the J_1j coupling scheme is given by:

$$Q = \left(4f^{n-1}(\alpha S_1 L_1 J_1), 6pj; JM \middle| \sum_{i>j=1}^{n} C_i^{(2)} \cdot C_j^{(2)} \middle| 4f^{n-1}(\alpha S_1 L_1 J_1), 6pj; JM\right)$$
$$= (n-1)(4f^{n-1}(\alpha S_1 L_1 J_1), 6pj; JM \| C_{n-1}^{(2)} \cdot C_n^{(2)} | 4f^{n-1}(\alpha S_1 L_1 J_1), 6pj; JM)$$
$$= (n-1)(-1)^{j+J_1+J}(f^{n-1}\alpha S_1 L_1 J_1 \| C^{(2)} \| f^{n-1}\alpha S_1 L_1 J_1)(pj \| C^{(2)} \| pj) \begin{Bmatrix} J_1 & J_1 & 2 \\ j & j & J \end{Bmatrix}. \tag{1.171}$$

(1) For $j = \frac{1}{2}$ one has

$$\begin{Bmatrix} J_1 & J_1 & 2 \\ \frac{1}{2} & \frac{1}{2} & J \end{Bmatrix} = 0, \quad \text{hence} \quad Q = 0. \tag{1.172}$$

It may therefore be concluded that the splittings of the doublets should be small, see for instance the doublets $^3H_{4,5,6}$, $^1D_2$ in fig. 1.6. When larger splittings occur, they are caused either by the exchange interaction 4f–6p, or, when there is a breakdown in the $J_1 j$ coupling, by matrix elements of the direct 4f–6p interaction not diagonal in J_1 and/or in j; the splittings may also be due to CI effects.

(2) For $j = \frac{3}{2}$ one obtains

(i) $$(p_{\frac{3}{2}}^{\frac{3}{2}} \| C^{(2)} \| p_{\frac{3}{2}}^{\frac{3}{2}}) = -2(5)^{-1/2}$$

(ii) $$(n-1)(f^{n-1}\alpha S_1 L_1 J_1 \| C^{(2)} \| f^{n-1}\alpha S_1 L_1 J_1)$$
$$= (n-1)(f \| C^{(2)} \| f)(f^{n-1}\alpha S_1 L_1 J_1 \| u^{(2)} \| f^{n-1}\alpha S_1 L_1 J_1)$$
$$= (f \| C^{(2)} \| f)(f^{n-1}\alpha S_1 L_1 J_1 \| U^{(2)} \| f^{n-1}\alpha S_1 L_1 J_1),$$

and $(f \| C^{(2)} \| f) = -2(\frac{7}{15})^{1/2}$

(iii) $$(-1)^{J_1+J+3/2} \begin{Bmatrix} J_1 & J_1 & 2 \\ \frac{3}{2} & \frac{3}{2} & J \end{Bmatrix} = A(J_1)[K(K+1) - 5J_1(J_1+1)] = A(J_1)N(J),$$

where

$$K = J(J+1) - J_1(J_1+1) - \tfrac{15}{4}, \qquad \text{and}$$
$$A(J_1) = [20(2J_1-1)2J_1(2J_1+1)(2J_1+2)(2J_1+3)]^{-1/2}.$$

We therefore get for the quadrupole interaction the expression

$$Q = B \cdot A(J_1) \cdot N(J)(f^{n-1}\alpha S_1 L_1 J_1 \| U^{(2)} \| f^{n-1}\alpha S_1 L_1 J_1), \tag{1.173}$$

where B and $A(J_1)$ are positive numbers and $N(J)$ includes all the dependence of Q upon J.

The evaluation of $N(J)$ for all the values of J generated from a particular value of J_1 gives

$$N(J_1 + \tfrac{3}{2}) = 2J_1(2J_1 - 1),$$
$$N(J_1 + \tfrac{1}{2}) = -2(J_1 + 3)(2J_1 - 1),$$
$$N(J_1 - \tfrac{1}{2}) = -2(J_1 - 2)(2J_1 + 3),$$
$$N(J_1 - \tfrac{3}{2}) = 2(J_1 + 1)(2J_1 + 3), \tag{1.174}$$

with

$$N(J_1 + \tfrac{3}{2}) - N(J_1 + \tfrac{1}{2}) = N(J_1 - \tfrac{3}{2}) - N(J_1 - \tfrac{1}{2}) = 2(2J_1 - 1)(2J_1 + 3) > 0. \tag{1.175}$$

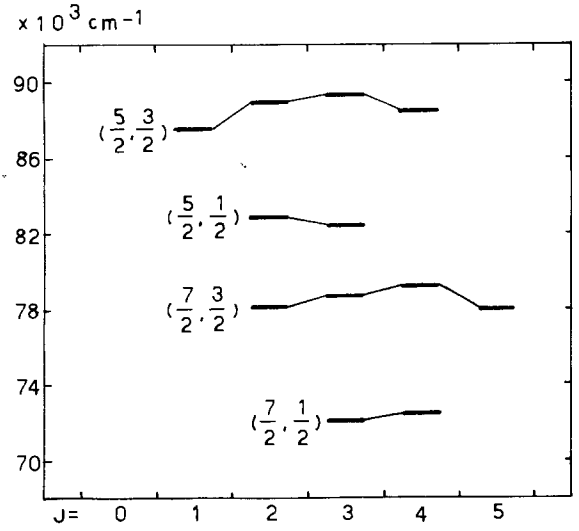

Fig. 1.34. Energy levels of YbIII $4f^{13}6p$.

Inspection of the last formulae shows that for quartets generated from core levels for which $(f^{n-1}\alpha S_1L_1J_1\|U^{(2)}\|f^{n-1}\alpha S_1L_1J_1)$ is positive, the quadrupole interaction Q is positive when J_1 and j are parallel or antiparallel, and negative when J_1 and j are nearly perpendicular*.

For core levels having negative $(f^{n-1}\alpha S_1L_1J_1\|U^{(2)}\|f^{n-1}\alpha S_1L_1J_1)$, the contributions of the quadrupole interaction Q to the energy levels reverse their sign. These features of Q are reflected in the Grotrian diagrams of the $4f^{n-1}6p$ configurations in the following way: quartets of the first kind are bowl shaped, whereas quartets of the second kind are umbrella shaped.

In the 4f6p configuration, $(4f\ ^2F_{5/2,7/2}\|U^{(2)}\|4f\ ^2F_{5/2,7/2})$ is positive for both J_1 values, therefore both quartets are expected to be bowl shaped. This is confirmed by experiment, see the Grotrian diagram of PrIV 4f6p in fig. 1.2.

In the $4f^{13}6p$ configuration, $(4f^{13}\ ^2F_{5/2,7/2}\|U^{(2)}\|4f^{13}\ ^2F_{5/2,7/2})$ is negative for both J_1 values, therefore both quartets are expected to be umbrella shaped. See the Grotrian diagram of YbIII $4f^{13}6p$ in fig. 1.34.

In PrIII $4f^26p$ (fig. 1.6) both kinds of quartets occur. The correspondence between the signs of $(f^{n-1}\alpha S_1L_1J_1\|U^{(2)}\|f^{n-1}\alpha S_1L_1J_1)$ and the shapes of the quartets in this configuration is given in table 1.34.

The values of the parameters obtained in the calculations of the various $4f^{n-1}6p$ configurations are given in table 1.35.

12.4. *The* $4f^{n-1}5d$ *configurations*

The $4f^{n-1}5d$ are found among the low lying configurations of the lanthanide spectra: in the second spectra they belong to the group "low B"; in the third and fourth spectra they generally come second in height, after the ground configura-

*Quartets are obtained for $J_1 \geq \frac{3}{2}$. The values $J_1 = \frac{3}{2}$, 2 are exceptions to the rule formulated above, since $N(J_1 - \frac{1}{2}) > 0$ for $J_1 = \frac{3}{2}$ and $N(J_1 - \frac{1}{2}) = 0$ for $J_1 = 2$.

TABLE 1.34.
Quartet structure in PrIII $4f^2 6p$[a,b].

Core level	Sign of $(f^{n-1}\alpha S_1 L_1 J_1 \| U^{(2)} \| f^{n-1}\alpha S_1 L_1 J_1)$	Quartet structure
$^3H_4$	+	bowl
$^3H_5$	+	bowl
$^3H_6$	+	bowl
$^1I_6$	+	bowl
$^3P_2$	−	umbrella
$^3F_2$	−	umbrella

[a]Z.B. Goldschmidt (1968a); [b]Z.B. Goldschmidt (1968b).

TABLE 1.35.
Parameter values for $4f^{n-1}6p$ configurations in lanthanide ions (cm^{-1}).

Parameters / Ion configuration	F_2	G_2	G_4	ζ_{4f}	ζ_{6p}
PrIV $4f6p$[a,b]	104 ± 3	13 ± 1	14 ± 1	864 ± 9	3241 ± 28
LuIV $4f^{13}6p$[c]	105 ± 1	14.0 ± 0.3	12 ± 1	3369 ± 3	6111 ± 8
CeIII $4f6p$[a,b]	37	10	15	676	2228
PrIII $4f^2 6p$[a,b]	52 ± 5	5 ± 2	15 ± 3	759 ± 18	2411 ± 42
EuIII $4f^6(^7F)6p$[d]	76 ± 2	9.0 ± 0.3	9.0 ± 0.4	(1333)	2925 ± 11
GdIII $4f^7(^8S)6p$[e]		$5G_2 + 4G_4 =$ 82			3050
TbIII $4f^8(^7F)6p$[f]	76 ± 3	8.3 ± 0.5	9.6 ± 0.8	(1605)	3267 ± 22
TmIII $4f^{12}6p$[g]	80 ± 1	10.2 ± 0.3	10.2 ± 7	2634 ± 3	3850 ± 8
YbIII $4f^{13}6p$[a,b]	81	10	10	2921	4020
LaII $4f6p$[a,b]	85	13	7	410	1102
CeII $4f^2 6p$[a,b]	64 ± 3	12 ± 1	6 ± 2	529 ± 12	1234 ± 36
GdII $4f^8(^7F)6p$[h]	38 ± 9	6 ± 1	[7]	1191 ± 27	1578 ± 60

Parameters / Ion configuration	E^1	E^2	E^3	α	β	γ
PrIII $4f^2 6p$[a,b]	5036 ± 45	23.8 ± 0.4	491 ± 3	33 ± 3	[0]	−97 ± 16
TmIII $4f^{12}6p$[g]	7018 ± 32	34.35 ± 0.20	684 ± 2			
CeII $4f^2 6p$[a,b]	3828 ± 50	18.3 ± 4	370 ± 6	[28]	[−700]	[−60]

[a]Z.B. Goldschmidt (1968a); [b]Z.B. Goldschmidt (1968b); [c]Sugar and Kaufman (1972); [d]Sugar and Spector (1974); [e]Callahan (1963); [f]Meinders, van Kleef and Wyart (1972); [g]Sugar (1970); [h]Blaise, van Kleef and Wyart (1971).

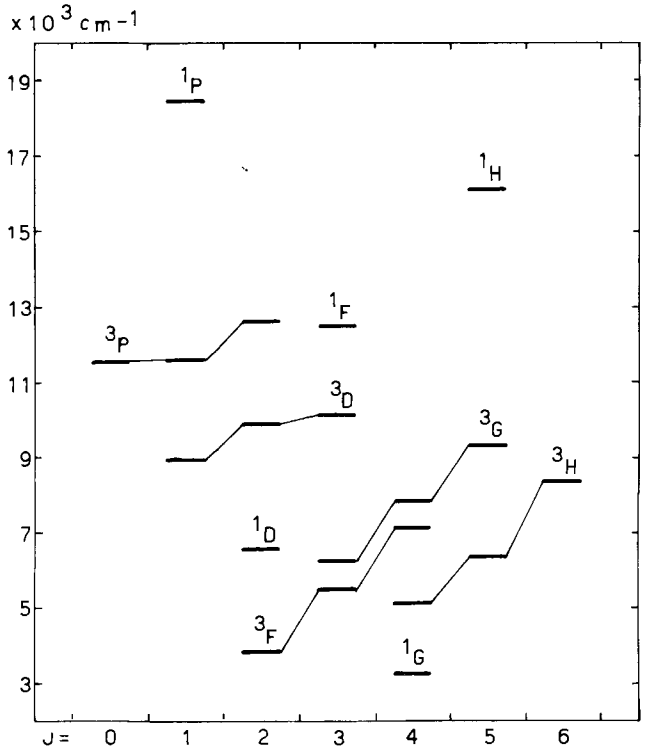

Fig. 1.35. Energy levels of CeIII 4f5d.

tion $4f^n$, except for LaIII and GdIII where $4f^{n-1}5d$ does constitute the ground configuration (with $n-1=0$ and 7 respectively). Levels belonging to the $4f^{n-1}5d$ configuration were experimentally found and theoretically analysed in the spectra of many lanthanide ions, as specified below. Although the configurations $4f^{n-1}5d$ and $4f^{n-1}6s$ are energetically close to each other, or even overlap, in the second and third lanthanide spectra, CI between them is quite small, and does not affect the energy level structure in any significant manner. Therefore, its effects will not be discussed in this section.

The results of a systematic study of the $4f^{n-1}5d$ configurations up to 1968 have been presented by Z.B. Goldschmidt (1968a,b). These results included the values of the electrostatic parameters $E^i(4f,4f)$, F_2, F_4, G_1, G_3, $G_5(4f,5d)$, and of the spin-orbit parameters ζ_{4f} and ζ_{5d}, as well as the values of the effective electrostatic parameters α β γ of the $4f^{n-1}$ core. It was shown that for ions lying on the left-hand side of the lanthanide group, the coupling was close to LS coupling (see the Grotrian diagram of CeIII 4f5d in fig. 1.35), whereas for ions lying on the right hand side of the group, the coupling has changed into J_1j coupling. There are two causes for this change of coupling:

(1) The core parameters, especially ζ_{4f}, increase appreciably; ζ_{5d} also increases, whereas the parameters representing the electrostatic 4f–5d interaction slightly decrease.

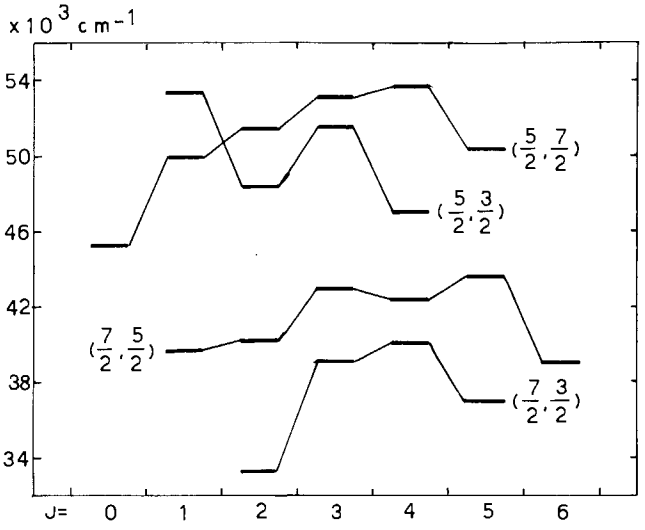

Fig. 1.36. Energy levels of YbIII $4f^{13}5d$.

(2) For $n-1>7$, the dominant parameter G_1 of the 4f–5d interaction, contributes only to states generated from $4f^{13}5d(^1P_1)$, and vanishes elsewhere. Thus, in spite of the fact that the values of the 4f–5d electrostatic parameters remain relatively large, a quite good J_1j coupling is valid for the $4f^{n-1}5d$ configurations on the right hand side of the lanthanide group. This is clearly demonstrated in the Grotrian diagram of YbIII $4f^{13}5d$ given in fig. 1.36: the umbrella shape of the quartets and the sextets is due to the quadrupole interaction represented by $F_2(4f, 5d)$, as already proved for the $4f^{n-1}6p$ configurations. The large departure of the quartet $(\frac{5}{2}, \frac{3}{2})$ from the umbrella shape demonstrates the breakdown of the J_1j coupling for $J = 1$, due to the exchange interaction represented by $G_1(4f, 5d)$.

At that time, first attempts were made to improve the fit between observed and calculated levels of the $4f^{n-1}5d$ configurations, through the inclusion of effective electrostatic interactions of the type (Z.B. Goldschmidt, 1968a,b):

$$\left(\sum_i \boldsymbol{l}_{fi} \cdot \boldsymbol{l}_d\right) \cdot El + \left(\sum_i \boldsymbol{s}_{fi} \cdot \boldsymbol{s}_d\right) \cdot Es \tag{1.176}$$

This last operator was later on augmented to the operator representing the complete two-electron 4f–5d effective electrostatic interaction, as given in formulae 1.151–1.153 and in table 1.12. As seen from the table, the effective electrostatic interaction in this case is described by the four "effective Slater parameters" F^1, F^3, G^2, G^4.

The inclusion of this interaction in the energy-level calculations of the 4f5d configuration in PrIV, CeIII and LaII and of the $4f^{13}5d$ configuration in YbIII (Z.B. Goldschmidt, Salomon and Starkand, 1971; Crosswhite, 1971) led to a remarkable improvement of the fit between observed and calculated levels. This is demonstrated by the reduction of the mean errors as given in table 1.36, which also

TABLE 1.36.
Parameter values for the 4f5d configuration in PrIV, CeIII and LaII and for the $4f^{13}5d$ configuration in YbIII(cm^{-1})[a,b,c]

	PrIV 4f5d		CeIII 4f5d		LaII 4f5d		YbIII $4f^{13}5d$	
Parameter	$H_1 + H_2$	$+ H_A^2$	$H_1 + H_2$	$+ H_A^2$	$H_1 + H_2$	$+ H_A^2$	$H_1 + H_2$	$+ H_A^2$
F_0	68 142 ± 52	68 070 ± 3	9408 ± 56	9337 ± 2	21 620 ± 162	21 172 ± 16	44 026 ± 54	44 178 ± 34
F_2(4f5d)	209 ± 5	213.6 ± 0.3	176 ± 5	185.0 ± 0.1	125 ± 14	132 ± 1	192 ± 4	192 ± 2
F_4(4f5d)	24.1 ± 1.3	26.0 ± 0.1	20.9 ± 1.3	22.7 ± 0.05	14.7 ± 3.0	17.3 ± 0.3	16.5 ± 1.4	18 ± 1
G_1(4f5d)	297 ± 6	300.7 ± 0.3	298 ± 7	303.4 ± 0.2	300 ± 18	315 ± 2	198 ± 4	199 ± 2
G_3(4f5d)	39 ± 2	37.9 ± 0.1	38.7 ± 2.8	34.8 ± 0.1	28 ± 7	29 ± 1	25.8 ± 3.4	23 ± 2
G_5(4f5d)	5.8 ± 0.4	5.21 ± 0.03	4.9 ± 0.4	4.50 ± 0.01	3.8 ± 1.0	3.0 ± 0.1	4.6 ± 0.8	3.1 ± 0.4
ζ_{4f}	929 ± 51	858 ± 3	669 ± 56	637 ± 2	495 ± 170	391 ± 14	2924 ± 27	2921 ± 11
ζ_{5d}	1015 ± 85	1067 ± 4	765 ± 110	686 ± 4	127 ± 311	412 ± 28	1161 ± 40	1149 ± 16
F_1(4f5d)*		−21.2 ± 0.6		−20.4 ± 0.4		−84 ± 3		−15 ± 5
F_3(4f5d)*		−3.0 ± 1.0		−7.3 ± 0.7		−44 ± 5		−9 ± 9
G_2(4f5d)*		−38.1 ± 0.8		−43.0 ± 0.5		−34 ± 3		−32 ± 5
G_4(4f5d)*		−1.85 ± 0.06		−1.54 ± 0.04		[0]		−2.4 ± 1.0
Δ	209	10	227	7	657	55	179	71

[a]Z.B. Goldschmidt, Salomon and Starkand (1971); [b]Z.B. Goldschmidt (1973a); [c]Z.B. Goldschmidt (1973b); *The D_k's for the "effective Slater parameters" are the following: $D_1 = 6\sqrt{70}$, $D_3 = 14\sqrt{15}$, $D_2 = 70$, $D_4 = 1260$.

includes the values of the parameters obtained for these configurations*, and by the reduction of the individual O_i–C_i deviations between observed and calculated energy levels, as seen by comparing columns 5 and 7 of tables 1.37–1.40.

The inclusion of the effective electrostatic interaction also greatly affected the compositions of the eigenvectors, as can be seen on comparing the contents of columns 11 and 12 of table 1.38; in particular, it should be noted that the lowest level of CeIII 4f5d has no good "name" in the conventional calculations (column 11), but is 72% ^{1}G according to the recent calculations which include the effective interaction (column 12).

The changes in the compositions of the eigenvectors are reflected in the calculated values of the g-factors associated with the energy levels. The considerable improvement achieved in the calculated values of the g-factors through the inclusion of the effective parameters can be seen by comparing columns 8, 9 and 10 of table 1.38.

The improvements obtained here for the energy levels, eigenvector compositions and g-factors of $4f^{n-1}5d$ configurations, make it possible to understand the necessity of the inclusion of the effective electrostatic interaction in energy-level calculations of groups of interacting configurations as will be discussed below.

The values of the parameters obtained for the various $4f^{n-1}5d$ configurations are given in table 1.41.

Spin-dependent interactions in the 4f5d *configurations of* PrIV *and* CeIII

An additional glance at tables 1.37 and 1.38 shows that the remaining deviations are of pronounced magnetic character. This fact led Z.B. Goldschmidt and Cohen (1975) to include in the hamiltonian of the 4f5d configuration of PrIV and CeIII the still missing spin-dependent interactions, namely, the ss, soo and effective EL–SO interactions. The parameters describing these interactions are listed in table 1.42; of these, K^{1-} and K^{5-} do not constitute independent parameters, since their angular coefficients are proportional to those of N^{-1} and N^5 respectively.

Even if the corresponding parameters of the ss and soo interactions are forced to remain equal to each other in a least-square calculation (as justified by their definitions), twenty new independent parameters have been added to the already existing ten electrostatic and two spin–orbit parameters. But since the 4f5d configuration comprises 20 levels, at most eight new SDI parameters could be

*As seen from table 1.36, the values obtained for the effective Slater parameters in LaII are inconsistent with the values of the corresponding parameters obtained for PrIV, CeIII and YbIII. The reason for this inconsistency is that in LaII the 4f5d configuration cannot be treated as an isolated configuration. In order to obtain meaningful results for LaII, the energy levels of the configurations

4f5d + 4f6s + 5d6p + 6s6p

should be calculated together, including direct CI between these four configurations, in addition to the effective electrostatic interaction. The results of this calculation will be given in section 13.1.

TABLE 1.37.
Energy levels of PrIV 4f5d (cm^{-1}).

Term	J	Obs	Calc(1) $H_1 + H_2$[a]	O–C(1)	Calc(2) $+ H_A^2$[b]	O–C(2)	Calc(3) + SDI[c]	O–C(3)	g-Calc(3)	Composition percentage (3)
^1G	4	61 171	61 300	−129	61 174	−3	61 173	−2	0.954	64% + ^3H 30%
^3F	2	61 458	61 673	−215	61 469	−11	61 458	0	0.775	69% + ^1D 30%
	3	64 124	64 105	19	64 121	3	64 127	−3	1.023	82% + ^3G 18%
	4	66 518	66 665	−147	66 514	4	66 516	2	1.188	74% + ^1G 13%
^3G	3	63 356	63 224	132	63 349	7	63 356	0	0.825	76% + ^3F 18%
	4	65 640	65 579	61	65 644	−4	65 640	0	1.074	87% + ^3F 13%
	5	67 899	67 801	98	67 902	−3	67 899	0	1.196	98% + ^1H 2%
^3H	4	63 581	63 487	94	63 576	5	63 576	5	0.884	69% + ^1G 23%
	5	65 240	64 905	335	65 244	−4	65 241	−1	1.034	100%
	6	68 078	67 822	256	68 077	1	68 080	−2	1.167	100%
^1D	2	65 322	65 718	−396	65 316	6	65 322	0	0.922	60% + ^3F 31%
^3D	1	66 968	66 838	130	66 959	9	66 970	−2	0.531	95% + ^1P 3%
	2	68 412	68 494	−82	68 427	−15	68 412	0	1.164	92% + ^1D 5%
	3	68 496	68 506	−10	68 487	9	64 494	2	1.222	69% + ^1F 28%
^3P	0	70 843	70 771	72	70 850	−7	70 842	1	$\frac{0}{0}$	100%
	1	70 755	70 704	51	70 754	1	70 755	0	1.452	93% + ^1P 5%
	2	72 185	72 361	−176	72 179	6	72 186	−1	1.472	94% + ^1D 5%
^1F	3	71 725	71 777	−52	71 730	−5	71 726	−1	1.096	64% + ^3D 31%
^1H	5	75 266	75 361	−95	75 266	0	75 266	0	1.004	98% + ^3G 2%
^1P	1	78 777	78 724	53	78 777	0	78 777	0	1.017	92% + ^3P 6%

[a]Z.B. Goldschmidt (1968a). [b]Z.B. Goldschmidt, Salomon and Starkand (1971). [c]Z.B. Goldschmidt and Cohen (1975).

TABLE
Energy levels of

Term	J	Obs	Calc(1) H_1+H_2[a]	O–C(1)	Calc(2) $+H_A^2$[b]	O–C(2)	Calc(3) +SDI[c]
^{1}G	4	3 277	3 451	−174	3 279	−2	3 279
^{3}F	2	3 822	3 907	−85	3 828	−6	3 820
	3	5 502	5 563	−61	5 501	1	5 505
	4	7 150	7 327	−177	7 145	5	7 148
^{3}H	4	5 127	5 092	35	5 120	7	5 120
	5	6 361	6 018	343	6 369	−8	6 367
	6	8 350	8 162	188	8 348	2	8 349
^{3}G	3	6 265	5 957	308	6 262	3	6 266
	4	7 837	7 748	89	7 839	−2	7 837
	5	9 326	9 181	145	9 329	−3	9 326
^{1}D	2	6 571	7 020	−448	6 567	4	6 572
^{3}D	1	8 922	8 850	72	8 915	7	8 924
	2	9 900	9 949	−49	9 910	−10	9 900
	3	10 127	10 094	33	10 122	5	10 124
^{3}P	0	11 577	11 640	−63	11 581	−4	11 576
	1	11 613	11 624	−11	11 611	2	11 613
	2	12 642	12 720	−78	12 640	2	12 644
^{1}F	3	12 501	12 636	−135	12 504	−3	12 502
^{1}H	5	16 152	16 178	−26	16 151	1	16 152
^{1}P	1	18 444	18 400	44	18 444	0	18 444

[a]Stern (1955). [b]Z.B. Goldschmidt, Salomon and Starkand (1971). [c]Z.B. Goldschmidt and Cohen

allowed to act as free parameters in the least-squares calculations. Some preliminary information was, therefore, needed concerning the values of these "new" parameters. Z.B. Goldschmidt and Cohen obtained this information by performing Hartree–Fock and "parametric potential" (Klapisch, 1971) calculations for the configurations 4f5d, 4f6d and 5f5d in both PrIV and CeIII. On considering the values obtained for the "new" SDI parameters by means of these calculations, and taking into account the magnitudes of their angular coefficients, it was concluded that the calculated multiplet splittings in PrIV and CeIII 4f5d were mainly affected by the effective EL–SO interaction, whereas the effects of the ss and soo interactions were negligible. This conclusion was confirmed by means of least-squares calculations. Furthermore, of the two sequences of perturbing configurations – one obtained through the $5d \leftrightarrow n'd$ jumps and the second through the $4f \rightarrow n''f$ jumps – the first sequence was found to be mainly responsible for the improvement of the fit between observed and calculated multiplet splittings.

The final results were obtained by performing a least-squares calculation in which all "new" parameters were fixed on the values obtained in the parametric-potential calculation, except for $S^2(4f5d, 4fn'd)$ and T^1, $T^3(4f5d, n'd4f)$ which were treated as free parameters, and the ratios S^4/S^2 and T^5/T^1 which were

1.38.
CeIII 4f5d (cm^{-1}).

O–C(3) +SDI[c]	g-obs	g-calc(1)	g-calc(2, 3)	Composition percentage(1)	Composition percentage(2, 3)
−2	0.99	0.904	0.969	43% + ^{3}H 53%	72% + ^{3}H 22%
2	0.76	0.749	0.762	76% + ^{1}D 23%	72% + ^{1}D 27%
−3	1.10	1.007	1.073	75% + ^{3}G 22%	95% + ^{3}G 3%
2	1.30	1.148	1.216	51% + ^{3}G 44%	85% + ^{1}G 8%
7	0.80	0.935	0.859	46% + ^{1}G 42%	77% + ^{1}G 18%
−6	1.07	1.033	1.033	100%	100%
1	1.17	1.167	1.167	100%	100%
−1	0.76	0.838	0.772	73% + ^{3}F 25%	93% + ^{3}F 4%
0	1.06	1.114	1.056	55% + ^{3}F 35%	93% + ^{3}F 4%
0	1.22	1.197	1.198	99%	99% + ^{1}H 1%
−1	0.88	0.944	0.924	69% + ^{3}F 23%	66% + ^{3}F 28%
−2	0.52	0.526	0.519	96%	97% + ^{1}P 2%
0	1.18	1.164	1.163	93%	96% + ^{1}D 4%
3	1.34	1.236	1.243	72% + ^{1}F 25%	75% + ^{1}F 23%
1		0/0	0/0	100%	100%
0	1.29	1.461	1.469	94%	95% + ^{1}P 4%
−2	1.38	1.477	1.484	95%	97% + ^{1}D 3%
−1	1.03	1.086	1.080	70% + ^{3}D 27%	73% + ^{3}D 24%
0	1.06	1.003	1.002	99%	99% + ^{3}G 1%
0	0.99	1.013	1.011	93%	94% + ^{3}P 4%

(1975).

forced to remain fixed on the values obtained in the parametric-potential calculation. The mean error reduced from 10 cm^{-1} to 4 cm^{-1} and from 7 cm^{-1} to 5 cm^{-1} in PrIV and CeIII respectively. The improvement in the fit between observed and calculated multiplet splittings is shown in tables 1.37 and 1.38 and in figs. 1.37 and 1.38.

Examination of the results obtained in the last calculation shows that the improvement of the fit between observed and calculated multiplet splittings is greater in PrIV than in CeIII. This can be explained by the fact that in PrIV the distances between the perturbed 4f5d configuration and the various perturbing configurations* are greater than the corresponding ones in CeIII. Therefore, the results obtained by treating 4f5d as an "isolated" configuration and using the second-order perturbation theory, are better in PrIV as compared to CeIII.

The values obtained for the SDI parameters are given in table 1.43. The following conclusions concerning the values of these parameters can be drawn: (1) All parameters for PrIV are greater than the corresponding ones in CeIII.

*For example, the distances 4f6d–4f5d are 131 000 cm^{-1} and 82 000 cm^{-1} in PrIV and CeIII respectively.

TABLE 1.39.
Energy levels of LaII 4f5d (cm^{-1}).

Term	J	Obs	Calc(1) H_1+H_2[a]	O–C(1)	Calc(2) $+H_A^2$[b]	O–C(2)	g-obs	g-calc(2)	Composition percentage(2)
^{1}G	4	16 599	17 563	−964	16 594	5	0.969	0.973	77% + ^{3}H 19%
^{3}F	2	17 212	17 706	−494	17 210	2	0.754	0.760	72% + ^{1}D 27%
	3	18 236	18 461	−225	18 247	−11	1.086	1.083	100%
	4	19 215	19 398	−183	19 213	2	1.232	1.230	92% + ^{1}G 7%
^{3}H	4	17 826	16 813	1013	17 800	26	0.846	0.847	81% + ^{1}G 16%
	5	18 580	17 956	624	18 579	1	1.017	1.033	100%
	6	19 750	19 009	741	19 778	−28	1.178?	1.167	100%
^{1}D	2	18 895	19 456	−561	18 892	3	0.923	0.918	70% + ^{3}F 27%
^{3}G	3	20 403	20 385	18	20 406	−3	0.757	0.760	96% + ^{1}F 3%
	4	21 332	21 247	85	21 332	0	1.049	1.050	100%
	5	22 283	22 114	169	22 280	3	1.197	1.199	99% + ^{1}H 1%
^{3}D	1	21 442	21 592	−150	21 536	−94	0.542	0.527	96% + ^{1}P 3%
	2	22 106	22 321	−215	22 112	−6	1.167	1.167	98% + ^{1}D 1%
	3	22 537	22 648	−111	22 434	103	1.288	1.296	90% + ^{1}F 9%
^{3}P	0	22 684	22 510	174	22 647	37		0	100%
	1	22 705	22 765	−60	22 695	10	1.431	1.467	95 + ^{1}P 3%
	2	23 247	23 780	−533	23 288	−41	1.459	1.488	97% + ^{1}D 2%
^{1}F	3	24 523	24 053	470	24 535	−12	1.034	1.028	87% + ^{3}D 10%
^{1}P	1	27 424	28 015	−591	27 421	3	0.876	1.007	95% + ^{3}P 3%
^{1}H	5	28 526	27 732	794	28 526	0	1.004	1.001	99% + ^{3}G 1%

[a]Stern (1955). [b]Z.B. Goldschmidt, Salomon and Starkand (1971).

TABLE 1.40.
Energy levels of YbIII $4f^{13}5d$ (cm^{-1}).

Level	J	Obs	Calc(1) $H_1 + H_2$[a]	O–C(1)	Calc(2) $+ H_A^2$[b]	O–C(2)	g-calc(2)	Composition percentage(2)
$(\frac{7}{2}, \frac{3}{2})$	2	33 386	33 555	−169	33 480	−94	1.467	79% + $(\frac{7}{2}, \frac{5}{2})$ 19%
	3	39 141	38 984	157	39 147	−6	1.210	94% + $(\frac{7}{2}, \frac{5}{2})$ 6%
	4	40 160	40 050	110	40 101	60	1.116	93% + $(\frac{7}{2}, \frac{5}{2})$ 6%
	5	37 020	37 027	−7	37 042	−22	1.023	96% + $(\frac{7}{2}, \frac{5}{2})$ 3%
$(\frac{7}{2}, \frac{5}{2})$	1	39 721	39 706	15	39 619	102	1.353	67% + $(\frac{5}{2}, \frac{3}{2})$ 18%
	2	40 288	40 589	−301	40 289	−1	1.023	81% + $(\frac{7}{2}, \frac{3}{2})$ 19%
	3	43 019	43 066	−47	43 047	−28	1.112	93% + $(\frac{7}{2}, \frac{3}{2})$ 5%
	4	42 425	42 521	−96	42 405	20	1.099	92% + $(\frac{7}{2}, \frac{3}{2})$ 5%
	5	43 623	43 552	71	43 633	−10	1.167	95% + $(\frac{7}{2}, \frac{3}{2})$ 3%
	6	39 085	38 834	251	39 072	13	1.167	100%
$(\frac{5}{2}, \frac{3}{2})$	1	53 365	53 370	−5	53 375	−10	0.989	72% + $(\frac{7}{2}, \frac{5}{2})$ 26%
	2	48 415	48 621	−206	48 412	3	0.915	95% + $(\frac{5}{2}, \frac{5}{2})$ 4%
	3	51 582	51 517	65	51 524	58	0.881	97% + $(\frac{5}{2}, \frac{5}{2})$ 2%
	4	47 057	46 962	95	47 080	−23	0.841	93% + $(\frac{5}{2}, \frac{5}{2})$ 3%
$(\frac{5}{2}, \frac{5}{2})$	0	45 277	45 345	−68	45 202	75	$\frac{0}{0}$	100%
	1	50 029	49 845	184	50 007	22	0.658	84% + $(\frac{5}{2}, \frac{3}{2})$ 9%
	2	51 463	51 392	71	51 474	−11	0.928	95% + $(\frac{5}{2}, \frac{3}{2})$ 4%
	3	53 123	53 160	−37	53 185	−62	0.965	96% + $(\frac{5}{2}, \frac{3}{2})$ 2%
	4	53 736	53 870	−134	53 772	−36	1.044	96% + $(\frac{5}{2}, \frac{3}{2})$ 4%
	5	50 357	50 375	−18	50 331	26	1.043	98% + $(\frac{7}{2}, \frac{3}{2})$ 2%

[a]Z.B. Goldschmidt (1968a). [b]Z.B. Goldschmidt, Salomon and Starkand (1971).

TABLE
Parameter values for $4f^{n-1}5d$

Ion configuration	F_2	F_4	G_1	G_3	G_5
PrIV $4f5d^a$	213.6 ± 0.3	26.0 ± 0.1	300.7 ± 0.3	37.9 ± 0.1	5.21 ± 0.03
LuIV $4f^{13}5d^b$	233 ± 2	22.7 ± 0.7	236 ± 1	30 ± 2	4.1 ± 0.5
CeIII $4f5d^a$	185.0 ± 0.1	22.7 ± 0.1	303.4 ± 0.2	34.8 ± 0.1	4.50 ± 0.01
PrIII $4f^25d^{*c}$	182.0 ± 0.9	21.4 ± 0.3	283.0 ± 1.4	32.6 ± 0.5	4.35 ± 0.10
EuIII $4f^6(^7F)5d^{*d}$	182 ± 2	17.7 ± 0.7	222 ± 3	24.5 ± 1.7	4.6 ± 0.1
GdIII $4f^7(^8S)5d^e$			$\frac{3}{5}[G_1 + 4G_3 + 22G_5] = 203$		
TbIII $4f^8(^7F)5d^{*f}$	194 ± 2	19.9 ± 0.6	185 ± 3	26.2 ± 1	2.9 ± 0.3
ErIII $4f^{11}5d^{*c}$	195 ± 3	20.1 ± 0.6	213 ± 7	25.9 ± 1.3	3.45
TmIII $4f^{12}5d^{*c}$	193.7 ± 1.2	19.4 ± 0.4	205.1 ± 1.2	26.3 ± 0.9	3.5 ± 0.2
YbIII $4f^{13}5d^a$	192 ± 2	18 ± 1	199 ± 2	23 ± 2	3.1 ± 0.4
LaII $4f5d^a$	132 ± 1	17.3 ± 0.3	315 ± 2	29 ± 1	3.0 ± 0.1
LaII $4f5d^{*g}$	150.8 ± 1.4	17.8 ± 0.4	315 ± 1	32.0 ± 0.7	4.0 ± 0.2
CeII $4f^25d^{*g}$	148.9 ± 1.1	17.0 ± 0.2	274.9 ± 1.4	29.0 ± 0.5	3.5 ± 0.1
PrII $4f^35d^{*c}$	149.3 ± 1.5	15.8 ± 0.6	245.9 ± 1.5	25.3 ± 0.8	3.5 ± 0.2
NdII $4f^45d^{*c}$	139 ± 5	15.5 ± 0.3	224 ± 3	27.0 ± 0.5	2.9 ± 0.3
GdII $4f^85d^{*h}$	145 ± 3	10.9 ± 0.8	144 ± 7	17 ± 2	1.7 ± 0.4
DyII $4f^{10}5d^{*i}$	144 ± 3	12.4 ± 0.8	165 ± 8	17 ± 4	2.6 ± 0.4
TmII $4f^{13}5d^{*c}$	136 ± 3	12 ± 1	159 ± 14	16 ± 2	2.2
	E^1	E^2	E^3	α	β
PrIII $4f^25d^{*c}$	4934 ± 15	22.8 ± 0.1	478.4 ± 0.8	18.1 ± 1	–
EuIII $4f^6(^7F)5d^{*d}$	5863	27.5	558	23	–
ErIII $4f^{11}5d^{*c}$	7061 ± 44	32.2	650	20	–
TmIII $4f^{12}5d^{*c}$	7222 ± 53	34.5 ± 0.3	681 ± 4	17	–
CeII $4f^25d^{*g}$	3771 ± 24	17.0 ± 0.2	368 ± 1	23 ± 2	−899 ± 64
PrII $4f^35d^{*c}$	4260 ± 70	19.7	396	10	–
NdII $4f^45d^c$	4441 ± 49	24 ± 2	437 ± 2	3 ± 2	–
GdII $4f^85d^h$	5502 ± 26	23	560		
DyII $4f^{10}5d^i$	6033 ± 44	26.0 ± 1.6	529 ± 4	[20]	[0]

*An * means that the calculations, the results of which are cited here, included CI. [a]Z.B (1974). [d]Sugar and Spector (1974). [c]Callahan (1963). [f]Meinders, van Kleef and Wyart (1972). [g]Z.B

TABLE 1.42.
List of SDI parameters for the 4f5d configuration.

Interaction	Direct part	Exchange part
Spin–spin	M^0, M^2, M^4(4f5d) M^0, M^2(5d4f)	N^1, N^3(4f5d)
Spin–other-orbit	M^0, M^2, M^4(4f5d) M^0, M^2(5d4f)	N^{-1}, N^1, N^3, N^5(4f5d) K^{1-}, K^{3-}, K^{5-}(4f5d)
Effective EL–SO	S^2, S^4(4f5d, 4fn'd) S^2, S^4(4f5d, n''f5d)	T^1, T^3, T^5(4f5d, n'd4f) T^1, T^3, T^5(4f5d, 5dn''f)

1.41.
configurations in lanthanide ions (cm^{-1}).

F_1	F_2	G_2	G_4	ζ_{4f}	ζ_{5d}	γ
-21.2 ± 0.6	-3.0 ± 1.0	-38.1 ± 0.8	-1.85 ± 0.06	858 ± 3	1067 ± 4	-52 ± 5
-18.7 ± 6	0 (fixed)	-33 ± 6	-2.5 ± 1	3368 ± 11	1821 ± 17	-
-20.4 ± 0.4	-7.3 ± 0.7	-43.0 ± 0.5	-1.54 ± 0.04	637 ± 2	656 ± 4	-55.5
-14.4 ± 1.6	-9.7 ± 4	-35.8 ± 2	-1.3 ± 0.2	767 ± 5	734 ± 11	-53 ± 6
-41 ± 5	0	-57 ± 7	-2.1 ± 1.5	1181 ± 12	898 ± 30	-65 ± 7
-	-	-	-		1050	-50
-12 ± 3		-36	-1.3			-
-15.4 ± 1.4	-9.3	-33.4 ± 5.1	-1.8	2383 ± 7	1090 ± 8	
-11.4 ± 1.8	-	-37.9 ± 3.8	-2.0 ± 0.3	2635 ± 7	1126 ± 9	
-15 ± 5	-9 ± 9	-32 ± 5	-2.4 ± 1	2921 ± 11	1149 ± 16	-75 ± 10
-84 ± 3	-44 ± 5	-34 ± 3	0	391 ± 14	412 ± 28	
$-18 \pm$	-7	-36	-1.5	368 ± 16	448 ± 28	
-18 ± 2	-7 ± 2	-35 ± 2	-1.6 ± 0.1			
-16.0 ± 1.6	-	-22.2 ± 3.1	-1.4 ± 0.2	656 ± 1	427 ± 6	
-16.2 ± 2.0	-12 ± 13	-31.0 ± 7.2	-1.3 ± 0.9	781 ± 2	451 ± 9	
-	-	-	-	1737 ± 54	608 ± 56	
-15.0 ± 1.6	-8.6	-18.5 ± 8.2	-2.2 ± 0.4	1771 ± 3	537 ± 9	
-13 ± 6	-8.6	-24.0 ± 8.2	-1.7 ± 0.8	2505 ± 20	552 ± 30	

Goldschmidt, Salomon and Starkand (1971). [b]Sugar and Kaufman (1972). [c]Wyart, Blaise and Camus Goldschmidt (1972). [h]Blaise, van Kleef and Wyart (1971). [i]Wyart (1976).

(2) The M^k's and N^k's are positive decreasing functions of k with N^{-1} having a smaller value than N^5.
(3) The K^{k-}'s are negative; their absolute values are decreasing functions of k.
(4) The effective EL–SO parameters representing the two sequences of perturbing configurations ($5d \leftrightarrow n'd$) and ($4f \rightarrow n''f$) are of opposite signs, with those representing the first sequence being one order of magnitude greater than the corresponding parameters representing the second sequence.

It is to be expected that the SDI interactions will be stronger on the right-hand side of the lanthanide group, but no explicit results are as yet available in the literature.

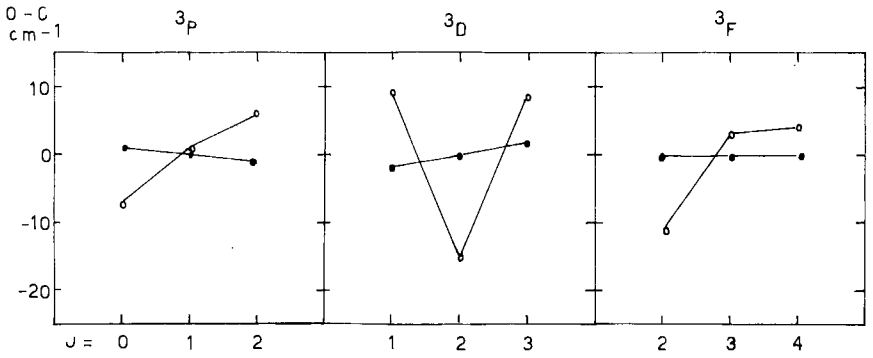

Fig. 1.37. PrIV 4f5d: improvement in the multiplet splittings due to the SDI. ○ – without SDI, ● – including SDI.

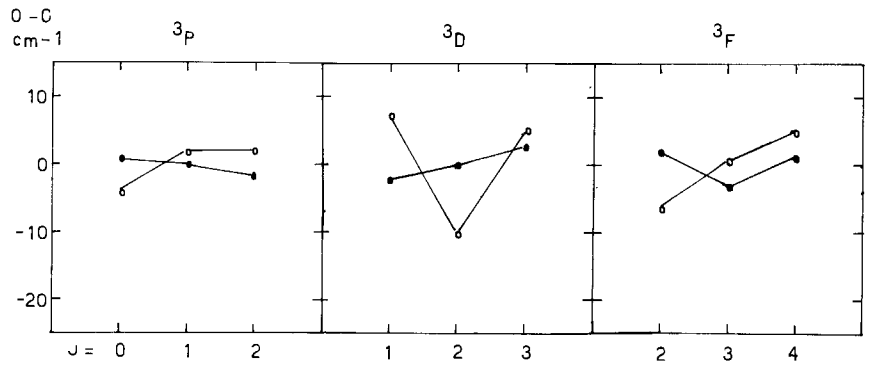

Fig. 1.38. CeIII 4f5d: improvement in the multiplet splittings due to the SDI. ○ – without SDI, ● – including SDI.

12.5. *The* $4f^{n-1}5g$ *configurations*

The sole representative of the $4f^{n-1}5g$ configurations is the configuration 4f5g of CeIII discovered by Sugar (1965a). Since $4f^{n-1}$ are "internal" electrons and 5g is an "external" electron, both the electrostatic $4f^{n-1}$–5g interaction, especially its exchange part, and the spin–orbit interaction of the 5g electron are weak. Consequently, the coupling is a pure *jK*, with pair splittings varying from 9 cm^{-1} to less than 1 cm^{-1}, as reflected in figs. 1.3 and 1.39. A glance at these figures shows that the energy levels are divided into two groups, corresponding to the two values $j_1 = \frac{5}{2}, \frac{7}{2}$ of the total angular momentum of the 4f electron; the energetic distance between these groups equals $\frac{7}{2}\zeta_{4f}$. For each of these groups, the centers of gravity of the pairs, characterized by the quantum number K, are determined by the direct part of the electrostatic interaction 4f–5g, particularly by that part of the interaction represented by the Slater parameter F^2. The

TABLE 1.43.
Parameter values for PrIV 4f5d and CeIII 4f5d ($H_1 + H_2 + H_A^2$ + SDI) (cm^{-1})[a].

Parameter	PrIV 4f5d	CeIII 4f5d
F_0	68075 ± 1	9339 ± 2
F_2	213.4 ± 0.1	184.9 ± 0.1
F_4	26.25 ± 0.04	22.84 ± 0.06
G_1	300.8 ± 0.1	303.5 ± 0.2
G_3	38.00 ± 0.07	34.92 ± 0.08
G_5	5.27 ± 0.01	4.54 ± 0.01
ζ_{4f}	854 ± 1	634 ± 2
ζ_{5d}	1058 ± 2	681 ± 3
F_1	−20.8 ± 0.2	−20.2 ± 0.3
F_3	−3.0 ± 0.5	−7.6 ± 0.6
G_2	−39.0 ± 0.3	−43.4 ± 0.4
G_4	−1.71 ± 0.03	−1.49 ± 0.03
M^0(fd)	[0.300]*	[0.202]*
M^0(df)	[0.517]	[0.372]
M^2(fd)	[0.139]	[0.095]
M^2(df)	[0.195]	[0.137]
M^4(fd)	[0.090]	[0.062]
N^1	[0.105]	[0.074]
N^3	[0.088]	[0.061]
N^5	[0.070]	[0.049]
N^{-1}	[0.053]	[0.038]
K^{1-}	[−0.490]	[−0.369]
K^{3-}	[−0.256]	[−0.192]
K^{5-}	[−0.146]	[−0.110]
S^2(4f5d, 4f*n*′d)	67 ± 15 (87)*	57 ± 21 (75)*
S^4(4f5d, 4f*n*′d)	[32] (41)*	[27] (35)*
T^1(4f5*d*, *n*′d4f)	−42 ± 15 (−81)*	−33 ± 19 (−76)*
T^3(4f5d, *n*′d4f)	−98 ± 18 (−32)*	−91 ± 29 (−29)*
T^5(4f5d, *n*′d4f)	[−14] (−27)*	[−11] (−25)*
S^2(4f5d, *n*″f5d)	[−4.4]	[−2.2]
S^4(4f5d, *n*″f5d)	[−3.4]	[−1.7]
T^1(4f5d, 5d*n*″f)	[26.4]	[16.4]
T^3(4f5d, 5d*n*″f)	[6.4]	[3.5]
T_5(4f5d, 5d*n*″f)	[4.6]	[2.4]
Δ	4	5

[a]Z.B. Goldschmidt and Cohen (1975). *Values written between round or square brackets were obtained in the "parametric potential" calculation.

coefficients of F^2 are given by the following formula:

$$f_2(j_1K) = \{\tfrac{1}{2}fj_1, g, K, \tfrac{1}{2}, J|C^{(2)} \cdot C^{(2)}|\tfrac{1}{2}fj_1, g, K, \tfrac{1}{2}, J\}$$
$$= (-1)^{K+1/2}(3\|C^{(2)}\|3)(4\|C^{(2)}\|4)[j_1] \begin{Bmatrix} 3 & 3 & 2 \\ j_1 & j_1 & \frac{1}{2} \end{Bmatrix} \begin{Bmatrix} 4 & 4 & 2 \\ j_1 & j_1 & K \end{Bmatrix} \qquad (1.177)$$

On substituting in this formula the explicit expressions for the reduced matrix

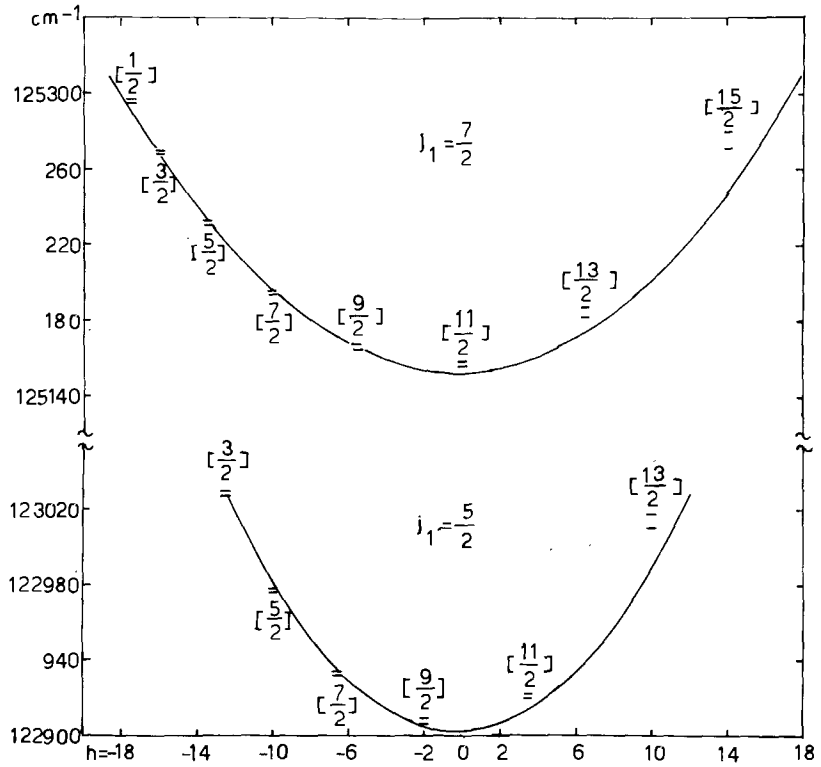

Fig. 1.39. The energy levels of CeIII 4f5g as functions of h lie close to two parabolas.

elements of $C^{(2)}$ and for the last $6j$-symbol, (Edmonds, 1957), and multiplying $f_2(j_1K)$ by $D_2 = 1155$, one obtains for the coefficients of F_2:

$$f^2(j_1K) = 2\sqrt{105}(-1)^{j_1+3/2}\begin{Bmatrix} 3 & 3 & 2 \\ j_1 & j_1 & \frac{1}{2} \end{Bmatrix} \times [3h(2h+1) - 40j_1(j_1+1)][(2j_1+1)/(2j_1-1)j_1(j_1+1)(2j_1+3)]^{1/2} = \begin{cases} [\frac{9}{7}h(2h+1) - 150] & \text{for} \quad j_1 = \frac{5}{2} \\ [\frac{5}{7}h(2h+1) - 150] & \text{for} \quad j_1 = \frac{7}{2} \end{cases} \tag{1.178}$$

where

$$h = (\boldsymbol{j}_1 \cdot \boldsymbol{l}_2) = \tfrac{1}{2}[K(K+1) - j_1(j_1+1) - 20] \tag{1.179}$$

Thus, in the approximation of the quadrupole electrostatic interaction described by f^2F_2, the centers of gravity of the pairs, when drawn as a function of h, lie on two parabolas, one for each value of j_1; the minima of both parabolas occur at $h = -\frac{1}{4}$; these are drawn in fig. 1.39 with $F_0 = 124\,238\ \text{cm}^{-1}$, $\zeta_{4f} = 643\ \text{cm}^{-1}$ and $F_2 = 0.325\ \text{cm}^{-1}$, and with the experimental pairs for comparison. Both the observed values for the centers of gravity of the pairs, and their calculated values in the quadrupole approximation, are listed in table 1.44. It can be seen

TABLE 1.44.
Energy values for the centers of gravity of the pairs in CeIII 4f5g (cm^{-1}).[a]

j_1	K	h	Observed	Calculated in the quadrupole approximation
$\frac{5}{2}$	$\frac{3}{2}$	$-\frac{25}{2}$	123 029	123 029
	$\frac{5}{2}$	-10	122 978	122 983
	$\frac{7}{2}$	$-\frac{13}{2}$	122 933	122 936
	$\frac{9}{2}$	-2	122 907	122 906
	$\frac{11}{2}$	$\frac{7}{2}$	122 921	122 915
	$\frac{13}{2}$	10	123 014	122 991
$\frac{7}{2}$	$\frac{1}{2}$	$-\frac{35}{2}$	125 296	125 292
	$\frac{3}{2}$	-16	125 269	125 269
	$\frac{5}{2}$	$-\frac{27}{2}$	125 232	125 236
	$\frac{7}{2}$	-10	125 195	125 198
	$\frac{9}{2}$	$-\frac{11}{2}$	125 167	125 167
	$\frac{11}{2}$	0	125 157	125 154
	$\frac{13}{2}$	$\frac{13}{2}$	125 184	125 175
	$\frac{15}{2}$	14	125 275	125 249

[a]Z.B. Goldschmidt (1976b).

both from table 1.44 and from fig. 1.39 that the overall agreement between theory and experiment is very good, except for the pairs with the highest K values, the calculated values of which are smaller than their observed values by about 25 cm^{-1}. As shown by Crosswhite (1971), this disagreement can readily be removed, through the inclusion, in the hamiltonian of 4f5g, of the effective electrostatic interaction H^2_A. The dominant part of this interaction is represented by $F_1(= F^1/12\sqrt{105})$, the coefficients of which are given by the following formula:

$$f^1(j_1K) = 12\sqrt{105}\{\tfrac{1}{2}fj_1,\ g,\ K,\ \tfrac{1}{2},\ J|\boldsymbol{u}^{(1)}\cdot\boldsymbol{v}^{(1)}|\tfrac{1}{2}fj_1,\ g,\ K,\ \tfrac{1}{2},\ J\}$$
$$= 12\sqrt{105}(-1)^{K+3/2}[j_1]\begin{Bmatrix}3 & 3 & 1\\ j_1 & j_1 & \frac{1}{2}\end{Bmatrix}\begin{Bmatrix}4 & 4 & 1\\ j_1 & j_1 & K\end{Bmatrix} \qquad (1.180)$$

On including the effective electrostatic interaction in the energy-level calculations of this configuration, the mean error reduced to 0.5 cm^{-1}, as compared to 10 cm^{-1} obtained in the conventional calculations including $H_1 + H_2$ only. The values obtained for the parameters describing the relevant interactions are (Crosswhite, 1971):

$$\zeta_f = 643\ cm^{-1},\quad F_2 = 0.367\ cm^{-1}\quad \text{and}\quad F_1 = 1.228\ cm^{-1}.$$

13. Groups of interacting configurations; study of electrostatic CI effects

The methods of approach to the interpretation of lanthanide spectra in which several configurations interact, were demonstrated by Z.B. Goldschmidt (1966,

1968a,b) by means of relatively simple examples, where the separate effect of each interaction could clearly be visualized. The examples chosen were LaII $5d^2+5d6s+6s^2$, CeIII $4f5d+4f6s$, LuII $5d^2+5d6s+6s^2$, LuII $5d6p+6s6p$, by means of which the competition between the electrons 5d and 6s was illustrated, and CeIII $4f6p+5d^2+5d6s$, which illustrated the competition between the pairs of electrons 4f6p, $5d^2$ and 5d6s. In these simple problems, the effects of each CI were studied in detail, by calculating the repulsions it induced on the individual terms, and its influence on the compositions of the eigenvectors.

The following conclusions were drawn:

(1) The inclusion in the theoretical calculations of CI between neighbouring configurations is essential for obtaining "true" and, therefore, consistent values for the various interaction parameters.

(2) The repulsions caused by the CI represented by $J(5d6p, 6s6p)$ and $K(5d6p, 6p6s)$ are the largest: in LuII $5d6p+6s6p$ they amount to $8500\,cm^{-1}$ between the ^1P terms and to $600\,cm^{-1}$ between the ^3P terms.

(3) The repulsions caused by the CI represented by $H(5d^2, 5d6s)$ and $G_2(5d^2, 6s^2)$ are large: in LaII $5d^2+5d6s+6s^2$ the repulsions of the ^1D terms due to H amount to $4160\,cm^{-1}$ and those of the ^1S terms due to G_2 amount to $2600\,cm^{-1}$.

(4) The CI represented by $R_1(4f6p, 5d^2)$ is quite strong. In CeIII $4f6p+5d^2+5d6s$ it does not only bring about deviations of the order of $1400\,cm^{-1}$ for the ^1G terms, but also causes a breakdown of the *jj* coupling in the 4f6p configuration.

(5) The CI represented by $T_1(4f6p, 5d6s)$ and $T_3(4f6p, 6s5d)$ is of medium strength: in CeIII $4f6p+5d^2+5d6s$, the repulsions due to these interactions amount to about $700\,cm^{-1}$.

(6) The CI represented by $M(4f5d, 4f6s)$ and $N(4f5d, 6s4f)$ is negligible, as far as the repulsions of the terms are concerned. However, the extremely small 4f5d-4f6s admixtures caused by this CI may explain the forbidden $4f6s–4f^2$ transitions observed by Sugar (1965a) in CeIII.

The detailed description of the analyses of the above mentioned groups of configurations will not be repeated in this chapter. Rather, the analyses of the following two, more comprehensive, groups of configurations LaII $4f5d+4f6s+5d6p+6s6p$ (Z.B. Goldschmidt, 1968a, 1972, 1973a, b) LaII $5d^2+5d6s+6s^2+4f6p+4f^2+6p^2+6s6d$ (Z.B. Goldschmidt, 1968a, 1976a), each of which comprises all configurations of the same parity belonging to both systems, will be discussed here.

13.1. LaII $4f5d+4f6s+5d6p+6s6p$.

The configurations 4f5d, 4f6s, 5d6p and 6s6p constitute the "low B" and "high I-A" groups of configurations of LaII (see fig. 1.15). They comprise 20 terms, which split into 40 levels, all of which are experimentally known. The Grotrian diagram of these configurations is given in fig. 1.40. A glance at this diagram shows that the four configurations partially overlap; this is a typical example of the above mentioned competition between all four 4f, 5d, 6s and 6p electrons. CI should therefore be included not only between $4f5d+4f6s$, belonging to the

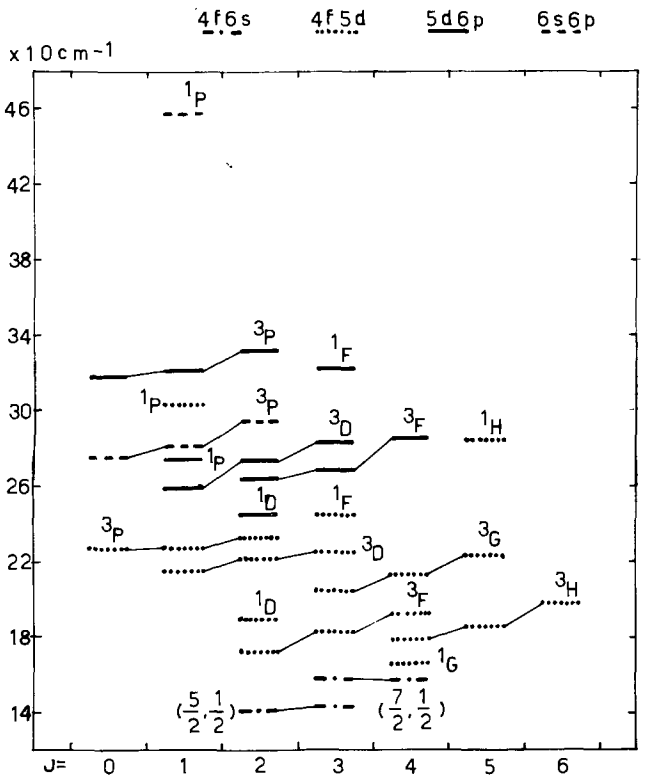

Fig. 1.40. Energy levels of LaII 4f5d + 4f6s + 5d6p + 6s6p.

group "low B", and between 5d6p + 6s6p belonging to "high I-A" but rather between any pair of these four configurations. Furthermore, from the distribution of the energy levels and the values of their g-factors, one can conclude that in the 4f6s configuration, the electrons are jj coupled; in the 6s6p configuration, the electrons are LS coupled; in 4f5d and 5d6p the couplings are also close to LS.

The parameters to be evaluated are given in table 1.45. Since the number of the electrostatic parameters (real and effective) is 30, against 20 terms, these parameters cannot be directly evaluated by comparing the theoretical formulae to the experimental values of the terms. Consequently, the interpretation of the odd configurations of LaII could be carried out only after completing the interpretation of other lanthanide spectra, such as those of CeIII 4f5d + 4f6s and LuII 5d6p + 6s6p mentioned in section 13 above, and also of more complicated lanthanide spectra, such as those of CeII (Z.B. Goldschmidt 1968a, 1972), GdII (Z.B. Goldschmidt and Nir, 1971), and YbII(Racah, et al., 1965). Initial values for the various interaction parameters of the odd configurations of LaII were obtained by extrapolating the values of the corresponding parameters in CeIII and in CeII–GdII–YbII–LuII. These initial values, which served for the first

TABLE 1.45.
Parameters for LaII 4f5d + 4f6s + 5d6p + 6s6p.

	4f5d	4f6s	5d6p	6s6p
4f5d	F_0, F_2, F_4, G_1, G_3, G_5(fd) F_1, F_3, G_2, G_4(fd) ζ_{4f}, ζ_{5d}			
4f6s	M(fd, fs) N(fd, sf)	F_0, G_3(fs) ζ_{4f}		
5d6p	R_1, R_3(fd, dp) R_2, R_4(fd, pd)	T_1(fs, dp) T_2(fs, pd)	F_0, F_2, G_1, G_3(dp) ζ_{5d}, ζ_{6p}	
6s6p	T_3(fd, sp) T_2(fd, ps)	–	J(dp, sp) K(dp, ps)	F_0, G_1(sp) ζ_{6p}

diagonalization of the energy matrices, are given in column 2 of table 1.46. In the least-squares calculations which followed, only 20 electrostatic parameters were allowed to vary freely. The following parameters were forced to remain fixed on their initial values:

the effective Slater parameters F_1, F_3, G_2, G_4(fd),

$M(\text{fd, fs}) = 0 \qquad N(\text{fd, sf}) = 60\ \text{cm}^{-1}$

$R_2(\text{fd, pd}) = R_4(\text{fd, pd}) = R_3(\text{fd, dp}) = 0$

in addition, T_2(fs, pd) and T_2(fd, ps) were forced to remain equal. The application of the iterative diagonalization–least squares procedure resulted in a very good agreement between theory and experiment, the mean error Δ being 40 cm^{-1}. The observed and calculated energy levels as well as the composition percentages of their eigenvectors and their observed and calculated g-factors are given in table 1.47. The final values obtained for the parameters are given in column 3 of table 1.46.

Discussion and conclusions

(1) The final values obtained for the various interaction parameters are close to their initial values extrapolated from neighbouring spectra. This confirms the fact mentioned in section 10, that the values of the parameters change systematically while moving along an isoionic row or along different degrees of ionization of the same element.

(2) The good agreement between theory and experiment obtained in these calculations, concerning both the energy levels and the corresponding g-factors, is a direct result of the simultaneous inclusion of both the CI between neighbouring configurations and the effective electrostatic interaction (which represents interaction with distant configurations). The omission of both of these

TABLE 1.46.
Parameter values for LaII 4f5d + 4f6s + 5d6p + 6s6p (cm^{-1})[a,b,c]

Parameter	Initial value	Final value
F_0(4f5d)	20 750	21 961 ± 15
F_2(4f5d)	150	151 ± 1
F_4(4f5d)	17.5	17.7 ± 0.3
G_1(4f5d)	300	315 ± 1
G_3(4f5d)	32	32.0 ± 0.5
G_5(4f5d)	3.8	4.0 ± 0.2
F_1(4f5d)	−18.0	[−18.0]
F_3(4f5d)	−7.5	[−7.5]
G_2(4f5d)	−36.0	[−36.0]
G_4(4f5d)	−1.5	[−1.5]
F_0(4f6s)	15 550	15 711 ± 204
G_3(4f6s)	200	174 ± 59
F_0(5d6p)	28 650	28 321 ± 154
F_2(5d6p)	304	343 ± 15
G_1(5d6p)	373	387 ± 8
G_3(5d6p)	6	2 ± 3
F_0(6s6p)	36 960	36 105 ± 250
G_1(6s6p)	5 800	5 763 ± 149
M(4f5d, 4f6s)	0	[0]
N(4f5d, 6s4f)	60	[60]
R_1(4f5d, 5d6p)	130	128 ± 4
R_3(4f5d, 5d6p)	0	[0]
R_2(4f5d, 6p5d)	0	[0]
R_4(4f5d, 6p5d)	0	[0]
T_1(4f6s, 5d6p)	−1 300	−1 365 ± 267
T_2(4f6s, 6p5d)	−50	−36 ± 15
T_2(4f5d, 6p6s)	−50	
T_3(4f5d, 6s6p)	−107	−108 ± 11
J(5d6p, 6s6p)	−1 650	−1 687 ± 93
K(5d6p, 6p6s)	−3 050	−3 210 ± 125
ζ_{4f}(4f5d)	390	369 ± 16
ζ_{4f}(4f6s)	400	411 ± 12
ζ_{5d}(4f5d)	412	452 ± 27
ζ_{5d}(5d6p)	550	597 ± 57
ζ_{6p}(5d6p)	1 380	1 325 ± 68
ζ_{6p}(6s6p)	1 800	1 903 ± 93
Δ		40

[a]Z.B. Goldschmidt (1968a). [b]Z.B. Goldschmidt (1972).
[c]Z.B. Goldschmidt (1973a).

interactions results in large deviations between observed and calculated energy levels (see column 5 of table 1.39) and between observed and calculated g-factors. The inclusion of only one of these interactions also leads to unsatisfactory results. For example, if only the effective electrostatic interaction is included, the following results are obtained:

TABLE 1.47.
Energy levels of LaII 4f5d + 4f6s + 5d6p + 6s6p (cm^{-1})[a,b].

Configuration	Term	J	Obs	Calc	O–C	g-obs	g-calc	Composition percentage
4f6s	$(\frac{5}{2},\frac{1}{2})$	2	14 148	14 177	−29	0.664	0.667	95% + 5d6p ^{3}F 4%
		3	14 375	14 346	29	1.056	1.056	96% + 5d6p ^{3}F 2%
	$(\frac{7}{2},\frac{1}{2})$	3	15 774	15 789	−15	1.017	1.028	96% + 5d6p ^{1}F 2%
		4	15 699	15 684	15	1.247	1.250	97% + 5d6p ^{3}F 3%
4f5d	^{1}G	4	16 599	16 650	−51	0.969	0.966	73% + ^{3}H 22% + ^{3}F 4%
4f5d	^{3}F	2	17 212	17 177	35	0.754	0.762	70% + ^{1}D 26% + 5d6p ^{1}D 2%
		3	18 236	18 245	−9	1.086	1.083	98% + 5d6p ^{3}F 2%
		4	19 215	19 224	−9	1.232	1.227	90% + ^{1}G 8% + 5d6p ^{3}F 1%
4f5d	^{3}H	4	17 826	17 802	24	0.846	0.856	77% + ^{1}G 19% + ^{3}F 4%
		5	18 580	18 560	20	1.017	1.033	100%
		6	19 750	19 768	−18	1.178?	1.167	100%
4f5d	^{1}D	2	18 895	18 892	3	0.923	0.916	64% + ^{3}F 28% + 5d6p ^{1}D 6%
4f5d	^{3}G	3	20 403	20 409	−6	0.757	0.761	96% + ^{1}F 3%
		4	21 332	21 337	−5	1.049	1.050	100%
		5	22 283	22 288	−5	1.197	1.199	99%
4f5d	^{3}D	1	21 442	21 490	−48	0.542	0.548	79% + 5d6p ^{3}D 15% + 4f5d ^{3}P 2%
		2	22 106	22 102	4	1.167	1.174	83% + 5d6p ^{3}D 13% + 4f5d ^{3}P 2%
		3	22 537	22 476	61	1.288	1.291	79% + ^{1}F 10% + 5d6p ^{3}D 10%
4f5d	^{3}P	0	22 684	22 662	22		$\frac{0}{0}$	84% + 5d6p ^{3}P 11% + 6s6p ^{3}P 4%
		1	22 705	22 712	−7	1.431	1.444	79% + 5d6p ^{3}P 11% + 4f5d ^{3}D 4%

		2	23 247	23 271	−24	1.459	1.478	82% + 5d6p ^{3}P 11% + 4f5d ^{1}D 3%
5d6p	^{1}D	2	24 463	24 483	−20	0.887	0.892	56% + ^{3}F 33% + 4f5d ^{1}D 5%
4f5d	^{1}F	3	24 523	24 486	36	1.034	1.033	84% + ^{3}D 10% + ^{3}G 2%
5d6p	^{3}D	1	25 973	25 946	27	0.782	0.760	44% + ^{1}P 27% + 4f5d ^{3}D 13%
		2	27 388	27 383	5	1.168	1.168	83% + 4f5d ^{3}D 13% + 5d6p ^{3}P 2%
		3	28 315	28 327	−12	1.308	1.309	81% + 4f5d ^{3}D 10% + 5d6p ^{3}F 4%
5d6p	^{3}F	2	26 414	26 367	47	0.825	0.802	59% + ^{1}D 33% + 4f6s ^{3}F 2%
		3	26 838	26 866	−28	1.088	1.095	90% + ^{3}D 4% + 4f6s ^{3}F 4%
		4	28 565	28 565	0	1.245	1.250	95% + 4f6s ^{3}F 3% + 4f5d ^{3}F 2%
5d6p	^{1}P	1	27 424	27 446	−22	0.876	0.885	23% + ^{3}D 37% + 4f5d ^{1}P 15%
6s6p	^{3}P	0	27 546	27 547	−1		0/0	70% + 5d6p ^{3}P 19% + 4f5d ^{3}P 12%
		1	28 155	28 157	−2	1.267	1.318	44% + 4f5d ^{3}P 30% + 5d6p ^{3}P 17%
		2	29 498	29 492	−6	1.471	1.479	45% + 5d6p ^{3}P 40% + 4f5d ^{3}P 10%
4f5d	^{1}H	5	28 526	28 543	−17	1.004	1.001	99%
4f5d	^{1}P	1	30 353	30 359	−6	1.074	1.054	49% + 5d6p ^{1}P 22% + 6s6p ^{3}P 12%
5d6p	^{3}P	0	31 786	31 801	−15		0/0	70% + 6s6p ^{3}P 26% + 4f5d ^{3}P 4%
		1	32 161	32 140	−21	1.492	1.488	65% + 6s6p ^{3}P 29% + 4f5d ^{3}P 3%
		2	33 204	33 208	−4	1.494	1.496	45% + 6s6p ^{3}P 52% + 4f5d ^{3}P 1%
5d6p	^{1}F	3	32 201	32 202	−1	1.005	1.013	91% + ^{3}D 4% + 4f6s ^{1}F 3%
6s6p	^{1}P	1	45 692	45 692	0	0.999	1.004	77% + 5d6p ^{1}P 20% + 4f5d ^{1}P 2%

[a]Z.B. Goldschmidt (1968a). [b]Z.B. Goldschmidt (1972).

TABLE 1.48.
CI effects in LaII 4f5d + 4f6s + 5d6p + 6s6p[a].

Pairs of repulsing terms		CI responsible for repulsion	Individual repulsions (cm^{-1})	Admixture (%)
(dp–sp)	^1P	J(dp, sp), K(dp, ps)	5550	20
	^3P		1770	45
(fd–dp)	^1P	R_1(fd, dp)	1550	22
	^3P		1300	11
	^1D		800	6
	^3D		1060	15
	^1F		350	2
	^3F		310	1
(fs–dp)	^1F	T_1(fs, dp), T_2(fs, pd)	1020	2
	^3F		890	4
(fd, sp)	^1P	T_3(fd, sp), T_2(fd, ps)	550	2
	^3P		180	12
(fd, fs)	^1F	M(fd, fs), N(fd, sf)	10	0.17
	^3F		5	0.12

[a]Z.B. Goldschmidt (1972).

(i) The parameters representing this interaction in LaII 4f5d take values which are inconsistent with those obtained for the neighbouring spectra. This can be clearly seen by comparing columns 3, 5, 7 and 9 of table 1.36.
(ii) The mean error $\Delta(=55\ cm^{-1})$ for LaII 4f5d is larger than the mean error $\Delta(=40\ cm^{-1})$ for LaII 4f5d + 4f6s + 5d6p + 6s6p, although, in the calculation of LaII 4f5d, the number of electrostatic parameters, real and effective, is equal to the number of terms.
(iii) The deviations between observed and calculated g-factors, especially for $J = 1$ levels which are sensitive to the composition of the eigenvectors, are much larger for LaII 4f5d than for LaII 4f5d + 4f6s + 5d6p + 6s6p.
(3) CI effects, namely, the magnitudes of the repulsions of the interacting terms and the extent of admixture of these terms are summarized in table 1.48. Inspection of this table confirms the conclusions obtained in section 13 concerning the strengths of the various CI.
(4) The displacements of the various terms of the 4f5d configuration due to the effective interaction are given in table 1.49.

The results given in both tables 1.48 and 1.49 demonstrate conclusion (2) concerning the extreme importance of the CI and the effective electrostatic interactions.

TABLE 1.49.
Effective electrostatic interaction (EEI) effects in LaII $4f5d + 4f6s + 5d6p + 6s6p$ (cm^{-1})[a].

Term	Displacement due to EEI
^1P	−370
^3P	−340
^1D	−290
^3D	170
^1F	88
^3F	−190
^1G	97
^3G	220
^1H	−75
^3H	300

[a]Z.B. Goldschmidt (1972).

13.2. LaII $5d^2 + 5d6s + 6s^2 + 4f6p + 4f^2 + 6p^2 + 6s6d$

The interpretation of the even configurations of LaII has been carried out in several steps. The calculation of the energy levels of

$5d^2 + 5d6s + 6s^2$ ("low A")

was conducted by Amiel (1955), and reviewed by Z.B. Goldschmidt (1968a, b) for the purpose of studying CI effects. The main results of these calculations, as far as CI effects are concerned, were summarized in section 13 of this chapter. The calculation of the energy levels of the configuration

4f6p ("high I-B")

was also conducted by Amiel (1955). The bowl structure of both $(\frac{5}{2}, \frac{3}{2})$ and $(\frac{7}{2}, \frac{3}{2})$ *jj*-coupling quartets was explained by Z.B. Goldschmidt (1968a, b), in terms of the quadrupole interaction represented by $F_2(4f, 6p)$ (see section 12.3 above). The configurations

$4f^2$("high II-B") and

$6p^2, 6s6d$ (third floor of system A, not included in fig. 1.15)

were already introduced in section 12.1.1.3 of this chapter. In that section, correct designations of the ^1D levels belonging to the $4f^2$ and $6p^2$ configurations were given and the energy level calculation of $4f^2$ (treated as an isolated configuration) was discussed; furthermore, the necessity for the inclusion of CI between $6p^2$ and 6s6d was pointed out. In what follows, the methods for evaluating the parameters for the $6p^2 + 6s6d$ configurations will be described. The parameters thus obtained, together

with the parameters obtained for all other configuration subgroups mentioned above will then be used for calculating the whole complex of seven even configurations of LaII.

The configurations $6p^2 + 6s6d$

The formulae for the electrostatic interaction within and between the configurations $6p^2 + 6s6d$ are given in table 1.50. The configuration 6s6d, comprising the two terms ^1D and ^3D, is described by the two internal Slater parameters F_0' and G_2. Since the number of parameters equals the number of terms, an exact solution to the electrostatic problem is possible whenever both terms are experimentally known. However, the values of the parameters obtained in this fashion are effective ones, which include the effects of the repulsion by the configuration $6p^2$. The three terms of $6p^2$ are described by only two internal Slater parameters, F_0 and F_2. If these parameters are evaluated so as to fit the two terms ^1S and ^3P unperturbed by 6s6d, there exists a large deviation between the calculated and the observed values of the perturbed term ^1D. (see section 12.1.1.3). This deviation measures the strength of the CI, and permits the evaluation of the CI parameter $K(6p^2, 6d6s)$ and of the unperturbed position of the term 6s6d $^1D = F_0' + G_2$. This evaluation is achieved through the requirement that the eigenvalues of the electrostatic matrix of ^1D should be equal to the observed ^1D terms. The value obtained for the sum $F_0' + G_2$, together with the equation $6s6d(^3D) = F_0' - G_2$, give the separate values of F_0' and G_2. In the case of LaII $6p^2 + 6s6d$, $6s6d(^1D)$ is not known experimentally. Additional information was, therefore, needed for the purpose of evaluating the electrostatic parameters of these configurations. This information was obtained by performing HF calculations for the configurations 5d6s and 6s6d and demanding that the following equality holds: $G_2(6d6s)_{\text{semiempirical value}}/G_2(6d6s)_{\text{HF}} = G_2(5d6s)_{\text{semiempirical value}}/G_2(5d6s)_{\text{HF}}$. The value thus obtained for $G_2(6d6s)$ was 700 cm^{-1}. F_0' was then evaluated from the formula $^3D = F_0' - G_2$, and the unperturbed value of ^1D was evaluated from the formula $^1D = F_0' + G_2$. The value of K was obtained by solving the secular equation derived from the electrostatic matrix of ^1D and the experimental value of $6p^2(^1D)$. The spin–orbit parameters ζ_{6p} and ζ_{6d} were directly evaluated from the splittings of the various terms.

TABLE 1.50.
Theoretical formulae of the electrostatic interaction for the configurations $p^2 + ds$.

$p^2\ ^1S = F_0 + 10F_2$

$ds\ ^3D = F_0' - G_2$

$p^2\ ^3P = F_0 - 5F_2$

^1D	p^2	ds
p^2	$F_0 + F_2$	$2(15)^{1/2}K/5$
ds	$2(15)^{1/2}K/5$	$F_0' + G_2$

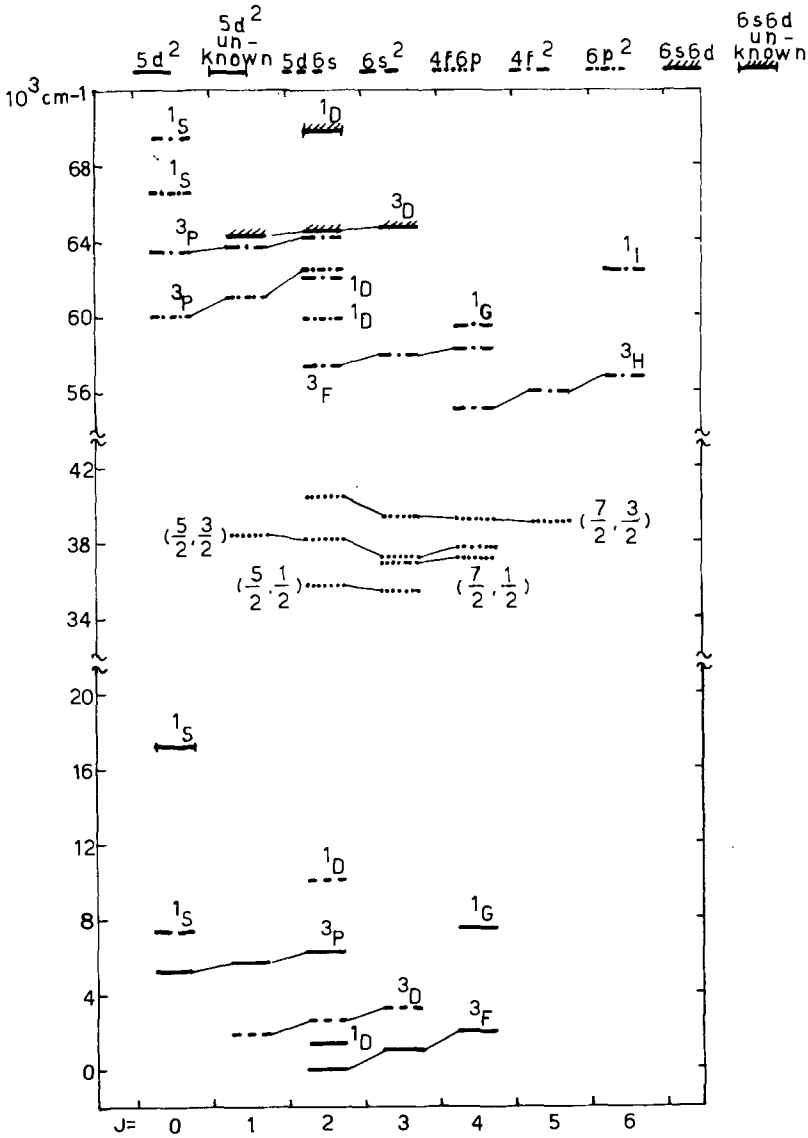

Fig. 1.41. Energy levels of LaII $5d^2 + 5d6s + 6s^2 + 4f6p + 4f^2 + 6p^2 + 6s6d$.

The configurations $5d^2 + 5d6s + 6s^2 + 4f6p + 4f^2 + 6p^2 + 6s6d$

There are 26 terms belonging to these configurations, which split into 48 levels, all of which, excepting $5d^2(^1S)$ and $6s6d(^1D)$, are experimentally known. Their Grotrian diagram is given in fig. 1.41. The diagram shows that in the 4f6p configuration the electrons are *jj* coupled, as already mentioned above, whereas in all other configurations the coupling is close to *LS*. The 45 electrostatic and 7

TABLE 1.51.
Parameters for LaII $5d^2 + 5d6s + 6s^2 + 4f6p + 4f^2 + 6p^2 + 6s6d$.

	$5d^2$	5d6s	$6s^2$	4f6p	$4f^2$	$6p^2$	6s6d
$5d^2$	A, B, C ζ_{5d}						
5d6s	$H(d^2, ds)$	F_0, $G_2(5d6s)$ ζ_{5d}					
$6s^2$	$G_2(d^2, s^2)$	–	F_0				
4f6p	R_1, $R_3(fp, d^2)$	$T_1(fp, 5d6s)$ $T_3(fp, 6s5d)$	–	F_0, F_2, G_2, $G_4(fp)$ ζ_{4f}, ζ_{6p}			
$4f^2$	G_1, G_3, $G_5(f^2, d^2)$	$N(f^2, 5d6s)$	$G_3(f^2, s^2)$	L_2, $L_4(f^2, fp)$	E^0, E^1, E^2, E^3 α, β, γ ζ_{4f}		
$6p^2$	G_1, $G_3(d^2, p^2)$	$K(p^2, 5d6s)$	$G_1(p^2, s^2)$	$P_2(fp, p^2)$	G_2, $G_4(f^2, p^2)$	F_0, $F_2(p^2)$ ζ_{6p}	
6s6d	not included	not included	–	$T_1(fp, 6d6s)$ $T_3(fp, 6s6d)$	$N(f^2, 6d6s)$	$K(p^2, 6d6s)$	F_0, $G_2(6d6s)$ ζ_{6d}

spin–orbit parameters representing the various interactions within and between these configurations, are listed in table 1.51. The energy levels of these configurations were calculated through the use of the diagonalization – least squares procedure. Only 22 electrostatic and the 7 spin–orbit parameters were allowed to change freely in the least squares calculations. The values of the parameters G_2, G_4(4f4f, 6p6p) and G_2(5d5d, 6s6s) were forced to remain equal to those of the internal parameters G_2, G_4(4f6p) and G_2(5d6s) respectively. The parameters G_1, G_3, G_5(4f4f, 5d5d), G_3(4f4f, 6s6s), G_1, G_3(5d5d, 6p6p), G_1(6s6s, 6p6p), R_1, R_3(4f6p, 5d5d), T_1(4f6p, 5d6s), T_3(4f6p, 6s5d) and K(6p6p, 5d6s) were

TABLE 1.52.
Parameter values for LaII $5d^2 + 5d6s + 6s^2 + 4f6p + 4f^2 + 6p^2 + 6d6s$ (cm^{-1})[a].

Parameter	Initial value	Final value
$A(5d^2)$	4 000	4 149 ± 99
$B(5d^2)$	313	338 ± 4
$C(5d^2)$	1 200	1 185 ± 37
F_0(5d6s)	4 700	5 016 ± 115
G_2(5d6s)	1 700	2 149 ± 69
$F_0(6s^2)$	10 000	11 091 ± 215
F_0(4f6p)	38 000	37 982 ± 98
F_2(4f6p)	85	73 ± 4
G_2(4f6p)	5	9 ± 1
G_4(4f6p)	7	4 ± 2
$E^0(4f^2)$	58 200	58 266 ± 94
$E^1(4f^2)$	1 783	1 792 ± 35
$E^2(4f^2)$	6.7	6.7 ± 0.2
$E^3(4f^2)$	163	158 ± 2
$\alpha(4f^2)$	−33	−23 ± 2
$\beta(4f^2)$	−725	−1 208 ± 89
$\gamma(4f^2)$	9	−6 ± 10
$F_0(6p^2)$	63 000	63 086 ± 208
$F_2(6p^2)$	250	263 ± 35
F_0(6d6s)	65 000	65 246 ± 102
G_2(6d6s)	700	[700]
H(5d5d, 5d6s)	−361	−388 ± 5
G_2(5d5d, 6s6s)	1 700	[2 149]
R_1(4f6p, 5d5d)	128	[128]
R_3(4f6p, 5d5d)	0	[0]
T_1(4f6p, 5d6s)	−1 365	[−1 365]
T_3(4f6p, 6s5d)	−108	[−108]
G_1(4f4f, 5d5d)	315	[315]
G_3(4f4f, 5d5d)	32	[32]
G_5(4f4f, 5d5d)	4	[4]
N(4f4f, 5d6s)	−32	[−32]
G_3(4f4f, 6s6s)	170	[170]
L_2(4f4f, 4f6p)	−4	[−4]
L_4(4f4f, 4f6p)	−2.5	[−2.5]
G_1(5d5d, 6p6p)	391	[391]

TABLE 1.52. (*Contd.*)

Parameter	Initial value	Final value
G_3(5d5d, 6p6p)	3	[3]
K(5d6s, 6p6p)	−3 235	[−3235]
G_1(6s6s, 6p6p)	5 734	[5 734]
P_2(4f6p, 6p6p)	30	[30]
G_2(4f4f, 6p6p)	5	[9]
G_4(4f4f, 6p6p)	7	[4]
T_1(4f6p, 6d6s)	−260.7	[−260.7]
T_3(4f6p, 6d6s)	34	[34]
N(4f4f, 6d6s)	42	[42]
K(6d6s, 6p6p)	2 950	3 056 ± 98
$\zeta_{5d}(5d^2)$	498	492 ± 19
ζ_{5d}(5d6s)	543	545 ± 35
ζ_{4f}(4f6p)	410	426 ± 14
ζ_{6p}(4f6p)	1 102	1 174 ± 61
$\zeta_{4f}(4f^2)$	314	295 ± 12
$\zeta_{6p}(6p^2)$	1 250	1 247 ± 45
ζ_{6d}(6d6s)	130	131 ± 35
Δ		63

[a]Z.B. Goldschmidt (1976a).

fixed on the values of the corresponding internal and CI parameters obtained for the odd configurations of LaII (see section 13.1). L_2, L_4 (4f4f, 4f6p) were fixed on their values obtained in CeII (Z.B. Goldschmidt, 1972). The parameters G_2(6d6s), N(4f4f, 5d6s), N(4f4f, 6s6d), P_2(4f6p, 6p6p), T_1(4f6p, 6d6s) and T_3(4f6p, 6s6d) were fixed on values obtained by performing HF calculations. Good agreement was obtained, both for the energy levels and their g-factors, with a mean error of 63 cm^{-1}. The final results obtained concerning the values of the parameters, and the energy levels and their g-factors are given in tables 1.52 and 1.53 respectively. CI effects are summarized in table 1.54.

14. The spectrum of CeII

The known levels of CeII belong to the five odd configurations

$4f5d^2$, $4f5d6s$, $4f6s^2$ (low A)
$4f^26p$ (high I–B)
$4f^3$ (high II–B)

and to the seven even configurations

$4f^25d + 4f^26s$ (low B)
$4f5d6p + 4f6s6p$ (high I–A)
$5d^3 + 5d^26s + 5d6s^2$ (high II–A)

TABLE 1.53.
Energy levels of LaII $5d^2 + 5d6s + 6s^2 + 4f6p + 4f^2 + 6p^2 + 6s6d$ (cm^{-1})[a].

Configuration	Term	J	Obs	Calc	O–C	g-obs	g-calc	Composition percentage
$5d^2$	^3F	2	0	−2	2	0.721	0.725	83% + ^1D 11% + 5d6s ^1D 5%
		3	1 016	1 025	−9	1.083	1.083	100%
		4	1 971	1 964	7	1.248	1.248	99% + $5d^2$ ^1G 1%
$5d^2$	^1D	2	1 394	1 397	−3	0.977	0.975	36% + 5d6s ^1D 33% + $5d^2$ ^3F 16%
5d6s	^3D	1	1 895	1 900	−5	0.498	0.500	100%
		2	2 592	2 575	17	1.133	1.140	85% + $5d^2$ ^1D 10% + 5d6s ^1D 4%
		3	3 250	3 260	−10	1.334	1.333	100%
$5d^2$	^3P	0	5 250	5 243	7		$\frac{0}{0}$	92% + ^1S 4% + $6s^2$ ^1S 4%
		1	5 718	5 728	−10	1.497	1.500	99% + $4f^2$ ^3P 1%
		2	6 227	6 224	3	1.481	1.486	96% + 5d6s ^1D 3%
$6s^2$	^1S	0	7 395	7 395	0		$\frac{0}{0}$	75% + $5d^2$ ^1S 17% + ^3P 6%
$5d^2$	^1G	4	7 473	7 474	−1	1.000	1.002	98% + ^3F 1%
5d6s	^1D	2	10 095	10 095	0	1.005	1.007	53% + $5d^2$ ^1D 42% + $5d^2$ ^3P 1%
4f6p	$(\frac{5}{2}, \frac{1}{2})$	2	35 788	35 696	92	0.719	0.723	80% + $(\frac{5}{2}, \frac{3}{2})$ 18% + $(\frac{7}{2}, \frac{3}{2})$ 1%
		3	35 453	35 510	−57	0.876	0.898	92% + $(\frac{5}{2}, \frac{3}{2})$ 7% + $(\frac{7}{2}, \frac{3}{2})$ 1%
4f6p	$(\frac{7}{2}, \frac{1}{2})$	3	36 955	36 896	59	1.061	1.063	48% + $(\frac{5}{2}, \frac{3}{2})$ 43% + $(\frac{7}{2}, \frac{3}{2})$ 6%
		4	37 173	37 226	−53	1.127	1.154	86% + $(\frac{7}{2}, \frac{3}{2})$ 12% + $(\frac{5}{2}, \frac{3}{2})$ 2%
$5d^2$	^1S	0		17 307			$\frac{0}{0}$	76% + $6s^2$ ^1S 18% + $4f^2$ ^1S 3%
4f6p	$(\frac{5}{2}, \frac{3}{2})$	1	38 534	38 562	−28	0.497	0.500	100%
		2	38 221	38 187	34	1.071	1.063	81% + $(\frac{5}{2}, \frac{1}{2})$ 18%
		3	37 210	37 217	−7	0.944	0.925	48% + $(\frac{7}{2}, \frac{1}{2})$ 34% + $(\frac{7}{2}, \frac{3}{2})$ 12%
		4	37 791	37 851	−60	1.113	1.095	82% + $(\frac{5}{2}, \frac{3}{2})$ 17%
4f6p	$(\frac{7}{2}, \frac{3}{2})$	2	40 458	40 369	89	1.036	1.047	97% + $(\frac{5}{2}, \frac{1}{2})$ 1% + 5d6s ^1D 1%
		3	39 403	39 386	17	1.274	1.280	80% + $(\frac{7}{2}, \frac{1}{2})$ 18% + $(\frac{5}{2}, \frac{3}{2})$ 2%
		4	39 222	39 305	−83	1.059	1.052	70% + $(\frac{5}{2}, \frac{3}{2})$ 16% + $(\frac{7}{2}, \frac{1}{2})$ 13%
		5	39 019	39 175	156	1.21	1.200	100%

TABLE 1.53. (*Contd.*)

Configuration	Term	J	Obs	Calc	O–C	g-obs	g-calc	Composition percentage
$4f^2$	^3H	4	55 107	55 138	−31	0.883	0.804	98% + ^1G 2%
		5	55 982	55 948	34	1.033	1.033	100%
		6	56 838	56 808	30	1.14	1.166	100%
$4f^2$	^3F	2	57 400	57 370	30	0.675	0.675	97% + ^1D 2%
		3	57 919	57 923	−4	1.085	1.083	100%
		4	58 259	58 211	48	1.196	1.191	77% + ^1G 22% + ^3H 1%
$4f^2$	^1G	4	59 528	59 541	−13	1.046	1.055	75% + ^3F 23% + ^3H 1%
$6p^2$	^1D	2	59 900	59 900	0	1.035	1.038	58% + 6s6d ^1D 32% + $6p^2$ ^3P 7%
$6p^2$	^3P	0	60 095	60 101	−6		[a]	90% + ^1S 6% + $4f^2$ ^3P 3%
		1	61 129	61 119	10	1.528	1.500	95% + $4f^2$ ^3P 5%
		2	62 506	62 509	−3	1.416	1.417	79% + $4f^2$ ^1D 11% + ^3P 5%
$4f^2$	^1D	2	62 026	62 023	3	1.054	1.072	78% + ^3P 12% + $6p^2$ ^3P 4%
$4f^2$	^1I	6	62 408	62 409	−1	1.003	1.001	100%
$4f^2$	^3P	0	63 464	63 373	91		[a]	91% + $6p^2$ ^3P 4% + $4f^2$ ^1S 4%
		1	63 703	63 768	−65	1.471	1.500	94% + $6p^2$ ^3P 5% + $5d^2$ ^3P 1%
		2	64 279	64 306	−27	1.414	1.461	82% + $6p^2$ ^3P 9% + $4f^2$ ^1D 7%
6s6d	^3D	1	64 361	64 375	−14	0.506	0.500	100%
		2	64 530	64 506	24	1.217	1.167	99%
		3	64 693	64 702	−9		1.333	100%
$6p^2$	^1S	0	66 592	66 585	7		[a]	56% + $4f^2$ ^1S 35% + $6p^2$ ^3P 4%
$6f^2$	^1S	0	69 592	69 515	−10		[a]	58% + $6p^2$ ^1S 34% + $5d^2$ ^1S 3%
6s6d	^1D	2		69 814			1.003	61% + $6p^2$ ^1D 38% + ^3P 1%

[a] Z.B. Goldschmidt (1976a).

TABLE 1.54.
CI effects in LaII $5d^2 + 5d6s + 6s^2 + 4f6p + 4f^2 + 6p^2 + 6s6d$[a].

Pairs of repulsing terms	CI responsible for repulsion	Individual repulsions (cm^{-1})	Admixture %
$(6p^2–6s6d)^1D$	K(6p6p, 6s6d)	4450	35
$(5d^2–5d6s)^1D$	H(5d5d, 5d6s)	4300	38
$(5d^2–6s^2)^1S$	G_2(5d5d, 6s6s)	3600	18
$(4f^2–5d^2)^1S$	G_1, G_3, G_5(4f4f, 5d5d)	2800	3
^3P		900	0.8
^1D		620	0.5
^3F		215	0.2
^1G		365	0.3
$(6s^2–6p^2)^1S$	G_1(6s6s, 6p6p)	2180	2
$(5d^2–6p^2)^1S$	G_1, G_3(5d5d, 6p6p)	820	2
^3P		220	0.1
^1D		70	0.1
$(4f^2–6p^2)^1S$	G_2, G_4(4f4f, 6p6p)	670	35
^3P		210	5
^1D		60	1
$(5d6s–6p^2)^1D$	K(6p6p, 5d6s)	650	0.7
$(4f6p–5d6s)^1D$	T_1(4f6p, 5d6s), T_3(4f6p, 6s5d)	635	1
^3D		300	0.3
$(4f6p–5d^2)^1D$	R_1(4f6p, 5d5d)	15	0.1
^3F		130	0.2
^1G		440	0.7

CI effects due to the remaining interactions are small and will not be included in this table.

[a]Z.B. Goldschmidt (1976a).

232 odd levels are predicted for the five odd configurations; of these, 192 levels have been experimentally found. 305 even levels are predicted for the seven even configurations; of these, 288 levels have been experimentally found. A complete list of the known levels of CeII, including also the names of the authors who contributed to that list, is given by Corliss (1973). The block diagram of CeII, demonstrating the heights and widths of the various configurations (and therefore also the extent of their overlappings) is given in fig. 1.17.

The calculations of the energy levels of CeII have been carried out by Z.B. Goldschmidt (1968a, 1972, 1973a). These calculations were performed in intermediate coupling, including CI between all configurations having the same parity, and including two-electron 4f–4f and 4f–5d effective electrostatic interactions. The parameters describing the various interactions are listed in tables 1.15 and 1.16.

It was for achieving an understanding of this spectrum that the "comparison method" was developed (see section 10 above): the relatively simple two-electron spectra at both ends of the group were investigated (see section 13), and additional more complicated spectra, such as those of PrIII (Z.B. Goldschmidt, 1968a), GdII (Z.B. Goldschmidt and Nir, 1971) and YbII (Racah et al., 1965), were analyzed. In all these spectra, reliable quantitative information was obtained, concerning the strengths of the various interactions and their effects on the energy level structure. Thus, the endeavor of interpreting the spectrum of CeII, resulted in a complete understanding of many lanthanide spectra.

The energy level calculations of CeII resulted in an excellent agreement between observed and calculated energy levels and g-factors, with mean errors of 38 cm^{-1} and 57 cm^{-1} for the odd and even groups of configurations respectively. The inclusion of both direct CI and the effective electrostatic interactions was essential for achieving these results (or any meaningful results whatsoever).

Detailed results will not be given in this chapter, but their character is demonstrated in table 1.55, through a small number of levels belonging to the seven even configurations of CeII. The levels selected for this table all have $J = \frac{9}{2}$, and range from levels possessing a pure "name" in a single configuration to levels having no "name" at all in mixed configurations (see column 8 of the table). The excellent agreement between theory and experiment is seen by comparing columns 3 and 4 on the one hand and columns 7 and 8 on the other hand.

The values of the parameters representing various interactions in CeII are listed in section 15, and compared to the values of the corresponding parameters in other lanthanide spectra.

15. Conclusion

Many more lanthanide spectra have lately been analysed, to various degrees of completeness, as can be seen by following the references given in table 1.18. However, the space in this chapter is too limited to discuss them all. Rather, this chapter will now be ended by citing some of the general results and conclusions obtained in the course of the numerous investigations carried out on the lanthanide spectra.

In most investigated spectra, excellent agreement between theory and experiment was obtained.

The values obtained for the parameters describing the various interactions are consistent, and change systematically both on moving along the group at a fixed

TABLE 1.55.

CeII: $4f^25d + 4f^26s + 4f5d6p + 4f6s6p + 5d^3 + 5d^26s + 5d6s^2$[a,b]. $J = \frac{9}{2}$ representative levels (cm^{-1}).

Configuration	Designation	Obs	Calc	O–C	g-obs	g-calc	Composition percentage
$4f^26s$	$^3H_{4,1/2}$	4 166	4 150	15	0.949	0.949	93%
$4f^25d$	$^3H\ ^2H$	7 012	7 023	−11	0.889	0.881	65% + $^3H\ ^4I$ 19% + $^3F\ ^2H$ 12%
4f5d6p	$^1G\ ^2H$	24 663	24 725	−62	0.933	0.922	34% + $^3H\ ^2H$ 25% + $^3H\ ^4I$ 18%
$4f^25d$	$^1I\ ^2H$	27 905	28 014	−109	0.920	0.919	77% + $^3F\ ^2H$ 7% + $^3H\ ^2H$ 3%
mixed	mixed	32 198	32 133	65	1.195	1.190	$4f^25d\ ^1I\ ^2G$ 28% + 4f5d6p ($^3G\ ^4F$ 16% + $^3F\ ^2G$ 15% + $^3H\ ^4G$ 15%
4f6s6p	$\frac{5}{2}, {}^3P_2$	36 202	36 191	11	1.186	1.192	43% + $\frac{7}{2}, {}^3P_1$ 24% + 4f5d6p $^3H\ ^4G$ 14%
$5d^3$	^2G	38 542	38 433	109	1.097	1.098	35% + 4f5d6p($^1H\ ^2G$ 10% + $^1H\ ^2H$ 9%

[a]Z.B. Goldschmidt (1968a); [b]Z.B. Goldschmidt (1972).

degree of ionization, and on moving from one degree of ionization of a given element to another. Tables 1.56 and 1.57 include respectively the values of the parameters for the groups of configurations $4f^N(5d+6s)^2$ and $4f^N(5d6p+6s6p)$ in the second lanthanide spectra. As seen from these tables, the mode of change of the various parameters is in complete agreement with the conclusions obtained in the qualitative discussion of section 9.2.4. For example, the electrostatic interactions 6s–6p, 5d–5d and the spin–orbit interactions increase on moving from left to right along the group. The same holds for the electrostatic interaction 5d–6s, for the exchange part of the electrostatic interaction 5d–6p, and for the CI represented by H(5d5d, 5d6s), G_2(5d5d, 6s6s), J(5d6p, 6s6p) and K(5d6p, 6p6s). The electrostatic interaction 4f–6s is constant along the group. The electrostatic interaction 4f–5d, especially its exchange part, decreases on moving to the right hand side of the group.

It can be further seen from these tables that the values of the parameters change in a regular manner also on going from one configuration to another in the same spectrum. For example, the 4f–5d electrostatic parameters increase

TABLE 1.56.
Parameter values for the $4f^N(5d+6s)^2$ configurations in the second lanthanide spectra (cm^{-1}).

Parameter*	La II[a,b] $(5d+6s)^2$	Ce II[a,c] $4f(5d+6s)^2$	Gd II[d] $4f^7(^8S)(5d+6s)^2$	Yb II[e] $4f^{13}(5d+6s)^2$	Lu II[a] $4f^{14}(5d+6s)^2$
$B(d^2)$	313 ± 1	344 ± 2	372 ± 6	378 ± 3	391 ± 2
$C(d^2)$	1200 ± 7	1269 ± 14	1216 ± 46	1278 ± 29	[1330]
G_2(ds) }	1703 ± 13	1854 ± 38	2079 ± 39	2442 ± 52	2581 ± 20
G_2(dd, ss) }					
H(dd, ds)	−361 ± 1	−375 ± 4	395 ± 8	−407 ± 11	−438 ± 5
F_2(fd)		154 ± 1		158 ± 2	
F_2'(fd)		169 ± 1		170 ± 2	
F_4(fd)		18.6 ± 0.1		12 ± 1	
F_4'(fd)		20.7 ± 0.2		15 ± 1	
G_1(fd)		257 ± 1		148 ± 2	
G_1'(fd)		278 ± 2		177 ± 4	
G_3(fd)		29.3 ± 0.3		16 ± 1	
G_3'(fd)		32.5 ± 0.5		21 ± 2	
G_5(fd)		3.54 ± 0.06		3.5 ± 0.4	
G_5'(fd)		4.48 ± 0.09		3.8 ± 0.6	
G_3(fs)		220 ± 19	230 ± 9	230 ± 60	
M(fd, fs)		26 ± 6		−49 ± 35	
N(fd, sf)		77 ± 6		141 ± 48	
ζ_f		630 ± 4		2922 ± 7	
ζ_d	498 ± 4	544 ± 7	817 ± 28	845 ± 14	888 ± 12
ζ_d'	543 ± 7	600 ± 14	817 ± 28	970 ± 21	1000 ± 18
Δ	12	38	144	144	37

*The prime means that the parameter belongs to the configuration $4f^N5d6s$. [a]Z.B. Goldschmidt (1968a); [b]Z.B. Goldschmidt (1968b); [c]Z.B. Goldschmidt (1972); [d]Z.B. Goldschmidt and Nir (1971); [e]Racah, Z.B. Goldschmidt and Bordarier (1965).

TABLE 1.57.
Parameter values for the $4f^N$ 5d6p + $4f^N$ 6s6p configurations in the second lanthanide spectra (cm^{-1}).

Parameter	La II[a,b] 5d6p + 6s6p	Ce II[a,b] 4f(5d6p + 6s6p)	Gd II[c] $4f^7(^8S)$(5d6p + 6s6p)	Yb II[d] $4f^{13}$(5d6p + 6s6p)	Lu II[a,e] $4f^{14}$(5d6p + 6s6p)
F_2(dp)	343 ± 15	306 ± 5	318 ± 8	325 ± 3	320 ± 8
G_1(dp)	387 ± 8	383 ± 7	451 ± 10	514 ± 3	529 ± 7
G_3(dp)	3 ± 3	7 ± 1	8 ± 2	9 ± 1	15 ± 6
G_1(sp)	5763 ± 149	5865 ± 73	6000 ± 148	6620 ± 74	6958 ± 164
F_2(fp)		68 ± 3		67 ± 2	
G_2(fp)		7 ± 3		9 ± 1	
G_4(fp)		5 ± 2		9 ± 2	
F_2(fd)		177 ± 1		181 ± 1	
F_4(fd)		21.4 ± 0.4		15.5 ± 0.3	
G_1(fd)		284 ± 2		186 ± 1	
G_3(fd)		33.5 ± 0.5		19 ± 1	
G_5(fd)		4.5 ± 0.1		4.3 ± 0.3	
G_3(fs)		[298]	295 ± 20	[300]	
J(dp, sp)	−1669 ± 93	−1647 ± 43	−1985 ± 54	−2189 ± 55	−2579 ± 211
K(dp, ps)	−3203 ± 125	−3035 ± 39	−3619 ± 65	−4305 ± 55	−4176 ± 197
M(fd, fs)	[0]	[0]			
N(fd, sf)	[60]	[55]			
ζ_f		650 ± 14		2919 ± 4	
ζ_d	597 ± 57	688 ± 16	895 ± 32	1147 ± 11	1100 ± 32
ζ_p	1325 ± 68	1486 ± 21	1989 ± 37	2688 ± 18	2907 ± 70
ζ_p'	1903 ± 94	1853 ± 58	2665 ± 124	3419 ± 30	3493 ± 54
Δ	40	57	138	104	56

[a]Z.B. Goldschmidt (1968a); [b]Z.B. Goldschmidt (1972); [c]Z.B. Goldschmidt and Nir (1971); [d]Racah, Z.B. Goldschmidt and Bordarier (1965); [e]Z.B. Goldschmidt (1968b).

both in CeII and YbII on going from

$$4f5d^2 \rightarrow 4f5d6s \rightarrow 4f5d6p$$

and from

$$4f^{13}5d^2 \rightarrow 4f^{13}5d6s \rightarrow 4f^{13}5d6p$$

respectively. Furthermore the value of ζ_{5d} increases on moving from $4f^N5d^2 \rightarrow 4f^N5d6s$ and the value of ζ_{6p} increases on moving from $4f^N5d6p \rightarrow 4f^N6s6p$.

A complete understanding of the effects of the separate interactions on the energy level structure of the investigated spectra was achieved. In particular, couplings in the various configurations were defined, and correlated in each case with the strong interactions, and finer structural details of the energy level schemes were explained in terms of the weak interactions, whether being electrostatic, spin–orbit or spin-dependent interactions. CI effects on the energy level structure were also studied in detail.

The stage has been reached where it is possible to make detailed predictions about the structure of the lanthanide spectra, even in those cases where the experimental material is rather scant.

The time is now ripe for a two-directional development in the investigation of the lanthanide spectra:
(1) In the third and fourth spectra complete lists of the energy levels of $4f^N(4 \leq N \leq 11)$ configurations are needed, in order to extend the investigation of the effects of the two- and three-electron effective electrostatic interactions and of the spin-dependent interactions.
(2) In the first and second spectra complete new lists of energy levels are needed; in this way, the understanding obtained till now of relatively simple spectra at both ends and in the middle of the group can be used for interpreting the still remaining complex spectra.

References

Albertson, W.E., 1937, Phys. Rev. **52**, 644.
Albertson, W.E., G.R. Harrison and J.R. McNally Jr., 1942, Phys. Rev. **61**, 167.
Amiel, S., 1955, M.Sc. Thesis, The Hebrew University of Jerusalem.
Arnoult, C. and S. Gerstenkorn, 1966, J. Opt. Soc. Amer. **56**, 177.
Bacher R.F. and S. Goudsmit, 1934, Phys. Rev. **46**, 948.
Ben Ahmed, Z., J. Blaise, J. Verges and J.F. Wyart, 1973, Abstract 20, in: Summaries of Contributions to the Fifth Annual Conference of the European Group for Atomic Spectroscopy, Lund, Sweden.
Ben Ahmed, Z., J. Verges, M. Wilson and A. Giacchetti 1976, Physica, **84C**, 275.
Bethe, H.A. and E.E. Salpeter, 1957, Quantum Mechanics of One- and Two-Electron Atoms (Springer-Verlag, Berlin).
Blaise, J., C. Morillon, M.G. Schweighofer and J. Verges, 1969, Spectrochem. Acta, Part B **24**, 405.
Blaise, J., J. Chevillard, J. Verges and J.F. Wyart, 1970, Spectrochem. Acta, Part B **25**, 333.
Blaise, J., J. Chevillard, J. Verges, J.F. Wyart and T.A.M. van Kleef, 1971, Spectrochem. Acta, Part B **26**, 1.
Blaise, J., T.A.M. van Kleef and J.F. Wyart, 1971, J. Phys. (Paris) **32**, 617.
Blaise, J., J.F. Wyart, R. Hoekstra and P.J.G. Kruiver, 1971, J. Opt. Soc. Amer. **61**, 1335.
Blaise, J., P. Camus, G. Guelachvili, J. Verges and J.F. Wyart, 1972a, C.R.Acad. Sci., Paris. Ser. B **274**, 1302.
Blaise, J., P. Camus, G. Guelachvili, J. Verges and J.F. Wyart, 1972b, C.R. Acad. Sci., Paris, Ser. B **275**, 81.
Blaise, J., J. Verges, J.F. Wyart, P. Camus and R. Zalubas, 1973a, Abstract 22, in: Summaries of Contributions to the Fifth Annual Conference of the European Group for Atomic Spectroscopy, Lund, Sweden.
Blaise, J., J. Verges, J.F. Wyart, P. Camus and R. Zalubas, 1973b, J. Opt. Soc. Amer. **63**, 1315.
Blume, M. and R.E. Watson, 1962, Proc. Roy. Soc. London, **A270**, 127.
Blume, M. and R.E. Watson, 1963, Proc. Roy. Soc. London, **A271**, 565.
Blume, M., A.J. Freeman, and R.E. Watson, 1964, Phys. Rev. **134**, A320.
Bordarier, Y., Private communication (1966).
Bordarier, Y., 1970, Ph.D. Thesis, Laboratoire Aime Cotton, 91 Orsay, France.
Breit, G. 1930, Phys. Rev. **36**, 383.
Bovey, L.F.H. and R.W.B. Pearse, 1956, U.K. Atomic Energy Research Establishment AERE C/R 1976, Harwell, 19 pp.
Bovey, L., E.B.M. Steers and H.S. Wise, 1960, U.K. Atomic Energy Establishment AERE-R 3225, Harwell, 8 pp.
Brewer, L., 1971a, J. Opt. Soc. Amer. **61**, 1101.
Brewer, L., 1971b, J. Opt. Soc. Amer. **61**, 1666.
Bryant, B.W., 1965, J. Opt. Soc. Amer. **55**, 771.
Callahan, W.R., 1963, J. Opt. Soc. Amer. **53**, 695.
Camus, P., 1966, J. Phys. (Paris), **27**, 717.
Camus, P. and F.S. Tomkins, 1969, J. Phys. (Paris), **30**, 545.
Camus, P., 1970, J. Phys. (Paris), **31**, 985.
Camus, P., 1971, Ph.D. Thesis, Univ. Paris, Orsay.
Camus, P and J. Sugar, 1971a, Physica Scripta, **4**, 257.
Camus, P. and J. Sugar, 1971b, Physica Scripta, **4**, 263.
Camus, P. and F.S. Tomkins, 1972, J. Phys. (Paris), **33**, 197.
Camus, P. and K. Mamoudi, 1972, Physica, **60**, 513.
Carlier, A. (1967), These de 3eme Cycle, Univ. Paris, Orsay.
Carter, W.J. (1966), Ph.D. Thesis, Johns Hopkins University.
Condon, E.U. and G.H. Shortley, 1951, The Theory of Atomic Spectra (Cambridge University Press).
Conway, J.G. and E.F. Worden, 1971, J. Opt. Soc. Amer. **61**, 704.
Copland, G.M., D.J. Newman and C.D. Taylor, 1971a, J. Phys. B. **4**, 1388.

Copland, G.M., D.J. Newman and C.D. Taylor, 1971b, J. Phys. B. **4**, 1605.
Corliss, C.H., 1973, J. Res. Nat. Bur. Stand., A, **77A**, 419.
Cowan, R.D., 1973, Nuclear Instruments and Methods, **110**, 173.
Crosswhite, H., H.M. Crosswhite and B.R. Judd, 1968, Phys. Rev. **174**, 89.
Crosswhite, H. and H.M. Crosswhite, 1970, J. Opt. Soc. Amer. **60**, 1556A.
Crosswhite, H.M., 1971, Phys. Rev. A., **4**, 485.
Davis, S.P. and J. Reader, 1972, J. Opt. Soc. Amer. **62**, 1370A.
Dupont, A., 1967, J. Opt. Soc. Amer. **57**, 867.
Edmonds, A.R., 1957, Angular Momentum in Quantum Mechanics (Princeton University Press, New Jersey).
Epstein, G.L. and J. Reader, 1971, J. Opt. Soc. Amer. **61**, 1590A. The error estimate is from unpublished material, J. Reader (1974).
Fano, U. and G. Racah, 1959, Irreducible Tensorial sets (Academic Press, New York).
Fano, U., F. Prats and Z.B. Goldschmidt, 1963, Phys. Rev. **129**, 2643.
Feneuille, S., 1966, C.R. Acad. Sc. Paris **262**, 23.
Feneuille, S. and N. Pelletier–Allard, 1968, Physica, **40**, 347.
Garton, W.R.S. and M. Wilson, 1966, Astrophys. J. **145**, 333.
Goldschmidt, Z.B., 1963, J. Opt. Soc. Amer. **53**, 594.
Goldschmidt, Z.B., 1966, Configuration Interaction in Rare Earth Spectra, in: Moser, M.C. and M.R. Lefebvre, eds., La Structure Hyperfine Magnetique des Atomes et des Molecules (Editions du Centre National de la Recherche Scientifique – Paris) pp. 365–384.
Goldschmidt, Z.B. and S. Nir, unpublished material (1967).
Goldschmidt, Z.B., 1968a, Ph.D. Thesis, The Hebrew University of Jerusalem.
Goldschmidt, Z.B. 1968b, Properties and Methods of Interpretation of Rare-Earth Spectra, in: Bloch, F., S.G. Cohen, A. De-Shalit, S. Sambursky, and I. Talmi, eds., Spectroscopic and Group Theoretical Methods in Physics (North-Holland Publishing Company, Amsterdam) pp. 411–457.
Goldschmidt, Z.B., A. Pasternak and Z.H. Goldschmidt, 1968, Phys. Lett. **28A**, 265.
Goldschmidt, Z.B., 1970, J. Phys. (Paris) Suppl. **31**, 163.
Goldschmidt, Z.B. and A. Pasternak, unpublished calculations (1970).
Goldschmidt, Z.B., A. Pasternak and Z.H. Goldschmidt unpublished material (1970).
Goldschmidt, Z.B. and D. Salomon, unpublished calculations (1970).
Goldschmidt, Z.B. and J. Starkand, 1970, J. Phys. **B3**, L141.
Goldschmidt, Z.B., 1971, Phys. Rev. A. **3**, 1872.
Goldschmidt, Z.B., J.V. Mallow and J. Starkand, 1971, Abstract 42, in: Summaries of Contributions to the Third Annual Conference of the European Group for Atomic Spectroscopy, Reading, England.
Goldschmidt, Z.B. and S. Nir, 1971, Physica, **51**, 222.
Goldschmidt, Z.B., D. Salomon and J. Starkand, 1971, Bull. Soc. Phys. Israel, p. 63.
Goldschmidt, Z.B., Unpublished calculations (1972).
Goldschmidt, Z.B. (1973a). Recent Advances in the Interpretation of Complex Spectra, in: Smith, S.J. and G.K. Walters, eds., Atomic Physics, Vol. 3 (Plenum Publishing Corporation, New York) pp. 221–246.
Goldschmidt, Z.B., 1973b, Abstract 1, in: Summaries of Contributions to the Fifth Annual Conference of the European Group for Atomic Spectroscopy, Lund, Sweden.
Goldschmidt, Z.B. and D. Ben-Ezra, 1975, Abstract 33, in Summaries and Contributions to the Seventh Annual Conference of the European Group of Atomic Spectroscopy, Grenoble, France.
Goldschmidt, Z.B., and M. Cohen, 1975, Abstract 34 in: Summaries and Contributions to the Seventh Annual Conference of the European Group of Atomic Spectroscopy, Grenoble, France.
Goldschmidt, Z.B., 1976a, Abstract 32, in: Summaries of Contributions to the Eighth Annual Conference of the European Group for Atomic Spectroscopy, Oxford, England.
Goldschmidt, Z.B., unpublished calculations (1976b).
Goldschmidt, Z.H., unpublished calculations (1966).
Goldschmidt, Z.H., 1967, Abstract 32 in: Atomic Spectroscopy Symposium, National Bureau of Standards Gaithersburg, Maryland.
Harrison, G.R., W.E. Albertson and N.F. Hoshford, 1941, J. Opt. Soc. Amer. **31**, 439.
Held, S., 1971, Astrophys. J. **167** (pt. 1), 203.
Herman, F. and S. Skillman, 1963, Atomic Structure Calculations (Prentice Hall, New Jersey).
Horie, H., 1953, Progr. Theoret. Phys. (Kyoto) **10**, 296.
Innes, F.R., 1953, Phys. Rev. **91**, 31.
Johansson, S. and U. Litzén, 1971, J. Opt. Soc. Amer. **61**, 1427.
Johansson, S. and U. Litzén, 1972, Physica Scripta **6**, 139.
Johansson, S. and U. Litzén, 1973, Physica Scripta **8**, 43.
Jørgensen, C.K., 1962, Mol. Phys. **5**, 271.
Jucys, A., R. Dagys, J. Vizbaraite and S. Zvironaite, 1961, Trudy, Akad. Nauk. Litovsk S.S.R. **B3** (26), 53.
Judd, B.R., 1962, Phys. Rev. **125**, 613.
Judd, B.R. and L.C. Marquet, 1962, J. Opt. Soc. Amer. **52**, 504.
Judd, B.R., 1963, Operator Techniques in Atomic Spectroscopy (McGraw-Hill, New York).
Judd, B.R., 1966, Phys. Rev. **141**, 4.
Judd, B.R., 1967, Physica **33**, 174.
Judd, B.R., H.M. Crosswhite and H. Crosswhite, 1968, Phys. Rev. **169**, 130.
Judd, B.R., 1970, Comments At. Mol. Phys. **1**, 173.

Griffin, D.C., J.S. Ross and R.D. Cowan, 1972, J. Opt. Soc. Amer., 62, 571.

Kaufman, V. and J. Sugar, 1971, J. Opt. Soc. Amer. **61**, 1693.
Kaufman, V. and J. Sugar, 1973, J. Opt. Soc. Amer. **63**, 1168.
Kielkopf, J.F. and H.M. Crosswhite, 1970, J. Opt. Soc. Amer. **60**, 347.
Klapisch, M., 1971, Comp. Phys. Com. **2**, 239.
Klinkenberg, P.F.A., 1954, Physica **21**, 53.
Klinkenberg, P.F.A., 1966, Physica **32**, 1113.
Klinkenberg, P.F.A. and E. Meinders, 1966, Physica **32**, 1617.
Klinkenberg, P.F.A., 1967, Physica **37**, 197.
Klinkenberg, P.F.A. and T.A.M. van Kleef, 1970, Physica **50**, 625.
Klinkenberg, P.F.A., 1972, Physica **57**, 594.
Koopmans, T., 1934, Physica **1**, 104.
Lang, R.J., 1936, Can. J. Res. **A14**, 127.
Livingston, A.E., Jr. and E.H. Pinnington, 1971, J. Opt. Soc. Amer. **61**, 1429.
Marquet, L.C. and S.P. Davis, 1965, J. Opt. Soc. Amer. **55**, 471.
Marquet, L.C. and W.E. Behring, 1965, J. Opt. Soc. Amer. **55**, 576.
Martin, W.C., 1971, Phys. Rev. **A3**, 1810.
Martin, W.C., 1971, J. Opt. Soc. Amer. **61**, 1682.
Martin, W.C., 1972, Opt. Pura Y Apl. **5**, 181.
Martin, W.C. and J. Sugar, 1973, Astrophys. J. **184**, 671.
Martin, W.C., L. Hagan, J. Reader and J. Sugar, 1974, J. Phys. Chem. Ref. Data **3**, 771.
Marvin, H.H., 1947, Phys. Rev. **71**, 102.
Mayer, M.G., 1941, Phys. Rev. **60**, 184.
McElaney, J.H., 1967, J. Opt. Soc. Amer. **57**, 870.
McNally, J.R., Jr. and K.L. Vander Sluis, 1959, J. Opt. Soc. Amer. **49**, 200.
Meggers, W.F. and B.F. Scribner, 1930, J. Res. Nat. Bur. Stand. **5**, 73.
Meggers, W.F., 1932, J. Res. Nat. Bur. Stand. **9**, 239, RP468.
Meggers, W.F. and C.H. Corliss, 1966, J. Res. Nat. Bur. Stand., A, **70A**, 63.
Meggers, W.F., 1967, J. Res. Nat. Bur. Stand., A, **71A**, 396.
Meinders, E. and P.F.A. Klinkenberg, 1968, Physica **38**, 253.
Meinders, E., 1969, Physica **42**, 427.
Meinders, E., T.A.M. van Kleef and J.F. Wyart, 1972, Physica **61**, 443.
Morillon, C., 1970, Spectrochem. Acta, Part **B25**, 513.
Morrison, J.C. and K. Rajnak, 1971, Phys. Rev. **A4**, 536.
Newman, D.J. and C.D. Taylor, 1971, J. Phys. **B4**, 241.
Nielson, C.W. and G.F. Koster, 1964, Spectroscopic Coefficients for p^n, d^n and f^n configurations (M.I.T. Press, Cambridge, Mass.).
Nir, S., 1969, Ph.D. Thesis, The Hebrew University of Jerusalem.
Nir, S. and Z.B. Goldschmidt, unpublished material (1969).
Nir, S., 1970, J. Opt. Soc. Amer. **60**, 354.
Nir, S. and Z.B. Goldschmidt, unpublished material (1976).
Nugent, L.J. and K.L. Vander Sluis, 1971, J. Opt. Soc. Amer. **61**, 1112.
Odabasi, H., 1967, J. Opt. Soc. Amer. **57**, 1459.
Oreg, J., 1973a, Ph.D. Thesis, The Hebrew University of Jerusalem.
Oreg, J., 1973b, J. Com. Phys. **11**, 153.
Oreg, J., D. Salomon and Z.B. Goldschmidt, 1973, Abstract 21 in: Summaries of Contributions to the Fifth Annual Conference of the European Group for Atomic Spectroscopy, Lund, Sweden.
Parr, A.C., 1971, J. Chem. Phys. **54**, 3161.
Pasternak, A. and Z.B. Goldschmidt, unpublished calculations (1968).
Pasternak, A. and Z.B. Goldschmidt, 1972, Phys. Rev. **A6**, 55.
Pasternak, A. and Z.B. Goldschmidt, 1974, Phys. Rev. **A9**, 1022.
Pinnington, E.H., 1963, Can. J. Phys. **41**, 1294.
Pinnington, E.H., 1967, J. Opt. Soc. Amer. **57**, 1252.
Racah, G., 1942a, Phys. Rev. **61**, 186.
Racah, G., 1942b, Phys. Rev. **62**, 438.
Racah, G., 1943, Phys. Rev. **63**, 367.
Racah, G., 1949, Phys. Rev. **76**, 1352.
Racah, G., 1951, Group Theory and Spectroscopy, mimeographed notes, Princeton. These notes were reproduced by Corn (61–68) (1961), and by Springer–Verlag, Berlin, in Ergebnisse der exakten Naturwissenschaften **37**, 27 (1965).
Racah, G., 1952, Phys. Rev. **85**, 381.
Racah, G., 1954, The present state and Problems of the Theory of Atomic Spectra, in: Proceedings of the Rydberg Centennial conference on Atomic Spectroscopy, Lunds Universitets Arsskrift, N.F. Avd. 2 Bd. 50. Nr. 21. Kungl. Fysiografiska Sallskapets Handlingar, N.F. Bd 65. Nr 21, pp. 31–42.
Racah, G., 1960, J. Opt. Soc. Amer. **50**, 408.
Racah, G., Z.B. Goldschmidt and A. Lonka, unpublished material (1960).
Racah, G., 1960–1963, unpublished lectures.
Racah, G., J. Quant. Spectrosc. Radiat. Transfer. **4**, 617 (1964).
Racah, G. and Z.B. Goldschmidt, unpublished material (1964).
Racah, G., Z.B. Goldschmidt and Y. Bordarier, unpublished material (1965).
Racah, G., Z.B. Goldschmidt and S. Toaff, 1966, J. Opt. Soc. Amer. **56**, 407.
Racah, G. and J. Stein, 1967, Phys. Rev. **156**, 58.
Rajnak, K., 1962, J. Chem. Phys. **37**, 2440.
Rajnak, K. and B.G. Wybourne, 1963, Phys. Rev. **132**, 280.
Rajnak, K. and B.G. Wybourne, 1964, Phys. Rev. **134**, A596.
Reader, J. and J. Sugar, 1966, J. Opt. Soc. Amer. **56**, 1189.
Reader, J. and S.P. Davis, 1967, J. Res. Nat. Bur. Stand., A, **71A**, 587.
Reader, J. and J. Sugar, 1970, J. Opt. Soc. Amer. **60**, 1421.
Reader, J. Unpublished material (1973).
Reader, J. and G.L. Epstein, 1975, J. Opt. Soc. Amer. **65**, 638.

Moore, C.E., 1958, Atomic Energy Levels, as Derived from the Analysis of Optical Spectra, U.S. Natl. Bur. Stands. Circ. 467 (U.S. Govt. Printing Office, Washington, D.C.) Vol. III.

Reilly, E.F., 1953, Phys. Rev. **91**, 876.
Rosen, N., G.R. Harrison and J.R. McNally Jr., 1941, Phys. Rev. **60**, 722.
Rosenzweig, N., 1952, Phys. Rev. **88**, 580.
Rotenberg, Bivins, Metropolis and Wooton, Jr., 1959, The 3*j* and 6*j* Symbols (Technology Press, M.I.T., Cambridge, Mass.).
Runciman, W.H., 1962, J. Chem. Phys. **36**, 1481.
Russell, H.N. and W.F. Meggers, 1932, J. Res. Nat. Bur. Stand. **9**, 625, RP497.
Russell, H.N., A.B. King and R.J. Lang, 1937, Phys. Rev. **52**, 456.
Russell, H.N. and A.S. King, 1939, Astrophys. J. **90**, 155.
Russell, H.N., W. Albertson and D.N. Davis, 1941, Phys. Rev. **60**, 641.
Russell, H.N., 1950, J. Opt. Soc. Amer. **40**, 550.
Salomon, D., 1973, Ph.D. Thesis, The Hebrew University of Jerusalem.
Schuurmans, P.H., 1946, Physica **11**, 419.
Slater, J.C., 1929, Phys. Rev. **34**, 1293.
Slater, J.C., 1960, Quantum Theory of Atomic Structure Vol. 2, (McGraw-Hill, New York).
Smith, G. and B.G. Wybourne, 1965a, J. Opt. Soc. Amer. **55**, 121.
Smith, G. and B.G. Wybourne, 1965b, J. Opt. Soc. Amer. **55**, 1278.
Smith, G. and B.S. Collins, 1970, J. Opt. Soc. Amer. **60**, 866.
Smith, G. and M. Wilson, 1970, J. Opt. Soc. Amer. **60**, 1527.
Spector, N., 1965a, J. Opt. Soc. Amer. **55**, 492.
Spector, N., 1965b, J. Opt. Soc. Amer. **55**, 576.
Spector, N., 1966, J. Opt. Soc. Amer. **56**, 341.
Spector, N., 1967a, J. Opt. Soc. Amer. **57**, 308.
Spector, N., 1967b, J. Opt. Soc. Amer. **57**, 312.
Spector, N., 1970a, J. Opt. Soc. Amer. **60**, 763.
Spector, N., 1970b, J. Phys. (Paris) Colloq. C 4 **31**, 173.
Spector, N., 1971a, J. Opt. Soc. Amer. **61**, 1350.
Spector, N., 1971b, Astrophys. J. **167** (Pt. 1), 205.
Spector, N., 1973, J. Opt. Soc. Amer. **63**, 358.
Spedding, F.H., 1940, Phys. Rev. **58**, 255.
Stein, J., 1967a, Ph.D. Thesis, The Hebrew University of Jerusalem.
Stein, J., 1967b, J. Opt. Soc. Amer. **57**, 333.
Stern, D., 1955, M.Sc. Thesis, The Hebrew University of Jerusalem.
Sugar, J., 1963, J. Opt. Soc. Amer. **53**, 831.
Sugar, J., 1965a, J. Opt. Soc. Amer. **55**, 33.
Sugar, J., 1965b, J. Opt. Soc. Amer. **55**, 1058.
Sugar, J. and V. Kaufman, 1965, J. Opt. Soc. Amer. **55**, 1283.
Sugar, J. and J. Reader, 1965, J. Opt. Soc. Amer. **55**, 1286.
Sugar, J., 1968, J. Opt. Soc. Amer. **58**, 1519.
Sugar, J., 1969, J. Res. Nat. Bur. Stand., A, **73A**, 333.
Sugar, J., 1970a, J. Opt. Soc. Amer. **60**, 454.
Sugar, J., 1970b, J. Opt. Soc. Amer. **60**, 571.
Sugar, J., 1971, J. Opt. Soc. Amer. **61**, 727.
Sugar, J. and V. Kaufman, 1972, J. Opt. Soc. Amer. **62**, 562.
Sugar, J., W.F. Meggers and P. Camus, 1973, J. res. Nat. Bur. Stand., A, **77A**, 1.
Sugar, J. and J. Reader, 1973, J. Chem. Phys. **59**, 2083.
Sugar, J., 1974, J. Res. Nat. Bur. Stand., A, **78A**, 555.
Sugar, J. and N. Spector, 1974, J. Opt. Soc. Amer. **64**, 1484.
Trees, R.E., 1951, Phys. Rev. **82**, 683.
Trees, R.E., 1964, J. Opt. Soc. Amer. **54**, 651.
Vander Sluis, K.L. and J.R. McNally, Jr., 1970, J. Opt. Soc. Amer. **60**, 94.
Vander Sluis, K.L. and L.J. Nugent, 1972, Phys. Rev. **A6**, 86.
Vander Sluis, K.L. and L.J. Nugent, 1974, J. Opt. Soc. Amer. **64**, 687.
van Kleef, T.A.M., J. Blaise and J.F. Wyart, 1971, J. Phys. (Paris), **32**, 609.
van Kleef, T.A.M. and J.J.A. Koot, 1973, J. Opt. Soc. Amer. **63**, 1315.
Wilson, M. and M. Fred, 1969, J. Opt. Soc. Amer. **59**, 827.
Wyart, J.F., 1970a, J. Phys. (Paris), **31**, 559.
Wyart, J.F., 1970b, C.R. Acad. Sci., Paris, Ser. **B271**, 849.
Wyart, J.F., 1971, C.R. Acad. Sci., Paris, Ser. **B272**, 933.
Wyart, J.F., 1973, Ph.D. Thesis, Univ. Paris-Sud, Orsay.
Wyart, J.F., J. Blaise, J. Verges, P. Camus and M. Fred, 1973, Abstract 23, in: Summaries of contributions to the Fifth Annual Conference of the European Group for Atomic Spectroscopy, Lund, Sweden.
Wyart, J.F., J. Blaise and P. Camus, 1974, Physica Scripta, **9**, 322 and 325.
Wyart, J.F., 1976, Physica **83C**, 361.
Wybourne, B.G., 1961, J. Chem. Phys. **35**, 340.
Wybourne, B.G., Math. J., Phys. **4**, 354 (1963).
Wybourne, B.G., 1965, Spectroscopic Properties of Rare Earths (Interscience Publishers, New York).
Zalubas, R. and B.R. Borchardt, J. Opt. Soc. Amer. **63**, 102.
Zeldes, N., 1953, Phys. Rev. **90**, 413.

Handbook on the Physics and Chemistry of Rare Earths, edited by K.A. Gschneidner, Jr. and L. Eyring

Chapter 2

PREPARATION AND BASIC PROPERTIES OF THE RARE EARTH METALS*

B.J. BEAUDRY and K.A. GSCHNEIDNER, Jr.
Ames Laboratory – DOE and Department of Materials Science and Engineering, Iowa State University, Ames, Iowa 50011, USA

Contents

Symbols

a = lattice constant along the x-axis
c = lattice constant along the z-axis
CN = coordination number
L = total angular momentum quantum number
v = valence

*This work was partially supported by the U.S. Department of Energy under Contract Number W-7405-eng. 82.

1. Preparation

The rare earth metals are being prepared on a large scale industrially for scavengers in steels and irons, as alloying additives in high strength, high temperature alloys to improve oxidation and corrosion resistance and many other uses. Although these industrial preparations are of great importance economically, the preparation of high purity metals for intrinsic property determinations will be given the most attention in this chapter. Most of the properties given in this chapter were determined on these high purity metals or at least on well characterized metals. The importance of high purity metals for property measurements was discussed by Pfann (1962). He questioned the value of detailed investigations of a metal that contains unspecified impurities, especially when these impurities are later shown to have a critical bearing on the behavior of the metal. In addition to the need for pure metals for determining their intrinsic properties, the success of several recent developmental programs involving rare earth compounds have depended on high purity rare earth metals for preparing the pure compounds. For example, high purity Gd is required to prepare Gd_2Se_3 for an n-type semiconductor as one of the elements in a high performance thermoelectric generator (Beaudry et al., 1976). Another example is the need for high purity Eu metal to prepare the ferromagnetic semiconducting EuX chalcogenides, which are important, not necessarily for their commercial utilization, but because they are ideal models for studying magnetic, optical and semiconducting phenomena in solids (see ch. 19).

The preparation of a high purity metal can be approached in two basic ways. The metal can be crudely made and then purified or the starting materials such as the salt and the reducing agents can be purified with precautions taken to keep them pure and the high purity metal produced directly from the reaction of the salt with the reducing agent. The chosen process depends on the basic properties of the metal involved; its reactivity, vapor pressure and melting point are important factors. To achieve the ultimate purities both approaches are used together.

About 150 years ago metallic cerium was the first rare earth metal to be reduced to its metallic state by reduction of $CeCl_3$ with Na or K (Mosander, 1827). This was about 40 years after the discovery of the rare earths by Lt. Arrhenius in 1787 in the town of Ytterby, Sweden. The cerium metal prepared by Mosander was a highly contaminated powdered product. Subsequently many other scientists have tried similar procedures and ended up with the same results. It was not until 1937 that Klemm and Bommer (1937) successfully reduced the rare earth chlorides with K in a sealed quartz ampule to prepare reasonably pure powdered rare earth metals. The metals were not separated from the KCl but were suitable for X-ray and magnetic property studies in their as-reduced form.

Electrolytic methods for preparing rare earth metals were not tried until about 100 years ago when Hillebrand and Norton (1875) successfully prepared La, Ce and didymium (a mixture of $\approx$1 part Pr to $\approx$3 parts Nd). Their metal was also

highly contaminated, especially with C and Fe from the electrode materials. Subsequent investigators using similar procedures also ended up with impure metals. Again it was not until the early to mid-1930's that the Fe and C contamination problem was solved by replacing C and Fe with a Mo cathode (Billy and Trombe, 1931; Trombe, 1932, 1933, 1936 and 1938) and reasonably pure metals were obtained.

The first massive quantities of the light rare earth metals prepared by a metallothermic method was accomplished by Spedding et al. (1952) who reduced the chloride with Ca. When the process was tried for the higher melting metals, the volatility of the chloride interferred and low yields resulted. In the following years Daane and Spedding (1953) showed that the Ca reduction of the fluorides of the higher melting rare earth metals could be used to prepare pound quantities. A few years later the Li reduction of the chloride was applied successfully by Nolting et al. (1960), and Moriarty (1968) to prepare the higher melting metals. The purest and best characterized rare earth metals are currently produced by the Ca reduction of the fluoride on a laboratory scale. The highly volatile lanthanide metals Sm, Eu, Tm and Yb were shown by Spedding and Daane et al. (1956) to be most easily prepared by the direct reduction of the oxide with a non-volatile reductant such as La. Achard (1966) and Kobisk and Grisham (1969) have also applied this technique to prepare some of the less volatile rare earth metals.

The methods of preparation of the rare earth metals by the Ca reduction of fluoride and the La reduction of the oxide have been continuously refined. The progress to 1965 was summarized by Gschneidner (1965) along with the mean values of some of the properties of the rare earth metals known to that date. The use of high purity reactants and an inert atmosphere in which to handle them was discussed by Spedding et al. (1968a) who also reported on analytical methods and listed some of the properties of the pure metals. The results of several years of experience concerned with the application of inert atmospheres in the metal preparation procedures were reported by Beaudry and Palmer (1974a). Many of the details concerning the discussions in the following sections on the preparation can be found in these three publications. Metallothermic methods involving a variety of salts and reductants have been tried, however, the methods described below in sections 1.1–1.4 have been most successfully applied.

1.1. *Metallothermic reduction of the fluoride*

Preparation of high purity rare earth metals starts with the pure oxide. Since most of the cation impurities which are present in the oxide will be present in the final metal product, it is imperative that the oxide be as pure as possible with respect to other cations. The exception is any cation which is volatile and will evaporate during vacuum melting of the rare earth metal, e.g. the alkali and alkaline earth metals. The oxides prepared in the Ames Laboratory for our studies were 99.999 wt.% pure with respect to all rare earth impurities and all other naturally occurring cation impurity elements. The separation and purification of the oxides are discussed in ch. 22. The cation impurities in the

oxides are determined by a spark source mass spectrometer method which is described in ch. 37C.

The preparation of the rare earth metals by the metallothermic reduction of the fluorides can be divided into 3 groups based on the procedure used to prepare them. The properties which are important in determining the groups are melting and boiling points. The first group is made up of La, Ce, Pr and Nd which have low melting points but high boiling points. The second group consists of Y, Gd, Tb and Lu which have moderate to high melting points and high boiling points. Sc, Dy, Ho and Er which make up the third group have high melting points and moderate boiling points. The remaining four rare earths, Sm, Eu, Tm and Yb, are not included here because their low boiling points allow them to be reduced directly from the oxides and this is discussed in section 1.2.

1.1.1. *Preparation of* La, Ce, Pr *and* Nd

The quantitative conversion of the oxide to the fluoride is accomplished in a two step process described by Spedding and Henderson (1971). In the first step a mixture of anhydrous HF and 60% Ar is passed over the R_2O_3 at 700°C for 16 hours. To prevent contamination of the fluoride, the Inconel furnace tube is lined with Pt and the oxide is contained in a Pt boat. After this initial step the fluoride has about 300 ppm by wt. O. This remaining O is lowered to less than 20 ppm in the second step by heating the fluoride to approximately 50° above its melting point in a Pt crucible in a graphite cell with a graphite resistance heater under a dynamic HF:60% Ar atmosphere. The length of time required to obtain O-free fluoride will vary, but about 1 hr at temperature for each 20 g of fluoride usually is required. After this step, the LaF_3 and CeF_3 are clear and colorless while PrF_3 and NdF_3 are clear with green and violet color, respectively. The optical transparency, or lack thereof, of the fluorides is an indicator of the O content; highly transparent fluoride crystals contain less than 10 ppm by wt. O, while milky or translucent crystals contain >20 ppm O. These fluorides are inert and may be handled in air. The fluoride which has undergone only the first step is termed "untopped" RF_3, while that material which has been through both steps is called "topped" RF_3. One of the important differences between material prepared at the Ames Laboratory and that prepared commercially is that topping the fluorides is not done commercially. It is important that a separate graphite cell be used for each rare earth, otherwise there will be serious contamination from the rare earth which was previously "topped" in the cell.

The Ca metal reductant is purchased commercially as "triply distilled" metal and is further purified by distillation under a partial pressure of 6 Torr (8×10^2 Pa) of He. The Ca as prepared contains less than 10 ppm by wt. O. However, when Ca is exposed to the air it quickly picks up oxygen – probably as adsorbed H_2O – and therefore, after purification it is essential that the Ca be handled and stored under an inert atmosphere. To do this the Ca distillate is placed in a He filled glove box, removed from the condenser and placed in Pyrex fruit preserving jars. The lids are tightened and the jars are transported to another glove box system and stored until needed.

The Ta crucibles are fabricated from Ta sheet obtained from commercial suppliers as "high purity, pickled and annealed sheet". The crucibles are formed and the seams are welded in an inert gas welding chamber described by Miller et al. (1963). A typical reduction crucible is 6.4 cm diameter by 25.4 cm long with 0.076 cm walls. After fabrication, the crucible is heated in a vacuum of 1×10^{-6} Torr (1.3×10^{-4} Pa) to 1900°C to boil off any volatile impurities.

In a typical reduction of CeF_3, 360 g of Ca which is 15% in excess of the theoretical amount required to reduce the fluoride, is mixed with 1030 g of CeF_3 and then packed into the Ta crucible in a He-filled glove box. The crucible is placed in an induction heated vacuum system and evacuated to 1×10^{-6} Torr (1.3×10^{-4} Pa). An atmosphere of pure Ar is admitted to the system and the crucible and contents are heated to a temperature above the melting point of the highest melting reactant or product. The temperature is maintained for about 15 min to allow the metal to settle to the bottom and the CaF_2 slag to float to the top. After the crucible is cool, it is transported to a He atmosphere glove box to remove the CaF_2 slag which is loose in the crucible and easily removed. Since the resultant 735 g of Ce occupies only about 10% of the crucible a second charge can be loaded and the second reduction made. After the second reduction, the slag is removed in the glove box. At this point the as-reduced Ce (or La, Pr or Nd) contains Ca, CaF_2 and H which must be removed by vacuum melting. Since the Ce (La, Pr or Nd) metal containing these impurities readily reacts with H_2O, the as-reduced metal should always be handled under an inert atmosphere. Although the Ca and H can be removed by heating the as-reduced metal to just above its melting point, it must be heated to at least 1800°C for 30 min to remove the fluoride impurity quantitatively. At this temperature these metals dissolve large amounts of Ta, for instance 0.10 at.% in Ce (Dennison et al. 1966a). However, the Ta impurity can be lowered to less than 20 ppm by wt. by holding the temperature just above the melting point of Ce (La, Pr or Nd) to allow the Ta to precipitate out of solution and settle to the bottom of the crucible. An empirical rule for the length of time needed to allow complete settling of the Ta is 24 min per cm of height of the liquid metal column. The Ta crucible and the Ta dendrites which have settled to the bottom of the crucible are machined off and the billet sampled for complete analysis. The impurities that are of special interest are those which might have been added during the process, and not completely removed. Typical analyses of these metals for these common impurities are given in table 2.1.

The preparation of these high purity metals is dependent on a strict adherence to the rule of using pure reactants and keeping them pure. Beaudry and Palmer (1974a) showed that handling the Ca reductant in air resulted in a 30-fold increase in the O content of the Ce metal so prepared. The preparation of the fluoride without melting it under a dynamic atmosphere of HF–Ar gas results in about a 10-fold increase in the O content of the metal prepared. The effect of impure Ca is the same as handling the purified Ca in air. Although the O impurity can enter from the Ca, fluoride, crucible or atmosphere, it usually does not exceed a level of about 1000 wt. ppm in the metal prepared due to a slagging

TABLE 2.1
Typical analysis in ppm atomic of La, Ce, Pr and Nd prepared by the Ca reduction of topped fluoride followed by vacuum melting when the reactants and products are handled under inert conditions, values given in parenthesis are in wt. ppm.

Impurity	La	Ce	Pr	Nd	Method of[a] Determination
O	304 (35)	385 (44)	379 (43)	315 (35)	Vacuum fusion
N	50 (5)	70 (7)	50 (5)	62 (6)	Vacuum fusion
H	275 (2)	277 (2)	140 (1)	285 (2)	Vacuum fusion
C	126 (11)	47 (4)	82 (7)	108 (9)	Combustion-chromatography
F	73 (10)	110 (15)	37 (5)	23 (3)	Chemically
Ca	0.1 (<0.1)	<0.1 (<0.1)	0.1 (0.1)	0.1 (<0.1)	Mass spectro.
Pt	<0.1 (<0.1)	<1 (<1)	<1 (<1)	< (<1)	Mass spectro.
Ta	4 (5)	6 (8)	10 (12)	20 (25)	Mass spectro.

[a]The particular methods are discussed in detail in ch. 37.

TABLE 2.2
Analysis of Pr before and after extraction with CaF_2–Ca slag in wt. ppm.

	O	H	N
Before	9360	890	400
After	265	8	140

effect of the CaF_2 and excess Ca. This effect can be used to purify the low melting rare earth metals when they are highly impure. Spedding et al. (1968b) sealed highly impure Pr metal in a Ta crucible with CaF_2 and Ca. The mixture was heated to 1550°C for 15 min, cooled, and the CaF_2–Ca slag removed. An analysis after vacuum melting the Pr showed the O, N, and H concentration had been lowered significantly, see table 2.2.

1.1.2. *Preparation of* Y, Gd, Tb *and* Lu

The moderate to high melting points of this group of metals necessitate a distillation step instead of precipitation to remove the Ta impurity introduced during the reduction and vacuum melting steps. That is, the solubility of Ta in these metals, which ranges from 0.06 at.% Ta in Gd to 1.4 at.% Ta in Lu at their melting points (Dennison et al. 1966b), is much too high to be left in the metals and for them to be considered as "high purity" materials.

The fluoride preparation of these elements is the same as for the four lanthanides in the first group. The appearance of the fluoride after it has been removed from the high temperature furnace is different due to a phase transformation that occurs during cooling (Thoma and Brunton, 1966). Instead of

large, clear crystals found for (La, Ce, Pr or Nd)F_3, small crystals which give a white appearance to the fluorides are present after the topping operation. However, each crystal when viewed under magnification appears clear if the O content is <10 ppm by wt.

The Ca must be pure and handled under inert conditions, just as with the first group, since Y, Gd, Tb and Lu are not purified significantly with respect to O during the distillation step. Lu is an exception; if it is sublimed at a slow rate (~ 0.5 g/hr), a significant purification with respect to O can be achieved. The reduction and vacuum casting operations are performed in the same way as for the first group, except that the temperature for the reduction step is higher because of the higher melting point of the metal. The vacuum casting is done at the same temperature, ~ 1800°C and in a vacuum of 1×10^{-6} Torr (1.3×10^{-4} Pa).

The distillation of Y, Gd and Tb is done in W crucibles since refluxing of some of the distilled metal erodes the Ta crucibles causing them to leak. The condenser is also lined with W since Ta diffuses into the hot condensate more readily than W. A typical distillation unit for Y, Gd or Tb is shown in fig. 2.1. Since Lu is sublimed, refluxing of the distilled metal is not a problem and the Lu is sublimed from a Ta crucible into a W lined condenser as described by Spedding et al. (1970). The temperatures of vacuum melting and distillation, the common impurities, the condenser temperature, typical size of run, and dis-

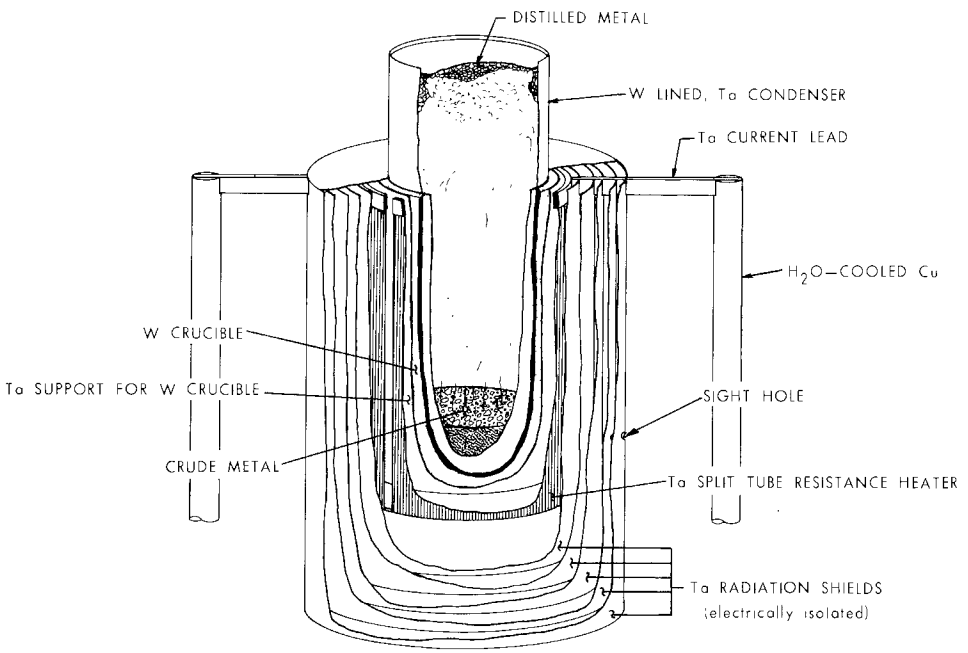

Fig. 2.1. Distillation assembly used for Y, Gd and Tb metals in a 3×10^{-9} Torr (4×10^{-7} Pa) vacuum.

tillation rate are given in table 2.3. The rate of distillation or sublimation is quite slow – 1 g/hr rate only 168 g are purified in one week, and at 1.5 g/hr rate 252 g per week. This slow distillation rate helps maintain a low level of impurities from the crucible in the distillate. Commercial metals are generally distilled at a much higher rate. A vacuum of better than 1×10^{-8} Torr (1.3×10^{-6} Pa) must be maintained to prevent contamination of the distillate.

The substitution of W crucibles for Ta in the preparation of Gd can eliminate the distillation step if approximately 0.012 at.% W can be tolerated in the Gd. After the vacuum casting operation the excess W dissolved at the high temperatures must be allowed to precipitate and settle to the bottom of the crucible in the same way Ta is allowed to settle in La, Ce, Pr and Nd (see section 1.1.1). An analysis of Gd prepared in a W crucible is given in table 2.3. W crucibles could be used for Tb and Y if 0.03 and 0.07 at.% W, respectively, could be tolerated in these metals (Dennison et al. 1966a).

1.1.3. *Preparation of* Sc, Dy, Ho *and* Er

These metals have melting points in the same range as found for the second group discussed above, but the vapor pressure at their melting points is con-

TABLE 2.3

Typical analysis[a] in ppm atomic of Y, Gd, Tb and Lu prepared by the Ca reduction of topped fluoride then vacuum melted and distilled when the reactants and products are handled under inert conditions. Values given in parenthesis are in wt. ppm.

Impurity	Y	Gd	Tb	Lu	Gd[b]
O	322 (58)	472 (48)	665 (67)	1090 (100)	600 (61)
N	19 (3)	11 (1)	91 (8)	50 (4)	112 (10)
H	352 (4)	311 (2)	945 (6)	520 (3)	467 (3)
C	148 (20)	236 (18)	132 (10)	234 (16)	249 (19)
F	<14 (<3)	<25 (<3)	<25 (<3)	<25 (<3)	<25 (<3)
Ca	1 (0.5)	<2 (<0.5)	0.4 (0.1)	<0.1 (<0.1)	<2 (<0.5)
Ta	<1 (2)	5 (4)	11 (14)	<3 (<3)	<0.4 (<0.4)
W	12 (24)	<0.4 (<0.4)	6 (7)	<20 (<24)	120(140)
Pt	<0.1 (<0.1)	<0.1 (<0.1)	<0.1 (<0.1)	<0.2 (<0.2)	<0.4 (<0.4)
Vacuum melting temp. (°C)	1850	1800	1750	1800	1800
Distillation temp. (°C)	1725	1725	1575	1645[c]	b
Condenser temp. (°C)	900	900	800	850	b
Distillation rate (g/hr)	1	1.5	1.5	1	b
Size of run (g)	150	250	225	250	2000

[a]See table 2.1 for methods of analysis. [b]Prepared in a W crucible and only vacuum cast. [c]Sublimation for Lu.

siderably higher. Thus, purification of these metals by vaporization is comparatively easy. The common interstitial impurities which form stable compounds such as N, C, or O remain in the residue when these metals are sublimed at a slow rate. Therefore, the great care taken to remove O from the fluoride and to prevent the introduction of it and the other interstitial impurities in the first two groups of metals is not necessary since Sc, Dy, Ho and Er metals are purified with respect to these three interstitial impurities during the sublimation step which primarily removes the Ta impurity. In the case of Sc this is indeed fortunate, since the vapor pressure of ScF_3 occurs when it is melted under a dynamic HF–Ar atmosphere. The fluorides of Dy, Ho and Er can be melted under a dynamic HF–Ar atmosphere, but usually this is not done for routinely prepared metal.

The procedure used to reduce the fluoride of these four elements is the same as discussed above (sections 1.1.1 and 1.1.2). Since the fluorides are not fused and are in a finely divided state, they tend to adsorb moisture and other impurities from the air, and should be stored and handled under an inert atmosphere. This is especially true for ScF_3 which will adsorb sufficient moisture in about 2 days to cause a violent reaction with the Ca reductant when heated. After the reduction step, the CaF_2 slag is removed and the as-reduced metals must be vacuum

TABLE 2.4

Typical analysis[a] in ppm atomic of Sc, Dy, Ho and Er prepared by the Ca reduction of the fluoride. Also vacuum melting temperature and time, sublimation temperature, condenser temperature, sublimation rate and size of run. Values in parenthesis are in wt. ppm.

Impurity	Sc	Dy	Ho	Er
O	267 (95)	398 (39)	309 (30)	231 (22)
N	26 (8)	12 (1)	35 (3)	12 (1)
H	357 (8)	965 (6)	653 (4)	166 (1)
C	56 (15)	108 (8)	55 (4)	153 (11)
F	37 (8)'	120 (14)	52 (6)	44 (5)
Ca	0.5 (0.5)	<4 (<1)	2 (0.5)	<0.2(<0.1)
Ta	0.5 (2)	22 (25)	<0.6 (<0.8)	6 (7)
W	19 (77)	<1 (<1)	1 (1)	8 (9)
Pt	<0.2 (<0.2)	<0.3 (<0.3)	<0.1 (<0.1)	<0.5 (<0.5)
Vacuum melting temp. (°C)	1550	1440	1480	1540
time (min)	10	45	45	30
Sublimation temp. (°C)	1425	1175	1220	1300
Condenser temp. (°C)	900	700	725	825
Sublimation rate (g/hr)	1	2.5	2.1	2.1
Size of run (kg)	0.1	1	0.6	1

[a]See table 2.1 for method of analysis.

melted to remove the excess Ca, residual fluoride and H. The high vapor pressure of these metals which helps in their purification by vaporization makes the quantitative removal of the fluorine impurity difficult. When these metals are vacuum melted for the length of time given in table 2.4, which will quantitatively remove the fluorine impurity, about 30% of the Sc and Dy, and 20% and 10% of the Ho and Er, respectively, are lost. This evaporated metal and the volatilized impurities are collected in a Ta cylinder placed above the crucible to make recovery of the metal easier. The vacuum melting time can be shortened to reduce the metal loss if several hundred ppm fluorine can be tolerated in the final product. Since these metals are sublimed, the refluxing of molten metal which causes crucible failure in the case of Y, Gd and Tb does not occur. Thus the metal can be sublimed from the same Ta crucible used for the reduction and vacuum melting steps allowing considerably larger batches to be sublimed (compare table 2.3 and 2.4). The chemical analysis of the metals prepared, the vacuum melting times and temperatures, the sublimation temperatures, condenser temperatures, sublimation rates and size of runs are given in table 2.4. Except for Sc the sublimation rates are about twice as high as for the Y, Gd, Tb and Lu group, but are still much lower than the distillation rates used in the commercial preparation of rare earth metals.

1.2. *Metallothermic reduction of the oxide – The preparation of* Sm, Eu, Tm, *and* Yb

The metals Sm, Eu, Tm and Yb all have high vapor pressures and are prepared by the reaction $La(s) + R_2O_3(s) \rightarrow La_2O_3(s) + R(g)$ in which the reaction goes to completion due to the removal of Sm, Eu, Tm or Yb by volatilization from the reaction chamber. In this procedure, the oxide is heated in air to 800°C for 15 hours to drive off absorbed compounds such as H_2O and CO_2. The La metal which has been vacuum melted at 1800°C or higher is made into chips or turnings on a lathe. La, especially impure La, will spark readily and burn, and therefore, the turnings should not be allowed to accumulate on the lathe. The turnings can be made in air if they are immediately transferred to an inert atmosphere. The turnings and freshly ignited oxide are packed into a 6.4 cm diameter by 25.4 cm long Ta crucible which is fitted with a 20 cm long Ta condenser and a Ta optical baffle arrangement to prevent excessive entrainment of oxide particles. The crucible and contents are evacuated, heated in an induction furnace over a period of 2 hours to a maximum temperature of 1400°C for Eu and Yb and 1600°C for Sm and Tm and then held at this temperature for an additional 2 hours. The slow increase in temperature is important, since a fast heating rate causes the La to melt and run to the bottom of the crucible and for all practical purposes the run is finished with only a small yield. As the reductant reacts with the oxide, a La–La_2O_3 solution is formed which melts at a higher temperature than pure La. The temperature can then be raised to increase the diffusion rate as the melting point of the reducing medium increases.

A typical reduction of Sm_2O_3 would consist of 550 g of Sm_2O_3 and 540 g of La

turnings which is about 15 wt.% over the stoichiometric amount. With a normal 98% yield on the reduction-distillation step, about 465 g of Sm are obtained. The reduction crucible can be cleaned, reloaded with La and Sm_2O_3 and reused for additional reduction-distillation runs. The reduced-distilled metal contains several hundred ppm La, as well as O and H. A subsequent sublimation of the metal at the temperature given in table 2.5 results in removal of these impurities to the levels listed. The sublimation can be done in the same crucible which was used for the reduction-distillation step, provided the following operations are carried out before the sample is sublimed. The optical baffles, which reduce entrainment during the reduction-distillation step, are removed for the low temperature sublimation, the crucible is leached with acid and then vacuum degassed at 1800°C to remove any volatile impurities.

The as-sublimed metals frequently contain many small crystals which gives them a large surface area to react with air and introduce impurities, and thus it is a good practice to consolidate these metal crystals as soon as possible. This can be done by sealing them in a Ta crucible in an inert gas welder and then heating the sealed crucible in vacuum to above the melting point of the metal. Since Eu is so reactive, the as-sublimed metal must be handled under an inert atmosphere. The as-sublimed metal usually contains H as an impurity, which can be removed quantitatively in the consolidation step by holding the temperature above the melting point for 24 hours in a dynamic vacuum. The H diffuses through the Ta and is pumped away.

TABLE 2.5

Typical analysis[a] in ppm atomic of sublimed Sm, Eu, Tm and Yb. Also the sublimation temperature, condenser temperature, sublimation rate and size of run. Values in parenthesis are in wt. ppm.

Impurity	Sm	Eu	Tm	Yb
O	310 (33)	665 (70)[b]	85 (8)	410 (38)[b]
N	214 (20)	N.D.[c]	<12 (<1)	112 (9)
H	595 (4)	1950 (13)	1500 (9)	685 (4)
C	75 (6)	1270 (100)	197 (14)	144 (10)
Ca	7 (2)	35 (10)	1 (0.2)	<10 (<13)
La	3 (3)	1 (1)	6 (5)	5 (4)
Ta	24 (30)	<0.6 (<0.6)	<1 (<1)	<1 (<1)
W	<2 (<2)	<3 (<3)	<3 (<3)	<1 (<1)
Sublimation temp. (°C)	800	700	950	625
Condenser temp. (°C)	~500	~400	~550	~350
Sublimation rate (g/hr)	3	3	3	4
Size of run (kg)	1	0.5	0.5	0.8

[a]See table 2.1 for methods of analysis. [b]Determined by neutron activation analysis. [c]N.D. = Not determined.

To reduce the cost of the reductant for Sm, Eu and Yb, mischmetal* which has been vacuum melted to 1800°C to remove the volatile impurities works well as a reductant in place of La. In the case of Tm the higher reduction-distillation temperatures as well as the higher sublimation temperatures sometimes cause a few ppm of Nd or the volatile heavy lanthanide metals in the mischmetal to be introduced in the sublimed Tm. La or Ce is used for the reduction of Tm when high purity is required.

The reduction of the rare earth oxides by the reduction-distillation technique has also been applied by Kobisk and Grisham (1969) to the preparation of special isotopes of high purity rare earth metals with La and Th as reductants.

1.3. *Metallothermic reduction of the chloride*

The pioneering work of Klemm and Bommer (1937) in which rare earth chlorides were reduced with K metal in a sealed glass tube resulted in a mixture of metal and KCl which they did not separate. They determined the lattice parameters and some of the magnetic properties of the rare earth metals in the presence of the KCl. Nolting et al. (1960) reduced YCl_3 with Li vapor in a sealed stainless steel chamber in Ta crucibles. After the reduction of the YCl_3 to Y metal was complete, one end of the chamber was cooled. The LiCl salt then distilled away from the Y crystals and condensed in the cool portion of the chamber. The Y was arc melted to consolidate the small crystals. The microstructure of the arc melted metal was clean. However, the interstitial impurity level was about 20 times higher than the laboratory scale metal prepared by the

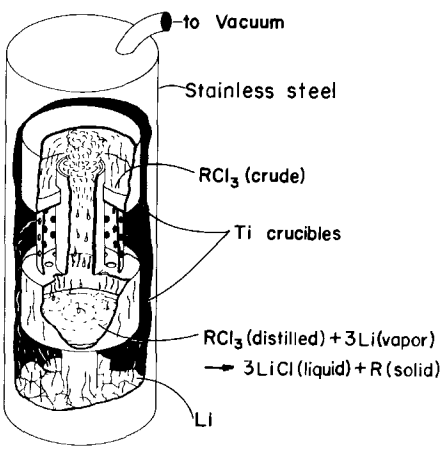

Fig. 2.2. Reduction crucible used for the Li reduction of RCl_3.

* Mischmetal is an alloy which contains the rare earth metals in the same proportions as found in the original ore source from which the mischmetal was made. Mischmetal prepared from bastnasite contains 33% La, 50% Ce, 4% Pr, 12% Nd and 1% Y plus the remaining lanthanides; while that prepared from monazite contains 21% La, 47% Ce, 6% Pr, 20%Nd, 2% Gd, 2% Y and 2% the remaining lanthanides.

Ca reduction of the fluoride followed by distillation as described above (section 1.1.2).

The Li reduction of the rare earth chloride was adapted to a commercial scale, as described by Moriarty (1968). In this process, crude chloride was placed in a Ti crucible with a tube down the center (see fig. 2.2). This crucible was separated by a spacer from a second Ti crucible below it. Both crucibles were placed in a stainless steel chamber on a pedestal. Commercial grade Li was placed around the pedestal as chunks. The steel chamber was evacuated and the upper Ti crucible was heated to distill the RCl_3 into the lower crucible. After the chloride was distilled, the entire steel chamber was heated. The Li vapor filled the chamber and some of the Li condensed in the vacuum line which sealed the chamber. The Li vapor also reacted with the molten RCl_3 to give R + LiCl. When the reaction was complete the steel chamber was partially removed from the furnace. The LiCl slag distilled from the reaction crucible to the cold part of the steel chamber which was out of the furnace. After it was cooled the sealed steel chamber was opened and the metal crystals were consolidated by arc melting or induction melting for the low melting rare earth metals. The low temperature (800 to 1000°C) of the reduction results in very low contamination of the rare earth metal crystals with the crucible material. The O content of the rare earth metals produced by this method ranged from 225 ppm by wt. for Ho to 1600 ppm by wt. for Tb. The nitrogen was less than 40 ppm by wt. in all cases.

The Li reduction of $DyCl_3$, $HoCl_3$ and $ErCl_3$ was studied by Croat (1969). By doubly distilling the chloride prior to the reduction and using high purity Li vapor as the reductant, he was able to obtain as-reduced metals of the purity listed in table 2.6. As mentioned in section 1.1.3, these metals can be purified with respect to O, N, C and H by sublimation.

Another approach, as described by Carlson and Schmidt (1967), involved the preparation of yttrium metal by the Ca reduction of YCl_3 in the presence of Mg. The Mg and Ca were removed from the Y by a vacuum heat treatment followed by arc melting the resultant Y sponge. In a similar process Schmidt and Carlson (1974) prepared scandium metal by reducing $ScCl_3$ with Ca and/or Mg. The reduced metal was purified by arc melting or vacuum distillation.

TABLE 2.6
Analysis of as-reduced Dy, Ho and Er prepared by the Li reduction of doubly distilled chloride in ppm atomic. Values in parentheses are in wt. ppm.

Impurity	Dy	Ho	Er
O	1370 (135)	835 (81)	1145 (109)
N	81 (7)	35 (3)	84 (7)
H	965 (6)	816 (5)	1673 (10)
C	527 (39)	233 (17)	153 (11)
F	<25 (<3)	<25 (<3)	<25 (<3)
Cl	<14 (<3)	<14 (<3)	<4 (<3)
Li	<0.1 (<0.005)	<0.1 (<0.005)	<0.2 (<0.005)

1.4. *Metallothermic methods used on a large scale*

The Ca reduction of the fluoride can be scaled up into a semicontinuous process with a reduction and pouring furnace similar to that described by Carlson and Schmidt (1961a) for the preparation of Y metal (see fig. 2.3). Granular Ca is mixed with the YF_3 and placed in both the hopper and the

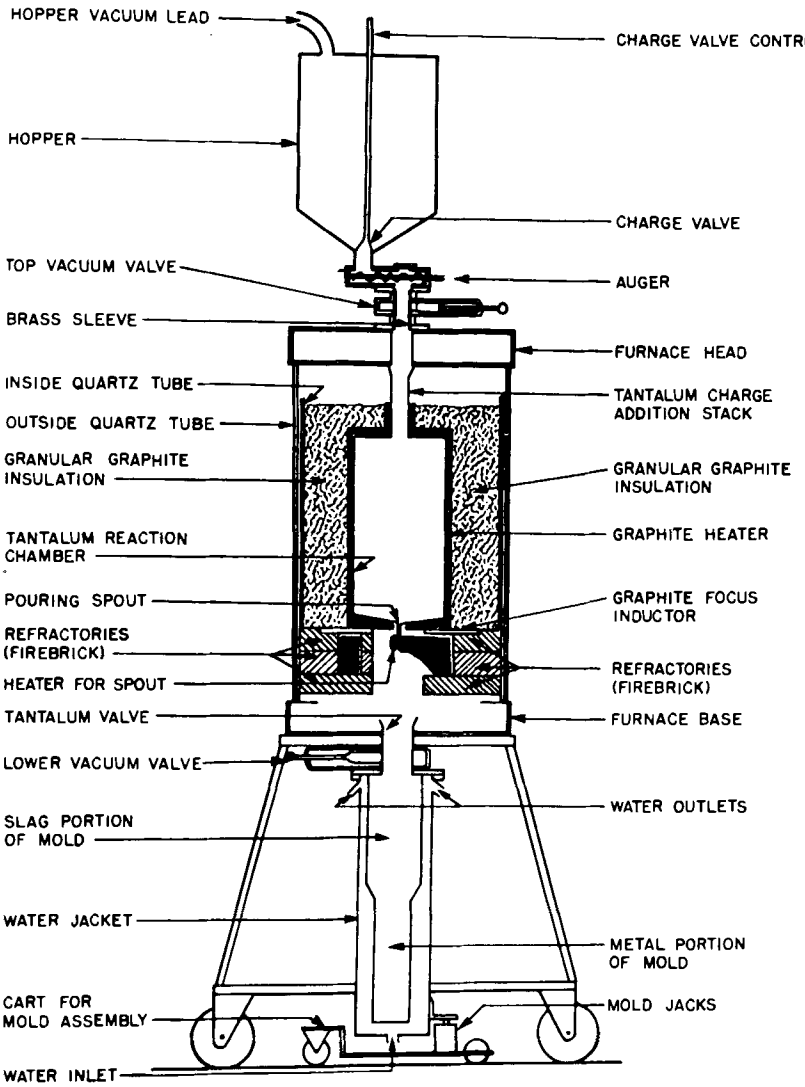

Fig. 2.3. Reduction and pouring furnace for semicontinuous preparation of Y metal (after Carlson and Schmidt, 1961a).

reaction chamber. The system is evacuated and backfilled with argon. After the initial heating of the reduction chamber to effect a reduction, additional reactants are introduced through the top vacuum valve from the hopper until the reaction chamber is filled with reduced metal and CaF_2 slag. The coil is then lowered and the plug of Y metal in the pouring spout is melted. The metal and slag run into the water cooled mold which can be separated and emptied while the next reduction is being run. The reactants are again admitted to the reaction chamber from the hopper by means of the auger while the chamber is still hot. After the second reduction the coil is again lowered and the metal poured into the empty water-cooled mold. The procedure can be repeated until sufficient metal is obtained or a portion of the equipment fails.

To remove the Ca and residual fluoride the Y is vacuum arc melted twice. Y prepared in this way contained 0.14 to 0.20 wt.% O, 0.05 wt.% F, 0.02 wt.% N, 0.01 wt.% C, 0.001 wt.% Ca and 0.4 wt.% Ta. Although Y metal prepared on a laboratory scale today is considerably more pure than metal produced in 1960 (see table 2.3), an analysis for Y produced on a large scale (>20 kg) would probably be about the same today as it was in 1960.

The small scale low temperature process for the preparation of the fluoride described in §1.1.1 can be scaled up to produce larger quantities of the fluorides. However, the depth of the oxide should not exceed about 4 cm to ensure complete reaction of the oxide with the HF gas. Greater depths of oxide, however, may be fluorinated by utilization of a rotating tube furnace (Carlson and Schmidt, 1961b). Because of the ease of handling and the low temperature required to complete the reaction, NH_4HF_2 is a good fluoriding agent for large scale production. In this process R_2O_3 is mixed with 30% excess NH_4HF_2 and heated to 300°C with dry air passing over the mixture. The residual O in the RF_3 ranges from 300 to 800 ppm by wt.

Commercial grade granular Ca may be used as the reductant. However, the resulting rare earth metal will contain large quantities of interstitial impurities which are absorbed from the Ca. As discussed in section 1.1.1 not all of the interstitial impurities go into the rare earth metal when the concentration of these impurities is high. Instead an equilibrium distribution of the impurities is established between the Ca–CaF_2 slag and the rare earth metal. This equilibrium concentration depends on the activity of the slag relative to the metal and will change with temperature. Therefore, the higher melting rare earth metals will have a different equilibrium concentration of interstitial impurities than the lower melting rare earth metals.

When the high melting rare earth metals are prepared, high concentrations of Ta remain if the metals are not purified by distillation. This crucible problem can be circumvented by adding a metal to alloy with the rare earth metal and lower the melting point and by adding a salt to lower the melting point of the slag. Large quantities of Y metal were prepared by Carlson and Schmidt (1961a) with Mg as the alloying additive and $CaCl_2$ as the salt. The process with various refinements is also reported by Carlson et al. (1960). For example Ti or Zr was

substituted for the more expensive Ta as a crucible material. In their process Mg and Ca are heated in a Ti crucible to 750°C under vacuum, then to 900°C under a He atmosphere. The desired quantity of YF_3 and $CaCl_2$ are fed slowly into the reaction chamber from a hopper above the retort. The crucible containing the reactants and products is heated to 960°C, removed and tilted before the alloy and slag solidify. When cool the slag and alloy are removed, the alloy is crushed and heated under vacuum to 950 for 25 hrs to remove the Mg and Ca. The Y sponge which remains is packed into rods which are used as consumable electrodes and vacuum arc-melted into a 10 cm diameter water-cooled copper mold. The 10 cm diameter billets in turn are used as consumable electrodes and vacuum arc-melted into 15 cm diameter billets.

In another variation a fused salt extraction step was added to the process in which a fused mixture of YF_3 and $CaCl_2$ was stirred in contact with the molten Y–Mg alloy. An analysis of the metal prepared with and without the extraction step is given in table 2.7. Carlson et al. (1960) also prepared small batches of Y in Ta crucibles in which the molten Y–Mg alloy was extracted several times with YF_3–$CaCl_2$ and then with YCl_3. The analysis of this metal is also given in table 2.7.

1.5. *Electrolytic methods*

Today electrolytic methods account by far for the largest amounts of rare earth metal produced throughout the world – thousands of tons per year. The main reason for this is that the electrolytic method is cheaper than any metallothermic process one can devise, either practically or theoretically. However, because of the reactivity of the materials the electrolytic method is usually limited to operating temperatures of 1100°C or lower. Because of this limitation generally only the first four lanthanide metals, La, Ce, Pr and Nd (and their mixture-mischmetal), are prepared by electrowinning. Limited quantities of

TABLE 2.7
Analyses of Y metal prepared by the Mg-alloy process prior to 1960 in ppm by wt.

Impurity	Without salt extraction	With YF_3–$CaCl_2$ extraction in Ti	With YF_3–$CaCl_2$ and YCl_3 extraction in Ta
O	1200 to 2500	500	150
N	150	N.G.[a]	20
F	800	600	60
C	200	N.G.	90
Ti	1500	5000	N.G.
Ca	10	10	10
Mg	30	30	10

[a]N.G. = not given.

other rare earth metals, primarily Sm, Gd, Dy and Y, have been prepared electrolytically, but metallothermic methods are almost exclusively used to prepare the remaining rare earth metals. To date the highest purity metals have been prepared by the calcium metallothermic method. This may be due to the fact that not as great an effort has been made to achieve such purities by the electrolytic method. But it is possible that the electrolytic method may inherently limit the ultimate purity to something less than that which can be attained by the metallothermic method.

Most of the earlier work on electrolytic methods has been well summarized in a comprehensive review by Morrice and Knickerbocker (1961). More recent, but limited, reviews have been written by Hirschhorn (1968) and Fölsch (1970) on industrial processes.

1.5.1. *Basic principles*

The basic electrolytic process for reducing metals from their salts is quite simple, but many variations have been successfully employed. In general a salt of the metal desired is dissolved in another salt or a solution of salts which are melted in an inert container. Two electrodes (a cathode and anode) are put into the batch and an electric current is passed through the circuit with a voltage sufficient to reduce the salt in question. Current densities ranging from 3 to 11 amp/cm^2 have been reported. The molten salt, in addition to serving as a solvent for the metallic salt to be reduced, must be a conductor of the electric current, have a melting point below the temperature at which the cell is operated, have a low vapor pressure, and be more stable than the salt to be reduced. The desired properties of the electrolyte are usually obtained with the addition of an alkali or alkaline earth fluoride or chloride, or a combination of them. The cell which comes in a variety of sizes and shapes is usually made of Fe, graphite, a ceramic (such as fire brick, alumina, etc.) Mo or a combination of these materials. In some designs the cell also serves as the cathode, at which the cation is reduced and the resultant metal is collected. The anode is generally made of graphite because it is relatively inert to the Cl_2 or O_2 liberated at the anode. The cathode is usually made of Mo or W (in laboratory preparation of pure metals) or Fe (in commercial production of metals).

The various combinations of materials, and cell design and size chosen depend upon the purity, cost and quantities of metal desired. If commercial production of 95–98% pure metal is the goal, then graphite and iron along with inexpensive ceramics are the choice for the cell and electrodes. The cells will be large and designed for continuous operation. The electrolytic bath will probably contain NaCl or KCl and perhaps a small quantity of $CaCl_2$ in addition to RCl_3. No special precautions will be taken to purify the chlorides. Generally such metal will contain appreciable amounts of Fe and other common metallic elements.

If high purity metals are required the cell is made of or at least lined with Mo and the cathode is made of Mo or W. The electrolyte is generally a complex one containing more expensive halides (LiF, CaF_2, LiCl) than used in commercial

processes. Generally salts for the electrolyte are purchased pure or, if necessary, the salts are purified by distillation or other means before the run. Metals of 99 wt.% pure or greater have been prepared by this method.

1.5.2. *Reduction of halides*

For the commercial preparation of the pure individual metals, La, Ce, Pr and Nd, and mischmetal the electrolyte is composed of the chlorides because they are cheap and molten at the temperature of electrolysis. A second (and sometimes a third) chloride is added (NaCl, KCl or $CaCl_2$) to lower the melting point, to improve the conductivity of the electrolyte and to increase the efficiency of the cell. The temperature and current density also effect the efficiency, e.g. Shiokawa et al., 1968, found that for the $LaCl_3$·2KCl bath the optimum conditions were obtained at 920°C and a current density of 4.0 amp/cm^2. The major difficulty with the chlorides is the hygroscopic nature of RCl_3 and the added chlorides. The rare earth trichloride must be dried by heating (1) in a vessel from which air is excluded until a porous, solid product is obtained or (2) in a vacuum chamber at a temperature lower than that used in (1). For commercial production most electrolytic cells are designed for continuous operation. This is accomplished by tapping the bottom of the cell to drain off the accumulated molten rare earth metal. Additional rare earth chloride must be added to replenish the chloride which has been reduced to metal.

For the preparation of small, high purity quantities of the first four lanthanide metals (La–Nd) for research purposes, the electrolyte is composed of fluorides. The main reason is that the rare earth trifluorides are not hygroscopic, as are the trichlorides, and thus are much easier to handle. But because of their much higher melting points, a second or third fluoride must be added to lower the melting point of the bath. In general LiF or a LiF–CaF_2 combination is added to accomplish this, although BaF_2 has been used in place of CaF_2. As in the chloride systems, the efficiency of the cell will depend upon the various fluoride salts present and their relative concentrations in the electrolyte, the current density and temperature. At low temperatures the current efficiency decreases because of the development of a metal "fog" (a colloidal suspension of metal in the electrolyte), while at high temperatures the solubility of the metal in the electrolyte and perhaps in some instances evaporation of one of the bath components are common causes for the reduction in the efficiency. The purity of the final product must be considered in addition to current efficiencies. Usually the lower the temperature the lower the concentration of O and other non-metallic impurities in the metal produced at the cathode.

In the processes where the cell temperature is above the melting point of the metal, the reduced metal at the cathode is molten. For cell designs in which the cathode is immersed in the bath, the molten metal builds up until it becomes heavy enough to drip-off of the end of the electrode and falls to the bottom of the cell due to gravity. In cell designs where the wall is the cathode the metal collects at the wall and settles to the bottom. For cells which operate below the

melting point of the deposited metal, a dendritic deposit builds up. The amount of metal collected in this case is generally less than that which can be obtained from cells which operate above the melting point. This is due to the fact that as the dendrites grow they will eventually reach the anode and short-out the cell, thereby ending the electrolysis.

1.5.3. *Reduction of oxides*

A good share of the research on electrowinning of the rare earth metals in the past 15 years has been devoted to the reduction of the rare earth oxide. Although good quality metals have been produced on a laboratory scale by this method and economically it appears to be cheaper than the chloride process, to date no company has successfully demonstrated that large quantities can be produced over an extended period of time (6 months to one year) by this technique.

In order to reduce the oxide by the electrolytic method one needs to consider the volatility of the salts, oxide solubility, an anion constituent which would not be oxidized in preference to the carbon oxides formed at the anode, and a cation constituent which would not be co-reduced with the rare earth metal. Chlorides are eliminated since they would be reduced in preference to the oxide forming chlorine at the anode. Of the common fluorides, only LiF, CaF_2 and BaF_2 are significantly more stable than the rare earth fluorides and thus would not be co-reduced during electrowinning. In a study by Henrie (1964), LiF (30 to 80 mol %) was added to increase the corresponding rare earth oxide solubility (2 to 4%) in the molten fluoride bath and BaF_2 was added (5 to 50 mol %) to lower the melting point. All constituents were carefully vacuum dried to remove moisture before addition to the electrolytic cell. The cell was placed in a chamber which contained He and the carbon oxides which were released during electrolysis. Henrie (1964) also described a cell for continuous operation with intermittent tapping to remove the molten metal. Because of the low oxide solubility carefully controlled additions of the oxide feed material was required. Further details can be found in papers by Shedd et al. (1964 and 1970) Morrice and Henrie (1967) and Morrice et al. (1968).

In the cases of electrowinning Ce and Pr metals Henrie (1964) and Morrice and Henrie (1967) found that the normal oxides, CeO_2 and Pr_6O_{11}, caused severe corrosion (or burning) of the graphite anode at the melt surface due to the high CO_2–CO ratio in the gas over the cell. This problem was eliminated by adding Ce_2O_3 or Pr_2O_3 to the electrolyte instead of the respective higher oxide. Another solution was to add CeO_2 or Pr_6O_{11} along with powdered graphite as the feed material, but the carbon content in the final metal was significantly higher than in the metal prepared from the sesquioxide.

The above method has been successfully used to prepare the first four lanthanides (La, Ce, Pr and Nd) and mixtures of these metals, specifically mischmetal and a cerium-free mischmetal. It has not been successfully applied to prepare the other rare earths because of their higher melting points. Henrie and Morrice (1966) have, however, described a modification of the above

technique to prepare Y, Gd and Dy (their melting points are 1522, 1313 and 1412°C, respectively). Because of the high temperatures BaF_2 was not needed to lower the electrolyte's fusion temperature. Instead a 50:50 mol % solution of LiF and RF_3 was used in all cases with ~2 wt.% of the respective R_2O_3. A large temperature gradient was maintained in the cell such that in the upper region around the electrodes the bath was 50 to 75°C above the melting point of the metal, and the bottom of the cell was 300 to 500°C below the melting point. As the metal was reduced and collected at the cathode, liquid drops would build-up and eventually drop-off. As these drops sank to the bottom, they would solidify as nodules and come to rest on the electrolyte which was frozen on the bottom, and thus reduce the reaction of the nodule with the graphite wall of the cell. The authors noted that the higher the temperature in the metal collection zone at the bottom of the cell, the lower the yields and the higher the impurity levels of oxygen and carbon. For Gd metal nodules weighing 5 to 20 g were recovered and had typically 0.05 wt.% C, 0.01 wt.% O_2 and 0.05% W as major impurities. For Dy and Y the C concentration was almost double and the O content about ten times higher than those in Gd. This is undoubtedly related to the higher operating temperatures of the cells which is required by the higher melting points of Y and Dy.

1.5.4. *Alloy processes*

Several different processes have been studied with two different objectives in mind – preparation of pure rare earth metals and the preparation of master alloys.

Two distinctly different methods have been described for preparing Sm metal by a combination electrolysis-distillation method. Morrice et al. (1969a) prepared a Sm–Fe low melting alloy by using iron as a consumable electrode. The electrolyte was similar to that described in section 1.5.3, 25% SmF_3 – 75% LiF with 2 to 4% Sm_2O_3 dissolved in the molten fluoride salt. The Sm deposits on the Fe cathode and forms a low-melting alloy, which drips off and sinks to the bottom of the crucible. As the cathode is consumed it is necessary to lower a new section. The 87 wt.% Sm–13 wt.% Fe alloy is prevented from reacting with the graphite crucible by a layer of frozen electrolyte on the bottom of the crucible. When the reaction is completed the electrolyte is allowed to solidify, and the alloy nodules are recovered and mechanically cleaned to remove adhering salts. The alloy is then heated in a distillation apparatus to separate the Sm from the Fe. The resulting Sm was reported to contain 50 ppm by weight Fe, with an 85% Sm recovery. Ishikawa et al. (1974) employed a liquid Zn cathode and a 1 : 1 molar $SmCl_3$–NaCl electrolyte to obtain a Sm–Zn alloy at 500°C. The product alloy had a composition close to $SmZn_{12}$. By vacuum distillation at 700°C most of the Zn was separated from the Sm. The Sm residue contained 7 wt.% Zn after distillation, and the authors thought that this could be further reduced by successive distillations, but no experiments were

performed to show this. As noted earlier, see table 2.5, the sublimation temperature for preparing pure Sm is 800°C and distillations carried out at 700°C would probably result in significant Sm losses.

Master alloys containing rare earth metals have been prepared by using a molten cathode (Al and Mg) and a consumable solid cathode (Cr, Fe, Co and Ni). The molten cathode work has been primarily centered on the preparation of Y master alloys containing either Mg (49 wt.% Y) or Al (28 wt.% Y), Bratland et al. (1972 and 1973) and Aamland, et al. (1973). The Mg or Al cathode floats on top of the molten LiF–YF_3 electrolyte, which also contains a few percent Y_2O_3.

Morrice et al. (1968 and 1969b) described their technique for preparing master alloys of transition metals (Cr, Fe, Co and Ni) with a number of the rare earth metals (Y, La, Ce, Pr, Nd, Sm, Gd, Dy and some of their mixtures). The RF_3–LiF electrolyte contained about 2–4 wt.% R_2O_3. Electrolysis was carried out at a temperature below the melting point of the transition metal (M) cathode and above the eutectic temperature on the rare-earth-rich side of the R–M phase diagram. In the case of Co, Morrice et al. (1969b) noted that these master alloys were suitable for preparing RCo_5 permanent magnet materials.

1.6. *Comparison of the calcium reduction and electrolytic methods*

Although only about half of the rare earth metals have been prepared by an electrolytic method while all have been prepared by a metallothermic method, it is instructive to compare the two methods. In order to make the comparison meaningful we will limit it to one metal – cerium. Much that follows, however, applies equally well to many of the other rare earth metals, especially the light lanthanides – La, Pr and Nd.

1.6.1. *Similarities*

For a number of criteria there is little difference between the two methods. These would include the scale of the operation, the crucible materials and the construction of the facilities. Either method could be applied equally well for small scale (10 g), large scale (1 kg) and even semicontinuous operations.

Although Mo is generally the container for the molten fused salt bath and Ce in the electrolytic method and Ta in the Ca reduction method, there is no reason why these two metals could not be substituted for one another as long as the level of the Mo or Ta impurity can be tolerated. Of the refractory metals, W is the least reactive with Ce, Ta is next and Mo is the most reactive. The choice of the refractory metal is not dictated by the method, but by costs and purity levels in the final product.

The facilities needed to carry out these reductions are in general the same – a vacuum or an inert gas furnace chamber. The only basic difference is the need to bring electrical power leads into the chamber for the electrolytic method.

1.6.2. *Starting materials*

The quality of the final product is greatly dependent upon the starting materials. If impurities can be tolerated in the final product it is recommended that the CeF_3 be prepared by the simplest fluorination method. This would be either the precipitation of CeF_3 from an aqueous solution using 48% HF as described by Daane and Spedding (1953) or the reaction of CeO_2 with NH_4HF_2 as described by Spedding and Daane (1956).

If low impurity levels are required, the method of preparing the fluoride for the electrolytic method is not as critical as for the Ca reduction method – at least with respect to the O content of CeF_3. In the electrolytic method CeO_2 or Ce_2O_3 is added to the fluoride flux, and it is the oxide which is reduced to the metal. For the Ca reduction method the O content of the fluoride is quite critical since any oxide present in the fluoride will end up in the metal. Furthermore, as noted by Carlson et al. (1960) the fluoride flux may serve to extract some of the impurities. These authors found that the levels of C, N, O, F, Mg and Ni in a Y–Mg alloy are reduced by extraction with a fused salt. Similarly, in the electrolytic preparation one might expect that the long contact time of the metal with the fluoride flux may decrease the level of some impurities in the metal. This behavior of the fluoride flux, however, may lead to difficulties if the flux is contaminated from the previous runs, since continued use would saturate the flux with certain impurities, and they would no longer be extracted, and even might be introduced into the next metal sample.

The other materials are also a source of impurities – the Ca in the Ca reduction method and the BaF_2 and LiF in the electrolytic method. Again, the quality of the final product required determines whether high purity or just ordinary chemically pure materials are needed.

For the highest purity Ce the direct fluorination of the oxide (see section 1.1.1) is recommended for either process.

1.6.3. *Purity*

As noted above, the quality of the starting materials determines the purity of the metal produced. To date, the purest Ce produced has been prepared by the Ca reduction method. Table 2.8 shows the impurity levels in the best Ce prepared by either method for which chemical analyses were given. Unfortunately, there is no F analysis given for Ce prepared by the electrolytic method, but on the basis of the data reported for Pr and Nd (Morrice and Henrie, 1967) one might expect to find between 100 and 400 ppm F in Ce.

There are several improvements one can suggest for the electrolytic method which would yield a higher purity product. One is to use a Ta liner or crucible to lower the Mo concentration. A second is to prepare the CeF_3 by reaction of the oxide with anhydrous HF (see section 1.1.1) which might lower the Al, Fe and Cu impurities which are introduced from the NH_4HF_2. The Li, C, O and F concen-

TABLE 2.8
Impurity levels in the best Ce metal prepared by either the Ca reduction or electrolytic method

	Concentration (ppm by wt.)	
Impurity	Ca reduction[a]	Electrolytic
H	2	30
Li	<0.001	20
C	4	100
N	7	not given
O	44	160
F	15	b
Mg	<0.01	40
Al	0.02	<100
Ca	<0.1	40
Fe	<0.5	70
Cu	2	10
Mo	<0.2	760
Ta	8	—
W	<0.4	20

[a]Same as Ce analysis in table 2.1 except additional impurities given here. [b]Fluorine analysis was not given, but values ranging from 100 to 400 ppm for Pr and Nd suggests similar levels might be expected in Ce.

trations would, however, be unaffected by the purity of the fluoride. The lithium and fluorine come from the fused fluoride flux, thes oxygen from the CeO_2 (or Ce_2O_3) starting material and the C from the graphite anode and/or cell walls. Only by changing the design or the operating parameters might it be possible to modify the Li, C, O and F concentrations. A third is to vacuum melt the electrodeposited metal. This would help to reduce some of the more volatile impurities (Li and F as CeF_3).

1.6.4. *Yields*

The Ca reduction of the fluoride method yields an average of about 95% of the Ce in the starting CeF_3. This compares to about 85% for the electrolyte method. For the Ca reduction method this value includes both the reduction step and the subsequent vacuum melting step, but does not include machining off the Ta layer and outer edge of the Ce to remove the precipitated Ta (see section 1.1.1). For the electrolytic method the yield only includes the metal preparation and not any further operation, such as melting the nodules together to form an ingot.

1.6.5. *Cost*

The electrolytic method is by far the cheapest method for preparing these metals. For Ce Morrice et al. (1961) report that only 7.5 kw-hours are required to prepare 1 kg Ce, and at a cost of 5 cents per kw-hour it would cost \$0.38 to prepare this Ce. This figure does not include the cost of the starting Ce_2O_3 or CeO_2, the fluoride flux, the equipment and heating costs, since these would be comparable to costs of similar items in the Ca reduction method.

The cost of Ca for preparing Ce by the metallothermic process would be \$1.25 per kg of Ce. This figure was arrived at assuming Ca costs \$2.25 per kg, a 100% yield and no costs for equipment and heating. However, to make this figure comparable to the electrolytic method, we need to add the cost of preparing the fluoride from the oxide, the cost of the vacuum melting step, and the cost of removing the Ta by machining off the outer 0.3 cm of the ingot. This makes the Ce prepared by the metallothermic reduction method about ten times more expensive than Ce prepared by electrolysis.

2. Purification

2.1. *Vacuum melting*

The procedure for the preparation of the rare earth metals by the Ca reduction of the fluoride on a laboratory scale described in section 1.1.1 includes a vacuum melting step in which the metals are heated to a temperature 500 to 1000°C above their melting points. However, metals prepared on a commercial scale are not heated this high so as to prevent excessive erosion of the crucible. Therefore, the commercial metals usually contain residual fluoride impurities and other volatile impurities which could be removed by vacuum melting. Vacuum arc melting or electron beam melting will also remove the volatile impurities from the rare-earth metals which have less than 0.1 Torr (13.3 Pa) vapor pressure at their melting points. These include Sc, Y, La, Ce, Pr, Nd, Gd, and Tb and Lu. Although Sm, Eu, Dy, Ho and Er can be arc melted under an argon atmosphere, the separation of impurities by volatilization is difficult due to the loss of the metal. Because of their high vapor pressure these five metals are easily distilled leaving the less volatile impurities behind.

2.2. *Distillation*

The removal of impurities which are more volatile than the rare earth metals is usually called "vacuum melting" as described above and since "distillation" of the rare earth metals is done after the vacuum melting operation, the two processes together could be called "fractional distillation." About half of the rare earth metals are purified by fractional distillation (sections 1.1.2 and 1.1.3). The more volatile impurities Ca, CaF_2 and H are removed by vacuum melting, while

impurities such as Ta or W are separated by distilling the rare earth metal leaving the less volatile impurities behind. The rare earth metals (Sc, Sm, Eu, Dy, Ho, Er, Tm and Yb) which are quite volatile and can be distilled (or sublimed) below 1500°C, can be purified considerably with respect to C, N and O as well as Ta by sublimation. When the distillation temperature is over 1650°C (see table 2.3), the volatile suboxide species, RO, starts to codistill with the metal, resulting in limited purification with respect to O. A slow distillation or sublimation rate gives the greatest degree of purification. High distillation rates result in impurities being transferred to the distillate by entrainment or by evaporation of compounds which become volatile at the higher temperatures.

In early studies on the distillation of the rare earth metals by Habermann and Daane (1963) baffles were placed above the distilland to reduce entrainment of impurities and to collimate the vapor. To increase the distillation rate to an acceptable level, the temperature had to be quite high ~2000°C. By removing the baffles and lowering the temperatures, a higher degree of purification was obtained as shown by Spedding et al. (1968a). As shown in tables 2.3–2.5 the actual temperatures employed on a laboratory scale today are considerably lower than 2000°C.

Busch et al. (1971) purified Eu by a fractionating column arrangement. The baffles of the column were at different temperatures due to their distance from the high frequency induction coil which heated the crucible containing the crude metal. The temperature of the various baffles was not reported. Eu with total impurities less than 0.02 at.% was obtained as determined by mass spectroscopy. The reason for the higher purity of this Eu compared to the Eu purified by sublimation (see table 2.5) is not clear but could be due to differences in analytical techniques, since the purification methods are essentially the same. The mass spectrometer method used by Busch et al. (1971) to analyze the Eu was not checked against standard methods such as vacuum fusion for H, Kjeldahl for N, combustion for C and neutron activation for O. As explained in ch. 37C, the mass spectrometric results for these impurities could be in error by a factor of 10.

Evers et al. (1975) studied the purification of Gd by reactive distillation. The analyses of their distillate indicated they obtained a high degree of purification by a double distillation. The interstitial impurities H, O, N, and C were reported as 4000 (which was 870 after the first distillation), 260, 10 and 30 at. ppm, respectively. These values are considerably lower than those observed for Gd distilled under a vacuum of 3×10^{-9} Torr (4×10^{-7} Pa) (see table 2.3). As in the case of Eu, the mass spectrometric results of Evers et al. for these interstitial impurities were not checked with the standard methods and could be low by a factor of 10.

2.3. *Electrotransport*

The method of solid state electrotransport has produced rare earth metals of higher purity than any other method. The principle of purifying metals by

electrotransport was reviewed by Verhoeven (1966) and by Jordan (1974). In this method, a large dc current is passed through a rod, typically 6 mm in diameter by 150 mm in length, for 1 to 3 weeks at a temperature 100 to 200°C below the melting point. Peterson (1971) gave a detailed discussion of the experimental factors which effect the purification of metals by electrotransport. The following discussion summarizes these factors.

During electrotransport, the impurities move under the influence of the electric field to one end of the bar. The greater the electric field, the faster the impurities move and the purer one end of the rod becomes. The passage of the current heats the rod and thus the maximum electric field is limited by the rate at which the heat can be removed from the bar. Under vacuum conditions the heat is lost by radiation. Addition of an inert atmosphere aids in the cooling by conduction. A smaller diameter rod gives a greater surface to volume ratio which increases the cooling per unit length and permits an increase in electric field. However, decreasing the diameter has the disadvantage of reducing the quantity of metal which can be obtained. Increasing the temperature to permit a greater electric field is limited by the melting point and vapor pressure of the metal being purified. The degree of purification is directly dependent on the purity of the surroundings and a vacuum of 1×10^{-9} Torr (1.3×10^{-7} Pa) or an equally pure inert atmosphere is the minimum requirement to permit movement of gaseous impurities to one end of the bar faster than they enter from the surroundings.

Since the ends of the rod are somewhat cooler and transport is therefore slower, the cold end from which the impurities are being removed can act as a source of impurities after the center portion of the rod has reached maximum purification. One method to eliminate this problem, is to butt weld an electrotransported rod to the end from which the impurities are being removed. The final steady state will then depend on contamination from the surroundings and the back diffusion due to the chemical gradient which is established. The success of the electrotransport method is therefore based on maximizing transport by the electric field, minimizing contamination from the atmosphere or the cold end, and minimizing back diffusion of impurities. Additional information concerning the theory of electrotransport and correlations involving the rate and direction of migration of interstitial and metallic solutes in the rare earth metals is discussed in ch. 12 §5. The rare earth metals which have high vapor pressures near their melting points, distill too quickly to be purified by the standard electrotransport methods. Those rare earth metals with low vapor pressures can be purified by this method and many of them have been, as discussed below.

The first report of purification of a rare earth by electrotransport was that given by Williams and Huffine (1961) for Y. They showed that O and N are quite mobile in Y and move to the anode end of the rod. The electrotransport parameters of C, N, and O in Y were determined by Carlson et al. (1966). Metals purified by electrotransport are frequently too pure to measure the impurities present quantitatively. As a means of indicating total purity both with respect to interstitial impurities and other lattice imperfections, the ratio of the resistance at room temperature to the resistance at 4.2 K ($R_{300}/R_{4.2}$) is reported. The Y

purified by Carlson et al. (1966) had a resistivity ratio of 45 compared with 12 in the starting material. In later studies on yttrium Carlson et al. (1975) obtained a sample with a resistance ratio of 127 by increasing the current density during electrotransport. In both of these studies the vacuum was 2×10^{-7} Torr (2.7×10^{-5} Pa) which limited the ultimate purification possible.

The electrorefining of Ce was studied by Marchant et al. (1962) in an inert gas chamber. This early study showed Fe, C, Cu and Si could be moved toward the anode by the electric field. The importance of the high vacuum or ultra-pure inert atmosphere is evident from this study, since the O content of their metal increased during electrorefining. Moore et al. (1965) in their study of Ce noted a movement of the Mn, Fe, Co, Ni and Cu impurities, but they apparently did not have a sufficiently clean atmosphere to purify the Ce with respect to O, N or C. A small movement of C was noted, but not sufficient to be termed "purification". Amonenko et al. (1966) studied the purification of Ce with a combination of zone melting and electrotransport. They showed that Ce containing 0.11 wt.% O could be reduced to 0.045% O by electrotransport or by the combination of the two methods. Their study was also done under an insufficiently pure atmosphere.

The first study of electrotransport purification of a rare earth metal which met the pure atmosphere condition was done by Peterson and Schmidt (1969) on the purification of Lu. A Lu sample with a resistance ratio of 151 compared to 21 for the starting metal was prepared by electrotransport in a vacuum of 2×10^{-10} Torr (2.7×10^{-8} Pa). Carlson et al. (1975) reported the O and N content had been lowered in Lu from 118 and 27 to 13 and 6 wt. ppm, respectively. They did not observe any movement of C in their study of Lu.

Peterson and Schmidt (1972) studied the electrotransport velocities of C, N and O in Gd. In addition, two separate experiments were performed in an attempt to purify rods of Gd in two types of atmospheres. In the first experiment a pressure of 5×10^{-10} Torr (6.7×10^{-8} Pa) was maintained with the rod at 1075°C for 150 hours. The best portion of the rod had a resistance ratio of 87 compared with 40 in the starting material. In the second experiment the rod was heated under a partial pressure of purified He, allowing an increase in both the temperature and the current density. The temperature of the rod was 1245°C, 10°C above the hcp-bcc transformation temperature. At 1245°C Gd has a bcc structure and the migration velocities of the impurities are greater than in the hcp phase. In this experiment they obtained a resistance ratio of 405 in the purest section, Carlson et al. (1975) later reported the O, N, and C content of the Gd purified as given in table 2.9.

Schmidt and Carlson (1976a) studied the electrotransport of C, N and O in Sc. In addition to determining the mobility, diffusivity and effective valence for each solute at four different temperatures, a rod of Sc was purified to a resistance ratio of 520 from 32 in the original Sc. They also observed the movement of Fe and Ni toward the anode.

In addition to the studies being made by Carlson, Peterson and Schmidt at the Ames Laboratory, extensive studies are now being made by Jones and co-workers at the University of Birmingham, United Kingdom, on the purification

of the rare earths by electrotransport. Their initial objective was to purify commercially available metals. Jordan and Jones (1973) in their first study purified several rods of Gd and then by taking the best sections and recycling the Gd, they were able to obtain a product with less than 100 at. ppm C, 106 at. ppm O, and no detectable N with a resistance ratio of 175. Jordan et al. (1975) have also succeeded in purifying commercial Tb by electrotransport with the double purification scheme noted for Gd. Their results are listed in table 2.10.

Current studies at the University of Birmingham include the electrotransport purification of Ce, Pr and Nd metal. Mattocks et al. (1976) have purified Nd supplied by the Ames Laboratory to obtain a sample with a resistance ratio of 118. The purest section contained 144 at. ppm O, 143 at. ppm H and 278 at. ppm N.

TABLE 2.9
Analysis of Gd before and after purification by electrotransport in ppm atomic. Values given in parentheses are in wt. ppm.

	Original analysis	After purification
C	300 (23)	<26 (<2)
N	314 (28)	<6 (<0.5)
O	824 (81)	157 (16)
$R_{300}/R_{4.2}$	40	405

TABLE 2.10
Analysis[a] of commercial Tb and Tb purified by electrotransport in ppm atomic. Values given in parentheses are in wt. ppm.

Impurity	As received[b]	As double-processed by electrotransport
H	445–730 (3–5)	350 (2)
N	60–350 (5–30)	180 (16)
O	3710–3840 (370–385)	260 (24)
Mg	1–6 (<1–1)	<3 (<1)
Al	10–25 (2–5)	20–100 (4–20)
Si	3–7 (<1–1)	8–30 (1.5–5)
Sc	210–550 (55–135)	20–40 (5–10)
Fe	10–100 (3–35)	10 (3)
La	10–20 (9–18)	5–30 (4–27)
Ce	2–6 (2–5)	2–10 (2–9)

[a]O, N, H were determined by vacuum fusion. Metallic impurities were determined by mass spectrometry. [b]Range of impurities determined in 3 separate Tb rods.

2.4. *Zone melting*

The application of zone melting to the purification of semiconductor materials has been well established. In this technique a molten zone is passed along the length of a solid rod in one direction several times. Impurities more soluble in the molten metal will move in the direction in which the molten zone is moved while impurities less soluble in the liquid metal will be deposited in the solid metal and will tend to move in the opposite direction. Since the degree of purification depends on the solubility of the impurities in the solid metal, those impurities which are soluble in the solid cannot be removed to below the equilibrium concentration. Thus the interstitial impurities which are quite soluble in the solid rare earths just below their melting point cannot be completely removed.

Early studies of the zone refining of the rare earth metals were reported by Huffine and Williams (1961). A molten zone 4.5 cm wide was passed ten times along a rod of Gd at a rate of 3.8 cm/hr. Metallographic examination showed substantial concentration of impurities at the rod ends and purification in the center. However, chemical analyses were not obtained to show which impurities had moved. Huffine and Williams (1961) studied the zone refining of Y and reported chemical analyses of portions of the rod. Their results indicated Cr, Cu, Fe and Zr were moved somewhat while O, N, Ni and Ti did not move. They concluded that zone refining is not a practical purification process for Y. It would appear the use of pure chemicals in the preparation of the metals as described in section 1.1 to prevent the introduction of metallic impurities is a more practical method of obtaining rare earth metals in the pure state than zone refining.

Revel et al. (1974) studied the zone refining of Ce in an induction heated cold crucible. They showed that 12 passes of a molten zone reduced a number of metallic impurities to the part per billion range. They did not determine the concentration of interstitial impurities in their samples. However, it is not likely that purification with respect to interstitials was attained due to the inadequate vacuum used and the high solubility of these impurities in solid Ce. Thus when only impure Ce is available, many metallic impurities can be reduced by zone refining.

Hukin and Jones (1976) zone refined Tb and observed that O, N and C moved in the direction opposite to the molten zone. They obtained significant purification with respect to these interstitial impurities as well as the metallic impurities. The zone melting was done under an atmosphere of pure argon in a horizontal cold crucible with induction heating.

3. Handling

3.1. *Storage*

The rare earth metals become more oxidation resistant with decreasing metallic radius. Eu which has the largest radius is by far the most reactive. Yb which has the second largest atomic radius is the lone exception and its reactivity with the atmosphere at room temperature falls between Sm and Gd. The lanthanides follow Eu in order from La through Tm and Lu. Sc can be placed at the end after Lu and Y between Tb and Dy. However, there is so little difference from Tb through Sc that the entire group can be classified as inert and can be stored in air. In part the reactivity of the metals also depends upon the structure of the oxide formed. For La through Nd the normal oxide is the hexagonal A-type, that for Sm and Gd is the monoclinic B-type while the remainder form the cubic C-type oxide. The first four metals are much more reactive than Sm and Gd, which are slightly reactive and the remainder as noted are inert.

Eu reacts quickly with moist air and should be handled at all times in an inert atmosphere. La oxidizes slowly, but continuously in air. As discussed below, electropolishing passivates the surface of La and it will stay shiny in air for 24 hours when the surface has been electropolished. However, a filed, sawed or sheared La surface will tarnish in less than $\frac{1}{2}$ hour. Thus La can be handled in air for short periods of time, ~10 minutes, without excessive tarnishing, but when stored for a long period, it should be stored in an inert atmosphere. Storage in a vacuum dessicator at 10^{-2} Torr (1.3 Pa) is acceptable, but slow oxidation still occurs. A more satisfactory method for long periods of storage is to seal the metal in evacuated Pyrex tubes sealed off with a torch. The same is true for Ce, Pr and Nd. All four, La, Ce, Pr and Nd, will oxidize completely when stored in air for long periods of time.

Storage in oil which is frequently used for alkali and alkaline earth metals is not recommended for the rare earth metals. A dry inert atmosphere is much better. The surface of the light lanthanide metals, Ce, Pr and Nd, also can be passivated by the methanol-perchloric acid electropolish described in section 3.3. The electropolished surface remains shiny from 1 to 3 days, depending on the perfection of the surface achieved.

3.2. *Cutting*

Large billets of the rare earth metals with the exception of Eu can be cut on an oil-cooled power hack saw or water-cooled carborundum cut-off wheel. Since the reactivity of these metals increases with temperature, any method chosen should have a means of keeping the metal cool. Intermediate size billets can be cut with a hack saw, but must be kept cool to prevent contamination especially by hydrogen which is formed by reaction of the metal with H_2O. The metal chips from sawing the light lanthanides, especially Ce and La, will readily ignite and

burn white hot. The metal saw chips from high purity heavy lanthanides, Y and Sc metals will not readily ignite, but those from impure metals will ignite from sparks generated by the saw. Therefore, the area should be kept free of the metal saw chips. The metals can be sheared. However, the sheared surface is more reactive than a cut or filed surface and should be filed and electropolished before the sample is heated to minimize contamination. After cutting, filing and machining operations the cold-worked surfaces should be removed to prevent contamination of the sample in subsequent operations. This is best accomplished by electropolishing, see section 3.3.

Water cooled carborundum wheels or oil cooled power hack saws can also be utilized to prepare small size, high purity samples with high surface to volume ratios. Again, the cold worked surface must be removed either chemically or electrochemically before the sample is heated to prevent introduction of interstitial impurities. The samples cut by the spark erosion machine, which traditionally is believed to yield a highly strain free surface, must also be ground smooth on a suitable emery paper and electropolished before the sample is heated. The most satisfactory device for cutting samples is a diamond impregnated Cu wheel run at a low speed employing a suitable cutting fluid. The surface which results is smooth and strain-free. Since the surface remained cool during cutting the contaminants introduced from the cutting fluid remain on the surface and can be removed from the metal surface with acetone. The slight traces of cold work introduced on the surface can be removed by electropolishing (see section 3.3). Single crystals can also be cut in this way without introducing strains.

Yb which is much softer than the trivalent metals tends to fill the teeth of the hack saw. For this reason shearing or cutting with a sharp blade works better than sawing. A carborundum wheel also works better than a saw, but the SiC particles from the wheel sometimes become imbedded in the surface of the metal. The saw blades used to cut La, Ce, Pr and Nd frequently become filled with metal. The metal caught in the saw blades oxidizes in a few days and the blades can be reused after cleaning off the oxide powder.

Eu is extremely soft and it also gums up the saw blades. A sharp knife or razor blade works the best for small pieces. Large pieces can be sawed if the blades are changed frequently. As mentioned above Eu should be handled in an inert atmosphere at all times.

In order to prevent cross contamination of one rare earth in another, a blade is reserved for each rare earth metal. If the blades are still sharp, they are stored for future use. Needless to say all cutting tools are cleaned and degreased before cutting or machining a rare earth metal sample.

3.3. *Cleaning*

The metals, La, Ce, Pr, Nd and to a small degree, Sm, continuously oxidize in air. A corroded piece of these metals can be cleaned with a file or a wire-brush wheel. The surface should be cleaned until it is shiny and an additional 1 mm of

metal surface should be removed to ensure complete removal of the intergranular corrosion products which are present near the surface. The cold worked surface introduced by filing is reactive toward moisture and should be removed chemically or electrochemically (see below). The surface of Eu can be cleaned by scraping with a sharp blade. There is no known chemical or electrochemical method for cleaning or polishing Eu.

An electropolishing procedure which has proved to be very useful for the rare earth metals was developed by Peterson and Hopkins (1964) and was extended to a "Universal" method by Hopkins et al. (1965). In this method, an electrolyte of 1% (or up to 6%) perchloric acid in absolute methanol is stirred and cooled continuously in a dry ice-acetone bath. In the original work a stainless steel cylinder served as the cathode. Pt is frequently employed as the cathode, especially when sample surfaces are being prepared for mass spectrometric studies. With a variable dc voltage supply, the amperage can be controlled to about 0.5 amps/cm^2. The amperage should be maintained at a level sufficient to generate small bubbles at the surface. Excessive bubbling of the electrolyte should be avoided. The sample is rinsed while cold in the dry-ice acetone bath, then rinsed with copious quantities of methanol to bring it to room temperature and remove all traces of acid. Due to the transformations which occur just below 0°C in Ce and Yb, an electrolyte that can be used at 0°C or above is generally required. The metallographic preparation of Ce is summarized in ch. 4 section 3.2. For Yb an electrolyte to 10 vol.% HCl in methanol may be employed at room temperature to clean the surface, but it does not leave a shiny finish as the low temperature perchloric-methanol procedure does.

3.4. *Cold working*

The preparation of fine-grained samples of the rare earth metals by alternately cold working and heat treating is frequently accompanied by contamination of the rare earth metal by interstitial impurities. The source of the impurities is the atmosphere, rolling mill or swaging dies. If small reductions are taken so as to keep the sample from becoming warm, the impurities will remain on the surface. Removal of the surface contamination before heat treatment by electropolishing (see section 3.3) will minimize the contamination.

A procedure developed by Owen and Scott (1973) for the preparation of 2 mm diameter rods of Gd can be used for most of the heavy rare earth metals. The Gd metal was arc melted into finger-shaped rods about 1.2 cm diameter. They were reduced 30% in diameter by swaging at room temperature, annealed for 1 hr. at 923 K and again swaged to give another 30% reduction in diameter. The alternate heat treatment and swaging was continued until 2.5 mm diameter was attained. The interstitial impurity O increased from 75 to 150 ppm by wt. during this procedure. Owen and Scott (1974) described a different procedure for Dy which required fewer heat treatments. The 1.2 cm diameter rods were encapsulated in mild steel and reduced 45% in diameter by swaging at 873 K. After removing the jackets by machining, the rods were swaged an additional 15%, then annealed at

1023 K in a 10^{-8} Torr (1.3×10^{-6} Pa) vacuum for 1 hour. The rods were again encapsulated in mild steel and swaged at 873 K to 3.8 mm diameter, the jackets removed and the rods swaged cold to 2.5 mm diameter. This procedure however, increased the O content from 19 to 294 ppm by wt.

The introduction of sufficient cold work to facilitate recrystallization can be accomplished by a simple 25% reduction in thickness if the starting sample is not more than 4 mm thick. The disturbed metal on the surface introduced by sawing or shearing must be removed by electropolishing to prevent contamination of the rare earth metal during cold rolling. After cold working the surface must again be electropolished before the sample is heated. By following this procedure, small grained samples can be produced with minimal contamination as shown by Spedding and Beaudry (1971) for Sc, Y, Gd, Tb, Dy, Ho, Er, Tm and Lu and by Beaudry and Palmer (1974b) for all the other rare earth metals except Eu.

The normally divalent metals Eu and Yb are very soft and can be cold worked extensively. Spedding et al. (1958) extruded Eu into a 3 mm diam. wire at 18,000 psi at room temperature. Owen and Scott (1970) reduced a 2.5 cm diam. rod of Yb to 0.2 cm by swaging and extruding without intermediate heat treatment.

3.5. *Heat treatment*

The recrystallization temperature of a metal is dependent on sample purity and amount of prior cold work as well as the melting point. High purity metals will recrystallize at a lower temperature than low purity metals. Metals with analyses approximately the same as given in tables 2.1, 2.3–2.5 were found by Spedding and Beaudry (1971) and Beaudry and Palmer (1974b) to be completely recrystallized in 20 hours when heated to the temperatures listed in table 2.11 after a 25% reduction in thickness.

In a study of the recrystallization and work hardening characteristics of 13 of the rare earth metals of commercial grade purity, Ross (1967) gave the temperatures listed in table 2.11 as "recommended annealing temperatures". The difference between the temperatures given might possibly reflect the difference in purity between the laboratory and commercial grade metals. Ross did not give a complete analysis of his metals. The temperature required to relieve stress and not cause recrystallization is somewhat lower than the temperatures given in table 2.11, which is the same as observed for other metals.

La which has a transition from dhcp to fcc at 310°C on heating retains some of the fcc when cooled. The complete conversion of an as-cast structure to the room temperature dhcp form cannot be accomplished by simply maintaining a temperature just below the transition. A cycle which has been shown to be quite effective is to cold roll the La to about 25% reduction in thickness, clean the surface electrochemically, heat in high vacuum to 425°C for 2 hours, cool to less than 200°C, heat to 290°C and maintain that temperature for 10 days. Mowry et al. (1976) showed recently that if the cast structure has sufficient strain in it, recrystallization in the dhcp range at 300°C will occur in about 10 days and will result in pure dhcp.

TABLE 2.11
Recrystallization temperatures of laboratory purity rare-earth metals and of commercial grade purity.

Rare-earth metal	Annealing temperature (°C)	
	Laboratory purity[a]	Commercial grade[b]
Sc	520	—
Y	520	750
La	c	—
Ce	325	450
Pr	400	450
Nd	400	600
Pm	(450)[d]	—
Sm	440	600
Eu	300	—
Gd	500	450
Tb	500	450
Dy	500	750
Ho	520	750
Er	520	600
Tm	600	—
Yb	300	400
Lu	600	—

[a]Metals with the analyses given in tables 2.1, 2.3–2.5 were recrystallized after 20 hrs at the temperatures given. [b]Ross (1967). [c]Recrystallization will occur at 300°C in dhcp La, however, a small amount of fcc usually remains. See the text for an alternate method of obtaining fully recrystallized pure dhcp La. [d]Estimated.

The thermal cycles and heat treatments required to obtain the various forms of Ce are discussed in ch. 4 sections 3.2 and 3.3. The hcp form of Yb was reported by Kayser (1971) to be the stable form below 270 K. The room temperature fcc form of Yb transforms martensitically to an hcp form when cooled below 270 K. The transformation is reversible with about a 20 degree hysteresis of the start of transformation on cooling and heating. The transformation is especially sensitive to the presence of impurities. A "new transformation" reported by Hurd and Alderson (1973) was shown by Beaudry and Gschneidner (1974) to be due to the presence of hydrogen in their sample and not a new polymorphic phase of Yb.

3.6. *Melting*

The vapor pressure of the rare earth metal at its melting point determines the method chosen to melt the metal. The low melting metals, La, Ce, Pr and Nd, which have low vapor pressures can be melted by any of the common methods,

e.g. arc-melting, electron beam melting, or melting in a Ta crucible with induction or resistance heating. The higher melting metals, Y, Gd, Tb and Lu, which have low vapor pressures can also be melted under vacuum or inert atmosphere by the various heating methods. However, when these metals are melted in refractory metal crucibles, contamination from the crucible occurs, due to the solubility of the refractory metal in the molten rare earth metal. Of the two refractory metals (Ta and W) used most frequently for crucibles, W is less soluble than Ta (Dennison et al. 1966a and 1966b), while Mo, Re, Nb and Hf are more soluble than Ta (Gschneidner, 1961a and Griffin and Gschneidner, 1971). The rare earth metals should not be melted in refractory oxide crucibles, since they will react and dissolve copious amounts of the oxide crucible. As far as we are aware the molten rare earth metals will react with and/or dissolve all other known refractory materials which might possibly be considered for crucibles.

The number of methods which can be used to melt Sc, Dy, Ho and Er is limited by the high vapor pressure of these metals at their melting points. Vacuum melting by induction in a cold crucible or refractory metal crucible or electron beam melting results in the loss of large quantities of metal. Cold crucible melting by induction as well as arc melting under an atmosphere of Ar decreases the vaporization to a tolerable amount. Because of its low mass He is not as effective as Ar. Melting in refractory metal crucibles results in the introduction of crucible materials as impurities.

Sm and Eu can be arc melted under argon with moderate losses due to volatilization. However, Yb which has a vapor pressure of 20 Torr (2.6×10^3 Pa) at its melting point and Tm which has a vapor pressure of about 73 Torr (9.5×10^3 Pa) at its melting point cannot be arc melted satisfactorily. Tm can be consumable-electrode-arc-cast without excessive vaporization. Since Eu and Yb do not dissolve Ta or W to any significant degree at their melting points, see table 2.5, these metals can be sealed in these type crucibles and melted. In spite of the 0.63% Ta and 0.32% W which are soluble in Tm at its melting point, sealed crucibles offer the most practical way of melting Tm. An alternate method to consolidate Tm is to pack as-distilled crystals of Tm in a Ta crucible, heat to 750°C for 2 hours to sinter, then swage or press at 25°C and reheat to 750°C for 2 hours. A third cold working and heat treating results in a nearly void-free piece of Tm metal.

3.7. *Machining*

All of the rare earth metals can be machined with the possible exception of Eu. However, specimens of Eu with various shapes can be produced by extrusion. The standard procedures for machining soft steels should be followed. The turnings of the light lanthanide metals and impure Sc, Y and heavy lanthanides metals ignite easily and burn white hot, therefore, they should not be allowed to accumulate on the lathe, drill, or other machining device.

4. Metallography

The metallographic examination of the pure rare-earth metals must be differentiated from the examination of impure rare earth metals which have a large quantity of second phase impurities. The preparation of impure metals for metallographic examination must take into account second-phase particle retention, the reactivity of the second phase and its hardness in addition to the properties of the pure metal.

The techniques described for cutting the rare earth metals in section 3.2 can also be applied to the preparation of metallographic specimens. The standard metallographic procedures outlined in Knechtel, et al. (1973) are recommended for preparing the rare-earth metal surfaces through the final grinding operation on 600 grit silicon carbide paper. However, the grinding procedure is somewhat improved if alcohol or kerosene is used as a lubricant instead of water. Metallographic procedures have not been developed for Eu. Because mechanical polishing methods always leave some worked material on the surface, the samples must be chemically or electrochemically treated to remove the cold worked surface. The best method of chemically or electrochemically polishing the pure rare earth metals for microscopic examination is the method described by Peterson and Hopkins (1964), see section 3.3 on cleaning the rare earth metals. The advantage of this electropolishing method is the resultant strain-free, unstained surface. The sample can be etched by simply turning off the current for about 1 minute before removing it from the electrolyte.

A chemical polish was reported by Roman (1965) for Gd, Dy, Ho and Er which worked well on commercial grade purity metals. His procedure starts with mounting the specimen in epoxy resin and grinding on 180, 400 and 600 grit silicon carbide abrasive papers with kerosene as a lubricant. After washing with acetone, the specimen is coarse polished with 9 μm diamond paste followed by 3 μm diamond paste. The chemical polish used for samples with a small amount of oxide inclusions contains 20 ml lactic acid, 5 ml phosphoric acid, 10 ml acetic acid, 15 ml nitric acid and 1 ml sulfuric acid. The solution is applied with a cotton swab for 10 to 15 sec, rinsed with ethyl alcohol and dried with a stream of air. The companion etchant contains 10 ml phosphoric acid, 10 ml lactic acid, 30 ml nitric acid and 20 ml acetic acid. If the specimen contains large amounts of oxides, the sample is mechanically polished with 1 μm and $\frac{1}{2}$ μm diamond paste before applying the above chemical polish for 2 or 3 seconds. This procedure probably works equally well on Sc, Y, Tb, Tm and Lu. As mentioned above the electropolishing method is the best for these metals if they do not contain second phase impurities.

Baker and Peterson (1976) have found that Roman's (1965) procedure will also work for La, Ce, Pr and Nd. It is especially valuable when slight traces (and greater amounts) of second phase impurities are present in these metals because the electropolishing method frequently leaves large stained areas on the surface near the second phase particles in these metals.

Yb which has a transition from fcc to hcp at about 260 K upon cooling cannot

be electropolished in the dry ice-acetone bath (200 K) if the pure fcc structure is of interest. Baker and Peterson (1976) have found that a chemical polish of 5–8 ml HNO_3, 58 ml H_3PO_4 and 22 ml of methanol swabbed on for 10 seconds works well. Kayser (1971) electrochemically thinned Yb in a 10 vol.% HCl in methanol solution at room temperature.

A metallographic technique which involved anodizing La and Ce (for Ce see ch. 4 section 3.1) was reported by Koch and Picklesimer (1967). In their method the samples are mounted in epoxy and the surface ground on silicon carbide papers to 600 grit using ethyl alcohol as a lubricant. The surface of La is then chemically polished with Roman's solution. After the surface is polished, it is anodized in a solution of 2 wt.% KOH in H_2O at 22 V. The anodic film gives good color contrast between grains. Although Koch and Picklesimer (1967) reported they could differentiate between fcc and dhcp grains in Ce and La due to the different colors, the present authors were not able to repeat the colors on pure dhcp La or Ce.

5. Preparation of single crystals

The first single crystals of the rare earth metals were grown by Behrendt et al. (1957 and 1958) who employed the Bridgman method with a pointed Ta crucible to grow a Nd crystal 3 mm on a cube edge and a Dy crystal about 4 mm on a cube edge. A year later an Y single crystal 1 cm in diameter by 2.5 cm long was grown by Carlson et al. (1959) by annealing an arc melted rod of Y at 1250°C for several hours. This method which is sometimes called the strain-anneal method, has been studied by many laboratories and their experiences are discussed in section 5.1. The other methods which have been used to grow rare-earth metal crystals are discussed below under the particular method.

5.1. *Recrystallization method*

The method of growing single crystals which involves the heat treatment of an arc melted button or any rapidly cooled sample to obtain single crystals is sometimes referred to as the "strain-anneal" method. In order to fit the strain-anneal category as defined by Aust (1963), a certain minimum strain must be introduced into a fully recrystallized specimen which is then heated to allow a few nuclei to form and to grow. It is more accurate to call the method simply "grain growth" which according to Aust is the annealing of a polycrystalline, cast material to obtain large grains. McEwen and Touborg (1973) called the heat treatment of an arc melted button the "recrystallization method" which according to Aust (1963) includes seven possible mechanisms, including grain growth and strain-anneal. We will include all samples heat treated in the solid state for the purpose of growing single crystals under the heading of "recrystallization", since in most cases the specific mechanism is not known. Table 2.12 lists the

TABLE 2.12
Largest known single crystal grown of each of the rare earth metals and the method used.

Metal	Size	Method	Reference
Sc	1.6 cm diam. × 3.5 cm	Recrystallization	Spedding et al. (1971)
Y	1.9 cm diam. × 4 cm	Recrystallization	Carnahan and Scott (1973)
La	None reported		
Ce (γ)	1 cm diam. × 1.5 cm	Floating zone	McMasters et al. (1978)
Pr	1 cm diam. × 2 cm	Floating zone	McMasters et al. (1978)
Nd	1 cm diam. × 2 cm	Floating zone	McMasters et al. (1978)
Pm	None reported		
Sm[a]	1.5 × 1.0 × 0.48 cm	Recrystallization	Reed (1971)
Eu	0.8 cm diam. × 2 cm	Czochralski	McEwen and Touborg (1973)
Gd	2.5 × 2.0 × 1.5 cm	Recrystallization	Present authors (see text)
Tb	3.6 cm diam. × 2 cm	Recrystallization	Present authors (see text)
Dy	3.0 × 1.5 × 0.5 cm	Recrystallization	Nigh (1963)
Ho	3.6 cm diam. × 2.1 cm	Recrystallization	Present authors (see text)
Er	1.6 cm diam. × 10 cm	Arc zone melting	Schmidt and Carlson (1976b)
Tm	1.0 × 1.0 × 0.5 cm	Recrystallization	Edwards and Legvold (1968)
Yb	1.0 × 1.0 × 1.0 cm	Bridgman	Present authors (see text)
Lu	1.3 cm diam. × 10 cm	Arc zone melting	Carlson et al. (1975)

[a]See text.

largest crystal grown of each of the rare-earth metals and the method used to grow it.

The method of Carlson et al. (1959) of annealing an arc melted rod to grow crystals was extended by Nigh (1963) to Gd, Tb, Dy, Ho, Er and Tm. Nigh obtained his best results for Gd by annealing in a temperature gradient of 25°C/cm with a maximum temperature of 1225°C. For Tb, Ho and Er his best results were obtained by heating in a constant temperature zone for 18 hours approximately 125°C below the melting point of the metal. Dy was heated to 1200°C for 18 hours, then to 1250°C for 6 hours, and finally 1300°C for 18 hours to obtain his largest crystal which is listed in table 2.12. A similar scheduled increase of temperature for Y with a maximum temperature of 1350°C for 8 hours gave the best results. Nigh reported good grain growth for Tm at 1350°C for 6 hours.

A study of the growth of Gd crystals was reported by Peterson et al. (1965) who used a tapered tensile specimen to determine the critical stress needed to promote grain growth. A crystal of Gd 2.5 cm long and 1 cm diameter was obtained. A similar method was investigated by Tonnies and Gschneidner (1971) for Pr and Nd but crystals only a few mm in length were obtained.

In several cases authors have reported growing crystals by the recrystallization technique, but did not state a size for the crystals grown. Whittaker (1968) prepared rods by a cold-crucible technique in which the samples were levitated and melted by high frequency induction. The rods were then heated by induction to 100°C below their melting point for 8 hours. Grains up to 20 mm in length and 7 mm diameter were prepared. In his studies Whittaker (1968) noted an inverse relationship between the size of crystals grown by this technique and

the presence of a second phase. Impurities either act as nucleation sites for new grains or retard the growth of grains. Savitskii et al. (1965) had noted that metals purified by distillation before the arc melting step resulted in larger crystals than the same process did with less pure metals.

The large Ho crystal (168 g) referred to in table 2.12 was grown in several steps. After the initial heat treatment of an arc melted button at 1340°C for 24 hours, several large and a few small grains were present. The smaller grains were lightly peened to induce sufficient strain to encourage continued growth of the large crystal, but insufficient to cause nucleation of new grains. Then the sample was heated to 1340°C for 16 hours. After the second treatment, the sample was nearly one crystal. The small grains again were peened and the sample heated to 1360°C for 18 hours. After this third heat treatment the entire button was one grain. Two separate buttons of this size were grown. The method is, unfortunately, difficult to put in quantitative terms because the amount of peening is based on a "trial and error" type experience. Excessive peening will cause new grains to form and to grow. In the case of Tb the arc-melted button was peened before it was heated to 1220°C for 25 hours. One crystal weighing 152 g resulted. The large crystal of Gd referred to in table 2.12 was grown by heating an arc melted button to 1225°C for 24 hours. The Ho, Tb and Gd were of the high purity discussed in section 1.1. The large crystals which were obtained probably reflects the high purity of the metals, and these results are consistent with the relationship suggested by Whittaker (1968) and Savitskii et al. (1965).

The major advantage of the recrystallization method is that alloys can be prepared of the desired composition by arc melting or some other suitable method of melting and then heat treated without changing composition. This is even true of metals with wide differences in vapor pressure. Alloys with a volatile component can be heat treated under pressure or in a sealed refractory metal crucible. McEwen and Touborg (1973) used an overpressure of 4 atmospheres while arc melting Tm alloys to prevent excessive vaporization of Tm. The alloys were then sealed in Ta to prevent loss during heat treatment. They also produced crystals of Y, Sm, Gd, Tb, Dy, Ho, Er, Tm, and many other intra-rare earth alloys.

Reed (1971) grew large crystals of the isotopes of Sm, Dy and Er which have low neutron capture cross-sections. The large Sm^{154} crystal which he grew and is referred to in table 2.12 was grown by heat treating an arc melted button at 917°C for 96 hours. Since Mardon and Koch (1970) have shown Sm transforms from an hcp structure to the rhombohedral structure below this temperature, the crystal either transformed to a pseudocrystal during cooling or was in a metastable hcp form at room temperature.

5.2. *Vapor deposition*

The first crystal of the rare earth metals grown from the vapor for a property determination (its crystal structure) was a Sm sample grown by Daane, et al. (1953). Schieber (1967) reported crystals of Sm up to 25 mm long grown by vapor

deposition. However, since the temperature of the deposited crystal was 857°C which is above the rhombohedral to hcp transition of Sm (see section 6.2), the crystal either transformed on cooling or was in a metastable hcp form at room temperature. The largest crystals of Eu and Tm he obtained were 2 to 3 mm long, and the Yb crystal he grew was 5 mm long. Cadieu and Douglass (1969) grew a crystal of Gd 1 cm^3 in volume by depositing Gd vapor on a W rod which extended several cm above the Ta crucible and acted as a radiator to keep the substrate cool. The openings between W rod and crucible lid were initially sealed with condensed Gd vapor under a vacuum of 3×10^{-7} Torr (4×10^{-5} Pa) resulting in a sealed crucible which prevented the introduction of gaseous impurities during the 36 hours of crystal growth.

5.3. *Bridgman method*

The Bridgman method which was employed by Behrendt et al. (1957 and 1958), Green et al. (1961) and Hall et al. (1960) for the higher melting rare earth metals, has the disadvantage of contamination from the crucible material. This technique also has a second disadvantage in that as the temperature is lowered the dissolved crucible material becomes supersaturated and begins to precipitate out of solution giving rise to nucleation sites for new grains to form and to grow. This problem, however, can be overcome as shown by Green et al. (1961) who grew an Er crystal 1 cm in diameter by 5 cm in length. The low melting rare-earth materials which do not dissolve appreciable amounts of Ta or W at their melting points may be grown by the Bridgman technique. The crystal of Nd grown by Behrendt et al. (1957) by the Bridgman method probably did not contain more than 50 ppm Ta, but the crystals were small compared to the Nd crystals grown by the floating zone method (see section 5.5). The authors have grown a crystal of Yb by the Bridgman method which measures about 1 cm on an edge (cube). The pointed Ta crucible was lowered through the temperature gradient at a rate of 2.5 cm per hour. To prevent excessive refluxing of the Yb, the space above the metal was filled with a Ta crucible as shown in fig. 2.4.

5.4. *Czochralski method*

The Czochralski method was reportedly used for growing a Gd crystal by Rutter and Lawyer [see Graham (1962)], but no details were given. The traditional Czochralski method has the same disadvantage as the Bridgman method – impurities are introduced from the crucible. This disadvantage was overcome by Hukin (1971) who used a cold crucible levitation technique to contain the molten metal. In addition to pulling a crystal from the molten pool of metal, he also grew crystals by slowly reducing the power which allowed the levitated pool of metal to touch the water cooled copper in one spot. The molten metal froze at this point, nucleating one grain which then was allowed to grow by gradual reduction of the power until the whole sample was frozen. In spite of the transformation in Gd and Y close to their melting point, 2 cm × 1 cm crystals were grown of the hcp allotrope by this method.

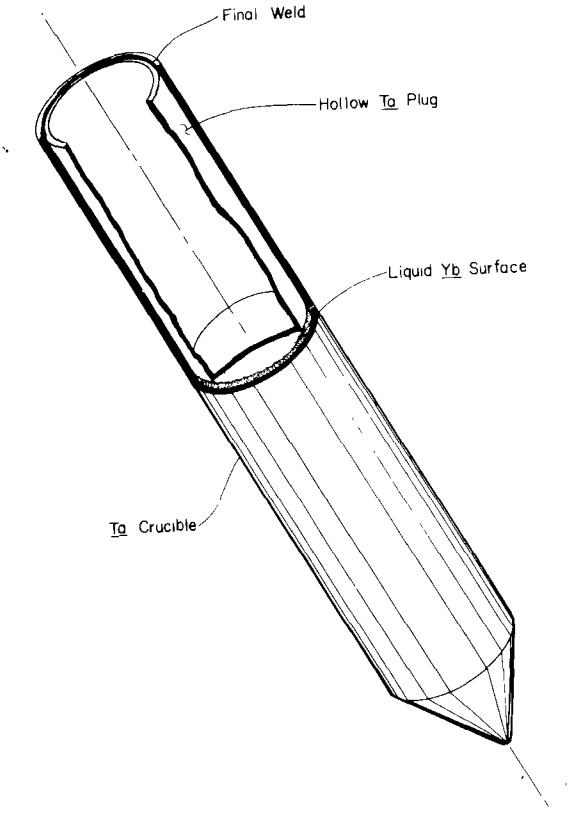

Fig. 2.4. Bridgman crucible for volatile metals.

5.5. *Zone melting*

The first rare earth crystal grown by moving a molten or hot zone along a bar of metal was Y (Carlson et al., 1964). The Y was contained on a water cooled copper hearth and an arc zone was moved along the top of the bar keeping the temperature of the zone below the transformation temperature. Y crystals 1.2 cm diameter × 3 cm long were grown by this method. In 1975 Carlson et al. reported the growth of a crystal of Lu 1 cm diameter × 10 cm long. Since Lu does not have a high temperature transformation, a molten zone was moved along the bar to grow the Lu crystal. Schmidt and Carlson (1976b) also grew a single crystal of Er 1.3 cm diameter × 10 cm long by arc zone melting.

Brissot and Martres (1965) employed a floating zone technique to grow crystals of Gd but did not report the size. Crystals of unspecified size of Sc, Y, Gd, Tb, Dy, Ho and Er were grown by Whittaker (1968) by induction heating employing a specially designed water cooled copper concentrator.

Tonnies and Gschneidner (1971) used an electron beam floating-zone method and obtained a Pr crystal 0.6 cm × 0.4 cm × 4 cm long. However, they were

unable to obtain large Nd crystals. McMasters et al. (1978) have obtained crystals of Nd and Pr 1 cm diameter × 2 cm long by passing a levitated molten zone along a sample held on a cold crucible.

5.6. *Crystallographic transformation method*

This method could possibly be classified as a "recrystallization method" since the crystals grow in the solid state but it is treated separately because of the requirement for temperature cycling. Tonnies and Gschneidner (1971) grew crystals of Pr and Nd by this method. Pr and Nd transform from dhcp to bcc on heating at 795 and 863°C, respectively. Tonnies and Gschneidner (1971) heated an arc melted bar of Nd to 985°C for 6 hours, cooled to 800°C and held for 96 hours, repeated this cycle 3 times and held the sample at 800°C for 168 hours on the last cycle. They obtained a crystal 0.4 cm × 0.5 cm × 1 cm. A similar cyclic heating for Pr yielded a crystal 1.6 cm diameter × 2.5 cm long.

5.7. *Solid state electrotransport*

This method might also be classified as a "recrystallization method". Experimentalists have observed that large grains form when the samples they are purifying by solid state electrotransport are maintained at high temperature for a long period of time (see section 2.3). The advantage of this method is that highly purified crystals are obtained. The disadvantage is that the crystals generally have one particular orientation parallel to the length of the rod axis, while the size of the crystal in the other directions is limited to the diameter of the rod (0.25 to 0.6 cm). Generally the other orientations do not grow parallel to the rod axis during electrotransport.

In an electrotransport purification study Jordan et al. (1974) grew a Gd crystal 0.6 cm diameter by 2.5 cm long which had a resistance ratio of 250. A small sphere approximately 0.3 cm diameter was spark machined from this crystal, polished and etched. X-ray Laue patterns of the sphere showed it to have a maximum mosaic spread of approximately 1 minute of arc.

When larger crystals of a particular orientation are required, the solid state electrotransport method can still be used to achieve purification. The single crystal is grown by another method, oriented, and cut in the desired direction with the long dimension parallel to the rod axis and with a cross-section which matches the diameter of a polycrystalline rod of the same metal. The single crystal is butt welded to the polycrystalline rod and then purified by electrotransport. Schmidt (1976) purified a single crystal of Gd 0.6 cm diameter by 2 cm long with the *c*-axis parallel to the rod length by this method. Carlson et al. (1975) cut a single crystal of Lu 0.31 cm × 0.31 cm × 10 cm from a larger crystal which had been grown by arc zone melting, then purified it by electrotransport, and obtained a pure section with a resistance ratio of 60.

6. Crystal structure

6.1. *Room temperature structures*

The room temperature structures for most of the rare earth metals have been known for about 40 years. The values for the room temperature lattice constants which had been reported prior to 1965 were summarized and averaged by Gschneidner (1965). The average deviations were large, ranging from 0.002 Å for Sc to as much as 0.06 Å for Sm. Since some of the values had been determined on less pure metals, the deviations were believed to be due to impurities in the metals. However, Spedding and Beaudry (1971) noted that the lattice parameters determined on the same purity metal by different workers also varied indicating that impurities were introduced in the preparation of the X-ray samples. They carried out extensive studies on sample preparation of Sc, Y and the heavy lanthanides (Gd–Lu) and showed that the impurities were introduced in the preparation of annealed filings. They developed a technique which overcame this problem. Solid samples in the form of cylinders were filed out of larger well-characterized small-grain samples. The cold worked surface introduced by filing was removed by electropolishing. In this way, the surface to be X-rayed was not heated after preparation. They showed that H had a large effect on room temperature lattice parameters and could explain the variations noted in the lattice parameters when the samples were prepared by different methods. Since the samples they prepared were well characterized and their method was shown to give accurate, reproducible results, their values for the hcp type rare earth metals are given in table 2.13. The analyses of the metals given in section 1.1 are typical of the purity of the metals examined in their lattice parameter study. Beaudry and Palmer (1974b) extended the study to the remaining rare earth metals and their results are also given in table 2.13.

Since the light lanthanide metals are more reactive in air one might expect a greater change in the lattice parameters of these metals when they are determined from filings than the change observed in the less reactive hcp type rare earth metals. However, there is very little, if any, change due to using filings compared with a solid sample for the light lanthanide metals. The change is the most pronounced in the lanthanides from Tb to Lu (excluding Yb) and Sc and Y. This change in lattice parameter is apparently related to the solubility of hydrogen in these metals. Beaudry and Spedding (1975) showed the solubility of hydrogen increased from less than 0.1 at.% in Gd to 20.6 at.% in Lu. The effect of H on the lattice parameters also increased from essentially 0 in Gd to a maximum in Lu.

The crystal structure sequence as one proceeds along the lanthanide series from La to Lu goes from fcc to hcp with two intermediate structures which are composed of a mixture of both fcc and hcp close-packed layers, one being 50% of each and the other being $\frac{2}{3}$ hcp and $\frac{1}{3}$ fcc. The relationship of the close-packed layer sequences in these four structures is shown in fig. 2.5. A layer is classified as an h (hexagonal) layer if the atoms just above and below the layer are aligned

TABLE 2.13
Crystal structure of the rare earth metals and related properties at 24°C

Rare earth metal	Crystal structure[a]	Lattice Constants(Å)		Metallic Radius CN = 12 (Å)	Atomic Volume $\left(\frac{cm^3}{mol}\right)$	Density (g/cm^3)
		a_0	c_0			
La	dhcp	3.7740	12.171	1.8791	22.602	6.146
Ce	fcc	5.1610	—	1.8247	20.696	6.770
Pr	dhcp	3.6721	11.8326	1.8279	20.803	6.773
Nd	dhcp	3.6582	11.7966	1.8214	20.583	7.008
Pm	dhcp	3.65	11.65	1.811	20.24	7.264
Sm	rhomb[b]	3.6290	26.207	1.8041	20.000	7.520
Eu	bcc	4.5827	—	2.0418	28.979	5.244
Gd	hcp	3.6336	5.7810	1.8013	19.903	7.901
Tb	hcp	3.6055	5.6966	1.7833	19.310	8.230
Dy	hcp	3.5915	5.6501	1.7740	19.004	8.551
Ho	hcp	3.5778	5.6178	1.7661	18.752	8.795
Er	hcp	3.5592	5.5850	1.7566	18.449	9.066
Tm	hcp	3.5375	5.5540	1.7462	18.124	9.321
Yb	fcc	5.4848	—	1.9392	24.841	6.966
Lu	hcp	3.5052	5.5494	1.7349	17.779	9.841
Sc	hcp	3.3088	5.2680	1.6406	15.039	2.989
Y	hcp	3.6482	5.7318	1.8012	19.893	4.469

[a]dhcp = double-c hexagonal close-packed; fcc = face-centered cubic; bcc = body-centered cubic; hcp = hexagonal close-packed. [b]Rhombohedral is the primitive cell. Lattice parameters given are for the non-primitive hexagonal cell. A value of 6.022045×10^{23} for Avogadro's number was used in calculating the atomic volume and density.

directly above one another, as shown in fig. 2.5A for the atoms in the A-layers above and below the B-layer. A layer is classified as a c (cubic) layer if the atoms in the neighboring layers do not line up directly over one another, but are rotated 60°. This is illustrated by considering layer B in fig. 2.5B where the atoms in the C-layer do not lie directly above the A-layer. Thus for a hcp structure the stacking sequence is hh, hh and for the fcc it is ccc, ccc. In the dhcp structure the sequence is chch, chch, i.e. 50% hexagonal – 50% cubic and in the Sm-type the sequence is chhchhchh, chhchhchh, i.e. 33% cubic and 66.7% hexagonal. Gschneidner and Valletta (1968), Gschneidner and Pearson (1968) and Falicov and Goncalves da Silva (1971) suggested that the crystal structure sequence can be explained by hybridization of some of the 4f electrons and s and d valence electrons which is a maximum at the beginning of the lanthanide series and accounts for the fcc structure. The 4f–sd valence interaction is thought to decrease with increasing atomic number and no longer becomes effective for elements beyond Gd, thus giving rise to the hcp structure. Between Ce and Gd, one finds the dhcp phase with 50% hexagonal character for Pr, Nd and Pm and the unique Sm-type structure with $\frac{2}{3}$ hexagonal character for Sm. However, Hodges (1967) and Havinga et al. (1969) offered alternate explanations for the crystal structure sequence which do not involve the 4f electrons. But these latter

theories are unable to account for the variation of the melting and boiling points of the lanthanide metals. However, the variation in these properties can be explained if the 4f electrons contribute to the bonding, see section 7.

Crystallography of the Rare-Earth Metals

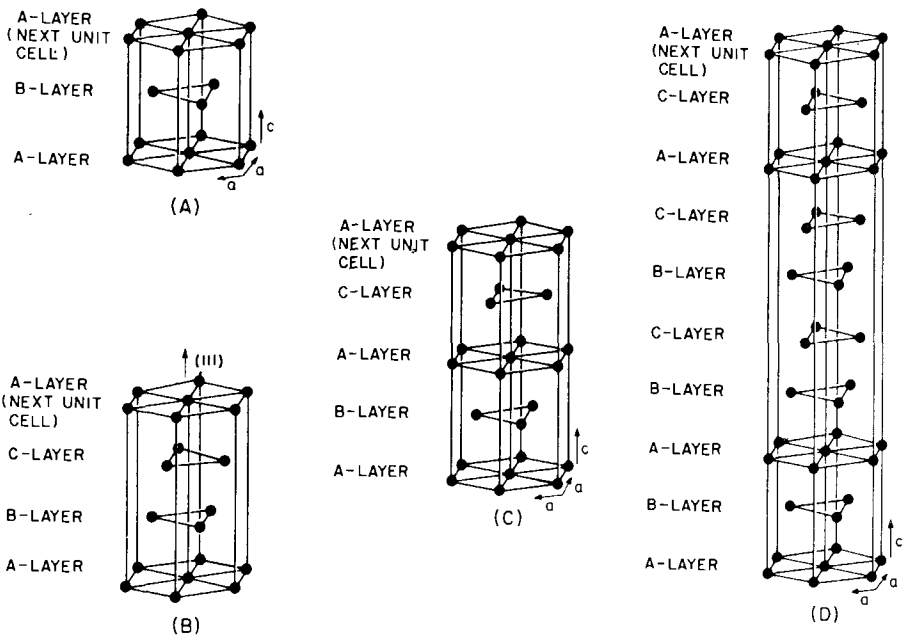

Fig. 2.5. The four closed-packed structures observed in the rare earth metals. A – the normal hcp structure (Mg-type), B – the normal fcc structure (Cu-type), C – the double c-axis hexagonal close-packed (dhcp) structure (La-type), and D – the triply primative hexagonal Sm-type structure (after Gschneidner, 1961b).

6.2. *Allotropic forms above room temperature*

The room temperature close-packed structures of the rare earth metals transform to body-centered cubic (bcc) in 12 of the 17 rare earth metals when heated. Eu is bcc over the entire temperature range that it is solid. The transformations in most cases were first observed by thermal analysis and/or resistivity measurements (e.g. Spedding et al., 1957).

The high temperature structure of La, Ce, Pr, Nd, Gd and Yb was shown to be bcc by Spedding et al. (1961) who also determined the lattice parameters of the bcc form of these metals. The bcc nature of the high temperature form of Y was inferred from phase diagram studies of the Y–Mg system by Gibson and Carlson (1960) and the Th–Y system by Eash and Carlson (1960). The continuous solid solubility observed by Spedding et al. (1962) in the La–Y and Gd–Y systems also confirmed the high temperature bcc nature of Y. The high temperature form of

Sc (β–Sc) is probably also bcc because β–Sc and β–Ti, which is bcc, form a continuous series of solid solutions (Beaudry and Daane 1962). Miller and Daane (1964) quenched rare earth-magnesium alloys from a high temperature and measured the lattice parameters of the bcc form which was retained at room temperature. An extrapolation of the lattice constant versus Mg content to 0% Mg gave the reported lattice constant of the bcc form of the heavy lanthanide metals. Although a bcc phase can be stabilized for each of the rare earth metals this does not necessarily mean they all have a high temperature bcc form because some of them remain hcp until they melt – Ho, Er, Tm and Lu. In a study of the phase equilibria of the heavy lanthanide metals, Spedding et al. (1973) showed that pure Ho and Er do not have a bcc form, even though earlier published results on less pure metals suggested a high temperature transformation. The presence of a bcc form of Tm and Lu is also doubtful since no thermal arrest was observed in these metals by differential thermal analysis (DTA). The high temperature bcc lattice parameters of the rare-earth metals are given in table 2.14.

TABLE 2.14
Structures, transition temperatures and lattice parameters of the allotropic forms of the rare earth metals stable above room temperature.

Rare Earth	Transition[a] Temp. (°C)	Structure	Lattice Parameter (Å)	Temp. (°C)	Reference
Sc	1337	bcc	Not determined	—	
Y	1478	bcc	4.11[b]	24	Eash & Carlson (1960)
			4.04[c]	24	Gibson & Carlson (1960)
La	310 heating 260 cooling	fcc	5.303	325	Spedding et al. (1961)
	865	bcc	4.26	887	Spedding et al. (1961)
Ce	726	bcc	4.12	757	Spedding et al. (1961)
Pr	795	bcc	4.13	821	Spedding et al. (1961)
Nd	863	bcc	4.13	883	Spedding et al. (1961)
Pm	890	bcc	—	—	
Sm	734 heating 727 cooling	hcp	$a = 3.6630$ $c = 5.8448$	450[d]	Mardon & Koch (1970)
	922	bcc	Not determined		
Gd	1235	bcc	4.05[c]	24	Miller & Daane (1964)
			4.06	1265	Spedding et al. (1961)
Tb	1289	bcc	4.02[c]	24	Miller & Daane (1964)
Dy	1381	bcc	3.98[c]	24	Miller & Daane (1964)
Yb	795	bcc	4.44	763[e]	Spedding et al. (1961)

[a]The transition temperatures are the best values from the Ames Laboratory determined by differential thermal analysis on metals of the purity listed in tables 2.1, 2.3, 2.4 and 2.5 except for Pm which is taken from Angelini and Adair (1974). [b]Determined by extrapolation to 0% solute of a vs. composition data for Y–Th alloys. [c]Determined by extrapolation to 0% solute of a vs. composition data for R–Mg alloys. [d]The hcp phase was stabilized by impurities and the temperature of measurement was below the transition temperature listed in column two. [e]The bcc phase was stabilized by impurities and the temperature of measurement was below the transition temperature listed in column two.

La and Sm have an additional transformation above room temperature. La transforms from dhcp to fcc at 310°C on heating. Impurities tend to stabilize the high temperature fcc form. La containing 0.8 at.% O heat treated at 400°C for 15 minutes and quenched to room temperature will retain about 95% of the fcc form. However, La of the purity given in table 2.1 will transform to over 50% dhcp even when quenched. The fcc to dhcp transition was shown to be a martensitic type transition by Marcinkowski and Hopkins (1968). The *complete* conversion of fcc to dhcp is also difficult. Beaudry and Palmer (1974b) showed that heat treatment of an as-cast structure for 2 weeks at 275°C did not result in complete conversion to dhcp. They showed that a cold worked sample, heat treated for 2 hours at 425°C to give a recrystallized and strain-free sample of fcc phase would transform completely to dhcp when cooled 100°C below the transformation (210°C), then reheated to within 25°C of the transformation and maintained at that temperature (285°C) for 10 days.

Marden and Koch (1970) showed by resistivity, X-ray diffraction and dilatometry that Sm transforms from the room temperature rhombohedral form to another close packed form at about 600°C. The high temperature form was shown to be hcp. They also observed that the transition temperature was purity dependent. Further studies by DTA in our laboratory on Sm with the purity listed in table 2.5 gave the transition temperature listed in table 2.14 which is considerably higher than the 600°C reported by Mardon and Koch (1970). Kumar and Srivastava (1969) observed an hcp structure in thin films of Sm by electron diffraction. The lattice parameters which they determined were considerably larger than those reported by Mardon and Koch (1970). Boulesteix et al. (1970a) observed Sm to be dhcp in a study of thin films by X-ray diffraction. However, the X-ray data of Mardon and Koch (1970) on bulk samples showed that the hcp form is the stable form between the low temperature rhombohedral form and the high temperature bcc allotrope.

Bucher et al. (1969) have observed an fcc form of Pr and Nd in splat-cooled samples. Since the metals were quite impure, it is possible the fcc phase observed was impurity induced and/or induced by the strains of splat-cooling.

There have been several papers which have appeared in the last five years concerning unusual lattice parameters and crystal structures in thin films of the rare earth metals. It is believed that these results are for highly contaminated metal which results from the high reactivity of the metallic rare earth thin films with residual gaseous impurities in the "high" vacuums [$\sim 10^{-8}$ Torr (10^{-6} Pa)]. Boulesteix et al. (1970b) and Gasgnier et al. (1974) have shown many of these structures to be impurity induced.

6.3. *Allotropic forms below room temperature*

The crystallographic transitions which occur in the Ce below room temperature are discussed in ch. 4 section 2.2. Yb has been observed to transform on cooling from its room temperature fcc form to an hcp structure at 270 K by Kayser (1970). The transformation occurs martensitically with an M_s temperature of

approximately 260 K and an A_s temperature of 280 K. The lattice constants determined by Kayser (1971) at 296 K are $a = 3.8799$ Å, $c = 6.3859$ Å. Studies by Bucher et al. (1970) have confirmed the existence of an hcp structure of Yb below room temperature.

The many magnetic transitions below room temperature in the rare earth metals are discussed in ch. 6. The ferromagnetic ordering of Tb at 220 K was shown to be accompanied by a transition from an hcp to an orthorhombic symmetry by Darnell (1963) who measured the lattice parameters versus temperature of single crystal Tb and found the h00 and hk0 reflections were each split into two components. These components were indexed on the basis of an orthorhombic cell which showed an expansion along the b direction from 6.244 Å at 220 K to 6.263 Å at 77 K and a contraction along the a direction from 3.605 Å to 3.588 Å over the same temperature interval. This distortion corresponds to the positive magnetostriction observed in Tb by Belov et al. (1961).

A discontinuous change in the lattice parameters of Dy was reported by Darnell and Moore (1963) to occur at 86 K, the temperature of the first order antiferromagnetic-ferromagnetic transition. The a parameter which is the same for the hcp form as for the orthorhombic form changes from 3.587 to 3.595 Å at 86 K on cooling while the b of the orthorhombic form ($b = a\sqrt{3}$) changes from 6.212 to 6.184 Å. Below 86 K the distortion which occurs is opposite in sign to Tb, that is, the a parameter increases and the b parameter decreases. None of the other lanthanide metals have been observed to transform crystallographically when they undergo a magnetic transition.

6.4. *Metallic radius, atomic volume and density*

The metallic radius, atomic volume and density are listed in table 2.13 and were derived from the room temperature lattice parameters also given in the same table. The metallic radius for the hexagonal metals is the average of the distance between atoms in a close-packed plane and the distance between the atoms in neighboring planes. For bcc Eu the radius was corrected from a coordination number, CN, of 8 to a CN of 12 by using the method of Teatum et al. (1968). A plot of the metallic radii is shown in fig. 2.6, and it is seen that the radii for the trivalent lanthanides exhibit a general decrease from La to Lu with a cusp at Gd. Also noted are deviations from the trivalent curve at Ce, Eu and Yb, which are due to a valence in excess of 3 for Ce (see ch. 4 section 2.3), and divalency for Eu and Yb. Anomalies in other physical properties, including the magnetic susceptibility, confirm these valence states for Ce, Eu and Yb metals (see table 2.13 and sections 7 and 8). Indeed, Gschneidner (1969) noted that in their chemical, metallurgical and physical behaviors, Eu and Yb can be considered to be members of the "baride" series of elements, where Ba has no 4f electrons, Eu a half-filled $4f^7$ level and Yb a completely filled $4f^{14}$ level, analogous to the corresponding trivalent lanthanides La, Gd and Lu.

A plot of the atomic volumes of the lanthanide metals would be similar to that

of the radii, with the Ce value falling below the curve established by the trivalent lanthanides and the Eu and Yb values rising significantly above the curve. The plot of the density would show an inverse behavior – a rise in the density on going form La to Lu and large dips at Eu and Yb with a slight departure to larger values at Ce.

For a number of years chemists have been discussing small variations from a smooth plot of a lanthanide property (P) vs. the atomic number. These properties include thermodynamic quantities, stability constants, ionic radii and oxidation potentials (for a review of the state-of-the art see Sinha, 1975). Scientists found that P formed two branches approximately symmetrical about Gd, and each branch consisted of two segments joined by Nd–Pm in the first half and Ho–Er in the second half. These have been called the "double-double" effect by the Polish investigators Fidelis and Siekierski and the "tetrad" effect by the American investigators headed by Peppard (Sinha, 1975). In order to see if this occurs for the metallic lanthanides, the radius for trivalent metals has been plotted on an expanded scale in fig. 2.7a, and it is seen that no such segments are found in either the first half or second half of the series. Instead one sees that the points lie on a single straight line in each half if one ignores La, Gd and Lu, which have respectively no 4f electrons, a half filled 4f level and a completely filled 4f level. The "inclined W" plot of Sinha (P vs the L quantum number) is

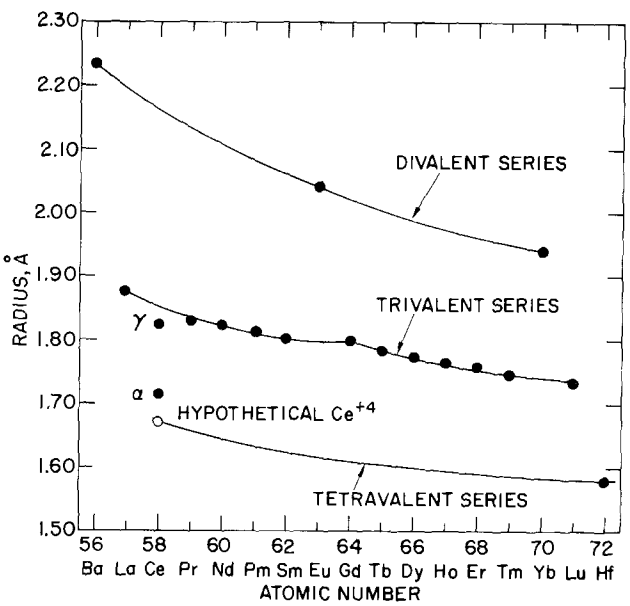

Fig. 2.6. The metallic radii for CN of 12 vs. the atomic number for Ba, the lanthanides and Hf metals. γ refers to γ–Ce, the fcc room temperature form and α refers to α–Ce, the collapsed fcc low temperature or high pressure form (see ch. 4 sections 2.1 and 2.2). The radius of hypothetical Ce^{+4} is taken from Gschneidner and Smoluchowski (1963).

shown in fig. 2.7b and except for the Gd–Ho segment the agreement is poorer than that observed in (1) the simple radius vs. atomic number plot (for Nd–Sm and Tb–Tm) shown in fig. 2.7a, and (2) that normally observed by Sinha in his inclined W plots for other properties.

The anomalous radii of La, Gd and Lu compared to the radii of the other lanthanides is thought to be due to crystal field effects (Gschneidner and Valletta, 1968). For La, Gd and Lu there is no crystal field contractions of the radius because the 4f wave functions are spherically symmetrical. For the other 4f configurations the crystal fields cause a contraction of the radius. And since the radial extent of the 4f wave function is larger for the first half of the series the crystal field contraction would be expected to be greater for the Pr–Sm series than for the second half of the series, Tb–Tm. This is evident by the difference seen in fig. 2.7a between the experimentally observed radius for La, Gd and Lu and the radius which is obtained by extrapolation of the radii vs. atomic number segments for the lanthanides with non-spherically symmetrical 4f configurations, i.e. Δr (where r is the radius) = 0.033 for La, = 0.015 or 0.009 for Gd and = 0.006 for Lu. It is quite possible that the effect which gives rise to the double-double or tetra effect is operative in the metals, but is over shadowed by the crystalline field contraction of the radius.

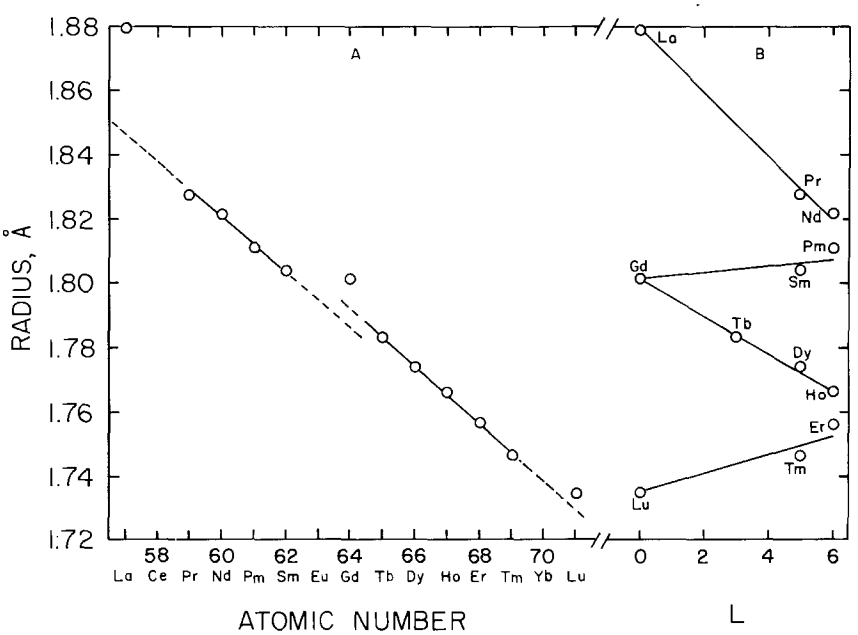

Fig. 2.7. (a) An expanded plot of the metallic radius (CN = 12) of the trivalent lanthanide metals vs. the atomic number. (b) The "inclined W" plot for the metallic radius (CN = 12) vs. the total angular momentum quantum number, *L*.

7. Transformation, melting and boiling points, vapor pressure and heat of sublimation

The high temperature (>25°C) transformations for the rare earth metals are found listed in table 2.14 and those for the close-packed (fcc, dhcp or hcp) to bcc transformation of the lanthanide metals are shown in fig. 2.8. The low temperature transformations (<25°C) for Ce are discussed in ch. 4 section 2, and for Tb, Dy and Yb in section 6.3 of this chapter. Examination of fig. 2.8 shows that the close-packed to bcc transformation temperatures roughly parallels the melting points, but interestingly enough the difference (which is the temperature range for the existence of the bcc phase) is a maximum on both sides of Eu and decreases as one goes toward each end of the lanthanide series. This is shown plotted in fig. 2.9, where we see an almost symmetrical curve about Pm. The reason for this behavior is not known.

The melting points of the rare earth metals (see tables 2.15 and fig. 2.8) have been redetermined by the authors over the past 6 years on metals which have chemical purities comparable to those listed in section 1.1, except for Pm, which is taken from Angelini and Adair (1974). The rare earth metal melting points are listed in table 2.15 and are plotted in fig. 2.8 for the lanthanides. The low melting points for Eu and Yb are related to their divalent character, in agreement with other physical properties for these two elements as compared with the trivalent lanthanides (sections 6.4 and 8.0). The melting points of the trivalent lanthanide metals as a whole are anomalous when compared to those of Sc, Y and the remainder of the periodic table. That is, the melting points of the light lanthanides are 500 to 700°C too low from that expected from the trends in the melting points in the first and second transition groups of metals, but those of the heavies are near what one expects, especially near the end of the lanthanide series. Matthias et al. (1967) and Gschneidner (1971) have suggested that the low melting points are due to hybridization of the 4f electrons with the sd valence electrons. To date this is the only reasonable explanation proposed for the melting point trends for the lanthanide metals, and is in agreement with the explanation advanced for the observed crystal structure sequence in the lanthanide metals (see section 6.1).

The boiling points, heats of sublimation at 25°C, and the temperatures at selected vapor pressures are also summarized in table 2.15. The values are taken from Hultgren et al. (1973) who have critically analyzed the available literature data and determined the best values for these quantities. The boiling point and heat of sublimation of Pm were estimated by the authors from the suggested electronic configurations for metallic Pm (Gschneidner, 1971). The calculations were based on a reversal of Gschneidner's (1971) scheme for deriving the electronic configurations of the solid lanthanide metals from these measured values and the melting points. The boiling points and heats of sublimation of the lanthanide metals are plotted in fig. 2.10, where it is seen that there is no regular, smooth variation as is generally found in plots of a physical property vs. atomic number. This "saw tooth" variation can qualitatively be understood when one considers the valence state in the solid ($\nu = 3$ or 2) and the electronic configura-

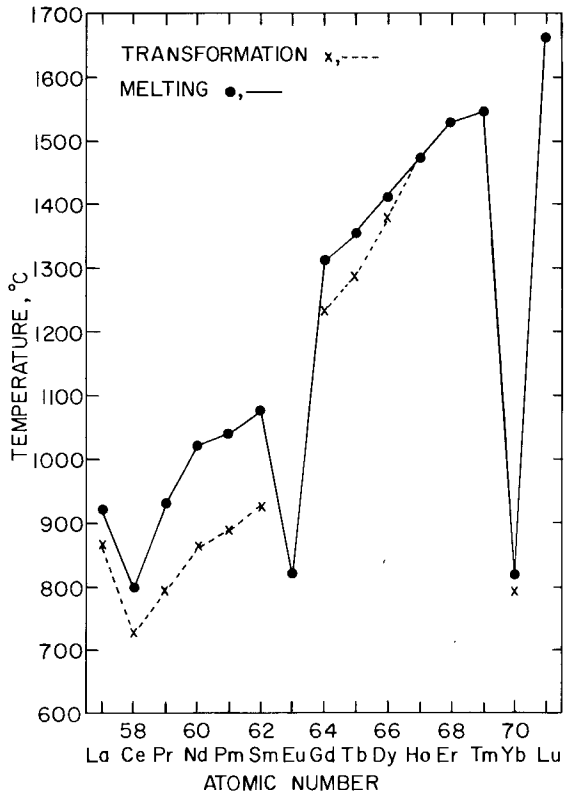

Fig. 2.8. The close-packed to bcc phase transformation and melting points vs. the atomic number for the lanthanide metals. The high temperature phase below the melting point has the bcc structure. In a study of the Dy–Ho system by Spedding et al. (1973) the hcp to bcc transformation was found to coincide with the melting point at 75 at.% Ho–25 at.% Dy.

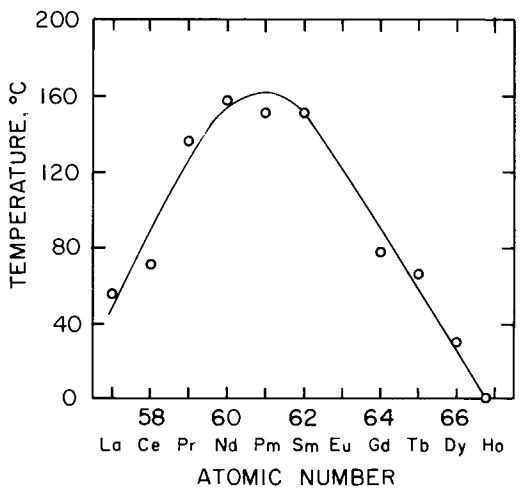

Fig. 2.9. The temperature range (i.e. the difference between the close-packed to bcc transition temperature and the melting point) of existence of the bcc phase of the trivalent lanthanide metals.

TABLE 2.15
Melting and boiling points, vapor pressures and heats of sublimation of the rare earth metals.

Rare earth metal	Melting point (°C)	Boiling point (°C)	Temperature in °C for a vapor pressure of				Heat of sublimation at 25°C (kJ/mol)
			10^{-8} atm (0.001 Pa)	10^{-6} atm (0.101 Pa)	10^{-4} atm (10.1 Pa)	10^{-2} atm (1013 Pa)	
La	918	3464	1301	1566	1938	2506	431.0
Ce	798	3433	1290	1554	1926	2487	422.6
Pr	931	3520	1083	1333	1701	2305	355.6
Nd	1021	3074	955	1175	1500	2029	327.6
Pm	1042	3000[a]	—	—	—	—	348[a]
Sm	1074	1794	508	642	835	1150	206.7
Eu	822	1529	399	515	685	963	~~144.7~~ 175.3
Gd	1313	3273	1167	1408	1760	2306	397.5
Tb	1365	3230	1124	1354	1698	2237	388.7
Dy	1412	2567	804	988	1252	1685	290.4
Ho	1474	2700	845	1036	1313	1771	300.8
Er	1529	2868	908	1113	1405	1896	317.1
Tm	1545	1950	599	748	964	1300	232.2
Yb	819	1196	301	400	541	776	152.1
Lu	1663	3402	1241	1483	1832	2387	427.6
Sc	1541	2836	1036	1243	1533	1999	377.8
Y	1522	3338	1220	1458	1809	2356	424.7

[a]Estimated, see text.

tion in the vaporized phase (gas) which is either $4f^n5d6s^2$ or $4f^{n+1}6s^2$. For La, Ce, Gd and Lu the solid metal has a valence of 3 (for γ–Ce it is slightly greater than 3, see ch. 4 section 2.3) and the gas phase (i.e. ground state) has a $4f^n5d6s^2$ configuration. We designate this as a $3 \rightarrow 3$ change of state. One notes that the boiling points and heats of sublimation are about the same for these metals (~3400°C and ~420 kJ/mole, respectively). For Eu and Yb the metallic valence is 2, the ground state configuration is $4f^{n+1}6s^2$, the boiling points are near 1400°C and heats of sublimation near ~~148~~ 164 kJ/mole. For these two metals we designate this as a $2 \rightarrow 2$ phase transformation. These values are also about the same as observed for the alkaline earth metals. For the remaining metals the metallic valence is 3 but the gas ground state has a $4f^{n+1}6s^2$ configuration, and this is designated as a $3 \rightarrow 2$ change of state. In fig. 2.10 we note that when the 4f level is empty, half-filled and completely filled we have a $3 \rightarrow 3$ vaporization process. As additional 4f electrons are added, Pr and Nd after Ce and Tb and Dy after Gd, there is a tendency for both the boiling points and heats of sublimation to drop off in a more or less regular manner for the $3 \rightarrow 2$ metals until one reaches the half-filled or completely-filled 4f levels in divalent Eu and Yb, the metals which exhibit a $2 \rightarrow 2$ change of state. Because of the stability of the half-filled 4f level the next electron is added to the 5d level (Gd) and for Lu because there are no available 4f levels the 5d level must also be occupied, we find a large increase in the boiling points and heats of sublimation at these points on going from Eu to Gd and from Yb to Lu. That is, the boiling points and sublimation

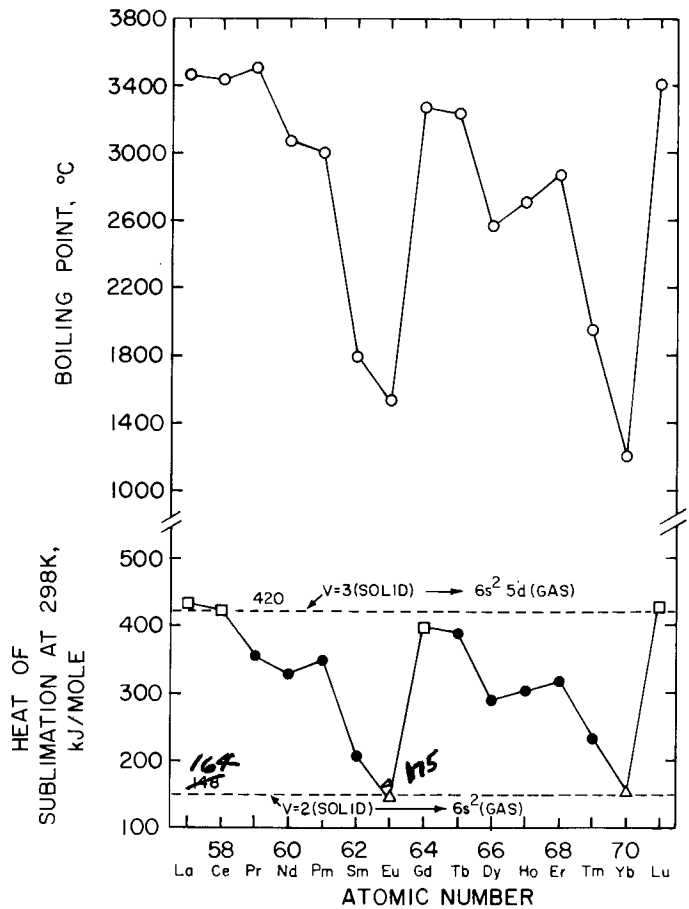

Fig. 2.10. The boiling points and heats of sublimation at 25°C of the lanthanide metals vs. the atomic number. The values for Pm are estimated. For the heat of sublimation the open squares are for the 3→3 metals, the open triangles for the 2→2 metals and the solid circles are for the 3→2 metals – see text for further discussion.

energies decrease as the tendency toward divalency increases with increasing atomic number in each half of the lanthanide series.

8. Thermal expansion

The coefficients of linear thermal expansion at 25°C for the rare earth metals are listed in table 2.16 and are plotted as a function of atomic number for the lanthanides in fig. 2.11. The coefficients were calculated from the X-ray data published by Spedding et al. (1961) except for Pm, which were estimated by the authors, and for Sm which were calculated by the authors from the lattice

parameter versus temperature data of Mardon and Koch (1970). The values for Gd were calculated at 100°C rather than at 25°C because the magnetic ordering at 20°C gives rise to an anomalous thermal expansion which is still evident at 25°C.

Examination of fig. 2.11 immediately reveals that Eu and Yb are anomalous due to their divalency. But one can also see an inverted correlation between the thermal expansion values and the boiling point and heat of sublimation (fig. 2.10) variation for the lanthanide metals. That is, the thermal expansion increases as the tendency toward divalency increases on going from Ce (or Gd) to Eu (or Yb); for the boiling points and heats of sublimation the values decrease in each half of the series (section 7).

9. Summary

For many years scientists have considered the rare earth elements as a group of nearly identical elements, and if something was known about one of them it was generally assumed to be the same for all of them. As rare earth scientists continue to work on these metals more exceptions are found each day. Indeed the differences in many cases are greater than those found for elements which lie in the same group, e.g. the alkaline earth metals, or the noble metals – Cu, Ag and Au.

TABLE 2.16
Coefficient of linear thermal expansion at 25°C

Rare earth metal	Coefficient of expansion × 10^6($°C^{-1}$)		
	poly-crystal	along *a*-axis	along *c*-axis
La	12.1	4.5	27.2
Ce	6.3	6.3	—
Pr	6.7	4.5	11.2
Nd	9.6	7.6	13.5
Pm	11[a]	9[a]	16[a]
Sm	12.7	9.6	19.0
Eu	35.0	35.0	—
Gd	9.4[b]	9.1[b]	10.0[b]
Tb	10.3	9.3	12.4
Dy	9.9	7.5	15.6
Ho	11.2	7.0	19.5
Er	12.2	7.9	20.9
Tm	13.3	8.8	22.2
Yb	26.3	26.3	—
Lu	9.9	4.8	20.0
Sc	10.2	7.6	15.3
Y	10.6	6.0	19.7

[a]Estimated, see text. [b]Values at 100°C.

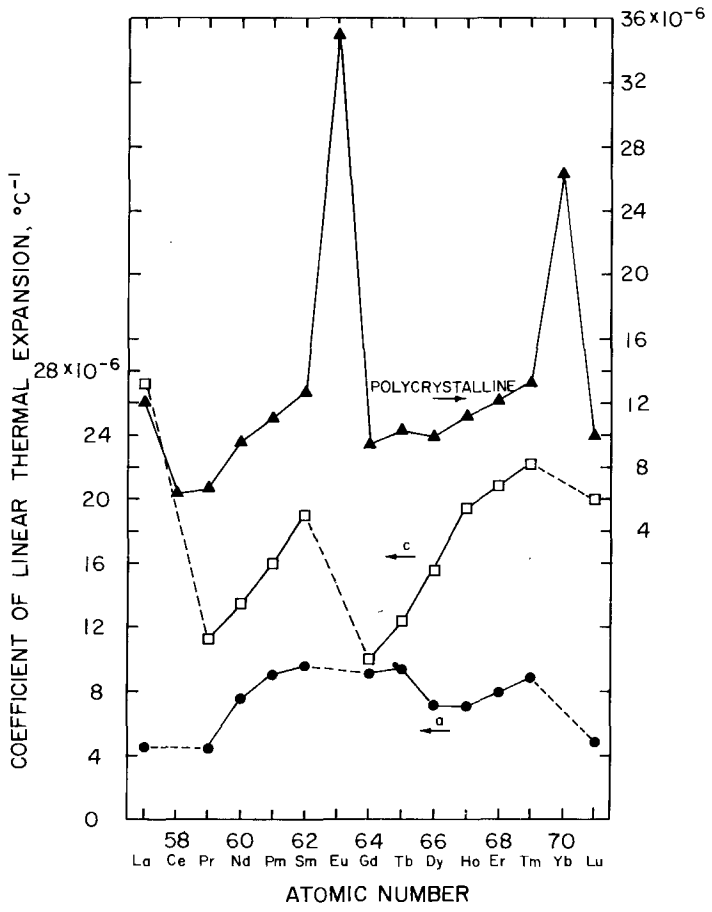

Fig. 2.11. The coefficients of linear thermal expansion at 25°C of the lanthanide metals vs. the atomic number. The values for Pm are estimated.

The differences due to the divalency of Eu and Yb as compared to the normal trivalent rare earth metals are the most obvious in consideration not only of their physical properties, but also in the method of preparing the pure metals. For the trivalent rare earths there are four major methods used to prepare these 14 metals (sections 1.1.1 to 1.1.3 and 1.2), and within each group there are minor but significant differences. A comparison of the basic physical properties shows significant and widely varying behaviors in their crystal structures (fcc → dhcp → Sm-type → hcp), melting points, (a difference of a factor of two between Ce and Lu), boiling points (the "saw-tooth" characteristic so vividly displayed in fig. 2.10), and vapor pressures (a difference of a factor of *one million* in the vapor pressures of La and Tm at 1300°C). Even the smooth, regular and systematic variation as implied in the term "lanthanide contraction" is not found in the

metallic radii which exhibit anomalies at La, Gd and Lu, and between the light and heavy lanthanides (fig. 2.7a).

Although, as noted, wide differences exist in the properties between certain rare earth elements, the systematic variation from *one neighboring rare earth to the next* (especially for the lanthanides) does occur, and allows one to predict properties which have not been determined experimentally. In making these predictions one should be aware that anomalies can occur and exercise caution. In so doing the application of systematics to rare earth materials can be a powerful tool for understanding their nature and predicting their behaviors in new surroundings.

References

Aamland, E., D.J. MacDonald and D.G. Kesterke, 1973, U.S. Bureau of Mines, Rept. Invest. No. 7722.

Achard, J.C., 1966, Rev. Hautes Temp. Refract. **3**, 281.

Amonenko, V.M., A.A. Kruglykh, V.S. Pavlov and L.M. Mosova, 1966, Izv. Akad. Nauk. SSSR, Neorg. Mater. **2**, 578. Engl. transl. Inorg. Mater. **2**, 500.

Angelini, P. and H.L. Adair, 1974, Preparation and determination of the melting point and phase transformation temperatures of ^{147}Pm metal, in: Haschke, J.M. and H.A. Eick, eds., Proceedings of the 11th Rare Earth Research Conf., Traverse City, Mich. (CONF-741002, Part 2, NTIS, Springfield, Virginia 22151) pp. 662–671.

Aust, K.T., 1963, Large crystals grown by recrystallization, in: Gilman, J.J., ed., The Art and Science of Growing Crystals (John Wiley and Sons, Inc., New York), p. 453.

Baker, H.H. and D.T. Peterson, 1976, Private communication, Ames Laboratory, ERDA, Iowa State University, Ames, Iowa 50011.

Beaudry, B.J. and A.H. Daane, 1962, Trans. Met. Soc. AIME **244**, 770.

Beaudry, B.J. and K.A. Gschneidner, Jr., 1974. Solid State Commun. **15**, 791.

Beaudry, B.J. and P.E. Palmer, 1974a, The use of inert atmospheres in the preparation and handling of high purity rare earth metals, in: Haschke, J.M., and H.A. Eick, eds., Proceedings of the 11th Rare Earth Research Conf. Traverse City, Mich. (CONF-741002, Part 2, NTIS, Springfield, Virginia 22151) pp. 612–620.

Beaudry, B.J. and P.E. Palmer, 1974b, J. Less-Common Metals **34**, 225.

Beaudry, B.J. and F.H. Spedding, 1975, Metall. Trans. **6B**, 419.

Beaudry, B.J., P.E. Palmer and K.A. Gschneidner, Jr., 1976, The Preparation of gadolinium metal for thermoelectric devices, in: Eleventh Intersociety Energy Conversion Engineering Conference Proceedings, Sept. 12–17, 1976, State Line, Nevada (Amer. Institute of Chemical Engineers, New York) p. 1556.

Behrendt, D.R., S. Legvold and F.H. Spedding, 1957, Phys. Rev. **106**, 723.

Behrendt, D.R., S. Legvold and F.H. Spedding, 1958, Phys. Rev. **109**, 1544.

Belov, K.P., R.Z. Levitin and S.A. Nikitin, 1961, Izv. Akad. Nauk, SSSR, Ser. Fiz. **25**, 1328. Engl. transl. Bull. Acad. Sci. USSR, Phys. Ser. **25**, 1394 (1962).

Billy, M. and F. Trombe, 1931, C. R. Acad. Sci. **193**, 421.

Boulesteix, C., L. Valiergue, M. Gasgnier and Ch. Henry la Blanchetais, 1970a, Thin Solid Films **6**, 51.

Boulesteix, C., P.E. Caro, M. Gasgnier, Ch. Henry la Blanchetais, B. Pardo and L. Valiergue, 1970b, Acta Crystallogr. **B26**, 1043.

Bratland, D., G.H. Boe, K. Grjotheim, H. Rensvik and E. Aamland, 1972, Rev. Roum. Chim. **17**, 41.

Bratland, D., G. Boe and K. Grjotheim, 1973, Rev. Chim. Miner. **10**, 347.

Brissot, J.J. and R. Martres, 1965, J. Appl. Phys. **36**, 3360.

Bucher, E., C.W. Chu, J.P. Maita, K. Andres, A.S. Cooper, E. Buehler, and K. Nassau, 1969, Phys. Rev. Lett. **22**, 1260.

Bucher, E., P.H. Schmidt, A. Jayaraman, K. Andres, J.P. Maita, and P.D. Dernier, 1970, Phys. Rev. **B2**, 3911.

Busch, G., E. Kaldis, J. Muheim and R. Bischöf, 1971, J. Less-Common Metals **24**, 453.

Cadieu, F.J. and D.H. Douglass, Jr., 1969, J. Appl. Phys. **40**, 2376.

Campbell, T.T. and F.E. Block, 1959, J. Metals **11**, 744.

Carlson, O.N. and F.A. Schmidt, 1961a, Metallothermic preparation of yttrium metal, in: Spedding, F.H. and A.H. Daane, eds. The Rare Earths, (John Wiley & Sons, Inc., New York) p. 113.

Carlson, O.N. and F.A. Schmidt, 1961b, Preparation of the rare-earth fluorides, in: Spedding, F.H. and A.H. Daane, eds., The Rare Earths, (John Wiley & Sons, Inc., New York) p. 79.

Carlson, O.N. and F.A. Schmidt, 1967, Metallurgy division, Research and development report IS-1600, Ames Laboratory-USAEC,

Iowa State University, Ames, Iowa 50011, p. M-10.
Carlson, O.N., D.W. Bare, E.D. Gibson and F.A. Schmidt, 1959, Symposium on Newer Metals, ASTM Special Technical Publication No. 272, 144.
Carlson, O.N., J.A. Haefling, F.A. Schmidt, and F.H. Spedding, 1960, J. Electrochem. Soc. **107**, 540.
Carlson, O.N., F.A. Schmidt and W.M. Paulson, 1964, ASM Trans. Q. **57**, 356.
Carlson, O.N., F.A. Schmidt and D.T. Peterson, 1966, J. Less-Common Metals **19**, 1.
Carlson, O.N., F.A. Schmidt and D.T. Peterson, 1975, J. Less-Common Metals **39**, 277.
Carnahan, T.G. and T.E. Scott, 1973, Metall. Trans., **4**, 27.
Croat, J.J., 1969, The preparation of high purity dysprosium, holmium and erbium by the lithium reduction of their trichloride salts. Report No. IS-T-346 from Ames Laboratory - ERDA, Iowa State University, Ames, Iowa 50011.
Daane, A.H., and F.H. Spedding, 1953, J. Electrochem. Soc. **100**, 442.
Daane, A.H., D.H. Dennison and F.H. Spedding, 1953, J. Amer. Chem. Soc. **75**, 2272.
Darnell, F.J., 1963, Phys. Rev. **132**, 1098.
Darnell, F.J. and E.P. Moore, 1963, J. Appl. Phys. **34**, 1337.
Dennison, D.H., M.J. Tschetter and K.A. Gschneidner, Jr., 1966a, J. Less-Common Metals **11**, 423.
Dennison, D.H., M.J. Tschetter, K.A. Gschneidner, Jr., 1966b, J. Less-Common Metals **10**, 108.
Eash, D.T. and O.N. Carlson, 1960, Trans. Amer. Soc. Met. **52**, 1097.
Edwards, L.R. and S. Legvold, 1968, Phys. Rev. **176**, 753.
Evers, J., E. Kaldis, J. Muheim, and C. Zürcher, 1975, Helv. Phys. Acta **48**, 462.
Falicov, L.M. and C.E.T. Goncalves da Silva, 1971, Phys. Rev. Lett. **26**, 715.
Fölsch, H., 1970, Metal **24**, 755.
Gasgnier, M., J. Ghys, G. Schiffmacher, Ch. Henry la Blanchetais and P.E. Caro, 1974, J. Less-Common Metals **34**, 131.
Gibson, E.D. and O.N. Carlson, 1960, Trans. Amer. Soc. Met. **52**, 1084.
Graham, C.D., Jr., 1962, J. Phys. Soc. Jap. **17**, 1310.
Green, R.W., S. Legvold and F.H. Spedding, 1961, Phys. Rev. **122**, 827.
Griffin, R.B. and K.A. Gschneidner, Jr., 1971, Met. Trans. **2**, 2517.
Gschneidner, K.A., Jr., 1961a, Rare Earth Alloys (Van Nostrand, Princeton, N.J.).
Gschneidner, K.A., Jr., 1961b, Crystallography of the rare earth metals, in: Spedding, F.H. and A.H. Daane, eds. The Rare Earths (John Wiley & Sons, Inc., New York) p. 190.
Gschneidner, K.A., Jr., 1965, The application of vacuum metallurgy in the purification of rare earth metals, in: Bianchi, L.M., ed. Trans. Vacuum Metallurgy Conference, 1966, (Am. Vac. Soc., Boston, Mass.) p. 99.
Gschneidner, K.A., Jr., 1969, J. Less-Common Metals **17**, 1.
Gschneidner, K.A., Jr., 1971, J. Less-Common Metals **25**, 405.
Gschneidner, K.A., Jr., and W.B. Pearson, 1968, Mater. Res. Bull. **3**, 951.
Gschneidner, K.A., Jr. and R. Smoluchowski, 1963, J. Less-Common Metals **5**, 374.
Gschneidner, K.A., Jr. and R.M. Valletta, 1968, Acta Met. **16**, 477.
Gvelesiani, G.G., D.I. Bagdavadze, 1966, Soobshch. Akad. Nauk Gruz. SSR **42**, 427.
Habermann, C.E. and A.H. Daane, 1963, J. Less-Common Metals **5**, 134.
Hall, P.M., S. Legvold and F.H. Spedding, 1960, Phys. Rev. **177**, 971.
Havinga, E.E., J.H.N. van Vucht, K.H.J. Buschow, 1969, Philips Res. Repts. **24**, 407.
Henrie, T.A., 1964, J. Metals **16**, 978.
Henrie, T.A. and E. Morrice, 1966, J. Metals **18**, 1207.
Hillebrand, W. and T. Norton, 1875, Ann. Phys. Chem. **155**, 633.
Hirschhorn, I.S., 1968, J. Metals **20**, [3], 19.
Hodges, C.H., 1967, Acta Met. **15**, 1787.
Hopkins, E.N., D.T. Peterson and H.H. Baker, 1965, A universal electropolishing method, in: Gray, R.J. (compiler), Nineteenth Metallographic Group Meeting, April 1965, United States AEC Rept. No. ORNL-TM-1161, Oak Ridge National Laboratory, Oak Ridge, Tenn. p. 1.
Huffine, C.L. and J.M. Williams, 1961, Refining and purification of rare earth metals, in: Spedding, F.H. and A.H. Daane, eds., The Rare Earths, (John Wiley & Sons, Inc., New York) p. 145.
Hukin, D.A., 1971, A new design of cold crucible and its application to the growth of rare earth metal single crystals, Clarendon Laboratory rept. no. 24/71, Parks Road, Oxford, England.
Hukin, D.A. and D.W. Jones, 1976, J. Cryst. Growth, to be published.
Hultgren, R., P.D. Desai, D.T. Hawkins, M. Gleiser, K.K. Kelley and D.D. Wagman, 1973, Selected Values of the Thermodynamic Properties of the Elements (Amer. Soc. for Metals, Metals Park, Ohio).
Hurd, C.M. and J.E.A. Alderson, 1973, Solid State Commun. **12**, 375.
Ishikawa, H., T. Utsunomiya, T. Hatano, Y. Hoshino and M. Sato, 1974, Bull. Tokyo Inst. Tech. [120], 103.
Jordan, R.G., 1974, Contemp. Phys. **15**, 375.
Jordan, R.G. and D.W. Jones, 1973, J. Less-Common Metals **31**, 125.
Jordan, R.G., D.W. Jones and P.G. Mattocks, 1974, J. Less-Common Metals **31**, 125.
Jordan, R.G., D.W. Jones and V.J. Hems, 1975, J. Less-Common Metals **42**, 101.
Kayser, F.X., 1970, Phys. Rev. Lett. **25**, 662.
Kayser, F.X., 1971, Phys. Status Solidi **8**, 233.
Klemm, W. and H. Bommer, 1937, Z. Anorg. Allg. Chem. **231**, 138.
Knechtel, H.E., W.F. Kindle, J.W. McCall and R.D. Buchheit, 1973, Metallographic practice

generally applicable to all metals, in: Metals Handbook, 8th edition, Metallography, Structures and Phase Diagrams **8**, 1 (American Society for Metals, Metals Park, Ohio).
Kobisk, E.H. and W.B. Grisham, 1969, Mater. Res. Bull. **4**, p. 651.
Koch, C.C. and M.L. Picklesimer, 1967, Trans. Met. Soc. AIME **239**, 759.
Kumar, J. and O.N. Srivastava, 1969, Acta Crystallogr. **B25**, 2654.
Marchant, J.D., E.S. Shedd and T.A. Henrie, 1962, Solid-state electrorefining of rare earth metals, in: Nachman, J.F. and C.E. Lundin, eds., Rare Earth Research (Gordon and Breach, Science Publishers, New York) p. 143.
Marcinkowski, M.J. and E.N. Hopkins, 1968, Trans. Met. Soc. AIME **242**, 579.
Mardon, P.G. and C.C. Koch, 1970, Scr. Metall. **4**, 477.
Matthias, B.T., W.H. Zachariasen, G.W. Webb, and J.J. Engelhardt, 1967, Phys. Rev. Lett. **18**, 781.
Mattocks, P.G., C. Muirhead, D.W. Jones, B.J. Beaudry and K.A. Gschneidner, Jr., 1977, J. Less-Common Metals **53**, 253.
McEwen, K.A. and P. Touborg, 1973, J. Phys. F: **3**, 1903.
McMasters, O.D., G.E. Holland and K.A. Gschneidner, Jr., 1978, J. Cryst. Growth, to be published.
Miller, A.E. and A.H. Daane, 1964, Trans. Met. Soc. AIME **230**, 568.
Miller, A.E., A.H. Daane, C.E. Habermann and B.J. Beaudry, 1963, Rev. Sci. Instrum. **34**, 644.
Moore, R.H., F.M. Smith and J.R. Morrey, 1965, Trans. Met. Soc. AIME **233**, 1259.
Moriarty, John L., Jr., 1968, J. Metals **20**, 41.
Morrice, E. and T.A. Henrie, 1967, U.S. Bureau of Mines Rept. Invest. No. 6957.
Morrice, E. and R.G. Knickerbocker, 1961, Rare-Earth Electrolytic Metals, in: Spedding, F.H. and A.H. Daane, eds., The Rare Earths (Wiley, New York) p. 126.
Morrice, E., B. Porter, E.A. Brown, C. Wyche and R.G. Knickerbocker, 1961, U.S. Bureau of Mines, Rept. Invest. No. 5868.
Morrice, E., E.S. Shedd and T.A. Henrie, 1968, U.S. Bureau of Mines, Rept. Invest. No. 7146.
Morrice, E., J.E. Murphy and M.M. Wong, 1969a, U.S. Bureau of Mines Rept. Invest. No. 7308.
Morrice, E., E.S. Shedd, M.M. Wong and T.A. Henrie, 1969b, J. Metals **21**, [1] 34.
Mosander, G.G., 1827, Ann. Phys. (Leipzig), formerly Pogg. Ann. **11**, 406.
Mowry, G., B.J. Beaudry and K.A. Gschneidner, Jr., 1976, Unpublished data. Ames Laboratory, Iowa State University, Ames, Iowa 50011.
Nigh, H.E., 1963, J. Appl. Phys. **34**, 3323.
Nolting, H.J., C.R. Simmons and J.J. Klingenberg, 1960, J. Inorg. Nucl. Chem. **14**, 208.
Owen, C.V. and T.E. Scott, 1970, J. Less-Common Metals **21**, 427.
Owen, C.V. and T.E. Scott, 1973, J. Less-Common Metals **30**, 113.
Owen, C.V. and T.E. Scott, 1974, J. Less-Common Metals **37**, 353.
Peterson, D.T., 1971, Experimental factors in the purification of metals by electrotransport, in: Lodding, A. and T. Lagerwall, eds. Atomic Transport in Solids and Liquids (Verlag der Zeitschrift für Naturforschung, Tübingen) p. 104.
Peterson, D.T. and E.N. Hopkins, Electropolishing the rare earth metals, IS-1036, Ames Laboratory – ERDA, Iowa State University, Ames, Iowa 50011, 1964.
Peterson, D.T. and F.A. Schmidt, 1969, J. Less-Common Metals **18**, 111.
Peterson, D.T. and F.A. Schmidt, 1972, J. Less-Common Metals **29**, 321.
Peterson, I.M., M. Smutz and E.H. Olson, 1965, J. Less-Common Metals **8**, 352.
Pfann, W.G., 1962, Why ultra-pure metals, in: Ultra High-Purity Metals (American Society for Metals, Cleveland, Ohio) p. 1.
Reed, R.E., 1971, Growth of large single crystals of rare earth metal isotopes, in: Field, P.E., ed. Proc. 9th Rare Earth Research Conf., Blacksburg, Virginia, 24061, (NTIS, U.S. Dept. of Commerce, Springfield, Virginia, 22151) p. 657.
Revel, G., J.-C. Rouchand, and J.-L. Pastol, 1974, Preparation and neutron activation analysis of high purity cerium, in: Haschke, J.M. and H.E. Eick, eds., Proc. 11th Rare Earth Research Conf., Traverse City, Michigan (CONF-741002 Part 2, NTIS, Springfield, Virginia 22151) p. 602.
Roman, W.A., 1965, J. Less-Common Metals **10**, 152.
Ross, I.N., 1967, J. Inst. Met. **95**, 337.
Savitskii, E.M., V.F. Terekhova, O.P. Naumkin and I.V. Burov, 1965, Rost Kristallov **6**, 301; Engl. transl., Growth Crystals. **6**, 111.
Schieber, M., 1967, Growth of Sm, Eu, Tm and Yb metal by vapor deposition, in: Perser, H.S., ed. Crystal Growth, (Pergamon Press, New York) p. 271.
Schmidt, F.A., 1976, Private communication. Ames Laboratory, ERDA, Iowa State University, Ames, Iowa 50011, U.S.A.
Schmidt, F.A. and O.N. Carlson, 1974, United States patent No. 3, 846, 121, Method for preparing scandium metal.
Schmidt, F.A. and O.N. Carlson, 1976a, J. Less-Common Metals, **50**, 237.
Schmidt, F.A. and O.N. Carlson, 1976b, Private communication, Ames Laboratory – ERDA, Iowa State University, Ames, Iowa 50011.
Shedd, E.S., J.D. Marchant and T.A. Henrie, 1964, U.S. Bureau of Mines, Rept. Invest. No. 6362.
Shedd, E.S., J.D. Marchant and M.M. Wong, 1970, U.S. Bureau of Mines, Rept. Invest. No. 7398.
Shiokawa, J., T. Kurita and T. Ishino, 1968, Denki Kagaku **36**, 142.
Sinha, S.P., 1975, Helv. Chim. Acta **58**, 1978.

Spedding, F.H. and B.J. Beaudry, 1971, J. Less-Common Metals, **25**, 61.
Spedding, F.H. and D.C. Henderson, 1971, J. Chem. Phys. **54**, 2476.
Spedding, F.H. and A.H. Daane, 1956, Progr. Nucl. Energy, Ser. 5, **1**, 413.
Spedding, F.H., H.A. Wilhelm, W.H. Keller, D.H. Ahmann and A.H. Daane, 1952, Ind. Eng. Chem. **44**, 553.
Spedding, F.H., A.H. Daane and K.W. Herrmann, 1957, J. Metals **9**, Trans. AIME **209**, 895.
Spedding, F.H., J.J. Hanak and A.H. Daane, 1958, Trans. Met. Soc. AIME **212**, 379.
Spedding, F.H., J.J. Hanak and A.H. Daane, 1961, J. Less-Common Metals **3**, 110.
Spedding, F.H., R.M. Valletta and A.H. Daane, 1962, ASM Trans. Q **55**, 483.
Spedding, F.H., B.J. Beaudry, J.J. Croat and P.E. Palmer, 1968a, The properties, preparation and handling of "pure" rare earth metals, in: Materials Technology – An Interamerican Approach (Am. Soc. Mech. Eng., New York) p. 151.
Spedding, F.H., J.J. Croat and B.J. Beaudry, 1968b, Metallurgy division, Research and development report IS-1900, Ames Laboratory, USAEC, Iowa State University, Ames, Iowa 50011, p. M-94.
Spedding, F.H., B.J. Beaudry, J.J. Croat and P.E. Palmer, 1970, The preparation and properties of "ultrapure" metals, in: Les Éléments Des Terres Rares **1** (Centre National de la Recherche Scientifique, Paris) p. 25.
Spedding, F.H., D. Cress and B.J. Beaudry, 1971, J. Less-Common Metals **23**, 263.
Spedding, F.H., B. Sanden and B.J. Beaudry, 1973, J. Less-Common Metals **31**, 1.
Teatum, E.T., K.A. Gschneidner, Jr. and J.T. Waber, 1968, Compilation of calculated data useful in predicting metallurgical behavior of the elements in binary alloy systems, LA-4003, Los Alamos Scientific Laboratory, Los Alamos, NM (December 24, 1968).
Thoma, R.E. and G.D. Brunton, 1966, Inorg. Chem. **5**, 1937.
Tonnies, J.J. and K.A. Gschneidner, Jr., 1971, J. Crys. Growth, **10**, 1.
Trombe, F., 1932, C. R. Acad. Sci. **194**, 1653.
Trombe, F., 1933, C. R. Acad. Sci. **196**, 704.
Trombe, F., 1936, Ann. Chim. **6**, 349.
Trombe, F., 1938, Tech. Mod. **30**, 855.
Verhoeven, J.D., 1966, J. Metals **18**, 26.
Whittaker, M., 1968, J. Cryst. Growth **3, 4**, 317.
Williams, J.M. and C.L. Huffine, 1961, Nucl. Sci. Eng. **19**, 500.

Handbook on the Physics and Chemistry of Rare Earths, edited by K.A. Gschneidner, Jr. and L. Eyring

Chapter 3

ELECTRONIC STRUCTURE OF RARE EARTH METALS*

S.H. LIU
Department of Physics, University of California, Berkeley, CA 94720, USA

and

Ames Laboratory – US DOE and Department of Physics, Iowa State University, Ames, IA 50011,† USA

Contents

Symbols

A = external Fermi surface cross sectional area; or amplitude of a wave

A_n = expansion coefficients of APW wave function in terms of plane waves

B = magnetic induction

$\hat{c}$ = unit vector along c axis of crystal

C_{lm} = expansion coefficients of APW wave function in terms of spherical waves

$D(E, \omega)$ = optical density of states

e = electron charge

*Research supported by the U.S. Energy Research and Development Administration under contract No. W-7405-eng.-82.

†Permanent address.

$\boldsymbol{E}$ = electric field vector

$E(4f^n5d^m)$, $E(n, m)$ = energy of the $4f^n5d^m$ configuration

$E^{(corr)}(n, m)$ = correlation energy part of $E(n, m)$

$E^{(exp)}(n, m)$ = experimental value of $E(n, m)$

$E_B(n, m)$ = binding energy of metal in $4f^n5d^m$ configuration

$E_M(n, m) = E(n, m)$ in metallic state

$E_{FA}(n, m) = E(n, m)$ for free atom

$E_{RA}(n, m) = E(n, m)$ for renormalized atom

E_b = bottom of energy band

E_F = Fermi energy

E_{ex} = exchange energy

E_{nk} = energy of conduction electron

$E_f(\boldsymbol{k})$ = energy of final state

$E_i(\boldsymbol{k})$ = energy of initial state

f_{nk} = Fermi distribution function

$|f\rangle$ = final state

F = de Haas–van Alphen frequency

F_{if} = magneto-optic Kerr effect matrix element square

$F(\boldsymbol{p}, \boldsymbol{k})$ = momentum distribution function of electron–positron pair

g = gyromagnetic ratio

$h, \hbar$ = Planck's constants

$\hbar\omega_q$ = energy of magnon

H = hamiltonian

H_s = effective spin hamiltonian

$|i\rangle$ = initial state

I_0, I_{45}, I_{90} = intensity of reflected light at 0°, 45°, and 90° angles respectively

$I(nk, n'k')$, I = total d–f exchange matrix element

$I_m(nk, n'k')$ = d–f exchange matrix element for a single 4f orbital

$\langle I \rangle$ = average d–f exchange matrix element

J = total angular momentum quantum number for the 4f shell

$\boldsymbol{J}$ = total angular momentum vector for the 4f shell

J_{ix}, J_{iy}, J_{iz} = cartesian components of $\boldsymbol{J}$ for the ith ion

$J_{if}(\omega)$ = Joint density of states

$\mathcal{J}(\boldsymbol{R})$ = Ruderman–Kittel–Kasuya–Yosida coupling energy

$\mathcal{J}(\boldsymbol{q})$ = the Fourier transform of $\mathcal{J}(\boldsymbol{R})$ with wave vector $\boldsymbol{q}$.

k = amplitude of wave vector, or imaginary part of index of refraction

$\boldsymbol{k}$ = wave vector of band electron

k_B = Boltzmann constant

k_F = Fermi wave vector

K, K_x, K_y = linear dimensions of Brillouin zone

$\boldsymbol{K}_n$ = nth reciprocal lattice vector

l = orbital angular momentum quantum number for one electron

L = orbital angular momentum quantum number for the 4f shell

$\boldsymbol{L}$ = orbital angular momentum vector for the 4f shell

L_l = logarithmic derivative of the radial wave function with angular momentum l

m = electron mass; or magnetic quantum number

m_c^* = effective cyclotron mass

$\boldsymbol{M}$ = magnetization vector

M_s = saturation magnetization

M_{if} = optical matrix element

M_{mn} = APW matrix element

$M(nk, n'k')$ = spin dependent part of electron–ion scattering matrix element

n = band index, or real part of index of refraction

N = total number of ions

$N(E)$, $N(\epsilon)$ = band density of states

$N(\theta)$ = angular distribution of positron annihilation γ-rays

$N_\uparrow(\theta)$, $N_\downarrow(\theta)$ = $N(\theta)$ in a magnetic field parallel/antiparallel to the positron momentum

$N_f(E)$ = density of final states

$N_i(E)$ = density of initial states

$N(E, h\nu)$ = energy distribution curve

$\boldsymbol{p}, \boldsymbol{p}_i$ = momentum of conduction electron

$\boldsymbol{p}_\perp$ = perpendicular component of p

$P(\theta)$ = spin polarization of positron annihilation γ-ray distribution

$\boldsymbol{q}$ = wave vector of magnon or magnetic order

$\boldsymbol{q}_\perp$ = perpendicular component of $\boldsymbol{q}$

q_z = z component of $\boldsymbol{q}$

$\boldsymbol{r}_i$ = position of the ith electron

r_{MT} = muffin-tin sphere radius

R = optical reflectivity

R_p = reflectivity for p polarization

R_s = reflectivity for s polarization

$R_l(E, r)$ = radial wave function

$\boldsymbol{s}$ = conduction electron spin operator

$\boldsymbol{s}_f$ = 4f electron spin operator

S = total spin quantum number for the 4f shell
$\boldsymbol{S}$ = total spin vector for the 4f shell
T = temperature
T_D = Dingle temperature
U = effective Coulomb repulsion
$V(\boldsymbol{r})$ = muffin-tin potential
$V_a(\boldsymbol{r})$ = Hartree–Fock potential
$V_H(\boldsymbol{r})$ = Hartree potential
$\bar{V}_x$ = average exchange energy of uniform electron gas
V_{nk} = d–f hybridization matrix element
$V_{xa}(\boldsymbol{r})$ = Hartree–Fock exchange potential
$V_{xs}(\boldsymbol{r})$ = Slater exchange potential for electron in spin state s
$\boldsymbol{X}_l$ = position of lth ion
$Y_{lm}(\hat{\boldsymbol{r}})$ = spherical harmonics
Z = number of ionic charge
α = scale factor for local exchange potential
$\alpha(\omega)$ = optical absorptivity
Γ = center of Brillouin zone
Γ_q = magnon damping constant
δ = mismatch parameter
Δ = phase of the ratio of reflectivities R_p/R_s
Δ_+ = promotion energy of band electron into the 4f shell
Δ_- = promotion energy of 4f electron into the conduction band
θ_p = paramagnetic Curie temperature
ϵ = dielectric function, or orbital energy
ϵ_i, ϵ_a = orbital energy in Hartree–Fock scheme
$\boldsymbol{\epsilon}$ = polarization vector
ϵ_0 = dielectric constant of quartz prism
$\epsilon_1(\omega)$ = real part of dielectric function
$\epsilon_2(\omega)$ = imaginary part of dielectric function
μ_B = Bohr magneton
ν = photon frequency
$\boldsymbol{\pi}$ = magneto-optic effective momentum operator
ρ = density of uniform electron gas; or amplitude of the ratio of reflectivities R_p/R_s
$\rho(\boldsymbol{r})$ = electron density
$\rho_s(\boldsymbol{r})$ = density of electron in spin state s
$\boldsymbol{\sigma}$ = Pauli spin matrices
$\overleftrightarrow{\sigma}$ = conductivity tensor
$\sigma(\omega)$ = optical conductivity
σ_{xx} = diagonal element of conductivity tensor
σ_{xy} = off-diagonal element of conductivity tensor
$\sigma_{xy}^{(1)}(\omega)$ = real part of σ_{xy}
$\sigma_{xy}^{(2)}(\omega)$ = imaginary part of σ_{xy}
ϕ = phase angle
$\phi_a(\boldsymbol{r})$ = orbital basis function
χ_a = spin basis function
χ_p = magnetic susceptibility in the paramagnetic state
$\chi(\boldsymbol{q})$ = generalized susceptibility
ψ = conical angle
$\psi_k^{\mathrm{I}}(\boldsymbol{r})$ = APW wave function inside muffin-tin sphere
$\psi_k^{\mathrm{II}}(\boldsymbol{r})$ = APW wave function between muffin-tin spheres
$\psi_+(\boldsymbol{r})$ = positron wave function
$\psi_{l,E}(\boldsymbol{r})$ = component of electron wave function with angular momentum l and energy E
ω = angular frequency
Ω_0 = atomic volume
∇ = gradient operator

1. Introduction

In the quantum theory of matter the study of the physical properties of any system, an atom, a molecule, or a solid, begins with the determination of the energy levels and the wave functions of the many electrons in the system. For this reason the theoretical and experimental investigations of the electronic structure of rare-earth metals have always occupied an important position in rare earth research. The pioneering calculations of the energy band structure of rare earth metals were motivated by the attempt to understand the complicated magnetic structures of these metals as revealed by neutron scattering. These

calculations gave the energy levels and wave functions of the conduction electrons. The optical absorption spectroscopy and ultraviolet and X-ray photoemission spectroscopy methods have been used to probe the structure of the filled bands as well as the core states. Recent developments in metallurgical techniques resulted in high quality single crystals of rare earth metals, thereby enabling precise measurements of the Fermi surface by the de Haas–van Alphen method. These experiments have stimulated more refined calculations. The purpose of this chapter is to review these developments and to summarize the challenges we are facing today.

For physical systems with more than one electron, the problem of calculating the electronic properties is a quantum mechanical many-body problem. The prospect of an analytic solution is remote. For metals even the best approximate methods in use today must rely on over-simplications. Nevertheless, these methods have provided us with a great deal of insight, and will continue to be the major theoretical tool for many years to come.

The central idea of all approximate methods is the reduction of the many-body problem into a one-body problem. The one electron under investigation is assumed to move in an effective potential due to the nuclei and all the other electrons. Naturally the success or failure of the approximation hinges on the construction of the potential. This problem will receive increasing attention when more refined calculations are desired.

The interpretation of experimental results based on the one electron picture also raises fundamental questions. It has been shown that the low energy elementary excitations in metals can be described as quasi-particles. By making suitable many-body corrections one can convert the one electron states into quasi-particle states. For excitations from inner shells, which become possible when the excitation energy is high, the change of state of one electron is accompanied by a rearrangement of the states of many other electrons in the same core. This is a complicated many-body problem that can not be handled by the simple methods of band calculation. To what extent should one include many electron effects when an electron is excited from a deep band state remains an open question.

There are two exhaustive reviews of the band structure of rare earth metals by Dimmock (1971) and Freeman (1972). The first article gives a complete discussion of the band calculation results and the second article emphasizes the magnetic properties as delineated by the electronic properties. Earlier calculations on the energy bands and Fermi surface of rare-earth-like metals Sc and Y by the cellular method have been reviewed by Cracknell (1971). Whenever feasible we will avoid duplicating the materials contained in these articles.

2. Energy bands of rare earth metals

The electronic structure of the free rare earth atoms is discussed in ch. 1. In each atom there are two or three electrons in 6s and 5d shells outside an unfilled

4f shell and a xenon core. In the metallic state the outer shell electrons go into band states and the 4f shell remains largely intact. Therefore, in most cases the 4f states are not included in the band calculations. The only exceptional case is Ce metal whose 4f levels fall very close to the Fermi energy. Since electrons in a 4f shell are strongly correlated by the Hund's rule interactions, one can not describe the 4f levels by the one electron theory. For this reason there exists no reliable way to calculate the full band structure of this metal.

The 4f shells of most rare earth metals possess a magnetic moment, and in the ground state the moments are ordered. The exchange field thus produced complicates the band structure considerably, All early band calculations ignored this effect and treated the 4f shells as nonmagnetic. Impetus for the first exchange split band calculation (Harmon and Freeman, 1974a) was provided by the neutron form factor measurement for Gd (Moon et al., 1972). The recent detailed de Haas–van Alphen measurements on Gd has given quantitative check of the theoretical spin polarized band structure.

2.1. *The effective potential in band calculation*

The hamiltonian for the many electrons in a solid is

$$H = \sum_i \frac{\boldsymbol{p}_i^2}{2m} - \sum_i \sum_l \frac{Ze^2}{|\boldsymbol{r}_i - \boldsymbol{X}_l|} + \sum_i \sum_{j \neq i} \frac{e^2}{|\boldsymbol{r}_i - \boldsymbol{r}_j|}, \tag{3.1}$$

where $\boldsymbol{r}_i$, $\boldsymbol{p}_i$ are the position and momentum of the ith electron, $\boldsymbol{X}_l$ is the location of the lth nucleus, Z is the nuclear charge, the sum on l is over all the N nuclei and the sum on i and j are over all the ZN electrons. The two potential terms in eq. (3.1) represent the attractive nuclear potential and the Coulomb repulsion between electron pairs respectively. The first step in transforming this many-body problem into a one-body problem is the Hartree–Fock approximation which assumes a single Slater determinant wave function for the electrons [see Slater (1965, 1967)]. We denote the basis functions of the Slater determinant as $\{\phi_a(\boldsymbol{r})\chi_a\}$, where $\phi_a(\boldsymbol{r})$ is the orbital part and χ_a the spin part of the basis function. Then one finds that the spatial part of an optimum basis function satisfies the one electron equation

$$\left(\frac{p^2}{2m} + V_a(\boldsymbol{r})\right) \phi_a(\boldsymbol{r}) = \epsilon_a \phi_a(\boldsymbol{r}), \tag{3.2}$$

where

$$V_a(\boldsymbol{r}) = -\sum_l \frac{Ze^2}{|\boldsymbol{r} - \boldsymbol{X}_l|} + V_H(\boldsymbol{r}) + V_{xa}(\boldsymbol{r}). \tag{3.3}$$

In the above equation the Hartree potential is

$$V_H(\boldsymbol{r}) = e^2 \int \frac{\rho(\boldsymbol{r}')}{|\boldsymbol{r} - \boldsymbol{r}'|} \mathrm{d}^3 r', \tag{3.4}$$

which is the electrostatic potential of the charge distribution of all the electrons.

The electron density is given by

$$\rho(\boldsymbol{r}) = \sum_{\mathrm{a}} |\phi_{\mathrm{a}}(\boldsymbol{r})|^2. \tag{3.5}$$

The exchange potential is

$$V_{\mathrm{xa}}(\boldsymbol{r}) = -e^2 \sum_{\mathrm{b}} \int \frac{\phi_{\mathrm{b}}^*(\boldsymbol{r}')\phi_{\mathrm{a}}(\boldsymbol{r}')\chi_{\mathrm{b}}^{+}\chi_{\mathrm{a}}}{|\boldsymbol{r}-\boldsymbol{r}'|}\, \mathrm{d}^3r' \frac{\phi_{\mathrm{b}}(\boldsymbol{r})}{\phi_{\mathrm{a}}(\boldsymbol{r})}. \tag{3.6}$$

The product of the spin functions χ_{a} and χ_{b} implies that exchange potential is effective only between electrons of parallel spin. The total potential $V_{\mathrm{a}}(\boldsymbol{r})$ is different for each different basis function, and the determination of the potential requires the detailed knowledge of the wave functions. Thus complete solution of the Hartree–Fock equations involves many iterations until self-consistency is reached.

The exchange potential is further simplified by the Xα approximation of Slater (1951). For the free electron gas of density ρ one can show that the average exchange energy is

$$\bar{V}_{\mathrm{X}} = -3e^2(3\rho/8\pi)^{1/3}.$$

Slater therefore proposed the following approximation for the exchange potential

$$V_{\mathrm{xs}}(\boldsymbol{r}) = -3e^2(\tfrac{3}{4}\pi)^{1/3}[\rho_s(\boldsymbol{r})]^{1/3}, \tag{3.7}$$

where $\rho_s(\boldsymbol{r})$ is defined by a sum similar to that in eq. (3.5) except that only those states in spin state s are included. In a paramagnetic metal the spin up and spin down states are degenerate, so $\rho_s(\boldsymbol{r})$ is equal to one-half of the total density. We exhibit the spin dependence of the exchange potential so that it will be easier to describe the spin polarized band calculation later.

The arguments leading to the Slater exchange have been examined closely by Gáspár (1954) and Kohn and Sham (1965). They contended that it is more reasonable to reduce the exchange potential by a factor $\frac{2}{3}$. Since both the Slater exchange and the Kohn–Sham–Gáspár exchange are rough approximations of a complicated problem, and that the Hartree–Fock approximation leaves out the correlation effects, many workers prefer to put a factor α, whose value lies between $\frac{2}{3}$ and 1, in front of the Slater exchange potential. The value for α is chosen differently for different metals based on physical grounds. The consequences of various choices of α are reviewed by Dimmock (1971) and Callaway (1974). It should be noted that, after this simplification, the effective potential depends only on the electron density for each spin, and is the same for all basis states of the same spin.

To start a band calculation for rare-earth metals it has been customary to use the potential constructed from overlapping atomic charge densities (Mattheiss, 1964). The calculations performed this way are not self-consistent because we expect the distribution of the valence electrons to be very different in the solid

from that in the atom. The question of self-consistency has been studied in detail for a number of transition metals and compounds (Snow and Waber, 1967; Connolly, 1967; Papaconstantopoulos et al., 1972). It has been found that 1), the final result of a self-consistent calculation depends on the choice of α, and 2), there is remarkable similarity between the result of a self-consistent calculation with $\alpha = \frac{2}{3}$ and that of a non-self-consistent calculation with $\alpha = 1$. The latter observation gives us confidence in the band structure calculations of rare earths because they have all been done with full Slater exchange and with no attempt at self-consistency. The self-consistency question is less meaningful when one compares the calculated results with experiments. As Dimmock pointed out in his review, it is very likely that, for best comparison between theory and experiment, one should use different potentials for different physical problems. There is no reason to expect the potential which gives the best Fermi surface will also give the best binding energy. In many instances a band calculation is done repeatedly, with the potential adjusted each time, until one obtains agreement with a particular experiment. Until recently there had been no detailed experimental results on rare earth metals to enable such adjustments to be made.

The mathematical problem of solving the Schrödinger equation is made easier by idealizing the potential according to the muffin–tin (MT) approximation of Slater (1937). A set of non-overlapping spheres is drawn, one around each ion. The potential is spherically symmetrized within each sphere and is approximated by a constant in the interstitial region between the spheres. In the next level of sophistication one adds a correction term to the MT potential to bring in the non-uniform part of the potential outside the MT spheres (Koelling et al., 1970). In general the warping does not affect the energy very much, but does affect the distribution of the bonding charges and the anisotropy of the neutron form factor (Harmon and Freeman, 1974a). A method has been formulated to correct for the warping effect in the potential inside the MT sphere (Williams et al., 1974). However, the method has not yet been applied to rare earth metals.

2.2. *The augmented plane wave method*

The APW method is a variational method for calculating the eigenfunctions and eigenvalues of the periodic MT potential. There are a number of comprehensive reviews of this method and its relativistic generalization (RAPW) (Mattheiss et al., 1968; Loucks, 1967; Dimmock, 1971; Callaway, 1974). We will briefly mention the philosophy of the method and some practical considerations that arise in connection with rare-earth metals.

Inside each MT sphere the trial wave function is a linear combination of spherical waves

$$\psi_{\mathbf{k}}^{\mathrm{I}}(\mathbf{r}) = \sum_{lm} C_{lm} R_l(E, r) Y_{lm}(\hat{\mathbf{r}}), \tag{3.8}$$

where $\mathbf{r}$ is measured from the center of the MT sphere, and the radial function

satisfies the differential equation

$$\left(\frac{\hbar^2}{2m}\frac{\mathrm{d}^2}{\mathrm{d}r^2}+V(r)+\frac{\hbar^2 l(l+1)}{2mr^2}\right) rR_l(E,r)=ErR_l(E,r), \tag{3.9}$$

where $V(r)$ is the spherical potential within the muffin-tin sphere. Outside the MT sphere the wave function is a linear superposition of plane wave states

$$\psi_{\boldsymbol{k}}^{\mathrm{II}}(\boldsymbol{r})=\sum_{\boldsymbol{K}_n} A_n \exp[\mathrm{i}(\boldsymbol{k}+\boldsymbol{K}_n)\cdot\boldsymbol{r}], \tag{3.10}$$

where $\boldsymbol{K}_n$ are the reciprocal lattice vectors. It is clear that $\psi_{\boldsymbol{k}}^{\mathrm{II}}(\boldsymbol{r})$ is of the Bloch form. The two pieces of wave functions are matched at the surface of the MT sphere. This gives a set of linear relations between the coefficients C_{lm} and A_n. A variational calculation, taking into account of the fact that the gradients of the wave functions are not matched a priori across the MT sphere, give a set of linear homogeneous equations for the coefficients A_n,

$$\sum_n M_{mn}A_n=0. \tag{3.11}$$

The condition for nontrivial solution determines the energy eigenvalues $E(\boldsymbol{k})$ for each wave vector $\boldsymbol{k}$. The normalized sets of solutions for A_n determine the wave functions. The relativistic method (Loucks, 1965) is very similar in principle except that the variational equations are deduced from the Dirac equation and the trial wave functions are spinors. The spin–orbit coupling is automatically included in the calculation.

The matrix elements M_{mn} depend on the energy and the potential through the logarithmic derivative of the radial function

$$L_l=\frac{\mathrm{d}}{\mathrm{d}r}R_l(E,r)|_{r=r_{\mathrm{MT}}}/R_l(E,r_{\mathrm{MT}}). \tag{3.12}$$

The importance of each partial wave can be estimated by comparing L_l with the logarithmic derivative for the free particle, i.e. the solution of eq. (3.9) with $V(r)=0$. For sufficiently large l the centrifugal potential becomes the dominant term, so the radial function becomes close to the free particle solution. As a result one needs to include only the lower l values in the sum in eq. (3.8). For rare earth band calculations it is sufficient to go up to $l=4$.

The number of reciprocal lattice vectors is dictated by the convergence criterion of the numerical solution. For heavy rare earths in the hcp structure the first few band energies at the center of the Brillouin zone converge within 0.002 Ry when one includes in the sum about 30 well chosen plane wave states. Similar degree of convergence at an arbitrary $\boldsymbol{k}$ point in the zone may be achieved by an additional 10 more $\boldsymbol{K}_n$ vectors. Matching the derivatives of the wavefunctions across the MT sphere gives the most stringent convergence criterion. According to Harmon et al. (1973) the kink in the d state wavefunction is smoothed out only with over 80 basis functions. The authors also pointed out that, for the purpose of calculating matrix elements, such high degree of

convergence is not necessary because the d charge is mostly confined in the MT sphere and a slight error in the tail part is not important. For dhcp crystals about twice as many basis functions are needed for the same level of convergence.

2.3. *Results of band calculation*

It is convenient to discuss the results of the calculations by separating the rare earth metals into groups. We will discuss the metals Y and Sc together with the trivalent heavy lanthanides Gd, Tb, Dy, Ho, Er, Tm and Lu because of their close similarity in band structure. The trivalent light lanthanides La, Pr and Nd and Pm form another group because they have the dhcp structure, see ch. 2, section 6. The Ce is in a class of its own. The complicated structure of Sm makes a band calculation prohibitively difficult.

2.3.1. *Trivalent heavy rare earths*

The trivalent heavy lanthanides Gd, Tb, Dy, Ho, Er, Tm, and Lu, together with Sc and Y, all have the hcp structure. The lattice parameters vary smoothly with the atomic number. It was anticipated that these metals have very similar band structure. However, the widely held notion that the energy bands were free electron like was proved wrong by the first band calculation of Dimmock and Freeman (1964). This calculation stimulated a thorough examination of the electronic structure of rare earth metals, and led to the subsequent breakthrough in correlating the electronic properties with the magnetic ordering of lanthanide metals.

The band calculation of Dimmock and Freeman was done for paramagnetic Gd, i.e. by putting equal numbers of 4f electrons in spin-up and spin-down states in constructing the potential. Two different starting potentials were used in the non-relativistic APW calculation, but the results were remarkably similar. The energy bands obtained from one of these calculations are plotted along high symmetry axes of the Brillouin zone as shown in fig. 3.1. The two bottom bands

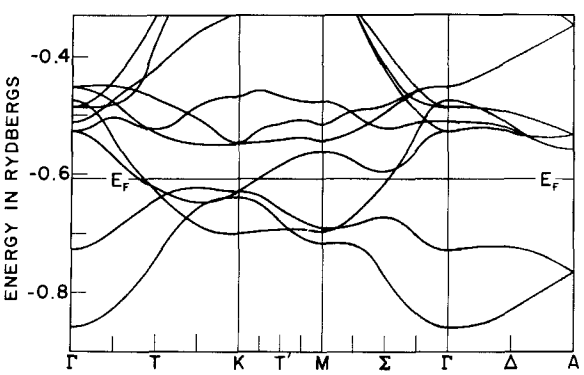

Fig. 3.1. The non-relativistic energy bands for Gd (Dimmock and Freeman, 1964).

have the s, p character, but near the Fermi level they intersect and hybridize with a set of flat d bands. The band structure is typical of transition metals rather than nearly free electron metals.

Bearing in mind the inherent uncertainties in the starting potential, Freeman et al. (1966) investigated a number of different potentials constructed from different atomic configurations. The overall band structure was found to remain very much the same. Just like in transition metals the location of the d band relative to the s, p band might vary as much as 0.5 eV with the assumed d state occupation in the starting atomic configuration. The total bandwidth was more sensitive to the choice of α, the scale factor of the Slater exchange. The authors also studied the band structure across the series, Gd, Tm, Lu and a hypothetical hcp La. The 5d band was found to move up with increasing atomic number relative to the s, p band, but otherwise all the metals had the same general band structure.

The density of states for the Gd bands in fig. 3.1 is shown in fig. 3.2. There is a region of high density of states near the Fermi level, labelled in the figure as E_F, reflecting the fact that the d bands are flat compared with the s, p bands. At the Fermi level the density of states is three times that at the Fermi level E_F^0 of the free electron model with the same number of electrons. This explains in part the very high electronic specific heat of rare earth metals (see ch.5). Also, as pointed out by Dimmock and Freeman, a high density of states is needed to account for the large excess magnetic moment, about 0.6 Bohr magneton per Gd atom, which arises from the polarization of the conduction bands by the ordered 4f moments.

In all of these calculations a very narrow 4f band appears below the conduction bands, and the location of the 4f band is very sensitive to the potential. As mentioned earlier it is not meaningful to think of the 4f electrons in band terms, so one should not attach too much significance to this result.

The calculated Fermi surfaces for hcp La, Gd, Tm and Lu are also very similar in essential features. In fig. 3.3 we show the Fermi surface for Gd

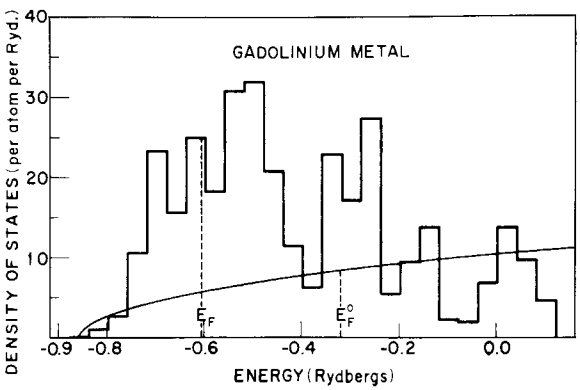

Fig. 3.2. The density of states of Gd (Dimmock and Freeman, 1964).

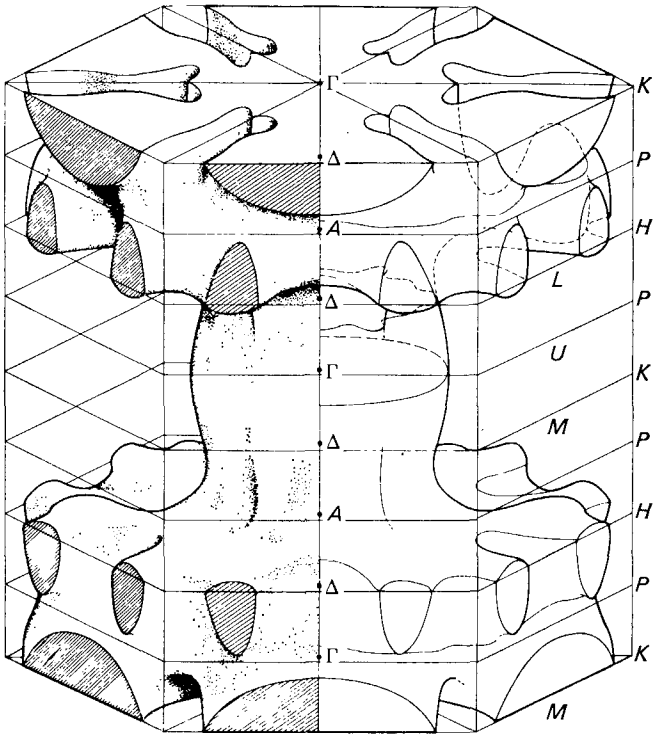

Fig. 3.3. The Fermi surface of Gd (Freeman et al., 1966).

(Freeman et al., 1966). For clarity the Fermi surface is presented in the double zone scheme by folding the bands between Γ and A into the extended zone $\Gamma A\Gamma$. It is an open surface, namely, it connects from one Brillouin zone to the next. The main feature of the surface is a central column with arms reaching out in the AHL and ΓKM planes. More detail of this surface can be found in Freeman (1972). It is a hole surface in the sense that the states outside the large cylinder are occupied. The sizes of the smaller pieces depend on the potential but the general shape of the surface does not. The lack of sensitivity of the Fermi surface to the potential is due to the fact that the d bands have a much higher density of states than the s, p bands. Although the d bands may shift relative to the s, p bands by as much as 0.5 eV, the transfer of electrons from the d bands to the s, p bands is relatively small. This causes the Fermi level to float with the d bands, and the effect on the Fermi surface structure may be simulated by taking one set of bands and moving the Fermi level up or down by a much smaller amount, about 0.05 eV. Thus only the shapes and sizes of the small pieces may be affected. As a rule it is possible to obtain a fairly reliable Fermi surface for transition metals based on a rather crude band structure calculation.

The lanthanide metals are nearly as heavy as lead, so the spin-orbit coupling should be significant. Shortly after formulating the relativistic APW method

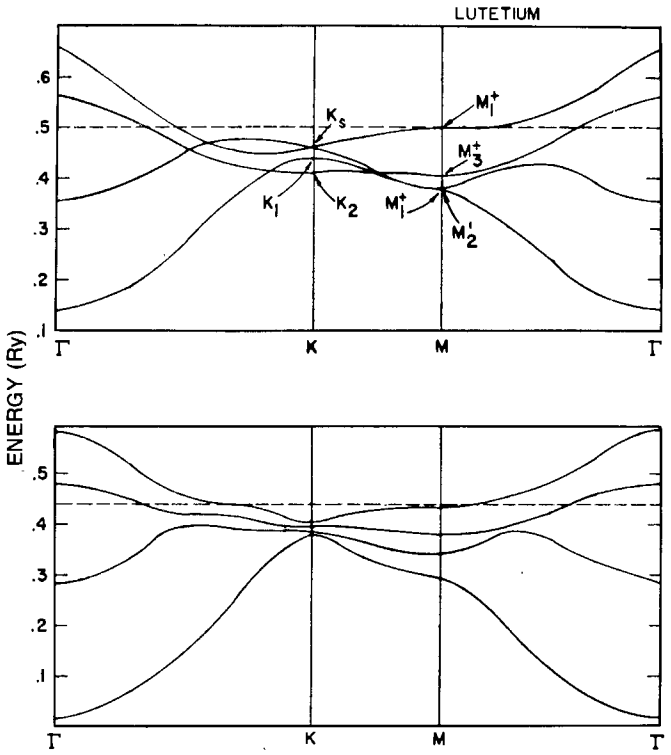

Fig. 3.4. Comparison between the non-relativistic (top) and the relativistic energy bands of Lu (Keeton and Loucks, 1966).

(Loucks, 1965), Loucks and his collaborator (Keeton and Loucks, 1966, 1968) performed a series of RAPW calculations for Gd, Dy, Er, and Lu. The starting potentials were constructed from the relativistic charge densities of Liberman et al. (1965). The results showed that the spin-orbit coupling had the effect of eliminating all the band crossings. In addition, it removed the two-fold degeneracy on the AHL plane except along the AL axis (Herring, 1937; Cohen and Falicov, 1960). A comparison between the non-relativistic and relativistic band structures of Lu is shown in fig. 3.4. The relativistic bands of Dy are shown in fig. 3.5.

The relativistic bands give Fermi surfaces very similar to the non-relativistic results except in one subtle but important aspect. The Gd Fermi surface is the same as that reported by Freeman et al. (1966), but for Dy, Er and Lu the region around the AL axis between the small arms in the AHL plane are filled up, very similar to the Fermi surface of Y reported earlier by Loucks (1966) shown in fig. 3.6. This "webbing" feature gives rise to large pieces of nearly parallel surfaces perpendicular to the *c* axis. The webbing becomes thicker and the boundary surfaces flatter with increasing atomic number as shown in cross-section plots in fig. 3.7. Keeton and Loucks (1968) pointed out the correlation between the

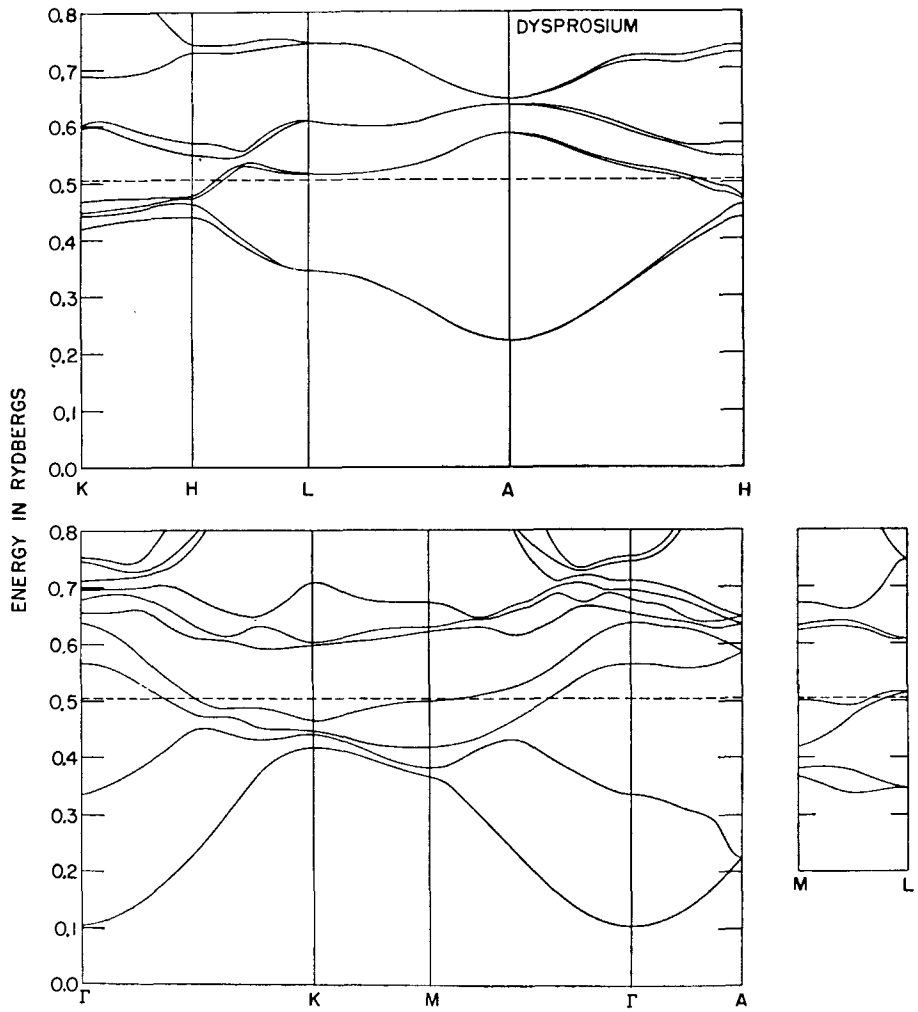

Fig. 3.5. Relativistic energy bands of Dy (Ketton and Loucks, 1968).

webbing feature and the magnetic ordering property of the metal when it first orders. The lack of webbing favors ferromagnetic ordering in Gd. The thickness of the webbing in other metals correlates very well with the observed periodicity of the magnetic structure of the metals just below the ordering temperature. This will be discussed in more detail in section 4.2 and ch. 7, section 3.2.

In fig. 3.7 the Fermi surface cross-section for Tb was constructed from interpolating between Gd and Dy. Band calculations by Mackintosh (1968) and Jackson (1969), together with a later calculation by Fleming and Liu (1970), showed that the conjecture made by Keeton and Loucks was correct.

The dependence of the webbing feature on the starting potential was studied

Fig. 3.6. The Fermi surface of Y (Loucks, 1966).

by Keeton and Loucks (1968) using two different potentials for Dy and Er. The differences in the results were minimal. However, it is not clear whether a different potential used in RAPW calculation of Gd will produce a webbing. One can not rule out the possibility that a small webbing may exist in Gd but the d–f exchange matrix element renders it ineffective in determining the magnetic ordering property of Gd (see section 4.3.1). It will require more careful cal-

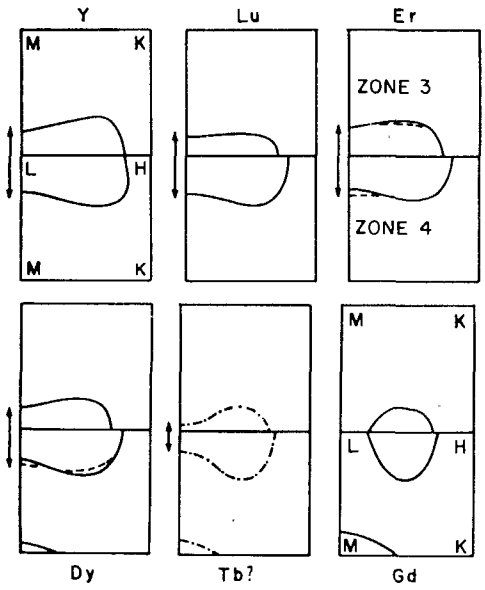

Fig. 3.7. The webbing feature on the Fermi surface of hexagonal heavy rare earths (Keeton and Loucks, 1968).

culations coupled with measurements of the Fermi surface geometry to answer this question.

The energy bands and Fermi surface of Sc metal have been found to resemble the rare earths Dy, Er, Tm, and Lu (Fleming and Loucks, 1968; Rath and Freeman, 1975). The APW calculation of Rath and Freeman using warped MT potential gives a very similar result to the early RAPW work of Fleming and Loucks. This may be regarded as further evidence that the webbing is not sensitive to the starting potential.

The ground state of Gd is actually ferromagnetic with the spins of all the 4f shells lined up in the same direction. This causes a difference in the exchange potential gives a very similar result to the early RAPW work of Fleming and section 2.1). The 4f shell of Gd has a very simple structure, with seven electrons all in the same spin state. The charge distribution of 4f electrons is spherically symmetric. The first spin polarized band calculation by Harmon and Freeman (1974a) was done by APW method with warped MT potential and different Slater exchange potentials for different spins. The starting atomic configurations are $4f^{7}5d^{0.5}6s^{1}$ for spin up and $5d^{0.5}6s^{1}$ for spin down. The band structure shown in fig. 3.8 consists of two sets, with spin up bands lower than spin down bands by 0.8 eV on the average. The shapes of the bands are very similar to the non-relativistic paramagnetic bands, again indicating that the band structure is insensitive to the potential.

In fig. 3.9 the densities of states and the integrated density of states for the two spin bands are plotted. The Fermi level is determined by filling the bands

with six electrons per cell, which contains two atoms. This puts 3.72 electrons in the spin-up band and 2.28 in the spin-down band. The net moment per atom obtained this way is 0.75 Bohr magneton, which is slightly larger than the excess moment of 0.63 Bohr magneton per atom (Roeland et al., 1975). There may be a number of reasons for this discrepancy, for instance, (1) the mesh of $\boldsymbol{k}$ points in the calculation is not fine enough to give an accurate determination of the

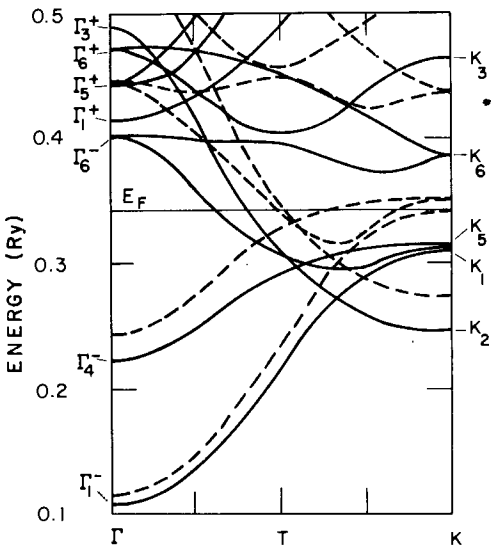

Fig. 3.8. The non-relativistic spin split bands of ferromagnetic Gd (Harmon and Freeman, 1974a). The solid lines are for the spin up bands and the dashed lines are for the spin down bands.

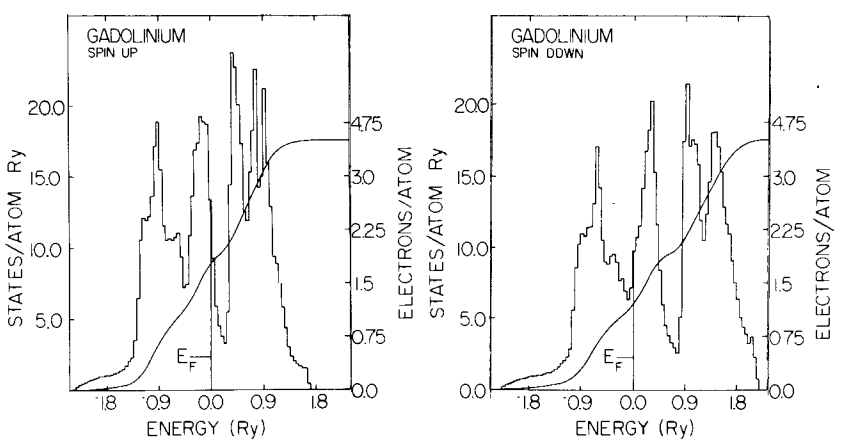

Fig. 3.9. The densities of states of (histogram) and the integrated density of states (smooth curve) of the two spin bands of ferromagnetic Gd (Harmon and Freeman, 1974a).

density of states, and (2) the calculation is non-relativistic so that the conduction electron orbital moment contribution is left out. The spin–orbit interaction makes the orbital moment line up opposite from the spin, so a part of the spin moment is cancelled out. This would bring the calculated moment per atom closer to the experimental value. Other experimental information on the size of the band splitting will be discussed later in connection with optical properties (section 3.1) and de Haas–van Alphen effect (section 2.4).

It can be seen in fig. 3.9 that the Fermi level falls on the right of a large peak in density of states for the spin-up band, and on the left of the peak for the spin-down band. In a paramagnetic calculation the Fermi level is situated at the middle of the peak (Keeton and Loucks, 1968). This means that total density of states is reduced when the bands are split, from 28.5 states/Ry·atom to 23 states/Ry·atom. One must keep in mind this complication when one compares the calculated density of states for the paramagnetic metal with the experimental data, such as the low temperature electronic specific heat. The same consideration applies to all magnetic rare-earth metals.

The main motivation of the spin polarized band calculation was to study the spatial distribution or form factor of the conduction electron spin. This will be discussed more thoroughly in ch. 7, section 4.

2.3.2. *Trivalent light lanthanides* La, Pr, *and* Nd

The metal La can exist in both the dhcp and fcc crystal structures. Pr and Nd, which have a thermodynamically stable dhcp structure, have been prepared in the fcc structure under unusual conditions of rapid cooling and/or addition of impurities. The RAPW energy bands in the dhcp phase were reported by Fleming et al. (1968), and the APW bands by Ghosh et al. (1970). In fig. 3.10 the RAPW bands for La are shown in high symmetry directions. The APW bands for La and the RAPW bands of Pr and Nd are substantially the same. Aside from the fact that the number of bands is doubled because there are now four atoms per unit cell, the general structure is very similar to that of heavy rare earths. A high concentration of flat bands are seen near the Fermi level, indicating the d band nature of these metals.

It is difficult to visualize the Fermi surface of these metals because there are too many pieces. The bands are relativistic, so it is not possible to fold them out into the extended zone as was done for heavy rare earths. This makes the graphical representation of the Fermi surface rather difficult. In fig. 3.11 we show the cross sections of the various pieces of Fermi surface with the high symmetry planes of the Brillouin zone. A detailed description of the Fermi surface structure is given in the original article.

One important difference between this Fermi surface and that of heavy rare earths is the lack of large, flat, and nearly parallel webbing pieces perpendicular to the c axis. The authors pointed out a possible relation between the lack of webbing and the occurrence of the dhcp crystal structure. If in the hcp phase of these metals the thickness of the webbing is nearly one-half the distance from

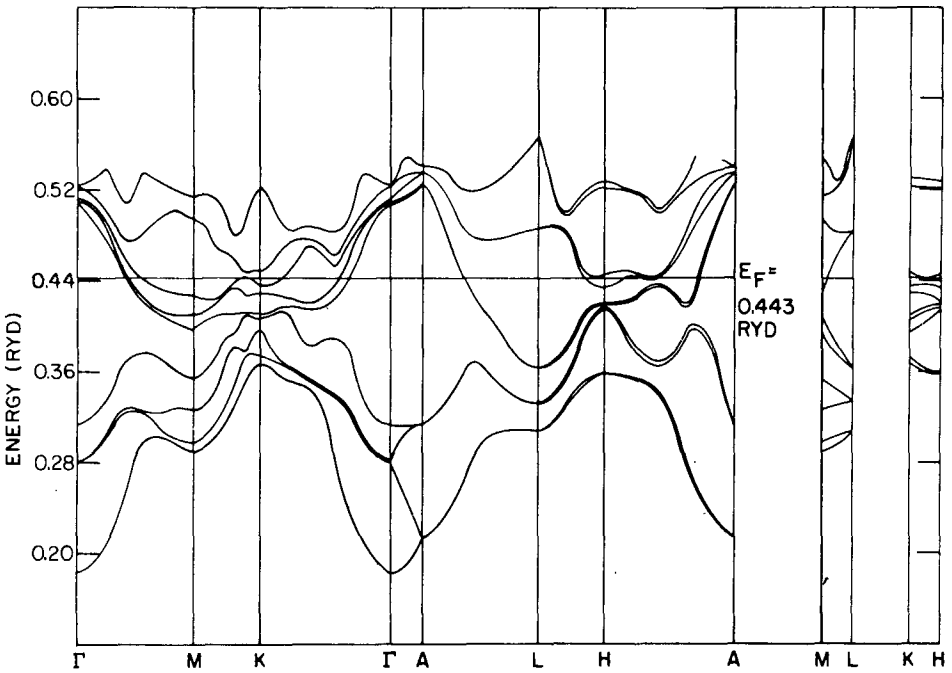

Fig. 3.10. The relativistic bands of dhcp La (Fleming et al., 1968).

the zone center Γ to the zone surface A, then the lattice becomes unstable against a doubling of the periodicity. This would destroy the webbing pieces and a drastic reduction of the density of states at the Fermi level would result. The latter effect can be seen by comparing the value 28.5 states/Ry·atom for Gd with 19.4 states/Ry·atom for La. The complicated nine layer periodic structure of Sm may also be a consequence of this type of lattice instability.

The magnetic structure of Nd and polycrystalline Pr may be explained on the basis of nearly parallel (nesting) pieces of Fermi surface. The authors suggested a number of such pieces which may nest in the a direction of the crystal as shown in fig. 3.12. More detailed discussion will be found in section 4.2. Recent neutron scattering results in β–Ce (Stassis, 1975) seem to indicate that it has a similar magnetic structure to Nd. Pm has the dhcp structure (Koehler et al., 1973), and is situated between Nd and Sm on the periodic table. We may conjecture that the two metals β–Ce and Pm in the dhcp phase have the same band structure as is discussed here.

Myron and Liu (1970) studied the energy bands of fcc La and the hypothetical fcc Pr by the relativistic APW method. The potentials were constructed from the relativistic atomic charge densities of the configurations $5d^16s^24f^0$ for La and $4d^06s^24f^3$ for Pr. The 4f charge distribution for Pr was assumed to be paramagnetic. The three lowest energy bands for La are shown in fig. 3.13. The resemblance of these bands to those for Th (Gupta and Loucks, 1969) is

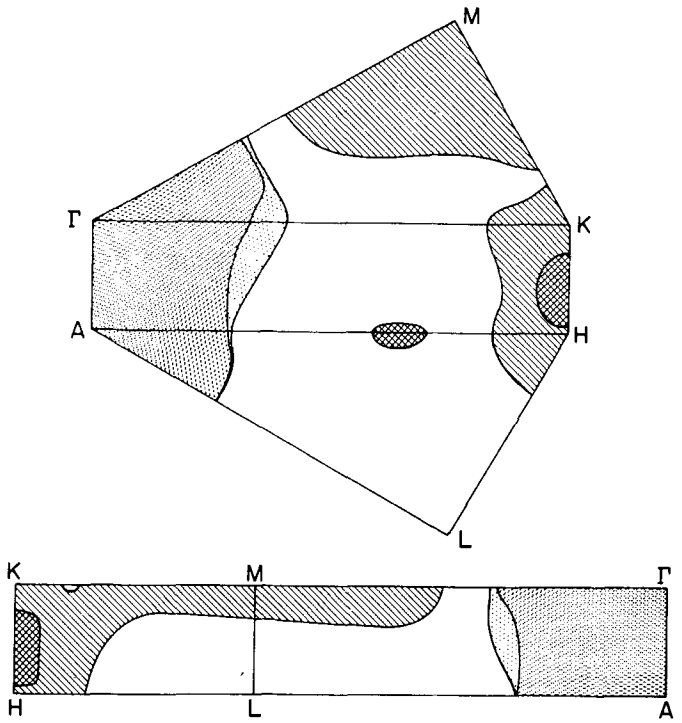

Fig. 3.11. Cross sections of the Fermi surface of dhcp La with the high symmetry planes of the Brillouin zone. The shaded region is the fifth zone hole surface, the lightly shaded region is the sixth zone hold surface, the crosshatched regions in the shape of two ellipsoids are the seventh and eighth zone electron surfaces, and the large diagonally shaded region is the major part of the seventh zone electron surface (Fleming et al., 1968).

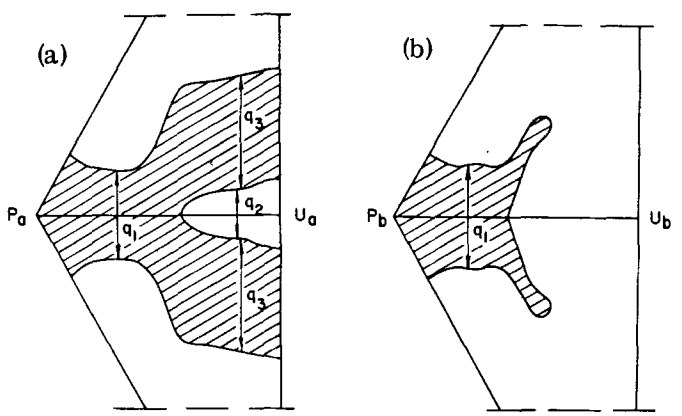

Fig. 3.12. Possible nesting pieces of Fermi surface for dhcp lanthanides (Fleming et al., 1968).

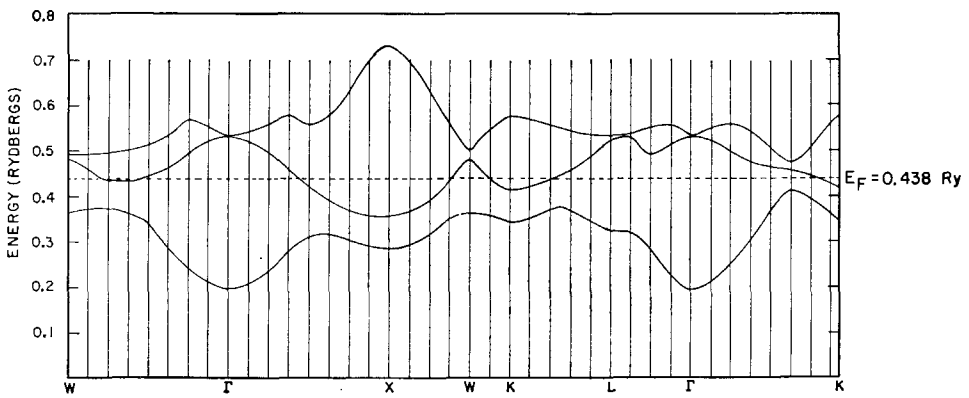

Fig. 3.13. The relativistic energy bands of fcc La (Myron and Liu, 1970).

striking. Although the bands for the hypothetical fcc Nd has not been calculated, it seems safe to predict that they too should have the same structure. Just like Th metal the 4f levels of La and Pr tend to lie within the energy range of the conduction bands. For this reason Myron and Liu adopted the technique proposed by Gupta and Loucks (1969) to remove the 4f levels by smoothing out the singularity in the logarithmic derivative of the 4f radial wavefunction. The Fermi surface is multiply connected very much like that of Th. The cross-sections of Fermi surface in high symmetry planes are depicted in the original article. They are not reproduced here because it is not very likely that the shapes of the pieces will be verified experimentally in the foreseeable future. It suffices to mention that there is a lack of nearly parallel or nesting pieces of Fermi surface. The authors pointed to this as the reason for the simple ferromagnetic ordering property observed in Nd and polycrystalline Pr in the metastable fcc phase.

The density of states at the Fermi level for fcc La was found to be 24.8 states/Ry·atom, compared with the value 19.4 states/Ry·atom for dhcp La (Fleming et al., 1968). Experimental values as determined from the low temperature specific heat are 33.6 and 27.2 respectively. Although the experimental numbers are much larger, presumably due to electron-phonon mass enhancement, the ratio of the theoretical values for the two structures agree very well with the ratio of the experimental values.

2.3.3. *Divalent* Eu *and* Yb

The metals Eu and Yb have very different electronic structures from their near neighbors. They are both divalent, and their 4f occupancy, $4f^7$ and $4f^{14}$, is one more than what one would expect from interpolating between their nearest neighbors. The 4f shell appears to be highly stable when it is half-filled or completely filled, to the extent that in these metals one valence electron goes

into the 4f shell to gain this stability. Quite naturally, these metals have different crystal structures from the trivalent rare earths.

The energy bands of bcc Eu were calculated by Freeman and Dimmock (1966) using APW method and by Andersen and Loucks (1968) using RAPW method. The non-relativistic bands are shown in fig. 3.14 and the relativistic bands in fig. 3.15. In both papers the authors stressed the similarity between the structure of

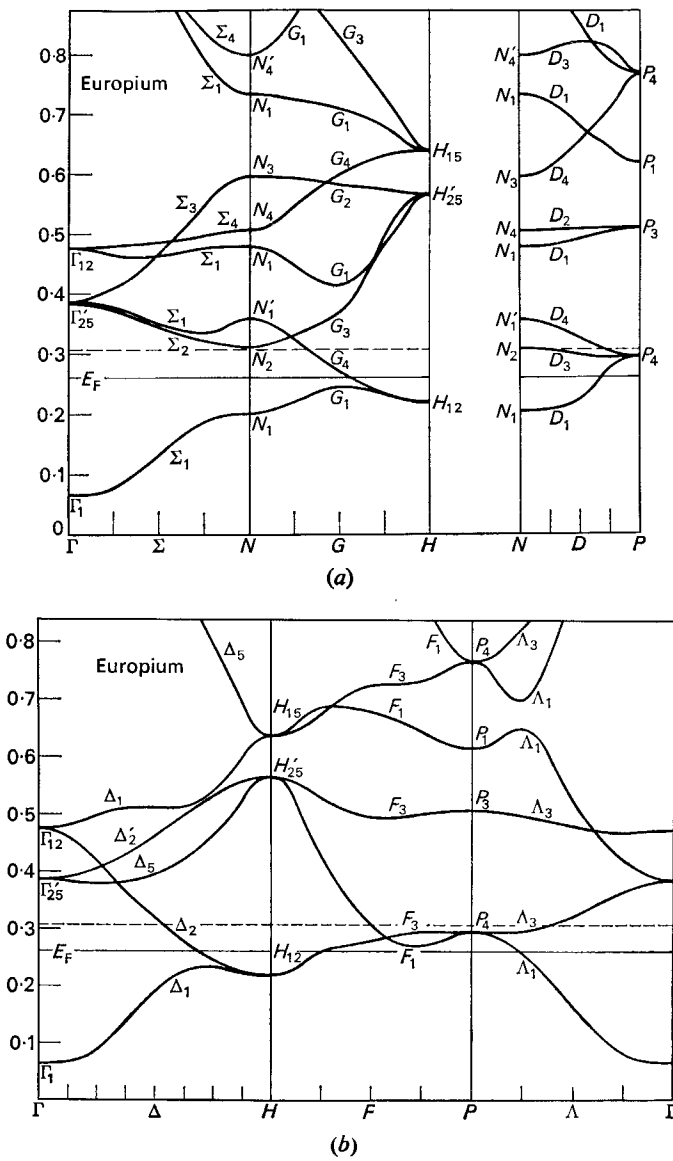

Fig. 3.14. The non-relativistic energy bands of bcc Eu (Freeman, 1972).

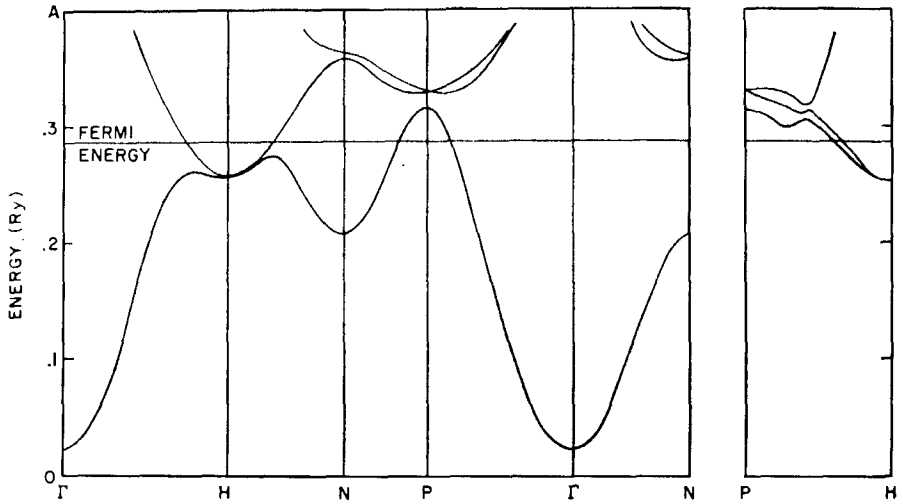

Fig. 3.15. The relativistic energy bands of bcc Eu (Andersen and Loucks, 1968).

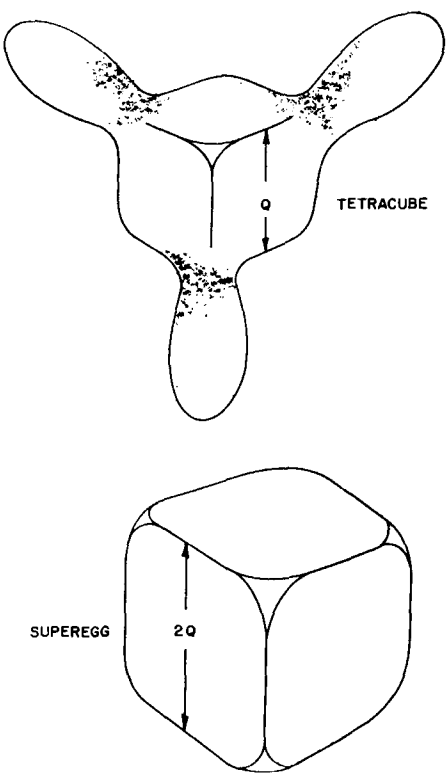

Fig. 3.16. The Fermi surface of bcc Eu (Andersen and Loucks, 1968).

these bands and those of the bcc transition metals. The Fermi surface determined by Andersen and Loucks consists of two pieces shown in fig. 3.16. The large electron surface centered around H has the shape of a cube with corners rounded off, and the hole surface centered around P is shaped like a rounded-off cube with ellipsoids tetrahedrally attached on four of the corners. The separation between the flat pieces of the hole cube agrees well with the experimentally determined magnetic structure periodicity of Eu. The effects of these flat pieces and the flat pieces in the electron cube should be observable in the phonon spectrum as well. Andersen and Loucks also worked out the sizes of several extremal areas of the Fermi surface in the hope that future experiments may be conducted to check their findings.

The Yb metal was the first rare earth metal studied with the de Haas–van Alphen measurement. Tanuma et al. (1967) purified a piece of raw metal by the vacuum distillation method. A single crystal specimen was obtained by spark cutting a large grain in a vapor condensed ingot. The resistivity ratio of the specimen was not reported. The crystal structure was determined to be fcc by X-ray analysis at room temperature. Two de Haas–van Alphen frequencies were observed, and the authors suggested that they came from two separate pieces of Fermi surface. Datars and Tanuma (1968) deduced from magnetoresistance measurements at 1.3 K with fields up to 20 KG that there were no open orbits in Yb. Therefore, they concluded that Yb is semimetallic with two small, closed pieces of Fermi surface.

The ab initio RAPW band calculation carried out by Johansen and Mackintosh (1970) on the fcc Yb resulted in a small energy gap between filled and empty bands as shown in fig. 3.17. However, a small change in potential could conceivably alter the band structure enough to produce over-lapping bands. Instead of constructing a different potential the authors arbitrarily raised the

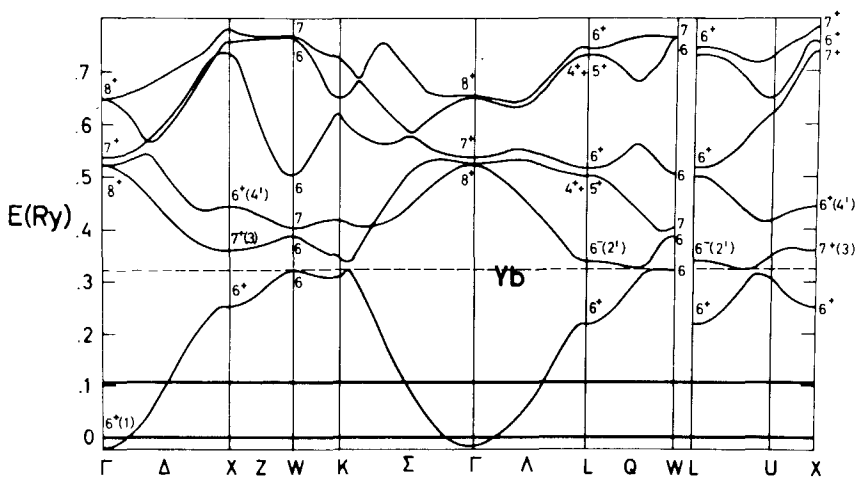

Fig. 3.17. The relativistic energy bands of fcc Yb (Johansen and Mackintosh, 1970).

position of the d resonance (the energy at which the $l = 2$ logarithmic derivative is singular) by 0.1 Ry and demonstrated that the energy gap could be made to disappear. Koelling and Harmon (1972) showed that the warping of the MT potential could cause a significant change of the s–d hybridization and make the bands overlap.

Bucher et al. (1970) and Kayser (1970) independently reported that the stable low temperature phase of Yb is hcp rather then fcc. Tanuma et al. (1970) reexamined the de Haas–van Alphen effect and confirmed that Yb transforms to hcp after a cooling cycle to 1.2 K. A specimen prepared in this way may be predominantly in the hcp phase, but it inevitably contains some amount of the fcc phase. To what extent this mixture of phases may affect the de Haas–van

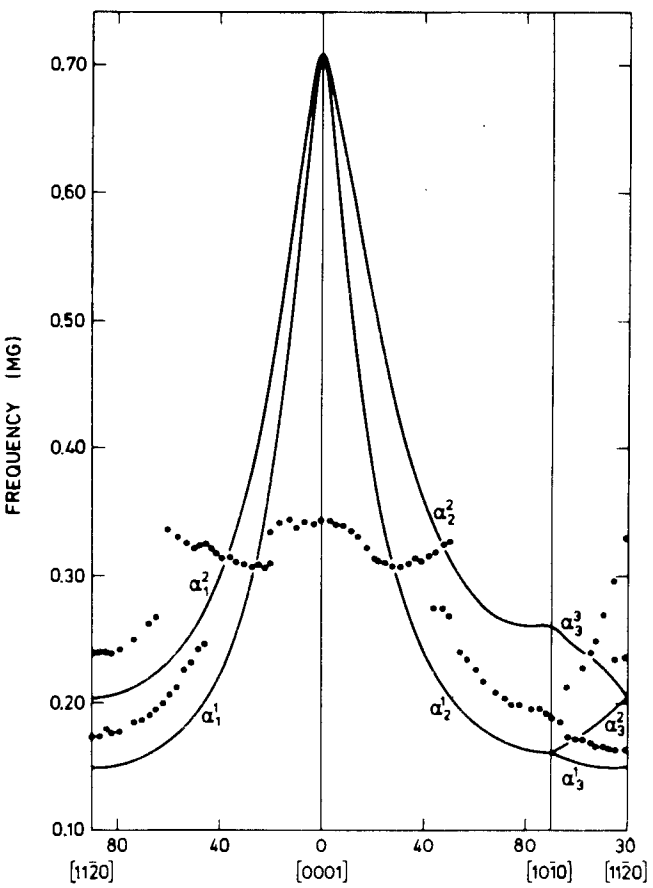

Fig. 3.18. The low frequency portion of the de Haas–van Alphen frequency branches for hcp Yb. The solid curves are the predictions of Jepsen and Andersen (1971), and the dots are the data of Tanuma et al. (1970).

Alphen data is not known. The observed dHvA frequencies were all in the 1–10 MG range. The low frequency branches are shown in fig. 3.18 and the high frequency branches in fig. 3.19. Subsequently Jepsen and Andersen (1971) did the ab initio RAPW calculation for hcp Yb in the MT potential approximation. The band structure and the Fermi surface are shown in fig. 3.20. The calculated dHvA frequencies are compared with the data in figs. 3.18 and 3.19. The low frequency branches were interpreted as coming from the electron pocket α on the ΓM axis. The branch at 0.3 MG was unaccounted for by the Fermi surface model, so the authors argued that they might come from beats between other frequencies. The frequencies of the μ piece are too small, but they have the correct angular dependence. A lowering of the d band by 10 mRy relative to the sp band would bring all the theoretical frequencies into agreement with the data. This shift of bands can be rationalized in many ways, for instance, the uncertainty in lattice parameter and the inaccuracy in the potential, especially the neglect of the non-muffin-tin part. The authors also noted that the Fermi level was in a region of very high density of states. They suggested this as a possible reason for the fcc–hcp phase transition.

The application of hydrostatic pressure of about 40 kbar induces a crystallographic phase transition in Yb from fcc to bcc. Johansen and Mackintosh (1970) studied this effect by calculating the energy bands of Yb under a simulated high

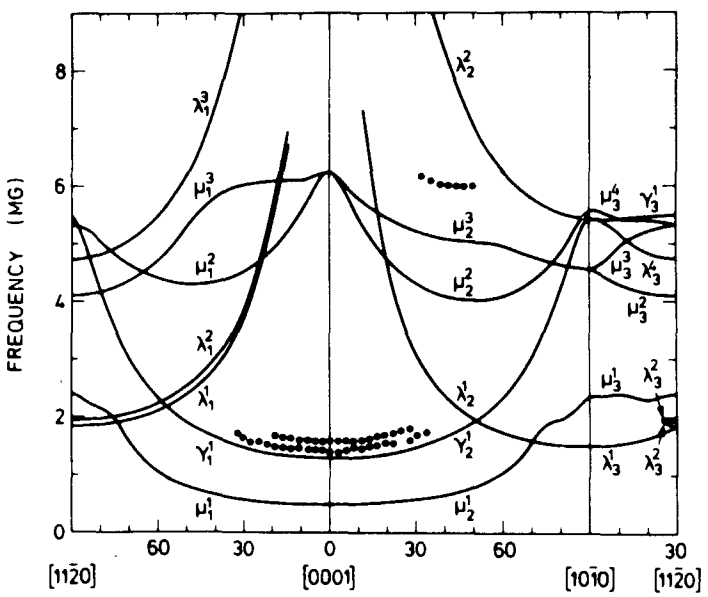

Fig. 3.19. The high frequency portion of the de Haas–van Alphen frequency branches for hcp Yb. The solid curves are calculated by Jepsen and Andersen (1971), and the dots are the data of Tanuma et al. (1970).

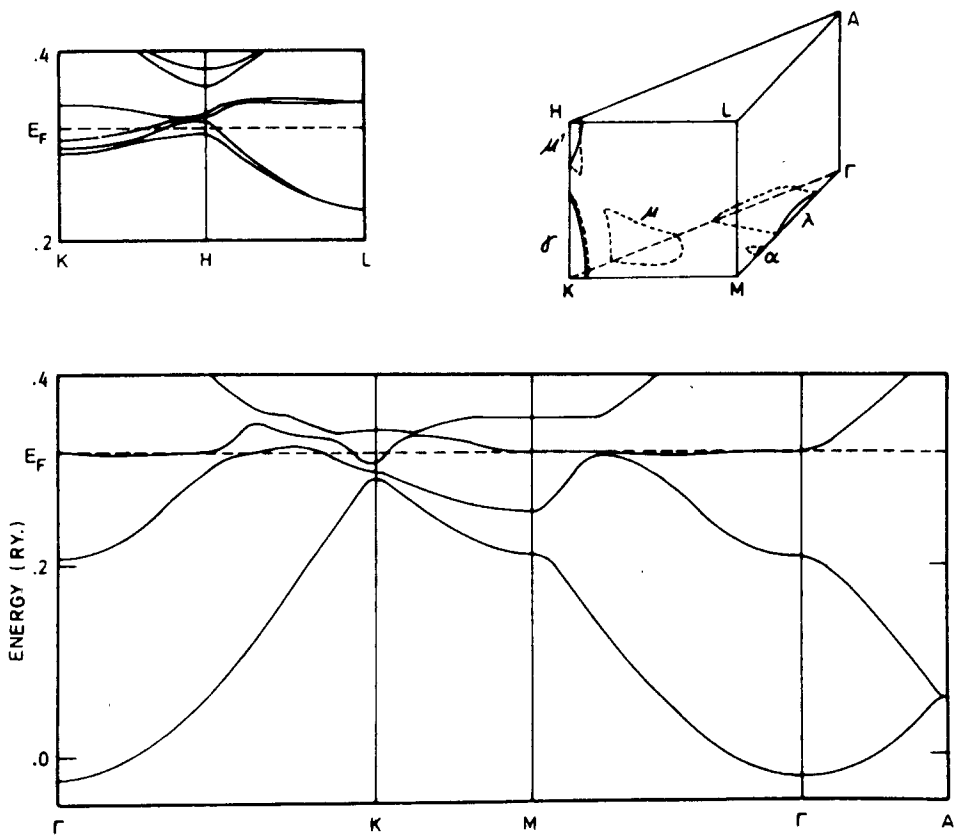

Fig. 3.20. The relativistic band structure and Fermi surface of hcp Yb (Jepsen and Andersen, 1971).

pressure, i.e. by reducing the cell volume to 0.8 and 0.6 of the volume under atmospheric pressure. Upon compression the increased electron density raises the kinetic energy, making the s, p type states rise relative to the bottom of the band. The d states also rise in energy but the major effect is a broadening of the total bandwidth because of the increased overlap between the nearest neighbor charge densities. This puts more d character into the occupied states so that the electronic structure shifts from Ca type (Vasvari et al., 1967) to Ba type (Johansen, 1969). This, the authors argued, is the reason that Yb prefers to take up the structure of Ba, which is bcc, under high pressure. In this connection Kmetko (1969) studied the pressure effect on many metals and concluded that the shift of occupied states from s, p-like states to states with increasing d character is a very general phenomenon which may be the underlying cause of all crystallographic phase transitions under pressure.

2.3.4. Ce

The band calculation of Ce is a formidable challenge to theorists. On the one hand there is ample evidence that the f level is very close to the Fermi level so that its population can be influenced by temperature and pressure, etc. (see ch. 4 sections 2.3 and 5 and ch. 9 section 2.1), but on the other hand we can not treat the f levels as a band because the strong Coulomb correlation effect within the shell of each atom makes the f state excitations highly localized in space. For this reason it is meaningless to discuss the band structure of Ce because it implies the treatment of the elementary excitations as Bloch states. Nevertheless band calculations have been done and the results are at times rather suggestive.

Waber and Switendick (1965) showed that the position of the "f band" is extremely sensitive to the potential, or equivalently the starting atomic configuration. Assuming the configuration $6s^25d^24f^0$ one finds the f band to be below the band complex, thereby making the f band fully occupied. However, on the assumption of occupied f states, $6s^25d^04f^2$, the f band rises above the occupied bands and so they end up being empty. Recently Mukhopadyay and Majumdar (1969) suggested a self-consistent band calculation as the way out of this difficulty. But the real issue here is not where a self-consistently determined f band will lie relative to the Fermi level, but how to handle the Coulomb correlation problem when the 4f occupation varies. This is outside the scope of the band calculation. By the same token the band calculation of Kmetko (1969) for γ–Ce, showing that the f bands are at the Fermi level, must also be viewed with skepticism.

2.4. *Experimental knowledge on the Fermi surface of rare earth metals*

Inspite of all the theoretical predictions about the Fermi surface geometry of rare earth metals, there was scanty experimental confirmation until recently. The difficulty in carrying out the measurements was due to the unavailability of crystals of high purity. Early experiments used the method of positron annihilation, which did not require high purity crystals. Unfortunately, the information obtained this way is not sufficient to map out the Fermi surface. With the development of the electrotransport method of sample purification, see ch. 2 sections 2.3 and 5.7, it is now possible to grow high quality crystals of a number of rare earth metals for de Haas–van Alphen experiments. We will review these results with emphasis on the latest findings.

2.4.1. *Positron annihilation in heavy rare earths*

In the positron annihilation experiment the single crystal specimen of the metal is bombarded with a beam of positrons. Once entering into the crystal lattice, the positrons lose their kinetic energy very rapidly and attain thermal

equilibrium with the lattice. Then each positron annihilates one electron in the metal to produce a pair of γ rays. If the electron–positron pair annihilates while at rest, the two photons will come out exactly opposite to each other in order to conserve momentum. The energy of each photon will be equal to the rest energy of the electron, mc^2. If the two initial particles move relative to each other, the relative momentum will be imparted to the photons. In particular, if the photons come out in a direction nearly perpendicular to the relative momentum, they will not be exactly antiparallel in direction but will make an angle $\pi-2\theta$ with each other. The angle θ measured the ratio of the relative momentum of the electron–positron pair and the momentum of the photon, $mc/\hbar$. Thus the distribution of the photons as a function of the angular deviation from antiparallelism gives information on the component of the relative momentum of the pair in the direction perpendicular to that of the photons. The thermal momentum of the positron is much smaller than the Fermi momentum or orbital momentum of the electron, so the relative momentum is mostly due to the electron. The initial momentum of the positron gives a predictable broadening of the angular distribution. Because of its positive charge the positron in the lattice tends to occupy the interstitial positions. As a result it tends to annihilate more readily with the band electrons than the core electrons.

The band electrons have a continuous distribution of momentum up to the Fermi momentum, and only the distribution of one component of the momentum is measured. So the final angular distribution of photons contains information on an average property of the Fermi surface. The information is not specific enough to help map out the Fermi surface, but it can be used to check theoretical models. The interpretation of the data is usually based on the independent particle model. The angular distribution $N(\theta)$ is given by

$$N(\theta) \propto \int \mathrm{d}\boldsymbol{p}_\perp \sum_{\boldsymbol{k}} F(\boldsymbol{p}, \boldsymbol{k}), \tag{3.13}$$

where the sum on $\boldsymbol{k}$ is over all occupied states, $\boldsymbol{p}$ is the momentum of the conduction electron, and the integration over $\boldsymbol{p}_\perp$ sums up all components of $\boldsymbol{p}$ not measured by the experiment. The function $F(\boldsymbol{p}, \boldsymbol{k})$ is the momentum distribution of the electron–positron pair

$$F(\boldsymbol{p}, \boldsymbol{k}) = \left| \int \psi_{\boldsymbol{k}}(\boldsymbol{r}) \psi_+(\boldsymbol{r}) \exp(-\mathrm{i}\boldsymbol{p}\cdot\boldsymbol{r}/\hbar) \mathrm{d}^3 r \right|^2, \tag{3.14}$$

where $\psi_{\boldsymbol{k}}(\boldsymbol{r})$ is the Bloch wave function for the electron in state $\boldsymbol{k}$, $\psi_+(\boldsymbol{r})$ is the positron wave function.

The experiments on rare earths were reported by Williams et al. (1966), Williams and Mackintosh (1968) and Szuszkiewicz (1973). In fig. 3.21 the data for Y in the c-axis is compared with the free electron theory and the theory based on the band calculation. The steep drop of the experimental curve at 2 mrad and the hump at 3 mrad are in sharp contrast with the free electron theory, but are reproduced quite well by the band theory. Both features are associated with the

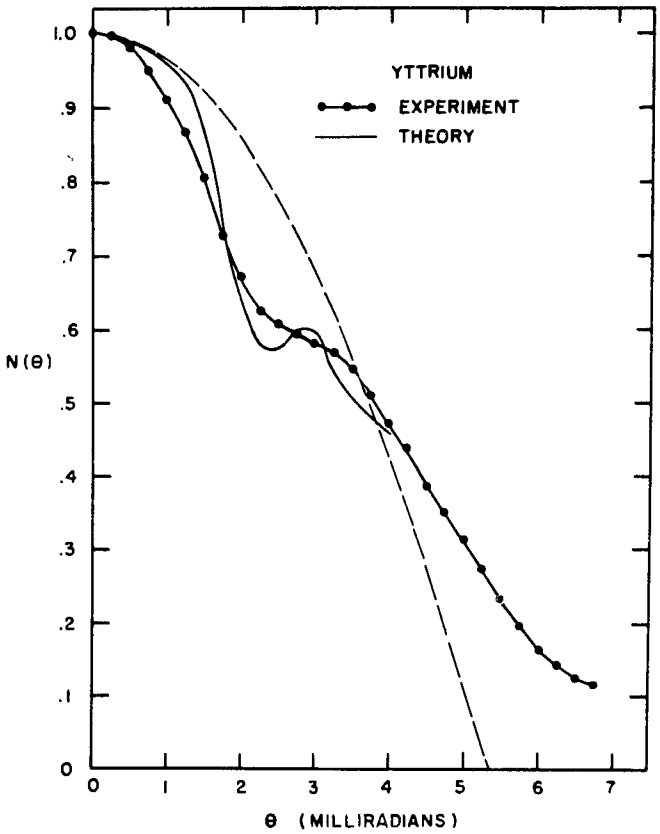

Fig. 3.21. The angular distribution of positron and annihilation γ rays for Y (Williams et al., 1966). The dashed curve is the calculated angular distribution in the free electron approximation.

rapid increase in hole surface area near the AHL plane. In the calculated curve the positron wave function was solved from the Schrödinger equation with a potential the same as that for the electrons but with the opposite sign and without the exchange part. There is some uncertainty in the calculation, not only in leaving out the many-body effects. A refined independent particle calculation by Gupta and Loucks (1968) gave a sharper drop off and a more pronounced hump. Nevertheless, the qualitative agreement between theory and experiment confirms the main features of the calculated shape of Fermi surface.

In fig. 3.22 the data on holmium in two different directions and at two different temperatures are shown. The near parabolic shape for the data along the *b* axis indicates that there is more symmetry in the Fermi surface around the hexagonal axis. However, the surface is not spherical because the data deviate considerably from the free electron theory. The slight temperature dependence of the *c* axis data for Ho reflects the change in band structure and Fermi surface due to magnetic ordering.

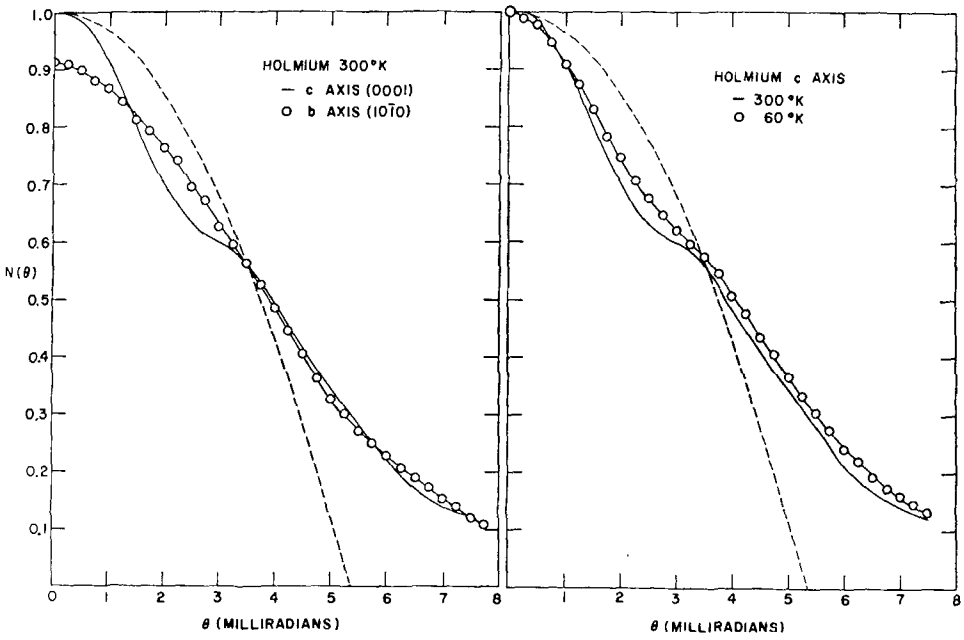

Fig. 3.22. The angular distributions of positron annihilation γ rays for Ho in two different directions at two different temperatures (Williams and Mackintosh, 1968). The dashed curves are the calculated angular distributions in the free electron approximation.

The angular distribution of coincident photons for Gd, Tb, Dy, Ho and Er are compared in fig. 3.23 (Williams and Mackintosh, 1968). There is a systematic change of the shape of the data curve between 2 to 3 mrad, and the authors attributed the variation to the progressive thickening of the webbing when going from Gd to Er.

Szuszkiewicz (1973) reported positron annihilation results for the entire series from La to Yb. The data appear to have less resolution than those of Williams and Mackintosh in that the fine structure due to the d bands is not evident in any of the metals. Furthermore, the data analysis was done in the most simple-minded manner. It consisted of finding how many sections of parabola were needed to fit the curve, for instance one for Eu and Yb but two for La and Ce. Not surprisingly, the data also indicated a great deal of similarity in electronic structure between the dhcp members of the group.

Details on positron annihilation studies on Ce are found in ch. 4 section 4.5.

2.4.2. *De Haas–van Alphen effect in* Lu, Y *and* Gd

When a strong magnetic field is applied to a metal the orbits of the band electrons are drastically modified into quantized Landau orbits. When the field increases the orbits with energies just below the Fermi level move up above the Fermi level and become depopulated. Because of the orbit quantization the

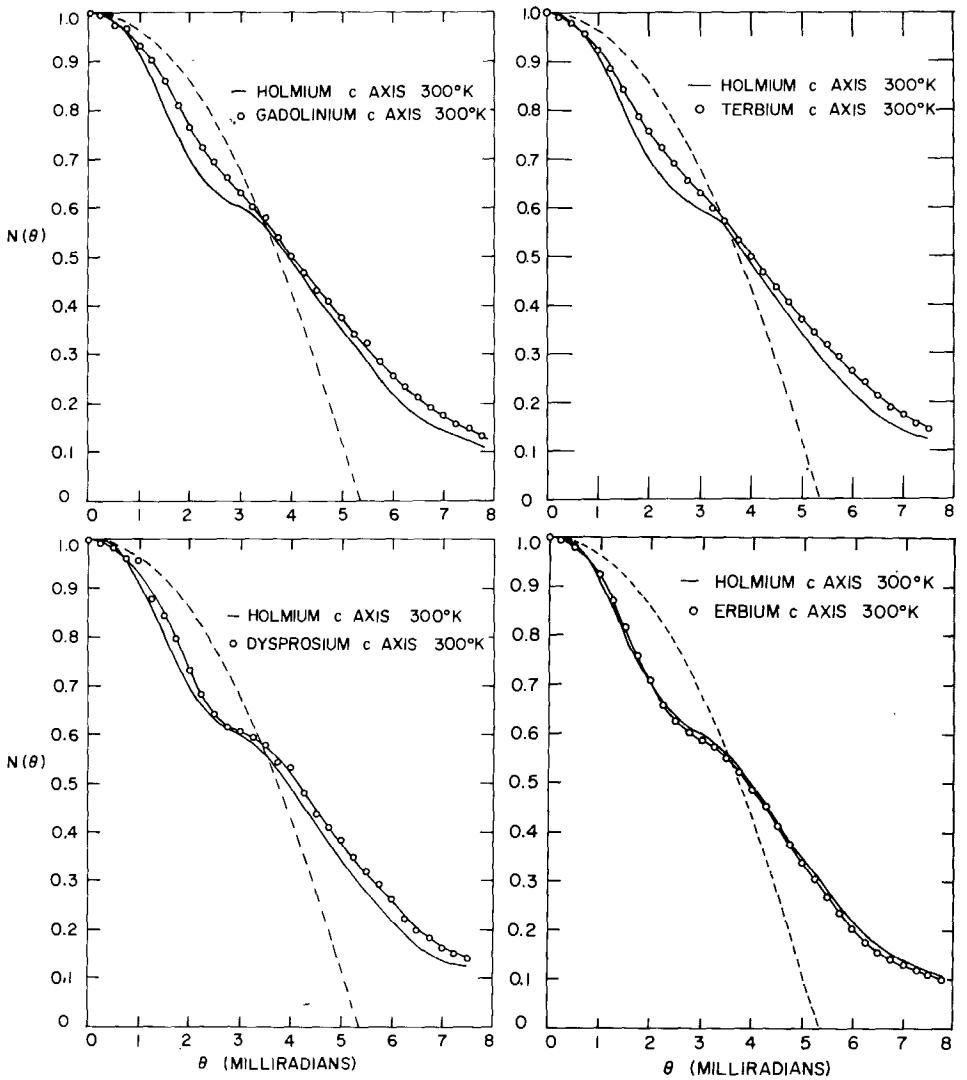

Fig. 3.23. The angular distributions of positron annihilation γ rays for Gd, Tb, Dy, Ho and Er (Williams and Mackintosh, 1968). The dashed curves are the calculated angular distributions in the free electron approximation.

depopulation takes place in discontinuous steps, and this can be seen as an oscillation in the magnetic moment of the metal. The oscillation is periodic in $(B)^{-1}$, where B is the magnetic induction, and the frequency F is proportional to the extremal cross-sectional area A of the Fermi surface in the plane perpendicular to the field, i.e.

$$F = (\hbar/2\pi e)A. \tag{3.15}$$

In a nonmagnetic metal B is the same as the magnetic field H. By rotating the magnetic field one can measure the extremal cross-sectional area of the Fermi surface over a range of angles, and from the data deduce the shape of the Fermi surface. For a complicated Fermi surface one often sees many oscillations superimposed on and beating with one another. The resolution of the data and the subsequent reconstruction of the Fermi surface is often difficult without a theoretical model for guidance. Once the oscillations are identified as coming from certain parts of the model Fermi surface, a quantitative verification of the band model becomes possible. To facilitate the comparison the calculated Fermi surface cross-sectional areas are often given in units of magnetic field in megagauss (MG).

The amplitude of the oscillations depends exponentially on the factor $m_c^*(T + T_D)/B$, where m_c^* is the effective cyclotron mass, T the temperature, T_D the Dingle temperature which measures the mean scattering probability of the electrons by impurities and lattice imperfections. By measuring the amplitude at a number of temperatures one can determine both the mass and the Dingle temperature. The mass is compared with the band calculation, thus providing an additional check on the theoretical model.

In order to observe the oscillation from a particular orbit the electron must be able to travel a large part of the full orbit before it is scattered. Therefore, high fields, low temperature, and single crystals with high purity are essential to the success of the experiment. The quality of a crystal is measured by the resistivity ratio, which is defined as the ratio of the room temperature resistivity (due to photon scattering) to the helium temperature value (due to scattering from impurity and imperfections). Successful high resolution experiments on metals were often performed on specimens with resistivity ratio $\sim 10\,000$. It has not been possible to purify rare earth metals to this degree. Thus, the de Haas–van Alphen measurements in rare earths are only at a beginning state of development.

Using the electrotransport technique (Peterson and Schmidt, 1969) the scientists at Ames Laboratory of Iowa State University first succeeded in growing a single crystal of Lu with the resistivity ratio of 60. While this was not high enough for mapping out the Fermi surface, Hoekstra and Phillips (1971) were able to observe one oscillation at 3.75 MG when the field is in the c direction. By tilting the field toward $[10\bar{1}0]$ and $[11\bar{2}0]$ directions, they found that the frequency of the oscillation increases until the tilt angle reaches 22° whereby the oscillation disappears. The data, plotted in fig. 3.24, imply a hyperboloidal shaped Fermi surface whose cross-section increases rapidly when the normal of the plane is rotated away from the c axis. The surface is a short column because the oscillation disappears at a relatively small tilt angle. No other oscillation was observed, presumably because all others occur at higher frequencies and would require better specimen for their detection.

The authors tentatively identified the orbit as the one around the point H in the Brillouin zone, because the predicted frequency, 6 MG (Keeton and Loucks, 1968), was rather close to the observed frequency. But there is an inconsistency

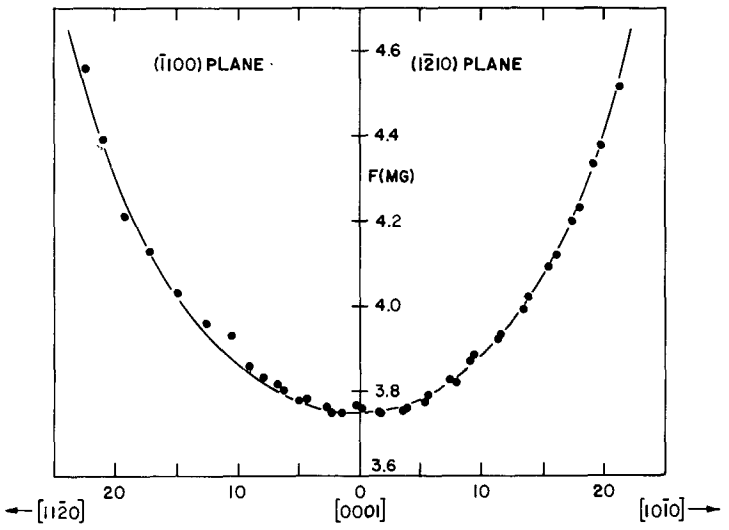

Fig. 3.24. The angular dependence of the de Haas–van Alphen frequency of Lu (Hoekstra and Phillips, 1971).

between theory and experiment at this point. According to the calculation the lowest frequency should come from the electron cylinder around the HK axis (see fig. 3.25). This cylinder has a rather straight face so that the oscillation should persist until the field is tilted to 40° from the c axis. The next higher frequency comes from the hole cylinder which has the geometric shape to give the field tilt effect seen experimentally. If one identifies the signal as coming from the hole cylinder, one must face the problem of explaining why the signal of lower frequency from the electron cylinder was not detected. The authors suggested that perhaps the calculation was in error, because a slight shift of the energy bands can cause the electron cylinder to pinch off at the point H. At present there is enough uncertainty in both theory and experiment that no definite conclusion can be drawn.

The Y metal has a Fermi surface very much like that of heavy lanthanides. Like Lu it is nonmagnetic, so its energy bands are not modified by magnetic ordering. Young et al. (1974) grew a single crystal of Y and refined it by the electrotransport method until a resistivity ratio of 120 was attained. With a spherical specimen of 3 mm diameter cut from this crystal, they observed two oscillations, one main oscillation at 3.27 ± 0.04 MG, and one at 3.9 ± 0.1 MG with much smaller amplitude beating with the main oscillation. When the field was tilted away from the c axis, the main oscillation increased in frequency while the smaller oscillation decreased slightly in frequency and increased in amplitude. Beyond about 12° from the c-axis the two oscillations became comparable in frequency and amplitude, and they combined to give a very complicated pattern of oscillation (fig. 3.26).

The authors interpreted the results in terms of the Fermi surface calculated by

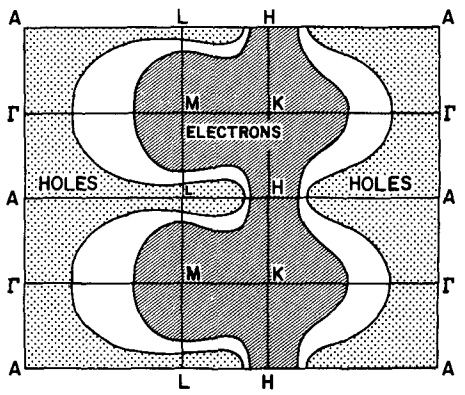

Fig. 3.25. Cross section of the relativistic Fermi surface of Lu (Hoekstra and Phillips, 1971).

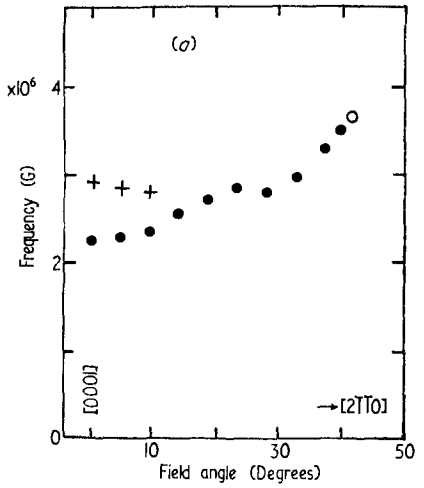

Fig. 3.26. The de Haas–van Alphen frequency branches for Y (Young et al., 1974).

Loucks (1966). In fig. 3.27 we show the cross-sections of the Fermi surface with planes cut perpendicular to the c axis as shown in fig. 3.28. Both the observed frequencies are in near agreement with the cross-sectional area of the electron cylinder around the HK axis. One can see from fig. 3.27 that the cylinder narrows at a point slightly away from the AHL plane. This gives rise to the δ_1 orbit shown in fig. 3.29. Without spin-orbit coupling the Fermi surface may be folded out into the double zone representation, and consequently there is no extremal orbit on the AHL plane. A slight spin–orbit coupling, however, removes the band degeneracy and creates another extremal orbit δ_2, with a calculated frequency 3.1 MG. In fig. 3.29 the difference in size between δ_1 and δ_2 is exaggerated for clarity. When the field is tilted out of the c axis the area of δ_1 increases and that of δ_2 decreases so that the two oscillations merge together very rapidly, in agreement with observations. There is no evidence of any oscillation from the hole surface around H, perhaps because its frequency is just beyond the range of detection.

The δ_1 oscillation is well resolved at 4.2 K. By lowering the temperature the effective mass of this orbit was determined to be 0.39 ± 0.01 times the free electron mass. No smaller orbit was observed even down to 0.9 K. This agrees with the band model of Loucks (1966) but disagrees with the cellular calculation of Altmann and Bradley (1967) who predicted a small neck at K and a small pocket at the ΓK line.

The common deficiency of both the Lu and the Y experiments is that only the small orbits were observed. These orbits are most difficult to predict with accuracy, and this makes the interpretation prone to uncertainties. It requires the observation of many more orbits, especially the large ones, to verify the complicated Fermi surface of rare earth metals.

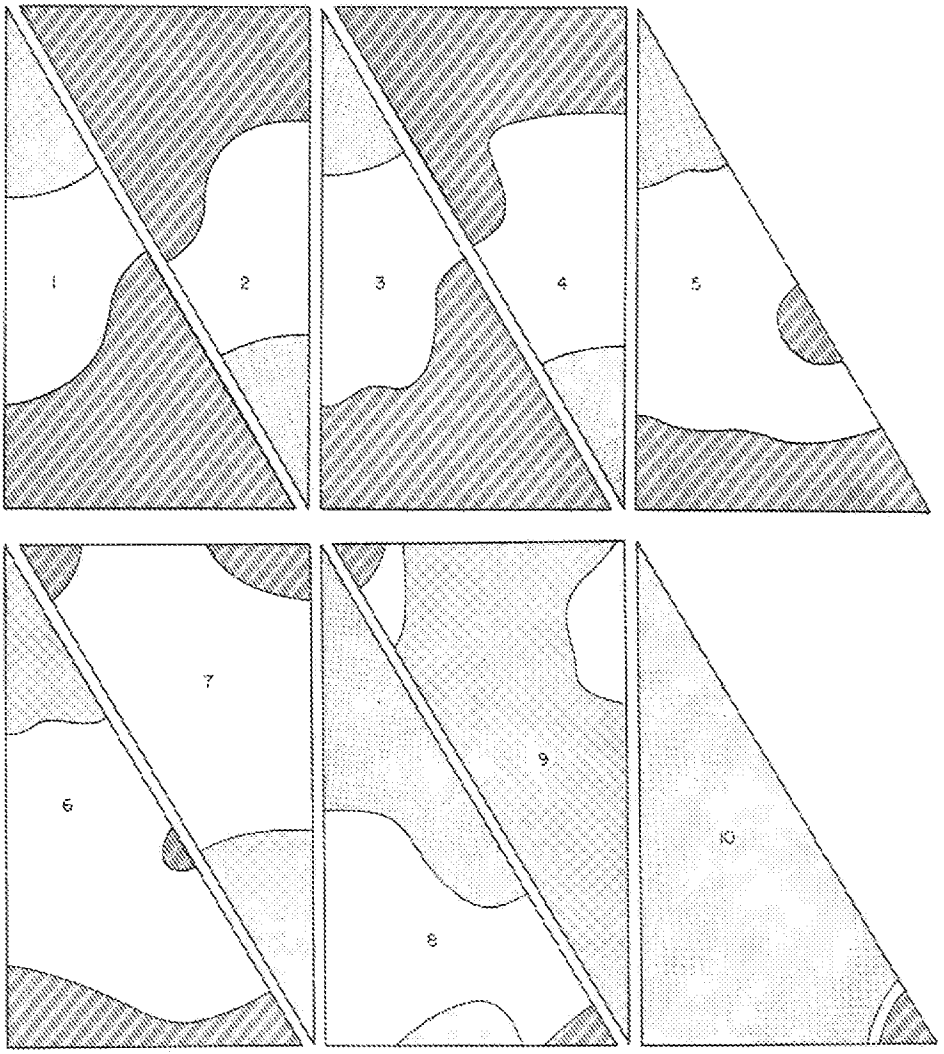

Fig. 3.27. The cross sections of the Fermi surface of Y (Loucks, 1966). The shaded region is inside the third band hole surface, and the diagonally shaded region is inside the fourth band electron surface.

The de Haas–van Alphen effect in ferromagnetic Gd has been observed by two groups, using crystals purified by the same electrotransport technique. Young et al. (1973) obtained a crystal with resistivity ratio 240. They carried out the measurement at 0.9 K over various field directions and observed a total of seven oscillations. By varying the temperature from 2 K to 0.9 K Young and Hulbert (1974) determined the cyclotron mass of four of the orbits. Schirber et al. reported nine orbits on a specimen with resistivity ratio 260. The three orbits with largest areas have been identified.

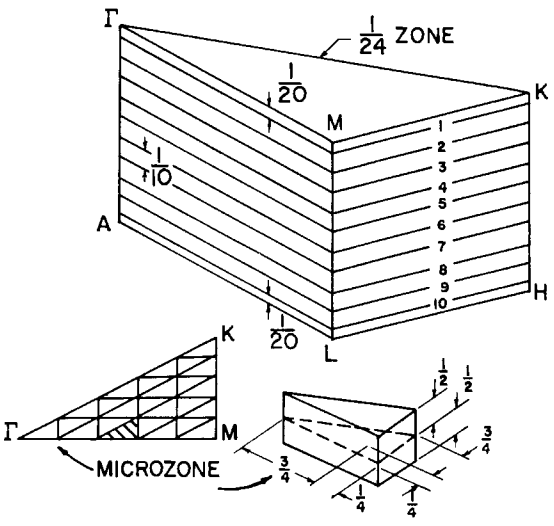

Fig. 3.28. A section of the Brillouin zone of hcp crystal showing the planes cutting the Fermi surface of Y shown in fig. 3.27 (Loucks, 1966).

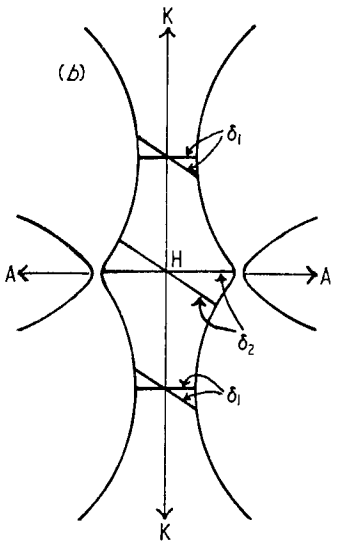

Fig. 3.29. The possible orbits which give rise to the observed dHvA frequencies in Y (Young et al., 1974).

In the ferromagnetic state the exchange field of the 4f electrons splits the conduction band into two sets. In the non-relativistic theory the two sets may be identified simply as spin-up and spin-down bands. The spin–orbit coupling mixes the two sets of bands wherever they intersect. The Fermi surface also separates into two sets, with spin–orbit splitting at places where the surfaces intersect. Thus, we can get information on both the band structure and the band splitting, but at the same time the identification of some orbits is rather difficult. Recall that the oscillation in the magnetization is periodic in the total magnetic induction B. For a spherical specimen $B = H + (8\pi/3)M_s$, where M_s is the saturation magnetization of the ferromagnetic metal. In determining the size of the orbits the magnetization correction must be done carefully. The saturation magnetization can be measured independently, and this serves as a check of the analysis of the orbit data. Young et al. extracted from their data the value 7 kG for the internal field, but Schirber et al. obtained the value 18.6 ± 0.7 kG. The static measurement gives 7.63 ± 0.02 Bohr magnetions per atom (Roeland et al., 1975), which corresponds to an internal field of 18.1 kG, in agreement with Schirber et al. Therefore, all the orbit frequencies detected by Young et al. must be revised, and we will review the new values here (Young, 1976).

The de Haas–van Alphen frequencies in the high symmetry directions are tabulated in table 3.1, and the angular variations measured by Young et al. are shown in fig. 3.30. The large orbits are much easier to identify. The orbit A is of almost constant area over 60° from the c-axis and then disappears sharply, suggesting a spherical surface of radius 0.35 $Å^{-1}$ whose central section is cut off at 60° by necks which extend in the c direction. If we assign the orbit B to the

TABLE 3.1
De Haas-van Alphen frequencies of Gd

Field direction	Frequency (MG) 1	2	Index	Range	Identity
[0001]	39.0	40.7	A	60[a]	$3\downarrow -\alpha_1$
	—	6.9	—	—	?
	13.5	13.9	B	22[a]	$3\downarrow -\alpha_2$
	1.97	1.96	C	15[a]	?
	0.28	0.3	D	40[a]	?
[11$\bar{2}$0]	46.5	46.6	E	24[b], 15[c]	$3\uparrow -\beta$
	2.93	—	F	27[a], 15[c]	?
	1.62	1.71	G	20[a], 12[c]	?
	0.46	0.5	—	—	?
[10$\bar{1}$0]	0.284	—	—	—	?
	1.55	1.6	G	—	?
	0.46	—	—	—	?

1. Young (1976); 2. Schirber et al. (1976); [a]Toward [10$\bar{1}$0]; [b]Toward [11$\bar{2}$0]; [c]Toward [0001].

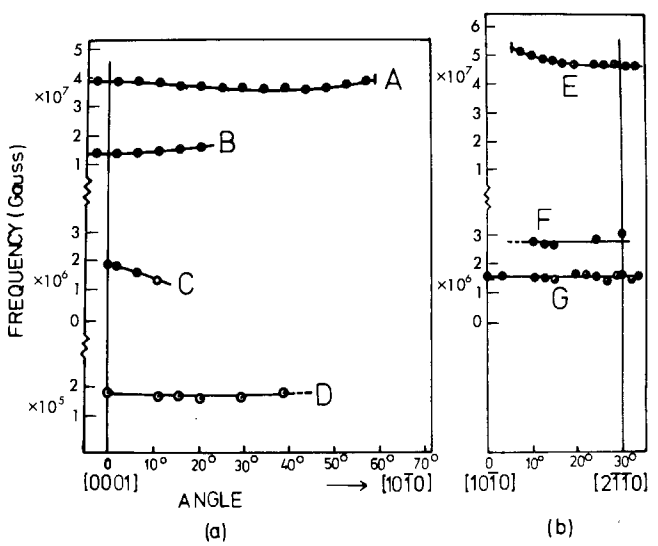

Fig. 3.30. The dHvA frequency branches for ferromagnetic Gd (Young et al., 1973). The frequency scale has been corrected according to the latest data (Schirber et al., 1976; Young, 1976).

neck, it will have a minimum radius of 0.20 $Å^{-1}$ and will occur at approximately a distance 0.35 $Å^{-1}$ (0.2 cot 30°) from the center of the sphere. This surface is marked I in fig. 3.31b, and it can be seen as a shrunken version of the paramagnetic Fermi surface marked as II. That the surface is a shrunken hole surface indicates that it belongs to the majority spin band. There must also be an expanded version of II corresponding to the minority spin band. This is marked as III in fig. 3.31b, and the resulting neck orbit β has the correct shape and size to identify it as E in table 3.1. The other oscillations are not as well understood, but work is in progress toward their identification.

The amount of splitting between the majority and minority Fermi surfaces corresponds to a band splitting of 0.95 eV, quite close to the value 0.8 eV calculated by Harmon and Freeman (1974). Together with the calculated density of states for Gd, this gives a spin moment of 0.78 Bohr magneton per atom, somewhat larger than the measured value of 0.63.

The magnetoresistance of Gd has been reported by Young et al. (1976) for a specimen with the resistivity ratio 340. The field dependence of the magnetoresistance is not understood in detail, but one can reliably conclude from the data that there are open orbits when the field is in the c direction as well as in the basal plane. This is consistent with the Fermi surface model of Gd with an exchange splitting of 0.95 eV, but not as large as 1.2 eV as deduced by Young et al. (1973) from the wrong internal field value, because such a large splitting would create closed orbits on the majority spin Fermi surface in the basal plane directions.

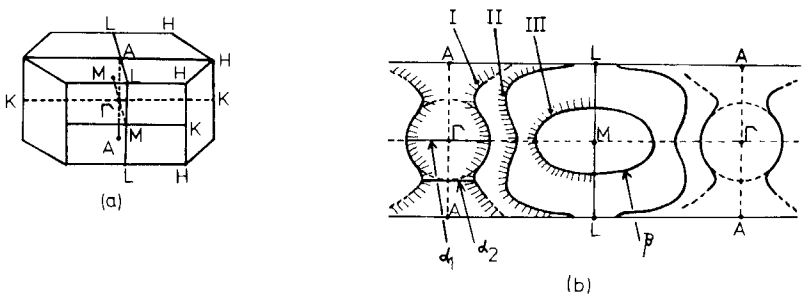

Fig. 3.31. The Fermi surface cross sections of ferromagnetic Gd, showing the orbits which give rise to the three highest dHvA frequencies (Young et al., 1973).

3. Optical studies of rare earth metals

Photons interact with solids by exciting an electron from an occupied state to an unoccupied state. The energy of the photon is absorbed by the excited electron, and the rate of absorption gives information on the number of filled electron states available for excitation, the number of vacant states to receive the excited electron, and the matrix element of transition. If the photon energy is high enough, the electron may acquire enough kinetic energy to escape from the

surface, giving rise to the photoelectric effect. Then counting the number of photoelectrons is a direct way to study the photon–electron interaction.

With photons in the infra-red frequency range only the electrons very near the Fermi level may be excited. This method was used to detect the modification of the energy bands of rare earth metals by magnetic ordering. Measurements of the entire conduction band structure by either optical reflection or photoemission are possible with photons in the ultraviolet range. With X-ray photons one can use the photoelectric effect to study not only the band states but also the location of the core states. This gives a direct answer to the question that was raised in the last section on band structure calculations, namely where the 4f-levels are relative to the band levels.

3.1. *Optical conductivity of rare earth metals*

The optical properties of metals are determined by the complex dielectric function $\epsilon_1(\omega) + i\epsilon_2(\omega)$. The imaginary part $\epsilon_2(\omega)$ is related to the optical conductivity $\sigma(\omega)$ by

$$\epsilon_2(\omega) = 4\pi\sigma(\omega)/\omega. \tag{3.16}$$

The complex index of refraction $n + ik$ is simply the square root of the dielectric function, thus

$$n^2 - k^2 = \epsilon_1(\omega), \qquad 2nk = \epsilon_2(\omega). \tag{3.17, 18}$$

The absorptivity $\alpha(\omega)$ is defined by

$$\alpha(\omega) = 2k\omega/c, \tag{3.19}$$

and is related to $\epsilon_2(\omega)$ by

$$\epsilon_2(\omega) = \alpha(\omega)nc/\omega. \tag{3.20}$$

In standard reflectivity measurements one measures the reflectivity

$$R = \left|\frac{n - 1 + ik}{n + 1 + ik}\right|^2 \tag{3.21}$$

from a metal surface over a wide range of frequencies. Then one makes use of the Kramers–Kronig relation to determine the complex index of refraction, dielectric function, and the optical constants $\sigma(\omega)$ and $\alpha(\omega)$. In order to perform the Kramers–Kronig transformation one needs the reflectivity data for all photon energies. Since in a typical experiment the data are taken over a finite range of energies, say 0.5–5 eV, the data must be extrapolated to both high and low energies. This introduces uncertainties in the data and affects the quality of the converted results.

The need for extrapolation may be avoided by measuring the reflectance and transmittance through a metal film simultaneously (Schüler, 1966). The ellipsometry method offers by far the best way to determine the complex dielectric function. A metal film is deposited in high vacuum onto the base of a silica

prism. A linearly polarized beam of light is incident on the metal-prism interface and is reflected by the surface. The polarization vector makes a 45° angle with the plane of incidence so that there are equal amounts of s and p polarized waves. Let the ratio of the complex reflectivities of these two waves be $R_p/R_s = \rho\, e^{i\Delta}$, then the measured quantities are ρ and Δ. These are deduced by measuring the intensity of reflected light at three directions of polarization, say parallel to (I_0), perpendicular to (I_{90}) and at 45° angle with (I_{45}) the plane of incidence. Then

$$\rho = (I_0/I_{90})^{1/2}, \tag{3.22}$$

$$\cos\Delta = (I_0 + I_{90} - 2I_{45})/2(I_0 I_{90})^{1/2}. \tag{3.23}$$

The quantities ρ and Δ are in turn related to the complex dielectric function ϵ and the incident angle θ by

$$\frac{(\epsilon - \epsilon_0 \sin^2\theta)^{1/2}}{\epsilon_0 \tan\theta \sin\theta} = \frac{1+\rho\, e^{i\Delta}}{1-\rho\, e^{i\Delta}}, \tag{3.24}$$

where ϵ_0 is the dielectric constant of the prism. The quality of the data depends on the accuracy of the angular measurements, these include the angle of incidence and the polarization angles. The angular measurements in turn depend critically on the quality of the metal surface.

The hexagonal rare-earth metals are highly anisotropic, so for a single crystal surface the optical constants are functions of the directions of incidence and polarization. In most experiments the metal surface is polycrystalline, and the measured optical constants are average properties of the crystal.

In the non-interacting particle model the optical conductivity may be calculated from the band structure and crystal wave functions,

$$\sigma(\omega) = \frac{4\pi^2 e^2}{m^2 c\omega} \sum_{i,f} \sum_{k} |\langle f|\boldsymbol{p}\cdot\boldsymbol{\epsilon}|i\rangle|^2 \delta[E_f(\boldsymbol{k}) - E_i(\boldsymbol{k}) - \hbar\omega], \tag{3.25}$$

where $\hat{\boldsymbol{\epsilon}}$ is the polarization vector of the photon, i denotes a filled initial band and f an empty final band. This formula excludes intraband transitions because they must take place at the Fermi level, and are therefore not allowed by energy conservation. Intraband transitions do occur when the electrons are scattered by phonons, impurities, and crystal imperfections. This Drude term is especially important at low frequencies, and it must be added to eq. (3.25) or subtracted from the data before one can compare the data with the theory.

A few attempts have been made to calculate the interband absorptivity for metals according to eq. (3.25). In most cases the interpretation of the data is done in either one of two oversimplified ways. In one of the approximations the matrix element is assumed to be slowly varying over the energy bands, so it is taken out of the sum to obtain

$$\sigma(\omega) = (4\pi^2 e^2/m^2 c\omega) \sum_{i,f} \langle M_{if}^2\rangle J_{if}(\omega), \tag{3.26}$$

where

$$J_{if}(\omega) = \sum_{k} \delta[E_f(k) - E_i(k) - \hbar\omega] \tag{3.27}$$

is the joint density of states of the bands i and f. This quantity peaks up at the energy $\hbar\omega$ where the two bands are nearly parallel. By comparing the measured $\sigma(\omega)$ with the joint density of states curve, one can often identify the sets of bands that are responsible for the peaks in the experimental curve. The shortcoming of this method is that the matrix elements are not constants in reality because there are transitions that are forbidden by symmetry. The second approximation method relies on the fact that the energy bands tend to be flat at high symmetry points of the Brillouin zone, so the states nearby are more likely to give the peaks in the joint density of states. A detailed study is made of the selection rules at the high symmetry points, and the various allowed transitions are identified with features of the absorptivity curve. This method suffers the disadvantage that it completely disregards the possibility that there may be two bands that are not flat but run parallel to each other inside the Brillouin zone, thus giving rise to a peak in absorptivity. In practice both methods may be used to give first understanding of the data, and the conclusions of both kinds of analysis are often quite similar. A more detailed discussion of the principle and practice of optical measurements on metals and alloys can be found in a recent review by Nilsson (1974).

The optical measurements on rare earth metals are difficult because of their high reactivity with their environment. Most experiments were carried out with films deposited in high vacuum and measured in situ. Such films are by nature polycrystalline and highly strained. The film thickness and the history of heat treatment both affect the optical data. With bulk samples the method of polishing the surface and the amount of exposure of the fresh surface to the atmosphere are important factors. Furthermore, when optical constants are extracted from the reflectivity data, the method of extrapolating the data to high and low frequency ends can bring in more uncertainty. For these reasons the data from different groups of investigators often disagree, and at this time it is not possible to determine which work is the most representative. We will review the experimental results by using Gd as a prototype, and discuss in detail the similarities and differences of the published results from various research groups. We feel that the qualitative features common to most of the results must carry more weight on the reliability scale than the peculiar features seen only by one group.

The reviewer was able to locate twelve reports on the optical conductivity of Gd. Some pertinent information on the type of sample and method of measurement of these studies is summarized in table 3.2. In fig. 3.32 we reproduce the optical conductivity data of Schüler taken on a thick film (2800 Å) of Gd in the paramagnetic phase. In fig. 3.33 the latest data of Myers for a thick film (~1400 Å) at 10 K and 295 K are plotted. In the high temperature data on both plots we see a large increase in optical conductivity at low frequencies coming

TABLE 3.2
Reports on the optical conductivity of Gd

Investigators	Sample	Method
Schüler (1966)	Film	Reflectance and Transmittance
Blodgett et al. (1966)	Film	Reflectance
Hodgson and Cleyet (1969)	Film	Reflectance
Knyazev and Noskov (1970)	Bulk Polycrystal	Ellipsometry
Knyazev and Noskov (1971a)	Bulk Polycrystal	Ellipsometry
Knyazev and Noskov (1971b)	Bulk Polycrystal	Ellipsometry
Pétrakian (1972)	Film	Reflectance and Transmittance
Miller et al. (1974)	Film	Ellipsometry
Erskine et al. (1974)	Film	Ellipsometry
Krizek and Taylor (1975)	Film	Ellipsometry
Weaver and Lynch (1975)	Bulk Single Crystal	Reflectance
Myers (1976)	Film	Ellipsometry

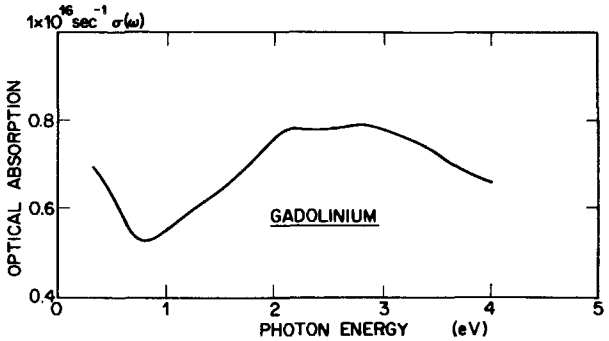

Fig. 3.32. The optical conductivity of Gd film (Schüler, 1966).

from the Drude term, a valley at 1 eV, and a peak at around 2 eV. The results of other investigators on polycrystalline samples show similar features. From these we may conclude that the interband transition starts near 1 eV, and the width of the large interband absorption region is about 2 eV. The joint density of states of Gd in fig. 3.34, which was calculated by Knyazev and Noskov (1970) based on the relativistic energy bands of Keeton and Loucks (1968), shows just such an interband transition peak. Cornwall (1965) tabulated the allowed interband transitions at the high symmetry points of Gd based on the energy bands of Dimmock and Freeman (1964) in fig. 3.1. As seen in table 3.3 most of the allowed transitions are in the 2–3 eV range. One may say that there is substantial agreement between the calculated band structure and the data.

Now we deal with the differences among the investigators. The reasons for

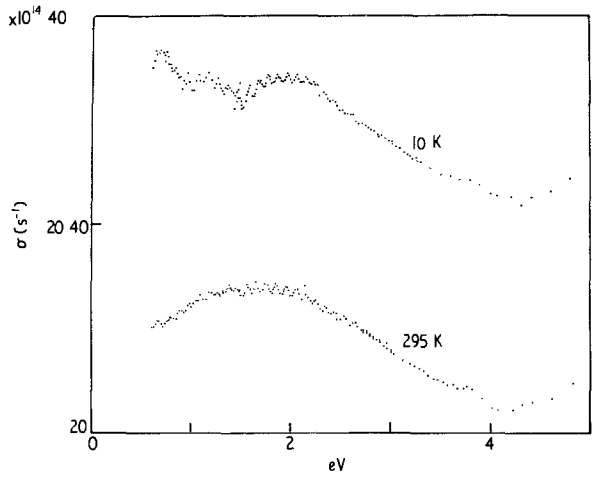

Fig. 3.33. The optical conductivity of Gd film at two temperatures (Myers, 1976). Note the shift in scales for the two curves.

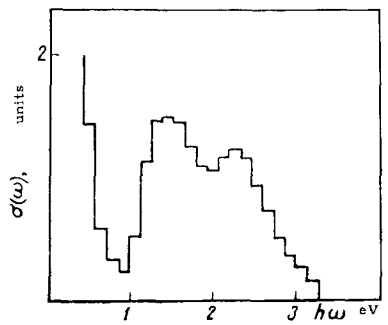

Fig. 3.34. The joint density of states of Gd (Knyazev and Noskov, 1970).

most of their differences are not precisely known. Hodgson and Cleyet (1969) observed that the optical conductivity peak near 2 eV became narrower when the temperature was reduced from room temperature to liquid nitrogen temperature. This effect was looked for by later investigators but the observed changes were not so pronounced (Krizek and Taylor, Myers). A low temperature peak reported by Hodgson and Cleyet and Myers near 1.1 eV was not reproduced by Krizek and Taylor. Pétrakian worked with thin films (~200 Å) and observed the first interband transition in the reflectivity at 3.2 eV. Krizek and Taylor suggested that the film thickness might have an effect on the position of the peak. The data of Miller et al. consist of many well-resolved wiggles in the peak region. The authors attributed these to the fine structures in the energy bands. The same kind of structure was seen in an annealed Gd film by Myers, but he felt that it was more likely an artifact coming from the measuring

TABLE 3.3
Selection rules for interband transitions, after Cornwell (1965) and associated energies according to calculated energy bands

Symmetry point	Transition	Direction of radiation	Energy (eV)
Γ	$\Gamma_4^- \rightarrow \Gamma_5^+$	x, y	2.8
	$\Gamma_4^- \rightarrow \Gamma_3^+$	z	3.0
A	$A_1 \rightarrow A_3$	x, y	2.8
	$A_1 \rightarrow A_1$	z	2.5
M	$M_1^+ \rightarrow M_2^-$	y	2.8
	$M_3^+ \rightarrow M_1^-$	x	1.8
	$M_3^+ \rightarrow M_4^-$	y	2.1
	$M_2^- \rightarrow M_1^+$	y	1.6
	$M_1^- \rightarrow M_4^-$	z	2.8
	$M_3^+ \rightarrow M_2^-$	z	3.0
K	$K_2 \rightarrow K_6$	y	2.2
	$K_5 \rightarrow K_3$	y	2.3
	$K_2 \rightarrow K_3$	z	3.3
	$K_5 \rightarrow K_6$	z	1.1

instruments. Knyazev and Noskov (1970), using a polished bulk polycrystal surface, measured a much lower optical conductivity than other investigators, and Erskine et al. believed that it was the result of surface contamination. In addition, Pétrakian found another interband feature at 5.7 eV, and Blodgett et al. suggested the 4f–5d transition as the cause of a reflectivity dip at 8 eV. The latter result was confirmed by XPS measurements (see ch. 3 section 3.4).

In the ferromagnetic phase of Gd another structure was seen by many authors (Schüler; Hodgson and Cleyet; Knyazev and Noskov, 1971b; Krizek and Taylor; Myers). This peak in conductivity is seen in the low temperature curve of Myers in fig. 3.33 and the data of Schüler in fig. 3.35. The peak diminishes with increasing temperature, and disappears in the paramagnetic phase. This feature was explained by the optical excitation of an electron from the spin-down to the spin-up band in the ferromagnetic phase (Dimmock et al., 1966). The spin flip during the transition is made possible by the sizable spin–orbit coupling in the band electron wave functions.

Investigations on other hexagonal heavy rare earths are summarized in table 3.4. Just like their band structures the optical properties of these metals are very much alike. Optical measurements on polycrystal samples can not detect the differences in the Fermi surface geometry of these metals. The optical conductivities of Gd, Tb, Dy, Ho, and Er obtained by Krizek and Taylor are shown in fig. 3.36. The same kind of similarity in optical properties of different metals is seen in Schüler's results on Gd, Dy and Lu, the data of Knyazev and Noskov (1970) on Gd and Dy, those of Miller et al. on Gd and Tb, those of Erskine et al. on Gd, Tb and Dy, and in those of Pétrakian on Gd and Tm. There is also the same kind of inconsistency among the results of different investigators as in Gd.

This points to the differences in sample handling and data analysis as the major reasons for the discrepancies.

In the ordered phase Cooper and Reddington (1965) first reported that the optical transition across the band gap created by magnetic ordering was independent of the type of ordering in Dy, whether it was ferromagnetic or helical. Krizek and Taylor made the same observation in Tb, Dy, and Ho. The band gaps were found to be 0.65 in Tb (Krizek and Taylor, 1974), 0.44 in Dy (Cooper and

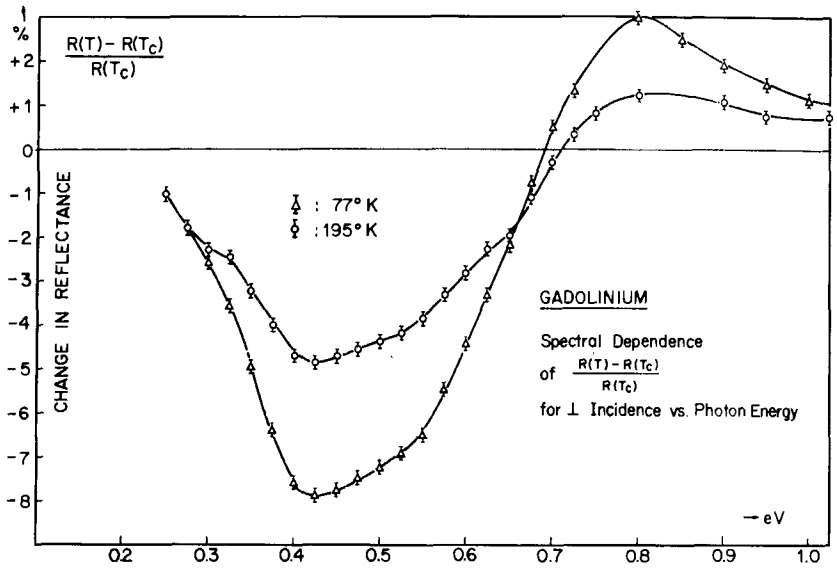

Fig. 3.35. Low temperature optical reflectance of Gd film, showing the structure at the ferromagnetic energy gap (Schüler, 1966).

TABLE 3.4
Investigators of the optical properties of hexagonal heavy rare earths

Element	Investigators
Tb	Schüler (1966), Miller et al. (1974), Erskine et al. (1974), Krizek and Taylor (1975), Knyazev and Noskov (1975)
Dy	Schüler (1966), Cooper and Reddington (1965), Knyazev and Noskov (1970), Erskine et al. (1974), Krizek and Taylor (1975)
Ho	Schüler (1964), Krizek and Taylor (1975)
Er	Krizek and Taylor (1975)
Tm	Pétrakian (1972)
Lu	Schüler (1966)

Reddington, 1965; Schüler, 1966; Krizek and Taylor, 1975), and 0.35 eV (Schüler, 1964) in Ho. The changes in optical conductivity between ordered and disordered phases for the various metals are summarized in fig. 3.37. Dimmock et al. (1966) pointed out that the magnetic gap in different metals should scale like the spin of the trivalent metal ion. This simple model accounts for the observations.

In contrast to the film measurements Weaver and Lynch reported a series of absorptivity measurements on single crystals of Y (1973) and hexagonal heavy lanthanides (1975). The samples were cut from single crystals to expose the c-axis. The surfaces were mechanically polished to obtain specular surfaces, and then electropolished to remove work damage. While the heavy rare earths are highly reactive at high temperatures, the reaction rate is slow at room temperature and particularly so for strain-free, single crystal, electropolished surfaces. The authors made two measurements on one Y sample, one 3 to 5 minutes after the surface was freshly prepared and one 14 days later, both measured at 4.2 K. The absorptivity curves showed differences above 3 eV, so the authors attributed the data in the range 0.15–3 eV to the metal single crystal. For heavy rare earths the authors reported their data taken at 4.2 K in the 0.2 to 4.4 eV range. The effect of photon polarization was studied with the electric field $\boldsymbol{E}$ parallel and perpendicular to the c-axis. The results for the optical absorptivity and conductivity curves are plotted in figs. 3.38 and 3.39. It is clear that the metals have anisotropic optical properties, and with single crystals the metals no longer resemble each other so strongly. The peak in conductivity at 1.6 eV for

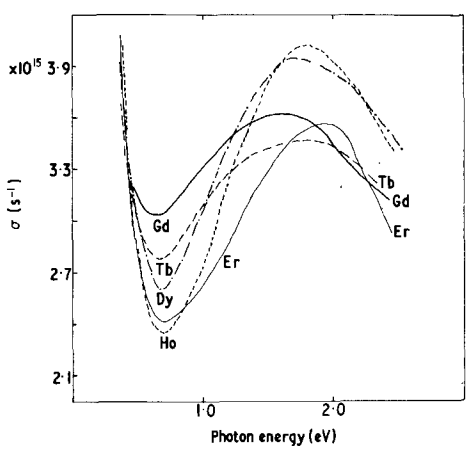

Fig. 3.36. Comparison of the optical conductivities of Gd, Tb, Dy, Ho, and Er (Krizek and Taylor, 1975).

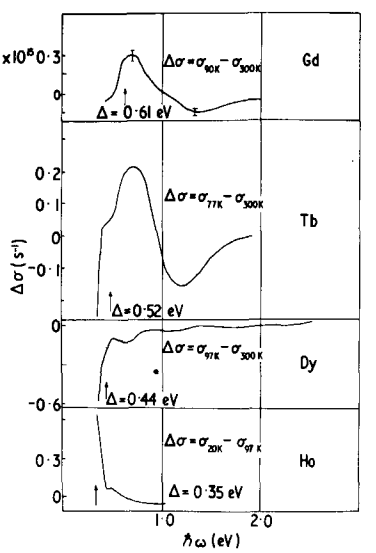

Fig. 3.37. The change in optical conductivities of Gd, Tb, Dy, and Ho between magnetically ordered and disordered phases (Krizek and Taylor, 1975).

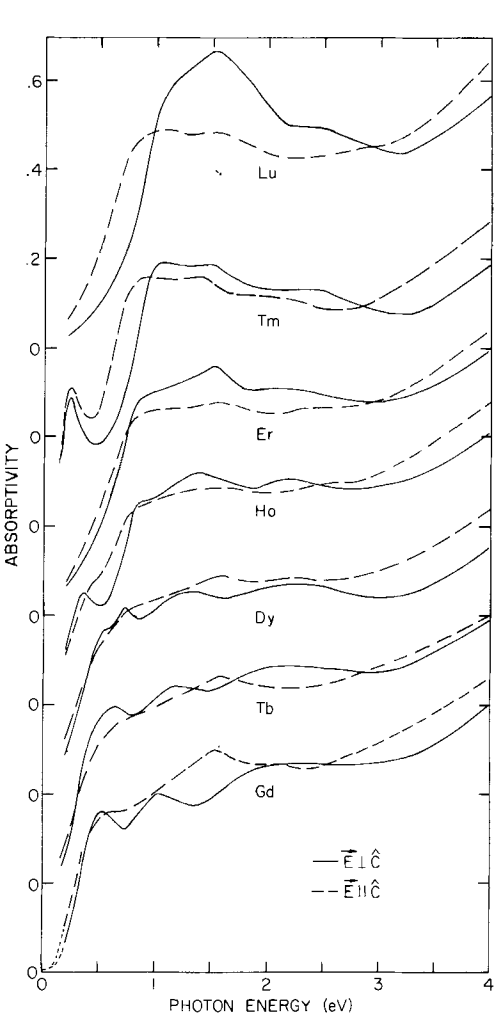

Fig. 3.38. The optical absorptivities of single crystal hexagonal heavy lanthanides (Weaver and Lynch, 1975).

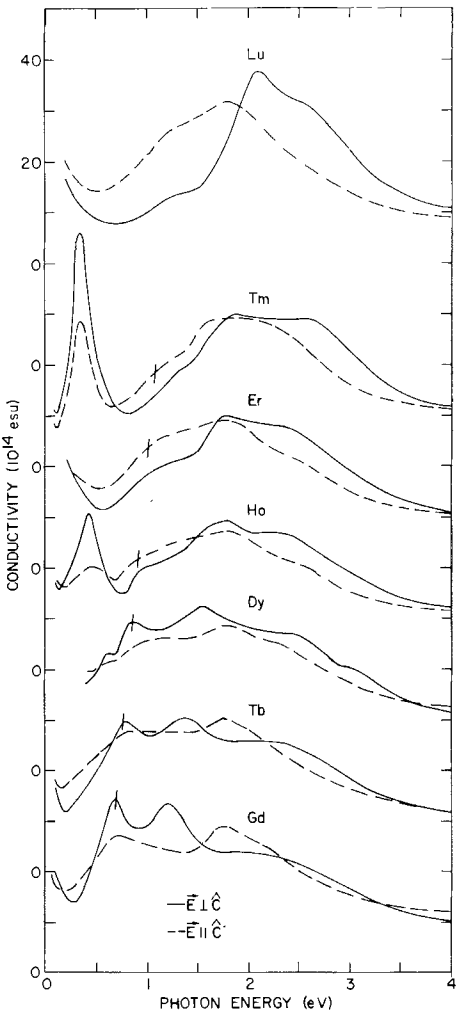

Fig. 3.39. The optical conductivities of single crystal hexagonal heavy lanthanides (Weaver and Lynch, 1975).

$\boldsymbol{E}\parallel\hat{c}$ and that at 2.5 eV for $\boldsymbol{E}\perp\hat{c}$ are common to all members of the group. They must be associated with the gross features of the band structure. The peak at 1.1 eV in Gd, seen by Hodgson and Cleyet (1969) and Myers (1976), was found only when $\boldsymbol{E}\perp\hat{c}$. The corresponding peak in other members shifts to higher energy with increasing atomic number until it reaches 2.1 eV in Lu. These must be associated with some fine features on the band structure that depend sensitively on changes of the crystal potential. The authors cautioned against any attempt to assign features of the data to parts of the band structure because the uncertainty in such interpretations might be very large.

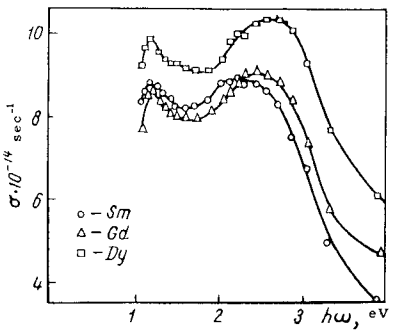

Fig. 3.40. Comparison of the optical conductivities of Gd, Dy and Sm, showing the Sm has very similar electronic structure to that of the hexagonal rare earths (Knyazev and Noskov, 1970).

The authors pointed out another systematic shift starting from the peak in conductivity at 0.7 eV in Gd, moving steadily to higher energies in other metals, ending at 1.3 eV in Lu. Recall that the peak at 0.7 eV in Gd was the one associated with the band splitting in the ferromagnetic phase. The authors suggested that there was another interband transition and that in Gd and Tb the magnetic ordering peak was masked by the interband peak. In Dy the magnetic peak begins to separate from the interband peak, and in Ho and Tm the magnetic peaks become more prominent while the interband peak flattens out. It is hoped that the authors would repeat this part of the measurement with increasing temperature so that the relative importance of interband transition versus spin-flip transition in Gd and Tb might be more reliably assessed.

In Y the authors reported a shoulder in the absorptivity curve at 9.45 eV and two peaks at 1.5 and 2.1 eV for $\boldsymbol{E} \| \hat{\boldsymbol{c}}$. For $\boldsymbol{E} \perp \hat{\boldsymbol{c}}$ the shoulder is not apparent but the peaks occur at the same energies. These peaks are probably due to band effects. An earlier thin film experiment by Pétrakian et al. (1970) revealed absorption peaks at 2.5 and 5.6 eV. The lower peak is most likely of band origin.

The metal Sm has a complicated nine-layer hexagonal structure. Its optical conductivity, as determined by Knyazev and Noskov (1970) for a bulk polycrystal surface using the ellipsometry method, is compared in fig. 3.40 with Gd and Dy. Clearly all three metals have very similar properties, even though the Sm band structure is expected to be much more complicated. As pointed out before, the measured optical conductivity of Gd by the authors is too low, possibly due to surface contamination. The differences between Sm and other rare earths should be studied with clean single crystal surfaces using polarized light.

Müller (1965) measured the optical reflectivity of Eu and Yb and compared the results with those for the alkali earths Sr and Ba. Endriz and Spicer (1970) did a more refined study and inverted the reflectivities by the Kramers–Kronig relation into optical constants ϵ_1, ϵ_2, σ and α. In fig. 3.41 the interband parts of the absorptivities of these four metals are plotted versus the normalized frequency ω/ω_p, where ω_p is the plasma frequency. One can see that the bcc metals Eu and Ba have very similar absorptivity curves, and so do the fcc metals Yb and Sr.

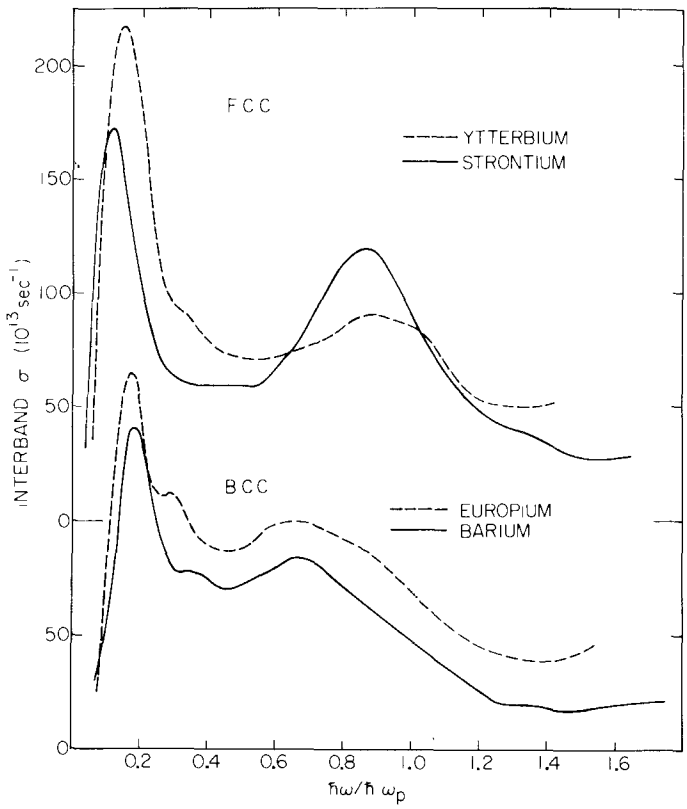

Fig. 3.41. The optical conductivities of Eu and Yb, showing the close similarity between Yb and Sr, and Eu and Ba (Endriz and Spicer, 1970).

The conclusion is that the absorption is due to interband transitions involving d bands. The authors correlated the various features of the absorptivity curve of Eu with the APW bands calculated by Freeman and Dimmock (1965) shown in fig. 3.14. In fig. 3.42 the quantity $\omega\sigma$ calculated from the band structure assuming a constant matrix element is compared with the experimental result. The onset of interband transition at 1 eV is well accounted for by the band structure. The broad peak in the ultraviolet region was calculated to be at 4 eV rather than 7 eV observed experimentally. The authors suggested that a systematic contraction of the energy scale (or an expansion of the band structure) will improve the agreement. It is also shown in fig. 3.42 that the nearly free electron model gives poor agreement with the experiment, indicating that the bands responsible for the absorption are of d character.

Although the transitions from the 4f levels were predicted to be in this frequency range, they were not seen in these experiments. The authors discussed the absence of f level transition in terms of the Fano and Cooper theory (1968). The f–d transition is allowed but is ten times weaker than the f–g

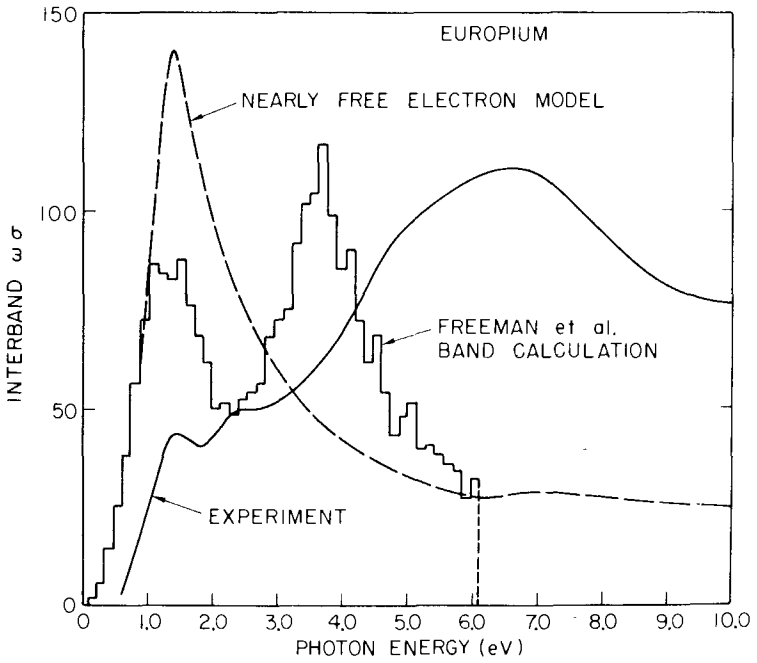

Fig. 3.42. Comparison of the interband optical constant with the joint density of states of Eu. The free electron model gives poor agreement with the experiment (Endriz and Spicer, 1970).

transition because when the electron increases its energy, it prefers to increase its angular momentum also. The f–g transition is out of the energy range of the experiment, and the f–d transition is too weak to be seen. The best way to excite an electron from the f level is by X-ray photoemission.

Pétrakian (1974) studied Yb films by the same method and arrived at the same conclusion. The two peaks in the absorptivity curves at 1.5 eV and 2.8 eV correlate rather well with the features on the energy bands of Johansen and Mackintosh (1970) shown in fig. 3.17. The comparison is given in table 3.5. An earlier experiment by Chander and Kumar (1973) reported similar results.

TABLE 3.5
Comparison between interband transitions with energy band features of Yb

Experiment	Theory	
1.5 eV	1.44 eV	(K_1-K_1)
	1.62	$(L_1-L_{2'})$
	1.53	(U_1-U_3)
2.8	2.58	$(X_1-X_{4'})$

Light rare earths Ce and Nd have been studied by Pétrakian (1972), and La and Pr by Derbez and Pétrakian (1974). By comparing the reflectivity curves of a number of films of various thicknesses, the authors pointed out that a minimum in reflectivity at 5.7 eV for Ce and Nd and at 5.8 eV for La and Nd were of band origin. These results need independent substantiation.

The considerable uncertainty in the optical data on rare earths reflects the difficulties in doing the experiments as mentioned at the beginning of this section. Judging from the recent rapid development in both materials preparation and experimental technique, we have reached the point that optical data on polycrystalline films of rare earths from different groups are converging. The optical experiments on single crystals have been attempted. More experiments of this kind should be performed to clear up many uncertainties in the optical data.

There is also a lack of theoretical calculation of the optical conductivity from energy bands and crystal wave functions. Computational techniques are now available (Williams et al., 1972; Janak et al., 1975). It is hoped that progress will be made in this direction in the next few years.

3.2. *Magneto-optic Kerr effect in* Gd

In a Kerr effect experiment a beam of linearly polarized monochromatic light is incident upon the surface of a ferromagnetic metal. The reflected light is in general elliptically polarized, with the major axis slightly rotated from the original polarization direction. The rotated part of the reflected light is proportional to the magnetization of the sample. It is convenient to describe the effect by a conductivity tensor. For a cubic crystal the conductivity tensor, with the magnetization M in the z direction, has the form

$$\overleftrightarrow{\sigma} = \begin{pmatrix} \sigma_{xx} & \sigma_{xy} & 0 \\ -\sigma_{xy} & \sigma_{xx} & 0 \\ 0 & 0 & \sigma_{xx} \end{pmatrix}. \tag{3.28}$$

This form also applies in an average sense to a polycrystal of Gd. The diagonal element σ_{xx} was designated by σ in the previous discussion of optical conductivity. The off-diagonal element σ_{xy} causes the optical rotation, so the Kerr effect gives a measure of this quantity. Symmetry requirements also demand that the diagonal element σ_{xx} be an even function of M and the off-diagonal element an odd function. The real and imaginary parts of $\sigma_{xy} = \sigma_{xy}^{(1)} + i\sigma_{xy}^{(2)}$ satisfy the dispersion relations as required by causality. The imaginary part represents the magneto-optic absorption, and it can have either sign because it is proportional to the difference in absorption for left and right circularly polarized light. The real part is the dispersive part.

In the non-interacting particle model the off-diagonal absorptive part of the dielectric function can be written in the form

$$\sigma_{xy}^{(2)}(\omega) = \frac{\pi e^2}{4m^2\omega} \sum_{i,f} \sum_{\boldsymbol{k}} F_{if}\delta(E_f(\boldsymbol{k}) - E_i(\boldsymbol{k}) - \hbar\omega), \tag{3.29}$$

where

$$F_{if} = |\langle f\uparrow|\pi^-|i\uparrow\rangle|^2 - |\langle f\downarrow|\pi^+|i\downarrow\rangle|^2 + |\langle f\downarrow|\pi^-|i\downarrow\rangle|^2 - |\langle f\downarrow|\pi^+|i\downarrow\rangle|^2. \tag{3.30}$$

The operators $\pi^{\pm} = \pi_x \pm i\pi_y$ are the components of

$$\boldsymbol{\pi} = \boldsymbol{p} + \frac{\hbar}{4mc^2}\boldsymbol{\sigma} \times \nabla\nabla(\boldsymbol{r}) \tag{3.31}$$

where the last term is the spin-orbit coupling. The initial states $|i\rangle$ for both spins are occupied and the final states $|f\rangle$ are unoccupied. Just like in the optical conductivity studies there are intraband and interband contributions to σ_{xy}. The intraband part may be estimated by an extension of the Drude model. This part has an ω^{-1} dependence and contributes to a smooth background. The interband square matrix element F_{if} is usually approximated by a constant, then

$$\sigma_{xy}^{(2)} \cong \frac{\pi e^2}{4m^2\omega}\sum_{i,f}\langle F_{if}\rangle J_{if}(\omega), \tag{3.32}$$

where $J_{if}(\omega)$ is the joint density of states defined previously.

Erskine and Stern (1973) reported the most careful Kerr effect measurement for Gd. The samples were films deposited in vacuum and measured in situ. They are magnetized in the plane of the films. The rotation of the polarization axis and the ellipticity were measured, and from these quantities the off-diagonal conductivity tensor was deduced. The results for the real and imaginary parts of σ_{xy} at 105 K are shown in fig. 3.43. Comparing the imaginary part $\sigma_{xy}^{(2)}$ with the joint density of states curve for Gd in fig. 3.43, we find that the peak at 2 eV in the

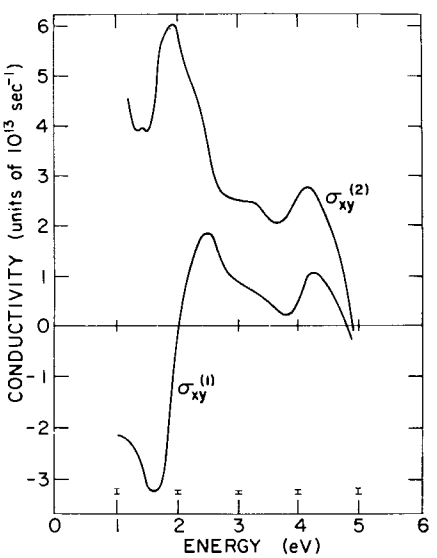

Fig. 3.43. The off-diagonal magneto-optic conductivities of Gd film (Erskine and Stern, 1973).

data curve coincides very well with the interband transition peak. The observed peak at 4 eV is not seen in the joint density of states curve, nor is it observed in the reflectivity or absorptivity measurements. The authors pointed out a peak at 4 eV above the Fermi energy in the density of states of Gd in fig. 3.2. Then they explained the peak at 4 eV by invoking a very narrow p band just at the Fermi level. The transition from the p band to the d band at 4 eV gave a joint density of states curve as observed experimentally. This explanation is not acceptable because calculations show that the band states have p character over a wide energy range, from near the bottom of the bands to above the ten d bands. Also, if such a narrow p band existed, it would cause a peak to appear at 4 eV in the diagonal element of the conductivity tensor, in contradiction to the experimental data. Therefore, if the observed peak has anything to do with the band states at 4 eV above E_F, it must be a result of the energy dependence of the matrix element.

The $\sigma_{xy}^{(2)}(\omega)$ function drops abruptly above 4 eV. Recently Erskine (1976) extended the frequency range of the measurement up to 12 eV by using synchrotron radiation. He found the off-diagonal optical conductivity to turn around and form two large peaks at 6 and 8 eV. The author identified the first peak as the 4f electron absorption edge because Erskine and Flynn (1976) observed a corresponding peak in the optical absorption spectrum. The peak at 8 eV is also due to 4f absorption. The reason for the two peaks was explained qualitatively by Erskine (1976) as coming from two different final states of excitation. When an electron is excited from the 4f shell into the conduction band, it may form a bound state with the 4f hole. The optical threshold is the energy of this bound state. At higher photon energies the bound state may be broken up, leaving the excited electron to move freely throughout the crystal. The peak at 8 eV, which is also observed in the XPS spectrum of Gd (section 3.4), corresponds to the energy of this final state.

In conclusion, the magneto-optic Kerr effect is a very promising method for probing the electronic structure of ferromagnetic metals. The method is new, and a certain amount of uncertainty in the interpretation of the data is to be expected. Further experiments should be conducted on samples prepared under different conditions to see if this has any influence on the data. Single domain, single crystal specimens are preferable to films. Other ferromagnetic rare earths should be studied to look for trends in behavior. Of equal importance, the energy dependence of the matrix element should be examined by using metallic-state wave functions.

3.3. *Ultraviolet photoemission spectroscopy* (UPS) *studies*

In a photoemission experiment monochromatic photons at uv or X-ray frequency are incident upon a clear surface of the solid. The number of emitted electrons in a specific energy range is counted. With incident photon energy $h\nu$ the number of photoelectrons in the energy interval $(E, E + \Delta E)$ is denoted by $N(E, h\nu)\Delta E$, and the quantity $N(E, h\nu)$, named energy distribution curve (EDC),

gives information about the energy band structure. In the uv region ($h\nu \lesssim 20$ eV) only the band electrons are excited. The photoelectron may be thought of as created in three stages (Berglund and Spicer, 1964a). First the band electron is excited into an empty state, then the excited electron moves to the surface, and finally the electron escapes into vacuum. The excited electrons suffer collisions during the transport process, so only those electrons created in the 5–15 Å thickness from the surface may escape (Lindau and Spicer, 1974). Also, the kinetic energy lost by an excited electron may be picked up by other band electrons, and the latter may emerge from the surface as secondary electrons. Berglund and Spicer (1964a,b) worked out a practical method to subtract out the spectrum of secondary electrons, and the corrected curve is called the optical density of states (ODS) of the solid. The ODS is to be compared with that calculated from the band model.

The proper way to calculate the theoretical ODS was a subject of controversy for some years. Taking the band electrons as independent particles, one can easily formulate the probability of excitation of a band electron,

$$D(E,\omega)=\frac{2\pi e^2}{m^2c^2\hbar\omega}\sum_{i,f}\sum_{\boldsymbol{k}}|M_{if}|^2\delta[E-E_f(\boldsymbol{k})]\delta[E-\hbar\omega-E_i(\boldsymbol{k})], \tag{3.33}$$

where the initial state, final state, and matrix element are defined in the same way as in eq. (3.35). It is clear that $D(E,\omega)$ is related to the imaginary part of the dielectric function

$$\omega^2\epsilon_2(\omega)\propto\int_{E_F}^{\infty}D(E,\omega)\mathrm{d}E. \tag{3.34}$$

Since $D(E,\omega)$ is like a derivative of the optical constant, it follows that the photoemission study can give more detailed information than optical studies.

Spicer and his coworkers (Berglund and Spicer, 1964a,b; Blodgett and Spicer, 1966) proposed a very different model for the excitation probability. They argued that the momentum conservation is not relevant in photoemission (nondirect transition), and the only selection rule is the conservation of energy. Therefore $D(E,\omega)$ is proportional to the product of the initial and final densities of states,

$$D(E,\omega)\propto N_i(E-\hbar\omega)N_f(E). \tag{3.35}$$

The final band may be broad because it approaches the free electron band at sufficiently high energy. So $N_f(E)$ is a smooth function and

$$D(E,\omega)\propto N_1(E-\hbar\omega) \tag{3.36}$$

to a good approximation. The scattering and escape effects may be approximately accounted for by a broadening of the energy resolution by about 0.5 eV. This way one can just take the calculated density of states below the Fermi level, broaden out the sharp features, and compare with the experimental ODS curve.

Although all the data on rare-earth metals to be reviewed are analyzed according to this model, the theoretical basis of the nondirect transition has been

questioned. Clearly if we ignore the electron–electron interaction, the transition must be direct. Doniach (1970) analyzed the interaction between the electron gas and the hole state left by the excited electron. The interaction causes a reduction of the direct transition probability, especially in cases where the hole is in a narrow band. This has been cited as the reason that nondirect transitions are important in d band metals.

Eastman and Cashion (1970) first noticed that even a very small amount of surface contamination could alter the shape of EDC for Cu in significant ways. They suggested that the data on newly prepared Cu gave support to the direct transition model. Detailed calculation by Williams et al. (1972) based on direct transition and including matrix elements resulted in ODS curves which look different from the simple band density of states in fine detail but not in gross features, such as the d band width. It is therefore not surprising that with slightly contaminated surfaces so many fine features of the EDC are lost, the observed ODS should agree with the band density of states. In any case the simple, nondirect transition model has been widely used as a practical way to interpret the photoemission data.

The first band structure determination of a rare-earth metal by photoemission was reported by Blodgett et al. (1966). The specimen of Gd metal was evaporated in high vacuum, and the energy distribution curves were measured for photon energies from 3.1 to 11.8 eV. The EDC's are characterized by a peak at the high energy end, a shoulder around 2.5 eV below the peak, and a low energy peak about 6 eV below the main peak. These features remain approximately at constant positions as the photon energy varies, so they are attributed to valence band effects. After subtracting out the secondary electrons, the authors presented the ODS for Gd as shown in fig. 3.44. On the same graph the density of states calculated by Dimmock and Freeman is also plotted for comparison. The ODS has the general shape and energy width as the calculated bands.

Eastman (1969) reported the ODS for Sc, Y and Gd and compared the data with the band density of states. For Gd he used the theoretical result of Keeton and Loucks (1968), for Y the result of Loucks (1964), and for Sc the result of Loucks for Y scaled in energy according to the band width calculated by Eastman (1971). As seen in fig. 3.45 the overall agreement in band width between theory and experiment is good. Lapeyre (1969) reported the same finding for Dy, shown in fig. 3.46. In particular the peak in density of states at E_F and 1.05 eV below were seen as a peak at 0.3 ± 0.1 eV (marked in fig. 3.46 as 1) and a shoulder at 1.1 ± 0.1 eV (marked in the figure as 2). Both Blodgett et al. (1965) and Lapeyre (1969) investigated the effect of magnetic ordering on the EDC and reported negative results. Since the band splitting is small and the energy resolution in the photoemission experiments is not fine enough, the lack of observable effect is not surprising.

The photoemission data of Er and Sm have been reported by Brodén (1972), and the ODS curve for Er is shown in fig. 3.47. The theoretical density of states curve in the comparison was obtained by broadening the calculated curve of Keeton and Loucks (1968) with a Lorentzian resolution function with a width of

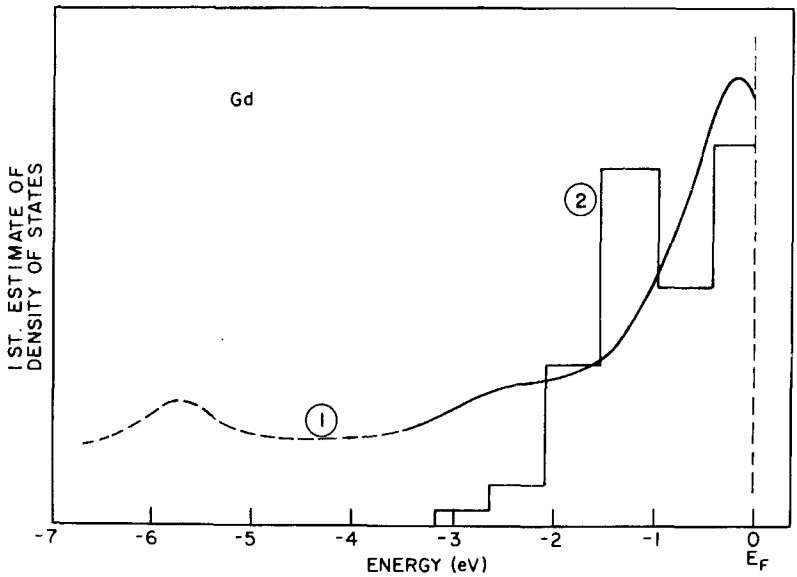

Fig. 3.44. The optical and band densities of states of Gd (Blodgett et al., 1969). Curve 1 is the optical density of states and curve 2 is the band density of states.

0.35 eV. The result for Sm is very interesting because there is no band calculation available for comparison. Nevertheless, the EDC's shown in fig. 3.48 indicate a narrow d band with a sharp peak at the Fermi level, a broader peak at 1 eV below, and an overall width of the occupied bands of 4.5 eV. This makes Sm very similar in electronic structure to the trivalent rare earths, although the crystal structure is much more complicated.

The cubic divalent metal Eu and Yb were studied by Brodén et al. (1970), Brodén et al. (1971), and Brodén et al. (1973). In fig. 3.49 the EDC's for Eu are compared with those of Ba. Just like their optical properties, the photoemission properties of these metals, features marked by A and D in fig. 3.49, are also similar. A small difference in the region between 1.5 eV and 3.2 eV below the Fermi level (features B and C in fig. 3.49) is evidence of 4f electron excitation (see section 3.4). That the bottom of the valence band appears to be 3 eV below the Fermi level is in good agreement with the calculation of Freeman and Dimmock (1966). Recall that the optical absorption data of Endriz and Spicer (1970) suggested a broader band than the calculated result by nearly a factor of 2. Since the photoemission data are easier to interpret, we would attach more weight to the information gained from this experiment.

The low photon energy (6–10 eV) EDC's for Yb in fig. 3.50 (Brodén et al., 1973) show a very narrow peak at the Fermi level, indicating a narrow valence band with a high density of states. The band calculation of Jepsen and Andersen (1971), though performed for the hcp phase, give just such a valence band. The data suggest that the fcc Yb is probably also a semi-metal with flat overlapping bands, as given by the warped MT-potential band calculation (Koelling and

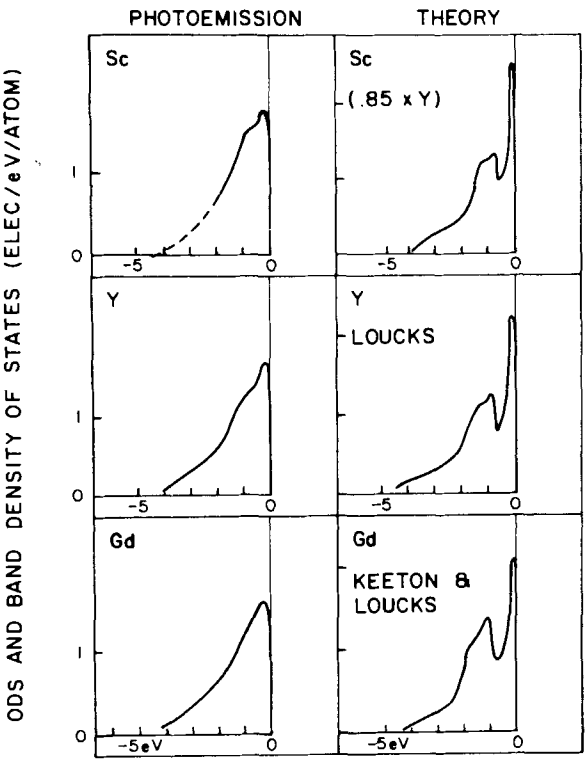

Fig. 3.45. The optical and band densities of states of Sc, Y, and Gd (Eastman, 1969).

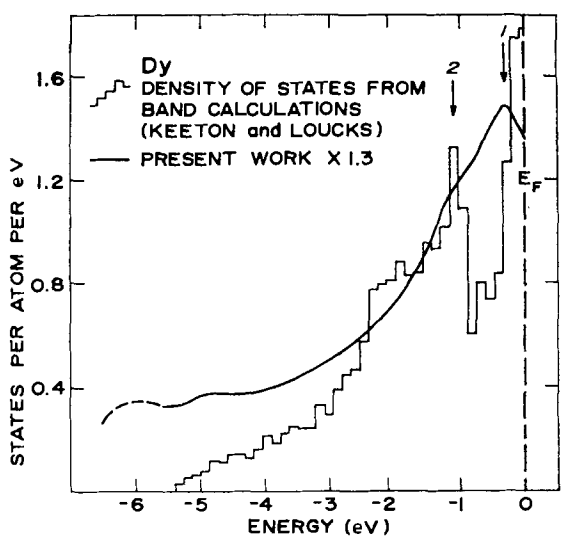

Fig. 3.46. The optical and band densities of states of Dy (Lapeyre, 1969).

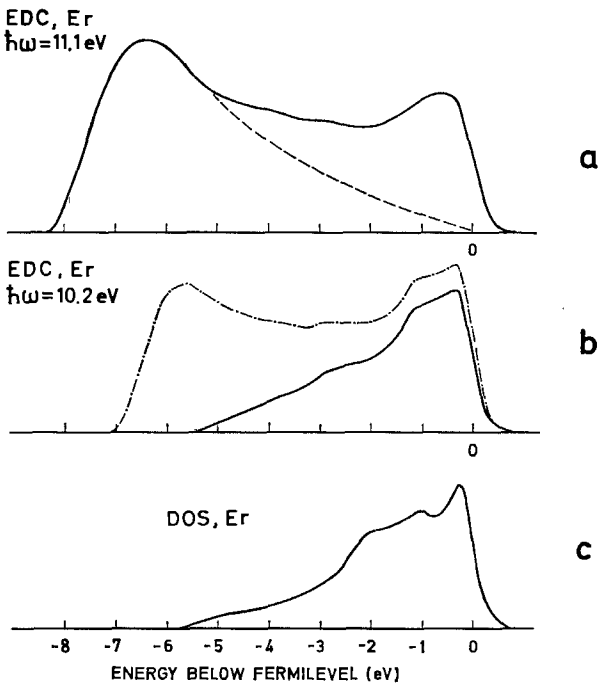

Fig. 3.47. The photoemission data and optical density of states of Er (Brodén, 1972).

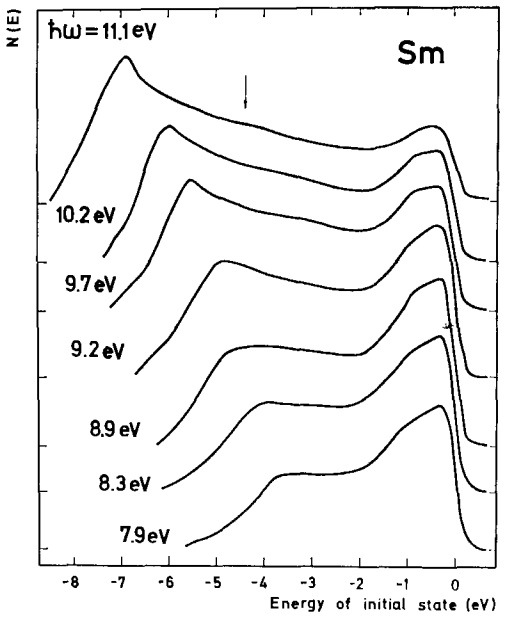

Fig. 3.48. The energy distribution curve of photoemission electrons for Sm (Brodén, 1972).

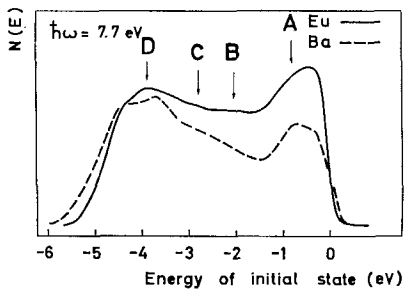

Fig. 3.49. Comparison of the energy distribution curves of Eu and Ba. The small features B and C may indicate 4f electron excitation (Brodén et al., 1971).

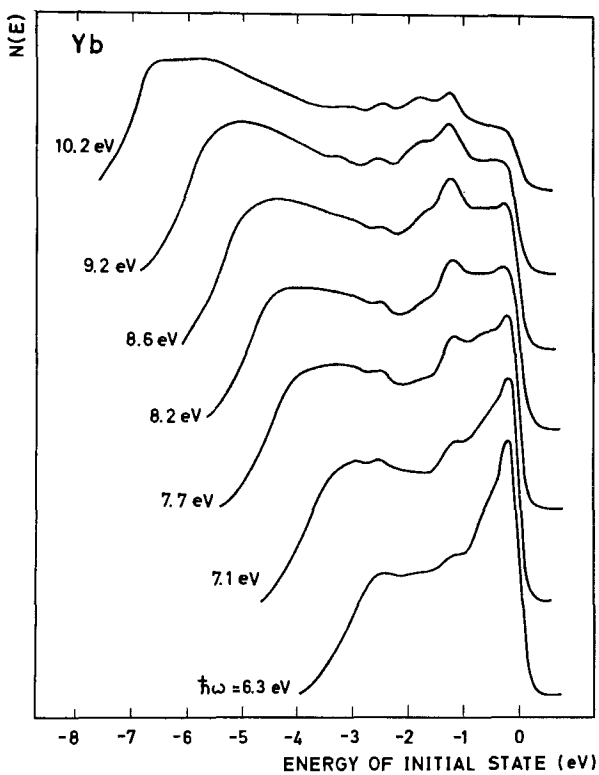

Fig. 3.50. The energy distribution curves for Yb at various photon energies (Brodén et al., 1973).

Harmon, 1972). For high photon energies (10–20 eV) two peaks in EDC at 1.2 and 2.8 below the Fermi energy grow steadily with increasing photon energy (Brodén et al., 1971). In fig. 3.51 the EDC at 21.2 eV photon energy is shown. The authors identified these peaks as the 4f level excitation. This conclusion was confirmed later by X-ray photoemission (section 3.4). The reason that there are two peaks has to do with the state of the final 4f hole. The hole has the orbital and

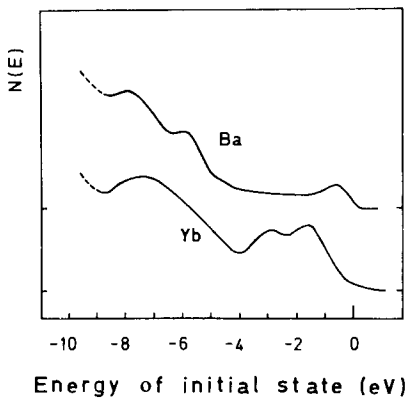

Fig. 3.51. The energy distribution curve for Yb at 21.2 photon energy, showing 4f excitation peaks at 1.2 and 2.8 eV below the Fermi energy (Brodén et al., 1973).

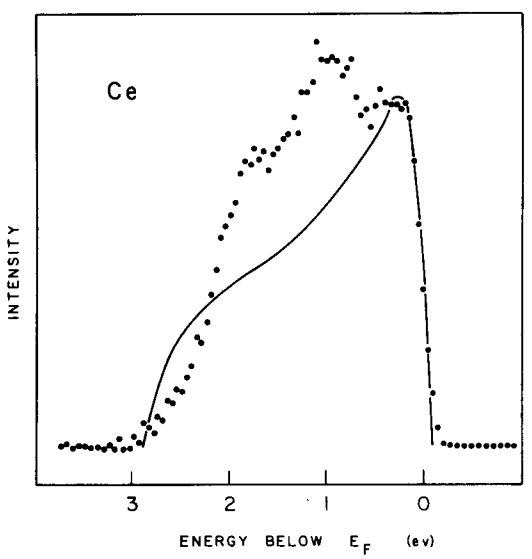

Fig. 3.52. The optical density of states of Ce. The solid curve is the UPS result of Helms and Spicer (1972) and the points are the XPS data of Bear and Busch (1974).

spin angular momentum quantum numbers $l = 3$, $s = \frac{1}{2}$. The spin-orbit coupling splits the many degenerate levels into two multiplets with total angular momentum $j = \frac{5}{2}$ and $\frac{7}{2}$ respectively, and these two groups of levels appear as two peaks in the EDC.

The ODS of Ce metal shown in fig. 3.52 was reported by Helms and Spicer (1972). The shape of the curve looks very much like the other trivalent rare earths. The conduction band extends to about 3 eV below the Fermi level, also consistent with trivalent rare earths. The excitation spectrum of the 4f level does

not appear on the graph because the matrix element of excitation is too small. On the same graph the spectrum of X-ray photoemission is also exhibited (Baer and Busch, 1973). The difference between the two curves, namely, the peak at 1 eV below the Fermi level, may indicate 4f excitation. This will be discussed further in section 3.4. Although the crystal structure of the Ce film is not known, we may infer from the data that it is in the dhcp or γ phase. Helms and Spicer studied in detail the effect of oxidation on the ODS of the film. Even with relatively small amount of exposure to oxygen, the main peak of ODS at E_F broadens and the shoulder at 2 eV below grows into a new peak. This result demonstrates in a dramatic way that the structures in the low energy region of the ODS curves of rare earths must be interpreted with caution.

3.4. *X-ray photoemission spectroscopy* (XPS) *studies*

With X-ray photons in the energy range around 1 keV the final energy of the photoelectron is so high that its wave function is very nearly a plane wave. Since a plane wave contains a large number of angular momentum states, the probability of exciting an electron out of the 4f shell becomes favorable. This is the most powerful tool to probe the structure of the partially filled 4f shell of rare-earth metals.

The electrons in a 4f shell move in a highly correlated manner, so the excitation process can not be visualized in the quasi-particle picture. Assume that one of the n 4f electrons is excited to the Fermi level. Then the initial configuration of the 4f shell is $4f^n$ and the final configuration is $4f^{n-1}5d$, where the 5d electron is in the Bloch state. The energy difference $E(4f^{n-1}5d) - E(4f^n)$, also called the 4f electron promotion energy, represents the measured "position" of the 4f level. Therefore, the excitation is a complicated atomic process, and it is wrong to associate the energy of excitation with the location of the "f-band" obtained from a band calculation, regardless of how the calculation is done.

The XPS spectrum of 4f excitation often exhibits a series of peaks corresponding to the multiplet structure of the final 4f shell. The spin-orbit splitting in Yb has been discussed in section 3.3. The splitting of final states with different L quantum numbers in the Russell–Saunders scheme is evident in Sm and heavier members. The spin multiplet structure is seen in rare earths with more than half-filled shells (Tb–Tm). For example, the final state of $Tb(4f^7)$ may be in the state $4f_\uparrow^7$ ($S = \frac{7}{2}$) or $4f_\uparrow^6 4f_\downarrow$ ($S = \frac{5}{2}$). The splitting of these groups of states measures the exchange interaction between the 4f electrons.

The ease with which an electron may be excited out of the 4f shell is of great interest because it determines the extent to which the 4f electrons may be regarded as local or itinerant. Models of itinerant 4f electrons have been proposed to explain the superconducting property of La, the lattice and valence instabilities of Ce and a number of rare earth compounds.

The XPS method also measures with high resolution the structure of the valence bands of transition and rare earth metals. The formula of the ODS is the same as was written down for UPS, eq. (3.33). However, since the final state is a

broad free-particle state with little structure, there should be little difference between the direct transition model and the non-direct transition model. The ODS compares readily with the valence band density of states. The contribution to the spectrum by the inelastically scattered electrons is unimportant, and if necessary, can be subtracted out in a much better controlled way as described by Hagström (1972). This is the reason for the recent popularity of XPS as a standard tool for probing the valence band structure of solids.

The various groups of investigators who contributed to the XPS studies of rare earth metals are listed in table 3.6 along with the metals they studied. The data from different groups agree, often within the experimental resolution of 0.3 eV in the latest works. In choosing the representative data for this review, we will show the sets of EDC with the best resolution so that the fine structures are best exhibited.

The XPS spectra of La, Ce, Pr, and Nd are shown in fig. 3.53 (Baer and Busch, 1973). The metal La has no 4f electron, so the peak just below E_F comes from excitations of valence electrons. The sharpness of the leading edge, about 1 eV, is a measure of the resolution width. The width of the valence band, somewhat less than 5 eV, is in good agreement with the calculated value 3.5 eV (Fleming et al., 1968). The structure below 5 eV corresponds to 5p electron excitations by an X-ray satellite. The spectrum of Ce shows a broader peak

TABLE 3.6
References on XPS studies of lanthanide metals

Element	References
La	6
Ce	6, 8
Pr	6
Nd	3, 5, 6
Sm	3, 5, 8
Eu	2, 4, 5
Gd	4, 5, 7
Tb	5, 7, 8
Dy	3, 7, 8
Ho	5, 8
Er	3, 8
Tm	5, 8, 9
Yb	1, 2, 4, 5, 8, 9, 10
Lu	5, 9, 10

[1]Hagström et al. (1970); [2]Brodén et al. (1971); [3]Hedén et al. (1971); [4]Hedén et al. (1972); [5]Hagström (1972); [6]Baer and Busch (1973); [7]McFeely et al. (1973); [8]Baer and Busch (1974); [9]Fabian et al. (1974); [10]Lang et al. (1974).

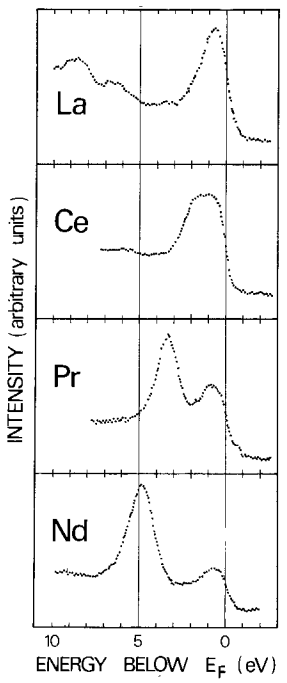

Fig. 3.53. The XPS spectra for La, Ce, Pr, and Nd (Baer and Busch, 1973).

between 1 and 2 eV below the Fermi energy. The interpretation of this feature becomes clear when the more recent data (Baer and Busch, 1974) are compared with the UPS data in fig. 3.52. Since the 4f excitation is very weak in UPS, the difference between the two curves must be due to the 4f electrons. Thus, we find that the excitation energy of the 4f electron in Ce is about 0.9 eV, somewhat lower than the earlier estimate of 1.8 eV (Baer and Busch, 1973). Neither set of data can rule out the possibility that the 4f level is strongly hybridized with the s–d bands, forming a complicated set of valence bands.

The 4f excitation energies for Pr and Nd are found to be 3.4 eV and 4.8 eV respectively, and the spectra appear as single lines. Cox et al. (1973) discussed the number of lines and their relative intensities on the basis of the Russell–Saunders coupling. The implicit assumption of a spherically symmetric environment for the 4f shells is justified when the temperature is high enough so that all the crystal field levels are equally populated. Then the ground state $^3H_4$ of Pr may lose one f electron and go into either $^2F_{7/2}$ or $^2F_{5/2}$. The spin–orbit splitting of the two lines, being on the order of 0.3 eV, is too small for the lines to be resolved. Now we turn to the final state of Nd, $4f^2$. Consider the coupling energies in the Russell–Saunders scheme in descending order of importance. The exchange energy is very strong so that the spin of the final state is $S = 1$. The orbital angular momentum L may have the values from 1 to 5. The corresponding ^3P, ^3D, ^3F, ^3G, ^3H are further split into their J multiplets. The J multiplets are

not resolvable because of the small spin–orbit splitting. The relative intensities of the L multiplets can be related to the fractional parentage coefficients. Cox et al. tabulated the intensities of all the important lines, reproduced here in table 3.7. For Nd they showed that the ^{3}H line dominates, the ^{3}F line is much weaker, and all other lines are unobservable. The single line on the spectrum must be the ^{3}H line, and the barely discernible shoulder at 5.4 eV, which is 0.6 eV above the main peak, is attributable to the ^{3}F line. The energy splitting of the two lines corresponds very well to the ^{3}H to ^{3}F separation in the trivalent Pr ion. That energy splitting of the excited state of $4f^n$ may be estimated from the ground state of $4f^{n-1}$ was pointed out by Wertheim et al. (1971).

It is also clear from the spectra of La, Pr and Nd that the valence bands of these three metals are very similar in structure.

We encounter the first instance of well-resolved 4f levels in the XPS spectrum of Sm, shown in fig. 3.54 (Baer and Busch, 1974). The various peaks are identified and their relative intensities as calculated from the coefficients of fractional parentage are described by the lengths of the lines drawn underneath each peak. The level separations ^{5}F–^{5}I (1.7 eV), ^{5}G–^{5}I(2.3 eV), and ^{5}D–^{5}I(4.0 eV) are comparable with the values 1.7, 2.2, 3.9 eV for Pm^{3+}. The spectrum of the valence band confirms the result of UPS that Sm is very similar in band structure to the trivalent heavy rare earths.

The XPS spectrum of Eu, reported by Hedén et al. (1972) is shown in fig. 3.55. The main peak due to the 4f shell lies about 2.1 eV below the Fermi level, somewhat lower than the value 2.5 eV reported earlier by Brodén et al. (1971). Since Eu is divalent, the ground state is $^8S_{7/2}$ and the excited state is $^7F_3$. With spin–orbit splitting unresolved, only one line is expected.

The XPS spectra of Gd is shown in fig. 3.56 (McFeely et al., 1973). The single peak from the final state ^{7}F is 8.0 eV below the Fermi level. This shows that although Eu and Gd have isoelectronic 4f shells, the 4f shell of Gd is far more stable.

The XPS spectra of the next six heavy lanthanides Tb, Dy, Ho, Er, Tm, and Yb, are shown in figs. 3.57 and 3.58 (Baer and Busch, 1973). In Tb we see the first instance of exchange splitting where the 7 electrons in the final state may align their spins to get $S = \frac{7}{2}$ or $\frac{5}{2}$. The ^{8}S level is 2.3 eV below the Fermi level. The next peak, which is the unresolved line of ^{6}P, ^{6}I, and ^{6}D, lies 5.1 eV below ^{8}S. This energy splitting may be compared with the values 4.0 eV (^{6}P), 4.5 eV (^{6}I), and 5.0 eV (^{6}D) for Gd^{3+}. The observed value is clearly higher than the average of the three expected values. Similarly the line for ^{6}G is expected to be at 6.2 eV but observed at 7.0 eV; the line for ^{6}H is expected at 7.3 eV but observed at 8.1 eV. This systematic shift of energy levels to higher values reflects the various relaxation processes that take place in the excited atom (Shirley, 1972; Jørgensen, 1974). On the crudest level we observe that the excited 4f shell of Tb sees one more nuclear charge than the ground state 4f shell of Gd. Taking the 4f levels as hydrogen-like orbitals outside the neon core, we find that the effective charges for Tb and Gd are 11 and 10 respectively. Consequently, all energy-level separations of Tb must be scaled up from the corresponding values of Gd by the

TABLE 3.7

Normalized probabilities of terms (in Russell–Saunders coupling) formed by ionization. Only values above 0.3 are included. This condition is satisfied by all accessible terms having the maximum value of S. After Cox et al. (1973).

Ground State										
f^3	$^4I_{9/2}$	$^3H(2.333)$	$^3F(0.667)$							
f^4	$^5I_4$	$^4I(2.545)$	$^4G(0.955)$	$^4F(0.500)$						
f^5	$^6H_{5/2}$	$^5I(2.758)$	$^5G(1.266)$	$^5F(0.500)$	$^5D(0.476)$					
f^6	$^7F_0$	$^6H(3.143)$	$^6F(2.000)$	$^6P(0.857)$						
f^7	$^8S_{7/2}$	$^7F(7.000)$								
f^8	$^7F_6$	$^8S(1.143)$	$^6I(1.857)$	$^6H(1.571)$	$^6G(1.286)$	$^6F(1.000)$	$^6D(0.714)$	$^6P(0.429)$		
f^9	$^6H_{15/2}$	$^7F(2.333)$	$^5L(1.545)$	$^5K(1.364)$	$a^3I(0.919)$	$^5H(1.000)$	$a^5G(0.422)$			
f^{10}	$^5I_8$	$^6H(2.800)$	$^6F(0.800)$	$^4M(1.462)$	$^4L(1.308)$	$a^4K(0.594)$	$a^4I(0.636)$	$c^4H(0.299)$		
						$b^4K(0.559)$				
f^{11}	$^4I_{15/2}$	$^5I(3.182)$	$^5G(1.193)$	$^5F(0.625)$	$^3M(1.462)$	$^3L(1.308)$	$a^3K(0.594)$	$a^3H(0.467)$	$d^3H(0.299)$	
							$b^3K(0.559)$			
f^{12}	$^3H_6$	$^4I(3.677)$	$^4G(1.688)$	$^4F(0.667)$	$^4K(0.635)$	$^2L(1.545)$	$^2K(1.364)$	$a^2H(1.000)$	$a^2F(0.333)$	
f^{13}	$^2F_{7/2}$	$^3H(4.714)$	$^3F(3.000)$	$^3P(1.286)$	$^1I(1.857)$	$^1G(1.286)$	$^1D(0.714)$			

ratio of the squares of charges, i.e. $(\frac{11}{10})^2 = 1.21$. The observed scale factor is roughly 1.1.

The spectrum of Dy shows many more resolved peaks, and the level separations are scaled up from those of Tb^{3+} by 12%. In Ho the spin–orbit splitting of

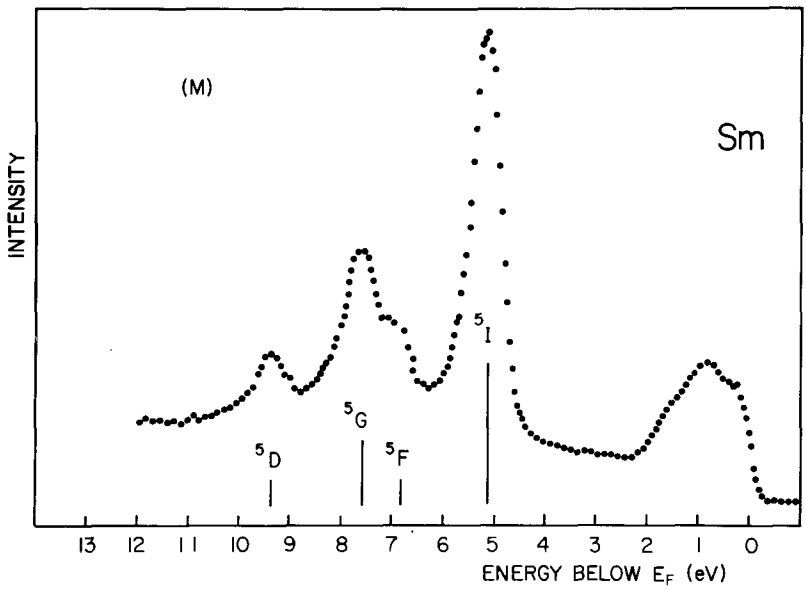

Fig. 3.54. The XPS spectrum of Sm (Baer and Busch, 1974).

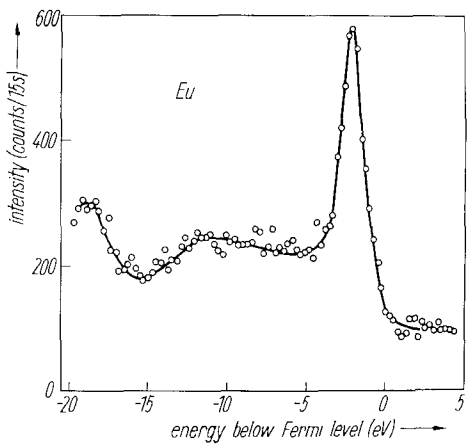

Fig. 3.55. The XPS spectrum of Eu (Hedén et al., 1972).

the ^{6}H levels (0.4 eV) is barely resolved. In Er the spin–orbit effect splits the ^{5}I levels. Although the levels ^{3}L and ^{3}M are also spin-orbit split, the intensities are concentrated in the levels $^3L_9$ and $^3M_{10}$. Thus only single lines are seen. In Tm we see clearly resolved spin–orbit split states $^4I_{13/2}$ and $^4I_{15/2}$. Compared with the spectrum of Er^{3+} the energy level spacings are scaled up by approximately 8%.

The Yb metal is divalent, so its XPS spectrum may be directly compared with the absorption spectrum of Yb^{3+}. The two peaks at 1.2 and 2.5 eV below the Fermi level are identified as the $^2F_{7/2}$ and $^2F_{5/2}$ states. The spin–orbit splitting of

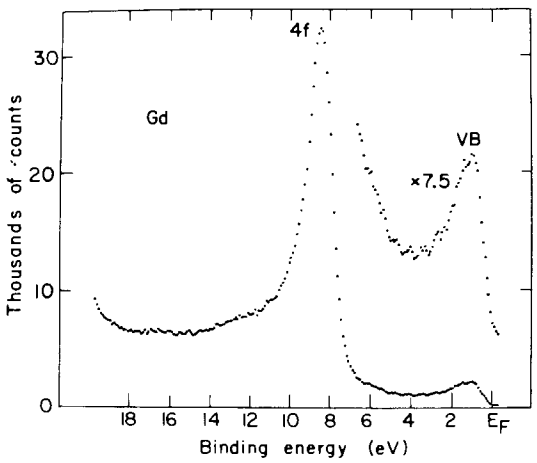

Fig. 3.56. The XPS spectrum of Gd (McFeely et al., 1973). The peak marked VB is due to the valence band.

1.3 eV agrees very well with the value 1.24 eV determined from the absorption spectrum. The spectrum of Lu is very similar to that of Yb as shown in fig. 3.59 (Lang et al., 1974). The initial and final states of both metals are isoelectronic. The slightly larger spin–orbit splitting in Lu, 1.4 eV, may be rationalized as due to the difference in the nuclear charges. Just like the comparison between Eu and Gd, the 4f level in Yb (1.2 eV) is much closer to the Fermi level than in Lu (7.5 eV).

The valence band spectra of Gd, Dy and Er are shown in fig. 3.60 (Baer and Busch, 1974). They follow very faithfully the density-of-states curves of Keeton and Loucks (1968). The fine resolution of the data testifies to the power of XPS method.

3.5. *Calculation of* 4f *promotion energy*

The calculation of 4f promotion energy requires the combination of an atomic calculation for the 4f shell and a band calculation for the 5d band. The two calculations are based on such drastically different approximations that the combination of the two under one algorithm is a seemingly impossible task. Herbst et al. (1972) overcame this difficulty by using the renormalized atom method first proposed for the d band metals by Watson et al. (1970) and reported in detail by Hodges et al. (1972). We will review here the philosophy of the method, with particular emphasis on the meaning of the various approximations. The computational details are found in the original article. The relativistic version of the calculation has been published recently by Herbst et al. (1976).

The promotion energy is identified as the difference between the total energy per atom of the trivalent metal and that of the tetravalent metal. On first sight this seems to imply that every atom in the metal must make a transition, which is

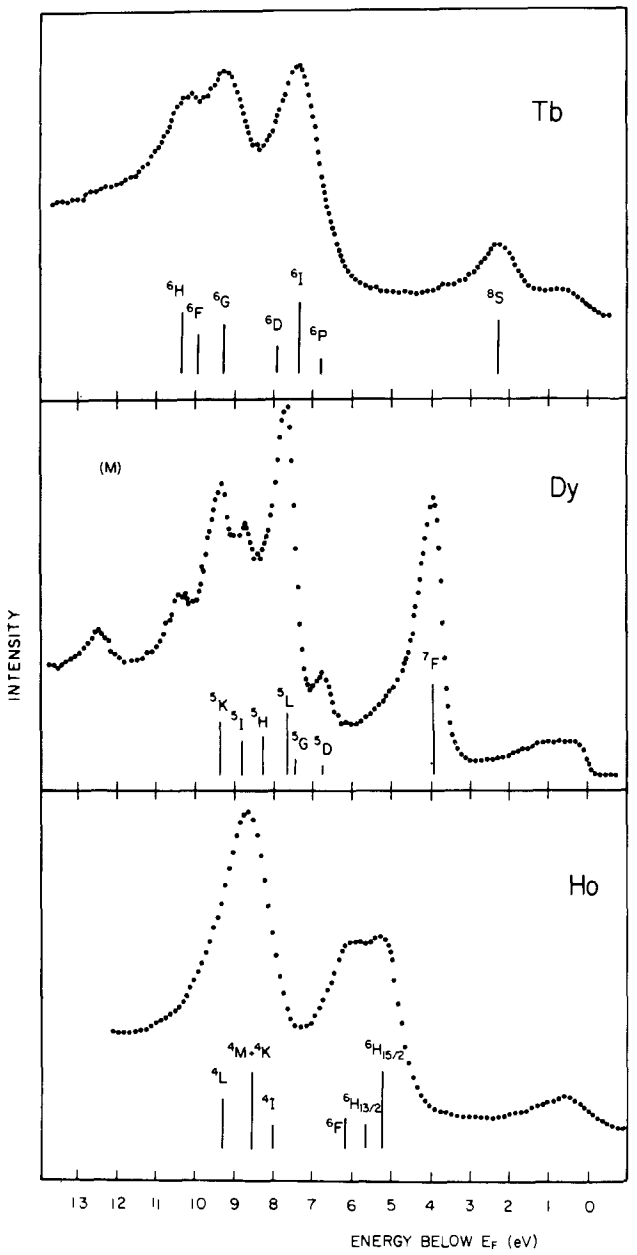

Fig. 3.57. The XPS spectra of Tb, Dy, and Ho (Baer and Busch, 1974).

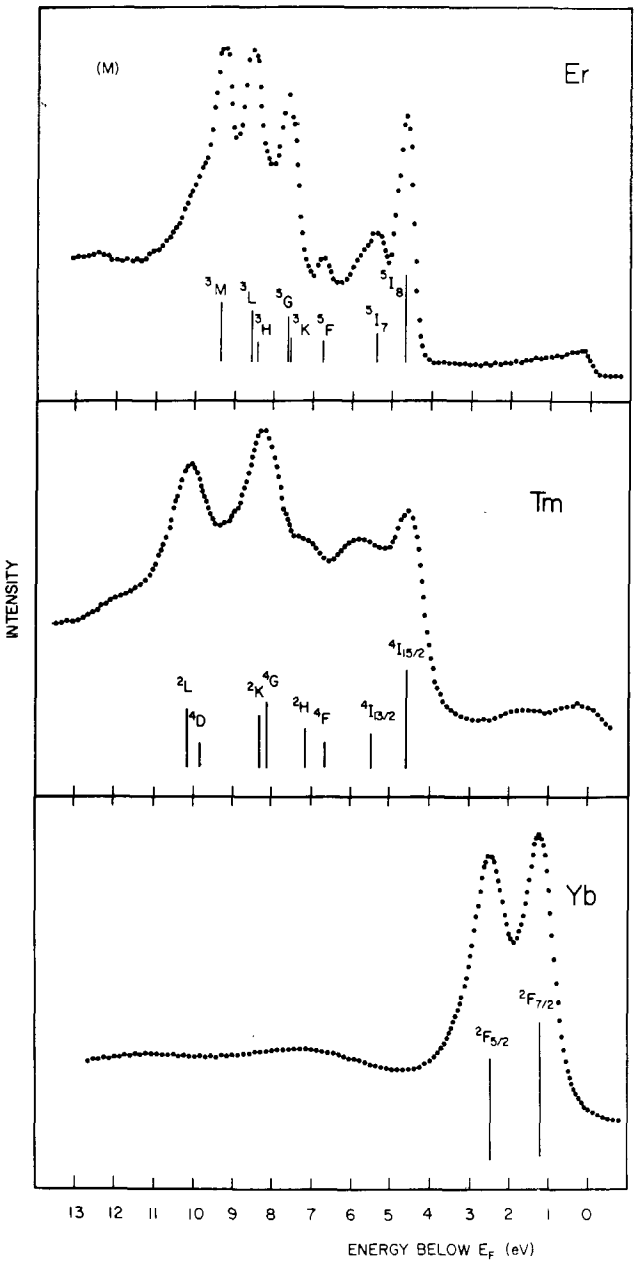

Fig. 3.58. The XPS spectra of Er, Tm, and Yb (Baer and Busch, 1974).

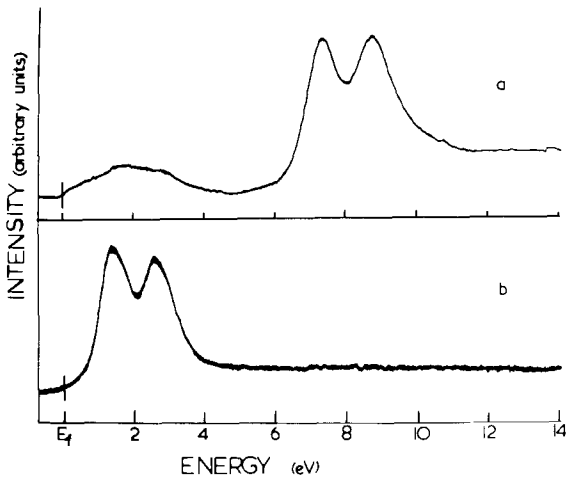

Fig. 3.59. The XPS spectra of Lu (curve a) and Yb (curve b) (Lang et al., 1974).

obviously not the case in a photoemission process. One can rationalize this step by assuming that when a site in a metal makes a transition, the effect is only felt within the site. The electrons on the site can relax to the new neutral configuration, and the electrons on the neighboring sites as well as the crystal lattice remain unaffected. Under this approximation the promotion energy Δ_- is written as

$$\Delta_- = E_M(n-1, m+1) - E_M(n, m), \tag{3.37}$$

where $E_M(n, m)$ means the energy per metal atom with n electrons in the 4f shell and m electrons in the conduction band.

In a crystal the electron wave functions satisfy very different boundary conditions so that all the electron charges are confined in the cell. Although only the wave functions of the outer shell electrons change significantly, the redistribution of the charges affect the entire self-consistent potential and the energies of the inner shells relative to the vacuum. The local exchange approximation, which is a one electron approximation, renders a rather poor account of the inner shell energies, so one must generalize the atomic Hartree–Fock calculation to the new charge distribution. The renormalized atom method was designed to do just this. If we cut off the neutral free atom wave functions at the Wigner–Seitz (WS) radius, we lose the normalization of the outer shell electrons. This may be remedied by scaling up the wave functions inside the WS sphere so that normalization is restored. The inner shell electron wave functions are very little affected. These renormalized wave functions are then used to construct the new Hartree–Fock potential, and the atomic problem is resolved. The total Hartree–Fock energy of the renormalized atom is then

$$E_{RA}^{(HF)}(n, m) = \sum_i \epsilon_i - (\text{double counted two-electron terms}), \tag{3.38}$$

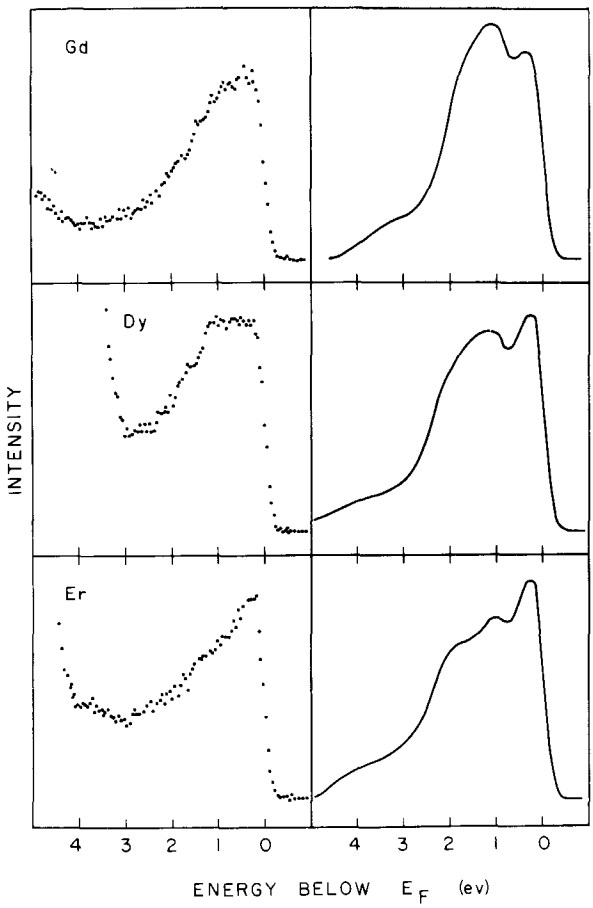

Fig. 3.60. The valence band XPS spectra of Gd, Dy, and Er (Baer and Busch, 1974). The solid curves on the right are the density-of-states curves calculated by Keeton and Loucks (1968).

where ϵ_i are the HF one-electron energies. In choosing the atomic configurations for the energy calculation the following scheme is used: the 4f electrons are in the Russell–Saunders coupled state, and the outer shell electrons, one in 6s and the rest in 5d, are in the average-of-configuration state. The various two center integrals involved are calculated for the unscreened Coulomb potential. The use of unscreened Coulomb potential introduces errors in the total energy. When tested in the free atom calculation, the total error was found to be between 0.01 and 0.025 Ry. In the sum on i only the electrons on and outside the 4f shell are counted because the inner core electrons are not affected by the promotion of a 4f electron.

The Hartree–Fock method leaves out the correlation energy. This is compensated by assuming that the correlation energy in the renormalized atom equals that in the free atom, and the latter is obtained by comparing the Hartree–Fock

energy of the free atom with the experimental value, i.e.

$$E_{RA}^{(corr)}(n, m) \cong E_{FA}^{(corr)}(n, m) = E_{FA}^{(exp)}(n, m) - E_{FA}^{(HF)}(n, m). \tag{3.39}$$

The approximation here is that the change in correlation due to the redistribution of the outer shell charges is negligible. Then we obtain the total energy of the renormalized atom

$$E_{RA}(n, m) = E_{RA}^{(HF)}(n, m) + E_{RA}^{(corr)}(n, m). \tag{3.40}$$

Now we are ready to pack the renormalized atoms together into a crystal. The outer shell states must broaden into bands, so the energy in the metal must differ from that of the renormalized atom because of this redistribution of electrons in the band states. Written explicitly

$$E_M(n, m) = E_{RA}(n, m) + \int_{E_b}^{E_F} \epsilon N(\epsilon) d\epsilon - \sum_i \epsilon_i, \tag{3.41}$$

where $N(\epsilon)$ is the band density of states, E_b is the bottom of the band, and the sum on i involves only the 5d, 6s electrons. The crucial question is how to place the band with the renormalized atom states. It was shown that the bottom of the band is at the energy for which the radial wave function of the renormalized atom has zero slope at the WS radius, and the top of the band at the energy for which the radial wave function has a node there (Watson et al., 1970). This helps to locate the bottom of the s, d bands and the width of the d band. Then, the Fermi energy is located by assuming its position relative to the d band extrema to be the same as in a full band calculation. In calculating the integral in eq. (3.41) one takes the density of states $N(\epsilon)$ from a band calculation, scales it to fit within the band extrema found by the renormalized atom scheme, and integrates numerically. This completes the metal calculation, and the results for the two different configurations are put into eq. (3.37) for the promotion energy. All the approximations in the calculation are of such a nature that the same errors are made for both configurations and tend to cancel in the final step.

The assumption behind eq. (3.37), that the effect of the 4f promotion is only felt within the site, is only valid if the Fermi levels for both the initial and final configurations relative to the vacuum level come out equal. This seems rather difficult to justify because in the final state there is one more electron in the band. On the other hand the loss of one electron from the core reduces the screening and makes the crystal potential more attractive. Consequently the bottom of the band E_b relative to the vacuum level is lowered. The Fermi level relative to E_b is increased because of the added electron in the band, but relative to the vacuum level the change could be small and unimportant.

For the heavy lanthanides in which exchange split final states are observed, the exchange splitting is calculated by perturbation. The Hartree–Fock two center exchange integrals are computed and scaled down by a factor 0.75 to crudely take into account the correlation effects.

The comparison between theory and experiment is summarized in fig. 3.61 (Baer and Busch, 1974). The lower curve for the heavy lanthanides corresponds

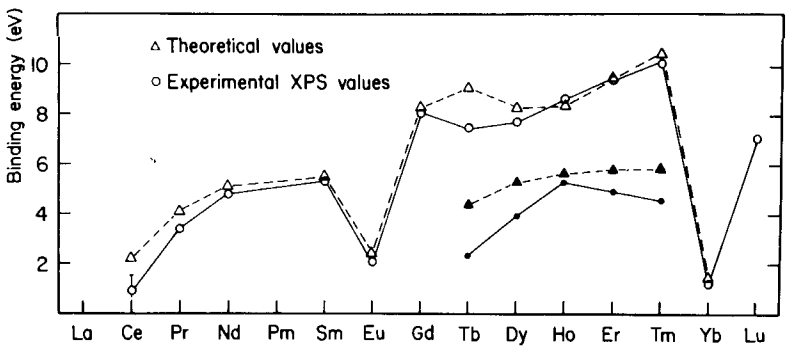

Fig. 3.61. Comparison between the calculated and the measured 4f promotion energies of the lanthanide metals (Baer and Busch, 1974). The calculation was made by Herbst et al. (1972) using the renormalized atom method.

to excitations of a minority spin electron (multiplets of higher S in final state). In case of L multiplets the energy of the line with the highest intensity is used for comparison. The success of the theory is evident. The high promotion energy of Gd reflects the great stability of the half-filled 4f shell. The low promotion energy of Ce, Eu and Yb makes it possible for the valence of these metals to change under external influences.

Recall that the energy of the excited configuration is calculated under the assumption of equilibrium state, i.e. the relaxation of the remaining electrons is complete. This assumption has been questioned recently (Baer and Busch, 1974), but so far there is no evidence to the contrary.

The authors also calculated another interesting quantity by the same method. This is the energy of promoting a band electron into the 4f shell, i.e.

$$\Delta_+ = E_M(n+1, m-1) - E_M(n, m). \tag{3.42}$$

In the language of the Anderson model of local moments (Anderson, 1961), the quantities Δ_+ and Δ_- are identified as

$$\Delta_+ = \epsilon + U, \qquad \Delta_- = -\epsilon \tag{3.43, 44}$$

where ϵ is the energy of the local orbital measured from the Fermi energy and U is the effective Coulomb repulsion. The following relation is easily established

$$U = \Delta_+ + \Delta_-. \tag{3.45}$$

Using unscreened Coulomb interaction the parameter U was found by the authors to be 2 Ry. In contrast, the renormalized atom calculation, which took into consideration the screening and relaxation effects, yielded a value $U \cong 0.5$ Ry for all rare earth metals.

Accepting the assumption of complete relaxation in the final configuration, Johansson (1974; see also Johansson and Rosengren, 1975) gave an intuitive calculation of the 4f promotion energy based exclusively on experimental data. The basic relation is also eq. (3.37), but the calculation of the energy terms

proceeds in a different manner. The difference between $E_M(n, m)$ for the metallic atom and $E_{FA}(n, m)$ for the free atom is the experimental binding energy $E_B(n, m)$,

$$E_B(n, m) = E_{FA}(n, m) - E_M(n, m). \tag{3.46}$$

Take for example a trivalent rare earth making a transition to tetravalence. For a few elements such as La, Gd, Tb, and Lu whose free atoms are in the $5d6s^2$ state, the experimental binding energies are directly applicable, but for the other rare earths with $6s^2$ free atoms the binding energy in eq. (3.46) must be taken as the sum of the experimental binding energy and the free atom excitation energy from $6s^2$ to $5d6s^2$ configuration. The binding energies of tetravalent rare earth metals are not available, but Johansson pointed out a remarkable consistency in the difference in binding energy of approximately 45 kcal/mole (2.0 eV per atom) between trivalent and tetravalent transition metals, e.g. Y: 101, Zr: 146, Lu: 102, Ac: 100, and Th: 143. This gives the universal value $E_B(n-1, 4) - E_B(n, 3) = 2.0$ eV, and consequently

$$\Delta_- = E_{FA}(n-1, 4) - E_{FA}(n, 3) - 2.0\,\text{eV}. \tag{3.47}$$

For the free atom excitation energy Johansson took the spectroscopic value when available and extrapolated when unavailable. The result, plotted in fig. 3.62, is remarkably close to that calculated by Herbst et al. The deviation between the two theoretical curves is never greater than 1 eV for the higher spin final states.

To estimate the exchange splitting in Tb, Johansson argued that the increase in exchange energy between Tb and Gd, 4.5 eV, could be regarded as the total interaction between one minority spin electron and seven majority spin electrons. In the $4f_\uparrow^6 4f_\downarrow$ final state of Tb there are six pairs of electrons with opposite spins, so the exchange splitting is reduced by $\frac{6}{7}$, or 3.9 eV. The same argument shows that the exchange splitting goes down linearly as one proceeds to heavier elements until it vanishes for Lu. The spin–orbit splitting seen in Yb and Lu can be equated to the corresponding free atom value. Thus, the author was able to explain the exchange and spin–orbit splittings in the heavier elements.

3.6. *Other optical studies*

We report briefly here two experiments designed to locate the empty 4f level of La above the Fermi energy, or to be more precise, the energy required to promote a 5d band electron into the empty 4f shell. The results of the two experiments are contradictory. The principles of both experiments are poorly understood, so one can not draw reliable conclusions from their findings.

Mariot and Karnatak (1974) studied the X-ray emission spectrum of La. The La metal film was bombarded by high energy electrons so that some of the atoms are excited by the process $3d^{10}4f^0 \rightarrow 3d^9 4f^1$. X-ray photons are emitted during the subsequent relaxation back to the ground state. Two emission lines

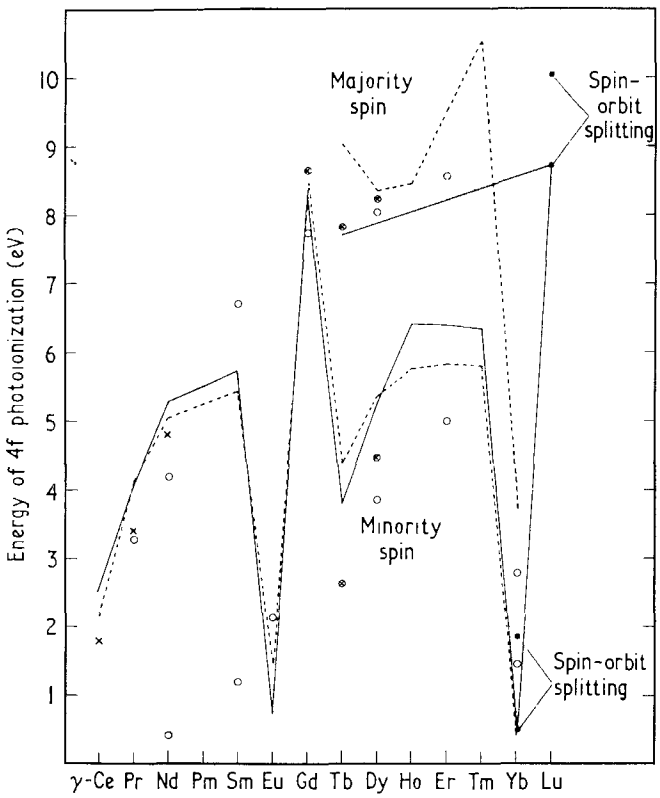

Fig. 3.62. The 4f promotion energy of the lanthanides metals as calculated by Johansson (1974, solid curve), by Herbst et al. (1972, dotted curve). ○ Experimental results of Hedén et al. (1971); □ experimental results of McFeely et al. (1973); × experimental results of Baer and Busch (1973).

were observed, and these were the strongest two of many lines which come from the multiplet structure of the initial excited state. The authors compared the emission lines with the soft X-ray absorption lines obtained by Bonnelle et al. (1974). Both emission and absorption lines have the same general structure with peaks falling at the same energies. But Mariot and Karnatak pointed out a low energy shoulder on the M_V emission line which was not present on the corresponding absorption line. They interpreted this as due to transitions of electrons from occupied 4f states near the Fermi level into the 3d hole. If this interpretation is correct, then the data suggest a hybridized d–f band just below the Fermi level. The shoulder could also be interpreted as due to transitions of 5d or 6s electrons into the 3d hole, but the authors argued that the matrix elements of these processes were too small to be significant. Aside from such qualitative considerations, the measurement gave no quantitative information on the 4f level of La.

Smith et al. (1975) attempted to observe transitions involving the empty 4f level in La by the appearance potential spectroscopy method (APS). The theory

and the experimental method have been reviewed recently by Park and Houston (1974) and Kanski and Nilsson (1975). The basic principle is as follows. The metal specimen is excited by electron bombardment. The bombarding electron interacts with a core electron via the Coulomb interaction, and in the final state they both end up in empty band states. Soft X-rays are emitted when both electrons relax back to lower band levels, and the photon yield depends, according to the simple theory, on the convoluted density of states of the empty bands. If there exists a narrow f band in La above the Fermi level, it should give rise to a high density of states and the photon yield should show a narrow feature. The result of Smith et al. did not support this idea because no sharp feature was seen. In fact, the photon yield could not be explained by the existing theory, whether one included the 4f level or not. The authors emphasized the need for a more realistic theory of the appearance potential spectroscopy.

The authors noted a great deal of similarity between the APS spectrum and the soft X-ray absorption spectrum. This suggests the following mechanism as the dominant interaction. The bombarding electrons lose their energy by Bremstrahlung. The emitted photons are selectively absorbed by the core electrons, and this is why the absorption features appear in the final spectrum.

3.7. *Electron spin polarization in* Gd

As mentioned in section 2.3.1, the energy bands of Gd are polarized when the 4f moments are ferromagnetically ordered. There are a number of experiments on the spin polarization effects. These studies have more in common with each other than with the band structure and Fermi surface studies using the same methods. We will review here a positron annihilation experiment (Hohenemser et al., 1968), two field emission experiments (Hofmann et al., 1967; Chrobok et al., 1968), and a UPS experiment (Busch et al., 1969).

In the polarized positron annihilation experiments the Gd sample was magnetized to saturation by a 20 kG field. The angular distribution functions $N_{\uparrow}(\theta)$ and $N_{\downarrow}(\theta)$ were measured for a field parallel and antiparallel to the average positron momentum, θ being the angle between the annihilation photons. The polarization curve was defined as $P(\theta) = [N_{\uparrow}(\theta) - N_{\downarrow}(\theta)]/[N_{\uparrow}(\theta) + N_{\downarrow}(\theta)]$. The individual $N(\theta)$ curves resemble those of Williams and Mackintosh (1968). The polarization curve measured along both the b and c-axes showed a positive polarization in the 4–10 mrad range, with more polarization in the c-axis. This indicates a substantial anisotropy in the Fermi surface geometry. As the temperature was varied the polarization was found to scale with the magnetization. It was also deduced from the data that the electrons were polarized in the direction of the magnetization, in agreement with the theoretical result that the spin-up bands have a higher density of states at the Fermi level (Harmon and Freeman, 1974a).

Hofmann et al. (1967) first measured the spin polarization of field emitted electrons for polycrystalline Gd. The sample was magnetized by a square pulsed field of 130 sec duration and with a strength of up to 10 kG. The spin of the

emitted electrons was measured by the Mott scattering technique. The polarization of the emitted electrons is defined by $P = (n_+ - n_-)/(n_+ + n_-)$ where n_+, n_- are the number of emitted electrons with spins parallel and antiparallel to the magnetization direction respectively. The authors reported a measured polarization of $8\% \pm 1.5\%$ at low temperatures, and that the polarization scaled with the magnetization at high temperatures. There was some confusion over the direction of the polarization at first, but a later paper by Chrobok et al. (1968) made it clear that the polarization was in the direction of the magnetization. The experiment of Chrobok et al. employed a field of up to 50 kG to saturate the sample. The polarization was found to be a strong function of the magnetic field, having zero value at zero field, a maximum of about 10% at 10 kG, and a very small value above 20 kG.

In a theoretical paper by Müller et al. (1967) and a detailed paper by Obermair (1968) it was pointed out that the field emitted electrons came from the immediate vicinity of the Fermi level. According to the spin polarized band calculation of Harmon and Freeman (1974a) the density of the spin-up states at the Fermi level is 30% higher than that of the spin-down states. This corresponds to a 12% polarization, in accord with the maximum polarization measured by Chrobok et al. However, the high field data present a puzzle which makes this simple interpretation questionable. In the ferromagnetic state of Gd the energy bands are polarized regardless of whether the sample is magnetized or not. The magnetic field merely lines up the domains and can not modify the size of the band gap in any appreciable way. If the experiment actually measured the effect of band polarization inside the solid, the data should approach a constant level when the sample became saturated. The fact that the polarization drops off at high fields makes it doubtful that the measured effect really represents the bulk property.

A spin polarized photoemission at uv frequency for Gd was reported by Busch et al. (1969). The sample was an evaporated film magnetized by a magnetic field perpendicular to the film. The incident photon beam was directed normal to the film and the spin state of the emitted electrons are measured by the Mott scattering technique. The polarization was found to be about 5% in the direction parallel to the magnetization. It appears at first sight that the data are consistent with the band theory because the photoelectrons come from within 1 eV from the Fermi level and there is a higher density of majority electrons in this energy range in Gd. But the situation is more subtle. It was reported by Bänninger et al. (1970) that the same experiment done on Ni yielded the same result that the emitted electrons were predominantly polarized in the direction of the magnetization. On the other hand, the band theory predicts that in Ni the minority spin band has higher density of states near the Fermi level. A detailed calculation by Politzer and Cutler (1972), taking into consideration the effect of the crystal surface on the energy bands, seems to remove the contradiction between the band theory and the photoemission data for Ni. We may need to interpret the Gd data on the same basis.

Meservey and Tedrow (1972) measured the spin polarization of electrons that

tunnel from magnetized Gd to Al through a layer of Al_2O_3. The magnetizing field was from 20 to 30 kG, and the average polarization of 5% was observed in the direction of the magnetization. The data are consistent with photoemission. Again the interpretation is not simple when the data for Gd and Ni are compared. The tunneling electrons must originate from within 10^{-3} eV from the Fermi level. Yet for Ni the spin polarization of the tunneling electrons was seen to be in the direction of magnetization, in contradiction to the band theory. So, all the above mentioned experiments show that the band electrons in Gd are polarized. Whether the results of the experiments may be interpreted in a straightforward manner by the band theory is questionable.

The definitive way to measure the spin polarization effect is by polarized neutron scattering, because it gives not only the size of the band polarization but also its spatial distribution. The latter information is contained in the magnetic form factor. The experiment was done by Moon et al. (1972) in which the total 4f and 5d form factor was obtained. After subtracting out the 4f part, which can be calculated from the atomic wave functions, one finds the form factor of the band electrons. The band form factor calculation of Harmon and Freeman (1974a) using band wave functions gave good agreement with the experiment (see ch. 7, section 4).

4. Relation between electronic structure and magnetic properties of the lanthanide metals

According to the Russell–Saunders coupling scheme an unfilled atomic shell carries a total angular momentum J and a magnetic moment $g\mu_B J$, where $J = L + S$ or $|L - S|$ depending on whether the shell is more or less than half filled, μ_B is the Bohr magneton, and

$$g = 1 + \frac{J(J+1) - L(L+1) + S(S+1)}{2J(J+1)} \tag{3.48}$$

is the gyromagnetic ratio or the Landé factor. For those lanthanide metals with partially filled 4f shells, this moment is possessed by the 4f shell of each atom. At high temperatures the metals have Curie–Weiss paramagnetic susceptibility with Curie constants very close to $(g\mu_B)^2 J(J+1)$. At low temperatures the metals become magnetically ordered. For those metals with a ferromagnetic ground state the saturation magnetization is very close to $g\mu_B J$ per atom. In this section we deal with the question of how the magnetic moments on different crystal sites communicate with each other and establish magnetic order. We will develop the theory of indirect exchange interaction through the conduction electrons, then relate the magnetic properties to the band structure.

4.1. *Indirect exchange interaction*

In fig. 3.63 we show the radial charge distribution of 4f, 5d and 6s electrons in the Wigner–Seitz sphere of Gd (Harmon and Freeman, 1974b). The 4f charge drops off rapidly and becomes vanishingly small at the WS sphere radius.

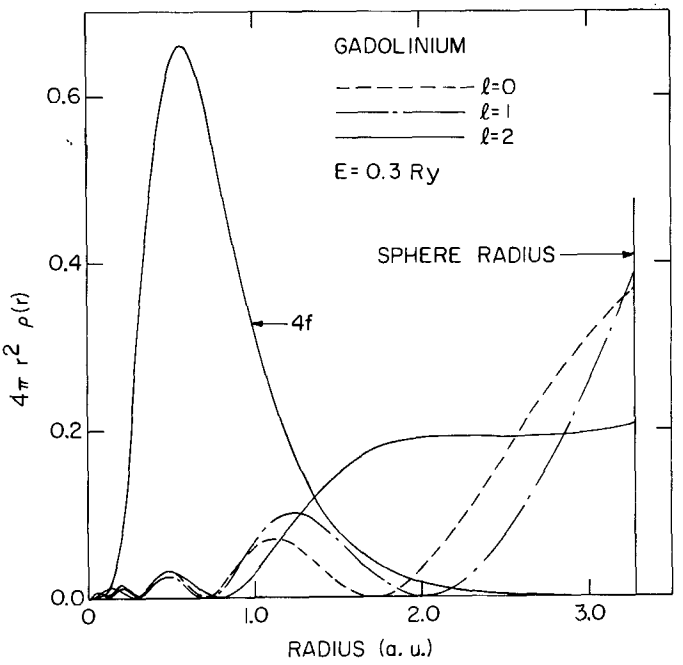

Fig. 3.63. The radial charge densities of 4f, 5d, and 6s electrons in the Wigner–Seitz sphere of Gd metal (Harmon and Freeman, 1974b).

Therefore, it was puzzling at first how the 4f electrons on different atomic sites could interact when there appeared to be no overlap between their wave functions. In the late fifties a number of authors (Kasuya, 1956; Mitchell, 1957; Yosida, 1957) worked out the details of the s–d model first proposed by Zener (Zener and Heikes, 1953) for magnetic transition metals and their alloys. The model stipulates that the magnetic moments are mainly carried by localized d electrons, and because of the exchange interaction between the d electrons and the conduction electrons (s electrons), a spin density cloud is set up around each atomic site. The spin cloud extends out to a considerable distance from the site. The direction of the d spin at each site is determined by the net polarization of the s electrons at that site induced by all other spins within a radius measured by the size of the spin cloud. The theory for this type of indirect interaction was first worked out by Ruderman and Kittel (1954) for the effective long-range interaction between nuclear spins in metals, and for this reason it is commonly called the Ruderman–Kittel–Kasuya–Yosida (RKKY) interaction. DeGennes (1958) was the first to give an extensive discussion of the application of RKKY interaction in lanthanide metals. Investigations since then have established the RKKY interaction as the dominant spin–spin interaction in the lanthanide metals.

The basic interactions between the conduction electrons and the localized d or f electrons have been studied by many authors. There are two important

interactions; one is the s–d (or s–f, d–f) exchange and the other is s–d (or s–f, d–f) admixing. We will give only cursory descriptions of the interaction mechanisms here. The reader is urged to consult the reviews by Kondo (1969) and Freeman (1972) for detailed discussions.

The d–f exchange interaction is the straightforward Heisenberg exchange interaction between a conduction electron and an electron in the 4f shell. Assume for simplicity that there is one 4f electron with the wave function $\phi_m(r)$ in the angular momentum state $(3, m)$. A conduction electron in band n and wave vector $\boldsymbol{k}$ is scattered by the 4f electron into band n' and wave vector $\boldsymbol{k}'$, and the spin dependent part of the matrix element has the form (Kasuya, 1956)

$$M(n\boldsymbol{k}, n'\boldsymbol{k}') = -2I_m(n\boldsymbol{k}, n'\boldsymbol{k}')s\cdot s_f, \tag{3.49}$$

where

$$I_m(n\boldsymbol{k}, n'\boldsymbol{k}') = \int d^3r_1 \int d^3r_2 \phi_m^*(r_1)\psi_{n'k'}^*(r_2)\frac{e^2}{r_{12}}\phi_m(r_2)\psi_{nk}(r_1), \tag{3.50}$$

s is the spin operator of the conduction electron and s_f is the spin operator of the 4f electron. This interaction is basically ferromagnetic, i.e. it tends to line up the conduction electron spin with the 4f spin.

For more than one electron in the 4f shell the symmetry of the many-electron 4f wave function must be considered (Liu, 1961). In the case of Gd which has an exactly half-filled 4f shell, the shell has zero orbital angular momentum and the interaction has the same form as eq. (3.49) except that the spin operator s_f is replaced by the total spin $\boldsymbol{S}$ of the entire shell. The matrix element $I(n\boldsymbol{k}, n'\boldsymbol{k}')$ is the average exchange integral of all seven 4f electrons,

$$I(n\boldsymbol{k}, n'\boldsymbol{k}') = \tfrac{1}{7}\sum_m I_m(n\boldsymbol{k}, n'\boldsymbol{k}'). \tag{3.51}$$

For 4f shells with non-zero total orbital moment L the effective interaction is very complicated. Only under some restrictive assumptions can one approximate the exchange interaction by the $s\cdot\boldsymbol{S}$ operator, where $\boldsymbol{S}$ is the total spin of the shell. However, since the total angular momentum is $\boldsymbol{J}$, one must project $\boldsymbol{S}$ onto $\boldsymbol{J}$ and obtain

$$M(n\boldsymbol{k}, n'\boldsymbol{k}') = 2I(n\boldsymbol{k}, n'\boldsymbol{k}')(g-1)\boldsymbol{S}\cdot\boldsymbol{J}, \tag{3.52}$$

where the gyromagnetic ratio g is given in eq. (3.48) (DeGennes, 1958).

The d–f admixing interaction is important when the 4f promotion energy is low. Let ϵ be the promotion energy, $\epsilon + U$ be the energy required to put an extra electron in the 4f shell. To use the notation defined in section 3.5, we can write $\epsilon = -\Delta_- = E_M(n, m) - E_M(n-1, m+1)$ and $\epsilon + U = \Delta_+ = E_M(n+1, m-1) - E_M(n, m)$. Then the d–f admixing interaction gives rise to an effective spin interaction of the form eq. (3.49) (Schrieffer and Wolff, 1966; Coqblin and Schrieffer, 1969), with the effective exchange interaction matrix element

$$I'(n\boldsymbol{k}, n'\boldsymbol{k}') = V_{n'k'}^* V_{nk}\left[\frac{1}{\epsilon} - \frac{1}{\epsilon + U}\right], \tag{3.53}$$

where V_{nk} is the d–f hybridization matrix element defined by

$$V_{nk} = \int_c \phi_m^*(\boldsymbol{r}) V(\boldsymbol{r}) \psi_{nk}(\boldsymbol{r}) \mathrm{d}^3 r, \tag{3.54}$$

$V(\boldsymbol{r})$ is the effective one electron crystal potential, and the integration in eq. (3.54) is carried out in the unit cell. In a band calculation the value of V_{nk} determines the width of the f band. The interaction in eq. (3.53) is basically antiferromagnetic. The present experimental evidence is that it is only important in Ce. If we take the bandwidth from the work of Kmetko (1969), we find $|V_{nk}| = 0.2$ eV. The quantity Δ_- has the value 1 eV as extracted from photoemission data, and U has been estimated as 7 eV by Herbst et al. (1972) using the renormalized atom method (section 3.5). Thus, one obtains $I' \cong -0.04$ eV, which is of the correct order of magnitude as estimated from the experimental properties of Ce and its alloys (Coqblin and Ratto, 1968; Coqblin et al., 1971; Liu et al., 1976). In contrast the d–f exchange interaction has been calculated by Harmon and Freeman (1974b) to have the average value 0.14 eV for conduction electron states near the Fermi energy, and the value estimated from the band splitting in ferromagnetic Gd is 0.1 eV. In other magnetic lanthanide metals there are more 4f electrons, which raises the d–f exchange interaction, and the promotion energy is greater, which reduces the d–f admixing. Thus the latter becomes quite negligible in comparison.

Regardless whether the d–f interaction is predominantly exchange or admixing, the second order effect of the spin interaction in eq. (3.52) is the RKKY interaction between the lanthanide spins (Kim, 1966). The effective hamiltonian of this interaction is

$$H_s = -\sum_{i,j} \mathcal{J}(\boldsymbol{R}_{ij})(g-1)^2 \boldsymbol{J}_i \cdot \boldsymbol{J}_j, \tag{3.55}$$

where

$$\mathcal{J}(\boldsymbol{R}_{ij}) = \frac{2}{N^2} \sum_{nk} \sum_{n'k'} |I(nk, n'k')|^2 \frac{f_{nk}(1-f_{n'k'})}{E_{n'k'} - E_{nk}} \exp[\mathrm{i}(\boldsymbol{k} - \boldsymbol{k}') \cdot \boldsymbol{R}_{ij}], \tag{3.56}$$

f_{nk} is the Fermi distribution function, and N is the total number of atoms. The terms with $i = j$ are self-energy terms of the spins and are independent of spin ordering. The $i \neq j$ terms provide coupling between pairs of spins.

The original work of Ruderman and Kittel is concerned with the interaction between nuclear spins due to the indirect interaction of the conduction electrons in simple s band metals. There the interaction between the electrons and the spins comes from the Fermi contact hyperfine interaction, so the matrix elements are independent of the initial and final wave vectors. The band structure is parabolic. If the same assumptions are made for the rare earths, the indirect coupling energy in eq. (3.56) has the form

$$\mathcal{J}(\boldsymbol{R}) = \frac{m|I|^2}{4\pi^3 R^4} [2k_F R \cos(2k_F R) - \sin(2k_F R)]. \tag{3.57}$$

Thus for large distances the interaction has the spatial dependence $\cos(2k_F R)/R^3$. The outstanding feature of the coupling energy as a function of distance is the long range oscillatory behavior. This makes it difficult at first to predict the most stable configuration when the spins order. The wave length of the oscillation, $2\pi/2k_F$, has the same origin as the Friedel oscillation which enters in many problems involving conduction electrons. With more complicated Fermi surfaces, we find that the linear caliper of the Fermi surface determines the period of the oscillation.

An immediate consequence of the indirect exchange model is the scaling of the paramagnetic Curie temperature of heavy lanthanides with the factor $(g-1)^2 J(J+1)$. DeGennes (1958) showed this by using the form of the interaction as given in eq. (3.57). Actually the scaling relation can be proved in a much more general way. The high temperature paramagnetic susceptibility of a spin system with the interaction hamiltonian in eq. (3.55) is

$$\chi_p = N(g\mu_B)^2 J(J+1)/3k_B(T-\theta_p), \tag{3.58}$$

where k_B is the Boltzmann constant and θ_p is the paramagnetic Curie temperature defined by

$$k_B\theta_p = \tfrac{2}{3}(g-1)^2 J(J+1)\sum_j \mathcal{J}(\boldsymbol{R}_{ij}). \tag{3.59}$$

Heavy lanthanide metals from Gd to Tm are all trivalent and have the common hcp crystal structure. It is reasonable to expect that the sum in eq. (3.59) is nearly the same for all metals of this group. Then we find

$$\theta_p \propto (g-1)^2 J(J+1). \tag{3.60}$$

The proportionality constant may be found by fitting the experimental value for Gd. For the other metals the θ_p predicted from the scaling relation are compared with experimental values in table 3.8. The experimental values are taken from the review by Koehler (1972). In cases where the paramagnetic property is anisotropic, the average θ_p is used for comparison. The small discrepancies between the theory and experiment should be viewed as evidence that the electronic structures of these metals are not identical. Applications of the RKKY theory to explain the magnetic behavior of rare-earth intermetallic compounds is discussed in ch. 14, sections 2.1.4 and 2.1.5.

TABLE 3.8
Comparison between θ_p and the prediction by DeGennes scaling for heavy lanthanides

Elements	Gd	Tb	Dy	Ho	Er	Tm
θ_p (theory) (K)	317	211	147	90	51	23
θ_p (exp) (K)	317	217	145	81	47	17

4.2. *Relation between band structure and magnetic ordering*

The magnetic structures of hcp heavy lanthanides have been well studied by neutron diffraction (Koehler, 1972). The types of ordering are shown in fig. 3.64. The moments in each hexagonal layer are parallel and fig. 3.64 indicates how the total moment of each layer is aligned relative to the plane of the layer and how the layers stack up. For example, Gd has the ferromagnetic structure below 293 K, while Tb and Dy first order in a helical structure and make a phase transition to the ferromagnetic structure at lower temperatures. Ho orders in a helical structure, then transforms into a conical structure. Er has, in order of decreasing temperature, helical, conical and longitudinal sinusoidally modulated structures. Tm has longitudinal sinusoidally modulated and antiphase domain structures.

Villain (1959) investigated first how the helical structure might be stabilized by long-range exchange interaction, such as the indirect exchange. A discussion of the other structures may be found in the review by Nagamiya (1967). Consider the helical ordering. Let the z-axis be the c-axis of the crystal. Then in a helical

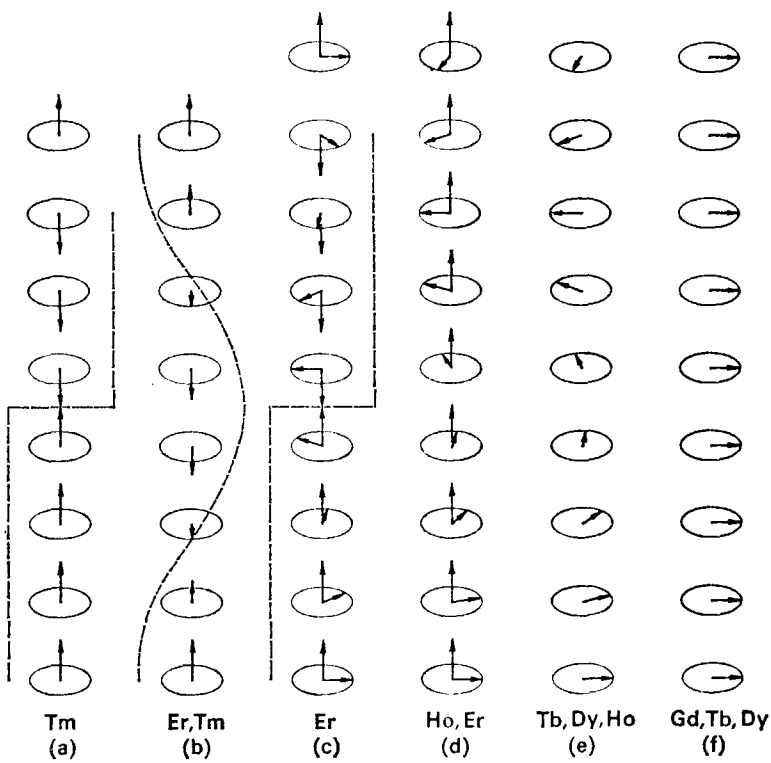

Fig. 3.64. The magnetic structures of hcp heavy lanthanide metals as revealed by neutron diffraction (Koehler, 1972).

structure the average components of the spins are given by

$$J_{ix} = A\cos(\boldsymbol{q}\cdot\boldsymbol{R}_i + \phi), \qquad J_{iy} = A\sin(\boldsymbol{q}\cdot\boldsymbol{R}_i + \phi), \tag{3.61}$$

where A is an amplitude factor, $\boldsymbol{q}$ is the wave vector which determines the periodicity of the helical structure, and ϕ is an arbitrary phase angle. The ferromagnetic structure is a special case where $\boldsymbol{q} = 0$. The exchange energy of the structure may be calculated,

$$E_{ex} = -(g-1)^2A^2\sum_{i,j}\mathcal{J}(\boldsymbol{R}_{ij})\cos(\boldsymbol{q}\cdot\boldsymbol{R}_{ij}). \tag{3.62}$$

If we define the Fourier transform of the exchange coupling constant by

$$\mathcal{J}(\boldsymbol{q}) = (g-1)^2\sum_{j}\mathcal{J}(\boldsymbol{R}_{ij})\exp(i\boldsymbol{q}\cdot\boldsymbol{R}_{ij}), \tag{3.63}$$

then

$$E_{ex} = -A^2N\mathcal{J}(\boldsymbol{q}). \tag{3.64}$$

Thus, the energy of the spin system is a function of the wave vector $\boldsymbol{q}$, and the most stable configuration is the one whose $\boldsymbol{q}$ maximizes the Fourier transform $\mathcal{J}(\boldsymbol{q})$ of the exchange constant.

In the conical ferromagnetic structure (fig. 3.64d) the average values of the spin components are

$$J_{ix} = A\sin\psi\cos(\boldsymbol{q}\cdot\boldsymbol{R}_i + \phi), \qquad J_{iy} = A\sin\psi\sin(\boldsymbol{q}\cdot\boldsymbol{R}_i + \phi), \tag{3.65}$$
$$J_{iz} = A\cos\psi,$$

where ψ is the conical angle. The exchange energy can be written as

$$E_{ex} = -A^2N[\mathcal{J}(0)\cos^2\psi + \mathcal{J}(\boldsymbol{q})\sin^2\psi]. \tag{3.66}$$

One can readily see that this structure can not be stabilized by exchange interaction alone, because if $\mathcal{J}(\boldsymbol{q}) > \mathcal{J}(0)$, the energy is minimized by $\psi = \frac{1}{2}\pi$, which is the helical structure, but if $\mathcal{J}(\boldsymbol{q}) < \mathcal{J}(0)$, the stable structure is $\psi = 0$, the ferromagnetic structure. The structure is actually stabilized by the combined effect of exchange energy, anisotropy and magnetoelastic energies. The existence of the conical structure implies that the maximum of $\mathcal{J}(\boldsymbol{q})$ occurs at $\boldsymbol{q} \neq 0$. Similarly the conical antiferromagnetic structure and the longitudinal periodic structures are stabilized by anisotropy and a $\mathcal{J}(\boldsymbol{q})$ with maximum at $\boldsymbol{q} \neq 0$. Thus, the first step toward the understanding of the magnetic structures of the heavy lanthanide is to explain why $\mathcal{J}(\boldsymbol{q})$ is a maximum at $\boldsymbol{q} = 0$ for Gd, and at $\boldsymbol{q} \neq 0$ for Tb, Dy, Ho, Er and Tm. Furthermore, experimental data have revealed that the $\boldsymbol{q}$ vector of most of the periodic magnetic structures are incomensurate with the lattice. The reason for this must also be explained.

The Fourier transform of the exchange coupling constant in eq. (3.56) can be

readily evaluated. The result is

$$\mathcal{J}(\boldsymbol{q}) = \frac{2(b-1)^2}{N} \sum_{nn'} \sum_{\boldsymbol{k}} |I(n\boldsymbol{k}, n', \boldsymbol{k}+\boldsymbol{q})|^2 \frac{f_{n\boldsymbol{k}}(1-f_{n',\boldsymbol{k}+\boldsymbol{q}})}{E_{n',\boldsymbol{k}+\boldsymbol{q}} - E_{n\boldsymbol{k}}}, \tag{3.67}$$

where it may be necessary to add or subtract a reciprocal lattice vector to fold $\boldsymbol{k}+\boldsymbol{q}$ back into the first Brillouin zone. This expression for $\mathcal{J}(\boldsymbol{q})$ shows very clearly that the $\boldsymbol{q}$ dependence comes from both the band structure and the d–f exchange matrix element. The matrix element has very complicated dependence on $\boldsymbol{k}$, $\boldsymbol{q}$ and the band indices (Watson and Freeman, 1969; Harmon and Freeman, 1974b). In early attempts to calculate $\mathcal{J}(\boldsymbol{q})$ the matrix element was approximated either by a constant or by a simple function of $\boldsymbol{q}$. This gives

$$\mathcal{J}(\boldsymbol{q}) = 2(g-1)^2 |I(\boldsymbol{q})|^2 \chi(\boldsymbol{q}), \tag{3.68}$$

where $\chi(\boldsymbol{q})$ is the $\boldsymbol{q}$ dependent susceptibility function of the band electrons defined by

$$\chi(\boldsymbol{q}) = \frac{m\Omega_0 K^0}{8\pi^2\hbar^2}, \frac{f_{n\boldsymbol{k}}(1-f_{n',\boldsymbol{k}+\boldsymbol{q}})}{E_{n',\boldsymbol{k}+\boldsymbol{q}} - E_{n\boldsymbol{k}}}. \tag{3.69}$$

The importance of the generalized susceptibility function $\chi(\boldsymbol{q})$ in the theory of magnetism in metals was discussed by many authors (see the review by Herring, 1966). Crudely speaking, $\chi(\boldsymbol{q})$ is the approximate response function of the band electrons to a sinusoidally modulated magnetic field. The true response function contains the dipole matrix elements, but if they are approximated as constant or a simple function of $\boldsymbol{q}$, the simple form of $\chi(\boldsymbol{q})$ in eq. (3.69) follows.

Before we discuss the effect of band structure on $\chi(\boldsymbol{q})$, it is instructive to study some simple band models as was done by Kasuya (1966). For an isotropic parabolic band, $E_k = \hbar^2 k^2/2m$, the sum of $\boldsymbol{k}$ can be easily done at very low temperatures when the Fermi distribution function is either 0 or 1. The result is

$$\chi(\boldsymbol{q}) = \frac{m\Omega_0 k_F}{8\pi^2\hbar^2}\left[1 + \left(\frac{4k_F^2 - q^2}{4k_F q}\right) \ln\left|\frac{2k_F + q}{2k_F - q}\right|\right], \tag{3.70}$$

where Ω_0 is the volume of the unit cell, and k_F is the Fermi wave vector. As a function of $\boldsymbol{q}$, $\chi(\boldsymbol{q})$ has a maximum at $\boldsymbol{q} = 0$ and decreases monotonously with increasing $\boldsymbol{q}$. The Fermi surface is a sphere of diameter $2k_F$. The first derivative of $\chi(\boldsymbol{q})$ has a singularity at $q = 2k_F$, the Fermi surface caliper, and this singularity manifests itself in the spatial oscillation of $\mathcal{J}(\boldsymbol{R})$ in the Ruderman–Kittel theory, eq. (3.57).

If the energy is assumed to be independent of the z component of the momentum, we obtain the two-dimensional electron gas model, $E_k = \hbar^2(k_x^2 + k_y^2)/2m$. The Fermi surface is a cylinder with diameter $2k_F$. The functional form of $\chi(\boldsymbol{q})$ is

$$\begin{aligned} \chi(\boldsymbol{q}) &= \frac{m\Omega_0 K}{8\pi^2\hbar^2}, \qquad q_\perp < 2k_F, \\ &= \frac{m\Omega_0 K}{8\pi^2\hbar^2}\left[1 - \sqrt{1 - 4k_F^2/q_\perp^2}\right], \qquad q_\perp > 2k_F, \end{aligned} \tag{3.71}$$

where K is the size of the Brillouin zone in the z direction, and $q_\perp$ is the component of $\boldsymbol{q}$ in the xy plane. This function is flat for $q_\perp < 2k_F$, then drops off steadily with increasing $q_\perp$ for $q_\perp > 2k_F$.

Finally, if E_k is assumed to depend on k_z alone, $E_k = \hbar^2 k_z^2/2m$, we obtain the one-dimensional model with two parallel planes as the Fermi surface. The form for $\chi(\boldsymbol{q})$ is

$$\chi(\boldsymbol{q}) = \frac{m\Omega_0 K_x K_y}{8\pi^3\hbar^2}\frac{1}{q_z}\ln\left|\frac{2k_F + q_z}{2k_F - q_z}\right|, \tag{3.72}$$

where K_x, K_y are the sizes of the Brillouin zone in the x, y directions, and q_z is the z component of $\boldsymbol{q}$. This function is singular at $q_z = 2k_F$, the separation between the two sheets of Fermi surface. The $\chi(\boldsymbol{q})$ for the three ideal models are shown in fig. 3.65.

Real Fermi surfaces are never perfectly planar. But the one-dimensional model is far less restrictive than it may appear to be. For example, if two sheets of Fermi surface of arbitrary shape may be brought into point-by-point coincidence by a translation vector $\boldsymbol{Q}$, the generalized susceptibility function will have the logarithmic singularity at $\boldsymbol{Q}$. Such two sheets of Fermi surface are said to "nest", and the vector $\boldsymbol{Q}$ need not be oriented normal to the sheets. In practice even this less restrictive form of nesting is not realized because the

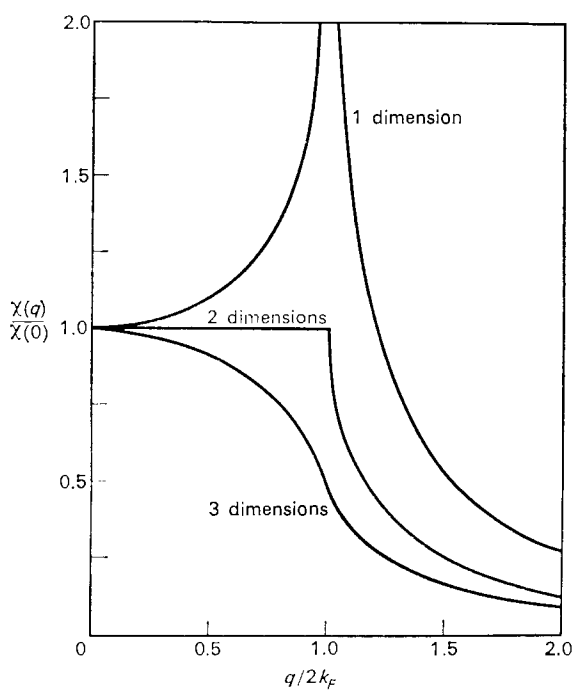

Fig. 3.65. The generalized susceptibility functions of one-, two-, and three-dimensional free electron models (Kasuya, 1966).

matching of the two surfaces is not perfect. The problem of imperfect nesting has been discussed by Roth et al. (1966), Liu (1968), and Rice (1970). For the present purpose we will discuss one simple case where the two pieces of Fermi surface mismatch slightly, as shown in fig. 3.66. The amount of mismatch is measured by the wave vector δ. Then the $\chi(q)$ curve is still given by eq. (3.72) as long as $|2k_F - q_z| \gg \delta$. When $q_z = 2k_F$ the curve has maximum equal to

$$\chi_{max} = \frac{m\Omega_0 K_x K_y}{8\pi^3\hbar^2}\frac{1}{k_F}[1 + \ln(2k_F/\delta)]. \tag{3.73}$$

The contrast between this behavior and the perfect nesting case is illustrated in fig. 3.67. In real metals one only finds gentle peaks in $\chi(q)$ rather than divergences.

From the above discussion it becomes clear that $\chi(q)$ can have a maximum at $q \neq 0$ only if there exist large, nearly parallel sheets of Fermi surface. The q for the stable magnetic structure is measured by the average separation of the two nesting sheets of Fermi surface. Since the Fermi surface geometry is not simply related to the lattice periodicity, this explains why the periodicity of the spin structure is not necessarily commensurate with the lattice.

Keeton and Loucks (1968) applied these ideas to the lanthanide metals by searching for nesting pieces of Fermi surface in the heavy lanthanides. The only candidates were the webbing pieces discussed in section 2.3.1 and illustrated in fig. 3.7. The webbing pieces are separated by a displacement in the c direction; this agrees with the observation that all periodic ordering in these metals have

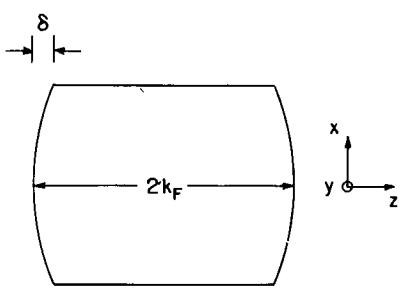

Fig. 3.66. A simple model for imperfect nesting of Fermi surface (Liu, 1968).

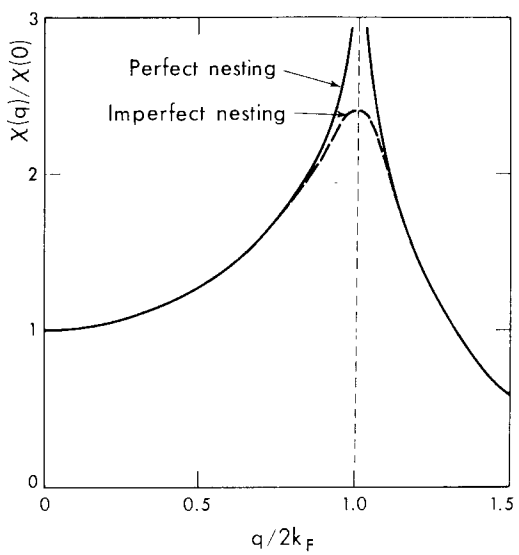

Fig. 3.67. The generalized susceptibility functions for the perfect nesting model and the imperfect nesting model.

wave vectors along the hexagonal axis. Recall that the Gd Fermi surface does not have the webbing. The authors pointed to this as the reason for the ferromagnetic ordering. In Dy and Er the thickness of webbing was found to agree with the wave vector of the initial helical ordering just below the ordering temperature. In the non-magnetic metals Lu and Y, the thickness agreed with the helical ordering wave vectors of their alloys with magnetic lanthanide metals.

Evenson and Liu (1968, 1969) confirmed the webbing hypothesis of Keeton and Loucks by calculating the $\chi(\boldsymbol{q})$ for Gd, Dy, Er and Lu for $\boldsymbol{q}$ along the c-axis. The hexagonal-closed-packed structure has two atoms per unit cell, and this fact necessitates some special considerations. Since $\chi(\boldsymbol{q})$ is only sensitive to the Fermi surface geometry, Evenson and Liu included in the sum in eq. (3.69) just the two bands which crossed the Fermi level. These are the third and fourth bands in the relativistic band structure in fig. 3.5. They added the lower bands as well as a number of higher bands later and determined that the shape of $\chi(\boldsymbol{q})$ changed very little. A number of other approximations were also made. If the spin–orbit splitting of the band on the AHL plane is ignored, we may extend the Brillouin zone out along the ΓA direction to twice its volume and fold out band 4 so that it becomes the extended part of band 3. Evenson and Liu assumed that the matrix element was constant in the extended zone scheme. The implication of this is that if $\boldsymbol{k}$ and $\boldsymbol{k}+\boldsymbol{q}$ are both within the original unextended zone, only intraband matrix elements are kept, and if $\boldsymbol{k}+\boldsymbol{q}$ is outside the zone and must be shifted back by adding a reciprocal lattice vector, only interband matrix elements are counted. This approximation is valid if the bands do not cross. In reality the bands do cross in the non-relativistic calculation, but the crossing is removed by spin–orbit coupling (see fig. 3.4). Therefore, the above approximation for the matrix elements breaks down near the crossing points of the bands. This was brought out clearly in the first-principles calculation of Harmon and Freeman (1974b).

With these simplifications the authors worked out the sum on $\boldsymbol{k}$ by the trapezoidal method with 27 000 points in the Brillouin zone, using the band data of Keeton and Loucks. The results are shown in figs. 3.68 and 3.69 where the $\chi(\boldsymbol{q})$ is plotted in the extended zone scheme for Gd, Dy, Er and Lu. On the same graphs the wave vectors separating the possible nesting features on the Fermi surface are marked. Although the noise level of the calculation is high, reflecting the crudeness of the integration mesh, the peaks in the curves for Dy, Er and Lu are clearly seen. The most prominent peak corresponds to the webbing thickness in every case. There is no similar peak in Gd, which may be taken as the indication that Gd does not prefer helical ordering. To establish that these conclusions were not sensitive to the various uncertainties in the band calculation, the authors shifted the Fermi level up and down by 0.005 Ry and showed that no essential change in the shape of $\chi(\boldsymbol{q})$ occurred.

Liu et al. (1971) repeated the calculation with a much finer mesh of about 450 000 points in the Brillouin zone. The $\chi(\boldsymbol{q})$ curves were very smooth, as seen from the result for Tb shown in fig. 3.70. The low noise level of the calculation allowed Fleming and Liu (1970) to investigate small shifts in $\chi(\boldsymbol{q})$ due to

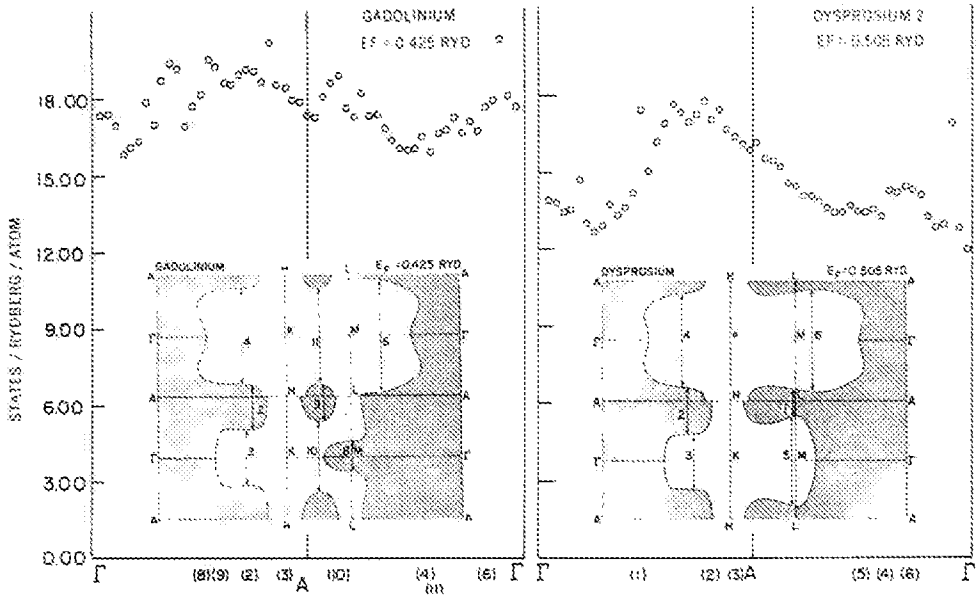

Fig. 3.68. The generalized susceptibility functions for Gd and Dy for wave vectors along the c-axis of the crystal (Evenson and Liu, 1968).

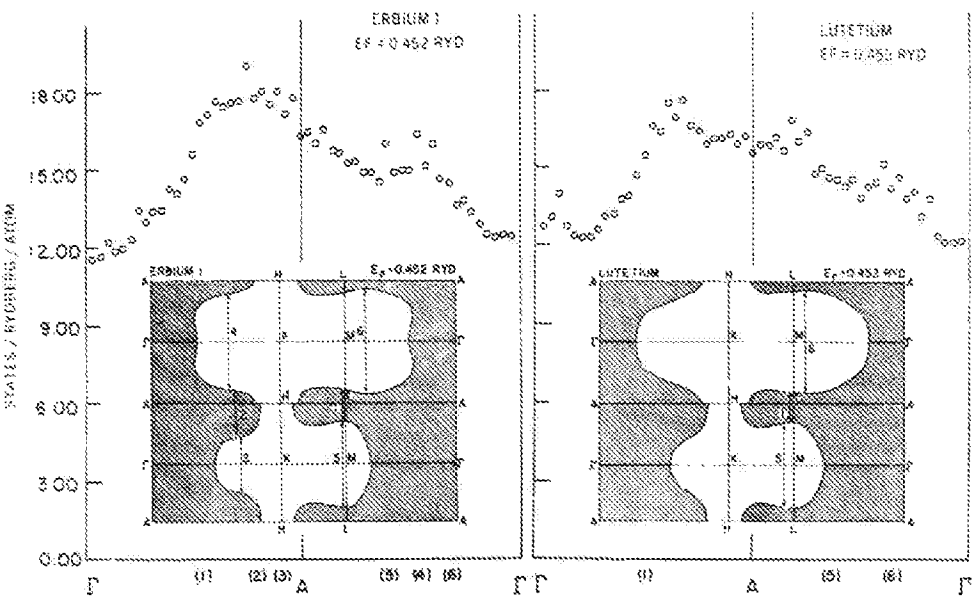

Fig. 3.69. The generalized susceptibility functions for Er and Lu for wave vectors along the c-axis of the crystal (Evenson and Liu, 1968).

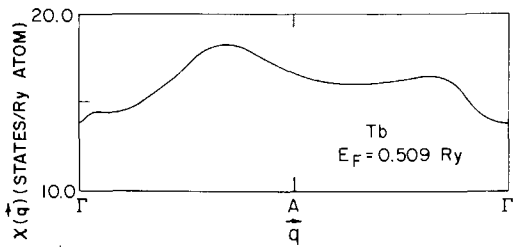

Fig. 3.70. The generalized susceptibility function of Tb along the c-axis of the crystal (Liu et al., 1971).

hydrostatic pressure. The energy bands for Gd, Tb, and Dy were computed for the normal lattice and for the compressed lattice under 20 kbar of hydrostatic pressure. Systematic shifts of $\chi(q)$ were seen above the noise level. In Gd the major shift was a decrease of density of states at the Fermi level, and this was correlated by the authors to the decrease in Curie temperature under pressure (Liu, 1962). For Tb as well as Dy the reduction in peak value of $\chi(q)$ was in agreement with the decrease in Néel temperature of the metal under pressure.

The most advanced method for $\chi(q)$ calculation was worked out recently by Rath and Freeman (1975) and Lindgård (1975). It is based on the method proposed by Gilat and Raubenheimer (1966) for the density of states in solids and by Jepsen and Anderson (1971) for volumes enclosed by Fermi surfaces. The Brillouin zone is divided into small tetrahedral volume elements in which the energy bands may be approximated by linear functions of $\boldsymbol{k}$. The Fermi surface is approximated by a plane in each tetrahedron. This allows an analytic integration within each tetrahedron, and the contributions from the tetrahedrons are summed up. This calculation is virtually noise-free, and its accuracy improves with increasing numbers of volume elements. A sample result of this calculation, the $\chi(q)$ for Sc published by Rath and Freeman, is shown in fig. 3.71. With this computational technique the calculation of the generalized suscep-

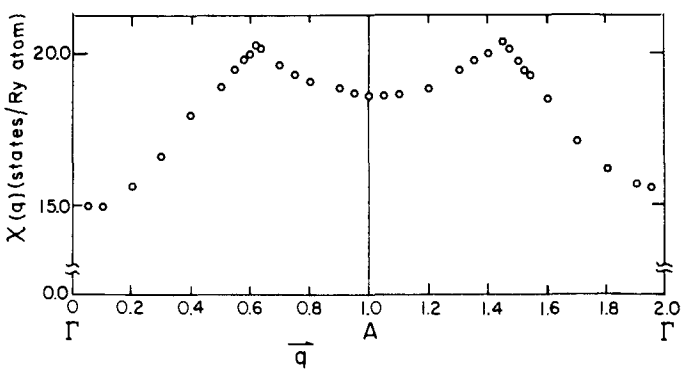

Fig. 3.71. The generalized susceptibility function of Sc along the c-axis of the crystal (Rath and Freeman, 1975).

tibility function with constant matrix elements has reached near perfection.

The light lanthanides Pr and Nd both have dhcp structure. Their magnetic ordering properties are very complicated. Both Nd and polycrystalline Pr show magnetic periodicity in the basal plane as well as in the c-axis (Koehler, 1972). Calculations of $\chi(\boldsymbol{q})$ for these metals have been attempted by Fleming et al. (1969) and Liu et al. (1971). The bands are so complicated that the folding of bands into the extended zone is trouble prone, and the constant matrix element assumption is more questionable. In the results the peaks of $\chi(\boldsymbol{q})$ for $\boldsymbol{q}$ in basal plane directions agreed with the nesting features, and might explain the observed periodicity in the basal plane. There is no clear understanding of the periodicity in the c direction. The authors suggested the matrix element effect as a possible explanation.

The magnetic structure of Eu was found to be helical antiferromagnetic below 90 K. The magnetic structure periodicity agrees with the caliper of the hole cube, and the $\chi(\boldsymbol{q})$ has a sharp peak at this value of $\boldsymbol{q}$ (Evenson et al., 1969). Another peak at larger $\boldsymbol{q}$ in the ΓH direction corresponds to the caliper of the superegg. That the actual periodicity is determined by the tetracube rather than the superegg must be a matrix element effect.

The above discussion is based exclusively on the band structure in the paramagnetic phase of the metals, so the conclusions are only valid at the point when the magnetic order first occurs. When the long-range order is established, the exchange splitting of the energy bands modifies the Fermi surface structure. In the ferromagnetic state the energy bands for spin-up and spin-down electrons are shifted relative to each other as discussed previously (section 2.3.1). On the indirect exchange model the splitting is given by $2(g-1)I(\boldsymbol{nk}, \boldsymbol{nk})J$. Assuming constant matrix elements and small splitting, one finds that this produces a net magnetization in the band electrons of the amount $(g-1)\langle I\rangle JN(E_F)$. The saturation moment per Gd atom has been measured recently to be 7.63 μ_B (Roeland et al., 1975), with the extra amount 0.63 μ_B per atom attributable to the conduction electrons. From this information and the calculated density of states, one may deduce the band splitting as 0.7 eV and the value for $\langle I\rangle$ as 0.1 eV.

The effects of helical ordering on the energy bands is more complicated (Miwa, 1963; Elliot and Wedgwood, 1964). The magnetic periodicity produces new energy gaps in the bands, called superzone gaps. These gaps tend to remove the nesting parts of the Fermi surface. The gaps may be observed in optical absorption measurements (section 3.1). The reduction in Fermi surface area may be seen in the sudden changes in the transport properties at the helical ordering temperature (ch. 6, sections 5 and 6). The positions of the superzone gaps in hexagonal rare earths have been calculated in detail by Watson et al. (1968).

Elliott and Wedgwood (1964) and Kasuya (1966) studied the effect of band splitting on $\chi(\boldsymbol{q})$ using an imperfect nesting Fermi surface model which was derived from a spherical Fermi surface model. For a trivalent metal with a spherical Fermi surface, the surface extends outside the Brillouin zone in the c direction. When the pieces of the surface outside the zone are folded back into the first zone, there arises a surface in the shape of a concave lens as shown in

fig. 3.72. This model was first studied by Yosida and Watabe (1962). The $\chi(q)$ along the c-axis shows a gentle peak as shown in fig. 3.73. On the same graph the $\chi(q)$ for the exchange split bands are drawn. The effect of exchange splitting is seen as a reduction of the peak and a shift of the position of the peak to smaller q values. The corresponding increase of magnetic ordering period has been observed in Tb, Dy, Ho and Er. Evenson and Liu (1959) did the same calculation for the perfect nesting model and their results are shown in fig. 3.74. The ordinate of the graph is $\chi(q)/\chi(0)$ for the split band, and the parameter η represents the ratio of exchange splitting to the effective Fermi energy. The two models give substantially the same behavior for $\chi(q)$. The effective Fermi energy is not measured from the bottom of the s, p band, but is the distance from the Fermi level to the bands at the L point (fig. 3.5). The value of the effective E_F can be estimated as 0.14 eV for Dy. Recalling that the full band splitting in the ferromagnetic ground state of Gd is about 0.7 eV, and the band splitting scales with the magnetization at finite temperatures, one finds that it takes but a small amount of spin ordering to virtually wipe out the peak in $\chi(q)$, making the ferromagnetic state stable. This may explain the transition from helical ordering to ferromagnetic ordering in Tb shortly after the onset of long-range order. The similar transition in Dy seems to be assisted by magnetoelastic interactions (Cooper, 1967; Evenson and Liu, 1969). The distinction between the two metals became clear after inelastic neutron scattering experi-

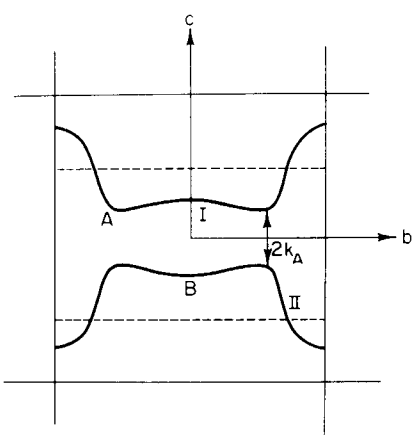

Fig. 3.72. The Fermi surface of hcp rare earths according to the nearly free electron model (Kasuya, 1966).

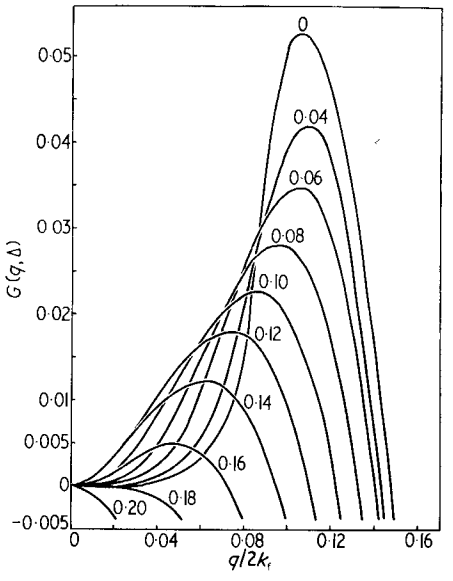

Fig. 3.73. The effect of magnetic ordering on the generalized susceptibility function of the nearly free electron model (Elliott and Wedgwood, 1964).

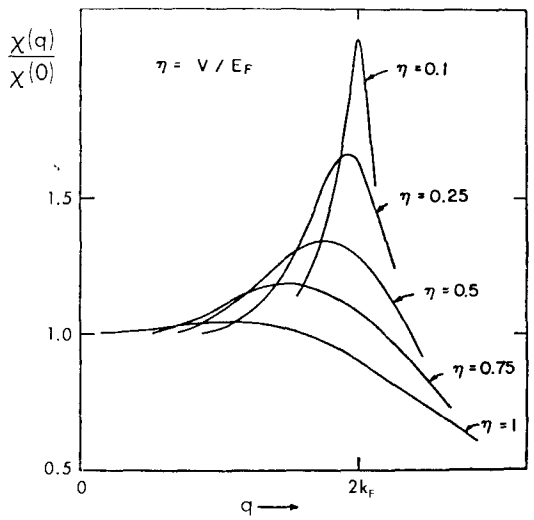

Fig. 3.74. The effect of magnetic ordering on the generalized susceptibility function of the perfect nesting model (Evenson and Liu, 1969).

ments had been performed to measure $\chi(\boldsymbol{q})$ from their spin wave spectra (see the review by Mackintosh and Møller, 1972). The $\chi(\boldsymbol{q})$ for Tb in the ferromagnetic phase is peaked at $\boldsymbol{q} = 0$, but for Dy the peak at $\boldsymbol{q} \neq 0$ persists in the ferromagnetic phase.

4.3. *Magnetic excitations*

4.3.1. *Spin wave spectrum of* Gd

The properties of the spin waves (magnons) in heavy lanthanide metals have been reviewed recently by Mackintosh and Møller (1972). In the ferromagnetic state the spin wave spectrum of an isotropic spin system with long range interaction has the form

$$\hbar\omega_{\boldsymbol{q}} = 2J[\mathcal{J}(0) - \mathcal{J}(\boldsymbol{q})]. \tag{3.74}$$

The metal Gd is very well described by this model, so a measurement of the magnon spectrum by the inelastic neutron scattering technique gives a direct measurement of $\mathcal{J}(\boldsymbol{q})$. In the other heavy lanthanides the anisotropy energy arising from the crystal field and magnetoelastic effects modifies the magnon spectrum. The extraction of $\mathcal{J}(\boldsymbol{q})$ from the data is a more subtle problem than is commonly recognized (Lindgård, 1976). Therefore, we will discuss the case of Gd to see how the measured magnon spectrum may be understood from first principles.

The magnon spectrum of Gd with wave vector in the c direction is shown in fig. 3.75. A comparison between the data and the curve for $\chi(\boldsymbol{q})$ in fig. 3.68 makes it obvious that the d–f exchange matrix element must not be a constant

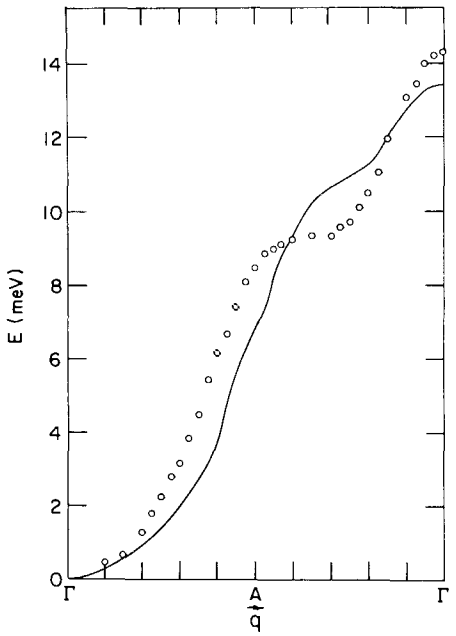

Fig. 3.75. The magnon spectrum of ferromagnetic Gd along the c-axis. The circles are the data of Koehler et al. (1970), and the solid line is the result of a model calculation by Liu et al. (1971).

because $\chi(\boldsymbol{q})$ does not vary much with $\boldsymbol{q}$ but $\mathcal{J}(\boldsymbol{q})$ has a variation of the order 2 meV. Evenson and Liu (1969) and Liu et al. (1971) took the suggestion of Watson and Freeman (1965, 1966) and approximated the matrix element as a function of $|\boldsymbol{k}-\boldsymbol{k}'|$. When they used a Gaussian form for the wave vector dependence, they obtained a magnon spectrum for Gd as shown in fig. 3.75. The significance of this result is that in order to explain the observed magnon spectrum, a strongly $\boldsymbol{q}$ dependent matrix element must be assumed.

Harmon and Freeman (1974b) made the first detailed calculation of the d–f exchange matrix element from the atomic-like 4f wave functions and the Bloch wave functions for the conduction electrons. The band wave functions were calculated by using the APW method in the paramagnetic state with full Slater exchange. The exchange integral $7I(\boldsymbol{nk}, \boldsymbol{n'k'})$ in eq. (3.51) with $I_m(\boldsymbol{nk}, \boldsymbol{n'k'})$ in eq. (3.50) was numerically calculated for a mesh of $\boldsymbol{k}$ and $\boldsymbol{k}'$ values and various pairs of bands. The bare Coulomb interaction enters the expression, and this means that the Coulomb screening effect is ignored. This tends to overestimate the size of the matrix element, but probably not the dependence on $\boldsymbol{k}$ and $\boldsymbol{k}'$.

The conduction electron wave function usually consists of a mixture of l values. The authors first studied the relative importance of the angular momentum states by taking the conduction electron wave function $\psi_{\boldsymbol{nk}}(\boldsymbol{r})$ as a state of pure l, i.e.

$$\psi_{l,E}(\boldsymbol{r}) = R_l(E, r)Y_{lm}(\boldsymbol{r}). \tag{3.75}$$

The radial wave function is normalized in the unit cell, and the normalization is done approximately by integrating inside two WS spheres for the two atoms in the hcp unit cell. The same $\psi_{l,E}(\boldsymbol{r})$ is used for both ψ_{nk} and $\psi_{n'k'}$ in the exchange integral. The result of this calculation is in fig. 3.76 in which it is shown that near the Fermi energy the d and f parts of the conduction electron wave function give the largest exchange effect, because the overlap of these wave functions with the 4f wave functions is much larger than the s, p states (fig. 3.63). There is very little f component in the conduction electron wave function, so the most important part of the exchange integral comes from the d–f overlap. This in turn means that the d bands near the Fermi level play the most important role in indirect exchange. Next the authors investigated the energy dependence of the exchange integral by putting $\psi_{l,E}$ with $E = E_F$ as one of the conduction electron wave functions in the d–f exchange integral and $\psi_{l,E'}$ as the other. The outstanding feature of the result, shown in fig. 3.77, is that the exchange integral does not fall off for large energy differences. Thus, in the calculation of the indirect exchange coupling constant $\mathcal{J}(\boldsymbol{q})$ in eq. (3.67), the sum on the bands must be carried out over all the ten d bands, although the contributions of the two bands which cross the Fermi energy will be the most important. The results for the full exchange integral are represented by figs. 3.78 and 3.79. The $\boldsymbol{q} = 0$ results show that the intraband exchange interaction is large compared with the interband interaction, as Evenson and Liu (1968) postulated. As $\boldsymbol{q} \neq 0$, this rule is strongly

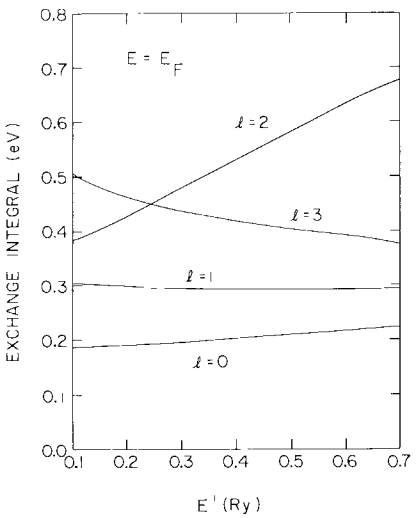

Fig. 3.76. Dependence of the conduction electron-4f exchange integral on the angular momentum of the conduction of the electron wave function. The result shows large d exchange effect (Harmon and Freeman, 1974b).

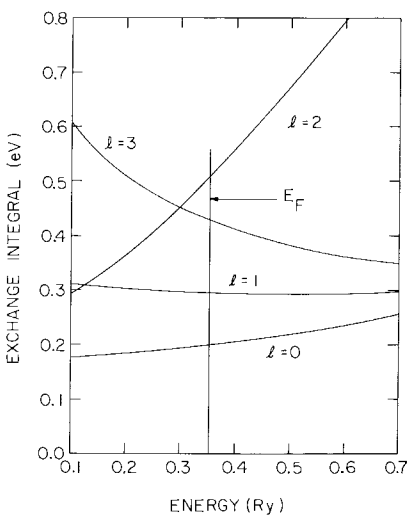

Fig. 3.77. Dependence of the conduction electron-4f exchange integral on the energies of the initial and final states conduction electron. The result shows that the exchange integral does not fall off with large energy difference (Harmon and Freeman, 1974b).

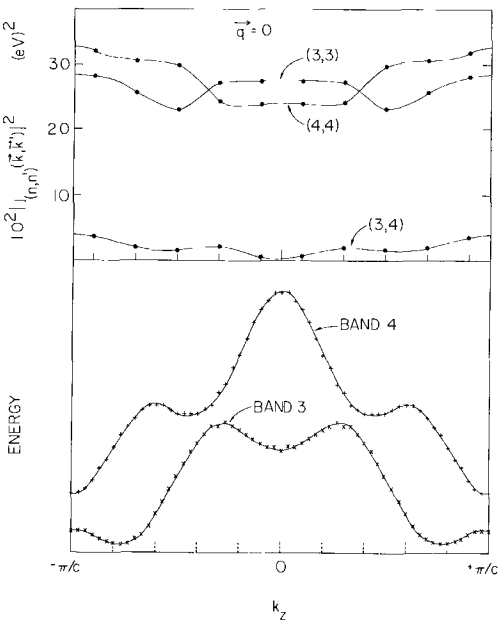

Fig. 3.78. The full exchange integral for bands 3 and 4 with zero wave vector transfer (Harmon and Freeman, 1974b).

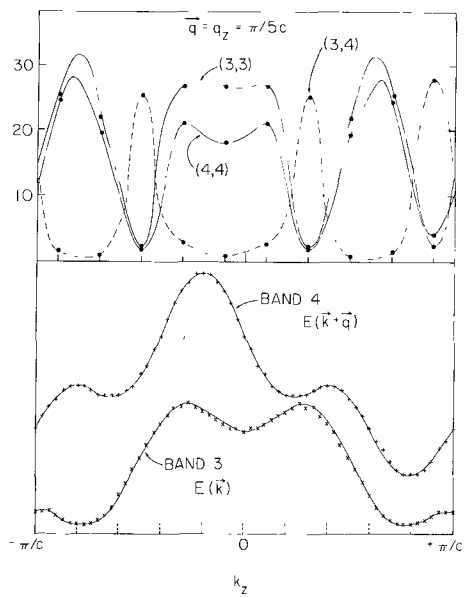

Fig. 3.79. The full exchange integral for bands 3 and 4 with finite wave vector transfer (Harmon and Freeman, 1974b).

violated at the points where the two bands cross ($k_c \cong \pm 0.35\ \pi/c$). The intraband interaction drops abruptly and the interband interaction takes over in a narrow range of k_c. Near the zone boundary the abrupt change of relative importance of the two kinds of interactions was contained in the model of Evenson and Liu.

Lindgård et al. (1975) made the first calculation of $\mathcal{J}(\boldsymbol{q})$ or magnon spectrum of Gd for $\boldsymbol{q}$ along the c-axis using the matrix elements of Harmon and Freeman. The sum of $\boldsymbol{k}$ was performed by the tetrahedron method using 14,000 volume elements in the Brillouin zone for the two bands that cross the Fermi surface and 2500 for the other bands. The exchange matrix element was approximated by a constant within each volume element. The result for $\mathcal{J}(\boldsymbol{q})$ is in fig. 3.80, where it is shown that the contribution from the bands 3 and 4 is important for most $\boldsymbol{q}$ values except near the hexagonal zone boundary point A. The matrix element effect is just as important as the Fermi surface geometry in determining the shape of $\mathcal{J}(\boldsymbol{q})$. This is especially noticeable in the optical branch about half way from A to Γ. The $\mathcal{J}(\boldsymbol{q})$ curve has a peak in this region as shown in fig. 3.68, but when multiplied by a Gaussian matrix element, the peak is no longer recognizable, as shown in fig. 3.75. When the actual matrix element is brought in, the peak again becomes pronounced. The importance of this feature of $\mathcal{J}(\boldsymbol{q})$ is that a strong wiggle or plateau is observed in the $\mathcal{J}(\boldsymbol{q})$ around this region of $\boldsymbol{q}$ for every hexagonal lanthanide metal. The origin of this feature was thought to be in the Fermi surface geometry (Evenson and Liu, 1968), but it now seems that the matrix element effect plays a dominant role.

The variation of $\mathcal{J}(q)$ gave a magnon band width about four times as wide as the measured value. To a large extent this was due to the neglect of Coulomb screening in the calculation of the exchange matrix element. When a uniform scale factor was applied to the calculated $\mathcal{J}(q)$, the comparison between the theoretical magnon spectrum and the data of Koehler et al. (1970) came out as shown in fig. 3.81. There is good overall agreement, although the deviation seems to be larger at small q. This may indicate the existence of a q dependent screening effect, but such an effect is poorly understood at present.

The sharp drop-off of the $\mathcal{J}(q)$ curve at small q indicates a strong matrix element effect. If we apply this drop-off to the $\mathcal{J}(q)$ of Dy, Er or Lu, the result will be a reduction of the size of the peak, and a shift of the position of the peak to a smaller value of q_c. Both effects tend to modify the conclusions of section 4.2 that the magnetic ordering is solely due to Fermi surface geometry. However, it is not yet the time to make a new study of the magnetic ordering problem, because the accuracy of the small q part of the calculated $\mathcal{J}(q)$ curve for Gd is still in doubt, and it is this part of the matrix element that will affect the magnetic ordering property the most.

4.3.2. *Magnon decay*

The formula for the ferromagnetic magnon spectrum, eq. (3.74), is but an approximation which ignores the dynamic response of the electron gas to the spin excitation. A self-consistent theory of the magnon spectrum gives the result

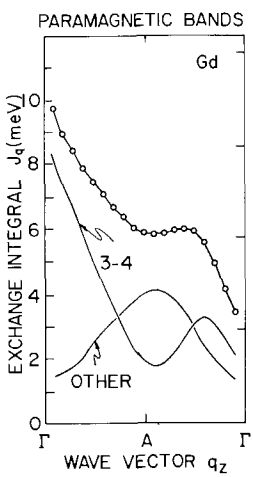

Fig. 3.80. The calculated $\mathcal{J}(q)$ for Gd with q along the c-axis (Lindgård et al., 1975).

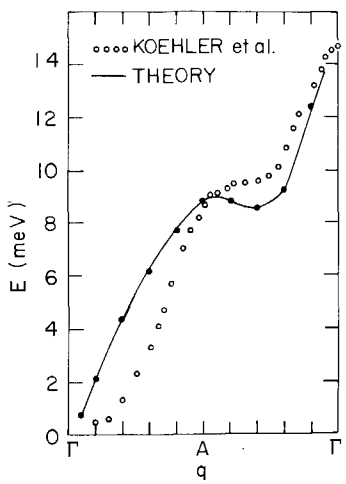

Fig. 3.81. Comparison between the calculated magnon spectrum of Gd with the data of Koehler et al. (1970) (Lindgård et al., 1975).

(Izuyama and Kubo, 1964; Nagaoka, 1962; Liu, 1976)

$$\hbar\omega_q = \left(\frac{2J}{N}\right)(g-1)^2 \sum_{nn'} \sum_{k} \left\{ |I(nk, n'k)|^2 \frac{f_{nk\uparrow} - f_{n'k\downarrow}}{E_{n'k\downarrow} - E_{nk\uparrow}} - |I(nk, n', k+q)|^2 \frac{f_{nk\downarrow} - f_{n',k+q\uparrow}}{E_{n',k+q\uparrow} - E_{nk\downarrow} + \hbar\omega_q} \right\}. \tag{3.76}$$

The dynamic correction in the energy denominator makes very little difference to the magnon energy, but it gives rise to a magnon damping when the energy and momentum of the magnon are such that it can decay into an electron-hole pair. If we write the complex solution of eq. (3.76) as $\hbar\omega_q - i\Gamma_q$, then the damping factor is given by

$$\Gamma_q = (2\pi J/N)(g-1)^2 \sum_{k} |I(nk, n', k+q)|^2 (f_{nk\downarrow} - f_{n',k+q\uparrow}) \delta(E_{n'k+q\uparrow} - E_{nk\downarrow} + \hbar\omega_q). \tag{3.77}$$

At very low temperatures the damping is finite only when the condition

$$E_{n',k+q\uparrow} - E_{nk\downarrow} + \hbar\omega_q = 0 \tag{3.78}$$

is satisfied by some value of k, with E_{nk}, $E_{n',k+q}$ on opposite sides of the Fermi surface. The value of q for which this is first satisfied is called the Stoner threshold, and at this value of q the damping of the magnon mode increases suddenly. In Tb this was observed for q near the zone boundary point A (Mackintosh and Møller, 1972). This information gives us an estimate of the amount of band splitting. Since the magnon energy is very small on the scale of the energy bands, eq. (3.78) can be approximately satisfied by $E_{n',k+q} = E_{nk}$ where q is the vector ΓA and both energies are on the Fermi level. This condition is fulfilled when some points on the spin-up Fermi surface may be put on top of some points on the spin-down Fermi surface by a translation ΓA. A look at the spin split Gd Fermi surface (fig. 3.31) reveals that a smaller exchange splitting would put the extremum point along AL on the spin-up (shrunken) Fermi surface and that along ΓM on the spin-down (expanded) Fermi surface into alignment. Using the same band structure for Gd to represent Tb, we find that the required band splitting is about 0.04 Ry, or close to 0.6 eV. If we take the band splitting of Gd as 0.7 eV and scale the s–d exchange interaction by the de Gennes relation, we predict just this value for Tb. The same value for the band splitting also agrees with that deduced from the preliminary de Haas–van Alphen data of Young (1976).

4.3.3. *Anomalous magnon-phonon mode mixing*

Along the c-axis of the Tb crystal strong magnon–phonon mode mixing was observed to occur as shown in fig. 3.82. The mixing between the acoustic magnon (MA) mode and the acoustic transverse phonon (TA) mode, giving rise to the splitting Δ_1, was explained on the basis of magnetoelastic interaction by

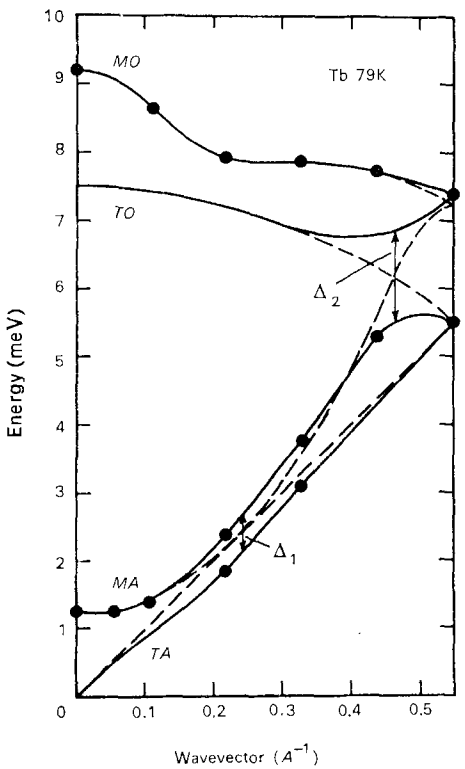

Fig. 3.82. The magnon–phonon mode mixing along the c-axis of Tb (Jensen, 1971).

Jensen (1971) and Vigren and Liu (1972). The theory is an extension of the static magnetostriction to the dynamic situation, and this kind of interaction failed to explain the splitting Δ_2 between the MA mode and the transverse optic phonon (TO). A similar situation exists in Dy where the mixing of the optic magnon (MO) and TA mode was seen (Nicklow et al., 1972).

Liu (1972) pointed out the reason why the conventional theory failed by using symmetry considerations. For hcp crystals the dispersion relations of all modes may be folded out into the extended zone scheme provided that there is no interaction which invalidates the double zone representation. It follows that in the double zone scheme the dispersion curves of MA and TO modes do not cross, so these modes should not mix. The same is true for MO and TA modes. Therefore, the observed mixing Δ_2 must come from a type of interaction which causes the double zone scheme to break down, and the only such interaction is the spin–orbit coupling of the conduction electrons (Herring, 1937; Cohen and Falicov, 1960). Then the mode mixing mechanism could arise when the phonon breaks up into a virtual electron–hole pair with the pair in the same spin state. Due to the spin–orbit coupling either the electron or the hole may reverse its spin. When they recombine the resulting particle will carry one unit of angular

momentum, therefore a magnon. This interaction takes place whenever the phonon and magnon modes cross in the single zone representation. Numerical estimates of the size of Δ_2 from the electron–magnon, electron–phonon, and electron spin–orbit interaction strength gave good agreement with the experiment.

In contrast to the magnetostriction mechanism the spin–orbit coupling is insensitive to the temperature. Experimentally Δ_1 was observed to disappear very rapidly with raised temperature. At the same time the magnon energy diminished so that the Δ_2 gap appeared at the crossing point of MO and TA modes, but with no appreciable reduction in size. Thus, the mixing of MO-TA and MA-TO modes confirms the importance of spin–orbit coupling in the conduction band states of heavy lanthanides.

Further discussions of the implications of this interaction are contained in a series of papers on Tb (Jensen et al., 1975; Jensen and Houmann, 1975; Houmann et al., 1975).

Acknowledgments

The author is indebted to his colleagues Professor K. Gschneidner, Professor B.N. Harmon, Professor I. Lindau, Professor D.W. Lynch, and Professor D.A. Shirley for their generous help in collecting material for this review. The paper was written while the author was a visiting faculty member at the University of California, Berkeley. The financial and technical assistance provided by the Physics Department at Berkeley in preparing the manuscript is gratefully acknowledged. Most of all, he would like to thank Professor L.M. Falicov and the Solid State Theory group at Berkeley for their hospitality.

References

Andersen, O.K. and T.L. Loucks, 1968, Phys. Rev. **167**, 551.

Anderson, P.W., 1961, Phys. Rev. **124**, 41.

Baer, Y. and G. Busch, 1973, Phys. Rev. Lett. **31**, 35.

Baer, Y. and G. Busch, 1974, J. Electron Spectrosc. & Relat. Phenom. (Netherlands) **5**, 611.

Banninger, V., G. Busch, M. Campagna, and H.C. Siegmann, 1970, Phys. Rev. Lett. **25**, 585.

Berglund, C.N. and W.E. Spicer, 1964a, Phys. Rev. **136**, A1030.

Berglund, C.N. and W.E. Spicer, 1964b, Phys. Rev. **136**, A1044.

Blodgett, A.J. Jr., W.E. Spicer, and A.Y.-C. Yu, 1966, The band structure of godalinium, photoemission and optical studies, Abeles, F., ed., Proceedings of the International Colloquium on Optical Properties and Electronic Structure of Metals and Alloys, Paris, 1965 (North-Holland Publishing Co., Amsterdam), pp. 246–256.

Bonnelle, C., R.C. Karnatak, and J. Sugar, 1974, Phys. Rev. **A9**, 1920.

Brodén, G., 1972, Phys. Kondens. Mater. (Germany) **15**, 171.

Brodén, G., S.B.M. Hagström, and C. Norris, 1970, Phys. Rev. Lett. **24**, 1173.

Brodén, G., S.B.M. Hagström, P.O. Hedén, and C. Norris, 1971, Ultraviolet and X-ray photoemission from europium and barium, Bennett, L.H., ed., Electronic Density of States, National Bureau of Standards Special Publications No. 323, pp. 217–220.

Brodén, G., S.B.M. Hagström, and C. Norris, 1973, Phys. Kondens. Mater. (Germany) **15**, 327.

Bucher, E., P.H. Schmidt, A. Jayaraman, K. Andres, J.P. Maita, K. Nassau, and P.D. Dernier, 1970, Phys., Rev. **B2**, 3911.

Altmann, S.L. and C.J. Bradley, 1967, Proc. Phys. Soc. (London) 92, 764.

Busch, G., M. Campagna, C. Cotti, and H.C. Siegmann, 1969, Phys. Rev. Lett. **22**, 597.
Callaway, J., 1974, Quantum Theory of the Solid State, Part A (Academic Press, New York), pp. 339–341.
Chander, R. and R. Kumar, 1973, Phys. Stat. Solidi (A) **20**, 739.
Chroboček, G., M. Hofmann, and G. Regenfus, 1968, Phys. Lett. **26A**, 551.
Cohen, M.H. and L.M. Falicov, 1960, Phys. Rev. Lett. **5**, 544.
Connolly, J.W.D., 1967, Phys. Rev. **159**, 415.
Cooper, B.R., 1967, Phys. Rev. Lett. **19**, 900.
Cooper, B.R. and R.W. Reddington, 1965, Phys. Rev. Lett. **14**, 1066.
Coqblin, B. and C.F. Ratto, 1968, Phys. Rev. Lett. **21**, 1065.
Coqblin, B. and J.R. Schrieffer, 1969, Phys. Rev. **185**, 847.
Coqblin, B., M.B. Maple, and G. Toulouse, 1971, Int. J. Magn. **1**, 333.
Cornwell, J.F., 1966, Phys. Kondens. Mater. (Germany) **4**, 327.
Cox, P.A., Y. Baer, and C.K. Jørgensen, 1973, Chem. Phys. Lett. **22**, 433.
Cracknell, A.P., 1971, Advan. Phys. **20**, 1.
Datars, W.R. and S. Tanuma, 1968, Phys. Lett. **27A**, 182.
DeGennes, P.G., 1958, Compt. Rend. **247**, 1836.
Derbez, C.T. and J.P. Pétrakian, 1974, Appl. Optics **13**, 599.
Dimmock, J.O., A.J. Freeman, and R.E. Watson, 1966, Electronic band structure and optical properties of rare earth metals, Abeles, F. ed., Proceedings of the International Colloquium on Optical Properties and Electronic Structure of Metals and Alloys, Paris, 1965, (North-Holland Publishing Co., Amsterdam), pp. 273–245.
Dimmock, J.O., 1971, The calculation of electronic energy bands by the augmented plane wave method, Ehrenreich, H., F. Seitz, and D. Turnbull, eds., Solid State Physics, Vol. 26, pp. 104–274.
Dimmock, J.O. and A.J. Freeman, 1964, Phys. Rev. Lett. **13**, 750.
Doniach, S., 1970, Phys. Rev. **B2**, 3898.
Eastman, D.E., 1969, Solid State Commun **7**, 1697.
Eastman, D.E., 1971, Photoemission studies of scandium, titanium and zirconium, Bennett, L.H., ed., Electronic Density of States, National Bureau of Standards Special Publications No. 323, pp. 205–215.
Eastman, D.E. and J.K. Cashion, 1970, Phys. Rev. Lett. **24**, 310.
Elliott, R.J. and F.A. Wedgwood, 1964, Proc. Phys. Soc. (London) **84**, 63.
Endriz, J.G. and W.E. Spicer, 1970, Phys. Rev. **B2**, 1466.
Erskine, J.L., 1976, Phys. Rev. Lett. **37**, 157.
Erskine, J.L., G.A. Blake, and C.J. Flaten, 1974, Opt. Soc. of Amer. **64**, 1332.
Erskine, J.L. and C.P. Flynn, 1976, Phys. Rev. **B14**, 2197.
Erskine, J.L. and E.A. Stern, 1973, Phys. Rev. **B8**, 1239.
Evenson, W.E., G.S. Fleming, and S.H. Liu, 1969, Phys. Rev. **178**, 930.
Evenson, W.E. and S.H. Liu, 1968, Phys. Rev. Lett. **21**, 432.
Evenson, W.E. and S.H. Liu, 1969, Phys. Rev. **178**, 783.
Fabian, D.J., B.D. Padalia, and W. Lang, 1974, Phys. Fenn. (Finland) **9**, S1, 313.
Fano, U. and J.W. Cooper, 1968, Rev. Mod. Phys. **40**, 441.
Fleming, G.S. and S.H. Liu, 1970, Phys. Rev. **B2**, 164.
Fleming, G.S., S.H. Liu, and T.L. Loucks, 1968, Phys. Rev. Lett. **21**, 1524.
Fleming, G.S. and T.L. Loucks, 1968, Phys. Rev. **173**, 685.
Fleming, G.S., T.L. Loucks, and S.H. Liu, 1969, J. Appl. Phys. **40**, 1285.
Freeman, A.J., J.O. Dimmock, and R.E. Watson, 1966, The augmented plane wave method and the electronic properties of rare earth metals, Löwdin, P.O., ed., Quantum Theory of Atoms, Molecules and the Solid State, a Tribute to John C. Slater (Academic Press, New York), pp. 361–380.
Freeman, A.J. and J.O. Dimmock, 1966, Bull. Am. Phys. Soc. **11**, 216.
Freeman, A.J., 1972, Energy band structure, indirect exchange interactions and magnetic ordering, Elliott, R.J., ed., Magnetic Properties of Rare Earth Metals (Plenum Press, London and New York), pp. 245–333.
Gáspár, R., 1954, Acta Phys. Acad. Sci. Hung. **3**, 263.
Gilat, G. and L.J. Raubenheimer, 1966, Phys. Rev. **144**, 390.
Gupta, R.P. and T.L. Loucks, 1968, Phys. Rev. **176**, 848.
Gupta, R.P. and T.L. Loucks, 1969, Phys. Rev. Lett. **22**, 458.
Hagström, S.B.M., 1972, J. Electron Spectrosc. & Relat. Phenom. (Netherlands) **5**, 515.
Hagström, S.B.M., P.O. Hedén, and H. Löfgren, 1970, Solid State Commun. **8**, 1245.
Harmon, B.N., D.D. Koelling, and A.J. Freeman, 1973, J. Phys. C. **6**, 2294.
Harmon, B.N. and A.J. Freeman, 1974a, Phys. Rev. **B10**, 1979.
Harmon, B.N. and A.J. Freeman, 1974b, Phys. Rev. **B10**, 4849.
Hedén, P.O., H. Löfgren, and S.B.M. Hagström, 1971, Phys. Rev. Lett. **26**, 432.
Hedén, P.O., H. Löfgren, and S.B.M. Hagström, 1972, Phys. Stat. Solidi (B) **49**, 721.
Helms, C.R. and W.E. Spicer, 1972, Appl. Phys. Lett. **21**, 237.
Herbst, J.F., D.N. Lowy, and R.E. Watson, 1972, Phys. Rev. **B6**, 1913.
Herbst, J.F., R.E. Watson, and J.W. Wilkins, 1976, Phys. Rev. **B13**, 1439.
Herring, C., 1937, Phys. Rev. **52**, 361.
Herring, C., 1966, Magnetism, Rado, G.T. and H. Suhl, eds., (Academic Press, New York), Vol. IV.
Hodges, L., R.E. Watson, and H. Ehrenreich, 1972, Phys. Rev. **B5**, 3953.
Hodgson, J.N. and B. Cleyet, 1969, J. Phys. C **2**, 97.

Ghosh, A., K. Santosh, and K.C. Das, 1970, Indian J. Pure and Appl. Phys. 8, 685.

Hoekstra, J.A. and R.A. Phillips, 1971, Phys. Rev. **B4**, 4184.
Hofmann, M., G. Regenfus, O. Schärf, and P.J. Kennedy, 1967, Phys. Lett. **25A**, 270.
Hohenemser, C., J.M. Weingart, and S. Berko, 1968, Phys. Lett. **28A**, 41.
Houmann, J.G., J. Jensen, and P. Touborg, 1975, Phys. Rev. **B12**, 332.

Jackson, C., 1969, Phys. Rev. **178**, 949.
Janak, J.F., A.R. Williams, and V.L. Moruzzi, 1975, Phys. Rev. **B11**, 1522.
Jensen, J., 1971, Int. J. Magn. **1**, 271.
Jensen, J. and J.G. Houmann, 1975, Phys. Rev. **B12**, 320.
Jensen, J., J.G. Houmann, and H. Bjerrum Møller, 1975, Phys. Rev. **B12**, 303.
Jepsen, O. and O.K. Andersen, 1971, Solid State Commun. **9**, 1763.
Johansen, G., 1969, Solid State Commun. **7**, 731.
Johansen, G. and A.R. Mackintosh, 1970, Solid State Commun. **8**, 121.
Johansson, B., 1974, J. Phys. F **4**, L169.
Johansson, B. and A. Rosengren, 1975, Phys. Rev. **B11**, 1367.
Jørgensen, C.K., 1974, Photoelectron spectra showing relaxation effects in the continuum and electrostatic and chemical influences of the surrounding atoms, Löwdin. P.O., ed., Advances in Quantum Chemistry, (Academic Press, New York), Vol. 8, pp. 137–18a.
Kanski, J. and P.O. Nilsson, 1975, Physics Scripta (Sweden) **12**, 103.
Kasuya, T., 1956, Prog. Theoret. Phys. (Japan) **16**, 45.
Kasuya, T., 1966, s–d and s–f interaction and rare earth metals, Rado, G.T. and H. Suhl, eds., Magnetism (Academic Press, New York), Vol. IIB, pp. 215–294.
Kasuya, T. and D.H. Lyons, 1965, J. Phys. Soc. Japan **21**, 287.
Kayser, F.X., 1970, Phys. Rev. Lett. **25**, 662.
Keeton, S.C. and T.L. Loucks, 1966, Phys. Rev. **146**, 429.
Keeton, S.C. and T.L. Loucks, 1968, Phys. Rev. **168**, 672.
Kim, D.J., 1966, Phys. Rev. **149**, 434.
Kmetko, E.A., 1969, Calculated effects of compression upon the band structure and density of states of several metals, Bennett, L.H., ed., Electronic Density of States, National Bureau of Standards Special Publications No. 323, pp. 67–73.
Knyazev, Yu. V. and M.M. Noskov, 1970, Fiz. Met. Metalloved **30**, 214; Phys. Metals and Metallography **30**, No. 1, 230.
Knyazev, Yu. V. and M.M. Noskov, 1971a, Fiz. Met. Metalloved **31**, 1099; Phys. Metals and Metallography, **31**, No. 5, 211.
Knyazev, Yu. V. and M.M. Noskov, 1971b, Fiz. Met. Metalloved **32**, 1189; Phys. Metals and Metallography **32**, No. 6, 70.
Knyazev, Yu. V. and M.M. Noskov, 1975, Opt. Spectrosc. **38**, 672.
Koehler, W.C., 1972, Magnetic structures of rare earth metals and alloys, Elliott, R.J., ed., Magnetic Properties of Rare Earth Metals (Plenum Press, London and New York), pp. 81–128.
Koehler, W.C., H.R. Child, R.M. Nicklow, H.G. Smith, R.M. Moon, and J.W. Cable, 1970, Phys. Rev. Lett. **24**, 16.
Koehler, W.C., R.M. Moon, and H.R. Child, 1973, Neutron scattering studies of ^{147}Pm, Graham, C.D., Jr. and J.J. Rhyne, eds., Proceedings of the 18th Annual Conference on Magnetism and Magnetic Materials, Denver, 1972, AIP conference Proceedings **10**, 1319.
Koelling, D.D., A.J. Freeman, and F.M. Mueller, 1970, Phys. Rev. **B1**, 1318.
Koelling, D.D. and B.N. Harmon, 1972, Bull. Amer. Phys. Soc. **17**, 94.
Kohn, W. and L.J. Sham, 1965, Phys. Rev. **140**, A1133.
Kondo, J., 1969, Theory of dilute magnetic alloys, Seitz, F., D. Turnbull, and H. Ehrenreich, Solid State Physics (Academic Press, New York), Vol. 23, pp. 183–281.
Krizek, J. and K.N.R. Taylor, 1975, J. Phys. F **5**, 774.
Lang, W.C., B.D. Padalia, D.J. Fabian, and L.M. Watson, 1974, J. Electron Spectrosc. & Relat. Phenom. (Netherlands) **5**, 207.
Lapeyre, G.J., 1969, Phys. Rev. **179**, 623.
Liberman, D., J.T. Waber, and D.T. Cromer, 1965, Phys. Rev. **137**, A27.
Lindau, I. and W.E. Spicer, 1974, J. Electron Spectrosc. & Relat. Phenom (Netherlands) **3**, 409.
Lindgård, P.-A., 1975, Solid State Commun. **16**, 481.
Lindgård, P.-A., B.N. Harmon, and A.J. Freeman, 1975, Phys. Rev. Lett. **35**, 383.
Liu, S.H., 1961, Phys. Rev. **121**, 451.
Liu, S.H., 1962, Phys. Rev. **127**, 1889.
Liu, S.H., 1968, Phys. Lett. **27A**, 493.
Liu, S.H., 1972, Phys. Rev. Lett. **29**, 793.
Liu, S.H., 1976, Phys. Rev. **B13**, 3962.
Liu, S.H., P. Burgardt, K.A. Gschneidner, Jr., and S. Legvold, 1976, J. Phys. F **6**, L55.
Liu, S.H., R.P. Gupta, and S.K. Sinha, 1971, Phys. Rev. **B4**, 1100.
Loucks, T.L., 1965, Phys. Rev. **137**, A1333.
Loucks, T.L., 1966, Phys. Rev. **144**, 504.
Loucks, T.L., 1967, Augmented plane Wave Method (Benjamin, New York).
McFeely, F.R., S.P. Kowalczyk, L. Ley, and D.A. Shirley, 1973, Phys. Lett. **45A**, 227.
Mackintosh, A.R., 1968, Phys. Lett. **28A**, 217.
Mackintosh, A.R. and H. Bjerrum Møller, 1972, Spin waves, Elliott, R.J., ed., Magnetic Properties of Rare Earth Metals (Plenum Press, London and New York), pp. 187–244.
Mariot, J.M. and R.C. Karnatak, 1974, J. Phys. F **4**, L223.
Mattheiss, L.F., 1964, Phys. Rev. **133**, A1399.
Mattheiss, L.F., J.H. Wood, and A.C. Switendick, 1968, Methods in Computation Physics **8**, 64.
Meservey, R. and P.N. Tedrow, 1972, Solid State Commun **11**, 336.
Miller, R.F., L.S. Julien and A. Taylor, 1974, J. Phys. F **4**, 2338.
Mitchell, A.H., 1957, Phys. Rev. **105**, 1439.

Miwa, H., 1963, Prog. Theoret. Phys. (Japan) **29**, 477.
Moon, R.M., W.C. Koehler, J.W. Cable, and H.R. Child, 1972, Phys. Rev. **B5**, 997.
Moruzzi, V.L., A.R. Williams, and J.F. Janak, 1974, Phys. Rev. **B9**, 3316.
Mukhopadhyay, G. and C.K. Majumdar, 1969, J. Phys. C **2**, 924.
Müller, N., G. Obermair, and H.C. Siegmann, 1967, Phys. Lett. **24A**, 733.
Müller, W.E., 1965, Phys. Lett. **17**, 82.
Myers, H.P., 1976, J. Phys. F **6**, 141.
Myron, H.W. and S.H. Liu, 1970, Phys. Rev. **B1**, 2414.
Nagamiya, T., 1967, Helical spin ordering – I theory of helical spin configurations, Seitz, F., D. Turnbull, and H. Ehrenreich, eds., Solid State Physics (Academic Press, New York and London), Vol. 20, pp. 306–411.
Nicklow, R.M., N. Wakabayashi, M.K. Wilkinson, and R.E. Reed, 1971, Phys. Rev. Lett. **27**, 334.
Nilsson, P.O., 1974, Optical Properties of Metals and Alloys, Ehrenreich, H., F. Seitz, and D. Turnbull, eds., Solid State Physics (Academic Press, New York and London), Vol. 29, pp. 139–234.
Obermair, G., 1968, Z. Phys. **217**, 91.
Papaconstantopoulos, D.A., J.R. Anderson, and J.W. McCaffrey, 1972, Phys. Rev. **B5**, 1214.
Park, R.L. and J.E. Houston, 1974, J. Vac. Sci. Tech. **11**, 1.
Peterson, D.T. and F.A. Schmidt, 1969, J. Less-Common Metals **18**, 111.
Pétrakian, J.P., 1972, J. Opt. Soc. Am. **62**, 401.
Pétrakian, J.P., 1974, Thin Solid Films **20**, 297.
Pétrakian, J.P., J.P. Palmari, and G. Rasigni, 1970, Appl. Opt. **9**, 2115.
Politzer, S.B.A. and P.H. Cutler, 1972, Phys. Rev. Lett. **28**, 1330.
Rath, J. and A.J. Freeman, 1975, Phys. Rev. **B11**, 2109.
Rice, T.M., 1970, Phys. Rev. **B2**, 3619.
Roeland, L.W., G.J. Cock, F.A. Muller, A.C. Moleman, R.G. Jordan, and K.A. McEwen, 1975, private communication.
Roth, L.M., H. Zeiger, and T. Kaplan, 1966, Phys. Rev. **149**, 519.
Ruderman, M.A. and C. Kittel, 1954, Phys. Rev. **96**, 99.
Shirley, D.A., 1972, Chem. Phys. Lett. **16**, 220.
Schirber, J.E., F.A. Schmidt, B.N. Harmon, and D.D. Koelling, 1976, Phys. Rev. Lett. **36**, 448.
Schrieffer, J.R. and P.A. Wolff, 1966, Phys. Rev. **149**, 491.
Schüler, C.C., 1964, Phys. Lett. **12**, 84.
Schüler, C.C., 1966, Recent studies on the optical properties of rare-earth metals, Abeles, F., ed., Proceedings of the International Colloquium on Optical Properties and Electronic Structure of Metals and Alloys, Paris, 1965 (North-Holland Publishing Company, Amsterdam), pp. 221–235.
Slater, J.C., 1937, Phys. Rev. **51**, 846.
Slater, J.C., 1951, Phys. Rev. **81**, 385.
Slater, J.C., 1965, Quantum Theory of Molecules and Solids (McGraw-Hill, New York), Vol. 2.
Slater, J.C., 1967, Quantum Theory of Molecules and Solids (McGraw-Hill, New York), Vol. 3.
Smith, R.J., M. Piacentini, and D.W. Lynch, 1975, Phys. Rev. Lett. **34**, 476.
Snow, E.C. and J.T. Waber, 1967, Phys. Rev. **157**, 570.
Stassis, C., 1975, private communication.
Szuszkiewicz, S., 1973, Acta Phys. Pol. (Poland) **A44**, 691.
Tanuma, S., Y. Ishizawa, H. Nagasawa, and T. Sugawara, 1967, Phys. Lett. **25A**, 669.
Tanuma, S., W.R. Datars, H. Doi, and A. Dunsworth, 1970, Solid State Commun. **8**, 1107.
Vasvari, B., A.O.E. Animalu, and V. Heine, 1967, Phys. Rev. **154**, 535.
Vigren, D.T. and S.H. Liu, 1972, Phys. Rev. **B5**, 2719.
Villain, J., 1959, J. Phys. Chem. Solids **11**, 303.
Waber, J.T. and A.C. Switendick, 1965, Results of augmented plane wave calculation of the band structure of cerium metal, Proceedings of the Fifth Rare Earth Research Conference, Ames, Iowa, 1965, Book II. pp. 75–88.
Watson, R.E., H. Ehrenreich, and L. Hodges, 1970, Phys. Rev. Lett. **24**, 829.
Watson, R.E. and A.J. Freeman, 1965, Phys. Rev. Lett. **14**, 695.
Watson, R.E. and A.J. Freeman, 1966, Phys. Rev. **152**, 566.
Watson, R.E. and A.J. Freeman, 1969, Phys. Rev. **178**, 725.
Watson, R.E., A.J. Freeman, and J.O. Dimmock, 1968, Phys. Rev. **167**, 497.
Weaver, J.H. and D.W. Lynch, 1973, Phys. Rev. **B7**, 4737.
Weaver, J.H. and D.W. Lynch, 1975, Phys. Rev. Lett. **34**, 1324.
Wertheim, G.K., A. Rosencwaig, R.L. Cohen, and H.J. Guggenheim, 1971, Phys. Rev. Lett. **27**, 505.
Williams, A.R., J.F. Janak, and V.L. Moruzzi, 1972, Phys. Rev. Lett. **28**, 671.
Williams, A.R. and J. Morgan, 1974, J. Phys. C **7**, 37.
Williams, R.W., T.L. Loucks, and A.R. Mackintosh, 1966, Phys. Rev. Lett. **16**, 168.
Williams, R.W. and A.R. Mackintosh, 1968, Phys. Rev. **168**, 679.
Young, R.C., 1976, private communication.
Young, R.C., R.G. Jordan, and D.W. Jones, 1973, Phys. Rev. Lett. **31**, 1473.
Young, R.C., R.G. Jordan, and D.W. Jones, 1974, J. Phys. F **4**, L84.
Young, R.C., R.G. Jordan, and D.W. Jones, 1976, J. Phys. F **6**, L37.
Young, R.C. and J.K. Hulbert, 1974, Phys. Lett. **47A**, 367.
Yosida, K., 1957, Phys. Rev. **106**, 893.
Yosida, K. and A. Watabe, 1962, Prog. Theoret. Phys. (Japan) **28**, 361.
Zener, C. and R.R. Heikes, 1953, Rev. Mod. Phys. **25**, 191.

Handbook on the Physics and Chemistry of Rare Earths, edited by K.A. Gschneidner, Jr. and L. Eyring

Chapter 4

CERIUM*

David C. KOSKENMAKI‡
Armco Steel Corporation, Armco Research Center, Middletown, Ohio 45042, USA

Karl A. GSCHNEIDNER, Jr.
Ames Laboratory – DOE and Department of Materials Science and Engineering, Iowa State University, Ames, Iowa 50011, USA

Contents

Symbols

A_f = end of transformation on heating
A_s = start of transformation on heating
C_M = magnetic contribution to the heat capacity
C_p = heat capacity at constant pressure
C_v = heat capacity at constant volume
E_{exc} = energy necessary to make an inter-configurational excitation
G = magnitude of the electron–electron or electron-hole interaction
$\hbar$ = Planck's constant/2π

*This work was partially supported by the U.S. Department of Energy under Contract Number W-7405-eng.-82.

‡Formerly spelled Koskimaki.

M_d = temperature at which a deformed sample begins to transform
M_f = end of transformation on cooling
M_s = start of transformation on cooling
n_c = number of conduction electrons
N = number of atoms
p_{eff} = effective magnetic moment
P = pressure
R = gas constant
R_H = Hall coefficient
T = temperature in kelvin
U = intra-atomic Coulomb repulsion energy
γ = electronic specific heat constant
Δ = band width
θ = paramagnetic ordering temperature
μ_B = Bohr magneton
ρ = electrical resistivity
χ = magnetic susceptibility

1. Introduction

In its elemental form cerium is the most fascinating member of the periodic table. Cerium, under various conditions of temperature and pressure, is an antiferromagnet, a superconductor, and the only pure element to exhibit Kondo scattering and a solid–solid critical point. These phenomena occur because the energy of the inner 4f level is nearly the same as that of the outer or valence 5d and 6s levels, and thus only small amounts of energy are necessary to change the relative occupancy of these electronic levels giving rise to a variable electronic structure. Although metallic cerium has been known for 150 years (Mosander, 1827) the discovery of the above phenomena are of recent origin – antiferromagnetism in β-Ce was suggested by Lock in 1957 on the basis of magnetic susceptibility measurements and confirmed by neutron diffraction in 1961 by Wilkinson et al.; the existence of the critical point between α- and γ-Ce was observed by Ponyatovskii in 1958; superconductivity in α'-Ce was discovered by Wittig in 1968; and most recently the Kondo effect in β-Ce was revealed by Gschneidner et al. in 1976.

Probably of the greatest interest to both experimentalists and theorists is the polymorphic transformation between two face-centered cubic phases, γ-Ce (the room temperature-ambient pressure phase) and α-Ce (the collapsed phase), which at high pressure and temperature become indistinguishable from one another at the solid–solid critical point. Although the structures of the various phases and the cerium pressure-temperature diagram below 5 GPa (50 kb) have been well established for over 10 years, the electronic and magnetic natures of the cerium allotropes have been a matter of much controversy due partly to the fact that until recently all physical property measurements below 0.5 GPa pressure and below room temperature were measured on samples containing two or three cerium allotropic phases. Experimentally, the problem is that as γ-Ce is cooled below 273 K it is unstable and begins to transform incompletely to β-Ce (a double-hexagonal close-packed phase); upon further cooling to ~ 100 K, γ-Ce transforms to α-Ce (but only partially). Thus it was difficult if not impossible, to extract meaningful values from the physical property measurements. Naturally, because of this, many of the theories proposed for the $\alpha \rightleftarrows \gamma$ transformation could not be verified or disproven. But in the early 1970's two important techniques were developed to prepare allotropically pure α-Ce (Panousis and

Gschneidner, 1970) and β-Ce (Koskimaki et al., 1974). Already several unexpected results have been realized from the first few experimental measurements, e.g. as noted above β-Ce exhibits Kondo scattering. The next few years should yield a wealth of reliable experimental information about the nature of the cerium allotropes. From this knowledge and understanding a great deal more will be known about the electronic nature of many of the other elements in the periodic table – cerium is the keystone element. What we learn from cerium can be extended to the actinide elements and to metals which exhibit electronic transitions at high pressure.

2. General description and allotropy

There are five established allotropic forms of cerium and some evidence for two or three others which actually may be metastable or impurity stabilized. The pressure–temperature relationships of the stable phases, their crystal structures and valences are discussed first under equilibrium conditions. Then non-equilibrium and hysteresis effects relative to the five established phases are reviewed. Finally the known information on the less reliably established phases is examined.

2.1. *Equilibrium phase diagram*

The pseudo-equilibrium pressure–temperature diagram of cerium is shown in fig. 4.1 and the low pressure–low temperature portion on an expanded scale is shown in fig. 4.2. The pressure–temperature diagram shown in the two figures is based on the results reported in some 25 independent investigations dealing with various aspects of the phase relationships among the five solid and liquid phases of cerium. Eleven important points in the cerium phase diagram are listed in table 4.1; most values are average values taken from the various investigations.

The accepted melting point and $\gamma \rightleftarrows \delta$ transformation point at one atmosphere are taken from the review by Gschneidner (1966). The pressure dependence of melting and the γ/δ phase boundary, the $\gamma \rightleftarrows \delta \rightleftarrows$ L triple point and liquidus minimum are taken from the results of Jayaraman (1965).

The pressure–temperature dependence of the $\alpha \rightleftarrows \gamma$ phase boundary is based on results reported by Likhter et al. (1957), Herman and Swenson (1958), Ponyatovskii (1958), Beecroft and Swenson (1960), Livshits et al. (1960), Gschneidner et al. (1962), Itskevick (1962), Livshits et al. (1962), Davis and Adams (1964), Jayaraman (1965) and Kutsar (1974). In addition James et al. (1952), McHargue and Yakel (1960), Smith and Morrice (1964), Rashid and Altstetter (1966), Elliott and Miner (1967) and Pavlov and Rybal'chenko (1970) have reported temperature values for the $\gamma \rightleftarrows \alpha$ transformation at atmospheric pressure, while Bridgman (1951), Voronov et al. (1960), MacPherson et al. (1971), and King and Harris (1972) give pressure values for the $\gamma \rightleftarrows \alpha$ transformation pressure at room temperature. The α/γ phase boundary ends at a critical point

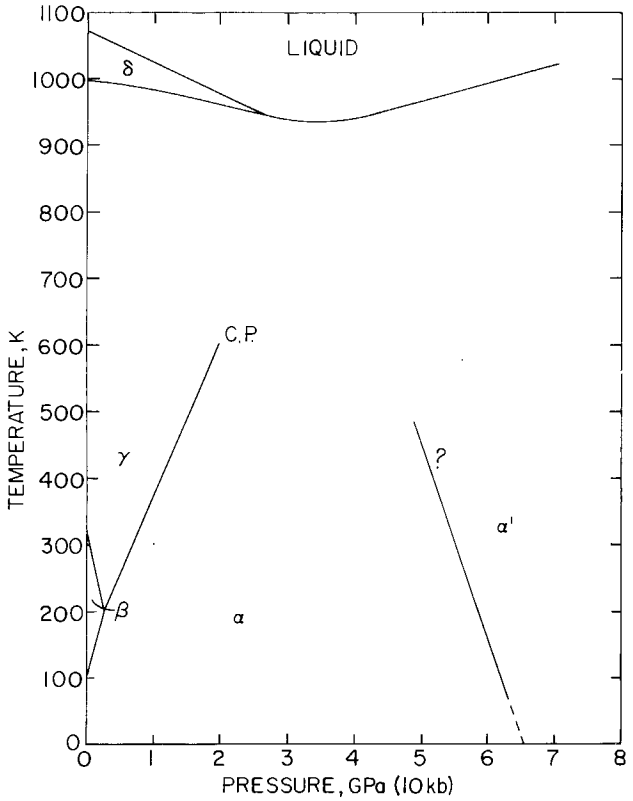

Fig. 4.1. Pseudo-equilibrium pressure-temperature phase diagram of cerium. The phase boundaries involving δ-Ce and liquid are true equilibrium boundaries. The letters C.P. mean critical point. The question mark for the α/α' phase boundary indicates that there is considerable doubt about the slope of this boundary, see text for further discussion.

where the two fcc phases are indistinguishable. Thermal analysis data (Ponyatovskii, 1958), volumetric data (Beecroft and Swenson, 1960 and Kutsar, 1974), resistivity data (Livshits et al., 1962 and Jayaraman, 1965) and X-ray data (Davis and Adams, 1964) all show that the quantity measured for the $\alpha \rightleftarrows \gamma$ transformation becomes smaller and smaller until it is no longer measurable as the temperature and pressure are increased. There is, however, considerable scatter for the values reported for the critical point (table 4.1). Except for one investigation, the results fall into two groups. The results of Ponyatovskii and of Jayaraman indicate a critical point at the lower limits (i.e., ~550 K and ~1.8 GPa) while the results of Beecroft and Swenson and of Davis and Adams indicate a critical point at ~640 K and ~2.05 GPa. Livshits et al. believe the critical point exists above 623 K and 2.1 GPa, which tends to favor the latter two investigations. The 480 K–1.45 GPa value for the critical point reported by Kutsar (1974) varies considerably from the above results, although this point falls close to the α/γ phase boundary line shown in figs. 4.1 and 4.2. Unless verified

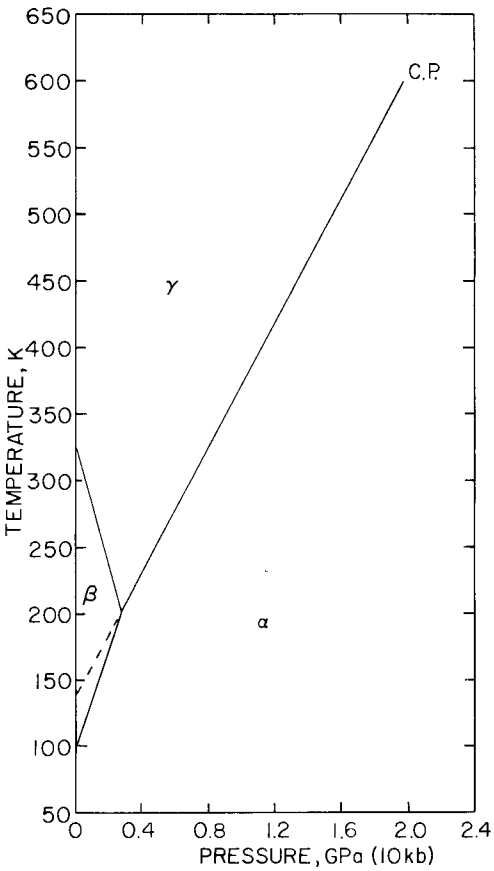

Fig. 4.2. Low pressure-low temperature region of pseudo-equilibrium phase diagram of cerium. The dashed line in the β-Ce phase region is the extension of the α/γ phase boundary to lower temperatures and pressures. The letters C.P. mean critical point.

we believe the value obtained by Kutsar for the critical point is erroneous. Furthermore, results of Beecroft and Swenson and of Livshits et al. suggest that the α/γ phase boundary curves slightly towards the temperature axis above ~400 K and ~1.2 GPa, while the other three investigations showed a linear boundary. Interestingly, a straight line is obtained by drawing it through the average values given in table 4.1 for the $\alpha \rightleftarrows \gamma$ transformation temperature at one atmosphere, the $\alpha \rightleftarrows \gamma$ transformation pressure at 298 K and the critical point. This reinforces our confidence in the critical point value in spite of the scatter and it also suggests that there is no curvature in the α/γ boundary above 1.2 GPa.

The pressure dependence of the β/γ boundary was determined by Gschneidner et al. (1962). These data were combined with the results for the $\beta \rightleftarrows \gamma$ transformation temperature at one atmosphere reported by McHargue and Yakel

TABLE 4.1.
Important points in the cerium pressure-temperature diagram

Transformation	Temperature		Pressure	
	(K)	(°C)	(GPa)[a]	Remarks
$\alpha \rightleftarrows \beta$	96 ± 6	−177	0	pseudo-equilibrium
$\beta \rightleftarrows \gamma$	326 ± 14	53	0	pseudo-equilibrium
$\gamma \rightleftarrows \delta$	999 ± 5	726	0	equilibrium
$\delta \rightleftarrows L$	1071 ± 3	798	0	equilibrium
$\alpha \rightleftarrows \gamma$	141 ± 10	−132	0	metastable, pseudo-equilibrium
$\alpha \rightleftarrows \beta \rightleftarrows \gamma$	201 ± 12	−72	0.28 ± 0.05	pseudo-equilibrium triple point
$\alpha \equiv \gamma$	600 ± 50	327	1.96 ± 0.20	critical point
$\gamma \rightleftarrows \delta \rightleftarrows L$	947	674	2.6	equilibrium triple point
$\alpha \rightleftarrows \gamma$	298	25	0.7 ± 0.06	pseudo-equilibrium
$\alpha \rightleftarrows \alpha'$	297	24	5.4 ± 0.5	pseudo-equilibrium
$\gamma \rightleftarrows L$(min.)[b]	935	662	3.3	equilibrium

[a]1 GPa = 10 kb. [b]The minimum in the liquids curve may actually be a triple point between γ, liquid and α' but further research needs to be done in this region of the phase diagram to determine the exact nature of this point.

(1960) and Rashid and Altstetter (1966) to give the β/γ boundary line shown in figs. 4.1 and 4.2. The intersection of the β/γ and α/γ boundary lines established the pseudo–equilibrium triple point $\alpha \rightleftarrows \beta \rightleftarrows \gamma$. The α/β phase boundary line was obtained by connecting the $\alpha \rightleftarrows \beta$ transformation temperature at atmospheric pressures (McHargue and Yakel, 1960 and Pavlov and Rybal'chenko, 1970) with the $\alpha \rightleftarrows \beta \rightleftarrows \gamma$ triple point.

The α/α' boundary line was determined by Livshits et al. (1962) from 200 to 800 K, by Stager and Drickamer (1964) at 77 and 296 K, and by King et al. (1970) from 77 to 480 K. Apparently the latter two groups of investigators were unaware of the earlier work by Livshits et al. who report that the α/α' boundary has a positive slope as opposed to the negative slope found by Stager and Drickamer and by King et al. In addition the magnitudes of the slope found by the latter two groups differ significantly. An extrapolation of the Stager–Drickamer α/α' boundary to high temperatures appears to intersect at the critical point, while the extrapolated boundary of King et al. intersects at the minimum in the liquidus as suggested by Jayaraman (1965). We believe the data of King et al. to be the most representative of the α/α' boundary, because it is the most recent and because it falls between the other two results. But because of the wide divergence, more careful research needs to be carried out before we can have a high degree of confidence in this portion of the cerium pressure diagram. Other researchers (Bridgman, 1952; Vereshchagin et al., 1961; Wittig, 1968; and King and Harris, 1972) have reported this transformation occurs at various pressures ranging from 5.0 to 9.1 GPa at room temperature. In addition X-ray studies (see section 2.2 below) show a crystal structure change above 5 to 6 GPa.

Stager and Drickamer (1964) also report the existence of another first order transformation at ~16 GPa and 296 K and at ~20 GPa and 77 K, suggesting the existence of a sixth polymorphic phase for cerium.

Evidence for phase transformations in cerium has been reported by many other investigators and as early as 1912 (see for example Gschneidner et al., 1962, for earlier citations). But since the purity of the cerium available before ~1950 is significantly lower than that available after 1950 the results reported by these earlier authors have not been included in the data shown in figs. 4.1 and 4.2 and in table 4.1. However, we should like to note that Trombe and Foex (1944 and 1947) discovered the existence of β-Ce and the influence the presence of this phase had on the volume of transformation observed in a sample when γ-Ce transformed to α-Ce. Indeed the nomenclature generally used today to identify these three cerium phases is the same as proposed by Trombe and Foex.

2.2. *Crystal structures*

The earliest investigations of the crystal structure of cerium (Hull, 1921) indicated that cerium had both a face centered cubic (fcc) and a hexagonal close-packed (hcp with $c/a = 1.62$) structure at room temperature and one atmosphere. Subsequent studies revealed only the fcc phase with $a \simeq 5.15$ Å, which today is identified as γ-Ce (see table 4.2 for additional crystallographic data). About 25 years ago the α-Ce phase was identified by X-ray methods at both high pressure and room temperature (Lawson and Tang, 1949) and at low temperature and atmospheric pressure (Schuck and Sturdivant, 1950) to have a fcc structure but with $a \simeq 4.83$ Å. The α phase, with a volume about 17% less than that of γ-Ce, is also known as the "collapsed" fcc phase. This large volume difference is also observed in dilatometric and volumetric studies of the $\alpha \rightleftarrows \gamma$ transformation.

The next phase to be identified was β-Ce, which forms from γ-Ce as a sample

TABLE 4.2.
Crystal structures, lattice parameters, metallic radii and atomic volumes of five cerium allotropes

Phase	Crystal Structure	Lattice Parameters (Å)			Conditions		Metallic Radius (CN = 12)[a] (Å)	Atomic Volume (Å^3/atom)	Ref.
		a	b	c	Temp. (K)	Press. (GPa)			
α'	C-centered orthorhombic	3.049	5.998	5.215	298	5.8	1.615	23.84	b
α	fcc	4.824	–	–	298	0.81	1.706	28.06	c
		4.85	–	–	77	0	1.71	28.5	d
β	dhcp	3.6810	11.857	–	298	0	1.8321	34.784	e
γ	fcc	5.1610	–	–	298	0	1.8245	34.367	e
δ	bcc	4.11	–	–	1041	0	1.83	34.7	f

[a]CN means coordination number; [b]Zachariasen and Ellinger (1976); [c]Adams and Davis (1962); [d]McHargue et al. (1957); [e]Beaudry and Palmer (1974); [f]Spedding et al. (1961).

of cerium is cooled below about 260 K (~ -15°C). McHargue and co-workers (1957) found β-Ce to have a double hexagonal close-packed (dhcp) structure, with $a \simeq 3.68$ Å, $c \simeq 11.92$ Å and $c/a \simeq 3.24$, which is about twice that observed for an ideal hcp metal ($c/a \simeq 1.63$). A few years later Spedding et al. (1961) showed that δ-Ce has a body-centered cubic (bcc) structure.

Four studies have been carried out at high pressures, >5.0 GPa, and room temperature to determine the structure of α'-Ce. Franceschi and Olcese (1969) identified α'-Ce as being fcc with a lattice parameter about 4% smaller than that of α-Ce. A year later McWhan (1970) reported α'-Ce to have a hcp structure with $a = 3.16$ Å and $c = 5.20$ Å. Ellinger and Zachariasen (1974) report a third structure for α'-Ce, namely C-centered orthorhombic, which is isotypic with α-U. Ellinger and Zachariasen suggest that Franceschi and Olcese did not attain sufficient pressures to transform α to α' since their lattice constant is consistent with the lattice parameter found by Ellinger and Zachariasen for α-Ce before it transformed to α'-Ce. Ellinger and Zachariasen also reanalyzed McWhan's data and found that the observed lines agreed better with their orthorhombic structure and lattice constants than they did for the hexagonal structure and lattice parameters given by McWhan. A year later Schaufelberger and Merx (1975) favored the co-existence of the fcc and hcp structures at $P > 5$ GPa, but they could not rule out the orthorhombic structure for α'-Ce. Furthermore, we note that the metallic radius and atomic volume calculated from the hcp lattice parameters are about 10% smaller than one might expect for tetravalent α'-Ce, but those calculated from the orthorhombic lattice parameters are within 1% of the expected values (Gschneidner and Smoluchowski, 1963). More recently Zachariasen and Ellinger (1976) presented additional experimental details confirming that α'-Ce has the C-centered orthorhombic structure and that McWhan's hcp structure cannot be correct.

The crystallographic data for the five cerium allotropic phases are summarized in table 4.2. The lattice parameters listed are those we feel are the best values for each of the five allotropes taking into account the chemical and phase purities of the samples and the X-ray techniques employed. The metallic radii and atomic volumes were calculated from the lattice parameters and thus correspond to the conditions given in table 4.2.

Several investigators have reported the co-existence of two of the cerium phases, such as γ and α, or β and α, or α and α', under conditions of pressure and temperature where only one phase would be expected from the known phase relationships and hysteresis effects (see section 2.4). The lack of truly hydrostatic pressure in the high pressure X-ray device probably accounts for most of the problem, but slow reaction kinetics may also contribute.

2.3. *Valences*

The simplest explanation for the large volume change between the γ and α, and the β and α phases is that the localized 4f level is at least partially delocalized and enters the valence band of cerium. The initial explanation,

proposed independently by Zachariasen (1949) and Pauling (1950) suggested that the volume change for the $\alpha \rightleftarrows \gamma$ transformation was due to a valence change from 3 in γ-Ce to 4 in α-Ce. But several years later Lock (1957) and Murao and Matsubara (1957) independently suggested that the magnetic susceptibility change for the $\alpha \rightleftarrows \gamma$ transformation corresponded to a valence change of 0.5 and not 1 electron per atom. The latter workers suggested valences of 3 for γ-Ce and 3.5 for α-Ce. In the early 1960's Evans and Raynor (1962) proposed a valence of 3.2 for γ-Ce, which increased with pressure to 3.5 at the γ–α transformation pressure (at 298 K), and a valence of 4 for α-Ce. A year later Gschneidner and Smoluchowski (1963) made an extensive analysis of all of the available experimental data, especially the metallic radii and magnetic susceptibility data, and also neutron diffraction and Hall coefficient results, and concluded that β- and γ-Ce have valences of 3.06 at room temperature and atmospheric pressure and α-Ce has a valence of 3.67 at 116 K and one atmosphere (see table 4.3). Furthermore, they claimed that the valence of γ-Ce increases with increasing pressure to a maximum value of 3.26 at the critical point, while that of α-Ce decreases with increasing pressure (3.54 at 0.78 GPa and 298 K) to 3.26 at the critical point. To date most scientists have accepted the latter set of valences as the most reasonable.

More recent high pressure studies (>5 GPa) have revealed the existence of α'-Ce, which is superconducting (Wittig, 1968) and has an atomic volume ~3.2% smaller than α-Ce at the $\alpha \rightleftarrows \alpha'$ transition pressure (Ellinger and Zachariasen, 1974). From metallic radii considerations Ellinger and Zachariasen consider α'-Ce to be tetravalent (see table 4.3), and thus to have no localized 4f electrons, which is consistent with its superconducting behavior. The existence of tetravalent α'-Ce is in accord with the valency scheme proposed by Gschneidner and Smoluchowski (1963), and this valence rules out most of the other proposed valence schemes.

Although more reliable X-ray and magnetic susceptibility data have become available since Gschneidner and Smoluchowski made their analysis, the use of

TABLE 4.3.
Metallic radii (corrected to atmospheric pressure and 298 K) and valences

Phase	Radius (Å)	Valence
Hypothetical trivalent Ce	1.846[a]	–
β-Ce	1.8321	3.04[b]
γ-Ce	1.8245	3.06[a,c]
δ-Ce	1.82	3.06
α-Ce	1.73	3.67[a,c]
α'-Ce	1.669	4.00[b]
Hypothetical tetravalent Ce	1.672[a]	–

[a]Gschneidner and Smoluchowski (1963); [b]See text; [c]Changes as a function of pressure and temperature, see text.

these data would not change the resultant valences by more than ±0.02 from those noted above. However, the revised lattice parameters (Beaudry and Palmer, 1974) and recent magnetic susceptibility data (Burgardt et al., 1976) of β-Ce suggest that the valence of this phase is about 0.02 lower than that of γ-Ce.

It should be noted that there are some experimental measurements (such as positron annihilation) which are apparently inconsistent with these valences. The difficulty arises from the fact that, although this valency scheme is useful and is consistent with many experimental facts, it is an over simplified description of the electronic nature of cerium and its allotropes. This problem is dealt with in the discussions concerning the various models proposed to explain the $\alpha \rightleftarrows \gamma$ transformation and the electronic nature of α, α' and γ phases (sections 5.1–5.7).

2.4. *Non-equilibrium and hysteresis effects*

The pressure–temperature diagrams presented in figs. 4.1 and 4.2 appear to be reasonable and explain the phase relationships between the various allotropes. The actual situation, however, is much more complicated and frustrating, especially in the region of temperatures <300 K and pressures <0.5 GPa. The major difficulty arises from the fact that all the phase transformations, except the $\gamma \rightleftarrows \delta$, $\gamma \rightleftarrows$ L and $\delta \rightleftarrows$ L transformations, exhibit large hystereses when either the temperature or the pressure is varied. The second difficulty is that some of the transformations do not go to completion, or if they do unusual conditions or procedures are required to complete the transition. Because of these difficulties most of the cerium samples studied below room temperature contain at least two and sometimes three different phases. Thus, most of the measurements made on these samples are of questionable value because it is almost impossible to separate out the individual contributions of the constituent phases.

2.4.1. *The non-equilibrium cerium phase diagram*

The experimentally observed transformations for $\beta \rightarrow \gamma$, $\gamma \rightarrow \beta$, $\gamma \rightarrow \alpha$ and $\alpha \rightarrow \gamma$ are shown in fig. 4.3 as a function of pressure and temperature. The lines in fig. 4.3 represent the start of transformations, M_s (cooling) or A_s (heating). The $\beta \rightarrow \gamma$ and $\gamma \rightarrow \beta$ transformations have only been measured by Gschneidner et al. (1962), while the $\gamma \rightarrow \alpha$ and $\alpha \rightarrow \gamma$ transformations are average values based on the investigations of Ponyatovskii (1958), Herman and Swenson (1958), Livshits et al. (1960) and Gschneidner et al. (1962). It is evident from fig. 4.3 that in samples which have never been cooled below -10°C γ-Ce is the observed phase at room temperature and pressure, although as seen in figs. 4.1 and 4.2 it is a metastable phase under these conditions.

Upon cooling atmospheric pressure γ-Ce will partially transform to β-Ce at a temperature near -10°C (263 K) (see table 4.4). To date no one has been able to cool a bulk cerium sample fast enough to avoid the formation of β phase. Upon further cooling the untransformed γ-Ce will transform to α-Ce at ~ 100 K (table

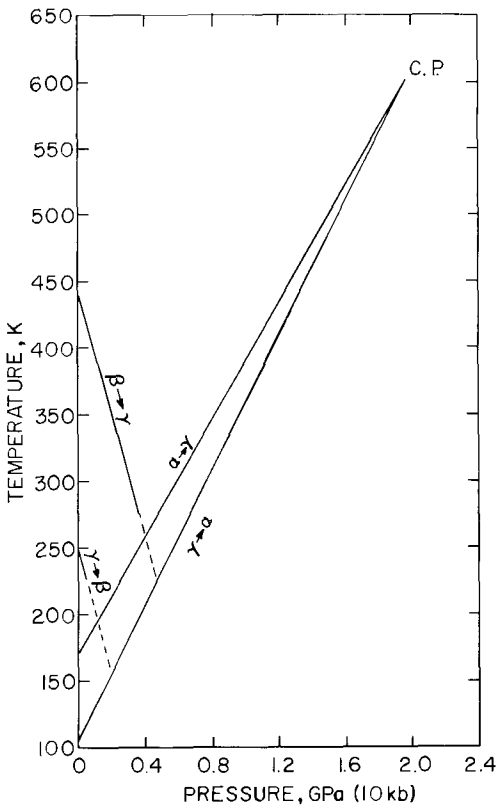

Fig. 4.3. The $\gamma \rightarrow \beta$, $\beta \rightarrow \gamma$, $\gamma \rightarrow \alpha$ and $\alpha \rightarrow \gamma$ transformations as experimentally observed. Averaged results taken from several investigations were used to construct the $\gamma \rightarrow \alpha$ and $\alpha \rightarrow \gamma$ transformation boundaries. Only one study has been made of pressure dependence of the $\gamma \rightarrow \beta$ and $\beta \rightarrow \gamma$ transformations. The letters C.P. mean critical point.

4.4). Continued cooling will cause β-Ce to be partially converted to α-Ce if the cooling rate is slow enough between 50 and 15 K. Upon warming, the α phase transforms back to β and γ, and at room temperature the sample will consist of two phases, β and γ. Conversion back to single phase γ-Ce requires heating the sample to above ~500 K. These transformations will be discussed separately below.

2.4.2. *The $\gamma \rightarrow \beta$ transformation*

The transformation of fcc γ to dhcp β is martensitic (McHargue and Yakel, 1960 and Rashid and Altstetter, 1966) and has been reported to take place over a wide range of temperatures (see table 4.4). The M_s temperature depends upon the purity (the higher the overall purity the lower the M_s temperature – Gschneidner et al., 1962), and the grain size (the smaller the grain size the lower the M_s temperature – Koch and McHargue, 1968). The amount of β-Ce formed

TABLE 4.4.
Experimental transformation temperatures at atmospheric pressure

	Cooling (K)		
Transformation	M_s	M_f	Ref.
$\gamma \rightarrow \beta$	237 to 278	?	a, b, c
$\gamma \rightarrow \alpha$	86 to 116	~4.2	a, b, c, d
$\beta \rightarrow \alpha$	45	15	e, f
	Heating (K)		
	A_s	A_f	
$\alpha \rightarrow \beta$	125	200	a
$\alpha \rightarrow \beta + \gamma$	158 to 180	190 to 210	a, b, c
$\beta \rightarrow \gamma$	373 to 451	420 to >451	a, b, c

[a]McHargue and Yakel (1960); [b]Gschneidner et al. (1962); [c]Rashid and Altstetter (1966); [d]Elliot and Miner (1967); [e]Gschneidner et al. (1976); [f]Burgardt et al. (1976a).

depends upon (1) the cooling rate, (2) the temperature to which a sample is cooled and (3) the number of times a specimen has been cycled (cooled to liquid N_2 or lower and then warmed to room temperature), see fig. 4.4. As shown by Gschneidner et al. (1962) it is almost impossible to cool a γ-Ce sample fast enough to prevent the formation of β-Ce. Extrapolation of their data indicate that a cooling rate of 10^7 K/min or greater is required (fig. 4.4). McHargue and Yakel (1960), Wilkinson et al. (1961) and Gschneidner et al. (1962) have shown that the lower the temperature to which a cerium sample is cooled and held the greater the amount of β-Ce formed (the dashed line in fig. 4.4 is based on the average of the latter two investigations). McHargue and Yakel using an X-ray technique found a somewhat higher percentage of β-Ce at a given temperature than Wilkinson et al., who used neutron diffraction, and Gschneidner et al., who used dilatometry. This suggests that there is a higher concentration of β-Ce near the surface than in the interior. Lock (1957) noted that the amount of β-Ce could be increased by cycling the sample between room temperature and liquid helium temperature. Subsequent investigators confirmed his findings, although some of them showed cooling to liquid N_2 gave similar results (see fig. 4.4). The curve shown in fig. 4.4 (after Gschneidner et al., 1962) is typical, and indicates that the fraction of β-Ce increases only slightly after about 20 cycles. It is doubtful that anyone has prepared pure β-Ce by just cycling, although McHargue and Yakel (1960) and Rashid and Altstetter (1966) have made such claims.

McHargue and Yakel (1960) proposed a dislocation model similar to that found for the fcc–hcp transformation in Co to explain the mechanism of the $\gamma \rightarrow \beta$ cerium transformation. This transformation occurs by a succession of $a/6$

⟨112⟩ glides in the cubic phase on two adjacent close-packed planes {111} with no glide on the next two neighboring planes (see fig. 4.5). Rashid and Altstetter (1966) and Shimura (1969) have also found this model to be acceptable and consistent with their investigations. Rashid and Altstetter also point out that the transformation can proceed both athermally and isothermally.

Plastic deformation has been found to induce the $\gamma \rightarrow \beta$ transformation from 196 K up to the M_d temperature (the temperature at which a deformed γ-Ce sample begins to transform to β-Ce, ~500 K) (Koch and McHargue, 1968).

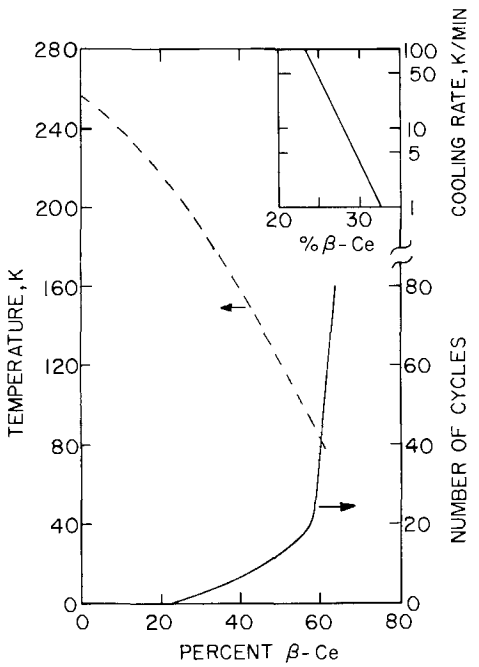

Fig. 4.4. Influence of the temperature to which a sample is cooled (dashed line), the cooling rate (insert) and the number of cycles (solid line) on the amount of β-Ce formed during the $\gamma \rightarrow \beta$ transformation.

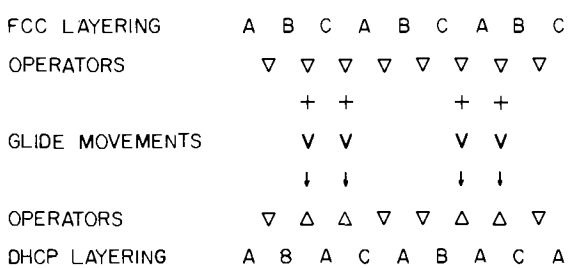

Fig. 4.5. A model showing glide motion for γ-Ce transforming to β-Ce. The symbol ∇ is used to represent the transition between two adjacent planes in the ABC layering sequence, Δ in the CBA layering sequence, and v is the vector representing a glide displacement.

Neutron diffraction studies carried out by Wilkinson et al. (1961) on an annealed and a cold worked sample support the observations of Koch and McHargue. Furthermore, they (K and McH) note that the M_d temperature is higher than the A_s and A_f temperatures, which is unusual (for a typical martensitic transformation $A_f > A_s > M_d > M_s > M_f$). The pressure dependence of this transformation (fig. 4.3) is based on the results of Gschneidner et al. (1962).

2.4.3. *The β-γ transformation*

Much less is known about the transformation of β-Ce to γ-Ce than the reverse reaction (see above). The A_s and A_f temperatures are given in table 4.4. The A_s temperature increases with increasing purity (Gschneidner et al., 1962) but is essentially independent of grain size (Koch and McHargue, 1968). The A_s temperature depends on the heating rate, the slower the rate of heating the lower the A_s value (Koskimaki et al., 1974). These authors have shown that below 348 K β-Ce will not transform to γ-Ce even after holding at this temperature for one year, but at 361 K 12% of the β-Ce will have transformed to γ-Ce after 6 days at this temperature. Holding at higher temperatures results in the transformation of successively larger amounts. The application of pressure lowers the A_s temperature as is shown in fig. 4.3 (Gschneidner et al., 1962).

According to the model of McHargue and Yakel (1960), see fig. 4.5, β-Ce transforms to γ-Ce by glide on the $\{0001\}$ planes in the $\langle 10\bar{1}0\rangle$ directions in the dhcp structure. The glides take place on two adjacent planes while the neighboring pairs of two adjacent planes remain stationary.

2.4.4. *The $\beta \rightleftarrows \gamma$ hysteresis*

As is shown in fig. 4.3 there is considerable hysteresis exhibited with this transformation, more than for the $\alpha \rightleftarrows \gamma$ transformation. The hysteresis is quite dependent upon the purity of the cerium used, as noted by Gschneidner et al. (1962) who report that a 99.5 at.% Ce sample had a hysteresis of 191 K, a 99.0 at.% Ce sample one of 110 K and a 96.4 at.% Ce specimen one of 80 K. This is consistent with the previous discussions concerning the lowering of M_s and the raising of A_s of the $\gamma \rightleftarrows \beta$ transformations as the purity of the cerium samples was increased. Grain size should also influence the hysteresis, with the smaller the grain size the larger the hysteresis (see above discussions).

2.4.5. *The $\gamma \rightarrow \alpha$ transformation*

The $\gamma \rightarrow \alpha$ is unique in that there is no crystallographic change, just a large volume collapse of about 17%. The M_s temperature has been reported to vary over a range of about 25 K (see table 4.4). Rashid and Altstetter (1966) found that M_s increases on the second and succeeding cycles (also confirmed by Elliot and Miner, 1967). A metallographic study by Rashid and Altstetter showed that small cellular areas of γ-Ce random in size and shape collapsed to α-Ce,

apparently independent of the neighboring areas. They concluded that the $\gamma \rightarrow \alpha$ transformation does not appear to be a shear transformation. The M_f temperature was determined from X-ray data by McHargue and Yakel (1960). These authors also noted that after considerable cycling γ-Ce (and also β-Ce) will no longer transform to α-Ce, which is consistent with results reported by Lock (1957), Gschneidner et al. (1962) and Rashid and Altstetter (1966). Deformation of γ-Ce below M_s increases the amount of α-Ce (McHargue and Yakel, 1960).

Rosen (1969) and Clinard (1969) found a softening (as evidenced by a large decrease in the elastic moduli) of the cerium lattice (presumably a mixture of γ and β-Ce) below 175 K and 200 K, respectively, which was temporarily arrested at the $\gamma \rightarrow \alpha$ transformation. An X-ray study by Pavlov and Finkel (1967) confirms that at least part of the softening of the cerium sample is due to the softening of the γ-Ce lattice, which is manifested by a large increase in the coefficient of thermal expansion of γ-Ce below 200 K. This softening of the γ-Ce lattice as the $\gamma \rightarrow \alpha$ transformation is approached is also evident in the high pressure volumetric and X-ray compressibility data (Bridgman, 1948 and Evidokimova and Genshaft, 1964) and sound velocity measurements (Voronov et al., 1960). At high pressure this softening is entirely due to γ-Ce, since no β-Ce is present in the samples.

The pressure dependence of the $\gamma \rightarrow \alpha$ transformation is shown in fig. 4.3. High pressure studies of γ-Ce and the $\gamma \rightarrow \alpha$ transformation at room temperature or above have an advantage over low temperature, one atmosphere studies in that β-Ce does not form to complicate the interpretation of data. In contrast to the low temperature transformation the $\gamma \rightarrow \alpha$ transformation at 300 K takes place rapidly and completely over a narrow range of pressure (<0.05 GPa). The reported values vary from 0.74 to 0.85 GPa.

2.4.6. *The $\beta \rightarrow \alpha$ transformation*

McHargue and Yakel (1960) using X-rays and Wilkinson et al. (1961) using neutron diffraction reported that β-Ce begins to transform to α-Ce at a temperature between 50 and 77 K. These experiments were carried out on samples which contained all three low temperature allotropes of cerium. Recently Gschneidner et al. (1976) and Burgardt et al. (1976a) using resistivity and magnetic susceptibility measurements on an allotropically pure β-Ce sample found the $\beta \rightarrow \alpha$ M_s temperature to be 45 K. They also found that if the β-Ce sample was rapidly cooled to 4.2 K (cooling rates were varied such that it took 5 to 90 min. to cool from 298 to 4.2 K) β-Ce would not transform to α-Ce. Neutron diffraction data by these authors confirmed the absence of any α-Ce within the limits of detection. Upon warming a quenched β-Ce sample from 4.2 K they found it began to transform to α-Ce at 15 K. The pressure dependence of this transformation has not been investigated.

It is quite likely that the $\beta \rightarrow \alpha$ transformation is partly a shear transformation involving the motion of atoms from a dhcp lattice to a fcc lattice, but in addition there is a large volume collapse ($\sim 17\%$) occurring approximately

simultaneously with the change in symmetry. That is, one can visualize this transformation as a combination of $\beta \rightarrow \gamma \rightarrow \alpha$ transformations.

2.4.7. *The $\alpha \rightarrow \beta$ and $\alpha \rightarrow \beta + \gamma$ transformations*

When α-Ce is warmed up to above 125 K it begins to transform only to β-Ce according to the X-ray study of McHargue and Yakel (1960). Examination of the dilatometric curve given by Gschneidner et al. (1962) and the resistivity curve of Smith and Morrice (1964) suggests that the M_s for $\alpha \rightarrow \beta$ may be as low as 100 K and 85 K, respectively. It should be noted, however, that resistivity and dilatometric curves published by others did not show any evidence for the $\alpha \rightarrow \beta$ transformation. Upon continued warming the α-Ce phase begins to transform slowly to γ-Ce at 160 K (McHargue and Yakel, 1960), but at about 180 K the transformation proceeds quite rapidly. During this same temperature interval the β-Ce is continuing to form but at a slow rate, such that above A_f 80% of the α-Ce present has transformed to γ-Ce and the remaining 20% to β-Ce. Dilatometric, magnetic susceptibility and electrical resistivity data reported by others are consistent with the X-ray results.

At high pressure and room temperature, since β-Ce is unstable, the α-Ce transforms entirely to γ-Ce. The pressure dependence of the $\alpha \rightarrow \gamma$ transformation is shown in fig. 4.3. It is seen that the hysteresis for the $\alpha \rightleftarrows \gamma$ transformation decreases with increasing pressure and temperature and appears to disappear at the critical point. The pressure dependence of the $\alpha \rightarrow \beta$ transformation has not been determined.

2.5. *Other phases – metastable or impurity stabilized or erroneous identifications*

A simple close-packed hexagonal structure has been reported for cerium at ambient temperature and pressure (Hull, 1921) and above 5 GPa pressure and 298 K (McWhan, 1970). The former probably had observed the dhcp β-Ce phase along with fcc γ-Ce in an impure cerium sample and incorrectly indexed the non-cubic phase as simple hcp. The high pressure X-ray pattern observed by McWhan was also indexed by Ellinger and Zachariasen (1974) to be orthorhombic (see section 2.2).

There have been three investigations in which a fcc structure with a lattice parameter about 1% smaller than that of γ-Ce has been observed (Dailer and Rothe, 1955; Weiner and Raynor, 1959; and Gschneidner et al., 1962). The lattice parameters observed by Dailer and Rothe, and Gschneidner and co-workers may be for the same phase, but those observed by Weiner and Raynor were obtained under very different conditions and are not related to the other two observations (see Gschneidner et al., 1962). About five years after Weiner's and Raynor's report, it was shown that their so-called "γ'-Ce" was probably a cerium interstitial compound, CeX, having the NaCl type structure (Gschneidner and Waber, 1964). The cubic phase noted by Gschneidner et al. (1962) was observed in X-ray powder samples, which were cycled through the $\gamma \rightleftarrows \alpha$

transformation and studied by X-rays at 298 K. This phase had a lattice parameter of 5.1233 Å and was called "α-γ intermediate" by the authors. This phase could be converted to γ-Ce by heating and when the sample was cycled once again to liquid N_2 it transformed to the "α-γ intermediate" – indicating that this was not due to a surface reaction forming a CeX compound. Interestingly the "α-γ intermediate" was not observed by these authors in another cerium sample of lower purity. Furthermore, it is quite likely that McHargue and Yakel (1960) did not observe the "α-γ intermediate" phase in their X-ray study, and Rashid and Altstetter (1966), who made a special attempt to find this phase, also did not observe it. Thus the "α-γ intermediate" phase, which has been observed once or possibly twice, still remains an unexplained mystery.

A monoclinic high pressure cerium phase (α''-Ce) was observed by Ellinger and Zachariasen (1974). They believe α''-Ce is a metastable phase which forms from α-Ce at about 6 GPa. If the pressure is lowered α''-Ce transforms back to α-Ce, but if the pressure is increased above 6 GPa α''-Ce changes sluggishly and irreversibly to α'-Ce. New results given by Zachariasen and Ellinger (1976) show that the body-centered monoclinic α''-Ce is a slightly distorted fcc structure with $a = 4.762$, $b = 3.170$, $c = 3.169$ Å and $\beta = 91.73°$.

3. Preparation and handling

3.1. *Problems in handling*

Cerium is a reactive metal which easily oxidizes when exposed to the air. The metal must be stored in an inert atmosphere or vacuum and ideally should be handled in a glove box. However, short exposures (< 15 minutes) to the air can be tolerated since the oxide layer can usually be removed by electropolishing. Oxide layers formed over longer periods (~ 1 hour) are difficult to remove by electropolishing unless the surface is first filed or ground on abrasive paper. In any event, the layer should not be allowed to become too thick, nor should the metal be stored in this condition due to the tendency of the oxide to penetrate the grain boundaries.

The most common electropolishing method is the application of approximately +40 volts to the sample in a 6% solution of perchloric acid in methanol cooled to dry ice temperature of $-78°$ C (Peterson and Hopkins, 1964). Afterwards the surface appears to be protected for an hour by an anodized layer. One drawback is the formation of β-Ce (M_s for β-Ce is $\sim -10°$ C) which needs to be avoided if a single phase γ-Ce sample is desired.

A chemical polish which can be used at room temperature consists of 25 ml dimethylformamide, 20 ml lactic acid, 5 ml phosphoric acid, 10 ml acetic, 15 ml nitric acid and 1 ml sulfuric acid (Koch and Picklesimer, 1967). The above solution is a dilution (with dimethylformamide) of Roman's solution (1966) which was developed for polishing the heavy rare earth elements. A modification of the

above solution, which has also been successfully used by us, is equal parts of dimethylformamide, nitric acid, acetic acid, and lactic acid. The chemical polish method is more difficult since the sample surface must be carefully swabbed during polishing to prevent buildup of various residues on the surface.

Koch and Picklesimer (1967) found that a protective anodized layer can be formed on the sample surface by applying +22 volts to the sample in a 1% solution of KOH immediately after polishing. This layer seems to protect the sample for up to a day but is difficult to subsequently remove except by grinding the sample on abrasive paper.

3.2. *Preparation of single phase α-cerium*

As indicated in section 2.4 any sample of pure γ-Ce cooled directly from room temperature will inevitably contain various mixtures of α- and β-Ce at liquid helium temperature. However, single phase α-Ce can be produced at room temperature by simply compressing γ-Ce to pressures above 0.8 GPa. The method used to apply the pressure is restricted by the physical requirements of the particular measurement to be performed. For example, heat capacity or magnetic susceptibility measurements have been made on samples contained in pressurized Cu-Be capsules with the contribution to the measurements from the capsule subtracted out after the measurement (Philips et al., 1968; MacPherson et al., 1971). X-ray measurements have been made using a variety of low atomic number materials, such as beryllium (Lawson and Tang, 1949; Davis and Adams, 1964) boron (Schaufelberger and Merx 1975) and diamond (Adams and Davis, 1962; Ellinger and Zachariasen, 1974). Resistivity measurements, which are subject to few physical limitations except for the electrical leads to the sample, can be made using a wide variety of techniques including some very high pressure methods such as the Bridgman anvil technique (e.g., see King and Harris, 1972).

For zero pressure studies single phase α-Ce can be prepared by by-passing the β-phase field (Panousis and Gschneidner, 1970; Nicolas-Francillon and Jerome, 1973; and Koskimaki et al., 1974). To do this a pure γ-phase sample is compressed to ~0.8 GPa, the sample is cooled to liquid nitrogen temperature, and the pressure is released while the temperature is maintained at 77 K. Due to the nature of the $\gamma \rightarrow \alpha$ transformation, some deformation of the sample is inevitable, even if the pressure device were to exert only isostatic stresses. In practice this deformation does not seem to effect the purity of the resulting α-Ce in so far as the formation of β-Ce is concerned; however, deformation of the α-Ce after the pressure is released may lead to formation of β-Ce (Koskimaki and Gschneidner, 1975). Needless to say, much care must be taken to keep the sample cold (< 150 K) during subsequent handling, which can sometimes be quite difficult in situations where the sample must be mounted in a sample holder in a chamber which is normally sealed and evacuated.

3.3. *Preparation of single phase β-cerium*

The $\gamma \rightarrow \beta$ transformation is very sluggish and does not go to completion (see section 2.4). Therefore an initially single phase γ-Ce sample cooled into the β-phase region will contain at most $\sim 50\%$ β-Ce. Compressive stresses due to the larger specific volume of β-Ce limit the transformation. Continued cooling into the α-phase region releases the stress when the remaining γ-phase begins to transform to the α-phase with its much lower specific volume. Apparently during some part of the $\gamma \rightleftarrows \alpha$ transformation, probably during heating, additional β-Ce forms. Therefore, numerous cooling and heating cycles can yield up to 90–95% β-Ce (Lock, 1957). Later Koskimaki et al. (1974) expanded this technique by addition of a long annealing step at 75° C in an attempt to relieve the compressive stresses which it was felt were preventing the final amount of γ- (or α-) Ce from transforming to β-Ce. Accordingly, single phase γ-Ce was thermally cycled between room temperature and helium temperature 10 times. The sample was then annealed at 75° C for 1 week. The whole process was repeated three or four times. Subsequent heat capacity measurements seemed to indicate a final percentage of at least 99% β, although some susceptibility measurements made at the same time (Koskimaki, unpublished) seemed to indicate that a partial ($\sim 6\%$) $\beta \rightarrow \alpha$ transformation occurred somewhere below 77 K. Later resistivity and susceptibility measurements (Gschneidner et al., 1976 and Burgardt et al., 1976a) have shown that cooling rate in the 15 to 50 K temperature range has a significant bearing on whether the $\beta \rightarrow \alpha$ transformation occurs. The $\beta \rightarrow \alpha$ transformation occurs mainly on the surface of the sample so that the larger the sample the smaller the fraction of α-Ce formed.

One additional method used to study single phase β-Ce is by alloying with an element which stabilized the β-phase field such as lanthanum (Roberts and Lock, 1957) or yttrium (Panousis and Gschneidner, 1972). The properties of the pure β-phase may be estimated by extrapolation of data measured at several alloy compositions to 100% β-Ce.

3.4. *Phase identification*

At room temperature the γ- and β-phases may coexist due to the large hysteresis in the $\gamma \rightleftarrows \beta$ transition. The two phases do not differ sufficiently in their magnetic or transport properties to determine relative percentages from these measurements; therefore the best method for phase identification is by diffraction methods. One can, however, make use of the fact that γ-Ce will always transform to α-Ce when cooled below 100 K and from resistance or magnetic susceptibility measurements one can detect small amounts of γ-Ce in β-Ce (see below). As mentioned previously (sections 2.4 and 3.3) the surface of the sample may contain more of a particular phase than the bulk; hence neutron diffraction methods are more reliable than X-ray methods. However, neutron diffraction may require a significantly larger sample.

A metallographic method to differentiate between the γ and β phases on the surface has been developed by Koch and Picklesimer (1967). The surface can be anodized using a KOH solution (see section 3.1). The dhcp β-Ce areas are then optically active under polarized light while the fcc areas (γ-Ce) are not. In addition, the color of the anodized coating will vary for the two phases, although it also varies with the thickness of the layer.

At low temperatures the α- and β-phases can be differentiated by the fact that β-Ce orders antiferromagnetically at 12.5 K. Thus small amounts of β-Ce can be detected in α-Ce by the large break in the specific heat, resistivity or magnetic susceptibility caused by this phase. The reverse situation is more difficult. A single phase β-Ce sample does not show any hysteresis in resistivity or magnetic susceptibility between 80 and 180 K due to the $\gamma \rightleftarrows \alpha$ transition, provided it is (1) not cooled below 60 K, or (2) if it is cooled below 60 K, it is cooled or heated rapidly enough through the temperature range of 15–50 K to prevent the $\beta \rightarrow \alpha$ transformation. The difference in resistivity and susceptibility between α- and γ-Ce is significant and there is a large hysteresis associated with the $\gamma \rightarrow \alpha$ and $\alpha \rightarrow \gamma$ transformations. Thus even small amounts ($\sim 1\%$) of α or γ in β-Ce should be detectable in the resistance and susceptibility vs. temperature curves. However, the possible occurrence of the $\beta \rightarrow \alpha$ transition between 15–50 K may complicate matters, adding uncertainty to whether a single phase β-Ce sample has been initially achieved below 15 K. The presence of γ-Ce can also be detected by noting the start of $\beta\ (\gamma) \rightarrow \alpha$ transformation; for pure β-Ce the M_s temperature is 45 K, but a few percent γ-Ce raises it to 100 K (Burgardt et al., 1976a).

4. Physical properties

This section deals with the physical properties (other than the crystal structures and phase relationships which were discussed previously) of the allotropes α-, β- and γ-Ce. Because of the paucity of information little or nothing will be discussed about the properties of the allotropic phases δ-, α'- and α''-Ce. Much of the published information on the properties of α-, β-, and γ-Ce at low temperatures (< 273 K) and low pressures (< 0.5 GPa) will be ignored primarily because the measurements were made on samples containing two or three phases and the data are difficult to partition uniquely into the contributions of the individual phases. Even in cases where careful attempts were made to extract useful data the information was ambiguous and generally not meaningful.

4.1. *Heat capacity*

4.1.1. *α-cerium*

The heat capacity of α-Ce is uncomplicated. A plot of C/T versus T^2 is shown in fig. 4.6. These results are believed to be the most accurate since the starting

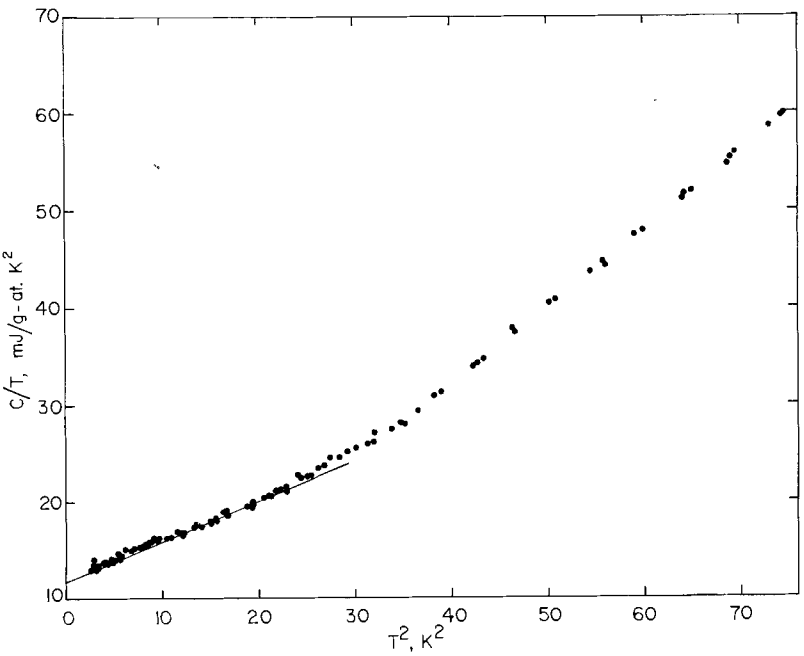

Fig. 4.6. The low temperature (< 9 K) heat capacity of α-Ce (after Koskimaki and Gschneidner, 1975).

material was the purest used to date since there is no evidence for a peak near 12.5 K to indicate the presence of small amounts of β-Ce. The electronic specific heat constant is 12.8 ± 0.2 mJ/g-at. K^2 and the Debye temperature at 0 K is 179 ± 2 K (Koskimaki and Gschneidner, 1975). The electronic specific heat constant compares favorably with the value at 1 GPa pressure of 11.3 mJ/g-at. K^2 (Phillips et al., 1968). The high value of this constant – the highest known for a pure metal – is probably due to substantial contribution to the density of states at the Fermi level by the 4f electron.

Several authors have found slight peaks and/or a low temperature tail in the specific heat (Parkinson and Roberts, 1957; Lounasmaa, 1964; Panousis and Gschneidner, 1970; and Conway and Phillips, 1974). It is likely that the peaks and tails are due to magnetic ordering of impurities and/or the presence of β-Ce in the predominately α-Ce samples (see ch. 5 section 2.2 for further details).

4.1.2. *β-cerium*

The heat capacity measurement of essentially allotropically pure β-Ce was first made by Koskimaki and Gschneidner (1974). These authors claimed that their sample was 99.5% or greater pure β-phase, but more recent studies by Burgardt et al. (1976a) revealed that K and G's sample might have contained an additional 0.8% α-Ce due to the transformation of some β-Ce to α-Ce between 15 and 50 K (see Tsang et al., 1976). A redetermination of the low temperature

heat capacity of β-Ce, in which the sample was rapidly cooled to 4 K to prevent the formation of α-Ce, indicated that if some α-Ce formed in Koskimaki's and Gschneidner's sample it had no effect on their results and conclusions (Tsang et al., 1976).

As a result of the heat capacity measurements Koskimaki and Gschneidner (1974) were the first to discover that magnetic ordering occurs at the two different symmetry sites in dhcp β-Ce (cubic and hexagonal) at 12.45 and 13.7 K. They thought, on the basis of the similarity of α-Nd and α-Sm structures, that the higher temperature is associated with ordering on the hexagonal sites and the lower temperature with the cubic sites. The small difference of 1.25 K between the two ordering peaks is much less than that observed in Nd (11.7 K) and Sm (95 K) and probably accounts for the fact that it was not observed previously.

An analysis of the various contributions to the heat capacity gave a reasonable explanation of the observed data (see fig. 5.1). More details can be found in ch. 5 section 2.2.

4.1.3. *γ-cerium*

Although it is impossible to measure the heat capacity of γ-Ce at low temperatures, < 20 K, it is possible to get a fairly reliable estimate of the electronic specific heat constant from an evaluation of the various contributions to the room temperature heat capacity. For γ-Ce these contributions are: the lattice heat capacity (24.68 J/g-at. K) assuming an average Debye temperature of 138 K from 15 to 300 K; a 4f contribution (0.04) from the thermal excitation of 4f electrons from the ground to the first excited level of the 4f multiplet; and a dilation contribution (0.10) due to the difference between C_p and C_v (Gschneidner, 1965). When these are subtracted from the measured heat capacity of Spedding et al. (1960) – 27.07 J/g-at. K – an electronic contribution of 2.25 is obtained (Gschneidner, 1965). Since the electronic contribution is given by γT, where γ is the electronic specific heat constant, a value of 7.5 mJ/g-at. K^2 is obtained for the γ value of γ-Ce. This value is probably reliable to ± 0.5 mJ/g-at. K^2. Thus it appears that the electronic specific constant of γ-Ce is less than that of β-Ce (9.4) and much less than that of α-Ce (12.8). And since the density of states at the Fermi surface is proportional to γ, the density of states increases on going from γ-Ce to β-Ce to α-Ce.

This type of analysis, however, does not yield a Debye temperature at 0 K and thus the β-Ce and α-Ce values cannot be compared to the 138 K value noted above for γ-Ce.

4.2. *Magnetic susceptibility*

4.2.1. *α-cerium*

The magnetic susceptibility of α-Ce as a function of temperature has been measured under pressure by MacPherson et al. (1971) and at zero pressure by

Grimberg et al. (1972) and by Koskimaki and Gschneidner (1975). In general the three investigations gave similar results (see fig. 4 of Koskimaki and Gschneidner, 1975). The α-Ce samples of both MacPherson et al. and Grimberg et al. contained magnetic impurities, and the latter's sample also contained some β-Ce. Because the sample of Koskimaki and Gschneidner was much purer than the other two α-Ce samples, their data are considered to be the most reliable and are shown in fig. 4.7. These data show that α-Ce is essentially a Pauli paramagnet. The minimum value of the susceptibility is 4.5 times higher than the Pauli susceptibility calculated from heat capacity results. This discrepancy can be attributed to a Stoner exchange enhancement arising mainly from the partially occupied (or partially localized) 4f state. All three investigations found a low temperature rise which may be intrinsic to α-Ce but has not been explained to anyone's satisfaction. The rise could also be due to varying amounts of β-Ce impurities, magnetic impurities, and possibly microscopic β-like regions at lattice imperfections due to the deformation incurred during sample preparation. A third feature seen in the susceptibility curve shown in fig. 4.7 is a slow rise with temperature above 60 K. This rise is possibly due to changes in position or shape of the 4f band with changes in temperature.

4.2.2. *β-cerium*

The magnetic susceptibility of β-Ce follows the Curie–Weiss law from 300 K down to near its Néel temperature ($\sim$13 K) with $\theta = -41$ K and $p_{\text{eff}} = 2.61\ \mu_B$ (Burgardt et al., 1976a). This shows that β-Ce has one localized 4f electron since the expected theoretical value of p_{eff} is $2.54\ \mu_B$. Susceptibility measurements showed only one peak in contrast to the two peaks observed in the heat capacity measurements. Apparently the change in the susceptibility at the two ordering temperatures is too small to be observed when the ordering temperatures are so close together ($\sim$1.25 K). Furthermore, the susceptibility at the ordering temperature, 12.6 K, decreases with increasing magnetic field. Burgardt et al. (1976a)

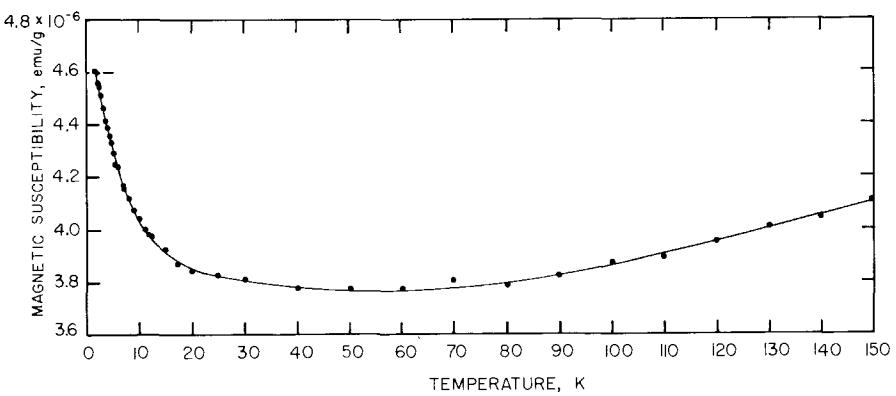

Fig. 4.7. The magnetic susceptibility of α-Ce from 2 to 150 K (after Koskimaki and Gschneidner, 1975).

thought the behavior of the magnetic moments on the cubic and hexagonal sites in β-Ce was complex and probably similar to that observed in α-Nd and α-Sm, but until single crystals are available, little else can be deduced from polycrystalline samples.

4.2.3. *γ-cerium*

Since γ-Ce transforms to β-Ce at $\sim$273 K most low temperature magnetic susceptibility measurements were made on samples of a mixture of γ- and β-Ce and thus the results do not yield reliable data for γ-Ce. The high temperature (>300 K) susceptibility measurements should be reliable since β-Ce is unstable with respect to γ-Ce. The data of Colvin et al. (1961) and Burr and Ehara (1966) show that γ-Ce obeys the Curie–Weiss law and that γ-Ce probably has one localized 4f electron. Their results however, differ somewhat: the results of Colvin et al. yield $\theta = -50$ K and $p_{\text{eff}} = 2.52\,\mu_B$, while those of Burr and Ehara give $\theta = -9$ K and $p_{\text{eff}} = 2.4\,\mu_B$. The theoretical effective moment, p_{eff}, for one unpaired 4f electron is $2.54\,\mu_B$.

4.3. *Electrical resistivity*

4.3.1. *α-cerium*

The resistivity of α-Ce has been measured by a number of workers (Katzman and Mydosh, 1972; Grimberg et al., 1972; Brodsky and Friddle, 1973; Nicolas–Francillon and Jerome, 1973; and Leger, 1976). Various pressure methods were used to prepare the samples. There has been some disagreement in results, mainly whether a T^2 dependence exists at low temperatures. Metals with large exchange enhancements are expected to exhibit spin fluctuation behavior which leads to a T^2 dependence in the low temperature resistivity (Kaiser and Doniach, 1970). Katzman and Mydosh found such a dependence but none of the other workers have, except as would be expected from β-Ce or impurities in their samples. Katzman and Mydosh also found that this T^2 dependence decreased with increasing pressure, while Nicolas–Francillon and Jerome found no change in resistivity up to pressures of 0.85 GPa. Thus, it is probable that the T^2 dependence shown by Katzman and Mydosh is due to a smaller amount of β-Ce in their sample which transforms to α-Ce as the pressure is increased. A second effect expected for spin fluctuation resistivity is a negative departure from a linear T law at higher temperatures (Jullian et al., 1974). The results of Brodsky and Friddle are linear to room temperature for α-Ce under 1.8 GPa pressure. Thus the departure from linearity, if it exists, occurs above 300 K. These results do not necessarily preclude the existence of spin fluctuations in α-Ce. The spin fluctuation resistivity of exchange enhanced palladium and platinum causes a departure from linearity above 300 and 400 K respectively. Also the coefficient of the T^2 dependence at low temperatures for palladium is only 3×

10^{-5} $\mu\Omega$ cm K^{-2} (Schindler and Rice, 1967). As indicated by Nicolas–Francillon and Jerome, a value this small could not be detected in their results.

High pressure studies by Probst and Wittig (1975) showed that α-Ce becomes superconducting at 20 mK and 2.0 GPa, and that the transition temperature is raised with increasing pressure (50 mK at 4.0 GPa). At the α/α' phase boundary ($\approx$4.0 GPa) the transition temperature increases by a factor of $\sim$40 to 1.9 K for α'-Ce.

4.3.2. *β-cerium*

The electrical resistivity of β-Ce has been measured by researchers at Iowa State University (Gschneidner et al., 1976 and Burgardt et al., 1976a) from 2 to 300 K, see fig. 4.8. It is seen that the temperature dependence of the resistivity of β-Ce is unusual in two respects – the large drop below 20 K and the slight decrease in resistivity upon cooling from 300 to 50 K (i.e. $\rho_{300}/\rho_{50} \simeq 1.3$ for β-Ce which compares to a ratio of 5 to 10 for normal metals). An analysis indicated that this effect could not be explained by existing models which have been used to explain large increases in the electrical resistivity in other metals. The authors, however, noted that the high temperature resistivity could be fitted to a

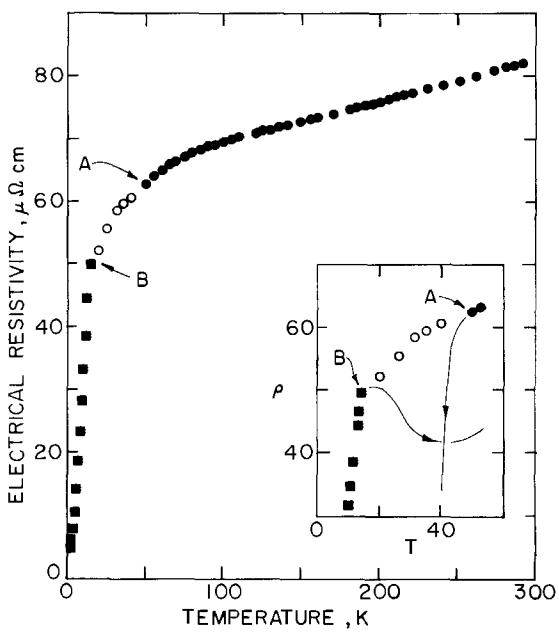

Fig. 4.8. Electrical resistivity of β-Ce. The solid points were measured under thermal equilibrium conditions and the open circles were taken on warming rapidly before β-Ce transformed to α-Ce. The solid squares were measured on slow warming of a sample which had been rapidly cooled to 4 K (within 5 to 10 min). The solid circles were taken on slow cooling from 300 K. The insert shows β-Ce transforming to α-Ce on cooling (point A) and on warming (point B).

Kondo model for scattering of conduction electrons and the rapid drop was probably due to a quenching of Kondo scattering by the magnetic ordering in β-Ce ($\sim$ 13 K). A more detailed theoretical analysis by Liu et al. (1976) resulted in a model which could account for Kondo scattering in the presence of strong spin correlation (i.e. magnetic ordering). The excellent agreement between theory and experiment is shown in fig. 4.9.

Magneto-resistivity measurements by Burgardt et al. (1976b) on β-Ce at five temperatures between 4.2 and 85 K showed that the spin resistivity is strongly negative above the Néel temperature up to the maximum fields measured ($\sim$80 kOe). This negative magneto-resistivity strongly supports the authors' previous conclusions of Kondo scattering in β-Ce. The 4.2 K results show a weak negative magneto-resistivity up to 70 kOe, above which a sudden positive upturn is observed. This sudden change is thought to be due to a flip of some of the magnetic moments in antiferromagnetic β-Ce.

4.3.3. *γ-cerium*

The electrical resistivity of γ-Ce is about 10% smaller than that of β-Ce and shows nearly the same temperature dependence as β-Ce down to $\sim$100 K at which temperature γ-Ce transforms to α-Ce, see fig. 4.10, Burgardt et al. (1976a). The similarities between β- and γ-Ce suggest that γ-Ce may also exhibit Kondo scattering, however, no detailed analysis has been made. Part of the difficulty is the fact that some of the γ-Ce transforms to β-Ce when cooled below 273 K (the small increase in ρ at $\sim$270 K) while the remaining γ-Ce transforms to α-Ce at $\sim$100 K.

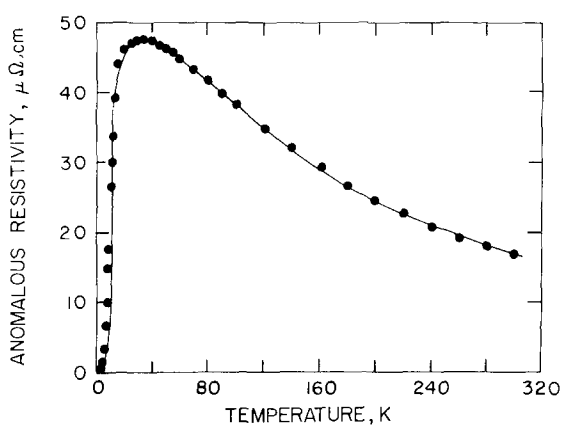

Fig. 4.9. The anomalous resistivity of β-Ce, which was obtained by subtracting the phonon and residual resistivities from the observed resistivity, as a function of temperature – solid points. The solid line is the theoretical resistivity based on the model of Liu et al. (1976).

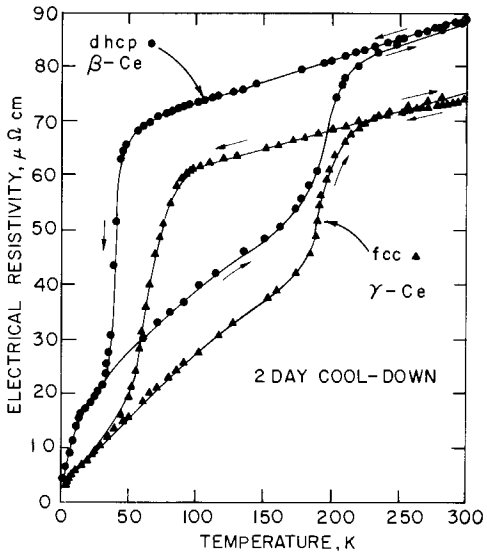

Fig. 4.10. The electrical resistivity of γ-Ce. For comparison purposes the resistivity of β-Ce is also shown.

4.4. *Neutron scattering*

Neutron diffraction measurements by Wilkinson et al. (1961) in addition to confirming the phase relationships deduced by X-ray studies (see section 2.4) also gave information concerning the magnetic nature of α-, β- and γ-Ce. The diffuse neutron scattering results were consistent with one localized 4f electron in both β- and γ-Ce and no 4f electron in α-Ce. These data, however, are not nearly as sensitive to the presence or absence of a localized 4f electron as magnetic susceptibility data. These authors also observed antiferromagnetic ordering in β-Ce at 4.2 K, and they suggested several models which could explain in three observed antiferromagnetic reflections from a polycrystalline sample. The true magnetic structure of β-Ce, however, will not be known until single crystals are available for study.

Inelastic scattering measurements on β-Ce by Stassis (1974) indicated that the two excited doublets associated with the hexagonal sites are 98 and 113 K above the ground state doublet and the excited quartet associated with the cubic sites is 206 K above the ground state doublet. Similar measurements on γ-Ce by Millhouse and Furrer (1974) showed that the Γ_8 quartet is 67 K above the ground state Γ_7 doublet. The results of Millhouse and Furrer are not applicable to the cubic sites of β-Ce since such a splitting would lead to a Schottky contribution near 20 K which is larger than the total specific heat of β-Ce. The wide divergence of the Γ_8 quartet in γ- and β-Ce is surprising and points to the importance of the interaction with second nearest neighbors or greater in crystal fields.

4.5. *Positron annihilation and angular correlation*

When a positron is injected into a metal it annihilates principally with the conduction and outer core electrons of the metal. Thus the lifetime of the positron in a metal and the angular correlation of the resultant photon are proportional to the density of the conduction electrons. On the basis of the promotional model of the cerium allotropes γ, α and α' one would expect to see a significant change in the lifetime and angular correlation as $\gamma \rightarrow \alpha$ and $\alpha \rightarrow \alpha'$. Such measurements have been carried out by Gustafson and co-workers on the $\gamma \rightarrow \alpha$ transformation at low temperatures and atmospheric pressure (Gustafson and Mackintosh, 1964), on the $\gamma \rightarrow \alpha$ transformation at both low temperature and 1 atm, and at 300 K and high pressure (Gustafson et al., 1969) and on the $\alpha \rightarrow \alpha'$ transformation at 300 K and high pressure (Gempel et al., 1972). The observed changes in lifetime and in angular correlation were small and the authors concluded that the number of conduction electrons in γ, α and α' are essentially the same, approximately three, and that the promotional model is not valid. But X-ray absorption spectra studies indicate that there is an electron transfer from the 4f level to the valence band when γ-Ce transforms to α-Ce (see section 4.9). Clearly any reliable model will need to take these apparently contradictory results into account.

4.6. *Hall effect*

The Hall effect in α- and γ-Ce has been measured as a function of temperature and pressure by several investigators. Kevane et al. (1953), reported a Hall coefficient, R_H, of 1.81×10^{-4} cm^3/coul. for γ-Ce at room temperature and measured the change in R_H upon cooling. Their results indicated a large decrease ($\sim$a factor of 3) when α-Ce formed from a β/γ mixture. Later investigators give larger values for R_H for γ-Ce at room temperature: 2.0×10^{-4} cm^3/coul. (Likhter and Venttsel', 1962) and 2.8×10^{-4} cm^3/coul. (Kaufman et al., 1961) and both find a large decrease in R_H as γ-Ce transforms to α-Ce at high pressures. Likhter and Venttsel' (1962) found R_H of γ-Ce to increase linearly with increasing pressure to a value of 2.26×10^{-4} cm^3/coul. at the $\gamma \rightarrow \alpha$ transformation pressure; the α-Ce R_H value at this transformation was 0.8×10^{-4} cm^3/coul. and it decreased in a non-linear fashion to 0.5×10^{-4} cm^3/coul. Both Likhter and Venttsel' (1962) and Kaufman et al. (1961) concluded that the change in the Hall coefficient at the $\gamma \rightarrow \alpha$ transformation could account for a valence change of 3 to 4. After an extensive analysis, Gschneidner and Smoluchowski (1963), however, concluded that the change in R_H is not sensitive to the choice of valence for α-Ce. That is, any valence between 3 and 4 is consistent with the R_H value observed for α-Ce, assuming that the Hall effect in α-Ce can be described in terms of a two band model.

4.7. *Thermoelectric power*

The thermoelectric power (TEP) of α- and γ-Ce have been measured by Khvostantsev et al. (1973) and Ramesh et al. (1974a and b). Both investigators

noted that there was a large variation in the TEP of γ-Ce as a function pressure, prior to the $\gamma \rightarrow \alpha$ transformation. The resistivity of γ-Ce in this pressure range shows only a small change. The general shapes of the TEP vs pressure curves are quite different and the absolute values for the TEP of γ-Ce at atmospheric pressure are of the opposite sign for the two investigations. During the $\gamma \rightarrow \alpha$ transformation, Rämesh et al. find the TEP drops rapidly (by a factor of about 5 times). Khvostantsev et al. explain their results on the basis of an electronic change at $\sim$0.75 GPa followed by a crystallographic structural change at $\sim$1 GPa but recent results by Léger et al. (1975) show that this cannot be. The TEP of α-Ce decreases and becomes negative at about 1.6 GPa and room temperature according to Ramesh et al. Furthermore, they note that pressure at which the TEP changes sign increases with increasing temperature. Khvostantsev et al., however, find that the TEP of α-Ce slowly rises, reaches a maximum at $\sim$2.2 GPa and remains positive up to the maximum pressure of their experiment, 3 GPa. From the significant differences in the results of the two investigations it would appear that the pressure dependence of α- and γ-Ce is quite sensitive to impurities and/or handling. Clearly more careful measurements and better characterized samples are needed before any reliance can be placed on TEP data.

4.8. *Elastic properties*

The elastic properties have been measured on cerium samples below room temperature by Rosen (1969) and Clinard (1969), but because their samples contain a mixture of phases (α-, β- and γ-Ce) it is difficult to derive meaningful data from these results. Voronov et al. (1960) measure the elastic moduli (Young's, bulk and shear moduli, and Poisson's ratio) and the Debye temperature of γ- and α-Ce as a function of pressure at room temperature. For γ-Ce the shear modulus increased slowly up to the γ–α transformation; Young's modulus remained nearly constant up to 0.4 GPa before slowly dropping; the bulk modulus and Poisson's ratio decreased rapidly; and the Debye temperature remained essentially constant. At the $\gamma \rightarrow \alpha$ transformation all of the moduli and the Debye temperature increased on going from γ-Ce to α-Ce. This increase in the elastic properties as γ-Ce transforms to α-Ce was also noted by Rosen (1969) and Clinard (1969) in their low temperature experiments. Furthermore, Voronov et al. (1960) found that the moduli and Debye temperature of α-Ce increased as a function of increasing pressure, except for Poisson's ratio which remained constant.

4.9. *Spectroscopic studies*

4.9.1. *Infrared*

Wilkins et al. (1962) measured the surface reflectance of γ-Ce and found several absorption peaks in the 2 to 35 μ region at room temperature, the largest

being at 15 μ. On the basis of these data Gschneidner (1965) suggested that the one-electron 4f band lies 0.076 eV below the Fermi surface in γ-Ce.

4.9.2. *X-ray absorption*

Ottewell et al. (1973) measured the X-ray absorption spectra around the M_4 and M_5 absorption edges of γ-Ce at room temperature and of a γ-Ce sample cooled to 77 K. The spectra of these metal samples were compared to those of CeF_3 and CeO_2. Their results showed that the γ-Ce spectrum was structurally similar to that of CeF_3 (trivalent Ce) and clearly different from that of CeO_2 (tetravalent Ce). On cooling γ-Ce to 77 K the M_4 and M_5 spectra change into a form which was resolved into a combination of trivalent (57%) and tetravalent (43%) curves. Although their sample undoubtedly contained some β-Ce in addition to α-Ce making it impossible to uniquely determine the α-Ce contribution to the spectra, their data clearly shows that some 4f electrons are transferred from the localized state to the valence band giving rise to a partial tetravalent state during the $\gamma \rightarrow \alpha$ transformation. This result is in apparent conflict with the positron annihilation studies (see section 4.5).

A year later Shaburov et al. (1974) arrived at a similar conclusion to Ottewell et al. (1973) on the basis of their measurement of the chemical shift of the K_{α_1}, K_{β_1} and $K_{\beta_{2,4}}$ X-ray lines during the $\gamma \rightleftarrows \alpha$ transformation. They concluded that 0.50 4f per atom is transferred to the 4d band during the $\gamma \rightarrow \alpha$ transformation at 77 K (their results may be too low since it is quite likely that some β-Ce was present in their samples) and 0.34 at 300 K and high pressure (>0.9 GPa).

4.9.3. *X-ray photoemission*

X-ray photoemission spectroscopy (XPS) of a number of rare earth metals, including γ-Ce, has been carried out by Baer and Busch (1973 and 1974) in order to determine the position of the 4f level relative to the Fermi energy. Although Baer and Busch (1974) found the observed spectrum of γ-Ce to change as evaporation conditions were varied, they felt that the peak at 0.9 eV, which was observed in all the samples, was due to the 4f electron. This is in variance with the infrared studies noted above, which suggested a 4f level is just 0.076 eV below the Fermi surface. A close examination of the data of Baer and Busch (1974) indicates that if the 4f level lay within 0.2 eV of the Fermi surface it would almost be impossible to detect due to the steep rise in the XPS spectrum at the Fermi surface. Furthermore it should be noted that the 5d band in lanthanum exhibits a peak at $\sim$0.8 eV (Baer and Busch, 1973). More careful studies are needed to see if the 4f level lies at $\sim$0.1 eV below the Fermi surface.

4.10. *Miscellaneous*

4.10.1. *Electron spin resonance*

The electron spin resonance, ESR, spectrum was determined by Goodrich and Everett (1966) at 300, 196 and 77 K. Since the ESR spectra of γ- and β-Ce can

be measured independently of one another the authors did not need to worry about phase purity in their samples. In addition to determining the g-factors for γ- and β-Ce, the authors found that there is a small trigonal distortion in the crystalline field of γ-Ce and that the 4f-conduction band exchange energy for γ-Ce is -0.062 eV at 300 K. At 77 K no resonance absorption (neither for α- nor β-Ce) was found in the sample after the $\gamma \rightarrow \alpha$ transformation was completed. The absence of the β-Ce ESR spectrum is thought to be due to strains in the sample due to the $\gamma \rightarrow \alpha$ transformation.

4.10.2. *Heat of transformation, $\alpha \rightleftarrows \gamma$*

Gonikberg et al. (1957) measured the heat of transformation of the $\alpha \rightleftarrows \gamma$ transformation at high pressure by differential thermal analysis. They obtained a value of 880 ± 40 cal/g-at. at 288 K and 0.7 GPa. This compares with 1070 ± 170 cal/g-at. as calculated from the data given in tables 4.1 and 4.2 and the known compressibilities for α- and γ-Ce (Gschneidner, 1964). Considering the error limits it is seen that the two values are in agreement.

5. Theoretical models for the $\gamma \rightleftarrows \alpha$ transformation

In this section we summarize the various theories and models that have been proposed to explain the $\gamma \rightleftarrows \alpha$ transition of cerium. These models are discussed with emphasis on their consistency with the experimental results described in the preceding sections. The $\gamma \rightleftarrows \alpha$ transition in cerium is often classed with the change-of-valence transitions observed in SmS, SmSe, CeP, and certain other rare earth compounds. Some of the numerous theories which attempt to explain these transitions apply equally well to cerium. However, since these transitions are treated in ch. 20 they will not be described here, except for those theories which have been specifically ascribed to cerium by their authors.

5.1. *Zachariasen–Pauling theory*

There are two general types of theories for $\gamma \rightleftarrows \alpha$ transition, those in which the localized 4f electron in γ-Ce (or a part of it) is believed to be transferred to the $(5d6s)^3$ conduction band in α-Ce and those in which the 4f state itself is believed to be delocalized. Theories of the first type have become known as "promotional" theories since the 4f electron is transferred or "promoted" to the conduction band. The original idea of promotion was first independently suggested by Zachariasen (1949) and by Pauling (1950). This idea accounted for the large volume collapse at the transition since the 4f electron in α-Ce would no longer be expected to shield the valence electrons from the nuclear charge. Later studies by a number of workers (see section 2.3) seemed to indicate that the 4f electron was only partially transferred to the valence band leading to a partial valence of about 3.7 for α-Ce at low temperatures and zero pressure.

5.2. *Coqblin–Blandin model*

One consequence of the promotional idea is that it implies that the localized 4f state in cerium is close in energy to the Fermi level and therefore should also be coincident with the conduction band. Coqblin and Blandin (1968) felt that under these conditions the 4f state should mix or hybridize with the conduction band states to form a 4f virtual bound state. Their treatment of the problem is based on the formalism developed by Friedel (1956, 1958) and Anderson (1961) to describe localized magnetic moments for transition metal impurity atoms in a nonmagnetic metal. Briefly, Anderson attributes the occurrence of localized moments to the formation of separate up-spin and down-spin virtual bound states, one of which lies below the Fermi level and is occupied. A transition to a single nonmagnetic virtual bound level can occur if broadening of the virtual levels by the s–d mixing interaction becomes comparable to the repulsive Coulomb energy between opposite spin d electrons on the same site. Coqblin and Blandin felt that a similar description could be applied to cerium since the spatial extent of the f orbitals was believed to be small enough to allow the cerium atoms to be treated as a collection of independent impurity atoms. In γ-Ce the occurrence of localized moments could be described as arising from a spin and orbital magnetic 4f virtual bound state lying about 0.1 eV below the Fermi level and having a half-width of around 0.02 eV. The mechanism for the transition to α-Ce was believed to arise from a cooperative interaction between a number of volume dependent terms in their free energy expression. These included an elastic term and an electronic energy term which was ultimately dependent on the position of the 4f virtual level relative to the Fermi level. The position of the virtual level was assumed to vary linearly with volume. During the transition the virtual level was expected to cross the Fermi level and to combine with the other spin and orbital f states to form a nonmagnetic, fourteenfold-degenerate virtual state lying about 0.1 eV to 0.15 eV above the Fermi level. The virtual state, due to its Lorentzian form, was expected to show a tail on the low energy side of the peak which would intersect and lie below the Fermi level. Thus a partial occupation of the virtual f level would result providing a contribution from the f electrons to the density of states at the Fermi level. The 4f contribution was also expected to give rise to an exchange enhancement of the magnetic susceptibility in agreement with specific heat and susceptibility results.

Edelstein (1968, 1970) has adopted the Coqblin–Blandin model for cerium but with an emphasis on the effect of spin compensation. This point of view was that the decrease or loss of the magnetic moment in α-Ce and the slightly decreased moments in γ- and β-Ce (based on Lock's data) was due to the antiferromagnetic polarization of conduction electrons around the 4f virtual state. Edelstein supported this idea in part by noting an apparent $T^{-1/2}$ dependence of the magnetic susceptibility of mixed phase cerium samples above 13 K (Lock, 1957). This temperature dependence had been suggested by Anderson (1967) for the spin compensation contribution to the susceptibility for Kondo alloys. However, subsequent susceptibility measurements of single phase α-Ce (see

section 4.2) have failed to show any $T^{-1/2}$ dependence in α-Ce and, at any rate, the temperature dependence of the susceptibility for a spin compensated system, in general, is believed to vary as $(T + 2T_K)^{-1}$ where T_K is the Kondo temperature (Krishna-murthy et al., 1975). In the presence of crystal fields the magnetic susceptibility of a Kondo system is more complicated (DeGennaro and Borchi, 1973). The $T^{-1/2}$ dependence for mixed phase Ce samples appears to be accidental rather than explicit prediction of any theory. For β-Ce (or γ-Ce) the temperature dependence of the susceptibility is dominated by a localized 4f electron magnetic ordering and crystal field effects; therefore any contribution from spin compensation would be difficult to detect. However, on the basis of resistivity measurements Gschneidner et al. (1976) have discovered a Kondo effect in β-Ce which is quenched by magnetic ordering. Thus Edelstein's hypothesis may have been correct at least for β-Ce.

5.3. *Ramirez–Falicov model*

Ramirez and Falicov (1971) have also proposed a promotional type model for the $\alpha \rightleftarrows \gamma$ transition. They assume that the f state in cerium exists as a narrow singly degenerate level lying about 0.1 eV to 0.2 eV above the Fermi level. One of the important features of their model is the inclusion of the Coulomb interaction between the electrons in the f states and electrons or holes in the conduction band. (The mixing or hybridization interaction of states is neglected). This Coulomb interaction, which they label G, acts to lower the free energy of the system by an amount $E = -NGn_c^2$ where N is the number of atoms and n_c is the occupancy of the f level. The energy E provides a cooperative feedback mechanism to drive the transition by counteracting the normal increase in free energy which would result when electrons are raised from the Fermi level to the f level. Various electronic entropy terms are also included providing a temperature dependence to the free energy. The result is a first order transition, which, by allowing the energy of the f level to increase linearly with pressure, ends in a critical point in the temperature–pressure phase diagram (figs. 4.1 and 4.2).

The Ramirez–Falicov model was not meant to be any more than a qualitative explanation of the main features of the transition. To improve the theory Alascio et al. (1973) and Olmedo et al. (1973) have extended the model to include hybridization between the f states and conduction band states. The result is a broadening of the f level so that the low energy tail of the f level lies partly below the Fermi level. The partial valence of α-Ce could thus be explained in the same manner as in the Coqblin–Blandin model.

One of the criticisms of the Ramirez–Falicov theory is that the free energy expressions at a given compression are parameterized in terms of pressure rather than volume (Hirst, 1974; Miyamoto and Nagamiya, 1975). A volume dependence is more natural in terms of the microscopic theory and also allows a direct expression for elastic energy. Miyamoto and Nagamiya have therefore reformulated the Ramirez–Falicov model in terms of a volume dependence and

have included an elastic energy term. One basic difference is their interpretation of the interaction G. They feel that G gives rise to an interaction between neighboring atoms through their respective conduction band hole clouds and that the interaction term, which is of the form $(\frac{1}{2})Gn_c^2$, is positive in α-Ce and negative in γ-Ce. Ramirez and Falicov treated the conduction band holes as completely itinerant and G as a constant. Numerical results by Miyamoto and Nagamiya, like those of Ramirez and Falicov, result in an integral valence for α-Ce at low temperatures.

Khomskii and Kocharjan (1976) have also discussed the interaction G, which they extend to include correlations or exciton pairing between f holes and conduction electrons. They show that this correlation leads to an extra broadening of the f states which, unlike the broadening due to hybridization of f states, increases as the f state approaches the Fermi level. The broadening is due to rapid fluctuations of the electron between f and conduction band states. Depending on the strength of the interaction G three situations can result: (1) a weak interaction leads to a gradual transition; (2) a stronger G leads to two successive first order transitions as in $\gamma \rightarrow \alpha \rightarrow \alpha'$; and (3) a still stronger G leads to one first order transition. In the second case the α phase is expected to have an intermediate valence characterized by valence or spin fluctuations. Typical values for the extra broadening of the f state were estimated to be 0.04 to 0.1 eV.

5.4 *Hirst model*

Hirst (1974) has proposed a theory for the transition in cerium and other 4f substances consistent with his ionic model for magnetic impurities in metals (Hirst, 1970). Briefly, the ionic model describes a metal which contains ions with localized shells such as 4f levels. Each localized shell has several electron energy levels corresponding to different integral occupations of the shell. An integral occupation is expected to be extra stable due to Hund's rules correlations. In effect, this means that there will be an energy gap E_{exc} which must be overcome before mixing interactions can occur between ions in the $4f^n$ and $4f^{n-1}$ state. In cerium E_{exc} is expected to change sign during the transition from γ to α, that is, the energy required to make an interconfigurational excitation from $4f^1$ to $4f^0$ becomes negative. One consequence is that $|E_{exc}|$ becomes very small at the transition and a mixing interaction can therefore occur. When this happens the individual ions will undergo rapid interconfigurational fluctuations (ICF) in which the occupancy of adjacent ions will fluctuate between integral values ($4f^0$ to $4f^1$ at a rate Δ/h where Δ is the width of the hybridized 4f level). α-Ce is expected to correspond to an ICF state while γ-Ce is expected to be a pure configurational state of integral occupation. The mechanism of the transition in cerium was expected to depend on several competing cooperative tendencies. These included an elastic term, an interaction G of the Ramirez–Falicov type, and a term providing for changes in the Fermi level with the number of conduction electrons. However, Hirst felt that the interaction G is reduced drastically by the tendency of the conduction electrons to correlate

with the localized f states and that the elastic term was therefore a more important part of the transition mechanism. Also, the elastic term, in the form Hirst expresses it, tends to result in only a partial collapse in agreement with the partial valence of α-Ce.

5.5 *Comparisons with experiment*

All of the models considered so far are based on the promotional idea. However, there are some experimental results which appear to conflict with this idea. One of these is the placement of the 4f level in γ-cerium at 0.9 eV below the Fermi level by X-ray photoemission studies (see section 4.9). If these results are correct then about 20 kcal/mole of energy would be required to lift the f level to the Fermi energy to allow transfer of electrons to the conduction band. The elastic work necessary to compress a γ-Ce sample to α-Ce at room temperature is two orders of magnitude smaller. This comparison is obviously an oversimplification but it serves to emphasize the importance of the proximity of the f level to the Fermi level in any promotional theory. Also, as noted in section 4.9, a 4f level could lie ~ 0.1 eV below the Fermi level but it would not be detected by the X-ray photoemission studies.

One might expect that the position of the f states could be determined by energy band studies. Such calculations have been performed for cerium by a variety of techniques (Kmetko, 1971; Mukhopadhyay, 1972; Rao et al., 1975; Herbst et al., 1972 and 1976). However, the results are uncertain and conflicting, with a range of over 2 eV in the position of the 4f band.

Some other results which appear to be inconsistent with the promotional idea are positron annihilation and angular correlation experiments which have shown that the number of valence electrons remains near 3 not only in γ-Ce but also in α- and α'-Ce. One attempt has been made to account for these results using the spin compensation idea (Edelstein, 1968). Apparently, this explanation would be that in α- (and α'-) Ce the number of f electrons remains near one but spin compensation by the conduction electrons gives an appearance in other types of measurements of a partial or complete transfer of f electrons to the conduction bands. This explanation is not very satisfying. It implies that the proposed low energy tail of the degenerate virtual band state of α-Ce intersects the Fermi energy just at the right position to allow exactly one f electron to occupy the portion of the tail below the Fermi level. Also, in this case there would be no apparent explanation of the decrease in atomic volume associated with $\gamma \rightarrow \alpha$ and $\alpha \rightarrow \alpha'$ transformations.

5.6 *Mott transition of f states*

A different approach from the promotional idea is that the 4f state itself becomes delocalized during the $\gamma \rightarrow \alpha$ transition. There are two possible ways that the 4f state could delocalize: by a Mott transition or by some type of hybridization mechanism. The idea of 4f delocalization by a Mott transition was

first expressed as a possible means to explain positron annihilation results (see section 4.5), but the main objection to this explanation has been that the 4f orbitals on adjacent ions were not expected to have a sufficient spatial extent (Herman and Skillman, 1963) to allow the overlap necessary for delocalization (Gempel et al., 1972). More recently Johansson (1974) has questioned the validity of this objection and has set forth some arguments in favor of the idea. In order for a 4f level to undergo a Mott transition the effective intra-atomic repulsion U between f electrons must be comparable to the 4f band width. Johansson estimates U to be around 3 or 4 eV and the 4f bandwidth to be around 1 eV. This bandwidth is larger by almost two orders of magnitude than the widths usually assumed in the promotional theories. Johansson maintains however that the f bandwidths are extremely difficult to calculate due to correlations in both the f states and the conduction band and also due to the large sensitivity of the f states to the assumed atomic potential. In addition the renormalized-atom approach for cerium (Herbst et al., 1972) indicates bandwidths of 0.4 eV for γ-Ce and, for the increased density of α-Ce, a value of 1 eV would not be unreasonable. A second argument by Johansson is one in which he uses cohesive energy values to refute the promotional theories. Comparisons of cohesive energies of trivalent and tetravalent elements close to cerium in the periodic table show that an absurdly high value of around 60 ± 20 kcal/mole would be required to change a $4f^1\ 5d^1\ 6s^2$ configuration in cerium metal to a $5d^2\ 6s^2$ configuration. Also the melting temperature of a tetravalent element having a $s^2\ d^2$ configuration is typically about 2000 K but α-Ce has a much lower melting point of around 940 K. It should be noted, however, that the trivalent and tetravalent configurations are not necessarily of the above form. A configuration consistent with melting points and heat of sublimation for γ-Ce is $4f^{0.6}\ 5d^{0.6}\ 5p^{0.1}\ 6s^{1.7}$ for the valence band electrons and a 4f localized level (Gschneidner, 1971). Based on some rules to correlate the change in melting point with changes in configuration (Gschneidner, 1971) a consistent guess for the configuration of α-Ce might be $4f^{0.7}\ 5d^{0.9}\ 5p^{0.1}\ 6s^{2.0}$ for the valence band electrons and a $4f^{0.3}$ localized level.

The Mott transition idea agrees well with most experimental results. Positron experiments can be explained by noting that the charge concentration in the 4f band in α-Ce lies mostly near the positive ion cores and would not be expected to annihilate positrons. Results of X-ray absorption spectra and chemical shift of X-ray lines (see section 4.9) seem to indicate, however, that there is a definite transfer of electrons to the conduction band during the transition to α-Ce. These conclusions are based on similarities in the results from metallic γ- (or β-) and α-Ce to the results obtained from trivalent and tetravalent compounds of cerium. The results of the chemical shift of X-ray lines can be reconciled to the Mott transition idea by noting that all these results really show is that there are similar numbers of localized electrons and bonding electrons in α-Ce and tetravalent cerium compounds. Nothing can be said about the actual form of the bonding electrons, that is, whether they are f or f-like versus s- or d-like. The absorption spectra results are more specific, showing no evident features in the spectrum of

α-Ce to indicate the presence of a 4f band. Whether f band features would be expected in the case of a hybridized $(4f\ 5d\ 5p\ 6s)^4$ band is not obvious.

5.7 *Hybridization of f states*

The effect of hybridization of the 4f states with the conduction band states was ignored by Johansson in his discussion of a Mott transition of f-states. Yet the effect appears to be important. For example, in the band picture (Slater, 1968) magnetic ordering would be expected to result for a sufficiently narrow band such as the f band of α-Ce. Hybridization can explain the absence of magnetic ordering by the larger effective band width which would result from the inclusion of the broad s and d states in a hybridized band. This explanation has been offered as the reason for the absence of magnetic ordering in α-U (Koelling and Freeman, 1973) and other early actinides (Jullien et al., 1972) and in α- and α'-Ce (Hill and Kmekto, 1975). Melting point and sublimation studies (Gschneidner, 1971) and energy band studies (Kmekto, 1971) have shown that there is substantial f-like character in the valence band of all the phases of cerium. For example, Gschneidner (1971) has proposed a configuration for γ-Ce of near $4f^{0.6}\,5d^{0.6}\,5p^{0.1}\,6s^{1.7}$. Thus in addition to the one localized f electron there is a 0.6 hybridized or band-like f electron. During the transition to α-Ce the amount of f-like character in the valence band would be expected to increase at the expense of the localized electrons. From positron experiments (see section 4.5) one would not expect significant changes in the total amount of s, p, and d character. The question of whether this picture is a type of promotional theory depends on whether the transfer of localized f electrons to the valence band occurs due to a crossing of the Fermi level by the localized f state and also on whether such a transfer can increase only the f-like portion of the hybridized band. Some type of direct delocalization by hybridization or a Mott transition seems more likely although the mechanism of a transition due to hybridization is not obvious. The picture of hybridization as giving rise to a virtual bound state (Coqblin and Blandin, 1968) works well for β- and γ-Ce and is consistent with the occurrence of a Kondo effect in β-Ce. But this is a localized approach in which the f states on adjacent atoms are treated as independent; this approach is not valid for α-Ce. Bahurmuz and Zuckermann (1974) have extended the Coqblin–Blandin model to take lattice periodicity into account but only to the extent of showing that the localized states can give rise to spin fluctuations or paramagnons; the f states are still assumed to be localized. Conversely, energy band studies can illustrate hybridization graphically (e.g. the elimination of band crossing degeneracies), but proper calculations for localized, magnetic states are difficult. Energy band calculations are thus more appropriate for α-Ce than γ- or β-Ce. The two approaches lead to wide differences in the expected width of localized and hybridized states. For example, Coqblin and Blandin (1968) expect a half width of 0.02 eV for the virtual level in γ-Ce while Kmekto (1971) calculates a width of about 0.6 eV for the same state. The problem of a suitable transition mechanism may come to light when these differences are resolved.

5.8. *Conclusion*

To summarize, it appears that there is as yet no adequate model to explain the $\gamma \rightleftarrows \alpha$ transition in cerium. A theory in which delocalization of the 4f states occurs simultaneously with a large hybridization effect appears closest to explaining all of the experimental results, but perhaps only because such a theory is not as yet well defined. A satisfactory theory should provide a mechanism for the transition, and this mechanism should not be based on certain assumptions about, for example, the variation in 4f level or elastic energy with volume, without an explanation of the reasons for these assumptions. We feel that when this problem is solved our understanding of the nature of the 4f electron will be advanced considerably.

Recent developments

The controversy concerning the structure of α'-Ce has continued into 1977 (see §2.2). Schaufelberger (1976) presented evidence that this phase is hexagonal, but the data of Zachariasen (1977) and Zachariasen and Ellinger (1977) and their analysis of Schaufelberger's experimental data leave little doubt that α'-Ce is orthorhombic. Zachariasen and Ellinger also present additional results concerning the metastable monoclinic α''-Ce (see §2.5). X-ray studies (Endo et al., 1977) and resistance measurements (Fujioka et al., 1977) at much higher pressures reveal that α'-Ce transforms to a tetragonal modification above 12 GPa, with $a = 2.92$ and $c = 4.84$ Å above 17.5 GPa. This structure is quite similar to α''-Ce with $a_t \cong b_m \cong c_m$, $c_t \cong a_m$ and $\beta_t(90°) \cong \beta_m = 91.70$, where t = tetragonal and m = monoclinic. This high pressure transformation is probably the same phase transformation detected by Stager and Drickamer (1964) (see §2.1).

Inelastic neutron scattering from both γ- and α-Ce under pressure was investigated by Rainford et al. (1977). Their results indicate that the s–f exchange interaction, J_{sf}, in γ-Ce increases with increasing pressure as predicted by Coqblin. Also they find no experimental evidence for a magnetic contribution to the inelastic neutron scattering intensity of α-Ce. They conclude that if there is some residual 4f electronic character in α-Ce its dynamical response is too weak or diffuse to be observed in their experiment.

References

Adams, L.H. and B.L. Davis, 1962, Proc. Nat. Acad. Sci. U.S. **48**, 982.

Alascio, B., A. Lopez, and C.F.E. Olmedo, 1973, J. Phys. F **3**, 1324.

Anderson, P.W., 1961, Phys. Rev. **124**, 41.

Anderson, P.W., 1967, Phys. Rev. **164**, 352.

Baer, Y. and G. Busch, 1973, Phys. Rev. Lett. **31**, 35.

Baer, Y. and G. Busch, 1974, J. Electron Spectrosc. Related Phenom. **5**, 611.

Bahurmuz, A.A. and M.J. Zuckermann, 1974, Solid State Comm. **15**, 1225.

Beaudry, B.J. and P.E. Palmer, 1974, J. Less-Common Metals **34**, 225.

Beecroft, R.I. and C.A. Swenson, 1960, J. Phys. Chem. Solids **15**, 234.

Bridgman, P.W., 1948, Proc. Amer. Acad. Arts Sci. **76**, 71.

Bridgman, P.W., 1951, Proc. Amer. Acad. Arts Sci. **79**, 149.

Bridgman, P.W., 1952, Proc. Amer. Acad. Arts Sci. **81**, 165.

Brodsky, M.B. and R.J. Friddle, 1973, Phys. Rev. B **7**, 3255.

Burgardt, P., K.A. Gschneidner, Jr., D.C. Koskenmaki, D.K. Finnemore, J.O. Moorman, S. Legvold, C. Stassis and T.A. Vyrostek, 1976a, Phys. Rev. B **14**, 2995.

Burgardt, P., S. Legvold, J. H. Queen and K.A. Gschneidner, Jr., 1976b, Magneto-Resistivity of Beta-Cerium, in: J.J. Becker, G.H. Lander and J.J. Rhyne, eds., Magnetism and Magnetic Materials–1975, AIP Conf. Proc. No. 29 (Amer. Inst. Physics, New York) pp. 527–528.
Burr, C.R. and S. Ehara, 1966, Phys. Rev. **149**, 551.
Clinard, F.W., Jr., 1969, J. Appl. Phys. **40**, 3067.
Colvin, R.V., S. Arajs and J. M. Peck, 1961, Phys. Rev. **122**, 14.
Conway, M.M. and N.E. Phillips, 1974, Low-Temperature Heat Capacity of α- and β-Cerium, in: K.D. Timmerhaus, W.J. O'Sullivan, E.F. Hammel, eds., Low Temperature Physics – LT13, vol. 2 (Plenum Press, New York) pp. 629–632.
Coqblin, B. and A. Blandin, 1968, Advan. Phys. **17**, 281.
Davis, B.L. and L.H. Adams, 1964, J. Phys. Chem. Solids **25**, 379.
DeGennaro, S. and E. Borchi, 1973, Phys. Rev. Lett. **30**. 377.
Dialer, K. and W. Rothe, 1955, Z. Elektrochem. **59**, 970.
Edelstein, A.S., 1968, Phys. Rev. Lett. **20**, 1348.
Edelstein, A.S., 1970, Solid State Comm. **8**, 1849.
Ellinger, F. H. and W. H. Zachariasen, 1974, Phys. Rev. Lett. **32**, 773.
Elliott, R.O. and W.N. Miner, 1967, Trans. Met. Soc. AIME **239**, 166.
Evans, D.S. and G.V. Raynor, 1962, J. Less-Common Metals **4**, 181.
Evdokimova, V.V. and Yu. S. Genshaft, 1964, Fiz. Tverd. Tela **6**, 2449; Eng. transl., Sov. Phys. – Solid State **6**, 1941.
Franceschi, E. and G.L. Olcese, 1969, Phys. Rev. Lett. **22**, 1299.
Friedel, J., 1956, Can. J. Phys. **34**, 1190.
Friedel, J., 1958, J. Phys. Radium **19**, 573.
Gempel, R.F., D.R. Gustafson and J.D. Willenberg, 1972, Phys. Rev. B, **5**, 2082.
Gonikberg, M.G., G.P. Shakhovskhoi and V.P. Butuzov, 1957, Zhur. Fiz. Khim. **31**, 350.
Goodrich, R.G. and G.E. Everett, 1966, Phys. Rev. **141**, 541.
Grimberg, A.J.T., C.J. Schinkel, and A.P.L.M. Zandee, 1972, Solid State Comm. **11**, 1579.
Gschneidner, K.A., Jr., 1964, Solid State Phys. **16**, 275.
Gschneidner, K.A., Jr., 1965, An Experimental Approach to a Simplified Band Structure of the Rare Earth Metals, in: Eyring, L. ed., Rare Earth Research III (Gordon and Breach, New York) pp. 153–185.
Gschneidner, K.A., Jr., 1966, The Application of Vacuum Metallurgy in the Purification of Rare-Earth Metals, in: Bianchi L.M. ed., Transactions Vacuum Metallurgy Conference 1965 (American Vacuum Society; Boston) pp. 99–135.
Gschneidner, K.A., Jr., 1971, J. Less-Common Metals **25**, 405.
Gschneidner, K.A. Jr. and R. Smoluchowski, 1963, J. Less-Common Metals **5**, 374.
Gschneidner, K.A., Jr. and J.T. Waber, 1964, J. Less-Common Metals **6**, 354.
Gschneidner, K.A., Jr., R.O. Elliott and R.R. McDonald, 1962, J. Phys. Chem. Solids **23**, 555.
Gschneidner, K.A., Jr., P. Burgardt, S. Legvold, J. O. Moorman, T.A. Vyrostek and C. Stassis, 1976 J. Phys. F **6**, L49.
Gustafson, D.R. and A.R. Mackintosh, 1964, J. Phys. Chem. Solids **25**, 389.
Gustafson, D.R., J.D. McNutt and L.O. Roellig, 1969, Phys. Rev. **183**, 435.
Herbst, J.F., D.N. Lowy, and R.E. Watson, 1972, Phys. Rev. B **6**, 1913.
Herbst, J.F., R.E. Watson and J.W. Wilkins, 1976, Phys. Rev. B **13**, 1439.
Herman, F. and S. Skillman, 1963, Atomic Structure Calculations (Prentice-Hall, Englewood Cliffs, New Jersey).
Herman, R. and C. A. Swenson, 1958, J. Chem. Phys **29**, 398.
Hill, H.H. and E.A. Kmetko, 1975, J. Phys. F **5**, 1119.
Hirst., L.L., 1970, Phys. Kondens. Mat. **11**, 255.
Hirst, L.L., 1974, J. Phys. Chem. Solids **35**, 1285.
Hull, A.W., 1921, Phys. Rev. **18**, 88
Itskevick, E.S., 1962, Zh. Eksp. Teor. Fiz. **42**, 1173; Eng. transl., Sov. Phys. – JETP **15**, 811.
James, N.R., S. Legvold and F.H. Spedding, 1952, Phys. Rev. **88**, 1092.
Jayaraman, A., 1965, Phys. Rev. **137**, A179.
Johansson, B., 1974, Phil. Mag. **30**, 469.
Jullien, R., E. Galleani d'A gliano, and B. Coqblin, 1972, Phys Rev. B **6**, 2139.
Jullien, R., M.T. Béal-Monod and B. Coqblin, 1974, Phys. Rev. B **9**, 1441.
Kaiser, A.B. and S. Doniach, 1970, Int. J. Magnetism **1**, 11.
Katzman, H. and J.A. Mydosh, 1972, Phys. Rev. Lett. **29**, 998.
Kaufman, L., S.V. Radcliffe, S.A. Kulin, M. Shatz, J. Kafalas, L.E. Tanner, H. Bernstein, A. Leyenaar and J.S. Harvey, 1961, "Research and Development on High-Pressure-High Temperature Metallurgy," WADD-TR-60-893, Wright Air Development Division, U.S. Air Force, Wright-Patterson Air Force Base, Ohio (August 1961), pp. 132–7.
Kevane, C.J., S. Legvold and F.H. Spedding, 1953, Phys. Rev. **91**, 1372.
Khomskii, D.I. and A.N. Kocharjan, 1976, Solid State Comm. **18**, 985.
Khvostantsev, L.G., L.F. Vereshchagin, and E.G. Shulika, 1973, High Temp. – High Press. **5**, 657.
King, E. and I.R. Harris, 1972, J. Less-Common Metals **27**, 51.
King, E., J.A. Lee, I.R. Harris and T.F. Smith, 1970, Phys. Rev. B **1**, 1380.
Kmetko, E.A., 1971, Calculated Effects of Compression Upon the Band Structure and Density of States of Several Metals, in: L.H.

Bennett, ed., Electronic Density of States, U.S. Nat. Bur. Stand., Special Publ. 323 (U.S. Government Printing Office, Washington, D.C.) pp. 67–73.
Koch, C.C. and C.J. McHargue, 1968, Acta Met. **16**, 1105.
Koch, C.C. and M.L. Picklesimer, 1967, Trans. Met. Soc. AIME **239**, 759.
Koelling, D.D. and A.J. Freeman, 1973, Phys. Rev. B **7**, 4454.
Koskimaki, D.C. and K.A. Gschneidner, Jr., 1974, Phys. Rev. B **10**, 2055.
Koskimaki, D.C. and K.A. Gschneidner, Jr., 1975, Phys. Rev. B **11**, 4463.
Koskimaki, D.C., K.A. Gschneidner, Jr. and N.T. Panousis, 1974, J. Cryst. Growth **22**, 225.
Krishna-murthy, H.R., K.G. Wilson, and J.W. Wilkins, 1975, Phys. Rev. Lett. **35**, 1101.
Kutsar, A.R., 1974, Phase Diagram and Characteristics of the $\gamma \leftrightarrow a$ Transformation of Cerium at High Hydrostatic Pressure, in: Ivanov, O.S. ed., Struktura faz, Fazovye Prevrashcheniya i Diagrammy Sostoyaniya Metallicheskikh Sistem (Izdatel'stvo Nauka, Moscow) pp. 76–80.
Lawson, A.W. and T.-Y. Tang, 1949, Phys. Rev. **76**, 301.
Léger, J.M., 1976, Phys. Lett. 57A, 191.
Léger, J.M., J.P. Bastide, H. Massat and Ph. Schaufelberger, 1975, High Temp. – High Press. **7**, 351.
Likhter, A. I. and V. A. Venttsel', 1962, Fiz. Tverd. Tela **4**, 485; Eng. transl., Sov. Phys. – Solid State **4**, 352.
Likhter, A.I., Yu. N. Ryabinin and L.F. Vereshchagin, 1957, Zh. Eksp. Teor. Fiz. **33**, 610; Eng. transl., Sov. Phys. – JETP **6**, 469.
Liu, S.H., P. Burgardt, K.A. Gschneidner, Jr. and S. Legvold, 1976, J. Phys. F. **6**, L55.
Livshits, L.D., Yu. S. Genshaft and Yu. N. Ryabinin, 1960, Fiz. Metal. Metalloved. **9**, 726.
Livshits, L.D., Yu. S. Genshaft and V.K. Markov, 1962, Zh. Eksp. Teor. Fiz. 43, 1262; Eng. transl., Sov. Phys. – JETP **16**, 894.
Lock, J.M., 1957, Proc. Phys. Soc. **70B**, 566.
Lounasmaa, O.V., 1964, Phys. Rev. **133**, A502.
MacPherson, M.R., G.E. Everett, D. Wohlleben, M.B. Maple 1971, Phys. Rev. Lett. **26**, 20.
McHargue, C.J. and H.L. Yakel, Jr., 1960, Acta Met. **8**, 637.
McHargue, C.J., H.L. Yakel, Jr. and L.K. Jetter, 1957, Acta Crystallogr. **10**, 832.
McWhan, D.B., 1970, Phys. Rev. B **1**, 2826.
Millhouse, A.H. and A. Furrer, 1974, Solid State Comm. **15**, 1303.
Miyamoto, K. and T. Nagamiya, 1975, J. Phys. Soc. Jap. **38**, 726.
Mosander, C.G., 1827, Ann. Phys. (Leipzig), (formerly Pogg. Ann.) **11**, 406.
Mukhopadhyay, G., 1972, J. Phys. F. **2**, 450.
Murao, T. and T. Matsubara, 1957, Progr. Theor. Phys. (Kyoto) **18**, 215.
Nicolas-Francillon, M. and D. Jerome, 1973, Solid State Comm. **12**, 523.
Olmedo, C.F.E., A.Lopez, and B. Alascio, 1973, Solid State Comm. **12**, 1239.
Ottewell, D., E.A. Stewardson and J.E. Wilson 1973, J. Phy. **B6**, 2184.
Panousis, N.T. and K.A. Gschneidner, Jr., 1970, Solid State Commun. 8, 1779.
Panousis, N.T. and K.A. Gschneidner, Jr., 1972, Phys. Rev. B **5**, 4767.
Parkinson, D.H. and L.M. Roberts, 1957, Proc. Phys. Soc. B **70**, 471.
Pauling, L., 1950, unpublished information quoted by A.F. Schuch and J.H. Sturdivant, J. Chem. Phys. **18**, 145.
Pavlov, V.S. and V.A. Finkel, 1967, Fiz. Metal. Metalloved. **24**, 1123; Eng. transl., Phys. Metals Metallogr. **24**, [6], 137.
Pavlov, V.S. and N.D. Rybal'chenko, 1970, Izv. Akad. Nauk SSSR, Metal., [1], 224; Eng. transl., Russ. Met. [1], 151.
Peterson, D.T. and E.N. Hopkins, 1964, "Electropolishing the Rare-Earth Metals," IS-1036 Ames Laboratory, Iowa State University, Ames, Iowa, (October 1964).
Phillips, N.E., J.C. Ho, and T.F. Smith, 1968, Phys. Lett. **27A**, 49.
Ponyatovskii, E.G., 1958, Dokl. Akad. Nauk SSSR **120**, 1021.
Probst, C. and J. Wittig, 1975, Superconductivity of Alpha Cerium, in: M. Krusius and M. Vuorio, eds., Low Temperature Physics – LT14, Vol. 5 (North-Holland/American Elsevier, Amsterdam/New York), pp. 453–456.
Ramesh, T.G., A.S. Reshamwala and S. Ramaseshan, 1974a, Pramana **2**, 171.
Ramesh, T.G., A.S. Reshamwala and S. Ramaseshan, 1974b, Solid State Comm. **15**, 1851.
Ramirez, R. and L.M. Falicov, 1971, Phys. Rev. **B3**, 2425.
Rao, R.S., C.K. Majumdar, B.S. Shastry, and R.P. Singh, 1975, Pramana **4**, 45.
Rashid, M.S. and C.J. Altstetter, 1966, Trans. Met. Soc. AIME **236**, 1649.
Roberts, L.M. and J.M. Lock, 1957, Phil. Mag. **2**, 811.
Roman, W.A., 1966, J. Less-Common Metals **10**, 150
Rosen, M., 1969, Phys. Rev. **181**, 932.
Schaufelberger, Ph. and H. Merx, 1975, High Temp.–High Press. **7**, 55.
Schindler, A.I. and M.J. Rice, 1967, Phys. Rev. **164**, 759.
Schuck, A.F. and J.H. Sturdivant, 1950, J. Chem. Phys. **18**, 145.
Shaburov, V.A., A.E. Sovestnov and O.I. Sumbaev, 1974, Phys. Lett. **49A**, 83.
Shimura, K., 1969, Jap. J. Appl. Phys. **8**, 870.
Slater, J.C., 1968, J. Appl. Phys. **39**, 761.
Smith, R.D. and E. Morrice, 1964, U.S. Bur. Mines, Rept. Invest. No. 6480.
Stager, R.A. and H.G. Drickamer, 1964, Phys. Rev. **133**, A830.
Spedding, F.H., J.J. McKeown and A.H. Daane, 1960, J. Phys. Chem. **64**, 289.
Spedding, F.H., J.J. Hanak and A.H. Daane, 1961, J. Less-Common Metals **3**, 110.

Stassis, C.J., 1974, Unpublished information quoted by D.C. Koskimaki and K.A. Gschneidner, Jr., Phys. Rev. B **10**, 2055.
Trombe, F. and M. Foex, 1944, Ann. Chim. (Paris) **19**, 417.
Trombe, F. and M. Foex, 1947, Rev. Met. **44**, 349.
Tsang, T.-W.E., K.A. Gschneidner, Jr., D.C. Koskenmaki and J.O. Moorman, 1976, Phys. Rev. B **14**, 4447.
Vereshchagin, L.F., A.A. Semerchan and S.V. Popova, 1961, Dokl. Akad. Nauk SSSR **138**, 1059; Eng. transl., Sov. Phys. – Doklady **6**, 488.
Voronov, F.F., L.F. Vereshchagin and V.A. Goncharova, 1960, Dokl. Akad. Nauk SSSR **135**, 1104; Eng. transl., Sov. Phys. – Doklady **135**, 1280.
Weiner, R.T. and G.V. Raynor, 1959, J. Less-Common Metals **1**, 309.
Wilkins, J.F., J.G. Clark and T.E. Leinhardt, 1962, Bull. Am. Phys. Soc. 7, 579.
Wilkinson, M.K., H.R. Child, C.J. McHargue, W.C. Koehler and E.O. Wollan, 1961, Phys. Rev. **122**, 1409.
Wittig, J., 1968, Phys. Rev. Lett. **21**, 1250.
Zachariasen, W.H., 1949, Unpublished information quoted by A.W. Lawson and T.-Y. Tang, Phys. Rev. **76**, 301.
Zachariasen, W.H. and F.H. Ellinger, "The Crystal Structures of Cerium Metal at High Pressure", LA-6251, Los Alamos Scientific Laboratory, Los Alamos, New Mexico (April 1976)

References to section 6

Endo, S., H. Sasaki and T. Mitsui, 1977, J. Phys. Soc. Jap. **42**, 882.
Fujioka, N., S. Endo and N. Kawai, 1977, Phys. Lett. **60A**, 340.
Rainford, B.D., B. Buras and B. Lebech, 1977, Physica **86–88B**, 41.
Schaufelberger, Ph., 1976, J. Appl. Phys. **47**, 2364.
Zachariasen, W.H., 1977, J. Appl. Phys. **48**, 1391.
Zachariasen, W.H. and F.H. Ellinger, 1977, Acta Cryst. **A33**, 155.

Handbook on the Physics and Chemistry of Rare Earths, edited by K.A. Gschneidner, Jr. and L. Eyring

Chapter 5

LOW TEMPERATURE HEAT CAPACITY OF THE RARE EARTH METALS

Lorna J. SUNDSTRÖM
Department of Physics, University of Helsinki, Siltavuorenpenger 20D, SF-00170 Helsinki 17, Finland

Contents

Symbols

a' = magnetic interaction parameter
C_E = electronic heat capacity
C_L = lattice heat capacity
C_N = nuclear heat capacity
C_M = magnetic heat capacity
C_P = total heat capacity at constant pressure
c_n = coefficient of T^{-n} in expansion of nuclear heat capacity on the high temperature side of the Schottky peak
E_{cry} = crystalline field interaction
E_{ex} = exchange interaction energy
eQ' = nuclear quadrupole moment
g_I = nuclear splitting factor
H_{eff} = effective magnetic hyperfine field
$\mathcal{H}$ = the hamiltonian
J_z = expectation value of J_z etc.
k_B = Boltzmann constant
P = quadrupole coupling constant
T_c = superconducting transition temperature, in particular for La and Ce
T_N = Néel temperature
W_m = energy eigenvalues of the nuclear hamiltonian
γ = coefficient of T in electronic heat capacity
$\theta_D(0)$ = Debye temperature at 0 K
μ_B = Bohr magneton
μ_I = nuclear magnetic moment
μ_N = nuclear magneton

1. Introduction

1.1. *General*

The rare earth metals abound in magnetic transitions of one kind or another, which strongly influence the heat capacities of these metals. Thus we might expect to find support for the theories put forward to explain the complex magnetic behaviour of these metals through heat capacity measurements. In non-magnetic metals we find only lattice (C_L) and electronic (C_E) contributions. In magnetic metals, we have an additional contribution from magnetic spin waves (C_M), and in the case of even–odd nuclei at very low temperatures a nuclear Schottky heat capacity (C_N) is observed. The effects are described in some detail below. Unfortunately, without guidance from theory or other types of experiment, it is not possible to determine unambiguously the various contributions to the heat capacity. To further complicate matters, early specimens of the rare earth metals generally contained contaminating elements, such as oxygen and hydrogen. These give rise to impurity ordering effects which mask the contributions of interest from the bulk metal at low temperatures (e.g. gadolinium oxide, section 3.1 below).

By "low temperature", we mean here temperatures below 30 K. Because of technical difficulties in making runs from 4.2 K to around 30 K, and also because of the unreliability of early temperature scales in this range, the early, pre-1960 work concentrated on the broader and more general behaviour of the lanthanide metals up to room temperature or below 4.2 K. This left a regrettable gap in the heat capacity measurement. However, with increasing technical skills these earlier problems have been surmounted and the 1960's saw a series of results in this intermediate "low temperature" region by Lounasmaa and co-workers. For experimental details one can consult Lounasmaa (1966a) and the Proceedings of the 1966 Low Temperature Calorimetry Conference. In the late 1960's and early 1970's the development of adiabatic demagnetization cryostats (e.g. Krusius et al., 1969; Collan et al., 1970a,b) made possible very low temperature ("v.l.t.") measurements in the temperature range 0.02 K to 0.8 K which have given indisputably fine sets of parameters for the nuclear hyperfine interactions of the lanthanide metals (see section 1.6 below).

The low temperature heat capacity of metals has been reviewed by Phillips (1971), who presented a detailed discussion of the state of the theory for the various contributions to the heat capacity. We shall therefore content ourselves here with highlighting only those aspects relevant to the lanthanide metals. In his review, Phillips did not go into details of the analyses of the experimental results for the lanthanides, although his table 23 presents a useful tabulation of references to the then available experimental results.

In the 1960's, when the bulk of the available results on the low temperature heat capacities of the lanthanides was determined, it was assumed that we could systematically divide these metals into two groups comprising the "light metals" from La to Eu and the "heavy metals" from Gd to Lu. The former is perhaps a less coherent grouping than the latter, with Ce and Eu forming face-centred cubic (fcc) and body-centred cubic (bcc) structures, respectively, while La, Pr,

Nd, and with additional modifications Sm, form the so-called double hexagonal structure (d-hcp) with atomic layer ordering along the c-direction following the sequence ABACAB . . . (cf. ch. 2, section 6). The metals of the second group all crystallise in the hexagonal close-packed (hcp) structure (except for divalent Yb) with c/a ratios ranging within the limits set by 1.5692 for Er and 1.5910 for Gd.

1.2. *Lattice heat capacity*

The lattice heat capacity, C_L, at low temperatures can be expanded in odd powers of T, where the first term is often referred to as the Debye T^3 term. Thus

$$C_L = A_3T^3 + A_5T^5 + \ldots . \tag{5.1}$$

The coefficient $A_3 = \frac{12}{5}\pi^2R/\theta(0) = 234R/\theta^3(0)$ gives the Debye θ. At temperatures less than $\theta_0/50$, where θ_0 is the low temperature Debye θ, it is generally sufficient to consider the T^3 term only. If the other contributions to the heat capacity can be subtracted off, then one can express the lattice contribution in terms of an effective Debye temperature, $\theta_D(T)$, determined from tables of the Debye function (Beattie, 1926; Gopal, 1966). Alternatively, one might assume (Lounasmaa, 1964a) that $\theta_D(T)$ should display similar features throughout the lanthanide series; $\theta_D(T)$ remains constant up to about 5 K, drops through approximately 27 K, then passes through a shallow minimum to level off at higher temperatures. This is indicated by results on lanthanum (Lounasmaa and Sundström, 1967) and lutetium (Culbert, 1967; Gerstein et al., 1969). Since the Debye temperature is proportional essentially to atomic weight, one can interpolate between the θ_D values obtained for the non-magnetic metals lanthanum and lutetium, and hence determine C_L from tables of the Debye function.

Elastic constants measured as a function of temperature are available for most of the lanthanides in polycrystalline form (Rosen, 1967, 1968) and for Tb, Dy, Ho and Er single crystals (Palmer, 1970; Palmer and Lee, 1973; and du Plessis, 1976). For a summary of the elastic properties of the lanthanides reference can be made to Taylor and Darby (1972, section 2.4) and to ch. 8, section 9. If a suitable lattice dynamical model were devised, we should be able to calculate C_L from first principles. This was done for Gd, Dy and Er metals (Sundström, 1968), but at the time of these calculations, elastic constants were available only for polycrystalline samples at a few fixed temperatures. Nevertheless the results obtained did indicate that Lounasmaa's (1964a) interpolation idea was reasonable. With the elastic constant data available today it should be possible to calculate C_L for the entire region of interest, although this appears not to have attracted much attention, presumably because the uncertainty involved in separating off the contributions in experimental heat capacity results makes comparison with theory unrewarding as far as C_L is concerned.

1.3. *Electronic heat capacity*

The electronic heat capacity is expressed as $C_E = \gamma T$, where γ is related to the electronic density of states at the Fermi energy $N(E_F)$ through the relation

$$\gamma = \tfrac{1}{3}\pi^2 k_B^2 N(E_F). \tag{5.2}$$

Since the lanthanides all have the same outer electron configuration, namely $5s^25p^66s^25d^1$, it was assumed in the early work that one could take a constant value for γ, either the value for α-La (9.4 mJ/mole·K^2) or that for Lu (11.27 mJ/mole·K^2) or a suitable weighted average (10.5 mJ/mole·K^2).

An attempt was made to measure isotopically enriched specimens of ^{152}Sm (Lounasmaa and Veuro, 1972), but this gave a γ value of 13.5 mJ/mole·K^2, a value much higher than was expected. Thus, far from being resolved, the situation became murkier and more confused. On the theoretical side, non-relativistic and relativistic band calculations have been carried out for a number of the lanthanides (for a review of the energy band structure of the rare earths see Freeman, 1972, and ch. 3 of this book). Although the relativistic calculations give higher electronic density of states values than the non-relativistic ones, the γ values obtained still do not approach the large reported experimental values. To get a clearer picture of the situation we would need more measurements on high purity samples. Recent work on high purity solid state electro-transported metals (see below sections 3.1, 3.2, 3.4 and 3.7), rather than confirming our earlier assumptions, gives electronic terms closer to the band theory calculations. In addition, theoretical evidence has been found in favour of a lower value of γ in the ordered magnetic state than in the paramagnetic state; spin-polarised band calculations in gadolinium by Harmon and Freeman (1974) give $\gamma_{ferro} \approx 75\%\ \gamma_{para}$. This arises from splitting of the electronic density of states curve into spin-up and spin-down bands in such a way that the peak in the density of states curve, due mainly to the 5d electrons, is shifted relative to the Fermi level to give a lower net density of states $N(E_F)$. Thus the γ values of the magnetic metals at low temperatures should, at best, be only a corresponding fraction of those for non-magnetic lanthanum and lutetium. This would seem to indicate a need for re-evaluation of earlier experimental results.

1.4. *Magnetic heat capacity*

The chief source of all this confusion and apparent indecision lies in our inability to ascribe a definite form to the magnetic spin wave contribution to the heat capacity. A number of theories were introduced in the early 1950's, for a review of which reference should be made to Mackintosh and Møller (1972) or, for a review in brief, one may consult Lounasmaa and Sundström (1966). For the sake of completeness, we present in table 5.1 the temperature dependences of the various models.

There have been attempts to calculate the spin wave contribution to the heat capacity from inelastic neutron scattering data for Tb and Gd (Sedaghat and Cracknell, 1971; Stevens and Krukewich, 1973). The former found the power of T to increase with increasing temperature for gadolinium from $n = 1.56$ to $n = 2.3$, but no simple power law above 14 K. The latter investigators found $n \sim 1.5$ for terbium and gadolinium. Wells et al. (1974) have confirmed that for

TABLE 5.1
Temperature dependences in various models

Spin wave theory for a simple ferromagnet gives a quadratic magnon dispersion relation at very low temperatures in the long wave-length limit:	$C_M \sim T^{3/2}$ (cf. Bloch $T^{3/2}$ law)	(5.3)
For an antiferromagnet spin wave theory gives a linear magnon dispersion relation:	$C_M \sim T^3$	(5.4)
Magnetic anisotropy arising from the crystalline field introduces a finite gap in the magnon dispersion curve even in the long wave-length limit. Thus $E_g \sim (K_2 K_6^6)^{1/2}$, where K_2 and K_6^6 denote the usual anisotropy constants. For the ferromagnet with strong anisotropy, therefore:	$C_M \sim T^{3/2} \exp(-E_g/k_B T)$	(5.5)
Antiferromagnetic spiral structure can give a linear dispersion law, and inclusion of the activation gap gives exponential dependence:	$C_M \sim T^3 \exp(-E_g/k_B T)$	(5.6)
Cooper (1962) has derived a more complex expression for the case of dysprosium with uniaxial ordering in the basal plane below 85 K:	$C_M \sim (E_g/k_B T + 2 + 2k_B T/E_g) \exp(-E_g/k_B T)$, when $k_B T \ll E_g$	(5.7)
	$C_M \sim T$, when $k_B T \geq E_g$	(5.8)

Gd $n \sim 1.75$ and that any possible spin wave activation energy has a vanishingly small effect.

Shender (1974) has applied the Ising model to the situation found in praseodymium. In particular, through comparison with the excitation spectrum of low-energy Frenkel excitations, he is able to obtain either $C_M \sim T^3$ for $\epsilon_0(0) < T$ or $C_M \sim T^{3/2} \exp(-\epsilon_0(0)/kT)$ for $\epsilon_0(0) > T$, where $\epsilon_0(0)$ is the zeroth Fourier component of the excitation spectrum at 0 K. Further theoretical work has been done by Kimura (1970) who included a magnon–phonon interaction in the hamiltonian which then gives a solution in terms of coupled modes such that for weak coupling the magnon–phonon interaction introduces only a small contribution to the entropy and specific heat. For strong coupling, on the other hand, the addition to C_M at low temperatures due to magnon–phonon coupling, ΔC_M, is large. Furthermore, Kimura finds that the temperature dependences of C_M and ΔC_M are very different and in particular that the temperature dependence of ΔC_M depends also on the exchange and anisotropy constants. Thus it is not surprising that analysis of experimental results can yield a variety of proposed behaviours for C_M from metal to metal and from temperature range to temperature range. Thus to date, except for isolated cases, we cannot with certainty say that we have unambiguously separated off and analysed the magnetic contribution to the heat capacity of the lanthanide metals.

1.5. *Graphical analysis*

This would seem a good point at which to say a few words about graphical analysis of the heat capacity data. For the sake of argument, let us consider

$$C_p = \gamma T + aT^3 + AT^{-2} + C_M \tag{5.9}$$

with

$$C_M = KT^n. \tag{5.10}$$

In this way we can represent the dominant terms in each of the four contributions to the heat capacity. Graphical analysis (e.g. Morrison and Newsham, 1968) is carried out in essentially two stages. Firstly, at very low temperatures, assume that C_L is negligible compared to C_E and C_N. Then consider

$$C_pT^2 = \gamma T^3 + A + C_MT^2 \tag{5.11}$$

A plot of C_pT^2 versus T^3 gives initial slope γ and intercept A. Secondly, at higher temperatures, where $C_N < 1\%$ of the total heat capacity, or is known from the first step, and where the Debye T^3 law is assumed to hold, which for the lanthanides means up to about 5 or 6 K, we can consider

$$C_p/T = \gamma + aT^2 + C_M/T \tag{5.12}$$

A plot of C_p/T versus T^2 then gives initial slope a and intercept γ.

These two steps can be reiterated until self-consistency is achieved. But what of the influence of C_M? Clearly the temperature dependence of C_M is important, especially in those cases where C_M is a large fraction of the total C_p even at low temperatures. We can differentiate the three most likely cases:

(a) n = 1. If $n = 1$, then C_M is linear in T and cannot be distinguished from $C_E = \gamma T$, and any "γ" found is "magnetically enhanced", $\gamma' = \gamma + K$. We can no longer say that the linear term is due to the conduction electrons alone. This effect is evident in Pr, Nd and Tm (see below sections 2.3, 2.4 and 3.6).

(b) n = 1.5. In a comparison with the other terms, a $T^{3/2}$ magnetic term still resembles a linear contribution in the first plot, and will introduce a downward curvature at low temperatures in the second plot (cf. fig. 2 of Wells et al., 1974). Both steps will result in a possible enhanced value for γ and over-estimation of a [and hence a low value for $\theta_D(0)$].

(c) n = 3. In this case the first plot should be relatively unaffected, unless the magnetic contribution is unusually strong, but the second plot will give an enhanced phonon term, $a' = a + K$. One cannot separate C_M from C_L without making some assumptions about C_L.

Introduction of the extra parameter E_g with the corresponding exponential term increases one's chances of fitting the data, but should not be used indiscriminately. Thus results obtained in the above manner should be interpreted warily, for who is to say if γ is the true electronic γ or a "magnetically enhanced" value. Furthermore, as Morrison and Newsham (1968) rightly point out, in this case little can be said about the lattice contributions. Equally sensible

results should be available from a least squares fit to the data in which some assumption has been made as to the values of C_E and C_L or as to the analytic form of C_M.

1.6. *Nuclear heat capacity*

In the lanthanide metals the 4f electrons, due to their orbital and spin angular momenta, produce an effective magnetic hyperfine field H_{eff} at the nucleus which interacts with the nuclear magnetic moment $\mu_I = g_I \mu_N I$. I is the nuclear spin, g_I a splitting factor and μ_N the nuclear magneton. If in addition to μ_I the nucleus carries a quadrupole moment eQ', there is an electrostatic interaction between it and the crystal field gradient eq at the nucleus due to the 4f electrons. These so-called hyperfine interactions have been reviewed in detail by Bleaney (1963, 1972), Lounasmaa (1967) and Phillips (1971). The nuclear contribution to the heat capacity arises when the $(2I+1)$ degeneracy of the nuclear state is lifted by these interactions. The leading terms in the resulting hamiltonian can be written as

$$\mathcal{H} = \left(\frac{\mu_I H_{eff}}{I}\right) I_z + \frac{3e^2qQ'}{4I(2I-1)}[I_z^2 - \tfrac{1}{3}I(I+1)] \tag{5.13}$$

It is assumed that H_{eff} and eq are parallel and define the z-axis, and that they include contributions from the core and conduction electrons, i.e. the Sternheimer shielding factor (cf. Sano et al., 1975). The eigenvalues of this hamiltonian are

$$W_m/k_B = a' + P[m^2 - \tfrac{1}{3}I(I+1)], \tag{5.14}$$

where we have introduced parameters defined by
(magnetic interaction parameter),

$$a' = \mu_I H_{eff}/k_B I \tag{5.15}$$

and (quadrupole coupling constant).

$$P = 3e^2qQ'/4k_B I(2I-1) \tag{5.16}$$

The nuclear term in the heat capacity can be calculated using statistical thermodynamics and has been presented in detail in each of the above reviews. Our interest lies in the parameters which can be extracted from the heat capacity data at low temperatures. The magnetic interaction parameter should vary as $\langle J_z \rangle$, which measures the 4f-electron magnetization, and the quadrupole coupling constant P as $\langle J_z^2 - \frac{1}{3}J(J+1)\rangle$, which is a measure of the average value of the electric quadrupole moment. J_z refers to the electronic ground state of the ion, which below a few degrees Kelvin is expected to have reached the saturation value J. Thus we find $a' \sim J$ and $P \sim J(2J-1)$. In other words, a' and P are temperature independent constants. Since I for the nucleus is known, we are left with two adjustable parameters a' and P to fit the nuclear heat capacity data, for each isotope. In experiments reaching the high temperature side of the C_N

Schottky peak, it is sometimes sufficient to expand C_N in a power series of inverse powers of T,

$$C_N = \sum_n c_n T^{-n} \tag{5.17}$$

The coefficients of the first few terms are given by

$$\begin{aligned} c_2/R &= \tfrac{1}{3}(a')^2 I(I+1) + \tfrac{1}{45}P^2 I(I+1)(2I-1)(2I+3) + \ldots \\ c_3/R &= -\tfrac{1}{15}(a')^2 PI(I+1)(2I-1)(2I+3) + \ldots \\ c_4/R &= -\tfrac{1}{30}(a')^4 I(I+1)(2I^2+2I+1) + \ldots \end{aligned} \tag{5.18}$$

Clearly, if the quadrupole interaction is zero, all odd powers disappear, and if $a' \ll T$, then just the first term is sufficient, i.e. $C_N = c_2 T^{-2}$.

Since the magnetic interaction parameter a' is of order 0.1 K, the associated Schottky anomaly in the C_p versus T curve will peak at around this temperature. Thus, for Tb, Ho and Tm we find that even in the analysis above 0.1 K we must include an estimate of the nuclear contribution (see table 5.2).

Direct comparison of hyperfine field values obtained from different types of measurements is not particularly rewarding because of imprecise knowledge of the values of the nuclear moments. Thus it is more meaningful to compare results for the magnetic interaction parameter defined by equation (5.15). Similarly, for the nuclear quadrupole interaction, the parameter used here for comparing results is the quadrupole coupling constant defined by equation (5.16). The values obtained for these parameters are presented in table 5.2 along with an indication of the type of experiment concerned. We find that very low temperature heat capacity measurements agree well for most of the lanthanide metals with the theoretical calculations of Bleaney (1963), who assumed saturation of the ionic moment, i.e. $\langle J_z \rangle = J$. An illustration of the beautiful agreement obtained is shown in fig. 5.1 for Pr, Nd, Sm and Eu, with similar agreement having been found for the heavy metals (Krusius, 1971). Furthermore, excellent agreement is reached with NMR and Mössbauer results, when available. Thus in any analysis of the heat capacity we can account for the nuclear contribution to the required degree of accuracy through appropriate choice of the full analytic expression for C_N, or the power series expansion (5.17), or just the T^{-2} term, and the parameters given in table 5.2.

In concluding this introduction we may observe that the majority of the heat capacity results reported in the literature have been analysed on the basis of one or other of the above discussed assumptions. Generally a least squares fit over some specified temperature range has been made within which the relative importance of the various terms has been taken into consideration. For example, for very low temperatures (v.l.t.), below around 0.5 K, say, the nuclear term is clearly dominant when it exists. There is danger, on the other hand, in putting too much stress on graphical analysis, as we have considered in section 1.5 above, for we must be clear as to what part of the linear T and cubic T^3 terms are attributable to the unenhanced electronic and lattice terms, respectively, as presented in sections 1.2 and 1.3 above. There have been some theoretical

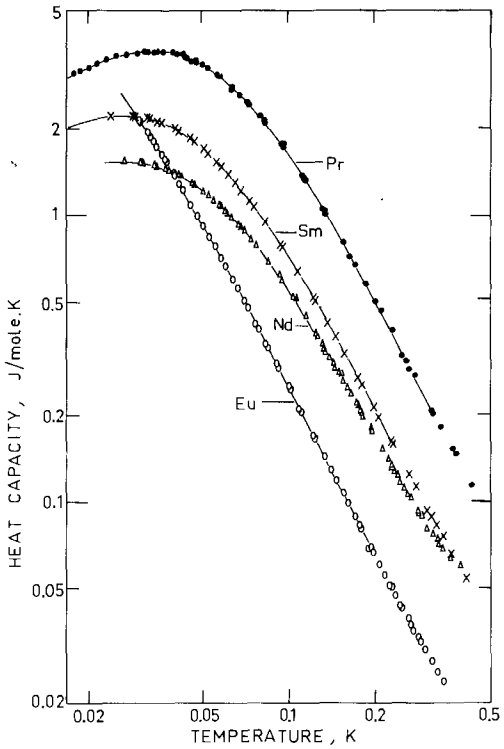

Fig. 5.1. Nuclear heat capacities of Pr, Nd, Sm and Eu (after Krusius, 1971).

TABLE 5.2.

Nuclear hyperfine interaction parameters for the lanthanide metals in degrees Kelvin. (Conversion factor – 1 MHz = 0.047994 mK) Note: The signs are given for those cases only where the sign can be unambiguously determined.

Element	I (units of $\hbar$)	a'(K)	P(K)	Method	Reference
^{141}Pr	$\frac{5}{2}$	+0.210	−0.00014	theory	a
		+0.0624	+0.00061	calorim	b
^{143}Nd	$\frac{7}{2}$	−0.0463	+0.000024	theory	a
	hex.	−0.0366	−0.0005	calorim	c
	cubic	−0.0251	−0.0005		
^{145}Nd	$\frac{7}{2}$	−0.0288	+0.000012	theory	a
	hex.	−0.0227	−0.0003	calorim	c
	cubic	−0.0156	−0.0003		
^{147}Sm	$\frac{7}{2}$	−0.0290	−0.000078	theory	a
		−0.0283	−0.0002	calorim	c
^{149}Sm	$\frac{7}{2}$	−0.0238	+0.000023	theory	a
		−0.0233	+0.00005	calorim	c

TABLE 5.2 (*Contd.*)

Element	I (units of $\hbar$)	a'(K)	P(K)	Method	Reference
^{151}Eu	$\frac{5}{2}$	−0.0173	−0.0000028	theory	a
		0.0132	0.00006	calorim vlt	d
		0.0130	—	calorim	e
		0.0134	—	Mössbauer	f
^{153}Eu	$\frac{5}{2}$	−0.00767	−0.0000073	theory	a
		0.00586	−0.00016	calorim vlt	d
		0.0057	—	calorim	e
		0.00593	—	Mössbauer	f
^{159}Tb	$\frac{3}{2}$	0.152	0.029	theory	a
		0.149	0.0158	calorim vlt	g
		0.150	0.021	calorim vlt	h
		0.152	0.013	calorim vlt	i
		0.1496	0.0161	NMR	j
		0.1497	0.0162	NMR	k
		0.147	0.0161	NMR (alloys)	l
^{161}Dy	$\frac{5}{2}$	−0.0394	+0.0072	theory	a
		−0.0396	+0.009	calorim	c
		0.03984	0.0093	NMR	m
		0.0388	0.0077	Mössbauer	n
^{163}Dy	$\frac{5}{2}$	+0.0547	+0.0086	theory	a
		+0.0554	+0.010	calorim	c
		0.0558	0.0098	NMR	m
		0.061	—	neutron trans.	o
^{165}Ho	$\frac{7}{2}$	0.312	0.003	theory	a
		+0.319	+0.004	calorim	g
		0.320	0.007	calorim	p
		0.320	0.008	calorim	i
		0.305	0.002	neutron trans.	u
		0.3095	0.0025	NMR	q
^{167}Er	$\frac{7}{2}$	−0.0451	−0.00326	theory	a
		0.0423	−0.0027	calorim	d
		0.047	—	calorim	r
		0.0438	0.00254	NMR	t
^{169}Tm	$\frac{1}{2}$	−0.113	—	theory	a
		−0.1072	—	calorim	b
		−0.105	—	Mössbauer	s
		−0.103	—	neutron trans.	v

Note: The signs are given for those cases only where the sign can be unambiguously determined.

a. Bleaney, 1963; b. Holmström et al., 1969; c. Anderson et al., 1969; d. Krusius et al., 1974; e. Lounasmaa, 1964b; f. Hüfner and Wernick, 1968; g. Krusius et al., 1969; h. Lounasmaa and Roach, 1962; i. Van Kempen et al., 1964; j. Kobayashi et al., 1967; k. Sano and Itoh, 1972; l. Sano et al., 1975; m. Kobayashi et al., 1966; n. Ofer et al., 1965; o. Brünhart, 1967 (unpublished); p. Lounasmaa, 1962b; q. Mackenzie et al., 1974; r. Parks, 1962; s. Kalvius et al., 1963; t. Sano et al., 1972; u. Brünhart et al., 1965; v. Al-Kital et al., 1967.

contributions towards understanding the magnetic enhancement of these terms; we discussed the C_M term above (section 1.4) in some detail. In the case of the electronic term, we might mention the work by Nakajima (1967) who investigated a model for the ferromagnetic lanthanides in which conduction electrons interact with the localized spins through an sf exchange type coupling, which can still be quite weak and yet produce an enhancement factor of order unity. When the localized spin system is in an ordered state, the exchange scattering of the conduction electrons may be described as emission and absorption of magnons. The analogy to the coupled electron–phonon system noted by Kondo (1965) is emphasised and expanded upon in a theoretically rigorous approach.

Finally, to give the reader a feeling for the magnitudes of the electronic coefficients γ and the Debye temperatures $\theta_D(0)$, table 5.3 presents the best available results for those cases where meaningful and relatively unambiguous analysis can be made of the heat capacity into its component parts.

TABLE 5.3
Estimated "unenhanced" electronic specific heat coefficient (mJ/mole·K^2) and low temperature Debye temperature $\theta_D(0)$ (K) for selected rare earth metals where such estimation is possible.

Metal	γ	$\theta_D(0)$	Reference
α-La	9.6	151	Finnemore and Johnson, 1966
	9.4	152	Johnson, 1966
	—	154	Rosen, 1968 (elast. const.)
β-La	11.3	139	Finnemore and Johnson, 1966
	11.5	140	Johnson, 1966
α-Ce	11.3	200	Phillips et al., 1968 (at 10 kb pressure)
	12.8	179	Koskimaki and Gschneidner, 1975
	—	139	Rosen, 1968 (not pure phase)
Sm	9.97	116	Dreyfus et al., 1961
	12.1	120–129	Lounasmaa, 1962a
	13.5	—	Lounasmaa and Veuro, 1972
	—	169	Rosen, 1968
Eu	5.8	—	Lounasmaa, 1964b
	(5.8)	~107.5	Gerstein et al., 1967
	—	117	Rosen, 1968
Gd	—	181	Sundström, 1968 (theoretical)
	3.7	187 ± 3	Wells et al., 1974 (if $C_M \sim T^{3/2}$)
	6.5	—	Hill, 1976 (if $C_M = 0$)
	4.94	—	Keeton and Loucks, 1968 (RAPW)
	—	184	Rosen, 1968
Tb	4.35	174 ± 1	Hill et al., 1974
	4.4	178 ± 2	Wells et al., 1976
	4.3	—	Hill, 1976
	5.62	—	Jackson, 1969 (RAPW)
	—	179	Rosen, 1968

TABLE 5.3 (*Contd.*)

Metal	γ	$\theta_D(0)$	Reference
Dy	9.0	207	Dreyfus et al., 1961
	<4.5	—	Hill, 1976
	4.80	—	Keeton and Loucks, 1968 (RAPW)
	4.21	—	-"- (with different potential)
	—	178	Rosen, 1968
	—	183	Palmer and Lee, 1970 (elast. const.)
Ho	6 ± 1	—	Hill, 1976
	—	114 ± 7	Dreyfus et al., 1961
	—	195	Rosen, 1968
		188.5	Palmer and Lee, 1970
Er	<9.5	—	Hill, 1976
	—	194.5	Satya and Wei, 1971
	4.21	—	Keeton and Loucks, 1968 (RAPW)
	4.09	—	-"- (with different potential)
	—	192	Rosen, 1968
Tm	—	200	Satya and Wei, 1971
Yb	2.9	118	Lounasmaa, 1963, 1966
	—	121	Rosen, 1968
Lu	11.27	210	Lounasmaa, 1964a, Culbert, 1967
	6.8	205 ± 3	Wells et al., 1976
	4.4	—	Keeton and Loucks, 1968 (RAPW)
Sc	10.34	346 ± 1	Tsang et al., 1976b
Y	8.2	248 ± 3	Wells et al., 1976
	4.7	—	Loucks, 1966 (RAPW)

2. The light lanthanide metals

2.1. *Lanthanum*

Lanthanum exists in modified hexagonal (α) and face-centred cubic (β) forms, each of which contributes independently to the electronic and lattice heat capacities. Both phases display superconductivity, the transition temperatures being $T_\alpha = 4.9$ K and $T_\beta = 6.0$ K, respectively (Finnemore et al., 1965; Finnemore and Johnson, 1966).

The normal state heat capacity obeys the usual $C_p = \gamma T + AT^3 + BT^5$ law. On 100% α-La samples Ohtsuka and Satoh (1966) found $T_\alpha = 4.9$ K, $\gamma_\alpha = 10.0$ mJ/mole·K^2 and $\theta_{D,\alpha}(0) = 142$ K. From the magnitude of the discontinuity in C_p at the superconducting transition comparison can be made with the law of corresponding states for the two lanthanum phases (Finnemore et al., 1965; Finnemore and Johnson, 1966; Lounasmaa and Sundström, 1967); similarly for superconducting alloys containing lanthanum (Ohtsuka and Satoh, 1966 – LaY; and Bonnerot et al., 1966 – LaGd).

According to the BCS theory of superconductivity, the electronic term of the heat capacity in the super conducting state can be expressed as $C_{Es}/\gamma T_c = f(t)$,

where $f(t) = a' \exp(-b'/t)$ with $t = T/T_c$ being the reduced temperature and a' and b' constants of order 9 and 1.5, respectively. Thus for the heat capacity discontinuity at T_c we have

$$(C_{Es} - C_{En})/\gamma T_c = f(1) - 1 = 1.43, \tag{5.19}$$

where the numerical result is as for the BCS theory. Ohtsuka and Satoh (1966) found this ratio to be of order 1.5 for LaY alloys with the α-La structure and Lounasmaa and Sundström (1967) found 1.48 for pure lanthanum of mixed phase. Thus it would appear that the BCS theory holds for superconducting La and La-alloys.

As the exact positions of the superconducting transition peaks are difficult to determine uniquely, slightly varying values have been reported for T_α and T_β, but the best available results point to $T_\alpha = 4.9\ K$ and $T_\beta = 5.9\ K$. The electronic term in the normal state is clearly linear in T, but in order to complete the analysis we must know either the relative concentrations of α and β-La, or make some assumption as to γ_α and γ_β. Berman et al. (1958) found $\gamma = 10.09\ \text{mJ/mole}\cdot\text{K}^2$, whereas Finnemore et al. (1965), Bonnerot et al. (1966) and Ohtsuka and Satoh (1966) all assumed $\gamma = 10.0\ \text{mJ/mole}\cdot\text{K}^2$. From measurements below 25 K Lounasmaa and Sundström (1967) deduced an effective $\gamma = 10.5\ \text{mJ/mole}\cdot\text{K}^2$, which is not inconsistent with Finnemore and Johnson's (1966) proposal that $\gamma_\alpha = 9.6\ \text{mJ/mole}\cdot\text{K}^2$ and $\gamma_\beta = 11.3\ \text{mJ/mole}\cdot\text{K}^2$ and Johnson's results (1966) $\gamma_\alpha = 9.4\ \text{mJ/mole}\cdot\text{K}^2$ and $\gamma_\beta = 11.5\ \text{mJ/mole}\cdot\text{K}^2$. The above values thus indicate an upper limit of $9.6\ \text{mJ/mole}\cdot\text{K}^2$ for γ_α.

As far as the effective Debye temperature is concerned, the earlier results indicated $\theta_{D,\alpha}\ (0) \sim 142$ K, whereas Finnemore et al. (1966) report $\theta_{D,\alpha}\ (0) = 151$ K and $\theta_{D,\beta}\ (0) = 139$ K, and ultrasonic measurements (Rosen 1968) give a value of 154 K. It would thus appear that earlier estimated $\theta_D(0)$ values for the lanthanides through an interpolation scheme originally based on $\theta_D(0) = 142$ K for lanthanum (Lounasmaa 1964a) should be revised to correspond to an α-La value of 151 ± 3 K.

Measurements on LaY alloys (Ohtsuka and Satoh 1966) failed to shed light on the role of the 4f electrons in the superconductivity of lanthanum. But we can say a few more words about γ. The variation of γ with yttrium content shows values of $10.0\ \text{mJ/mole}\cdot\text{K}^2$ at 100% α-La and $10.5\ \text{mJ/mole}\cdot\text{K}^2$ at 100% Y. The γ versus concentration curve falls from either end, but shows an irregularity in the region of $La_{0.5}Y_{0.5}$ where the alloy has the complex α-Sm structure. Thus γ for the rare earths is perhaps more closely structure dependent than was first assumed, and care must be taken when adopting a γ value for separating off the electronic term in the heat capacity (see also section 1.3 above).

Ratto et al. (1969) have developed a theoretical model which explains the superconductivity of lanthanum and of α-cerium at high pressures, with T_c increasing with pressure (cf. section 2.2 below). They postulate the presence of an inner 4f shell even for these metals such that the 4f character in La and non-magnetic α-Ce tends to inhibit superconductivity; this 4f character decreases with increasing pressure. Their model gives results in line with

experimental observation both as to the existence of superconductivity and the pressure variation of T_c in these two metals. A more extensive discussion of this subject will be found in ch. 10, section 3.

2.2. *Cerium*

Cerium, like lanthanum, possesses two crystallographic modifications at low temperatures, the relative concentrations depending on the thermal and cold-working history and on impurity content (see chapter 2). Thus we are here concerned with α-cerium (collapsed fcc, $a = 4.85$ Å) and β-cerium (d-hcp). The presence of impurities seems to stabilise the β-phase. From magnetic susceptibility (Lock 1957) and neutron diffraction experiments (Wilkinson et al. 1961) it has been established that, while α-cerium is non-magnetic, the hexagonal β-phase undergoes antiferromagnetic ordering with $T_N = 12.5$ K, which shows up as an anomaly in the heat capacity.

In the 1950's and 1960's measurements on cerium suffered from inexact knowledge of the phase concentrations, in addition to the usual problem of purity (Lounasmaa 1964b and references therein), so we shall pass on to more recent results on better defined specimens.

Phillips et al. (1968) measured the heat capacity of collapsed fcc α-cerium at a pressure of 11 kbar, between 0.3 and 6 K, in an attempt to check the behaviour of the 4f electron, which gives the room temperature fcc γ-phase a magnetic moment. Their results can be fitted by $\gamma_\alpha = 11.3$ mJ/mole·K^2 and $\theta_{D,\alpha}(0) = 200$ K. This high γ_α value, as compared with the tetravalent transition metals above and below Ce in the periodic table, is interpreted as evidence of a large 4f contribution to the density of states. To complement this picture of itinerant 4f electrons in cerium, whose "bands" at zero pressure must overlap well into the conduction band, Probst and Wittig (1975) established the existence of superconductivity in α-Ce with $T_c = 20$ mK at 20 kbar and $T_c = 50$ mK at 40 kbar, at which pressure the transition to α'-Ce (C-centered orthorhombic, see ch. 4 section 2.2) takes place with a jump in T_c to 1.9 K. $T_{c,\alpha}$, then decreases with increasing pressure, but becomes constant above 120 kbar. They propose that α-Ce possesses a strong Coulomb interaction which keeps T_c low. As the pressure increases, the Coulomb interaction is weakened and the electron–phonon interaction has more chance to play its role in forming Cooper pairs. The situation thus indicates narrow 4f bands in cerium rather than a localized 4f electron.

Conway and Phillips (1974) measured the heat capacities of mixed-phase samples, from which they extrapolated to the pure phases, using the magnetic ordering anomaly in the β-phase as a measure of the composition. Small concentration independent peaks near 0.15, 0.9 and 6 K were neglected as being impurity related. They found $\gamma_\alpha = 22$ mJ/mole·K^2 and $\theta_{D,\alpha}(0) \sim 125$ K, results which can be explained as above in terms of a shift in the 4f band or virtual bound state relative to the conduction band (Coqblin and Blandin 1968).

Koskimaki and Gschneidner (1975) measured on single-phase α-Ce.† They found $\gamma_\alpha = 12.8$ mJ/mole.K^2 and $\theta_{D,\alpha}(0) = 179$ K. They also discussed a number of models which have been put forward to explain the behaviour of C_p and the magnetic susceptibility of α-Ce. Although none was completely satisfactory, the present author tends to favour the delocalization of the 4f-electron shell into a 4f band similar to the delocalization which occurs in a Mott transition (Johansson 1974), especially in view of the pressure and superconducting studies discussed above.

As to the behavior of d-hcp β-Ce, Conway and Phillips (1974) could express the relevant part of the heat capacity as $C_{p,\beta} = 54T + 5.6T^3$ mJ/mole·K. The high linear term is attributed to "magnetic enhancement" of the electronic term; so too the high T^3 term (by comparison, recall that for α-La, $C_L \sim 0.55T^3$ mJ/mole·K). Furthermore, because of the nature of their samples, only one broad peak was evident so that it was not suspected that ordering was taking place on both types of lattice site in the d-hcp phase. Tsang et al. (1967a), on the other hand, redetermined the heat capacity of a well characterized sample of single-phase β-Ce, in the light of recent indications that β-Ce transforms to α-Ce between 15 and 50 K unless the sample is cooled or warmed rapidly through this temperature region (Gschneidner et al. 1976, Burgardt et al. 1976). This, along with lattice strains, has probably led to inaccurate estimates of the phase concentrations in earlier work. However, their results agree essentially with those of Koskimaki and Gschneidner (1974) except for a sharpening of the peak around 12 K and a more pronounced shoulder on the high temperature side of the peak (fig. 5.2).

In order to separate off the lattice and electronic terms, Tsang et al. (1976a) and Koskimaki and Gschneidner (1974) assumed for β-Ce that $\theta_D(0) = 152$ K and $\gamma_\beta = 9.4$ mJ/mole·K^2, the values obtained for α-La (Johnson, 1966). They found it necessary to include crystal field effects on the $^2F_{5/2}$ ground state level of the Ce^{3+} ion. By means of neutron inelastic scattering, the hexagonal site levels are identified as splitting into three doublets with excited levels at 98 K and 113 K, while the cubic site levels have a doublet ground state, with a quartet excited level at 206 K. The resulting Schottky curve has appreciable magnitude above 10 K, as shown in fig. 5.2. $\theta_{D,\beta}(T)$ is assumed to follow the behaviour of $\theta_D(T)$ for α-La. The remaining C_M is interpreted as evidence for separate ordering at 12.45 and 13.7 K for the two types of site symmetry, the lower temperature peak being associated with ordering on the cubic sites and the higher with ordering on the hexagonal sites. The associated magnetic entropy falls within 2% of the theoretical value R ln 2.

Tsang et al. (1976a) find an exponential behaviour for C_M of β-Ce below 1.33 K, with $C_M = 162.8 \exp(-1.41/T)$ mJ/mole·K. From 3.5 to 6.5 K a good fit is given by $C_M = 6.5T^3$ mJ/mole·K. The existence of both exponential and non-exponential behaviour is consistent with Cooper's theory (1962), but the absence

†Previous results on nearly single-phase α-Ce by Panousis and Gschneidner (1970) as originally reported are erroneous due to inadvertant neglect of the heat capacity of a copper plug in the sample holder – see Koskimaki and Gschneidner (1975) for details.

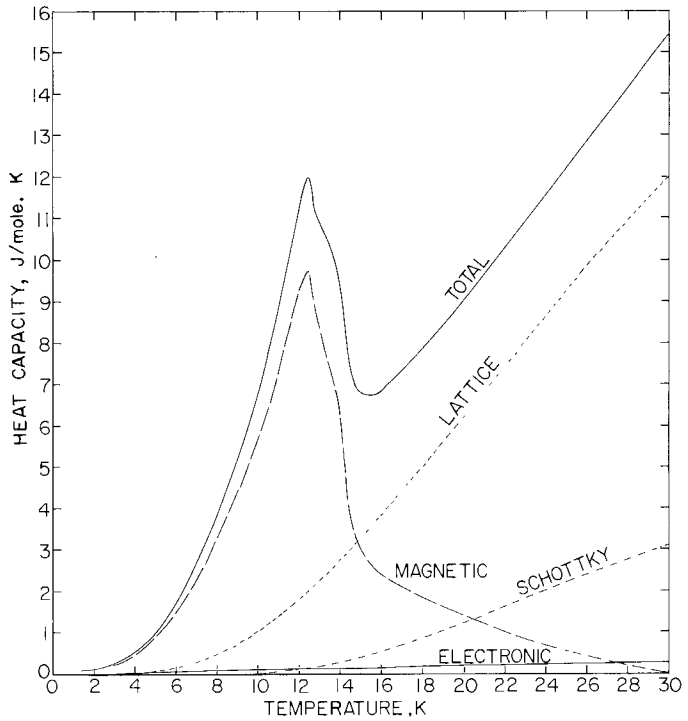

Fig. 5.2. The heat capacity of β-Ce showing the electronic, lattice, magnetic and Schottky contributions (private communication from K.A. Gschneidner, Jr.).

of T-dependence in front of the exponential term is unexpected. In view of the approximations made for C_L and C_E, this reported low temperature behavior for C_M in β-Ce should perhaps be viewed with caution.

2.3. *Praseodymium*

Praseodymium, being still close to the lanthanum end of the lanthanide series, like cerium, does not yet show a clear cut behaviour. This is mainly due to the close competition between the exchange interaction E_{ex}, favouring magnetic order, and the crystal field interaction E_{cry} (Gregers-Hansen et al. 1972, Lindelof et al. 1975, Lebech et al. 1975). Thus in the single crystal the ratio is $E_{ex}/E_{cry} = 0.95$ (Lebech et al. 1975) and hence no magnetic order, whereas the presence of strain can upset this delicate balance so that polycrystalline samples may display magnetic ordering phenomena. The heat capacity results on praseodymium are therefore strongly sample and sample history dependent. On the other hand, the proposal of the formation of ferromagnetic clusters of fcc Pr (Holmström et al. 1969, Bucher et al. 1969) has not been well supported by subsequent results.

Even the nuclear term in praseodymium has proved intractible to definite

analysis (Holmström et al. 1969), as indicated in table 5.2 above, presumably due to the sample dependence of the magnetic ordering. The information that has been extracted is that there appears to be sinusoidal modulation of the hyperfine fields on half the lattice sites. Thus early results (Lounasmaa 1964c, Dreyfus et al. 1964, Lounasmaa and Sundström 1967 and references therein) were by necessity only approximately analysed, with the electronic and lattice terms taken to be as for normal α-La. Dreyfus et al. (1965) measured the heat capacity of a series of Gd-Pr alloys and speculated that somewhere between 75% and 50% Pr the lowest electronic level undergoes a drastic change of J_z from 1 to 4 under the action of an increasing exchange field, this effect occurring on only the hexagonal sites. The ionic ground state is $^3H_4$, but the crystalline electric field apparently lifts the degeneracy, since the total entropy associated with C_M is close to R ln 9 (Parkinson et al. 1951).

It is now fairly well established (Andres et al. 1972, Gregers-Hansen et al. 1972, Lindelof et al. 1975, Lebech et al. 1975) that praseodymium metal provides an example of singlet ground state magnetism (Cooper and Vogt 1971, and for a review see Cooper 1972). In the crystal field both types of ion sites have singlet ground states. The hexagonal site ions have a first excited state around 30 K (Bleaney 1963-singlet, Curry, and Taylor 1973†-doublet) and the cubic site ions have a triplet excited state around 87 K.

When due consideration is taken of admixtures of the higher states $|s\rangle$ into the ground state $|0\rangle$ a small magnetic moment is induced under the influence of a magnetic field H in what is known as Van Vleck paramagnetism. The induced magnetisation is given by

$$M = 2NH \sum_s |\langle s|\mu_z|0\rangle|^2/E_{\mathrm{cry},s}. \tag{5.20}$$

However, if the ratio of the exchange parameter E_{ex} to the energy gap between the ground and first excited states $E_{\mathrm{cry},1}$ exceeds some critical value, spontaneous admixing can occur with resulting magnetic polarization of the ions (Cooper and Vogt 1971).

Interesting experiments by Gregers-Hansen et al. (1972) on Pr in an applied magnetic field at very low temperatures show convincingly that the cubic site ions display ordinary Van Vleck paramagnetism, while the hexagonal site ions show a field independent exchange induced magnetism. More recent heat capacity measurements under magnetic fields up to 1.55 Tesla (Lindelof et al. 1975) demonstrate how the nuclear moment of the Pr ion is itself sufficient to induce, through the Van Vleck mechanism, a polarization of the ion, which can then interact by exchange with the moment similarly induced on a neighbouring ion. Thus single crystal praseodymium has been shown to display this effective nuclear-nuclear exchange mechanism, the effect again clearly being confined to ions in a hexagonal environment.

This section on praseodymium can be concluded by mentioning that results of

†For details of Curry and Taylor's (1973) energy level scheme see Krizek (1975).

analysis of the heat capacity beyond the hyperfine region into its component parts depends very much on the technique used. Lounasmaa and Sundström (1967) took α-La as the measuring stick for $C_L + C_E$, and obtained, for the region below 3 K, $C_M = 3.98T^3$, as might be expected for an antiferromagnet. Alternatively, the graphical analysis of Morrison and Newsham (1968) yields $\gamma = 26.2$ mJ/mole·K^2 and $C_M = 41T^{3/2} \exp(-2.84/T)$ mJ/mole·K for T less than 2.5 K. In the present circumstances, given the complex ordering of praseodymium, it is not clear even theoretically which form of temperature dependence can be expected for C_M. Resolution of this point must await further theoretical and experimental investigations.

2.4. *Neodymium*

The complex magnetic structure of neodymium is reflected in the magnetic heat capacity, which cannot be expressed in terms of any straightforward temperature dependence. Moreover, C_M is clearly the dominant contribution at low temperatures. Thus, to date, the heat capacity of neodymium has not been satisfactorily analysed, except for the nuclear contribution (Anderson et al. 1969). The heat capacity curve features two cooperative type maxima at around 7.4 and 19.5 K (Lounasmaa and Sundström 1967) associated with ordering of ions on the cubic and hexagonal sites, respectively (fig. 5.3). As a first approximation, the heat capacity of α-La was taken as representative of the lattice and electronic terms, but in view of the anomalous and large thermal expansion coefficient of neodymium (Andres 1963), it is likely that C_L behaves in quite some different and anomalous way. The Schottky curve resulting from crystalline field splitting of the $J = \frac{9}{2}$ ground state, along with additional splitting through quadrupole-quadrupole interaction, does reproduce certain features of the measured heat capacity curve (Lounasmaa and Sundström 1967), but the cooperative effects have not been explained.

Janovec and Morrison (1965) and Morrison and Newsham (1968) carried out graphical analysis of Lounasmaa's (1964c) heat capacity measurements below 4 K and, ignoring the lattice contribution as being less than 2% of the total, they found for the temperature range 0.4 to 2.5 K a good fit with $C_E = 58T$, $C_N = 4.7T^{-2} + 0.2T^{-3}$, and $C_M = 1030\,T \exp(-2.44/T)$, all in mJ/mole·K. Unfortunately, this value for γ can only be explained away as some low temperature "magnetic enhancement" of C_E. Also, the temperature dependence of C_M does not correspond to any current theoretical proposal for neodymium, although the small value for the spin wave energy gap is more in line with recent work on the heavy lanthanide metals (see section 3 below).

Even the nuclear heat capacity of Nd is complicated by the magnetic structure. Anderson et al. (1969) have made an analysis with their best solution given by two unmodulated sub-lattices with electronic moments 2.58 μ_B and 1.77 μ_B attributed tentatively to the ions on hexagonal and cubic sites, respectively. In reaching this conclusion they made comparison with neutron diffraction results (Moon et al. 1964) which suggest sinusoidally modulated moments with amplitudes 2.3 μ_B and 1.8 μ_B, respectively (table 5.2).

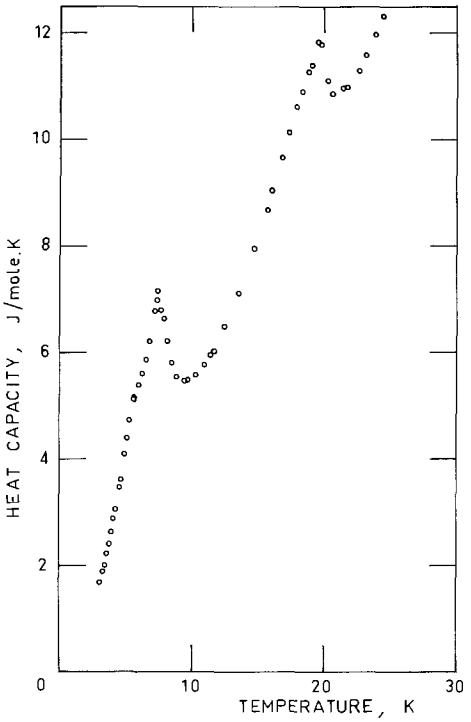

Fig. 5.3. The heat capacity of Nd between 4.2 and 25 K (after Lounasmaa and Sundström, 1967).

2.5. *Samarium*

Samarium has a complex hexagonal structure, with packing sequence ABABCBCAC... for layers normal to the c-axis. Thus ions in every third layer have cubic environment while the remaining layers have hexagonal environment. Koehler et al. (1972) have proposed a model for the antiferromagnetic ordering of samarium wherein each of the hexagonal and cubic site ion layers order with successive pairs of layers antiparallel. In both cases the moments are aligned along the c-axis. Thus straightforward application of spin wave theory, with or without strong magnetic anisotropy, will not necessarily apply. The hexagonal site ions order at 106 K, while those on cubic sites do not order until 14 K (Koehler et al. 1972), at which temperatures the heat capacity shows distinct peaks (Lounasmaa and Sundström 1967 and references therein). In addition, a smaller anomaly was observed around 9.5 K, but this is attributed to some impurity phase transformation.

After the usual assumption of $C_E + C_L = C_p(\alpha\text{-La})$, Lounasmaa and Sundström (1967) found $C_M \sim T^4$ over the region 2.5 to 10 K, a temperature dependence which does not correspond to any known theory. If, on the other hand, analysis is made of the heat capacity below 2.3 K, where C_M is expected to be relatively small and to follow the long wave length limit T^3 behaviour for an antiferromagnet, one finds $\gamma = 12.4\,\text{mJ/mole}\cdot\text{K}^2$ and the leading nuclear term

$8.56T^{-2}$ mJ/mole·K (Lounasmaa 1962a, Morrison and Newsham 1968). The remaining $0.88T^3$ mJ/mole·K is higher than expected if $\theta_D(0)$ were to follow the general trend of the lanthanides, and so clearly includes a magnetic contribution. As mentioned in section 1.3 above, Lounasmaa and Veuro (1972) measured the heat capacity of enriched ^{152}Sm metal between 0.45 and 6 K to reduce the number of variables in the analysis. They used the parameters found by Anderson et al. (1969) for the nuclear contributions of the small quantities of even-odd isotopes (table 5.2) and obtained the rather high value of 13.5 mJ/mole·K^2 for γ. As regards the nuclear terms (table 5.2), it should be noted that in the case of samarium the experimental parameters are approximately 2% lower than given by the theory (Bleaney 1963).

Thus, until either more heat capacity results on high purity samarium samples are available, or until theoretical predictions can be made for the magnetic term of this complex antiferromagnet, little more information can be extracted from the available heat capacity results. It might be speculated that the 4f electron levels in Sm, rather than forming localized magnetic states, occupy virtual bound states close to the Fermi level. Under pressure (cf. Bader et al. 1973 on SmS) these bound states, or narrow 4f bands, overlap into the conduction band and give a large linear term in the heat capacity.

2.6. *Europium*

Europium metal, like ytterbium at the end of the lanthanide series, loses only 2 electrons to the conduction band, and so retains a half filled 4f shell. Thus the observed C_N must be caused by core polarization effects; i.e. since $L = 0$, the magnetic field produced at the nucleus of the Eu^{2+} ion is due mainly to polarization of electrons in closed shells by the spin moments of the 4f electrons. In the other rare earths this interaction is completely masked by the much larger field due to the orbital angular momentum of the 4f electrons.

Between 0.61 and 1.2 K a least squares fit can be found assuming $C_M \sim T^3$ (Lounasmaa 1964b, 1966). The T^3 term is dominant, indicating a strong magnetic contribution. Morrison and Newsham (1968) found an exponential fit over a slightly wider temperature range, 0.4 to 1.5 K, but the form $T\exp(-2.51/T)$ has no ready theoretical basis. Lounasmaa (1966) found a sharp Ising type peak in his specimen at 16.1 K, which has since been attributed to impurity effects, possibly europium hydride (Gerstein et al. 1967). Gerstein et al. (1967) found no traces of any anomaly at 16 K in measurements covering 5 to 300 K. They found full development of the magnetic entropy for divalent Eu, $R \ln 8$, by room temperature and an average θ_D of 107.5 K.

Meadon and Sze (1969), on the other hand, found anomalies in the thermopower and resistivity of 99.9% pure Eu at around 22.5 K and 21 K, respectively. Cold-working raised the thermopower anomaly to 25 K, whereas annealing weakened it and depressed it to 18 K. They suggested an electronic transformation based on 4f virtual bound states close to the Fermi level, but this is doubtful in view of energy band calculations (Andersen and Loucks 1968) and

the X-ray photoemission spectrum (Hedén et al. 1972), the latter indicating that the 4f level in Eu is 2.1 ± 0.4 eV below the Fermi level. It does seem more likely that the observed anomalies are due to impurities, which being situated at the site of lattice defects and dislocations will obviously be influenced by cold-rolling and annealing thereby giving rise to changes in the intensity and position of the transport property anomalies associated with these impurities.

The hyperfine parameters of europium as found from heat capacity measurements (Krusius et al. 1974, Lounasmaa 1964b) agree well with those found from Mössbauer work (Hüfner and Wernick 1968). However, as shown in table 5.1, these values are somewhat smaller than Bleaney's (1963) theoretical values for Eu^{2+}. It has been suggested (Hüfner and Wernick 1968) that the conduction electron polarization in the metal contributes a mainly positive hyperfine field, as opposed to the field acting on Eu^{2+} ions diluted in ionic CaF_2 used in Bleaney's (1963) calculations.

In conclusion, we may say that the situation in europium is far from clear as regards heat capacity measurements. The most we can say is that $C_E = (5.8 \pm 1.0) \times T$ mJ/mole·K (Lounasmaa 1964b) and that C_N as determined experimentally disagrees slightly with theory. Nothing definite can be said about the lattice and magnetic terms.

3. The heavy lanthanide metals

The heavy metals of the lanthanide series, from gadolinium to thulium, and lutetium, have traditionally been looked upon as a more coherent, systematic grouping that the light metals. This can still be considered to be true for the most part, but until high purity specimens became available (Wells et al. 1974, 1976, Hill et al. 1974, Hill 1976) heat capacity analysis could be done only by assuming values for C_E and C_L. In early work, therefore, it was assumed that $C_E + C_L \approx C_p$ (Lu), which implied $\gamma \sim 11.27$ mJ/mole·K^2 and $\theta_D(0) \sim 210$ K. In the more recent work referred to, as will be discussed in detail below, much smaller values for γ are found, even for non-magnetic lutetium, where $\gamma = 6.8$ mJ/mole·K^2 (Wells et al. 1976). The $\theta_D(0)$ values, on the other hand, agree fairly well with values obtained from ultrasonic measurements (Rosen 1967, 1968, Palmer 1970, Palmer and Lee 1973) and follow the trend proposed for interpolation between the values for lanthanum and lutetium by Lounasmaa (1964a).

3.1. *Gadolinium*

The now familiar problem of impurity effects plagued early heat capacity results on gadolinium (Lounasmaa 1963, Lounasmaa and Sundström 1966 and references therein). Thus a wide variety of results have been obtained for γ. Beside the assumption (Lounasmaa and Sundström 1966) that $C_L + C_E = C_p$ (Lu), we find that Jelinek et al. (1966) assumed $\gamma = 9.2$ mJ/mole·K^2 and hence $\theta_D(0) = 153.7$ K. But the latter's lowest experimental temperature was 15 K and they do

not state whether allowance was made for the temperature dependence of θ_D; they concluded that an appreciable magnetic contribution to the heat capacity of Gd remains even above 360 K. Dreyfus et al. (1967), from measurements between 0.023 and 0.6 K, where they assumed both C_L and C_M to be negligible, used the minimum in $C_N + C_E$ at 0.25 K to determine $\gamma = 11$ mJ/mole·K^2 once C_N had been found. This appears to be the only reported occasion when this technique for finding γ has been used – i.e.

$$\gamma = (2A)^{1/3} T_{\min}^{-1}, \tag{5.21}$$

where A is the coefficient in the nuclear T^{-2} term, as in eq. (5.9) above. In those cases where C_M and C_L are not negligible, this could still perhaps be used as a first approximation for γ, provided that $T_{\min} < 1$ K.

Wells et al. (1974) have made heat capacity measurements on a gadolinium sample purified by solid-state electrotransport (S.S.E.) with RRR 160, in which no traces of impurity anomalies were found (fig. 5.4). Least squares analysis below 5 K yielded $\gamma = 3.7$ mJ/mole·K and $\theta_D(0) = 187 \pm 3$ K. This low value for γ, compared with that previously assumed (11.27 mJ/mole·K^2 as for lutetium), has been explained (Wells et al. 1976) on the basis of spin-polarized energy band calculations for Gd by Harmon and Freeman (1974) which show that in the paramagnetic state the electronic density of states at the Fermi level is about 25% greater than for the spin-polarized state (see above section 1.3). Thus we might expect γ for paramagnetic Lu to give too high an estimate of γ for the magnetically ordered metals. At this point we should note that Wells et al. (1976)

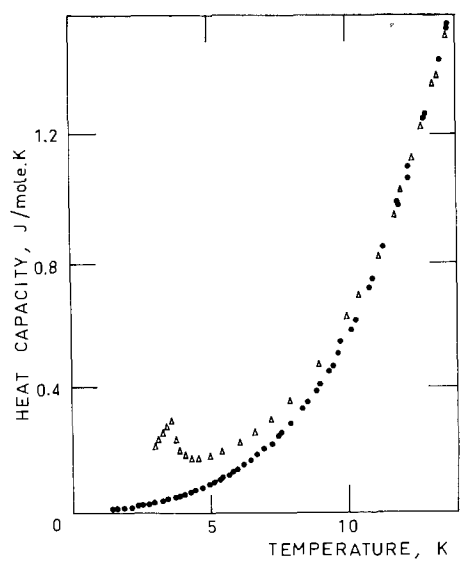

Fig. 5.4. The heat capacity of Gd between 1.5 and 14 K. △ Lounasmaa and Sundström (1966), ● Wells et al. (1974) (courtesy of R.G. Jordon).

also found a lower value for γ (Lu) than previously reported (see below, section 3.8), namely 6.8 ± 0.1 mJ/mole·K^2.

Finally, it appears that C_M for gadolinium does not follow one simple temperature dependence; if we allow $C_M \sim T^n$ then theoretically (Sedaghat and Cracknell 1971, Stevens and Krukewich 1973) n varies from 1.5 at low temperatures to 2.3 above 10 K. The above theoretical calculations are based on experimentally determined magnon dispersion relations. Lounasmaa and Sundström (1966) tentatively proposed $n \sim 2.7$ from analysis of heat capacity results. Wells et al. (1974), on the other hand, are able with more confidence to propose $n \sim 1.75$, and that if magnetic anisotropy were allowed then the introduced energy gap E_g will be very small, in the region of 0.05 K. If there were no anisotropy at all, then a T^3 behaviour would have been expected, as gadolinium, with $L = 0$, is a special case (see e.g. Lounasmaa and Sundström 1966).

3.2. *Terbium*

Let us begin the discussion of terbium by looking at the nuclear contribution (table 5.2). Krusius et al. (1969) found a good fit with parameters very close to the NMR results from 0.03 to 0.5 K, at which temperature their heat capacity results joined onto those of Lounasmaa and Roach (1962). Their values agree within 1% with those of van Kempen et al. (1964). Thus we might safely assume C_N of Tb to be well established.†

At higher temperatures the same sample (Lounasmaa and Roach 1962, Lounasmaa and Sundström 1966) showed an anomalous hysteresis effect centered around 16 K and an impurity related peak at 4.5 K. As neither of these phenomena have been satisfactorily explained, it is gratifying that Hill et al. (1974) and Wells et al. (1976) found no low temperature impurity anomaly in heat capacity measurements on S.S.E. purified terbium between 1.5 and 16 K. Thus their best results (Wells et al. 1976) indicate for Tb that $\gamma = 4.4 \pm 0.1$ mJ/mole·K^2 and $\theta_D(0) = 178 \pm 3$ K. The same arguments as above for Gd can be put forward to explain the unexpectedly low γ value. The limiting $\theta_D(0)$ value is in reasonable agreement with the elastic constant result of 177 K by Rosen (1968), but is considerably lower than the 187 K found from single crystal elastic constant data by Palmer (1973).‡

Lounasmaa and Sundström (1966), in view of the strong basal plane anisotropy of Tb at low temperatures, favoured introduction of a spin-wave energy gap as against a simple power law for C_M. They found a reasonable fit with $C_M = 36\, T^{3/2} \exp(-23.5/T)$ from 8 to 20 K, based on the assumption $C_E + C_L = C_p$ (Lu). In their analysis, Wells et al. (1976) used a theoretical expression

†Note that Anderson et al.'s (1968) results were based on an erroneous temperature scale, as discussed in Krusius et al., 1969. This underlines the importance of a correct temperature scale in low temperature heat capacity work.

‡The value of 182 K originally given by Palmer (1973) was apparently incorrect (Wells et al. 1976, note on table 3).

$C_M = 9.5\ T^{3/2} \exp(-14.8/T)$ mJ/mole·K. But, since C_L is not independently known, this cannot be regarded as the final value for C_M, even for measurements from this pure sample. Nevertheless, in view of earlier work, the evidence is strong in favour of C_M behaviour of the type proposed above.

Amongst other relevant work done recently on Tb may be mentioned spin-wave theoretical calculations by Brooks et al. (1968) based on inelastic neutron scattering data (Møller and Houmann 1966, Møller et al. 1968). The overall behaviour of the heat capacity of Tb could be reproduced below 60 K by Stevens and Krukewich (1973) using the same scattering data as Brooks et al. (1968) but allowing for variations of the interatomic parameters consistent with the dispersion curves. They found for both Gd and Tb that the temperature dependence of C_M is slightly greater than $T^{3/2}$. Although no allowance was made for an exponential factor, we can take this result as further support for a $T^{3/2}$ dependence along with an exponential term.

The higher γ values obtained during the 1960's in investigations of heat capacities below 4.2 K are clearly due to impurity effects, which are fortunately negligible at the very low temperatures where C_N is investigated, but which are enough to disturb any low temperature extrapolation of the type discussed in section 1.5 above (Morrison and Newsham 1968).

3.3. *Dysprosium*

Due mainly to impurity oxide, the low temperature heat capacity of dysprosium is strongly sample dependent, especially between about 0.5 and 0.8 K (see fig. 1 of Flotow and Osborne 1964). Thus any analysis based on this temperature range alone cannot be relied upon. The only safe criterion is that the purest samples presumably give the lowest heat capacity from which we can obtain an upper limit for γ and $\theta_D(0)$. On this basis $\gamma \leqslant 9.0$ mJ/mole·K^2 for Dy. To obtain any further information from the experimental results, some assumptions must be made about C_E and C_L. Single crystal elastic constant data for Dy (Palmer 1970) give $\theta_D(0) = 183$ K as against polycrystalline results (Rosen 1968) where $\theta_D(4.2) = 178$ K. Flotow and Osborne (1963) assumed $C_E = 10.5\ T$ mJ/mole·K and $\theta_D(0) = 186$ K and found a fit to Cooper's (1962) expression, eq. (5.7), with $E_g/k_B \sim 50$ K. Lounasmaa and Sundström (1966), on the other hand, using $C_E + C_L = C_p$(Lu) proposed the behaviour $C_M = 107\ T^{3/2} \exp(-31/T)$ mJ/mole·K.

In the light of the recent work on Y, Gd, Tb, Ho, and Lu, described in the appropriate sections of this chapter, it is likely that none of these analyses represents the final picture for dysprosium. We must await further heat capacity work on high purity samples.

The nuclear contribution, fortunately, is in a better situation (Anderson et al. 1969, and references therein) – table 5.2 – and indicates a fully developed 4f electronic moment of the dysprosium ions.

3.4. *Holmium*

Even at 4 K the nuclear contribution dominates the heat capacity of holmium by about 85%. Thus Krusius et al. (1969) in measurements below 0.6 K were essentially looking at C_N only, and obtained the hyperfine interaction parameters given in table 5.2. These parameters agree fairly well with those of van Kempen et al. (1964), whose C_N results showed considerably more scatter, although Krusius et al. (1969) felt that the fit to their own results was not as good as for the other lanthanides they have measured. The results of NMR (Mackenzie et al. 1974) give slightly lower parameter values.

The ferromagnetic spiral ordering of the moments in holmium, with cone angle 79°, makes the transition to a proper screw as the temperature is raised through 20 K (Koehler et al. 1962, and ch. 7 section 3.2.4), with a corresponding anomaly in the heat capacity around that temperature (Dempesy et al. 1966 around 16 K; Lounasmaa and Sundström 1966 around 17.5 K). Nevertheless, making use of our knowledge of C_N and confining analysis to below 4 K, we should be able to estimate C_L and C_E. Lounasmaa (1962b) found $\gamma = 10$ mJ/mole·K^2, whereas in recent, unpublished work Hill et al. (1976 private communication), measuring on what appears to be the purest holmium sample to date, estimate a lower γ value of 6 ± 1 mJ/mole·K^2. In both cases, however, the large observed T^3 term clearly includes a magnetic contribution and precludes unique determination of the Debye temperature. The most we can say is that the $\theta_D(0)$ obtained from elastic constants of holmium single crystals (Palmer 1970) is 188.5 K, as against the interpolation approximation of 191 ± 5 K (Lounasmaa 1964a) and the polycrystalline elastic constant value of 195 K (Rosen 1967) at 4.2 K.

Theoretical justification for a T^3 behaviour in C_M can be found (Kaplan 1961). One might also consider that holmium's magnetic structure is intermediate between that of dysprosium and erbium, the latter displaying a linear spin-wave dispersion relation in neutron scattering studies along the c-axis (Nicklow et al. 1971). No evidence has been found in support of an exponential factor other than in the graphical analysis by Morrison and Newsham (1968) of Lounasmaa's (1962b) results below 4 K. Confirmation of occurrence of this type of ordering in zero field at around 20 K is demonstrated by studies of the heat capacity in an applied field up to 40 K (Dempesy et al. 1966). Here the symmetric type of peak associated with the 85 K transition in dysprosium was found. In zero field, below 8 K, Dempesy et al. obtained a T^3 behaviour for C_M, while for a considerable range above that temperature they obtained a linear C_M in both zero and applied field, if they assumed that $C_L + C_E = C_p(\text{Lu})$. This agrees with the analysis of Lounasmaa and Sundström (1966), who found that up to 8 K, $C_M \sim T^{3.2}$. It would be interesting to make renewed attempts to analyse C_M using a more reliable estimate for $\theta_D(T)$ and the recently proposed value $\gamma \approx 6$ mJ/mole·K^2.

3.5. *Erbium*

Erbium has been scantily studied due to the usual problem of obtaining samples of sufficient purity, which here appears to have been more serious than for the other lanthanide metals. Widely conflicting results have been reported for the heat capacity of Er, which makes its presentation something of a hotch-potch.

The nuclear heat capacity, however, has been fairly well established (Krusius et al. 1974) and agrees well with NMR results (Sano et al. 1972), as shown in table 5.2. After subtraction of this C_N the remaining heat capacity does not yield to simple analysis. Hill et al. (1976 private communication) have obtained the lowest heat capacity results so far for erbium and extract a γ value of 9.5 mJ/mole·K^2 as an upper limit for γ, and a T^3 magnetic term. Their sample still contained apparent impurity effects, since a plot, of $(C_p - C_N)/T$ versus T^2 showed a minimum at about 1.3 K. Other γ estimates have ranged from 9.145 mJ/mole·K^2 assumed by Parks (1962) and quoted by him as being that for Lu but in fact being closer to the α-La value, to 17.2 mJ/mole·K^2 found by Satya and Wei (1971). The latter also studied erbium–thulium alloys and found γ to be strongly composition dependent. They proposed an itinerant 4f-band model where a narrow 4f-band with a substructure overlaps the conduction band around the Fermi level. This should be treated as pure speculation, as the 4f electron shell is both very narrow (~ 0.05 eV) and lies well below (~ 10 eV) the Fermi level (e.g. Dimmock and Freeman 1964, Watson et al. 1968 Andersen and Loucks 1968, Hedén et al. 1971). What might in fact be happening could perhaps be related to the peak in the electronic density of states around the Fermi level arising from the d-electrons, which itself contains some substructure. In the spin-polarized state and for alloying we might find shifting of this peak for spin-up and spin-down states relative to the Fermi level. Cf. the spin-polarized band calculation for gadolinium (Harmon and Freeman 1974) discussed above (section 3.1).

The T^3 magnetic term in the heat capacity is what would be expected from the ferromagnetic spiral (i.e. the cone) structure of erbium (Kaplan 1961) and has been supported by the discovery of a linear spin-wave dispersion law along the c-axis in neutron scattering experiments (Nicklow et al. 1971).

3.6. *Thulium*

Below 25 K the reported heat capacity data on thulium vary by as much as 20%, the discrepancy increasing towards lower temperatures (Lounasmaa and Sundström 1966, and references therein). Since no sharp anomaly has been observed, the cause of these discrepancies is not clear, but after subtracting the nuclear, electronic and lattice contributions in the usual way, Lounasmaa and Sundström (1966) found the remaining term to vary as $T^{2.3}$ over the temperature interval 4 to 20 K.

At the low temperatures of interest here, thulium has a net ferromagnetic

moment arising from a $+4, -3, +4, -3\ldots$ sequence in the c-direction. Thus no theoretical predictions are available for C_M in thulium. Likewise, the linear terms reported vary, but tend to have a coefficient considerably greater than 10.5 mJ/mole·K^2, which may generally be taken as an upper estimate for the heavy lanthanides. Thus also this indicates an unusually large magnetic term or some ever present impurity anomaly. For example, Satya and Wei (1971) obtained a term $55.9T$ mJ/mole·K.

Even the nuclear heat capacity of Tm has presented problems. Holmström et al. (1969) in measurements between 0.02 and 0.4, obtain a good fit with the parameters in table 5.2, provided that only $95.0 \pm 0.8\%$ (by weight) of the specimen is assumed to contribute to C_N. As these parameters, although smaller than the theoretical values (Bleaney 1963), agree well with those found from Mössbauer (Kalvius et al. 1963) and neutron transmission experiments (Al-Kital et al. 1967), they may be taken to represent the situation in thulium at low temperatures.

3.7. *Ytterbium*

The only published heat capacity results on ytterbium are those of Lounasmaa (1963, 1966) covering 0.4 to 25 K, and of Gerstein et al. (1964) from 15 to 300 K, the latter results being 2–3% higher in the overlapping region. The normally accepted structure for Yb has been divalent fcc. However, in recent years (in particular Kayser 1970, 1971) evidence has pointed to a martensitic transformation, starting around 260 K, from β(fcc) – Yb to α(hcp) – Yb, with an associated volume change of a mere 0.0091. Kayser (1971) proposes that in a high-purity, strain-free Yb sample the stable form below 270 K is hcp, but that over a broad range of temperatures the free energies of the two phases are so close that small concentrations of impurities can shift the range of stability. Thus varying amounts of the two phases might account for the 2–3% discrepancy between the heat capacity results. The small T^{-2} term observed below 1 K by Lounasmaa (1963) has been attributed to lanthanide impurities. At the time of these heat capacity measurements, there was no reason to suspect the presence of a second structural phase, which fortunately appears to be also divalent and non-magnetic, so that for the pure metal we might take one representative set of lattice and electronic terms for both phases. The low temperature heat capacity results therefore yield $\gamma = 2.90$ mJ/mole·K^2 and $\theta_D(0) = 118.1$ K. The Debye temperature drops through a minimum at about 13 K and levels off at a value of 110 K for higher temperatures. These values, as expected, differ considerably from those of the other heavy lanthanides, but compare favourably with elastic constant measurements by Rosen (1967) which give $\theta_D(4.2) = 121$ K and $\theta_D(300) = 113$ K.

3.8. *Lutetium*

Lutetium metal is trivalent, hexagonal close-packed, and has a full 4f shell which makes it non-magnetic. Furthermore, since its physical properties otherwise resemble the heavy lanthanides from Gd to Tm, non-magnetic Lu has often

been adopted as the model for the electronic and lattice contributions to the heat capacity of the magnetic heavy metals in lieu of a better approximation. Thus several independent studies have been made, a comparison of which is presented in Gerstein et al. (1969), who unfortunately do not analyse their own results other than to tabulate the smoothed thermodynamic functions and the (uncorrected for curvature) experimental data. The observed discrepancies between the variously reported heat capacities for Lu are attributed by Gerstein et al. to a hydrogen impurity, presumably lutetium hydride.

In their analysis of the heavy lanthanides, Lounasmaa and Sundström (1966) used the heat capacity of lutetium as measured by Lounasmaa (1964a) and Culbert (1967) on the same sample. This gave $\gamma = 11.27$ mJ/mole·K^2 and $\theta_D(0) = 210$ K. The Debye temperature drops rapidly above 4 K to a minimum of 158 K at approximately 25 K (Culbert, 1967).

A small, but measurable, T^{-2} term (Lounasmaa, 1964a) might be due to antishielding effects caused by crystal field distortion of the closed electronic shells. In this case the quadrupole coupling constant for ^{175}Lu becomes $P = 0.00072$ K. Alternatively, the T^{-2} term might arise from long-range exchange-type coupling between the magnetic moments of rare earth impurities in the lutetium sample.

The most recent data on a lutetium sample purified by S.S.E. processing (Wells et al., 1976) yields $\gamma = 6.8 \pm 0.1$ mJ/mole·K^2, which is closer to the band theoretical value of 4.4 mJ/mole·K^2 of Keeton and Loucks (1968) than that given earlier above. Furthermore, this new γ value follows the reported trend in the magnetic heavy lanthanides, which indicates that the electronic term is indeed closer to the band theoretical value than had previously been believed.

4. Concluding remarks

In conclusion, it may be said that the stumbling blocks in analysing heat capacity measurements on the rare earth metals are the difficulty of obtaining satisfactorily high purity samples and the current state of the theory for spin waves. There are too many unknown variables for unambiguous analysis. Nevertheless, in nearly all cases the nuclear contribution has been determined accurately, and for the majority some indication of the most likely form for the magnetic term exists.

The determination of the linear electronic term depends on the method of analysis and on the sample purity; as discussed in section 1.5, we find "magnetic enhancement" of γ in many cases. Likewise, the Debye temperature value is not always clear, although elastic constant results give good guidelines.

In this review we have not touched on the related metals yttrium and scandium. We may briefly mention here that recent measurements give results in line with those for non-magnetic lanthanum and lutetium. For yttrium the most recent results give $\gamma = 8.2$ mJ/mole·K^2 and $\theta_D(0) = 248 \pm 3$ K (Wells et al., 1976), while for scandium $\gamma = 10.34$ mJ/mole·K^2 and $\theta_D(0) = 346.1 \pm 0.9$ K (Tsang et al., 1976b).

Also somewhat neglected in their details are the various results on inter rare earth alloys. A number of such have been mentioned where appropriate, but the bulk have been left out as they do not at this stage add clarity to the situation in the pure metals. This does not mean to say that heat capacity work on inter rare earth alloys is of no consequence. On the contrary, there is a great need for systematic heat capacity studies of these alloys according to crystal structure and magnetic structure. Here also, theory cannot progress further without support from experiments on high purity specimens which have been well characterized with respect to the polymorphic phase(s) present.

5. Recent developments

Hydrogen tunneling between interstitial sites has been proposed as a mechanism which could give rise to the T^{-2} anomaly in the low temperature heat capacity, notable in lutetium (Thome et al. 1978, Gschneidner and Thome 1978). This effect occurs within a critical concentration range from about 0.1 to between 1.5 and 3.0 at.% H, with a maximum at 0.22 at.% H. The role of interstitial impurities i (where i is C, N, or O) is also considered vital in the thermal making and breaking of H–i bonds for the different interstitial configurations (octahedral, tetrahedral or triangular holes), so that it may not merely be the H concentration itself, but the H/i concentration ratio which determines the range and nature of the low temperature anomaly (Gschneidner and Thome 1978). This model may account for the discrepancies between very low temperature heat capacities for different samples of the heavy rare earths and scandium, for which the hydrogen solubility is high.

To table 5.3 should be added the results for $\theta_D(0)$ from more recent analysis of single crystal elastic constant results by Palmer and co-workers (Palmer 1977): Gd 180.2 K, Tb 185.6 K, Dy 180.7 K, Ho 186.8 K, Er 187.8 K, and Y 255.2 K.

Acknowledgements

The author wishes to thank Professor O.V. Lounasmaa for his guidance and assistance in collecting and assessing the materials required. She further wishes to thank Professor R.W. Hill and Drs. R.G. Jordon and P.C. Lanchester for their kindness in sending her their unpublished results, along with appropriate comments, on solid-state electrotransport purified samples of the heavy lanthanides. Finally, the Department of Solid State Physics of the University of Uppsala and that of the Technical University of Stockholm are to be thanked for their hospitality and provision of working space during the preparation of this chapter.

References

Al-Kital, R.A., G. Brünhart, S.S. Malik, J.P. Roberge and V.L. Sailor, 1967, Nucl. Phys. **A91**, 644.

Andersen, O.K. and T.L. Loucks, 1968, Phys. Rev. **167**, 551.

Anderson, A.C., B. Holmström and M. Krusius, 1968, Phys. Rev. Lett. **20**, 154.

Anderson, A.C., B. Holmström, M. Krusius and G.R. Pickett, 1969, Phys. Rev. **183**, 546.

Andres, K., 1963, Phys. Rev. Lett. **10**, 223.

Andres, K., E. Bucher, J.P. Maita, L.D. Longinotti and R. Flukiger, 1972, Phys. Rev. **B6**, 313.

Bader, S.D., N.E. Phillips and D.B. McWhan, 1973, Phys. Rev. **B7**, 4686.

Beattie, J.A., 1926/27, J. Math. Phys. **6**, 1.

Berman, A., M.W. Zemansky and H.A. Boorse, 1958, Phys. Rev. **109**, 70.

Bleaney, B., 1963, J. Appl. Phys. **34**, 1024.

Bleaney, B., 1972, Hyperfine interactions, in: Elliott, R.J., ed., Magnetic properties of rare earth metals (Plenum Press, London and New York) pp. 383–420.

Bonnerot, J., B. Caroli and B. Coqblin, 1966, in: Lounasmaa, O.V. ed., Proceedings of the 1966 Low Temperature Calorimetry Conference (Ann. Acad. Sci. Fennicae A VI, No. 210) pp. 120–128.

Brooks, M.S.S., D.A. Goodings and H.I. Ralph, 1968, J. Phys. C (Proc. Phys. Soc) [2] **1**, 1596.

Brünhart, G., 1967 unpublished (but see Anderson et al., 1969).

Brünhart, G., H. Postma and V.L. Sailor, 1965, Phys. Rev. **137**, B 1484.

Bucher, E., C.W. Chu, J.P. Maita, K. Andres, A.S. Cooper, E. Buehler and K. Nassau, 1969, Phys. Rev. Lett. **22**, 1260.

Burgardt, P., K.A. Gschneidner, Jr., D.C. Koskenmaki, D.K. Finnemore, J.O. Moorman, S. Legvold, C. Stassis and T.A. Vyrostek, 1976, Phys. Rev. **B14**, 2995.

Collan, H.K., T. Heikkilä, M. Krusius and G.R. Pickett, 1970a, Cryogenics **10**, 389.

Collan, H.K., M. Krusius and G.R. Pickett, 1970b, Phys. Rev. **B1**, 2888.

Conway, M.M. and N.E. Phillips, 1974, in: Timmerhaus, K.D., W.J. O'Sullivan and E.F. Hammel, eds., Low Temperature Physics–LT 13, Colorado 1972 (Plenum Press, New York and London) pp. 629–632.

Cooper, B.R., 1962, Proc. Phys. Soc. (London) **80**, 1225.

Cooper, B.R., 1972, Phenomenological theory of magnetic ordering: Importance of interactions with the crystal lattice, in: Elliott, R.J., ed., Magnetic properties of rare earth metals (Plenum Press, London and New York) pp. 17–80.

Cooper, B.R. and O. Vogt, 1971, J. Phys. (Paris) Suppl. 32, **C1**, 958.

Coqblin, B. and A. Blandin, 1968, Advan. Phys. **17**, 281.

Culbert, H.V., 1967, Phys. Rev. **156**, 701.

Curry, R. and K.N.R. Taylor, 1973, "to be published".†

Dempesy, C.W., J.E. Gordon and T. Soller, 1966, in: Lounasmaa, O.V., ed., Proceedings of the 1966 Low Temperature Calorimetry Conference (Ann. Acad. Sci. Fennicae A VI, No. 210) pp. 204–209.

Dimmock, J.O. and A.J. Freeman, 1964, Phys. Rev. Lett. **13**, 750.

Dreyfus, B., B.B. Goodman, A. Lacaze and G. Trolliet, 1961, Comptes Rendus **253**, 1764.

Dreyfus, B., J.C. Michel and A. de Combarieu, 1965, in: Daunt, J.G., D.O. Edwards, F.J. Milford and M. Yaqub, eds., Proceedings of the 9th International Conference on Low Temperature Physics, Columbus, Ohio 1964 (Plenum Press, London and New York) pp. 1054–1058.

Dreyfus, B., J.C. Michel and D. Thoulouze, 1967, Phys. Lett. **24A**, 457.

Finnemore, D.K., D.L. Johnson, J.E. Ostenson, F.H. Spedding and B.J. Beaudry, 1965, Phys. Rev. **137**, A550.

Finnemore, D.K. and D.L. Johnson, 1966, in: Lounasmaa, O.V., Ed., Proceedings of the 1966 Low Temperature Calorimetry Conference (Ann. Acad. Sci. Fennicae A VI, No. 210) p. 85.

Flotow, H.E. and D.W. Osborne, 1964, in: Vorres, K.S., ed., Proceedings of the Third Conference on Rare Earth Research, Clearwater, Florida 1963 (Gordon and Breach, New York) pp. 233–243.

Freeman, A.J., 1972, Energy band structure, indirect exchange interactions and magnetic ordering, in: Elliott, R.J., ed., Magnetic properties of rare earth metals (Plenum Press, London and New York) pp. 245–333.

Gerstein, B.C., J.R. Mullaly, N.E. Phillips, R.W. Miller and F.H. Spedding, 1964, J. Chem. Phys. **41**, 883.

Gerstein, B.C., F.J. Jelenik, J.R. Mullaly, W.D. Shickell and F.H. Spedding, 1967, J. Chem. Phys. **47**, 5194.

Gerstein, B.C., W.A. Taylor, W.D. Shickell and F.H. Spedding, 1969, J. Chem. Phys. **51**, 2924.

Gopal, E.S.R., 1966, Specific heats at low temperatures (Plenum Press, New York) at pp. 219–226.

Gregers-Hansen, P.E., M. Krusius and G.R. Pickett, 1972, Phys. Rev. Lett. **29**, 420.

Gschneidner, K.A. Jr., P. Burgardt, S. Legvold, J.O. Moorman, T.A. Vyrostek and C.

†Note: A search of the literature has not revealed the time or place of this publication, which has been extensively quoted by Krizek (1975) q.v.

Stassis, 1976, J. Phys. F: Metal Phys. **6**, L49.
Harmon, B.N. and A.J. Freeman, 1974, Phys. Rev. **B10**, 1979.
Hedén, P.O., H. Löfgren and S.B.M. Hagström, 1971, Phys. Rev. Lett. **26**, 432.
Hedén, P.O., H. Löfgren and S.B.M. Hagström, 1972, Phys. Stat. Sol. (b) **49**, 721.
Hill, R.W., 1976, private communication.
Hill, R.W., J. Cosier, D.A. Hukin, P. Wells and P.C. Lanchester, 1974, Phys. Lett. **49A**, 101.
Holmström, B., A.C. Anderson and M. Krusius, 1969, Phys. Rev. **188**, 888.
Hüfner, S. and J.H. Wernick, 1968, Phys. Rev. **173**, 448.
Jackson, C., 1969, Phys. Rev. **178**, 949.
Janovec, V. and J.A. Morrison, 1965, Phys. Lett. **17**, 226.
Jelinek, F.J., B.C. Gerstein, M. Griffel, R.E. Skochdopole and F.H. Spedding, 1966, Phys. Rev. **149**, 489.
Johansson, B., 1974, Phil. Mag. **30**, 469.
Johnson, D.L., 1966, Specific heat of fcc and d-hcp lanthanum from 1.0 to 10.0 K, Thesis, Iowa State University of Science and Technology, Ames, Iowa, IS-5-124.
Kalvius, M., P. Kienle, H. Eicher, W. Wiedemann and C. Schüler, 1963, Z. Phys. **172**, 231.
Kaplan, T.A., 1961, Phys. Rev. **124**, 329.
Kayser, F.X., 1970, Phys. Rev. Lett. **25**, 662.
Kayser, F.X., 1971, Phys. Stat. Sol. (a) **8**, 233.
Keeton, S.C. and T.L. Loucks, 1968, Phys. Rev. **168**, 672.
Kimura, I., 1970, J. Phys. Soc. Japan **28**, 1182.
Kobayashi, S., N. Sano and J. Itoh, 1966, J. Phys. Soc. Japan **21**, 1456.
Koehler, W.C., J.W. Cable, E.O. Wollan and M.K. Wilkinson, 1962, J. Phys. Soc. Japan Suppl. **17**, 32S.
Koehler, W.C., R.M. Moon, J.W. Cable and H.R. Child, 1972, Amer. Inst. Phys. Conf. Proc. **5**, 1434.
Kondo, J., 1965, Prog. Theor. Phys. **33**, 575.
Koskimaki, D.C. and K.A. Gschneidner, Jr., 1974, Phys. Rev. **B10**, 2055.
Koskimaki, D.C. and K.A. Gschneidner, Jr., 1975, Phys. Rev. **B11**, 4463.
Krizek, H., 1975, J. Phys. F: Metal Phys. **5**, 56.
Krusius, M., 1971, Calorimetric measurements of hyperfine interactions in some metals, Thesis, Helsinki University of Technology, Otaniemi, Finland.
Krusius, M., A.C. Anderson and B. Holmström, 1969, Phys. Rev. **177**, 910.
Krusius, M., G.R. Pickett and M.C. Veuro, 1974, Solid State Commun. **14**, 191.
Lebech, B., K.A. McEwen and P.A. Lindgård, 1975, J. Phys. C: Solid State Phys. **8**, 1684.
Lindelof, P.E., I.E. Miller and G.R. Pickett, 1975, in: Krusius, M. and M. Vuorio, eds., Proceedings of the 14th International Conference on Low Temperature Physics, Otaniemi, Finland 1975, Vol. V (North-Holland, Amsterdam and Oxford; Elsevier, New York) pp. 204–207.
Lock, J.M., 1957, Proc. Phys. Soc. (London) **B70**, 566.
Loucks, T.L., 1966, Phys. Rev. **144**, 504.
Lounasmaa, O.V., 1962a, Phys. Rev. **126**, 1352.
Lounasmaa, O.V., 1962b, Phys. Rev. **128**, 1136.
Lounasmaa, O.V., 1963, Phys. Rev. **129**, 2460.
Lounasmaa, O.V., 1964a, Phys. Rev. **133**, A219.
Lounasmaa, O.V., 1964b, Phys. Rev. **133**, A502.
Lounasmaa, O.V., 1964c, Phys. Rev. **133**, A211.
Lounasmaa, O.V., 1966, Phys. Rev. **143**, 399.
Lounasmaa, O.V., 1967, Nuclear specific heats in metals and alloys, in: Freeman, A.J. and R.B. Frankel, eds., Hyperfine interactions (Academic Press, New York) pp. 467–496.
Lounasmaa, O.V. and P.R. Roach, 1962, Phys. Rev. **128**, 622.
Lounasmaa, O.V. and L.J. Sundström, 1966, Phys. Rev. **150**, 399.
Lounasmaa, O.V. and L.J. Sundström, 1967, Phys. Rev. **158**, 591.
Lounasmaa, O.V. and M.C. Veuro, 1972, Phys. Lett. **40A**, 371.
Mackenzie, I.S., M.A.H. McCausland and A.R. Wagg, 1974, J. Phys. F: Metal Phys. **4**, 315.
Mackintosh, A.R. and H. Bjerrum Møller, 1972, Spin waves, in: Elliott, R.J., ed., Magnetic properties of rare earth metals (Plenum Press, London and New York) pp. 187–244.
Meaden, G.T. and N.H. Sze, 1969, in: Allan, J.F., D.M. Finlayson and D.M. McCall, eds., Proceedings of the 11th International Conference on Low Temperature Physics, St. Andrews 1968 (University of St. Andrews) pp. 1102–1104.
Møller, H.B. and J.C.G. Houmann, 1966, Phys. Rev. Lett. **16**, 737.
Møller, H.B., J.C.G. Houmann and A.R. Mackintosh, 1968, J. Appl. Phys. **39**, 807.
Moon, R.M., J.W. Cable and W.C. Koehler, 1964, J.Appl. Phys. Suppl. **35**, 1041.
Morrison, J.A. and D.M.T. Newsham, 1968, J. Phys. C (Proc. Phys. Soc.) Ser. 2, **1**, 370.
Nakajima, S., 1967, Prog. Theor. Phys. **38**, 23.
Nicklow, R.M., N. Wakabayhasi, M.K. Wilkinson and R.E. Reed, 1971, Phys. Rev. Lett. **27**, 334.
Ofer, S., M. Rakavy, E. Segal and B. Khurgin, 1965, Phys. Rev. **138**, A241.
Ohtsuka, T. and T. Satoh, 1966, in: Lounasmaa, O.V., ed., Proceedings of the 1966 Low Temperature Calorimetry Conference (Ann. Acad. Sci. Fennicae A VI No. 210) pp. 92–97.
Palmer, S.B., 1970, J. Phys. Chem. Solids **31**, 143.
Palmer, S.B. and E.W. Lee, 1973, in: Proceedings of the 1973 International Conference on Magnetism, Vol. 1, pp. 169–173.
Panousis, N.T. and K.A. Gschneidner, Jr., 1970, Solid State Commun. **8**, 1779.
Parks, R.D., 1962, in: Nachman, J.F. and C.E. Lundin, eds., Proceedings of the 2nd Conference on Rare Earth Research, Glenwood Springs, Colorado 1961 (Gordon and Breach, New York) pp. 225–231.
Phillips, N.E., 1971, Low-temperature heat

Parkinson, D.H., F.E. Simon and F.H. Spedding, 1951, Proc. Roy. Soc. (London) A207, 137.

capacity of metals, in: CRC Critical Reviews in Solid State Sciences (1971) pp. 467–553.
Phillips, N.E., J.C. Ho and T.F. Smith, 1968, Phys. Lett. **27A**, 49.
du Plessis, P. de V., 1976, J. Phys. F: Metal Phys. **6**, 873.
Probst, C. and J. Wittig, 1975, in: Krusius, M. and M. Vuorio, eds., Proceedings of the 14th International Conference on Low Temperature Physics, Otaniemi 1975, Vol. III (North-Holland, Amsterdam and Oxford; Elsevier, New York) pp. 453–456.
Ratto, C.F., B. Coqblin and E. Galleani d'Agliano, 1969, Advan. Phys. **18**, 489.
Rosen, M., 1967, Phys. Rev. Lett. **19**, 695.
Rosen, M., 1968, Phys. Rev. **174**, 504.
Sano, N. and J. Itoh, 1972, J. Phys. Soc. Japan **32**, 95.
Sano, N., M. Teraoka, K. Shimizu and J. Itoh, 1972, J. Phys. Soc. Japan **32**, 571.
Sano, N., K. Shimizu and J. Itoh, 1975, J. Phys. Soc. Japan **39**, 84.
Satya, A.V.S. and C.T. Wei, 1971, Low-temperature specific heats of hexagonal close-packed erbium–thulium alloys, Nat. Bur. Stand. (U.S.) Spec. Publ. No. 323, pp. 571–577.
Sedaghat, A.K. and A.P. Cracknell, 1971, J. Phys. C: Solid State Phys. **4**, 3215.
Shender, E.F., 1974, Zh. Eksp. Teor. Fiz. **66**, 2198 [English transl. Sov. Phys.-J.E.T.P. **39**, 1083 (1974)].
Stevens, W.N.R. and K. Krukewich, 1973, J. Phys. F: Metal Phys. **3**, 1229.
Sundström, L.J., 1968, A Theoretical investigation of the lattice specific heat of gadolinium, dysprosium and erbium metals (Ann. Acad. Sci. Fennicae A VI, No. 280).
Taylor, K.N.R. and M.I. Darby, 1972, Physics of rare earth solids (Chapman and Hall, London).
Tsang, T.-W.E., K.A. Gschneidner, Jr. and F.A. Schmidt, 1976b, Solid State Commun. **20**, 737.
Tsang, T.-W.E., K.A. Gschneidner, Jr., D.C. Koskenmaki and J.O. Moorman, 1976a, Phys. Rev. **B14**, 4447.
van Kempen, H., A.R. Miedema and W.J. Huiskamp, 1964, Physica **30**, 229.
Watson, R.E., A.J. Freeman and J.O. Dimmock, 1968, Phys. Rev. **167**, 497.
Wells, P., P.C. Lanchester, D.W. Jones and R.G. Jordan, 1974, J. Phys. F: Metals Phys. **4**, 1729.
Wells, P., P.C. Lanchester, D.W. Jones and R.G. Jordan, 1976, J. Phys. F: Metal Phys. **6**, 11.
Wilkinson, M.K., H.R. Child, C.J. McHargue, W.C. Koehler and E.O. Wollan, 1961, Phys. Rev. **122**, 1409.

References to section 5

Gschneidner, K.A., Jr. and D.K. Thome, 1978, in Proceedings of the 13th Rare Earth Conference (Plenum Press) to be published.
Palmer, S.B., 1977, private communication.
Thome, D.K., K.A. Gschneidner, Jr., G.S. Mowry and J.F. Smith, 1978, Solid State Comm. **25**, 297.

Handbook on the Physics and Chemistry of Rare Earths, edited by K.A. Gschneidner, Jr. and L. Eyring

Chapter 6

MAGNETIC AND TRANSPORT PROPERTIES OF THE RARE EARTHS

K.A. McEWEN
Department of Pure and Applied Physics, University of Salford, Salford M5 4WT, UK

Contents

Symbols

a = lattice parameter
$\hat{a}$ = unit vector parallel to $\langle 11\bar{2}0 \rangle$ directions
a_i^+, a_i = spin deviation creation and annihilation operators
a_q^+, a_q = magnon creation and annihilation operators
A = fourth-order magnetostriction parameter
A_l^m = crystal field potential
$A_q(T,H)$ = spin wave energy term [see eq. (6.13)]
$b(T,H)$ = ellipticity parameter defined by eq. (6.14)
$\hat{b}$ = unit vector parallel to $\langle 10\bar{1}0 \rangle$ directions
B = magnetic induction
B_l^m = microscopic single-ion magnetic anisotropy coefficient
$B_q(T,H)$ = spin wave energy term [see eq. (6.13)]
$B^{\Gamma,i}$ = magnetoelastic coupling constant
$B_s(y)$ = Brillouin function
$B_s'(y)$, $B_s''(y)$ = first and second derivatives of $B_s(y)$
c = lattice parameter
c_{ij}^{Γ} = elastic modulus corresponding to strain of hcp lattice
c_{kl} = elastic modulus corresponding to cartesian strain
C = second-order magnetostriction parameter

D = magnetostriction parameter [see eq. (6.55b)]
$E(\boldsymbol{k})$ = conduction electron dispersion relation
E_{ex} = exchange energy
E_F = Fermi energy
E_H = transverse Hall electric field
E_i = energy of crystal field level
E_{me} = magnetoelastic energy
$E_0(T, H)$ = spin wave energy gap (at zero wavevector)
$E_q(T, H)$ = energy of spin wave of wavevector q
$F(\theta, \phi)$ = free energy for magnetization along direction (θ, ϕ)
$F_q(T, H)$ = exchange term in spin wave energy [see eq. (6.18)]
g = gyromagnetic ratio, Landé splitting factor
G = magnetostriction parameter [see eq. (6.55b)]
$\hbar$ = Planck's constant/2π
H_{app} = applied magnetic field
H_{c1} = critical field for spiral-fan transition
H_{c2}, H_{c3} = critical fields for magnetic structure transitions
H_d = applied magnetic field needed to form single domain
H_{int} = internal magnetic field
$\mathcal{H}_{an}$ = effective single-ion anisotropy hamiltonian
$\mathcal{H}_{cf}$ = crystal field hamiltonian
$\mathcal{H}_e$ = elastic hamiltonian
$\mathcal{H}_{ex}$ = isotropic exchange hamiltonian
$\mathcal{H}_{me}$ = magnetoelastic hamiltonian
$\mathcal{H}_{sf}$ = conduction electron – local moment hamiltonian
$\mathcal{H}_{Zee}$ = Zeeman hamiltonian
$|i\rangle$ = eigenfunction of $\mathcal{H}_{cf}$
$\hat{I}_m$ = reduced hyperbolic Bessel function
J = total angular momentum, also current density
$J_n = J(J-\frac{1}{2})(J-1)\ldots(J-\frac{1}{2}[n-1])$
J_{sf} = coupling strength of s and f electrons
$J_\pm, J_z$ = angular momentum operators
$\mathcal{J}(R)$ = intra-sublattice exchange interaction in $\mathcal{H}_{ex}$
$\mathcal{J}'(R)$ = inter-sublattice exchange interaction in $\mathcal{H}_{ex}$
$\mathcal{J}(q), \mathcal{J}'(q)$ = spatial Fourier transforms of $\mathcal{J}(R), \mathcal{J}'(R)$
$\mathcal{J}_1, \mathcal{J}_2 \ldots \mathcal{J}_5$ = interplanar exchange parameters
k = Boltzmann constant
$\boldsymbol{k}$ = conduction electron wavevector
k_i = magnetoresistivity anisotropy parameter
K = kelvin
$K_{22}(\boldsymbol{q})$ = anisotropic exchange parameter
l = orbital quantum number
L = total orbital angular momentum
$\mathcal{L}^{-1}$ = inverse Langevin function
$m(T, H)$ = reduced magnetization [see eq. (6.15)]
m^* = conduction electron effective mass
M = bulk magnetization
M_0 = bulk magnetization at zero internal field
n_q = spin wave population factor, $[\exp(\beta\hbar\omega - 1)]^{-1}$
N = number of ions/unit volume, also demagnetization factor
$O_l^m(J)$ = operator equivalent of spherical harmonic, defined by Elliott and Stevens (1953)
p = pressure, also parameter in eq. (6.20)
P_{ij} = matrix defined by eq. (6.64)
$P_l(\cos\theta)$ = Legendre polynomial
q = magnon wavevector, also parameter in eq. (6.20)
q_c = Debye cut-off wavevector
$\boldsymbol{Q}$ = magnetic structure modulation wavevector
Q_{ij} = matrix defined by eq. (6.64)
$\langle r^l \rangle$ = expectation value of r^l with respect to 4f wave function
$R(T)$ = renormalization factor [see eq. (6.37)]
R_0 = ordinary Hall coefficient
R_s = spontaneous Hall coefficient
R_1 = extraordinary Hall coefficient
s = spin quantum number
S = total spin angular momentum
$S_\pm, S_z$ = spin operators
T = absolute temperature
T = tesla
T_C = Curie temperature
T_N = Néel temperature
Tr = trace
v_i = component of conduction electron velocity
V_l^m = macroscopic anisotropy coefficient used in expansion of $F(\theta, \phi)$

in terms of Legendre polynomials [see eq. (6.50)]
$Y_l^m(\theta, \phi)$ = spherical harmonic normalized by integration over sphere of unit radius
α = wavevector independent term in $E_q(T, H)$ [see eq. (6.18)], also angular momentum matrix element between crystal field states [see eq. (6.35)]
α_i = direction cosines of magnetization
α_J = second-order Stevens' factor
$\alpha_l = \frac{1}{2}l(l+1)$, exponent characterizing temperature dependence of magnetic anisotropy
$\beta = (kT)^{-1}$, also term in $E_q(T, H)$ [see eq. (6.18)]
β_i = direction cosines of strain measurement direction
β_J = fourth-order Stevens' factor
$\beta_{66}^{\pm}$ = exponents characterizing temperature dependence of α and β
γ_J = sixth-order Stevens' factor
Δ = spin wave energy gap
$\Delta(T, H)$ = magnetization deviation parameter defined by eq. (6.14)
$\Delta\rho$ = magnetoresistivity
$\Delta\rho^H$ = magnetoresistivity above H_d
$\varepsilon^{\Gamma,j}$ = irreducible strains of hcp lattice
ε^{xy} = Cartesian strains
θ_l = Stevens' factors $\alpha_J, \beta_J, \gamma_J$
θ_0 = angle of easy magnetization direction from c-axis
$\theta_{\parallel c}, \theta_{\perp c}$ = paramagnetic Curie temperatures derived from c-axis and basal plane susceptibilities
κ_l^m = macroscopic anisotropy coefficient used in expansion of $F(\theta, \phi)$ in terms of spherical harmonics [see eq. (6.39)]
λ = molecular field parameter
$\lambda_i^{\Gamma,j}$ = magnetostriction coefficient [see eq. (6.35)]
μ_{Aj} = magnetic moment on jth ion in layer A
μ_B = Bohr magneton
μ_h, μ_c = magnetic moment on ions with local hexagonal or cubic site symmetry
ρ = electrical resistivity
$\rho_{long}, \rho_{trans}$ = resistivity due to longitudinal or transverse spin fluctuations
ρ_{mag} = contribution to resistivity arising from magnetic scattering
ρ_H = Hall resistivity
ρ_0 = spin disorder resistivity in high temperature limit $\div J(J+1)$
$\rho(E)$ = conduction electron density of states
σ = conduction electron spin, also $[1 - \Delta M(T, H)]$
σ_{ij} = electrical conductivity tensor
τ = relaxation time
$|\phi_i\rangle$ = eigenfunction of $\mathcal{H}_{cf} + \mathcal{H}_{Zee}$
χ_{ce} = measured conduction electron susceptibility
χ_{cf} = susceptibility of crystal field system
χ_p = Pauli susceptibility
χ_ζ = susceptibility for magnetic field applied in ζ-direction
ω = magnon frequency
ω_c = cyclotron frequency (eB/m^*)

1. Introduction

This chapter reviews the available knowledge of the bulk magnetic and transport properties of the rare earth metals with a particular emphasis on the ways in which these macroscopic properties may be interpreted to improve our understanding of the fundamental microscopic interactions. The review comprises five basic components: in section 2 we discuss the magnetization and susceptibility of these metals followed by their magnetic anisotropy in section 3 and magnetostriction in section 4. Section 5 considers the electrical resistivity, whilst section 6 deals with magnetoresistance and the Hall effect.

Although we shall concentrate our attention on the developments of the last

five years or so, earlier work will naturally be reviewed to some extent, not only for the sake of completeness, but also to set the more recent studies in perspective. Further details of earlier investigations may be found in the reviews of Rhyne (1972), Legvold (1972) and Taylor and Darby (1972).

2. Magnetization and susceptibility

The strong Russell–Saunders coupling between the spin and orbital angular momenta of electrons in unfilled 4f shells produces a ground state multiplet characterized by a total angular momentum (J) given by Hund's rules. This has values $L+S, |L-S|$ for shells greater or less than half full, respectively. In general the first excited multiplet is sufficiently separated in energy from the ground multiplet that the ion reflects the properties of this latter multiplet alone. In the crystalline state, the electric field from surrounding ions removes the $(2J+1)$-fold degeneracy of the ground multiplet, but the crystal field splittings remain much less than the spin–orbit coupling energies (except in the case of samarium).

It has been established for many years now that the variety of co-operative magnetic phenomena displayed by the lanthanides is a manifestation of the indirect coupling of angular momenta of neighbouring ions via the conduction electrons – the RKKY interaction. Subject to a number of simplifying assumptions, this two-ion coupling may be considered isotropic and indeed many magnetic properties may be interpreted on this basis. Detailed studies of the excitation spectra of some of the lanthanides (see ch. 7 section 5) have, however, revealed the importance of anisotropic two-ion couplings.

Before reviewing the experimental magnetization and susceptibility data, we outline the appropriate features of a microscopic theory with which the magnetization may be calculated from a detailed knowledge of the spin wave dispersion relations. Such a calculation has recently been carried out for terbium following a comprehensive study of the magnetic excitations in the ferromagnetic phase of this element (see sections 2.1.1, 2.2.1). Following the discussion of the Tb results, the elements Dy, Ho, Er and Tm are considered. A review of the two elements with $4f^7$ configurations (half filled shells), Gd and Eu, follows. Section 2.3 contains a discussion on induced moments and crystal field effects, together with experimental results for Pr and Nd. The advent of a number of single crystals of these elements and their alloys has enabled considerable progress in the understanding of these metals to take place in recent years. Samarium crystals are also now available: Sm magnetization and susceptibility results are described in section 2.4. For the convenience of the reader we have summarized the bulk magnetic properties of the magnetic lanthanides in table 6.1 in the order in which the metals are discussed in the text.

The non-magnetic rare earths Y, Sc, La and Lu have frequently been used as hosts for dilute alloy measurements (see, for example section 3.4). The scatter of early magnetization results reported for the elements themselves suggests this

TABLE 6.1
Summary of the bulk magnetic properties of the elements discussed in section 2.2 to section 2.4.

Ion	$4f^n$	Ground state	gJ	Observed saturation moment (μ_B)	T_N (K)	T_c (K)	Easy direction at 4.2 K	$\theta_{\|c}$ (K)	$\theta_{\perp c}$ (K)
Tb^{3+}	8	$^7F_6$	9	9.33	230	220	b-axis	195	239
Dy^{3+}	9	$^6H_{15/2}$	10	10.3	178	86	a-axis	121	169
Ho^{3+}	10	$^5I_8$	10	10.3	133	19	b-axis	73	88
Er^{3+}	11	$^4F_{15/2}$	9	9.0	84	18	30° to c-axis	62	32.5
Tm^{3+}	12	$^3H_6$	7	7.12	56	32	c-axis	41	−17
Gd^{3+}	7	$^8S_{7/2}$	7	7.63	–	293	30° to c-axis	317	317
Eu^{2+}	7	$^8S_{7/2}$	7	5.1*	90	–	⟨110⟩	18	18
Pr^{3+}	2	$^3H_4$	3.20	2.7*	0.03	–	a-axis		
					19.2[h]		b-axis[h]		
Nd^{3+}	3	$^4I_{9/2}$	3.27	2.2*	7.8[c]	–	a-axis[c]		
					106[h]		a-axis		
Sm^{3+}	5	$^6H_{5/2}$	2.14	0.5†	14[c]	–	(see section 2.4)		

*values at 38 T, 4.2 K; †estimated for cubic sites (see section 2.4); [h]hexagonal sites; [c]cubic sites.

alloying was often inadvertent. Definitive data on these elements and also Yb are presented in section 2.5, concluding this section.

2.1. *Spin wave theory of magnetization*

As a framework for the discussion of the magnetization, magnetic anisotropy and magnetostriction we consider a hamiltonian which comprises the following isotropic exchange, effective single-ion anisotropy, elastic, magnetoelastic and Zeeman terms:

$$\mathcal{H} = \mathcal{H}_{ex} + \mathcal{H}_{an} + \mathcal{H}_{el} + \mathcal{H}_{me} + \mathcal{H}_{Zee}. \tag{6.1}$$

Anisotropic contributions to the exchange may be included in the single-ion anisotropy, within the molecular field approximation. Since the hcp structure contains two atoms per unit cell, $\mathcal{H}_{ex}$ may be described in terms of exchange interactions between magnetic ions on the same and different sublattices, respectively $\mathcal{J}(R)$ and $\mathcal{J}'(R)$

$$\mathcal{H}_{ex} = -\sum_{l>l'} \mathcal{J}(R_{ll'})\, \boldsymbol{J}_l \cdot \boldsymbol{J}_{l'} - \sum_{m>m'} \mathcal{J}(R_{mm'})\, \boldsymbol{J}_m \cdot \boldsymbol{J}_{m'}$$
$$- \sum_{l,m} \mathcal{J}'(R_{lm})\, \boldsymbol{J}_l \cdot \boldsymbol{J}_m \tag{6.2}$$

The crystal field contribution to $\mathcal{H}_{an}$ must, by symmetry, be of the form

$$\mathcal{H}_{cf} = B_2^0 O_2^0 + B_4^0 O_4^0 + B_6^0 O_6^0 + B_6^6 O_6^6, \tag{6.3}$$

where O_l^m are the operator equivalents defined by Elliott and Stevens (1953). In terms of the irreducible strains of the hcp lattice $\varepsilon^{\Gamma,i}$ the elastic energy is

$$\mathcal{H}_{\rm el} = \tfrac{1}{2}\sum_{\Gamma,i,j} c_{ij}^{\Gamma}\varepsilon^{\Gamma,i}\varepsilon^{\Gamma,j}. \tag{6.4}$$

c_{ij}^{Γ} are the elastic constants corresponding to the strains $\varepsilon^{\Gamma,i}$ which transform as $\Gamma(=\alpha,\ \gamma,\ \varepsilon)$ and are numbered i if Γ occurs more than once. In terms of the cartesian strains they are given by

$$\begin{aligned} &\varepsilon^{\alpha,1} = \varepsilon_{xx} + \varepsilon_{yy} + \varepsilon_{zz}, && \varepsilon^{\alpha,2} = (3\varepsilon_{zz} - \varepsilon^{\alpha,1})/2\sqrt{3}, \\ &\varepsilon^{\gamma,1} = \tfrac{1}{2}(\varepsilon_{xx} - \varepsilon_{yy}), && \varepsilon^{\gamma,2} = \varepsilon_{xy}, \\ &\varepsilon^{\varepsilon,1} = \varepsilon_{yz}, && \varepsilon^{\varepsilon,2} = \varepsilon_{xz}. \end{aligned} \tag{6.5}$$

Callen and Callen (1963) expanded the magnetoelastic hamiltonian as

$$\mathcal{H}_{\rm me} = -\sum_{\Gamma,i} B^{\Gamma,i} S^{\Gamma,i} \varepsilon^{\Gamma,i} \tag{6.6}$$

$B^{\Gamma,i}$ define the magnetoelastic coupling constants and $S^{\Gamma,i}$ are appropriate linear combinations of Stevens operators. The number of terms may be reduced by noting that the operators of the α-strain terms correspond to those of $\mathcal{H}_{\rm cf}$: hence these terms will change the effective crystal field parameters B_l^m. Moreover, if the moments are confined to the basal plane as in Tb and Dy, the ε-strains do not contribute and only the γ-strains need be retained. The Zeeman term is simply

$$\mathcal{H}_{\rm Zee} = -g\mu_{\rm B}\boldsymbol{H}\cdot\boldsymbol{J}. \tag{6.7}$$

In order to proceed with the diagonalization of $\mathcal{H}$, it is convenient to rotate the z-axis into the magnetization direction. Prescriptions for the rotation of Stevens operators have been discussed by Danielsen and Lindgård (1972). In the representation with the magnetization axis as quantization axis we have therefore

$$\mathcal{H} = \mathcal{H}_{\rm ex} + \sum_{l=0,\ l>m=0,\ 2,\ 4,\ 6}^{6} C_l^m O_l^m \tag{6.8}$$

The diagonalization of $\mathcal{H}_{\rm ex}$ is normally accomplished by a transformation from angular momentum operators to spin deviation operators (Holstein and Primakoff, 1940). A spin deviation at the ith site of one quantum of angular momentum is created and annihilated by operators a_i^+ and a_i respectively

$$a_i^+|m_i\rangle = \sqrt{m_i+1}\,|m_i+1\rangle, \qquad a_i|m_i\rangle = \sqrt{m_i}\,|m_i-1\rangle. \tag{6.9}$$

$a_i^+ a_i$ represents the number operator, and it may readily be shown that a_i^+ and a_i obey boson commutation relations. The magnon operator

$$a_q^+ = N^{-1/2}\sum_i \exp(-i\boldsymbol{q}\cdot\boldsymbol{R}_i)a_i^+ \tag{6.10}$$

creates a collective excitation of the spin system, in which a deviation from the ordered state propagates through the lattice. $\mathcal{H}_{\rm ex}$ may be expressed in terms of

the spin wave operators a_q^+ and a_q together with the Fourier transforms $\mathcal{J}(\boldsymbol{q})$ and $\mathcal{J}'(\boldsymbol{q})$ of the exchange interactions $\mathcal{J}(\boldsymbol{R})$ and $\mathcal{J}'(\boldsymbol{R})$ (see, for example, Mackintosh and Møller 1972).

The remainder of $\mathcal{H}$ may be cast into a similar form by an expansion of the Stevens operators $O_l^m(i)$ belonging to the ith site into a well-ordered series of the operators a_i^+ and a_i. Lindgård and Danielsen (1974) derived this expansion by matching corresponding matrix elements of Racah operators (linear combinations of Stevens operators) with the Bose operators. For example, O_2^0 becomes

$$O_2^0 = 2J(J-\tfrac{1}{2})\left(1-\frac{3}{J}a^+a+\frac{3}{2J(J-\frac{1}{2})}a^+a^+aa\right). \tag{6.11}$$

As a result of this expansion, followed by a decoupling of four operator products (two magnon terms) in the Hartree–Fock approximation, and subsequent Fourier transformation, Lindgård and Danielsen (1975) deduce the full hamiltonian in the form

$$\mathcal{H} = E_0 + \tfrac{1}{2}\sum_q \{A_q(T, H)\,(a_q^+a_q + a_qa_q^+) + B_q(T, H)(a_{-q}a_q + a_q^+a_{-q}^+)\}. \tag{6.12}$$

The elementary excitations of the system are thus non-interacting renormalized spin waves with energies $E_q(T)$ determined by the diagonalization of $\mathcal{H}$ as

$$E_q(T, H) = \{(A_q(T, H) + B_q(T, H))(A_q(T, H) - B_q(T, H))\}^{1/2} \tag{6.13}$$

As a result of the decoupling, two characteristic temperature and field dependent functions appear:

$$\Delta M(T, H) = \frac{1}{NJ}\sum_q \langle a_q^+a_q\rangle,$$

$$b(T, H) = \frac{1}{NJ}\sum_q \langle a_q^+a_{-q}^+\rangle. \tag{6.14}$$

The function $\Delta M(T, H)$ is related to the bulk magnetization $\langle NJ_z\rangle$ and the reduced magnetization $m(T, H)$ by

$$\begin{aligned}\langle NJ_z\rangle &= \left\langle NJ - \sum_q a_q^+a_q\right\rangle = NJ[1-\Delta M(T, H)] \\ &= NJ\,m(T, H)\,[1-\Delta M(O, H)].\end{aligned} \tag{6.15}$$

whilst $b(T, H)$ arises from the non-spherical precession of the angular momentum in the presence of anisotropy

$$\langle J_x^2\rangle - \langle J_y^2\rangle = 2J^2[1-\tfrac{3}{2}\Delta M(T, H)]b(T, H). \tag{6.16}$$

$\Delta M(T, H)$ and $b(T, H)$ may be calculated from a summation over the Brillouin

zone of the parameters defining the spin wave energies:

$$\Delta M(T, H) = \frac{1}{NJ}\sum_q \left([n_q(T, H) + \tfrac{1}{2}] \frac{A_q(T, H)}{E_q(T, H)} - \tfrac{1}{2} \right),$$

$$b(T, H) = \frac{1}{NJ}\sum_q \left([n_q(T, H) + \tfrac{1}{2}] \frac{B_q(T, H)}{E_q(T, H)} \right), \tag{6.17}$$

where $n_q(T, H) = \{\exp [E_q(T, H)/kT] - 1\}^{-1}$ is the spin wave population factor.

2.1.1. *Application to terbium*

The systematic investigation of the temperature and field dependence of the spin wave energies in terbium, which has been carried out at Risø by Jensen, Houmann and Bjerrum Møller (1975a, b) provided Roeland , Cock and Lindgård (1975) with sufficient information to calculate the magnetization of Tb in the following way. By re-writing the dispersion relation in the form:

$$E_q(T, H) = \{[JF_q(T, H) + \alpha(T, H)][JF_q(T, H) + \beta(T, H)]\}^{1/2} \tag{6.18}$$

which separates the exchange terms comprising $F_q(T, H)$ from the wavevector independent terms α and β containing the anisotropy, magnetoelastic and Zeeman contributions, and from an examination of the spin wave energy gap in Tb, $E_0(T, H) = (\alpha\beta)^{1/2}$, Roeland et al. deduced effective single-ion parameters B_2^0, B_4^0, B_6^0, and B_6^6 together with the magnetostriction parameters A and C (see section 4). Measurements of $E_q(T, H)$ were then used to extract $F_q(T, H)$ and estimates of $\mathcal{J}(q)$ and $\mathcal{J}'(q)$ from

$$F_q(T, H) = [\mathcal{J}(0) - \mathcal{J}(q) + \mathcal{J}'(0) \pm \mathcal{J}'(q)]m(T, H). \tag{6.19}$$

A least squares fit to the dispersion relations with 7 exchange parameters $\mathcal{J}(R)$ and 5 inter-sublattice parameters $\mathcal{J}'(R)$ enabled $\mathcal{J}(q)$, $\mathcal{J}'(q)$ and E_q to be determined at any q, enabling the wavevector sums comprising ΔM and b to be evaluated. The result has to be made self-consistent since the $F_q(T, H)$ functions are renormalized by scaling with the reduced magnetization $m(T, H)$.

2.1.2. *Conduction electron polarization*

In mediating the indirect exchange coupling between 4f electrons of neighbouring ions, the conduction electrons themselves acquire a net polarization. It has been generally assumed that this polarization is parallel to the 4f moment, accounting for an observed bulk magnetization in excess of the maximum ionic moment $gJ\mu_B$. In the heavy rare earths, this excess moment (which amounts to some 4% of gJ in the case of Tb) roughly follows $(g - 1)J$, the projection of the ionic spin onto the total angular momentum, as expected if the sf exchange and the conduction electron susceptibility remain constant over the series.

However, the validity of this simple picture becomes questionable when the spin–orbit coupling of the conduction electrons, which mixes spin-up and

spin-down states, is considered. As discussed by Jensen and Houmann (1975), such a mixing is equivalent to a deviation between the direction in which the conduction electrons are polarized and the direction of the 4f moment. The spin component perpendicular to the magnetization is found to be proportional to a spin–orbit coupling parameter λ_{so}, the sf exchange and the conduction electron susceptibility. The existence of this perpendicular spin component has been invoked by Liu (1972) in an explanation of the observed coupling between acoustic magnons and optic phonons in Tb. Such an interaction violates the selection rules for magnon–phonon coupling in a basal plane ferromagnet, unless the above mechanism is also included. The experimental results for Tb of Jensen and Houmann (1975) are consistent with the assumption that the perpendicular spin component of the conduction electrons lies within the basal plane.

2.2. *Comparison with experiment*

2.2.1. *Terbium*

Terbium orders ferromagnetically at 220 K: the powerful uniaxial anisotropy confines the spins to the basal plane with the $b\langle 10\bar{1}0\rangle$ direction as the easy axis. Hegland et al. (1963) measured the magnetization, in fields up to 1.8 T, over the entire temperature range of the ferromagnetic phase whilst Feron et al. (1970) and Rhyne et al. (1968) reported measurements to somewhat higher fields, using their results to extract the uniaxial anisotropy coefficients (see section 3.2). Roeland et al. (1975a) measured the magnetization at several temperatures, in the easy (b) and hard (a) basal plane directions, in applied fields up to 34 T. Their results, shown in figs. 6.1, 6.2 are in excellent agreement with the earlier low field data. The saturation moment is somewhat higher than the maximum ionic moment of the ground multiplet, $g\mu_B J = 9\,\mu_B$. The self-consistent ionic moment J_Z was calculated by the method described above and is shown in the figures as

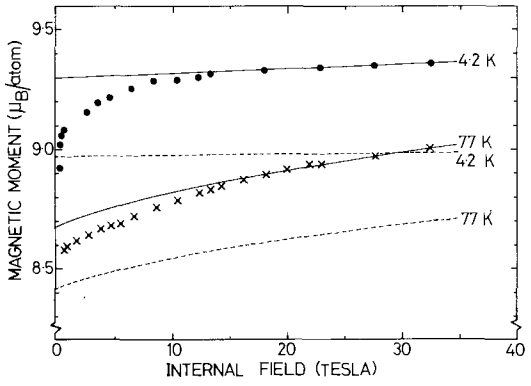

Fig. 6.1. The high field magnetization of terbium as a function of internal field in the easy (b) direction. Broken lines represent the calculated ionic moment whilst the solid lines indicate the total moment per terbium atom (after Roeland et al. 1975a).

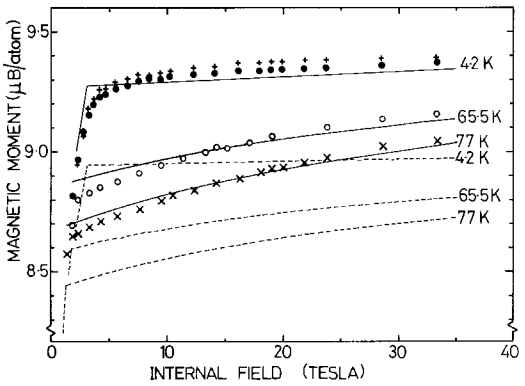

Fig. 6.2. The high field magnetization of terbium as a function of internal field in the hard (a) direction. The calculated ionic moment and total moment are shown as broken and solid lines, respectively (after Roeland et al. 1975a). The symbols represent measurements at 1.8 K(+), 4.2 K(●), 65.5 K(○) and 77 K(×).

dotted lines. Because of the zero-point motion, the moment is slightly quenched by the crystal field and the $T = 0$ moment is thus some 0.04 μ_B below the $g\mu_B J$ value. The difference between the experimental magnetization curves and the calculated ionic moment is usually ascribed to a polarization of the conduction electrons. From the b-direction results this may be deduced to be $(0.33 \pm 0.05)\mu_B$/ion in zero field at 4.2 K. Allowing for this conduction electron polarization, there is good agreement between the calculated and measured results for both the b- and a-directions. The critical field required to overcome the basal plane anisotropy and pull the moments into the a-direction is clearly revealed.

Roeland et al. investigated the conduction electron susceptibility χ_{ce} from a study of the high-field susceptibility, considering a phenomenological expression for the relation between the ionic and conduction electron magnetization of the form

$$M_{ce}(T, H) = \chi_{ce}(T)[H + \lambda M_{ion}(T, H)]$$

$$\text{with} \qquad \chi_{ce}(T) = p + qT^2. \tag{6.20}$$

These parameters were determined to be $\lambda = 26.4\ T\mu_B^{-1}$,

$$p = (1.4 \pm 0.8) \times 10^{-3}\ \mu_B T^{-1},$$

$$q = -3.8 \times 10^{-8}\ \mu_B T^{-1} K^{-2}.$$

$\chi_{ce}(T = 0)$ is apparently considerably enhanced above the Pauli susceptibility $\chi_P = \frac{1}{2}(g\mu_B)^2 \rho(E_F) = 2.4 \times 10^{-4}\ \mu_B T^{-1}$ calculated from Keeton and Loucks' (1968) estimate of the density of states at the Fermi level. However, a note of caution needs to be injected into these estimates of the conduction electron susceptibility. It is apparent from figs. 6.1 and 6.2 that some 10 to 15 T are required to complete the magnetization process by overcoming residual domain walls and the effects of crystal imperfections. Measurements of the high-field susceptibility

and anisotropy of magnetization should therefore be considered with some reservation.

The temperature dependence of the reduced magnetization $m(T, 0)$, as calculated by Lindgård and Danielsen (1975) is compared in fig. 6.3 with the available experimental results. The conduction electron polarization has been subtracted from the measured magnetization using eq. 6.20 but the effect of ignoring this correction is very small. To a good approximation the data may be characterized by the analytic expression of Mackintosh (1963) after the suggestion of Niira (1960)

$$\Delta M(T, 0) = T^{3/2}\exp(-\Delta/kT), \tag{6.21}$$

where $\Delta = E_0(T = 0) = 20$ K. Such data fits have not usually included the renormalization of the energy gap.

In the antiferromagnetic phase (between 220 and 230 K), magnetization and neutron diffraction studies (Koehler et al. 1963) indicate that the moments remain in the basal plane and form a spiral structure with a 20° interplanar angle. The narrow temperature range of its existence suggests that this structure is energetically weak: indeed, applied fields of 1 T in the basal plane align the moments ferromagnetically.

Above 230 K the susceptibility follows Curie–Weiss behaviour with an effective paramagnetic moment of 9.77 μ_B/atom (Hegland et al. 1963). As a result of the uniaxial anisotropy, the paramagnetic Curie temperatures $\theta_{\parallel c}$ and $\theta_{\perp c}$ are displaced, and have the values 195 and 239 K respectively.

2.2.2. *Dysprosium*

Dysprosium also exhibits a basal plane spiral structure, but this state is stable over a much greater temperature range ($T_N = 178$ K, $T_C = 86$ K) than in Tb. In the ferromagnetic phase the easy axis is $\langle 11\bar{2}0\rangle$, the a-axis. Behrendt et al. (1958) found a low temperature saturation moment of 10.2 μ_B/atom, as did Cock (1976),

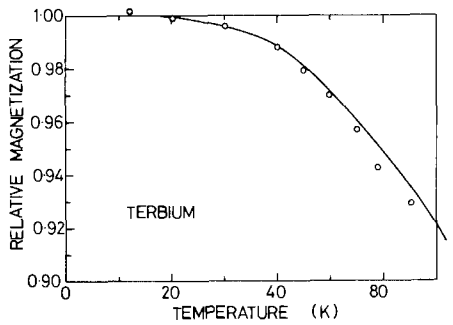

Fig. 6.3. The relative magnetization $m(T, 0)$ of terbium, calculated by Lindgård and Danielsen (1975), together with the experimental results of Hegland et al. (1963), shown as open circles.

whilst Feron et al. (1970) report a value of 10.4 μ_B/atom. The anisotropy-induced reduction of the saturation moment from the fully aligned moment is calculated to be about 0.08 μ_B (Lindgård and Danielsen 1975), so that the conduction electron polarization amounts to at least 0.28 μ_B. Graham et al. (1973) measured the relative magnetization of Dy as a function of temperature for a number of fields, up to 10 T, applied along the a and b directions (see fig. 6.4). Figure 6.5 shows several of Feron's magnetization curves for a Dy sphere. Whilst a field along the easy axis produces a single domain at the demagnetizing field $H_{app} = \frac{1}{3}M$, a field along the b-axis involves a two stage magnetization process. From six initial domains, two equivalent domains with spins 30° to the applied field are first formed at H_a and a field H_b is subsequently required to overcome the basal plane anisotropy, and produce full alignment. Fields along the c-axis only slightly tilt the spins out of the basal plane – by some 6.5° in 5 T at 1.65 K.

The results at 148.5 K illustrate Nagamiya and co-workers' (1962) theory of the

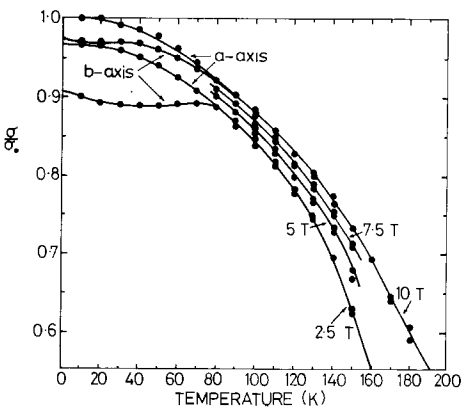

Fig. 6.4. The relative magnetization of dysprosium, as measured by Graham et al. (1973) for various fields in the easy (a) and hard (b) directions.

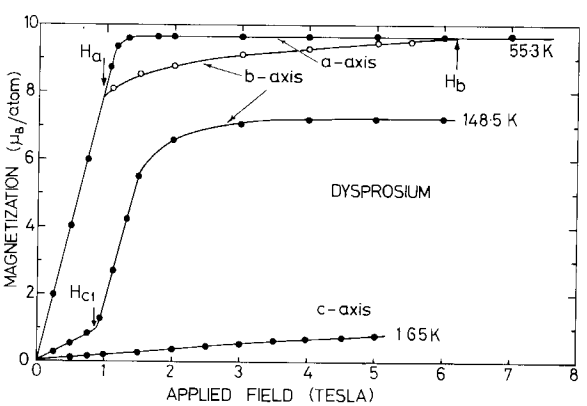

Fig. 6.5. The magnetization of dysprosium as a function of applied field (after Feron et al. 1970).

magnetization in modulated structures. An applied field initially pulls each layer of spins towards the field direction. At a critical field H_{c1} a sharp transition from spiral to fan structures occurs. With increasing field, the angular spread of the moments diminishes and full alignment is achieved at $\sim 2\,H_{c1}$. Between 135 K and $T_C = 86$ K, the intermediate fan structure disappears and at a critical field a first order transition to the ferromagnetic phase is found (Behrendt et al. 1958, Flippen 1964). X-ray measurements (Finkel and Belovol, 1973) reveal a discontinuous change in lattice parameter at the transition, confirming its first-order character, as does the thermal hysteresis of about 5 K in T_C detected by Wilkinson et al. (1961).

The precise mechanism that drives the spiral-ferromagnet transition remains controversial. In essence, the transition results from a temperature dependent competition between the exchange interaction $\mathcal{J}(q)$ favouring a spiral structure and the magnetostriction, which together with the planar anisotropy, favours a ferromagnetic alignment. General agreement has been reached about the magnitude of these latter contributions: Cooper's analysis (1968, 1972), subsequently extended by Evenson and Liu (1969) indicates that the total magnetoelastic energy may be written in terms of the equilibrium strains as:

$$E_{me} = -\tfrac{1}{2}c_{11}^{\alpha}(\varepsilon^{\alpha,1})^2 - \tfrac{1}{2}c_{22}^{\alpha}(\varepsilon^{\alpha,2})^2 - \tfrac{1}{8}c^{\gamma}(\varepsilon^{\gamma,2})^2, \tag{6.22}$$

where the elastic moduli have been written in a hexagonal notation c_{ij}^{α} related to cartesian moduli by

$$\begin{aligned} c_{11}^{\alpha} &= (2c_{11} + 2c_{12} + 4c_{13} + c_{33})/9, \\ c_{22}^{\alpha} &= 2(c_{11} + c_{12} - 4c_{13} + 2c_{33})/3, \\ c^{\gamma} &= 2(c_{11} - c_{12}) \end{aligned} \tag{6.23}$$

The γ-strain provides the major contribution to the difference in E_{me} for the two states, since orthorhombic distortions in the spiral state are prevented by the lattice-clamping effect ($\varepsilon^{\gamma,2} = 0$). Direct measurements of the lattice parameters and hence $\varepsilon^{\gamma,2}$ by X-ray diffraction (Darnell 1963, Finkel and Belovol 1970) combined with the elastic constant data of Rosen and Klimker (1970) yield an estimated ΔE_{me} favouring ferromagnetism of ~ 0.3 meV/ion at 85 K, some three times larger than Cooper's original estimate derived from a renormalization of low temperature data. Although the planar anisotropy, which also favours ferromagnetism, is comparable with E_{me} at $T = 0$ K, it decreases much more rapidly with increasing temperature and is, therefore, relatively insignificant at and above T_C.

Cooper's examination of the exchange energy difference ΔE_{ex} between the two structures contains a number of simplifications that have been subsequently criticised by del Moral and Lee (1975). To describe the long-range interaction $\mathcal{J}(\boldsymbol{R})$, Cooper employed only two parameters $\mathcal{J}_1$ and $\mathcal{J}_2$. Not only was $\mathcal{J}_1$ assumed to be temperature independent below T_N ($\mathcal{J}_2$ being derived from $\mathcal{J}_1$ and the interplanar turn angle), but $\mathcal{J}_1$ and $\mathcal{J}_2$ were also considered to have the same value just above and below T_C. On this basis, Cooper found that the difference

between ΔE_{ex} and ΔE_{me} was in good agreement with the Zeeman energy calculated from the critical field required to drive the spiral→ferromagnet transition above T_C, and he concluded that the magnetostriction term was dominant in driving the transition at T_C.

However, the spin wave measurements of Nicklow et al. (1970) allow seven interplanar exchange parameters to be deduced: $\mathcal{J}_2$, $\mathcal{J}_3$, $\mathcal{J}_4$ and $\mathcal{J}_5$ all have similar magnitudes. $\mathcal{J}(q)$ has a maximum at finite q at 78 K and at 98 K. The maximum at 78 K (i.e. below T_C) indicates that even in the ferromagnetic phase the exchange interaction alone favours a helical structure. But, the magnitude of exchange at 98 K that favours the spiral structure, i.e.

$$\tfrac{1}{2}S^2[\mathcal{J}_{AF}(\boldsymbol{Q}) - \mathcal{J}_{AF}(0)] \tag{6.24}$$

is so large (~ 2 meV/ion) that the reduction in magnetoelastic energy alone is quite insufficient to drive the ferromagnetic transition. Del Moral and Lee therefore suggest that the major contribution must come from a substantial change in the exchange interaction itself. Deletion of the superzone boundaries (see section 5) at T_C will change the conduction electron band structure and hence the exchange interaction so that $\mathcal{J}_F(0) \neq \mathcal{J}_{AF}(0)$. Indeed, Nicklow et al. derived different interplanar constants for the two states.

The net exchange energy difference between the two structures

$$\tfrac{1}{2}S^2[\mathcal{J}_{AF}(Q) - \mathcal{J}_F(0)] \tag{6.25}$$

may also be derived via a thermodynamic argument, using Clapeyron's equation (see, for example, Pippard 1964)

$$\Delta E_{ex} = \Delta V\left(\frac{1}{T_C}\frac{dT_C}{dp}\right)^{-1}. \tag{6.26}$$

ΔV and the pressure dependence of T_C have been determined by Finkel and Belovol (1973) and by Bartholin et al. (1971), respectively, from which we deduce $\Delta E_{ex} = 0.34$ meV/ion, in good agreement with the estimate of ΔE_{me}.

Thus it appears that the spontaneous transition at T_C and the ease with which small applied fields can drive the transition above T_C result principally from a lowering of the exchange energy of the ferromagnetic phase relative to the spiral phase. The basal plane magnetoelastic and, to a lesser extent, anisotropy energies produce a further reduction in the total energy of the ferromagnetic phase, overcoming the contribution from $\mathcal{J}_F(Q) - \mathcal{J}_F(0)$ to ensure its stability in zero field.

2.2.3. *Holmium*

Holmium orders magnetically at 133 K to form a basal plane spiral structure with an interplanar turn angle decreasing monotonically from 50° at T_N to 36° at 35 K, below which it drops steeply to 30° at $T_C = 19$ K. The neutron diffraction study of Koehler et al. (1966) revealed, below T_C, a ferromagnetic c-axis moment of 1.7 μ_B: the moments lift out of the plane by some 10° to form a conical structure.

For fields applied along the c-axis the magnetization process below T_C involves initial domain reversals with the movement of 180° domain walls, succeeded by a gradual tilting of the moments towards the c-axis. Thus the discontinuity at zero internal field in the 4.2 K magnetization results of Bozorth et al. (1972), shown in fig. 6.6 is a measure of the cone angle $\theta = \cos^{-1}\{M(H=0)/M_{sat}\} = 77° -$ in good agreement with the neutron diffraction data. Increasing the applied field reduces the cone angle to about 60° at 11.5 T, at which field a first-order transition to ferromagnetic alignment along $\langle 0001 \rangle$ occurs as the Zeeman energy overcomes the uniaxial anisotropy energy.

The large basal plane anisotropy below T_C (see section 3.2) implies that an interplanar turn angle of 30° is energetically unfavourable and the moments, therefore, bunch preferentially about the easy $b\langle 10\bar{1}0 \rangle$ axes. Small fields applied in the basal plane induce a distortion of the bunched spiral, followed by a fan-type structure and then ferromagnetic ordering. All these modifications are achieved below 1 T. At low temperatures, this ordering is along the b-axis even when the field is applied along the a-axis. The extrapolated zero-field a-axis moment is 8.90 μ_B/atom, which is cos 30° times the value of 10.30 μ_B/atom found for fields along the b-axis (Strandburg et al. 1962, Bozorth et al. 1972). Measurements in the Amsterdam high-field magnet indicate that, at 4.2 K, some 40 T is required to completely align the moments along the a-axis (Cock 1976).

Above $T_C = 19$ K, the magnetization curves of Strandburg (1962) and Feron (1970) reflect the standard spiral→fan→ferromagnetic structures produced by fields in the basal plane. At temperatures above 35 K, Koehler et al. (1967) detected a number of intermediate fan structures which are clearly evident in the magnetization data: the b-axis isotherms at 30, 50.2 and 65.2 K show one, two and three critical fields, respectively (fig. 6.7).

Vishnyakov et al. (1970) have reported Ho magnetization measurements between 80 K and 300 K, in pulsed fields up to 24 T. From 80 K until just below $T_N = 133$ K, the spiral-fan transition apparently remains at 2 T. Fields along the c-axis pull the moments gradually into the field direction, in a process which still requires some 13 T to complete, at 80 K. The data were analysed to determine the uniaxial anisotropy (see section 3.2).

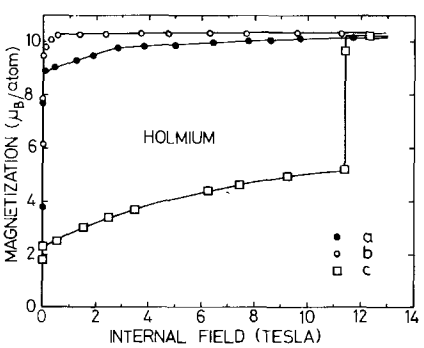

Fig. 6.6. The high field magnetization of holmium at 4.2 K (after Bozorth et al. 1972).

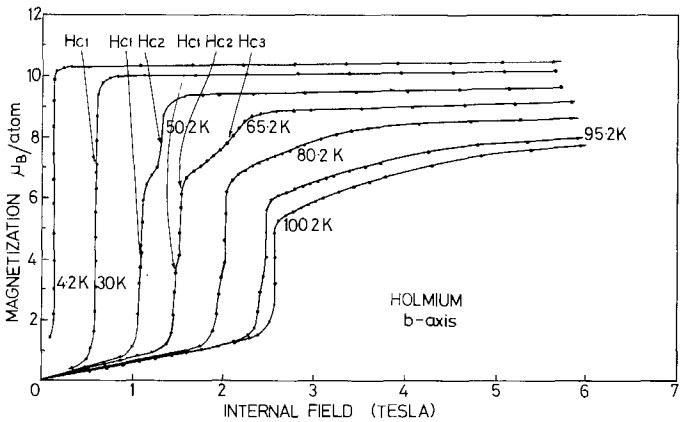

Fig. 6.7. The magnetization of holmium as a function field along the b-axis. H_{c1} is the spiral $\rightarrow$fan transition field: before the onset of ferromagnetic alignment intermediate transitions are observed at H_{c2} and H_{c3} (after Feron et al. 1970).

Several indications of possible additional magnetic phase transitions in Ho have been reported. In an analysis of the structures dictated by the balance between exchange and anisotropy forces Sherrington (1973) proposed that an intermediate "tilted spiral" configuration should be developed between the flat spiral and cone structures at a temperature close to T_C. Such a phase is obtained by tilting the spiral planes of spins about an axis in the basal plane. Since the available neutron diffraction data did not reveal such a phase above T_C, Sherrington suggested that it might be quenched by magnetoelastic effects. However, Tachiki et al. (1974) found an anomalous attenuation peak at 24 K for ultrasonic shear waves transmitted along the c-axis, whilst no such anomaly was found using longitudinal waves. These results are consistent with a transition to a tilted spiral phase.

Another anomaly in the ultrasonic attenuation of c-axis shear waves has been detected at 95.5 K by the same group (Lee et al. 1975). Applied fields along both a- and c-directions shifted the peak to higher temperatures. Volkov et al. (1974) found an extremum in the a-axis susceptibility (but not in χ_c) together with an anomaly in the Hall resistivity at 93 K. The origin of these effects is not clearly understood, but it is presumably reflected in the magnetization curves (fig. 6.7) as the disappearance, between 95.2 K and 100.2 K, of the transition at H_{c2}. Additional neutron diffraction studies extending Koehler's examination beyond 75 K would be helpful here.

In the paramagnetic phase, the Ho effective moment is 11.2 μ_B/atom, somewhat larger than the $g[J(J+1)]^{1/2}$ value of 10.6 μ_B/atom. The relatively small difference, compared with Tb and Dy, of the paramagnetic Curie temperatures $\theta_{\|c} = 73$ K, $\theta_{\perp c} = 88$ K reflects the smaller uniaxial anisotropy of this element.

2.2.4. *Erbium*

Three distinct magnetically ordered states of erbium have been delineated by the neutron diffraction studies of Cable et al. (1965), Habenschuss et al. (1974) and Atoji (1974). At $T_{N\parallel} = 84.4\,K$ the c-axis moment orders in a sinusoidally modulated structure with the wave vector parallel to the c-axis and a periodicity close to seven atomic layers. With decreasing temperature, the competition between the exchange, which favours a modulated structure with one fundamental wave vector, and the axial anisotropy favouring a c-axis alignment of the total available moment, tends to develop a square wave pattern, as evinced by the appearance of higher-order odd harmonics. Below $T_{N\perp} = 52.4\,K$ a spiral ordering of the basal plane moment is superimposed on the c-axis modulation. Habenschuss et al. observed third and fifth order harmonics of the basal plane moment between 50 and 18 K.

Er has a c-axis cone structure, with a periodicity of almost eight atomic layers, below $T_C = 18\,K$. Neutron diffraction measurements at 6 K indicated c-axis and basal plane moments of $(4.44 \pm 0.12)\mu_B$ and $(7.80 \pm 0.12)\mu_B$, respectively, i.e. a total ionic moment of $(8.98 \pm 0.18)\mu_B$ and cone angle of $29.6 \pm 0.8°$. Jensen's (1976) prediction of a 1% reduction of the fully ordered moment by zero point effects is thus within the experimental error.

The 4.2 K magnetization measurements of Bozorth et al. (1972) support these results. Figure 6.8 illustrates how a field applied along the c-axis closes up the cone, after initial 180° domain reversals (as in the case of holmium). Rhyne et al.'s (1968) results are similar but some 3.7% higher. The successive modifications of the spin structure, produced by a field in the basal plane, are reflected in the magnetization curves. At $H_c = 2.0\,T$, the distorted spiral

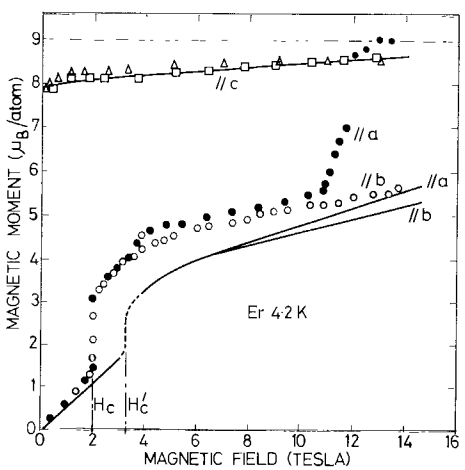

Fig. 6.8. The magnetization of erbium at 4.2 K for magnetic fields along the a, b and c-directions (Bozorth et al. 1972) together with the c-axis results of Rhyne et al. (1968) scaled by a factor of 0.963 and shown as squares. Jensen's (1976) calculated magnetic moment is displayed by the solid lines.

component changes abruptly into an inclined fan-type structure in which the spin components parallel to the field are close to alignment. As the field is increased further, the amplitude of the oscillating basal plane component – the spread of the fan perpendicular to the field – decreases monotonically. Calculations by Nagamiya and co-workers (1964, 1967) predict a second-order transition, at approximately $2H_c$, to a state with the moments ferromagnetically aligned at an angle close to that of the original cone. Although fig. 6.8 shows the magnetization at $2H_c = 4.0$ T to be almost $g\mu_B J \sin 30°$, Rhyne and Pickart (1971) were still able to detect the fan structure in a neutron diffraction experiment at 6 T.

Jensen's calculation (1976) of the basal plane magnetization agrees qualitatively with the experimental data. He employed a molecular field model with exchange parameters deduced from the spin wave dispersion (Nicklow et al. 1971) and four crystal field parameters. The discrepancies may indicate anisotropic exchange couplings additional to the $K_{22}(q)$ term considered by Jensen. The abrupt increase of the magnetization along the easy a-axis at 12 T was also not reproduced, but magnetoelastic effects may be significant here.

The susceptibility of Er, measured by an AC technique with peak fields of $\sim 10^{-3}$ T, reveals anomalies (fig. 6.9) at 27 K and 34 K in addition to those at $T_{N\parallel}$, $T_{N\perp}$ and T_C (Taylor et al. 1975). Habenschuss et al. did not observe magnetic transitions at these temperatures but suggested instead that the low field susceptibility will exhibit singularities when the magnetic and crystallographic periodicities become commensurate. The extra susceptibility anomalies and their associated thermal hysteresis correspond to the regions of eight and fifteen layer periodicity.

The complexity of the Er magnetization process is again illustrated by the data of Feron et al. (1970), extending up to $T_{N\parallel}$ (fig. 6.10). The critical field along [0001] required to decouple the c-axis modulated moments (above T_C) increases

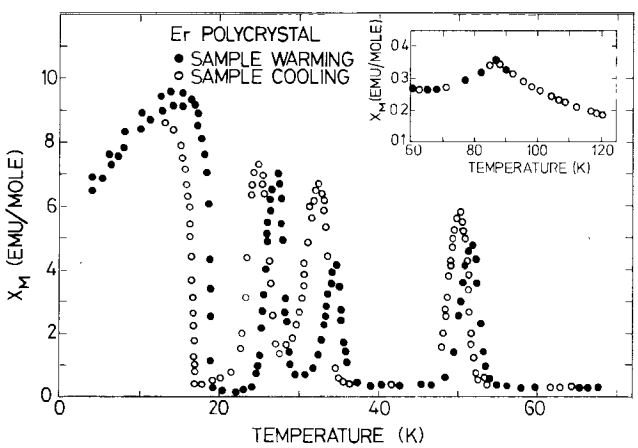

Fig. 6.9. Temperature dependence of the susceptibility of erbium measured by an AC method in a field of amplitude 6.4×10^{-4} tesla (after Taylor et al. 1975). Results for the sample warming and cooling are shown. For conversion 1 emu/g = $4\pi 10^{-3}$ m^3 kg^{-1}.

almost linearly with temperature, reflecting the energy difference between the modulated and ferromagnetic configurations, to a maximum value of 2.24 T, some 15 K below $T_{N\|}$. For fields parallel to the a-axis, the spiral-fan transition field H_{c1} is temperature independent below T_C, as expected, but then rises rapidly with temperature and the transition becomes less distinct (fig. 6.11). A complete description of the magnetic structure above T_C requires a knowledge of the phases of the various harmonics of the moment modulation. Unfortunately this is not available, but according to Jensen the structure between 18 K and 30 K should be cycloidal, i.e. a spiral tilted perpendicular to the basal plane. At higher temperatures, variations in the magnitude of the moments render this model inadequate.

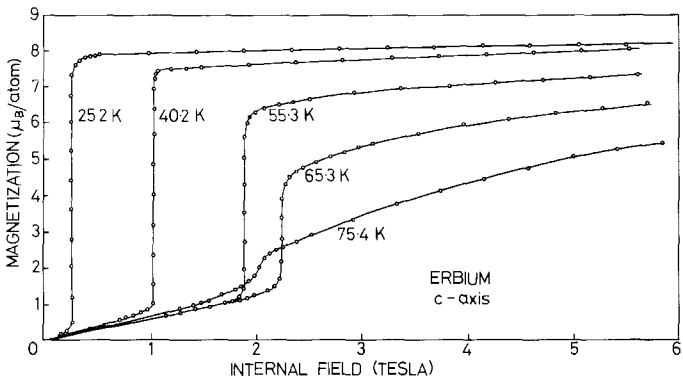

Fig. 6.10. The c-axis magnetization of erbium, showing the temperature dependence of the field required to align the modulated moments (after Feron et al. 1970).

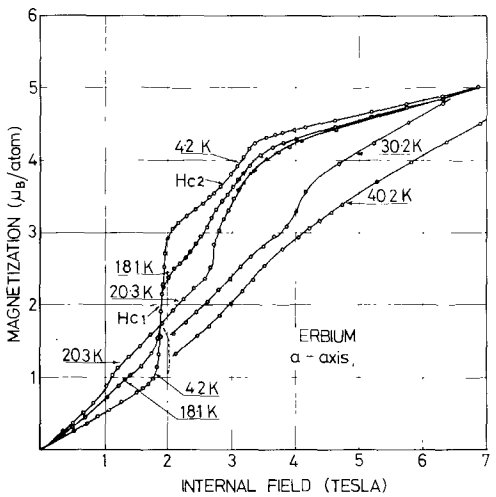

Fig. 6.11. Results of Feron et al. (1970) for the a-axis magnetization of erbium. The spiral→fan transition at H_{c1} is followed by a transition at H_{c2} between two fan structures.

In the paramagnetic region, Green et al. (1961) deduced an effective moment of 9.9 μ_B/atom, and Curie temperatures $\theta_\parallel = (62 \pm 5)$ K; $\theta_\perp = (32.5 \pm 5)$K.

2.2.5. *Thulium*

The magnetic structure of thulium is simpler than that of erbium since the basal plane component remains disordered below $T_N = 56$ K whilst a c-axis sinusoidally modulated structure develops. The appearance of higher harmonics of the modulation is a prelude to the formation of a ferrimagnetic arrangement at about 32 K (Brun et al. 1970), consisting of four layers of moments parallel to the c-axis, followed by 3 antiparallel layers. Such a structure clearly explains the 4.2 K magnetization curves of Richards and Legvold (1969). Figure 6.12 demonstrates that the 4 up–3 down structure with its net moment of 1 μ_B can be decoupled by a parallel field of 2.8 T to produce a ferromagnetic structure with the maximum ionic moment. Extrapolation to zero internal field yields a moment, including the conduction electron contribution, of 7.12 μ_B/atom. The b-axis is magnetically hard with only 0.76 μ_B/atom developed in 10 Tesla. The magnetization curves are qualitatively similar at temperatures up to 40 K: the critical field required to decouple the structure diminishes rapidly between 40 K and 55 K.

In the paramagnetic phase, the inverse susceptibility follows Curie–Weiss behaviour with an effective moment of 7.61 μ_B/atom, $\theta_\parallel = 41$ K and $\theta_\perp = -17$ K.

2.2.6. *Gadolinium*

Since the indirect exchange coupling is between spins, Gd is distinguished by the highest Curie temperature (292.7 K) of the lanthanides as a result of its $4f^7$

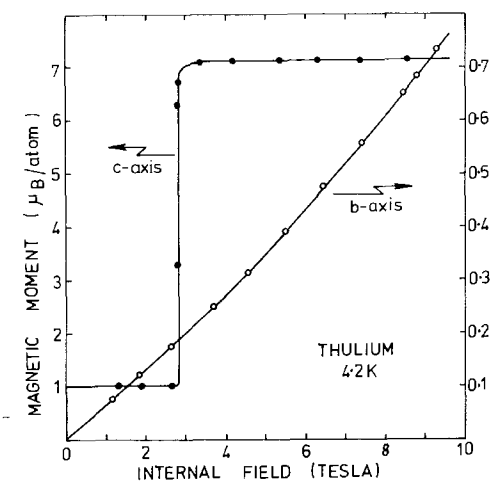

Fig. 6.12. The magnetization of thulium at 4.2 K (after Richards and Legvold 1969). A field of 2.8 Tesla along the c-axis is required to uncouple the ferrimagnetic structure.

configuration and $^8S_{7/2}$ ground state. The absence of an orbital contribution to the moment implies that the anisotropic interactions in eq. 6.1 arise from perturbations of higher order than we have, so far, considered (see section 3). Nevertheless, the residual anisotropy is manifested in the temperature dependence of the easy axis of magnetization. This has been studied several times, most recently by Corner and Tanner (1976) who investigated a single crystal of Gd which had been purified, by Jordan and Jones (1973), using the solid state electrotransport technique. These new results agree well not only with Corner's earlier work (1962), but also with neutron diffraction measurements (Cable and Wollan, 1968) and may, therefore, be regarded as definitive (fig. 6.13). Immediately below T_C, the easy axis is the c-direction. Some fifty degrees below T_C, the easy axis begins to tilt away from [0001], reaching a maximum cone angle of 60° at 180 K before decreasing to just below 30° at 4.2 K. Since the angular dependence of the total anisotropy energy is very weak around 200 K (see section 3.2), local inhomogeneities or strains may readily stabilise the moments in the basal plane, as reported by Graham (1962).

The sensitivity of the magnetization at 4.2 K to impurities has recently been investigated by Roeland et al. (1975b). Their single crystal Gd-A was prepared from commercially available Gd whilst crystal Gd-B was obtained from material purified by solid state electrotransport processing, which reduced the oxygen content from a few atomic percent to 0.01 atomic per cent. Figure 6.14 illustrates a striking difference in the c-axis magnetization of these two samples. Gd-B saturates in a very small field and may be described as magnetically very soft. Substantial fields are required to saturate Gd-A, presumably due to the pinning of residual domain walls by crystal defects. Moreover, the c-axis moment $M_0 = (7.55 \pm 0.02)\mu_B$/atom obtained by Nigh et al. (1963) via an expansion $M = M_0 + \alpha B^{-1}$ concurs with a similar analysis for Gd-A and contrasts with the

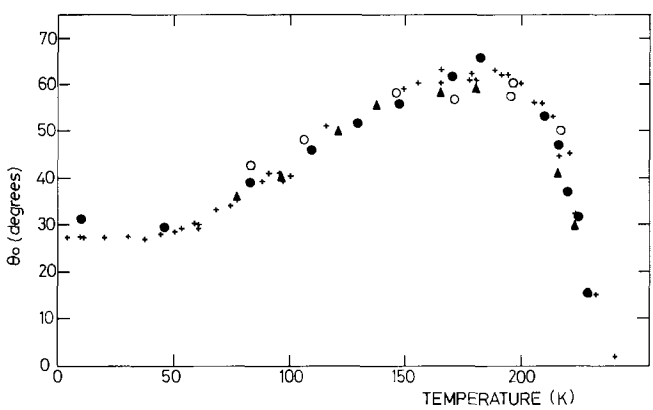

Fig. 6.13. Temperature dependence of the angle between the easy magnetization direction and the c-axis, for gadolinium. Open and closed circles represent the neutron diffraction results of Cable and Wollan (1968) as determined from different reflections. Crosses denote the torque results of Corner and Tanner (1976) at $0.85T$: triangles show their $H = 0$ extrapolated values.

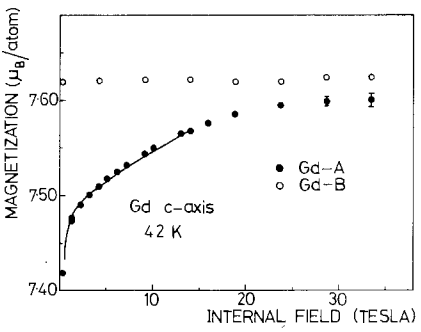

Fig. 6.14. Comparison of the high field magnetization of two gadolinium crystals. Gd–B was two orders of magnitude purer than Gd–A (after Roeland et al. 1975b).

value $M_0 = (7.62 \pm 0.01)\mu_B$/atom obtained for Gd-B. The anisotropy of the magnetization was estimated to be no more than 0.1%: for the b-direction, $M_0 = (7.63 \pm 0.01)\mu_B$/atom. This discrepancy between Gd-A and Gd-B may be accounted for by the presence in Gd-A of an oxygen concentration of some 2 atomic percent in the form Gd_2O_3, which saturates in about 20 T to $6.9\mu_B$/atom. In an attempt to determine the conduction electron susceptibility, Roeland et al. analysed the Gd-B data with the expansion $M = M_0 + \chi B + \alpha B^{-1}$. No evidence for an enhancement over the Pauli susceptibility was found, in contrast to the Tb results (section 2.2.1). Additional measurements on purer Tb would obviously be valuable.

The zero-field moment of $7.63\mu_B$ permits a direct estimate of the conduction electron polarization as $0.63\mu_B$, since the anisotropy-induced zero point motion is negligible for Gd. This increased estimate of the conduction electron polarization is of particular significance for energy band calculations. Harmon and Freeman's spin-polarized APW calculation (1974) requires little adjustment to concur with the experimental result.

The temperature dependence of the relative magnetization was determined by Nigh et al. (1963). From 0 K to 100 K, the magnetization decreases with temperature almost twice as fast as does the $S = \frac{7}{2}$ Brillouin function expression, owing to the two-dimensional character of the spin wave dispersion relation (see ch. 7). Above T_C, the susceptibility displays evidence of short-range ordering (also observed in the resistivity, section 5), whilst above 400 K Curie–Weiss behaviour is exhibited, with a paramagnetic Curie temperature of 317 K and an effective moment of $7.98\mu_B$/atom, close to the $g[J(J+1)]^{1/2}$ value of $7.94\mu_B$.

2.2.7. *Europium*

In its metallic state, Eu is divalent in order to achieve the energetically favourable half-filled shell ($4f^7$) configuration. Apart from the presence of the 4f electrons, Eu is isoelectronic to the alkaline earth metal Ba: the influence of the d-bands on the conduction electron energies is largely responsible for the

resultant bcc crystal structure and Fermi surface of these two metals (Andersen and Loucks 1968, McEwen 1971). Because Eu is divalent, the density of states at the Fermi level is less than for the trivalent metals: a correspondingly lower indirect exchange interaction is manifested in a magnetic ordering temperature for Eu much lower than for Gd.

In the ordered state below $T_N = 90.5$ K, the moments form a spiral structure described by a wave vector along ⟨100⟩ directions, such that the interplanar turn angle is close to 50°. Neutron diffraction measurements (Millhouse and McEwen 1973) have clearly demonstrated the first-order character of the magnetic transition (fig. 6.15a). Within a temperature interval of less than 3 K, the zero-field spontaneous magnetization changes from zero to 40% of its $T = 0$ K value. Mössbauer studies by Cohen et al. (1969) also indicate a first-order transition, which is probably due to magnetoelastic effects, and it is also apparent in the isofield magnetization plots of McEwen and Touborg (1971). As expected, the anisotropy is rather small: fig. 6.15b indicates ⟨110⟩ and ⟨100⟩ as the easy and hard directions. An extension of the isofield measurements to 4.2 K revealed anomalous increases in the magnetic moment around 75 K and again near 15 K. These anomalies were found in earlier measurements of polycrystals by Bozorth and Van Vleck (1960), who attributed their results to an $Eu^{2+} \rightarrow Eu^{3+}$ valence change at low temperatures. However, it appears more likely that the very high chemical reactivity of Eu has resulted in contamination of the samples by the ferromagnetic compounds EuO ($T_c = 77$ K) and EuH_2 ($T_c = 18$ K).

Several magnetization isotherms for temperatures between 4.2 and 106.4 K are shown in fig. 6.16. With an applied field along [100], observation of the appropriate neutron diffraction satellites indicated the gradual formation of a single domain, with the field normal to the plane of the spiral, that is completed by about 0.8 T. In such a configuration the magnetization arises from a lifting of the ordered moments out of the plane and, in the absence of anisotropy, the

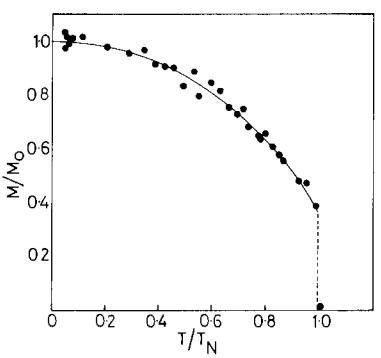

Fig. 6.15(a). Reduced magnetization of europium as a function of reduced temperature, determined by neutron diffraction measurements (after Millhouse and McEwen 1973).

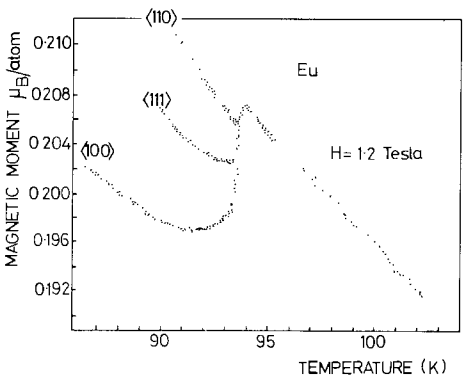

Fig. 6.15(b). The magnetic moment of europium measured in a field of 1.2 T as a function of temperature near T_N. The ordering transition is first-order (after McEwen and Touborg 1971).

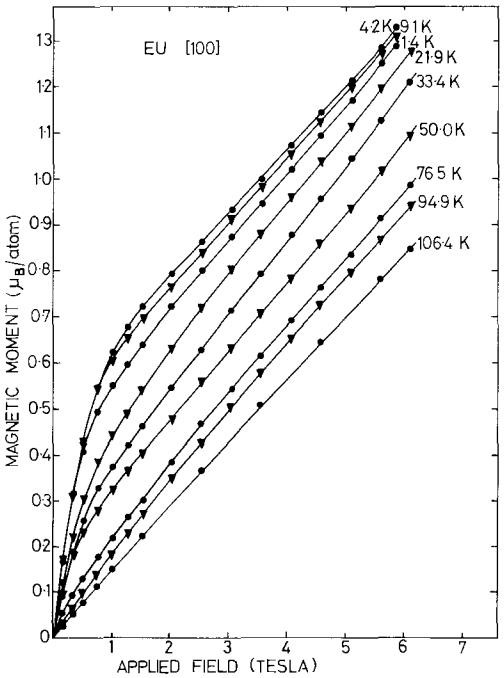

Fig. 6.16. Magnetization curves for europium with a magnetic field along [100].

susceptibility near T_N is given by (Nagamiya et al. 1962)

$$\chi_z = \frac{(g\mu_B)^2}{2(g-1)^2[\mathcal{J}(Q)-\mathcal{J}(0)]}. \tag{6.27}$$

$[\mathcal{J}(Q)-\mathcal{J}(0)]$ is the exchange energy favouring helical rather than ferromagnetic ordering, for which a value of 7.3 K may be deduced from the molecular field formulae for T_N and the paramagnetic Curie temperature ($\theta_p = 18$ K). The susceptibility then calculated from eq. 6.27 agrees well with the experimental value of $0.18\mu_B$/atom Tesla in the single domain region.

McEwen and Touborg found qualitatively identical magnetization results for fields along [110], the moment being typically 5% to 10% larger. Since the anisotropy energy of Eu is very small, we may anticipate that the ordered spins will not necessarily remain confined close to the (100) plane. Nagamiya (1962) showed that tilting the ordered moment out of the plane of the helix requires less energy than distorting the helix in its plane (i.e. $\chi_z > \chi_{\text{plane}}$). A rotation of the helix such that the moment plane remains perpendicular to the field direction is consistent with the magnetization and neutron diffraction data. Thus the spiral→ fan→ferromagnet transitions, observed with a field in the basal plane of Tb, Dy and Ho, remain absent in Eu. Measurements of the [110] magnetization at higher fields indicated a moment of $5.1\mu_B$/atom at 38 T, with saturation ($7\mu_B$) requiring perhaps 100 T (McEwen et al. 1973).

2.3. *Induced moments and crystal fields*

2.3.1. *Praseodymium magnetization and susceptibility*

The understanding of the magnetic properties of Pr has been considerably extended since the reviews of Cooper (1972) and Mackintosh and Møller (1972). For a number of years Pr has been a metal of particular interest: indeed, there has even been a controversy about the existence of magnetic ordering in Pr, with apparent conflict between the data from polycrystalline and single crystal samples.

We shall concentrate on the dhcp allotrope of Pr. Single crystals are still much more difficult to prepare than the heavy rare earth metals, but recent successes in crystal preparation have yielded great dividends.

In the dhcp crystal structure, which has a stacking sequence ABAC, the Pr ion (with $J = 4$) experiences a crystal field of approximately local cubic symmetry at the A sites and of approximately local hexagonal symmetry at the B and C sites. The ratio $c/(2a)$ is 1.611, nearer the ideal value of $(8/3)^{1/2} = 1.633$ than the heavy rare earths. With the c-axis as the quantization direction, the crystal field hamiltonian may be written as

$$\mathscr{H}_{\mathrm{cf}}^{\mathrm{c}} = B_2^0 O_2^0 + B_4^0[O_4^0 + 20\sqrt{2}O_4^3] + B_6^0\left[O_6^0 - \left(\frac{35}{8}\sqrt{8}\right) O_6^3 + \frac{77}{8} O_6^6\right] \tag{6.28}$$

for the cubic sites. $B_2^0 = 0$ when the $c/(2a)$ ratio is ideal. For the hexagonal sites

$$\mathscr{H}_{\mathrm{cf}}^{\mathrm{h}} = B_2^0 O_2^0 + B_4^0 O_4^0 + B_6^0 O_6^0 + B_6^6 O_6^6. \tag{6.29a}$$

Again $B_2^0 = 0$ when $c/(2a) = (8/3)^{1/2}$ but the frequently quoted relation

$$B_6^6 = \frac{77}{8} B_6^0 \tag{6.29b}$$

does not, in the case of the hexagonal sites, follow directly from symmetry considerations alone, but is a consequence of the nearest neighbour point-charge model combined with an ideal $c/2a$ ratio.

Bleaney (1963) made the first estimates of the crystal field parameters of Pr by fitting the Schottky anomaly in the heat capacity (Parkinson, Simon and Spedding 1951) with the use of two parameters B_4^0 and B_6^0. He concluded that Pr has a singlet ground state and thus magnetic ordering requires a sufficiently large exchange interaction (see eq. 6.35). However, the magnetic contribution to the heat capacity is sensitive only to the energy eigenvalues of the ionic states and not to the character of the eigenfunctions of $\mathscr{H}_{\mathrm{cf}}$. Magnetization and susceptibility measurements represent a much more demanding test of proposed crystal field level schemes and we, therefore, examine these properties.

The average magnetic moment of a single ion in an external field may be calculated in the following way. In small fields we may expand the energy of an eigenfunction $|i\rangle$ of $\mathscr{H}_{\mathrm{cf}}$ as

$$E_i = E_0(i) + E_1(i)H + E_2(i)H^2 + \ldots. \tag{6.30}$$

and calculate the terms in this series from matrix elements of the Zeeman operator $\mathcal{H}_{Zee} = -g\mu_B \boldsymbol{J} \cdot \boldsymbol{H} = -g\mu_B J_\zeta H$. For a singlet ground state, the first term $E_1(i)H = \langle i|\mathcal{H}_{Zee}|i\rangle$ vanishes and we are left with

$$E_2(i)H^2 = \sum_j \frac{|\langle i|\mathcal{H}_{Zee}|j\rangle|^2}{E_0(i) - E_0(j)} \tag{6.31}$$

plus higher order terms. The magnetic moment and the ζ-direction susceptibility $\chi = (\partial M_\zeta/\partial H)_{H\to 0}$ may be evaluated from the Gibbs free energy to give

$$\chi_{cf} = 2g^2\mu_B^2 \left(\sum_i \exp(-\beta E_i)\right)^{-1} \sum_j \frac{|\langle i|J_\zeta|j\rangle|^2}{E_0(j) - E_0(i)}. \tag{6.32}$$

Inclusion of an exchange contribution in the molecular field approximation yields

$$\chi^{-1} = \chi_{cf}^{-1} - 2\mathcal{J}(Q)/g^2\mu_B^2 \tag{6.33}$$

and hence the criterion for magnetic ordering is simply

$$2\mathcal{J}(Q)\chi_{cf}/g^2\mu_B^2 \geqslant 1. \tag{6.34}$$

Considering only the lowest levels coupled to give a matrix element α with $T \to 0$, the condition becomes

$$\frac{4\alpha^2\mathcal{J}(Q)}{\Delta} \geqslant 1. \tag{6.35}$$

In larger fields the hamiltonian $\mathcal{H}_{cf} + \mathcal{H}_{Zee}$ is diagonalized to find its eigenfunctions $|\phi_i\rangle$ and the magnetization calculated from

$$M_\zeta = g\mu_B \sum_i \left\{\langle\phi_i|J_\zeta|\phi_i\rangle \exp(-E_i/kT)\right\} \Big/ \left(\sum_i \exp(-E_i/kT)\right). \tag{6.36}$$

The first magnetic susceptibility measurements on Pr were made by Johansson et al. (1970, 1971) and revealed a large anisotropy which could not be explained by Bleaney's crystal field level scheme. Lebech and Rainford (1971) subsequently measured the magnetic moments on both types of site by neutron diffraction. For magnetic fields parallel to the c-direction virtually no magnetic moment was found on the hexagonal sites. In a new analysis Rainford (1972) included the B_2^0 term and deduced a different set of crystal field parameters to explain the available susceptibility, neutron diffraction and specific heat data. The strong axial crystal field at the hexagonal sites leads to a pure $|J_z = 0\rangle$ ground state and a pure $|J_z = \pm 1\rangle$ excited doublet at approximately 30 K. Fields along the c-axis thus do not couple this ground state with any excited state, whilst fields applied in the basal plane readily induce a moment via coupling to the $|\pm 1\rangle$ doublet. For the cubic sites the first excited state is a triplet at approximately 80 K. Rainford found that for a reasonable fit to both the specific heat data and the magnetic susceptibility data, different parameters B_2^0 were necessary for the

cubic and hexagonal sites. Using

$$B_2^0(\text{cubic}) = 0 \qquad B_2^0(\text{hex}) = 4.92\ \text{K};$$
$$B_4^0 = 0.0232\ \text{K}; \qquad B_6^0 = 9.84 \times 10^{-4}\ \text{K}$$

a reasonable fit with the specific heat data above 20 K was obtained, and with the inclusion of the exchange interaction in a two parameter molecular field model the susceptibility features were reproduced as in fig. 6.17. There are considerable deviations from the experimental results below 15 K and above 30 K for $\chi_\parallel$ and $\chi_\perp$ respectively*. With these parameters the energy separation between the ground and excited states on the hexagonal sites is 25 K.

This energy separation has also been derived from inelastic neutron scattering determinations of the magnetic excitation spectrum of Pr. The excitations in a singlet ground state system are known as magnetic excitons and their dispersion is given by

$$E(q) = [\Delta^2 - \alpha^2\Delta\{\mathcal{J}(q) \pm \mathcal{J}'(q)\}R(T)]^{1/2} \tag{6.37}$$

where Δ is the energy separation, $\mathcal{J}(q)$ and $\mathcal{J}'(q)$ describe the intra-planar and inter-planar exchange and $R(T)$ is the renormalization factor.

The extraction of Δ can be achieved by a study of either the temperature dependence or the magnetic field dependence of the excitation spectrum. From the latter approach Rainford and Houmann (1971) deduced $\Delta = (2.14 \pm 0.1)$ meV $= (24.8 \pm 1.2)$K for the hexagonal sites. In a subsequent investigation, using

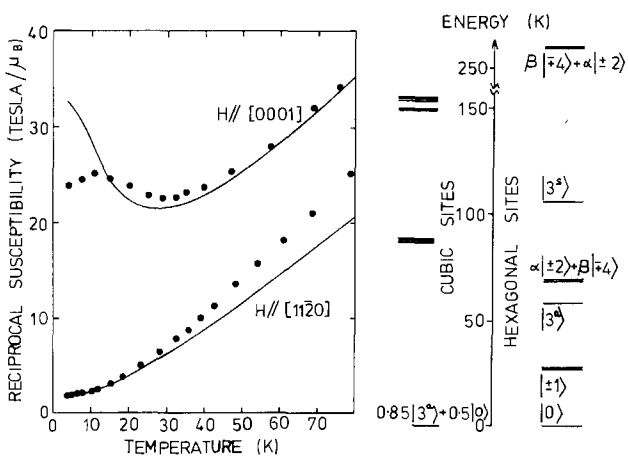

Fig. 6.17. Experimental results for the temperature dependence of the reciprocal susceptibility of praseodymium (Johansson et al. 1971). The solid lines indicate the behaviour calculated by Rainford (1972) using the crystal field energy level scheme shown on the right.

*Recent measurements by Sakamoto et al. (1976) of χ^{-1} vs temperature show only a minimum around 25 K, in good qualitative agreement with Rainford's calculation.

a much larger crystal, Houmann et al. (1975) fitted the temperature dependence of three modes to the random phase approximation renormalization factor and deduced a value of $\Delta = 3.2$ meV (37.2 K). With the same data, a more sophisticated RPA calculation by Lindgård (1975), in which the dispersion of the excitons was explicitly included, yielded a somewhat greater value of

$$\Delta = 3.74 \pm 0.01 \text{ meV } (43.4 \text{ K}).$$

Additional information about the low lying crystal field levels in Pr has been derived from the magnetization measurements of McEwen et al. (1973). In fig. 6.18 the magnetization for fields along the [11$\bar{2}$0] direction are shown. At 4.2 K there is a smooth increase towards saturation, although the maximum observed value of 2.71 μ_B/atom is much lower than the free ion value of $gJ\mu_B = 3.2\ \mu_B$/atom. Applying a field along the c-axis produces only a small magnetic moment at 4.2 K for fields up to 30 T as shown in fig. 6.19. This anisotropy agrees with the behaviour found by Johansson et al. (1970, 1971) in low fields. At 31.8 T a sudden increase of 1.04 μ_B/atom was observed. This jump in the magnetization was studied by a special field pulse and a hysteresis of 0.2 T was found. At a temperature of 14.2 K the transition was considerably broadened and by 77 K all signs of the anomaly had disappeared.

According to the level scheme of fig. 6.17, the ground state on the hexagonal sites is not coupled to any higher states by a field along the c-direction, which thus at low temperatures induces a moment only on the cubic sites. For the hexagonal sites, the field reduces the energy of the $|-1\rangle$ state relative to the ground state as indicated in fig. 6.19 and at the critical field at which they cross, a moment of $g\mu_B = 0.8\ \mu_B$ per hexagonal site atom would develop discontinuously at 0 K. Ascribing the total increase in magnetization found experimentally at 4.2 K to the hexagonal sites alone, suggests a moment increase of 2.08 μ_B/site. It

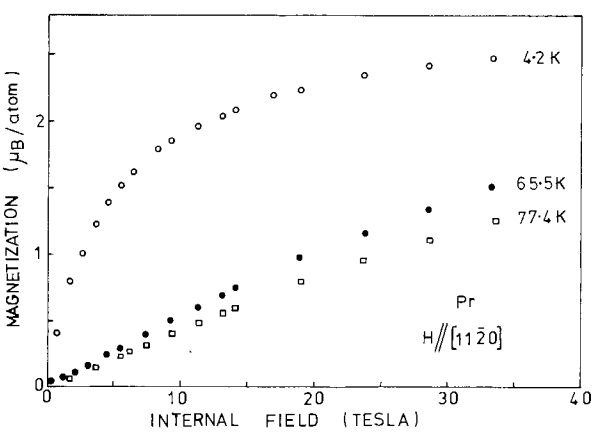

Fig. 6.18. The high field magnetization of praseodymium as a function of internal field along [11$\bar{2}$0] (after McEwen et al. 1973, Cock 1976).

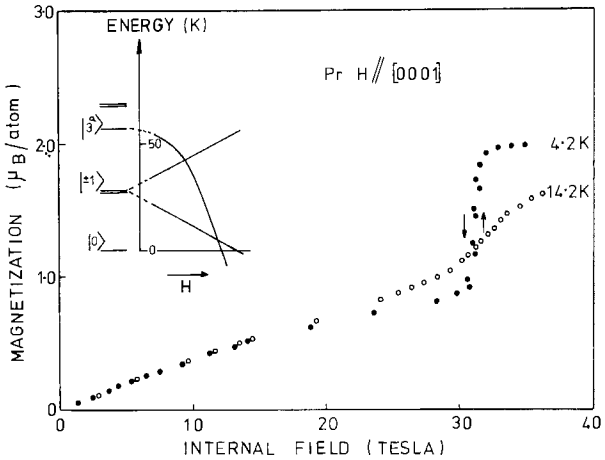

Fig. 6.19. The high field magnetization of praseodymium, as a function of internal field along [0001]. Arrows represent results for increasing and decreasing fields. The schematic field dependence of the low-lying crystal field levels for the hexagonal sites is also indicated (after McEwen et al. 1973, Cock 1976).

is, therefore, more likely that the transition is due to the higher state $|3^a\rangle = 2^{-1/2}\{|+3\rangle - |-3\rangle\}$ which mixes in an axial field with the state $|3^s\rangle = 2^{-1/2}\{|+3\rangle + |-3\rangle\}$ and drops rapidly in energy. If the state $|3^a\rangle$ has become a pure $|3\rangle$ state at the crossing with the ground state $|0\rangle$, a moment of 2.4 μ_B would be developed, which is slightly more than the observed value. Cock and Roeland attempted to fit the magnetization data with three crystal field parameters B_2^0, B_4^0, B_6^0 and three molecular field parameters λ_{CC}, λ_{HH} and λ_{HC} but they were unable to reproduce the magnetization of both the hexagonal and cubic sites with the same set of parameters. When the coupling between the two sites was neglected (i.e. $\lambda_{HC} = 0$), Rainford's parameters could be used to fit the c-axis magnetization. A large hexagonal exchange ($\lambda_{HH} = 15.2\ T\mu_B^{-1}$) is necessary to sharpen the transition, whilst the cubic–cubic exchange is much smaller ($\lambda_{CC} = 2.57\ T\mu_B^{-1}$). Using the same parameters for the data at higher temperatures a surprisingly good fit is obtained. Applying these exchange parameters to the calculated basal plane magnetization yields a ferromagnetic moment on the hexagonal sites. This is, of course, not supported experimentally and suggests that the exchange is anisotropic, as found by Houmann et al. (1975).

Thus six parameters are inadequate to describe the magnetization of Pr. Extra information on the separate magnetization (and its temperature dependence) of the hexagonal and of the cubic sites would greatly assist further calculations.

2.3.2. *Magnetic ordering in* dhcp Pr

For a number of years the question of magnetic ordering in dhcp Pr has been puzzling. An antiferromagnetic structure below 25 K was found by Cable et al. (1964) in neutron diffraction experiments on a powder sample, with a spon-

taneous moment of $\sim 0.7\,\mu_B$ on the hexagonal sites only. This result has been reproduced several times: antiferromagnetic ordering was also found in a polycrystalline rod (Birgeneau et al. 1972). Moreover, nuclear specific heat measurements below 0.5 K (Gregers-Hansen et al. 1972) are consistent with the observation that polycrystalline samples are ordered, with an induced moment of $\sim 0.6\,\mu_B$ on the hexagonal sites.

In contrast, no evidence of magnetic ordering in single crystals was revealed in the magnetization measurements reviewed above or in any of the neutron diffraction studies which were carried out at Risø down to 0.4 K by Lebech et al. (1975) and Houmann et al. (1975). The nuclear specific heat measurements were extended by Lindelof et al. (1975) who used the same single crystal which had been studied by Rainford and Houmann (1971) and was known not to order above 1.8 K. A sharp increase in the nuclear specific heat, resembling the higher temperature side of a λ anomaly, was found and associated with a co-operative magnetic ordering of the hexagonal-site nuclei at 25–30 mK. The electronic ordering appears to arise via the hyperfine interaction. In a series of papers, Murao (1971, 1972, 1975) has shown that ordering can occur at sufficiently low temperatures even for values of $\mathcal{J}/\Delta$ less than critical. The nuclear moment is enhanced via the hyperfine interaction and the Van Vleck polarizability of the ion leads to an exchange coupling which appears as a very large effective interaction between the nuclei. The ordering of the nuclei then drives the ordering of the 4f moments.

Magnetic ordering in Pr may also be induced by magnetic impurities. Adding a material with a doublet ground state will induce ordering at very small impurity concentrations and may be the cause of the antiferromagnetism in polycrystalline Pr. Lebech and McEwen examined single crystals of three Pr–Nd alloys in neutron diffraction and magnetization studies. The compositions $Pr_{0.97}Nd_{0.03}$, $Pr_{0.945}Nd_{0.055}$ and $Pr_{0.737}Nd_{0.263}$ were found to order on the hexagonal sites at 6.3 K, 6.5 K and 11.4 K respectively. The wave vector describing the longitudinal modulation of the antiferromagnetic ordering is 0.24 Å along ΓM, which corresponds very closely to that of the incipient soft mode in pure Pr. The concentration dependence of T_N can be understood (Lebech et al., 1975) in terms of a molecular field theory for a mixture of singlet–doublet ($S_{eff} = 1$) ions and Kramers' doublet ($S_{eff} = \frac{1}{2}$) ions, with three parameters $\mathcal{J}^{PP}$, $\mathcal{J}^{PN}$, and $\mathcal{J}^{NN}$ to describe the exchange coupling between the two components. The result of a least squares fit is shown in fig. 6.20. $\mathcal{J}^{NN}$ was constrained to yield $T_N = 19.5$ K for pure Nd and the splitting between $S_{eff} = 1$ levels of Pr was fixed with $\Delta = 43$ K (see section 2.3.1). The ratio between the exchange interaction and the crystal field for pure Pr is found to be $(4\alpha^2\mathcal{J}^{PP}(Q)/\Delta) = 0.96 \pm 0.01$, in excellent agreement with estimates from the magnetic exciton data (Houmann et al., 1975; Lindgård, 1975). This molecular-field description for random alloys is appropriate because of the long range exchange interaction in rare earth metals. Even at small concentrations there is a direct interaction between impurities. This is not the case for nearest neighbour interactions for which the molecular field description fails at low concentrations. It was not possible to obtain a good fit to

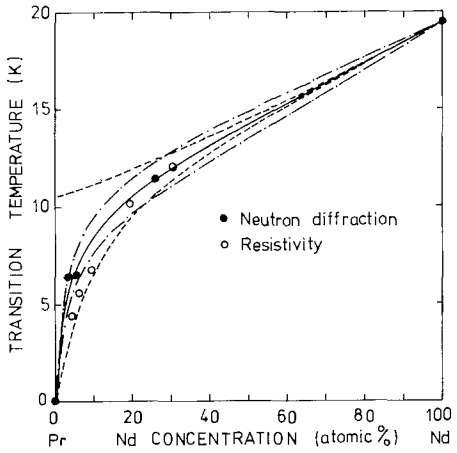

Fig. 6.20. Concentration dependence of T_N calculated by Lebech et al. (1975). The solid line is a least squares fit to their neutron diffraction results, giving $4\alpha^2\mathcal{J}^{PP}/\Delta = 0.96$. The dashed and dot-dashed lines correspond to 10% variations in $\mathcal{J}^{PP}$ and $\mathcal{J}^{PN}$, respectively. Recent results of Sarkissian (1976) obtained from resistance measurements are also shown.

the Pr–Nd data using the Fulde and Peschel (1972) theory for this reason.

Magnetization measurements on some Pr–Nd alloys for fields along the c-axis at 4.2 K showed that the transition found in pure Pr (fig. 6.19) persists in the magnetically ordered alloy system indicating that the crystal field at the Pr sites is not drastically altered by the addition of Nd. The transition broadens with Nd concentration as would be expected for an inhomogeneous system, and the magnitude of the magnetization change decreases, reflecting the decrease in the number of Pr ions. The movement of the transition to lower fields is in accord with the increase in molecular field due to the presence of Nd but could also reflect a modification of the crystal fields. Very recent resistivity and low field susceptibility measurements (Sarkissian, 1976) indicate that long range ordering requires some 2% Nd in Pr. Alloys of lower concentrations apparently exhibit the spin glass phase found in Y–Tb and Y–Gd alloys.

2.3.3. *FCC praseodymium*

Quenching from approximately 1300 K enables an fcc phase of Pr to be procured, although no single crystals of this allotrope have yet been made. Bulk magnetization measurements (Bucher et al., 1969) suggest that fcc Pr becomes ferromagnetic below 8.7 K with a saturation moment of 0.76 μ_B/atom. Subsequent neutron diffraction studies by Birgeneau et al. (1972), using material from the same source, indicated a magnetic transition at 20 K but no anomaly around 8.7 K could be detected. The zero temperature saturation moment was estimated as 0.65 ± 0.1 μ_B/atom. Birgeneau et al. were unable to explain these paradoxical observations but speculated that the ordering at 20 K is to a long wavelength modulated structure with a second transition to a simple ferro-

magnetic state at 8.7 K. A small remanence in the bulk magnetization apparently persists to 20 K.

2.3.4. *Neodymium*

The crystal structure of neodymium is dhcp, like that of praseodymium. The fact that these two elements conveniently form a solid solution for all compositions has already been utilised in section 2.3.2. Moon et al. (1964) investigated the magnetic structure of single crystal Nd, in zero magnetic field, by neutron diffraction. The moments on the hexagonal and cubic sites order below 19.2 K and 7.8 K, respectively, to form periodic antiferromagnetic structures. The main features of the diffraction patterns are explained by a simple model in which the moments in the B and C layers are antiferromagnetically coupled and sinusoidally modulated in the basal plane, with both the moment and modulation vector $\boldsymbol{Q}_h$ parallel to a b-direction $\langle 10\bar{1}0\rangle$. For the A layers, with local cubic symmetry, the modulation vector $\boldsymbol{Q}_c$ is also along a b-direction, but the moments are turned $\pm 30°$ with respect to $\boldsymbol{Q}_c$. The moment on the jth atom in a particular layer is thus described by:

$$\boldsymbol{\mu}_{Bj} = -\boldsymbol{\mu}_{Cj} = \mu_h \hat{b} \cos(\boldsymbol{Q}_h \cdot \boldsymbol{R}_j + \phi_h) \tag{6.38a}$$

$$\boldsymbol{\mu}_{Aj} = -\boldsymbol{\mu}_{A'j} = \mu_c \hat{a} \cos(\boldsymbol{Q}_c \cdot \boldsymbol{R}_j + \phi_c) \tag{6.38b}$$

Equation (6.38) cannot describe some of the coherence effects observed in the diffraction patterns. These discrepancies, and possible improvements to the model, are discussed by Moon et al. and by Lebech and Rainford (1973).

No detailed experimental knowledge of the crystal field is yet available although Kowalewski and Lehmann–Szweykowska (1973a,b) and Lehmann–Szweykowska (1973) have considered the symmetry restrictions imposed on possible splittings of the $J = \frac{9}{2}$ multiplet by eqs. 6.28 and 6.29. These authors further categorized level schemes whose ground state wavefunctions are consistent with the observed basal plane ordering. Lehmann's estimates of the energy levels, based on the point charge model with an antishielding correction, suggested an overall splitting of less than 100 K on both types of site, consistent with the interpretation of Lebech et al. (1975).

Johansson's (1970, 1971) low temperature single crystal magnetization measurements extend up to 6 T and confirm earlier data up to 1.8 T of Behrendt et al. (1957). Interpretation of the results relies heavily on Lebech and Rainford's (1971, 1973) systematic neutron diffraction studies of Nd in an applied field (fig. 6.21): their technique enabled the field dependence of the ferromagnetic and modulated moments to be distinguished at both types of site. In zero applied field, a crystal in the magnetically ordered state contains three domains of hexagonal site ions and six domains of cubic site ions, each characterized by a modulation vector and moment direction given by eq. 6.38. According to Lebech and Rainford, the application of a field along an a-direction $\langle 11\bar{2}0\rangle$ causes the modulated moments on the cubic sites to form a single domain with wavevector

Q_c perpendicular to the field direction. At 4.2 K this process requires 0.8 T for completion: the accompanying reduction of some 0.4 μ_B in the periodic moment is compensated by an increase in the ferromagnetic moment (fig. 6.21) clearly seen in the magnetization curves (fig. 6.22). Concurrent with the formation of a

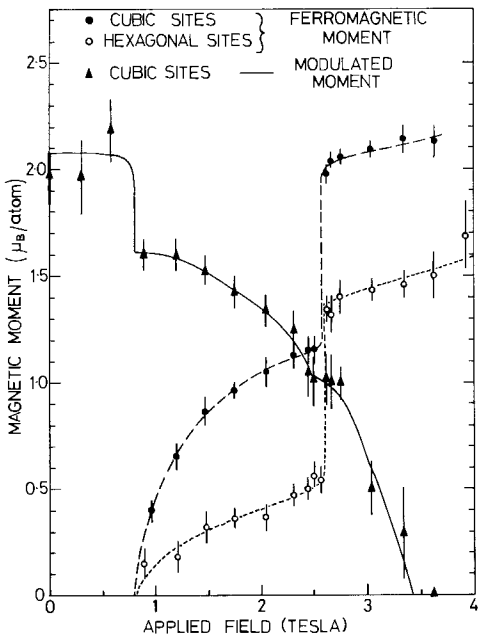

Fig. 6.21. The effect of a magnetic field applied along [11$\bar{2}$0] on the modulated moment on the cubic sites in neodymium, and on the induced ferromagnetic moments on the cubic and hexagonal sites (after Lebech and Rainford 1973).

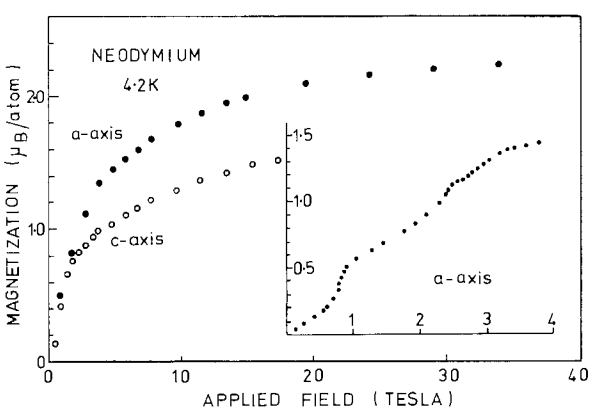

Fig. 6.22. The high field magnetization of neodymium at 4.2 K (after McEwen et al. 1973). The inset shows Johansson's (1971) data with the anomalies discussed in the text.

single domain on the cubic sites, the hexagonal moments turn parallel to those on the cubic sites. With increasing fields, the ferromagnetic moment on both sites develops at the expense of the periodic moment and the magnetization increases accordingly. An abrupt rise of about $0.8\,\mu_B$ in the induced ferromagnetic moments on the hexagonal sites was detected at 2.6 T and ascribed to a crossing of crystal field levels. The corresponding change in the molecular field may be expected to induce a concomitant increase in the cubic moments. Furthermore, these effects create a single domain on the hexagonal sites, and are reflected as an anomaly in the magnetization. The modulated moment on the cubic sites rapidly diminishes (and the ferromagnetic moments increase) with larger fields: the magnetization anomaly at 3.2 T marks the disappearance of the periodic moment. A steady approach to saturation is apparent in the high field measurements. At 34 T, the bulk moment is $2.23\,\mu_B$/atom, still well below the free ion value of $3.2\,\mu_B$/atom. We also note that when the temperature is reduced to 2 K, the increase in magnetization associated with the domain formation on the cubic sites sharpens, whilst the anomalies at higher fields shift apart slightly.

Lebech and Rainford (1971) found that a field applied along the hexagonal axis easily pulls the cubic moments out of the basal plane, whereas a larger axial anisotropy constrains the hexagonal moments in the plane. This anisotropy is also apparent from the high field magnetization: the moment at 34 T is only $1.8\,\mu_B$/atom.

The temperature dependence of the magnitude of the modulated moment on the hexagonal sites follows a scaled Brillouin curve (with $S = \frac{3}{2}$) above 8 K (Lebech et al., 1975). This is consistent with a ground state doublet and an excited doublet at an energy of perhaps only 6 K. Ordering of the cubic sites at 7.5 K leads to a slight reduction of the hexagonal moment, which is $2.6\,\mu_B$ at 4.2 K.

2.4. *Samarium*

Sm exhibits a rhombohedral crystal structure at low temperatures. In the nine layer sequence of close packed planes, two layers of atoms with a locally hexagonal environment alternate with one atomic layer in a locally cubic environment, so that the stacking pattern is of the form hhchhchhc. Hund's rules predict a ground state of the Sm^{3+} ion with $L = 5$, $S = \frac{5}{2}$ and $J = \frac{5}{2}$, with a small theoretical saturation moment of $\frac{5}{7}\,\mu_B$/atom.

Koehler and Moon (1972) detected, by neutron diffraction, that below $T_{Nh} = 106$ K the hexagonal site moments align along the c-direction in a type Al antiferromagnetic arrangement. Two spin-up ferromagnetic sheets normal to the c-axis alternate with two spin-down sheets. In this configuration, the cubic sites are thus not coupled to the hexagonal sites in the absence of an applied field. A separate type Al magnetic structure is formed by the cubic sites below $T_{Nc} = 14$ K: the moments align along the hexagonal axis but in this case the ferromagnetic sheets are parallel to $(10\bar{1}1)$ planes. Characteristic features around the Néel points are clearly evident in the low field susceptibility measurements (fig. 6.23) of McEwen et al. (1974).

Figure 6.24 illustrates the high field magnetization for fields applied parallel to [11$\bar{2}$0] at 4.2 K and parallel to [0001] at 4.2 K and 20.4 K. The basal plane magnetization rises linearly with field, as expected for the perpendicular susceptibility of an antiferromagnet. However, only about 0.1 μ_B/atom – much less than the free ion moment – is developed at 30 T. The [0001] directions is magnetically hard at low fields (corresponding to the parallel susceptibility) but the magnetization exhibits a rapid rise between 25 and 30 T so that in the highest fields the c-axis magnetization exceeds that of the basal plane. This effect was not observed in measurements at 20.4 K, i.e. above T_{Nc}, and has, therefore, been ascribed to a spin-flop of the moments on the cubic sites.

McEwen et al. (1974) analysed their measurements in terms of independent contributions from the two crystallographic sites. Whilst the magnetization and

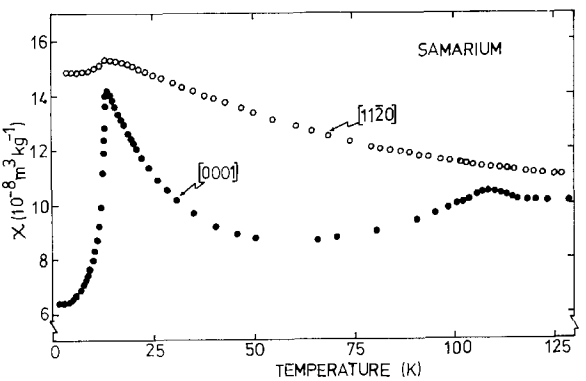

Fig. 6.23. The susceptibility of samarium (after McEwen et al. 1974) showing anomalies at the ordering of the moments on the cubic sites (at 14 K) and on the hexagonal sites (at 106 K).

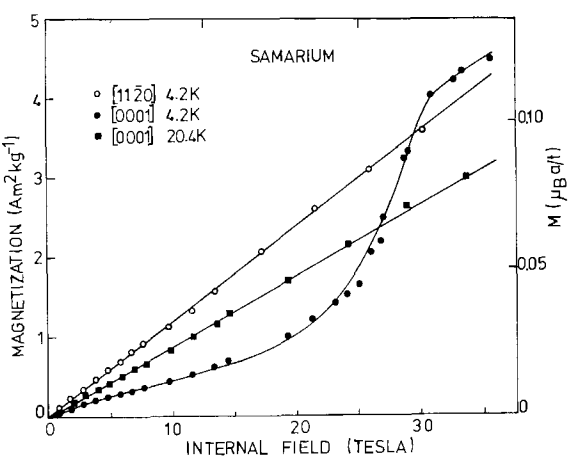

Fig. 6.24. High field magnetization of samarium at temperatures above and below T_{Nc} = 14 K (after McEwen et al. 1974).

susceptibility results for the moments on the cubic sites were consistently characterized by a simple molecular field theory involving four parameters, further experiments are necessary to elucidate the behaviour of the moments on the hexagonal sites. With such a model, the saturation moment on the cubic sites was estimated to be $(0.47 \pm 0.07)\mu_B$/atom, in fair agreement with the value $(0.57 \pm 0.05)\mu_B$/atom, obtained by Moon and Koehler (1973) from their analysis of the magnetic form factor. The temperature dependence of the c-axis susceptibility above T_{Nc} is consistent with the assumption that the crystal field acting on the cubic sites produces a ground state Γ_8 quartet, a conclusion later supported by de Wijn et al. (1974). The spin-flop field (27.2 T) provides a measure of the uniaxial anisotropy. In the notation of eq. 6.39, $\kappa_2^0 = 2.3 \times 10^5$ J m^{-3}.

The proximity of the excited $J = \frac{7}{2}$ multiplet to the ground $J = \frac{5}{2}$ multiplet ($\Delta E \sim 1500$ K) has a profound effect on the susceptibility as demonstrated by its increase with the temperature (fig. 6.25). Because the crystal field induces admixtures of the different multiplets, the susceptibility does not follow the simple Van Vleck (1932) theory. Although de Wijn et al. (1973) managed to extract information on the crystal field parameters in some Sm cubic intermetallic compounds, the presence of two types of crystallographic site in Sm metal prohibits, at present, a detailed comparison in this case.

Around 900 K, McEwen and Touborg observed anomalies in both χ_a and χ_c, with hysteresis of some 15 K. We attribute these to a rhombohedral – hcp crystal structure transition detected by X-ray diffraction. Mardon and Koch (1970) found such a transition, in polycrystalline Sm, at temperatures ranging from 710 to 870 K – higher temperatures being associated with higher purity material (also see ch. 2 section 6.2).

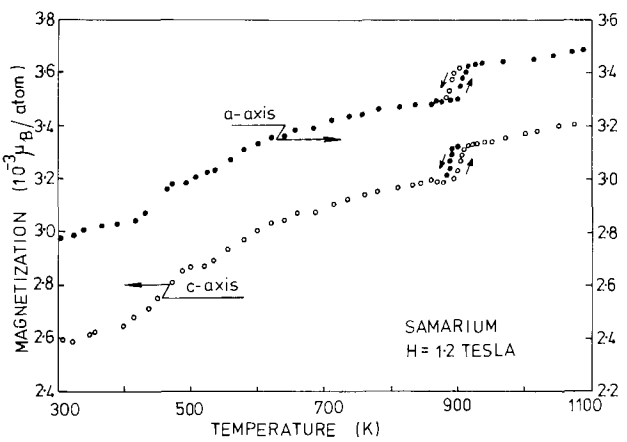

Fig. 6.25. High temperature susceptibility of samarium (after McEwen and Touborg 1976).

2.5. *Scandium, yttrium, lanthanum, ytterbium and lutetium*

The magnetic susceptibilities of these elements are worthy of interest because the absence of a partially filled 4f shell enables other, weaker, contributions to the susceptibilities of the rare earths to be examined. These terms include the conduction electron susceptibility and the diamagnetic susceptibility of the core electrons. Obviously the susceptibilities of Sc, Y, La, Yb and Lu are particularly sensitive to magnetic impurities: both Y and La have been studied on a number of occasions, with conflicting results. Recently Spedding and Croat (1973a,b) prepared a number of samples (polycrystalline and single crystal) of Sc, Y, La and Lu, and systematically investigated their susceptibilities as a function of sample purity. Figure 6.26 shows Spedding and Croat's data for their purest samples. On a molar basis the susceptibilities of Y and Lu are remarkably similar. Both are almost independent of temperature and exhibit broad maxima at 120 K (Lu) or 300 K (Y). The a-axis susceptibility is greater than that measured for the c-axis and the relationship $\chi(\text{polycrystalline}) = \frac{1}{3}\chi_c + \frac{2}{3}\chi_a$ holds for Y, Sc and Lu provided the samples originate from the same starting material. Minute amounts of paramagnetic rare earth impurities led to commensurate increases in the susceptibility, whilst non-magnetic impurities were found to reduce the susceptibility, most noticeably in the case of Sc.

The susceptibility of Sc, and its temperature dependence, is much greater than

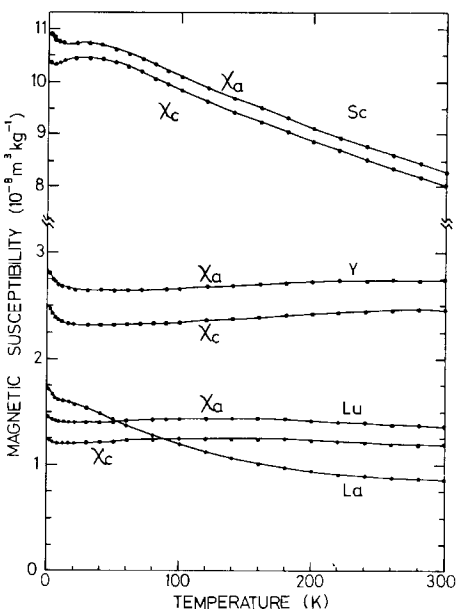

Fig. 6.26. Susceptibility of yttrium, scandium, lanthanum and lutetium (after Spedding and Croat 1973a, b).

that of Y, La and Lu. Above 70 K, it follows Curie–Weiss behaviour with an effective moment of 1.65 μ_B/atom and a paramagnetic Curie temperature of −850 K. Although the temperature dependence of Sc has usually been interpreted by a band model (Gardner and Penfold, 1963), Spedding and Croat suggested that it might arise from an unpaired electron in a bound or highly localized d state. The theoretical $g[J(J+1)]^{1/2}$ effective moment of a single d electron having both a full spin and orbital moment ($L = 2$, $S = \frac{1}{2}$, $J = \frac{3}{2}$) would be 1.55 μ_B, whilst that of a bound d electron with quenched orbital angular momentum ($J = \frac{1}{2}$) would be 1.73 μ_B. Thus the observed 1.65 μ_B may indicate either a partially localized d electron or a fully localized d electron with a partially unquenched orbital angular momentum, a state proposed by Wohlleben and Luo (1969). The anomaly around 30 K suggests antiferromagnetic ordering, but no field dependence was found. Moreover, no anomalies in the Sc resistivity or specific heat have been detected in this region. However, Spedding and Croat noted that the susceptibility anomaly disappeared upon addition of either magnetic or non-magnetic impurities.

Lanthanum does not order magnetically but previous susceptibility results have been confused by the presence of both fcc and dhcp phases co-existing below room temperature (see, for example, Finnemore et al., 1968). According to Spedding and Croat, however, the high temperature fcc phase cannot be stabilised at room temperature in La of the highest available purity. The addition of more than one atomic percent oxygen was required to stabilise the fcc phase on quenching. Figure 6.26, therefore, shows the susceptibility of dhcp La : χ for pure fcc La is estimated about 10% higher at 300 K and almost the same as χ for dhcp La at low temperatures.

Bucher et al. (1970) found that high purity ytterbium metal manifested a first order paramagnetic–diamagnetic transition, with considerable hysteresis, between 100 and 360 K. The phenomenon appears to be associated with an fcc–hcp martensitic transformation. The low temperature hcp phase is characterized by a diamagnetic susceptibility of about $1.7 \times 10^{-10}\,m^3\,kg^{-1}$, whilst the fcc phase (which can be also obtained at low temperatures by straining the hcp phase) exhibits a temperature dependent paramagnetic susceptibility. The observed susceptibilities and small volume change at the transition are consistent with a partial conversion of divalent Yb^{2+} (which has the $4f^{14}$ configuration) to Yb^{3+} (which has a magnetic $^2F_{7/2}$ ground state). The existence of the transition has also been reported by Kayser (1970) and Tanuma et al. (1970), who detected de Haas–van Alphen oscillations in the magnetization of the hcp phase.

3. Magnetic anisotropy

The strong coupling of the angular momentum L to the large 4f spin S in the presence of a crystalline electric field leads to a giant magnetic anisotropy of electrostatic origin in most of the lanthanides. At the beginning of the series, the large radii of the 4f charge clouds results in an anisotropy which is of compar-

able magnitude to the exchange energy and, as we have seen in the case of Pr (section 2.3), directly influences the type of magnetic order. For elements beyond Gd, the anisotropy can be treated to a first approximation as a perturbation on the exchange and has only a small effect on the magnitude of the $T = 0$ moment given by the ground state value of J_z [see eqs. (6.15)–(6.17)]. However, the anisotropy does have a pronounced effect on the stable magnetization direction, and hence may be elucidated by torque or magnetization measurements, which are used to derive appropriate macroscopic anisotropy parameters. A careful study of the spin wave energy gap at zero wave vector permits microscopic analogues of these parameters to be deduced (eq. 6.18). In section 3.1 we review the basic theory as applicable to the rare earths. After considering the connection between the microscopic and macroscopic anisotropy parameters (section 3.1.1) we discuss their expected temperature dependence in both weakly and highly anisotropic systems (section 3.1.2). Section 3.2 reviews the available experimental results obtained from measurements in the ordered phases, the paramagnetic phases, and from dilute alloy studies.

3.1. *Theory of magnetic anisotropy*

3.1.1. *Relations between microscopic and macroscopic parameters*

The macroscopic anisotropy parameters are simply the coefficients in a symmetry-determined expansion of the free energy in terms dependent on the magnetization direction as specified by polar co-ordinates (θ, ϕ) relative to the crystallographic axes. For hexagonal symmetry the free energy may be written in an expansion of spherical harmonics as

$$F(\theta, \phi) = \kappa_0(T) + \kappa_2^0(T) Y_2^0(\theta, \phi) + \kappa_4^0(T) Y_4^0(\theta, \phi) + \kappa_6^0(T) Y_6^0(\theta, \phi) + \kappa_6^6(T)[Y_6^6(\theta, \phi) + Y_6^{-6}(\theta, \phi)] \tag{6.39}$$

where θ and ϕ are the angles of the magnetization relative to the c and a-axes. The spherical harmonics are normalized over a solid angle of 4π. The κ_l^0 terms describe the dominant uniaxial anisotropy: positive values of κ_l^0 favour the alignment of the moments in the basal plane, whilst negative values favour the c-axis. The κ_6^6 term, which has the form $\sin^6\theta \cos 6\phi$, describes the anisotropy within the basal plane. If the hexagonal symmetry is distorted by strains, additional terms of the appropriate symmetry should be included in eq. 6.39.

In some early work, an expansion in powers of $\sin\theta$ has been employed. However, the spherical harmonics form an orthogonal basis and are thus more appropriate. An expansion in Legendre polynomials $P_l^0(\cos\theta)$ has also been frequently used. Although these functions are equivalent to the $Y_l^0(\theta, \phi)$, due account of the scaling factor has not always been included in previous comparisons of anisotropy results. The microscopic anisotropy parameters comprise the terms of various physical origins which enter into the hamiltonian for the system. If the hamiltonian is written in a representation $\mathcal{H}(\theta, \phi)$ in which the quantization axis is along the magnetization direction, the microscopic and

macroscopic parameters are related by

$$F(\theta, \phi) = -kT \ln \mathrm{Tr}\{e^{-\beta \mathcal{H}(\theta,\phi)}\} \tag{6.40}$$

Before employing eq. 6.40 to evaluate the contributions to the macroscopic coefficients $\kappa_l^m(T)$ from the single-ion anisotropy terms of $\mathcal{H}_{cf}$, the Stevens operators of eq. 6.3 must first be transformed to a co-ordinate system with the z-axis along the magnetization direction. Equation 6.40 then yields, for example,

$$\kappa_6^6(T) = B_6^6\{\langle O_6^0\rangle + \tfrac{15}{2}\langle O_6^2\rangle + 3\langle O_6^4\rangle + \tfrac{1}{2}\langle O_6^6\rangle\} \tag{6.41}$$

On the assumption that the spins precess with cylindrical symmetry about the magnetization direction, $\langle O_l^m\rangle$ for which $m \neq 0$ may be discarded and we find that at $T = 0$ K:

$$\begin{aligned} &\kappa_2^0(0) = 2J_2B_2^0, \qquad \kappa_4^0(0) = 8J_4B_4^0, \\ &\kappa_6^0(0) = 16J_6B_6^0, \qquad \kappa_6^6(0) = J_6B_6^6 \end{aligned} \tag{6.42}$$

where

$$J_n = J(J - \tfrac{1}{2})(J - 1) \ldots (J - \tfrac{1}{2}[n - 1]) \tag{6.43}$$

The microscopic coefficients B_l^m are frequently expressed in the form

$$B_l^m = A_l^m \langle r^l \rangle \theta_l \tag{6.44}$$

where the A_l^m are crystal field potentials which include the effects of charge screening, $\langle r^l \rangle$ denotes averages over the 4f wave functions and $\theta_2 = \alpha_J$, $\theta_4 = \beta_J$, $\theta_6 = \gamma_J$, scalar factors derived by Stevens (1952) which are proportional to the l-pole moment of the 4f electrons. Considerable attention has been given to the contribution of the magnetoelastic terms (eq. 6.6) to the anisotropy coefficients as measured by bulk magnetization and torque experiments or from a study of the spin wave energy gap (see eq. 6.18). In the rapid precession of spins which occurs when spin waves are propagated in an anisotropic system, the lattice strains remain fixed at their equilibrium values deduced from the strain derivatives of $\mathcal{H}_e + \mathcal{H}_{me}$ and are thus independent of the actual spin direction (θ, ϕ). In this so-called "frozen-lattice" model, those frozen strains with hexagonal symmetry contribute to the single-ion anisotropy in a way which can be described by a modification of the crystal field parameters B_l^m. The remaining γ and ϵ magnetoelastic terms introduce a correction to the basal plane anisotropy which is particularly significant in terbium (although the ϵ strains do not contribute unless the magnetization is pulled out of the basal plane.) When a magnetic field is applied in the basal plane hard direction, the magnetization rotates to an angle δ (with respect to the hard direction) which may be easily calculated by minimising the free energy to yield

$$Ng\mu_B J[1 - \Delta M(T, H)]H \sin \delta = 6\kappa_6^6 \sin 6\delta \tag{6.45}$$

Thus the critical field H_c required to pull the moments into the hard (basal plane)

direction provides a measure of κ_6^6:

$$\kappa_6^6(T) = \tfrac{1}{36} N g \mu_B J H_c [1 - \Delta M(T, H)] \tag{6.46}$$

A comparison of the critical field, calculated within the frozen lattice model, in terms of the microscopic crystal field and magnetoelastic coefficients gives

$$\kappa_6^6(0) = J_6 B_6^6 + \tfrac{1}{2} c^\gamma A C \tag{6.47}$$

where C and A are the second and fourth order magnetostriction parameters defined in section 4.1. In an attempt to explain certain ferromagnetic resonance experiments in Dy and Tb, Cooper (1968) introduced a "flexible-lattice" model in which the lattice is assumed to follow the instantaneous moment direction. The model was analyzed via a phenomenological expression for the macroscopic free energy from which Cooper deduced that the spin wave energy gap should be zero when H equals the critical field H_c. In fact, however, not all the resonance experiments could be explained on this basis. Moreover, a microscopic analysis by Jensen (1971) established that although the lattice is completely flexible, the spins actually perceive the lattice as frozen. In subsequent papers Houmann et al. (1975) and Jensen (1975) have shown that when the magnetization lies along a symmetry direction, the resonance energy is in accord with the microscopic calculations. Differences between the macroscopic and microscopic energy gap parameters were ascribed by Houmann et al. to two-ion anisotropy terms of non-magnetoelastic origin.

3.1.2. *Temperature dependence of magnetic anisotropy coefficients*

The expressions assumed for the angular dependence of the free energy and the simple relations (eq. 6.42) between the coefficients κ_l^m and B_l^m are strictly valid only in the limit where the anisotropy is much smaller than the isotropic two-ion exchange interaction. Under these conditions the expectation values of the Stevens operators renormalize with temperature in the straight-forward manner calculated by Callen and Callen (1965, 1966):

$$\langle O_l^0 \rangle_T = \langle O_l^0 \rangle_0 \hat{I}_{l+1/2}[\mathscr{L}^{-1}(\sigma)] \tag{6.48}$$

$\hat{I}$ denotes a reduced hyperbolic Bessel function, $\mathscr{L}^{-1}$ is the inverse Langevin function and $\sigma = 1 - \Delta M(T, H)$ from eq. 6.15. For $T \ll T_C$ the temperature dependence of the single-ion anisotropy coefficients B_l^m becomes $\sigma^{l(l+1)/2}$ or σ^{α_l} where $\alpha_l = \frac{1}{2} l(l+1)$: at high temperatures the dependence is of the form σ^l.

However, in a highly anisotropic system, such as Tb or Dy, the $\langle O_l^m \rangle$ terms with $m \neq 0$ cannot be neglected as was done in the derivation of eq. 6.42 from eq. 6.41. Mathematically, a highly anisotropic ferromagnet may be characterized by having finite expectation values for certain products of spin operators (functions of $\langle J_+ J_+ \rangle$ and $\langle J_- J_- \rangle$ that do not commute with J_z). As described in eq. 6.16 the precession of the moments in such a system is generally non-spherical: the moments tilt less in the hard than in the easy directions, leading to changes in the magnitude and temperature dependence of the anisotropy coefficients. When the

axial anisotropy confines the moments to the basal plane (as in Tb and Dy), the resulting elliptic precession reduces the temperature dependence of the macroscopic axial anisotropy whilst the basal plane anisotropy and γ-strain coefficients acquire a more rapid temperature dependence. Extensive calculations of the appropriate renormalization factors have been made by Brooks and Egami (1973), Lindgård and Danielsen (1975) and by Jensen (1975).

The results of Jensen, which follow the method of Lindgård and Danielsen, lead to results very similar to those of Brooks and Egami. Including only the most important magnetoelastic terms (B_2^2 and B_4^4, the γ-strain parameters C and A), Jensen deduced that the microscopic parameters B_l^0 and B_l^m should renormalize as

$$\sigma^{\alpha_l}(1+\tilde{b})^{\alpha_l-2}(1+\tilde{b}^2)^{3-\alpha_l/2}, \qquad \sigma^{\alpha_l}(1+\hat{b})^{-\alpha_{l-1}}(1+\tilde{b}^2)^{\alpha_{l-1}/2} \tag{6.49}$$

with $\tilde{b} = b\sigma^{-3/2}$ respectively at temperatures satisfying $\Delta M(T) = 1 - \sigma(T) \ll 2/l$. With the appropriate values of $\Delta M(T)$ and $b(T)$ for Tb and Dy, Jensen derived effective power laws and zero-point temperature corrections for the contributions to the anisotropy terms α and β in the spin wave energy expression eq. 6.18. The deviations from the α_l power laws appear less dramatic than earlier calculations suggested. Compared with an exponent for the basal plane anisotropy B_6^6 of $\alpha_6 = 21$ from eq. 6.48, Jensen's exponents for the α and β terms in eq. 6.18 are $\beta_{66}^- = 26.8$ and $\beta_{66}^+ = 21.6$. However, for technical reasons discussed by Jensen these values should only be considered qualitatively reliable, pending additional information on some of the spin wave parameters.

3.2. *Experimental results*

As we have already noted, Tb and Dy have such large axial anisotropies that at low temperatures their moments can only be pulled a few degrees out of the basal plane. Conventional torque magnetometry techniques are thus unsuitable, but estimates of the axial anisotropy coefficients have been made from analyses of the magnetization measurements (Feron et al., 1970; Rhyne et al., 1968) and also from measurements of the zero torque position of a torque magnetometer with uncoupled servo (Rhyne and Clark, 1967). All of these experiments were actually interpreted with the aid of an expression for the macroscopic anisotropy energy of the form:

$$F(\theta,\phi) = V_2^0 P_2(\cos\theta) + V_4^0 P_4(\cos\theta) + V_6^0 P_6(\cos\theta) + V_6 \sin^6\theta \cos 6\phi \tag{6.50}$$

However, Rhyne (1972) subsequently employed the spherical harmonic expansion (eq. 6.39) without allowance for appropriate scaling of the coefficients due to

$$Y_l^0(\theta,\phi) = \left[\frac{(2l+1)}{4\pi}\right]^{1/2} P_l^0(\cos\theta). \tag{6.51}$$

We shall rigorously follow the notation of eq. 6.39 and, where necessary, scale the original data accordingly.

In the case of Tb, the most systematic data for $\kappa_2^0(T)$ are those of Feron et al. deduced from measurements of the c-axis magnetization leading to $\kappa_2^0(0) = 9.0 \pm 1.8 \times 10^7\,\mathrm{Jm^{-3}}$. From the zero–torque method, Rhyne and Clark estimated $\kappa_2^0(0) = 8.7 \pm 2.2 \times 10^7\,\mathrm{Jm^{-3}}$. In their analysis of the spin wave energy gap in Tb (section 2.1.1) Roeland et al. (1975) derived a value (0.23 meV/ion) for the microscopic parameter B_2^0. Using eq. 6.42, this result is equivalent to $\kappa_2^0(0) = 7.6 \times 10^7\,\mathrm{Jm^{-3}}$, in agreement with the macroscopic values within experimental error.

From the slight curvature of the c-axis magnetization, Feron et al. deduced $\kappa_4^0(0) = 5.4 \pm 1.4 \times 10^6\,\mathrm{Jm^{-3}}$. The result of Roeland et al. equivalent to $\kappa_4^0(0) = -3.0 \times 10^6\,\mathrm{Jm^{-3}}$ is, however, consistent with the negative sign of the appropriate Stevens factor (eq. 6.44).

The temperature dependence of $\kappa_2^0(T)$ does not follow the $\hat{I}_{5/2}$ expression (eq. 6.48) particularly well. Instead of a σ^3 renormalization, fig. 6.27 indicates a rather larger exponent (4.0 ± 0.2), in contrast to the value of 2.6 obtained from eq. 6.49. In view of the uncertainty connected with κ_4^0, which may be reflected in the determination of κ_2^0, further measurements would be most helpful, in order to establish a more definite conclusion.

Several attempts have been made to elucidate the crystal field and magnetoelastic contributions to the basal plane anisotropy of Tb. Feron et al. deduced κ_6^6 via eq. 4.46 from their magnetization measurements, estimating $\kappa_6^6(0) = 1.85 \pm 0.18 \times 10^5\,\mathrm{Jm^{-3}}$. Figure 6.2 reveals the difficulty of accurately determining H_c from magnetization results. Rhyne's (1965) analysis of the basal plane magnetostriction included κ_6^6 as a fitting parameter: he found $\kappa_6^6(0) = 2.4 \pm 0.2 \times 10^5\,\mathrm{Jm^{-3}}$. The torque magnetometer results of Bly et al. (1969) are broadly similar to those of Feron and Rhyne but extend down to only 55 K. A

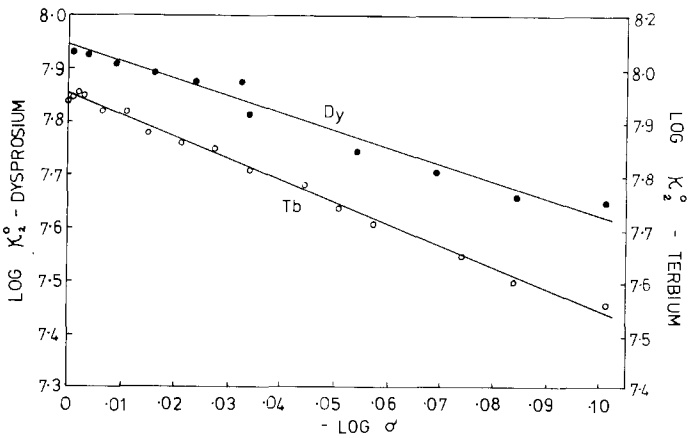

Fig. 6.27. The results of Feron et al. (1970) for the uniaxial anisotropy coefficient κ_2^0 of dysprosium and terbium plotted as a function of the reduced magnetization.

recent study of κ_6^6 by Shepherd (1976) in which measurements were made of the emf induced in a pick-up coil during the rotation of a sample in a steady field produced $\kappa_6^6(0) = 3.0 \pm 0.1 \times 10^5\ \mathrm{Jm^{-3}}$. From their spin wave data, Houmann et al. (1975) deduced a $T = 0$ critical field of 3.23 T equivalent to $\kappa_6^6(0) = 2.3 \times 10^5\ \mathrm{Jm^{-3}}$. Roeland et al.'s analysis provides an indication of the separate microscopic contributions to $\kappa_6^6(0)$: they estimated the magnitude of the magnetoelastic term $\frac{1}{2}c^{\gamma}AC$ as 0.072 meV/ion ($3.6 \times 10^5\ \mathrm{Jm^{-3}}$) and the effective crystal field term $B_6^6 = -1.7 \times 10^{-6}$ meV/ion ($-0.9 \times 10^5\ \mathrm{Jm^{-3}}$). The appropriate sum of these yields $2.7 \times 10^5\ \mathrm{Jm^{-3}}$ in good agreement with the macroscopic investigations.

Results for the temperature dependence of $\kappa_6^6(T)$, expressed in terms of the critical field, are summarised in fig. 6.28. Houmann et al.'s data follow a σ^{15} power law arising from the renormalization of the dominant magnetoelastic term. On the simple theory (eq. 6.48) C and A have temperature dependences σ^3 and σ^{10} whilst corrections for the ellipticity produce $\sigma^{3.3}$ and $\sigma^{12.3}$ (Jensen, 1976) or alternatively $\sigma^{3.4}$ and $\sigma^{14.6}$ (Lindgård and Danielsen, 1975). Clearly, a product of the former pair agrees very satisfactorily with the experimental results. We are thus unable to draw any conclusions about the temperature dependence of the crystal field term in this case.

The uniaxial anisotropy coefficients of Dy have been deduced from macroscopic measurements in the manner outlined for Tb. With the notation of eq. 6.39, Feron et al. (1970) found $\kappa_2^0(0) = 8.7 \pm 1.7 \times 10^7\ \mathrm{Jm^{-3}}$ and $\kappa_4^0(0) = 6.4 \pm 1.7 \times 10^6\ \mathrm{Jm^{-3}}$ whilst Rhyne et al. (1967) deduced $\kappa_2^0(0) = 7.8 \pm 0.8 \times 10^7\ \mathrm{Jm^{-3}}$ from the magnetization and $8.7 \pm 2.2 \times 10^7\ \mathrm{Jm^{-3}}$ via the zero-torque technique. The temperature dependence of $\kappa_2^0(0)$ (fig. 6.27) apparently follows $\sigma^{3.1 \pm 0.2}$ and is thus indistinguishable from the prediction of eq. 6.48.

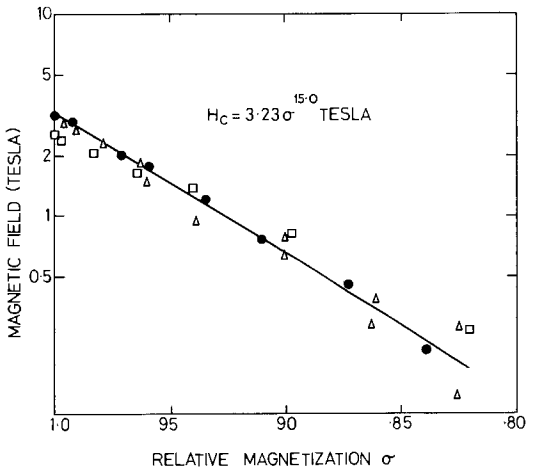

Fig. 6.28. The basal plane anisotropy of terbium, expressed as a critical field, plotted as a function of the reduced magnetization. Closed circles denote the neutron scattering results of Houmann et al. (1975): triangles and squares correspond to the macroscopic measurements of Rhyne (1965) and Feron et al. (1970), respectively.

Following the J-dependence of the appropriate Stevens factor, Dy exhibits a crystal field contribution to the basal plane anisotropy considerably larger than Tb and, as already noted (section 2.2.2), the a-axis is the easy direction so that κ_6^6 is negative. Although Feron et al. estimated κ_6^6 from 1.7 to 105 K, below 50 K the available magnetic field was insufficient to pull the magnetization completely into the hard direction. Thus the extrapolations used to calculate $\kappa_6^6(0) = -1.1 \pm 0.1 \times 10^6\,\mathrm{Jm^{-3}}$ should be treated with caution.

Rhyne's (1965) analysis of his magnetostriction results produced $\kappa_6^6(0) = -0.76 \times 10^6\,\mathrm{Jm^{-3}}$, considerably below the estimate of Feron. However, as in the magnetization measurements, the sample did not comprise a single domain for fields applied close to the hard basal plane directions at low temperatures. In a re-analysis of Rhyne's experiments, Martin (1977) has shown that consideration of this domain effect significantly alters the values deduced for κ_6^6 (as well as for the magnetostriction constants, see section 4.2) leading to $\kappa_6^6(0) = -1.38 \pm 0.06 \times 10^6\,\mathrm{Jm^{-3}}$. Figure 6.29 illustrates that the revised $\kappa_6^6(T)$ follows a $\sigma^{26.3\pm0.4}$ dependence, confirming the dominance of the crystal field contribution in Dy in contrast to Tb. Moreover, the magnetization exponent is decidedly larger than $\alpha_6 = 21$ and strongly supports the renormalization calculations for highly anisotropic ferromagnets (section 4.1.2).

The magnitude of κ_6^6 in Dy appears large enough to induce a ϕ dependence of the magnetization and ellipticity parameters $\Delta M(T, H)$ and $b(T, H)$ defined in eq. 6.14. In such a case, the phenomenological free energy expression (eq. 6.39)

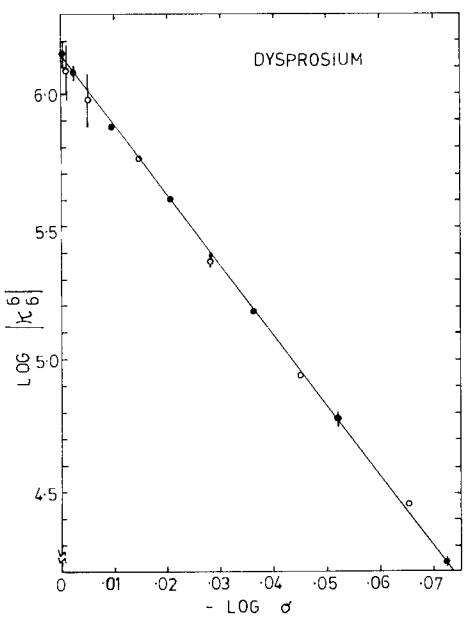

Fig. 6.29. The basal plane anisotropy of dysprosium as a function of reduced magnetization. The results of Martin's re-analysis of Rhyne's (1965) magnetostriction measurements are shown. (Martin and Rhyne, 1977).

requires additional terms with a $\cos 6n\phi$ dependence: alternatively, κ_6^6 may be regarded as a ϕ-dependent quantity. For Dy at zero temperature, Jensen (1975) estimated $\kappa_6^6(\text{easy}) \simeq 1.35\,\kappa_6^6(\text{hard})$. Whilst the measurements of H_c from the magnetization curves provide a determination of κ_6^6(hard), κ_6^6(easy) represents the parameter deduced from the spin wave energy gap (in $H = 0$) as measured by neutron scattering (Nicklow and Wakabayashi, 1972) or ferromagnetic resonance (Marsh and Sievers, 1969). The relative difference between κ_6^6(hard) and κ_6^6(easy) should decrease with increasing temperature, and the convergence of the static and dynamic energy gap parameters confirms this hypothesis.

Brooks and Egami (1974) calculated that the field dependence of $M(T, H)$ and $b(T, H)$ should produce a sizeable field dependence of κ_6^6 at low temperatures: a similar calculation by Jensen (1975) estimated this effect to be an order of magnitude smaller. Torque magnetometer measurements in pulsed fields up to 14 T (Melville and Rayner, 1977) indicate a field dependence of κ_6^6 which has an intermediate magnitude and a $T = 0$ value of $1.27 \pm 0.05 \times 10^6\,\text{Jm}^{-3}$, in good agreement with Martin's results. From a study of the anisotropy torque at 77.4 K, Egami (1976) extracted the field dependence of the sixth and twelfth order terms. The ratio κ_6^6 (easy)/κ_6^6 (hard), which was 1.29 at the critical field ($H_c = 2.1$ T) decreased with increasing field (following the reduction of $b(T, H)$ with field) whilst the mean value of κ_6^6 increased with field (following the increasing reduced magnetization).

For holmium, there are discrepancies between the values of the axial coefficients estimated from magnetization data by Rhyne et al. (1967) and by Feron et al. (1970). Rhyne's analysis yielded zero temperature values of $\kappa_2^0 = 3.2 \times 10^7\,\text{Jm}^{-3}$, $\kappa_4^0 = 1.65 \times 10^6\,\text{Jm}^{-3}$ and $\kappa_6^0 = -1.6 \times 10^6\,\text{Jm}^{-3}$, with considerable uncertainty in the latter, whereas Feron found $\kappa_2^0 = 6.6 \pm 1.7 \times 10^7\,\text{Jm}^{-3}$ and $\kappa_4^0 = 2.1 \pm 0.5 \times 10^6\,\text{Jm}^{-3}$. However, Rhyne's results are probably more reliable since they incorporate the effects of the sudden increase of the c-axis magnetization near 12 T (fig. 6.6): Feron's measurements extended to only 6 T and the temperature dependence of $\kappa_2^0(T)$ exhibits wide scatter on a $\log \kappa_2^0 - \log \sigma$ plot. A value of $1.45 \pm 0.15 \times 10^7\,\text{Jm}^{-3}$ for $\kappa_2^0(0)$ has been estimated by Vishnyakov et al. (1970) from measurements in pulsed fields up to 24 T.

Both Rhyne and Feron estimated $\kappa_6^6(0)$ as $2.7 \pm 0.3 \times 10^6\,\text{Jm}^{-3}$ whilst Cock (1976) deduced a value of $3.4 \pm 0.3 \times 10^6\,\text{Jm}^{-3}$. The basal plane anisotropy in Ho is thus larger than in any other lanthanide, a result of the 4f charge distribution associated with the large orbital moment ($L = 6$). As in the case of κ_2^0, the temperature dependence of κ_6^6 cannot be readily parameterized and requires further investigation.

For both erbium and thulium the easy direction is the c-axis (section 2.2.4, section 2.2.5) and thus the overall axial anisotropy is negative. Consequently, when a field is applied along a hard direction, the angle between neighbouring spins in the conical configuration is field dependent, so that the exchange energy varies with field. Hence the anisotropy deduced from magnetization or torque measurements must be carefully analysed to separate crystal field and anisotropic exchange effects. As described in section 2.2.4, Jensen (1976) has self-

consistently fitted the Er magnetization data with a molecular field model using exchange parameters deduced from the spin wave dispersion (including the effects of anisotropic exchange) and four effective crystal field parameters B_2^0, B_4^0, B_6^0 and B_6^6. Using eq. 6.42, Jensen's fit gives

$$\kappa_2^0 = -9.7 \times 10^6\ \mathrm{Jm^{-3}}, \qquad \kappa_4^0 = -4.1 \times 10^6\ \mathrm{Jm^{-3}}, \qquad \kappa_6^0 = 5.1 \times 10^6\ \mathrm{Jm^{-3}}$$

and $\kappa_6^6 = -2.1 \times 10^6\ \mathrm{Jm^{-3}}$ at $T = 0$ K.

Appropriately combined changes in these parameters of the order of 10% also fit the magnetization data. The substantial basal plane anisotropy thus has a magnitude second only to that of holmium.

Since gadolinium is an S-state ion, the magnitude of the anisotropy is much smaller than in the other lanthanides. In the absence of single-ion contributions, the departure of the c/a ratio from its ideal value is manifested as a dipolar anisotropy (Brooks and Goodings, 1968). The residual anisotropy of Gd has been measured several times and the early torque magnetometer studies were collated by Rhyne (1972). Corner et al. (1962) found that κ_2^0 actually changed sign between T_C and $T = 0$. This unusual temperature dependence, resulting from the two-ion origin of the anisotropy, is further revealed as a variation of the easy magnetization direction with temperature, as shown in fig. 6.13.

More recent data of Feron et al. (1969) and Mishima et al. (1975) are in general agreement with the earlier data, although the accuracy remains rather poor. At $T = 0$ K, Feron et al. found $\kappa_2^0 = -2.1 \pm 0.5 \times 10^5\ \mathrm{Jm^{-3}}$ and $\kappa_4^0 = 8.2 \pm 0.2 \times 10^4\ \mathrm{Jm^{-3}}$ whilst Mishima et al. deduced $\kappa_2^0 = -1.4 \times 10^5\ \mathrm{Jm^{-3}}$, $\kappa_4^0 = 7.3 \times 10^4\ \mathrm{Jm^{-3}}$ and $\kappa_6^0 = -1.4 \times 10^4\ \mathrm{Jm^{-3}}$. Graham (1967) measured the very small basal plane anisotropy, estimating $\kappa_6^6(0) = 6.3 \times 10^2\ \mathrm{Jm^{-3}}$.

3.3. *Results from paramagnetic measurements*

In an attempt to determine the crystal field contribution (eq. 6.3) to the magnetic anisotropy, Touborg and Høg (1974) systematically investigated the magnetization of dilute alloys of Tb, Dy and Er in the host elements Y, Sc and Lu. With atomic concentrations of 0.1 to 1 atomic percent, the exchange interactions become sufficiently small that the magnetization of such single crystal alloys can be interpreted directly in terms of eqs. 6.32 and 6.36. Two molecular field parameters served to describe residual exchange interactions: apart from $\lambda_{\parallel c}$, $\lambda_{\perp c}$ and B_2^0, B_4^0, B_6^0, B_6^6, the atomic concentration was also employed as a fitting parameter. A value close to the nominal concentration was always deduced. In a later extension to Ho and Tm solutes, Høg and Touborg (1976) reanalyzed some of their earlier work (particularly the Dy alloys) to overcome ordering effects. Their data are reviewed by Touborg (1977). Figure 6.30 shows the deduced values of B_l^m, divided by appropriate Stevens' factors (eq. 6.44), for Tb–Tm in Y, La and Sc hosts. Within the sensitivity of the fitting procedure, a common set of crystal field parameters accounts for the susceptibility data for all solutes in the same host. For the different hosts, a considerable variation of B_2^0/α_J is evident, whilst B_4^0/β_J and B_6^0/γ_J are each almost the

TABLE 6.2

Anisotropy parameters for Tb, Dy, Ho, Er and Tm. The units of κ_l^m and B_2^0/α_J are 10^6 J m^{-3} and K/ion respectively. Macroscopic measurements have been collated from the references cited in the text together with the parameters deduced by Touborg (1977) from dilute alloy studies. κ_2^0 has also been calculated from paramagnetic Curie temperatures quoted in the text, and from the paramagnetic susceptibility at 273 K (Boutron and Aléonard 1976) and at 300 K (Touborg 1977). Equivalent values of B_2^0/α_J are included for comparison. Touborg's average values of B_4^0/β_J and B_6^0/γ_J are 6.8 ± 0.9 K/ion and 13.6 ± 1.6 K/ion, respectively.

Metal	κ_2^0	κ_6^0	κ_6^0	κ_6^6	B_2^0/α_J	Method
	89 ± 15	5.4 ± 1.4	–	0.25 ± 0.05	-310 ± 30	Torque and magnetization
	76 ± 7	-3.0 ± 0.3	-1.2 ± 0.1	0.27 ± 0.03	-265 ± 25	Spin wave analysis of magnetization
Terbium	–	–	–	0.23 ± 0.02	–	Spin wave critical field
	23 ± 3	-2.3 ± 0.3	-1.1 ± 0.1	0.66 ± 0.06	-81 ± 12	Dilute alloys
	25 ± 2	–	–	–	-88 ± 8	Paramagnetic Curie temperatures
	31 ± 3	–	–	–	-110 ± 10	Paramagnetic susceptibility
	84 ± 15	6.4 ± 1.7	–	-1.35 ± 0.15	-290 ± 50	Torque and magnetization
	–	–	–	-0.97 ± 0.10	–	Spin wave critical field
Dysprosium	23 ± 4	2.9 ± 0.4	5.5 ± 0.6	-3.3 ± 0.4	-81 ± 12	Dilute alloys
	29 ± 2	–	–	–	-99 ± 6	Paramagnetic Curie temperatures
	30 ± 2	–	–	–	-103 ± 5	Paramagnetic susceptibility

Holmium	32 ± 3	1.65 ± 0.2	-1.6 ± 0.8	2.7 ± 0.3	-270 ± 30	Magnetization
	14.5 ± 1.5	–	–	3.4 ± 0.3	-120 ± 10	Magnetization (pulsed fields)
	$8.1^{+0.8}_{-1.6}$	2.2 ± 0.3	-11.3 ± 1.3	6.8 ± 0.8	-69^{+7}_{-14}	Dilute alloys
	9.3 ± 1	–	–	–	-79 ± 8	Paramagnetic Curie temperatures
	9.0 ± 0.5	–	–	–	-76 ± 4	Paramagnetic susceptibility
Erbium	-9.7 ± 1	-4.1 ± 1.0	5.1 ± 0.4	-2.1 ± 0.2	-81 ± 8	Magnetization
	-11.0 ± 1.7	-2.2 ± 0.3	11.4 ± 1.3	-6.9 ± 0.8	-92 ± 14	Dilute alloys
	-18 ± 4	–	–	–	-155 ± 35	Paramagnetic Curie temperatures
	-14.7 ± 1	–	–	–	-122 ± 8	Paramagnetic susceptibility
Thulium	-30 ± 4	-3.0 ± 0.4	-5.8 ± 0.7	3.5 ± 0.4	-99 ± 12	Dilute alloys
	-35.5 ± 2	–	–	–	-116 ± 5	Paramagnetic Curie temperatures
	-33 ± 3	–	–	–	-107 ± 8	Paramagnetic susceptibility

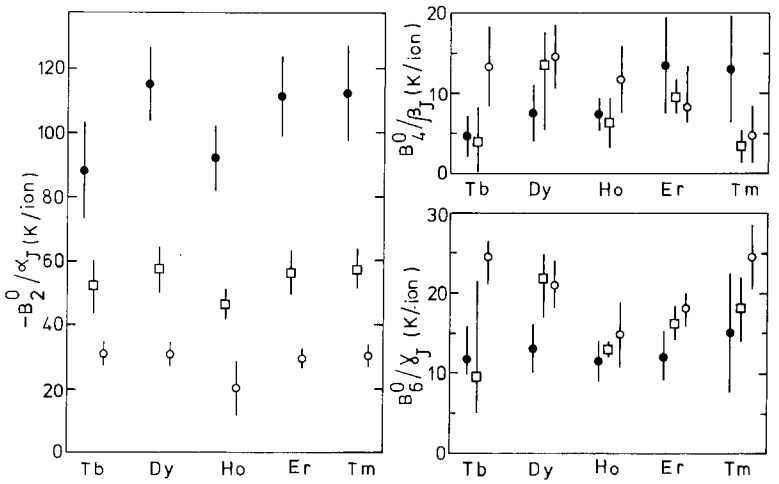

Fig. 6.30. Crystal field parameters, divided by appropriate Stevens' factors, for dilute alloys of Tb, Ho, Er and Tm in the hosts Y(●), Lu(□) and Sc(○), as deduced from magnetization and susceptibility measurements (after Touborg 1977).

same for Y and Lu, and slightly larger for Sc. The magnitude of B_2^0/α_J increases with the deviation of the host metal c/a ratio (1.573 for Y, 1.584 for Lu and 1.592 for Sc) from the ideal value of 1.633.

It is interesting that the ratios of B_l^m/θ_l for different solutes in the same host display no clear tendency to vary as $\langle r^l \rangle$ in accordance with eq. 6.44. Freeman and Watson (1962) calculated that $\langle r^l \rangle$ decreases from Tb to Tm with a variation compared to the Tb values of 14%, 25% and 36% for $\langle r^2 \rangle$, $\langle r^4 \rangle$, and $\langle r^6 \rangle$ respectively. A study of dilute alloys with solutes of Pr, Nd and Sm, which have much larger mean radii, may substantiate these conclusions.

Touborg (1977) has estimated B_2^0 for the pure metals by interpolation for the c/a ratio. Values of B_4^0 and B_6^0 were deduced from the average of the results for Y and Lu hosts, as these exhibit the closest resemblance (in respect of lattice parameters and band structure) to the magnetic lanthanides. These estimates have been converted to $\kappa_l^m(0)$ values and are compared in table 6.2 with the data reviewed in section 3.2. The overall agreement is fair, considering that the coefficients for the pure metals include not only crystal field but also magnetoelastic and possibly anisotropic exchange contributions as well. They should thus be regarded as model-dependent parameters.

The uniaxial anisotropy may also be evaluated from the anisotropy in the paramagnetic susceptibility or, equivalently, from the difference between the paramagnetic Curie temperatures:

$$B_2^0 = 5k(\theta_\perp - \theta_\parallel)/6(J - \tfrac{1}{2})(J + \tfrac{3}{2}) \tag{6.52}$$

Estimates for the pure metals are in reasonable agreement (table 6.2) with those determined from the dilute alloy studies. Indeed Aléonard et al. (1969) found a variation of B_2^0/α_J (deduced from the paramagnetic susceptibility) on the c/a

ratio similar to that of Touborg and Høg. Subsequently Boutron et al. (1971) interpreted the anisotropy they detected in the field dependence of the paramagnetic susceptibility as evidence for an anisotropic exchange interaction. However, Kazakov (1974) later explained the high temperature behaviour of $\kappa_2^0(T, H)$ in a higher order molecular field calculation without invoking anisotropic exchange.

4. Magnetostriction

Whenever the total magnetic energy depends on the lattice parameters, we may expect the minimization of this energy to be manifested as magnetostrictive distortions. In general terms the total energy comprises exchange, anisotropy and Zeeman contributions. If the exchange energy depends only on the relative orientation and magnitude of the spins, and is not changed by the application or rotation of a magnetic field, we may usually neglect its strain dependence. (This does not hold for the spiral state.) A variation of the demagnetizing factor with specimen shape leads, in principle, to a strain dependence of the demagnetization energy (known as the form effect), but again this may normally be neglected in the case of the rare earths. The key contribution to the magnetostriction thus arises from a strain dependence of the anisotropy energy. In section 4.1 we review Callen and Callen's (1963) elegant theory of magnetostriction, and discuss appropriate modifications for highly anisotropic systems. The resulting symmetry-dictated strain modes and the techniques by which they may be observed are then described. Experimental results (section 4.2) were earlier reviewed by Rhyne (1972) and remain essentially limited to the elements Gd, Tb, Dy, Ho and Er together with some preliminary data for Pr. As for the magnetic anisotropy, the most extensive studies are confined to Tb and Dy: reasonably definitive results for their ferromagnetic, helical and paramagnetic phases exist.

4.1. *Review of magnetostriction theory*

Callen and Callen (1963) considered the interactions of a single ion with its surrounding charge environment in terms of an expression of the form (eq. 6.6) together with possible two-ion effects expressed using spin polynomials in the product spaces of the ions. After expanding $\mathscr{H}_{\mathrm{me}}$, the free energy may then be calculated by a perturbation method and minimized with respect to the irreducible hexagonal strains. A subsequent transformation of the equilibrium strains back to Cartesian symmetry yields the following well-known expression for the magnetostriction of a hexagonal ferromagnet, correct to second order in direction cosines α_i of the magnetization:

$$\frac{\Delta l}{l} = [\lambda_1^{\alpha,0} + \lambda_1^{\alpha,2}(\alpha_z^2 - \tfrac{1}{3})](\beta_x^2 + \beta_y^2) + [\lambda_2^{\alpha,0} + \lambda_2^{\alpha,2}(\alpha_z^2 - \tfrac{1}{3})]\beta_z^2$$
$$+ \tfrac{1}{2}\lambda^{\gamma,2}[(\alpha_x\beta_x + \alpha_y\beta_y)^2 - (\alpha_x\beta_y - \alpha_y\beta_x)^2] + 2\lambda^{\epsilon,2}(\alpha_x\beta_x + \alpha_y\beta_y)\alpha_z\beta_z. \qquad (6.53)$$

The direction cosines β_i designate the strain measurement direction and the magnetostriction coefficients λ may therefore be deduced from measurements of the fractional length changes of the specimen as a function of magnetization direction. Of the six magnetostriction coefficients in eq. 6.53, $\lambda_1^{\alpha,l}$ and $\lambda_2^{\alpha,l}$ terms correspond to uniform expansions of the basal plane and c-axis, respectively. $\lambda^{\gamma,2}$ describes the distortion of the basal plane from hexagonal to orthorhombic symmetry, whilst $\lambda^{\epsilon,2}$ represents a shearing of planes perpendicular to the c-axis. Equation 6.53 may be readily extended to fourth order in α_i with the addition of a further five magnetostriction coefficients.

Mason (1954) also described the magnetostriction, to the same degree of symmetry as Callen and Callen, from a consideration of the elastic enthalpy. Mason's expression has frequently been used as a working relation for investigations of Tb and Dy below the Néel temperature (see section 4.2).

As a result of minimizing $\mathcal{H}_e + \mathcal{H}_{me}$, the magnetostriction coefficients are functions of the elastic constants c_{ij}, the magnetoelastic coupling constants $B^{\Gamma,i}$ and expectation values of spin operators (Clark et al., 1965). In general, the coefficients include contributions from both single-ion and multi-ion interactions, but the anisotropic part ($l \geqslant 2$) of the magnetostriction is dominated by the terms of single-ion origin, representing the strain response to the angular variation in electrostatic crystal field energy plus an additional contribution due to a strain-induced rearrangement of the conduction electrons (Tsuya et al., 1965). For example, the single-ion form of $\lambda^{\gamma,2}$ is given by Clark et al. (1965) as

$$\lambda^{\gamma,2} = -\frac{B^{\alpha,2}}{c_{11} - c_{12}} \langle (S^{\zeta})^2 - \tfrac{1}{3} S(S+1) \rangle \tag{6.54}$$

The fully symmetric terms $\lambda_1^{\alpha,0}$ and $\lambda_2^{\alpha,0}$ are, however, of multi-ion origin, being related to the anomalous thermal expansion.

Lacheisserie (1970) and Brooks and Egami (1974) have introduced coefficients defined via a spherical harmonic expansion, but since almost all experimental work has been analysed in terms of either eq. 6.53 or Mason's expansion, we shall retain these latter expressions for our purposes.

The temperature dependence of the magnetostriction coefficients follows from the expectation values of the Stevens operators: the calculation proceeds analogously to that for the anisotropy coefficients, discussed in section 3.1.2. When the ellipticity parameter may be neglected, the single-ion contributions to $\lambda_i^{\Gamma,l}$ follow the $\frac{1}{2}l(l+1)$ power law as a consequence of eq. 6.48. Mason's coefficients follow a similar temperature dependence if only the leading $l \geqslant 2$ term is considered. Corrections for the ellipticity parameter (Brooks and Egami, 1974) modify the temperature dependence of, for example, $\lambda^{\gamma,2}$ from σ^3 to $\sigma^{3.3}$ (Jensen, 1975) or alternatively $\sigma^{3.4}$ (Lindgård and Danielsen, 1975). Since they arise from multi-ion interactions, the temperature dependence of the $l = 0$ terms is more complex and cannot normally be expressed as a simple power law in the magnetization.

4.2. *Experimental results*

Measurements of $\Delta l/l$ have been accomplished by three methods. Strain gauges are widely used (e.g. Rhyne, 1965) but this technique suffers from a variation of the gauge factor with temperature. The usual method of gauge measurement incorporates a compensating gauge which should, ideally, be mounted on a substrate with the same thermal expansion coefficient as the magnetostricting sample, but this is rarely possible. Thus strain gauge measurements are expected to be more reliable for anisotropic determinations ($\lambda^{\gamma,2}$, for example) than for $\lambda_1^{\alpha,0}$ and $\lambda_2^{\alpha,0}$. Moreover, the magnitudes of these latter coefficients are sensitive to the choice of the state of zero strain.

Capacitance dilatometer methods are substantially more sensitive than the strain gauge technique (Slavin, 1972; Lacheisserie, 1975) but accurate low temperature calibration requires considerable care, as does the mounting of highly anisotropic materials (Tb and Dy) for rotation measurements (Keeler and Pearson, 1978).

Magnetostriction coefficients have also been deduced from measurements of interplanar lattice spacings by X-ray diffraction (Darnell, 1963; Finkel and Belovol, 1974). However, it is open to question whether the microscopic strain determined in a multidomain, (and sometimes powdered or polycrystalline) sample is equivalent to the bulk strain in a single domain crystal measured by either of the first two methods. Again the determination of $\lambda_1^{\alpha,0}$ and $\lambda_2^{\alpha,0}$ involves an extrapolation from the paramagnetic region, which is a source of some uncertainty.

4.2.1. *Terbium and dysprosium*

Whilst in principle the anisotropic magnetostriction coefficients may be readily deduced by measuring $\Delta l/l$ as a function of magnetization direction, the magnitude of the magnetic anisotropy imposes strong limitations. For Tb and Dy the effective confinement of the spins to the basal plane ($\alpha_z = 0$) at low temperatures eliminates the $\lambda^{\epsilon,2}$ term from eq. 6.53 which then has the form

$$\Delta l/l = D(\beta_x^2 + \beta_y^2) + G\beta_z^2 + C[(\alpha_x\beta_x + \alpha_y\beta_y)^2 - (\alpha_x\beta_y - \alpha_y\beta_x)^2] + A[2\alpha_x\alpha_y\beta_x + (\alpha_x^2 - \alpha_y^2)\beta_y]^2 \tag{6.55a}$$

In this equation, correct now to fourth order in α_x and α_y, the coefficients D, G, C, A contain the following combinations:

$$D = \lambda_1^{\alpha,0} - \tfrac{1}{3}\lambda_1^{\alpha,2} + \tfrac{9}{5}\lambda_1^{\alpha,4},$$

$$G = \lambda_2^{\alpha,0} - \tfrac{1}{3}\lambda_2^{\alpha,2} + \tfrac{9}{5}\lambda_2^{\alpha,4},$$

$$C = \tfrac{1}{2}(\lambda_2^{\gamma,2} - \tfrac{1}{7}\lambda_1^{\gamma,4}) \tag{6.55b}$$

and A corresponds to $\lambda_2^{\gamma,4}$ with a shift in zero level. Only the γ-strain coefficients A and C can be directly determined by a rotation of the field in the basal plane. For an angle ϕ between the magnetization direction and the a-axis, the aniso-

tropy of the linear strain becomes

$$\Delta l/l = \pm A \sin^2 2\phi \pm 2C \sin^2 \phi \tag{6.56}$$

The choice of signs in eq. 6.56 reflects the directions of strain measurement and easy magnetization. A and C for Tb and Dy were extracted by Rhyne (1965) from strain gauge experiments in an applied field of 3 T. However, the basal plane anisotropy results of section 3.2 indicate that 3 T is insufficient to produce a single domain in Dy below ~100 K and in Tb below ~40 K. Martin and Rhyne (1977) has re-analysed the experimental data of Rhyne to allow for the multidomain nature of the samples. Whilst the A and C results for Tb are only slightly changed by this procedure and are in reasonable agreement with measurements in 4 T by the capacitance technique (Keeler and Pearson, 1978), those of Dy are substantially modified – C is increased whilst the fourth order term A is diminished. Houmann et al. (1975) found that for Tb, the temperature dependence of C follows the reduced magnetization as $\sigma^{2.42\pm0.04}$ whilst A follows $\sigma^{7.5\pm0.15}$. It was suggested that the difference between these expressions and the larger exponents predicted (section 4.1.2) may indicate the importance of two-ion contributions. For the Dy data of fig. 6.31, C follows a $\sigma^{4.4\pm0.2}$ dependence – in contrast again with the predicted exponent.

The coefficients D and G are independent of magnetic field directions in the basal plane and thus cannot be determined from rotation measurements. Rhyne

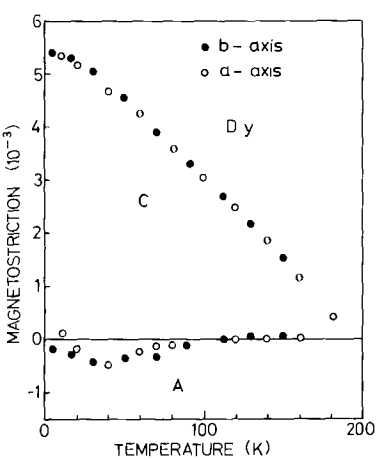

Fig. 6.31. Temperature dependence of the second and fourth order magnetostriction constants (C and A) for dysprosium, as deduced by Martin (1977) from Rhyne's (1965) strain measurements along a and b directions.

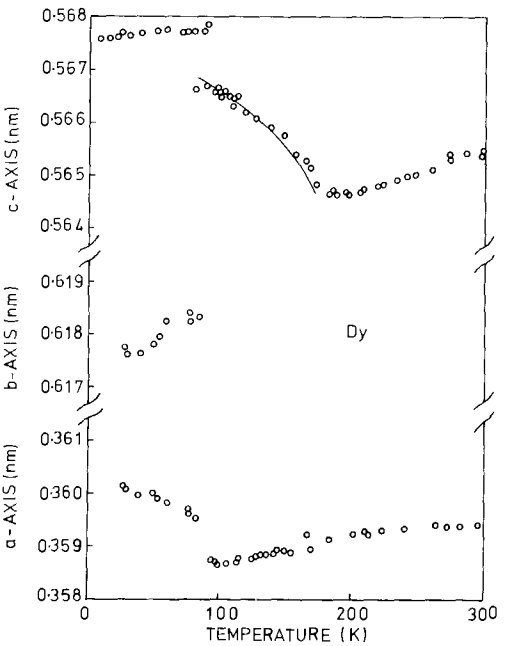

Fig. 6.32. The temperature dependence of the lattice parameters of dysprosium (after Darnell, 1963).

evaluated D and G by subtracting the thermal expansion (extrapolated from above T_N) from the measured basal plane and c-axis strains.

Finkel and Belovol (1973, 1974) investigated the deformations by accurate lattice parameter studies of polycrystalline Tb and Dy with X-ray diffraction techniques, following earlier work by Darnell (1963). Figure 6.32 illustrates the rapid expansion with decreasing temperature along the c-axis of Dy in the antiferromagnetic region, and the discontinuity of about 0.3% at T_C. This effect, together with similar changes in the a and b directions, is directly comparable with the results of Rhyne (1965) for the length changes due to a field-induced ferromagnetic transition (see fig. 6.33). The c-axis magnetostriction in the helical phase is normally attributed (Lee 1964, Evenson and Liu 1969) to a strain dependence of the crystal field energy which dominates in the ferromagnetic phase. Finkel and Belovol deduced that for Dy $\lambda_2^{\alpha,2}$ is positive but $\lambda_1^{\alpha,2}$ and $\lambda^{\gamma,2}$ are negative. Their field dependence correlates well with predictions based on studies of the anisotropy of the dependence of T_N on compression parallel to the a and c directions (Bartholin et al. 1971) and the following equation

$$\left(\frac{\partial\lambda}{\partial H}\right)_{p,T} = -\frac{T}{T_N}\left(\frac{\partial\sigma}{\partial T}\right)_{p,H}\left(\frac{\partial T_N}{\partial p}\right) \tag{6.57}$$

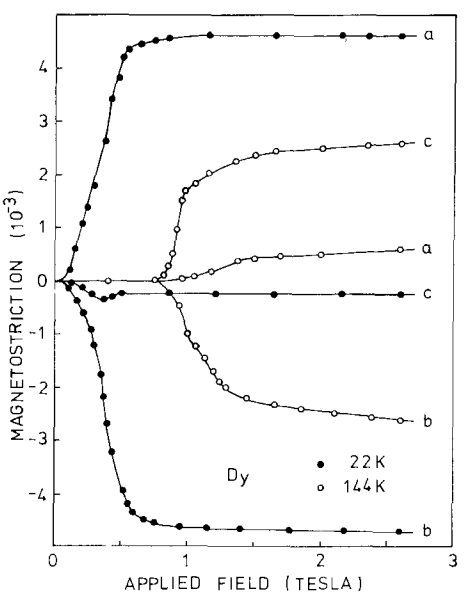

Fig. 6.33. The a, b and c-axis strains of dysprosium as a function of field applied along the a-axis. Results are shown for both ferromagnetic and spiral phases (after Rhyne, 1965).

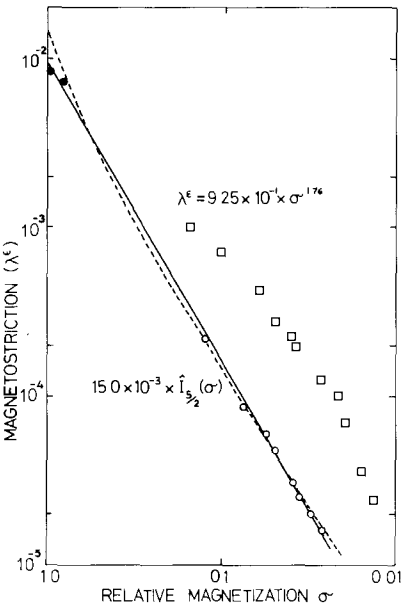

Fig. 6.34. The shear magnetostriction parameter of terbium as a function of the relative magnetization. Closed circles, open circles and squares denote the results deduced by Jensen and Houmann (1975), De Savage and Clark (1965) and Du Plessis (1968), respectively.

Below T_C the field dependence assumes a quite different form (fig. 6.33). The positive sign of C for Dy corresponds to an expansion along the easy a-axis and a contraction in the transverse basal plane direction. As expected, the c-axis strain is very small. Tb exhibits qualitatively similar results with b and a-directions interchanged. When a single domain has been formed, the forced magnetostriction is linear with applied field, as predicted (Callen and Callen 1965, del Moral and Brooks 1974) for a highly anisotropic ferromagnet, and its temperature dependence follows the high field (paraprocess) susceptibility:

$$\chi_{hf} = g\mu_B J(1-\sigma)/kT_{N,c}. \tag{6.58}$$

For $\sigma > 0.8$, Houmann et al. (1975) found that the field dependence of the Tb γ-strain terms was well represented by χ_{hf}. Above T_N the forced magnetostriction of Tb and Dy (Rhyne 1965) is proportional to H^2 in agreement with Callen and Callen (1965).

Three estimates of the shear magnetostriction parameter λ^ϵ have been made for Tb (fig. 6.34). By measuring the field dependence of the velocity of transverse sound waves propagating in the c-direction, Moran and Luthi (1970) deduced $\lambda^\epsilon = 7.3 \times 10^{-3}$ at 140 K ($\sigma = 0.82$). Jensen and Houmann (1975) determined a value of 8.5×10^{-3} at 53 K ($\sigma = 0.97$) from their analysis of magnon–phonon interactions in the c-axis dispersion relation. These results are consistent with the strain gauge measurements of De Savage and Clark (1965), taken in the paramagnetic phase.

4.2.2. *Holmium and erbium*

Magnetostrictive effects in Er are clearly visible in the temperature variation of the lattice parameters determined in the neutron diffraction study of Habenschuss et al. (1974). The appearance of the c-axis modulated structure below $T_{N\parallel} = 84.4$ K has little effect on the lattice constants (fig. 6.35), but below the basal plane ordering temperature $T_{N\perp} = 52.4$ K, the c-axis expands in the manner of the exchange magnetostriction found in the spiral phases of Tb and Dy. Ferromagnetic alignment of the c-axis moment at $T_C = 18$ K is marked by a

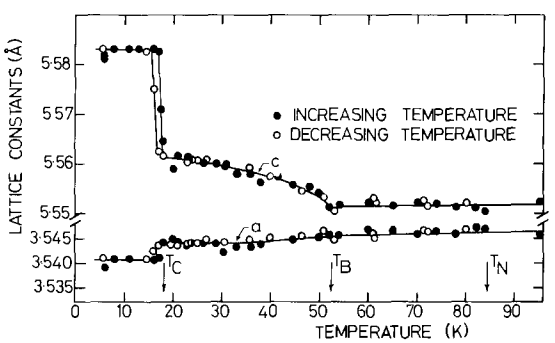

Fig. 6.35. The temperature dependence of the c and a-axis lattice constants of erbium. T_N and T_B correspond to the c-axis and basal plane ordering temperatures $T_{N\parallel}$ and $T_{N\perp}$ (after Habenschuss et al. 1974).

discontinuous increase in the c-axis lattice constant of some 0.4% as the clamping effect of the modulated structure is removed. Smaller changes, of the opposite sign, occur in the a-direction, These observations are in good agreement with the X-ray investigations of Darnell (1963). Application of a 3T magnetic field parallel to the c-axis produces a more rapid increase (between T_N and T_C) of the c-axis lattice constant which becomes a continuous function of temperature across the 18 K transition, as a result of the ferromagnetic moment produced (see fig. 6.10). Darnell's data indicate that the a and b directions behave similarly: the orthorhombic distortion detected in Tb and Dy does not materialise. Because the easy axis is ⟨0001⟩, the irreproducibility in zero field strain gauge measurements is much less than in Tb and Dy, and thus the lattice parameter studies are reasonably well supported by Rhyne's (1965) results. However, the field rotation measurements are less satisfactory. Due to a lack of knowledge about the exact details of the field-induced modifications of the ordered phases, $C = \frac{1}{2}\lambda^{\gamma,2}$ could not be evaluated reliably below 53 K. On the basis of a σ^3 temperature dependence, extrapolation to $T = 0$ yields $\lambda^{\gamma,2} = -5.1 \times 10^{-3}$.

In Ho, as in Er, the basal plane strain is isotropic at all temperatures whilst the c-axis expands with decreasing temperature (Darnell 1963, Rhyne et al. 1967). Again the analysis in applied fields is complicated by the complex magnetization process (see section 2.2.3) and the $T = 0$ K value of $\lambda^{\gamma,2} = 2.5 \times 10^{-3}$ has been extrapolated from data in the paramagnetic phase.

4.2.3. *Gadolinium*

Gd has been thoroughly studied because the weak anisotropy (section 3.2) enables practical fields to align the magnetization in any desired direction specified by α_i. Since the anisotropy is small, the magnetostriction constants are typically two orders of magnitude smaller than for the other elements we have

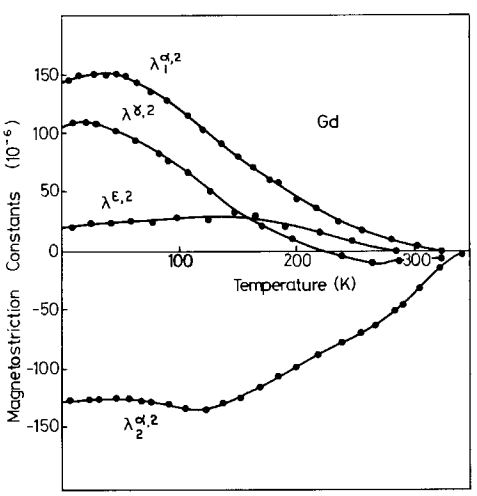

Fig. 6.36. The temperature dependence of the magnetostriction constants of gadolinium (after Mishima et al. 1976).

discussed, and their different temperature dependence reflects two-ion contributions.

Mishima et al. (1976) determined λ_1^{α}, λ_2^{α}, λ^{γ} and λ^{ε} from field rotation measurements using the strain gauge technique. Results in reasonable agreement with the earlier studies of Bozorth and Wakiyama (1963) and Alstad and Legvold (1964) were achieved. Figure 6.36 shows the temperature dependence of the $l = 2$ magnetostriction coefficients. The sign change of the $\lambda^{\gamma,2}$ term at 220 K has been interpreted as evidence for the presence of both single-ion and two-ion effects. Below 80K, an anomalous behaviour is apparent in Mishima et al.'s field rotation curves for *ac*-plane samples. Subsidiary extrema in the strain were observed on both sides of the *a*-axis. Although the anomalies may be interpreted in terms of higher order (up to $l = 8$) magnetostriction constants, they are presumably an artefact of the easy magnetization direction (fig. 6.13). It is noteworthy that no evidence for $l > 2$ contributions to λ^{γ} was found.

4.2.4. *Praseodymium*

The magnetostriction parallel and perpendicular to the *c*-axis of Pr has been measured by Ott (1975) over the temperature range 1.5 to 25 K. A quadratic field dependence was observed, as expected for a paramagnet (see section 2.3), and fig. 6.37 shows the measured strains in a field of 1 T. At the lowest temperatures the magnetoelastic coupling is highly anisotropic, reflecting the anisotropy in the susceptibility (fig. 6.17). The dominant field dependence of the γ-strains, compared to the α-strains, agrees with the theoretical estimates of Jensen (1976). From an analysis of the coupling between the phonons and the magnetic excitations in Pr, Jensen deduced a magnetoelastic coupling coefficient B^{22} of 20 meV, almost three times the equivalent value found in Tb.

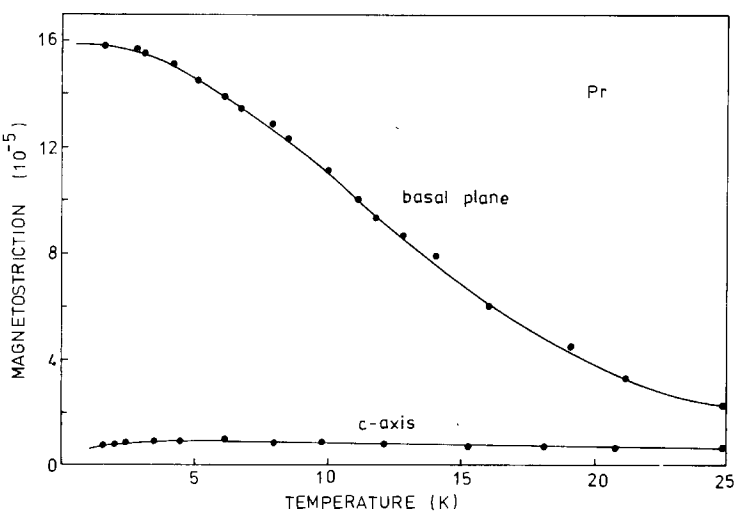

Fig. 6.37. The magnetostriction of praseodymium as a function of temperature, measured in a field of 1 T (Ott 1975).

Ott's thermal expansion measurements indicate that in zero field the α-strains are non-zero, corresponding to a change in c/a ratio. Combining these results with the magnetostriction data, a value of the susceptibility dependence on c/a ratio was estimated as $\partial(\ln \chi)/\partial[\ln(c/a)] \approx 40$, probably inadequate to account alone for the magnetic ordering in polycrystalline samples of Pr.

5. Electrical resistivity

The rare earth metals display a rich variety of transport phenomena, which we shall discuss in the remaining sections. Transport properties were last reviewed by Legvold (1972), who presented data for the resistivity, thermal conductivity and Seebeck coefficient of almost all the rare earth metals together with Hall effect results for the elements Gd – Er. Since 1972 little attention has been given to the thermal conductivity and Seebeck coefficient and, accordingly, we shall concentrate on the resistivity, magnetoresistivity and Hall effect measurements, with particular attention to recent studies.

We recall that the electrical resistivity of a metal is derived from an inversion of the conductivity tensor, which is given in the relaxation time (τ) approximation (see, for example, Ziman 1964) by

$$\sigma_{ij} = \frac{e^2}{4\pi\hbar} \int_{FS} \tau v_i \, dS_j \tag{6.59}$$

where v_i and dS_j denote components of the conduction electron velocity and Fermi surface projected area.

If the operative scattering mechanisms are independent, contributions to the resistivity may be separated in the well-known manner:

$$\rho_{total} = \rho_{residual} + \rho_{phonon} + \rho_{magnetic} \tag{6.60}$$

The strong d-like character of large sections of the Fermi surface of the rare earths (Harmon and Freeman 1974) results in a relatively low conduction electron mobility. Furthermore, even in the purest material available, $\rho_{residual}$ – describing the temperature independent scattering by non-magnetic impurities and lattice defects – is some $3 \times 10^{-9}\,\Omega$m (Jordan et al. 1974). Thus the electron mean free path is presently limited to a value several orders of magnitude lower than has been achieved for other metals.

However, our primary concern is with the magnetic contributions to the resistivity. The exchange coupling between the spin of a conduction electron and the 4f moment of an ion (which we have seen leads in second order to a strong two-ion coupling) directly affects the current carrying capacity of the lanthanides. If each of the ionic moments were exactly aligned parallel to a particular direction, there would be no scattering from this perfectly ordered system. At a finite temperature, when each ion possesses a thermal energy sufficient to partially randomize the orientation of the 4f moment, departures

from the aligned state provide a source of conduction electron scattering. In paramagnets, these effects are manifested as a spin-disorder resistivity. We examine this in section 5.1, assuming the ionic ground state is $(2J+1)$-fold degenerate, before considering the effects of crystal field splitting, as in Pr. In the magnetically ordered state, thermal fluctuations of the 4f moments may be analysed by molecular field theory (section 5.2) at temperatures above $0.1-0.2T_C$; section 5.3 considers the scattering by spin waves, and the large magnetic anisotropy of the lanthanides is again in evidence.

An unusual feature of the resistivity of some lanthanides appears when the magnetic system orders with a periodicity different to that of the ionic lattice. The development of additional energy gaps in the band structure, and the consequent diffraction of the conduction electrons, produces an increase of resistivity with decreasing temperature around certain magnetic transitions (see section 5.4).

5.1. *Spin disorder resistivity in paramagnets*

De Gennes and Friedel (1958) and Kasuya (1959) developed a model in which the conduction electrons are assumed to be scattered by the difference between the actual spin $\boldsymbol{S}$ of the ion at site $\boldsymbol{R}$ and the average value $\langle \boldsymbol{S} \rangle$:

$$\mathcal{H}_{sf} = -J_{sf}\boldsymbol{\sigma} \cdot (\boldsymbol{S} - \langle \boldsymbol{S} \rangle)\delta(\boldsymbol{r} - \boldsymbol{R}) \tag{6.61}$$

If J_{sf} is assumed to be independent of conduction electron wavevector, the scattering from a completely disordered spin system (i.e. the paramagnetic state, $\langle \boldsymbol{S} \rangle = 0$) may be readily evaluated within the first Born approximation to yield a resistivity contribution:

$$\rho_{mag} = (3\pi N m^*/8\hbar e^2 E_F) J_{sf}^2 (g-1)^2 J(J+1) \tag{6.62}$$

Spin – orbit coupling of the localized moments has been included and the $(2J+1)$ eigenstates are assumed equally populated, as in a paramagnet at high temperatures. N denotes the number of scattering centres per unit volume, and m^* the conduction electron effective mass: the free electron approximation has been used to calculate eq. 6.62. The magnetic contribution to the resistivity of the elements Gd – Tm (shown in figs. 6.38, 6.39) may be deduced by an appropriate subtraction of the phonon resistivity. As expected, Gd exhibits the largest spin disorder resistivity (almost $10^{-6}\Omega$m) and ρ_{mag} calculated from the c-axis resistivity of the series Gd – Tm follows the $(g-1)^2 J(J+1)$ dependence of eq. 6.62. Good agreement is also found for the basal plane results provided allowance is made for changes in the basal plane direction (Legvold 1972).

The expression (eq. 6.62) has assumed an equal population of the ground J-multiplet. For a paramagnet at a temperature well below the overall crystal field splitting of the multiplet, the 4f ions in the different eigenstates will be distributed randomly over the lattice sites with occupation numbers determined by the Boltzmann distribution. Since the 4f ions in these states have different cross-sections for conduction electron scattering, this contribution to the resistivity will be sensitive to changes in the population of crystal field levels. The

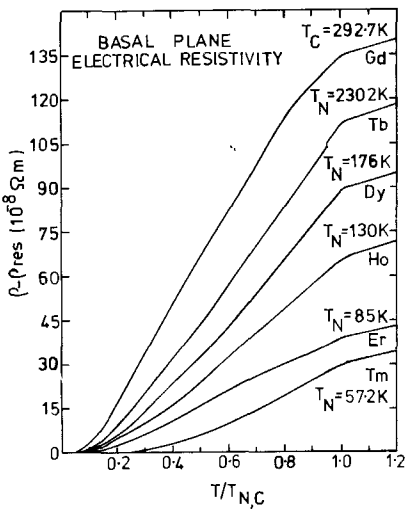

Fig. 6.38. The basal plane electrical resistivity of the elements Gd–Tm (after Legvold, 1972).

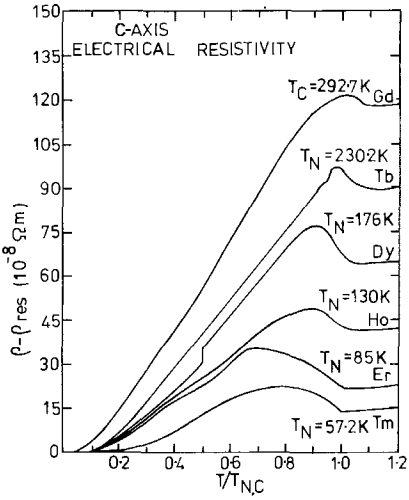

Fig. 6.39. The c-axis electrical resistivity of the elements Gd–Tm (after Legvold, 1972).

relevance of this mechanism as a significant contribution to the temperature dependence of the resistivity of elements such as Pr and Nd was first pointed out by Elliott (1954), before any detailed information about their crystal fields was available.

Following the approach of Van Peski-Tinbergen and Dekker (1963) and Andersen et al. (1974), the temperature dependent resistivity due to elastic and inelastic scattering of conduction electrons from the 4f states may be written as

$$\rho = \rho_0 \mathrm{Tr}(PQ) \tag{6.63}$$

where the trace is taken over the $(2J+1)$ crystal field states of energy E_i and the symmetric matrices P_{ij} and Q_{ij} are defined by

$$P_{ij} = \frac{\exp(-\beta E_i)}{\Sigma_i \exp(-\beta E_i)} \frac{2}{1+\exp[\beta(E_j - E_i)]}; \qquad \beta = (kT)^{-1},$$

$$Q_{ij} = |\langle i|J_z|j\rangle|^2 + \tfrac{1}{2}|\langle i|J_+|j\rangle|^2 + \tfrac{1}{2}|\langle i|J_-|j\rangle|^2. \tag{6.64}$$

The first factor in P_{ij} yields the Boltzmann population of the ith eigenstate whilst the second arises from a combination of Fermi distribution functions. Q_{ij} represents the matrix elements of eq. 6.61 between available states.

Temple and McEwen (1977) have evaluated the temperature dependence of Tr (PQ) for Pr, using the crystal field level scheme shown in fig. 6.17. In the absence of detailed information about the Fermi surface, ρ_0 was determined by fitting the calculation to experimental data (after subtraction of the residual resistance) at 10 K, where the phonon contribution is much smaller than the magnetic contribution. As indicated by fig. 6.40, the spin-disorder resistivity has almost

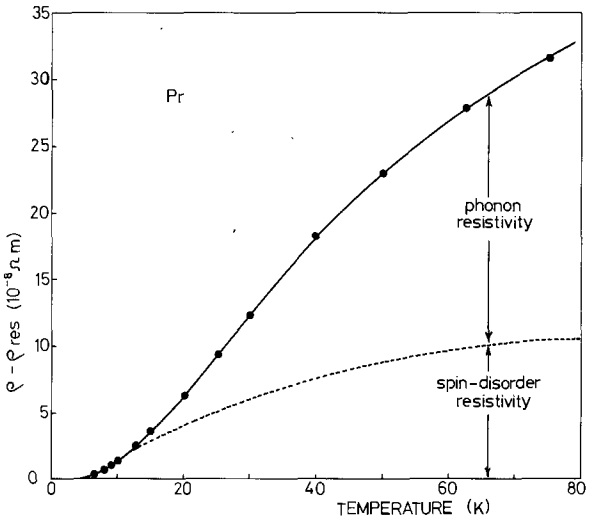

Fig. 6.40. The electrical resistivity of polycrystalline praseodymium separated into spin-disorder and phonon contributions as described in the text.

saturated by about 100 K: measurements of Smirnov and Prokhorov (1974) reveal a roughly linear dependence of the resistivity of Pr from 300 to 850 K, as expected for electron – phonon scattering.

5.2. *Resistivity in the ordered state*

The development of magnetic ordering with decreasing temperature reduces the conduction electron scattering because of correlations between ionic moments on different sites. A calculation starting from eq. 6.61 but with $\langle S\rangle \neq 0$ leads to a magnetic contribution to the resistivity of the form $[S(S+1)-\langle S\rangle^2]$, reflecting the degree of disorder amongst the spins. A rapid decrease in ρ_{mag} below T_c (or T_N) is therefore anticipated.

Yamada and Takada (1972, 1973) have extended earlier calculations and analyzed the effect of spin correlations on ρ_{mag} for both ferromagnets and antiferromagnets. Using a molecular field model to calculate $\langle S_i\rangle$ from the Brillouin function $B_s(y)$, the effect of spin correlations on ρ_{mag} for both ferromagnets and antiferromagnets. transverse spin fluctuations (within each magnetic sublattice, for an antiferromagnet).

$$\rho_{mag}(T,H) = \rho_{long}(T,H) + \rho_{trans}(T,H),$$

$$\rho_{long}(T,H) = CB_s'(y),$$

$$\rho_{trans}(T,H) = \tfrac{1}{2}C\,y\,B_s(y)\sinh^{-2}(\tfrac{1}{2}y) \qquad (6.65)$$

The argument y of the Brillouin function $B_s(y)$ describes the total field (applied plus molecular) acting on the ith ion.

Before quantitative comparison between eq. 6.65, evaluated for $H = 0$, and the experimental data can be made, the phonon contributions have to be subtracted from the results shown in figs. 6.38 and 6.39. However eq. 6.65 cannot be expected to be valid at the lowest temperatures (see section 5.3) where the phonon contribution is small. Moreover, there is an additional subtlety to the scattering problem in that the conduction electron band structure is itself temperature dependent below $T_{c,N}$. As the localized spins order with decreasing temperature, so the exchange interaction J_{sf} develops the periodicity of the lattice, leading to a modification of the band structure such that spin-up and spin-down conduction electrons with the same wavevector have different energies. Although Harmon and Freeman (1974) have examined this exchange splitting in Gd, it is not yet possible to make quantitatively reliable calculations of its effect on $\rho_{mag}(T)$ for ferromagnets. In antiferromagnets, the additional potential experienced by the conduction electrons no longer has the periodicity of the lattice, with the consequences discussed in section 5.4.

5.3. *Spin wave scattering*

At low temperatures, $B_s'(y)$ becomes exponentially small and $\rho_{long}(T)$ may be neglected, reflecting the insignificance of longitudinal spin fluctuations as the moment approaches saturation at $T = 0$. The transverse spin fluctuations, however, remain but are more accurately described within the spin wave approximation, because of the inadequacy of the molecular field model in describing the collective excitations. Calculations (Kasuya 1959, Yamada and Takada 1972) of the electron – magnon scattering cross-section yield a resistivity contribution:

$$\rho_{mag}(T) = A\int_0^{q_c} dq.\, q^3 \frac{\beta h\omega}{[\exp(\beta h\omega) - 1][1 - \exp(-\beta h\omega)]} \tag{6.66}$$

The integrand includes factors arising from the magnon occupation number and from a combination of Fermi distribution functions for the conduction electrons: it may be evaluated subject to a number of simplifying assumptions. At low temperatures only low wavevector magnons are appreciably excited and we may extend the limit of integration to infinity. Dispersion relations of the type $\omega \propto q^2$ and $\omega \propto q$ then yield resistivity contributions proportional to T^2 and T^4, respectively.

For Gd the dispersion relations for magnons propagating in the basal plane and along the c-axis are almost linear and quadratic, respectively. Figure 6.41 illustrates good qualitative agreement with the predicted temperature dependence of the resistivity. The experimental data up to 16 K actually follow $\rho_{mag} \propto T^n$ with $n = 3.7 \pm 0.1$ (basal plane) and $n = 2.2 \pm 0.1$ (c-axis), corresponding to deviations of the dispersion relation from the simple model.

The significance of the spin wave energy gap (Δ) for the transport properties of anisotropic ferromagnets was first recognized by Mackintosh (1962 and 1963), who

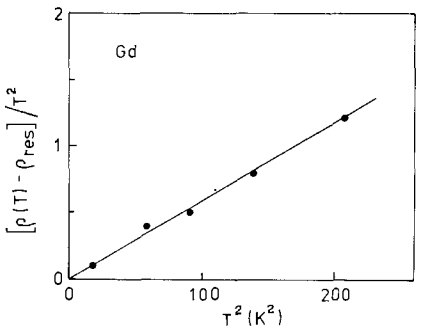

Fig. 6.41. The *b*-axis resistivity of gadolinium at low temperatures, plotted to afford comparison with the simple model described in section 5.3. The ordinate units are 10^{-11} Ωm K^{-2}.

showed that the combination of an energy gap and a quadratic magnon dispersion relation leads to a magnetic resistivity of the form:

$$\rho_{mag}(T) = AT^2 \exp(-\beta\Delta) \tag{6.67}$$

Thus the phonon contribution becomes relatively more significant than in, for instance, Gd and attempts (Sze et al. 1969, Cress 1970) to deduce Δ from the available data for Tb and Dy (Hegland et al. 1963, Boys and Legvold 1968, Nellis and Legvold 1969) have not been particularly successful, yielding values from 20 to 40 K.

5.4. *Superzone effects in antiferromagnets*

The spin fluctuation contribution to the resistivity of antiferromagnets below T_N may be calculated, within the molecular field model, from equations of the form of eq. 6.65 for each sublattice (Yamada and Takada 1973). However, in addition to this contribution, we observe a larger effect as the conduction electrons experience, via the sf interaction, the periodicity of the ordered magnetic structure. Just as the periodic Coulomb potential introduces energy gaps in the conduction electron band structure at the Brillouin zone boundaries, so an extra set of energy gaps appears, below T_N, at the boundaries of the magnetic superzones (Mackintosh 1964). The resulting distortions of the Fermi surface modify the metal's transport properties.

Since the wavevector describing the magnetic periodicity of the antiferromagnetic phases of the elements Tb-Tm is parallel to the *c*-axis, it transpires that the superzone energy gaps effectively remove a considerable fraction of the Fermi surface area projected normal to the *c*-axis, which thus produces a sharp increase in the *c*-axis resistivity below T_N (see fig. 6.39). The only portions of the calculated (hole) Fermi surface which have significant velocity components parallel to the *c*-axis are found in the network of arms located near the hexagonal faces of the Brillouin zone (see ch. 3 section 2.3.1).

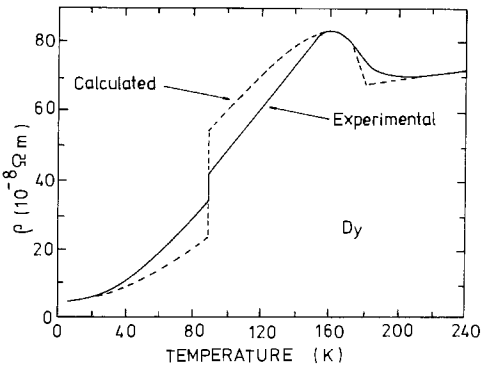

Fig. 6.42. Comparison for dysprosium of the measured c-axis electrical resistivity (Boys and Legvold 1968) with the calculation of Elliott and Wedgwood (1963).

Elliott and Wedgwood (1963) and also Miwa (1963) evaluated the superzone contribution to the resistivity of the elements Tb – Tm, subject to a number of simplifying assumptions. Figure 6.42 illustrates the good qualitative agreement achieved: a free electron Fermi surface was utilised and other magnetic scattering mechanisms were neglected. Since the periodicity of the magnetic structures show a temperature dependence between T_N and T_C, the concomitant variations in the relaxation of the conduction electrons produce an unusual temperature variation of the resistivity in this interval. The superzone scattering disappears at T_c, with a consequent drop in resistivity. A similar decrease takes place at higher

TABLE 6.3
References to electrical resistivity measurements

Element	Reference
Y	Hall et al. (1959)
Sc	Spedding et al. (1971)
La	Alstad et al. (1961); Nicolas–Francillon and Jerome (1973)
Ce	Gschneidner et al. (1976); Liu et al. (1976)
Pr	Arajs and Dunmyre (1967); Krithivas et al. (1972); Smirnov and Prokhorov (1975)
Nd	Alstad et al. (1961)
Sm	Arajs and Dunmyre (1966); Krithivas and Meaden (1975)
Eu	Meaden and Sze (1970)
Gd	Nigh et al. (1963); Hiraoka and Suzuki (1971)
Tb	Hegland et al. (1963); Nellis and Legvold (1969)
Dy	Boys and Legvold (1968); Craven and Parks (1973); Guntherodt et al. (1974); Rao et al. (1975)
Ho	Strandburg et al. (1962); Nellis and Legvold (1969); Guntherodt et al. (1974); Volkov et al. (1974)
Er	Boys and Legvold (1968)
Tm	Edwards and Legvold (1968)
Yb	Kayser (1970)
Lu	Boys and Legvold (1968)

temperatures when an applied magnetic field may be employed to produce a ferromagnetic alignment – as demonstrated with Tb by Hegland et al. (1963).

5.5. *Summary of experimental results*

In the preceding sections we have reviewed the most important mechanisms which produce magnetic contributions to the resistivity. The range of applicability of these scattering mechanisms has been discussed and illustrated with a number of specific examples. Details of the experimental results for each of the rare earth elements may be found in the references given in table 6.3. The list is necessarily representative rather than exhaustive: reference is made to definitive studies over a wide range of temperatures, together with more recent developments, where appropriate.

6. Galvanomagnetic effects

With the application of a magnetic field to a metal, the Lorentz force acting on the conduction electrons causes them to attempt to rotate around the Fermi surface at the cyclotron frequency $\omega_c = eB/m^*$. Many metals may be obtained sufficiently pure that it is possible, with suitable combinations of low temperatures and high magnetic fields, to achieve a frequency of collisions between carriers and scattering centres that is much less than the cyclotron frequency, i.e. $\omega_c\tau \gg 1$. In such a case, the motion of the conduction electrons will be completely described by their dispersion relation $E(k)$ and the external field. A study of the galvanomagnetic phenomena then provides valuable information on $E(k)$ and the Fermi surface. However, the available crystals of the rare earths are not yet sufficiently pure, in general, to enable this information to be extracted. Only in Gd (Young et al. 1976) has direct evidence of the topology of the Fermi surface emerged from magnetoresistance studies.

It may, therefore, be assumed that $\omega_c\tau \ll 1$: a conduction electron samples only a small fraction of the Fermi surface between collisions. Thus field dependent coherence effects are not manifested and the variation of the scattering mechanisms with magnetic field may be directly determined.

Three possible galvanomagnetic configurations have been generally considered: (a) current and magnetic field parallel, to measure the longitudinal magnetoresistance; (b) current and magnetic field perpendicular, with voltage measurement parallel to the current (transverse magnetoresistance); and (c) current, magnetic field and voltage measurement directions mutually perpendicular (Hall effect). A complete investigation of these phenomena for the major crystallographic directions, over a range of temperatures, constitutes a formidable task. A reasonably thorough survey exists so far only for Gd, Dy and Ho.

The first effect of applying a magnetic field to a ferromagnet is the alignment of domains, which is reflected in the spontaneous anisotropy described in section

6.1. Section 6.2 then discusses the influence of a field on the spin fluctuation scattering of section 5.2, for both ferromagnets and antiferromagnets. In the latter case, field induced magnetic structural changes produce corresponding changes in the relaxation time τ. Finally we consider the Hall effect in section 6.3.

6.1. *Anisotropic magnetoresistance*

Although the phenomenon of anistropic magnetoresistance has been investigated at some length in the transition metal ferromagnets, following its discovery by Thomson (1857), it has been almost completely ignored in the lanthanides. The experimental situation is illustrated by measurements on a Gd crystal, shown in fig. 6.43. Above technical saturation, the transverse magnetoresistance is a few percent larger than the longitudinal magnetoresistance. This spontaneous anisotropy $\Delta\rho/\rho$ may be characterized by a phenomenological expression of the same form as that used to describe the spontaneous magnetostriction. In eq. (6.53), the β's now represent direction cosines of the current direction, and the λ's are replaced by a set of magnetoresistance anisotropy constants k_i (see, for example, Hurd 1974). $\Delta\rho$ measures the difference between the resistance at the demagnetizing field and that at zero field $\rho(0)$. The constants k_i have been deduced for Gd, from 77 to 400 K, by Hiraoka and Suzuki (1971) from appropriate differences in $\Delta\rho/\rho$ between saturated states. For example, from the data of fig. 6.43 we obtain

$$k_1 = (\Delta\rho/\rho)_{H\parallel b} - (\Delta\rho/\rho)_{H\parallel c} \tag{6.68}$$

The microscopic origin of this orientational effect was discussed for the 3d metals by Smit (1951) in terms of a model in which spin-up and spin-down electrons conduct in parallel but with different mobilities. Campbell et al. (1970)

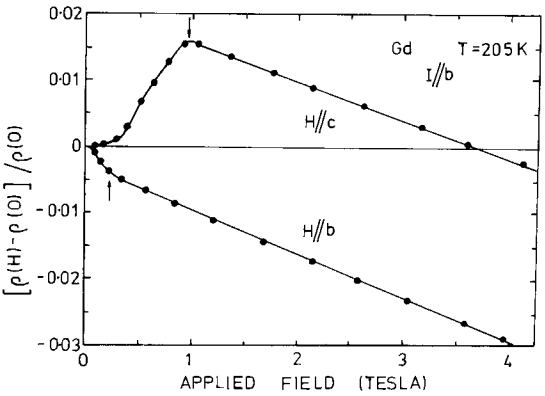

Fig. 6.43. The magnetoresistance of gadolinium at 205 K, showing the spontaneous anisotropy described in section 6.1 and the linear negative magnetoresistance discussed in section 6.2. The arrows indicate the applied field needed to create a single domain in the two configurations (after McEwen and Webber 1976).

related this two current model to the anisotropic magnetoresistance by considering the mixing of states of opposite spin, due to the spin–orbit interaction between the conduction electrons and the ferromagnetic spin system. Since the conduction electrons in the lanthanides have a strong d-like character, these interactions (which are discussed in more detail in section 6.3) produce an asymmetry of scattering between up- and down-spin conduction electrons (i.e. they have unequal relaxation times). As the spin–orbit interaction is sensitive to the relative orientation of the current flow and the magnetization direction, the resistivity of an aligned ferromagnet is anisotropic. Following recent successful quantitative explanations of the extraordinary Hall effect, progress towards a detailed understanding of the anisotropic magnetoresistance may be anticipated. The more tractable case of scattering from isolated (paramagnetic) lanthanide ions in non-magnetic hosts has been recently examined by Fert and Friederich (1976).

6.2. *Field dependent magnetoresistance*

The spin fluctuation model of section 5.2 may be readily extended to describe the magnetic field dependence of this contribution. We define the magnetoresistance above the field H_d required to form a single domain as

$$\Delta\rho^H(T, H) = \rho(T, H) - \rho(T, H_d). \tag{6.69}$$

In the molecular field approximation, we predict from eq. 6.65 that, for a ferromagnet, $\Delta\rho^H$ is negative and linear in H, since the applied field suppresses the number of spin fluctuations. This behaviour is indeed evident in the results for Gd shown in fig. 6.43. Equation 6.65 also predicts a temperature dependence for $\mathrm{d}(\Delta\rho^H)/\mathrm{d}H$ of the form $[1-(T/T_C)]^{-1/2}$: from about 120–260 K the Gd data

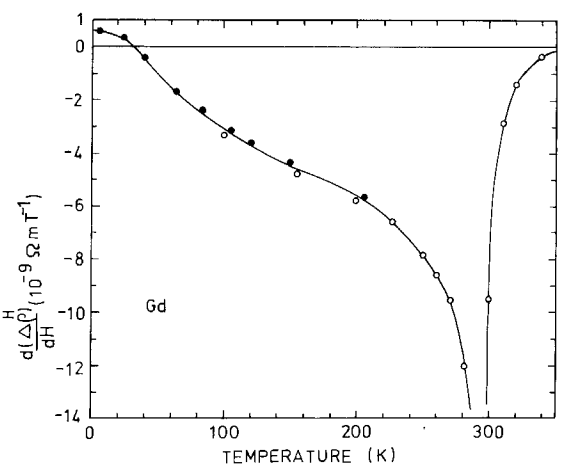

Fig. 6.44. The temperature dependence of the magnetoresistance coefficient of gadolinium. Open and closed circles denote the results of Hiraoka and Suzuki (1971), and McEwen and Webber (1977), respectively.

(fig. 6.44) are well represented by such an expression. In the spin wave scattering regime, an RPA calculation by Yamada and Takada (1973) indicated a magnetoresistance of the form:

$$\Delta\rho^H(T, H) \sim -T^2(\mu H/kT)/\ln(\mu H/kT). \tag{6.70}$$

Although $\omega_c\tau$ is almost invariably too small to yield information about the Fermi surface topology, the modifications to the conduction electrons' trajectories produce a modest positive magnetoresistance, which apparently dominates at the lowest temperatures (fig. 6.44). A satisfactory separation of the spin-wave scattering and electron trajectory effects has not yet been achieved.

As the temperature approaches T_C, neither the molecular field nor the RPA models are reliable: a consideration of the interactions between the spin fluctuations, which become very large in both space and time, is essential. The singularity around T_C is evident from fig. 6.44.

The magnetoresistance exhibited (in the molecular field approximation) by a simple two-sublattice antiferromagnet is indicated in fig. 6.45. A field applied in the direction of the sublattice magnetization decreases the spin fluctuations of the parallel sublattice, whilst reinforcing those on the antiparallel sublattice. The combination produces a positive magnetoresistance proportional to H^2.

When the Zeeman energy due to the applied field overcomes the anisotropy energy, the magnetic structure displays a spin-flop transition (as observed in Sm, see section 2.4). In this configuration, the magnetoresistance is very small until ferromagnetic alignment is achieved, and the magnetoresistance becomes negative. A similar situation holds for fields applied perpendicular to the original sublattice magnetization.

Calculations based on the spin wave scattering model (Yamada and Takada, 1973) indicate that, at low temperatures, the magnetoresistance in the perpendicular configuration reflects the competition between the softening of the acoustic spin wave mode (tending to increase the resistivity) and the increase of the optic mode energy gap which tends to decrease the resistivity.

Magnetoresistance measurements on Sm (see section 2.4) would test these

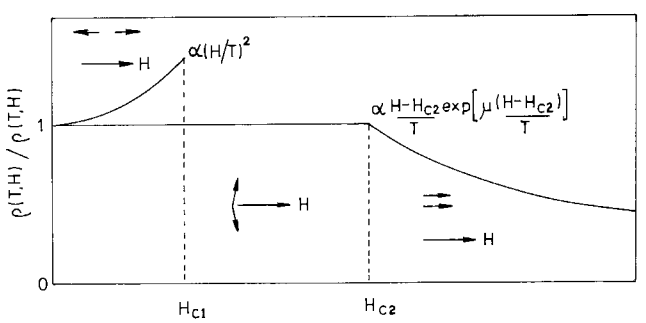

Fig. 6.45. The schematic magnetoresistance of a simple antiferromagnet, calculated in the molecular field approximation by Yamada and Takada (1973).

predictions for the response of the conduction electrons to magnetic structural changes in the simple antiferromagnet. Data for $T < T_{Nc} = 14$ K would permit the spin wave regime and the effect of the spin-flop transition to be examined: results at higher temperatures (below $T_{Nh} = 106$ K) would, after correction for the disordered spins on the cubic sites, check the predicted H^2 field dependence. For the antiferromagnetic phases of the elements Nd, Dy, Tb, Ho, Er and Tm, the situation is complicated by the superzone scattering effect (section 5.4). Only modest magnetic fields are required to disrupt the modulated or spiral structures of these elements (see section 2.2 and 2.3.4). A magnetization process of the type spiral → fan → ferromagnet progressively reduces the magnetic energy gaps in the conduction electron band structure, restores segments of the Fermi surface and hence gives rise to a rapid negative magnetoresistance. From the discussion in section 5.4, we expect this effect to be much larger for the c-axis resistivity than for that in the basal plane, and the measurements on Dy and Ho of Mackintosh and Spanel (1964) provided a striking affirmation of these predictions. Applied fields of some 2 Tesla (in the b-direction) are sufficient to align the moments in Ho, resulting in a dramatic reduction in the c-axis resistivity which amounts to some 30–40% below 25 K (fig. 6.46). The b-axis longitudinal magnetoresistance exhibits a more rapid (because of the demagnetizing effect) but somewhat smaller reduction with the development of ferromagnetic alignment. This latter effect cannot be directly attributed to an elimination of superzone scattering since the zero field basal plane resistivity (fig. 6.38) shows no evidence for such a contribution. The magnetoresistance may, therefore, be attributed to modifications of the magnon spectrum and the exchange splitting of the conduction electron bands due to ferromagnetism.

More extensive measurements on Ho by Akhavan and Blackstead (1976)

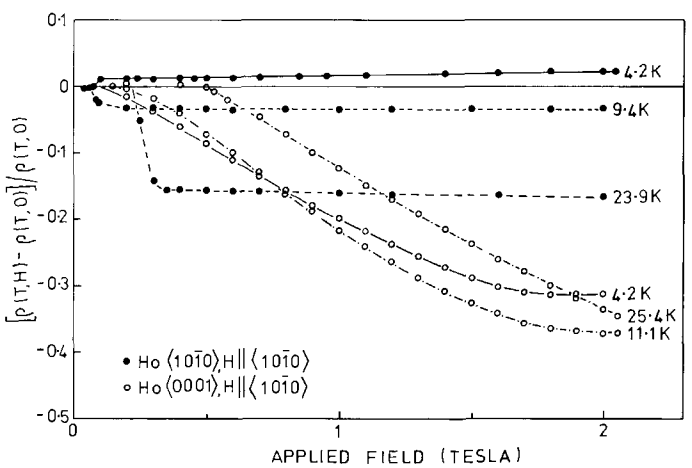

Fig. 6.46. The b and c-axis resistivity of holmium as a function of fields applied in the easy direction (after Mackintosh and Spanel (1964)).

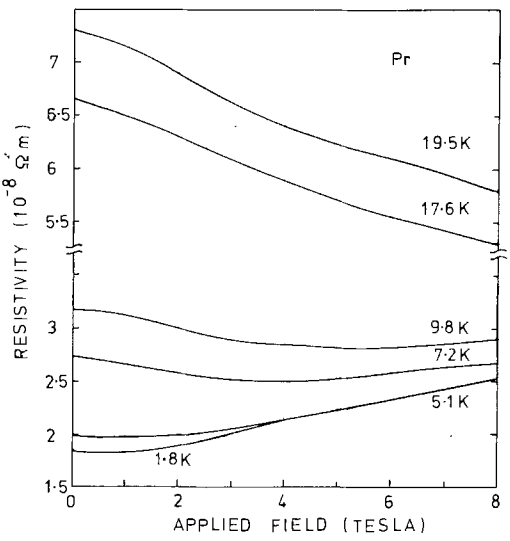

Fig. 6.47. The transverse magnetoresistance of polycrystalline praseodymium (McEwen and Webber 1977).

confirm these results. These authors utilised the sensitivity of the resistance to magnetic structural changes to plot H–T magnetic phase diagrams. General agreement with the neutron diffraction studies of Koehler et al. (1966, 1967) was found, although the persistence of an intermediate structure to lower temperatures is suggested.

The results of Mackintosh and Spanel (1964) for Dy in the $H\|a$, $I\|c$ configuration are qualitatively similar to the $H\|b$, $I\|c$ Ho data. The resistance anomaly was used by Akhavan et al. (1973) to determine the temperature dependence of the critical field H_{c1} (see section 2.2.2) to within 1 K of the Néel point. As expected, an approximately linear negative magnetoresistance was observed above H_{c1}.

Less extensive measurements have been reported for polycrystalline Pr (Nagasawa and Sugawara, 1967; McEwen and Webber, 1977) and for Nd (Nagasawa, 1972). The transverse magnetoresistance of Pr (fig. 6.47) displays a competition between positive and negative contributions, due to changes in spin-disorder scattering as a result of the magnetic field dependence of the crystal field levels (see section 5.1). At 1.4 K and 4.2 K (i.e. below $T_{NC} = 7.8$ K) the transverse magnetoresistance of Nd is initially positive, reaching a maximum at the field corresponding to the formation of a single domain on the cubic sites (see section 2.3.4). Thereafter the resistance decreases with field, presumably reflecting the reduction in superzone scattering with the decrease of the modulated moment (see fig. 6.21) and possibly crystal field effects. Measurements on single crystals of these elements will permit a more detailed analysis of their magnetoresistance.

6.3. *Hall effect*

The Hall effect in magnetic materials exhibits a number of unusual features which have defied successful explanation until recently. Defining the Hall resistivity $\rho_H = E_H/J$ as the transverse Hall electric field per longitudinal current density, typical results for a magnetic material display an initial rapid linear rise of the Hall voltage with applied field followed by a second linear portion with a considerably smaller field coefficient: this may be expressed as

$$\rho_H = R_0 B + 4\pi M R_s \tag{6.71}$$

B represents the applied magnetic induction, M the macroscopic magnetization intensity (below T_C, the spontaneous magnetization M_s). The Hall resistivity thus includes the ordinary Hall coefficient R_0 plus a much larger (in general) spontaneous Hall coefficient R_s which has a strong temperature dependence below T_C. The Hall resistivity has also been frequently expressed in terms of an alternative phenomenological expression

$$\rho_H = R_0 H_{int} + R_1 M, \tag{6.72}$$

with H_{int} as the internal field strength in the conductor and $R_1 = 4\pi(R_0 + R_s)$ being called the extraordinary Hall coefficient.

As in the case of the spontaneous magnetoresistance effect (section 6.1), the applied magnetic field is not the primary cause of the extraordinary Hall effect: it acts simply as an agent to align the magnetic domains of the sample. The origin of the effect may be qualitatively explained by the following argument. When an electron is scattered by a perturbation in the periodic array of aligned spins in a single domain, it is energetically favourable for it to pass preferentially to one side of the plane which is defined by its direction of motion and the spin direction of the scattering ion. Thus in a steady state, a flux of conduction electrons subject to such an asymmetric scattering potential will give rise to a spontaneous transverse electric field. However, although the conduction electron scattering due to thermal disorder accounts for the magnetic resistivity through the $\boldsymbol{\sigma} \cdot \boldsymbol{S}$ interaction, it does not produce asymmetric scattering provided the charge carriers are equally distributed between states of opposite spin.

Kondo (1962) therefore examined a number of spin–orbit coupling mechanisms which yield an odd power of spin–spin interactions in the scattering probability and hence allow skew-scattering to take place. Three types of spin–orbit interaction in the lanthanides may be envisaged (see, for example, Hurd, 1975). These are shown in fig. 6.48. The intrinsic spin–orbit coupling of a conduction electron with its temporary orbital angular momentum about a non-magnetic scattering centre results in a preferred trajectory with the electron spin (shown as $\boldsymbol{s}$ in fig. 6.48) coupled antiparallel to its temporary $\boldsymbol{l}$. An unequal population of up- and down-spin conduction electrons is necessary for a net asymmetry. When the conduction electron interacts with a magnetic ion, there is a stronger extrinsic spin–orbit coupling $\boldsymbol{l} \cdot \boldsymbol{S}$ between the ion's net spin $\boldsymbol{S}$ and the electron's orbital angular momentum. If the ion itself has a finite orbital angular

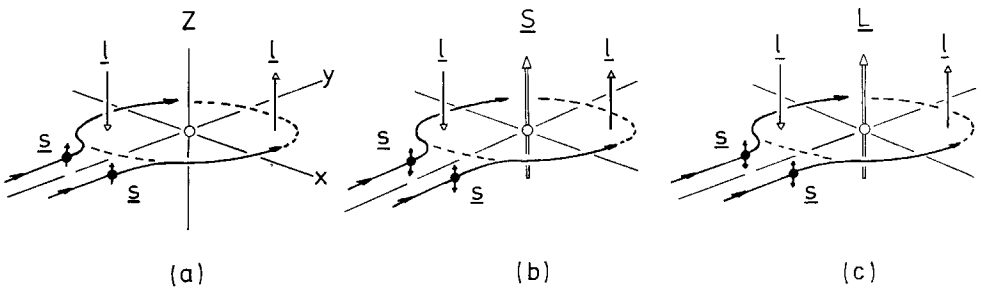

Fig. 6.48. A simple corpuscular picture of three cases where non-resonant scattering can be asymmetric. (a) Intrinsic spin–orbit coupling acts on an electron influenced by any attractive scattering centre. (b) Extrinsic spin–orbit coupling between the ionic spin $\boldsymbol{S}$ and the electron's temporary orbital angular momentum $\boldsymbol{l}$. (c) An ion with a nonzero $\boldsymbol{L}$ can couple with $\boldsymbol{l}$ via an electrostatic mechanism (after Hurd 1975).

momentum, Kondo derived a third mechanism, of electrostatic origin, resulting in a coupling of the form $\boldsymbol{l} \cdot \boldsymbol{L}$. However, the calculations of Kondo (1962) and Maranzana (1967) indicated that the anomalous Hall resistivity due to the first two mechanisms is much too small. Moreover, the $\boldsymbol{l} \cdot \boldsymbol{L}$ coupling could not be applied to Gd (because $\boldsymbol{L} = 0$) although Gd exhibits the largest extraordinary Hall effect of all the lanthanides (Lee and Legvold, 1967).

In an attempt to overcome these difficulties Kondo introduced a resonant scattering mechanism involving virtual f states. While resonantly captive an incident itinerant electron experiences an intrinsic spin–orbit coupling. However, as a result of the ionic spin $\boldsymbol{S}$, incident electrons also experience an exchange coupling $\boldsymbol{s} \cdot \boldsymbol{S}$ which deters the close approach of electrons of like spin. Thus the exchange interaction acts to spin polarize the incident electrons whilst the spin–orbit coupling produces the scattering asymmetry. The resultant Hall resistivity has a temperature dependence (in the molecular field approximation) of the form $B''_{\mathcal{J}}(y)$ which can explain Lee and Legvold's results for Gd (fig. 6.49) if the spin–orbit coupling parameter is assumed to have the rather large value of about 0.5 eV. Unfortunately this expression cannot explain the extraordinary Hall coefficients for Tb and Dy as these change sign between $T = 0$ and T_C (Rhyne, 1968, 1969) whilst $B''_{\mathcal{J}}(y)$ does not.

Further examination of the resonant scattering problem shows that as a result of its temporary orbital motion, the itinerant electron suffers a time delay in its translational motion. When combined with the intrinsic spin–orbit coupling, this delay is manifested as an abrupt sideways displacement of the centre of mass of the electron's wave packet. This side jump effect (Berger, 1970; 1972) also gives the electron an unequal probability of emerging from one side of the scattering centre rather than the other. Nozières and Lewiner (1973) calculated the transverse current induced by side jumps and hence the Hall field needed to prevent such a current. According to Fert (1974) the side jump contribution should be as effective as the overall skew scattering (Giovannini, 1971). A suitable com-

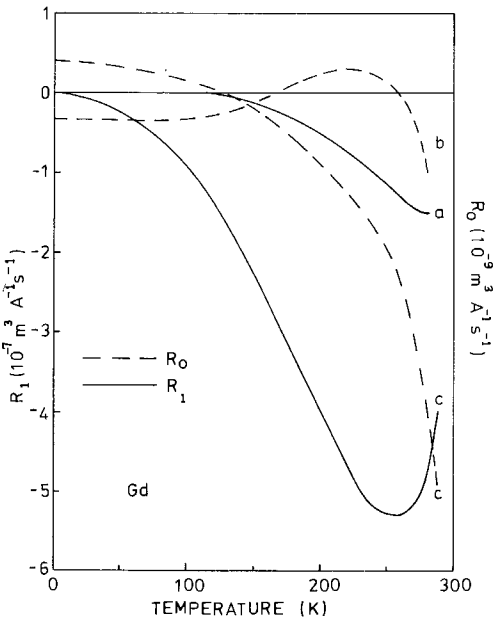

Fig. 6.49. The ordinary and extraordinary Hall coefficients of gadolinium (Lee and Legvold 1967).

bination of these mechanisms, with temperature dependences f_1 and h_2 involving the Brillouin function and its derivatives, can then be utilised to fit the experimental results for Tb and Dy. Figure 6.50 demonstrates excellent agreement within the expected limitations of the molecular field model. A fit to the results for Ho (Volkov et al., 1974) will provide an additional test of this theory.

Above T_C, the spontaneous contribution to the Hall resistivity vanishes but if the material has a large paramagnetic susceptibility an external field can

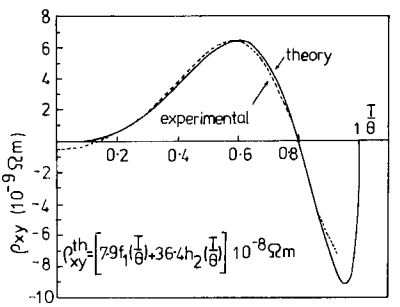

Fig. 6.50. The extraordinary Hall resistivity of terbium $\rho_{xy} = R_1 M$ as a function of reduced temperature. The experimental measurements (Rhyne 1969) were made with the field in the basal plane. Measurements between T_C and $\theta = T_N$ were made above H_{c1}, the field needed to create ferromagnetic alignment. The theoretical curve of Fert (1974) includes sidejump and skew scattering contributions.

sufficiently align the ionic moments to produce a macroscopic anomalous Hall field. Substituting $M = \chi H_{\text{int}}$ in eq. 6.71 allows the Hall resistivity to be written as

$$\rho_H = \{R_0 + 4\pi\chi^*[R_s + R_0(1 - N)]\}H_{\text{app}} \tag{6.73}$$

where $\chi^* = \chi/(1 + 4\pi N\chi)$ is an effective susceptibility which includes demagnetizing effects. If R_0 and R_s are independent, the Hall resistivity divided by the applied field depends linearly on χ^*. The results of Rhyne (1968, 1969) indicate that such a relationship holds for Dy and Tb from just above T_N to about 400 K. Values of R_0 and R_s in the paramagnetic phase have been obtained, with applied fields parallel and perpendicular to the c-axis, for Tb, Dy, Ho and Er (Cullen et al., 1970; Hurd, 1972).

Acknowledgments

I wish to thank G.J. Cock, J. Jensen, D.J. Martin, D. Melville, L.W. Roeland, B. Sarkissian, F.H. Spedding, J.A.G. Temple and G.D. Webber for communicating their results to me before publication and for helpful discussions.

I am also grateful to A.R. Mackintosh and G.J. Keeler for critically reading the manuscript and for a number of comments. Finally, I am particularly indebted to Mrs. J. Callaghan and Mrs. A. McEwen for their invaluable help in the typing and preparation of this review and to Mr. W.M. Lowe and Mr. J. Rippon for their careful preparation of the graphs.

References

Akhavan, M. and H.A. Blackstead, 1976, Phys. Rev. **B13**, 1209.
Akhavan, M., H.A. Blackstead and P.L. Donoho, 1973, Phys. Rev. **B8**, 4258.
Aléonard, R., P. Boutron and D. Bloch, 1969, J. Phys. Chem. Solids **30**, 2277.
Alstad, S., R.V. Colvin, S. Legvold and F.H. Spedding, 1961, Phys. Rev. **121**, 1637.
Alstad, S. and S. Legvold, 1964, J. Appl. Phys. **35**, 1752.
Andersen, N.H., P.E. Gregers-Hansen, E. Holm, H. Smith and O. Vogt, 1974, Phys. Rev. Lett. **32**, 1321.
Andersen, O.K. and T.L. Loucks, 1968, Phys. Rev. **167**, 551.
Arajs, S. and G.R. Dunmyre, 1966, Z. Naturforsch. **21**, 1856.
Arajs, S. and G.R. Dunmyre, 1967, J. Less-Common Metals **12**, 162.
Atoji, M., 1974, Solid State Commun. **14**, 1047.
Bartholin, H., J. Beille, D. Bloch, P. Boutron and J.L. Feron, 1971, J. Appl. Phys. **42**, 1679.
Behrendt, D.R., S. Legvold and F.H. Spedding, 1957, Phys. Rev. **106**, 723.
Behrendt, D.R., S. Legvold and F.H. Spedding, 1958, Phys. Rev. **109**, 1544.
Berger, L., 1970, Phys. Rev. **B2**, 4559.
Berger, L., 1972, Phys. Rev. **B5**, 1862.
Birgeneau, R.J., J. Als-Nielsen and E. Bucher, 1972, Phys. Rev. **B6**, 2724.
Bleaney, B., 1963, Proc. Roy. Soc. **A276**, 39.
Bly, P.H., W.D. Corner and K.N.R. Taylor, 1969, J. Appl. Phys. **40**, 4787.
Boutron, P. and R. Aléonard, 1976, Phys. Rev. **B13**, 174.
Boutron, P., J.L. Feron, G. Hug and P. Morin, 1971, J. Phys. (Paris) **32**, C1-368.
Boys, D.W. and S. Legvold, 1968, Phys. Rev. **174**, 377.
Bozorth, R.M., A.E. Clark and J.H. Van Vleck, 1972, Intern. J. Magnetism **2**, 19.
Bozorth, R.M. and J.H. Van Vleck, 1960, Phys. Rev. **118**, 1493.
Bozorth, R.M. and T. Wakiyama, 1963, J. Phys. Soc. Jap. **18**, 97.
Brooks, M.S.S. and T. Egami, 1973, J. Phys. C. **6**, 513.
Brooks, M.S.S. and T. Egami, 1974, J. Phys. C. **7**, 979.

Brooks, M.S.S. and D.A. Goodings, 1968, J. Phys. C. **1**, 1279.
Brun, T.O., S.K. Sinha, N. Wakabayashi, G.H. Lander, L.R. Edwards and F.H. Spedding, 1970, Phys. Rev. **B1**, 1251.
Bucher, E., C.W. Chu, J.P. Maita, K. Andres, A.S. Cooper, E. Buehler and K. Nassau, 1969, Phys. Rev. Lett. **22**, 1260.
Bucher, E., P.H. Schmidt, A. Jayaraman, K. Andres, J.P. Maita, K. Nassau and P.D. Dernier, 1970, Phys. Rev. B **2**, 3911.
Cable, J.W., R.M. Moon, W.C. Koehler and E.O. Wollan, 1964, Phys. Rev. Lett. **12**, 553.
Cable, J.W. and E.O. Wollan, 1968, Phys. Rev. **165**, 733.
Cable, J.W., E.O. Wollan, W.C. Koehler and M.K. Wilkinson, 1965, Phys. Rev. **140**, 1896.
Callen, E.R. and H.B. Callen, 1963, Phys. Rev. **129**, 578.
Callen, E.R. and H.B. Callen, 1965, Phys. Rev. **139**, A455.
Callen, H.B. and E.R. Callen, 1966, J. Phys. Chem. Solids **27**, 1271.
Campbell, I.A., A. Fert and O. Jaoul, 1970, J. Phys. C. Metal Phys. Suppl. no. 1, S95.
Clark, A.E., B.F. De Savage and R. Bozorth, 1965, Phys. Rev. **138**, A216.
Cock, G.J., 1976, Thesis, University of Amsterdam.
Cohen, R.L., S. Hufner and K.W. West, 1969, Phys. Rev. **184**, 263.
Cooper, B.R., 1968, Phys. Rev. **169**, 281.
Cooper, B.R., 1972, Magnetic Properties of Rare Earth Metals, ed. R.J. Elliott, (London: Plenum) Ch. 2.
Corner, W.D., W.C. Roe and K.N.R. Taylor, 1962, Proc. Phys. Soc. **80**, 927.
Corner, W.D. and B.K. Tanner, 1976, J. Phys. C. **9**, 627.
Craven, R.A. and R.D. Parks, 1973, Phys. Rev. Lett. **31**, 383.
Cress, W.D., 1970, Thesis, Iowa State University.
Cullen, J.R., J.J. Rhyne and F. Mancini, 1970, J. Appl. Phys. **41**, 1178.
Danielsen, O. and P.A. Lindgård, 1972, Risø Report No. 259 (Danish AEC).
Darnell, F.J., 1963, Phys. Rev. **130**, 1825 and **132**, 1098.
De Gennes, P.G. and J. Friedel, 1958, J. Phys. Chem. Solids **4**, 71.
Del Moral, A. and M.S.S. Brooks, 1974, J. Phys. C. **7**, 2540.
Del Moral, A. and E.W. Lee, 1975, J. Phys. C. **8**, 3881.
De Savage, B.F. and A.E. Clark, 1965, Proc. Fifth Rare Earth Research Conf., Ames, Iowa.
De Wijn, H.W., A.M. Van Diepen and K.H.J. Buschow, 1973, Phys. Rev. **B7**, 524.
De Wijn, H.W., A.M. Van Diepen and K.H.J. Buschow, 1974, Solid State Commun. **15**, 583.
Du Plessis, P. de V., 1968, Phil. Mag. **18**, 145.
Edwards, L.R. and S. Legvold, 1968, Phys. Rev. **176**, 753.
Egami, T. and P.J. Flanders, 1976, J. Phys. Soc. Jap. **40**, 78.
Elliott, R.J., 1954, Phys. Rev. **94**, 564.
Elliott, R.J. and K.W.H. Stevens, 1953, Proc. Roy. Soc. **218**, 553.
Elliott, R.J. and F.A. Wedgwood, 1963, Proc. Phys. Soc. **81**, 846.
Evenson, W.E. and S.H. Liu, 1969, Phys. Rev. **178**, 783.
Feron, J.L. and R. Pauthenet, 1969, C.R. Acad. Sci., Paris, Ser. **B269**, 549 and 611.
Feron, J.L., G. Hug and R. Pauthenet, 1970, Z. Angew. Phys. **30**, 61.
Feron, J.L., G. Hug and R. Pauthenet, 1970, Les Elements des Terres Rares, vol. 2 (Paris: CNRS), p. 19.
Fert, A., 1974, J. Phys. Lett. (Paris) **35**, L107.
Fert, A. and A. Friederich, 1976, Phys. Rev. **B13**, 397.
Finkel, V.A. and V.S. Belovol, 1970, Sov. Phys: JETP **30**, 424.
Finkel, V.A. and V.S. Belovol, 1973, Sov. Phys: JETP **37**, 90.
Finkel, V.A. and V.S. Belovol, 1974, Sov. Phys: JETP **38**, 953.
Finnemore, D.K., L.J. Williams, F.H. Spedding and D.C. Hopkins, 1968, Phys. Rev. **176**, 712.
Flippen, R.B., 1964, J. Appl. Phys. **35**, 1047.
Freeman, A.J. and R.E. Watson, 1962, Phys. Rev. **127**, 2058.
Fulde, P. and I. Peschel, 1972, Adv. Phys. **21**, 1.
Gardner, W.E. and J. Penfold, 1963, Phil. Mag. **11**, 549.
Giovannini, B., 1971, Phys. Lett. **36A**, 381.
Graham, C.D., 1962, J. Phys. Soc. Jap. **17**, 1310.
Graham, C.D., 1967, J. Appl. Phys. **38**, 1375.
Graham, C.D., P.J. Flanders and T. Egami, 1973, AIP Conf. Proc. **10**, 759.
Green, R.W., S. Legvold and F.H. Spedding, 1961, Phys. Rev. **122**, 827.
Gregers-Hansen, P.E., M. Krusius and G.R. Pickett, 1972, Phys. Rev. Lett. **29**, 420.
Gschneidner, K.A., P. Burgardt, S. Legvold, J.O. Moorman, T.A. Vyrostek and C. Stassis, 1976, J. Phys. **F6**, L49.
Guntherodt, H.J., E. Hauser and H.U. Kunzi, 1974, Phys. Lett. **47A**, 189 and **48A**, 201.
Habenschuss, M., C. Stassis, S.K. Sinha, H.W. Deckman and F.H. Spedding, 1974, Phys. Rev. **B10**, 1020.
Hall, P.M., S. Legvold and F.H. Spedding, 1959, Phys. Rev. **116**, 1446.
Harmon, B.N. and A.J. Freeman, 1974, Phys. Rev. **B10**, 1979.
Hiraoka, T. and M. Suzuki, 1971, J. Phys. Soc. Japan **31**, 1361.
Holstein, T. and H. Primakoff, 1940, Phys. Rev. **58**, 1098.
Houmann, J.G., M. Chapellier, A.R. Mackintosh, P. Bak, O.D. McMasters and K.A. Gschneidner, 1975, Phys. Rev. Lett **34**, 587.
Houmann, J.G., J. Jensen and P. Touborg, 1975, Phys. Rev. **B12**, 332.
Hurd, C.M., 1972, The Hall Effect in Metals and Alloys (New York: Plenum).
Hurd, C.M., 1974, Adv. Phys. **23**, 315.
Hegland, D.E., S. Legvold and F.H. Spedding, 1963, Phys. Rev. 131, 158.

Hurd, C.M., 1975, Contemp. Phys. **16**, 517.
Høg, J. and P. Touborg, 1975, Phys. Rev. **B11**, 520.
Høg, J. and P. Touborg, 1976, Phys. Rev. **B14**, 1209.
Jensen, J., 1971, Risø Report No. 252 (Danish AEC).
Jensen, J., 1975, J. Phys. **C8**, 2769.
Jensen, J., 1976, J. Phys. **C9**, 111 (Pr) and J. Phys. **F6**, 1145 (Er).
Jensen, J. and J.G. Houmann, 1975, Phys. Rev. **B12**, 320.
Jensen, J., J.G. Houmann and H. Bjerrum Møller, 1975, Phys. Rev. **B12**, 303.
Johansson, T., B. Lebech, M. Nielsen, H. Bjerrum Møller and A.R. Mackintosh, 1970, Phys. Rev. Lett. **25**, 524.
Johansson, T., K.A. McEwen and P. Touborg, 1971, J. Phys. (Paris) **32**, C1–372.
Jordan, R.G. and D.W. Jones, 1973, J. Less-Common Metals **31**, 125.
Jordan, R.G., D.W. Jones and P.G. Mattocks, 1974, J. Less-Common Metals **34**, 25.

Kasuya, T., 1959, Prog. Theor. Phys. (Kyoto) **22**, 227.
Kayser, F.X., 1970, Phys. Rev. Lett. **25**, 662.
Kazakov, A.A., 1974, Sov. Phys: Solid State **16**, 893.
Keeler, G.J. and P. Pearson, 1978, to be published.
Koehler, W.C., J.W. Cable, M.K. Wilkinson and E.O. Wollan, 1966, Phys. Rev. **151**, 414.
Koehler, W.C., J.W. Cable, H.R. Child, M.K. Wilkinson and E.O. Wollan, 1967, Phys. Rev. **158**, 450.
Koehler, W.C., H.R. Child, E.O. Wollan and J.W. Cable, 1963, J. Appl. Phys. Suppl. **34**, 1335.
Koehler, W.C. and R.M. Moon, 1972, Phys. Rev. Lett. **29**, 1468.
Kondo, J., 1962, Prog. Theor. Phys. (Kyoto) **27**, 772 and **28**, 846.
Kowalewski, L. and A. Lehmann-Szweykowska, 1973, Acta Phys. Polon. **A44**, 281 and 547.
Krithivas, G. and G.T. Meaden, 1975, J. Less-Common Metals **41**, 149.
Krithivas, G., G.T. Meaden and N.H. Sze, 1972, J. Phys. Soc. Jap. **33**, 1584.
Lacheisserie, E. du T., 1970, Ann. Phys. (Paris) **5**, 267.
Lacheisserie, E. du T., 1975, Revue Phys. Appl. (Paris) **10**, 169.
Lebech, B., K.A. McEwen and P.A. Lindgård, 1975, J. Phys. **C8**, 1684.
Lebech, B. and B.D. Rainford, 1971, J. Phys. (Paris) **32**, C1–370.
Lebech, B. and B.D. Rainford, 1973, Proc. Intern. Conf. Magn. (Moscow) **3**, 191.
Lee, E.W., 1964, Proc. Phys. Soc. **84**, 693.
Lee, M.C., R.A. Treder and M. Levy, 1975, J. Phys. Chem. Solids **36**, 1281.
Lee, R.S. and S. Legvold, 1967, Phys. Rev. **162**, 431.
Legvold, S., 1972, Magnetic Properties of Rare Earth Metals, ed. R.J. Elliott (London: Plenum) Ch. 7.
Lehmann-Szweykowska, A., 1973, Acta Phys. Polon. **A44**, 265.
Lindelof, P.E., I.E. Miller and G.R. Pickett, 1975, Phys. Rev. Lett. **35**, 1297.
Lindgård, P.A., 1975, J. Phys. **C8**, L178.
Lindgård, P.A. and O. Danielsen, 1974, J. Phys. **C7**, 1523.
Lindgård, P.A. and O. Danielsen, 1975, Phys. Rev. **B11**, 351.

Liu, S.H., 1972, Phys. Rev. Lett. **29**, 793.
Liu, S.H., P. Burgardt, K.A. Gschneidner and S. Legvold, 1976, J. Phys. **F6**, L55.
Mackintosh, A.R., 1962, Phys. Rev. Lett. **9**, 90.
Mackintosh, A.R., 1963, Phys. Lett. **4**, 140.
Mackintosh, A.R. and H. Bjerrum Møller, 1972, Magnetic Properties of Rare Earth Metals, ed. R.J. Elliot (London: Plenum) Ch. 5.
Mackintosh, A.R. and L.E. Spanel, 1964, Solid State Commun. **2**, 383.
Maranzana, F.E., 1967, Phys. Rev. **160**, 421.
Mardon, P.G. and C.C. Koch, 1970, Scripta Met. **4**, 477.
Marsh, H.S. and J. Sievers, 1969, J. Appl. Phys. **40**, 1563.
Martin, D.J. and J.J. Rhyne, 1977, J. Phys. C**10**, 4123.
Mason, W.P., 1954, Phys. Rev. **96**, 302.
McEwen, K.A., 1971, Proc. Roy. Soc. **A322**, 509.
McEwen, K.A., G.J. Cock, L.W. Roeland and A.R. Mackintosh, 1973, Phys. Rev. Lett. **30**, 287.
McEwen, K.A. and P. Touborg, 1971, J. Phys. (Paris) **32**, C1–484.
McEwen, K.A., P. Touborg, G.J. Cock and L.W. Roeland, 1974, J. Phys. **F4**, 2264.
McEwen, K.A., G.D. Webber and L.W. Roeland, 1977, Physica **88-88B**, 531.
McEwen, K.A. and P. Touborg, 1977, to be published.
Meaden, G.T. and N.H. Sze, 1970, Les Elements des Terres Rares, vol. 2 (Paris: CNRS), p. 107.
Melville, D. and D.L. Rayner, 1977, Physica **86-88B**, 38.
Millhouse, A.H. and K.A. McEwen, 1973, Solid State Commun. **13**, 339.
Mishima, A., H. Fujii and T. Okamoto, 1975, J. Phys. Soc. Jap. **38**, 284 and **39**, 873.
Mishima, A., H. Fujii and T. Okamoto, 1976, J. Phys. Soc. Jap. **40**, 962.
Miwa, H., 1963, Prog. Theor. Phys. (Kyoto) **29**, 477.
Moon, R.M., J.W. Cable and W.C. Koehler, 1964, J. Appl. Phys. Suppl. **35**, 1041.
Moon, R.M. and W.C. Koehler, AIP Conf. Proc. **10**, 1314. 1973,
Moran, T.J. and B. Luithi, 1970, J. Phys. Chem. Solids **31**, 1735.
Murao, T., 1971, J. Phys. Soc. Jap. **31**, 683.
Murao, T., 1972, J. Phys. Soc. Jap. **33**, 33.
Murao, T., 1975, J. Phys. Soc. Jap. **39**, 1629.
Nagamiya, T., 1967, Solid State Physics **20**, 305.
Nagamiya, T. and Y. Kitano, 1964, Prog.

Keeton, S.C. and T.L. Loucks, 1968, Phys. Rev. 168, 672.

Theor. Phys. (Kyoto) **31**, 1.
Nagamiya, T., K. Nagata and Y. Kitano, 1962, Prog. Theor. Phys. (Kyoto) **27**, 1253.
Nagasawa, H., 1972, Phys. Lett. **41A**, 39.
Nagasawa, H. and T. Sugawara, 1967, J. Phys. Soc. Jap. **23**, 701.
Nellis, W.J. and S. Legvold, 1969, Phys. Rev. **180**, 581.
Nicklow, R.M. and N. Wakabayashi, 1972, Neutron Inelastic Scattering (Vienna: IAEA) p. 611.
Nicklow, R.M., N. Wakabayashi, M.K. Wilkinson and R.E. Reed, 1971, Phys. Rev. Lett. **26**, 140 (Dy) and **27**, 334 (Er).
Nicolas-Francillon, M. and D. Jerome, 1973, Solid State Commun. **12**, 523.
Nigh, H.E., S. Legvold and F.H. Spedding, 1963, Phys. Rev. **132**, 1092.
Niira, K., 1960, Phys. Rev. **117**, 129.
Nozieres, P. and C. Lewiner, 1973, J. Phys. (Paris) **34**, 901.
Ott, H.R., 1975, Solid State Commun. **16**, 1355.
Parkinson, D.H., F.E. Simon and F.H. Spedding, 1951, Proc. Roy. Soc. **A207**, 137.
Pippard, A.B., 1964, Classical Thermodynamics (Cambridge University Press).
Rainford, B.D., 1972, AIP Conf. Proc. **5**, 591.
Rainford, B.D. and J.G. Houmann, 1971, Phys. Rev. Lett. **26**, 1254.
Rao, K.V., O. Rapp, C. Johannesson, D.J.W. Geldart and T.G. Richard, 1975, J. Phys. **C8**, 2135.
Rhyne, J.J., 1965, Thesis, Iowa State University.
Rhyne, J.J., 1968, Phys. Rev. **172**, 523.
Rhyne, J.J., 1969, J. Appl. Phys. **40**, 1001.
Rhyne, J.J., 1972, Magnetic Properties of Rare Earth Metals, ed. R.J. Elliott (London: Plenum) Ch. 4.
Rhyne, J.J. and A.E. Clark, 1967, J. Appl. Phys. **38**, 1379.
Rhyne, J.J., S. Foner, E.J. McNiff and R. Doclo, 1968, J. Appl. Phys. **39**, 892.
Rhyne, J.J., S. Legvold and E.T. Rodine, 1967, Phys. Rev. **154**, 266.
Rhyne, J.J. and S.J. Pickart, 1971, AIP Conf. Proc. **5**, 1436.
Richards, D.B. and S. Legvold, 1969, Phys. Rev. **186**, 508.
Roeland, L.W., G.J.Cock and P.A. Lindgård, 1975a, J. Phys. **C8**, 3427.
Roeland, L.W., G.J. Cock, F.A. Muller, A.C. Moleman, K.A. McEwen, R.G. Jordan and D.W. Jones, 1975b, J. Phys. **F5**, L233.
Rosen, M. and H. Klimker, 1970, Phys. Rev. **B1**, 3748.
Sakamoto, S., J. Nakai and Y. Nakagawa, 1976, J. Phys. Soc. Japan **40**, 686.
Sarkissian, B., 1976, private communication.
Shepherd, C.H., 1976, Thesis, University of Salford.
Sherrington, D., 1973, J. Phys. **C4**, 1037.
Slavin, A.J., 1972, Cryogenics **12**, 121.
Smirnov, Y.N. and I.A. Prokhorov, 1975, Sov. Phys.: JETP **40**, 504.
Smit, J., 1951, Physica **17**, 612.
Spedding, F.H. and J.J. Croat, 1973, J. Chem. Phys. **58**, 5514 and **59**, 2451.
Spedding, F.H., D. Cress and B.J. Beaudry, 1971, J. Less-Common Metals, **23**, 263.
Stevens, K.W.H., 1952, Proc. Phys. Soc. **A65**, 209.
Strandburg, D.L., S. Legvold and F.H. Spedding, 1962, Phys. Rev. **127**, 2046.
Sze, N.H., K.V. Rao and G.T. Meaden, 1969, J. Low Temp. Phys. **1**, 563.
Tachiki, M., M.C. Lee, R.A. Treder and M. Levy, 1974, Solid State Commun. **15**, 1071.
Tanuma, S., W.R. Datars, H. Doi and A. Dunsworth, 1970, Solid State Commun. **8**, 1107.
Taylor, K.N.R. and M.I. Darby, 1972, Physics of Rare Earth Solids (London: Chapman and Hall).
Taylor, W.A., B.C. Gerstein and F.H. Spedding, 1975, private communication.
Temple, J.A.G. and K.A. McEwen, 1978, to be published.
Thomson, W., 1857, Proc. Roy. Soc. **8**, 546.
Touborg, P. and J. Høg, 1974, Phys. Rev. Lett. **33**, 775.
Touborg, P., 1977, Phys. Rev. B **16**, 1201.
Tsuya, N., A.E. Clark and R.M. Bozorth, 1965, Proc. Intern. Conf. Magnetism (Nottingham) p. 250.
Van Peski-Tinbergen, T. and A.J. Dekker, 1963, Physica **29**, 917.
Van Vleck, J.H., 1932, Theory of Electric and Magnetic Susceptibilities (Oxford University Press).
Vishnyakov, Y.N., V.L. Ivannikov, R.Z. Levitin and B.K. Ponomarev, 1970, Sov. Phys.: JETP **30**, 1059.
Volkov, D.I., T.M. Kozlova, V.N. Prudnikov, N.A. Prudnikova and N.I. Moreva, 1974, Sov. Phys: JETP **40**, 98.
Wilkinson, M.K., W.C. Koehler, E.O. Wollan and J.W. Cable, 1961, J. Appl. Phys. **32**, 48S.
Wohlleben, D. and H.L. Lou, 1969, Phys. Rev. Lett. **22**, 842.
Yamada, H. and S. Takada, 1972, Prog. Theor. Phys. (Kyoto) **48**, 1828.
Yamada, H. and S. Takada, 1973, J. Phys. Soc. Jap. **34**, 51.
Yamada, H. and S. Takada, 1973, Prog. Theor. Phys. (Kyoto) **49**, 1401.
Young, R.C., R.G. Jordan and D.W. Jones, 1976, J. Phys. **F6**, L37.
Ziman, J.M., 1964, Principles of the Theory of Solids (Cambridge University Press).

Temple, J.A.G. and K.A. McEwen, 1977, Physica 86-88B, 533.

Handbook on the Physics and Chemistry of Rare Earths, edited by K.A. Gschneidner, Jr. and L. Eyring

Chapter 7

MAGNETIC STRUCTURES AND INELASTIC NEUTRON SCATTERING: METALS, ALLOYS AND COMPOUNDS

S.K. SINHA
Solid State Science Division, Argonne National Laboratory, Argonne, Illinois 60439, USA

Contents

Symbols

a = a-axis lattice constant
a^* = reciprocal lattice constant
$a_i^\dagger$, a_i = Holstein–Primakoff operators for spin deviations
A = criticality parameter for magnetic ordering in singlet ground state systems
$A(\boldsymbol{q})$ = function entering spin-wave energy [see eq. (7.100)]
A_{lm} = crystal field parameters
α = matrix element of J_2 between ground and excited states of singlet–singlet system
α_l = Stevens multiplicative factor
$\boldsymbol{b}_1, \boldsymbol{b}_2, \boldsymbol{b}_3$ = primitive vectors of reciprocal lattice
B_{lm} = coefficients of operator equivalents in crystal field hamiltonian
B^γ = magnetoelastic coupling constant
$B_J(x)$ = Brillouin function
$B(q)$ = function entering spin-wave energy [see eq. (7.100)]
$\beta = (kT)^{-1}$
$\beta' = g_J\mu_B H/kT$
c = c-axis lattice constant
c^* = reciprical lattice constant
C^γ = basal plane elastic constant
$C_{im}^\dagger$, C_{im} = creation and annihilation operators for state $|m\rangle$ on site i
χ = bulk susceptibility
χ_a = atomic susceptibility
$\chi(q)$ = generalized wave number-dependent susceptibility function of conduction electrons

$\chi_{\alpha\beta}(Q, \omega)$ = Q, ω dependent susceptibility tensor of system of magnetic ions
d_ξ, d_η = direction cosines of magnetization relative to ξ, η axes of crystal
$\delta\theta_i$ = deivations of polar and azimuthal angles of spin
$\delta\phi_i$ = direction from equilibrium structure values
Δ = level separation in singlet–singlet system
$\Delta(\boldsymbol{q}) = \omega_{-q} - \omega_q$ [defined in eq. (7.103)]
e = electron charge
$e^{-W\kappa}$ = Debye–Waller factor for κth atom
E_d = driving energy for ferromagnetic transition
E_{ms}^{γ} = magnetoelastic component of E_d
ϵ_1, ϵ_2 = symmetrized basal plane equilibrium stress tensors
$f(\boldsymbol{Q})$ = magnetic form factor
$F(\boldsymbol{G})$ = structure factor for reciprocal lattice vector $\boldsymbol{G}$
g_J = Landé spectroscopic factor
G = de Gennes factor $(g_J - 1)^2 J(J+1)$
$\boldsymbol{G}$ = reciprocal lattice vector
γ = neutron magnetic moment in nuclear magnetons
$\hbar$ = (Planck's constant)/2π
H = magnetic field
$\mathcal{H}$ = total spin hamiltonian
$\mathcal{H}_{ex}$ = exchange hamiltonian
$\mathcal{H}_{cf}$ = crystal field hamiltonian
$\mathcal{H}_{me}$ = magnetoelastic hamiltonian
I_n = squared amplitude of nth harmonic in neutron diffraction
$j(\boldsymbol{R})$ = exchange interaction between spins separated by distance R
j_k = radial wave function average of spherical Bessel function $j_k(Qr)$
J = total angular momentum quantum number
J_n = polynomial in J defined in eq. (7.102)
$J_n(x)$ = Bessel function of order n
J_i = total angular momentum operator for ith ion
$\boldsymbol{J}_q$ = Fourier component of ordered spin
$\mathcal{J}_{ij}$ = effective exchange interaction between $\boldsymbol{J}_i$, $\boldsymbol{J}_j$ [including $(g_J - 1)^2$ factor]
k = Boltzmann's constant; orbital angular momentum quantum number
$\boldsymbol{k}_0$ = incident neutron wave vector
$\boldsymbol{k}_1$ = scattered neutron wave vector
K = degrees Kelvin
l = orbital angular momentum quantum number
$\boldsymbol{L}$ = total orbital angular momentum operator
L = total orbital angular momentum quantum number
λ = neutron wavelength; molecular field constant
λ^{γ} = basal plane magnetostriction coefficient
m = orbital azimuthal quantum number; electron mass
$\boldsymbol{M}$ = magnetization
M = total orbital azimuthal quantum number
μ = atomic moment
μ_B = Bohr magneton
$\mu_\parallel$ = atomic moment in basal plane
$\mu_\perp$ = atomic moment normal to basal plane
$n_\uparrow(r)$, $n_\downarrow(r)$ = "up" and "down" components of electron spin
N = total number of unit cells in crystal
$O^m(J)$ = Steven's operator equivalents
ω = (neutron energy loss)/h
Ω = unit cell volume
$P(\boldsymbol{Q})$ = magnetic scattering amplitude for wave vector $\boldsymbol{Q}$
P_0 = unit magnetic scattering length = 0.269×10^{-12} cm
P_n = probability of thermal occupation of state $|n\rangle$
$P_l(\cos\theta)$ = Legendre polynomial
ϕ_j = azimuthal angle for moment in jth layer of spiral structure
ψ = tilt angle of spiral out of basal plane
$\boldsymbol{q}$ = wave vector
$\boldsymbol{q}_m$ = magnetic periodicity wave vector
$\boldsymbol{Q}$ = neutron scattering wave vector
r_0 = classical electron radius
$\langle r^l \rangle$ = atomic average of r^l
$\boldsymbol{r}_\kappa$ = basis vector for κth atom in unit cell
R = lanthanide
$\boldsymbol{R}_i$ = position of ith ion
$\boldsymbol{R}_{l\kappa}$ = position of κth ion in lth cell
S = total spin quantum number
$\boldsymbol{S}_i$ = total spin operator for ith ion
$\bar{S}$ = classical magnitude of spin
σ = reduced magnetization
$\boldsymbol{\sigma}$ = Pauli spin matrix operator
T = absolute temperature

T_{km} = irreducible tensor operators
T_C = Curie temperature
T_N = Néel temperature
θ = angle between c-axis and moment direction; half of neutron scattering angle
$U(q)$ = averaged matrix element of s–f exchange
v = seniority quantum number
V_n = axial anisotropy coefficients in $\mathcal{H}_{cf}$
V_6^6 = basal plane anisotropy coefficient in $\mathcal{H}_{cf}$
V_c^i = crystal field potential at site i
W = Lee–Leaske–Wolf parameter for scale of crystal-field splitting
$W_m^{(k_1,k_2)k}$ = Racah tensor
x = concentration; Lea–Leaske–Wolf crystal field parameter
$\boldsymbol{X}_{km}(\boldsymbol{Q})$ = vector spherical harmonic
Z = ionic charge
ξ-axis = easy direction of magnetization in basal plane
η-axis = normal to ξ-axis in basal plane
ζ-axis = hexagonal axis

1. Introduction

The study of the magnetism of the rare earth metals may be said to have begun in the 1950's with the availability of pure samples and, in particular, single crystals of the different rare earth metals due to the efforts of F.H. Spedding and his collaborators at the Ames Laboratory, Iowa State University. The magnetic behavior exhibited by these metals was studied by bulk techniques at Ames by Spedding, Legvold and their colleagues and by neutron diffraction techniques at Oak Ridge National Laboratory. The richness and diversity of the magnetic phenomena and the intricacies of the various microscopic patterns of magnetism in these metals has since been an unending source of fascination for solid state researchers. Neutrons have played a key role in the development of our understanding of these materials because of their ability to elucidate the microscopic magnetic structures, to probe the details of the spatial distribution of magnetization on the atoms, and also to study the spectrum of low-lying excited states of these magnetic systems, such as spin waves or transitions between crystal field levels. We shall discuss such experiments in detail in this chapter. Much of the earlier work was concentrated on the pure heavy lanthanide metals (except for those with enormously large neutron absorption cross sections). This was soon followed, however, by work on light lanthanides and on rare earth compounds. This phase of study may be said to be still actively in progress at the time of writing. Several excellent reviews of these topics are already available in the literature. In particular, the reader may refer to the articles of Cooper (1972), Koehler (1972) and Mackintosh and Bjerrum Møller (1972), which survey excellently the field up to the early seventies. More recent reviews have also been given by Cooper (1976) and Mackintosh (1977).

The magnetic properties of the lanthanide metals follow from the basic property that there is an unfilled shell of 4f electrons which is well separated from the conduction band electrons and which is also well localized on the ion sites, so that direct f-shell overlap or exchange effects are negligible. The ion containing the f-shell is tripositive, the three outer electrons going into the conduction band. The conduction electrons interact with the f-electrons and

provide the medium for the famous "indirect exchange" or RKKY (Ruderman and Kittel, 1954; Freeman, 1972) interaction between the magnetic moments on the f-shells. The subtleties of the conduction electron wave functions and energy bands for the various metals are partly responsible for the diversity of magnetic structures and properties of these materials. Another reason is the orbital contribution to the magnetic moments which interacts with the crystalline electric fields at the ion sites. The spin–orbit coupling in the f-shell is strong enough so that the total angular momentum J is a good quantum number. The total orbital angular moment L, the total spin S and the value of J are determined by Hund's rules, and the ionic magnetic moment in the ground state is given by $g_J\mu J$ where g_J is the Landé factor and μ_B the Bohr magneton. Exceptions to some of the above properties are found in metals and compounds involving some of the light lanthanides, in particular cerium and samarium. In such cases, the energies of the f-electrons are not as well separated from the conduction band energies, and interesting effects such as phase transitions can occur due to valence changes on the f-shell. These effects, however, are covered in chs. 4, 11 and 20 so we shall exclude them from discussion here. In some cases, where an ion containing an even number of electrons is situated in a strong crystalline electric field, a singlet (non-magnetic) ground state may result, and magnetic behavior can arise only through so-called "induced moment" behavior, i.e. the mixing of higher crystal field states into the ground state by the indirect exchange interaction.

Starting from the basic physical picture described above, the ultimate aim of a microscopic theory of magnetism in lanthanide materials is to achieve a fundamental understanding of the magnetic structures, excitations and bulk magnetic properties in terms of the electronic structures of the 4f shells and the conduction bands and their interactions with each other and possibly the crystal lattice. As may be imagined, along with the vast amount of experimental information gathered over the last few years, there has been a correspondingly intense theoretical effort, which has by now reached a high degree of sophistication. Nevertheless, we are still only on the threshold of a microscopic understanding of the details of how conduction electrons interact with the f-shells to produce the various magnetic structures and excitation spectra observed, and of the quantitative magnitude of the crystal field parameters. The reader may refer to ch. 3 for a survey of the microscopic theory. An earlier review has been given by Freeman (1972) and a more recent one by Lindgard (1976a).

2. The spin hamiltonian and magnetic ordering

In this section, we shall give a broad survey of the phenomenon of magnetic ordering in lanthanide metals, alloys and compounds, before discussing the individual experimental results. It is hoped that this will help the reader to place the results for individual materials in the appropriate context. We shall briefly

discuss the nature of the basic hamiltonian and interactions needed to describe these systems, and indicate how molecular field theories based on the hamiltonian can help us understand the very diverse magnetic behavior observed in these materials at various temperatures.

2.1. *The spin hamiltonian*

The total spin hamiltonian may be written as

$$\mathcal{H} = \mathcal{H}_{ex} + \mathcal{H}_{cf} + \mathcal{H}_{me}, \tag{7.1}$$

where $\mathcal{H}_{ex}$ stands for the exchange contribution, $\mathcal{H}_{cf}$ for the crystal field contribution, and $\mathcal{H}_{me}$ for the magnetoelastic contribution. We discuss $\mathcal{H}_{ex}$ first.

The RKKY theory of indirect exchange between 4f electrons (Ruderman and Kittel, 1954; Freeman, 1972; Lindgard, 1976a; Liu, 1977) proceeds by using perturbation theory to eliminate the conduction electron degrees of freedom from the full hamiltonian, leaving in lowest order an effective hamiltonian between spins which is of the isotropic Heisenberg form. In this theory, the conduction electrons are assumed to play a passive role in simply transmitting the exchange interaction between f-shells, a point we shall return to later in section 6 of this chapter. One obtains

$$\mathcal{H}_{ex} = -\sum_{i \neq j} j(\boldsymbol{R}_i - \boldsymbol{R}_j)\boldsymbol{S}_i \cdot \boldsymbol{S}_j, \tag{7.2}$$

where $j(\boldsymbol{R}_i - \boldsymbol{R}_j)$ is the exchange interaction between spins located at lattice sites $\boldsymbol{R}_i$ and $\boldsymbol{R}_j$ and $\boldsymbol{S}_i$, $\boldsymbol{S}_j$ are the corresponding total spin operators. Mapping this interaction on to the manifold of states of the ions labelled by the total angular momentum quantum numbers, we obtain

$$\mathcal{H}_{ex} = -(g_J - 1)^2 \sum_{i \neq j} j(\boldsymbol{R}_i - \boldsymbol{R}_j)\boldsymbol{J}_i \cdot \boldsymbol{J}_j = -\sum_{i \neq j} \mathcal{J}_{ij}\boldsymbol{J}_i \cdot \boldsymbol{J}_j, \tag{7.3}$$

where $\boldsymbol{J}_i$ is the total angular momentum operator $\boldsymbol{L}_i + \boldsymbol{S}_i$ for the ith ion. The simplest form of the microscopic theory yields for the exchange interaction, (Ruderman and Kittel, 1954; Freeman, 1972; Lindgard, 1976a; Liu, 1977)

$$j(\boldsymbol{R}_i - \boldsymbol{R}_j) = \frac{2}{N^2} \sum_{\boldsymbol{q}} |U(\boldsymbol{q})|^2 \chi(\boldsymbol{q}) e^{i\boldsymbol{q} \cdot (\boldsymbol{R}_i - \boldsymbol{R}_j)} \tag{7.4}$$

where $\chi(\boldsymbol{q})$ is the generalized susceptibility function (Freeman, 1972; Lindgard, 1976a; Liu, 1977) of the conduction electrons, N the total number of unit cells in the crystal and $U(\boldsymbol{q})$ is an averaged matrix element between conduction electron states separated by wave vector $\boldsymbol{q}$ of the exchange between the f-electrons and the conduction electrons. Recent calculations (Lindgard, 1976a; Liu, 1977; Harmon and Freeman, 1974a) indicate that the s–f exchange matrix element is strongly dependent on both the initial and final states of the conduction electron and hence that the form of eq. (7.4) is a poor approximation. Instead, $|U(\boldsymbol{q})|^2\chi(\boldsymbol{q})$

should be replaced by a matrix element weighted response function for the conduction electrons.

The exchange represented by eq. (7.3) above is isotropic, and represents an approximation. Various contributions to anisotropy of the interaction have been discussed by Jensen et al. (1975). Anisotropic terms can arise from: (1) Dependence of the s–f exchange matrix elements on the orbital states of the f-electrons. At present there is no realistic quantitative calculation of the magnitude of this effect, although estimates based on simplified approximations (Kaplan and Lyons, 1963; Kasuya and Lyons, 1965; Specht, 1967) indicate the anisotropic terms to be of order 10% of the isotropic terms. The effect may be larger for larger q values since it arises from anisotropy of the localized f-wave functions. (2) In the ordered phases, from polarization of the conduction electron bands and a corresponding splitting between the longitudinal and transverse components of the J_{ij} (Lindgard, 1976a). This effect is small since the exchange splitting of the conduction bands is $\sim 10^{-4}$ times the typical conduction electron bandwidths. (3) Spin–orbit coupling of the conduction electrons, which also produces an anisotropic susceptibility similar to effect (2) above. Again the magnitude of this effect is small ($\sim 10^{-3}$). (4) Modification of the s–f exchange matrix element by spin–orbit coupling of the conduction electrons, (Levy, 1968; White and White, 1968; Levy, 1969b) or indirect interactions via the spin–orbit coupling of the conduction electrons (Levy, 1969b). These effects are again estimated to be very small. (5) Direct quadrupole–quadrupole electrostatic interactions between the f-shells. (Wolf and Birgeneau, 1968; Birgeneau et al., 1968). These are also fairly small. (6) Phonon-induced electronic multipole interactions, i.e. effective ion–ion coupling through the electron–phonon interactions on the f-shells (Sugihara, 1959; Orbach and Tachiki, 1967; Elliott, 1972; Gehring and Gehring, 1975). Such effects are known to be important for some lanthanide vanadates and aluminates (Elliott, 1972; Gehring and Gehring, 1975; Birgeneau et al., 1974) where the so-called "collective Jahn–Teller distortion" occurs. It is not clear whether such effects are appreciable in metals. From the above discussion it may be seen that although individual contributions to the anisotropy of the exchange interaction are small, the sum of these may in certain cases be enough to produce appreciable anisotropic exchange. Recent spin-wave dispersion measurements in Tb (Jensen et al., 1975) and Er (Nicklow et al., 1976a) in fact indicated that very large two-ion magnetic anisotropy was present. However more recent analyses of the data on Er by Jensen (1974) and Lindgard (1976b) indicate that the two-ion anisotropy might not be as large as originally thought. This will be discussed in more detail in section 5.3. In the case of lanthanide compounds, e.g. DySb (Moran et al., 1971) and PrAg (Brun et al., 1976) it is known from bulk magnetic measurements that the simple bilinear exchange of the form given by eq. (7.3) must be supplemented by a higher order (biquadratic) exchange term, whose origins are not at present unambiguously clear. It may arise from an effective quadrupole–quadrupole coupling via the electron–phonon interaction. For the present we shall not include such effects.

The crystal field interaction terms may be calculated by expanding the

electrostatic potential around a lanthanide ion site in terms of spherical harmonics and using the Wigner–Eck art theorem to convert the spherical harmonics to equivalent angular momentum operators as first suggested by Stevens (Stevens, 1952). This method has been discussed in detail in several reviews (Newman, 1971; Abragam and Bleaney, 1970; Bleaney, 1963a,b). The point group symmetry of the site, and the angular momentum of f-electron orbitals ($l = 3$) restrict the number of terms quite severely. The general expression is of the form

$$\mathcal{H}_{\mathrm{cf}} = \sum_i \sum_{lm} B_{lm} O_l^m(\boldsymbol{J}_i), \tag{7.5}$$

where i sums over ion sites, the $O_l^m(\boldsymbol{J}_i)$ are the operator equivalents of the corresponding spherical harmonics, obtained by replacing the Cartesian components of the arguments of the spherical harmonics (suitably symmetrized) by the Cartesian components of $\boldsymbol{J}$;

$$\text{(e.g. } O_2^0(\boldsymbol{J}) = 3J_z^2 - J(J+1);\ O_6^6(\boldsymbol{J}) = \tfrac{1}{2}[(J_x + iJ_y)^6 + (J_x - iJ_y)^6]),$$

$$\text{and } B_{lm} = \alpha_l \langle r^l \rangle A_{lm} \tag{7.6}$$

where α_l is the Stevens factor and depends on the particular ion involved, (Hutchings, 1964) $\langle r^l \rangle$ denotes an expectation value over the radial 4f distributions, and the A_{lm} are the crystal field parameters, which can in principle be calculated from the charge distribution around the ion. For an ion at a hexagonal site, it is customary to choose the hexagonal axis as the ζ-axis, and the ξ-axis as the easy direction of magnetization in the hexagonal plane, and to regroup the terms in (7.5) according to powers of $J_{i\zeta}$ to obtain

$$\mathcal{H}_{\mathrm{cf}} = \sum_i \{V_2 J_{i\zeta}^2 + V_4 J_{i\zeta}^4 + V_6 J_{i\zeta}^6 - \tfrac{1}{2} V_6^6[(J_{i\xi} + J_{i\zeta})^6 + (J_{i\xi} - iJ_{i\eta})^6]\} \tag{7.7}$$

where the first three terms represent the axial anisotropy and the last three the (usually much smaller) basal plane anisotropy.

For sites of cubic symmetry, choosing the z-axis as a cubic axis, one has

$$\mathcal{H}_{\mathrm{cf}} = \sum_i \{V_4^0 O_4^0(\boldsymbol{J}_i) + 5V_4^0 O_4^4(\boldsymbol{J}_i) + V_6^0 O_6^0(\boldsymbol{J}_i) - 21 V_6^0 O_6^4(\boldsymbol{J}_i)\} \tag{7.8}$$

For the sites of "cubic" symmetry in the double-hexagonal and Sm structures, the above form is usually re-expressed choosing the z-axis as the three-fold axis (Bleaney, 1963).

In the case of many systems, magnetic ordering may be accompanied by a magnetostrictive strain which modifies the crystal fields to lower the energy of the ions. If the magnetization rotates sufficiently slowly, the strain field will also change resulting in a second order contribution to the magnetic anisotropy. However, the experimental results (discussed later) show that the lattice cannot respond quickly enough to the rapid spin precession in the spin-wave modes, and so one uses the "frozen lattice approximation" first discussed by Turov and Shavrov (1965). The magnetoelastic contributions to the hamiltonian can be

written down in terms of the equilibrium strains and the magnetostriction coefficients. For the hexagonal lanthanide metals one need only consider the strains in the basal plane as the others will give effective fields which are of the same form (but much smaller than) the axial anisotropy fields in eq. (7.7). To first order we have (Mackintosh and Bjerrum-Møller, 1972; Cooper, 1968a)

$$\mathcal{H}_{\mathrm{me}} = -\tilde{B}^{\gamma}\left[\tfrac{1}{2}\bar{\epsilon}_1^{\gamma}\sum_i (S_{i\xi}^2 - S_{i\eta}^2) + \bar{\epsilon}_2^{\gamma}\sum_i (S_{i\xi}S_{i\eta})\right] \tag{7.9}$$

where $\tilde{B}^{\gamma}$ is the magnetoelastic coupling constant and is related (Mackintosh and Bjerrum-Møller, 1972) to the elastic constant, the magnetostriction coefficient and the value of J; $\bar{\epsilon}_1^{\gamma}$ is the symmetrized equilibrium stress $\frac{1}{2}(\bar{\epsilon}_{\xi\xi} - \bar{\epsilon}_{\eta\eta})$ and $\bar{\epsilon}_2^{\gamma}$ is $\bar{\epsilon}_{\xi\eta}$.

2.2. *Magnetic ordering in the heavy lanthanide metals*

It is the interplay between $\mathcal{H}_{\mathrm{ex}}$, $\mathcal{H}_{\mathrm{cf}}$ and $\mathcal{H}_{\mathrm{me}}$ which provides the diverse variety of magnetic structures found in the lanthanide metals and in many compounds. $\mathcal{H}_{\mathrm{ex}}$ often provides the driving field for oscillatory magnetic moments because of the long range and oscillatory nature of the indirect exchange interaction, while the other terms favor a tendency to lock into the lattice, determine the orientation of the moments and often drive the systems ferromagnetic (or at least commensurate with the lattice periodicity) at lower temperatures. Magnetic ordering in these systems can be explained phenomenologically in terms of the above hamiltonian via a simple molecular field theory (Elliott, 1961; Yosida and Miwa, 1961; Miwa and Yosida, 1961; Kaplan, 1961). A recent review has been given by Cooper (1972).

Figure 7.1 schematically represents the magnetic structures of the hexagonal close packed structure heavy lanthanide metals. The same metal can have several of these structures at different temperatures, as discussed later. The structures include basal plane ferromagnets, basal plane spirals, cone shaped spirals about the c-axis modulated structures, and c-axis ferrimagnetic structures. The magnetic structures of the light lanthanide metals is more complex and will be discussed later. A general form for writing such structures is in the form:

$$\boldsymbol{J}_i = \sum_{\alpha} \boldsymbol{J}_{q_\alpha}\, \mathrm{e}^{\mathrm{i}\boldsymbol{q}_\alpha \cdot \boldsymbol{R}_i} \tag{7.10}$$

where the sum runs over all periodicities α (with associated wave vectors $\boldsymbol{q}_\alpha$) which are simultaneously present, and the vector amplitudes $\boldsymbol{J}_{q_\alpha}$ are in general complex. For spiral structures only $\boldsymbol{q}_{\mathrm{m}} = (0, 0, \pm q_{\mathrm{m}})$ are present and J_q^x is $\frac{1}{2}\pi$ out of phase with J_q^y. For cone structures, in addition to the above, a $\boldsymbol{q} = 0$ component (with $\boldsymbol{J}_0$ along the c-axis) is present. For c-axis modulated (CAM) structures, again only $\boldsymbol{q}_{\mathrm{m}} = (0, 0, \pm q_{\mathrm{m}})$ exists, but $\boldsymbol{J}_q = (0, 0, S_0)$. As this structure begins to "square up", extra periodicities corresponding to the harmonics of $\boldsymbol{q}_{\mathrm{m}}$ appear. Finally the case of basal plane ferromagnetism corresponds to $\boldsymbol{q} = 0$ and

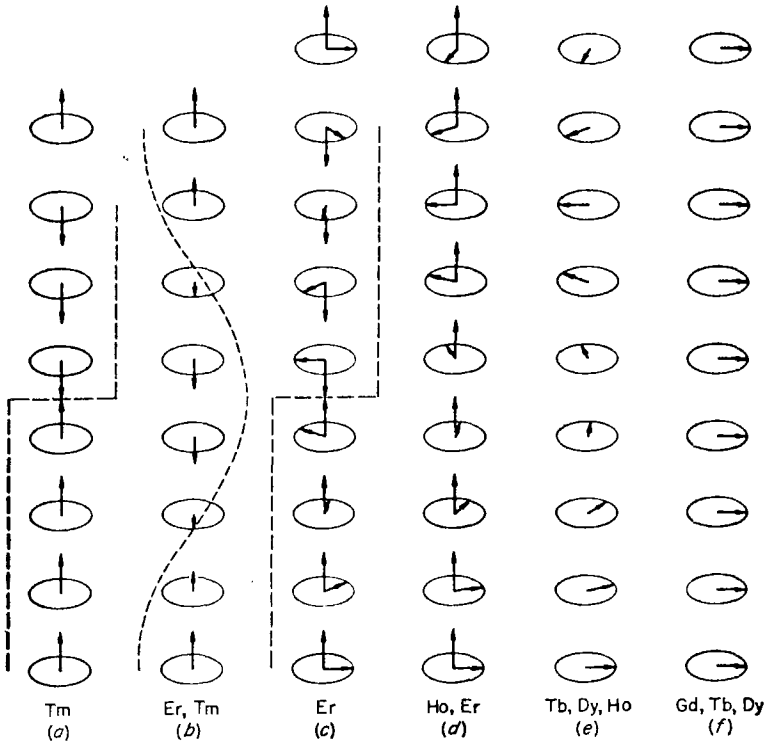

Fig. 7.1. Magnetic structures of heavy lanthanide metals [after Koehler (1972)].

J_0 in the basal plane. The representation in eq. (7.10) is particularly useful in discussing neutron diffraction studies of these structures.

For the phenomenological theory of magnetic ordering, it is often more convenient to write these structures in terms of the angle θ of the moment relative to the c-axis:

$$J_{i\xi} = \bar{S}\cos\theta, J_{i\zeta} = \bar{S}\sin\theta\cos(\boldsymbol{q}\cdot\boldsymbol{R}_i), J_{i\eta} = \bar{S}\sin\theta\sin(\boldsymbol{q}\cdot\boldsymbol{R}_i) \tag{7.11}$$

(This does not include the CAM and ferrimagnetic structures).

In the molecular field theory, the exchange energy per ion is given from eq. (7.3), by

$$E_{ex}/N = -\mathcal{J}(\boldsymbol{q})\bar{S}^2\sin^2\theta - \mathcal{J}(0)\bar{S}^2\cos^2\theta \tag{7.12}$$

where

$$\mathcal{J}(\boldsymbol{q}) = \sum_j \mathcal{J}_{ij}\, e^{i\boldsymbol{q}\cdot(\boldsymbol{R}_i-\boldsymbol{R}_j)}. \tag{7.13}$$

From eq. (7.12), it is obvious that the system will choose as the magnetic periodicity $\boldsymbol{q}_m$ the value of $\boldsymbol{q}$ for which $\mathcal{J}(\boldsymbol{q})$ is a maximum. The detailed discussion of the relationship of $\mathcal{J}(\boldsymbol{q})$ to the electronic structure and in particular

to the function $\chi(q)$ [see eq. (7.4)], is given in ch. 3, section 4.2. As discussed by Cooper (1968), entropy considerations do not play a role in determining the *relative* stability of spiral structures with different q_m, so one is justified in comparing internal energies. However, for the CAM structures, entropy considerations play an important role in the stability of the structure (Elliott, 1961). Thus, the main role of $\mathcal{H}_{ex}$ is to produce a modulated (or, in the case where $\mathcal{J}(q)$ is maximum at $q = 0$, a ferromagnetic) magnetic ordering. The actual orientation of the moments are determined by the anisotropy terms in $\mathcal{H}_{cf}$ and $\mathcal{H}_{me}$.

Let us assume the structure given by eq. (7.11) for a given q_m, and work out the total energy per ion of the system in the molecular field approximation, using eqs. (7.7), (7.9) and (7.12). The basal plane anisotropy terms do not contribute because they are of the single-ion type and for incommensurate q_m the phase factors make them average to zero. We obtain

$$E/N = -\mathcal{J}(q_m)\bar{S}^2 \sin^2\theta - [\mathcal{J}(0) - V_2]\bar{S}^2 \cos^2\theta + V_4\bar{S}^4 \cos^4\theta + V_6\bar{S}^6 \cos^6\theta \tag{7.14}$$

where $\bar{S}^n$ denotes the nth power of the amplitude of the mean ordered moment per ion. If one goes beyond molecular field theory, the anisotropy terms have a complicated temperature dependence. Specifically, the nth order anisotropy parameter V_n goes as (Callen and Callen, 1966)

$$V_n = \frac{1}{\sigma^n} V_n(0)\hat{I}_{1/2(2n+1)}(L^{-1}(\sigma)) \tag{7.15}$$

where σ is the reduced magnetization, $V_n(0)$ is the value at $T = 0$, $L^{-1}(\sigma)$ is the inverse Langevin function of the reduced magnetization, and $\hat{I}_{(2n+1)/2}(x)$ is the ratio of the hyberbolic Bessel function of order $\frac{1}{2}(2n+1)$ to that of order $\frac{1}{2}$. At low $T(\sigma \to 1)$, $\hat{I}_{(2n+1)/2}$ goes as $\sigma^{n(n+1)/2}$ while as $\sigma \to 0$, $\hat{I}_{(2n+1)/2}$ goes as σ^n.

We may minimize the energy given in eq. (7.14) with respect to the cone angle θ and obtain as possible solutions:

$$\sin\theta = 0 \text{ (axial ferromagnet)}, \qquad \cos\theta = 0 \text{ (basal plane spiral)}, \tag{7.16a,b}$$

$$3V_6\bar{S}^4 \cos^4\theta + 2V_4\bar{S}^2 \cos^2\theta + (\mathcal{J}(q_m) - \mathcal{J}(0) + V_2) = 0 \text{ (general cone structure)}. \tag{7.16c}$$

Cooper et al. (1962) have discussed the conditions for the stability of these various structures. In general, for high temperatures, the term involving V_2 is the largest one, and the magnitude and sign of V_2 determine whether the moments lie in the basal plane ($V_2 > 0$), form a cone structure, or line up along the c-axis in a CAM or ferrimagnetic structure ($V_2 \ll 0$).

2.3. *Bunched spirals and applied field effects*

The assumption of a perfectly regular spiral (or cone) in the previous section led to the vanishing of the hexagonal basal plane and magnetoelastic anisotropies from the expression for the energy. The effect of these smaller terms will be to

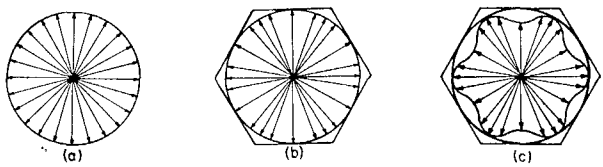

Fig. 7.2. Projections of (a) simple spiral, (b) bunched spiral and (c) a bunched spiral with a moment modulation [after Felcher et al. (1976)].

modify the spirals so as to produce a tendency to "bunch" along the easy axes of magnetization in the basal plane as shown in fig. 7.2. Such effects have been seen in several lanthanide systems by neutron diffraction, as discussed later. A theoretical discussion for the case of a planar spiral in a hexagonal crystal anisotropy field has been given by Yosida (1964). The general case of the cone structure, including magnetoelastic effects, can be treated similarly. If one treats the spins quasi-classically and uses the molecular field approximation, one may obtain the results by re-writing eq. (7.11) as

$$J_{i\xi} = \bar{S}\cos(\theta + \delta\theta_i), \qquad J_{i\zeta} = \bar{S}\sin(\theta + \delta\theta_i)\cos(\boldsymbol{q}\cdot\boldsymbol{R}_i + \delta\phi_i),$$
$$J_{i\eta} = \bar{S}\sin(\theta + \delta\theta_i)\sin(\boldsymbol{q}\cdot\boldsymbol{R}_i + \delta\phi_i). \tag{7.17}$$

One may then write down the conditions

$$\frac{\partial E}{\partial(\delta\theta_i)} = \frac{\partial E}{\partial(\delta\phi_i)} = 0 \tag{7.18}$$

and solve this set of equations iteratively in increasing orders of V_6^6 and $\tilde{B}^\gamma$. To first order, the results are

$$\delta\theta_i = \frac{\tilde{B}^\gamma/2[\tilde{\epsilon}_1^\gamma\cos(2\boldsymbol{q}\cdot\boldsymbol{R}_i) + \tilde{\epsilon}_2^\gamma\sin(2\boldsymbol{q}\cdot\boldsymbol{R}_i)] + V_6^6\bar{S}^2\cos(6\boldsymbol{q}\cdot\boldsymbol{R}_i)}{2\bar{S}^2[\mathcal{J}(0)\cot\theta + \mathcal{J}(\boldsymbol{q}_m)\tan\theta]}, \tag{7.19a}$$

and

$$\delta\phi_i = \frac{(\tilde{B}^\gamma/\bar{S}^2)[\tilde{\epsilon}_1^\gamma\sin(2\boldsymbol{q}\cdot\boldsymbol{R}_i) - \tilde{\epsilon}_2^\gamma\cos(2\boldsymbol{q}\cdot\boldsymbol{R}_i)] + 6V_6^6\sin(6\boldsymbol{q}\cdot\boldsymbol{R}_i)}{2\mathcal{J}(\boldsymbol{q}_m)}, \tag{7.19b}$$

i.e. the general result is a cone-shaped structure which is fluted as well as bunched. A molecular-field treatment where the spins are treated quantum mechanically also exists (J.W. Patterson, unpublished), but the non-classical effects are small. Using eq. (7.17), a Fourier representation of the bunched structure may be obtained. For simplicity, let us consider a basal-plane spiral structure ($\theta = \pi/2$) and no magnetoelastic anisotropy ($\tilde{B}^\gamma = 0$). Then we obtain from eqs. (7.17) and (7.19b),

$$J_{i\xi} = \bar{S}J_0(h)\cos(\boldsymbol{q}\cdot\boldsymbol{R}_i) - \bar{S}J_1(h)\cos(5\boldsymbol{q}\cdot\boldsymbol{R}_i) + \bar{S}J_1(h)\cos(7\boldsymbol{q}\cdot\boldsymbol{R}_i) + \cdots \tag{7.20a}$$

$$J_{i\eta} = \bar{S}J_0(h)\sin(\boldsymbol{q}\cdot\boldsymbol{R}_i) - \bar{S}J_1(h)\sin(5\boldsymbol{q}\cdot\boldsymbol{R}_i) + \bar{S}J_1(h)\sin(7\boldsymbol{q}\cdot\boldsymbol{R}_i) + \cdots \tag{7.20b}$$

$$J_{i\zeta} = 0 \tag{7.20c}$$

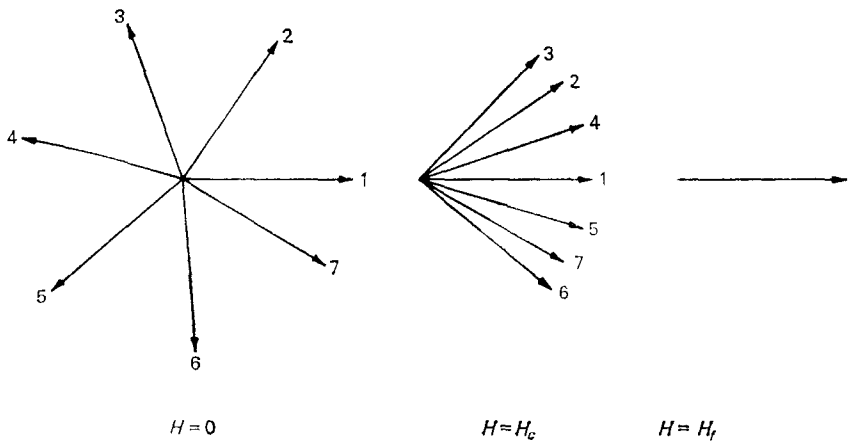

Fig. 7.3. Effect of applied magnetic field in basal plane on spiral structure [after Cooper (1972)].

where J_n is the Bessel function of order n, and $h = 3V_6^6/\mathcal{J}(q_m)$. Equations (7.20) show that in this case the structure develops equal amplitude fifth and seventh harmonics (and similarly equal amplitude eleventh and thirteenth harmonics, etc.).

When magnetic fields are applied to spiral or cone structures in these materials, for low fields there is a slight distortion of the structure with a small net moment along $\boldsymbol{H}$. For intermediate fields (~ 10 kOe) there may exist a fan-like structure (see fig. 7.3) in which the moments oscillate sinusoidally about the field direction, while for fields greater than a critical value ($\sim$20–30 kOe) this structure collapses into a ferromagnetic structure parallel to the field direction. If the basal plane anisotropy is sufficiently large, the fan-phase may not appear. The theoretical treatment of such effects has been given by Nagamiya and coworkers (Nagamiya, 1962, 1967; Nagamiya et al., 1962; Kitano and Nagamiya, 1964), and has been recently reviewed by Cooper (1972) for a basal plane spiral without planar anisotropy or magnetostriction. Earlier theoretical treatments have been given by Herpin and Meriel (1960, 1961) and by Enz (1960, 1961).

The experimental evidence for these effects from neutron diffraction studies of individual heavy lanthanide metals is discussed in section 3.

2.4. *Temperature dependence of magnetic ordering in the heavy lanthanide metals*

As discussed above, in the lanthanide earth metals and alloys at the highest temperatures, the exchange contribution to the magnetic energy is the dominant one (although the second order axial anisotropy may also be appreciable) and the spins will order in a periodic arrangement with $q = q_m$, the value at which $\mathcal{J}(q)$ (eq. (7.13)) is a maximum. (This may be at $q = 0$, as in Gd, in which case the "periodic arrangement" is really a ferromagnetic one.) Molecular field theories

of the ordering temperature predict (Elliott, 1961; Yosida and Miwa, 1961; Kaplan, 1961)

$$kT_N = \tfrac{2}{3}\mathcal{J}(q_m)J(J+1) = \tfrac{2}{3}j(q_m)(g_J - 1)^2 J(J+1) \tag{7.21}$$

for both helical and CAM structures (see eqs. 7.2 and 7.3). The inclusion of anisotropy effects complicates this expression somewhat. On the assumption that $j(q_m)$ is constant across this series of metals and alloys, eq. (7.21) would predict a linear variation of T_N with the "de Gennes factor" (de Gennes, 1958) $G = (g_J - 1)^2 J(J+1)$. In fact, T_N for this series of materials does follow a fairly universal curve vs. G (Bozorth, 1967) (the exception being alloys with scandium which have considerably lower T_N's, a point to be discussed again later). However, the proportionality is to $G^{2/3}$ rather than G. This may be related to the fact that the generalized susceptibility function $\chi(q)$ does depend on the subtle features of the band-structure, so that $j(q_m)$ is itself concentration dependent in the alloys (Lindgard, 1976c).

The values for the initial q_m (i.e. the periodicity adopted just below T_N in units of $2\pi/c$) for the heavy lanthanide metals and alloys also follow a universal curve vs. G (Koehler, 1972) (see fig. 7.4). According to current theories this is given by the q for which the generalized susceptibility function of the conduction electrons (together with the appropriate matrix elements $|U(q)|^2$ (see the discussion following eq. (7.4)) is a maximum. It is not obvious why this should be a universal function of G, although in principle the s–f exchange matrix elements as a function of q could exhibit systematic variations with G. Such calculations are only beginning at the present time. It should be noted, however, that the system of disordered spins will produce (via s–f exchange scattering) a finite mean free path for the electrons and this will in turn produce a modification of the generalized susceptibility function $\chi(q)$ of the conduction electrons which

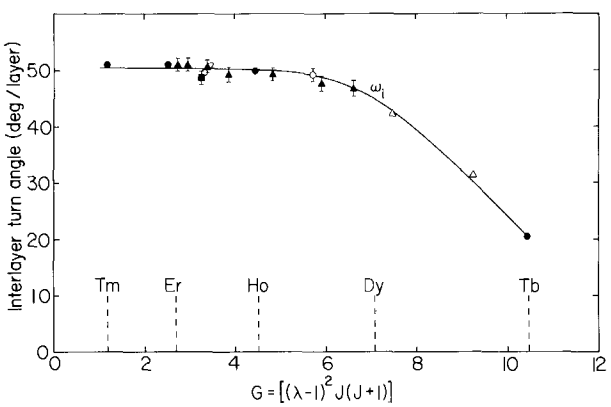

Fig. 7.4. Interlayer turn angle data vs. the de Gennes factor for the heavy lanthanide metals and binary alloys as determined from single crystal neutron diffraction experiments. ω_i is the initial turn angle (just below T_N) [after Koehler (1972)]. Legend: ● pure rare earth elements; ▲ Er–Dy alloys; ■ Er–Tb alloys; ▽ Er–Gd alloys; ○ Ho–Dy alloys; △ Ho–Tb alloys.

will cause the maximum to shift with the amount of spin-disorder scattering. Since $1/\tau$ is proportional to G (where τ is the conduction electron relaxation time), this could help to explain the systematics discussed above. These ideas were originally put forward by de Gennes (1962). De Gennes and Saint-James (1963) were in fact able to explain the behavior of q_m with G on this basis, but they used a somewhat unrealistic free-electron model for the conduction electrons. Calculations incorporating realistic band-structure and wavefunctions remain to be done.

As the temperature is decreased below T_N, the value of q_m changes, in general decreasing with temperature. For Tm on the other hand a small increase of q_m with decreasing temperature is observed (see fig. 7.5). The general features of the temperature dependence of q_m can be explained in terms of electronic effects, as pointed out by Elliott and Wedgewood (1964). Below T_N, the long range magnetic order induces superzone gaps in the conduction electron energy bands and this shifts the one-electron energies and the Fermi level. The total electronic energy due to the exchange interaction now looks more complicated than the RKKY formula (eq. (7.2)) which was derived using second order perturbation theory only. Elliott and Wedgewood calculated this energy as a function of q_m for different values of the superzone gaps, and obtained the position of the minimum as a function of temperature using a free electron model, a constant exchange interaction between f-electrons and conduction electrons and the observed temperature dependence of the ordered components of the magnetic moments for the series of heavy lanthanide metals Tb, Dy, Ho, Er, and Tm. They found qualitative agreement with experiment.

In addition to the shift of q_m with temperature, as discussed in section 2.2,

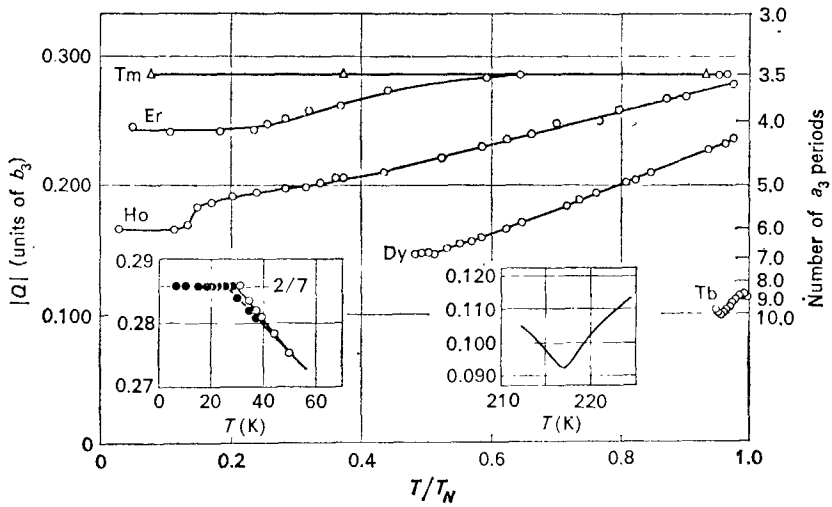

Fig. 7.5. Variation of q_m with reduced temperature for the heavy rare earths. Inserts show details of data for Tm (Brun et al., 1970) and Tb (Dietrich and Als-Nielsen, 1967) on left and right hand sides respectively [after Koehler (1972)].

several of the magnetic structures of the heavy lanthanides show the development of higher harmonics, as will be discussed in more detail in section 3. Thus the CAM structures (Tm and Er) both develop odd higher harmonics as the temperature is decreased, corresponding to a symmetrical squaring up of the sinusoidal structure. Elliott (1961) has discussed this effect using a molecular field theory. He shows that as the CAM structure develops, the amplitude of the sinusoidal moment reaches the full free ion moment at $T = \frac{1}{2}T_N$. Since the amplitude obviously cannot increase beyond this value, the system will lower its free energy by developing higher harmonics. Although a squaring up of the structure will result in a loss of entropy, at lower temperatures this will be more than offset by the lowering of the exchange energy due to larger moments on each site. The actual details of the squaring up process are extremely complicated to work out, even in molecular field theory. A proper treatment of the temperature dependence of both the magnetic periodicity and the squaring up of such structures will have to include a realistic band structure for the conduction electrons, introduce superzone boundaries corresponding to all the periodicities present (including harmonics), calculate the total exchange energy by solving a fairly large secular equation for the one-electron levels, include anisotropy effects and minimize the free energy with respect to the various amplitudes of the harmonics. Watson et al. (1968) discussed the superzone boundaries for a realistic Fermi surface for Tm, but have not attempted to study the effect on the magnetic periodicity. The basal plane spiral structures also develop higher harmonics. As discussed in section 2.3, these are due to "bunching effects" arising from basal plane anisotropy and possibly magnetoelastic anisotropy. Before we discuss the transitions to the lower temperature magnetic structures, it is worth pointing out that there are in fact occasionally more subtle transitions at higher temperatures, where anomalies are observed in the transport properties or the zero field susceptibilities but there appears to be no change in the magnetic structure. Such anomalies have been observed in Tm at 32 K (Edwards and Legvold, 1968; Jelinek et al., 1965) and Er at 28 K and 35 K (Gray and Spedding, 1968; Taylor et al., 1977). These are in fact associated with transitions at which the magnetic periodicity q_m "locks" itself into commensuracy with the lattice as clearly seen in the left insert in fig. 7.5 and in fig. 7.6. At 32 K, the Tm CAM-type periodicity locks itself from incommensurate to an exact 7 layer repeat distance (Brun et al., 1970). In some crystals of Ho at 19 K the spiral locks itself into an exact 12 layer repeat distance (Koehler, 1972) (although this is not seen in other samples of Ho (Koehler, 1972)), and in Er there is a tendency to lock in at a 15 layer repeat distance at 33 K and a locking in at an 8 layer repeat distance at 23 K (Habenschuss et al., 1974). It is easy to account for transport property anomalies at these temperatures, as when the structure becomes commensurate there will be a discontinuous change in the Fermi surface owing to the coalescing of magnetic superzone boundaries. The anomalies in the zero field susceptibility can be also explained on the basis of a molecular-field argument (Habenschuss et al., 1974) as follows. Consider a purely sinusoidal CAM structure and imagine a weak field δH applied along the c-axis. The

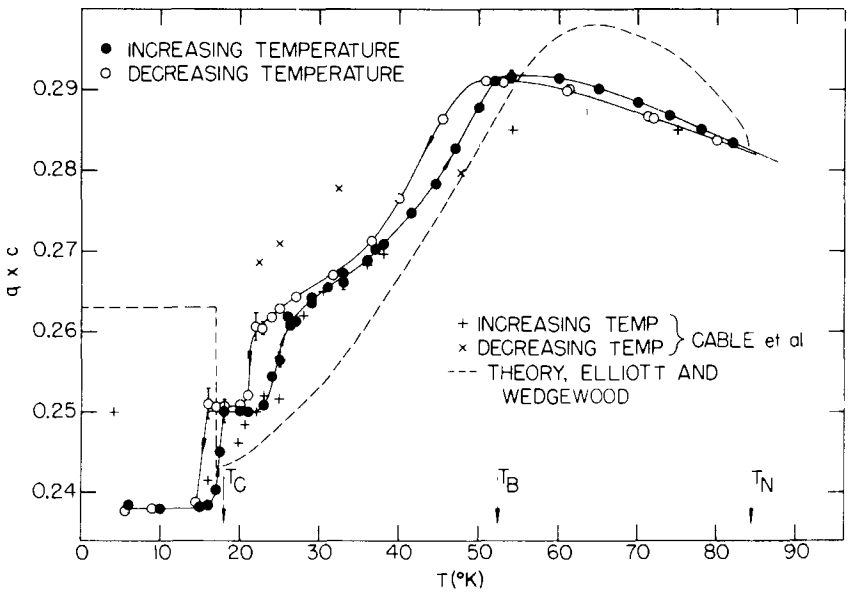

Fig. 7.6. Temperature dependence of the magnetic periodicity q_m in Er, as obtained from recent single crystal neutron diffraction results compared to earlier results of Cable et al. (1965) and the theoretical calculation (normalized to the data at 84 K) of Elliott and Wedgewood (1964) [after Habenschuss et al. (1974)].

induced moment along the c-axis on the ith atom will be given by

$$\delta M_i = (g_J\mu_B J/kT)^2 B'_J(g_J\mu_B J H_i^M)\delta H \tag{7.22}$$

where H_i^M is the molecular field along the c-axis and B'_J is the derivative of the Brillouin function. Since the molecular field is periodic, i.e.

$$H_i^M = H_0 \sin(\boldsymbol{q}_m \cdot \boldsymbol{R}_i) \tag{7.23}$$

we obtain for the bulk zero-field susceptibility

$$\chi = (g_J\mu_B J/kT)^2 \sum_i B'_J(g_J\mu_B J H_0 \sin(\boldsymbol{q}_m \cdot \boldsymbol{R}_i)/kT) \tag{7.24}$$

Expansion of the function B'_J in a Fourier series in $(\boldsymbol{q} \cdot \boldsymbol{R}_i)$ and applications of the Bloch theorem to the sum over i in eq. (7.24) leads to peaks in χ whenever $\boldsymbol{q}_m$ is a sub-multiple of a c-axis reciprocal lattice vector. The same argument can be made in the case of a spiral structure. The reasons for the incommensurate-to-commensurate $\boldsymbol{q}_m$ transition are to be found in (a) the single-ion anisotropy terms in the hamiltonian, including magnetoelastic effects. For CAM-type structures the axial anisotropy favors maximum ordered moment at each site which can only develop in a commensurate structure. For spiral-type structures the basal plane anisotropy will also favor a commensurate structure, as will the nagnetoelastic anisotropy; (b) the exchange will also favor a maximum ordered

moment provided this is developed with a periodicity not too incompatible with the maximum of $\mathcal{J}(q)$. This is presumably why Tm chooses $q_m = \frac{2}{7}(2\pi/c)$ as it is the closest periodicity to the maximum of $\mathcal{J}(q)$ which allows the CAM structure to develop maximum ordered moment on each site (in a 4 up, 3 down arrangement). The coalescing of superzone gaps in the commensurate phase can also lower the exchange energy. At the higher temperatures, presumably the increased entropy of the incommensurate structure plays a role in keeping q_m incommensurate. A quantitative theory of these transitions has not yet been developed. The above arguments imply that these types of transitions should be first order. The presence of hysteresis (in q_m vs. T curves) and the discontinuous nature of the transition in very pure crystals indicate that this is indeed the case.

At lower temperatures, the increase of the anisotropic terms in the hamiltonian cause first-order transitions to various structures. Thus, in Tb and Dy, the basal plane spiral structure transforms to a basal plane ferromagnetic arrangement. This was originally ascribed to the six-fold symmetric crystal field anisotropy in the basal plane, but Cooper (1967, 1968b) has shown that the dominant driving force for this transition is the energy of cylindrical symmetry associated with the first order magnetostriction terms in the hamiltonian (see eq. (7.9)). According to the mechanism, a transition to a basal-plane ferromagnetic structure allows strains to develop which minimize the elastic and magnetoelastic energy. Such strains are unable to develop in a spiral arrangement. This energy is cylindrically symmetric with regard to the direction of the basal plane moments, and it is in fact the much smaller crystal field anisotropy which determines the easy axis of magnetization. From eq. (7.9) and the expression for the elastic strain energy, one may obtain the equilibrium strains in terms of the magnetostriction coefficients (Rhyne, 1972) as

$$\bar{\epsilon}_1^\gamma = \tfrac{1}{2}\lambda^\gamma(d_\xi^2 - d_\eta^2), \qquad \bar{\epsilon}_2^\gamma = \lambda^\gamma d_\xi d_\eta \tag{7.25a,b}$$

where d_ξ, d_η are the direction cosines of the magnetization relative to the crystal axes, and λ^γ is the basal plane magnetostriction coefficient. Using eqn. (7.25), it may be shown that the decrease in magnetoelastic energy due to ferromagnetic alignment from the spiral is given by

$$\bar{E}_{ms}^\gamma = -\tfrac{1}{8}C^\gamma(\lambda^\gamma)^2 \tag{7.26}$$

where $C^\gamma = 2(C_{11} - C_{12})$ is a basal plane elastic constant. With decreasing temperature, $\bar{E}_{ms}^\gamma$ increases in magnitude more rapidly than E_{ex} and the transition occurs when $\bar{E}_{ms}^\gamma$ becomes equal to the exchange energy. The temperature dependence of $\bar{E}_{ms}^\gamma$ is mainly due to that of λ^γ, which is given by the theory of Callen and Callen (1966) as

$$\lambda^\gamma = \lambda^\gamma(0)\hat{I}_{5/2}[L^{-1}(\sigma)] \tag{7.27}$$

where the notation is the same as in eq. (7.15) and $\lambda^\gamma(0)$ is the value at zero temperature. Cooper (1967, 1968b) has shown that except at the highest temperatures close to T_N, $\hat{I}_{5/2} \sim \sigma^3$ so that $\bar{E}_{ms}^\gamma$ goes as σ^6, thus increasing sharply at lower temperatures. The total driving energy for the ferromagnetic transition

is obtained by combining $\bar{E}^{\gamma}_{ms}$ with the crystal field anisotropy whose temperature dependence is given by eq. (7.15)

$$E_d = -\tfrac{1}{8}C^{\gamma}[\lambda^{\gamma}(0)]^2\{\hat{I}_{5/2}(L^{-1}(\sigma))\}^2 - V_6^6 J^6 \hat{I}_{13/2}(L^{-1}(\sigma)) \tag{7.28}$$

where (see eq. (7.15) and discussion following) the temperature dependence of the second term is $\sim\sigma^{21}$. This term thus decreases very much more rapidly with temperature than the first term although they are comparable at $T = 0$. For Dy, Cooper (1967) estimated $\bar{E}^{\gamma}_{ms}$ $(T = 0) = -2.0$ K/atom, $V_6^6 J^6 = -2.4$ K/atom. At $T = T_C$, the Curie temperature, $\bar{E}^{\gamma}_{ms}$ was the dominant term. A more detailed microscopic theory of magnetoelastic effects and their role in stabilizing the ferromagnetic state has been given by Evenson and Liu (1969), who also included two-ion magnetoelastic effects. Their estimates of the magnetoelastic driving energy favoring ferromagnetism are of the same order of magnitude as above (i.e. one or two degrees K per atom). Note that the above explanation of the ferromagnetic ordering would still allow the function $\mathcal{J}(\boldsymbol{q})$ to be a maximum at some $\boldsymbol{q}_m \neq 0$ in the ferromagnetic state since the exchange energy is outweighed by the magnetoelastic energy. The appearance of a gap between up and down spin conduction states due to ferromagnetic ordering and the disappearance of the superzone gaps will in general change the function $\mathcal{J}(\boldsymbol{q})$ from that existing in the spiral phase, however, and as we shall see, in certain cases, may even make the maximum at $\boldsymbol{q}_m$ disappear. In such cases a maximum of $\mathcal{J}(\boldsymbol{q})$ at $\boldsymbol{q} = 0$ is to be viewed as a secondary result, rather than the cause of the ferromagnetic ordering.

In other cases as that discussed above, a cone structure (sometimes called a "ferromagnetic spiral") develops at lower temperatures from a higher temperature basal plane spiral (as in Ho) or a CAM structure (as in Er). The conditions for the occurrence of such a cone structure have been discussed from a molecular field point of view by several authors (Elliott, 1961; Yosida and Miwa, 1961; Miwa and Yosida, 1961; Kaplan, 1961) and in detail by Cooper et al. (1962) (see eqs. (7.16) in section 2.2). The reason for the transition to the cone structure lies in the temperature variation of the axial anisotropy coefficients (as given by eq. (7.15)). Cooper et al. (1962) also discussed the stability of these structures against long wavelength spin excitations. However, more recently Woods et al. (1969) and Stringfellow et al. (1970) pointed out that if the anisotropy parameters vary smoothly with temperature, near the temperature of the transition from a spiral to a cone structure, an instability actually must develop for spin-waves of wave vector near $\boldsymbol{q}_m$, implying an intermediate phase between spiral and cone. Sherrington (1973) has investigated theoretically this intermediate phase and concludes that it is a *tilted* spiral, i.e. a spiral structure in which the pitch of the spiral is along the c-axis as before, but with the moments lying in a plane tilted out of the basal plane. He also shows that higher order effects produce modulations of the pitch and plane of this spiral. The net result is a structure given by (neglecting higher order terms),

$$J_{i\xi} = \bar{S}\cos(\boldsymbol{q}\cdot\boldsymbol{R}_i) \tag{7.29a}$$

$$J_{i\eta} = \bar{S} \sin(\boldsymbol{q} \cdot \boldsymbol{R}_i), \tag{7.29b}$$

$$J_{i\zeta} = -S \sin\psi \sin(\boldsymbol{q} \cdot \boldsymbol{R}_i) - \tfrac{1}{2}\alpha \sin(3\boldsymbol{q} \cdot \boldsymbol{R}_i), \tag{7.29c}$$

where ψ is the tilt angle of the spiral (assumed small) and α is a small amplitude. As we shall see in the next section, the neutron diffraction data on several heavy lanthanide metals and alloy systems do not reveal any intermediate temperature structure between the spiral and cone phases. This would presumably indicate in the light of the above arguments that the anisotropy parameters actually change discontinuously at the transition, possibly due to magnetostrictive effects. Recently, Tachiki et al. (1974) concluded from the existence of a peak in the ultrasonic shear wave attenuation in Ho at 24 K in the spiral phase (which was well separated from the peak at 20 K associated with the appearance of the cone structure) that Ho exhibits a tilted magnetic spiral structure between 20 and 24 K. However, careful recent neutron diffraction intensity measurements (Felcher et al., 1976) indicate that if such a phase existed, the tilt must be less than 10°. In some Er-rich alloys on the other hand, neutron diffraction results indicate the existence of an intermediate phase between the spiral and cone structures with moment arrangements given by a superposition of basal plane spiral and CAM structures, as in eqs. (7.29). In Er itself, the intermediate structure exists between the cone and CAM phases. It is at present unclear whether the experimental data can be analyzed in terms of a tilted spiral. It is also unclear what effects the greater entropy of a sinusoidal c-axis moment (as in the nearby CAM phases) would have on the intermediate structure. Thus the existence of the tilted spiral intermediate phase is still an open question.

Recently Jensen (1976a) has performed a self-consistent molecular field calculation of the magnetic structures of Er including the high-temperature, intermediate-temperature and cone phases, in terms of a set of effective crystal field parameters and an intra-planar two-ion interaction parameter, which were fitted to the experimental ordering temperatures and the bulk magnetization data. A seven-layer repeat distance was assumed (so that self-consistent calculations for the moments on seven different sites had to be performed) and the function $\mathcal{J}(\boldsymbol{q})$ was taken from fits to the spin-wave dispersion curve for Er (including an anisotropic exchange function). The details of the obtained magnetic structure at different temperatures were compared to the results of the neutron diffraction measurements on Er (Habenschuss et al., 1974) and while reasonably good agreement was obtained at high temperatures, the agreement at temperatures above T_C was only qualitative. However, the correct structures were obtained. An interesting feature of these calculations is that it indicates that the intermediate phase structure is confined to the $(\xi-\zeta)$ plane, i.e. a plane perpendicular to the basal plane, an extreme case of a tilted spiral! (The neutron diffraction results alone cannot fix the phase of the basal plane component relative to that of the c-axis component). It may be that the exchange interactions used by Jensen are not the best ones, e.g., there could be other types of anisotropic two-ion couplings than the ones considered or there could be a temperature dependence of the exchange interaction arising from the variation of the

superzone gaps with temperature. This could possibly account for the poor quantitative agreement at the lower temperatures.

2.5. *Magnetic ordering in alloys of heavy lanthanide metals*

Several neutron diffraction measurements have been done on random binary alloys of heavy lanthanide metals with each other and Y, Sc and Th. The last three serve as non-magnetic diluents, but only Y acts as a true diluent since there is no appreciable volume change in the hcp structure on alloying with Y, and the outer electronic structure of Y is the same as that of the lanthanide metals. In the random alloys one may still think of a homogeneous electronic band structure for the conduction electrons which transmit the RKKY interaction, although the peak in the generalized susceptibility $\chi(\boldsymbol{q})$ may be shifted upon alloying due to subtle changes in band structure. For such an alloy, eqs. (7.3) and (7.4) expressing the exchange interaction should be generalized to

$$\mathcal{H}_{ex} = -\sum_{i \neq j} (g_{A0} - 1)(g_{B0} - 1) j_{AB}(\boldsymbol{R}_i - \boldsymbol{R}_j) \boldsymbol{J}_i \cdot \boldsymbol{J}_j, \tag{7.30}$$

where site i has an atom of type A, and site j an atom of type B, g_A is the g-factor of an ion of type A, etc. and

$$j_{AB}(\boldsymbol{R}_i - \boldsymbol{R}_j) = \frac{2}{N^2} \sum_{\boldsymbol{q}} U^A(\boldsymbol{q}) U^B(\boldsymbol{q}) \chi(\boldsymbol{q})\, e^{i\boldsymbol{q} \cdot (\boldsymbol{R}_i - \boldsymbol{R}_j)} \tag{7.31}$$

One may combine (7.30) and (7.31) to write

$$\mathcal{H}_{ex} = -\sum_{i \neq j} \mathcal{J}_{ij}^{AB} \boldsymbol{J}_i \cdot \boldsymbol{J}_j \tag{7.32}$$

The exchange interaction will still attempt to drive the system to order with some magnetic periodicity $\boldsymbol{q}_m$ given by the wavevector where a maximum of

$$\mathcal{J}(q) = \frac{1}{N} \sum_{i \neq j} \mathcal{J}_{ij}^{AB}\, e^{i\boldsymbol{q} \cdot (\boldsymbol{R}_i - \boldsymbol{R}_j)} \tag{7.33}$$

occurs. The anisotropy terms will, however, be different for the different sites depending on the type of atom at the site, so that one might expect that the moments will order in directions determined by the local anisotropy on the particular ion at that site. In general, however, this is not the case. Most of the alloys studied so far possess a homogeneous magnetic structure, in the sense that the moments order in directions which do *not* depend on the type of ion. This is because of the dominance of the long range exchange interaction which couples the direction of one moment to that of a large number of neighbors. In addition, strain fields due to magneto-elastic interactions may similarly couple the ionic moments together. An exception has recently been observed for the Tb–Tm alloy system (Hansen et al., 1975) where it appears that a phase exists where the Tb-spins lie in the basal plane, while the Tm-spins lie along the hexagonal c-axis. Whether the magnetic structure of the alloy is homogeneous

or not depends obviously on a delicate balance between the exchange interaction and the magnitude of (and disparity between) the individual single-ion anisotropy terms in the hamiltonian. A mean field theory for magnetic order in random anisotropic magnetic alloys has recently been developed by Lindgard (1976c).

Dilution of the magnetic ions with Y will reduce the exchange interaction $\mathcal{J}(q)$ [see eq. (7.33)] and hence lowers the initial ordering temperature. In the basal plane spiral structures such as Dy and Tb, the addition of Y rapidly reduces the temperature at which the transition to basal plane ferromagnetic order occurs. This is presumably because the driving energy for this transition (which is related to magnetoelastic anisotropy effects, as discussed in section 2.4) goes as quite a high power of the ordered moment. Dilution of the magnetic ions with Sc, which has the same outer electronic configuration as the lanthanide metals and Y, reduces the initial ordering temperatures much more rapidly than dilution with Y. This is probably due to the much smaller atomic volume of Sc, resulting in a net volume decrease for the alloys, and also a change in the c/a ratio. Recent magnetization measurements of the conduction electron polarization (a measure of the strength of the s–f exchange interaction) in Gd based alloys by Legvold and collaborators (private communication) show a linear dependence on c/a. Harmon (private communication) has shown in the case of Gd that the nature of the conduction electron wave functions at the Fermi level, and hence the matrix elements which control the magnitude of the exchange interaction between the f-electrons and the conduction electrons, is quite sensitive to the c/a ratio.

2.6. *Magnetic ordering in the light lanthanides and compounds*

In the case of the heavy lanthanide metals, the exchange interaction dominates the hamiltonian. The crystal field effects, although very important for determining the detailed nature of the ordering, do not affect the question of whether magnetic ordering takes place at all. In the light lanthanide metals, and in some cubic lanthanide compounds, the crystal field effects are comparable to, or dominant over, the exchange effects. Thus, for example in the case of ions like Pr, (which have an even number of f-electrons and hence an integral J for the ground state multiplet), the crystal field can quench the magnetic moment completely by requiring a singlet ground state. Magnetism can then occur only by induced-moment behavior due to the mixing-in of the higher crystal field levels in the multiplet through the exchange interaction. For such systems, even at zero temperature, there is a critical value of the ratio of exchange to crystal field interaction below which magnetic ordering cannot occur. The first molecular field description of such systems was given several years ago by Trammell (1963) and Bleaney (1963). Trammell was concerned with explaining the reduction of moment and strong magnetic anisotropy in heavy lanthanide-pnictides with the rocksalt structure, while Bleaney considered double-hexagonal close packed (dhcp) Pr, which is a singlet ground state system. As we shall see in section 3, there appears to be no magnetic ordering in single crystals of dhcp Pr,

but metastable fcc Pr is weakly ferromagnetic at low temperatures and appears to be an example of such an induced moment system. We review briefly here the molecular field theory for the ground state of such systems. There has also been a great deal of experimental and theoretical interest in recent years in the collective modes associated with such systems, and we shall discuss these in a later section. Excellent recent reviews of the status of our understanding of such systems have been given by Cooper (1972, 1976).

The appropriate hamiltonian for such systems is (see eqs. (7.3) and (7.5)):

$$\mathcal{H} = \mathcal{H}_{\rm cf} + \mathcal{H}_{\rm ex} = \sum_i V_{\rm c}^i - \sum_{i\neq j} \mathcal{J}_{ij} \boldsymbol{J}_i \cdot \boldsymbol{J}_j, \tag{7.34}$$

where $V_{\rm c}^i$ is the crystal field potential (written in terms of the Stevens operator equivalents, as in eq. (7.5)) for the ion at site i. We may write this as

$$\mathcal{H} = \mathcal{H}_0 + \mathcal{H}_1 \tag{7.35}$$

where

$$\mathcal{H}_0 = \sum_i \left[V_{\rm c}^i - 2 \sum_{j\neq i} \mathcal{J}_{ij} \langle \boldsymbol{J}_j \rangle_0 \cdot \boldsymbol{J}_i \right] \tag{7.36a}$$

and

$$\mathcal{H}_1 = - \sum_{i\neq j} \mathcal{J}_{ij} (\boldsymbol{J}_i - \langle \boldsymbol{J}_i \rangle_0) \cdot (\boldsymbol{J}_j - \langle \boldsymbol{J}_j \rangle_0) \tag{7.36b}$$

where $\langle \boldsymbol{J}_i \rangle_0$ stands for the thermal expectation value. Here $\mathcal{H}_0$ is the molecular field (single ion) hamiltonian, and $\mathcal{H}_1$ gives rise to the collective excitations. We consider only $\mathcal{H}_0$. One may now for a given temperature assume a certain $\langle \boldsymbol{J}_j \rangle_0$, diagonalize $\mathcal{H}_0$ for each site independently, recalculate $\langle \boldsymbol{J}_j \rangle_0$ for the new states and continue until self-consistency is obtained. The ground state must be one for which $\Sigma_i [\langle V_{\rm c}^i \rangle - 2 \Sigma_{j\neq i} \mathcal{J}_{ij} \langle \boldsymbol{J}_i \rangle_0 \cdot \langle \boldsymbol{J}_j \rangle_0]$ is minimized, at low temperature. In general, one must assume certain general forms for the magnetic structure (ferromagnet, simple antiferromagnet, etc.).

A simpler example is offered by the case (Bleaney, 1963; Cooper, 1972) where we consider ferromagnetic ordering in a system with only two singlet levels $|0_{\rm c}\rangle$ and $|1_{\rm c}\rangle$. (The other crystal field levels being regarded as sufficiently high in energy so as to be relatively unimportant.) We consider the case for ordering along the z-axis, so that only J_z has a non-vanishing matrix element

$$\alpha = \langle 0_{\rm c} | J_z | 1_{\rm c} \rangle \tag{7.37}$$

between the ground and excited states. For singlet states, of course, all expectation values of J_x, J_y, J_z are zero.

The molecular field hamiltonian $\mathcal{H}_0$ is the same for each site i,

$$\mathcal{H}_0 = \sum_i \mathcal{H}_0^i = \sum_i [V_{\rm c}^i - 2\mathcal{J}(0) \bar{J} J_z^i] \tag{7.38}$$

This may be diagonalized in terms of $|0_{\rm c}\rangle$, $|1_{\rm c}\rangle$ (the eigenstates of $V_{\rm c}$) to yield the

eigenstates

$$|0\rangle = \cos\theta|0_c\rangle + \sin\theta|1_c\rangle, \qquad |1\rangle = -\sin\theta|0_c\rangle + \cos\theta|1_c\rangle \tag{7.39a,b}$$

and eigenvalues

$$E_0 = -E_1 = -\frac{\Delta}{2}[\cos 2\theta + (4\mathcal{J}(0)\alpha\bar{J}/\Delta)\sin 2\theta] \tag{7.40}$$

where Δ is the splitting between the crystal field levels $|0_c\rangle$ and $|1_c\rangle$ and

$$\tan 2\theta = 4\mathcal{J}(0)\alpha\bar{J}/\Delta. \tag{7.41}$$

A self-consistent equation for $\bar{J}$ may be obtained as a function of temperature. It is given by

$$\bar{J}/\alpha = \sin 2\theta \tanh\{(\Delta/T)[\tfrac{1}{2}\cos 2\theta + (2\mathcal{J}(0)\alpha\bar{J}/\Delta)\sin 2\theta]\} \tag{7.42}$$

At $T = 0$, the above equation yields as the condition for finite $\bar{J}$, i.e. for ferromagnetism to occur at all,

$$A \equiv 4\mathcal{J}(0)\alpha^2/\Delta > 1 \tag{7.43}$$

Figure 7.7 shows the behavior of the solutions for $\bar{J}$ and the Curie temperature T_C from eq. (7.42) vs. the parameter A. Note how the magnetization is reduced from its full "free ion" value as A gets close to its critical value. A similar treatment can be carried out for an antiferromagnetic structure. A simple collinear antiferromagnetic structure (where each atom has antiparallel moment to its neighbors) yields as the critical condiction for magnetism,

$$A < -1. \tag{7.44}$$

A mean field theory for the susceptibility of such systems (Cooper, 1972;

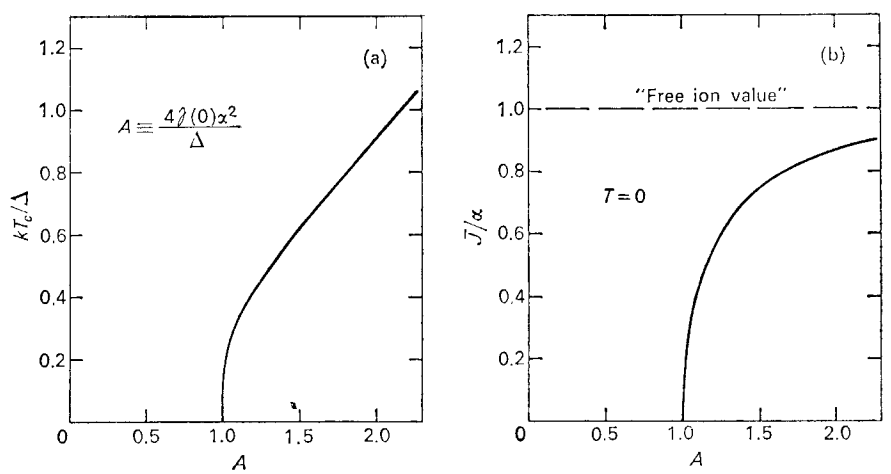

Fig. 7.7. (a) T_C/Δ vs. A for the two singlet level model. (b) Spontaneous magnetization (in dimensionless form) vs. the parameter A ($\equiv 4\mathcal{J}(0)\alpha^2/\Delta$) for singlet level model at $T = 0$.

Bleaney, 1963) also shows that eq. (7.43) is the condition for the bulk susceptibility to just diverge at $T = 0$, i.e. for the system to go unstable with respect to ferromagnetic ordering.

A review of the systematics of the spin hamiltonian, magnetic interactions and all possible magnetic structures relating to rare earth compounds may be found in the article by Bertaut (1972).

3. Neutron diffraction investigations of magnetic structures

3.1. *Experimental technique*

The conventional technique of neutron diffraction consists of letting a monochromatic beam of neutrons fall on the sample (single crystal or polycrystalline) and measuring the peaks in the intensity of the scattered neutrons in various directions. Since Bragg reflections in the sample will give sharp intense peaks in certain directions, energy analysis of the scattered beam is generally not required. The interaction between the atomic nuclei and the neutron produces diffraction patterns characteristic of the crystal structure, while the magnetic interaction between the dipole moment of the neutron and the atomic moments produces diffraction patterns characteristic of the long range magnetic order in the crystal. For details of the technique, the reader may refer to the books by Bacon (1975) or Marshall and Lovesey (1971) and to the experimental papers referred to in this section.

Let us consider a single crystal sample in the neutron beam, and regard all vectors as expressed with respect to a coordinate system tied to the crystal axes. Let the incident neutron wavevector be $\boldsymbol{k}_0$, the scattered neutron wavevector be $\boldsymbol{k}_1$ ($|\boldsymbol{k}_0| = |\boldsymbol{k}_1|$ for elastic scattering), and the neutron scattering vector $\boldsymbol{Q} = \boldsymbol{k}_0 - \boldsymbol{k}_1$. The differential cross-section for elastic coherent magnetic scattering from an ordered system of moments given by the general form of eq. (7.10) is (Marshall and Lovesey, 1971)

$$\frac{\mathrm{d}\sigma}{\mathrm{d}\Omega} = \frac{1}{4} p_0^2 \frac{N}{\Omega} (2\pi)^3 g_J^2 \sum_{\boldsymbol{G}} \sum_{\alpha} \delta(\boldsymbol{Q} - \boldsymbol{G} - \boldsymbol{q}_\alpha) [f(\boldsymbol{Q})]^2 |F(\boldsymbol{G})|^2 \{\boldsymbol{J}_{\boldsymbol{q}\alpha} \cdot \boldsymbol{J}^*_{\boldsymbol{q}\alpha} - |\hat{\boldsymbol{Q}} \cdot \boldsymbol{J}_{\boldsymbol{q}\alpha}|\}, \tag{7.45}$$

where p_0 is a characteristic magnetic scattering length ($= 0.269 \times 10^{-12}$ cm), N is the total number of unit cells, Ω the unit cell volume, $\boldsymbol{G}$ a reciprocal lattice vector, $f(\boldsymbol{Q})$ the magnetic form factor for the lanthanide ion at wave vector $\boldsymbol{Q}$ (which would be simply the Fourier transform of the spin density if there was no orbital moment, but is in general more complicated as discussed in the next section); and $F(\boldsymbol{G})$ is the structure factor for the reciprocal lattice vector $\boldsymbol{G}$, given by

$$F(\boldsymbol{G}) = \sum_{\kappa} \mathrm{e}^{\mathrm{i}\boldsymbol{G} \cdot \boldsymbol{r}_\kappa} \mathrm{e}^{-W_\kappa} \tag{7.46}$$

where r_κ denotes the position of the κth atom in the unit cell and e^{-W_κ} is its Debye–Waller factor. In eq. (7.45) $\hat{Q}$ denotes a unit vector along Q. It should be noted here that we have assumed a homogeneous magnetic structure as given by eq. (7.10), so that different basis atoms in the cell do not have different $J_{q\alpha}$, although eq. (7.45) can be easily generalized if that is the case. If there are non-magnetic atoms in the unit cell they are to be excluded in the sum in eq. (7.46).

Equation (7.45) reveals that long range magnetic order of periodicity q_α gives rise to so-called satellite reflections at values of Q displaced by $\pm q_\alpha$ from the positions of the nuclear reflections. (It should be noted that the occurrence of a satellite of q_α implies one at $-q_\alpha$ because of the reality condition on the atomic moments.) Higher harmonics of a sinusoidally modulated structure will appear as reflections at $\pm nq_\alpha$ (see fig. 7.8). Unfortunately, as can be seen from eq. (7.45), intensity measurements on magnetic reflections do not yield the relative *phases* of the J_{nq_m} relative to J_{q_m}, so that an additional physical assumption regarding these phases is necessary in order to describe in detail how a structure "squares up" from simple sinusoidal form. (See, for example, the phase arguments given by Koehler in his recent review article (1972)). The *directions* of the vectors J_{Q_α} can be obtained by measuring satellite reflections for several different directions of Q. Thus eq. (7.45) shows that if Q is parallel to $J_{q\alpha}$, the magnetic intensity vanishes. Hence, a CAM structure for example will exhibit satellites at $\pm q$ from reciprocal lattice vectors that are normal to the c-axis but

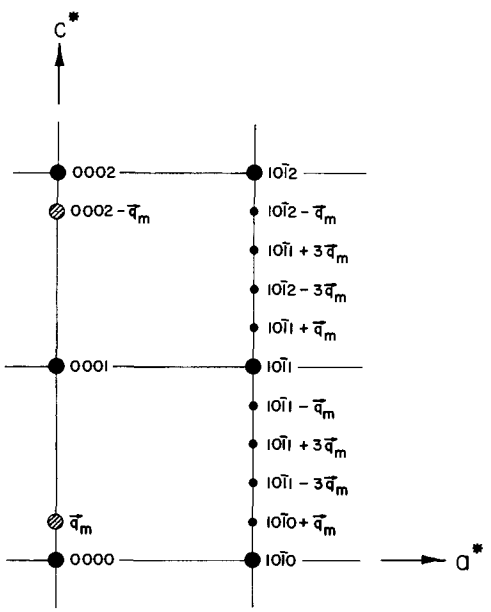

Fig. 7.8. Schematic diagram of positions of satellite reflections indicated by full circles observed in the a^*–c^* plane of the reciprocal lattice in the slightly squared-up CAM structure of erbium (high-temperature phase). In the intermediate temperature phase, additional satellites would appear along (001) (indicated by shaded circles) signifying ordering of the basal plane component.

none along 00l. A basal plane spiral, on the other hand, will have twice as much intensity for (00l) type reflections as for basal plane reflections (apart from form factor effects). A ferromagnetic component ($\boldsymbol{q}_\alpha = 0$) manifests itself by additional intensity at the reciprocal lattice vectors below T_C. Thus, a basal plane ferromagnet yields magnetic intensity superimposed on all nuclear reflections because in general there are six equally populated domains along the easy axes. A cone structure yields magnetic intensity on all nuclear reflections except those of the type (00l) in addition to satellites at $\pm \boldsymbol{q}_m$. The magnitude of the ordered moment associated with the structure is usually obtained by comparing the magnetic intensity to that of the nuclear reflections, since the nuclear coherent scattering lengths are generally well-known. In general, for accurate intensity measurements, one must ensure that the single crystal sample is free of extinction effects (Bacon, 1975). This is usually realized by utilizing crystals of large mosaic spread and small (1 or 2 mm) dimensions in the plane of scattering. For the case of powder samples, one must average the cross-section given in eq. (7.45) over all directions of $\boldsymbol{Q}$, and as is obvious, it is quite difficult to obtain details of a complex magnetic structure in such cases.

3.2. *The heavy lanthanide metals*

The neutron diffraction results on the heavy lanthanide metals have been recently reviewed by Koehler (1972). The main features are summarized in table 7.1. We shall briefly review the results here.

3.2.1. *Gadolinium*

Neutron diffraction studies have been carried out by Will, Nathans and Alperin (1964) and by Cable and Wollan (1968). The high neutron capture cross-section of naturally occurring Gd creates severe problems for such studies. Nevertheless, Cable and Wollan (1968) were able to make a fairly detailed study using a 0.353 Å wavelength neutron beam for which the absorption cross-section is much lower than for thermal neutrons. The results indicated that Gd is a ferromagnet at all temperatures below its initial ordering temperature. Liu, Gupta, and Sinha (1971) showed that the generalized susceptibility $\chi(\boldsymbol{q})$ for the conduction electrons of Gd had a maximum at $\boldsymbol{q} = 0$, although they neglected matrix elements in their calculation. More recently, Lindgard, Harmon and Freeman (1975) have shown that matrix element effects are very important but still obtain $\boldsymbol{q} = 0$ as the maximum of $\mathcal{J}(\boldsymbol{q})$.

The ferromagnetic moment in Gd is parallel to the c-axis from T_C (293 K) to 232 K, and below that starts moving away from that axis, reaching a maximum deviation of 65° near 180 K and then at still lower temperatures moving back to within 32° of the c-axis. This curious behavior is due to the temperature variation of the weak single-ion anisotropy constants for Gd. Since Gd is an S-state ion, there is no anisotropy to first order. However, higher order effects of the spin–orbit coupling can yield such anisotropy terms.

TABLE 7.1.
Magnetic structures of the lanthanide metals.

	Crystal structure	High temp. phase	Intermediate temp. phase	Low temp. phase	Ground state of free ion	de Gennes factor
Ce	dhcp	–	–	c-axis moment; antiferromagnetic (?) $T_N = 12.5$ K	$^2F_{5/2}$	0.18
Pr	dhcp	–	–	(Singlet ground state)	$^3H_4$	0.80
Nd	dhcp	basal plane moment modulated along $\boldsymbol{b}_1$ and parallel to $\boldsymbol{b}_1$ on hexagonal sites; B and C layers antiferromagnetically coupled: $T_N = 19.2$ K	–	Cubic sites order at 7.8 K, as in high temp. phase but moments modulated with different periodicity along $\boldsymbol{b}_1$ and pointing 30° to $\boldsymbol{b}_1$	$^4I_{9/2}$	1.84
Pm	dhcp	–	–	Ferromagnetic or singlet ground state (?) ($T_C = 98$ K)	$^5I_4$	3.20
Sm	Sm-structure	$T_N = 106$ K for ordering on hexagonal sites $(0++0--0++\cdots)$	–	Below 13.8 K cubic sites order in complex manner (see text)	$^6H_{5/2}$	4.46
Eu	bcc	–	–	$T_N = 90.5$ K; right-angle spiral along cube axis	$^8S_{7/2}$	15.75
Gd	hcp	–	–	$T_C = 293$ K; ferromagnetic	$^8S_{7/2}$	15.75
Tb	hcp	$T_N = 230.2$ K; basal plane spiral	–	$T_C = 220$ K; basal plane ferromagnet	$^7F_6$	10.50
Dy	hcp	$T_N = 176$ K; basal plane spiral	–	$T_C = 87$ K; basal plane ferromagnet	$^6H_{15/2}$	7:08
Ho	hcp	$T_N = 133$ K; basal plane spiral	bunched basal plane spiral	$T_C = 20$ K; bunched cone structure, semi-angle ~80°	$^5I_8$	4.50
Er	hcp	$T_N = 80$ K; CAM structure	CAM structure squares up; at $T_B = 52$ K basal plane moment orders with same periodicity	$T_C = 32$ K; c-axis ferrimagnetic cone-shaped structure	$^4I_{15/2}$	2.55
Tm	hcp	$T_N = 56$ K; CAM structure	CAM structure squares up symmetrically	$T_C = 32$ K; c-axis ferrimagnetic structure (4 up, 3 down) develops	$^3H_6$	1.17

3.2.2. *Terbium*

Neutron diffraction investigations have been carried out by Koehler and co-workers (Koehler, 1967; Koehler et al., 1963). Additional investigations have been performed by Dietrich and Als-Nielsen (1967) and by Umebayashi et al. (1968). The data are consistent with an initial ordering to a basal plane-spiral structure at $T_N = 230.2$ K. The range of stability of this structure is, however, very narrow and at 225 K, a first order transition to a basal plane ferromagnet begins with a region of about 10 K where both phases coexist. There is also some temperature hysteresis. This transition is in accord with the theory of the magnetoelastic driving force for ferromagnetism discussed in section 2.4. The ferromagnetic phase is stable down to the lowest temperatures. An ordered moment of 9.0 μ_B per ion was obtained at 4.2 K (Koehler et al., 1967; Koehler, 1967) consistent with the free ion ground state value as given by Hund's Rules. Magnetization measurements show that the easy direction is a b-axis. The ordered moment increases smoothly through the spiral-ferromagnetic transition. The variation of q_m with temperature is shown in detail in the right insert of fig. 7.5. It increases slightly and then decreases with decreasing temperature (as the superzone gaps open up due to the spiral order) and then starts increasing again once the mixed phase with ferromagnetic order sets in. Lindgard (1976a) has calculated the generalized susceptibility function $\chi(q)$ for Tb without matrix elements, however, and finds a peak close to the observed initial q_m. He also calculates the exchange energy with ferromagnetic band splitting and estimates the exchange energy of the spiral phase to be lower than that of the ferromagnetic phase by ~ 10 K/ion times the reduced magnetization squared. This is the energy that must be overcome by the magnetoelastic and basal plane anisotropy energies favoring ferromagnetism which have been estimated numerically by Cooper (1967, 1968a). Umebayashi et al. (1968) studied the effect of pressure on the magnetic structure of Tb up to 6 kilobars, in particular the effect on the magnetic periodicity q_m (or alternatively the turn angle per layer) in the spiral phase. Their results are shown in fig. 7.9. They obtain a value for $[(1/q_m)(dq_m/dp)]$ of $20 \pm 2 \times 10^{-3}$ kbar^{-1} at $T - T_N = -4$ K and $23 \pm 2 \times 10^{-3}$ kbar^{-1} at $T - T_N = -9$ K. The results were interpreted in terms of a theory by Miwa (1965) relating the change in q_m to the change in superzone gaps and the spin-disorder scattering. The agreement obtained was quite good.

3.2.3. *Dysprosium*

The magnetic structures are the same as those of Tb, except there is a larger region of stability of the basal plane spiral (from T_N at 176 K down to 90 K) (Wilkinson et al., 1961a). There is a narrow region of mixed spiral-ferromagnetic phase with the midpoint at 87 K and with some temperature hysteresis. At low temperature the magnetization measurements reveal easy a-directions in the basal plane. The turn angle per layer is 43.2° at T_N and decreases to 26.5° at 90 K. As in Tb, the ordered moment per ion increases continuously across the spiral-ferromagnetic transition. In an applied field parallel to the c-axis, no

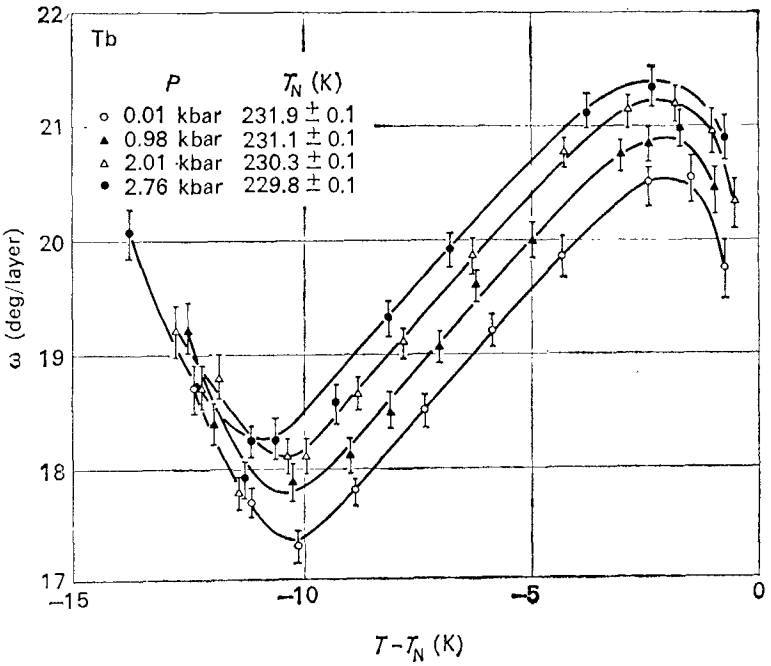

Fig. 7.9. Interlayer turn angle ω for Tb as a function of $(T - T_N)$ at various pressures [after Umebayashi et al. (1968)].

change was observed in the magnetic structure, but when the field was applied in the basal plane, a transition to the ferromagnetic phase was observed.

3.2.4. *Holmium*

Holmium has been studied in detail by the Oak Ridge Group (Koehler et al., 1966) and more recently by Felcher et al. (1976). Details of the magnetic structure appear to be sensitive to the particular crystal studied. The general features are the same, however. At $T_N = 133$ K, the magnetic structure is a basal-plane spiral. Below roughly 42 K, weak fifth and seventh order satellites were observed, indicating bunching of the spiral about the sixfold easy axes, as discussed in section 2.3. However, the squared amplitudes of the fifth and seventh harmonics are not equal as required by the simple bunching theory. Instead $I_5 \sim 2I_7$ (Felcher et al., 1976). A recent calculation by Arai and Felcher (1975) indicates that this can be accounted for by zero point motion associated with the spins in the spiral structure. At $T_C = 20$ K, the distorted spiral changes to a cone-shaped structure of semi-angle $\sim 80°$, still with bunching of the basal plane components. At 4.2 K, the net c-axis moment is 1.7 μ_B and the ordered basal plane moment is 9.5 μ_B.

The magnetic periodicity q_m and its temperature variation seem to be sensitive to the particular samples studied (Koehler, 1972). The turn angle per layer starts

off in all samples being ~50° just below T_N and decreases with decreasing temperature. However, it behaved differently for two different samples (A and B) studied at Oak Ridge (Koehler, 1972), in one case (A) smoothly saturating at 36.7° per layer, in the other (B) suddenly assuming a constant value of 30° per layer (commensurate into the lattice) at about 18 K. On the other hand, Felcher et al. (1976) find the turn angle discontinuously assuming a constant value of 33.3 K below 25 K, while a sample measured at Chalk River (Koehler, 1972) exhibited a final turn angle of 32.5°. Presumably at the lower temperatures, the periodicity is determined by a delicate balance between anisotropy, magnetostriction and exchange, with impurities and strains in particular samples affecting this balance in one direction or the other. As mentioned in section 2.4 there appears to be no evidence of a tilted spiral phase (at least with a tilt greater than about 10°) separating the spiral and conical phases.

Koehler et al. (1967) have also performed extensive studies of the magnetic structures of Ho in an applied field. At 4.2 K, a field applied in the basal plane causes a tipping of the moments in the cone-structure towards the basal plane, and eventually ferromagnetic alignment along the easy (b) axis nearest the field direction, owing to the considerable hexagonal basal plane anisotropy. The helix presumably becomes slightly distorted in lower fields (although the intensities of the additional zeroth and second harmonics resulting from such a distortion were too small to be observed), but the transition to the ferromagnetic alignment takes place without going through the so-called intermediate "fan phase", again due to the large hexagonal anisotropy. At higher temperatures, very complex diffraction patterns appear at intermediate fields, which Koehler et al. have analyzed in terms of two different types of intermediate fan phases, denoted I and II. Figure 7.10 shows their obtained phase diagrams for fields applied along the a- and b-axes. The magnetic periodicities of these intermediate oscillating phases are different from each other and from that of the original spiral. Neither phase I nor phase II behave like a simple fan structure (see fig. 7.3), where the moment direction oscillates sinusoidally about the field direction. For fields applied parallel to the a-axis, ferromagnetic alignment parallel to the field was not achieved at the highest fields (~22 kOe), but again intermediate fan phases were observed. The magnetic periodicity in these phases was different from that observed when the field was parallel to the b-axis. There is at present no detailed theoretical explanation for the existence of two intermediate fan phases and the observed changes in the magnetic periodicity on entering these phases.

Umebayashi et al. (1968) have also studied the effect of pressures up to 7 kbar on the magnetic periodicity in Ho with results similar to those in Tb except that the rate of percentage increase of turn angle with pressure is much smaller.

3.2.5. *Erbium*

This metal was first studied by Cable et al. (1965) who deduced the magnetic structure. More recently, a detailed study on high-purity single crystals has been carried out by Habenschuss et al. (1974). A detailed study has also been made by

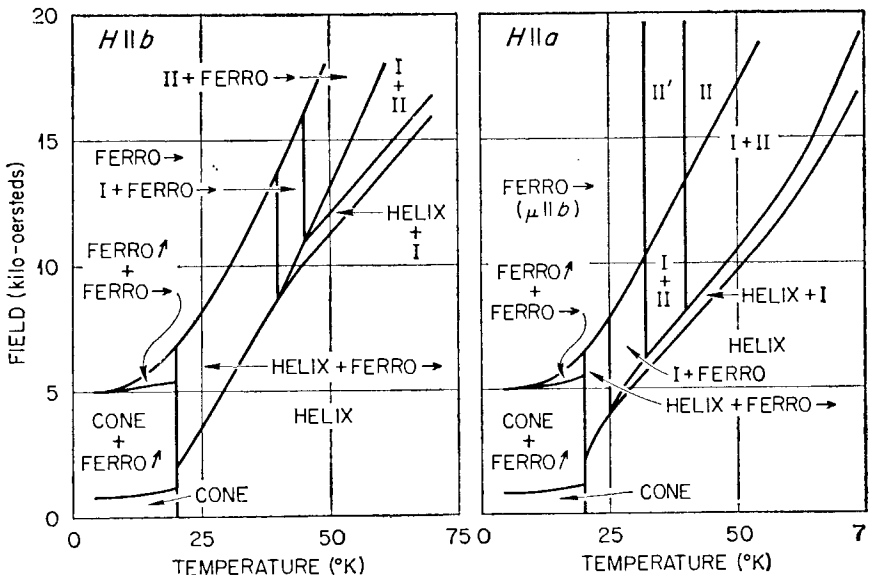

Fig. 7.10. Schematic H–T phase diagrams for single-crystal holmium in fields applied parallel to the (easy) b-axis (left) and to the (hard) a-axis (right) [after Koehler et al. (1967)].

Atoji (1974) with very similar results. There are three distinct regions of long-range order: (i) a high-temperature region (80 K–52 K) in which the c-axis moment orders in a purely sinusoidal CAM-type structure, (ii) an intermediate temperature region (52 K–20 K) in which the basal plane moment orders in a periodic fashion and a third-harmonic modulation of the c-axis moment is observed, (iii) a low temperature structure (20 K and lower) where a ferromagnetic cone-structure is observed. As in the case of Ho, there appears to be a sensitivity of the q_m vs. T curve to the particular sample used, as seen in fig. 7.6, where the results of Cable et al. do not always agree with those of Habenschuss et al. As discussed in section 2.4 from the latter work there appears to be locking of the magnetic periodicity to commensuracy with the lattice periodicity at 33 K and 23 K, which is probably related to the susceptibility anomalies observed by Taylor et al. (1977) and Gray and Spedding (1968) (see section 2.4). The theory of Elliott and Wedgewood (1964) using a simple free-electron model for the RKKY interaction gives remarkably good agreement with the observed temperature dependence of q_m as shown in fig. 7.6. However, below T_C they predict a discontinuous increase of q_m to a constant value whereas a *decrease* is observed, presumably due to a discontinuous increase in magnetoelastic energy at T_C, or to larger effects of the gap due to ferromagnetic ordering than estimated in the theory. As in the other lanthanide metals, there are small magnetostrictive changes in the lattice constants at the magnetic transitions, and the results of the neutron diffraction measurements (Habenschuss et al., 1974) are shown in fig. 7.11.

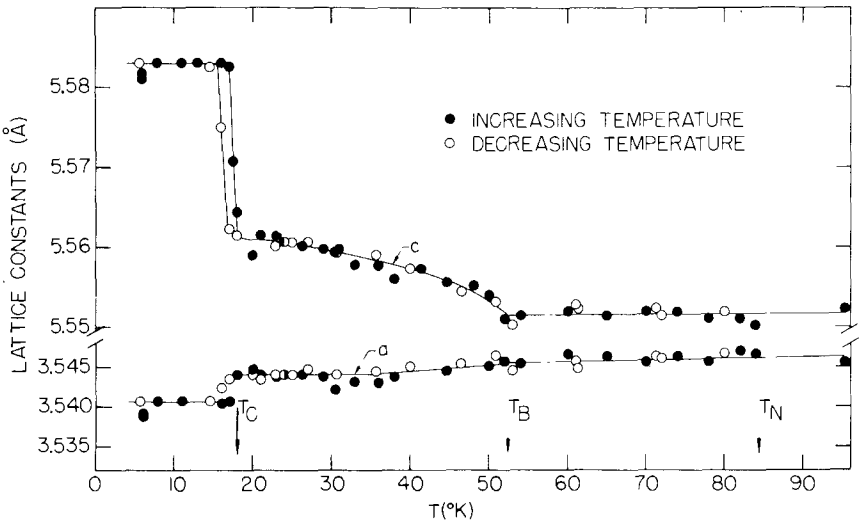

Fig. 7.11. Lattice constants c and a vs. temperature for Er. T_B is the basal plane ordering temperature [after Habenschuss et al. (1974)].

Below T_N, the CAM structure slowly "squares up" by developing higher harmonics, whose appearance does not seem to be directly connected to the appearance of ordered basal plane moments. As many as 17 harmonics of the c-axis modulation have been observed as the temperature is decreased to 22 K. The relative phases of the various harmonics are, of course, undetermined. In the earlier measurements (Cable et al., 1965) only first and third harmonics were observed and phase angles of $5\pi/8$ and $15\pi/8$ respectively, were assigned to these so as to not exceed on any site the maximum allowed moment along the c-axis. In the more recent measurements, a similar phase assignment of $n(5\pi/8)$ to the nth harmonic does cause the moment to exceed this value. However, just above T_C at 22 K, the root-mean-square moment calculated from the sum of the intensities of the harmonics is 7.7 μ_B which is almost equal to the value (7.8 μ_B) of the c-axis ordered moment in the cone phase at the lowest temperature, i.e. the maximum ordered c-axis moment allowed by the anisotropy. Thus the c-axis moment above T_C is approaching a completely squared up structure with half of the atoms having a maximum moment of 7.7 μ_B "up" and half having the same moments "down". At approximately 52 K, the basal plane moment orders with a q_m which always has the same periodicity as the c-axis modulation. At lower temperatures third and fifth harmonics of the basal plane modulation appear, which disappear at 22 K when the ferromagnetic cone structure appears. At 6 K, $\mu_\parallel$ and $\mu_\perp$ have been found to be (7.80 ± 0.12) μ_B and (4.44 ± 0.12) μ_B respectively, so that within experimental precision the magnetic moment per atom is the free-ion value of 9.0 μ_B. The cone angle is 29.6°. As stated above a semi-quantitative explanation of these results is given by the self-consistent molecular field calculation of Jensen (1976a). Neutron diffraction results for Er

in magnetic fields have been reported by Atoji (1974) and by Rhyne and Pickart (1972).

3.2.6. *Thulium*

The magnetic structure was first obtained by Koehler et al. (1962). Further work on high-purity crystals was carried out by Brun et al. (1970). At T_N of 56 K, the moments order along the c-axis in a CAM type structure which gradually squares up at lower temperatures once the amplitude begins to exceed the free-ion moment of 7.0 μ_B at roughly 40 K. At 32 K, a ferromagnetic component appears and at the lowest temperatures an anti-phase domain "square-wave" structure is obtained with four layers having "up" (i.e. parallel to c-axis) spin and the next three having "down" spin over an exact seven layer repeat distance. The ordered moment per atom is 7.0 μ_B with a resultant ferromagnetic moment of 1.0 μ_B in agreement with magnetization data. The data of Brun et al. (1970) for the temperature variation of the magnetic periodicity (see left insert of fig. 7.5) show that at 32 K, there is a first order transition below which q_m suddenly stays constant at a value of exactly $(0, 0, \frac{2}{7})2\pi/c$ corresponding to a seven-layer repeat distance. There is also some temperature hysteresis associated with this transition, which also accounts for anomalies seen in the transport properties of Tm crystals at 32 K as discussed in section 2.4. The sine-wave along the c-axis squares up *symmetrically* from 40 K to 32 K, then locks into commensuracy with the lattice and a zeroth harmonic (or ferromagnetic component) then sets in below 32 K.

3.3. *Alloys of heavy lanthanide metals*

As discussed in section 2.5, there has been quite a lot of work done on binary intra-lanthanide alloys. Practically all the systems studied to date have been discussed in the review article by Koehler (1972) and by Millhouse and Koehler (1971). These include the Er–Dy, Er–Tb, Er–Ho, Er–Gd, Ho–Tb, and Ho–Dy alloy systems. As stated previously, the results can be interpreted in terms of homogeneous magnetically ordered systems (with common ordering temperatures and moment directions for the constituent atoms) showing the dominance of exchange over anisotropy forces. Since Gd has negligible anisotropy, its main effect seems to be to increase the exchange interaction and raise the ordering temperatures of its host without changing the magnetic phases. Figure 7.12 indicates the magnetic phase diagram found for the Er–Dy system. As might be expected, addition of Dy to Er raises the temperature at which the basal plane moment orders relative to that at which the c-axis moment orders, so that with the addition of more than roughly 10% Dy it is in fact the basal plane moment which develops at T_N and the CAM-structure which is superimposed on it at lower temperatures. The same qualitative behavior is true for Er–Tb alloys. An interesting recent development is the discovery of *inhomogeneous* magnetic phases in the Tb–Tm system (Hansen et al., 1975). Single crystals of $Tb_{0.45}Tm_{0.55}$

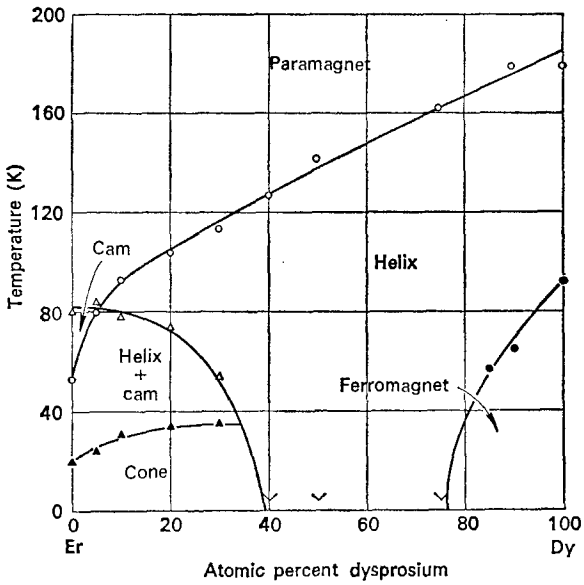

Fig. 7.12. Magnetic phase diagram for the Er–Dy system [after Koehler (1972)].

and $Tb_{0.35}Tm_{0.65}$ have been investigated. Just below T_N, a basal plane spiral develops, followed at lower temperatures by the appearance of a CAM-type moment. At still lower temperatures, the c-axis component becomes ferromagnetic. At low temperatures, the value of $(\mu_\parallel^2 + \mu_\perp^2)^{1/2}$ calculated from the c-axis and basal plane components respectively is less than the expectation value of μ for pure Tb and pure Tm. This is then interpreted as indicating the presence of a heterogeneous phase in which the Tb spins lie in the basal plane while the Tm spins lie along the c-axis. The breaking up of the homogeneous spin arrangement in this case is presumably caused by the large and widely disparate axial anisotropy energies for Tb and Tm respectively, making it energetically favorable for the structure to sacrifice some lowering of exchange energy by becoming heterogeneous.

Studies of alloys of heavy lanthanide metals with the non-magnetic metals Y, Lu, Sc and Th have also been performed. The first three are isoelectronic with the outer shells of the heavy lanthanide atoms and form continuous solid solutions having the hcp structure. However, of these, Sc causes a significant change in the lattice constants owing to its much smaller atomic volume, and as discussed in section 2.5 this can strongly affect the exchange interaction. Thus Y and Lu should be regarded as true non-magnetic diluents of the exchange interaction and ordered moment in heavy lanthanide systems. Most of the experiments have been performed on polycrystalline specimens of these alloys (Child et al., 1965; Child and Cable, 1969), and have been recently reviewed by Koehler (1972). Figure 7.13 summarizes the data for the initial ordering temperatures of R–Y alloys (which correspond to the high temperature ordered

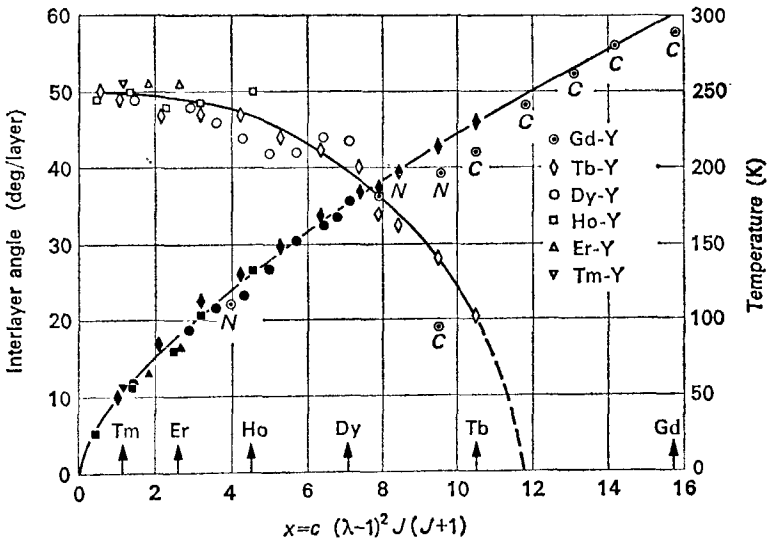

Fig. 7.13. Magnetic properties of R–Y alloys. The left hand side scale denotes the value of the initial interlayer turn angle (at T_N), and the right hand side scale the value of the initial ordering temperature vs. the effective de Gennes factor. For the Gd alloys, the symbol "C" denotes the Curie temperature, and "N" the Néel temperature [after Koehler (1972)].

phases of the pure lanthanide except for dilute Gd in Y alloys which order helically). These follow the expected universal $G^{2/3}$ variation with the effective de Gennes factor (as do the R–Lu alloys) (Child et al., 1965). Also shown is the variation of interlayer turn angle which saturates near the pure Y limit to a universal value of about 50° per layer. This corresponds closely to the q_m at which the generalized susceptibility function $\chi(q)$ for pure Y has a maximum (Liu et al., 1971). (See also the discussion in section 5.3.) The Curie temperature is rapidly suppressed on alloying Y into Tb, Dy and Er, as discussed in section 2.5. Alloying with Sc reduces the initial ordering temperatures much more rapidly than in the case of Y, so that above about 80% Sc no magnetic ordering remains in contrast to the observed ordering of 5% of Tb in Y, for example. In other respects, however, these alloys behave similarly to Y alloys, i.e. with regard to type of ordering and a universal limiting q_m in the dilute lanthanide limit. This q_m agrees quite well in position with one of elements. Gupta and Freeman (1976a) however, find that inclusion of the matrix elements suppresses the peaks in $\chi(q)$. They suggest that an incipient spin-density wave instability in Sc may strongly influence the magnetic ordering observed on adding lanthanide atoms to Sc and show that local field effects in the exchange enhancement of $\chi(q)$ for Sc help stabilize the q_m to the observed value.

Recently single crystal diffraction studies of $Er_{0.75}Lu_{0.25}$ (Habenschuss et al., 1973) and $Ho_{0.9}Sc_{0.1}$ (Felcher et al., 1976) have been performed. In the case of $Er_{0.75}Lu_{0.25}$, structures identical to those of the high and intermediate temperature phases of Er were observed but with the c-axis ordering temperature T_N lowered

to 68 K and the basal plane ordering temperature T_B lowered to 60 K. (The latter fact accounts for the magnetization anomalies seen at 40 K in the alloy (Gray and Spedding, 1968).) Squaring up of the c-axis modulation was observed, but no ferromagnetic transition was observed down to 4.9 K, i.e. the low-temperature phase of Er is suppressed. Both T_N and T_B appeared to correlate well with the effective de Gennes factor. In the case of $Ho_{0.9}Sc_{0.1}$, the observed structures (including basal plane bunching effects) were similar to those observed in pure Ho, but with lowered transition temperatures. The low-temperature value of q_m, however, was appreciably different from the various values observed for several samples of pure Ho and again reflects the strong sample dependence of q_m for this material.

The rare earth-thorium system, as might be expected (considering that Th is a tetravalent impurity), does not fall on the universal curves discussed above. Recent single crystal data have been taken (Child and Koehler, 1971) and are reviewed by Koehler (1972).

3.4. *The light lanthanide metals*

The lanthanide earth metals do not crystallize in the hcp structure common to the heavy lanthanide metals. Pr, Nd and certain phases of La and Ce crystallize in the double hexagonal close packed (dhcp) structure (see ch. 2, section 6). Thus if the stacking sequence of layers along the c-axis in hcp crystals is ABAB . . . , and that in fcc crystals along the [111] axis is ABCABC . . . , then the stacking sequence along the c-axis for dhcp crystals is ABACABAC . . . Atoms in the B and C layers have nearest neighbor environments of hexagonal symmetry and those in A layers have cubic environments. Thus, there are in general two different sets of crystal field levels, associated with atoms on cubic and hexagonal sites. As discussed in section 2.6, crystal field effects in light lanthanides are large enough to be comparable to exchange effects.

3.4.1. *Samarium*

Neutron diffraction studies of the magnetic structures have been performed by Koehler and Moon (1972) on a single crystal of Sm enriched with the low-capturing isotope ^{154}Sm. The crystal structure of Sm is quite complicated, and consists of a nine-layer stacking sequence ABABCBCAC . . . of hexagonal close-packed layers (with domains of the inverse sequence ACACBCBAB . . . coexisting in the structure). The B and C sites have hexagonal near neighbor environments, while the A sites have cubic environments. The Sm ion is trivalent in the $4f^5$ configuration which by application of Hund's rules yields the ground state $^6H_{5/2}$ ($L = 5$, $S = \frac{5}{2}$, $J = \frac{5}{2}$). The large cancellation of spin and orbital moments on this ion leads to interesting effects in the magnetic form factor and this will be discussed in section 6. Below 106 K, the moments on the hexagonal sites only order in ferromagnetic sheets (which are the hexagonal layers) parallel or antiparallel to the c-axis in the sequence $0++0--0++\cdots$ as shown in fig.

7.14(a). (Zeros represent the disordered cubic sites.) The magnetic unit cell is twice as long along the c-axis as the chemical unit cell. The symmetry of the structure is such that the exchange field on the cubic sites exactly vanishes, in complete agreement with the lack of observed order on those sites. Below 13.8 K, the cubic sites order and the structure changes to one in which the magnetic unit cell has its c- and one of its a-axes four times those of the chemical unit cell. The hexagonal site moments retain their high temperature structure. The extra reflections have been analyzed by Koehler and Moon, who propose a magnetic structure on the cubic site layers which consists of ferromagnetic rows parallel to the hexagonal a_2 axis, with a $+ + - - \cdots$ sequence

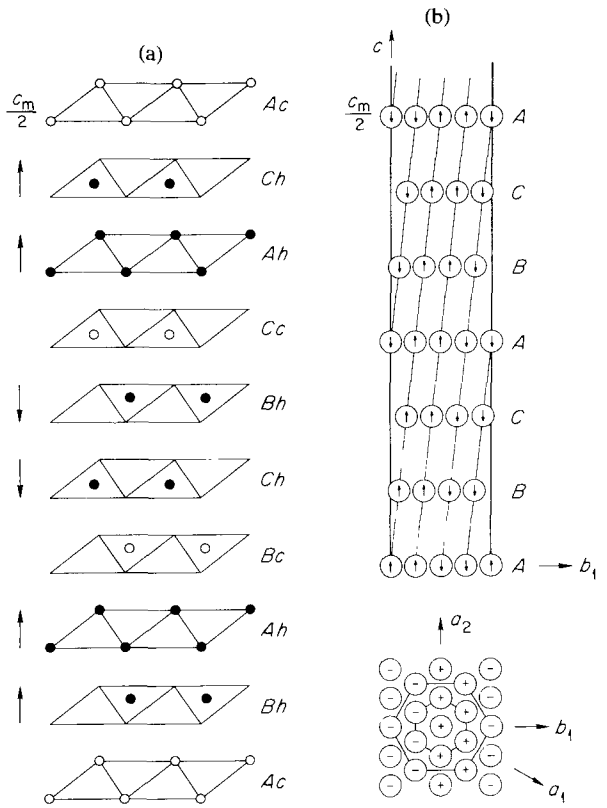

Fig. 7.14. Magnetic structures of Sm. (a) High temperature structure involving only the hexagonal-site ions. Closed circles, hexagonal sites (h); open circles, cubic sites (c). The hexagonal sites are coupled ferromagnetically within layers normal to the c-axis. The moment direction is indicated by arrows. Only half of the magnetic cell is shown. The upper half is the same as the lower half, but with all the moments reversed. (b) Low-temperature structure involving only cubic-site ions. The lower part shows the arrangement of spins within a layer normal to the c-axis. In the upper part is shown a projection of the magnetic unit cell onto the a^*–c^* plane. The arrows stand for rows of atoms along the a_2 direction with moments directed along the arrows. The hexagonal sites are shown. Only half the magnetic cell is shown. The upper half is generated by reversing all the moments in the lower half and translating by $\frac{1}{2}c_M$ (after Koehler and Moon, 1972).

along the a_1 axis (see fig. 7.14b), the moments again being parallel or antiparallel to the c-axis. The ferromagnetic rows in the different cubic layers are coupled to form ferromagnetic sheets parallel to $(\bar{1}01)$ planes, with a stackup sequence normal to these sheets of the form $++--\cdots$. Koehler and Moon have discussed the observed structures from the point of view of exchange interactions out to a few neighbors (for the cubic layers only exchange interactions within the layer were considered) and conclude that the exchange interaction must be oscillatory and fairly long range in accordance with the behavior expected from the RKKY (indirect exchange) interaction via the conduction electrons.

3.4.2. *Europium*

This metal has the body-centered cubic structure, and the ion is believed to be in a divalent $^8S_{7/2}$ state. Earlier diffraction investigations on polycrystalline samples were carried out by Nereson et al. (1964) and more recently a single crystal sample has been studied by Millhouse and McEwen (1973). At 90.5 K, there is a *first order* transition (observed as a discontinuous appearance of magnetic satellites) to an antiferromagnetic state corresponding to a spiral structure along a cube axis, the plane of the spiral being the plane normal to the cube axis. (Obviously, three equally populated domains corresponding to the three different cube axes will exist.) The turn angle per layer was observed to vary only slightly from 51.4° per layer at T_N to 50.0° per layer at 4.2 K. (The single crystal work reports $(47.6 \pm 1.2)°$ per layer at 4.2 K.) Diffraction studies were also made at 4.2 K on a single crystal in applied magnetic fields up to 41.7 kOe (Millhouse and McEwen, 1973). The results indicated stabilization of domains with the pitch of the helix along the field direction at the expense of those with the pitch normal to the field direction. The powder data yielded an ordered moment at 4.2 K of $(5.9 \pm 0.4)\ \mu_B$ per atom which is rather less than the expected value of $7.0\ \mu_B$. The observed q_m occurs at 15% less than the value for the separation of nearly parallel pieces of the Fermi surface of Eu as calculated by Andersen and Loucks (1968). More recently, Davis and Cooke (1977) have shown that matrix elements play a very important role in determining the maximum in $\mathcal{J}(q)$ and find reasonable agreement for Eu using an electronic band structure calculation.

3.4.3. *Cerium*

It has unfortunately not yet been possible to obtain a large enough single crystal of Ce for detailed neutron diffraction studies, although it appears likely that this situation will be changed before long. The properties of the various phases of Ce have been discussed in detail in ch. 4. Here we shall confine ourselves to the dhcp or β-phase, which is the only one which exhibits magnetic ordering. Powder diffraction studies carried out by Wilkinson et al. (1961b) showed three very weak additional reflections developing below a T_N of 12.5 K. They suggested a possible magnetic structure with moments parallel or

antiparallel to the c-axis, with an ordered moment per atom of $0.62\,\mu_B$. (The maximum ordered moment for the $^2F_{5/2}$ ground state of the Ce^{3+} ion is $2.14\,\mu_B$.)

3.4.4. *Prometheum*

This element has no stable isotope and is consequently intensely radioactive. Nevertheless, neutron studies have been carried out on a polycrystalline rod of ^{147}Pm by Koehler et al. (1972). The crystal structure is dhcp, and Hund's Rules predict the free ion ground state to be $^5I_4$ for which the fully ordered moment is $2.4\,\mu_B$. No direct evidence was found for magnetic ordering, i.e. no extra intensity appeared either on or between the Bragg reflections at low temperatures compared to that at room temperature, nor did there appear any observable change in diffuse scattering attributable to magnetic ordering. However, the depolarization of a polarized beam of neutrons transmitted through the sample increased below 98 K indicating the formation of ferromagnetic domains. From these measurements, the authors estimated a mean moment of $0.24\,\mu_B$ per atom and concluded that it would have been below the threshold of observation in the direct experiments. Since Pm has an even number of f-electrons (4) it is possible for the crystal field to produce a singlet ground state on both hexagonal and cubic sites so that it may be an example of weak induced magnetism as discussed in section 2.6. A point charge crystal field calculation however, yields doublet ground states at both sites (Koehler et al., 1972).

3.4.5. *Neodymium*

Single crystal diffraction studies of the magnetic structure have been performed by Moon et al. (1964) and more recently by Johansson et al. (1970). The crystal structure is dhcp. Below 19.2 K, the moments on the hexagonal (A and B) sites order in the basal plane parallel to the $[10\bar{1}0]$ reciprocal axis ($\boldsymbol{b}_1$) with a sinusoidal modulation also along $\boldsymbol{b}_1$, see fig. 7.15. The moments on the B and C layers are antiferromagnetically coupled. Below 7.8 K, the moments on the cubic (A) sites order in the basal plane with a modulation vector also along $\boldsymbol{b}_1$ (but of different magnitude to the hexagonal-site modulation vector), but with the moments 30° to $\boldsymbol{b}_1$. Moments in alternate A layers are also antiferromagnetically coupled. Thus, for B and C layers the ordered moment on the ith atom is given by

$$\boldsymbol{J}_{Bi} = -\boldsymbol{J}_{Ci} = \mu_h \boldsymbol{b}_1 \cos(\boldsymbol{q}_h \cdot \boldsymbol{R}_i + \phi_h) \tag{7.47}$$

while for the A layers, it is given by

$$\boldsymbol{J}_{Ai} = -\boldsymbol{J}_{A'i} = \mu_c \boldsymbol{b}_2 \cos(\boldsymbol{q}_c \cdot \boldsymbol{R}_i + \phi_c) \tag{7.48}$$

The low temperature value for θ_h is $(.\pm 0.2)\,\mu_B$ and for μ_c is $(1.8 \pm 0.2)\,\mu_B$, both lower than the full free ion moment of $3.2\,\mu_B$, indicating the importance of crystal field effects. $\boldsymbol{q}_h$ varies with temperature from $0.13\,\boldsymbol{b}_1$ at 19.2 K to $0.11\,\boldsymbol{b}_1$ *at* 7.8 K, while $\boldsymbol{q}_c = 0.15\boldsymbol{b}_1$, and both $\boldsymbol{q}_h$ and $\boldsymbol{q}_c$ do not vary below 7.8 K. A puzzling feature of the data is the inequality of intensities for the $+\boldsymbol{q}_h$ and $-\boldsymbol{q}_h$ satellites

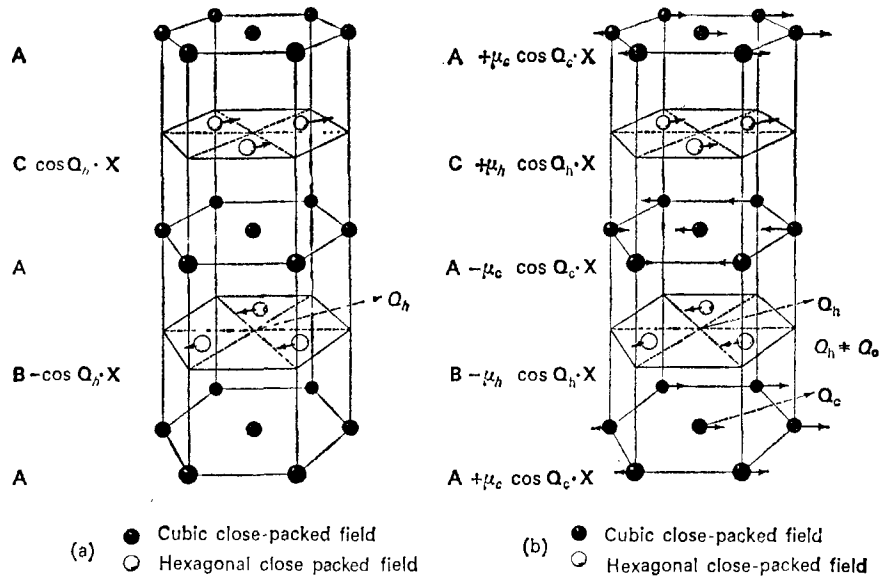

Fig. 7.15. Magnetic structures of neodymium, (a) $7.5 < T < 19$ K (b) $T < 7.5$ K [after Koehler (1972)].

around certain reciprocal lattice points; and the occurrence of weak hexagonal site satellites along the b_1 axis indicating some ordered moment normal to the b_1 axis. In addition, there appears to be some dependence of the magnetic periodicity vectors on the relative orientations of the moments in adjacent layers in different domains, as witnessed by a slight splitting in the satellite peaks below the cubic site ordering temperature. This splitting disappears on formation of a single-domain crystal in a field of 7 kOe at 4.2 K applied along the b_2 axis (Johansson et al., 1970). By 12 kOe, the moments on the hexagonal sites have turned parallel to those on the cubic sites, and ferromagnetic moments are induced on the cubic and hexagonal sites in the ratio of 5:2. At higher fields, the moment on the hexagonal sites shows abrupt increases, presumably due to crossing of crystal field levels. A detailed explanation of the magnetic structure and its field dependence in terms of crystal fields and molecular fields and exchange coupling between cubic and hexagonal sites has yet to be performed.

3.4.6. *Praseodymium*

Polycrystalline samples of dhcp Pr were studied by Cable et al. (1964a) and below 25 K, showed magnetic reflections indicating a structure very similar to that of Nd, with a low temperature ordered moment of about 1 μ_B per atom. Single crystal studies by Johansson et al. (1970) however showed no magnetic ordering down to 4.2 K, indicating that dhcp Pr is indeed a singlet ground state system as discussed in section 2.6. The effects of strain on the crystal fields and consequent induced moment effects could be responsible for the magnetic ordering observed in the polycrystalline samples, since as we shall see, there is

considerable evidence that the exchange in this system is close to the critical value for an induced moment to appear. Thus, application of a magnetic field along the $\boldsymbol{b}_2$ direction in the single crystal produces large induced moments on both sets of sites (Johansson et al., 1970). The molecular field theory of Bleaney (1963) described in section 2.6 provides a fairly good fit to the field dependence of the induced moment with some modification of Bleaney's crystal field parameters for dhcp Pr, and indicates a value of A close to its critical value of 1. Pr in the metastable fcc phase (Bucher et al., 1969) and the closely related cubic alloy Pr_3Tl (Birgeneau et al., 1971b) appear to be weakly ferromagnetic at low temperatures. A detailed discussion may be found in the review article by Cooper (1972).

3.4.7. Pr–Nd *alloys*

Lebech et al. (1975) have studied single crystal samples of Pr–5.5% Nd, Pr–3.0% Nd and Pr–26.3% Nd which all form solid solutions of dhcp crystal structure. They observed antiferromagnetic ordering as given by eq. (7.47) for Nd on the hexagonal sites with a T_N which decreased from 11.4 K for the Pr–26.3% Nd alloy to 6.3 K for the Pr–3.0% Nd alloy. No ordering was observed on the cubic sites. $\boldsymbol{q}_h$ was at all temperatures observed to be within 10% of the value for pure Nd. These authors carried out a fit of a molecular field theory of the random alloy (neglecting all but the singlet ground state and the first excited doublet for the Pr ions and the doublet ground state for the Nd ions and also neglecting the cubic sites) to the observed variation of T_N with concentration and obtained good agreement with experiment. This yielded for pure Pr a value of the parameter A (the ratio between the exchange interaction and crystal field generalized to the case of finite wave vector $\boldsymbol{q}_h$) of 0.96 very close to the critical value of 1 for antiferromagnetic ordering, and in excellent agreement with the value of 0.93 derived from magnetic excitation data (see section 5.2). These authors also carried out a fit of the magnetization vs. temperature curves to a theory involving exchange interactions between the various constituents, i.e., J_Q^{PP}, J_Q^{PN}, and J_Q^{NN} together with a complete crystal field level scheme for both types of ions in the random alloy. They obtained the results $J_Q^{PP} = (0.665 \pm 0.007)$K, $J_Q^{PN} = (0.86 \pm 0.04)$K, and $J_Q^{NN} = (1.08 \pm 0.006)$K, which scale reasonably well in the ratios predicted by the appropriate de Gennes factors of the ions. For this purpose they assumed a value for the crystal field splitting D for Pr obtained earlier by Rainford (1972) of 28.3 K, and assumed that the Nd crystal field splittings were scaled down by a factor of 2.5. However, this fit should be considered with some scepticism as the magnetic exciton spectrum measurements on pure Pr (see section 5.2) yield values of $D = 40.6$ K and $J_Q^{PP} = 0.93$ K, somewhat different from those above.

3.4.8. *Light lanthanide–heavy lanthanide alloys*

The Tb-light lanthanide alloys have been studied by Achiwa and Kawano (1973). They studied $Tb_{0.8}La_{0.2}$, $Tb_{0.8}Pr_{0.2}$ and $Tb_{0.75}Nd_{0.25}$, all of which have the

Sm-type crystal structure. They find (below T_N of 124 K, 130.5 K and 129 K for these three alloys respectively) an antiferromagnetic structure identical to the high-temperature magnetic structure of Sm (fig. 7.14) except that the moments lie *in* the basal plane layers rather than parallel to the c-axis, presumably due to the characteristic single ion anisotropy of the Tb ions. The identical nature of the magnetic periodicity for these alloys and for pure Sm indicates that the generalized susceptibility of the conduction bands associated with the Sm-type crystal structure plays an important role in determining the magnetic order. Below 30 K, the Pr and Nd alloys transform martensitically to a hcp crystal structure, and at these low temperatures, basal plane ferromagnetic order similar to that in pure Tb was observed.

3.5. *Rare earth compounds*

The number of all possible magnetic rare earth compounds is too vast to attempt a complete discussion in this chapter. We shall, instead, attempt to describe the results for the simplest and most well-characterized (mainly binary) rare earth compounds, and concentrate on systems for which neutron diffraction results are available.

A fairly recent review of the physical properties of a large number of the rare earth intermetallic compounds may be found in the article by Taylor (1971) (also see chs. 9, 11, 13, 14, 15 and 18). A comprehensive review of the magnetic properties of such compounds has also been given by Wallace (1971) and Kirchmayr and Poldy (ch. 14). The reader may also refer to the review article by Bertaut (1972). As discussed in section 2.6, the basic physics involved in the magnetism of these materials involves the interplay between comparable exchange and crystal field effects, as in the light lanthanide metals, with possible additional complications resulting from interactions with lattice phonons.

For those materials for which the neutron diffraction results are not given here, bulk magnetic measurements are usually available from which one may deduce the structure (although indirectly) and their properties may be looked up in one of the aforementioned reviews.

3.5.1. *Compounds with group-V elements (the lanthanide-pnictides)*

These were some of the earliest lanthanide compounds studied, and were first investigated by the Oak Ridge group (Child et al., 1963). Trammell (1963) was the first to provide a detailed theoretical description of their magnetic properties in terms of an interplay between crystal field and exchange effects, as discussed in section 2.6. Over the last few years these materials have been the subject of continuing experimental and theoretical interest. Busch (1967) and Junod et al. (1969) have given reviews of their magnetic properties (see also ch. 33).

The materials are all metallic (except possibly for some of the nitrides) and possess the NaCl structure. The exchange interaction between the lanthanide ions is thus probably of the RKKY type and involves oscillatory long range

components. The crystal field parameters may be estimated by fitting to susceptibility and magnetization data (Junod et al., 1969; Cooper and Vogt, 1970a,b) or from inelastic neutron scattering data (to be discussed in section 5). In general, point charge calculations of the crystal field are not too reliable, although they may yield qualitatively correct results. Table 7.2 summarizes some of the magnetic properties of these compounds. The lattice constants are smallest for the nitrides, owing to the small ionic radius of the nitrogen ion and increase with the size of the anions. They also decrease with the size of the cation as one goes across the lanthanide series.

The magnetic structures are, by and large, consistent with an exchange interaction which wants to impose a magnetic periodicity along a [111] direction, and strong crystal field anisotropy forces which keep the moments pointing along easy axes (e.g. [100] for Dy^{3+} and Ho^{3+}, [111] for Tb^{3+}, etc.) and perhaps also force the structure to be commensurate so that full advantage can be taken of the crystal field. Magneto-elastic forces may also play a similar role. Thus, HoN has a complex structure (Child et al., 1963) which corresponds to seven sheets of lanthanide spins normal to the [111] axis pointing along $+x$, then seven more sheets pointing along $+y$, and then the next seven sheets pointing along $+z$ (see fig. 7.16a), thus simulating a "bunched cone" with a net ferromagnetic moment. The neutron diffraction patterns for the other nitrides of the heavy rare earths are similar and indicate very similar structures, except that in TbN, the

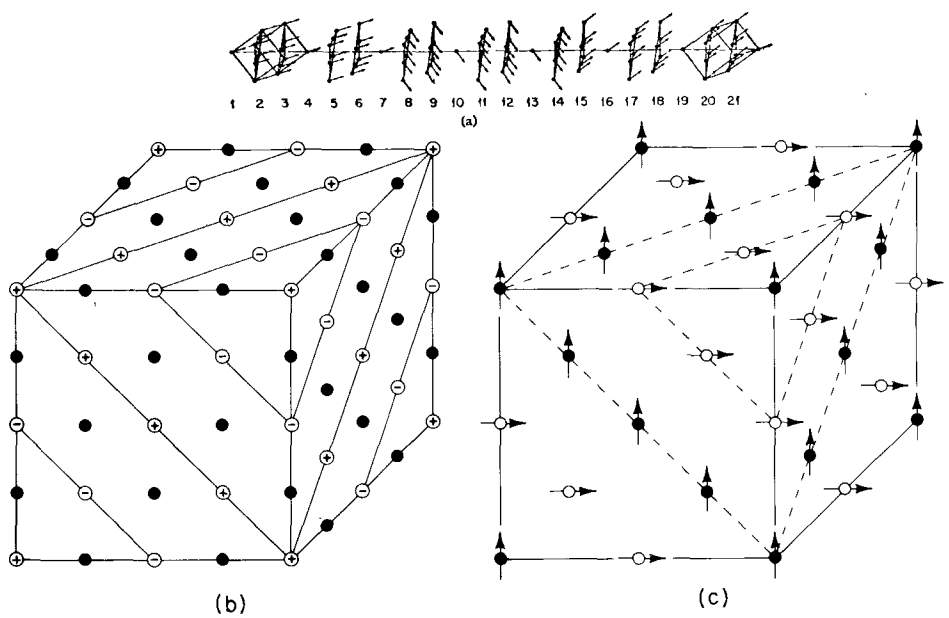

Fig. 7.16. (a) Possible magnetic structure of HoN [after Child et al. (1963)]. (b) Mn–O type (Type II) antiferromagnetic structure. The open circles represent the magnetic atoms with + and − symbols denoting moments parallel and antiparallel to the [111] direction. The closed circles represent the non-magnetic atoms. (c) Magnetic structure of HoP [after Child et al. (1963)].

TABLE 7.2.
Magnetic structures of the lanthanide monopnictides.

Compound	Magnetic structure	Ordering temp. T_N (T_C) (in K)	Max. ordered moment on lanthanide ion (μ_B)	Max. free ion moment (μ_B) ($g_J J$)	Ref.
CeN	Does not order			2.14	Fischer et al. (1976)
PrN	Does not order			3.2	Busch (1967)
NdN	Ferromagnetic μ along [001]	28	2.69	3.28	Schobinger-Papamantellos et al. (1973)
GdN	Ferromagnetic	72	6.6	7.94	Busch (1967)
TbN	Ferromagnetic spiral (μ along [111] directions)	42	7.0	9.0	Child et al. (1963)
DyN	Ferromagnetic spiral (moments along [100] directions)	26	7.4	10.0	Child et al. (1963)
HoN	Ferromagnetic spiral (μ along [100] directions) (or ferro, with s.r. order)	18	8.9	10.0	Child et al. (1963) Fischer and Kaldis (1976)
ErN	Ferromagnetic spiral ($\mu \perp$ to [111] directions)	5	6.0	9.0	Child et al. (1963)
TmN	Does not order			7.0	Child et al. (1963)
CeP	Type I along [001]	9.5	0.79	2.14	Rainford et al. (1968) Meier and Vogt (1976)
PrP	Does not order			3.2	Busch (1967)
NdP	Type I along [001]	11	1.82	3.28	Fischer et al. (1971) Schobinger-Papamantellos et al. (1973)
GdP	Antiferromagnetic	15		7.0	Busch (1967)
TmAs	Does not order			7.0	Busch (1967)
CeSb	Sinusoidal (CAM) μ and q_m along [001]	16	2.1	2.14	Lebech et al. (1971)
NdSb	Type I μ along [001]	16	2.98	3.27	Fischer et al. (1971) Schobinger-Papamantellos et al. (1973)

GdSb	Antiferromagnetic	28		7.0	Busch (1967)
TbSb	Type II (MnO) μ along [111]	14	8.2	9.0	Child et al. (1963)
DySb	Type II (MnO) μ along [001]	9.5	9.8	10.0	Felcher et al. (1973)
HoSb	Type II (MnO) μ along [001]	9	9.3	10.0	Child et al. (1963)
ErSb	Type II (MnO) $\mu \perp$ to [111]	3.7	5.7	9.0	Child et al. (1963)
TmSb	Does not order			7.0	Busch (1967)
CeBi	(High temp.) Type I along [001] (Low temp.) Type Ia along [001]	26 13	2.0	2.14	Nereson and Arnold (1971)
NdBi	Type I along [001]	24	3.1	3.28	Nereson and Arnold (1971)
TbBi	Type II (MnO) μ along [111]	18	7.9	9.0	Nereson and Arnold (1971)
DyBi	Type II (MnO)	13	8.7	10.0	Nereson and Arnold (1971)
TbP	Type II (MnO) μ along [111]	9	6.2	9.0	Child et al. (1963)
DyP	Ferrimagnetic (?)	8		10.0	Busch (1967)
HoP	"Flip-flop" (see text)	5.5	8.8	10.0	Child et al. (1963)
ErP	Type II (MnO) $\mu \perp$ to [111]	3.1	5.7	9.0	Child et al. (1963)
TmP	Does not order			7.0	Busch (1967)
CeAs	Type I μ along [001]	7.5	0.88	2.14	Rainford et al. (1968) Meier and Vogt (1976)
PrAs	Does not order			3.2	Busch (1967)
NdAs	Type I μ along [001]	11	2.18	3.27	Fischer et al. (1971) Schobinger-Papamantellos et al. (1973)
GdAs	Antiferromagnetic	25		7.0	Busch (1967)
TbAs	Type II (MnO) μ along [111]	12	7.7	9.0	Child et al. (1963)
DyAs	Ferrimagnetic (?)	8.5		10.0	Busch (1967)
HoAs	Type II (MnO)	4.8		10.0	Busch (1967)
ErAs	Type II (MnO)	3.5		9.0	Busch (1967)

moments lie along [111] directions, while in ErN they lie perpendicular to the [111] directions (probably [110] directions) (Trammell, 1963). It should be pointed out that the diffraction work was done on polycrystalline material, so it is difficult to say that the deduced structure is unique, since the various satellites reflections overlapped considerably. Fischer et al. (1976) have recently re-examined several more powder samples of HoN including samples of varying stoichiometry. They find a sensitivity of the diffraction peaks to sample stoichiometry and ascribe the broad powder peaks seen by Child et al. (1963) to short-range ferromagnetic ordering rather than a complex spiral structure with overlapping reflections. TmN does not order down to 1.5 K. In the case of the light lanthanide nitrides, CeN does not appear to order at all (Fischer and Kaldis, 1976), while NdN is ferromagnetic with an ordered moment of 2.69 μ_B (Schobinger-Papamantellos et al., 1973). Crystal field calculations (Trammell, 1963) indicate that the easy axes are in fact the directions the moments are observed to point along the various heavy lanthanide ions.

Most of the other heavy lanthanide compounds are antiferromagnetic and correspond to the MnO-type antiferromagnetic structure with ferromagnetic sheets perpendicular to the [111] axis, spins in adjacent sheets being antiparallel (Child et al., 1963). (See fig. 7.16b.) The moment directions are again along the easy axes for the appropriate lanthanide ions, as determined by the crystal field and are the same as in the corresponding nitrides. HoP (Child et al., 1963) has a structure shown in fig. 7.16(c) consisting again of ferromagnetic sheets normal to the [111] axis, but with the moments in alternate sheets being parallel to $+x$ and $+y$ respectively. Thus, there is a net ferromagnetic component parallel to the [110] direction and a net antiferromagnetic component parallel to the $[1\bar{1}0]$ direction. Trammell (1963) has shown that if the easy axes are in fact the (100) directions, and the antiferromagnetic interactions are only slightly larger than the ferromagnetic interactions, the above "flip-flop" structure can be stabilized by magnetic dipole-dipole interactions. However, as we shall see, higher order quadrupolar coupling (probably due to quadrupole-lattice interactions) are known to exist in these materials, and it is possible these may be more important in stabilizing this particular structure. The MnO-type antiferromagnetic structure (also called type II) has recently been confirmed for DySb in single crystal neutron diffraction measurements by Felcher et al. (1973). The moments lie along the [001] axis. Brun et al. (1974a) have performed neutron diffraction and magnetization measurements on DySb in fields of up to 60 kOe and find that the type II-phase goes into the HoP phase at high fields. A typical H–T phase diagram for H parallel to a [110] direction is indicated in fig. 7.17.

Although HoN (Child et al., 1963) was not observed to undergo any lattice distortions upon magnetic ordering, subsequently several of these compounds were observed to undergo such distortions (Levy, 1969a). Thus, the Nd^{+3}, Ho^{+3}, and Dy^{+3} compounds with easy axis along [100] were observed to distort tetragonally, while the Tb^{+3} compounds (easy axis along [111]) were observed to distort trigonally. The distortions were of the order of a few parts per thousand.

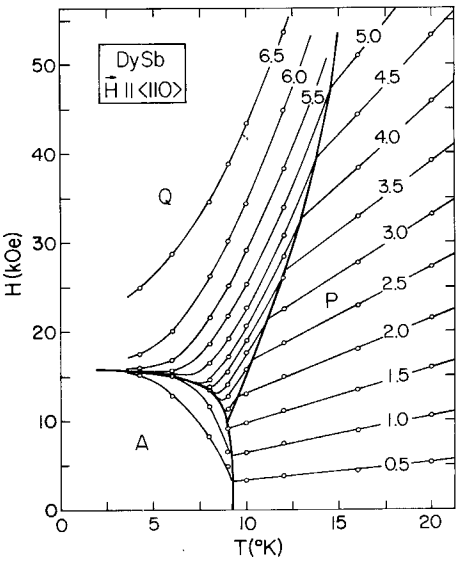

Fig. 7.17. The magnetic phase diagram of DySb for $\boldsymbol{H}$ parallel to ⟨110⟩. The phase marked P is paramagnetic, the A phase is the Type II antiferromagnetic state and the Q phase is the intermediate state with HoP structure (after Brun et al., 1974).

It was shown (Levy, 1969a) that the distortion lowered the crystal field ground state energy by about 10% of the overall spilling of the J-multiplet. (GdSb and TmSb did not distort, the former presumably because of the lack of orbital coupling to the lattice, and the latter because ordering was absent.) Initially the temperature of the transition to the distorted structure appeared to be a few degrees *above* the magnetic transition (Levy, 1969a). Levy and Chen (1971) formulated a theory including quadrupole-quadrupole coupling between the ions, and showed that if this was large enough compared to the usual bilinear exchange interaction, it could lead to a first-order transition in which the quadrupoles ordered (and led to a distortion of the lattice via quadrupole-lattice coupling) *without* net magnetic ordering, and a subsequent magnetic ordering at a slightly lower temperature, whose ordering temperature was enhanced above that due to bilinear exchange. Subsequently, however, careful measurements failed to reveal two ordering temperatures in any of these compounds. Thus Bucher et al. (1972) showed that the transition in DySb at 9.5 K was indeed first order but that the lattice distortion and magnetic ordering took place simultaneously. These authors found a 0.7% tetragonal contraction along the moment direction and an additional 0.1% distortion along the [111] axis parallel to the magnetic ordering vector. Felcher et al. (1973) observed a slight tilt of the moments away from the [001] axis just below T_N, which increased with temperature. The origin of the tilt is not yet clear. It is in fact likely, that the coupling to the lattice, via a quadrupole–lattice interaction, plays a vital role in determining the details of the ordered magnetic structure and the lattice distortion (as was in fact pointed out by Trammell (1963) in his original paper).

Stevens and Pytte (1973) have discussed this coupling along lines similar to the treatment of the cooperative Jahn–Teller effect observed in the rare earth vanadates (Elliott et al., 1972). They show that lattice distortions tend to stabilize selected minima of the crystal field potentials and that for ions which tend to order along a [100] axis the appropriate distortion is a tetragonal one, while for ions which tend to order along a [111] axis, trigonal distortions minimize the energy. They also present a model for the transition to the HoP structure by postulating a relative displacement of the P ions relative to the Ho ions in a $\pi/a(1, 1, 1)$ phonon mode and showing that such a distortion can stabilize the HoP structure given the right sign of exchange interactions. Neutron scattering studies of whether such a soft mode exists have yet to be performed. Stevens and Pytte also present similar ideas to explain the ordering in ErSb and ErP, where the moments lie perpendicular to the [111] axis, whereas the fourth order crystal field terms predict they should be parallel to it. They postulate a trigonal distortion and show that the observed moment directions can result. This distortion has also to await experimental verification.

Mullen et al. (1974) have made a systematic study of the temperature dependence of the susceptibility, specific heat and elastic constants of the heavy lanthanide antimonides. They are able to account for their data well with a theory which involves a hamiltonian containing a crystal field term, a purely elastic term, a term coupling the elastic strains to the quadrupole operators of the ions (due to the strain-dependence of the crystal field energies), and a quadrupole-quadrupole interaction (evaluated in a molecular field approximation) due to effects other than strains. (One such effect, that due to indirect quadrupole-quadrupole coupling via the conduction electrons is discussed by Sablik et al. (1973). Another such effect may be coupling via short wavelength or optical phonons (Elliott et al., 1972).) In particular, the coupling to the strains induces in some cases a softening of the shear modes with decreasing temperature which can drive the system into a structural phase transition (e.g. DySb and HoSb). In the case of ErSb no such softening of the shear modes was found. This is consistent with the previously mentioned ideas that transitions in ErSb (as in HoP) may be caused by coupling to zone boundary phonons rather than long wavelength modes. In all cases, the structural and magnetic phase transitions (Mullen et al., 1974) were observed to coincide. Uffer, Levy and Chen (1973) have presented a model similar to that described above, and with adjustment of the bilinear and biquadratic (quadrupole–quadrupole) parameters are able to obtain good agreement for the elastic and magneto-thermal behavior (at least above T_N) for DySb and to obtain a simultaneous first-order transition of crystal structure and magnetic ordering at 9.5 K. The lack of agreement below T_N may be due to domain-wall stress effects (Mullen et al., 1974). However, it seems likely that the simultaneous occurrence of both structural and magnetic transitions in all these compounds cannot depend on adjustment of biquadratic relative to bilinear coupling parameters, but must be an intrinsic feature of the dynamics of the system, which is not as yet satisfactorily understood.

To summarize, most of the lanthanide monopnictide systems are characterized

by the need to include coupling to lattice strains, as well as quadrupole–quadrupole coupling. This leads to significant biquadratic terms in the hamiltonian in addition to the usual bilinear exchange terms. It can also account for the elastic constant softening effects and lattice distortions observed in many of these materials.

A striking feature of these materials is the rapid decrease of the ordering temperatures as one moves away from the center of the lanthanide series to either side, in the direction of increasing orbital moments. Under these conditions, crystal field effects become larger relative to exchange. The extreme case is that of the Tm compounds, which do not order at all. Tm^{3+} is an even-f-electron ion ($J = 6$) and the crystal field produces a Γ_1 singlet as the ground state, while the exchange is below the critical value for ordering (see section 2.6). Cooper and Vogt (1970a) have analyzed the crystal field parameters for TmSb in terms of susceptibility and magnetization data, and obtain extremely good agreement with experiment. They find exchange is practically absent and that the fourth order term in the crystal field is dominant, the sixth order term being quite small. The same authors have analyzed similar data for the series of mixed $Tb_xY_{1-x}Sb$ compounds (Cooper and Vogt, 1970b). Tb^{3+} is also a $J = 6$ ion in a similar crystal field to that of TmSb. The effect of the dilution with Y being to "tune" the exchange from values below the critical value for ordering to values above it. The molecular field treatment proceeds as follows: if χ_{CF} is the susceptibility of the ions in the crystal field (in the limit $H \to 0$, as obtained by diagonalizing the crystal field hamiltonian in the usual way, and calculating χ from the resulting wave functions and energy levels), and M is the magnetization, we have

$$M = \chi_{CF}(H + \lambda M) \tag{7.49}$$

where H is the applied field and λ the molecular field constant. Equation (7.49) yields, on dividing by H,

$$1/\chi = 1/\chi_{CF} - \lambda \tag{7.50}$$

and λ is assumed to scale linearly with Tb concentration, i.e.

$$\lambda = C_{ex}X \tag{7.51}$$

The cubic crystal field strength (with only the fourth order term retained) can be expressed in terms of a single parameter W (Lea, Leask and Wolf, 1962) and C_{ex} and W are determined by fitting to the susceptibility curves. The magnetization curves may then be calculated by diagonalizing the hamiltonian $[\mathcal{H}_{cf} - g\mu_B \boldsymbol{J} \cdot \boldsymbol{H}_{app} + \lambda \boldsymbol{M})]$ and self consistently obtaining the thermal expectation value of $\boldsymbol{J}$. The Néel temperature for ordering in the MnO-type antiferromagnetic structure can be obtained from the condition,

$$g\mu_B\langle J_z\rangle = -\chi_{CF}\lambda g\mu_B\langle J_z\rangle \tag{7.52}$$

where we assume that each ion sees only exchange interactions from its neighboring ions, which are all supposed to be in the other sublattice. (For the

MnO-type structure this is not rigorously true but is satisfied, if the nearest-neighbor exchange is negligible compared to second-neighbor exchange. This appears to be the case in these compounds.) Equation (7.52) yields, for the ordering temperature T_N, the equation

$$\frac{1}{\chi_{CF}(T_N)} = -\lambda = -C_{ex}X \tag{7.53}$$

Cooper and Vogt were able to get good agreement for the susceptibility curves of a whole family of $Tb_xY_{1-x}Sb$ compounds with just the above two parameters

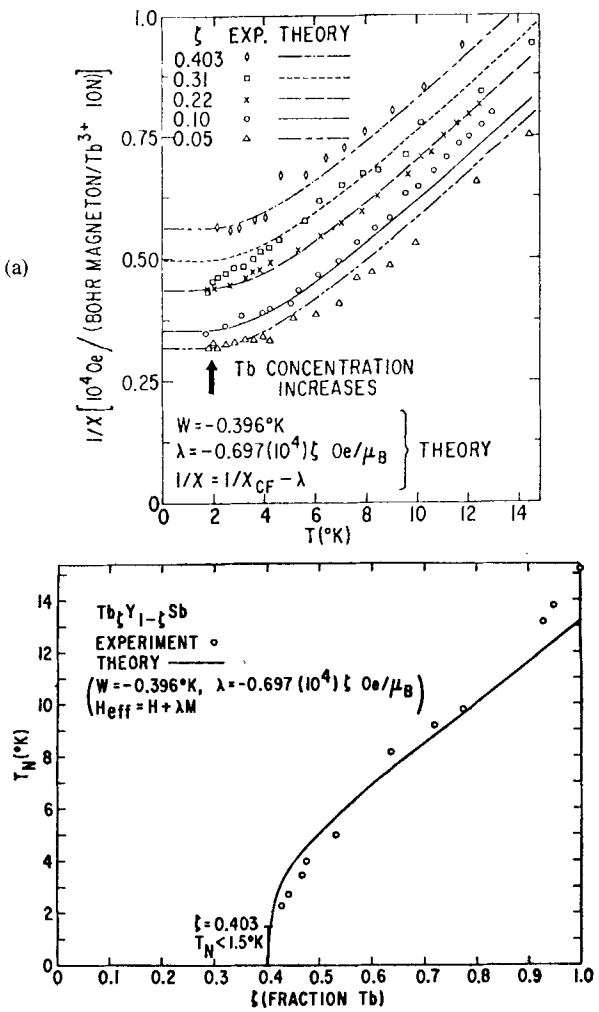

Fig. 7.18. (a) Inverse susceptibility per Tb ion vs. temperature for $Tb_\zeta Y_{1-\zeta}Sb$. (b) Néel temperature vs. terbium concentration in $Tb_\zeta Y_{1-\zeta}Sb$ (after Cooper and Vogt, 1970b).

(see fig. 7.18). Figure 7.18 also shows calculated and measured values of T_N vs. x using the same parameters. It is seen that good agreement is obtained, the critical value of exchange arising at a Tb concentration of 40.3%. These materials therefore are excellent examples of induced moment singlet ground state systems. (For these particular systems, it appears as though biquadratic exchange effects are not very important, although it may be seen from fig. 7.18 that for high x-values, the observed T_N's begin to be higher than the calculated values as would be the case if quadrupole interactions were present (Levy and Chen, 1971).)

The cerium monopnictides are the group in this family of compounds which behave anomalously. CeBi (Nereson and Arnold, 1971; Cable and Koehler, 1972) orders at 26 K in a type I antiferromagnetic structure, with ferromagnetic sheets perpendicular to the [001] axis, and alternate sheets having moments parallel and antiparallel to [001]. At $\sim\frac{1}{2}T_N$, there is a first order transition to a type Ia arrangement, where the sheets are now ordered two up, followed by two down. CeSb (Lebech, Fischer and Rainford, 1971) has a first order transition at ~ 16 K to a structure where there is a CAM-structure along the [001] direction with four lower temperature transitions into other such sinusoidal structures with differing periodicities. More recently Meier and Vogt (1976) have studied the mixed crystals $Ce_x(La, Y)_{1-x}Sb$, $Ce_xLu_{1-x}Sb$ and $Ce_x(La, T)_{1-x}Bi$, thereby diluting the Ce–Ce interaction. For $Ce_{0.4}(La, Y)_{0.6}Bi$ they find the type I structure stable down to 2 K. For $Ce_{0.7}(La, Y)_{0.3}Bi$, they find a type I structure at 16.5 K and a first-order transition to an incommensurate CAM arrangement at 10.5 K. For $Ce_{0.8}Lu_{0.2}Sb$ they observed a second order transition to a single incommensurate CAM structure at 14 K. For $Ce_x(La, Y)_{1-x}Sb$, they observed a stabilization of the type I structure and a lowering of T_N with decreasing x. CeP and CeAs order at 9.5 K and 7.8 K respectively (Rainford et al., 1968) into type I arrangements along [001]. A detailed discussion of these materials has recently been given by Cooper (1976). The easy axis of all these materials is [001] in contrast to the [111] direction predicted from a Γ_7 crystal field ground state. The latter is consistent with moment measurements and other evidence. Wang and Cooper (1970) were able to provide a phenomenological explanation of the structure and magnetization behavior, but only by postulating extremely anisotropic exchange interactions between the Ce^{3+} ions, the microscopic origin of which is still unclear. It is possible that some hybridization of the Ce f-levels with anion p-states or with conduction band states, as is known to happen in other Ce compounds (Varma, 1976) may be responsible for the unique behavior of these materials.

Powder diffraction data by Nereson and Arnold (1971) indicate that NdBi also has a type I ordering along the [001] axis. Fischer et al. (1971) have obtained the magnetic structures of NdP, NdAs and NdSb from powder neutron diffraction data, and find it to be the same as for NdBi. The ordered moments in NdBi and NdSb are comparable to the free ion moment, but are reduced in NdAs and NdP, reflecting the increase of crystal field due to decreasing lattice constants. In the case of Nd^{3+}, the [001] axis *is* an easy axis of magnetization.

3.5.2. *Compounds with noble metals and* Zn, Hg, Mg

These compounds are metallic and crystallize in the simple CsCl structure. Many of the RCu and RAg compounds have been studied by neutron diffraction and exhibit at low temperatures an antiferromagnetic phase in which the moments in adjacent (110) ferromagnetic planes are antiparallel i.e. the so-called (π, π, 0) structures (although the moment directions can vary for the different compounds, sometimes lying in the (001) planes and sometimes lying parallel to the [001] axis). Their magnetic properties are summarized in table 7.3. The low temperature values of the ordered moment range from practically the full free ion moment value (for the heavy lanthanide compounds) to about two-thirds of the free ion value (for the light lanthanide compounds) indicating crystal field effects are present but not as strong as in the lanthanide pnictides. The bulk properties of these compounds have been measured by Walline and Wallace (1964, 1965). These authors, however, find peaks in some of their susceptibility versus temperature curves which are not observed as magnetic structural transitions in the corresponding neutron diffraction measurements (e.g. in TbCu), and vice versa. They speculate that some of their susceptibility peaks may correspond to subtle magnetic transitions not readily visible in powder neutron diffraction data. It should be noted that in at least two of these compounds [HoAg (Nereson, 1973b) and ErAg (Nereson, 1973a)] a sinusoidally modulated phase has been observed at the initial ordering temperature, where the antiparallel (110) sheets of spins have superimposed on them a sinusoidal modulation parallel to the [100] axis. At lower temperatures, this locks into the commensurate (π, π, 0) structure. It is possible that in some of these compounds, a susceptibility anomaly may result from a subtle incommensurate-commensurate transition of the magnetic periodicity as discussed in section 2.4. There is also a slight tetragonal distortion along the [001] axis which accompanies the antiferromagnetic ordering. The lanthanide gold compounds presumably have similar magnetic structures, since they are known to become antiferromagnetic at low temperatures (Wallace, 1973) although no neutron diffraction work seems to have been done on these materials.

Upon adding an extra electron by compounding lanthanides with the divalent elements such as Zn, Mg and Hg the CsCl crystal structure is still retained. However, the magnetic structures are different (see table 7.3). The heavy lanthanide compounds are ferromagnetic at low temperatures, although the powder neutron diffraction data is unable to indicate the moment orientation. Specific heat data (Morin et al., 1974a) on TbZn and HoZn show first-order temperature transitions which, together with evidence from magnetization measurements, they attribute to moment reorientations. The light lanthanide compounds PrZn, NdZn, NdMg are found to order in the so-called (0, 0, π) antiferromagnetic structure, i.e. one in which the moments are arranged in ferromagnetic (001) planes with alternate sheets being antiparallel (see fig. 7.19). The magnetic unit cell thus doubles the chemical cell dimensions along the c-axis. Morin and de Combarieu (1975) also find a low temperature (18.1 K) specific heat anomaly in NdZn below T_N which they attribute to moment

TABLE 7.3.
Magnetic structures of some CsCl structure lanthanide compounds.

Compound	Magnetic structure	T_N (T_C)	Low temp. ordered moment (μ_B)	Max. free ion moment (μ_B) ($g_J J$)	Ref.
CeAg	Ferromagnetic	9	0.95	2.14	Wallace (1971)
PrAg	Antiferromagnetic $(\pi, \pi, 0)$ μ in (001) planes	14	2.1	3.2	Brun et al. (1974b)
NdAg	Antiferromagnetic $(\pi, \pi, 0)$ μ along [001]	22	2.19	3.28	Buschow et al. (1974a)
GdAg	Antiferromagnetic	150	–	7.0	Wallace (1971)
TbAg	Antiferromagnetic $(\pi, \pi, 0)$ μ along [001]	100	8.7	9.0	Cable et al. (1964c)
DyAg	Antiferromagnetic $(\pi, \pi, 0)$ μ along [001]	51	9.8	10.0	Arnold et al. (1967)
HoAg	Antiferromagnetic Modulated $(\pi, \pi, 0)$ for annealed samples. [$(\pi, \pi, 0)$ for unannealed]	33	8.0	10.0	Nereson (1973b)
ErAg	Antiferromagnetic Modulated $(\pi, \pi, 0)$ [$(\pi, \pi, 0)$ below 9.5 K]	18	7.2	9.0	Nereson (1973a)
TmAg	Antiferromagnetic	10	–	7.0	Wallace (1971)
GdCu	Antiferromagnetic	41	–	7.0	Wallace (1971)
TbCu	Antiferromagnetic $(\pi, \pi, 0)$ μ along [001]	115	8.9	9.0	Cable et al. (1964c)
DyCu	Antiferromagnetic $(\pi, \pi, 0)$ μ along [001] or possibly noncollinear	64	8.62	10.0	Winterberger et al. (1971)
HoCu	Antiferromagnetic	28	–	10.0	Wallace (1971)
ErCu	Antiferromagnetic $(\pi, \pi, 0)$ μ in (001) planes	33	6.0	9.0	Cable et al. (1964b)
TmCu	Antiferromagnetic	11	–	7.0	Wallace (1971)
PrZn	Antiferromagnetic $(0, 0, \pi)$ μ along [001]	70	2.34	3.2	Buschow et al. (1974a)
NdZn	Antiferromagnetic $(0, 0, \pi)$	66	2.53	3.28	Buschow et al. (1974a)
TbZn	Ferromagnetic	160	7.8	9.0	Cable et al. (1967c)
HoZn	Ferromagnetic	73	–	10.0	1975
NdMg	Antiferromagnetic $(0, 0, \pi)$ μ along [001]	48	2.09	3.28	Buschow et al. (1974a)
TbHg	Ferromagnetic	80	8.0	9.0	Cable et al. (1964c)

re-orientation. They propose two other possible non-collinear variations of the $(0, 0, \pi)$ structure (see fig. 7.19) and provide arguments based on crystal field energies to show that these two variations are in fact more stable at low temperatures than the collinear structure proposed by Buschow et al. (1974a),

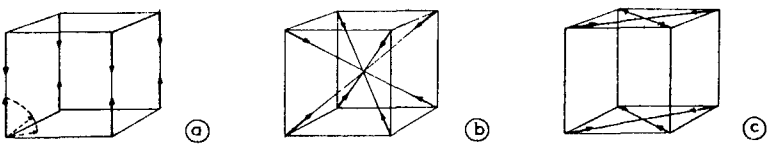

Fig. 7.19. (a) $(0, 0, \pi)$ antiferromagnetic structure. (b) and (c): Alternative non-collinear spin arrangements consistent with $(0, 0, \pi)$ periodicity as proposed by Morin and de Combarieu (1975).

and that the 18.1 K transition is in fact from one of these structures to the other. However, this is difficult to reconcile with the absence of magnetic (001) reflections in the neutron diffraction data (Buschow et al., 1974b) indicating magnetic moments parallel to [001]. Winterberger et al. (1971) have also proposed a noncollinear variation of the $(\pi, \pi, 0)$ structure as one consistent with the powder neutron diffraction data on DyCu, where the moments point along the four [111] axes, and indicate it is favored energetically on the basis of crystal field and dipolar energy calculations. Mattis and Donath (1962) performed an early calculation for $\mathcal{J}(q)$ based on the RKKY interaction between spins on a simple cubic lattice (which is the lattice of the lanthanide ions in these compounds) interacting via a free electron gas. In the absence of any nesting features for the Fermi surface, it is quite likely that the maximum of $\chi(q)$ and hence $\mathcal{J}(q)$ for such a case comes out to be a point of high symmetry, and this was in fact the case. For increasing values of $(k_f a)$ (k_f = Fermi wave vector, a = lattice constant) they found a maximum of $\chi(q)$ first at $q = 0$, then at $a^{-1}(0, 0, \pi)$, then at $a^{-1}(\pi, \pi, 0)$ and finally at $a^{-1}(\pi, \pi, \pi)$. Much has been made of the apparent conflict between this predicted trend and that of the observed structures with electron concentration. However, a free electron calculation is much oversimplified, considering the complicated band-structure of these compounds (Hasegawa and Kübler, 1974) and a more rigorously based $\mathcal{J}(q)$ calculation would be worth performing before the RKKY interaction is to be blamed. More recently, Sakurai et al. (1973) have performed a more accurate calculation of $\mathcal{J}(q)$, still using a free-electron model, but including matrix elements and employing methods leading to better convergence of the sums over reciprocal lattice vectors. They find satisfactory agreement of the behavior of magnetic structure with electron concentration for the CsCl structure compounds but not for the NaCl structure.

Yashiro et al. (1976) have recently performed neutron diffraction and magnetic measurements on the alloy system $TbCu_{1-x}Zn_x$. For $x \leq 0.5$, they find the $(\pi, \pi, 0)$ antiferromagnetic structure, as in TbCu (Cable et al., 1964) and for $x \geq 0.7$, they find the ferromagnetic structure as in TbZn (Cable et al., 1964). For intermediate values, they find a spin canted state (i.e. a state where alternate (110) planes of spins have moments that point first to one side, then to another of a mean direction, yielding both a ferromagnetic and a $(\pi, \pi, 0)$ component). The phase diagram is shown in fig. 7.20. Umehara and Kasuya (1976) have discussed theoretically how such a canted spin arrangement can be brought about via the s–f exchange interaction.

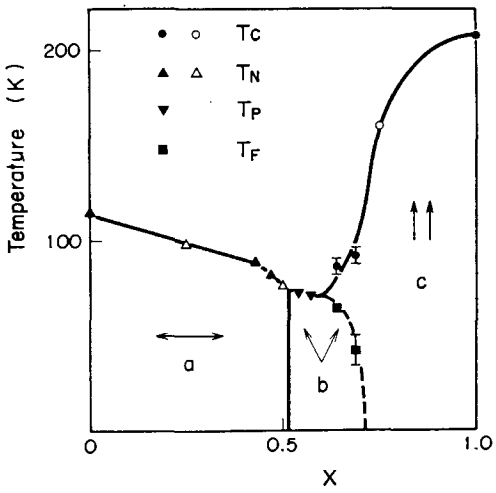

Fig. 7.20. Magnetic phase diagram for $TbCu_{1-x}Zn_x$. T_C and T_N are the Curie and Néel temperatures respectively. T_P and T_F are the transition temperatures from the canted state to a paramagnetic state and to a ferromagnetic state respectively. Region a represents the antiferromagnetic $(\pi, \pi, 0)$ phase, region b represents the canted ferromagnetic phase, and region c represents the ferromagnetic phase. The closed symbols represent data of Yashiro et al. (1976) and the open symbols those of Pierre (1969). (after Yashiro et al., 1976).

Brun et al. (1976) have done an extensive study, using neutron diffraction and magnetization measurements in fields up to 60 kOe of the effects of higher-order exchange (in particular, biquadratic exchange) on the magnetic properties of PrAg. They find a field-induced spin-flop transition for $H > H_c \sim 5$ kOe, to a canted spin arrangement, and a significant M^3 dependence of the exchange field (M = magnetization). They develop a mean field theory of biquadratic exchange to account for their results. An interesting qualitative prediction based on their theory and fitted parameters is a zero-field canted spin state at very low temperatures for PrAg. It may be true that in all these compounds, as in the lanthanide pnictides, higher order "exchange" effects play a significant role, although the situation is not yet clear in that regard, nor is there much other than speculation (e.g. quadrupole-lattice coupling) as to the microscopic origins of these higher order exchange effects.

3.5.3. *Cubic laves phase lanthanide intermetallic compounds* (RM_2)

The properties of these compounds are compiled in several reviews (Taylor, 1971; Wallace, 1973). They are practically all ferromagnetic (in the case of lanthanide – non-magnetic atom compounds) or ferrimagnetic (in the case of most of the lanthanide – magnetic atom compounds). Until very recently it has not been possible to grow single crystals of these materials, so practically all the neutron diffraction data have been taken on powders. Alloying with Y, La or Lu in place of the lanthanide decreases the Curie temperatures proportionally to the

non-magnetic trivalent ion concentration. It should be noted that in many cases, neutron diffraction results are valuable in establishing the moment on the non-lanthanide site, for otherwise a reduction in ordered bulk moment is ambiguous since it can be assigned to quenching of the lanthanide moment by crystal fields or to antiferromagnetically aligned M spins.

3.5.3.1. RAl_2 *compounds*

In the case of $DyAl_2$ (Nereson et al., 1968), at low temperatures, some very weak magnetic superlattice lines were observed leading to the possibility of a very small antiferromagnetic component. The data are all consistent with no magnetic moment developing on the Al sites.

$PrAl_2$ is calculated to have a singlet ground state for the Pr^{3+} ion in the crystal field and appears to be another example of an induced moment system (Wallace, 1973). Purwins et al. (1974) have shown that the magnetization measurements on these compounds can be explained reasonably consistently in terms of an isotropic exchange and a suitably scaled but universal set of crystal field parameters. Swift and Wallace (1968) studied the magnetic characteristics of $(R_1)_x(R_2)_{1-x}Al_2$ systems and found that the lanthanide ions always align their *spins* ferromagnetically (so that for R_1 = a light lanthanide ($J = L - S$) and R_2 = a heavy lanthanide ($J = L + S$), the *moments* actually align antiferromagnetically). This is consistent with a $q = 0$ peaked RKKY interaction. $EuAl_2$ and $CeAl_2$ appear to be antiferromagnetic (Swift and Wallace, 1968) although their structures are not known in detail. Mader and Wallace (1968) showed for $Eu_{1-x}La_xAl_2$ that for $x > 0.6$, the structure became ferromagnetic, showing that the change of electron concentration due to the addition of trivalent La changes the peak in $\mathcal{J}(q)$ back to $q = 0$.

3.5.3.2. RIr_2 *compounds*

Felcher and Koehler have studied $TbIr_2$ and $HoIr_2$ (Felcher and Koehler, 1963) in the ferromagnetic phase and found a Tb^{3+} moment of $\sim 7\ \mu_B$ (implying some crystal field quenching) and no moment on the Ir sites. Tanner et al. (1974) have analyzed the preferred moment directions in the ordered ferromagnetic phase by measurements of the transferred hyperfine fields at the Ir nuclei using the Mössbauer effect. The moments appear to be parallel to the [001] axis in all cases, except $GdIr_2$ where they are along [111].

3.5.3. RCo_2 *compounds*

Diffraction studies of $NdCo_2$, $TbCo_2$, $HoCo_2$ and $ErCo_2$ have been carried out by Moon et al. (1965). They find almost the full ordered free ion moment on the lanthanide sites for the heavy lanthanide compounds and an antiferromagnetically coupled $1\ \mu_B$ moment on the Co sites, indicating a nearly neutral $3d^9$ Co configuration and weak crystal fields. For $NdCo_2$, the Nd ion has a moment of $2.6\ \mu_B$ (the free ion value is $3.3\ \mu_B$) and the Co moment of $0.8\ \mu_B$ seems ferromagnetically coupled to it.

Recently, Gignoux et al. (1976) have performed accurate measurements (using

the polarized neutron technique (Koehler, 1972)) on a single crystal of $TmCo_2$ and have been able to actually map out the spin density in the ferrimagnetic state of this crystal. They find an ordering temperature of 7 K, and at 4.2 K a moment on the Tm atom of 5.4 μ_B (free ion value = 7.0 μ_B) and antiparallel to it moments of 0.8 μ_B on the Co atoms. The spin densities on the Co sites can be fitted well with a 3d Co spin distribution, and those on the Tm sites with relativistic Dirac–Fock wavefunctions calculated by Desclaux and Freeman and including crystal field splitting effects. In addition there is some diffuse spin density of an oscillatory nature. The crystal field parameters were calculated by fitting self consistently to the magnetization and form-factor measurements, and yielded a Γ_1 singlet ground state for the Tm^{3+} ion.

The properties of many of the RCo_2 compounds have been reviewed by Lemaire (1966). They are to be regarded as strongly exchange-enhanced itinerant d-electron systems (e.g. YCo_2 and $LuCo_2$ are strong Pauli paramagnets (Lemaire, 1966) with magnetic order developing from the cobalt-rare earth exchange interaction (Bloch et al., 1975)).

We omit from discussion here the technologically important RCo_5 and R_2Co_{17} compounds, since they are discussed in detail in ch. 14, section 6.

3.5.3.4. RFe_2 *compounds*

These materials are thoroughly reviewed in the book by Wallace (1973). Neutron diffraction studies have established the antiferromagnetic coupling between the R and Fe ions for $HoFe_2$ (Moreau et al., 1971) and $ErFe_2$ (Bargouth and Will, 1971). The magnetic properties have also been studied by Buschow and Van Stapele (1970) for heavy lanthanide-Fe_2 compounds and for compounds with the lanthanide diluted with Y. They find an almost constant Fe moment of 1.4 μ_B antiparallel to the lanthanide moment, with some crystal field quenching of the lanthanide moment. For very dilute lanthanide ions, the Fe moment increases rapidly to 2.1 μ_B indicating that the magnetism on the Fe ions is not a local moment phenomenon, but a band effect. Single crystals of these compounds large enough for inelastic neutron scattering have recently become available and these experiments will be discussed in section 5.

Oesterreicher (1973) has by neutron diffraction and other techniques studied the effect of replacing Al in RAl_2 compounds by Fe or Co. He finds that on initial substitution, the bulk moment decreases which is partly explicable in terms of an antiparallel transition metal ion moment, but appears also to be due to magnetic disorder produced on the lanthanide sublattice. The microscopic reasons for this are not yet completely clear.

3.5.4. *Lanthanide-group VIa compounds*

The heavy lanthanide oxides crystallize in the bixbyite (Moon et al., 1968) structure which contains 32 lanthanide ions and 48 oxygens in a cubic unit cell of lattice constant ~10.5 Å. They order antiferromagnetically at very low temperatures (~2–3 K). As might be expected the magnetic structure is extremely

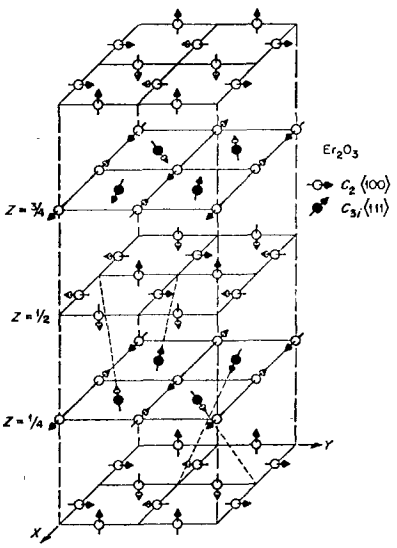

Fig. 7.21. Magnetic structure of Er_2O_3. The unit cell is cubic but has been expanded along the z direction for clarity. The C_2 sites are actually displaced from the positions shown by 1/30 of a cell edge. The oxygen atoms (not shown) are between the rare earth layers (after Moon et al., 1968).

complicated but was nevertheless unravelled for Er_2O_3 and Yb_2O_3 using single crystal diffraction by Moon et al. (1968) and by Bertaut and collaborators for Er_2O_3 (Bertaut and Chevalier, 1966) and Tb_2O_3 (Quezel, Bertaut and Quezel, 1969) using powder diffraction data and a group theoretical analysis for the allowed magnetic arrangements. The structure for Er_2O_3 is illustrated in fig. 7.21. A theoretical analysis of the structure by Moon et al. (1968) indicated that while magnetic dipole–dipole interactions may help stabilize these structures at their low ordering temperatures, superexchange via oxygen atoms was probably also necessary. These systems also correspond to a situation where the crystal field dominates. Thus in Tb_2O_3 (Quezel, Bertaut and Quezel, 1969) only half the Tb sites order, the remainder possibly remaining in singlet ground states with sub-critical exchange.

Recently, Moon and Koehler (1975) have studied the induced moments in Gd_2O_3 down to 1.8 K in an applied field and have shown that strong antiferromagnetic correlations exist to quite high temperatures between neighboring Gd^{3+} spins. The material orders antiferromagnetically below 1.6 K. Moon et al. were also able to fit the temperature dependence of their ordered moment with a molecular field treatment involving significant biquadratic exchange.

EuO and EuS (in which the Eu ion is in a divalent $^8S_{7/2}$ ground state) form NaCl crystal structures and are ferromagnetic below 69.2 K and 16.6 K respectively. They are extremely rare magnetic systems in that they are insulating local-moment Heisenberg ferromagnets. This has been exploited in a study of their critical behavior using neutron scattering (Als-Nielsen et al., 1971). EuSe has been most recently investigated by Fischer et al. (1969) using a single crystal sample. At 4.2 K, EuSe orders antiferromagnetically in ferromagnetic (111) sheets with the moments in the layers arranged as $++--$, etc. (+ denoting moments parallel to [111] and − moments antiparallel to [111]). At 1.9 K a new phase

appears which is ascribed to the co-existence of an antiferromagnetic MnO-type structure and a ferrimagnetic structure of $++-,\ldots$ ordered (111) ferromagnetic sheets. Such structures are speculated to arise due to the coupling of the Eu^{2+} ions via the free carriers in this semiconducting compound. EuTe orders below 7.8 K in an antiferromagnetic MnO-type structure (Will et al., 1963). This type of structure may arise due to a balance between a ferromagnetic nearest-neighbor direct exchange integral J_1 and a second-neighbor superexchange integral J_2 which is antiferromagnetic. For EuTe, it is estimated (Will et al., 1963) that $|J_2| \simeq 5|J_1|$.

The magnetic structures of CeS, NdS, NdSe, NdTe and TbSe have been investigated by Schobinger-Papamantellos et al. (1974). They find their powder diffraction data at low temperatures consistent with type II (MnO-type) antiferromagnetic ordering, as in the lanthanide monopnictides. However, they find a lot of sensitivity to the samples used (presumably due to problems of non-stoichiometry in various samples) and in some cases diffuse scattering characteristic of some short-range order superimposed on the magnetic Bragg peaks. The intensities are consistent with moments parallel or antiparallel to the [111] axis, except for NdS where the moments are tilted from this axis.

Some other lanthanide monochalcogenides such as SmS, or TmSe exhibit other interesting properties associated with valence fluctuations (Varma, 1976) and are the subject of much current interest (see ch. 20).

4. Magnetic form factors

There is a further category of information on lanthanide magnetism which may be obtained from elastic neutron scattering experiments, namely the details of the distribution of magnetization density on the ions themselves. This is obtained as the Fourier transform of the magnetic scattering amplitude as a function of the neutron momentum transfer vector. One obtains in this way detailed information on the 4f wavefunctions, either in the ordered or in the paramagnetic state, although as we shall see, the actual calculation of the form factor in terms of the spin and orbital parts of the wavefunction is a complicated procedure. Accurate form factor measurements (only available in the last few years) also yield information about the conduction electron polarized spin density and, in some cases, the effect of crystal fields on the 4f wavefunctions.

4.1. *Magnetic scattering of neutrons by ions*

We review briefly here the theory of magnetic scattering of neutrons by electrons in atomic multiplet states with strong Hund's rule and spin–orbit coupling. This subject has by now a long history with a succession of several developments in recent years. The theory was first given by Trammell (1953) and extended by Odiot and Saint-James (1960). A more powerful tensor operator

technique for calculating the matrix elements was developed by Johnston (1966) and extended and applied by Lovesey and Rimmer (1969) and several other authors. (A list of references may be found in Stassis and Deckman (1975).) The formalism is discussed in detail in ch. 6 of Marshall and Lovesey (1971).

The calculations are quite involved, although by now they have been tabulated in fairly easily usable form for most of the lanthanide ions (Marshall and Lovesey, 1971; Lander and Brun, 1970; Balcar, 1973) in terms of a few radial integrals over the 4f-wavefunctions. Perhaps the most rigorous and elegant treatment of the problem is the most recent one by Stassis and Deckman (1975, 1976a, 1976b) who treat the problem along the lines of the well known problem of the interaction of polarized electromagnetic radiation with atoms. They expand the scattering amplitude in terms of the magnetic and electric multipoles characterizing the atomic electrons and utilize the highly-developed theory of the symmetry properties of atomic states. Their approach also has the advantage of being easily generalized to the relativistic case. We briefly discuss their method here.

The magnetic scattering of neutrons arises from the interaction of both the spin and orbital currents of the electrons with the magnetic dipole of the neutron. We neglect here small higher order scattering processes such as the Schwinger interaction and the Foldy interaction (Stassis and Deckman, 1975). It may be shown (Stassis and Deckman, 1975) that the magnetic scattering amplitude for neutron momentum transfer vector $\boldsymbol{Q}$ is given by

$$p(\boldsymbol{Q}) = (|\gamma| r_0)\boldsymbol{\sigma} \cdot \boldsymbol{J}_\perp \tag{7.54}$$

where $\gamma = -1.91$ is the neutron magnetic moment in nuclear magnetons, r_0 is the classical electron radius, $\boldsymbol{\sigma}$ is a Pauli matrix operating on the spin state of the neutron and $\boldsymbol{J}_\perp$ is related to the (orbital and spin) current density $\boldsymbol{j}(\boldsymbol{r})$ of the system by

$$\boldsymbol{J}_\perp = -\mathrm{i}\left(\frac{m}{e\hbar Q}\right)\hat{\boldsymbol{Q}} \times \langle \mathrm{f}| \int \boldsymbol{j}(\boldsymbol{r}) \exp(\mathrm{i}\boldsymbol{Q} \cdot \boldsymbol{r})\, \mathrm{d}\boldsymbol{r}|\mathrm{i}\rangle \tag{7.55}$$

where m is the electron mass, $e = -|e|$ the electronic charge, $\hat{\boldsymbol{Q}}$ a unit vector along $\boldsymbol{Q}$, and $|\mathrm{i}\rangle$ and $|\mathrm{f}\rangle$ denote the initial and final states of the system.

An inspection of eq. (7.55) shows that the matrix elements needed for an evaluation of $p(\boldsymbol{Q})$ are the same as those appearing in the radiation problem. Thus $p(\boldsymbol{Q})$ can be expressed in terms of the multipole operators characterizing the ion, analogous to the expansion used in the formulation of the radiation problem. One obtains

$$p(\boldsymbol{Q}) = (|\gamma| r_0)\boldsymbol{\sigma} \cdot \sum_{k,m} \left(\frac{8\pi}{2k+1}\right)^{1/2} \{\boldsymbol{X}^*_{km}(\hat{\boldsymbol{Q}})\langle \mathrm{f}|T^{(\mathrm{e})}_{km}|\mathrm{i}\rangle - |(\hat{\boldsymbol{Q}} \times \boldsymbol{X}^*_{km}(\boldsymbol{Q}))\langle \mathrm{f}|T^{(\mathrm{m})}_{km}|\mathrm{i}\rangle\}, \tag{7.56}$$

where $\boldsymbol{X}_{km}(\hat{\boldsymbol{Q}})$ denotes the vector spherical harmonic (Hill, 1954) $\boldsymbol{Y}^m_{k,k,l}(\hat{\boldsymbol{Q}})$ (and is perpendicular to $\boldsymbol{Q}$) and $T^{(\mathrm{e})}_{km}$ and $T^{(\mathrm{m})}_{km}$ are irreducible tensor operators corresponding to the electric and magnetic multipoles of the system respectively.

Note that since both $\boldsymbol{X}_{km}$ and $(\boldsymbol{Q}\times\boldsymbol{X}_{km})$ are transverse to $\boldsymbol{Q}$, eq. (7.56) explicitly exhibits the fundamental property of magnetic scattering, namely, that the magnetic moment of the neutron couples only to the transverse components of the current density. It is also useful to recall at this point that the elastic and magnetic multipole operators of rank k have particles $(-1)^k$ and $(-1)^{k+1}$ respectively. In the limit $\boldsymbol{Q}\to 0$ these operators are, of course, proportional to the static multipole moments of the system. The number of multipoles entering the calculation of the magnetic scattering amplitude is limited by selection rules based on the symmetry properties of the ion e.g. parity and angular momentum conservation.

Let us consider only scattering *within* the l^n configuration ($l=3$ for the lanthanide ions). In this case, the selection rules restricting the number of multipoles which contribute to the scattering amplitude can be easily formulated. By parity conservation, only even order electric and odd order magnetic multipoles contribute to the scattering amplitude. In addition, since the multipole operators are one-electron operators, their rank k must be $\leqslant(2l+1)$ by one-electron angular momentum conservation. Thus, for the lanthanides, we need consider only the matrix elements of a limited number of electric ($k=2, 4, 6$) and magnetic ($k=1, 3, 5, 7$) multipoles. In addition, by conservation of angular momentum, $|J_f - J_i| \leqslant k \leqslant |J_f + J_i|$, and $M_f = M_i + m$, where J_i, M_i are the angular momentum quantum numbers of the initial state, and J_f, M_f those of the final state.

Let us consider the expressions for the multipole operators. These are given by Stassis and Deckman (1976a)

$$T^{(e)}_{km} = i^k\,[2\pi(2k+1)]^{1/2}\left(\frac{m}{e\hbar Q}\right)\frac{1}{Q}\int \nabla\times[(j_k(Qr)\boldsymbol{X}_{km}(\boldsymbol{r}))]\cdot\boldsymbol{j}(\boldsymbol{r})\,d\boldsymbol{r} \tag{7.57}$$

and

$$T^{(m)}_{km} = i^k\,[2\pi(2k+1)]^{1/2}\left(\frac{m}{e\hbar Q}\right)\int j_k(Qr)\boldsymbol{X}_{km}(\hat{\boldsymbol{r}})\cdot\boldsymbol{j}(\boldsymbol{r})\,d\boldsymbol{r} \tag{7.58}$$

where the current density is made up of orbital and spin parts

$$\boldsymbol{j}(\boldsymbol{r}) = \boldsymbol{j}_{orb}(\boldsymbol{r}) + \boldsymbol{j}_s(\boldsymbol{r}) \tag{7.59}$$

$$\boldsymbol{j}_{orb}(\boldsymbol{r}) = \sum_i \tfrac{1}{2}e\{\mathbf{V}_i\delta(\boldsymbol{r}-\boldsymbol{r}_i) + \delta(\boldsymbol{r}-\boldsymbol{r}_i)\mathbf{V}_i\} \tag{7.60}$$

and

$$\boldsymbol{j}_s(\boldsymbol{r}) = \sum_i (e\hbar/m)\nabla\times(\mathbf{s}_i\delta(\boldsymbol{r}-\boldsymbol{r}_i)), \tag{7.61}$$

where i refers to the ith electron, and $\mathbf{V}_i$ is the velocity operator given by

$$\mathbf{V}_i = \frac{i}{\hbar}[\mathcal{H}, \boldsymbol{r}_i] = \delta\mathcal{H}/\delta\mathbf{P}_i \tag{7.62}$$

In the extreme non-relativistic case, the only sizeable explicitly momentum-dependent part of $\mathcal{H}$ is the kinetic energy, and hence we put $\mathbf{V}_i = \mathbf{P}_i/m$. This

approximation is very good even for relatively heavy atoms such as the lanthanides. Substituting this result in eq. (7.60) and then the results of eqs. (7.60) and (7.61) in eqs. (7.57) and (7.58), Stassis and Deckman were finally able to express the multipole operators in terms of Racah tensors, which are simply related to the generators of the groups used in the classification of the ionic states. These operators, written $W_m^{(k_1,k_2)k}$ are non-electron operators of rank k having ranks k_1 and k_2 in the spin and orbital space of the ion respectively. Since they are one-electron operators $k_1 = 0$, 1, and $k_2 \leqslant 2l$. They obtain (Stassis and Deckman, 1975, 1976a)

$$T_{km}^{(m)} = i^{k+1}\left[R^{(m)}(0,k,k)W_m^{(0,k)k} + \sum_{k'=k,k\pm1} R^{(m)}(1,k',k)W_m^{(1,k')k}\right],$$
$$(k = 1,3,\ldots,2l+1) \tag{7.63}$$

$$T_{km}^{(e)} = i^{k+1}\left[R^{(e)}(0,k,k)W_m^{(0,k)k} + \sum_{k'=k,k\pm1} R^{(e)}(1,k',k)W_m^{(1,k')k}\right], \quad (k = 2,4,\ldots,2l) \tag{7.64}$$

where the terms involving $W^{(0,k)k}$ are associated with the purely orbital part of the multipoles, and the others with the spin part. Explicit expressions for the R's are given by Stassis and Deckman (1976a). They involve integrals over the radial wave functions, and $3j$ and $6j$ symbols. One now needs only matrix elements of the $W_m^{(k_1,k_2)k}$, which have already been extensively tabulated in reduced form. One can now also use further symmetry properties of the f^n electronic configuration to tabulate a comprehensive set of selection rules on the matrix elements of the Racah tensors. Thus, the f^n configurations are classified according to their transformation properties under the operations of the groups R(3), Sp$(4l+2)$, R$(2l+1)$ and G_2 and labelled by the corresponding set of quantum numbers (J, M), v, W, and U respectively (v is the seniority quantum number). Using the transformation properties of the Racah tensors under the operations of these groups and the well-known group theoretical matrix element selection rules, one can formulate selection rules for matrix elements of the $W^{(k_1,k_2)k}$ and these have been tabulated by Stassis and Deckman (1976a).

Equations (7.63) and (7.64), together with eq. (7.56) thus can be used to evaluate the contribution to $p(\boldsymbol{q})$ from transitions between any two Russell–Saunders states of the f^n configuration. Let us now consider the case of elastic magnetic scattering from a single saturated state $|\theta JM\rangle$ (as in the low temperature ordered phase); where J, M are the usual angular momentum quantum numbers, and θ the set of additional quantum numbers needed to completely specify the state. In this case, the expectation values of $W_0^{(0,k)k}$ and $W_0^{(1,k')k}$ vanish so that there is no electric multipole contribution. The magnetic multipole contributions may be evaluated to yield

$$p(\boldsymbol{Q}) = (|\gamma|r_0)\boldsymbol{\sigma}\cdot\boldsymbol{q}_m \sum_k i^{k+1}\left[\frac{2}{k(k+1)}\right]^{1/2} P_k^1(\cos\theta)\langle\theta JM|R^m(0,k,k)W_0^{(0,k)k}$$
$$+ \sum_{k'=k\pm1} R^m(1,k',k)W_0^{(1,k')k}|\theta JM\rangle, \qquad (k = 1,3,5,7) \tag{7.65}$$

Here $\boldsymbol{q}_m$ is the so-called magnetic scattering vector defined by

$$\boldsymbol{q}_m = (\hat{\boldsymbol{Q}} \cdot \boldsymbol{\epsilon}_3)\hat{\boldsymbol{Q}} - \boldsymbol{\epsilon}_3 \tag{7.66}$$

where $\boldsymbol{\epsilon}_3$ is a unit vector along the z-axis (axis of quantization). P_k' is the derivative of a Legendre polynomial and θ is the angle between the scattering vector and the axis of quantization of the ion. For most polarized neutron experiments, $\theta = \frac{1}{2}\pi$ and

$$[P_k'(\cos\theta)]_{\theta=\pi/2} = (-1)^{(k-1)/2}\frac{k(k-1)!}{2^{k-1}\{[(k-1)/2]!\}^2} \tag{7.67}$$

The magnetic form factor is obtained by writing

$$p(\boldsymbol{Q}) = f(\boldsymbol{Q})^{1/2}\gamma r_0 g_J M \tag{7.68}$$

where $g_J M$ is the ordered moment (in μ_B). Thus by eq. (7.65)

$$f(\boldsymbol{Q}) = -\frac{2}{gM}\sum_{k=1,3,5,7}\left(\frac{2}{k(k+1)}\right)^{1/2} P_k'(\cos\theta)\mathrm{i}^{k+1}\langle\theta JM|R^m(0,k,k)W_0^{(0,k)k}$$
$$+\sum_{k'=k\pm1} R^m(1,k',k)W_0^{(1,k')k}|\theta JM\rangle \qquad (k = 1,3,\ldots,2l+1)$$

The matrix elements $\langle\theta JM|\ldots|\theta JM\rangle$ have been tabulated by Stassis and Deckman (1976a) for the saturated ground state of the ion ($M = J$) in the multiplet state given by Hund's rules, in the form $\Sigma_k a_k \bar{j}_k$ ($k = 0, 2, 4, 6$), where

$$\bar{j}_k = \int_0^\infty r^2 f^2(r) j_k(Qr)\,\mathrm{d}r \tag{7.69}$$

and $f(r)$ is the radial wave function. The a_k are obtained as rational fractions. Equivalent results have been tabulated in decimal form by several authors using the other methods (Lander and Brun, 1970; Marshall and Lovesey, 1971; Balcar, 1973).

In the case where the ground state is not a pure $|\theta JM\rangle$ state due to crystal field effects the full calculation must be used to evaluate the magnetic scattering amplitude in the form

$$p(Q) = \sum_{M,M'} a_M^* a_{M'} P_{\theta JM'}^{\theta JM}(\boldsymbol{Q}) \tag{7.70}$$

In another important class of experiments one measures the coherent elastic magnetic scattering of neutrons by a paramagnetic crystal in an external magnetic field H. The degenerate ion state is split into $(2J+1)$ levels whose probability of occupation is

$$P_M = \mathrm{e}^{-\beta' M}\Big/\left(\sum_M \mathrm{e}^{-\beta' M}\right) \tag{7.71}$$

($\beta' = g_J\mu_J H/kT$). If $\beta \ll 1$ (as is true in most cases of experimental interest) we may expand

$$\mathrm{e}^{-\beta M} = 1 - \beta M + \frac{\beta^2 M^2}{2!} - \frac{\beta^3 M^3}{3!} + \cdots \tag{7.72}$$

It may be shown that if n is the largest power of M retained in eq. (7.72) then because of the sum over M, only magnetic multipoles of order $\leqslant n$ contribute to $p(\boldsymbol{Q})$. Retaining only the first three terms in eq. (7.72), we see that the paramagnetic scattering amplitude is determined only by the magnetic dipole term,

$$p(\boldsymbol{Q}) = -\gamma r_0 \frac{\chi_a(T)B}{g_J \mu_B [J(J+1)(2J+1)]^{1/2}} (\theta J \| T_1^{(m)} \| \theta J), \tag{7.73}$$

where $\chi_a(T)$ is the atomic susceptibility. Evaluation of the reduced matrix gives

$$p(\boldsymbol{Q}) = -\frac{\gamma r_0 \chi_a(T)B}{2\mu_B} \left\{ \bar{j}_0 + \left[\frac{J(J+1)+L(L+1)-S(S+1)}{2g_J J(J+1)} + \frac{1}{g_J} \left(\frac{2(J+1)}{J(J+1)} \right)^{1/2} \left(\frac{3l(l+1)(2l+1)}{(2l-1)(2l+3)} \right)^{1/2} (\theta \| W^{(1,2)} \| \theta) \right] \bar{j}_2 \right\}. \tag{7.74}$$

For small scattering angles ($Q\langle r \rangle \ll 1$), it can be shown that the magnetic dipole approximation also applies for scattering within the l^n configuration. Then, by the Wigner–Eck art theorem, the scattering amplitude between states $\langle \theta JM|$ and $|\theta JM'\rangle$ is proportional to the matrix elements of the operator $(\hat{\boldsymbol{Q}} \times \boldsymbol{J}_\perp)$ between the states ($\boldsymbol{J}$ = total angular momentum operator).

Stassis and Deckman (1976b) have also given a completely relativistic formulation of the problem, and the reduced matrix elements for the (effective) multipole operators needed in this case have also been tabulated. In addition, of course, one needs to replace the radial wavefunction $f(r)$ appearing in the expression for the $\bar{j}_k$ by relativistic (Dirac–Fock) radial wave functions.

Finally, there is the question of the conduction electron contribution to the form factor. As discussed in section 2, there is a strong exchange interaction between the spins of the f-electrons and those of the conduction electrons. In the ordered ferromagnetic state, this interaction will lead to a splitting between the energies of the up and down conduction spin states and hence to a net spin density. (The argument can be generalized to the case of an antiferromagnetic state.) Since the s–f exchange acts purely on the *spins* of the conduction electrons, there is no orbital moment density and the conduction electron contribution to the magnetic form factor is directly proportional to the Fourier transform of $(n_\uparrow(\boldsymbol{r}) - n_\downarrow(\boldsymbol{r}))$ where $n_\uparrow(\boldsymbol{r})$ is the net "up-spin" density of the conduction electrons and $n_\downarrow(\boldsymbol{r})$ is the net "down-spin" density. In the paramagnetic state, where the f-electrons are polarized by an externally applied field, the induced moment on the f-shells will polarize the conduction electrons in proportion to the ordered moment. In addition there will be a very small additional conduction electron spin and orbital polarization due to the applied field itself but for weak fields this is in general negligible.

Since the conduction electron densities are much more delocalized than the f-electron densities, the conduction electron contribution will only be appreciable (relative to that of the f-electrons) at relatively small values of Q (or $\sin\theta/\lambda$).

4.2. *Experimental results*

The experimental technique for measuring form factors by exploiting the properties of polarized neutron beams has been reviewed by Koehler (1972). The technique can be quite accurate, particularly in the region of large Q or small magnetic scattering amplitude. It has not yet been used very successfully with powder samples. Results of moderate accuracy can and have also been obtained by simply measuring the integrated intensities of various magnetic reflections (for single crystal or powder samples) and normalizing to the intensities of the nuclear reflections. The experimental situation, up to 1972, has been reviewed by Koehler (1972). Here we discuss briefly some recent high precision polarized neutron experiments and their implications regarding the electronic wave functions in rare earth systems.

Form factor measurements for ^{160}Gd using both polarized and unpolarized neutrons have been made (Moon and Koehler, 1971; Moon et al., 1972). It was found that the large Q values of $f(\boldsymbol{Q})$ could be fitted well by calculations based on ordinary Hartree–Fock radial wave functions (Blume et al., 1963, 1964) but extrapolated to $Q = 0$, this would predict a much smaller (5.63 μ_B) local moment on the ions than appears reasonable from susceptibility and magnetization measurements, and hence would require an unreasonably large conduction electron polarization. Moon et al. were able to analyze their data so as to be able to separate out a "local" (4f) part and a "diffuse" (conduction electron) part. The local part indicated that the 4f radial wave functions were somewhat more extended than the Hartree–Fock radial functions, and Cooke and Davis (1972) showed that such an expansion could be accounted for by performing a *relativistic* Hartree–Fock–Slater calculation with an adjustable exchange exponent (α). This was later clearly demonstrated by Freeman and Desclaux (1972) who performed a fully relativistic Dirac–Fock (D–F) calculation for Gd^{3+} and obtained very good agreement with experiment (see fig. 7.22). The deviations at small scattering angles are now of the right order of magnitude to be attributed to the polarization of the conduction electrons. In order to eliminate the latter effects, Moon et al. (1972) had also measured the form factor of Gd^{3+} in the ionic crystal Gd_2O_3 using paramagnetic diffuse scattering. A puzzling result was that the resulting form factor was in good agreement with that obtained from the *non-relativistic* wave functions. However, recently, Moon and Koehler (1975) remeasured the form factor of Gd^{3+} in Gd_2O_3 using induced moments in an applied field and standard polarized neutron techniques and obtained good agreement with the D–F calculated form factors. They attribute the earlier discrepancies to the effects of spin correlations between the Gd^{3+} ions on the paramagnetic diffuse scattering.

Lander et al. (1973) measured the Tb^{3+} form factor in another ionic material $Tb(OH)_3$, and also found excellent agreement with calculations using D–F electronic wave functions. Note that, unlike Gd^{3+}, Tb^{3+} possesses an orbital component in its form factor. However, the agreement does not appear quite as good for Tb metal (Brun and Lander, 1971; 1974), although again the metallic

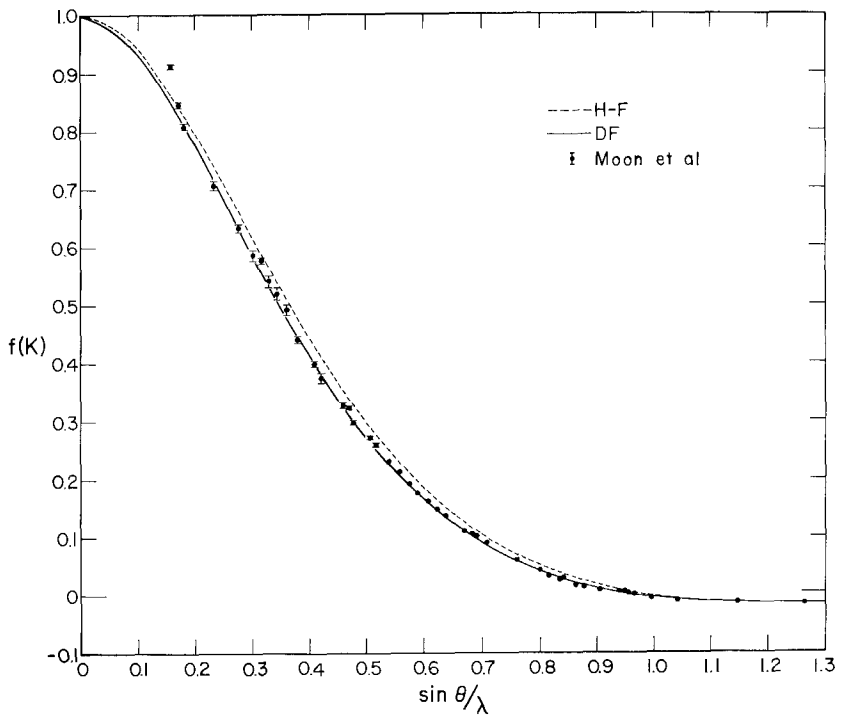

Fig. 7.22. Comparison of Dirac–Fock and Hartree–Fock calculations compared with the localized part of the measured magnetic form factor of Gd (after Freeman and Desclaux, 1972).

form factor corresponds to a more expanded radial function than the Hartree–Fock wave function. Similar effects were also observed in the form factor of metallic Tm (Brun and Lander, 1969) and although D–F atomic calculations do not yet exist for Tm^{3+}, Brun and Lander (1969) were able to fit an empirically expanded Hartree–Fock type radial function to the data. Recently measurements have also been performed on Er metal by Stassis et al. (1976) with the field applied both parallel and perpendicular to the c-axis of the crystal. Again the experimental results (fig. 7.23) are in excellent agreement with calculations using relativistic D–F wave functions for the free Er^{3+} ion. The deviations from the theoretical curves at small scattering angles are of the same order of magnitude as those observed in Gd and can be attributed to conduction electron polarization. In the analysis of the Gd, Er and $Tb(OH)_3$ data, the theoretical form factors were evaluated using the non-relativistic formalism of magnetic scattering but using relativistic wave functions. As discussed in section 4.1, Stassis and Deckman (1976b) have indicated slightly different results if one uses the relativistic formalism of scattering and pointed out that agreement with experiment is thereby slightly improved.

As discussed in section 3.5, the compound TmSb is a well-studied system in which exchange effects appear to be absent, and the crystal field produces a

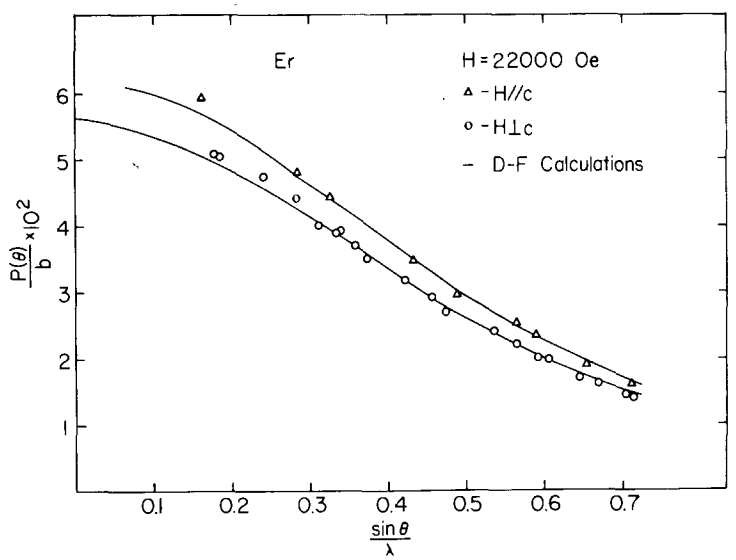

Fig. 7.23. Comparison of the coherent paramagnetic scattering amplitudes for $H \| c$ and $H \perp c$ with Dirac–Fock calculations of the magnetic form factor of paramagnetic Er (after Stassis et al., 1976).

singlet ground state. The crystal field parameters are also quite well-known (Cooper and Vogt, 1970a). The magnetic form factor for the Tm^{3+} ion in this compound for various directions of the applied field of 12.5 kOe was studied by Lander and Brun (1973). They calculated the induced moment form factor by obtaining the wave functions as linear combinations of the $|\theta JM\rangle$ states from a diagonalization of the crystal field hamiltonian (with the applied field included) and using the Lovesey-Rimmer tensor formulation (Lovesey and Rimmer, 1969) to calculate the matrix elements. The directional dependence was consistent with the crystal field calculations but again the form factor indicated a slightly more expanded Tm^{3+} radial 4f wavefunction than that given by the non-relativistic calculations. (In the case of $Tb(OH)_3$ described above, the crystal field produces a $|6, \pm 6\rangle$ doublet ground state yielding essentially the ordered moment form-factor (Brun and Lander, 1974).

Recently, Koehler and Moon (1972) obtained the form factor of Sm^{3+} on both cubic and hexagonal sites of Sm metal from intensity measurements in the ordered phases. Their results are shown in fig. 7.24. Unlike most other form factors, it does not have a maximum at $\sin\theta/\lambda = 0$. This is partly due to the opposition of the spin and orbital contributions to the moment for this ion. In addition, Koehler and Moon ascribe the very low value of the apparent moment on the Sm^{3+} ion to compensatory conduction electron polarization. However, they did not fully consider the strong crystal field effects which must be present. De Wijn et al. (1974) have attempted to calculate the form factor including crystal field effects but do not obtain good agreement. However, they use non-relativistic wave functions and also employ the dipole approximation,

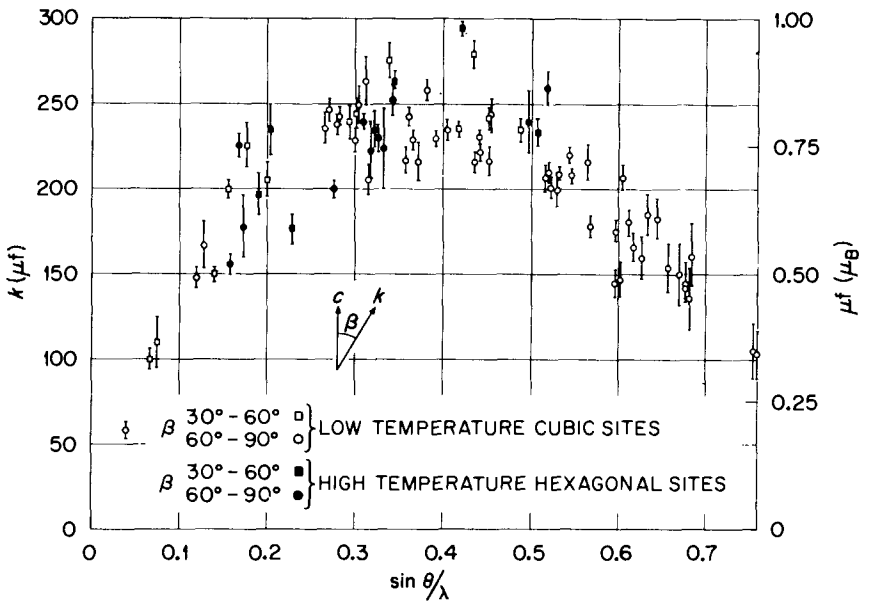

Fig. 7.24. Magnetic scattering amplitudes observed in metallic Sm. β refers to the angle between c and the scattering vector (after Koehler and Moon, 1972).

where as discussed above, the full expression (given by eq. (7.70)) should be employed. Such calculations should be performed if conclusions are to be drawn regarding conduction electron polarization, and the magnitude of the crystal field.

A slightly different type of form-factor measurement was performed by Felcher et al. (1976) who performed an experiment to look specifically at the aspherical component of the form factor of Ho. (The measurements were performed both for a pure Ho crystal and a $Ho_{0.9}Sc_{0.1}$ alloy.) They showed that for a spiral magnetic structure of ions having aspherical magnetization distributions, the form factor for ions in the jth layer at a given $\boldsymbol{Q}$ was given by

$$f_j(\boldsymbol{Q}) = \sum_{n=0}^{3} B_{2n}(Q, \theta) \cos(2n\phi_j) \tag{7.75}$$

where ϕ_j is the azimuthal angle for the direction of the moments in the jth layer, and θ is the angle between $\boldsymbol{Q}$ and the plane of the spiral. The B_{2n}'s are linear combinations of the $\bar{j}_{2n}$ integrals involving tabulated (Felcher et al., 1976) coefficients which depend on the M value of the ordered state ($M = 8$ for the completely ordered state of the Ho^{3+} $^5I_8$ multiplet). Since the moments themselves have components which vary as $(\cos\phi_j)$ and $(\sin\phi_j)$, and since the scattering amplitude is the product of the form factor and the moment, it may be seen that the $n = 1$ term in eq. (7.75) will give rise to a third-order satellite along the [001] axis of reciprocal space. This will be weak compared to the main satellite, but will have a leading term in its amplitude which involves $\bar{j}_2$ rather

than $\bar{j}_0$ as in the usual form factor. Hence its form factor will have quite a different behavior as a function of Q and will go to zero as $Q \to 0$. Figure 7.25 shows this form factor measured for both samples studied (after correcting for the higher-order $\bar{j}_{2n}$ and converting it to an effective $\bar{j}_2$ for Ho^{3+}) compared with that calculated from a Dirac–Fock calculation of Freeman and Desclaux. It may be seen that its shape is right, but that its magnitude is appreciably different from the calculated free ion $\bar{j}_2$. The same D–F calculation gave very good agreement with the form factor measured from the ordinary first-order satellites (the usual "spherical" form factor) in the same experiments. The temperature dependence of the third satellite intensities was also in excellent agreement with that calculated from the M-dependence of the B_{2n}'s. Since the experiment is sensitive *only* to the aspherical components of the magnetization distribution, in contrast to the other form factor measurements, it may indicate subtle solid state effects possibly associated with the conduction electrons.

As we have seen, on the whole the agreement with theory for the localized form factor associated with the 4f electrons in lanthanide metals and compounds is satisfactory provided one is careful to use relativistic calculations. The situation for the conduction electron polarization distribution is less clear. Conduction electron form factors were obtained for Gd by Moon et al. (1972) and for Er by Stassis et al. (1976). In both cases, these were obtained by separating from the measured form factor the localized 4f contribution, and in both cases appear to be different from either a 5d or 6s atomic form factor. A spin-polarized augmented-plane-wave (APW) calculation of the conduction electron polarization in ferromagnetic Gd was performed by Harmon and Freeman (1974). Their results are, however, only in qualitative agreement with the results of Moon et al. The theoretical form factor of Harmon and Freeman is in somewhat better agreement with the experimental results of Stassis et al. on Er.

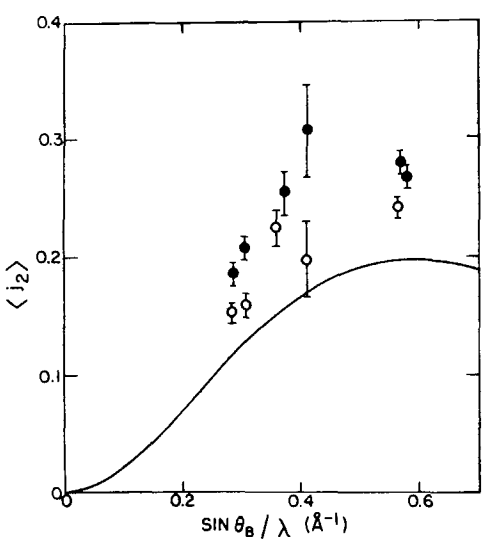

Fig. 7.25. Effective $\langle j_2 \rangle$ for Ho measured from third order satellite intensities. The open points refer to measurements on Ho; the closed to measurements on $Ho_{0.9}Sc_{0.1}$. The full line represents a Dirac–Fock calculation of $\langle j_2 \rangle$ (after Felcher et al., 1976).

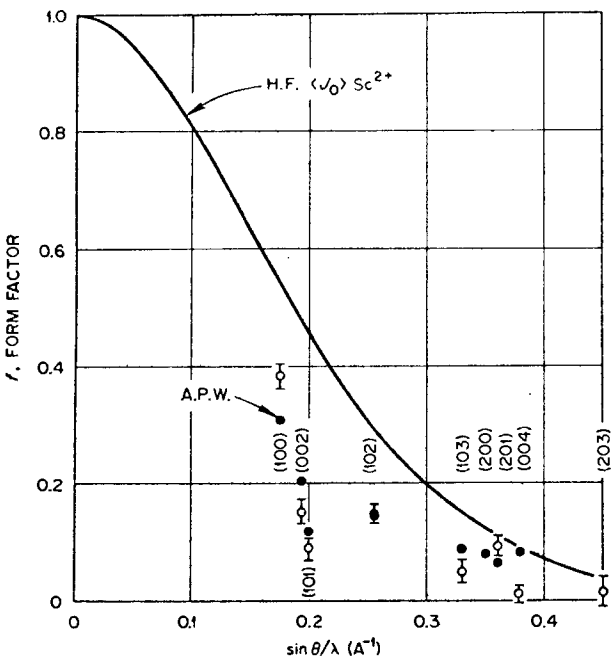

Fig. 7.26. Induced moment form factor for Sc metal. The open circles are the experimental points. The full circles are from the APW calculation of Gupta and Freeman (1976b). The solid line is a free-ion 3d form factor from a Hartree–Fock calculation. (After Koehler and Moon, 1976.)

The subtraction of the large 4f contribution from the measured form factor leads to serious uncertainties in the measured conduction electron form factor. Recently, the induced moment conduction electron form factor has been measured for Sc (Koehler and Moon, 1976) which is isoelectronic but without a 4f contribution. This form factor, it should be noted, will only be similar to the conduction electron form factor of the magnetic rare earth metals, if no appreciable orbital moment is induced by the applied field. (Here we are relying on the susceptibility of the conduction electrons themselves rather than exchange with the 4f electrons to produce a polarization.) If this is the case, the form factor is proportional to the Fourier transform of a density-of-states weighted average of the electron spatial density for electrons at the Fermi surface (Stassis et al., 1975). This has been calculated for Sc by Gupta and Freeman (1976b) and is in very good agreement with the measured form factor, although neither bears any similarity to atomic 3d form factors (see fig. 7.26). Similar measurements are in progress for Y (Koehler, to be published) and Lu (Stassis, private communication).

5. Inelastic neutron scattering studies

We have seen in the preceding sections that studies of magnetic ordering in lanthanide materials by neutron diffraction, together with bulk magnetization and susceptibility measurements, as well as other types of measurements such as

Mössbauer experiments, have yielded a great deal of information about the basic interactions in these materials. Most of this information is obtained via a molecular field theory of the magnetic phenomena. A more stringent test of our understanding of the basic interactions (crystal field, exchange, magnetoelastic, etc.) is to see whether one can successfully explain the spin dynamics in these systems. Inelastic neutron scattering studies have been invaluable in probing such dynamics since they may be used to study the spectrum of low-lying magnetic excitations (e.g. crystal field or magnon excitations). Over the last ten years or so such experiments have been used to obtain a great deal of detailed information on the microscopic interactions. We shall not discuss here the effects of interactions among the excitations or with other types of excitations such as phonons.

The partial differential scattering for neutrons from an assembly of lanthanide ions may be calculated in the Born approximation (Marshall and Lovesey, 1971). If we assume $Q\langle r\rangle \ll 1$, the dipole approximation (see section 4.1) may be used and we obtain

$$\frac{\mathrm{d}^2\sigma}{\mathrm{d}\Omega\,\mathrm{d}E'} = \frac{1}{4}g_J^2(\gamma r_0)^2\frac{k'}{k}\sum_{\alpha\beta}(\delta_{\alpha\beta}-\hat{Q}_\alpha\hat{Q}_\beta)\sum_{\lambda\lambda'}P_\lambda\sum_{\substack{ll'\\ \kappa\kappa'}}f_\kappa(\boldsymbol{Q})f_{\kappa'}(\boldsymbol{Q})$$
$$\times\exp\{\mathrm{i}\boldsymbol{Q}\cdot(\boldsymbol{R}_{l\kappa}-\boldsymbol{R}_{l'\kappa'})\}\langle\lambda|J^\alpha_{l\kappa}|\lambda'\rangle\langle\lambda'|J^\beta_{l'\kappa'}|\lambda\rangle\delta(\hbar\omega+E_\lambda-E_{\lambda'}) \qquad (7.76)$$

where E' is the scattered neutron energy, $\hbar\boldsymbol{Q}$, $\hbar\omega$ the neutron momentum transfer and energy loss respectively, $\boldsymbol{k}_0$, $\boldsymbol{k}_1$ the incident and scattered neutron wave vectors respectively, λ, λ' denote the initial and final states of the system with energies E_λ, $E_{\lambda'}$ respectively, P_λ denotes the thermal population of the state λ and $J^\alpha_{l\kappa}$ is the α component of the total angular momentum operator for the ion at site $\boldsymbol{R}_{l\kappa}$, κ denoting the sublattice index. $f_\kappa(\boldsymbol{Q})$ is the magnetic form factor in the dipole approximation, given in eq. (7.74). We have also assumed unpolarized neutrons. Alternative forms for writing the cross section in eq. (7.76) which are sometimes useful are (Marshall and Lovesey, 1971)

$$\frac{\mathrm{d}^2\sigma}{\mathrm{d}\Omega\,\mathrm{d}E'} = \frac{1}{4}g_J^2(\gamma r_0)^2\frac{k_1}{k_0}\sum_{\alpha\beta}(\delta_{\alpha\beta}-\boldsymbol{Q}_\alpha\boldsymbol{Q}_\beta)\frac{1}{2\pi\hbar}\sum_{\substack{ll'\\ \kappa\kappa'}}f_\kappa(\boldsymbol{Q})f_{\kappa'}(\boldsymbol{Q})\,\mathrm{e}^{-W_\kappa}\,\mathrm{e}^{-W_{\kappa'}}$$
$$\times\exp\{\mathrm{i}\boldsymbol{Q}\cdot(\boldsymbol{R}_{l\kappa}-\boldsymbol{R}_{l'\kappa'})\}\langle J^\alpha_{l\kappa}(0)J^\beta_{l'\kappa'}(t)\rangle \qquad (7.77)$$

where e^{-W_κ} is the Debye–Waller factor for sublattice κ; and the thermal expectation value in $\langle\ldots\rangle$ is over the Heisenberg operators for the times indicated. We may also write this result as

$$\frac{\mathrm{d}^2\sigma}{\mathrm{d}\Omega\,\mathrm{d}E'} = \frac{1}{4}g_J^2(\gamma r_0)^2\frac{k_1}{k_0}(\mathrm{e}^{-2W})f^2(\boldsymbol{Q})\frac{N}{\pi(g_J\mu_\mathrm{B})^2}$$
$$\times\sum_{\alpha\beta}(\delta_{\alpha\beta}-\boldsymbol{Q}_\alpha\boldsymbol{Q}_\beta)(1-\mathrm{e}^{-\beta\omega})^{-1}\,\mathrm{Im}\,\chi_{\alpha\beta}(\boldsymbol{Q},\omega) \qquad (7.78)$$

where we have dropped for simplicity the sublattice indices, N = total number of unit cells in the crystal and $\chi_{\alpha\beta}(\boldsymbol{Q},\omega)$ is the generalized susceptibility tensor

for the system of *ions* (not to be confused with $\chi(q)$ for the *conduction electrons* discussed in earlier sections).

We may, in keeping with the general principles discussed in section 2, separate the materials studied into three classes:
(a) materials in which exchange is negligible compared to the crystal field effects,
(b) materials in which exchange and crystal field effects are comparable,
(c) materials in which exchange is dominant.
We shall discuss experiments on each class of material in turn.

5.1. *Studies of crystal field splitting*

Crystal field effects in lanthanide materials form the subject of a separate chapter (17). In this section we briefly review the experimental neutron scattering results, of which by now there are a large number. Since exchange is negligible, the states of the system can be factorized into single ion states with no correlation between these states. In such a case, we obtain from eq. (7.76),

$$\frac{d^2\sigma}{d\Omega\, dE'} = \frac{1}{4} g_J^2 (\gamma r_0)^2 f^2(\boldsymbol{Q}) \sum_{n,n'} P_n \sum_{\alpha\beta} (\delta_{\alpha\beta} - \boldsymbol{Q}_\alpha \boldsymbol{Q}_\beta) \times \langle n|J^\alpha|n'\rangle\langle n'|J^\beta|n\rangle \delta(\hbar\omega + E_n - E_{n'}) \tag{7.79}$$

where we assume only one sublattice, and n, n' refer to the states of a single ion. In general, neutron scattering experiments are performed with energy transfers of up to only a hundred millivolts or so, and thus these states will be within the manifold of states split by the crystal field from the $(2J+1)$ fold degenerate ground state. Thus one should see peaks at energy transfers corresponding to the splitting within a multiplet, broadened by instrumental resolution and also by other effects such as thermal broadening or exchange broadening. (In such cases one generally replaces the δ-function in eq. (7.79) by a Gaussian or a Lorentzian.) By measuring the temperature dependence of the various lines or the relative intensities for up and down scattering, one can often identify the states between which the transitions are occurring (since P_n depends on both the initial state and the temperature) and thus construct a level scheme. Sometimes, particularly for single crystal samples, the matrix element selection rules may be used to identify states.

For lanthanide ions in crystal fields of cubic symmetry, the crystal field hamiltonian is of the form given by eq. (7.8), and thus the energy levels depend on two parameters V_4^0, V_6^0 (usually referred to as B_4 and B_6). It is often more convenient to deal with two other parameters introduced by Lea, Leask and Wolf (1962), which are referred to as W and x and are given by

$$\frac{B_4}{B_6} = \frac{x}{1-|x|}\frac{F(4)}{F(6)} \tag{7.80}$$

and

$$B_4 F(4) = Wx \tag{7.81}$$

The $F(4)$ and $F(6)$ are the inverses of the Stevens multiplicative factors for the ion of given J [see eq. (7.6)] and are tabulated by Lea et al. (1962) x is a measure of the ratio of fourth order to sixth order crystal field contributions, while W scales the overall splitting of the levels. Lea, Leask and Wolf have tabulated all the crystal field splittings for different J's as functions of x, W. Measured crystal field parameters for cubic systems are usually expressed in terms of these parameters, and then via knowledge of the $\langle r^4 \rangle$ and $\langle r^6 \rangle$, in terms of the more "fundamental" crystal field parameters A_4, A_6. In order to facilitate interpretation of neutron scattering experiments, Birgeneau (1972) has also tabulated matrix elements of J^α for all possible transitions in terms of the parameter x. For hexagonal symmetry, one may use the crystal field hamiltonian given in eq. (7.7).

5.1.1. *Lanthanide metals*

In general, exchange effects are too large in lanthanide metals to enable one to see pure crystal field transitions. However, for very dilute lanthanide alloys in non-magnetic isoelectronic hosts such as Y, Sc or Lu, exchange can be made sufficiently negligible. Recently neutron scattering determinations of such crystal field levels have been carried out by Rathmann et al. (1974) together with magnetization and susceptibility measurements on these systems (Høg and Touborg, 1974, 1975a,b, 1976). Measurements have been made for 1 or 2% of Er and Dy in Sc, Lu and Y. Figure 7.27 shows a crystal field transition observed in $Y_{0.98}Er_{0.02}$ (Rathmann et al., 1974) at 5 K. The measurements were performed along the a^*- and c^*-axes of a single crystal and with a polycrystalline sample, and a least squares fit was made of the four crystal field parameters (together with some broadening), after correction for instrumental resolution and phonon scattering. Good agreement was obtained with the crystal field parameters calculated from magnetization measurements on the same crystal. Table 7.4

TABLE 7.4.
Crystal field parameters for small concentrations of lanthanides dissolved in Y, Sc, Lu (divided by Stevens factors)

	B_{20}/α (K)	B_{40}/β (K)	B_{60}/γ (K)	c/a
Y (Er)	−111	13.5	12.0	
Y (Tb)	−94	4.8	13	1.573
Y (Dy)	−53	44	32	
Lu (Er)	−55.7	9.6	16.1	
Lu (Tb)	−63	5.2	12	1.584
Lu (Tb)	−22	48	33	
Lu (Ho)	−36	0.8	13	
Sc (Tb)	−31	13.4	24.4	
Sc (Dy)	−29.9	14.6	20.9	1.594
Sc (Er)	−29.0	8.2	18.1	

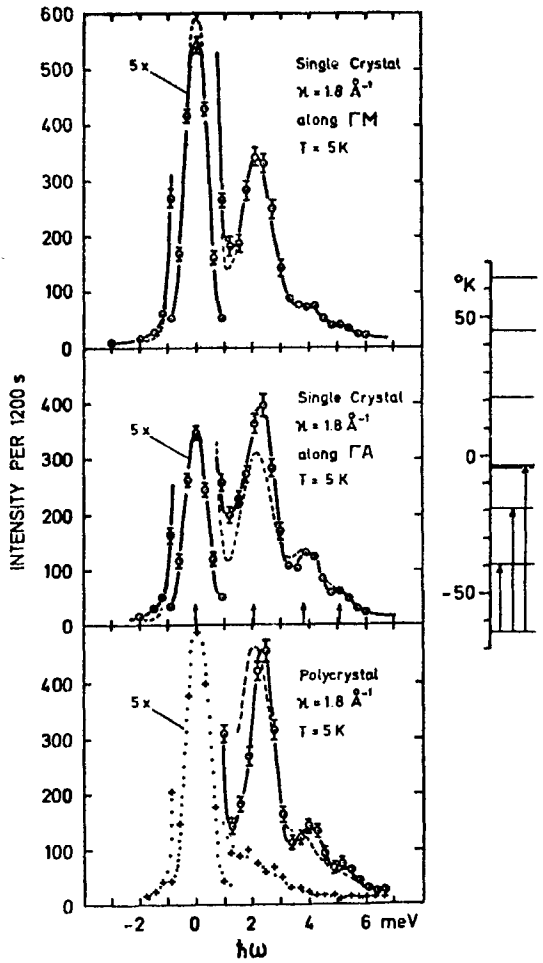

Fig. 7.27. Inelastic neutron spectra for $Er_{0.02}Y_{0.98}$ at $Q = 1.8$ Å^{-1}. The upper and middle figures refer to single crystal data with $\boldsymbol{Q}$ along the b- and c-axes respectively. The lower figure is on a polycrystalline sample. The scattering from a pure Y polycrystal is shown in the bottom figure by + symbols and a dotted line. The dashed line represents a fit of the crystal field model and the full lines are guides to the eye (after Rathmann et al., 1974).

shows the values for the crystal field parameters found for several such systems. From eq. (7.6), it may be seen that B_{lm}/α_l (α_l = the Steven's factor) depends only on the crystal field potential of the host lattice and $\langle r^l \rangle$ of the magnetic ion which does not vary appreciably among the heavy lanthanide metals. Hence, it should be roughly constant for a given host, independent of the lanthanide ion. This is indeed the case. Table 7.4 shows that B_{lm}/α_l (and in particular B_{20}/α_2) depends on the host lattice which provides the crystal field. In fact, the behavior of B_{20}/α_2 strongly correlates with the deviation of the c/a ratio of the host from the ideal hcp ratio. A point charge model for crystal fields in these systems was totally unsatisfactory (Rathmann et al., 1974).

5.1.2. NaCl *structure* RX *compounds*

These are the best studied with neutrons from the point of view of crystal fields. It is not true of course that exchange is completely negligible for all of these, since many of them do order magnetically at low temperatures, as discussed in section 3.5. As mentioned previously, TmSb is probably closest to being the ideal exchange free paramagnet. In agreement with this, no exchange broadening of the crystal field transitions was observed (Birgeneau et al., 1971a). Figure 7.28 shows the time-of-flight spectrum of neutrons scattered from a

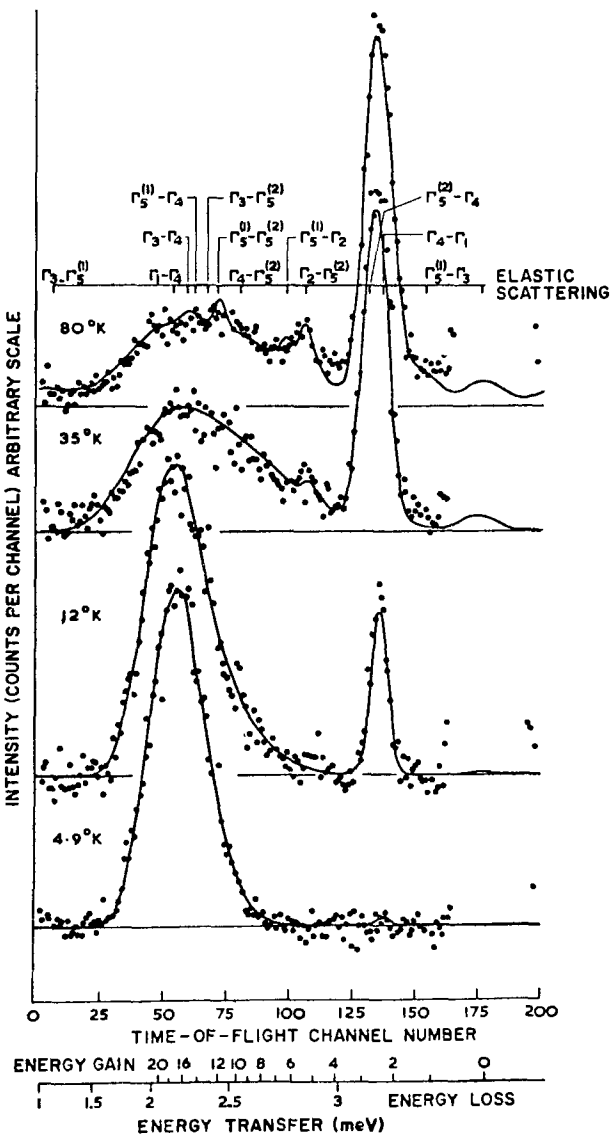

Fig. 7.28. Time-of-flight spectrum of neutrons scattered from polycrystalline TmSb at various temperatures. Smooth curves and associated background levels represent the results of fitting a crystal-field model (after Birgeneau et al., 1971a).

polycrystalline sample of TmSb at various temperatures, together with a fit to the data from a crystal field model. The crystal field parameters were in reasonable agreement with those derived by Cooper and Vogt from magnetization measurements (Cooper and Vogt, 1970a) and consistent with those used later by Lander et al. (1973) in analyzing the form factor of TmSb. Similar measurements have been carried out on the complete series of lanthanide phosphides (Birgeneau et al., 1973), Pr pnictides and chalcogenides (Tuberfield et al., 1970, 1971), Nd pnictides (Furrer et al., 1972), CeP, CeAs, CeSb, and CeBi (Rainford et al., 1968; Heer, 1975, 1976). The results on the Pr compounds (except for PrN) indicated good agreement with a surprisingly simple point charge calculation of the crystal fields with an effective ligand charge of -2, if one used the non-relativistic atomic calculations of $\langle r^n \rangle$. In view of the form factor work described in the previous section, it is actually necessary to use the relativistic Dirac–Fock calculations, however, so these values of Z should not be taken at face value. (Using relativistic values for $\langle r^n \rangle$ changes Z to -1.2 (Birgeneau et al., 1973)). PrN (Davis and Mook, 1972), NdN (Furrer and Halg, to be published), HoN (Furrer et al., 1976a), and TmN (Davis and Mook, 1975) require quite a different value of Z ($\simeq -3$), but there is some evidence that the nitrides are a different class of compounds (as already discussed in section 3.5) and may be semiconductors rather than metals (Bucher and Maita, 1973). The point charge model fails, however, to provide agreement for the sixth order crystal field parameters in TmSb and the Nd compounds. Since one expects the conduction electrons in these materials to strongly affect the crystal fields at the lanthanide sites, it is possible that the apparent good agreement with the predictions of the point charge model for a large number of these compounds is fortuitous. This is also borne out by the calculations of elastic constant softening due to strain-quadrupole coupling discussed in section 2.5, where derivatives of the crystal fields calculated from a point-charge model (Mullen et al., 1974) give poor agreement with experiment. Nevertheless, some remarkable systematics are apparent. Figure 7.29 shows the fourth order parameter $A_4\langle r^4 \rangle$ times the fifth power of the lattice constant (which in the point charge model would be proportional to Z) plotted against the number of 4f electrons, and it is seen that a reasonably universal curve is obeyed (except for the Ce compounds, which are also anomalous in many ways as has been discussed in section 3.5, and the nitrides). The sixth order parameters remain small and almost constant. Bucher and Maita (1973) were able to correlate $A_4\langle r^4 \rangle$ with the electronegativity of the pnictide compounds and another for the chalcogenides. Some measurements on single crystals of HoP, NdSb and NdS are discussed in section 5.2.

5.1.3. CsCl-*structure* RX *compounds*

Crystal field splittings in PrAg (Brun et al., 1974), ErCu (Morin et al., 1974b), ErZn (Morin et al., 1974b), ErAg (Morin et al., 1974b; Furrer, 1975) and HoAg (Tellenbach et al., 1975) have been studied by inelastic neutron scattering. The point charge model does not appear to be capable of giving good agreement for

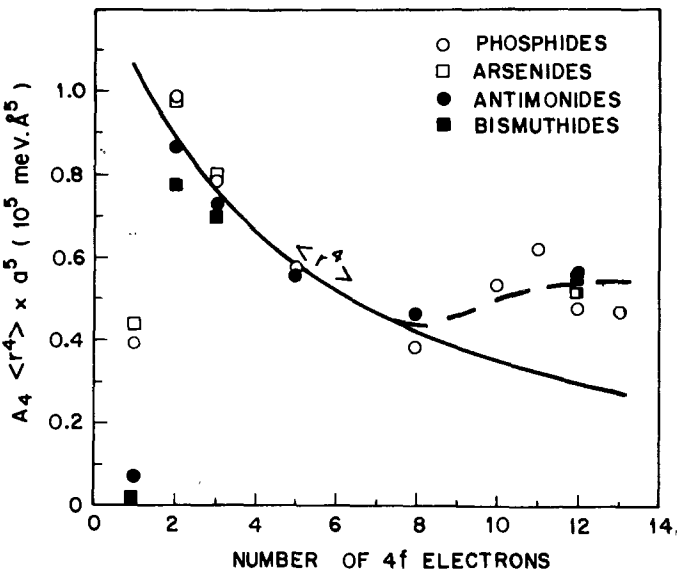

Fig. 7.29. Fourth-order crystal field parameter times the lattice constant, a, raised to the fifth power for a number of lanthanide monopnictides. The solid line is the point charge model prediction with $Z = -1.2$ and $\langle r^4 \rangle$ equal to that obtained from a Dirac–Slater calculation (after Birgeneau et al., 1973).

the measured values of the crystal field parameters, in particular the sixth order terms. Brun et al. (1974b) find reasonable agreement with one set of their obtained parameters for PrAg by assuming neutral Ag atoms and the crystal fields arising from next nearest-neighbor Pr^{3+} ions. However, Morin et al. (1974b) find Brun et al.'s alternative set of experimental parameters in much better agreement with their values obtained for ErAg, since the first set has an $A_6\langle r^6 \rangle$ which is an order of magnitude too small. In principle, of course the two compounds should have very similar crystal field parameters. The PrAg spectra (Brun et al., 1974b) as well as the pure ErAg data of Furrer (1975) showed considerable exchange broadening which complicates the analysis of the crystal field parameters. Morin et al. (1974a, 1974b) were able to decrease the exchange in their samples and sharpen the observed peaks by diluting with Y in place of the Er. These authors have used the crystal field parameters in these and similar compounds together with a molecular field theory, as outlined in section 2.6, to calculate bulk magnetic properties of these materials (Morin et al., 1974a,b). Tellenbach et al. (1975) have carried out similar experiments on $Ho_{0.2}Y_{0.8}Ag$ and also on HoAg. They find the exchange broadening in the latter wipes out the structure of the peaks, but that the spectra could still be fitted with a consistent set of crystal field parameters which agreed with those of the dilute alloys, where the peaks were resolved. They also find agreement with susceptibility and magnetization data calculated using these parameters and a molecular field.

5.1.4. *Cubic laves phase compounds* RX_2

The point symmetry in these materials at the lanthanide sites is cubic. Crystal field measurements on powdered samples of $Tm_xY_{1-x}Al_2$ have been made by Purwins et al. (1973a) and on $Er_xY_{1-x}Al_2$ by Heer et al. (1974). The Y was used to dilute the exchange interaction. Nevertheless, separate peaks due to individual transitions were not resolved in the spectra, and a least squares procedure was used to obtain the crystal field parameters. In the case of $Er_xY_{1-x}Al_2$, susceptibility and magnetization data were discussed to help decide on the best set of crystal field parameters (Heer et al., 1974). It should be noted that the A_4, A_6 deduced from these measurements are not in agreement with each other as they should be if the crystal field at the lanthanide site did not depend on the type of ions on those sites. Thus for the best fit results to $Tm_xY_{1-x}Al_2$, A_4 was positive and A_6 was negative. The signs of A_4, A_6 deduced from neutron, susceptibility, specific heat and EPR measurements in these compounds in fact appear to vary in a bewildering fashion and has been suggested (Devine, 1974) that the crystal fields may be dependent on the lanthanide concentration, which in turn could affect the degree of localization of the 5d virtual bound state on the rare earth ions. One should note however, that several different combinations of A_4, A_6 give quite good fits to the neutron data alone, so one cannot be sure whether the problem involves real physics or not.

5.2. *Studies of magnetic excitons*

A magnetic exciton is defined as an elementary excitation corresponding to a particular crystal field transition on an ion which is coupled by exchange to transitions on neighboring ions, and hence can propagate coherently through the crystal. Thus, instead of a transition between two discrete levels, as in the pure crystal field case, there will be a dependence of the excitation energy on wave vector, and the dispersion curves can, in principle, be mapped out by inelastic neutron scattering on single crystal samples. Particular interest has centered on the singlet ground state systems in the region close to where the threshold value of the exchange required to induce magnetic ordering is achieved, in view of the theoretical prediction made some years ago (Wang and Cooper, 1969, 1970) that the onset of magnetic ordering could be understood in terms of the "softening" (to zero frequency) of one of these collective modes, analogous to the relationship of crystallographic phase transformations to soft phonon modes. Unfortunately, as in the latter case, the experiments have revealed a situation more complicated than envisaged in the original predictions. The subject has been recently reviewed by Cooper (1972, 1976). We have briefly discussed molecular field treatment of induced moment systems in section 2.6. In order to discuss the collective modes of such systems, one is forced to improve on the molecular field approximation.

The first dynamical calculations were based on the singlet–singlet system already introduced in section 2.6 and were based on the Bogoliubov-type

approximation of defining pseudo-Boson operators which excited and de-excited an ion from the lower to the upper level respectively. (For a list of references see Cooper (1976).) This approximation is only good at low temperatures, since for appreciable occupation of the higher levels, the operators do not have boson-like commutation relations any more. In addition the formalism implicitly involves unphysical states with multiple occupation of the same site. The result obtained at low temperature, however, is equivalent to that obtained in the RPA, to be discussed below. Subsequent calculations have gone in two directions. One approach has concentrated on the singlet–singlet system and attempted to treat the dynamics in a better approximation. Thus one can recast the problem in terms of a pseudo-spin formalism (Wang and Cooper, 1970; Pink, 1968), and obtain the collective modes by a Green's function decoupling technique. The first approximation is the RPA. However, one can go even further and keep two-site correlations (Wang and Cooper, 1969, 1970). Pseudospin-formulations have also been developed for the singlet–triplet system (Pink, 1968; Hsieh and Blume, 1972). The other approach has been to keep the complete multi-level system and perform an RPA calculation using a pseudo-fermion formalism (Fulde and Peschel, 1971, 1972; Buyers, 1975). We briefly review this method below.

We write the hamiltonian as in eq. (7.35) (section 2.6) in terms of a molecular field part $\mathcal{H}_0$ and an interaction part $\mathcal{H}_1$. Let $|m\rangle$, $|m'\rangle$, etc. denote molecular field states on a single ion, and introduce pseudo-fermion operators C^+_{im}, C_{im} that create and annihilate states $|m\rangle$ on the ion i, respectively. Then

$$\mathcal{H}_0 = \sum_{m,i} \epsilon_m C^+_{im} C_{im}, \tag{7.82}$$

$$\mathcal{H}_1 = \sum_{\substack{i \neq j \\ m,m' \\ n,n'}} J_{ij} \langle m|\boldsymbol{J}_i|m'\rangle \cdot \langle n'|\boldsymbol{J}_j|n\rangle C^+_{im} C_{im'} C^+_{jn'} C_{jn} \tag{7.83}$$

We have assumed in the above that there is no ordered moment. One may then obtain the dynamical susceptibility of the spin system $\chi_{\alpha\beta}(\boldsymbol{Q}, \omega)$ in terms of the two-particle Green's functions $\langle\langle C^+_{im} C_{im'}; C^+_{jn'} C_{jn}\rangle\rangle$. These are obtained by the equation of motion technique (Buyers, 1975) by commuting $C^+_{im} C_{im'}$ with $\mathcal{H}$ and in the commutator replacing four-operator products by suitably averaged two-operator terms. One obtains

$$\chi_{+-}(\boldsymbol{Q}, \omega) = \chi^{(0)}_{+-}(\omega)/[1 - \mathcal{J}(\boldsymbol{q})\chi^{(0)}_{+-}(\omega)] \tag{7.84}$$

and

$$\chi_{zz}(\boldsymbol{Q}, \omega) = \chi^{(0)}_{zz}(\omega)/[1 - 2\mathcal{J}(\boldsymbol{q})\chi^{(0)}_{zz}(\omega)] \tag{7.85}$$

for the different components of the susceptibility. In eqs. (7.84) and (7.85),

$$\mathcal{J}(\boldsymbol{q}) = \sum_j \mathcal{J}_{ij} \exp\{i\boldsymbol{q} \cdot (\boldsymbol{r}_i - \boldsymbol{r}_j)\} \tag{7.86}$$

and $\chi^{(0)}$ is the dynamical susceptibility of the single ion in the molecular field given by

$$\chi^{(0)}_{\alpha\beta}(\omega) = \sum_{m,m'} \langle m|J^\alpha - \langle J^\alpha\rangle|m'\rangle\langle m'|J^\beta - \langle J^\beta\rangle|m\rangle(P_m - P_{m'})[E_{m'} - E_m - \omega]^{-1} \tag{7.87}$$

where P_m is the thermal occupation of state $|m\rangle$, etc. The neutron scattering may then be obtained from eq. (7.78). It will yield discrete peaks at ω values wherever eqs. (7.84) or (7.85) reveal that $\chi_{\alpha\beta}(Q, \omega)$ has poles. (In the above, we have assumed only one ion per unit cell.) In the singlet–singlet case only matrix elements of J^z exist and hence only χ_{zz}. In the paramagnetic state, $\langle J^z\rangle = 0$, and eq. (7.87) yields

$$\chi^{(0)}_{zz}(\omega) = \Delta\alpha^2(P_0 - P_1)/(\Delta^2 - \omega^2) \tag{7.88}$$

and by eq. (7.85), the collective modes will be given by

$$1 - [2\mathcal{J}(q)\Delta\alpha^2(P_0 - P_1)/(\Delta^2 - \omega_q^2)] = 0 \tag{7.89}$$

which yields the solution

$$\omega_q = \Delta[1 - (2\mathcal{J}(q)\alpha^2/\Delta)(P_0 - P_1)]^{1/2} \tag{7.90}$$

The Bogoliubov approximation described above obtains the same result without the $(P_0 - P_1)$ factor. At low temperatures, $P_0 = 1$, $P_1 = 0$, and for the situation where $\mathcal{J}(q)$ is a maximum at $q = 0$, we see that the collective mode will go soft at $q = 0$ when A (defined in eq. (7.44)) reaches 1, which is also the threshold value for induced moment ordering in the molecular field theory. The temperature renormalization of ω_q in this theory is contained in the factor $(P_0 - P_1)$ which may be evaluated in the molecular field approximation,

$$P_0 = \frac{1}{1 + e^{-\Delta/kT}}, \qquad P_1 = \frac{e^{-\Delta/kT}}{1 + e^{-\Delta/kT}} \tag{7.91}$$

However, one may go further than this and evaluate P_0 and P_1 self-consistently in the Green's function theory. This changes the threshold value of A from 1 to 1.04. The TSCA yields a critical value for A of 1.18 for a simple cubic lattice with nearest neighbor exchange (Cooper, 1976). The dispersion curve in the RPA approximation for A slightly greater than the critical value is shown in fig. 7.30, for several temperatures, together with the behavior of the magnetization. It may be seen that the mode at $q = 0$ softens as the temperature approaches T_C from above, reaching zero at T_C and then increasing again to a finite value at lower temperatures.

The dispersion relation for such collective modes was first measured by Rainford and Houmann (1971) for dhcp Pr and later studied in more detail by Houmann et al. (1975) (see also Bak (1975)). Figure 7.31 shows the excitation dispersion relations for the hexagonal sites in Pr at 6.4 K. The hexagonal sites show four branches corresponding to two "acoustic" and two "optic" modes (there are two such sites per unit cell) and to excitations from the singlet $|0\rangle$

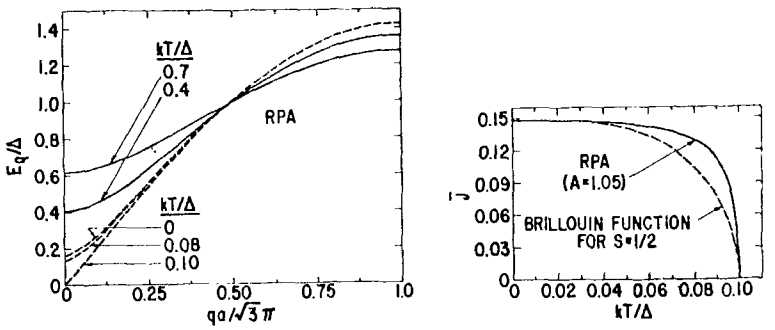

Fig. 7.30. (left) Change of dispersion curve as temperature is raised through T_C for ($A = 4\mathcal{J}(0)\alpha^2/\Delta = 1.05$, $kT/\Delta = 0.1$, $q\|\langle 111\rangle$) for a simple cubic lattice in the RPA. (right) Corresponding magnetization vs. temperature (after Wang and Cooper, 1970).

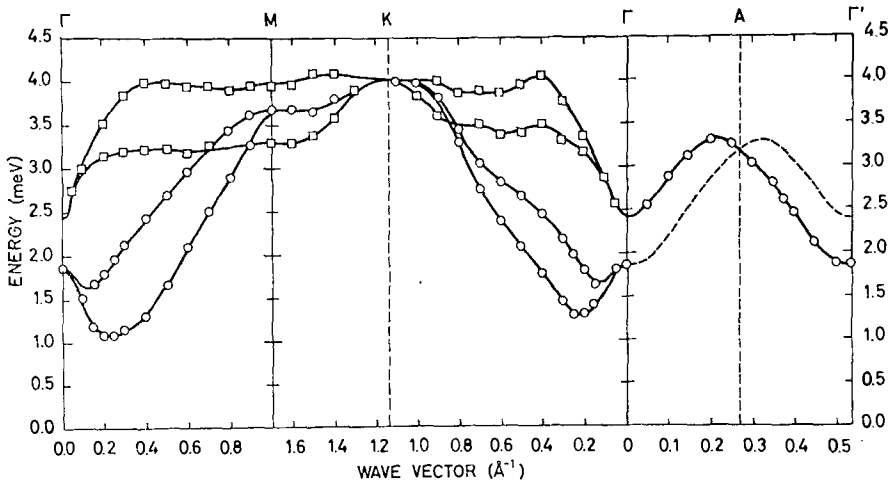

Fig. 7.31. Dispersion relations for magnetic excitations propagating on the hexagonal sites of dhcp Pr at 6.4 K. The circles represent acoustic-type modes and the squares optic-type modes (after Houmann et al., 1975).

crystal field state to the doublet $|\pm 1\rangle$ first excited states. The RPA theory yields for the dispersion relation (Lindgard and Houmann, 1971; Houmann et al., 1975)

$$\omega^2_{q\pm,\nu} = x,\ y = \Delta^2 - \alpha^2\Delta\{\mathcal{J}^{\nu\nu}(\boldsymbol{q}) \pm |\mathcal{J}^{i\nu\nu}(\boldsymbol{q})|\}(P_0 - P_1), \qquad (\nu = x, y) \tag{7.92}$$

where we have assumed anisotropic exchange interactions ($J^{xx} \neq J^{yy} \neq J^{zz}$), α is the matrix element of J^+ and J^- between the ground and excited states, and $\mathcal{J}(\boldsymbol{q})$, $\mathcal{J}'(\boldsymbol{q})$ represent interactions between the same and between different sublattices. For isotropic exchange, the two branches (acoustic as well as optic) should be degenerate along the c-axis, and fig. 7.31 shows that considerable anisotropy of the exchange must be present. The source of this anisotropy is as yet unclear. Figure 7.32 shows the temperature dependence of some of the

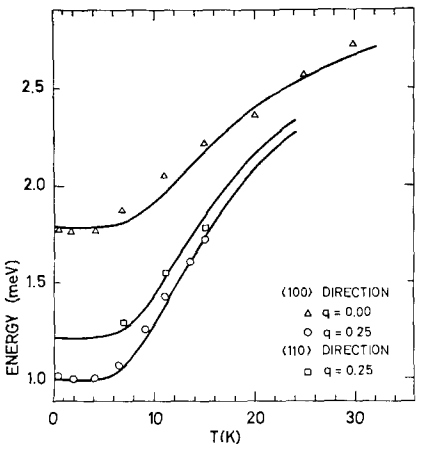

Fig. 7.32. Temperature dependence of selected magnetic excitations in Pr. The full lines are calculated in the RPA-approximation as discussed in the text (after Houmann et al., 1975).

excitation frequencies along the a^*-axis, together with the calculation based on the temperature dependence of $(P_0 - P_1)$ in eq. (7.92) in the molecular field approximation (Houmann et al., 1975). It may be seen that the agreement is quite good. As the temperature is lowered, the modes soften (especially near the q-vector for which there is a tendency for antiferromagnetism to set in) but not all the way to zero. The exchange interaction in this system is in fact only 90% of the critical value required for ordering.

We turn now to systems where ordering is known to occur such as the cubic singlet ground state systems Pr_3Tl (Birgeneau, 1973; Birgeneau et al., 1972b) ($T_C = 11.6$ K) and TbSb (Holden et al., 1974) ($T_N = 14.9$ K). Measurements have also been made for the alloy $(Pr_{0.88}La_{0.12})_3Tl$ which does not order magnetically (Birgeneau, 1973; Birgeneau et al., 1972b). In the case of Pr_3Tl and $(Pr_{0.88}La_{0.12})_3Tl$ the measurements were made on a polycrystalline sample for Q in the first zone and averaged over directions. Very little temperature dependence of the magnetic exciton frequency was observed down to $Q = 0.6$ Å^{-1}, in contrast to the expectations of the soft-mode theory based on the singlet–singlet model. This unexpected result caused the whole question of phase transitions in such systems to be reexamined. It has now been shown (Holden and Buyers, 1974; Buyers et al., 1975) that a multi-level RPA theory for the frequencies as given by the poles on the right hand sides of eqs. (7.84) and (7.85) is capable of explaining the data satisfactorily. At higher temperatures, in the paramagnetic phase, a new excitation appears, corresponding to the excitation from the first excited Γ_4 triplet crystal-field state of Pr^{3+} to a higher Γ_3 state. (This excitation has vanishing strength at lower temperatures because of the absence of any population in the Γ_4 state.) Its frequency is in the region of the $\Gamma_1 \rightarrow \Gamma_4$ exciton frequencies and because of like-mode repulsion effects, this keeps the collective mode from renormalizing with temperature as one might expect (see fig. 7.33). Holden and Buyers (1974) calculated the frequency corresponding to the weighted mean of the intensities of the two modes in the crossover region as a

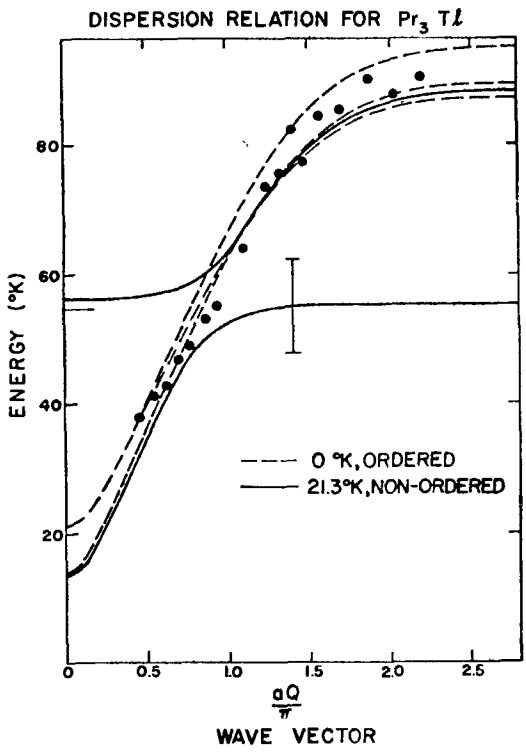

Fig. 7.33. Dispersion relations for magnetic excitations in Pr_3Tl. The low temperature neutron measurements of Birgeneau, 1973; Birgeneau et al., 1972b, are to be compared with the average of the three broken lines obtained from the pseudo-boson model at 0 K. Above T_C at $T = 21.3$ K, the solid lines indicate the predictions of the RPA-enhanced dynamical susceptibility theory described in the text and show the strong mode–mode interaction with the excited state Γ_3–Γ_4 transition (after Holden and Buyers, 1974).

function of temperature and found excellent agreement with the observed frequency in complete contrast to the predictions of the singlet–singlet model (see fig. 7.34). Similar calculations performed for $(Pr_{0.88}La_{0.12})_3Tl$ also showed satisfactory agreement with experiment. A similar effect has also been observed in $TbAl_2$ (Purwins et al., 1973b) where a split peak appears at higher temperatures corresponding to a spin wave interacting with a higher level exciton mode, once the excited state becomes significantly populated. Again the results are satisfactorily explained within the framework of the multi-level RPA theory.

In the case of TbSb (Holden et al., 1974), the magnetic exciton frequency at the wave-vector corresponding to the antiferromagnetic superlattice reflection was observed to fall as $T \to T_N$, but before reaching zero frequency the peak was obscured by the wings of an intense "central peak" (centered at $\omega = 0$) whose intensity diverged as $T \to T_N$ in a manner reminiscent of critical scattering. (Such a central peak has now been deduced at $q = 0$ in Pr_3Tl also by means of improved higher resolution experiments performed at smaller q values (Als-Nielsen et al., 1977). A central peak has also been observed recently in dhcp Pr (Houmann et al., 1977). Buyers (1975) ascribes this divergent central peak to a contribution to the dynamical susceptibility function $\chi_{zz}^{(0)}$ arising from z-axis moment fluctuations *within* an excited state multiplet, as distinct from the contributions to the susceptibility arising from virtual transitions between

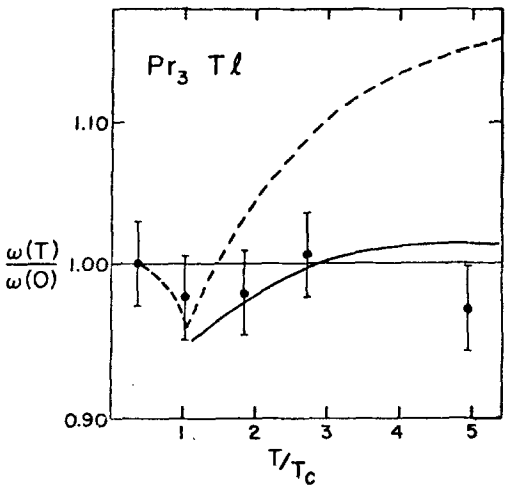

Fig. 7.34. Temperature dependence of the weighted exciton frequencies in Pr_3Tl according to experiment (Birgeneau et al., 1972b) singlet–singlet model (broken line) and dynamical susceptibility theory (full line) (after Holden and Buyers, 1974).

different crystal field states. (This is analogous to the Curie-like contribution to the susceptibility of a local moment system as distinct from the Van Vleck contribution.) Such a contribution will give, at finite temperatures, a finite central peak intensity at $\omega = 0$ (owing to the $(1 - e^{-\beta\omega})$ denominator in the scattering cross section; see eq. (7.78)). However, owing to the exchange enhancement factor $(1 - 2\mathcal{J}(\boldsymbol{q})\chi^{(0)}(0, T))^{-1}$ this intensity will diverge as $T \to T_C$. This is the soft mode, then, which causes a second-order transition for $\langle J^z \rangle$ to order, even though no finite frequency longitudinal exciton mode softens to zero. This idea was originally proposed by Smith (1972) and developed by Lines (1974) for the singlet–triplet mode.

It should be borne in mind that, as far as the dynamics go, the singlet–singlet system is highly artificial, as has been pointed out by Buyers (1975) since there is only the longitudinal exciton available as the degree of freedom through which ordering of J^z can proceed, and hence it *must* soften. Cooper (1976) however, suggests that the question of whether the phase transition is really brought about by softening of the collective mode at $\boldsymbol{q} = 0$ is still open, arguing that the RPA theory described above is not fully self-consistent in that the f_n are evaluated in the molecular field approximation, rather than with the interactions included. (Again, in the pseudo-fermion representation of eqs. (7.82) and (7.83) unphysical multiple occupation of the site would be a problem.) In fact he shows that for the singlet–singlet system, a truly self-consistent RPA calculation using the pseudo-spin formalism can in certain cases produce a first-order transition to the ordered phase.

Furrer and Kaldis (1976) have measured the excitations in a single crystal of HoP at a variety of temperatures. Even though this material orders in a "flopside" structure (see section 3.5), very little $\boldsymbol{q}$-dependence of the modes was observed. Some temperature renormalization for some of the modes was observed. The spectra were fitted to a single ion molecular field model including

quadrupolar couplings, as well as the usual bilinear exchange field. These authors find that the quadrupolar parameter λ_Q was negative as required by Levy and Chen's theory (1971) for such interactions to drive the moments into the unusual flop-die structure (see section 3.5). Similar studies have been performed on NdSb (Furrer et al., 1976b) where again relatively dispersionless magnetic excitons were observed. The frequencies showed surprisingly little renormalization with temperature.

Recently, Sinha et al. (to be published) have studied the inelastic neutron scattering from a single crystal of Nd in the paramagnetic phase at 30°K. The crystal field should be similar to that obtained from the analysis of the Pr excitation spectrum, except that Kramers degeneracy in this case assures the existence of a moment. Broad peaks were observed in the spectrum (presumably due to exchange broadening) and the levels associated with the hexagonal sites were not resolved. Two broad peaks associated observed at energies corresponding to 138 K and 180 K were identified as transitions from a $\Gamma_8^{(1)}$ ground state level on the cubic sites to Γ_6 and $\Gamma_8^{(2)}$ excited states. The peaks were almost dispersionless and showed little renormalization with temperature. Preliminary analysis shows that the crystal fields in Nd appear to be almost a factor of two larger than those in Pr, a somewhat surprising result, although the effects of exchange have yet to be analyzed.

5.3. *Studies of spin waves*

Most of the inelastic studies so far have been concentrated on the heavy lanthanide metals or alloys, although recently work has also begun on some of the intermetallic compounds. Strictly speaking, there is not as much of a difference between spin waves and magnetic excitons as one might think. While the latter are collective modes associated with transitions from one set of crystal-field-split levels to another, spin-waves may be regarded as collective modes associated with transitions between exchange-field-split levels of the $(2J + 1)$ fold multiplet, with crystal field anisotropy acting as a perturbation. The subject has been recently comprehensively reviewed by Mackintosh and Bjerrum-Møller (1972), and by Houmann and Bjerrum-Møller (1976).

The conventional treatment of spin-waves in magnetically ordered systems uses the Holstein–Primakoff transformation (1940). One transforms to operators a_i^+, a_i^- defined by

$$J_i^+ = J_i^x + \mathrm{i}J_i^y = (2J)^{1/2}\left(1 - \frac{a_i^+ a_i}{2J}\right)^{1/2} a_i \tag{7.93}$$

$$J_i^- = J_i^x - \mathrm{i}J_i^y = (2J)^{1/2}\, a_i^+ \left(1 - \frac{a_i^+ a_i}{2J}\right)^{1/2} \tag{7.94}$$

where

$$[a_i, a_j^+] = \delta_{ij} \tag{7.95}$$

so that the commutation relation

$$[J_i^+, J_i^-] = 2J_i^z \tag{7.96}$$

is satisfied. In terms of these operators,

$$J_i^z = J - a_i^+ a_i \tag{7.97}$$

so that a_i^+ is an operator which creates one quantum of angular momentum deviation along the axis of quantization at the site i. At low temperatures, this deviation has a very small thermal average so that we may neglect $a_i^+ a_i$ in eqs. (7.93) and (7.94) and write approximately

$$J_i^+ \simeq (2J)^{1/2} a_i, \; J_i^- \simeq (2J)^{1/2} a_i^+. \tag{7.98}$$

One may then write the exchange part of the hamiltonian in terms of the a_i, a_i^+. (In the case of spiral or cone structures, one must first carry out a coordinate rotation for each site so that the ordered moment is always along the axis of quantization.) The resulting hamiltonian, which is bilinear in the spin-deviation operators on the sites, is then diagonalized by a canonical transformation (Niira, 1960), and the normal mode (spin-wave) frequencies are thus obtained. If one includes single-ion anisotropy terms (let us say up to second order axial anisotropy and sixth order basal plane anisotropy) one may approximately represent these in terms of bilinear products of a_i, a_i^+ (such that the matrix elements of these operators are the same as those of the original hamiltonian between states on a particular ion (Mackintosh and Bjerrum-Møller, 1972)) and then proceed as before. One obtains the dispersion relation ω_q in the following very general form (Lindgard and Danielsen, 1975):

$$\hbar\omega_q = \{[A(q) + B(q)][A(q) - B(q)]\}^{1/2} \tag{7.99}$$

For the specific case of spin-waves propagating along the c-axis of a basal-plane ferromagnet, such as Tb for instance, we have in the double-zone scheme for q,

$$A(q) + B(q) = J[\mathcal{J}(0) - \mathcal{J}(q)] + 2J_1 V_2 + 6J_5 V_6^6 \tag{7.100}$$

$$A(q) - B(q) = J[\mathcal{J}(0) - \mathcal{J}(q) + 36J_5 V_6^6 \tag{7.101}$$

where

$$J_n = (J - \tfrac{1}{2})(J - 1) \ldots (J - \tfrac{1}{2}n) \tag{7.102}$$

Dispersion curves measured for Tb at 4.2 K (basal plane ferromagnetic phase) (Bjerrum-Møller and Houmann, 1966; Nielsen et al., 1968, 1970a) are shown in fig. 7.35. We see that $\{\mathcal{J}(0) - \mathcal{J}(q)\}$ is the only q-dependent term which enters into the expression for the spin wave dispersion curve, and hence may be determined from a measurement of the latter, provided the anisotropy constants are known. One also sees that the single-ion anisotropy terms result in a finite gap for the magnons at $q = 0$. This gap will be changed upon application of an external magnetic field. The procedure for deriving the magnon spectrum in an external field within the conventional Holstein–Primakoff formalism has been

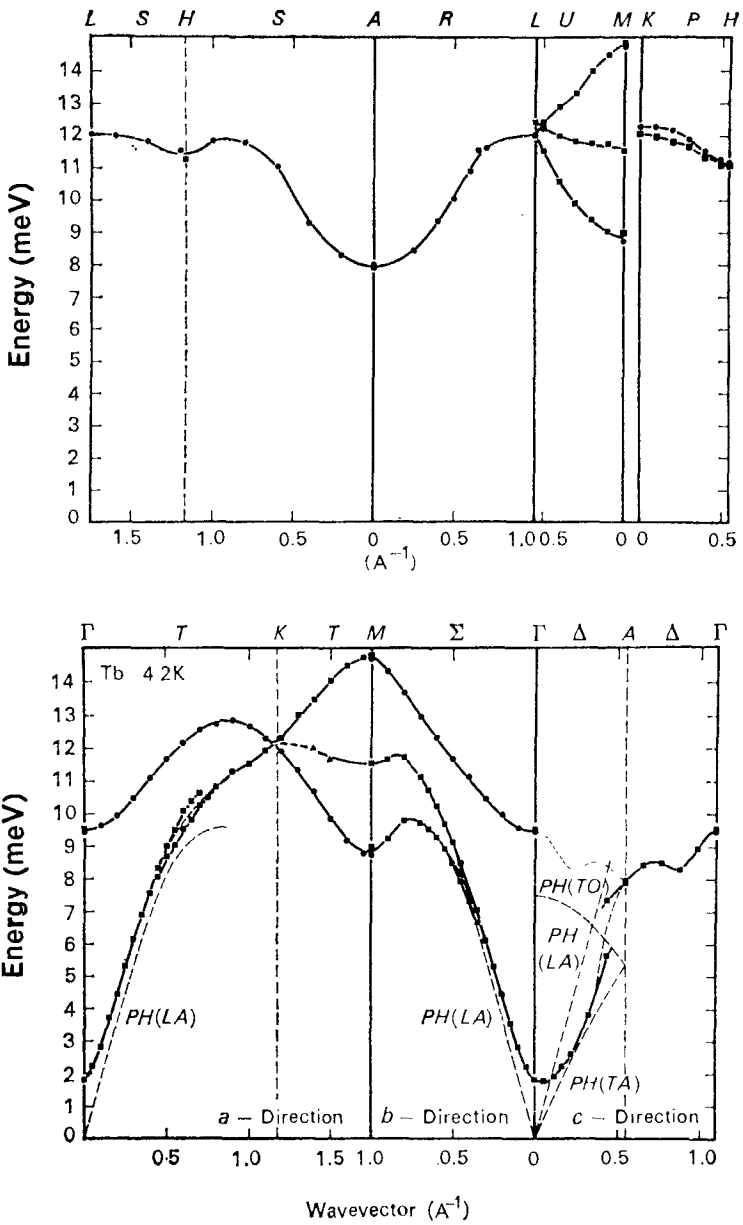

Fig. 7.35. Magnon dispersion relations for Tb along symmetry lines in the zone at 4.2 K. The effects of interactions with certain phonon branches (dashed lines) are also shown (after Mackintosh and Bjerrum-Møller, 1972).

discussed by Mackintosh and Bjerrum-Møller (1972) and Cooper (1972). It can be shown that for a field applied in the hard direction of magnetization the gap goes to zero for fields greater than the critical field H_c required to turn the moments into the hard direction. Experimentally, however, the gap softens at H_c but does not go to zero (Bjerrum-Møller et al., 1967, 1970; Nielsen et al., 1970b; Jensen et al., 1975). This has been explained in terms of the "frozen lattice model" (Cooper, 1968) of magnetoelastic strains. Since the strain-field cannot reorient rapidly enough to keep up with the spin precession, one must add to the hamiltonian the static magnetoelastic coupling terms (see eq. (7.9)) in deriving the spin-wave energies. Since these are axially symmetric they will contribute to the gap at $q = 0$ regardless of the direction of the applied field. Using the expression for the $q = 0$ spin-wave energy derived using this theory (Mackintosh and Bjerrum-Møller, 1972) the anisotropy and magnetoelastic anisotropy constants have been fitted to the experimental results. Note that the above deviation has assumed *isotropic* exchange interactions. The form of $[A(q) + B(q)]$ and $[A(q) - B(q)]$ in the case of the most general (anisotropic) interactions has been given by Jensen et al. (1975). For periodic structures of periodicity q_m, the quantities $\mathcal{J}(q_m + q)$ and $\mathcal{J}(q_m - q)$ also enter the expression for the dispersion relations. For spin-waves propagating in directions other than the c-axis, there will be an acoustic and an optic mode in the hcp structure with two atoms per cell.

Since the quantity $\mathcal{J}(q)$ as discussed in section 2 is of fundamental importance from the point of view of our microscopic understanding of lanthanide magnetism, its deduction from spin-wave measurements is one of the most important outcomes of this type of experiment. As discussed in section 2 for metals with periodic structure, $\mathcal{J}(q)$ must have its maximum at q_m, although the converse is not necessarily true. $\mathcal{J}(q)$'s calculated from experiments on a number of heavy lanthanide metals and alloys in the ferromagnetic phase along the c-axis are shown in fig. 7.36, and those for a number of metals and alloys in the spiral or cone phases along the c-axis are shown in fig. 7.37. The functions have been scaled by the de Gennes factor $(g_J - 1)^2$, and have been obtained under the assumption that exchange is isotropic and that the single-ion anisotropy terms can be treated properly within the Holstein–Primakoff formalism. As we shall see, this may not be justified except for Gd, which has no orbital moment, so one should not interpret these curves too quantitatively. Nevertheless, one may see that there are in fact appreciable differences between these functions for the different metals, reflecting differences in band structure (and hence $\chi(q)$ (Liu, 1977)) or else in s–f exchange matrix elements (Harmon and Freeman, 1974a). The results for Y in fig. 7.37 were obtained by measurements on $Y_{0.9}Tb_{0.1}$ and $Y_{0.9}Ho_{0.1}$ alloys (Wakabayashi and Nicklow, 1974) which order magnetically at low temperatures with the turn angle characteristic of pure Y of about 50°. Well defined spin waves were observed in both cases. The function $[\mathcal{J}(q) - \mathcal{J}(0)]$ was extracted from the measurements on the assumption that in the virtual crystal approximation the terms involving $[\mathcal{J}(q) - \mathcal{J}(0)]$ in the expression for the spin-wave energies will simply be multiplied by c ($c =$

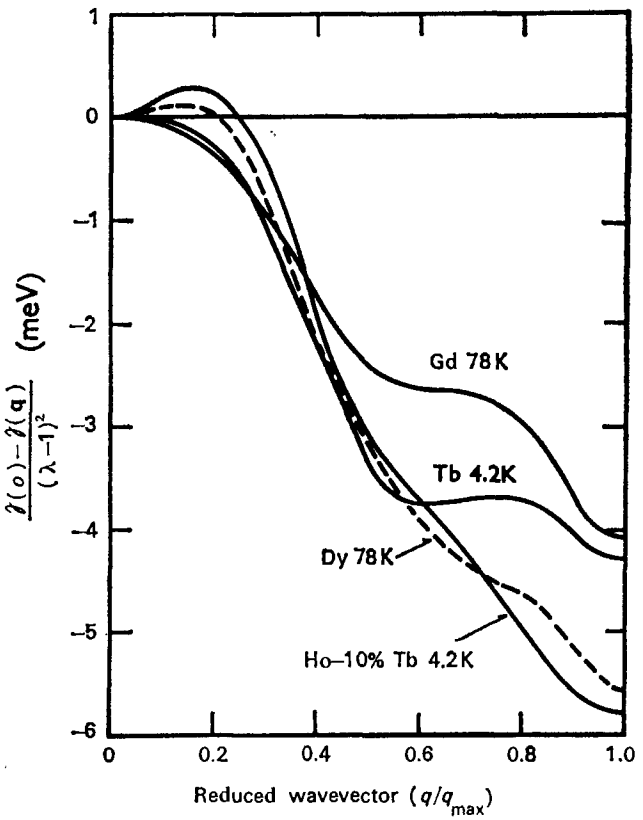

Fig. 7.36. The exchange function $[\mathcal{J}(\boldsymbol{q})-\mathcal{J}(0)]/(g_J-1)^2$ along the c-axis for a number of ferromagnetic heavy lanthanides (after Mackintosh and Bjerrum-Møller, 1972).

concentration of magnetic ions). The same result for $[\mathcal{J}(\boldsymbol{q})-\mathcal{J}(0)]$ was obtained from both alloys which indicates that, in these systems at least, the effects of anisotropy have not seriously affected the determination of $[\mathcal{J}(\boldsymbol{q})-\mathcal{J}(0)]$ from the spin-wave dispersion curves using the conventional formalism. One notices immediately the large peak in the case of Y, which explains the fact that the addition of Y to Tb or Dy rapidly increases the stability of the spiral phase. One also notices from figs. 7.36 and 7.37 that the changes in band splitting induced by ferromagnetic as opposed to spiral ordering changes the $\mathcal{J}(\boldsymbol{q})$ function, although in the case of Dy and Ho – 10% Tb, the peak at $\boldsymbol{q} \neq 0$ still survives in the ferromagnetic phase. (As discussed earlier, however, it is not large enough to overcome the magnetoelastic driving energy favoring ferromagnetism, which increases rapidly with decreasing temperature.)

Liu et al. (1971) calculated the magnon dispersion curve for Gd along the c-axis using a $\chi(\boldsymbol{q})$ calculated from APW energy bands in the constant matrix element approximation. They found reasonable agreement after adopting a somewhat arbitrary $\boldsymbol{q}$-dependent matrix element form factor and a suitably scaled interaction parameter. More recently Lindgard et al. (1975) have performed a more microscopic calculation of the dispersion curve for Gd along the

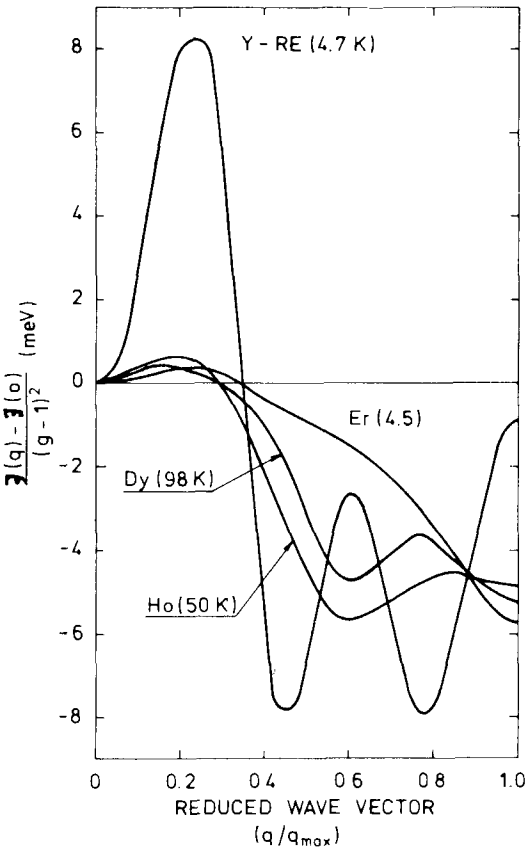

Fig. 7.37. The exchange function $[\mathcal{J}(q) - \mathcal{J}(0)]/(g_J - 1)^2$ along the c-axis for a number of heavy lanthanide metals in the cone (Er) and helical phases (after Houmann and Bjerrum-Møller, 1976).

c-axis including exchange matrix elements between f-electrons and conduction electrons. Reasonable agreement is obtained for the shape of the measured dispersion curve, which they find is determined strongly by matrix element effects rather than structure in $\chi(q)$ (see fig. 7.38). However, the overall magnitude has to be scaled down by a factor of approximately 4, which may be ascribed to the use of non-relativistic 4f wave functions and to screening effects. Also the q^2 behavior at small q for ω_q is not obtained.

We now discuss the question of possible anisotropy in the two-ion exchange terms in the hamiltonian. It may be shown (Mackintosh and Bjerrum-Møller, 1972; Nicklow, 1971; Nicklow et al., 1971) that ω_q is not a symmetric function of q for wave vectors along the c-axis of a cone-shaped magnetic structure. It may also be shown (Nicklow et al., 1971) that both single-ion and two ion (pure axial) anisotropy terms cancel in the expression for the difference in the spin-wave frequencies for $+q$ and $-q$,

$$\Delta(q) = \omega_{-q} - \omega_q = J[\mathcal{J}(q_m - q) - \mathcal{J}(q_m - q)], \tag{7.103}$$

and one may obtain directly the isotropic part of the exchange. This was done in

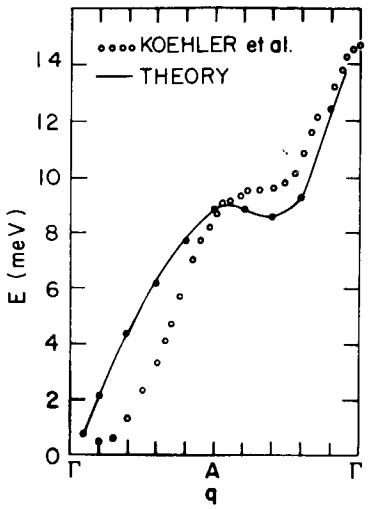

Fig. 7.38. The measured magnon spectrum (open circles) for Gd along the c-axis in the double zone scheme (1974) and the theoretically calculated spectrum multiplied by a scale-factor of 3.6 (after Lindgard et al., 1975).

the case of the low temperature phase of Er by Nicklow et al. (1976a) (see fig. 7.39). They then found that a q-independent single ion anisotropy term was unable to produce a good fit to the individual ω_q and ω_{-q} (dashed line in fig. 7.39), but that a good fit could be obtained using two-ion interactions with a large axial two-ion anisotropy. The same conclusion was arrived at by Jensen et al. (1975) in the case of Tb by measuring the change of ω_q^2 with applied field H in the ferromagnetic phase with H applied along an easy axis of magnetization. With an applied field H, the expression for ω_q^2 is given by (Jensen et al., 1975)

$$\omega_q^2(H) = [A(q) + B(q) + g_J\mu_B H][A(q) - B(q) + g_J\mu_B H] \tag{7.104}$$

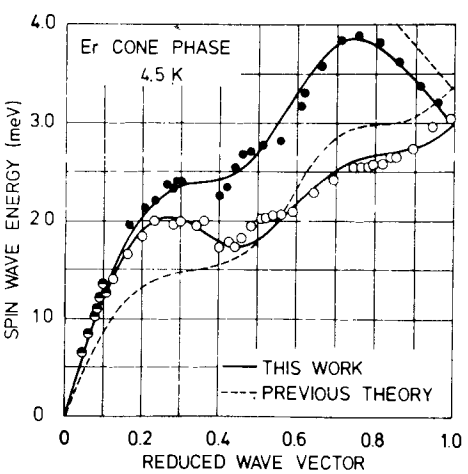

Fig. 7.39. The spin-wave data for Er by Nicklow et al. (1976). The lower curve (open circles represents the branch $\hbar\omega(+q)$ and the upper curve (solid circles) the branch $\hbar\omega(-q)$. The full line is a fit of the MME theory of Lindgard using six parameters and single-ion anisotropy. The dashed curve shows the best fit of the conventional spin-wave theory using eight parameters and single-ion anisotropy. Introducing two-ion anisotropy (Nicklow et al., 1976) leads to a fit almost identical to the full line with ten parameters (after Lindgard, 1976b).

so that the initial slope

$$\alpha(q) \equiv \frac{1}{g_J \mu_B} \frac{d}{dH} \omega_q^2(H)|_{H=0} = 2A(q). \tag{7.105}$$

Thus, from measurements of $\alpha(q)$ and $\omega_q^2(H=0)$ one can separately determine the functions $A(q)$ and $B(q)$, since by eq. (7.104),

$$B(q) = \tfrac{1}{2}(\alpha^2(q) - 4\omega_q^2(0)) \tag{7.106}$$

The theory shows (Jensen et al., 1975) that for isotropic exchange $[B(q) - B(0)]$ should be zero ($A(0)$, $B(0)$ can be determined by subsidiary experiments in magnetic fields). Jensen et al. found $[B(q) + B(0)]$ quite small when the field was applied along the hard axis, but quite large for the field applied along the easy axis.

Recently, Lindgard (1976b) has noted that if considerable single-ion anisotropy is present, the starting point of the conventional spin wave theory, which assumes a pure J^z single-ion state and equidistant (exchange) splittings as the unperturbed state, is not satisfactory. In a crystal with appreciable crystal field interactions, one gets appreciable ground state corrections due to mixing of these J^z states by the crystal field. Lindgard develops a new transformation using the matching of matrix element method as an expansion in powers of V_c/H_{ex} and obtains q-dependent terms in the expression for ω_q (specifically, in the function $B(q)$ in eqs. (7.100) and (7.101) arising from the *single-ion* anisotropy terms. He then obtains a good fit to the Er cone-phase spin-wave spectrum without assuming any anisotropic two-ion exchange, and without increasing the number of exchange parameters (see fig. 7.39). Cooke and Lindgard (to be published) have generalized the method in terms of a canonical transformation (which may in principle be calculated to any order in V_c/H_{ex}) which transforms the single-ion part of the hamiltonian so that it has no off-diagonal matrix elements between the J^z states. One then, of course, gets *effective* two-ion anisotropic interactions in the transformed hamiltonian.

Lindgard's ideas have recently been disputed by Jensen (1976b, 1977). Jensen points out that the Holstein–Primakoff transformation (which is in principle exact, being a canonical transformation) for the operators J_i^+, J_i^- can be expanded in a well-ordered expansion (Lindgard and Danielsen, 1975; Jensen, 1975) including terms up to *fourth* order in the spin-deviation operators in the hamiltonian, and the resulting equations of motion decoupled using a self-consistent Hartree–Fock (SCHF) approximation. A similar treatment has been given by Brooks and Egami (1973). The net result (Jensen, 1976b) is a number of correction terms, involving self-consistent averages over spin-wave states, to the functions $A(q)$ and $B(q)$ in eqs. (7.100) and (7.101), including a q-dependent term in $B(q)$ which in principle gives rise to dispersion in the spin-waves arising from single-ion anisotropy alone. However, Jensen estimates that the magnitude of this dispersive term for both Tb and Er is an order of magnitude smaller than the observed q-dependence of $B(q)$. He also points out that if one regards J^{-1} as the J^{-2}. Jensen also shows that if one includes consistently *all* second order terms

(in V_c/H_{ex}) in Lindgard's expression (which is of zero order in J^{-1}) then Lindgard's expressions for $A(q)$ and $B(q)$ become formally identical to the expressions obtained from the above SCHF theory, and thus discounts the possibility that single-ion anisotropy can be invoked as an explanation for the observed spin-wave dispersion in Er and Tb. To substantiate this claim, Jensen has carried out, in the case of Er, a numerical multi-level RPA calculation for the "best" single-ion molecular field states (including single-ion crystal field anisotropy) along the lines of the magnetic exciton theory described in the previous section, and finds agreement within a few percent with the results of the SCHF theory. Lindgard (1976c and to be published) agrees that the formal expression obtained for the spin-wave dispersion is the same in both theories, but appeals to experiment and the goodness of fit obtained with his parameters to conclude that the q-dependence of the single-ion anisotropy may in fact be larger than the SCHF theory would indicate, perhaps due to higher-order ground-state corrections. One of the problems, of course, is that there are few unique ways in which the predictions of the theory which postulates an empirically sizeable q-dependent single-ion anisotropy contribution to $B(\mathbf{q})$ can be distinguished from those of a theory which includes genuine two-ion anisotropic exchange. (One way would be to compare measured and predicted intensities in the neutron experiments on spin-waves.) It should be pointed out that Jensen (1974) has also reanalyzed the Er cone-phase spin-wave spectrum in terms of not the axial two-ion anisotropy used by Nicklow et al. (1971) but one which couples $m = 2$ Racah operators in the general expression for the exchange interaction, and finds agreement with experiment (about as good as Lindgard's) without a giant anisotropic contribution as Nicklow et al. had found. In fact, his anisotropic exchange is of the same order as the isotropic exchange. It is quite conceivable that a rigorous formulation of f–d exchange in the microscopic theory could lead to anisotropic exchange of this order of magnitude, but no realistic numerical calculations have yet been attempted.

Recently, spin wave dispersion curve measurements have also become available for some of the cubic Laves phase lanthanide intermetallic compounds, namely $TbAl_2$ (Buhrer et al., 1973), $Ho_{0.88}Tb_{0.12}Fe_2$ (Nicklow et al., 1976b), $ErFe_2$ (Rhyne et al., 1976) and $PrAl_2$ (Purwins et al., 1975). $TbAl_2$ is a good example of an RKKY system, i.e. the lanthanide ions are coupled by indirect exchange via the conduction electrons, and there are no other moments in the system. The analysis of the spin-wave dispersion curves (measured at 4.6 K) bears this out. Buhrer et al. (1973) find that the results can be fitted well in terms of long-ranged oscillatory exchange interactions between the lanthanide ions (very reminiscent of the RKKY interaction) and a significant crystal field anisotropy gap. As mentioned previously, at higher temperatures, the higher crystal field levels become significantly populated, there is an interaction between the magnons and the excited levels and a higher level exciton is observed (Purwins et al., 1973b). Similar effects are observed in $PrAl_2$ (Purwins et al., 1975). The RFe_2 compounds on the other hand provide interesting cases where the lanthanide ions are sitting in a system of electrons which is itself ferromagnetic and of the itinerant type.

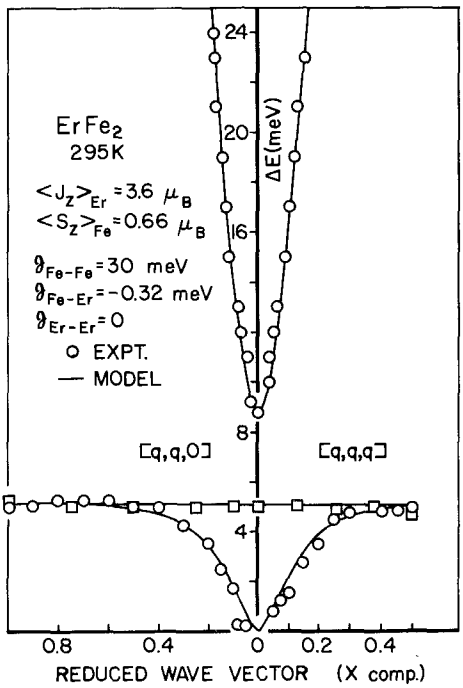

Fig. 7.40. Magnon dispersion in $ErFe_2$ along ⟨110⟩ and ⟨111⟩ symmetry directions. The squares denote points measured on the lower optic branch; the circles denote points on the acoustic and upper optic branches. The solid line is the result of the nearest neighbor exchange interaction fitting calculation described in the text (after Rhyne et al., 1976).

The lanthanide moments are aligned antiparallel to the iron moments. There is very little loss of the lanthanide moment from its free ion value but a relatively low value for the Fe moment compared to pure Fe. The results for the two compounds studied are quite similar (and quite different to those for $TbAl_2$). Figure 7.40 shows the dispersion relations measured for $ErFe_2$ at room temperature. (There are also calculated to be three branches at much higher frequencies which have not yet been observed.) The dispersion curves are extremely isotropic, and the lowest lying optic mode is quite dispersionless. An analysis of the dynamics shows that the lanthanide–lanthanide exchange interaction is effectively non-existent. The higher optic mode takes off very steeply in a manner reminiscent of the magnons in an itinerant ferromagnet such as Fe itself, and would form the acoustic magnon branch if it were not for interactions with the lanthanide ions. It would be interesting to see whether the upper branch magnons exhibit other characteristics of itinerant electron systems, (e.g. whether they disappear into a Stoner continuum, etc.) but such information will have to await neutron scattering experiments at much higher energies. The results in both cases can be fitted surprisingly well by a simple model involving only nearest neighbor Fe–Fe exchange and R–Fe exchange, as can be seen from fig. 7.40. Further, the R–Fe exchange interaction appears to scale within experimental error with the effective de Gennes factor $[(g_J - 1)]$ at least for these two samples (Rhyne et al., 1976). In both materials there is a negligible anisotropy

gap in the magnon spectrum at $q = 0$ at room temperature. At low temperatures, the frequencies renormalize downwards strongly and the gap increases. The origin of the strong magnon renormalization is not understood at present.

6. Concluding remarks

In this review, we have attempted to survey what has been learned so far about lanthanide magnetism from both elastic and inelastic neutron scattering experiments. In a field as vast as this, there have inevitably had to be several omissions. Thus, we have had to omit discussions of critical scattering from lanthanide systems, of the very interesting studies of cooperative Jahn–Teller effects in some rare earth compounds, of measurements of the phonon spectra of these systems, and of a large number of neutron diffraction studies of many rare earth compounds other than those described in section 3.5.

Our understanding of the physics of lanthanide magnetism, at least at a phenomenological level, is in a reasonably satisfactory state, although a few uncertainties still remain, such as the magnitude of the anisotropic exchange (or effective exchange) between ions in the hamiltonian, the relative importance of higher order (e.g. biquadratic) exchange terms or the best way to derive the spectrum of elementary excitations (magnon or magnetic exciton) when both anisotropy and exchange terms are present. To all of these questions, however, partial answers and promising approaches are already apparent. At a more microscopic level, however, a great deal still needs to be done. Microscopic calculations of $\mathcal{J}(q)$ and possibly anisotropic exchange involving the actual atomic f-electron wave functions and band calculated conduction wave functions and energy bands is still at a fairly early stage, particularly with regard to atoms with orbital moments. Calculations for Gd (Liu et al., 1971; Harmon and Freeman, 1974a; Cooke and Lindgard, 1976) and Sc (Gupta and Freeman, 1976b) have already established the importance of subtle matrix element effects hitherto ignored. The effect of interactions (exchange enhancement) among the conduction electrons themselves on the magnetic ordering on the crystal field and on the collective modes has not yet been investigated. Thus, if the conduction electrons play an active role rather than simply passively transmitting the indirect exchange between the 4f shells, we should expect higher energy magnon branches associated with spin-fluctuations on the conduction electrons as well. In the next few years, we may expect further neutron scattering experiments designed to elucidate such matters. No calculations of the exchange interactions based on realistic band structures have yet been performed for rare earth compounds. In order to provide a rigorous test of our understanding of the lanthanides it would be of interest to perform a truly self-consistent molecular field calculation of the magnetic ordering in, some material as a function of temperature, along the lines of Jensen's calculations for Er (Jensen, 1976a), but where the effects of superzone boundaries on the RKKY interactions and magnetoelastic effects were taken into account, and to see how well such a

calculation could reproduce in detail the observed temperature dependence of the magnetic structure, including the appearance of harmonics, etc. Although much information has been obtained on crystal fields in lanthanide systems, more first principles calculations including the effects of conduction electrons and configuration interactions would be desirable. Such calculations have already been attempted by Ray (1971), Dixon and Dupree (1973), and Newman et al. (1971). More information is also needed on the magnitude of the coupling of the lanthanide moments to the lattice phonons, and we may expect more theoretical and experimental work in this area. In addition, as single crystals of the different rare earth compounds become available, there will be more fertile areas for neutron scatterers to explore.

Acknowledgements

The author is indebted to several friends and colleagues for their valuable assistance in providing information relating to this subject matter and for helpful discussions. Particular mention must be made of Dr. C. Stassis, Dr. B.N. Harmon, Dr. G.H. Lander, Dr. N. Wakabayashi, Dr. S.G. Das, Dr. P.A. Lindgard, Dr. J. Jensen, Dr. W.J.L. Buyers and Reneé Diehl. He also wishes to thank Dr. J.G. Houmann, Dr. J.F. Cooke, and Dr. J.J. Rhyne for sending copies of some of their recent work prior to publication. Thanks are also due to Florence Belcher for her patience and diligence with the manuscript.

References

A. Abragam and B. Bleaney, 1970, *Electron Paramagnetic Resonance of Transition Ions* (O.U.P.).
N. Achiwa and S. Kawano, 1973, J. Phys. Soc. Japan **35**, 303.
J. Als-Nielsen, O.W. Dietrich, W. Kunnmann and L. Passell, 1971, Phys. Rev. Lett. **27**, 741.
J. Als-Nielsen, J.K. Kjems, W.J.L. Buyers and R.J. Birgeneau, 1975, J. Phys. **C10**, 2673 (1977).
O.K. Andersen and T.L. Loucks, 1968, Phys. Rev. **167**, 551.
T. Arai and G.P. Felcher, 1975, J. Phys. **C8**, 2095.
G. Arnold, N. Nereson and C. Olsen, 1967, J. Chem. Phys. **46**, 4041.
M. Atoji, 1974, Sol. St. Comm. **14**, 1047.
G.E. Bacon, 1975, *Neutron Diffraction*, 3rd Ed. (Oxford, Clarendon Press).
P. Bak, 1975, Phys. Rev. **B12**, 5203.
E. Balcar, 1973, Proc. Int. Magnetism Conf. Moscow, Vol. 2, (Moscow: Nauka) 250.
M.O. Bargouth and G. Will, 1971, J. Phys. Suppl. **32**, C1, 675.
E.F. Bertaut, 1972, Ann. Phys. (France) **7**, 203.
E.F. Bertaut and R. Chevalier, 1966, Comp. Rend. **B262**, 1707.
R.J. Birgeneau, 1972, J. Phys. Chem. Solids **33**, 59.
R.J. Birgeneau, 1973, AIP Conf. Proc. **10**, 1664.
R.J. Birgeneau, M.T. Hutchings and R.N. Rogers, 1968, Phys. Rev. **175**, 1116.
R.J. Birgeneau, E. Bucher, L. Passell and K.C. Turberfield, 1971a, Phys. Rev. **B4**, 718.
R.J. Birgeneau, J. Als-Nielsen and E. Bucher, 1971b, Phys. Rev. Lett. **27**, 1530.
R.J. Birgeneau, J. Als-Nielsen and E. Bucher, 1972a, Phys. Rev. **B6**, 2724.
R.J. Birgeneau, J. Als-Nielsen and E. Bucher, 1972b, Phys. Rev. **B6**, 2724.
R.J. Birgeneau, E. Bucher, J.P. Maita, L. Passell and K.C. Turberfield, 1973, Phys. Rev. **B8**, 5345.
R.J. Birgeneau, J.K. Kjems, G. Shirane and L.G. Van Uitert, 1974, Phys. Rev. **B15**, 1300.
H. Bjerrum-Møller and J.C.G. Houmann, 1966, Phys. Rev. Lett. **16**, 737.
H. Bjerrum-Møller, A.R. Mackintosh and J.C. Gylden Houmann, 1965, J. Appl. Phys. **39**, 1078.
H. Bjerrum-Møller, J.G. Houmann and A.R.

Mackintosh, 1967, Phys. Rev. Lett. **19**, 312.
H. Bjerrum-Møller, M. Nielsen and A.R. Mackintosh, 1970, in *Les Elements des Terres Rares*, (CNRS, Paris), Vol. II, p. 227.
B. Bleaney, 1963, Proc. Phys. Soc. (London) **A276**, 39.
D. Bloch, D.M. Edwards, M. Shimizu and J. Voiron, 1975, J. Phys. **5**, 1217.
M. Blume, A.J. Freeman and R.E. Watson, 1963, J. Chem. Phys. **37**, 1245.
M. Blume, A.J. Freeman and R.E. Watson, 1964, J. Chem. Phys. **41**, 1878.
R.M. Bozorth, 1967, J. Appl. Phys. **38**, 1366.
M.S.S. Brooks and T. Egami, 1973, J. Phys. **C6**, 3719.
T.O. Brun and G.H. Lander, 1969, Phys. Rev. Let. **23**, 1295.
T.O. Brun and G.H. Lander, 1971, J. Phys. (Paris), **32**, C7-571.
T.O. Brun, S.K. Sinha, N. Wakabayashi, G.H. Lander, L.R. Edwards and F.H. Spedding, 1970, Phys. Rev. **B1**, 1251.
T.O. Brun, G.H. Lander, F.W. Korty and J.S. Kouvel, 1974a, AIP Conf. Proc. **24**, 244.
T.O. Brun, G.H. Lander, D.L. Price, G.P. Felcher and J.F. Reddy, 1974b, Phys. Rev. **B9**, 248.
T.O. Brun, J.S. Kouvel and G.H. Lander, 1976, Phys. Rev. **B13**, 5007.
E. Bucher and J.P. Maita, 1973, Solid State Comm. **13**, 215.
E. Bucher, C.W. Chu, J.P. Maita, K. Andres, A.S. Cooper, E. Buehler and K. Nassau, 1969, Phys. Rev. Lett. **22**, 1260.
E. Bucher, R.J. Birgeneau, J.P. Maita, G.P. Felcher and T.O. Brun, 1972, Phys. Rev. Lett. **28**, 746.
W. Buhrer, M. Godet, H.G. Purwins and E. Walker, 1973, Sol. St. Comm. **13**, 881.
G. Busch, 1967, J. Appl. Phys. **38**, 1386.
K.N.J. Buschow and R.P. Van Stapele, 1970, J. Appl. Phys. **41**, 4066.
K.H.J. Buschow, J.P. de Jong, H.W. Zandbergen and B. Van Laar, 1974a, J. Appl. Phys. **46**, 1352.
K.H.J. Buschow, B. Van Laar and J.B.A.A. Elemans, 1974b, J. Phys. **F4**, 1517.
W.J.L. Buyers, 1975, AIP Conf. Proc. **24**, 27.
W.J.L. Buyers, T.M. Holden and A. Perreault, 1975, Phys. Rev. **B11**, 266.
J.W. Cable and W.C. Koehler, 1972, AIP Conf. Proc. **5**, 1381.
J.W. Cable and E.O. Wollan, 1968, Phys. Rev. **165**, 733.
J.W. Cable, R.M. Moon, W.C. Koehler and E.O. Wollan, 1964a, Phys. Rev. Lett. **12**, 553.
J.W. Cable, W.C. Koehler and E.O. Wollan, 1964b, Bull. Am. Phys. Soc. **9**, 312.
J.W. Cable, W.C. Koehler and E.O. Wollan, 1964c, Phys. Rev. **136**, A 240.
J.W. Cable, E.O. Wollan, W.C. Koehler and M.K. Wilkinson, 1965, Phys. Rev. **140**, 1896.
H.B. Callen and E. Callen, 1966, J. Phys. Chem. Solids **27**, 127.
H.R. Child and J.W. Cable, 1969, J. Appl. Phys. **40**, 1003.
H.R. Child and W.C. Koehler, 1971, J. de Physique **32**, C1-1128.
H.R. Child, M.K. Wilkinson, J.W. Cable, W.C. Koehler and E.O. Wollan, 1963, Phys. Rev. **131**, 922.
H.R. Child, W.C. Koehler, E.O. Wollan and J.W. Cable, 1965, Phys. Rev. **138**, A 1655.
J.F. Cooke and H.L. Davis, AIP Conf. Proc. **5**, 1441. 1972.
J.F. Cooke and P.A. Lindgard, 1976, Phys. Rev. **B14**, 5056.
B.R. Cooper, 1967, Phys. Rev. Lett. **19**, 900.
B.R. Cooper, 1968a, Solid State Physics **21**, 393 (Ed. Seitz, Turnbull, Academic Press, New York).
B.R. Cooper, 1968b, Phys. Rev. **169**, 281.
B.R. Cooper, 1972, in Magnetic Properties of Rare Earth Metals, edited by R.J. Elliott, (Plenum, London), ch. 2.
B.R. Cooper, 1976, in Magnetism in Metals and Metallic Compounds, edited by J.T. Lopuszanski, A. Pekalski and J. Przystawa (Plenum, New York), p. 225.
B.R. Cooper and O. Vogt, 1970a, Phys. Rev. **B1**, 1211.
B.R. Cooper and O. Vogt, 1970b, Phys. Rev. **B1**, 1218.
B.R. Cooper, R.J. Elliott, S.J. Nettel and H. Suhl, 1962, Phys. Rev. **127**, 57.
H.L. Davis and J.F. Cooke, 1977, to be published.
H.L. Davis and H.A. Mook, 1972, AIP Conf. Proc. **5**, 1548.
H.L. Davis and H.A. Mook, 1975, AIP Conf. Proc. **24**, 229.
P.G. de Gennes, 1958, Compt. Rend. Acad. Sci. (Paris) **247**, 1836.
P.G. de Gennes, 1962, J. Phys. Rad. **23**, 630.
P.G. de Gennes and D. Saint-James, 1963, Sold. St. Comm. **1**, 62.
R.A.B. Devine, 1974, J. Phys. **C7**, L71.
H.W. de Wijn, A.M. Van Diepen and K.H.J. Buschow, 1974, Sol. St. Comm. **15**, 583.
O.W. Dietrich and J. Als-Nielsen, 1967, Phys. Rev. **162**, 315.
J.M. Dixon and R. Dupress, 1973, J. Phys. **F3**, 118.
L.R. Edwards and S. Legvold, 1968, Phys. Rev. **176**, 753.
R.J. Elliott, 1961, Phys. Rev. **124**, 346.
R.J. Elliott, 1965, Magnetism (Eds. G.T. Rado and H. Suhl), IIA, p. 385.
R.J. Elliott, 1972, Proc. Roy. Soc. (London) **A328**, 217.
R.J. Elliott and F.A. Wedgwood, 1964, Proc. Phys. Soc. (London), **84**, 63.
R.S. Elliott, R.T. Harley, W. Hayes and S.R.P. Smith, 1972, Proc. Roy. Soc. **A328**, 217.
U. Enz, 1960, Physica **26**, 698.
U. Enz, 1961, J. Appl. Phys. **32**, 225.
W.E. Evenson and S.H. Liu, 1969, Phys. Rev. **178**, 783.
G.P. Felcher and W.C. Koehler, 1963, Phys. Rev. **131**, 1518.
G.P. Felcher, T.O. Brun, R.J. Gambino, M. Kuznietz, 1973, Phys. Rev. **B8**, 260.

G.P. Felcher, G.H. Lander, S.K. Sinha and F.H. Spedding, 1976, Phys. Rev. **B13**, 3034.
P. Fischer and E. Kaldis, 1976, "Neutronen-Streuung" Rept. AF-SEP-93 (Institut für Reaktortechnik ETHZ, E.I.R., Switzerland) p. 16.
P. Fischer, W. Hälg, W. von Wartburg, P. Schwob and O. Vogt, 1969, Phys. Kondens Materie **9**, 249.
P. Fischer, A. Furrer, H. Heer, W. Hälg, P. Schobinger-Papamantellos, A. Niggli, O. Vogt, J. Kjems and B. Rainford, 1971, Proc. of the Durham Conference on Rare Earths and Actinides (The Institute of Physics, London) p. 206.
P. Fischer, E. Kaldis and C. Zürcher, 1976, J. Magnetism and Mag. Materials, **3**, 200, also in "Neutronen-Streuung" Rept. AF-SSP-95 (Institut für Reaktortechnik ETHZ, E.I.R., Switzerland, 1976) p. 16.
A.J. Freeman, 1972, in Magnetic Properties of Rare Earth Metals, edited by R.J. Elliott (Plenum, London) Chap. 6.
A.J. Freeman and J.P. Desclaux, 1972, Int. J. Magnetism **3**, 311.
P. Fulde and I. Peschel, 1971, Z. Phys. **241**, 82.
P. Fulde and I. Peschel, 1972, Adv. Phys. **21**, 1.
A. Furrer, 1975, J. Phys. **C8**, 824.
A. Furrer and W. Hälg, 1977, to be published.
A. Furrer and E. Kaldis, 1976, AIP Conf. Proc. **29**, 264.
A. Furrer, J. Kjems and O. Vogt, 1972, J. Phys. **C5**, 2246.
A. Furrer, W. Hälg, E. Kaldis and C. Zurcher, 1976a, Neutronen-Streuung, AF-SSP-95 (Institut für Reaktortechnik ETHZ, E.I.R. Switzerland) p. 33.
A. Furrer, W.J.L. Buyers, R.M. Nicklow and O. Vogt, 1976b, Phys. Rev. **B14**, 179.
G.A. Gehring and K.A. Gehring, 1975, Rep. Prog. Phys. **38**, 1.
D. Gignoux, D. Givord, F. Givord, W.C. Koehler and R.M. Moon, 1976, Phys. Rev. **B14**, 162.
W.J. Gray and F.H. Spedding, 1968, Iowa State University Rept. IS-2044.
R.P. Gupta and A.J. Freeman, 1976a, Phys. Rev. **B13**, 4376.
R.P. Gupta and A.J. Freeman, 1976b, Phys. Rev. Lett. **36**, 613.
M. Habenschuss, C. Stassis, S.K. Sinha and F.H. Spedding, 1973, Phys. Lett. **45A**, 381.
M. Habenschuss, C. Stassis, S.K. Sinha, H.W. Deckman and F.H. Spedding, 1974, Phys. Rev. **B10**, 1020.
P.A. Hansen, P. Fynbo and B. Lebech, 1975, Risø Report No. 334, p. 12.
B.N. Harmon and A.J. Freeman, 1974a, Phys. Rev. **B10**, 4849.
B.N. Harmon and A.J. Freeman, 1974b, Phys. Rev. **B10**, 1979.
A. Hasegawa and J. Kübler, 1974, Z. Phys. **269**, 31.
H. Heer, Neutronen-Streuung, 1975, Rep. AF-AAP-87, (Institut für Reaktortechnik ETHZ, E.I.R. Switzerland) p. 33.
H. Heer, 1976, AF-SSP-87, pp. 28, 30.
H. Heer, A. Furrer, E. Walker, A. Treyvaud, H.G. Purwins and J. Kjems, 1974, J. Phys. **C7**, 1207.
A. Herpin and P. Meriel, 1960, Compt. Rend. Acad. Sci. (Paris), **251**, 1450.
A. Herpin and P. Meriel, 1961, J. Phys. Radium **22**, 237.
E.L. Hill, 1954, Am. J. Phys. **22**, 211.
H. Høg and P. Touborg, 1974, Phys. Rev. **B9**, 2920.
J. Høg and P. Touborg, 1975a, Phys. Rev. **B11**, 520.
J. Høg and P. Touborg, 1975b, Phys. Rev. **B11**, 2660.
J. Høg and P. Touborg, 1976, Phys. Rev. **B14**, 1209.
T.M. Holden and W.J.L. Buyers, 1974, Phys. Rev. **B9**, 3797.
T.M. Holden, E.C. Svensson, W.J.L. Buyers and O. Vogt, 1974, Phys. Rev. **B10**, 3864.
T.D. Holstein and H. Primakoff, 1940, Phys. Rev. **58**, 1098.
J.G. Houmann and H. Bjerrum-Møller, 1976, Proc. Conf. on Neutron Scattering, Gatlinburg, p. 793.
J.G. Houmann, M. Chapellier, A.R. Mackintosh, P. Bak, O.D. McMasters and K.A. Gschneidner, 1975, Phys. Rev. Lett. **34**, 587.
J.G. Houmann, B. Lebech, A.R. Mackintosh, W.J.L. Buyers, O.D. McMasters and K.A. Gschneidner, Jr., 1977, Physica **86–88B**, 1156.
Y.Y. Hsieh and M. Blume, 1972, Phys. Rev. **B6**, 2684.
M.T. Hutchings, 1964, Solid State Physics **16**, 227 (Ed. Seitz and Turnbull, Academic Press, New York).
F.J. Jelinek, E.D. Hill and B.C. Gerstein, 1965, J. Phys. Chem. Solids **26**, 1475.
J. Jensen, 1974, J. Phys. **F4**, 1065.
J. Jensen, 1975, J. Phys. **C8**, 2769.
J. Jensen, 1976a, J. Phys. **F6**, 1145.
J. Jensen, 1976b, Phys. Rev. Lett. **37**, 951.
J. Jensen, 1977, Physica **86–88B**, 32.
J. Jensen, J.G. Houmann and H. Bjerrum-Møller, 1975, Phys. Rev. **B12**, 303.
T. Johansson, B. Lebech, M. Nielsen, H. Bjerrum-Møller and A.R. Mackintosh, 1970, Phys. Rev. Lett **25**, 524.
D.F. Johnston, 1966, Proc. Phys. Soc. **88**, 37.
P. Junod, A. Menth and O. Vogt, 1969, Phys. Kondens. Materie **8**, 323.
T.A. Kaplan, 1961, Phys. Rev. **124**, 329.
T.A. Kaplan and D.H. Lyons, 1963, Phys. Rev. **129**, 2072.
T. Kasuya, 1956, Progr. Theoret. Phys. (Japan) **16**, 45.
T. Kasuya and D.H. Lyons, 1965, J. Phys. Soc. Japan **21**, 287.
Y. Kitano and T. Nagamiya, 1964, Prog. Theoret. Phys. (Kyoto) **31**, 1.
W.C. Koehler, 1967, in Trans of the American Crystallographic Association (H.G. Smith, Ed.), Polycrystal Book Service, Pittsburgh), Vol. **3**, p. 53.
W.C. Koehler, 1972, Magnetic Properties of Rare Earth Metals, Edited by R.J. Elliott (Plenum, London), ch. 3.

W.C. Koehler and R.M. Moon, 1972, Phys. Rev. Lett. **29**, 1468.
W.C. Koehler and R.M. Moon, 1976, Phys. Rev. Lett. **36**, 616.
W.C. Koehler, J.W. Cable, E.O. Wollan and M.K. Wilkinson, 1962, Phys. Rev. **126**, 6172.
W.C. Koehler, H.R. Child, E.O. Wollan and J.W. Cable, 1963, J. Appl. Phys. Suppl. **34** m 1335.
W.C. Koehler, J.W. Cable, M.W. Wilkinson and E.O. Wollan, 1966, Phys. Rev. **151**, 414.
W.C. Koehler, J.W. Cable, H.R. Child, M.K. Wilkinson and E.O. Wollan, 1967, Phys. Rev. **158**, 450.
W.C. Koehler, H.R. Child, R.M. Nicklow, H.G. Smith, R.M. Moon and J.W. Cable, 1970, Phys. Rev. Lett. **24**, 16.
W.C. Koehler, R.M. Moon and H.R. Child, 1972, AIP Conf. Proc. **10**, 1319.
W.C. Koehler et al., 1977, to be published.
G.H. Lander and T.O. Brun, 1970, J. Chem. Phys. **53**, 1387.
G.H. Lander and T.O. Brun, 1973, Phys. Rev. **B7**, 1988.
G.H. Lander, T.O. Brun, J.P. Desclaux and A.J. Freeman, 1973, Phys. Rev. **B8**, 3237.
K.R. Lea, M.J.M. Leask and W.P. Wolf, 1962, J. Phys. Chem. Solids **23**, 1381.
B. Lebech, 1968, Sol. St. Comm. **6**, 791.
B. Lebech, P. Fischer and B.D. Rainford, 1971, Proc of the Durham Conference on Rare Earths and Actinides (The Institute of Physics, London) p. 204.
B. Lebech, K.A. McEwen and P.A. Lindgard, 1975, J. Phys. **C8**, 1684.
R. Lemaire, 1966, Cobalt **33**, 201.
F. Levy, 1969a, Phys. Kondens. Materie **10**, 85.
P.M. Levy, 1968, Phys. Rev. Lett. **20**, 1366.
P.M. Levy, 1969b, Sol. St. Comm. **7**, 1813.
P.M. Levy and H.H. Chen, 1971, Phys. Rev. Lett. **27**, 1385.
P.A. Lindgard, 1976a, in Magnetism in Metals and Metallic Compounds, edited by J.T. Lopuszanski, A. Pekalski and J. Przystawa (Plenum, New York), p. 203.
P.A. Lindgard, 1976b, Phys. Rev. Lett. **36**, 385.
P.A. Lindgard, 1976c, Phys. Rev. **B14**, 4074.
P.A. Lindgard, 1976d, Phys. Rev. Lett. **37**, 954.
P.A. Lindgard and J.F. Cooke, 1977, to be published.
P.A. Lindgard and O. Danielsen, 1975, Phys. Rev. **B11**, 351.
P.A. Lindgard and J.G. Houmann, 1971, Proc. of Durham Conf. on Rare Earths and Actinides (The Institute of Physics, London), p. 207.
P.A. Lindgard, B.N. Harmon and A.J. Freeman, 1975, Phys. Rev. Lett. **35**, 385.
M.E. Lines, 1974, J. Phys. **C7**, L287.
S.H. Liu, 1977, Chapter 3 of this book.
S.H. Liu, R.P. Gupta and S.K. Sinha, 1971, Phys. Rev. **B4**, 1100.
S.W. Lovesey and D.E. Rimmer, 1969, Rep. Progr. Phys. **32**, 333.
A.R. Mackintosh, 1977, to be published.
A.R. Mackintosh and H. Bjerrum-Møller, 1972, Magnetic Properties of the Rare Earth Metals, edited by R.J. Elliott (Plenum, London), Chap. 5.
K.H. Mader and W.E. Wallace, 1968, J. Chem. Phys. **49**, 1521.
W. Marshall and S.W. Lovesey, 1971, Theory of Thermal Neutron Scattering, (London, Oxford University Press).
D. Mattis and W.E. Donath, 1962, Phys. Rev. **128**, 1618.
G. Meier and O. Vogt, 1976, Neutronen-Streuung, Rept. AF-SSP-95 (Institut für Reaktortechnik ETHZ, E.I.R., Switzerland) p. 9; see also Repts. AF-SSP-87, AF-SSP-93.
A.H. Millhouse and W.C. Koehler, 1971, Int. J. Magnetism **2**, 389.
A.H. Millhouse and K.A. McEwen, 1973, Sol. St. Comm. **13**, 339.
A.H. Millhouse, H.G. Purwins and E. Walker, 1972, Sol. St. Comm. **11**, 707.
H. Miwa, 1965, Proc. Phys. Soc. (London) **85**, 1197.
H. Miwa and K. Yosida, 1961, Progr. Theoret. Phys. (Kyoto) **26**, 693.
R.M. Moon and W.C. Koehler, 1971, Phys. Rev. Lett. **27**, 407.
R.M. Moon and W.C. Koehler, 1975, Phys. Rev. **B11**, 1609.
R.M. Moon, J.W. Cable and W.C. Koehler, 1964, J. Appl. Phys. Suppl. **35**, 1041.
R.M. Moon, W.C. Koehler and J. Farrell, 1965, J. Appl. Phys. **36**, 978.
R.M. Moon, W.C. Koehler, H.R. Child and L.J. Raubenheimer, 1968, Phys. Rev. **176**, 722.
R.M. Moon, W.C. Koehler, J.W. Cable and H.R. Child, 1972, Phys. Rev. **B5**, 997.
T.J. Moran, R.L. Thomas, P.M. Levy and H.H. Chen, 1971, Phys. Rev. **B7**, 3238.
J.M. Moreau, C. Michel, M. Simmons, T. O'Keefe and W.J. James, 1971, J. Phys. Suppl. **32**, **C1**, 670.
P. Morin and A. de Combarieu, 1975, Sol. St. Comm. **17**, 975.
P. Morin, J. Pierre and J. Chaussy, 1974a, Phys. Stat. Sol. (a) **24**, 425.
P. Morin, J. Pierre, J. Rossat-Mignod, K. Knorr and W. Drexel, 1974b, Phys. Rev. **B9**, 4932.
M.E. Mullen, B. Luthi, P.S. Wang, E. Bucher, L.D. Longinotti, J.P. Maita and H.R. Ott, 1974, Phys. Rev. **B10**, 186.
T. Nagamiya, 1962, J. Appl. Phys. **33**, 1029.
T. Nagamiya, 1967, Solid State Physics, **20**, 306 (Eds. Seitz, Turnbull and Ehrenreich) (Academic Press, New York).
T. Nagamiya, K. Nagata and Y. Kitano, 1962, Prog. Theoret. Phys. (Kyoto) **27**, 1253.
N. Nereson, 1973a, J. Appl. Phys. **44**, 4727.
N. Nereson, 1973b, AIP. Conf. Proc. **10**, 669.
N. Nereson and C. Arnold, 1971, J. Appl. Phys. **42**, 1625.
N.G. Nereson, C.E. Olsen and G.P. Arnold, 1964, Phys. Rev. **135**, A 176.
N. Nereson, C. Olsen and G. Arnold, 1966, J. Appl. Phys. **37**, 4575.

N. Nereson, C. Olsen and G. Arnold, 1968, J. Appl. Phys. **39**, 4605.
D.J. Newman, 1971, Adv. in Phys. **20**, 197.
D.J. Newman, S.S. Bishton, M.M. Curtis and C.D. Taylor, 1971, J. Phys. **C4**, 3234.
R.M. Nicklow, 1971, J. Appl. Phys. **42**, 1672.
R.M. Nicklow, N. Wakabayashi, M.K. Wilkinson and R.E. Reed, 1971, Phys. Rev. Lett **26**, 140.
R.M. Nicklow, N. Wakabayashi, M.R. Wilkinson and R.E. Reed, 1976a, Phys. Rev. Lett. **36**, 385.
R.M. Nicklow, N.C. Koon, C.M. Williams and J.B. Milstein, 1976b, Phys. Rev. Lett. **36**, 532.
M. Nielsen, H. Bjerrum-Møller and A.R. Mackintosh, 1968, J. Appl. Phys. **39**, 807.
M. Nielsen, H. Bjerrum-Møller and A.R. Mackintosh, 1970a, J. Appl. Phys. **41**, 1174.
M. Nielsen, H. Bjerrum-Møller, P.A. Lindgard and A.R. Mackintosh, 1970b, Phys. Rev. Lett. **25**, 1451.
K. Niira, 1960, Phys. Rev. **117**, 129.
J. Odiot and D. Saint-James, 1960, J. Phys. Chem. Solids **17**, 117.
R. Orbach and M. Tachiki, 1967, Phys. Rev. **158**, 524.
H. Oesterreicher, 1973, J. Phys. Chem. Solids **34**, 1267.
J.W. Patterson, 1972, unpublished.
J. Pierre, 1969, Sol. St. Comm. **7**, 165.
D.A. Pink, 1968, J. Phys. **C1**, 1246.
H.G. Purwins, E. Walker, P. Donze, A. Treyvaud, A. Furrer, W. Bührer and H. Heer, 1973a, Sol. St. Comm. **12**, 117.
H.G. Purwins, J.G. Houmann, P. Bak and E. Walker, 1973b, Phys. Rev. Lett. **31**, 1585.
H.G. Purwins, E. Walker, B. Barbara, M.F. Rossignol and P. Bak, 1974, J. Phys. **C7**, 3573.
H.G. Purwins, W.J.L. Buyers, T.M. Holden and E.C. Svensson, 1975, AIP Conf. Proc. **29**, 259.
S. Quézel, E.F. Bertaut and G. Quézel, 1969, Acta. Cryst. **25A**, S 252.
B.D. Rainford, 1972, AIP Conf. Proc. Magnetism and Magnetic Materials **5**, 591.
B.D. Rainford and J.G. Houmann, 1971, Phys. Rev. Lett. **26**, 1254.
B. Rainford, K.C. Turberfield, G. Busch and O. Vogt, 1968, J. Phys. **C1**, 679.
J. Rath and A.J. Freeman, 1975, Phys. Rev. **B11**, 2109.
O. Rathmann, J. Als-Nielsen, P. Bak, J. Høg and P. Toubo[illegible]rg, 1974, Phys. Rev. **B10**, 3983.
D.K. Ray, 1971, Proc of Durham Conf. on Rare Earths and Actinides (The Institute of Physics, London) p. 15.
J.J. Rhyne, 1972, in Magnetic Properties of Rare Earth Metals, edited by R.J. Elliott (Plenum, London) Chap. 4.
J.J. Rhyne and S.J. Pickart, 1972, AIP Conf. Proc. No. **5**, 1436.
J.J. Rhyne, N.C. Koon, J.B. Milstein and H.A. Alperin, 1976, Proc. of Neutron Scatt. Conf., Gatlinburg, Tennessee, p. 783.
M.A. Ruderman and C. Kittel, 1954, Phys. Rev. **96**, 99.
M.J. Sablik, H.H. Teitelbaum and P.M. Levy, 1973, AIP Conf. Proc. **10**, 548.
J. Sakurai, Y. Kubo, T. Kondo, J. Pierre and E.F. Bertaut, 1973, J. Phys. Chem. Solids **39**, 1305.
J.R. Sandercock, 1972, J. Phys. **C5**, 3126.
P. Schobinger-Papamantellos, P. Fischer, O. Vogt and E. Kaldis, 1973, J. Phys. **C6**, 725.
P. Schobinger-Papamantellos, P. Fischer, A. Niggli, E. Kaldis and V. Hildebrandt, 1974, J. Phys. **C7**, 2023.
D. Sherrington, 1973, J. Phys. **C6**, 1037.
G. Shirane and S.J. Pickart, 1966, J. Appl. Phys. **37**, 1032.
S.K. Sinha, N. Wakabayashi, O.D. McMasters and K.A. Gschneidner, Jr., 1977, to be published.
S.R.P. Smith, 1972, J. Phys. **C5**, L157.
F. Specht, 1967, Phys. Rev. **162**, 389.
F.H. Spedding, Y. Ito and R.G. Jordan, 1970, J. Chem. Phys. **53**, 1455.
F.H. Spedding, Y. Ito, R.G. Jordan and J. Croat, 1971, J. Chem. Phys. **54**, 1995.
C. Stassis, private communication.
C. Stassis and H.W. Deckman, 1975, Phys. Rev. **B12**, 1885.
C. Stassis and H.W. Deckman, 1976a, J. Phys. **C9**, 2241.
C. Stassis and H.W. Deckman, 1976b, Phys. Rev. **B13**, 4943.
C. Stassis, S.K. Sinha and G.R. Kline, 1975, Phys. Rev. **B11**, 2171.
C. Stassis, G.R. Kline, A.J. Freeman and J.P. Desclaux, 1976, Phys. Rev. **B13**, 3916.
K.W.H. Stevens, 1952, Proc. Phys. Soc. **A65**, 209.
K.W.H. Stevens and E. Pytte, 1973, Sol. St. Comm. **13**, 101.
M.W. Stringfellow, T.M. Holden, B.M. Powell and A.D.B. Woods, 1970, J. Phys. **C2**, 5189.
K. Sugihara, 1959, J. Phys. Soc. Japan **13**, 880.
W.M. Swift and W.E. Wallace, 1968, J. Phys. Chem. Solids **29**, 2053.
M. Tachiki, M.C. Lee, R.A. Treder and M. Levy, 1974, Sol. St. Comm. **15**, 1071.
G. Tanner, F.E. Wagner, G.M. Kalvius, G.K. Shenoy and K.H.J. Buschow, 1974, Proc. 18th Ampere Congress, Nottingham, p. 87.
K.N.R. Taylor, 1971, Advances in Physics **20**, 551.
W.A. Taylor, B.C. Gerstein and F.H. Spedding, 1977, to be published.
U. Tellenbach, A. Furrer and A.H. Millhouse, 1975, J. Phys. **C8**, 3833.
G.T. Trammell, 1953, Phys. Rev. **92**, 1387.
G.T. Trammell, 1963, Phys. Rev. **131**, 932.
K.G. Turberfield, L. Passell, R.J. Birgeneau and E. Bucher, 1970, Phys. Rev. Lett. **25**, 752.
K.C. Turberfield, L. Passell, R.J. Birgeneau and E. Bucher, 1971, J. Appl. Phys. **42**, 1746.
E.A. Turov and V.G. Shavrov, 1965, Fix. Tverd. Tela **7**, 217 (1965); Engl. transl. Soviet Physics Solid State **7**, 166.
L.F. Uffer, P.M. Levy and H.H. Chen, 1973, AIP Conf. Proc. **10**, 553.

H. Umebayashi, G. Shirane, B.C. Frazier and W.R. Daniels, 1968, Phys. Rev. **165**, 688.
M. Umehara and T. Kasuya, 1976, J. Phys. Soc. Japan **40**, 13.
C.M. Varma, 1976, Rev. Mod. Phys. **48**, 219.
N. Wakabayashi and R.M. Nicklow, 1974, Phys. Rev. **B10**, 2049.
W.E. Wallace, 1973, Rare Earth Intermetallics (Academic Press, New York) see also W.E. Wallace, Prog. in Solid State Chem. **6**, 1–5 (1971).
R.E. Walline and W.E. Wallace, 1964, J. Chem. Phys. **41**, 3285.
R.E. Walline and W.E. Wallace, 1965, J. Chem. Phys. **42**, 604.
Y.L. Wang and B.R. Cooper, 1969, Phys. Rev. **185**, 696.
Y.L. Wang and B.R. Cooper, 1970, Phys. Rev. **B2**, 2607.
R.E. Watson, A.J. Freeman and J.O. Dimmock, 1968, Phys. Rev. **167**, 497.
R.M. White and R.L. White, 1968, Phys. Rev. Lett. **20**, 62.
M.K. Wilkinson, W.C. Koehler, E.O. Wollan and J.W. Cable, 1961a, J. Appl. Phys. **32**, 48S.
M.K. Wilkinson, H.R. Child, C.J. McHargue, W.C. Koehler and E.O. Wallan, 1961b, Phys. Rev. **122**, 1409.
G. Will, S.J. Pickart, H.A. Alperin and R. Nathans, 1963, J. Phys. Chem. Solids **24**, 1679.
G. Will, R. Nathans and H.A. Alperin, 1964, J. Appl. Phys. **35**, 1045.
M. Winterberger, R. Chamard-Bois, M. Belakhovsky and J. Pierre, 1971, Phys. Stat. Sol. (b) **48**, 705.
W.P. Wolf and R.J. Birgeneau, 1968, Phys. Rev. **166**, 376.
A.D.B. Woods, T.M. Holden, B.M. Powell and M.W. Stringfellow, 1969, Phys. Rev. Lett. **23**, 81.
T. Yashiro, Y. Hamaguchi and H. Watanabe, 1976, J. Phys. Soc. Japan **40**, 63.
K. Yosida, 1957, Phys. Rev. **106**, 893.
K. Yosida, 1964, In Progress in Low Temperature Physics IV, edited by C.J. Garter (North-Holland, Amsterdam) p. 265.
K. Yosida and M. Miwa, 1961, J. Appl. Phys. **32**, 85.

Handbook on the Physics and Chemistry of Rare Earths, edited by K.A. Gschneidner, Jr. and L. Eyring

Chapter 8

ELASTIC AND MECHANICAL PROPERTIES*

T.E. SCOTT
Ames Laboratory – DOE and Department of Materials Science and Engineering, Iowa State University, Ames, Iowa 50011, USA

Contents

Symbols

A^* = Anisotropy ratio, C_{44}/C_{66}, for hexagonal structures
A_s = Temperature at which a polymorphic transformation begins during heating
α = Coefficient of linear thermal expansion
B^* = Anisotropy ratio, C_{33}/C_{11}, for hexagonal structures
C_p = Isobaric specific heat
C^* = Anisotropy ratio, C_{12}/C_{13}, for hexagonal structures
C_{ij} = Elastic stiffness constants
CYS = Compression yield strength
DPH = Diamond pyramid hardness
E = Young's modulus

*This work was supported by the U.S. Department of Energy under Contract Number W-7405-eng.-82.

E_H = Hill average Young's modulus
ϵ = Strain
$\dot{\epsilon}$ = Strain rate
$\dot{\epsilon}_{ss}$ = Steady-state creep rate
G = Shear modulus
G_H = Hill's average shear modulus
G_R = Reuss' average shear modulus
G_V = Voigt's average shear modulus
h = Planck's constant
θ = Pseudo Debye temperature given by eq. (8.18) in text when $T > 0$
θ_D = Debye temperature given by θ when $T \simeq 0$ K
k = Boltzmann's constant
K = Bulk modulus
K_H = Hill's average bulk modulus
K_R = Reuss' average bulk modulus
K_V = Voigt's average bulk modulus
M = Molecular weight
M_d = Temperature below which a polymorphic transformation begins to form as a result of deformation
M_s = Temperature at which a polymorphic transformation begins during cooling
M_H = Hill's average of any elastic property
M_R = Reuss' average of any elastic property
M_V = Voigt's average of any elastic property
N = Avogadro's number
ν = Poisson's ratio
P = Pressure
q = Number of atoms in a molecule
R = Gas constant
R.A. = Reduction in area
ρ = Density
S_{ij} = Elastic compliance constants
σ = Stress
TYS = Tensile yield strength
UCS = Ultimate compression strength
UTS = Ultimate tensile strength
U_p = Particle velocity
U_s = Shock wave velocity
V = Volume
V_D = Volume at atmospheric pressure
v_B = Bulk (isotropic) wave velocity
v_ℓ = Longitudinal wave velocity
v_m = Mean velocity
$\bar{v}_m$ = Anderson's average of the mean velocity
v_s = Shear wave velocity
v_{cl} = Longitudinal velocity of an acoustic wave propagated parallel to the c-axis
v_{al} = Longitudinal velocity of an acoustic wave propagated perpendicular to the c-axis
v_{asa} = Velocity of a shear wave propagated perpendicular to the c-axis with polarization also perpendicular to the c-axis
v_{cs} = Velocity of a shear wave propagated parallel to the c-axis with any polarization direction appropriate to a shear wave
v_{asc} = Velocity of a shear wave propagated perpendicular to the c-axis with polarization parallel to the c-axis
χ_s = Adiabatic compressibility
χ_T = Isothermal compressibility
ω = Atomic volume

1. Introduction

Scandium, yttrium, and the lanthanide metals comprise 17 elements for which systematically-determined mechanical property data are sparse. Pioneering work on the mechanical properties of rare earth metals was done in the mid to late 1950's and was conducted almost exclusively by three groups: B. Love and associates at Research Chemicals, Inc.; C.R. Simmons and associates at General Electric Co.; and E.M. Savitskiy and associates in the USSR. Since that time the number of investigations has increased and the property values have changed considerably with improvements in metal purification methods.

In this chapter an attempt is made to present all the available information, referring to the original source whenever possible. The literature on this topic is sometimes confusing because the original results, often available only in reports,

have been published repeatedly in various reviews and each time some of the pertinent ancillary information was omitted. Here the author has tried to provide such information as strain rates, annealing temperatures, purity, grain size and condition the metal was in when tested. All purity levels are given here on the weight basis.

2. Hardness

Despite the fact that results of hardness tests are impossible to interpret in terms of any single fundamental mechanical property of materials, they are probably the simplest "mechanical property" tests to perform. Also, it is frequently the only mechanical test that can be employed when material is not available in substantial quantities as has been the situation in rare earth research. Nevertheless, carefully conducted hardness tests often are a sensitive means for detecting differences in impurity concentrations and for classifying metals.

There are a variety of types of hardness tests, but the most popular in the case of rare earth metals seems to have been the Brinell test and the Vickers, or Diamond Pyramid Hardness (DPH) test as it is most commonly called. The DPH test is perhaps the most reliable hardness test and, in fact, should give hardness values in close agreement with the results of properly conducted Brinell and Knoop (when loads are >500 g) hardness tests. Consequently, the emphasis in this section is on DPH data, but Brinell data are also presented where they are instructive. Frequently, microhardness data are quoted in the rare earth literature. Since they are determined with a diamond pyramid indenter using lower loads than macrohardness, the author includes them with DPH values when they are in agreement with macroscopic values although it is recognized that microhardness results can be load sensitive.

Before presenting data, it is of value to discuss certain aspects of hardness testing that are not always mentioned and that are of particular importance for DPH testing of the non-cubic rare earth metals. With the exception of the three cubic metals, γ-cerium, europium, and β-ytterbium, all the rare earth metals, at room temperature, have a hexagonal structure which is strongly anisotropic. This inherent anisotropy appears in large grained as-cast structures and it is strong in polycrystalline materials which have been formed by rolling or swaging, even after full annealing. A good example of the effect of anisotropy on DPH values is provided by some unpublished results from the author's laboratory. Diamond pyramid indentations were taken parallel and transverse to the longitudinal axis of 0.318 cm diameter swaged wires of several fully recrystallized high purity rare earth metals.

In the case of fine grained cerium (cubic) the averages of many longitudinal and transverse DPH values were 28.7 and 28.5 kg/mm^2. In this instance, the indentation was usually within a single grain; yet the hardness values were not seriously affected by directionality. The average longitudinal and transverse DPH values of a moderate grain size ytterbium (cubic) sample were 17.6 and

13.7 kg/mm^2. Again, directionality had only a minor affect on the hardness values.

On the other hand, the average longitudinal and transverse DPH values of a fine grained praseodymium (hexagonal) sample were 26.7 and 24.2 kg/mm^2 respectively. Here the indenter covered several grains. For a coarse grained praseodymium sample, in which the indentations were within single grains, the longitudinal and transverse DPH values were 40.2 and 26.4 kg/mm^2 respectively. In this instance, the anisotropy affected hardness readings markedly. Other examples of this anisotropy effect were (kg/mm^2): dysprosium = 57.5 longitudinal, 38.6 transverse; yttrium = 81.9 longitudinal, 68.8 transverse; gadolinium = 57.0 longitudinal, 33.2 transverse. Furthermore, an yttrium single crystal was indented normal to the basal plane, normal to a first order prismatic plane of the type $(10\bar{1}0)$, and normal to a second order prismatic plane of the type $(11\bar{2}0)$. The corresponding DPH values were 98.1, 45.9 and 50.6 kg/mm^2 and there were great differences in the individual indentation diagonal lengths. Others have reported ratios of DPH on the basal plane to that on a first order prismatic plane ranging from 2.04 to 3.69 for scandium (Spedding et al., 1971, and Naumkin et al., 1963). Terekhova and Savitskiy (1967) and Carlson et al. (1959) have demonstrated hardness anisotropy in yttrium. When the above anisotropy features are coupled with the influence of impurities on hardness it becomes evident that large differences in reported hardness values might be expected, depending on grain size, forming operation, thermal history, and orientation of the indentation. These factors should be considered when evaluating reported hardness data. In fact, for a hypothetically pure rare earth with non-cubic structure, the hardness will vary greatly with relative orientation and the correct value to report is somewhat ambiguous. The author's choice is to select the lowest value because it is less ambiguous, but, unless a similar choice is available when comparing results among metals, even this selection criterion can produce erratic hardness values within a family such as the rare earth metals.

2.1. *Room temperature hardness*

Most, if not all, of the existing hardness data for the rare earth metals in the as-cast or annealed condition has been compiled in table 8.1. Figure 8.1 presents the DPH values for the rare earth metals as a function of atomic number. Both low and high values are represented to indicate the range. In most cases, the range of hardness values reflects the variation in purity with low values representing the highest purity as expected. However, there may be an effect of crystallographic orientation involved with the low values that is impossible to isolate based on the information available from the data sources. With the exception of the fact that the cubic metals always have lower hardness than the non-cubic metals, hardness does not appear to exhibit any definite trend with atomic number. The average low DPH values of the non-cubic rare earth metals is about 37 kg/mm^2 whereas the cubic metals have an average low DPH value of about 19 kg/mm^2.

TABLE 8.1.
Hardness summary for the rare earth metals (as cast or annealed)*.

	Vickers (DPH) and microhardness (kg/mm^2)		Brinell (kg/mm^2)		Rockwell		
Metal	Value	Ref.	Value	Ref.	Value	Scale	Ref.
Scandium	50	1	40	3	85	H	4
	36	2	47–196	7			
	36 {10$\bar{1}$0}	5	75–80	8[a]			
	132 (0001)	5	> 100	8[b]			
	42 {10$\bar{1}$0}	5	143	9			
	148 (0001)	5	95–120	10			
	103 {10$\bar{1}$0}	6	120–130	17[a]			
	210 (0001)	6	75–100	17[b]			
	100	7	50–60	17[c]			
	220	31					
Yttrium	83–118	11[a]	80–85	10, 31	81	E	12[a]
	63–73	8[c]	45–50	14	25	A	13
	80	16[a]	32–67	15[a]	67–89	F	15[d]
	130	18	40–54	15[b]	60	H	19
	45	19	39–69	15[c]	61	H	20
	38	20					
	69–82	21[a]					
	46 {10$\bar{1}$0}	21					
	98 (0001)	21					
	61 {10$\bar{1}$0}	22[a]					
	112 (0001)	22[a]					
	–/41	30					
	78/120	22[b]					
Lanthanum	37	20	35–40	10	55	H	20
	59	18	38	31	38	*	25[a]
	38	16[b]	36	32			
	30	23[a]					
	50	8, 23[b]					
	33	24[a]					
	50–52	11[b]					
	28/38	30					
Cerium			25–30	10	3	H	20[a]
	25	16[c], 26	26	31	38	*	25[b]
	24	20[a]	19	34			
	29–33	11[c]					
	30	8					
	21–29	21[b]					
	22/29	30					

TABLE 8.1 (Contd)

Metal	Vickers (DPH) and microhardness (kg/mm^2) Value	Ref.	Brinell (kg/mm^2) Value	Ref.	Rockwell Value	Scale	Ref.
Praseodymium	24–27	21[c]	35–50	10	38	H	20[a]
	26–40	21[d]	49	8			
	37	20[a]	45	31			
	31	16[d]	55	33			
	43–49	11[d]					
	20/37	30					
Neodymium	35	20[a]	35–45	10	50	H	20[a]
	45	16[e]	27	8			
	80–85	11[e]	46	31			
	33	24[b]	33	34			
	18/24	30					
Promethium							
Samarium	45	20	45–65	10	63	H	20
	55	16[f]					
	64	11[f]					
	39/40	30					
Europium	17	20[a]	15–20	10	26	L	20[a]
Gadolinium	33–57	21[a]	55–70	10	67	H	20
	57	20	54	8	36–40	E	27
	63	16[g]	70	31			
	58–74	11[g]					
	60–65	28					
	37/42	30					
Terbium	46	20	90–120	10	62	H	20
	65	16[h]	69	8			
	–/38–46	30					
Dysprosium	39–58	21[a]	55–105	10	57	H	20
	42	20	51	8	61	E	12[b]
	68	16[i]					
	80	18					
	80	29					
	87–99	11[h]					
	58/44	30					

TABLE 8.1 (Contd)

	Vickers (DPH) and microhardness (kg/mm^2)		Brinell (kg/mm^2)		Rockwell		
Metal	Value	Ref.	Value	Ref.	Value	Scale	Ref.
Holmium	42	20	50–125	10	57	H	20
	78	16[j]	76	8			
	93	18					
	90	11[i]					
	–/46	30					
Erbium	44	20	60–95	10	63	H	20
	73	16[k]	83	8	74	E	12[c]
	107–128	11[j]					
	–/42	30					
	135	31					
Thullium	48	20	55–90	10	69	H	20
			79	8			
Ytterbium	14–18	21[a]	20–30	10	−4	H	20[a]
	21	20[a]	35	8			
	14	16[l]					
	–/17	30					
Lutetium	77	20	120–130	10	86	H	20
			91	8			

*The Miller-Bravais indices following a hardness value indicate the crystallographic face on which the measurement was made.

References and Comments for Table 8.1

1. Naumkin, O.P. and D.V. Ignatov, 1964, Izv. Akad. Nauk SSSR, Met Gorn. Delo [5], 142. Engl. Transl., 1964, Russ. Met. Mining [5], 101.
2. Betterton, Jr. J.O. and J.O. Scarbrough, 1968, Phys. Rev. **168**, 715.
3. Naumkin, O.P., V.F. Terekhova and E.M. Savitskiy, 1967, Izv. Akad. Nauk SSSR, Neorg. Mater. **3**, 711. Engl. Transl., 1967, Inorg. Materials **3**, 628.
4. Spedding, F.H., A.H. Daane, G. Wakefield, D.H. Dennison, 1960, Trans. AIME **218**, 608.
5. Spedding, F.H., D. Cress and B.J. Beaudry, 1971, J. Less-Common Metals **23**, 263. Total of 2620 ppm impurity out of 36 elements analyzed.
6. Naumkin, O.P., V.F. Terekhova and E.M. Savitskiy, 1963, Fiz. Metal. Metalloved. **16** [5], 663. Engl. Trans., 1963, Phys. Met. Metallogr. **16**, 22. (99.6% pure Sc).
7. Geiselman, D., 1962, J. Less-Common Metals **4**, 362. Total of 7960 ppm impurities including about 4500 ppmO. Cold worked 87% and annealed 1 hour at 900°C.
8. Simmons, C.R., 1961, The Mechanical Properties of Yttrium, Scandium, and the Rare Earth Metals, in: Spedding, F.H., and A.H. Daane eds., *The Rare Earths* (John Wiley and Sons, New York), pp. 428–452. a) Lithium-reduced scandium fluoride, distilled and arc-melted into buttons. b) Calcium reduced scandium fluoride in tantalum crucibles; contain 2–5 w/o Ta. c) Arc-melted yttrium; low value for 500 ppm O and 700 ppm F, high value for 2500 ppm O, 3000 ppm F. (500 kg. load, 10 mm indenter.)

9. Achard, J-C., P. Caro, and J. Loriers, 1956, Compt. rend. **243**, 493. (3000 kg. load, 10 mm indenter) claimed less than 0.2% impurities but contained second phase.
10. Savitskiy, E.M., V.F. Terekhova, and O.P. Naumkin, 1963, Usp. Fiz. Nauk **79**, 263. Engl. Transl., 1963, Sov. Phys. Usp. **6**, 123.
11. Love, B., 1959, "Selection and Evaluation of Rare or Unusual Metals – Part II. The Metallurgy of Yttrium and the Rare Earth Metals," WADC-TR-57-666, Wright Air Development Center, U.S. Air Force, Wright-Patterson Air Force Base, Ohio (March 1959). a) Y: Ca-reduced fluoride; about 7030 ppm impurity including about 3900 ppm O. b) La: ≃2160 ppm impurity including 1800 ppm O. c) Ce: 2550 ppm impurity including 500 ppm O. d) Pr: 2640 ppm impurity including 1400 ppm O. e) Nd: 2310 ppm impurity including 1300 ppm O. f) Sm: 580 ppm impurity including 200 ppm O. g) Gd: 4470 ppm impurity including 1600 O. h) Dy: <4720 ppm impurity including 2000 O, <1000 ppm Ho and <1000 ppm Y. i) Ho: 3990 ppm impurity including 800 ppm O. j) Er: 7260 ppm impurity including 3500 ppm O + 2000 ppm Ta.
12. Love, B., 1960, "The Metallurgy of Yttrium and Rare Earth Metals – Part II. Mechanical Properties," WADD-TR-60-74 (Pt. 2), Wright Air Development Division, U.S. Air Force, Wright-Patterson Air Force Base, Ohio (June 1960). Calcium reduction of fluoride in tantalum crucibles, arc-cast in copper chill molds. a) Y: Contains 0.6 w/o to 1.05 w/o impurities including 0.2 to 0.4 w/o O and 0.25 to 0.50 w/o Ta. b) Dy: 3500–7500 ppm impurity including 1000–4000 ppm O + 1000–2000 ppm Ta. e) Er: 6000–9600 ppm impurity including 2000–4000 ppm O + 2500–5000 ppm Ta.
13. Bohlander, K.M., 1961, Mechanical Fabrication of Rare Earth Metals, in: Spedding, F.H. and A.H. Daane eds., *The Rare Earths* (John Wiley and Sons, New York) pp. 163–174.
14. Nolting, H.J., C.R. Simmons, and J.J. Klingenberg, 1960, J. Inorg. Nucl. Chem. **14**, 208. Yttrium prepared by lithium reduction of anhydrous yttrium chloride prepared from yttrium oxide; claim 99.8% purity but, in fact, contained <2372 ppm impurity including 1700 ppm non-metallic. (500 kg load, 10 mm indenter).
15. Carlson, O.N., D.W. Bare, E.D. Gibson, and F.A. Schmidt, 1959, Survey of the Mechanical Properties of Yttrium and Yttrium Alloys, in: *Symposium on Newer Metals*, A.S.T.M. Special Technical Publication No. 272 (American Society for Testing Materials, Philadelphia), pp. 144–159. Yttrium prepared by reduction of YF_3 with calcium in the presence of magnesium (intermediate alloy process) in a titanium reaction vessel.
    a) As arc-cast; contains 500 ppm O.
    b) Arc-cast then annealed at 950°C and slowly cooled; 500 ppm O.
    c) Values in different grains of arc-melted ingot.
    d) On different faces of a single crystal; low value on face nearly perpendicular to basal plane, high value on face nearly parallel to basal plane.
16. Ross, I.N., 1967, J. Inst. Mets. **95**, 337.
    a) Y: 1100 ppm Ta; O, N, H not given
    b) La: 1470 ppm impurities including 1060 ppm O
    c) Ce: 52 ppm impurities but O, N, H not given
    d) Pr: 52 ppm impurities but O, N, H not given
    e) Nd: 28 ppm impurities but O, N, H not given
    f) Sm: 1494 ppm impurities including 1000 ppm O
    g) Gd: 153 ppm impurities but O, N, H not given
    h) Tb: 150 ppm impurities but O, N, H not given
    i) Dy: 586 impurities including 200 ppm O
    j) Ho: 1239 ppm impurities including 680 ppm O
    k) Er: 412 ppm impurities including 180 ppm O
    l) Yb: 1526 ppm impurities including 1400 ppm O
17. Naumkin, O.P., V.F. Terekhova, and E.M. Savitskiy, 1964, Investigation of the Properties of Metallic Scandium, in: Savitskiy, E.M. and V.F. Terekhova, eds. *Voprosy Teorii i Primeneniya Redkozemel'nykh Metallov* (Science Publishing House, Moscow) pp. 71–78. Engl. Transl., *Problems of the Theory and Use of Rare Earth Metals*, JPRS: 28 849, Feb. 23, 1965 available

from U.S. Dept. of Commerce, Clearinghouse for Federal Scientific and Technical Information, Joint Publications Research Service, Washington, D.C., pp. 86–97.
a) 96–97% pure Sc; b) 99% pure Sc; c) 99.7% pure Sc.
18. Rabinowicz E. and P.A. March, 1973, J. Less-Common Metals **30**, 145.
19. Habermann, C.E. and A.H. Daane, 1963, J. Less-Common Metals **5**, 134. Vacuum distillation, contained 8000 ppm total impurities including 120 ppm O.
20. Spedding, F.H. and A.H. Daane, 1960, Met. Revs. **5**, 297. Hardness data taken by C.E. Habermann, 1959, USAEC Rept. IS-15. a) unannealed.
21. Unpublished work in author's laboratory.
a) low value from transverse section of polycrystalline rod and high value from longitudinal section of same rod.
b) low value = coarse grain cerium; high value = fine grain cerium
c) fine grain polycrystalline sample
d) coarse grain; high value from longitudinal section and low value from transverse section.
22. Terekhova, V.F., and E.M. Savitskiy, 1967, *Yttrium* (Academy of Sciences of the U.S.S.R., A.A. Baikov Inst. Metallurgy, Moscow) Engl. Transl. available as AEC-tr-6980 from U.S. Dept. of Commerce. a) 50 gram load. b) As-cast + 1 h/973 K anneal. Lower number is for zone refined yttrium (200–250 μm grain size) while higher value is for commercial yttrium (30 μm grain size).
23. Amonenko, V.M., A.A. Kruglikh, and V.S. Pavlov, 1966, Ukr. Fiz. Zhur. **11**, 1023.
a) Combined zone melting with electrotransport (320 ppm O, 40 ppm N, 800 ppm C)
b) 800 ppm O, 47 ppm N, 13 ppm H, 1400 ppm C.
24. Bol'shutkin, L.I., Yu.Ye. Krot, and V.A. Moskalenko, 1965, Fiz. Metal Metalloved. **20**, 465. Engl. Transl., 1965, Phys. Met. Metallogr. **20**, 151.
a) La: Claim 99.3% pure (0.3 wt/o Cu, 0.1 w/o Nd, 0.2 w/o Pr. 0.02 w/o Fe) but no non-metallics quoted. (5 kg load).
b) Nd: Claim 99.2% pure (<0.5% Pr, <0.1% Sm, <0.02% Ca, <0.05% Fe) but no non-metallics quoted.
25. Savitskiy, E.M. and V.F. Terekhova, 1955, Izv. Sekt. Fiz. Khim. Anal. (Inst. Obshehei Neorg. Khim., Akad. Nauk S.S.S.R.) pp. 148–155.
a) La: 90° vertex angle cone indenter.
b) Ce: 90° vertex angle cone indenter; claim 97.1% pure Ce.
26. Amonenko, V.M., A.A. Kruglikh, V.S. Pavlov, and L.M. Mosova, 1966, Izv. Akad. Nauk SSSR. Neorg. Mater. **2**, 578. Engl. Transl. Inorg. Mater. **2**, 500. Combined zone melting and electrotransport purification, final product had 840 ppm total impurity. (10 gram load)
27. Milstein, F. and J.A. Baldwin, Jr., 1972, J. Inst. Met. **100**, 337. About 1300–1800 ppm O. (annealed at 1173 K)
28. Nabutovskaya, O.A., 1969, Fiz. Tverd. Tela **11**, 1434. Engl. Transl., 1969, Sov. Phys.-Solid State **11** [5], 1172.
29. Hopkins, R.H., 1974, Met. Trans. **5**, 1183. Dy containing <3260 ppm impurities including 2000 ppm O. (Knoop indenter).
30. Beaudry, B.J., Ames Laboratory, unpublished research, 1977. Left-hand value is the as arc-cast value and right-hand value is for as arc-cast + rolled + annealed.
31. Savitskiy, E.M., 1959, *Redkie Metally i Splavy* (Rare Metals and Alloys) (Dom Tekhniki, Moscow) p. 19.
a) Sc: 90% pure; b) Y: 96.4% pure; c) La: 99.0% pure; d) Ce: 99.0% pure; e) Pr: 99.2% pure; f) Nd: 99.5% pure; g) Gd: 99.9% pure; h) Er: 99.3% pure. However impurities are not given.
32. Trombe, F., 1936, Ann. Chim. (Paris) **6**, 349.
33. Iandelli, A., 1947, Atti accad. nazl. Lincei Rend., Classe sci. fis. mat. e nat. **2**, 327.
34. Ahmann, D.H., 1950, "Metallurgy of the Rare Earths with Particular Emphasis on Cerium," AECD-3205, U.S. Atomic Energy Commission Report.

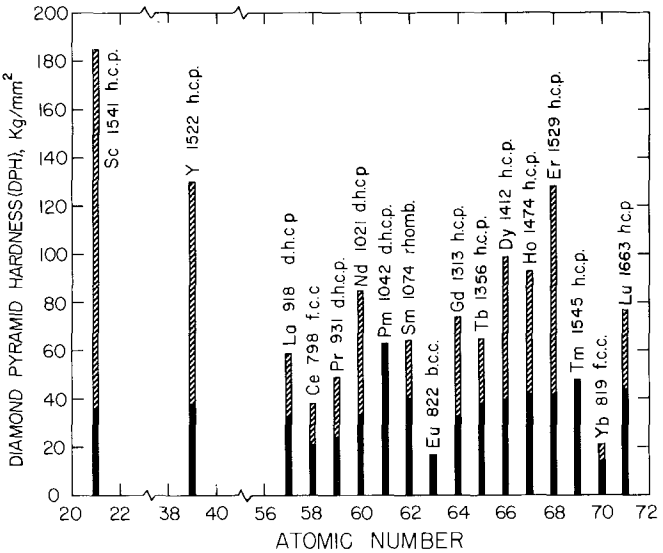

Fig. 8.1. A bar graph summary of room temperature diamond pyramid hardness values of the rare earth metals including melting temperatures (K) and room temperature crystal structures. Solid portions of the bars indicate the lowest known value while the cross-hatched portions represent the range of values reported.

The effects of impurities on room temperature hardness have been evaluated systematically only for the case of yttrium with varying amounts of oxygen. Carlson et al. (1959) determined the influence of oxygen concentration on the Brinell hardness of sponge process yttrium in the as arc-cast and in the annealed plus slow cooled condition. The results of annealing plus quenching were the same as those obtained for as arc-cast material. The results, given in fig. 8.2, indicated a linear increase in hardness with oxygen concentration. However, the rate of hardness increase was almost negligible for the annealed plus slow cooled metal. Subsequent work by the GE-ANPD group (Simmons, 1961) corroborated the findings of Carlson et al. on as-cast yttrium. But the latter researchers used yttrium which had been melted in tantalum crucibles and solidified in copper or graphite molds to produce a more equiaxed, smaller as-cast grain size. With this material, they observed no affect of annealing on the hardness in contradiction to the results of Carlson et al. (fig. 8.3). This discrepancy has not been resolved. Also, it has not been established whether the effect of oxygen on hardness is a result of dissolved oxygen or of dispersed oxide particles.

2.2. *Effect of temperature*

The available information on the effect of temperature on the hardness of rare earth metals is illustrated in fig. 8.4 which includes data for Y, La, Ce, Pr, Nd, and Gd. Two of the curves, representing neodymium (99.2% pure) and

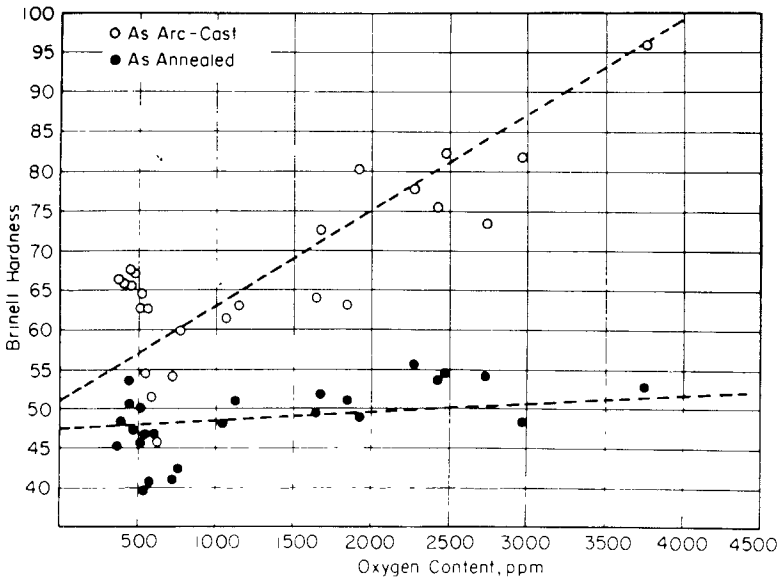

Fig. 8.2. Hardness versus oxygen content of yttrium in the arc-cast and annealed condition. From Carlson et al. (1959).

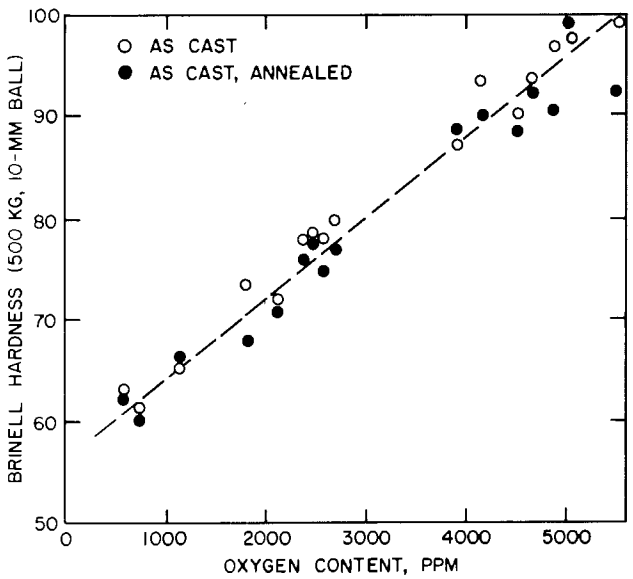

Fig. 8.3. Hardness versus oxygen content of yttrium in the cast and cast plus annealed conditions. From Simmons (1961).

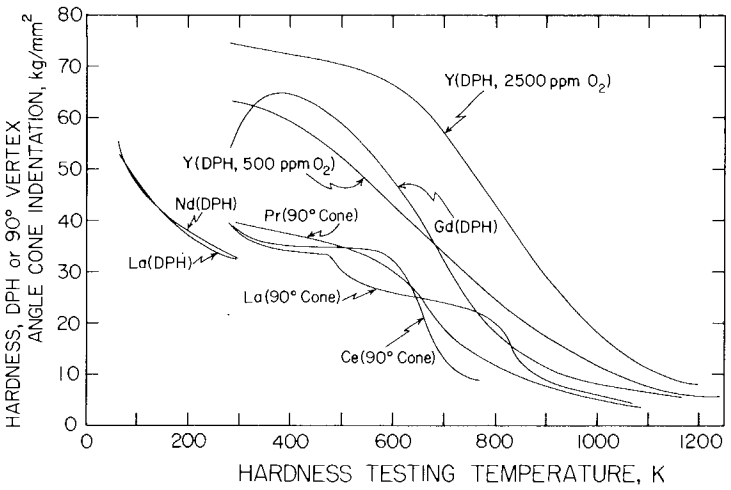

Fig. 8.4. Hardness versus testing temperature for six rare earth metals. La (90°Cone) and Ce (90°Cone) from Savitskiy and Terekhova (1955); Pr (90°Cone) from Savitskiy et al. (1962); La (DPH) and Nd (DPH) from Bol'shutkin et al. (1965); Gd and Y from Simmons (1961).

lanthanum (99.2% pure) in the as-cast plus annealed condition, were determined at subambient temperatures by Bol'shutkin et al. (1965). The temperature dependence of the hardness was described by the relation $DPH = Ae^{-BT}$ where A and B are constants. Curves for the same metals which had been cold worked by compressing 40 percent were parallel to the corresponding curves for the annealed metal but displaced to higher hardness values. The higher temperature hardness data for praseodymium, lanthanum, and cerium were taken with a conical indenter made of a W–Co–C–Ti alloy (Pobedit) having a vertex angle of 90° (the Rockwell "C" conical indenter has vertex angle of 120°C). Consequently, the absolute hardness values cannot be compared directly with other hardness data. Nevertheless, the qualitative trend, which reveals a transition near 650 K for Pr and Ce, should be reliable. The curve for La appears to exhibit a double transition, one near 500 K and the other near 825 K. The lower temperature hardness transition for lanthanum might be related to the α(d.h.c.p) to β(f.c.c.) transformation. The transitions for the other metals and the higher temperature hardness transition of lanthanum probably reflect changes in deformation mechanism with increasing temperature. Hardness versus test temperature plots for yttrium contaminated with two different levels of oxygen reveal that the hardening due to oxygen decreases with increasing temperature. Finally, the hardness of gadolinium exhibits a maximum at about 400 K which has been attributed (Simmons, 1961) to an aging process. All of the metals represented in fig. 8.4 approach a high temperature hardness level of about 5 kg/mm^2 whether determined with a diamond pyramid or 90° cone indenter. In conclusion, all the metals exhibit a hardness transition which, regardless of how one chooses to define it, does not appear to correlate with the absolute melting

temperatures of the metals. However, lack of correlation could be attributed to variation in purity which has a substantial influence as shown by the curves for yttrium of two oxygen levels.

An anomaly in the microhardness of gadolinium near its Curie temperature was noted by Nabutovskaya (1969). The microhardness dropped suddenly from a value of about 62 kg/mm^2 at room temperature (298 K) to about 31 kg/mm^2 at 292 K which is within 1 K of the Curie temperature. Upon further cooling the hardness rose to a sharp peak at 276 K; it dropped at 273 K to a value of about 50 kg/mm^2 where it remained relatively constant down to the lowest temperature used, 230 K. The peak hardness at 276 K was interpreted as being associated with a phase transformation accompanying deformation by the indenter.

2.3. *Effect of cold work*

According to the systematic study by Ross (1967) of the effect of cold rolling on the hardness of yttrium and twelve of the lanthanide metals, the hardness of all metals except La, Nd, Er, Y, and perhaps Sm tends to increase rapidly during the initial 20–25 percent reduction. Further hardening does not occur until reductions of the order of 60 percent (see fig. 8.5). This is in agreement with the earlier work by Love (1960) on erbium and dysprosium shown in fig. 8.6. A comparison of the effect of 50 percent cold work by swaging (Love, 1959) or

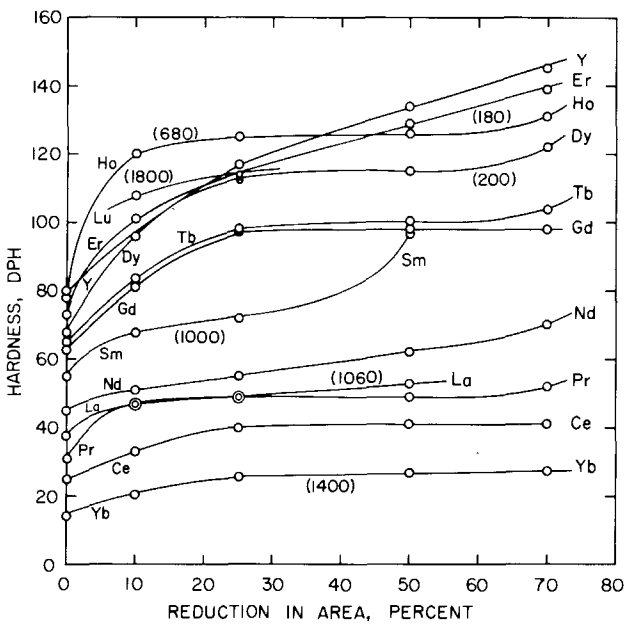

Fig. 8.5. Effects of cold reduction by rolling on the hardness of rare earth metals. Data from Ross (1967). Numbers in parenthesis refer to oxygen concentration in ppm (wt.).

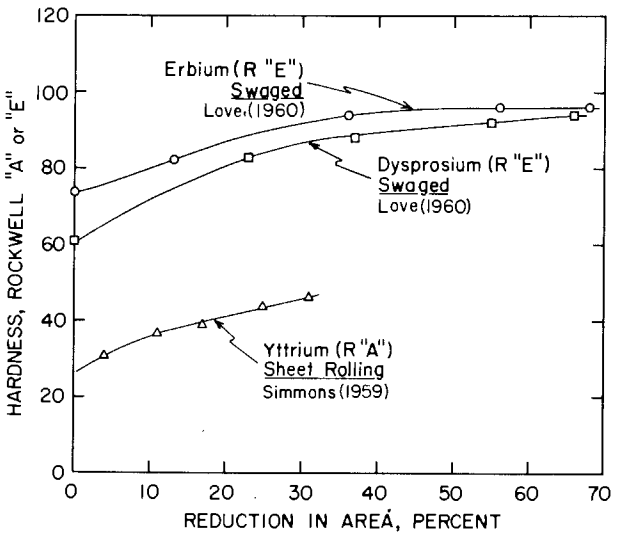

Fig. 8.6. Effect of cold working by swaging (Er and Dy) or cold rolling (Y).

cold rolling (Ross, 1967) on the DPH of several rare earth metals is given in table 8.2. With the exceptions of lanthanum and dysprosium the hardness increase agreed within the ranges observed. The increase in the hardness of lanthanum as measured by Love (1959) was much greater than the increase measured by Ross (1967). On the other hand, the hardness increase of dysprosium measured by Love (1959) was much less than that measured by Ross (1967). Different purity levels do not explain the disparity in results because the purity of Ross'

TABLE 8.2.
Effect of 50% cold working on hardness, DPH (kg/mm^2).

	Love (1959)			Ross (1967)		
Metal	As-cast	Swaged	Increase	Annealed	Rolled	Increase
Yttrium	83–118	140	22–57	80	134	54
Lanthanum	50–52	120–178	69–127	38	53	15
Cerium	29–33	43–53	10–24	25	41	16
Praseodymium	43–49	77*	28–34	26	49	23
Neodymium	80–85	76	(−4)–(−9)	45	62	17
Samarium	–	–	–	55	97	42
Gadolinium	58–74	97–98*	23–40	63	98	35
Terbium	–	–	–	65	100	35
Dysprosium	87–99	97–98*	(−2)–11	68	115	47
Holmium	–	–	–	78	126	48
Erbium	107–128	161	33-54	73	129	56

*Worked at elevated temperature because metal would not work readily at room temperature.

dysprosium was much higher than Love's which was softer after 50 percent cold work. Perhaps the initial condition of lanthanum was different. In the case of dysprosium reported by Love (1959) the metal had to be worked at elevated temperature consequently the final states were not comparable.

It appears that the hardness of yttrium increases rapidly during the first 10–25% reduction and then continues to increase linearly for greater reductions. This is indicated by the results of Simmons (1961), fig. 8.7; Ross (1967), fig. 8.5; and Simmons (1959), fig. 8.6. However, the results of Carlson et al. (1959), fig. 8.7, showed that purer yttrium (500 ppm oxygen) was hardened linearly by cold working from the lowest reductions (~2%) up to about 45% cold work where hardness ceased to increase significantly. Based on the curves illustrated in fig. 8.7, the initial work hardening behavior depends on the impurity concentration, especially that of oxygen. Higher purity yttrium work-hardens linearly in the early stages of deformation while lower purity yttrium work-hardens more rapidly at first but with a continually decreasing rate. Furthermore, as the oxygen content increases the initial rate of hardening seems to be greater and the

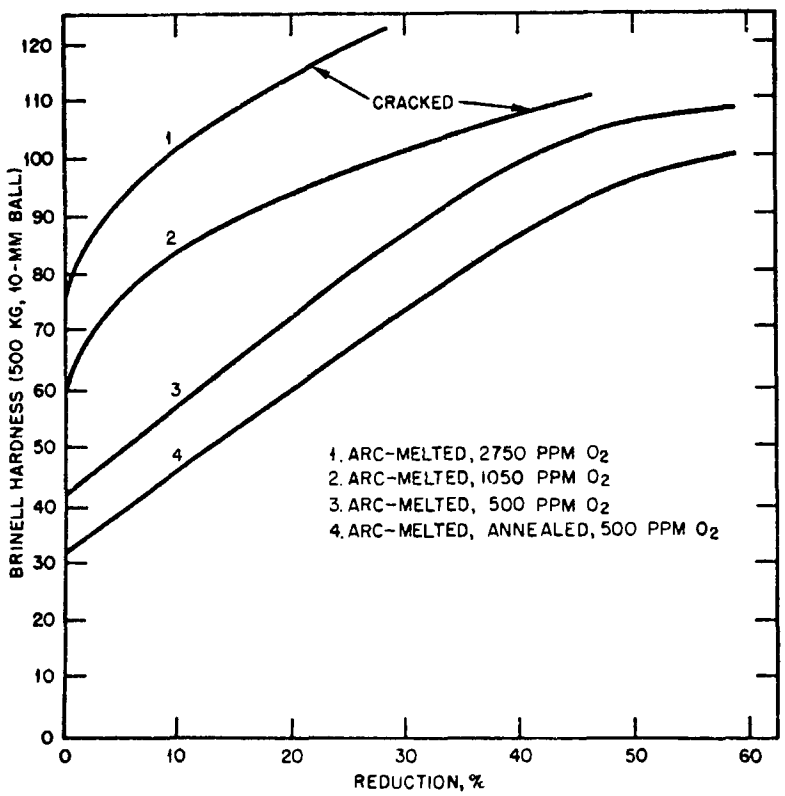

Fig. 8.7. Effect of cold reduction by rolling on the hardness of yttrium having three levels of oxygen impurity. Lower oxygen concentration data (curves 3 and 4) are from Carlson et al. (1959) while data for higher oxygen concentrations (curves 1 and 2) are from Simmons (1961). Taken from Simmons (1961).

cracking sets in earlier. It is very likely that both the initial high rate of work hardening and the early onset of cracking are associated with the presence of dispersed oxide particles.

2.4. *Effect of annealing*

After cold working it is customary to anneal metals to restore softness and workability. Annealing is accomplished by heating metals to temperatures where self-diffusion permits crystalline defects to be annihilated or rearranged. Hardness measurements provide one means for ascertaining annealing characteristics of cold worked metals. Hardness versus annealing temperature curves for Sc, Er, Gd, and Y are shown in figs. 8.8 and 8.9. In fig. 8.8 it can be seen that the hardness of gadolinium and erbium pass through minima at about 750 K and 825 K respectively according to Ross (1967). Based on these results Ross suggested an annealing temperature of 750 K for gadolinium. However, subsequent annealing studies by Milstein and Baldwin (1972) and Milstein et al.

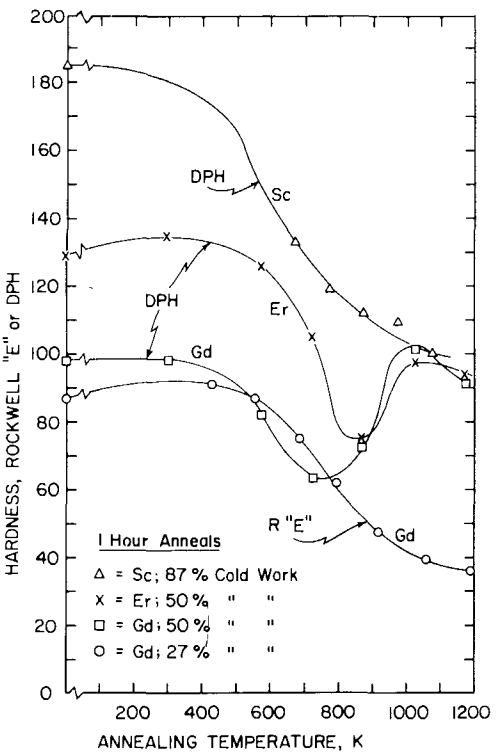

Fig. 8.8. Hardness versus annealing temperature for Sc, Gd, and Er. DPH values for Gd and Er from Ross (1967): Gd had 153 ppm impurities but O_2, N_2, C and H_2 not given; Er had 412 ppm impurities including 180 oxygen. Rockwell "E" data for Gd from Milstein and Baldwin (1972): about 2150 ppm impurities including an average of about 1300 ppm oxygen. DPH (microhardness, 17 gram load) results for Sc from Geiselman (1962): about 7960 ppm impurities including about 4500 ppm oxygen.

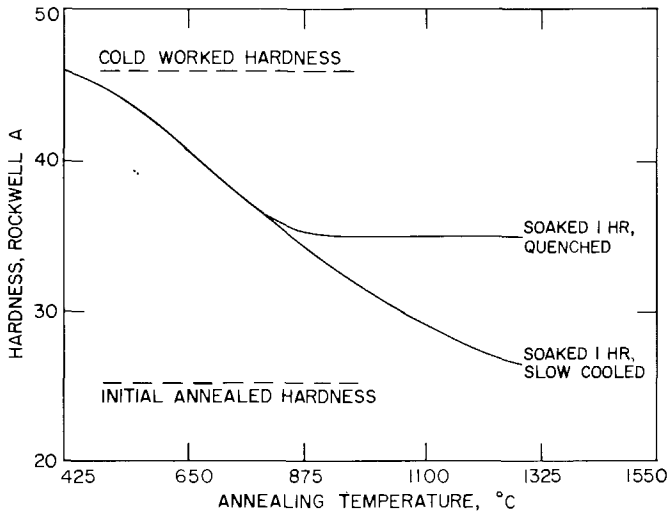

Fig. 8.9. Effect of annealing temperature and rate of cooling from annealing temperature on the hardness of 30 percent cold worked yttrium. From Bohlander (1961).

(1973) did not reveal the hardness minimum for gadolinium. They attributed the hardness minimum observed by Ross to contamination during higher temperature annealing; the contamination presumably increased the hardness at annealing temperatures above 750 K. This explanation seems reasonable. Nevertheless, the hardness of gadolinium in both studies was similar at 750 K. Even though two different hardness scales were employed (Rockwell "E" and DPH are virtually the same in the hardness range of concern), the similarity in hardness suggests that 750 K may be the appropriate annealing temperature since the inflection point in the hardness-annealing temperature curve generally signifies completion of recrystallization. Subsequent softening is produced by grain growth and further defect elimination or rearrangement. Figure 8.9 from Bohlander (1961) shows that the hardness of annealed yttrium depends on the cooling rate subsequent to holding at the annealing temperature. Samples of 30 percent cold-worked yttrium showed no further softening above the annealing temperature of about 1100 K when they were quenched to ambient temperature. Slow cooled samples continued to soften with increased annealing temperature. Perhaps quenching prevented impurities from precipitating, thus maintaining the hardness via solution hardening.

3. Single crystal deformation

Knowledge of basic deformation characteristics can be obtained from single crystal tests. Furthermore, the confounding effect of grain boundaries is eliminated in single crystal tests. Unfortunately, very few single crystal mechanical

tests have been made on the rare earth metals, probably because sufficiently large single crystals were not available. The slip and twinning systems that have been observed in the rare earth metals are given in tables 8.3 and 8.4 respectively. The primary slip system in the rare earth metals is $\{10\bar{1}0\}\langle 1\bar{2}10\rangle$ (Type I) prism slip while the secondary slip systems are $(0002)\langle 1\bar{2}10\rangle$ basal slip and $\{11\bar{2}2\}\langle \bar{1}\bar{1}23\rangle$ pyramidal slip.

In the case of yttrium where more systematic single crystal testing has been done than for the other rare earth metals, it is possible to provide greater detail. For example, $\{10\bar{1}0\}\langle 1\bar{2}10\rangle$ and $(0002)\langle 1\bar{2}10\rangle$ were found to be the primary and secondary slip systems at 77, 298, and 497 K by Carnahan and Scott (1973). However, these investigators indicated that the critical resolved shear stress for the secondary slip system was more than four times greater than for the primary slip system at room temperature and, in fact, the secondary system only operated when the primary system was inhibited by a restraint wall in a plane strain compression test where the sample orientation gave a Schmid factor of 0.49 (maximum is 0.50) for the secondary system. Sokaski (1975) confirmed that $(0002)\langle 1\bar{2}10\rangle$ slip had a critical resolved shear stress at least 2.3 times greater than the primary system. Sokaski (1975) claimed that the $\{11\bar{2}2\}\langle \bar{1}\bar{1}23\rangle$ slip system operated in yttrium at room temperature when the tensile axis was nearly

TABLE 8.3.
Rare earth metal slip systems.

Metal	Slip plane	Slip direction	Comments	Ref.
Yttrium	$\{10\bar{1}0\}$	$\langle 1\bar{2}10\rangle$	a) Compression along $\langle 10\bar{1}0\rangle$ b) Plane strain compression along a direction at 40° to the [0001] direction with the $(\bar{1}100)$ plane and $[11\bar{2}0]$ direction parallel to the restraint wall c) Bending with $(10\bar{1}0)$ plane as the neutral plane and the $[\bar{1}210]$ direction as the moment axis (all two-surface trace analysis)	1
	$\{10\bar{1}0\}$	–	Bending (single-surface trace analysis)	2
	$\{10\bar{1}0\}$	–	Compression (two-surface trace analysis)	3
	$\{10\bar{1}0\}$	$\langle 1\bar{2}10\rangle$	Tension at about 90° to [0001]: usually between $[10\bar{1}0]$ and $[11\bar{2}0]$ (two-surface trace analysis)	4
	(0002)	$\langle 1\bar{2}10\rangle$	Plane strain compression as described above (two-surface trace analysis)	1
	(0002)	–	Bending (single-surface trace analysis)	2
	$\{11\bar{2}2\}$	$\langle \bar{1}\bar{1}23\rangle$	Tension almost parallel to [0001]. Didn't appear until shear strain of $> 10\%$ (two-surface trace analysis)	4

TABLE 8.3 (Contd).

Metal	Slip plane	Slip direction	Comments	Ref.
Gadolinium	$\{10\bar{1}0\}$	–	Compression (single-surface trace analysis)	3
	(0002)	–	Compression (single-surface trace analysis)	3
Dysprosium	$\{10\bar{1}0\}$	–	Compression (single-surface trace analysis)	3
	(0002)	–	Compression (single-surface trace analysis)	3
	$\{10\bar{1}0\}$	$\langle 1\bar{2}10\rangle$	$\langle 11\bar{2}0\rangle$ Compression (two-surface trace analysis)	6
	$\{11\bar{2}2\}$	$\langle 11\bar{2}\bar{3}\rangle$	$\langle 11\bar{2}0\rangle$ Compression (two-surface trace analysis)	6
Holmium	$\{10\bar{1}0\}$	–	Compression (single-surface trace analysis)	3
	(0002)	–	Compression (single-surface trace analysis)	3
Erbium	$\{10\bar{1}0\}$	–	Compression (single-surface trace analysis)	3
	(0002)	–	Compression (single-surface trace analysis)	3

1. Carnahan, T.G. and T.E. Scott, 1973, Met. Trans. **4**, 27.
2. Rapperport, E.J. and C.S. Hartley, 1959, Trans. TMS-AIME **215**, 1071.
3. Westlake, D.G., 1967, Acta Met. **15**, 1407.
4. Sokaski, M., 1975, "Low Temperature Deformation Characteristics of Yttrium Single Crystals," Ph.D. Thesis, Oregon State University, Corvallis, Oregon.
5. Srivastava, O.N. and J. Kumar, 1968, Phys. Lett. **27A**, 675.
6. Liebermann, H.H. and C.D. Graham Jr., 1977, Acta Met. **25**, 715.

parallel to the [0001] direction after shear strains of more than 10%. In fact, it was suggested, but not confirmed, that this second order, Type II pyramidal system should operate whenever the tensile axis is less than 37 degrees from the [0001] direction. However, Carnahan and Scott (1973) did not observe this mode of slip when they tested yttrium in tension parallel to the (0001) direction. Sokaski (1975) observed that the slip character in yttrium changed from fine slip at 77 K to coarse wavy slip at 300 K and suggested that a peak in the flow stress-temperature curve at 195 K was caused by this transition.

Twinning is important in polycrystalline h.c.p. metals because extensive twinning is necessary to provide the degrees of freedom required for compatibility at grain boundaries when the number of independent slip systems is limited as in h.c.p. metals. The primary twinning planes in the rare earth metals are the $\{11\bar{2}1\}$ planes in spite of the fact that the theoretical shear is high (about 0.63); the secondary twinning planes are $\{10\bar{1}2\}$ even though the theoretical shear is much less (about 0.18).

TABLE 8.4.
Rare earth metal twinning systems

Metal	Twinning system Plane	Twinning system Direction	Second undistorted system Plane	Second undistorted system Direction	Comments	Ref.
Yttrium	$\{11\bar{2}1\}$	$\langle\bar{1}\bar{1}26\rangle$	(0001)	$\langle11\bar{2}0\rangle$	a) Compression along $\langle10\bar{1}0\rangle$ b) Only near platens when compressed along [0001] c) Compression along $\langle\bar{1}\bar{1}22\rangle$ d) Tension along [0001] e) Plane strain compression along a direction at 40° to the [0001] direction with the $(\bar{1}100)$ plane and the $[11\bar{2}0]$ direction parallel to the restraint wall. f) Bending with $(10\bar{1}0)$ plane as the neutral plane and the $[12\bar{1}0]$ direction as the moment axis. (All two-surface trace analysis)	1
	$\{11\bar{2}1\}$	–	–	–	Bending (single-surface trace analysis)	2
	$\{11\bar{2}1\}$	–	–	–	Compression (two-surface trace analysis)	3
	$\{11\bar{2}1\}$	–	–	–	Tension axis nearly parallel to the [0001] direction (two-surface trace analysis)	4
	$\{10\bar{1}2\}$	$\langle\bar{1}011\rangle$	$\{10\bar{1}\bar{2}\}$	$\langle10\bar{1}1\rangle$	a) Tension along [0001] b) Plane strain compression as described above. c) Bending as described above. (All two-surface trace analysis)	1
	$\{10\bar{1}2\}$	–	–	–	Bending (single-surface trace analysis)	2

	$\{10\bar{1}2\}$	–	–	–	Compression (two-surface trace analysis	3
	$\{10\bar{1}2\}$	–	–	–	Tension axis nearly parallel to the [0001] direction. (Two-surface trace analysis)	4
	$\{11\bar{2}2\}$	–	–	–	Bending (single-surface trace analysis)	2
Gadolinium	$\{11\bar{2}1\}$	–	–	–	Compression (single-surface trace analysis)	3
	$\{10\bar{1}2\}$	–	–	–	Compression (single-surface trace analysis)	3
	$\{10\bar{1}2\}$	$\langle\bar{1}011\rangle$	$\{10\bar{1}\bar{2}\}$	$\langle10\bar{1}1\rangle$	Heating foil in electron microscope (diffraction pattern analysis)	5
Dysprosium	$\{11\bar{2}1\}$	–	–	–	Compression (single-surface trace analysis)	3
	$\{10\bar{1}2\}$	–	–	–	Compression (single-surface trace analysis)	3
	$\{11\bar{2}1\}$	$\langle11\bar{2}6\rangle$	–	–	[0001] Compression (two-surface trace analysis)	6
	$\{10\bar{1}2\}$	$\langle10\bar{1}\bar{1}\rangle$	–	–	[0001] Compression (two-surface trace analysis)	6
Holmium	$\{11\bar{2}1\}$	–	–	–	Compression (single-surface trace analysis)	3
	$\{10\bar{1}2\}$	–	–	–	Compression (single-surface trace analysis)	3
Erbium	$\{11\bar{2}1\}$	–	–	–	Compression (single-surface trace analysis)	3
	$\{10\bar{1}2\}$	–	–	–	Compression (single-surface trace analysis)	3

1. Carnahan, T.G. and T.E. Scott, 1973, Met. Trans. **4**, 27.
2. Rapperport, E.J. and C.S. Hartley, 1959, Trans. TMS-AIME **215**, 1071.
3. Westlake, D.G. 1967, Acta Met. **15**, 1407.
4. Sokaski, M., 1975, "Low Temperature Deformation Characteristics of Yttrium Single Crystals," Ph.D. Thesis, Oregon State University, Corvallis, Oregon.
5. Srivastava, O.N. and J. Kumar, 1968, Phys. Lett. **27A**, 675.
6. Liebermann, H.H. and C.D. Graham Jr., 1977, Acta Met. **25**, 715.

A more complete analysis of yttrium by Carnahan and Scott (1973) established that at 77, 298 and 497 K the primary twinning system was $\{11\bar{2}1\}\langle\bar{1}\bar{1}26\rangle$ with the second undistorted plane and direction being $(0001)\langle11\bar{2}0\rangle$. The secondary system was $\{10\bar{1}2\}\langle\bar{1}011\rangle$ with the second undistorted plane and direction being $\{10\bar{1}\bar{2}\}\langle10\bar{1}1\rangle$. By interference microscopy they found the shears to be about 0.69 for the primary system and 0.20 for the secondary system in good agreement with theoretical predictions. The primary twins exhibited a characteristic long, thin morphology while the secondary twins were shorter and broader. Only one other twinning plane has been indicated for yttrium. Rapperport and Hartley (1959), who bent large grain polycrystalline samples, reported that twinning occurred on the $\{11\bar{2}2\}$ planes as determined by single-surface trace analysis. Carnahan and Scott (1973) performed a compression test along the [0001] axis which gave a Schmid factor of 0.46 for $\{11\bar{2}2\}$ twinning but did not observe this mode. It must be admitted that grain boundary constraints in the test of Rapperport and Hartley (1959) could have forced the $\{11\bar{2}2\}$ twin plane to operate.

Sokaski (1975) investigated the deformation rate-controlling mechanisms of yttrium and concluded that below 300 K deformation was controlled by impurities with a barrier energy of about 0.3 eV; the impurities were not oxygen. It was suggested that a dislocation interaction mechanism was rate-controlling at temperatures above 300 K.

Liebermann and Graham (1977) compressed samples of nominally 99.9 percent pure dysprosium along the $\langle11\bar{2}0\rangle$ and [0001] axes at both room temperature and 77 K. Two-surface trace analysis revealed that compression along the $\langle11\bar{2}0\rangle$ axis at room temperature produced $\{10\bar{1}0\}\langle1\bar{2}10\rangle$ prismatic slip and $\{11\bar{2}2\}\langle11\bar{2}\bar{3}\rangle$ pyramidal slip. No twinning occurred in this orientation. However, compression along the [0001] axis activated both $\{11\bar{2}1\}\langle11\bar{2}6\rangle$ and $\{10\bar{1}2\}\langle10\bar{1}1\rangle$ twins with the former being prevalent. Although it was not stated explicitly, the writer has inferred that the same deformation modes were found at 77 K. Liebermann and Graham indicated that deformation usually originated at corners and contact surfaces of the samples where stress concentrations exist.

4. Tensile and compression properties

4.1. *Room temperature tensile and compression properties*

Room temperature tensile and compression properties do not always provide reliable representation of the mechanical behavior of metals. However, they are the mechanical properties most frequently tabulated in handbooks. Often only room temperature properties are determined in an investigation of the effects of impurities or prior thermal and mechanical history. The drawback associated with tabulating only room temperature properties is overcome by the ease of testing at room temperature. However, though room temperature hardness serves as a common base for comparing metals, the reader should be cognizant

of the fact that room temperature is a varying fraction of the recrystallization temperature depending on the metal. It is fortunate that room temperature is less than about 0.4 the absolute melting temperature of all the rare earth metals. Consequently, no large variations among the mechanical properties of these metals is expected from relative temperature effects due to recrystallization during room temperature testing.

Virtually all the known room temperature tensile and compression properties of the rare earth metals are given in table 8.5. Where data for several not widely varying strain rates were available in a particular investigation only one of the strain rates was used. Properties did not vary greatly over the range of strain rates at room temperature. From the amassed data of table 8.5 the author has selected "best values." These are given in table 8.6. The selection was based on purity and combinations of low strength and high ductility values. Frequently, when strength and ductility are low simultaneously the metal is brittle for one reason or another and the properties are not representative of "good" material. All the data given in table 8.6 except those for La, Ho, and Lu are from worked and annealed (wrought) materials. This choice was made, in addition to the fact that almost all the "best values" were from wrought material, because the as-cast structure of rare earth metals is usually coarse grained with substantial anisotropy as indicated earlier for single crystal tests. Also, the as-cast grain boundaries often contain considerable second phase. In the case of holmium and lutetium, the only data available were for as-cast metal. The properties will undoubtedly improve when wrought material is tested. Data for wrought lathanum were available but results from the as-cast material were used because the as-cast material was much purer, a more complete set of data was available, and the combination of strength and ductility was equal to or better than the properties of the wrought material. Only compression properties were available for terbium and thulium (see table 8.5) and these were greatly different from the general trend for wrought material, probably as a result of lower purity. No data are available for promethium or europium. The "best value" data for 0.2% yield strength and ultimate tensile strength from table 8.6 are plotted on a bar graph in fig. 8.10 for ease of visualizing any trends that might exist. The low value for β-ytterbium is consistent with its divalent character as compared to the higher values for the trivalent rare earths. In the author's opinion there is no trend for the trivalent metals. Even crystal structure is not a determining factor: for example f.c.c. α-cerium and h.c.p. gadolinium both have comparable strengths. There are no obvious differences between light and heavy rare earth metals. The strength of scandium is high but this probably reflects a rather high impurity level ($\sim$8000 ppm including about 4600 ppm oxygen). The yield strength of lanthanum is probably high because it is in the as-cast condition while holmium and lutetium have high ultimate tensile strength because of high impurity and as-cast condition. Consequently, it appears that variation of purity clouds any inherent trend in the mechanical properties of the rare earth metals related to electron or crystal structure. Material of similar purity and condition for all these metals must be tested before expected trends will become evident.

TABLE 8.5.
Room temperature mechanical properties summary.

	Tensile				Compression			Impurities					
Metal	U.T.S.[A] (kg/mm^2)	0.2.T.Y.S.[B] (kg/mm^2)	Elong.[C] (%)	R.A.[D] (%)	U.C.S.[E] (kg/mm^2)	0.2C.Y.S.[F] (kg/mm^2)	Red.[G] (%)	Total[H] (ppm)	Oxygen (ppm)	Condition	Grain size (μm)	Strain Rate (sec^{-1})	Ref.[I]
Scandium	16.1	–	–	–	–	–	–	~8000	~4600	As-cast	200/400	1.7×10^{-4}	1
	13.9	13.8	1.0	1.5	–	–	–	~8000	~4600	As-cast	100/1000	1.7×10^{-4}	1
	26.0	17.7	5.0	8.0	–	–	–	~8000	~4600	Cold swaged, ann. 1 h/1123 K	6/25	1.7×10^{-4}	1
	24.7	18.8	2.9	3.1	–	–	–	~8000	~4600	Hot swaged, 1273 K ann.	40/100	1.7×10^{-4}	1
	–	–	–	–	54.2	38.9	8.7	~8000	~4600	As-cast	–	6.7×10^{-4}	1
	–	–	–	–	53.7	29.8	12.8	~8000	~4600	As-cast	–	1.7×10^{-4}	1
	–	–	–	–	100.0	–	26.0	20,000/ 40,000	–	As-cast	–	–	2
	–	–	–	–	40.0	–	–	10,000	–	As-cast	–	–	3[a]
	36.8	–	7.7	2.7	–	–	19.0	100	–	Wrought-ann.	–	2×10^{-2}	4[a]
Yttrium	15.5 ± 0.4	7.0 ± 0.6	25.0	–	–	–	–	7500	780	Cold rolled, ann. 1 h/1073 K	–	–	5[a,b,c,d]
	15.4 ± 0.5	8.3 ± 0.1	21.0	–	–	–	–	7500	780	Cold rolled, ann. 1 h/1073 K	–	–	5[e,f,g]
	13.2 ± 0.3	5.9 ± 0.1	34.0	–	–	–	–	7410	740	Cold rolled, ann. 1 h/1073 K	–	–	5[h,i,j,k]
	14.7	11.9	11.0	–	–	–	–	2372	1700	As-cast	–	–	6[a]
	24.3	18.2	7.0	–	–	–	–	–	6600	As-cast	–	–	7
	17.0	11.7	6.1	–	–	–	–	–	2560	As-cast	–	–	7
	10.5	6.9	12.6	–	–	–	–	–	1070	As-cast	–	–	7
	25.7	8.6	24.0	29.3	–	–	–	8450	1900	Swaged, ann. 1 h/866 K	–	–	8[a]
	26.2	8.9	17.1	13.9	–	–	–	8410	2500	Swaged, ann. 1 h/866 K	–	–	8[a]
	24.3	10.7	15.8	22.6	–	–	–	6550	2960	Swaged, ann. 1 h/866 K	–	–	8[a]
	23.6	11.4	27.3	22.7	–	–	–	5050/ 7020	1500/ 2150	Impact extruded 92%	–	–	9[a,b,c,d]
	16.0	–	–	–	80.0	–	17.0	36,000	–	As-cast	–	–	3[b]
	22.9	18.6	1.0	5.8	–	–	–	6000/ 10,500	2000/ 4000	As-cast	–	–	10
	19.5	13.8	2.0	16.0	–	–	–	6000/ 10,500	2000/ 4000	Swaged 20% at 1255 K	–	–	10[a]

	24.9	20.1	8.7	–	–	–	–	7030	3900	As-cast	–	–	11
	18.9	–	16.0	24.0	–	–	–	<2500	800	Swaged, ann. 1 h/1073 K	65	2.5×10^{-4}	12[a]
	31.6	28.9	7.0	2.0	–	–	–	26,000	–	Wrought-ann.	–	1×10^{-2}	13[a]
Lanthanum	13.3	12.8	7.9	–	–	–	–	2160	1800	As-cast	–	–	11
	7.1	–	2.0	4.0	24/34	–	–	20,000	–	–	–	–	14[a]
	16.6	–	7.0	14.0	–	–	–	14,000	–	Wrought-ann. (596 K)	–	2.3×10^{-2}	15[a]
α-Cerium	10.4	9.3	23.9	–	–	–	–	2550	500	As-cast	–	–	11
	12.0	–	2.0	5.0	29.5	–	33.0	10,000	–	–	–	–	14[b]
	11.9	2.9	22.0	30.0	–	–	–	287	40	Swaged, ann. 2 h/650 K	10	8.3×10^{-5}	16[a]
β-Cerium	14.1	8.8	–	24.0	–	–	–	287	40	Thermal cycled	–	8.3×10^{-5}	16
Praseodymium	15.0	7.4	15.4	67.0	–	–	–	307	148	Swaged, ann. 1 h/723 K	5	8.3×10^{-5}	17[a]
	–	–	–	–	–	–	36.0	10^5	–	Wrought-ann.	–	4.7×10^{-3}	18[a]
	11.2	10.2	9.8	–	–	–	–	2640	1400	As-cast	–	–	11
	9.5	–	20.0	–	20.0	–	31.0	–	–	As-cast	–	–	2
	–	–	–	–	33.0	–	18.0	9800	–	–	–	–	3[d]
Neodymium	16.7	7.2	25.0	72.0	–	–	–	<259	69	Swaged, ann. 2 h/800 K	10	8.3×10^{-5}	19[a]
	13.6	–	17.5	13.5	–	–	–	8400	–	Wrought	20	2.3×10^{-2}	20[a]
	17.8	16.8	10.6	–	–	–	–	2310	1300	As-cast	–	–	11
	13.0	–	1/2	–	25.0	–	36.0	9500	–	As-cast	–	–	3[e]
Promethium	–	–	–	–	–	–	–	–	–	–	–	–	–
Samarium	15.9	6.9	17.0	29.5	–	–	–	<1530	106	Hot worked, ann. 1 h/923 K	30/230	8.3×10^{-5}	21[a]
	12.7	11.4	2.5	–	–	–	–	<580	200	As-cast	–	–	11
	21.9	–	2.0	–	33.5	–	14.0	–	–	As-cast	–	–	2
Europium	–	–	–	–	–	–	–	–	–	–	–	–	–
Gadolinium	12.0	1.5	37.0	56.0	–	–	–	519	150	Swaged, ann. 1 h/1023 K	85	8.3×10^{-5}	22[a]
	19.5	18.5	7.8	–	–	–	–	<4470	1600	As-cast	–	–	11
	21.9	–	2.0	–	–	–	–	1000	–	As-cast	–	–	3[f]
	16.6	5.3	8.3	–	–	–	–	–	–	As-extruded at 1033 K	–	–	7

TABLE 8.5 (Contd).

Metal	Tensile				Compression			Impurities		Condition	Grain size (μm)	Strain Rate (sec^{-1})	Ref.[I]
	U.T.S.[A] (kg/mm^2)	0.2.T.Y.S.[B] (kg/mm^2)	Elong.[C] (%)	R.A.[D] (%)	U.C.S.[E] (kg/mm^2)	0.2C.Y.S.[F] (kg/mm^2)	Red.[G] (%)	Total[H] (ppm)	Oxygen (ppm)				
Terbium	–	–	–	–	71.0	–	16.0	–	–	As-cast	–	–	2
	–	–	–	–	–	–	63.0	62,000	–	Wrought-ann.	–	–	23[a]
Dysprosium	22.1	12.9	5.3	14.3	–	12.9	–	3500/ 7500	1000/ 4000	As-cast	–	1.5×10^{-4}	10
	24.7	22.9	5.6	–	–	–	–	4720	2000	As-cast	–	–	11
	–	–	–	–	52.0	–	20.0	–	–	As-cast	–	–	2
	14.2	4.4	30.0	30.0	–	–	–	<484	294	Swaged, ann. 2 h/1023 K	35/140	8.3×10^{-5}	24[a]
Holmium	26.4	22.6	4.9	–	–	–	–	3990	3800	As-cast	–	–	11
	–	–	–	–	51.0	–	20.0	–	–	As-cast	–	–	2
	26.7	–	2.7	1.0	–	–	33.0	26,000	–	–	–	4.7×10^{-3}	25[a]
Erbium	13.9	6.1	11.5	11.9	–	–	–	<1369	160	Swaged, ann. 1 h/1123 K	38	3.3×10^{-5}	26[a]
	23.3	12.4	4.7	14.0	–	14.3	–	6000/ 9600	2000/ 4000	As-cast	–	–	10
	29.1	27.2	4.0	–	–	–	–	7260	3500	As-cast	–	–	11
	29.0	–	<1.0	–	78.0	–	22.0	7000	–	As-cast	–	–	3[g]
	26.8	–	3.3	–	–	–	31.0	11,950	–	Hot extruded	–	2×10^{-2}	27[a]
Thulium	–	–	–	–	55.0	–	26.0	–	–	As-cast	–	–	2
Ytterbium	7.3	6.7	5.7	–	–	–	–	<650	100	As-cast	–	–	11
	6.6	–	13.0	–	–	–	–	–	–	Rolled, ann. 723 K	–	–	2
	5.9	0.7	43.0	92.0	–	–	–	<1000	203	Swaged, ann. 1 h/723 K	62	1.7×10^{-4}	28[a]
Lutetium	–	–	–	–	102.0	–	12.0	–	–	As-cast	–	–	2
	~31.0	–	~2.0	~2.0	–	~41.0	31.0	12,000	–	–	–	2.3×10^{-2}	29[a,b]

[A]U.T.S. = ultimate tensile strength. [B]0.2 T.Y.S. = 0.2% offset yield stress in tension; occasionally the value given was for 0.5% offset and these uses are indicated by the comments accompanying the references following the table. [C]Elong. represents total elongation with a few exceptions where the value represents uniform elongation and these are given with the accompanying reference following the table. [D]R.A. = reduction in area. [E]U.C.S. = ultimate strength in compression. [F]0.2 C.Y.S. = 0.2% offset yield stress in compression. [G]Red = maximum relative reduction in height in compression as indicated by a sudden drop in load. [H]Compositions given in parts per million (ppm) by weight. [I]Reference numbers refer to those listed following the table.

1. Geiselman, D., 1962, J. Less-Common Metals **4**, 362.
2. Savitskiy, E.M., V.F. Terekhova and O.P. Naumkin, 1963, Usp. Fiz. Nauk **79**, 263. Engl. Transl., 1963, Sov. Phys. Usp. **6**, 123.
3. Savitskiy, E.M. 1959, Redkie Metally i Splavy (Rare Metals and Alloys) (Dom Tekhniki, Moscow), p. 19. No actual analysis given, especially no mention of non-metallics.
   (a) Claimed ~90.0% Sc. (b) Claimed 96.4% Y. (c) Claimed 99.0% La. (d) Claimed 99.2% Pr. (e) Claimed 99.5% Nd. (f) Claimed 99.9% Gd. (g) Claimed 99.3% Er.
4. Sokolov, L.D., V.M. Solenov, V.A. Skudnov and A.N. Gladkikh, 1970, Izv. Akad. Nauk SSSR, Metal. [2], 181. Engl. Transl., 1970, Russ. Met. [2], 106.
   (a) Claim 99.99% Sc. but no analysis given.
5. Carlson, O.N., D.W. Bare, E.D. Gibson and F.A. Schmidt, 1959, Survey of the Mechanical Properties of Yttrium and Yttrium Alloys, in: *Symposium on Newer Metals*, A.S.T.M. Special Technical Publ. No. 272, (American Society for Testing Materials, Philadelphia) pp. 144–159.
   (a) Parallel to rolling direction; average of 10 tests.
   (b) 0.5% extension yield stress; parallel to rolling direction; average of 10 tests.
   (c) Uniform elongation; parallel to rolling direction; average of 10 tests.
   (d) 350 ppm carbon.
   (e) Transverse to rolling direction; average of 4 tests.
   (f) 0.5% extension yield stress; transverse to rolling direction; average of 4 tests.
   (g) Uniform elongation; transverse to rolling direction; average of 4 tests.
   (h) Parallel to rolling direction; average of 4 tests.
   (i) 0.5% extension yield stress; parallel to rolling direction; average of 4 tests.
   (j) Uniform elongation; parallel to rolling direction; average of 4 tests.
   (k) 110 ppm carbon.
6. Nolting, H.J., C.R. Simmons and J.J. Klingenberg, J. Inorg. Nucl. Chem. **14**, 208.
   (a) 170 ppm is total non-metallics.
7. Simmons, C.R., 1961, The Mechanical Properties of Yttrium, Scandium, and the Rare Earth Metals, in: Spedding, F.H., and A.H. Daane eds., *The Rare Earths* (John Wiley and Sons, New York), pp. 428–452.
8. Geary, A.L., E.S. Guidoboni and P. Lowenstein, 1962, Fabrication of Yttrium Metal, in: Nachman, J.F., and C.E. Lundin eds., *Rare Earth Research*, (Gordon and Breach Science Publishers, New York) p. 105.
   (a) 0.5% yield stress.
9. Owen, C.V., T.E. Scott, and O.N. Carlson, 1965, "Pneumatic-Mechanical High-Energy-Rate Extrusion of Yttrium" USAEC Rept. IS-1227, Ames Laboratory, Ames, Iowa (August 1965).
   (a) Results were virtually independent of extrusion temperature over the range from 298 to 873 K.
   (b) 0.5% offset yield stress.
   (c) Uniform elongation.
   (d) U.T.S.: max. = 28.8, min. = 19.0 (86 tests). 0.5% Y.S.: max. = 18.3, min. = 7.0 (91 tests). Elongation: max. = 39, min. = 5 (70 tests). R.A.: max. = 32, min. = 6 (71 tests).
10. Love, B., 1960, "The Metallurgy of Yttrium and Rare Earth Metals. Part II. Mechanical Properties," WADD-TR-60-74 (Pt.2). Wright Air Development Division, U.S. Air Force, Wright-Patterson Air Force Base, Ohio (June 1960).
    (a) After swaging 20 percent at 1255 K the yttrium grains were elongated but there was no evidence of cold work.
11. Love, B., 1959, "Selection and Evaluation of Rare or Unusual Metals—Part II. The Metallurgy of Yttrium and Rare Earth Metals," WADC-TR-57-666, Wright Air Development Center, U.S. Air Force, Wright-Patterson Air Force Base, Ohio (March 1959).

(a) Values obtained by extrapolation of plotted data.
14. Savitskiy, E.M. and V.F. Terekhova, 1955, Izv. Sekt. Fiz. Khim. Anal. (Inst. Obshehei Neorg. Khim., Akad. Nauk SSSR) [2] 148. No analysis given.
(a) Claim 98% pure La.
(b) Claim 99.0% pure Ce.
15. Gladkikh, A.N., V.A. Skudnov, and L.D. Sokolov, 1969, Izv. Akad. Nauk SSSR, Metal. [3], 94. Engl. Transl., 1969, Russ. Met [3], 75.
(a) Claim 98.6 percent pure but did not give non-metallics.
16. Owen, C.V. and T.E. Scott, 1976, J. Less-Common Metals **46**, 151.
(a) Uniform elongation.
17. Owen, C.V. and T.E. Scott, 1977, J. Less-Common Metals **51**, 117.
(a) Uniform elongation.
18. Skudnov, V.A., L.D. Sokolov, and A.N. Gladkikh, 1969a, Izv. Akad. Nauk Arm. SSR – Tekh. **22** [4], 43.
(a) Claim 90.2% Pr but no analysis given.
19. Owen, C.V. and T.E. Scott, 1975, J. Less-Common Metals **41**, 303.
(a) Uniform elongation.
20. Skudnov, V.A., L.D. Sokolov and A.N. Gladkikh, 1969b, Izv. Akad. Nauk BSSR. Ser. Fiz. – Tek. Nauk [2], 114 Engl. Transl. Available as Doc. No. AD-742-893 from National Technical Information Service, Springfield, VA. 22151.
(a) Non-metallics not analyzed.
21. Owen, C.V. and T.E. Scott, 1971, J. Less-Common Metals **25**, 161.
(a) Uniform elongation.
22. Owen, C.V. and T.E. Scott, 1973, J. Less-Common Metals **30**, 113.
(a) Uniform elongation.
23. Sokolov, L.D., V.M. Solenov, V.A. Skudnov and A.N. Gladkikh, 1970, Fiz. Metal. Metalloved. **30** [4], 894. Engl. Transl., 1970, Phys. Met. Metallogr. **30** [4], 232.
(a) Non-metallics not specified individually; also contains 41,000 ppm Dy.
24. Owen, C.V., and T.E. Scott, 1974, J. Less-Common Metals **37**, 353.
(a) Uniform elongation.
25. Gladkikh, A.N. *et al.*, 1969, Fiz. Khim. Obrabotka Mater. [4], 151.
(a) Claim 97.4% pure Ho.
26. Owen, C.V., and T.E. Scott, 1968, J. Less-Common Metals **16**, 447.
(a) Uniform elongation.
27. Sokolov, L.D., V.A. Skudnov and A.N. Gladkikh, 1969, Probl. Prochnosti [6], 104. Engl. Transl., 1969, Strength Mater. [6], 671.
(a) Non-metallics not included but claimed 98.8 percent Erbium.
28. Owen, C.V., and T.E. Scott, 1970, J. Less-Common Metals **21**, 427.
(a) Uniform elongation.
29. Gladkikh, A.N., 1975, Metalloved. i Term. Obrabotka Metallov (MiTOM) [7], 12. Engl. Transl., 1975, Met. Sci. Heat Treat. **17**, 558.
(a) Claim 98.78% pure Lu but no analysis was given.
(b) Strain-rate for the compression 0.2% yield strength was 1.5×10^{-2} sec.$^{-1}$.

TABLE 8.6.
Best values of room temperature tensile properties.

Metal	0.2% Offset Yield Strength (kg/mm^2)	Ultimate Tensile (kg/mm^2)	Uniform Elongation (%)	Reduction in area (%)	Strain[a] Hardening Exponent	Strain Rate ($Sec.^{-1}$)	Strain[b] Rate Sensitivity (ϵ)	Anneal Temp. (K)	Ref.[c]
Scandium	17.7	26.0	5.0[d]	8.0	–	1.7×10^{-4}	–	1123	1
Yttrium	4.3 ± 1[e]	13.2 ± 0.3	34.0	–	0.23	–	0.013(0.03)	1073	5
Lanthanum[f]	12.8	13.3	7.9[d]	–	–	–	–	–	11
γ-Cerium	2.9	11.9	22.0	30.0	0.27	8.3×10^{-5}	0.017(0.05)	650	16
β-Cerium	8.8	14.1	–	24.0	–	8.3×10^{-5}	–	–	16
Praseodymium	7.4	15.0	15.4	67.0	0.22	8.3×10^{-5}	0.007(0.04–0.12)	723	17
Neodymium	7.2	16.7	25.0	72.0	0.28	8.3×10^{-5}	0.007(0.05–0.15)	800	19
Promethium	–	–	–	–	–	–	–	–	–
Samarium	6.9	15.9	17.0	29.5	0.24	8.3×10^{-5}	0.011(0.02–0.1)	923	21
Europium	–	–	–	–	–	–	–	–	–
Gadolinium	1.5	12.0	37.0	56.0	0.44	8.3×10^{-5}	0.011(0.05–0.3)	1023	22
Terbium	Only compression data available								
Dysprosium	4.4	14.2	30.0	30.0	0.37	8.3×10^{-5}	0.005(0.05–0.15)	1023	24
Holmium[g]	22.6	26.4	4.9[d]	–	–	–	–	–	11
Erbium	6.1	13.9	11.5	11.9	0.25	3.3×10^{-5}	0.023(0.1)	1123	26
Thulium	Only compression data available								
Ytterbium	0.7	5.9	43.0	92.0	0.62	1.7×10^{-4}	~0(0.02–0.2)	723	28
Lutetium[h]	–	~31.0	–	–	–	2.3×10^{-2}	–	–	29

[a]Strain hardening exponent, n, from $\sigma = K\epsilon^n$; [b]Strain rate sensitivity given by $(\Delta \ln \sigma/\Delta \ln \epsilon)_{T,\epsilon}$; Strain given in parenthesis; [c]References are those used in table 8.5; [d]Total elongation; [e]Yield strength given as 5.9 ± 0.1 kg/mm^2 at 0.5% extension but the present author has adjusted this to 0.2% offset yield strength – an approximation from curves; [f]As-cast but of best purity and values are close to wrought-annealed values given by Ref. 15; [g]The only holmium tensile data were for the as-cast condition and then choice was based on the better purity compared to other sources; [h]The condition of the lutetium, for the only known tensile data, is unknown. It was probably in the as-cast state and not of good purity.

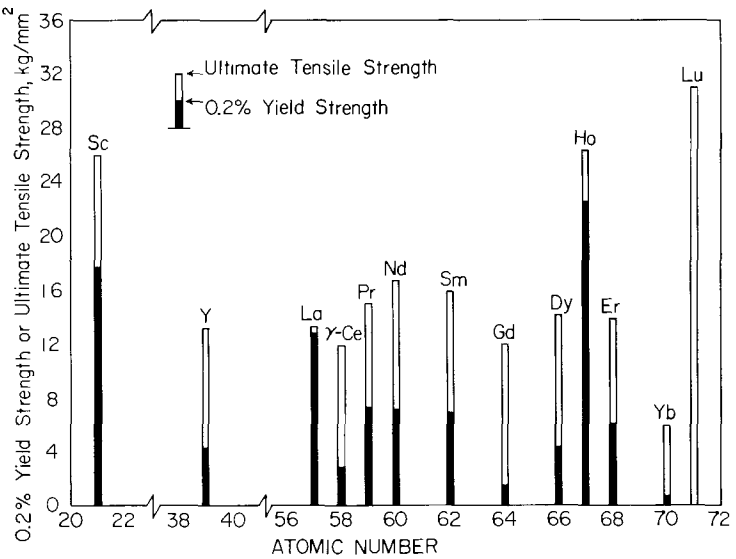

Fig. 8.10. Bar graph showing writer's selection of "best" values for the room temperature yield and tensile strengths of the rare earth metals.

4.2. *Effect of test temperature*

Temperature dependence of strength and ductility provides much more insight to the mechanical property characteristics of metals than room temperature properties. In this section the temperature dependence of the mechanical properties of all the rare earth metals except Pm, Eu, and Tm are presented graphically. It will be shown that most of these metals exhibit temperature dependencies that have characteristics usually associated with dynamic strain aging although in no instance, to the author's knowledge, has the impurity element responsible for strain aging been isolated. Perhaps changes in crystallographic deformation modes cause the apparent strain aging effects. Very large discrepancies in mechanical property data from different sources are evident. These discrepancies largely are due to impurity effects. Polymorphic transformations are noted to influence the mechanical properties in several instances.

4.2.1. *Scandium*

The temperature dependence of all the available tensile and compression properties of scandium are shown in fig. 8.11. The data are from three sources: Geiselman (1962), Sokolov et al. (1969a), and Sokolov et al. (1970a). The Soviet investigators' material was worked and annealed and they claimed a purity of 99.99 percent but no analysis was given. Geiselman (1962) used as-cast material with a large grain size (200–400 μm) and a total impurity concentration near 4600 ppm. None of the investigators reported a yield strength value. Sokolov et al. (1970a) reported compression flow stress ($\epsilon = 20\%$) curves for two strain rates

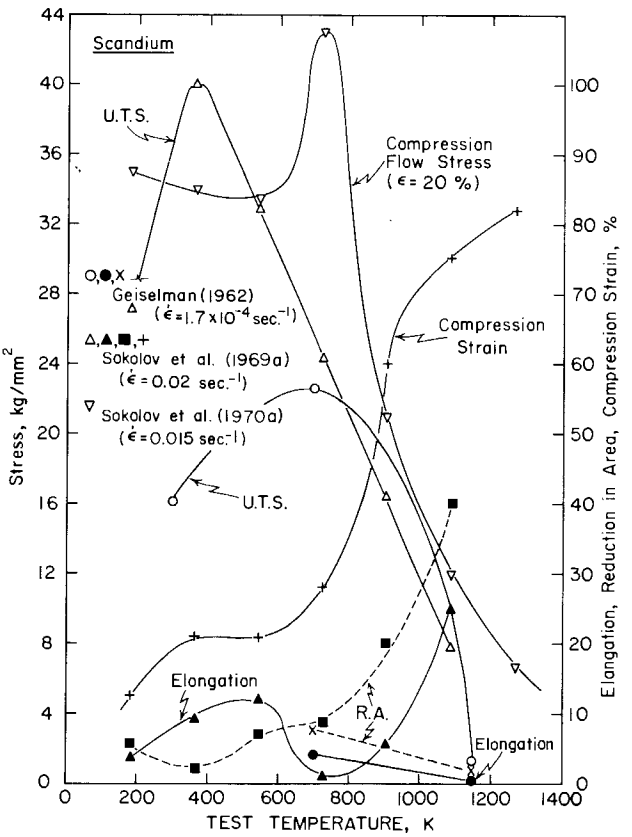

Fig. 8.11. Temperature dependence of the tensile and compressive mechanical properties of scandium. Geiselman (1962): as-cast; about 8000 ppm impurities including 4600 ppm oxygen. Sokolov (1969a) and Sokolov (1970a): wrought; claimed 99.99% Sc but no analysis was given.

in addition to the strain rate used for the compression strength data of fig. 8.11 (2×10^{-3} sec^{-1} and 0.15 sec^{-1}). Except for a slight shift of the curves to higher temperature with increasing strain rate there was no variation in the behavior. The peak strength at about 275 K shifted to higher temperatures with increased strain rate suggesting strain aging might be operating. Although the compression flow stress and the elongation data obviously were not from the same tests, the peak in compression flow stress agrees reasonably with the minimum in elongation near 725–750 K obtained by Sokolov et al. (1969a). The peak in the ultimate tensile strength from the results of Geiselman (1962) should not be attributed to a strain aging behavior. The lower value of strength at 298 K is a reflection of brittleness in that the specimen broke before yielding. Also, the low value at 1144 K is probably a reflection of brittleness because the ductility (both R.A. and elongation) is low, especially when compared to the elongation and R.A. from Sokolov et al. (1969a) at 1090 K. The strength and ductility from

Sokolov et al. (1969a) at about 175 K indicate their material was relatively brittle at this temperature. A rather rapid rise of ductility in tension (Sokolov et al., 1969a) and compression (Sokolov et al., 1970a) near 700 to 800 K is probably associated with recrystallization during testing since this should be the appropriate temperature range for dynamic recrystallization. It seems rather evident that none of the data shown in fig. 8.11 reveals the intrinsic mechanical properties of pure scandium.

4.2.2. *Yttrium*

Wide differences are evident in the mechanical properties of yttrium as determined by various investigations, figs. 8.12 and 8.13. For example, the ultimate tensile strength data obtained by Gladkikh (1970) are a factor of 2 or more higher than the data obtained by Koepke et al. (1967). The results from Koepke et al. (1967) were obtained with material that was hot swaged, cold swaged, and annealed at 1073 K to produce a final grain size of 65 μm. Their yttrium contained less than 2500 ppm impurities including 800 ppm oxygen and 150 ppm carbon plus several metallics. Gladkikh (1970) claimed a purity of 97.4 percent containing 2 percent Ta and Dy. However, no detailed analysis was given and there was no indication of the amount of non-metallics. The material

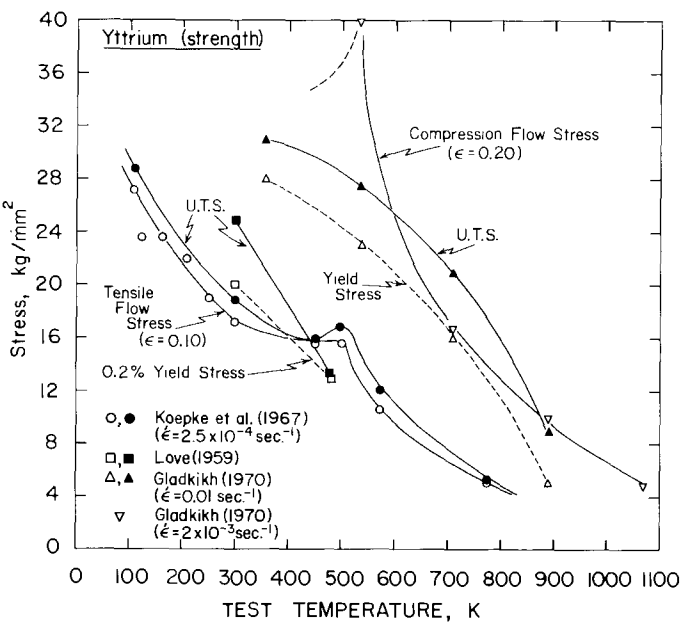

Fig. 8.12. Temperature dependence of the tensile and compressive strength properties of yttrium. Koepke et al. (1967): swaged and annealed; less than 2505 ppm impurities including 800 ppm oxygen; 65 μm grain size. Love (1959): as-cast, 7030 ppm impurities including 3900 ppm oxygen and 2500 ppm Ta. Gladkikh (1970): probably wrought; claimed 97.4% yttrium with 2% Ta and Dy.

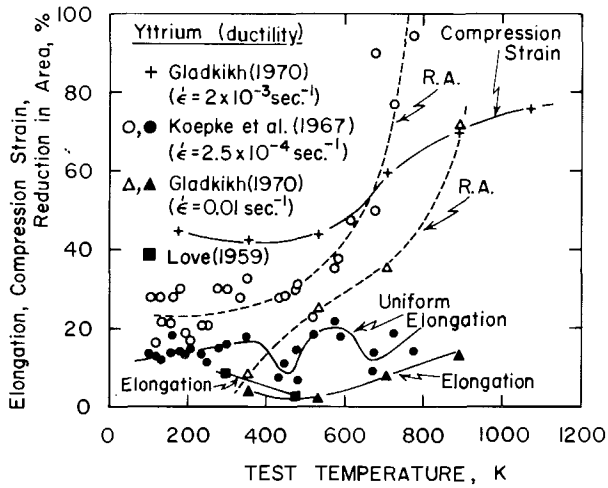

Fig. 8.13. Temperature dependence of the tensile and compressive ductility properties of yttrium. See fig. 8.12 caption for details.

was wrought but no details were given and no grain size was mentioned. Presumably Gladkikh's yttrium was less pure than that of Koepke et al. Furthermore, the results of the latter investigators showed a distinct peak in the stress-temperature curve between 450 and 550 K. Perhaps Gladkikh's test temperatures were too widely spaced to reveal the stress peak. On the other hand, Gladkikh (1970) showed a stress peak at about 550 K in the compression flow stress curve. The data plotted in fig. 8.12 do not reveal the peak but similar curves from Gladkikh's work at two higher strain rates have adequate data to establish that a peak exists. The stress peak was accompanied by a dip in the uniform elongation in the work of Koepke et al. (1967) but not in their reduction in area (fig. 8.13). However, a distinct minimum in their strain rate sensitivity data is evident at 475 K, fig. 8.14. The combination of stress peak, ductility minimum and rate sensitivity minimum suggests that a strain aging process was operative near 450–550 K but it might also reflect a change in crystallographic deformation mode as suggested by Sokaski (1975).

Simmons (1961) investigated the influence of oxygen content on the mechanical properties of as-cast yttrium made by the sponge process. The results, fig. 8.15, reveal large effects on strength below 1000 K but virtually no effect at about 1250 K. On the other hand, only a small change in elongation was affected by oxygen concentration until the temperature exceeded approximately 1000 K. A comparison of Simmons's results with those of Koepke et al. (1967) shows that factors other than composition play a major role in the mechanical properties. For example, the yield and ultimate strength of Simmons's yttrium containing 1070 ppm oxygen are lower by a factor of about two at 300 K than the values of Koepke et al. (1967) despite the fact that the latter's yttrium contained only 800 ppm oxygen. The rapid rise of reduction in area values from Koepke et al.

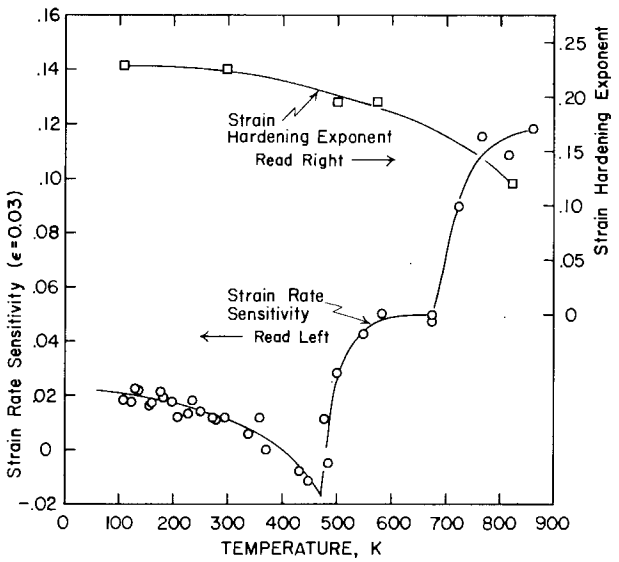

Fig. 8.14. Temperature dependence of tensile strain-hardening exponent and strain-rate sensitivity of yttrium from Koepke et al. (1967).

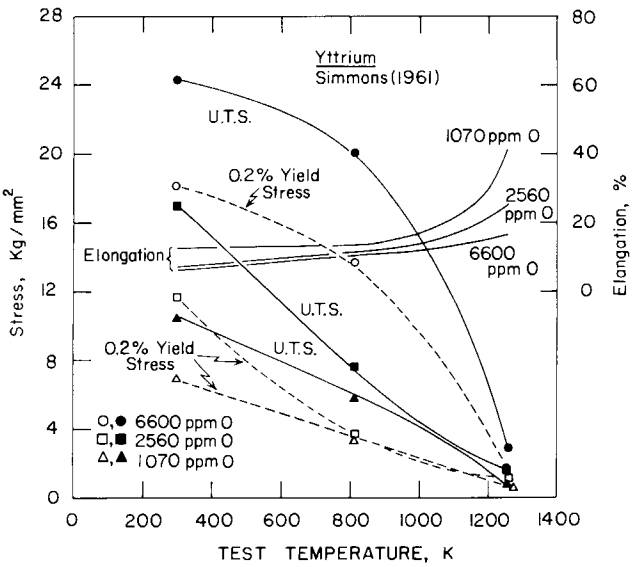

Fig. 8.15. Effect of three oxygen concentrations on the temperature dependence of the tensile properties of as-arc-melted sponge process yttrium.

(1967) and from Gladkikh (1970) occurs in the region where recrystallization would be expected during deformation.

Temperature dependence of the strain hardening exponent, n, in the equation $\sigma = K\epsilon^n$ is indicated in fig. 8.14. It decreases slowly with increasing temperature to about 600 K where it begins to drop rapidly, perhaps as a consequence of recrystallization during testing. As mentioned above, the strain rate sensitivity defined by $(\Delta \ln \sigma/\Delta \ln \dot{\epsilon})_{T,\epsilon}$ exhibits a distinct minimum with negative values near 475 K. Whether the "step" behavior in the 550 to 675 K region is physically "real" or just a manifestation of data scatter is not clear.

4.2.3. *Lanthanum*

The temperature dependence of the strength and ductility of the lanthanum metal tested by Gladkikh et al. (1969a) reveals complex patterns as shown in figs. 8.16 and 8.17. Their metal, which was hot worked, cold worked, then annealed at 596 K, was claimed to contain 1.4% impurities but no analysis was given and the non-metallics probably were not analyzed. Ultimate tensile strength (no yield strength values were given) and the compression flow stress from Solenov et al.

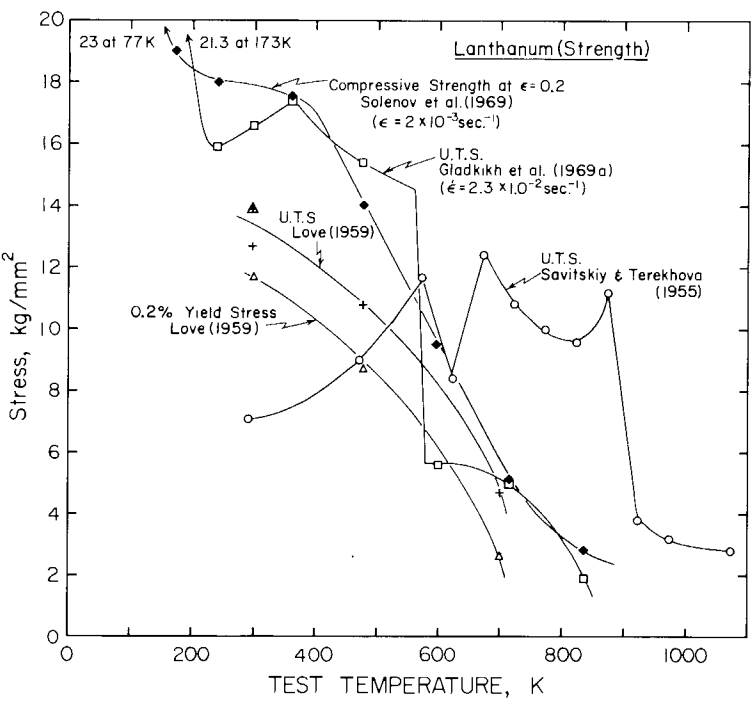

Fig. 8.16. Temperature dependence of the tensile and compressive strength properties of lanthanum. Love (1959): as-cast; 2160 ppm impurities including 1800 ppm oxygen. Gladkikh et al. (1969a) and Solenov et al. (1969): worked and annealed; claim 98.6% La but interstitials not analyzed. Savitskiy and Terekhova (1955): probably as-cast; no analysis given.

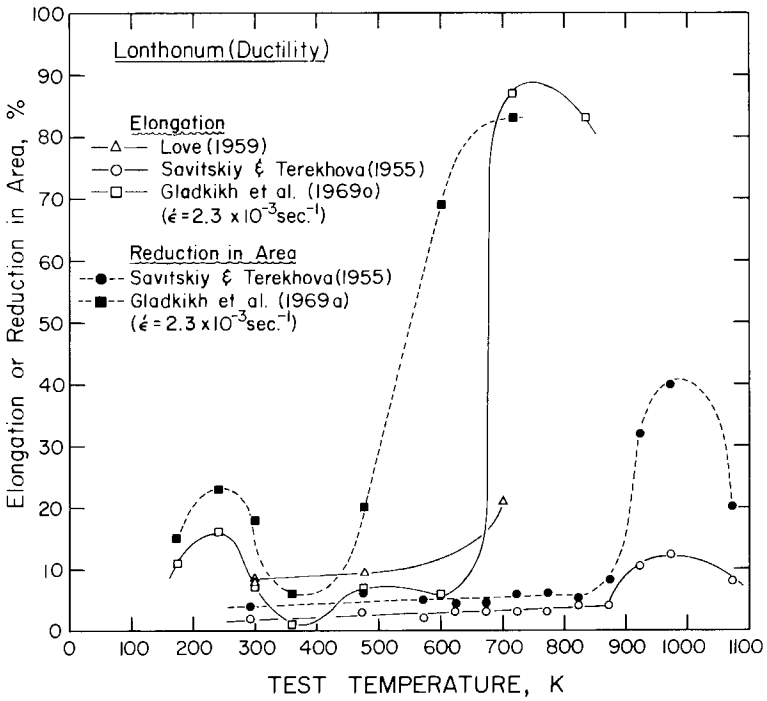

Fig. 8.17. Temperature dependence of the tensile ductility properties of lanthanum. See fig. 8.16 caption for details.

(1969), who used the same metal, reveal peaks or plateaux at about 350 K (fig. 8.16). Reduction in area and elongation data show a well-defined minimum at the same temperature. Such characteristics are generally found in strain aging. At about 560 K the ultimate tensile strength drops precipitously and the reduction in area rises rapidly. These changes are due, undoubtedly, to the α(d.h.c.p.) to β(f.c.c.) transformation which occurs on heating at about 575 K. Lower strength and higher ductility are expected for the higher temperature f.c.c. phase. The discontinuous change at 560 K does not appear in the compression behavior (Solenov et al., 1969) or in the tensile data of Love (1959). Love's as-cast material contained 2160 ppm impurities including about 1800 ppm oxygen. Consequently, it was considerably purer than the material used by Gladkikh et al. (1969a) and by Solenov et al. (1969). The higher purity is reflected in lower values of strength found by Love but the lower ductility values are probably associated with the as-cast structure. Love's material would be expected to reveal the α to β transformation but the test temperature spacing was too large to detect it. The rapidly-rising elongation values from both Love (1959) and Gladkikh et al. (1969a) may be associated with recrystallization during testing or they may be a result of the α to β transformation, or both.

The data of Savitskiy and Terekhova (1955) do not even approach agreement with the results of the other investigations. The material was probably in the as-cast state and of lower purity. The decrease in strength and rise in ductility near 875 K might be due to the suppression of the β to γ transformation by impurities.

4.2.4. *Cerium*

Polymorphic transformations complicate the mechanical properties and their temperature dependence in cerium. The 0.2% offset yield strength data from Owen and Scott (1976) shown in fig. 8.18 reveal the effect of the γ(f.c.c.) to β(d.h.c.p.) transformation beginning at about 280 K. The yield stress tends to increase with increased amount of β phase as the temperature decreases. At approximately 110 K the yield strength rises dramatically in association with the transformation of the remaining γ(f.c.c., $a = 5.16$) to α(f.c.c., $a = 4.85$), see ch. 4 section 2.4.5. With decreasing temperature the ultimate tensile strength rises rapidly at about 375 K. This rise probably reflects deformation-induced γ to β

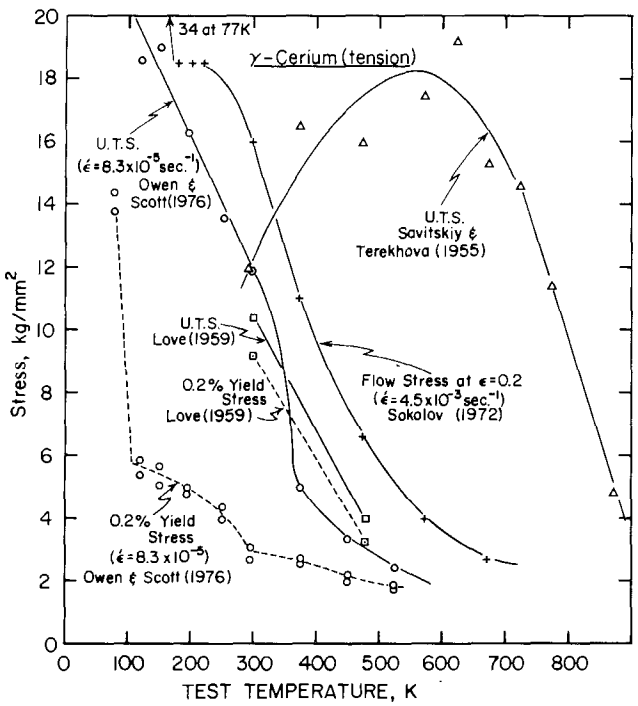

Fig. 8.18. Temperature dependence of the strength properties (in tension) of cerium. Owen and Scott (1976): in γ phase at room temperature prior to testing; swaged and annealed; 287 ppm impurities including 40 ppm oxygen, 42 ppm nitrogen and 37 ppm carbon; 10 μm grain size. Love (1959): as-cast; 2550 ppm impurities including 500 ppm oxygen. Savitskiy and Terekhova (1955): probably as-cast; claim 97.1% Ce but no analysis given. Sokolov (1972): claim 96% Ce, but no analysis given.

transformation during the test. However, the ultimate tensile strength does not exhibit an increase due to the γ to α transformation. It is likely that deformation tends to increase the amount of γ that transforms to β such that insufficient γ remains at 110 K to transform to α. The flow stress curve at 20% strain from Sokolov (1972) tends to indicate the γ to β and γ to α transformations and is in reasonable agreement with the ultimate tensile strength curve of Owen and Scott (1976) albeit at a somewhat higher stress level. Owen and Scott (1976) tested swaged and annealed (2 h/650 K) cerium which had a grain size of 10 μm and contained 287 ppm impurities including 40 ppm oxygen, 42 ppm nitrogen and 37 ppm carbon. Sokolov (1972) used cerium, probably wrought, claimed to be 96 percent pure with the remaining composition being other rare earth elements although no analysis was given.

Ultimate tensile strength and elongation data from Love (1959) on as-cast cerium are in reasonable agreement with the results of Owen and Scott (1976) but the yield strength data of Love are much higher than the latter observed. Lower purity (2550 ppm including 500 ppm oxygen) and cast structure probably are the reasons for the higher yield strength of Love's material. Data from Savitskiy and Terekhova (1955) disagree substantially with the results of other investigators. They claimed 97.1 percent pure as-cast material but no analysis was given and one suspects that the non-metallic impurities were present in rather high concentration.

According to the results of Owen and Scott (1976), the ductility of γ-cerium, fig. 8.19, behaved erratically as the test temperature decreased. Reduction in area is high, about 95 percent at 373 K, but drops precipitously between 373 and 300 K. Presumably the high value of reduction in area is characteristic of good purity cerium and the drop is associated with deformation-induced β-cerium (d.h.c.p.). However, the author has no ready explanation for the maximum in both uniform elongation and reduction in area at 200 K. Regardless, the ductility can be considered good.

Owen and Scott (1976) were able to test samples which were, before testing, virtually all β-cerium. The β-cerium samples were prepared by a clever method devised by Koskimaki et al. (1974), also see ch. 4, section 3.3. The strength and ductility of β-cerium are shown as a function of temperature in fig. 8.20. The 0.2 percent offset yield strength decreases smoothly as temperature is raised from 77 K to about 400 K where it begins to decrease more rapidly. The temperature 400 K correlates well with the A_s temperature of the β to γ transformation on heating. Thus, the more rapid strength decrease is caused by the presence of γ-cerium in the material. The reduction in area of β-cerium ranges between 20 and 40 percent until about 350 K and then it rises rapidly to values characteristic of γ-cerium.

Both the strain rate sensitivity and strain hardening exponent of cerium (initially in the γ phase) exhibit manifestations of the various transformations as shown in fig. 8.21. There is a gradual rise in the strain hardening exponent as the temperature decreases to the γ to β M_d temperature of 373 K. At this point deformation-induced β-cerium begins to form and contributes to the strain

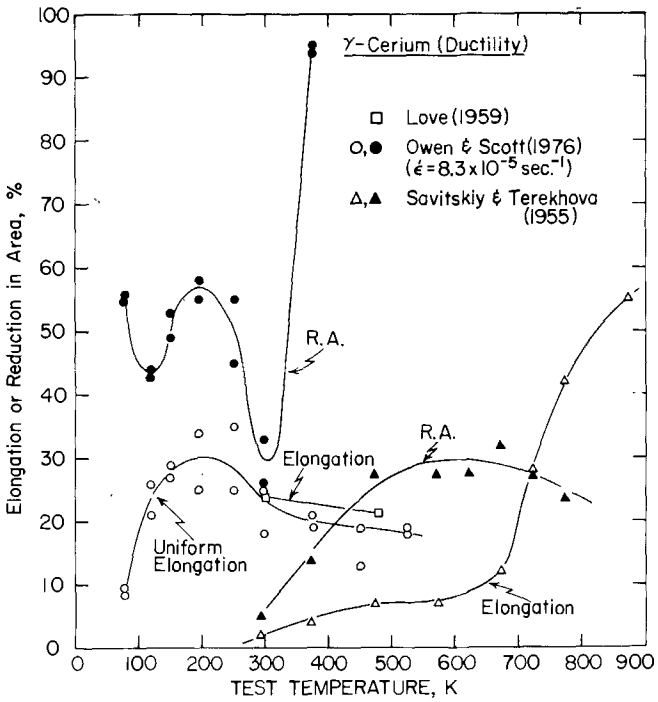

Fig. 8.19. Temperature dependence of the tensile ductility properties of cerium. Scott and Owen (1976): cerium was in the γ phase at room temperature prior to testing. See fig. 8.18 caption for other details.

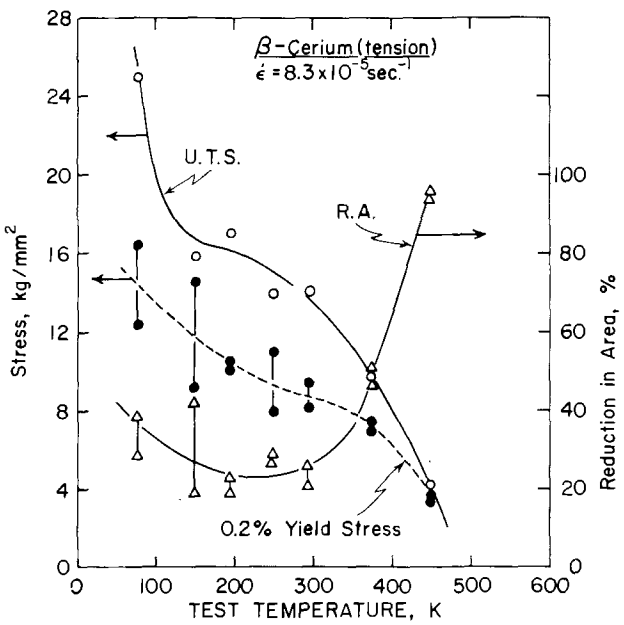

Fig. 8.20. Temperature dependence of tensile properties of cerium which was in the β phase at room temperature prior to testing. From Owen and Scott (1976).

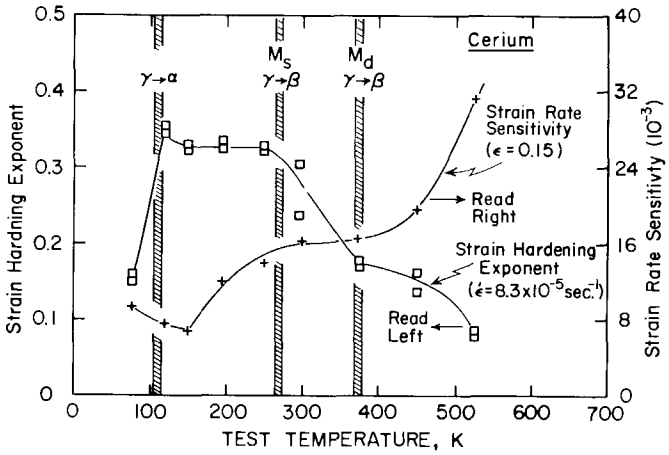

Fig. 8.21. Temperature dependence of the strain-rate sensitivity and the strain-hardening exponent (in tension) of cerium which was in the γ phase at room temperature prior to testing. Cross-hatched bars depict temperatures at which the indicated phase changes occur. From Owen and Scott (1976).

hardening. At 110 K the strain hardening exponent decreases rapidly when γ-cerium transforms to α-cerium.

4.2.5. *Praseodymium*

With the exception of several ocillations in the curve, the yield strength of praseodymium is relatively independent of test temperature from 77 to 525 K according to Owen and Scott (1977). Despite the lack of a satisfactory explanation for this erratic behavior, the oscillations shown in fig. 8.22 appear to be real. A second series of tests reproduced the oscillations. Peaks in the ultimate tensile strength obtained by these investigators, although not as pronounced, occur at the same temperature, ~200 K and ~ 300 K, as peaks in the yield strength. Also, a minimum is evident in both the reduction in area and the uniform elongation curves of fig. 8.23 at ~300 K. Furthermore, the maximum compression strain curve from the work of Skudnov et al. (1969a) exhibits a minimum between 300 and 400 K. Since their tests were run at a strain rate more than 100 times that used by Owen and Scott (1977), it is likely that the ductility minima from both investigations are produced by the same phenomenon, possibly strain aging. Over most of the temperature range the compression flow stress curve ($\epsilon = 0.2$) from Skudnov et al. (1969a) agrees well with the ultimate tensile strength curve from Owen and Scott (1977). This seems rather surprising in view of the fact that the impurity content of the praseodymium used by Owen and Scott was only 307 ppm including 148 ppm oxygen after being worked and annealed at 723 K while Skudnov et al. (1969a) used praseodymium which was claimed to be only 90.2 percent pure; their material was also worked and annealed. The relatively rapid increase in ultimate tensile strength and compression flow stress with decreasing temperature compared to the yield strength is consistent with the

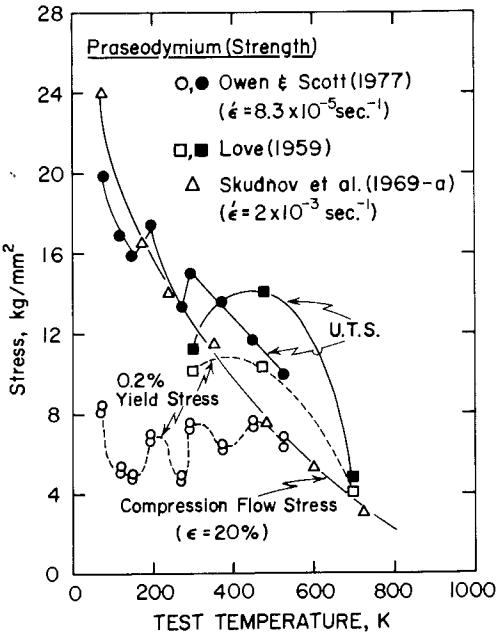

Fig. 8.22. Temperature dependence of the tensile and compressive strength properties of praseodymium. Love (1959): as-cast; 2640 ppm impurities including 1400 ppm oxygen. Owen and Scott (1977): worked and annealed; <307 ppm impurities including 148 ppm oxygen; 5 μm grain size. Skudnov et al. (1969a): claimed 90.2% Pr; worked and annealed.

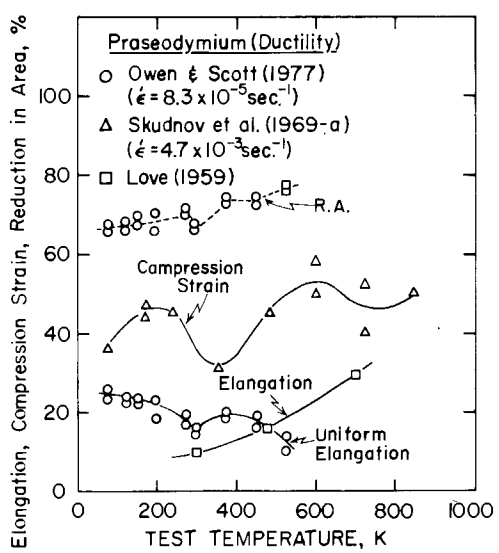

Fig. 8.23. Temperature dependence of the tensile and compressive ductility properties of praseodymium. See fig. 8.22 caption for details.

strong temperature dependence of the strain hardening exponent shown in fig. 8.24.

4.2.6. *Neodymium*

From the data shown in fig. 8.25 it can be concluded that the ultimate tensile strength and compression flow stress data of Owen and Scott (1975), Love (1959), Skudnov et al. (1969b) and Solenov et al. (1971) are in reasonable agreement despite substantial differences in metal purity. Except for Love's (1959) results which were insufficient to illustrate the details of temperature dependence, the ultimate tensile strength and compression flow stress curves all exhibit a region of low temperature sensitivity between 400 and about 550 K followed by a rather rapid decrease in strength. This strength decrease may be associated with the onset of recrystallization during testing since recrystallization would be expected near 600 K depending on the purity of the metal. The results of Owen and Scott (1975) reveal a rather rapid increase in temperature dependence below 150 K in both the ultimate tensile and yield strengths. No ready explanation is offered. Their yield strength results indicate virtually no temperature dependence from 150 to 600 K. The only other yield strength data

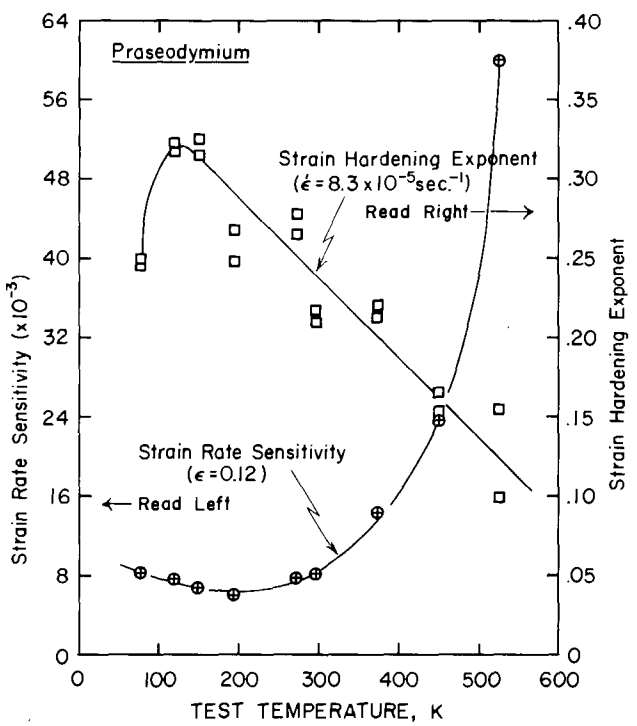

Fig. 8.24. Temperature dependence of the tensile strain-hardening exponent and strain-rate sensitivity of praseodymium. From Owen and Scott (1977).

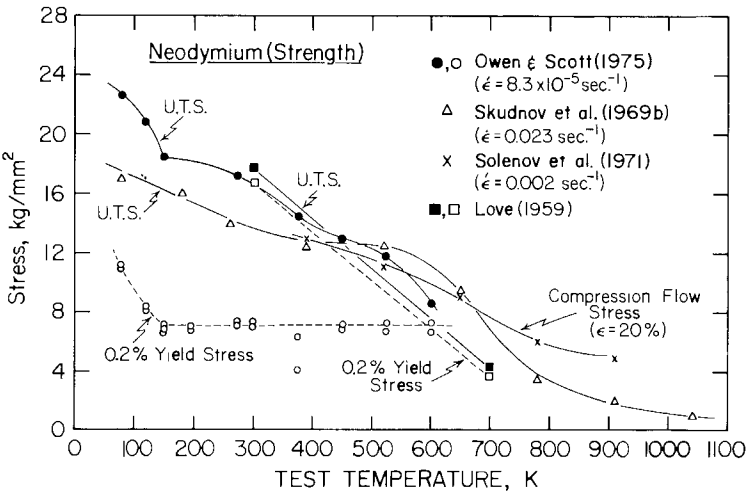

Fig. 8.25. Temperature dependence of the tensile and compressive strength properties of neodymium. Owen and Scott (1975): swaged and annealed; less than 259 ppm impurities including 69 ppm oxygen; 10 μm grain size. Love (1959): as-cast; 2310 ppm impurities including 1300 ppm oxygen. Solenov et al. (1971) and Skudnov et al. (1969b): wrought; 8400 ppm impurities including 3000 ppm Pr, and 5000 ppm Ta, but interstitials were not analyzed; 20 μm grain size.

(Love, 1959), obtained at room temperature and 700 K, differ significantly from the results of Owen and Scott; this probably reflects the different purity of the metals used (<259 ppm, Owen and Scott, versus 2310 ppm, Love) and the fact that Love's material was in the as-cast condition while Owen and Scott used a fine-grain, worked and annealed material.

Reduction in area and uniform elongation of good purity neodymium (Owen and Scott, 1975) are excellent with the reduction in area ranging from about 60% at 77 K to about 95% at 600 K. However, the reduction in area exhibited a sharp minimum at 250 K. Although the reduction in area values obtained by Skudnov et al. (1969b) were considerably lower, probably due to the lower purity metal used, their results also revealed a minimum at 250 K. The cause of these minima, shown in fig. 8.26, is unexplained. The rapid rise of the reduction in area observed in both investigations occurs in the temperature range, approximately 600 K, where recrystallization is expected. Strain rate sensitivity and strain hardening exponent temperature dependencies from Owen and Scott (1975) are illustrated in fig. 8.27. The strain rate sensitivity, except for an unexplained peak at 125 K, is relatively temperature insensitive to 375 K where it begins to rise monotonically. Similarly, the strain hardening exponent does not vary substantially from a value of approximately 0.30 until it begins to drop at 375 K; this property also seems to exhibit a small peak at 125 K.

4.2.7. *Samarium*

Only two sources of data for the temperature dependence of mechanical properties of samarium were found. The data are shown in figs. 8.28 and 8.29.

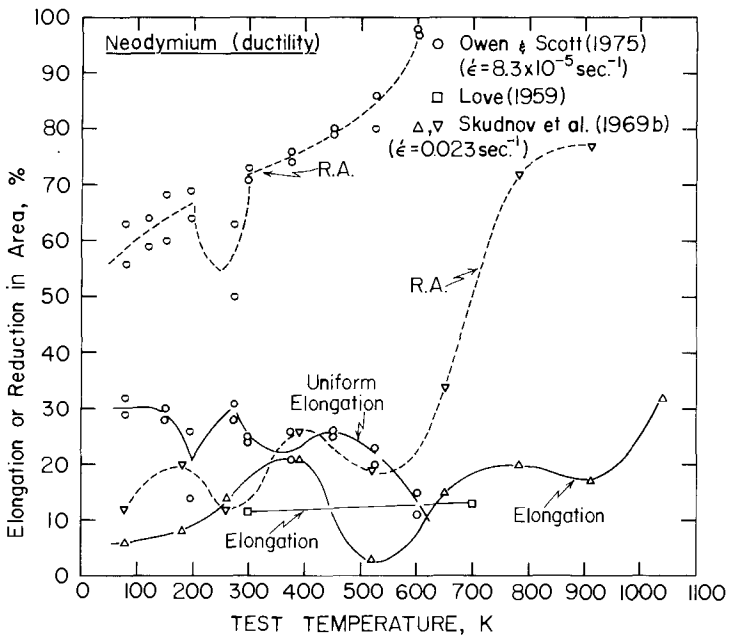

Fig. 8.26. Temperature dependence of the tensile ductility properties of neodymium. See fig. 8.25 caption for details.

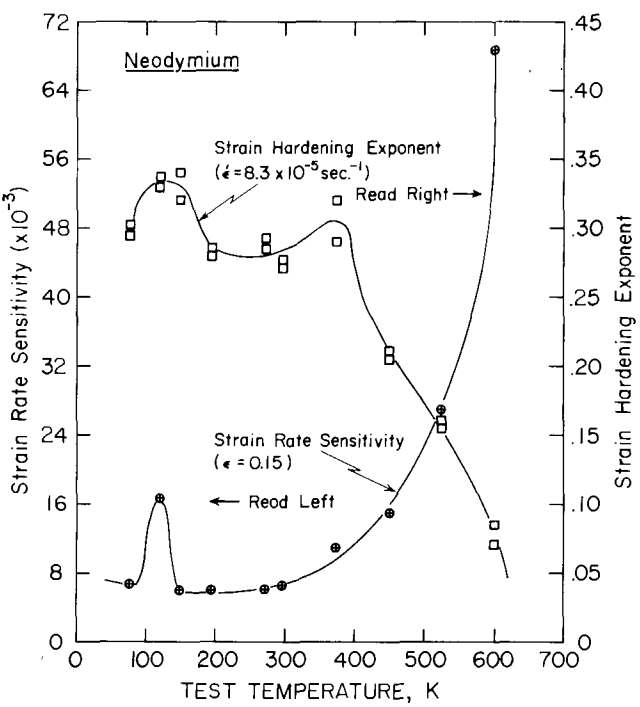

Fig. 8.27. Temperature dependence of the strain-hardening exponent and the strain-rate sensitivity of neodymium. From Owen and Scott (1975).

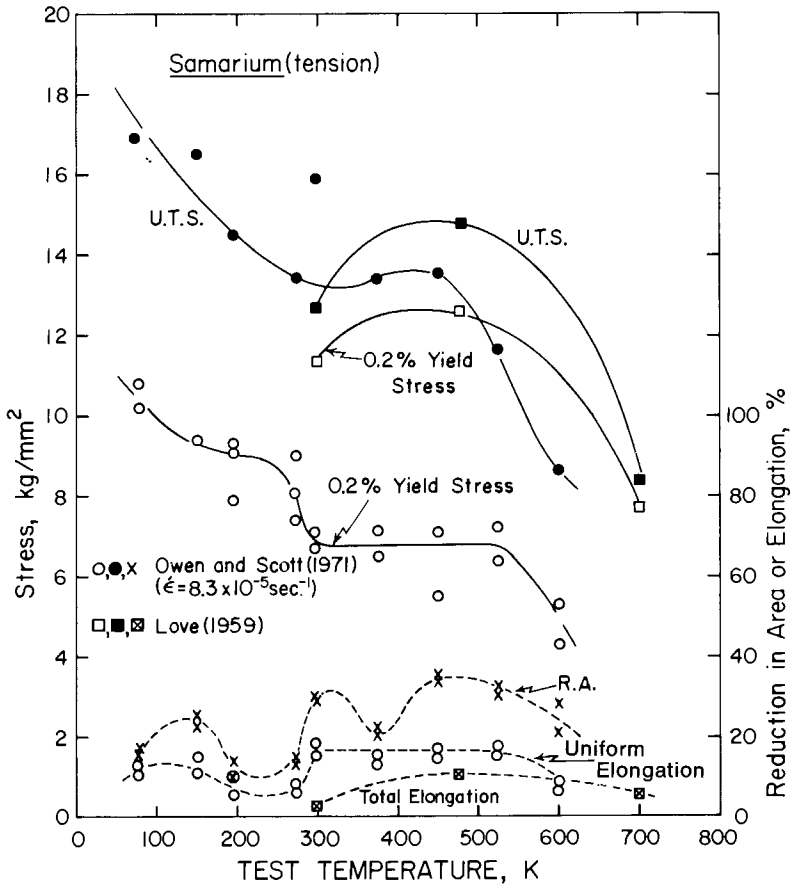

Fig. 8.28. Temperature dependence of the tensile properties of samarium. Owen and Scott (1971): worked and annealed; less than 1530 ppm impurities including 106 ppm oxygen; mixed (30 to 230 μm) grain size. Love (1959): as-cast; contained 200 ppm oxygen.

The data of Love (1959) were obtained from as-cast samarium while Owen and Scott (1971) used hot swaged–hot extruded-annealed material having a mixed grain size which ranged from 30 to 230 μm. Purity levels were close to the same in both studies – less than 580 ppm impurities including 200 ppm oxygen for Love and less than 1529 ppm impurities including 106 ppm oxygen plus somewhat less than 1000 ppm tungsten, tantalum and other rare earths for Owen and Scott. With the exception of yield strength, the mechanical properties obtained in both investigations were in reasonable agreement. The large difference in yield strength can be understood by the fact that Love (1959) used as-cast material which could have residual stresses that would elevate the yield strength above the values obtained with annealed material. Ultimate tensile strength exhibits a peak between 325 and 525 K where the yield strength has a broad plateau. Both yield and ultimate strengths decrease rapidly above 525 K which is near the

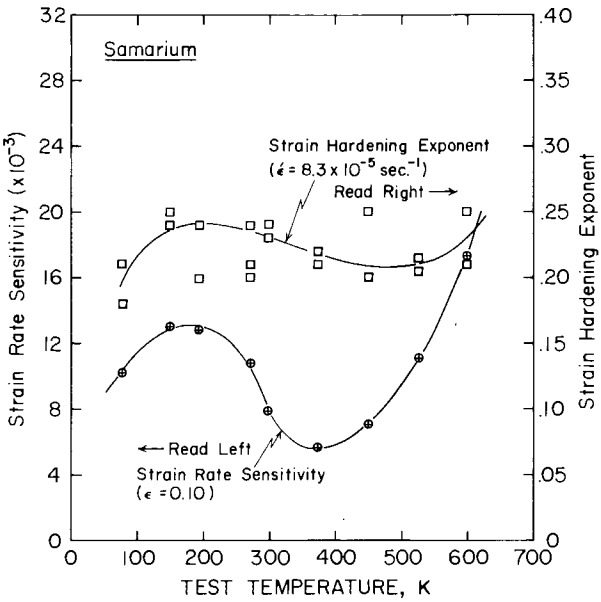

Fig. 8.29. Temperature dependence of the strain-hardening exponent and strain-rate sensitivity of samarium. From Owen and Scott (1971).

expected recrystallization temperature. In addition, the yield strength appears to rise rapidly just below 300 K where both the reduction in area and uniform elongation show minima. The stress plateau and the rise at 300 K could be manifestations of strain aging and/or a change in deformation mode. Based on the strain rate sensitivity minimum, fig. 8.29, at 375 K one might be tempted to conclude that the yield stress plateau region is a strain aging phenomenon while the strength rise just below 300 K is due to a change in deformation mode. However, neither of these explanations has been verified experimentally. With minor perturbations the strain hardening exponent, fig. 8.29, is relatively temperature independent at a value of about 0.22.

4.2.8. *Gadolinium*

All the available information concerning the temperature dependence of the tensile properties of gadolinium are shown in figs. 8.30, 8.31 and 8.32. Love (1959) used as-cast metal with less than 4470 ppm impurities including 1600 ppm oxygen and 2000 ppm tantalum. Material tested by Simmons (1961) was in the hot-extruded (1033 K) condition and the purity is uncertain. Owen and Scott (1973) used swaged and annealed (1023 K) metal having a grain diameter of 85 μm. The ultimate and yield strength data from Owen and Scott and from Simmons exhibited similar temperature dependencies although Simmons' values were somewhat higher than those obtained by Owen and Scott. Love's data are at variance with the others, possibly due to the as-cast condition and different

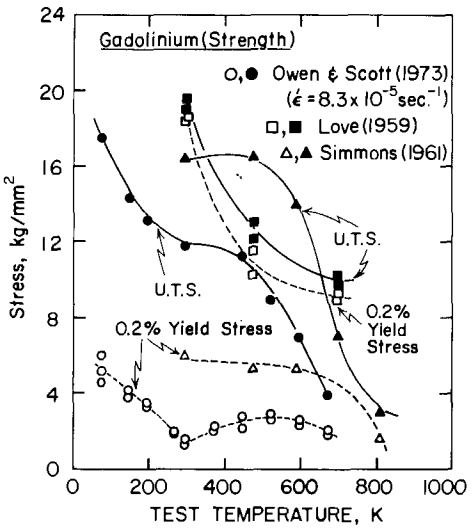

Fig. 8.30

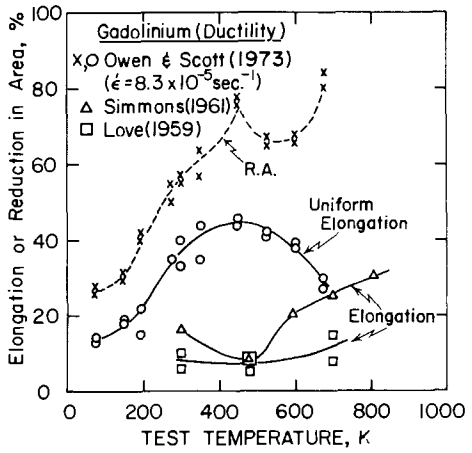

Fig. 8.31

Fig. 8.30. Temperature dependence the strength properties of gadolinium in tension. Love (1959): as-cast; less than 4470 ppm impurities including 2000 ppm Ta and 1600 ppm oxygen. Simmons (1961): as-extruded at 1033 K. Owen and Scott (1973): worked and annealed; 519 ppm impurities including 255 ppm other rare earths and 150 ppm oxygen; 85 μm grain size.

Fig. 8.31. Temperature dependence of the tensile ductility properties of gadolinium. See fig. 8.30 caption for details.

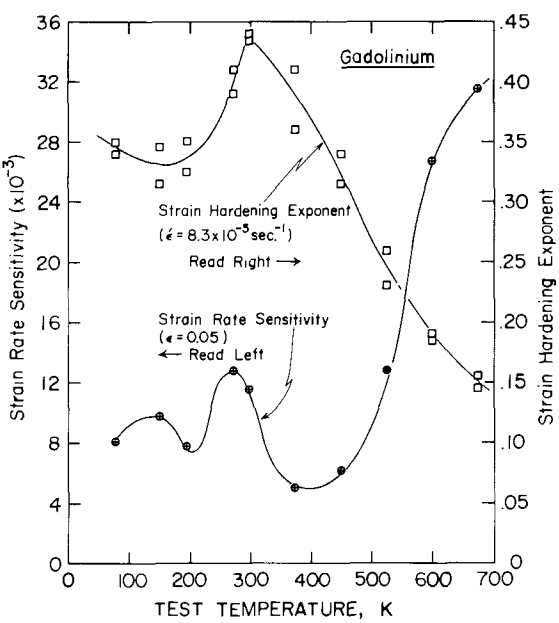

Fig. 8.32. Temperature dependence of the strain-hardening exponent and the strain-rate sensitivity of gadolinium. From Owen and Scott (1973).

purity of his metal. The yield and ultimate strengths reveal peaks near 500 K while the strain rate sensitivity, fig. 8.32, and the reduction in area, fig. 8.31, exhibit minima near this temperature. This combination of behaviors is suggestive of a strain aging phenomenon. A slight dip in yield strength at ~300 K, fig. 8.30, in combination with a peak in both the strain rate sensitivity and strain hardening exponent near room temperature may be associated with the paramagnetic to ferromagnetic transition of gadolinium.

4.2.9. *Terbium*

The only study of the temperature dependence of the mechanical properties of terbium was compression tests by Sokolov et al. (1970) who reported the purity of their metal to be 98.88 percent, but no analysis of non-metallics was made. Although fig. 8.33 shows only one compression flow stress (20% strain) versus temperature curve, Sokolov et al. did furnish curves for two additional strain rates. These additional curves were parallel to the flow stress curve reproduced in fig. 8.33 and the peak in the flow stress shown at 500 K shifted to higher temperatures with higher strain rates in the manner characteristic of strain aging or some other thermally-activated process. The dip in the maximum compression strain tends to support a strain aging phenomenon. No obvious manifestation of the α(h.c.p.) to α'(orthorhombic) phase change at about 220 K is evident in the mechanical properties. More data in the critical region are needed to determine whether the transformation produces an effect.

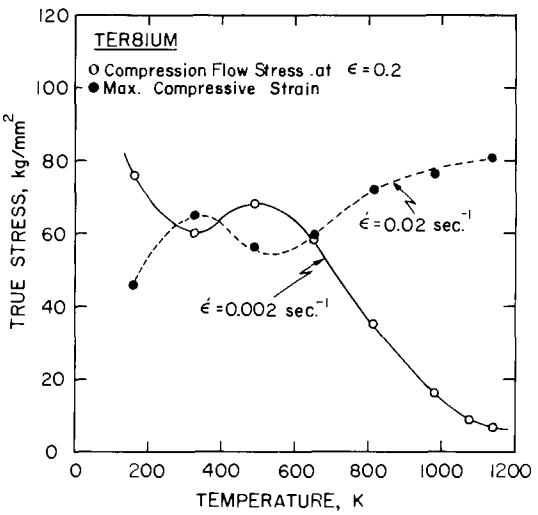

Fig. 8.33. Temperature dependence of the compression flow stress at 20% strain and the maximum compressive strain of terbium. Sokolov et al. (1970b): about 5% impurities including 4.1% Dy, but interstitials were not analyzed.

4.2.10. *Dysprosium*

The two available sets of data on the tensile properties of dysprosium, figs. 8.34 and 8.35, are not in agreement but this can be attributed to the large difference in purity of the metal and its condition when tested. Love (1959) used as-cast metal containing less than 4720 ppm impurities including 2000 ppm oxygen and less than 1000 ppm each of holmium and yttrium while Owen and Scott (1974) used swaged and annealed (1023 K) material containing less than 484 ppm impurities including 294 ppm oxygen. The yield strength, similar to samarium, exhibited a wide plateau from approximately 200 to 600 K. Ultimate tensile strength increased more or less smoothly with decreasing temperature down to about 100 K where it dropped, possibly in response to deformation induced transformation from the α(h.c.p.) to α'(orthorhombic) phase transformation temperature of 85 K. Uniform elongation was good, ranging from 20 to 40 percent, over the temperature interval of 150 to 700 K. Reduction in area increased from about 25% at 77 K to 95% at 750 K and revealed small peaks at 273 to 300 K and 450 K. These peaks correlate with small dips in the ultimate tensile strength but the magnitudes of these deviations are too small to assure they are physically significant. Strain rate sensitivity, fig. 8.35, shows no evidence of strain aging to associate with the dips and peaks in the ultimate tensile strength and reduction in area respectively.

4.2.11. *Holmium*

Compression flow stress (20 percent strain) and maximum compressive strain versus temperature data from Gladkikh et al. (1969b) are shown in fig. 8.36. They

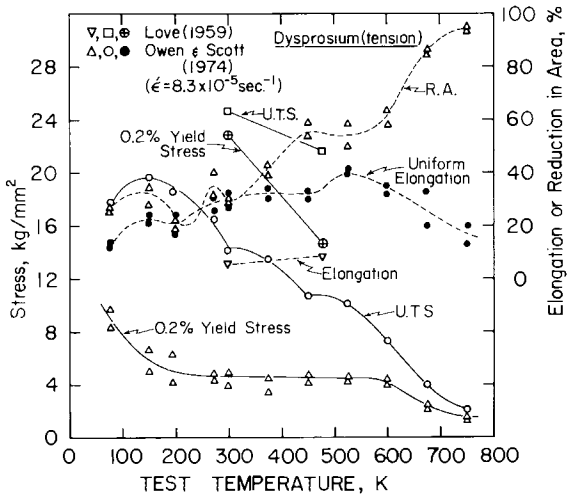

Fig. 8.34. Temperature dependence of the tensile properties of dysprosium. Love (1959): as-cast; less than 4720 ppm impurities including 1000 ppm Y, about 1000 ppm Ho, and 2000 ppm oxygen. Owen and Scott (1974): worked and annealed; less than 484 ppm impurities including 294 ppm oxygen; mixed grain sizes ranging from 35 to 140 μm.

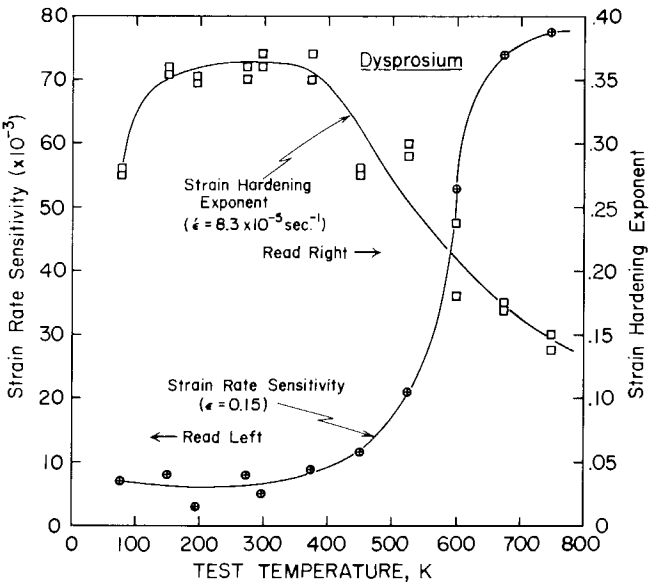

Fig. 8.35. Temperature dependence of the strain-hardening exponent and the strain-rate sensitivity of dysprosium. From Owen and Scott (1974).

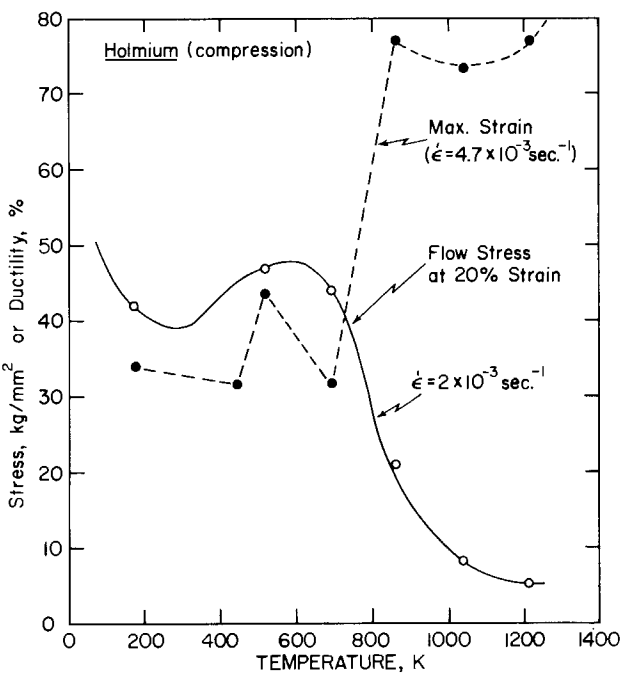

Fig. 8.36. Temperature dependence of the compressive flow stress at 20% strain and the maximum compressive strain of holmium. Gladkikh et al. (1969b): claim 97.4% Ho, but no analysis was given.

claimed a metal purity of 97.4 percent. Data for two additional strain rates were available but they only showed that the curves shifted to higher temperatures with increased strain rate. The rapid rise in maximum compression strain and fall in flow stress as the temperature rises to about 750 K may be related to recrystallization during testing. The broad peak from 400 to 800 K in compression flow stress tends to correlate with two seemingly spurious data points (one at 525 K and the other at 700 K) in the ultimate tensile strength curve from Gladkikh et al. (1969b) shown in fig. 8.37. There is also a dip in their elongation curve in the same temperature region. Reasonable agreement exists, fig. 8.37, between the tensile data of Gladkikh et al. and the tensile data of Love (1959) who tested as-cast holmium containing 3990 ppm impurities including 3800 ppm oxygen.

4.2.12. *Erbium*

Compression flow stress (20% strain) and ultimate tensile strength data from Sokolov et al. (1971), Sokolov et al. (1969b) and Love (1959) for erbium are in reasonable agreement with one another but deviate substantially from the ultimate tensile strength data from Owen and Scott (1968), fig. 8.38. Again the

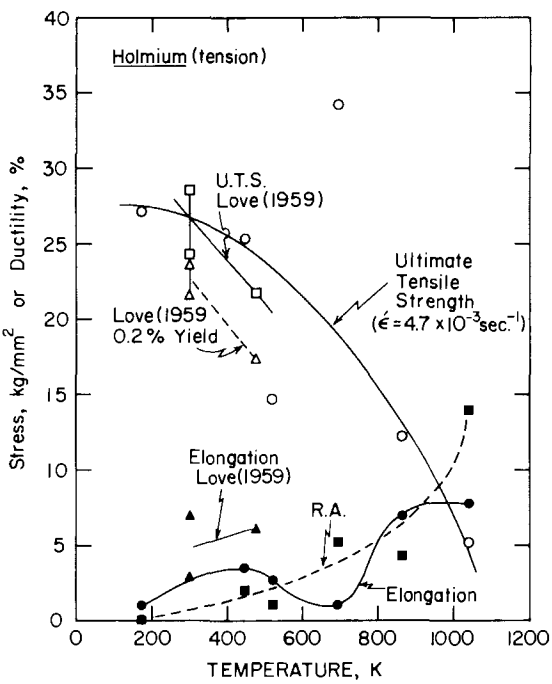

Fig. 8.37. Temperature dependence of the tensile properties of holmium. Love (1959): as-cast; 3990 ppm impurities including 3800 ppm oxygen. Gladkikh et al. (1969b): claim 97.4% Ho, but no analysis was given.

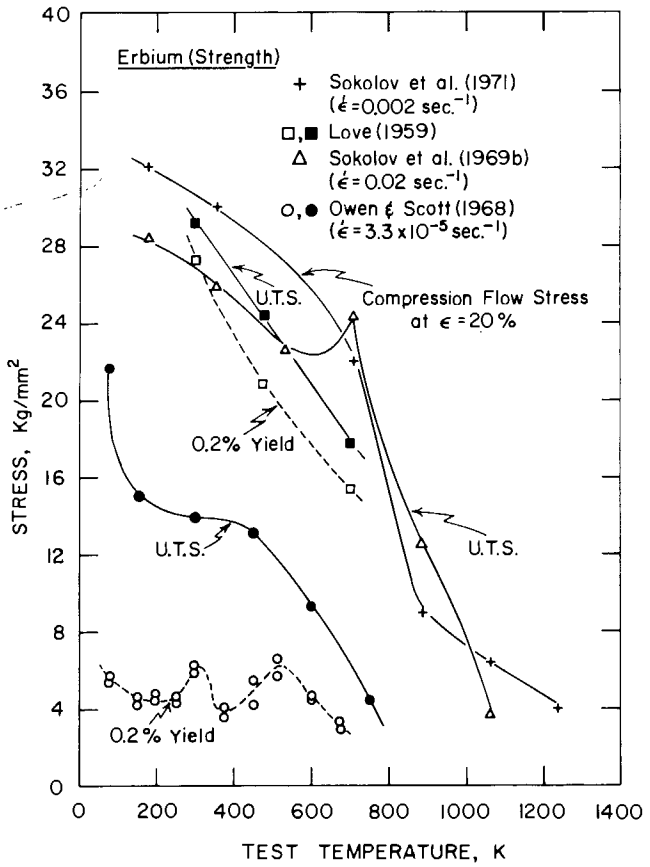

Fig. 8.38. Temperature dependence of the strength properties of erbium. Love (1959): as-cast; 6260 ppm impurities including 3500 ppm oxygen. Sokolov et al. (1969b and 1971): worked and annealed; claim 98.8% Er but no non-metallics were given. Owen and Scott (1968): swaged and annealed; less than 1690 ppm impurities including 160 ppm oxygen; 38 μm grain size.

difference probably can be attributed to purity and condition of the metal. Love (1959) used as-cast metal containing 6260 ppm impurities including 3500 ppm oxygen while Sokolov et al. (1969b) and Sokolov et al. (1971) used annealed metal claimed to be 98.8% pure but no non-metallics were analyzed. On the other hand Owen and Scott (1968) used swaged and annealed (1123 K) metal which had a grain diameter of 38 μm and contained less than 1396 ppm impurities including 160 ppm oxygen. The rapid decrease in ultimate tensile strength and compression flow stress and the rapid rise in maximum compression strain, fig. 8.39, all near 650 or 700 K, as determined by Sokolov et al. (1969b) and Sokolov et al. (1971), may reflect recrystallization during testing. Ultimate tensile strength data from Owen and Scott (1968) indicates a broad peak or plateau at about 250 to 500 K while the yield strength exhibits peaks at 300 K and 500 K. Corresponding to the yield strength peaks are minima in

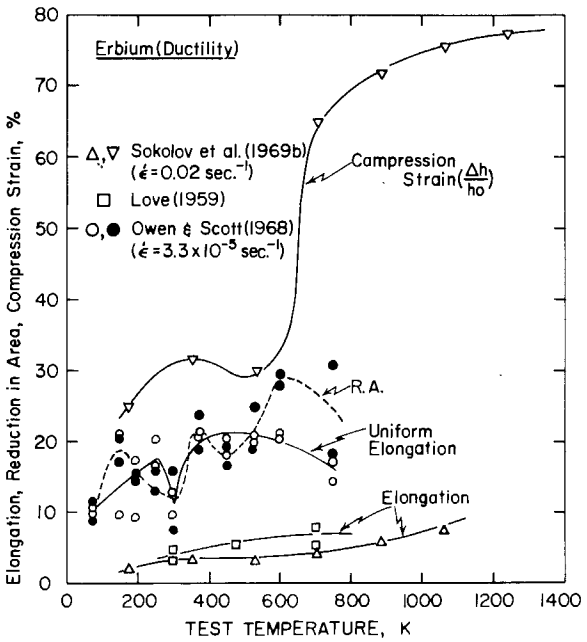

Fig. 8.39. Temperature dependence of the ductility properties of erbium. See fig. 8.38 caption for details.

reduction in area. A dip occurs in the uniform elongation at 300 K but the curve is smooth at 500 K. There are also minima in the strain rate sensitivity at 300 and 500 K as shown in fig. 8.40. One might tentatively conclude that these effects are related to strain aging. The strain hardening exponent, fig. 8.40, decreases monotonically with increasing temperature but some deviation from a smooth curve occurs over the temperature range where the yield strength peaks appear.

4.2.13. *Ytterbium*

The tensile properties of ytterbium, figs. 8.41 and 8.42, exhibit interesting effects because of the β(f.c.c.) to α(h.c.p.) phase change which occurs on cooling near 250 K. These effects do not appear in the results of Love (1959), fig. 8.41, because he only tested at room temperature and 477 K. The yield strength determined by Owen and Scott (1970) was virtually independent of temperature above 250 K. Just below 250 K the yield strength increased almost discontinuously. This increase is associated with the formation of α phase ytterbium at the M_s temperature (~250 K). Probably as a result of strain induced α-phase formation, the ultimate tensile strength began to rise rapidly at about 280 K. Both the uniform elongation and reduction in area decrease suddenly at approximately 280 K, also reflecting the presence of strain induced α phase.

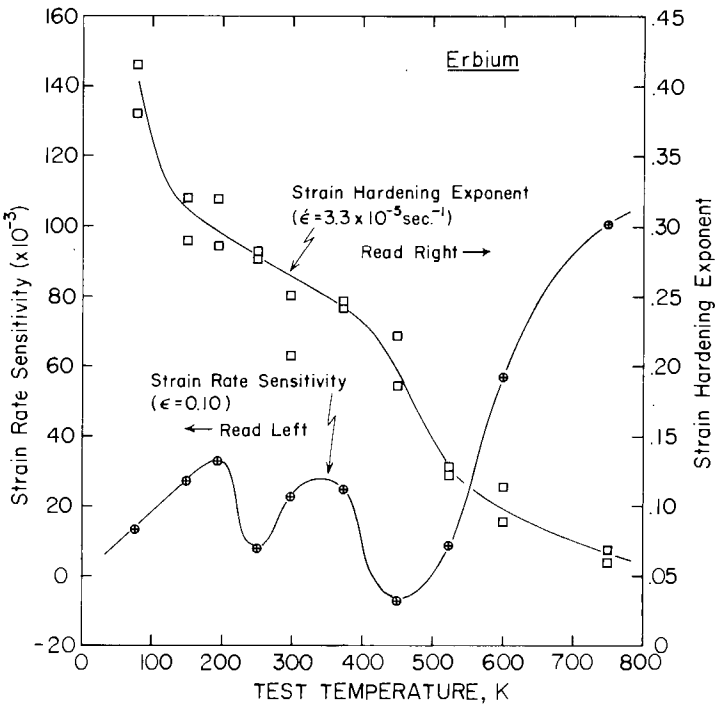

Fig. 8.40. Temperature dependence of the strain-hardening exponent and the strain-rate sensitivity of erbium. From Owen and Scott (1968).

Furthermore, the strain hardening exponent, fig. 8.42, dropped suddenly at 250 K as a result of elongation produced during the β to α transformation. The strain rate sensitivity, fig. 8.42, exhibited a distinct minimum centered at about 350 K. Whether this is associated with the β to α transformation or is related to another phenomenon is not known.

4.2.14. *Lutetium*

Gladkikh (1975) has reported the compression and tensile properties of lutetium as a function of temperature, fig. 8.43. The metal was claimed to be 98.7% pure but no analysis was given and the condition of the metal is unknown. The compression strength exhibits a peak at 580 K and a minimum appears, at the same temperature, in the maximum compression strain. Insufficient data are available to determine whether a similar behavior is manifest in the tensile properties. Both elongation and reduction in area are low, less than 10%, and the ultimate tensile strength is less than the compression yield strength. This discrepancy suggests the metal was relatively brittle, especially below about 600 K.

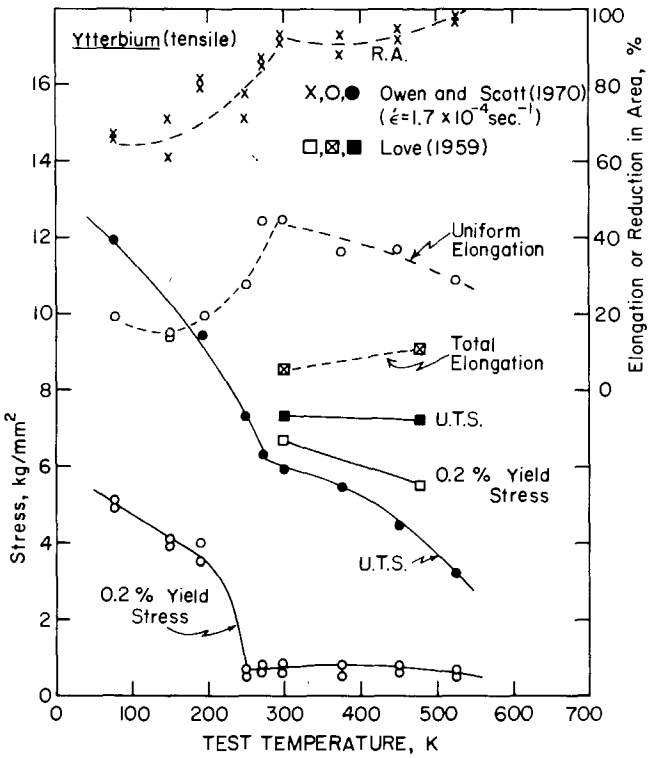

Fig. 8.41. Temperature dependence of the tensile properties of ytterbium. Love (1959); as-cast; 650 ppm impurities including 100 ppm oxygen and less than 500 ppm Lu. Owen and Scott (1970): worked and annealed; less than 1000 ppm impurities including 400 ppm Ta, 100 ppm Y, and 203 ppm oxygen; 62 μm grain size.

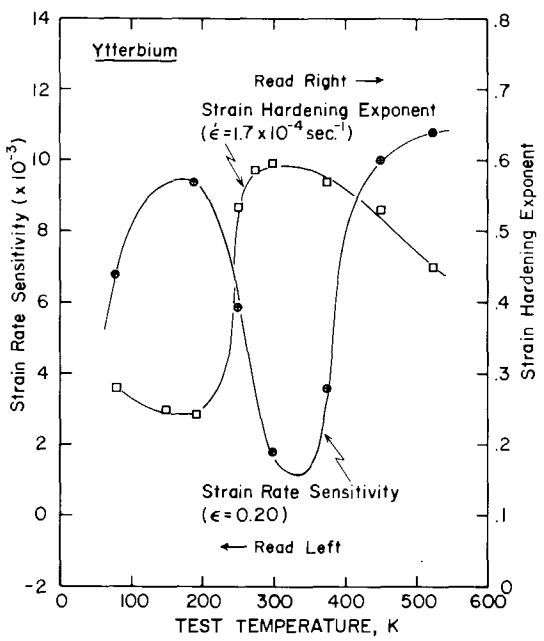

Fig. 8.42. Temperature dependence of the strain-hardening exponent and the strain-rate sensitivity of ytterbium. From Owen and Scott (1970).

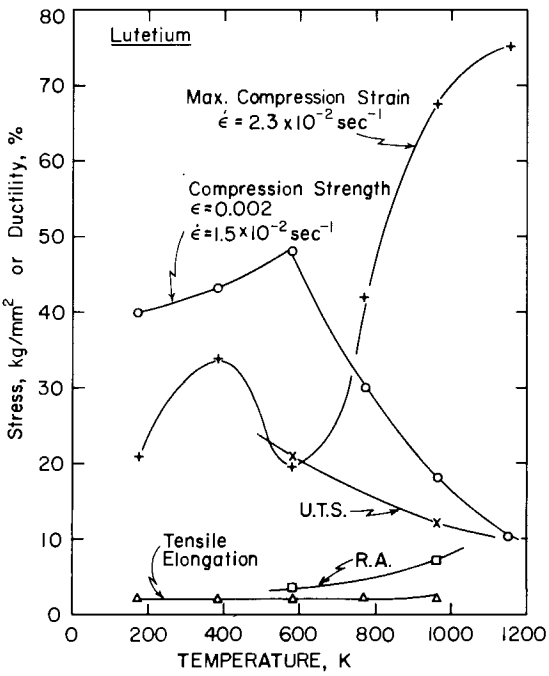

Fig. 8.43. Temperature dependence of strength and ductility of lutetium. Gladkikh (1975): Condition not given and purity variously quoted from 95.7% to 98.7% Lu. The writer is of the opinion that the lower purity is correct because there is a great difference in compressive and tensile ductility parameters.

5. Impact properties

All the available data on the impact properties of the rare earth metals are from Love (1959, 1960). The metals were prepared by calcium reduction of the anhydrous fluorides. Izod specimens having a standard V-notch were tested with a 100 inch-pound capacity impact machine that had a striking velocity of 11.3 feet per second. The specimens were all tested in the as-cast condition. Data from Love (1959) were from subsize-width specimens and the impact energy, taken in inch-pounds, was corrected from the subsize notch cross-section to standard notch cross-section and quoted in foot-pounds.

It can only be concluded, from the impact data tabulated in table 8.7, that all the rare earth metals have low fracture toughness in the as-cast condition. Although neodymium, holmium, and ytterbium have somewhat better impact properties than the other rare earth metals this is not explained by purity or crystal structure. Furthermore, the three metals (yttrium, dysprosium and erbium) tested at 477 K did not exhibit a strong tendency towards improved impact properties with increased test temperature.

TABLE 8.7.
Room temperature impact properties (foot-pounds).*

	(Love, 1959)	(Love, 1960)
Scandium	–	–
Yttrium	1.5, 1.5	0.9, 1.1, 1.3 1.5, 2.1, 1.6 (477 K)
Lanthanum	3.7, 5.3	–
Cerium	2.8, 1.6	–
Praseodymium	4.8	–
Neodymium	8.5, 8.0	–
Promethium	–	–
Samarium	0.5, 0.5	–
Europium	–	–
Gadolinium	1.3, 1.3	–
Terbium	3.1, 3.3	–
Dysprosium	1.5, 1.8	2.4, 2.3, 2.0 2.3, 2.4, 2.1 (477 K)
Holmium	6.9, 7.4	–
Erbium	1.3, 1.1	1.4, 1.8, 1.7 2.4, 2.1, 2.0 (477 K)
Thulium	–	–
Ytterbium	5.0, 5.6	–
Lutetium	–	–

*Sets of two and three numbers indicate the values of two or three tests.

6. Fatigue properties

Fatigue data for the rare earth metals are limited to tests on yttrium, dysprosium, and erbium by Love (1960) and lanthanum by Shibarov et al. (1971). The data by Love, given in fig. 8.44, are based on smooth bar tension-tension loading tests at 30 Hz frequency. Data points for samples which failed at defects have been omitted in fig. 8.44. The lower stress was always 10% of the upper stress which is plotted in terms of the percentage of ultimate tensile strength for the as-cast material. Although the data are limited and considerable scatter exists, it appears that the endurance limit of as-cast yttrium, dysprosium and erbium is between 40 and 50% of the ultimate tensile strength. However, impurities have considerable influence on the endurance limit of metals and the values for purer metals may be substantially different from those reported. As shown in fig. 8.45, Shibarov et al. (1971) observed a power law relation between fatigue life and tensile stress for lanthanum at ambient temperature. Furthermore, they noted that the fatigue life decreased as the cyclic frequency was increased from about 47 Hz to about 234 Hz in their rotating beam fatigue tests.

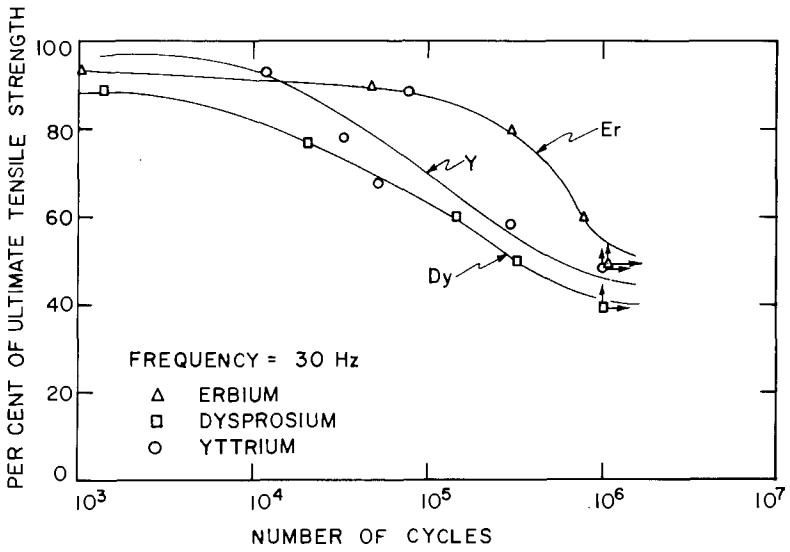

Fig. 8.44. Room temperature tension-tension fatigue-life curves for yttrium, dyprosium and erbium with maximum tensile stress given in terms of the fraction of the respective ultimate tensile strengths which were not given explicitly. From Love (1960).

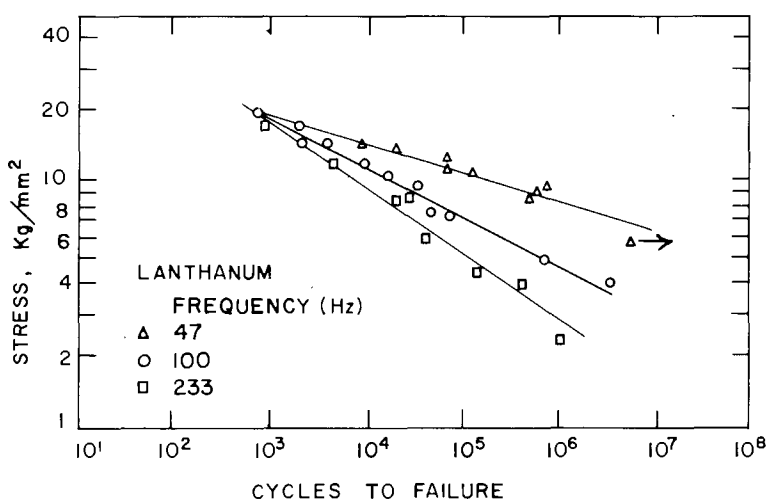

Fig. 8.45. Linear log–log relationship between cyclic stress amplitude and fatigue life of lanthanum in rotating beam tests at three different cyclic frequencies. From Shibarov et al. (1971).

7. Creep properties

Yttrium is the only rare earth metal for which creep information exists. Suganeyev et al. (1970) have examined the creep behavior of yttrium over the temperature range 595 to 700°C (0.39–0.47 absolute melting temperature). They used stresses from 0.7 to 4 kg/mm^2. The composition of their vacuum-distilled, arc-remelted metal in weight percent was: 0.1 O, 0.02 N, 0.05 C, <0.003 Ta, <0.002 Ca, <0.003 Ni, <0.003 Si, 0.03 Fe, 0.3 Cu, 0.12 Cd, less than 0.01 Al, and less than 0.06 other rare earth metals. However, it should be pointed out that the creep tests were run in a vacuum which attained 3×10^{-4} Torr pressure. It is well known that yttrium will absorb oxygen and nitrogen at the pressures and temperatures used for their tests. Consequently, even though the test durations were not over one hour, the samples should be suspected of contamination during the course of the creep tests. Nevertheless, Suganeyev et al. (1970) developed the following empirical expression for the steady-state creep rate of yttrium.

$$\dot{\epsilon}_{ss} = \frac{A}{T}\sigma^{3.6}\exp\left[-\frac{78.500}{RT}\right]$$

$$A = 5.49 \times 10^{16}\,\frac{K}{\text{sec}\,(\text{kg/mm}^2)^{3.6}}$$

σ = applied stress in kg/mm^2

T = temperature in K

R = gas constant in cal/mole – K

The value given here for the constant A is not that found in the reference; instead it is the value computed by the writer because the units for the constant and the stress were not given. The equation reproduces steady-state creep rates reasonably well for tension and compression loading over the stress range from 0.28 kg/mm^2 to 4 kg/mm^2 at temperatures from 594°C to 700°C. The accuracy decreases at higher creep rates which, in their tests, reached values as high as 1.56×10^{-3} sec^{-1}. Included in the data they used to develop the steady-state creep rate equation are two results from Simmons (1959) who used a lower range of stress (0.28 kg/mm^2 and 0.7 kg/mm^2) at 594°C. Simmons' tests also were of much longer duration (1000 hours and ~400 hours) than Suganeyev et al. used (apparently all less than 1 hour). Suganeyev et al. (1970) state that Weertmann's (1955, 1957) dislocation climb theory for steady-state creep adequately describes the creep results for yttrium.

8. Internal friction

Published internal friction data for the rare earth metals are limited. Work on lanthanum and cerium has been conducted by Dashkovskiy and Savitskiy (1961).

The results are shown in figs. 8.46 and 8.47 for lanthanum and cerium respectively. A frequency of 4.5 Hz was used and the heating or cooling rate was 0.042 K per second. Neither metal was of high purity: lanthanum (9.8% Nd, 1% Pr, 0.01% Fe, $<3 \times 10^{-4}$% Pb, Cd, and Bi, <0.01% O) and cerium (0.75% Nd, 0.75% Pr, 0.01% Fe, $<1.1 \times 10^{-4}$% Pb, <0.01% O). For lanthanum, fig. 8.46, they attributed the rather sharp peak near 300°C (curve B) during heating to the d.h.c.p. to f.c.c. transformation. The peak during cooling (curve A) appears at a slightly lower temperature than during heating, probably reflecting the known transformation hysteresis (see ch. 2, table 2.14). On the other hand, the rather broad peak between 300 and 500°C for cerium, fig. 8.47, was attributed to a grain boundary relaxation process. To substantiate this conclusion they compared two samples, one annealed for one hour at 600°C (curve A) and the other annealed for 20 minutes at 500°C (curve B). The lower annealing temperature resulted in a more clearly-defined and somewhat broader peak than the higher annealing temperature which produced a larger grain size material. In the writer's opinion, the interpretation of these internal friction peaks should be considered cautiously since incomplete internal friction work on yttrium in his laboratory indicates that the behavior is extremely sensitive to the thermal history and purity of the samples.

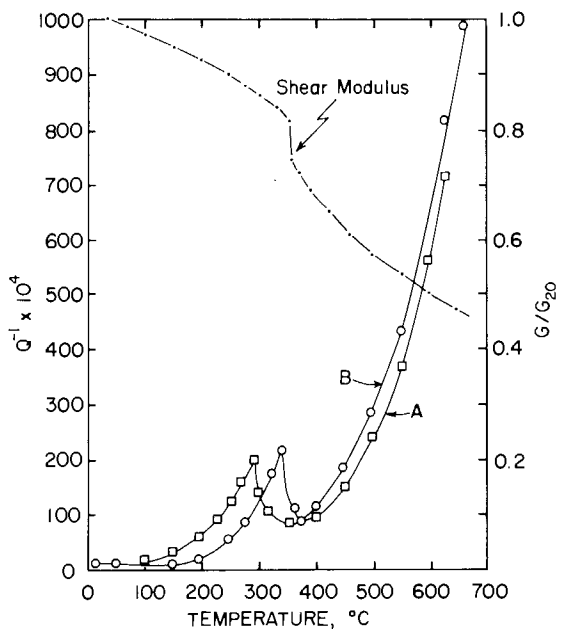

Fig. 8.46. Internal friction curves for lanthanum (annealed 30 min at 680°C) during heating (curve B) and during cooling (curve A). Included is a plot of the normalized shear modulus (G/G_{20}) where G at 20°C was 1480 ± 50 kg/mm^2. The frequency of oscillations was 4.5 Hz and the heating and cooling rates were 0.042°C sec^{-1}. From Dashkovskiy and Savitskiy (1961).

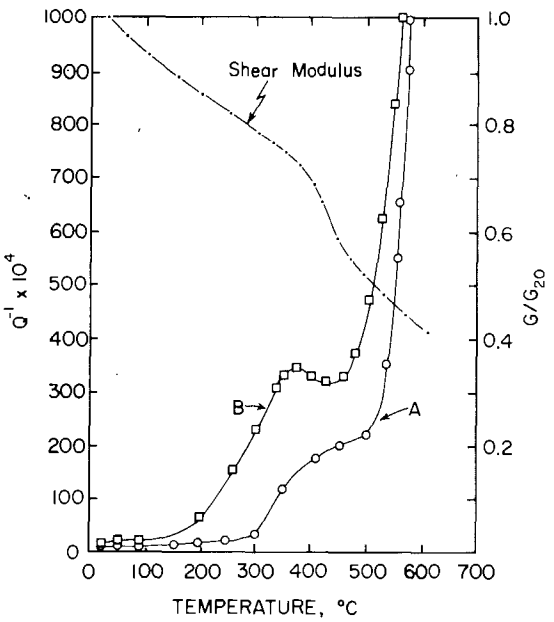

Fig. 8.47. Internal friction curves for cerium at an oscillating frequency of 4.5 Hz with a heating rate of 0.042°C sec^{-1}. Curve A represents a sample that had been annealed 1 hour at 600°C while curve B represents a sample annealed 20 min at 500°C. Included is a plot of the normalized shear modulus (G/G_{20}) where G at 20°C was 1350 ± 50 kg/mm^2. From Dashkovskiy and Savitskiy (1961).

Borisov and Vedenyapin (1971), using an oscillating frequency of 1 Hz, observed a grain boundary relaxation peak in yttrium at 620 K with an activation energy of 34.5 kcal/mole. Borisov et al. (1971) studied the relaxation spectrum of yttrium [0.06% O, 0.005% N, 0.05% C, 0.05% F, 0.036% Fe, <0.025% Cu, <0.003% Ni, <0.006% Al, <0.03% Ta, <0.003% Gd, by weight] from 293 to 573 K. They interpreted a rather complex series of relaxation peaks as being produced by interactions between dislocations and the interstitials carbon, nitrogen and oxygen. Based on their interpretation they obtained the following reasonable values for the diffusion coefficients: oxygen, $1.14 \times 10^{-2} \exp[-21{,}500/RT]$ cm^2/sec; nitrogen, $9 \times 10^{-2} \exp[-25{,}400/RT]$ cm^2/sec; carbon, $1.8 \times 10^{-2} \exp[-28{,}000/RT]$ cm^2/sec.

In a series of papers Burdett (1968, 1969, 1970) and Burdett and Layng (1967a, 1967b, 1968) have reported on the internal friction of gadolinum and terbium. Internal friction was determined with a torsion pendulum oscillating at a frequency of about 1 Hz and the results were given in terms of the logarithmic decrement. Two damping peaks were observed for gadolinum, one at about 182 K and the other at about 230 K as shown in fig. 8.48. The low temperature peak was independent of strain amplitude but dependent on frequency while the higher temperature peak was independent of frequency but dependent on strain amplitude. Neither peak apparently was due to a true relaxation process; they

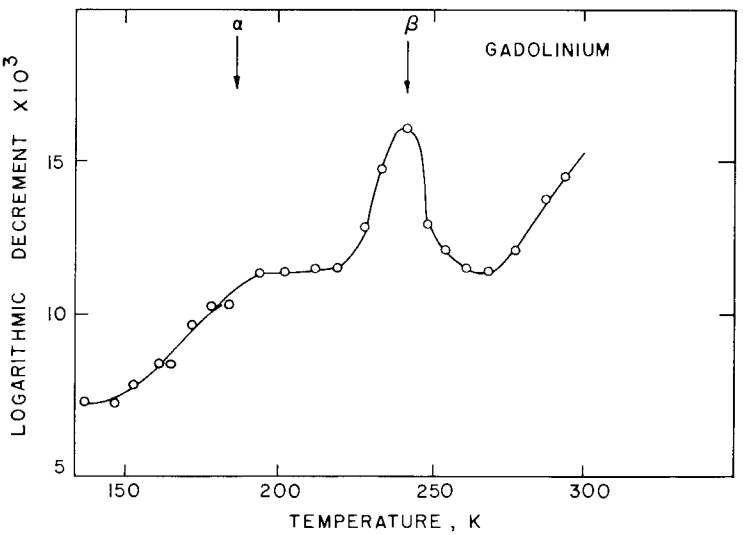

Fig. 8.48. Logarithmic decrement as a function of temperature for a gadolinium sample annealed at 900°C for 2 hours and tested in a torsion pendulum oscillating at about 1 Hz. From Burdett (1968).

were produced by temperature variations of the magnetic constants. The higher temperature peak was attributed to irreversible movement of domain boundaries pinned by dislocations. Microeddy currents caused by changes in magnetization accompanying the domain boundary motion led to an energy loss when the sample was cyclicly stressed in the torsion pendulum; this produced the low

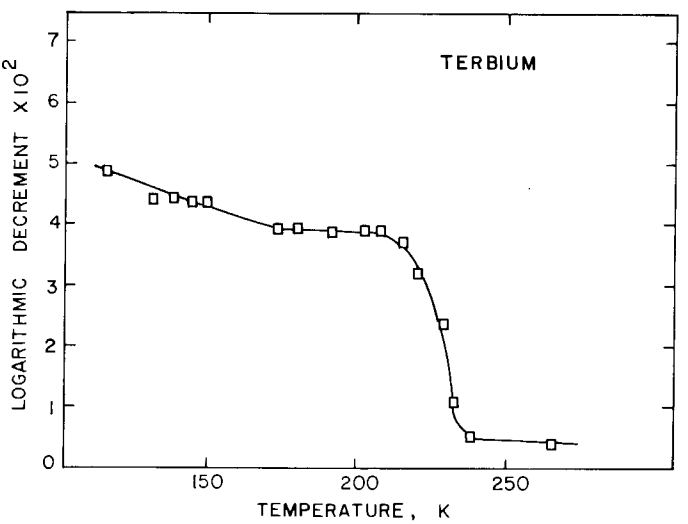

Fig. 8.48. Logarithmic decrement as a function of temperature for terbium which had been annealed for 1 hour at 1000°C and tested in a torsion pendulum oscillating at about 1 Hz. From Burdett (1969).

temperature frequency dependent peak. Instead of a distinct peak, terbium exhibited a step-wise decreasing logarithmic decrement with increasing temperature, fig. 8.49.

Belov et al. (1961) observed two anomalies in the internal friction of dysprosium, one at 88 K and the other at 175 K. The anomaly at 88 K consisted of a very sharp drop in the internal friction while the 175 K anomaly was a kink in the internal friction-temperature curve. They attributed the sharp drop at 88 K to a first order transition involving a change in the nature of the magnetic interaction between magnetic sublattices corresponding to the ferromagnetic-to-antiferromagnetic transition which is known to be between 85 and 90 K in dysprosium. The higher temperature anomaly, claimed to be characteristic of a second order transition, was associated with the antiferromagnetic-to-paramagnetic transition at 178 K, the Néel point for dysprosium. A frequency of 128 kHz was used in their experiments but they indicated that the same phenomena occurred in torsion pendulum experiments.

9. Elastic properties

Elastic properties serve an obvious utility in mechanics of materials, e.g., stress–strain relations and dislocation characteristics (Fisher and Dever, 1967; Fisher and Alfred, 1968). Moreover, elastic properties and their temperature dependencies provide important information and understanding of such physical characteristics as magnetic behavior, polymorphic transformations, and other fundamental lattice phenomena. In this section the elastic properties and their temperature dependencies are presented for all the rare earth metals except promethium, for which there is no data. To the writer's knowledge this is the first one-source compilation of the temperature dependencies of the elastic properties of the rare earth metals.

Before proceeding with the presentation of the specific elastic properties for the rare earth metals individually, it is appropriate to discuss pertinent general elastic-property relations, symbols, and assumptions used in the attainment of numerical values. Since single crystals are not always readily available, *bulk* elastic property measurements are frequently made with *polycrystalline* samples. An implicit assumption made when obtaining *bulk* elastic constants is that polycrystalline material is elastically *isotropic*. This is not always true, especially with hexagonal materials and particularly when the hexagonal material is used in the as-cast condition. Accordingly, in the writer's opinion, data obtained on single crystals are to be preferred. Unfortunately, single crystals cannot always be obtained and polycrystalline material must be used. The most accurate data are measured by ultrasonic methods whereby longitudinal and shear mode acoustic waves of high frequency are propagated through the sample. From a knowledge of the material density (ρ) and the measured longitudinal and shear wave velocities, all the bulk elastic properties can be obtained. The shear modulus, sometimes called the rigidity modulus, symbolized by the letter G in

this chapter, is directly obtained from the shear wave velocity, v_s, by the following relation:

$$G = \rho v_s^2. \tag{8.1}$$

When ρ is in units of g cm^{-3} and v_s is in units of cm sec^{-1}, the shear modulus has units of dynes cm^{-2} (10^{-10} GPa = 1 dyne cm^{-2}). Through relations between isotropic elastic constants the longitudinal velocity (v_ℓ) gives directly the following combination of bulk modulus (K) and shear modulus (G):

$$K + \tfrac{4}{3}G = \rho v_\ell^2. \tag{8.2}$$

Since G is known from the shear wave velocity measurement, K can be calculated. With K and G known, both Poisson's ratio (ν) and Young's modulus (E) can be calculated using appropriate relations for isotropic elastic constants. Two such relations, one for ν and one for E, are given below:

$$\frac{1}{E} = \frac{1}{3G} + \frac{1}{9K}, \tag{8.3}$$

and

$$\nu = \frac{1}{2}[1 - 3G/(3K + G)]. \tag{8.4}$$

Often the compressibility (χ) is used rather than the bulk modulus (K). These quantities are simple reciprocals for isotropic materials, i.e., $\chi = K^{-1}$. Ultrasonic methods for measuring elastic properties are inherently adiabatic processes. Compressibility, on the other hand, is frequently determined by hydrostatic pressurization techniques which are isothermal in nature. Conversion of isothermal values (χ_T) to adiabatic values (χ_s) is accomplished via the following relation:

$$\chi_s = \chi_T - \frac{9\alpha^2 \omega T}{C_p} \tag{8.5}$$

In eq. (8.5) the symbols have the meaning:

α = linear thermal expansion coefficient.
ω = atomic volume which is also the atomic weight divided by the density.
T = absolute temperature on the Kelvin scale.
C_p = isobaric specific heat.

Throughout this chapter the values for α, ω and C_p given by Gschneidner (1964) were used to convert isothermal compressibilities to adiabatic values. In all cases, however, the reciprocal of adiabatic compressibility (χ_s), i.e. the bulk modulus (K), is quoted in this chapter. From the experimental point of view, the most common method used to determine the isothermal compressibility (χ_T) involves the measurement of volume change ($\Delta V/V_0$) associated with applied pressure (P) to obtain a relative volume change versus pressure relation. Several

relations have been touted but Stephens (1964) claims that the following one gives the best fit with experimental data for the rare earth metals:

$$\frac{\Delta V}{V_0} = AP + BP^2 + CP^3, \tag{8.6}$$

Using eq. (8.6) and the defining equation (eq. (8.7)) for isothermal compressibility

$$\chi_T = -\frac{1}{V_0}\left(\frac{\partial V}{\partial P}\right)_T \tag{8.7}$$

one finds that the constant A in eq. (8.6) approaches χ_T as the pressure vanishes. In other words, the extrapolation of a $\Delta V/V_0$ versus P plot to zero pressure gives the isothermal compressibility. Adiabatic bulk moduli can be obtained from shock experiments also. (For example, see Gust and Royce, 1973.) Here the bulk modulus (K) is given directly by eq. (8.8)

$$K = \rho v_B^2. \tag{8.8}$$

In eq. (8.8) v_B is the bulk wave velocity often expressed as

$$v_B^2 = v_l^2 - \tfrac{4}{3}v_s^2.$$

When the shock velocity (U_s) is linearly related to the particle velocity (U_p), the shock velocity at zero particle velocity is approximately the bulk acoustic wave velocity (v_B). That is, $v_B = U_s$ when $U_p = 0$. Gust and Royce (1973) showed that U_s was linearly related to U_p for most of the rare earth metals.

For single crystals with transverse dimensions large enough to permit a plane wave condition to be attained, the results are unambiguous and virtually free from theoretical assumptions. Five *independent* elastic constants (stiffnesses or compliances) are required to describe the linear elastic stress–strain relations for hexagonal materials. Only three independent constants are required for cubic (γ-Ce, Eu, Yb) materials. Since there are no *single crystal* elastic constant data for the cubic rare earth metals, this discussion will concentrate on the relationships for hexagonal symmetry.

The five independent constants for hexagonal materials are C_{11}, C_{33}, C_{44}, C_{12} and C_{13}. Of the five, only four can be measured directly as indicated below:

$$C_{33} = \rho v_{cl}^2 \tag{8.9}$$

$$C_{11} = \rho v_{al}^2 \tag{8.10}$$

$$C_{66} = \tfrac{1}{2}(C_{11} - C_{12}) = \rho v_{asa}^2 \tag{8.11}$$

$$C_{44} = \rho v_{cs}^2 \tag{8.12a}$$

or

$$C_{44} = \rho v_{asc}^2 \tag{8.12b}$$

Wave velocity subscript symbols in eqs. (8.9) through (8.12b) have the following definitions:

v_{cl} = longitudinal wave propagated parallel to the unique axis (c-axis).
v_{al} = longitudinal wave propagated perpendicular to the unique axis (c-axis).
v_{asa} = shear wave propagated perpendicular to the unique axis with polarization also perpendicular to the unique axis.
v_{cs} = shear wave propagated parallel to the unique axis with any polarization direction appropriate to a shear wave.
v_{asc} = shear wave propagated perpendicular to the unique axis with polarization parallel to the unique axis.

The fifth independent constant (C_{13}) must be determined from a wave propagated at some oblique angle to the unique axis. With a knowledge of the wave velocity, the other constants, and the oblique angle, it is possible to compute C_{13}. Musgrave (1954) has derived the relations between density, wave velocity, and elastic constants and has written generalized equations for waves propagated at a general angle to the unique axis. Internal consistency checks can be made by employing various propagation and polarization directions.

Bulk properties can be obtained from the single crystal constants by appropriate averaging. Voigt (1928) and Reuss (1929) proposed averaging techniques that provide maximum and minimum values respectively. Their concepts and expressions for bulk properties are described by Huntington (1958). Voigt (1928) averages of C_{ij} for bulk (K_V) and shear (G_V) moduli of hexagonal materials are

$$9K_V = 2C_{11} + C_{33} + 2C_{12} + 4C_{13} \tag{8.13a}$$

and

$$15G_V = 2C_{11} + C_{33} + 6C_{44} + 3C_{66} - C_{12} - 2C_{13}, \tag{8.13b}$$

where

$$2C_{66} = C_{11} - C_{12}.$$

According to Reuss (1929) the bulk (K_R) and shear (G_R) moduli for materials with hexagonal symmetry are given by

$$K_R^{-1} = 2S_{11} + S_{33} + 2S_{12} + 4S_{13} \tag{8.14a}$$

and

$$15G_R^{-1} = 8S_{11} + 4S_{33} + 6S_{44} + 3S_{66} - 4S_{12} - 8S_{13}, \tag{8.14b}$$

where $S_{66} = 2(S_{11} - S_{12})$.

Relations between the stiffnesses (C_{ij}) and the compliances (S_{ij}) are given by Cline et al. (1967) and by Nye (1957). Poisson's ratio (ν) and Young's modulus (E), with the values of K and G determined by Voigt's or Reuss' averaging

procedures, can be computed from

$$2\nu = \frac{3K - 2G}{3K + G} \tag{8.15}$$

and

$$9E^{-1} = 3G^{-1} + K^{-1}. \tag{8.16}$$

The currently-accepted method for averaging single crystal constants to compute bulk properties was proposed by Hill (1952). Based on energy arguments, he proved that Voigt's method provided the upper bound and Reuss's method the lower bound such that the arithmetic mean of their averages would yield more accurate results than either individual average. This is expressed as

$$2M_H = M_V + M_R \tag{8.17}$$

where M_H, M_V and M_R represent the Hill, Voigt, and Reuss averages of any of the elastic moduli or Poisson's ratio. Hill's (1952) average has been used in this chapter where computed bulk (or isotropic polycrystalline) properties are given.

At or near absolute zero the elastic constants determine the thermal spectrum of lattice vibrations and, consequently, the Debye temperature. Since elastic constants can be determined with high precision, it is useful to calculate the Debye temperature from acoustic wave velocities, i.e. from elastic constants measured near absolute zero. In the Debye theory the characteristic temperature at absolute zero is given (Anderson, 1963) by

$$\theta^3 = \left(\frac{h}{k}\right)^3 \left[\frac{3qN\rho}{4\pi M}\right] v_m^3 \tag{8.18}$$

where $\theta = \theta_D$ when $T \simeq 0$, h and k = Planck's and Boltzmann's constants respectively, N = Avogadro's number, M = molecular weight, ρ = density, q = number of atoms in the molecule = 1 for pure metals, and v_m = a mean velocity.

Various methods have been proposed (for example, Wolcott, 1959, and Anderson, (1963)) for calculating a mean, or isotropic, acoustic wave velocity from elastic anisotropic crystals. In this chapter, Anderson's (1963) averaging scheme was employed where θ's were computed from C_{ij}'s because it is inherently suited to such calculations. In his scheme, Anderson approximates the mean velocity, v_m, by $\bar{v}_m$ which is defined in the following expression

$$\bar{v}_m^3 = \left(\frac{1}{3}\left[\frac{2}{\bar{v}_s^3} + \frac{1}{\bar{v}_l^3}\right]\right)^{-1} \tag{8.19}$$

where $\rho\bar{v}_s^2 = G_H$ and $3\rho\bar{v}_l^2 = 3K_H + 4G_H$. A few comparisons indicated that θ's calculated with Anderson's (1963) average were within one percent of the θ's calculated with Wolcott's (1959) mean velocity which is based on a more rigorous approach.

The literature on elastic properties is replete with references to Debye temperatures (θ_D) computed from wave velocities using eq. (8.18) at temperatures above absolute zero. In the strict sense, eq. (8.18) gives the Debye

temperature only when the elastic wave velocities have been measured near absolute zero. Accordingly, in this chapter, the term "theta" (θ) is used to describe the quantity often erroneously called the Debye temperature. In fact, the Debye temperature is equal to theta ($\theta_D = \theta$) only at absolute zero.

Elastic anisotropy of cubic crystals is describable by a single ratio: That is not the case for hexagonal materials. Three ratios of C_{ij}'s are necessary to define the anisotropy of hexagonal crystals and all three must equal unity simultaneously if the crystal is to be declared isotropic. The three ratios are (see Fisher and Alfred, 1968)

$$A^* = C_{44}/C_{66} = 2C_{44}/(C_{11} - C_{12}), \qquad B^* = C_{33}/C_{11}, \qquad C^* = C_{12}/C_{13}. \tag{8.20}$$

Anisotropy ratios are given in table 8.22 when C_{ij}'s were available.

Temperature and pressure dependencies of the elastic constants sometimes are required and are often informative. This chapter contains graphical presentations of the temperature dependence of polycrystalline constants and C_{ij}'s where data were available. However, pressure dependencies have not been included because so little data exists. Readers who are concerned with pressure dependencies of elastic properties are referred to a paper by Guinan and Steinberg (1974) which lists estimated temperature and pressure derivatives of the polycrystalline constants for all the rare earth metals except promethium. When experimental data for the pressure dependence of rare earth metal elastic constants were presented, the writer has provided appropriate references in the pertinent section for the metal involved.

Finally, magnetic transitions and the affect of applied magnetic fields must be mentioned in regard to their modification of the elastic constants. A host of magnetic-related phenomena have a variety of influences on the elastic constants and their measurement. Currently, the details of magnetic structures in several of the rare earth metals are not well understood. Consequently, the writer has refrained from interpretative comments about subtle anomalies in the temperature dependence of the elastic constants. In the measurement of elastic constants it is appropriate to correct acoustic path length for magnetostriction strains as well as thermal expansion because these factors influence the accuracy of acoustic wave velocity measurements and are not inherent characteristics of the resulting constants. However, the writer was confronted with a more problematic decision about whether to present C_{ij}'s determined from wave velocities measured in a magnetic field. Granted, magnetic saturation fields serve to eliminate domain wall motion in ferromagnetic phases and alter magnetoelastic and magnetostrictive effects which aid in the separation of fundamental phenomena involved in magnetic transitions. Nevertheless, the writer decided to present only data taken in zero magnetic field. There were two primary reasons for this choice. In the applications of the C_{ij}'s the user is concerned about the response to stress that the material undergoes and not about the various reasons for that response. Of course, from the crystal physics point of view, it is desirable to know the "real" elastic constants for interatomic force calculations etc. In order not to ignore this point of view, references are given for the investigations which studied

applied magnetic field effects. The user of such information is better prepared to extract the desired data from the reference than is the user of the constants for mechanics application. Secondly, it seemed inconsistent to present some data measured in magnetic fields when such data were not available for all the metals. Magnetostriction, *per se*, is not discussed in this chapter.

9.1. *Scandium*

The only single crystal elastic constant data for scandium were measured by Fisher and Dever (1968) over the temperature range 4 to 300 K. Although they employed crystals of three different purities and two Sc-Gd alloys, only the results from the highest purity (903 ppm impurity, not including non-metallics) material are reported here. Figure 8.50 illustrates the temperature dependence of the four constants C_{11}, C_{33}, C_{44} and C_{66}. Unfortunately, Fisher and Dever (1968) measured C_{13} only at room temperature and with a different crystal. Consequently, it is impossible to compute the temperature dependence of the polycrystalline elastic properties (bulk properties) from their single crystal elastic constant data. Following Gschneidner (1975), room temperature bulk elastic properties were computed with the assumption that C_{13} would not differ greatly from one crystal to the other. In fact, the maximum difference in the C_{ij} between the two crystals was 1.8%.

Brown et al. (1966) determined the room temperature Young's and shear moduli of scandium (~7250 ppm impurity including 5800 oxygen). Bulk modulus and Poisson's ratio were computed from the data. Calculation of the bulk modulus and Poisson's ratio from Young's and shear moduli implies that the material is homogeneous and isotropic. Despite the use of polycrystalline scandium made by swaging and annealing a rod that had solidified in a water-

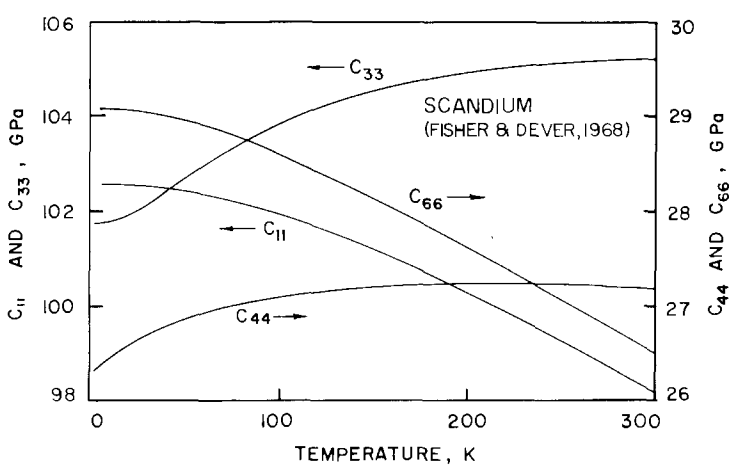

Fig. 8.50. Temperature dependence of the elastic stiffness constants of scandium. Fisher and Dever (1968).

TABLE 8.8.
Adiabatic elastic properties of scandium.

E(GPa)	G(GPa)	K(GPa)	ν	θ_D(K)	T(K)	Reference
74.4[a]	29.1[a]	56.6[a]	0.278[a]	–	298	Fisher and Dever (1968)
–	–	66.5[b]	–	–	298	Stephens (1964)
–	–	43.8[b]	–	–	298	Monfort and Swenson (1965)
75.5	28.8	65.9	0.309	–	298	Brown et al. (1966)
79.2	–	–	–	–	298	Geiselman (1962)
79.9	31.8	55.2	0.257	–	298	Gust and Royce (1973)
–	–	78.8[c]	–	–	295	Al'tshuler et al. (1968)

[a]Computed from experimental single crystal constants, see text; [b]Converted from the isothermal result using Gschneidner's (1964) values for α, ω and C_p in eq. (8.5); [c]From shock compression results for v_B in eq. (8.8).

cooled copper mold after arc-melting, they concluded that the compressibility (reciprocal of the bulk modulus) was low and Poisson's ratio was high as a result of some remnant directionality. Consequently, the bulk properties given by the Hill (1952) averages of Fisher and Dever's (1968) single crystal constants were deemed the best values and included in table 8.22. Data from other sources are given, for comparison, in table 8.8.

Stephens (1964) and Monfort and Swenson (1965) determined the room temperature isothermal compressibility of scandium up to 45 kbar and 20 kbar respectively.

9.2. *Yttrium*

Three sources of elastic property data for yttrium were found: Smith et al. (1957), Gust and Royce (1973), and Smith and Gjevre (1960). Only the latter determined the temperature dependence of the single crystal elastic constants; they are shown in fig. 8.51. Smith and Gjevre (1960) employed the ultrasonic pulse-echo technique (10 MHz) with crystals of better than 99% purity, titanium and oxygen being the primaary impurities. They made corrections for density and dimensional variations with temperature. It should be noted that C_{44} and C_{66} data were interchanged in their paper. Using their single crystal elastic constants, the polycrystalline values of Young's modulus (E), shear modulus (G), bulk modulus (K), Poisson's ratio (ν) and theta (θ) were computed. The temperature dependence of the computed values is illustrated in figs. 8.52 and 8.53 while values at room temperature (300 K) and absolute zero (usually 4.2 K) are given in table 8.9. Comparison of bulk properties computed from the single crystal constants with the experimental polycrystalline values (table 8.9) obtained by Smith et al. (1957) and by Gust and Royce (1973) reveals good agreement. Consequently, the writer has chosen as best values (summary table 8.22) those computed from single crystal constants in order to provide a consistent set of data from 4.2 K to 400 K.

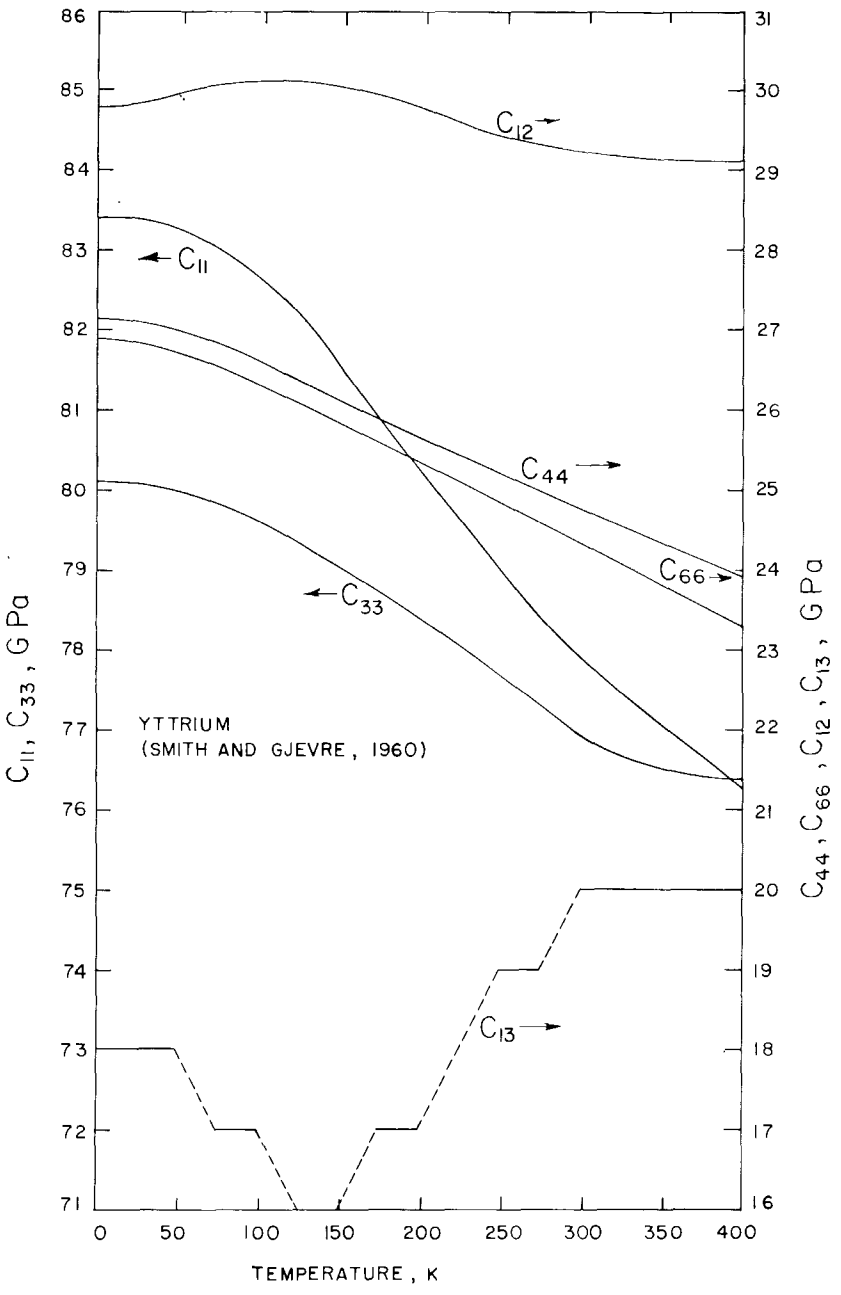

Fig. 8.51. Temperature dependence of the elastic constants of yttrium. Smith and Gjevre (1960).

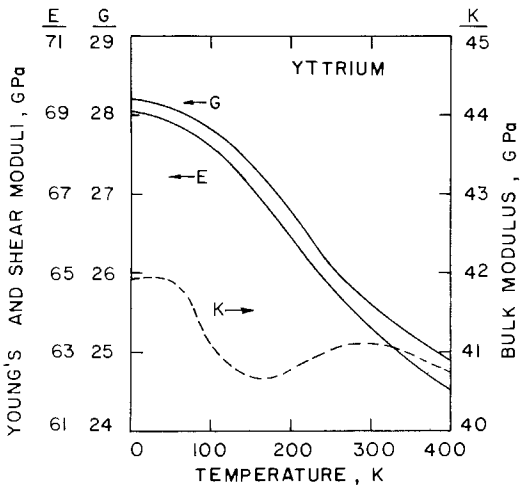

Fig. 8.52. Temperature dependence of Young's (E), shear (G), and bulk (K) moduli computed from the single crystal constants of yttrium.

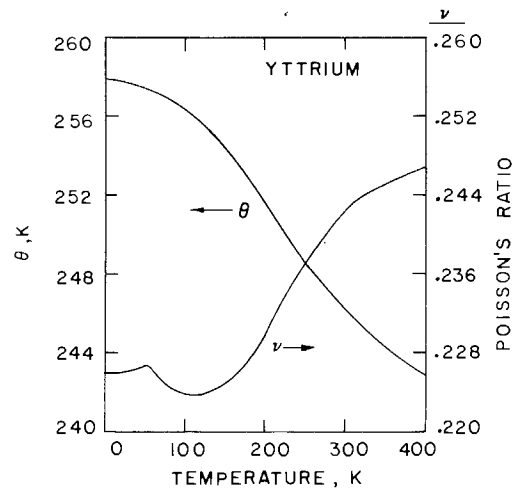

Fig. 8.53. Temperature dependence of Poisson's ratio (ν) and theta (θ) of yttrium. Computed from single crystal elastic constants.

TABLE 8.9.
Adiabatic elastic properties of yttrium.

E(GPa)	G(GPa)	K(GPa)	ν	θ_D(K)	T(K)	Reference
66.3	26.2	46.9	0.265	–	298	Smith et al. (1957)
60.9	23.5	49.8	0.296	–	298	Gust and Royce (1973)
63.5[a]	25.6[a]	41.2[a]	0.243[a]	–	300	Smith and Gjevre (1960)
69.1[a]	28.2[a]	41.9[a]	0.226[a]	258[a]	0	Smith and Gjevre (1960)
–	–	49.8[b]	–	–	295	Al'tshuler et al. (1968)

[a]Computed from experimental single crystal constants; [b]From shock compression results for v_B in eq. (8.8).

TABLE 8.10.
Adiabatic elastic properties of lanthanum.

E(GPa)	G(GPa)	K(GPa)	ν	θ_D(K)	T(K)	Reference
–	14.5	–	–	–	293	Dashkovskiy and Savitskiy (1961)
33.7	13.6	16.0	0.166	–	300	Rosen (1967)
35.0	13.3	16.0	0.135	154	0	Rosen (1967)
38.4	14.9	30.3	0.288	–	298	Smith et al. (1957)
36.6	14.3	27.9	0.280	–	298	Gust and Royce (1973)
–	–	28.7[a]	–	–	295	Al'tshuler et al. (1968)
–	–	25.0[b]	–	–	300	Syassen and Holzapfel (1975)
–	–	25.3[b]	–	–	298	Bridgman (1954)
–	–	24.8[b]	–	–	300	Vaidya and Kennedy (1970)

[a]From shock compression results for v_B in eq. (8.8). [b]Converted from isothermal values using Gschneidner's (1964) data for α, ω and C_p in eq. (8.5).

9.3. *Lanthanum*

Apparently, the only information about the temperature dependence of the elastic properties of lanthanum was obtained by Dashkovskiy and Savitskiy (1961). During internal friction studies at a frequency of 4.5 Hz they determined the shear modulus from 293 to about 923 K. The results are presented in fig. 8.46, with the internal friction data, as the ratio of $G(T)/G(293)$. Their $G(293)$ value was $(14.51 \pm 0.49$ GPa). A sharp change in shear modulus at about 630 K was attributed to the d.h.c.p. to f.c.c. polymorphic phase change. Their $G(293)$ value compares well with values of 13.6 GPa by Rosen (1967), 14.9 GPa by Smith et al. (1957) and 14.3 GPa by Gust and Royce (1973) all using ultrasonic methods. Literature values for other room temperature bulk elastic properties of lanthanum are summarized in table 8.10. The writer's choice of best values is those given by Gust and Royce (1973) (see table 8.22) because they are self-consistent and lower than all but Rosen's values which are suspect because of the extremely low values of Poisson's ratio and bulk modulus. The bulk modulus values obtained by isothermal techniques and converted to adiabatic values are somewhat lower than the values obtained in adiabatic experiments but are in reasonable agreement with them.

9.4. *Cerium*

No single crystal elastic constant data for cerium were found by the writer: This probably reflects the difficulty of obtaining suitable single phase crystals. The most complete and systematic investigation of the polycrystalline elastic properties of cerium was conducted by Rosen (1969a). He used an ultrasonic pulse technique employing a frequency of 10 MHz to measure sound velocities in spectrographically pure (99.9+%) metal and corrected the acoustic path

length for thermal expansion during both cooling and heating cycles. His results are illustrated in figs. 8.54, 8.55 and 8.56. All three elastic properties, Young's modulus (E), shear modulus (G), and compressibility (χ_s) reveal substantial differences between the measurements taken during cooling from room temperature and those taken during heating. The differences result from phase transformations and associated hystereses. The samples were in the γ phase at room temperature at the start of the cooling cycle. The abrupt rise of E and G and the decrease in compressibility near 270 K signal the onset of the γ(f.c.c.) to β(d.h.c.p.) transformation. Near 160 K, E and G begin to decrease and the compressibility begins to increase. Presumably, these trends reflect lattice softening as the temperature approaches that (110 K) at which the remaining γ transforms to α(f.c.c, $a = 4.85$, see ch. 4 section 2.4.5). There is a sharp rise in E and G and a dip in the compressibility associated with the γ-to-α transformation followed by a second, broader anomaly in each of the elastic properties at a slightly lower temperature: The origin of this anomaly is uncertain but Rosen suggested it might be associated with β-to-α transformation. Below about 91 K, both E and G continue to decrease while the compressibility increases down to about 31 K where a reversal in all the elastic properties occurs. Other types of measurements have revealed an anomaly ascribed to magnetic ordering at 13 K but none have been reported at 31 K. Consequently, there is no ready explanation for the appearance of the minimum in E and G and of the maximum in

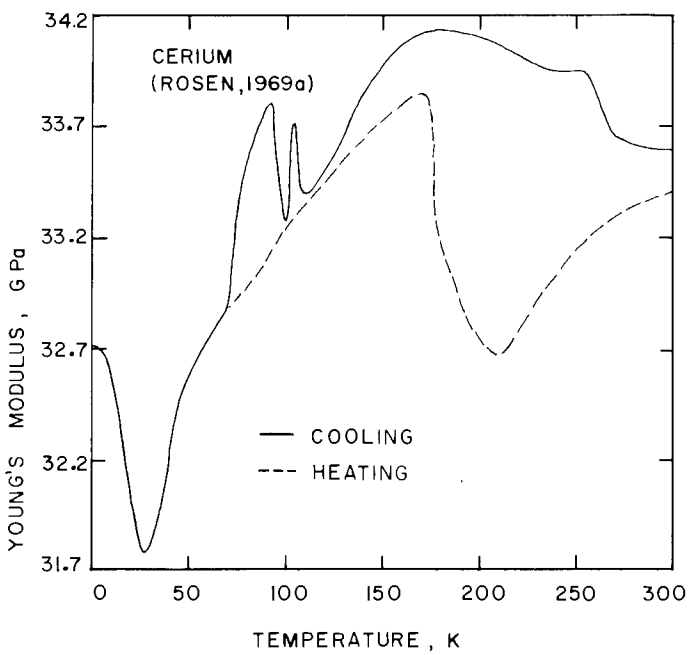

Fig. 8.54. Young's modulus of polycrystalline cerium during cooling and heating. Below about 80 K the heating and cooling data lie on the same curve. Rosen (1969a).

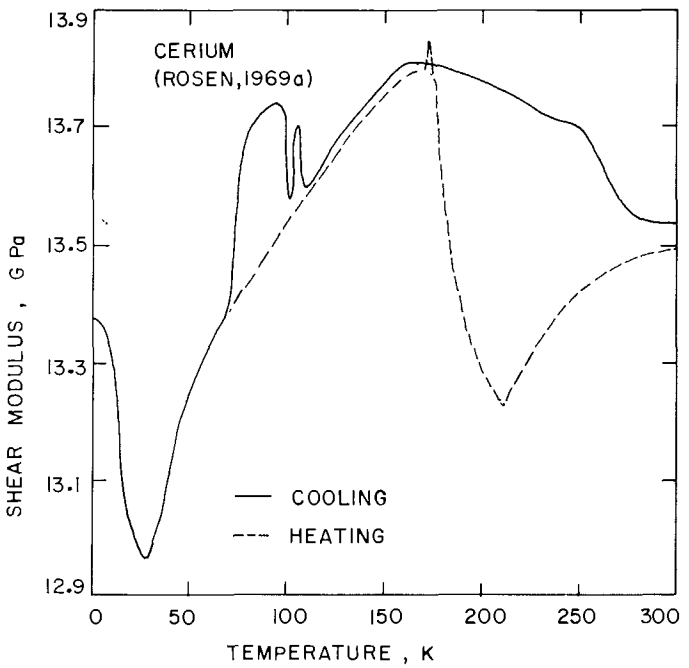

Fig. 8.55. Cooling and heating behavior of the shear modulus of cerium. Below about 70 K the heating and cooling data lie on the same curve. Rosen (1969a).

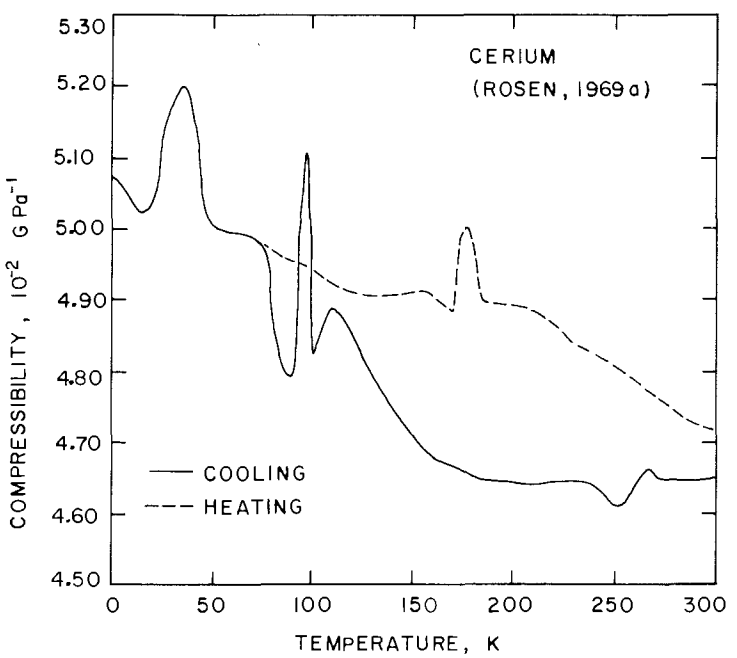

Fig. 8.56. Temperature dependence of the compressibility of cerium during cooling and heating. Below about 75 K heating and cooling data lie on the same curve. Rosen (1969a).

compressibility at 31 K; however, they are reproduced during heating from 4.2 K. During the heating cycle the structure is a mixture of α and β phases up to about 175 K where E and G drop sharply and the compressibility exhibits a peak. These are all associated with the α-to-β and α-to-γ transformations. From the minimum at about 213 K to room temperature both E and G rise while the compressibility decreases. At room temperature the elastic properties do not regain their prior room temperature values because the structure is not transformed completely back to the γ phase. Extrapolation of the heating and cooling curves indicates the samples would have to be heated to about 380 K to restore completely the γ structure. The abrupt rise in E at the γ-to-α transformation was also noted by Clinard (1969) who used a resonant bar technique but he did not notice the change associated with the γ-to-β transformation near 270 K. This may have been a matter of purity difference or sensitivity of measurement. Varanov et al. (1960) measured the adiabatic polycrystalline constants of cerium (presumably all γ-phase) at 289 K as a function of pressure. The bulk modulus (K) and Poisson's ratio (ν) decreased significantly while E decreased slightly and G rose slightly as the pressure was increased to approximately 0.74 GPa (7560 kg/cm^2) where the γ-to-α transformation occurred; when γ transformed to α the anomalous behavior ceased. On decreasing the pressure from a maximum of 0.93 GPa (9500 kg/cm^2), all the elastic properties, except Poisson's ratio, decreased until the α-to-γ transformation occurred at 0.58 GPa (5950 kg/cm^2). Evdokimova and Genshaft (1965) observed a similar pressure dependence for the isothermal Young's modulus. Only the zero pressure values are quoted in the summary given in table 8.11.

Although they are slightly higher than some of the others, Rosen's (1969a) values at room temperature and 4.2 K are given in table 8.22 as the best values because they provide a more complete set. It should also be noted that Savitskiy and Dashkovskiy (1961) have determined the shear modulus from 293 to about

TABLE 8.11.
Adiabatic elastic properties of gamma cerium.

E(GPa)	G(GPa)	K(GPa)	ν	θ_D(K)	T(K)	Reference
30.0	12.0	19.8	0.248	–	298	Smith et al. (1957)
30.0	11.8	21.7	0.269	–	298	Gust and Royce (1973)
33.6	13.5	21.5	0.244	–	300	Rosen (1969a)
32.7[a]	13.4[a]	19.8[a]	0.220[a]	139[a]	4.2	Rosen (1969a)
–	13.24 ± 0.49[b]	–	–	–	293	Savitskiy and Dashkovskiy (1961)
30.2	12.0	19.8	0.25	–	289	Varanov et al. (1960)
–	–	27.4[b]	–	–	298	Frolov et al. (1969)
–	–	11.2[a,b]	–	–	298	Frolov et al. (1969)
–	–	25.6[b]	–	–	292	Evdokimova and Genshaft (1965)
–	–	20.9[b]	–	–	298	Bridgman (1954)

[a]For alpha (α) cerium; [b]Converted from isothermal to adiabatic using Gschneidner's (1964) values for C_p, ω and α in eq. (8.5).

873 K by the internal friction method as shown in fig. 8.47. The shear modulus decreased almost linearly from 293 to about 673 K where a sudden change in slope occurred; the investigators attributed this to grain boundary relaxation effects. Bridgman (1954), Evdokimova and Genshaft (1965) and Frolov et al. (1969) have determined isothermal compressibilities. For the sake of comparison, these isothermal compressibilities have been converted to adiabatic bulk moduli (See table 8.11).

Schaufelberger and Merx (1975) have also investigated the pressure dependence of the relative volume from 2 GPa to 10 GPa.

9.5. *Praseodymium*

The elastic properties of praseodymium have been determined by Gust and Royce (1973), Smith et al. (1957), Rosen (1969b) and Greiner et al. (1973). Isothermal compressibilities have been measured by Stephens (1964) and Bridgman (1954). However, only Rosen (1969b) and Greiner et al. (1973) have investigated the temperature dependence of the properties and, although Lüthi et al. (1973) measured the sub-ambient temperature dependencies of C_{33} and C_{44}, only Greiner et al. employed single crystals.

The single crystal data of Greiner et al. (1973), measured by the ultrasonic pulse-echo-overlap method (10 MHz), are presented in fig. 8.57. The writer chose the C_{44} value obtained from their quasinormal shear wave at 90° to the c-axis because they did not correct for thermal expansion; this correction would be smaller for measurements normal to the c-axis. The forms of the temperature dependencies of C_{33} and C_{44} obtained by Lüthi et al. (1973) agree well with those of Greiner et al. (1973) but the latter's values are somewhat higher, especially in the case of C_{33}. Both groups of investigators noted a sharp minimum in C_{33} at about 35 K. Polycrystalline elastic properties computed from the single crystal data of Greiner et al. (1973) are shown in figs. 8.58 and 8.59. These graphs afford a comparison with the experimentally-determined polycrystalline properties obtained by Rosen (1969b). Most striking in figs. 8.58 and 8.59 is the appearance of a sharp minimum or maximum in all the properties at about 40 K (25 to 40 K for single crystal data). This anomaly has been observed in other physical properties but its cause has not been firmly established. The temperature dependencies of E, G, and θ from Rosen's (1969b) work agree qualitatively, but not quantitatively, with the data of Greiner et al. (1973) who obtained somewhat higher values. A significant point of disagreement between the results of these two investigations is evident in the compressibility or bulk modulus. Greiner et al. (1973) found only one dip in the bulk modulus. However, Rosen (1969b) detected two peaks in the compressibility (the reciprocal of bulk modulus). One peak near 25 or 30 K corresponds to the dip in bulk modulus of Greiner et al. The second compressibility peak occurred at about 75 K and has no counterpart in the results of Greiner et al. who observed a smoothly-increasing bulk modulus at this temperature. The reason for the discrepancy is uncertain. The data of Greiner et al. (1973) were selected for inclusion in table 8.22 because they were

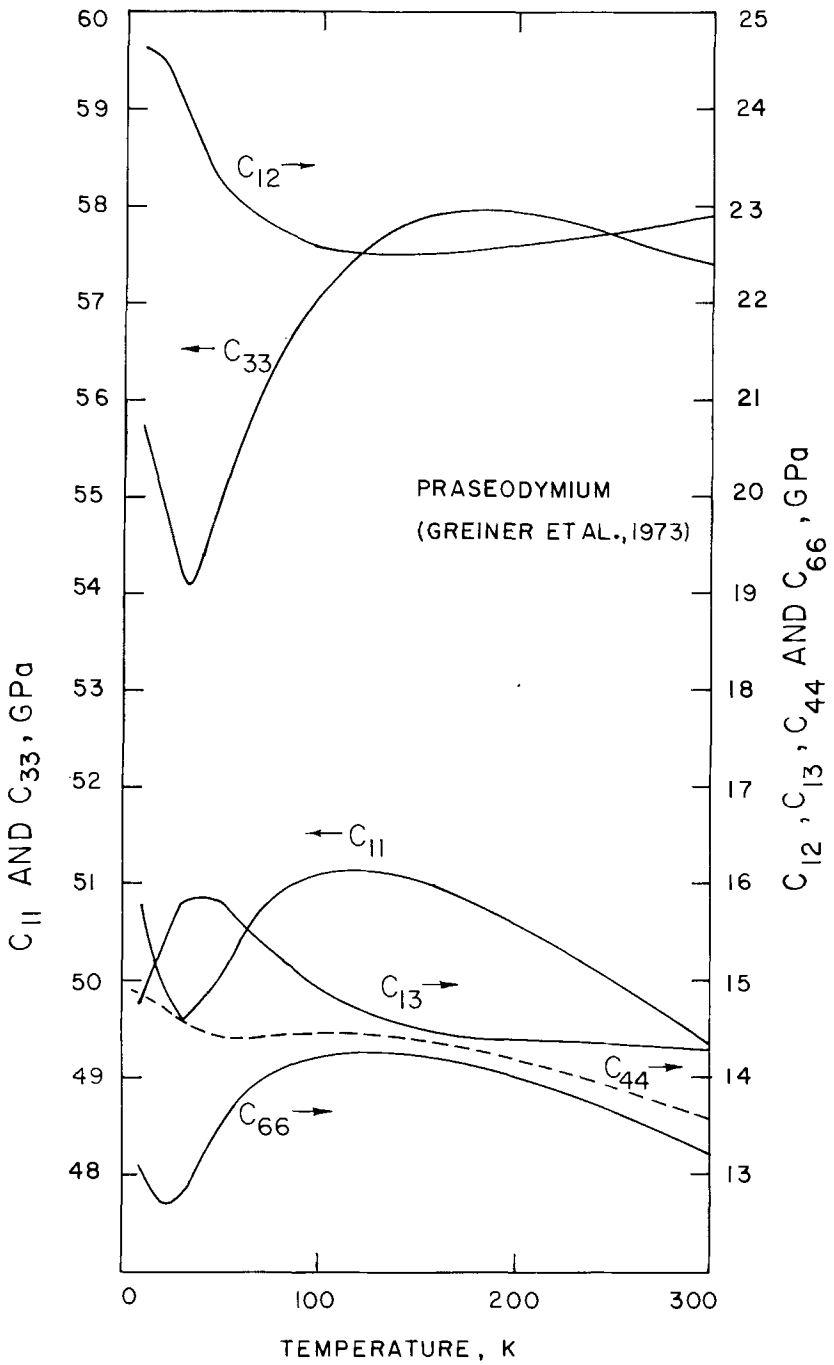

Fig. 8.57. Elastic stiffness constants of praseodymium. Greiner et al. (1973).

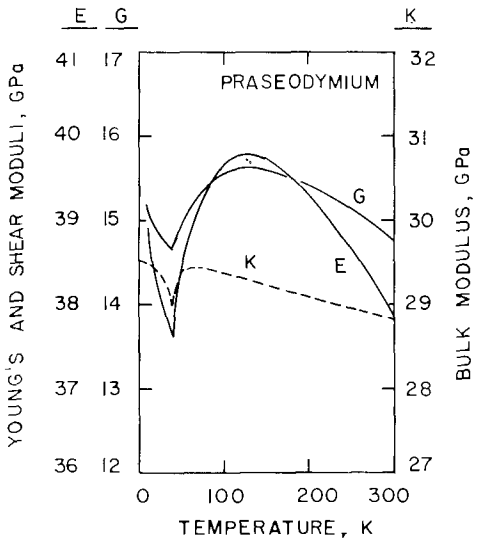

Fig. 8.58.

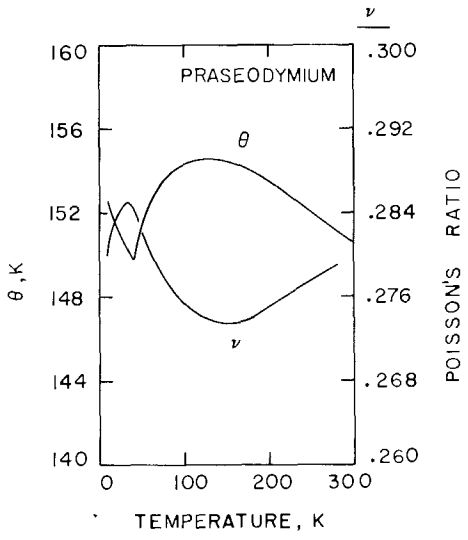

Fig. 8.59.

Fig. 8.58. Young's (E), shear (G), and bulk moduli (K) of praseodymium computed from the single crystal data shown in fig. 8.57.
Fig. 8.59. Poisson's ratio (ν) and theta (θ) of praseodymium computed from the single crystal constants shown in fig. 8.57.

TABLE 8.12.
Adiabatic elastic properties of praseodymium.

E(GPa)	G(GPa)	K(GPa)	ν	θ_D(K)	T(K)	Reference
38.5	15.0	29.9	0.283	–	298	Gust and Royce (1973)
35.2	13.5	29.9	0.305	–	298	Smith et al. (1957)
–	–	26.6[a]	–	–	298	Bridgman (1954)
36.0	13.9	28.0	0.291	–	300	Rosen (1969b)
36.1	13.9	29.8	0.297	146	4.2	Rosen (1969b)
37.8[b]	14.8[b]	28.8[b]	0.281[b]	–	300	Greiner et al. (1973)
38.9[b]	15.2[b]	29.5[b]	0.280[b]	153[b]	10	Greiner et al. (1973)
–	–	37.6[a]	–	–	298	Stephens (1964)

[a]Converted from the isothermal value using Gschneidner's (1964) values for α, ω and C_p in eq. (8.5). [b]Computed from experimental single crystal constants.

obtained from the only complete set of single crystal data available. Data from several sources are provided for comparison in table 8.12.

9.6. *Neodymium*

Smith et al. (1957) and Gust and Royce (1973) have measured the polycrystalline elastic constants of neodymium at ambient temperature with reason-

TABLE 8.13.
Adiabatic elastic properties of neodymium.

E(GPa)	G(GPa)	K(GPa)	ν	θ_D(K)	T(K)	Reference
40.7	15.8	31.0	0.288	–	300	Rosen (1969a)
45.6	17.6	33.7	0.295	163	0	Rosen (1969a)
37.9	14.5	32.5	0.306	–	298	Smith et al. (1957)
43.1	16.8	33.1	0.283	–	298	Gust and Royce (1973)
–	–	32.9[a]	–	–	298	Bridgman (1954)
41.8[b]	16.3[b]	31.8[b]	0.281[b]	–	300	Greiner et al. (1976)
45.6[b]	18.0[b]	33.0[b]	0.269[b]	163[b]	4.2	Greiner et al. (1976)
–	–	–	–	168	4	Lenkkeri and Palmer (1977)
–	–	30.3[c]	–	–	295	Al'tshuler et al. (1968)

[a]Converted from an isothermal result using Gschneidner's (1964) values for α, ω and C_p in eq. (8.5). [b]Computed from experimental single crystal constants. [c]From shock compression results for v_B in eq. (8.8).

ably good agreement as shown in table 8.13. The temperature dependence of the polycrystalline elastic properties was determined by Rosen (1969b). His results at room temperature, given in table 8.13, agree with those just cited. Below 50 K, anomalies appear in all the elastic properties. For E, G, and θ, a sharp rise begins at about 50 K and is followed by a rapid drop to a minimum at 18 K; this drop is associated with antiferromagnetic ordering. No anomaly was observed at 7.5 K where other physical properties revealed an additional magnetic-structure transformation. The adiabatic compressibility appears more complicated with two minima (one at about 50 K and another at about 18 K) and two peaks (one at 30 K and one near 12 K).

Lenkkeri and Palmer (1977) have determined four of the single crystal elastic constants from 4 to 280 K using the ultrasonic pulse-echo-overlap technique (15 MHz). Unfortunately, they did not measure C_{13} which is necessary for computing bulk properties to compare with experimental polycrystalline constants. Nevertheless, their single crystal constants reveal anomalies below 25 K. In the case of C_{11} and C_{66} minima appear at about 21.5 K, about 9 K, and about 6 K. Much smaller anomalies occur in C_{33} at these temperatures while C_{44} exhibits only one anomaly at 8 K. These anomalies have been interpreted in terms of antiferromagnetic ordering between B and C layers (hexagonal environment) for the 21.5 K anomaly and in terms of a more complicated magnetic ordering involving the A layer (cubic environment) for the 9 and 6 K anomalies in the ABAC stacked structure of neodymium.

Greiner et al. (1976) also have determined the single crystal elastic constants from 6 to 300 K using the ultrasonic pulse-echo-overlap (10 MHz) method. No thermal expansion corrections for density and acoustic path length were made because no thermal expansion data were available in the experimental temperature range. In addition to the four constants measured by Lenkkeri and Palmer (1977), Greiner et al. measured C_{13}; consequently, polycrystalline elastic

constants were computed from their single crystal data. The results of Greiner et al. (1976) are quantitatively somewhat lower than those of Lenkkeri and Palmer (1977) suggesting purer material. Greiner et al. (1976) observed cusped anomalies in the ultrasonic wave velocities near 19 K and 7.5 K; however, they are not evident in the single crystal elastic constants (fig. 8.60) or in the computed polycrystalline results (figs. 8.61 and 8.62). Lenkkeri and Palmer (1977) took measurements at close temperature intervals and found a double anomaly at 6

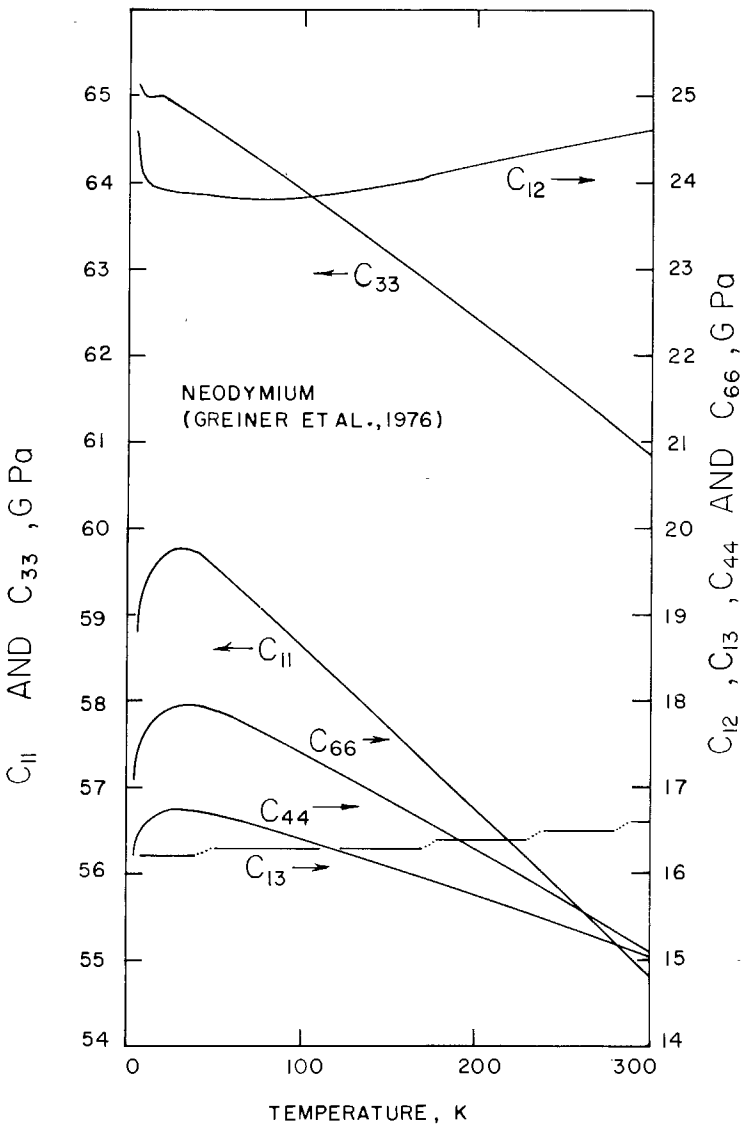

Fig. 8.60. Elastic stiffnesses of neodymium. Greiner et al. (1976).

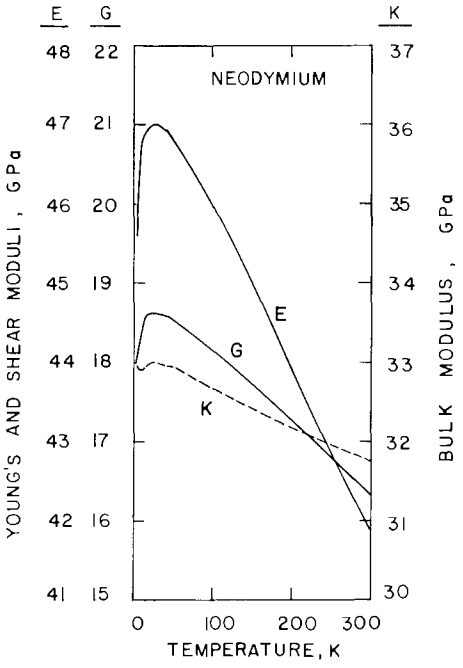

Fig. 8.61.

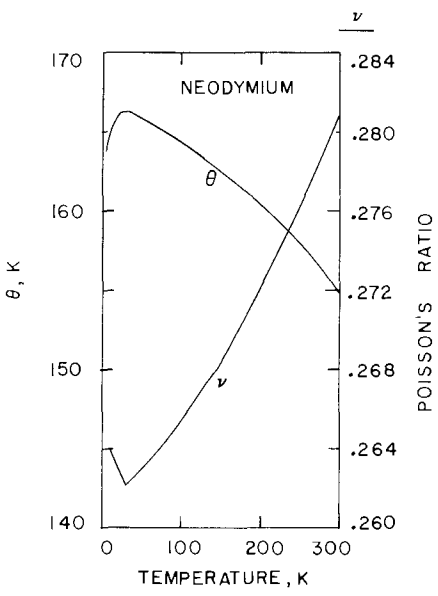

Fig. 8.62.

Fig. 8.61. Young's (E), shear (G), and bulk (K) moduli of neodymium computed from the single crystal data in fig. 8.60.
Fig. 8.62. Poisson's ratio (ν) and theta (θ) of neodymium computed from the single crystal data in fig. 8.60.

and 9 K. On the other hand, Greiner et al. (1976) found only a single anomaly at 7.5 K. Otherwise, there is good qualitative agreement between the results of the two groups of investigators. The temperature dependencies of the computed polycrystalline elastic properties do not reveal the same details in the region of magnetic ordering that were exhibited by Rosen's (1969b) data. Perhaps the magnetic behavior of polycrystalline material is sufficiently different from that of single crystals to alter the details of the behavior. Because they were determined with single crystals and provide a more complete set than offered by Lenkkeri and Palmer (1977), the results of Greiner et al. (1976) were chosen for inclusion in table 8.22. Their single crystal data are plotted in fig. 8.60 while the bulk properties computed from them are given in figs. 8.61 and 8.62.

9.7. *Promethium*

There are no elastic property data for promethium.

9.8. *Samarium*

The only determination of the temperature dependence of the elastic properties of samarium was done with polycrystalline material by Rosen (1969b) who used an ultrasonic pulse (10 MHz) technique and corrected the acoustic path length for thermal contraction. His results are shown in figs. 8.63 and 8.64. Smith et al. (1957) and Gust and Royce (1973) have determined room temperature values of the polycrystalline elastic properties while Bridgman (1954) has determined the room temperature compressibility (reciprocal bulk modulus). These data are summarized in table 8.14. According to Rosen's (1969b) results, the Young's (E) and shear (G) moduli increase normally with decreasing temperature to a broad maximum centered near 75 K. Further cooling causes rapid lattice softening until a minimum, which is associated with magnetic ordering, is reached at 14 K. Theta follows the pattern of E and G while the adiabatic bulk modulus (K) is approximately temperature independent down to about 165 K where it rises to form a broad peak with maximum at 109 K followed by a decrease to a minimum at 70 K. Anomalies due to ordering of the hexagonal sites in samarium have been observed in other properties at 109 K. A minimum in K is also observed at the magnetic ordering temperature of 14 K; this minimum is caused by ordering of the cubic sites.

The summary, table 8.14, shows that all the bulk modulus values except Bridgman's (1954) are in reasonable agreement. Room temperature values for E, G, and ν obtained by Gust and Royce (1973) and by Rosen (1969b) are very close but the values of E and G obtained by Smith et al. (1957) are considerably lower; consequently, ν is considerably higher suggesting purer material. Never-

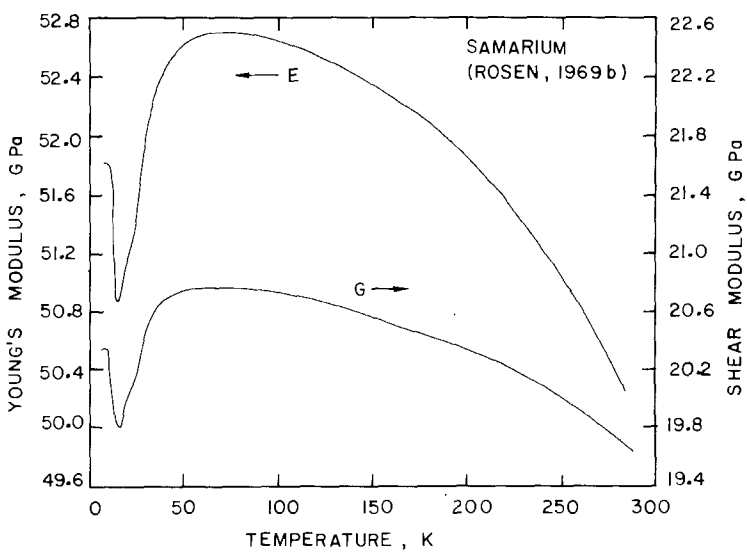

Fig. 8.63. Young's (E) and shear (G) moduli of polycrystalline samarium. Rosen (1969b).

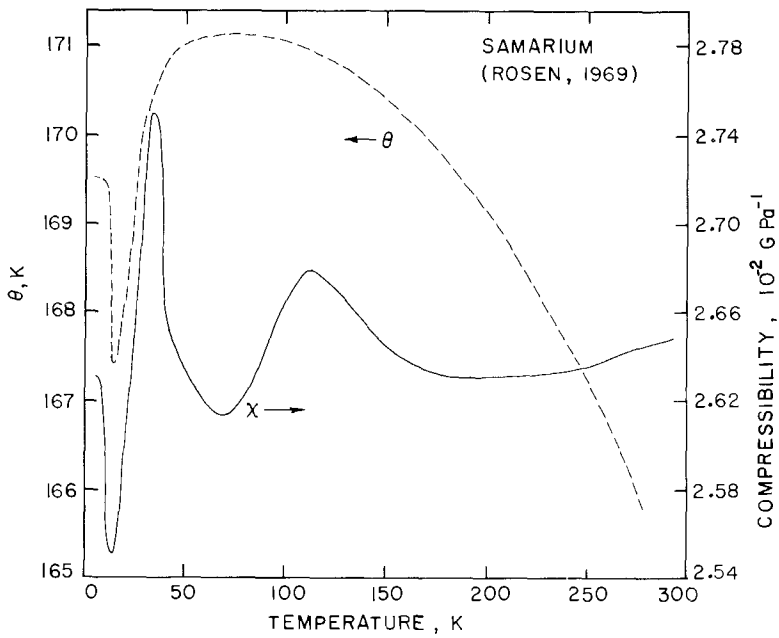

Fig. 8.64. Compressibility (χ_s) and theta (θ) of polycrystalline samarium. Rosen (1969b).

TABLE 8.14.
Adiabatic elastic properties of samarium.

E(GPa)	G(GPa)	K(GPa)	ν	θ_D(K)	T(K)	Reference
34.1	12.6	38.3	0.352	–	298	Smith et al. (1957)
50.6	19.9	37.3	0.272	–	298	Gust and Royce (1973)
49.7	19.5	37.8	0.274	–	300	Rosen (1969b)
51.8	20.3	38.0	0.276	169	0	Rosen (1969b)
–	–	28.2[a]	–	–	298	Bridgman (1954)
–	–	36.0[b]	–	–	295	Al'tshuler et al. (1968)

[a]Converted from an isothermal result using Gschneidner's (1964) data for α, C_p and ω in eq. (8.5). [b]From shock compression results for v_B in eq. (8.8).

theless, the writer selected Rosen's (1969b) results to tabulate in table 8.22 because they are more detailed and extensive.

9.9. *Europium*

The most extensive set of data for the elastic properties of europium was measured on polycrystalline material by Rosen (1968a) using an ultrasonic pulse method (10 MHz); thermal contraction corrections for acoustic path length were made. The temperature dependencies of the elastic moduli and theta are

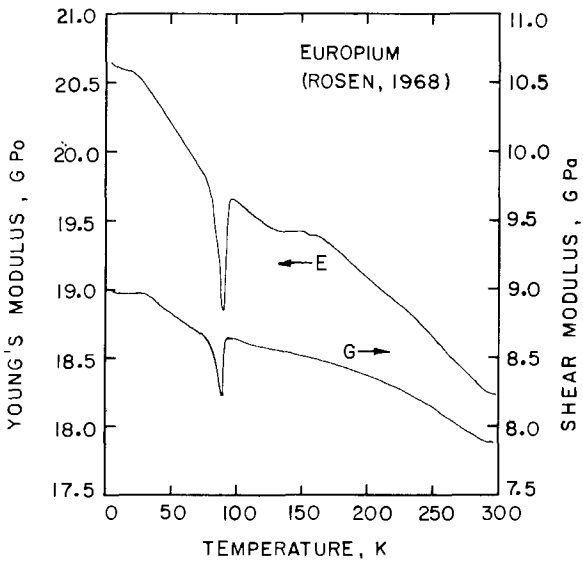

Fig. 8.65. Young's (E) and shear (G) moduli of polycrystalline europium. Rosen (1968).

shown in figs. 8.65 and 8.66. All the properties shown in figs. 8.65 and 8.66 indicate a sharp minimum at 91 K which is the Néel temperature for the antiferromagnetic transition. The compressibility exhibits an additional anomaly near 150 K which has been attributed (Rosen, 1968a) to an electronic structure transition.

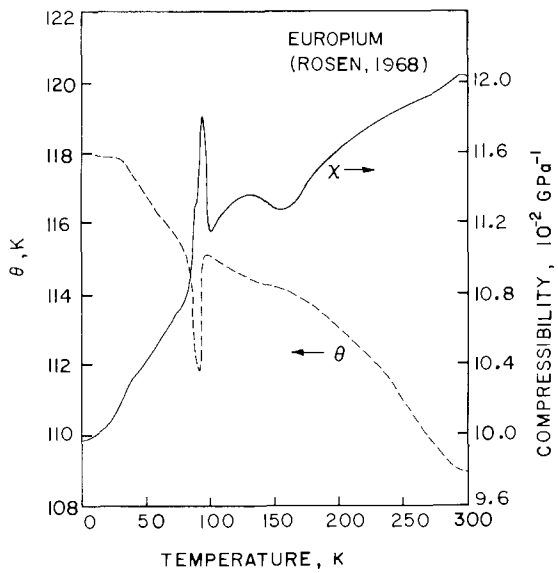

Fig. 8.66. Compressibility (χ_s) and theta (θ) of polycrystalline europium. Rosen (1968).

TABLE 8.15.
Adiabatic elastic properties of europium.

E(GPa)	G(GPa)	K(GPa)	ν	θ_D(K)	T(K)	Reference
–	–	12.9[a]	–	–	298	McWhan et al. (1966)
–	–	12.3[a]	–	–	297	Montfort and Swenson (1965)
–	–	13.7[a]	–	–	0	Montfort and Swenson (1965)
–	–	14.8[a]	–	–	298	Stephens (1964)
–	–	13.4[a]	–	–	300	Spedding et al. (1958)
19.6	7.5	17.1	0.308	–	298	Gust and Royce (1973)
18.2	7.9	8.3	0.152	–	300	Rosen (1969a)
20.6	9.0	10.0	0.144	118	4.2	Rosen (1968a)
21.4 ± 0.4	8.7 ± 0.2	13.2 ± 1	0.23 ± 0.01	–	293	Burkhanov et al. (1967)

[a]Converted from the isothermal result using Gschneidner's (1964) values for C_p, α and ω in eq. (8.5).

Burkhanov et al. (1967) have conducted measurements similar to Rosen but they did not extend their temperature range below 70 K. Although their results were qualitatively identical to those obtained by Rosen (1968a), the latter's values were lower indicating that the material was purer. The results of these investigators and several others are given in table 8.15 for comparison. Rosen's (1968a) results have been selected as best values for inclusion in table 8.22 because they cover the widest temperature range and appear to represent the highest purity europium. McWhan et al. (1966) and Monfort and Swenson (1965) have investigated the pressure dependence of the compressibility; their zero pressure results are included in table 8.15.

9.10. *Gadolinium*

The elastic properties of gadolinium have been studied by several investigators: Palmer et al. (1974), Fisher et al. (1973), Andreeva et al. (1971), Maeda (1971), Long et al. (1969), Rosen (1968a), and Belov et al. (1964). Palmer et al. (1974), Fisher et al. (1973), and Long et al. (1969) worked with single crystals while the others used polycrystalline samples. Long et al. (1969) only examined the behavior of C_{33} and C_{44}. With the exception of about two percent difference in the C_{11} results of Fisher et al. (1973) and Palmer et al. (1974), there is excellent agreement in the data from the three groups of investigators. Since the results of Palmer et al. (1974) are the most complete, the writer has chosen them for tabulation in the summary of best values, table 8.22, and for graphical exposition as shown in fig. 8.67. Bulk properties computed from them are shown in figs. 8.68 and 8.69. Table 8.16 gives data from several investigations for comparative purposes.

All the above-mentioned investigators observed anomalies in the elastic properties at about 290 K which corresponds to the Curie point of gadolinium (see

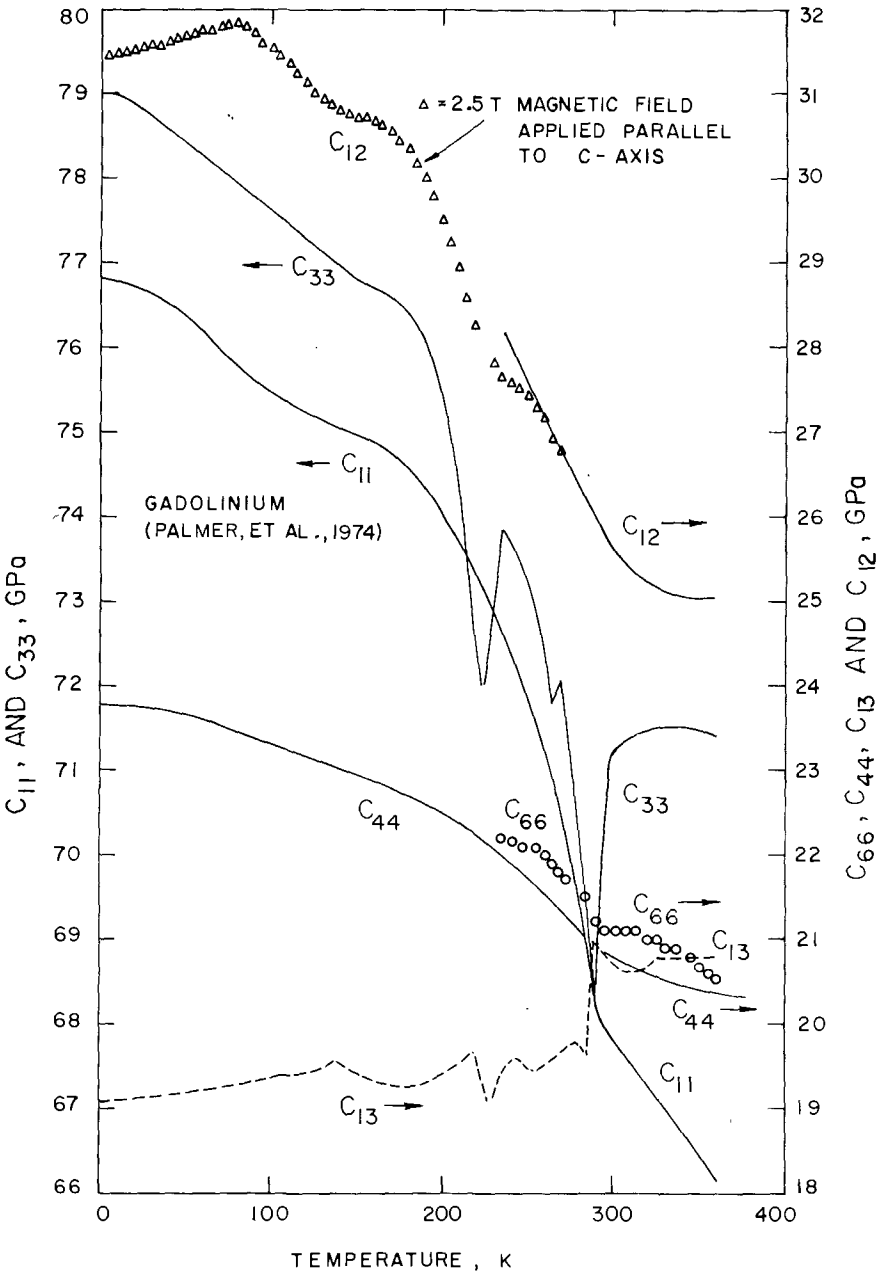

Fig. 8.67. Elastic stiffness constants of gadolinium. Triangles on the C_{12} curve indicate the data were taken in a 2.5 Tesla magnetic field applied parallel to the c-axis of the crystal. Palmer et al. (1974). Open circles for C_{44} have been used for clarity.

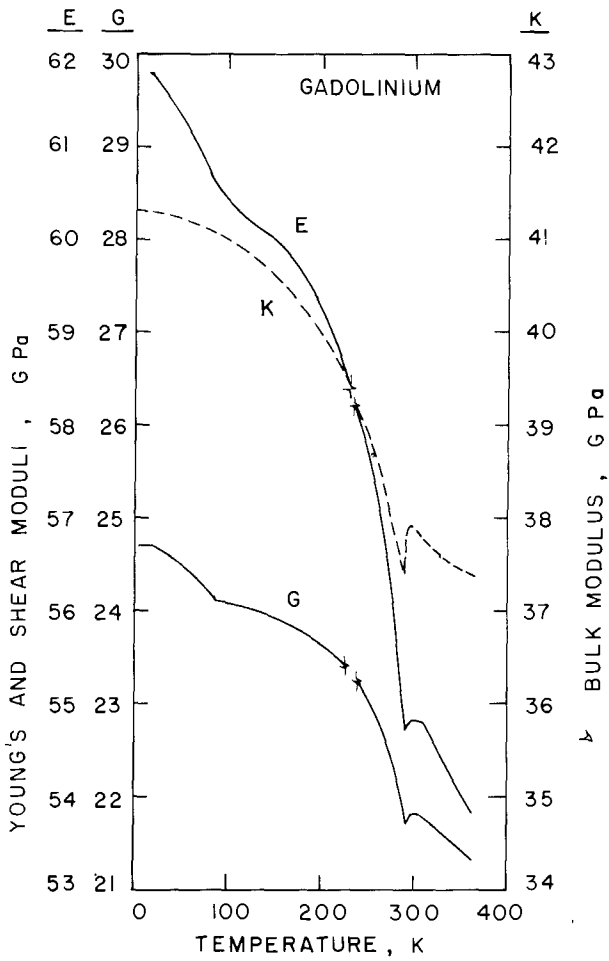

Fig. 8.68. Young's (E), shear (G), and bulk (K) moduli of gadolinium. Computed from single crystal constants shown in fig. 8.67. Breaks in the curves indicate that data for C_{12}, used in the computation, were taken in a magnetic field at temperatures below the break.

figs. 8.67, 8.68 and 8.69). The Curie point anomaly is most dramatic in the behavior of the constant C_{33} which shows a large well defined minimum. The other single crystal constants, except C_{44} and C_{12}, exhibit abrupt changes at about 290 K. Another C_{ij} anomaly begins at about 235 K and is followed by a pronounced minimum at about 223 K. It is especially evident in C_{33} and somewhat in C_{13} (see fig. 8.67) and was investigated in detail by Long et al. (1969). This anomaly was attributed to magnetostrictive effects and the breaking away of the ferromagnetic spin alignment from the c-axis. The maximum effect occurs at about 223 K and extends, according to Long et al., down to about 110 K. Rosen's (1968b) results from polycrystalline gadolinium also reveal clearly the

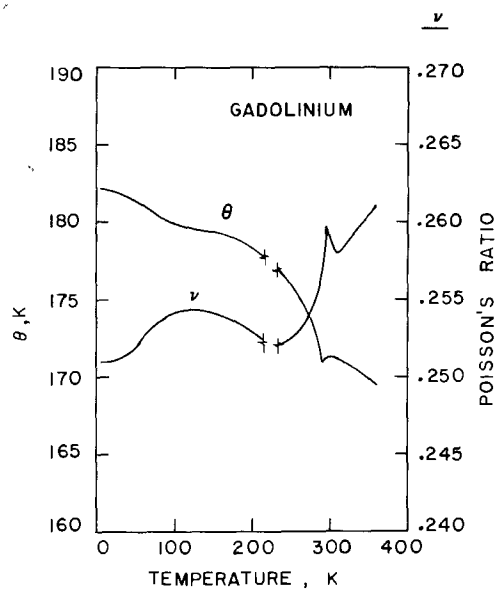

Fig. 8.69. Poisson's ratio (ν) and theta (θ) of gadolinium. Computed from single crystal constants shown in fig. 8.67. Breaks in the curves indicate that data for C_{12}, used in the computations, were taken in a magnetic field at temperatures below the break.

223 K anomaly. However, the bulk properties computed from the single crystal data of Palmer et al. (1974) do not exhibit any anomalous behavior at 223 K. This may be due to the averaging procedure used to obtain the bulk properties. In addition, it should be pointed out that the writer was forced to employ C_{12} values obtained by Palmer et al. (1974) in a 2.5 Tesla magnetic field parallel to the c-axis

TABLE 8.16.
Adiabatic elastic properties of gadolinium.

E(GPa)	G(GPa)	K(GPa)	ν	θ_D(K)	T(K)	Reference
56.1	22.3	38.5	0.257	–	298	Gust and Royce (1973)
56.2	22.3	38.9	0.259	–	298	Smith et al. (1957)
–	–	39.4[a]	–	–	298	Bridgman (1954)
54.8[b]	21.8[b]	37.9[b]	0.259[b]	–	300	Palmer et al. (1974)
61.8[b]	24.7[b]	41.3[b]	0.251[b]	182.2[b]	0	Palmer et al. (1974)
~59.2	23.8	38.6	0.244	–	300	Andreeva et al. (1971)
46.4	20.2	22.0	0.149	–	300	Maeda (1971)
55.6	22.2	38.1	0.252	–	300	Rosen (1968b)
62.7	25.2	39.9	0.244	184	0	Rosen (1968b)
–	–	40.1[c]	–	–	295	Al'tshuler et al. (1968)

[a]Converted from an isothermal result using Gschneidner's (1964) values for C_p, α and ω in eq. (8.5); [b]Computed from experimental single crystal constants; [c]From shock compression results for v_B in eq. (8.8).

below 235 K in the averaging procedure because no zero field data were available for C_{12}. These data are shown by triangular points in fig. 8.67; breaks in the curves in figs. 8.68 and 8.69 are to indicate that the C_{12} data taken in the magnetic field were used in the averaging. According to Palmer et al. (1974), the 2.5 Tesla field eliminated the cusp at 223 K in C_{33} in agreement with the experience of Long et al. (1969). In addition to the 290 K and 223 K anomalies, Rosen (1968b) observed an anomaly at about 15 K which was attributed to changes in transport properties noted previously by Arajs and Colvin (1964). However, none of the other elastic property investigations give results which corroborate the 15 K anomaly.

It should also be mentioned that Maeda (1971) also applied magnetic fields in his investigation. Furthermore, Klimker and Rosen (1973), Bartholin and Bloch (1969), and Fisher et al. (1973) examined the pressure dependence of the elastic properties of gadolinium.

9.11. *Terbium*

Belov et al. (1961) observed a large anomaly in Young's modulus (E) of terbium at 234 K and an internal friction maximum at 223 K which they attributed to the ferromagnetic-to-antiferromagnetic transition. Rosen (1968b) later determined the polycrystalline elastic properties by an ultrasonic pulse technique from 4.2 to 300 K; more recently Salama et al. (1972) and Palmer et al. (1974) measured the single crystal elastic constants of terbium. A comparison of room temperature properties from these investigations is given in table 8.17. Unfortunately, the reasonable agreement of the room temperature values does not reflect the significant qualitative differences in temperature dependencies observed by Rosen (1968b), Salama et al. (1972), and Palmer et al. (1974). For example, Palmer et al. (1974) observed a small anomaly in C_{11} at the Néel

TABLE 8.17.
Adiabatic elastic properties of terbium.

E(GPa)	G(GPa)	K(GPa)	ν	θ_D(K)	T(K)	Reference
57.5	22.8	40.0	0.261	–	298	Smith et al. (1957)
–	–	47.3[a,b]	–	–	298	Stephens (1964)
55.65[c]	22.08[c]	38.71[c]	0.261[c]	–	300	Salama et al. (1972)
–	–	38.88	–	–	300	Palmer et al. (1974)
57.9	22.9	40.4	0.264	–	300	Rosen (1968b)
60.2	23.6	44.2	0.275	177	4.2	Rosen (1968b)
–	–	40.3[a,d]	–	–	298	Montfort and Swenson (1965)
–	–	40.7[a,d]	–	–	298	Stephens and Johnson (1969)
–	–	45.5[a,e]	–	–	298	Stephens and Johnson (1969)

[a]Converted from isothermal value using Gschneidner's (1964) values for α, C_p and ω in eq. (8.5). [b]Mixed h.c.p. and Sm-structure terbium. [c]Computed from experimental single crystal constants. [d]h.c.p. terbium. [e]Precompressed to produce Sm-structure terbium.

temperature (229 K) followed by a rapid drop at the Curie point (221 K). According to Darnell (1963) there is also a transformation from the h.c.p. structure to an orthorhombic distortion of the hexagonal cell at 221 K which is a consequence of the magnetic ordering (see ch. 2, section 6.3). Salama et al. (1972) on the other hand, observed a rather broad maximum for C_{11} in the 230 K to 215 K region followed by a gradual decline to 150 K with no evidence of the 180 K minimum revealed by the results of Palmer et al. The results for C_{33} from both groups are in qualitative agreement although the values found by Salama et al. are lower. Salama et al. (1972) show a cusped minimum in C_{44} at the Néel temperature whereas Palmer et al. (1974) found no anomaly in C_{44} throughout the magnetic transition region.

Because these disparities exist, the temperature dependence of the C_{ij}'s obtained by both Palmer et al. (1974) and Salama et al. (1972) is compared in figs. 8.70 and 8.71. It should be pointed out that Palmer et al. (1974) made temperature corrections for the density and corrected the acoustic path length for thermal expansion *and* magnetostriction. Salama et al. (1972) made none of

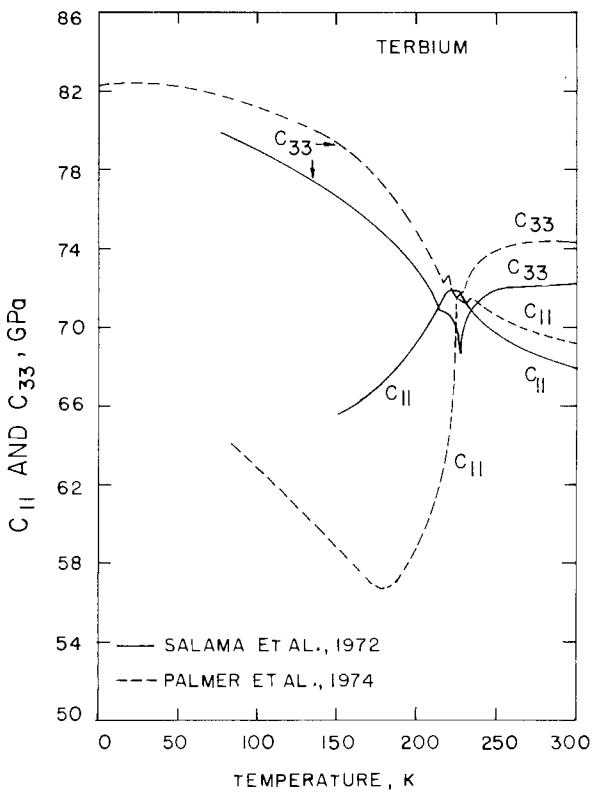

Fig. 8.70. Comparison of the temperature dependencies of C_{11} and C_{33} for terbium as determined by Palmer et al. (1974) and by Salama et al. (1972).

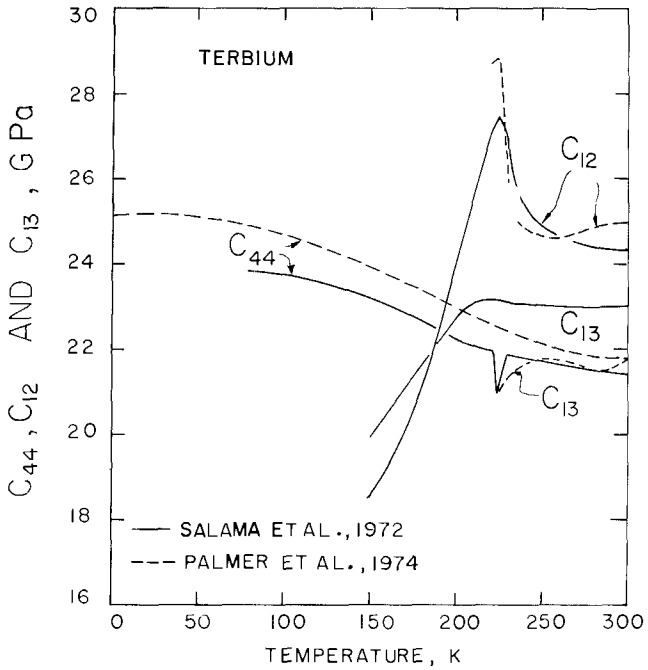

Fig. 8.71. Comparison of C_{44}, C_{12}, and C_{13} for terbium as determined by Palmer et al. (1974) and by Salama et al. (1972).

these corrections. Ignoring the temperature and magnetostriction corrections would have a significant effect on the acoustic wave velocities in the magnetic transition region because, as shown by Barson et al. (1957) and by Rhyne and Legvold (1965), the thermal expansion coefficient exhibits a substantial minimum (even reversing in sign) between about 273 K and 150 K. Consequently, the difference in the temperature dependencies of C_{11} and C_{13} reported by Palmer et al. and Salama et al. can be rationalized by the neglected corrections in the work of the latter group.

When the polycrystalline elastic properties determined experimentally by Rosen (1968b) are compared with the polycrystalline values computed from the data of Salama et al. (1972), further disparities are apparent. Rosen's data for E, G, and θ all rise with decreasing temperature to a maximum near 229 K; at this point they decrease slightly, then rise to a small peak near 221 K and subsequently decrease to a minimum near 150 K before they resume rising. On the other hand, the computed results for E, G and θ (see figs. 8.72 and 8.73) all rise as the temperature decreases to about 230 K where the elastic properties drop sharply to a minimum. Below 220 K they continue to rise with decreasing temperature. Most disturbing of all is the fact that Rosen (1968b) observed a peak in compressibility (or minimum in its reciprocal, the bulk modulus) in the magnetic transition region while Salama et al. (1972) noted the opposite

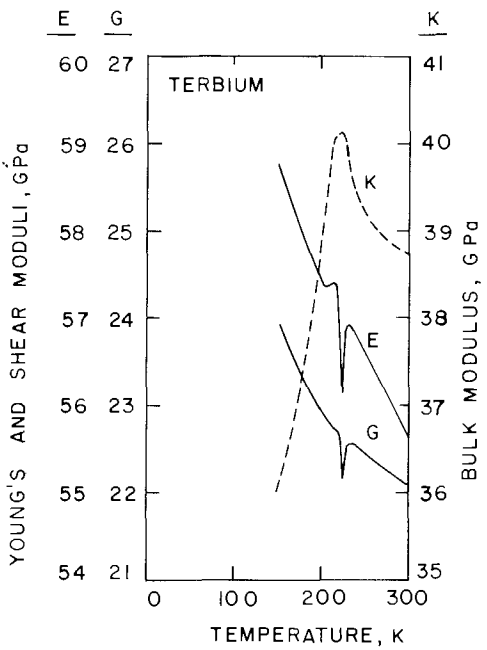

Fig. 8.72. Young's (E), shear (G), and bulk (K) moduli of terbium computed from the single crystal constants (figs. 8.70 and 8.71) determined by Salama et al. (1972).

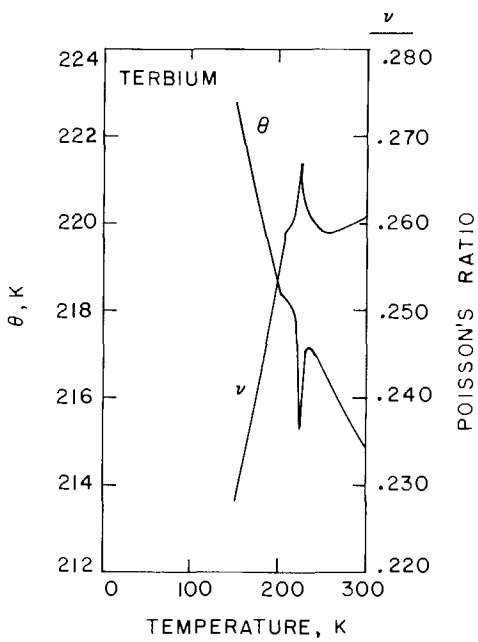

Fig. 8.73. Poisson's ratio (ν) and theta (θ) of terbium computed from the single crystal data (figs. 8.70 and 8.71) determined by Salama et al. (1972).

behavior. In this regard it should be emphasized that Salama et al. obtained a peak in their *linear* compressibility parallel to the c-axis (agreeing with Rosen). However, the *linear* compressibility normal to the c-axis exhibited a minimum in agreement with the computed volume compressibility (reciprocal bulk modulus). Rosen's (1968b) material may have had a strong crystallographic texture. It should be noted that Rosen (1968b) made path length corrections for thermal expansion effects. Therefore, the decrease he observed for E, G and θ following magnetic transitions is probably more accurate then the increase shown by the computed values based on the data of Salama et al. Clearly, more elastic constant work on terbium is needed.

Despite the fact that appropriate corrections were not made, the single crystal data of Salama et al. (1972) were chosen to compute the bulk properties included in table 8.22 for two reasons. Their C_{13} values encompassed a wider temperature range than Palmer et al. (1974) employed. In addition, the room temperature results of Salama et al. were lower, indicating their material was purer. Room temperature results should not require corrections.

During their investigation Palmer et al. (1974) examined the effect of a 2.5 Tesla magnetic field on the temperature dependence of the elastic constants of terbium. Monfort and Swenson (1965) and Stephens and Johnson (1969) obtained the pressure dependence of the compressibility.

9.12. *Dysprosium*

Levitin and Nikitin (1961) and Belov et al. (1964) demonstrated that the Young's modulus (E) of dysprosium increased normally with decreasing temperature until a small anomaly appeared between 170 and 180 K. Below 170 K Young's modulus rose sharply to a peak at about 108 K followed by a very large drop at about 85 K. The higher temperature anomaly was associated with the Néel point and the lower temperature anomaly with the Curie point of dysprosium. Later Fisher and Dever (1967) determined the single crystal elastic constants of dysprosium from 298 K to 923 K. All the C_{ij}'s except C_{12} decreased normally, and almost linearly, with increasing temperature. The constant C_{12} increased with increasing temperature. The bulk elastic properties were determined by Rosen (1968b) from 4.2 to 300 K; he observed that E, G, and θ increased normally with decreasing temperature down to about 178 K (Néel temperature) where a small anomaly occurred. Also, a precipitous drop in these properties occurred at about 86 K where the h.c.p. structure transforms to the orthorhombic structure (see ch. 2, section 6.3) due to the onset of ferromagnetism at the Curie point. Peculiarly, the adiabatic compressibility also increased with decreasing temperature down to the Néel point: No explanation was offered.

Single crystal elastic constants of dysprosium were determined by Rosen and Klimker (1970), Palmer and Lee (1972), and Fisher et al. (1973). Palmer (1975) investigated the effect of cooling and heating on just one constant, C_{33}. The results of Palmer and Lee (1972) and Fisher et al. (1973) showed qualitative and

reasonable quantitative agreement but both exhibited substantial qualitative disagreement with the results of Rosen and Klimker (1970). The disparities were primarily in the behavior of C_{12} and C_{13}. Palmer and Lee's (1972) values, generally lower than those of other investigators, were in good agreement with those of the independent investigation by Fisher et al. (1973) (who did not determine C_{13}). Consequently, the writer chose their data to use in computing the bulk properties. Their single crystal constants are illustrated in fig. 8.74 and the bulk properties computed from their data are shown in figs. 8.75 and 8.76 while the room temperature and absolute zero values are included in the summary of best values, table 8.22. A comparison of results from several investigations is given in table 8.18.

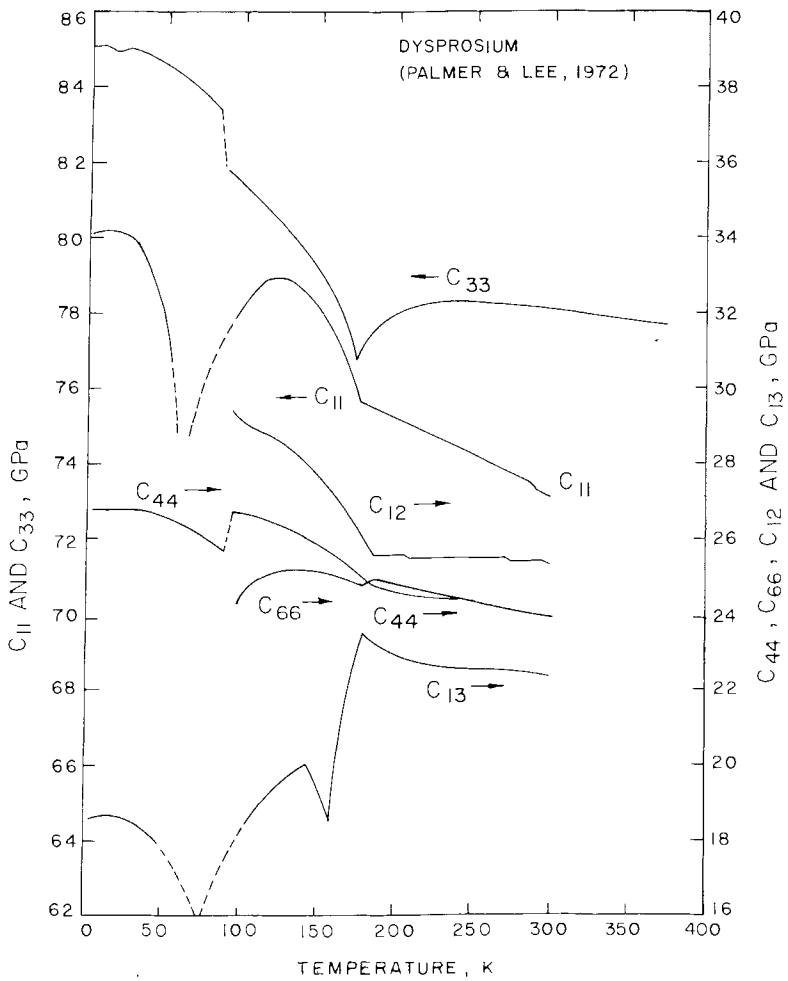

Fig. 8.74. Elastic stiffness constants of dysprosium. Palmer and Lee (1972).

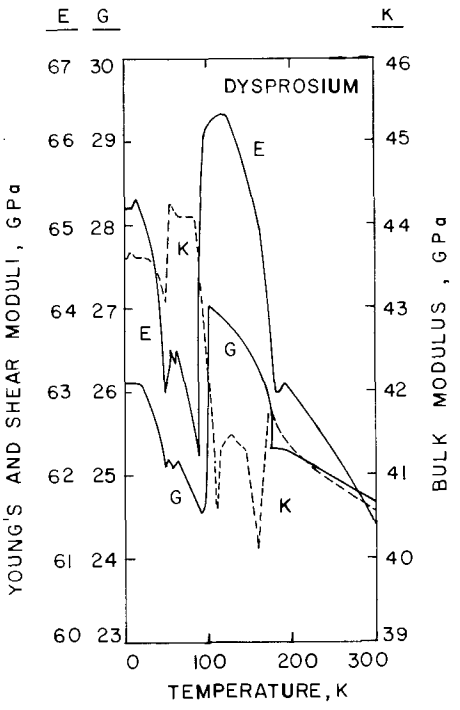

Fig. 8.75.

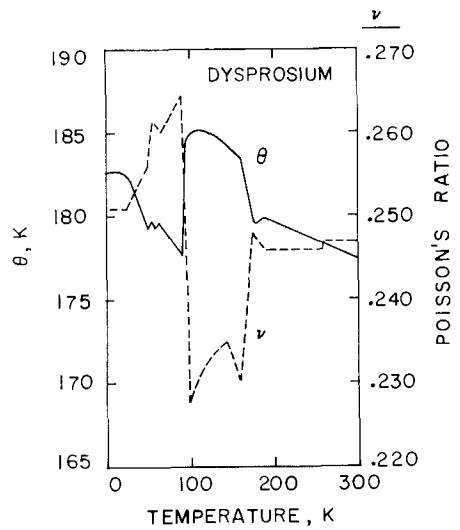

Fig. 8.76.

Fig. 8.75. Young's (E), shear (G), and bulk (K) moduli of dysprosium computed from the single crystal constants shown in fig. 8.74.

Fig. 8.76. Poisson's ratio (ν) and theta (θ) of dysprosium computed from the single crystal constants shown in fig. 8.74.

TABLE 8.18.
Adiabatic elastic properties of dysprosium.

E(GPa)	G(GPa)	K(GPa)	ν	θ_D(K)	T(K)	Reference
63.0	25.3	41.2	0.245	–	298	Gust and Royce (1973)
63.1	25.4	41.0	0.243	–	298	Smith et al. (1957)
–	–	38.0[a]	–	–	298	Bridgman (1954)
61.4[b]	24.6[b]	40.5[b]	0.247[b]	–	298	Palmer and Lee (1972)
65.2[b]	26.1[b]	43.6[b]	0.251[b]	182.6[b]	0	Palmer and Lee (1972)
63.5	25.6	40.6	0.240	–	300	Rosen (1968b)
62.6	24.9	42.9	0.257	179	0	Rosen (1968b)
–	–	40.3	–	–	300	Rosen and Klimker (1970)
–	–	41.8	–	191	0	Rosen and Klimker (1970)
~70.0	–	–	–	–	300	Belov et al. (1964)
~65.5	–	–	–	–	0	Belov et al. (1964)
–	–	47.9[c]	–	–	295	Al'tshuler et al. (1968)

[a]Converted from the isothermal result using Gschneidner's (1964) values for C_p, α and ω in eq. (8.5). [b]Computed from experimental single crystal constants. [c]Shock compression used to obtain v_B in eq. (8.8).

All of the single crystal constants (fig. 8.74) exhibit anomalies near the Néel temperature (~180 K) and the Curie temperature (~80 K). This is also true of the computed polycrystalline results (figs. 8.75 and 8.76). In contrast to the experimental polycrystalline results of Rosen (1968b), the computed bulk modulus (reciprocal of the adiabatic compressibility) increases with decreasing temperature down to about 175 K. In other words, the behavior is exactly reversed from the reported by Rosen (1968b). Perhaps, as was suggested in the discussion of terbium, the polycrystalline material used by Rosen was textured. Additional, unexplained anomalies appear to about 60 K; this is probably related to the magnetic behavior of dysprosium. Finally, it should be emphasized that the data of Palmer and Lee (1972) were obtained with an ultrasonic pulse technique (15 MHz) and were corrected for temperature and magnetostriction effects.

Palmer (1975) examined C_{33} as a function of cooling and heating from room temperature to 4.2 K. When a sample was reheated before the Curie temperature was reached during cooling, the values of C_{33} reproduced those obtained during cooling. However, if the sample was allowed to cool below the Curie temperature, C_{33} exhibited an anomalous drop near, or slightly above, the Curie temperature during heating. The difference between the values obtained during cooling to 4.2 K and those obtained during heating from 4.2 persisted to temperatures approaching the Néel point. The anomalous behavior was attributed to domains in the helical or spiral spin regime.

Fisher et al. (1973) investigated the pressure dependence of the C_{ij} while Palmer and Lee (1972) examined the effect of a 2.5 Tesla magnetic field on them.

9.13. *Holmium*

Several additional investigations of the elastic properties of holmium have been completed since Belov et al. (1964) first demonstrated that the Young's modulus behaved normally in its temperature dependence with the exception of anomalies at the Néel and Curie temperatures. Rosen (1968b) determined the polycrystalline elastic properties from 4.2 to 300 K while Palmer and Lee (1972), Salama et al. (1973) and Rosen et al. (1974) evaluated the single crystal elastic constants of holmium. Salama et al. (1973) did not take measurements below 77 K. Agreement of the temperature dependencies of the C_{ij} between Rosen et al. (1974) and Palmer and Lee (1972) is good with the latter obtaining slightly lower values at 300 K. However, there are qualitative discrepancies in the remaining C_{ij}. Since the ambient temperature values of Palmer and Lee (1972) were lower and because they made temperature corrections for the density and acoustic path length and made magnetostriction corrections for path length, the writer chose to illustrate their results in fig. 8.77. Their results were also used to compute the bulk properties shown in figs. 8.78 and 8.79 and were included in the summary of best values, table 8.22.

Although all the elastic constants except C_{66} exhibit some form of anomalous temperature dependence at the Néel point (~132 K), the most striking changes

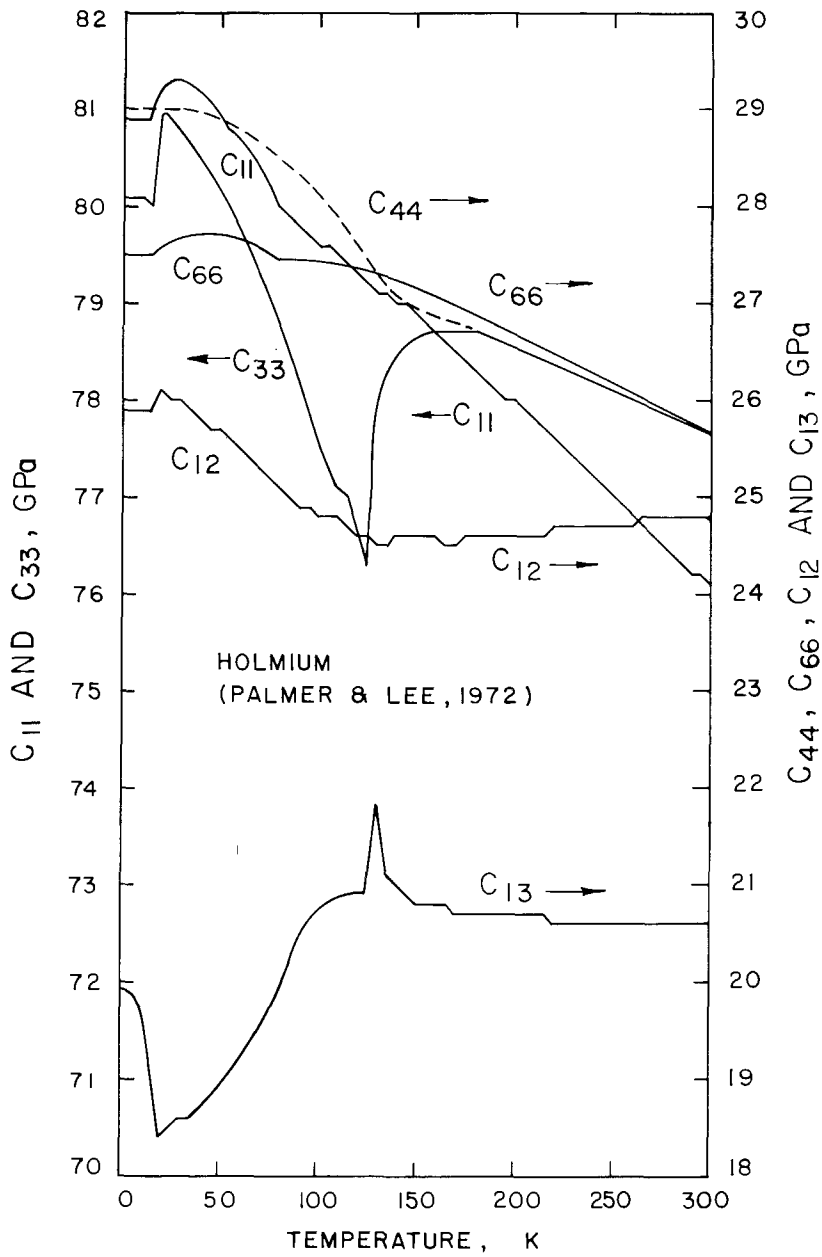

Fig. 8.77. Elastic stiffness constants of holmium. Palmer and Lee (1972).

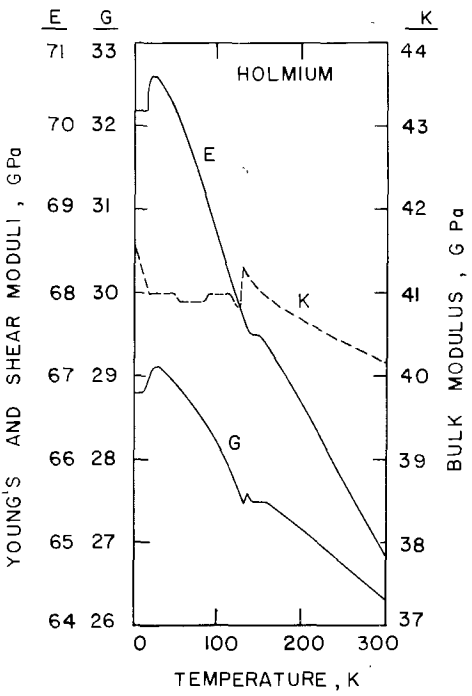

Fig. 8.78.

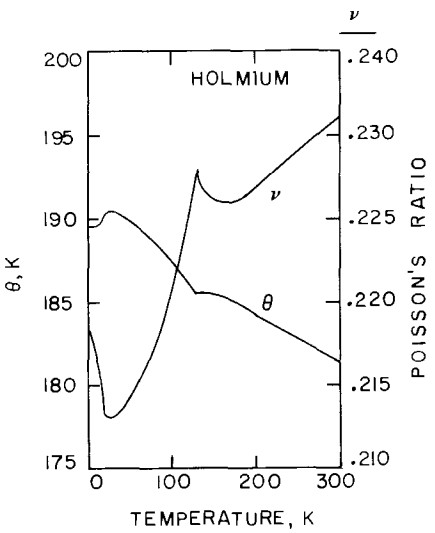

Fig. 8.79.

Fig. 8.78. Young's (E), shear (G), and bulk (K) moduli of holmium computed from the single crystal constants in fig. 8.77.

Fig. 8.79. Poisson's ratio (ν) and theta (θ) of holmium computed from the single crystal constants in fig. 8.77.

develop in C_{33} and C_{13}. Anomalies also appear at the Curie point (~20 K) but they generally are not as marked as at the Néel point; again C_{33} and C_{13} are prominent. The reason for the discrepancies between the temperature dependencies of the C_{ij} observed by Rosen et al. (1974) and Palmer and Lee (1972) are not clear but they might result from the neglect of Rosen et al. to correct the magnetostrictive effects. Perhaps impurities play an unforeseen role also.

With the exception of a small deviation at the Néel temperature and a sizable change at the Curie temperature, the computed bulk properties shown in figs. 8.78 and 8.79 behave normally. These results are in reasonably good qualitative agreement with Rosen's (1968b) experimental bulk properties with the exception that he obtained an additional anomaly at about 80 K which was unexplained. The volume compressibility obtained by Rosen et al. (1974) also revealed the anomaly between about 100 and 30 K and there is some evidence for it in the bulk modulus shown in fig. 8.78. In addition, the computed bulk properties are in reasonable quantitative agreement with Rosen's (1968b) results. Results from several investigations are presented for comparison in table 8.19. It should be noted that Palmer and Lee (1972) examined the effect of a 2.5 T magnetic field on the temperature dependence of the C_{ij}.

TABLE 8.19.
Adiabatic elastic properties of holmium.

E(GPa)	G(GPa)	K(GPa)	ν	θ_D(K)	T(K)	Reference
–	–	39.6[a]	–	–	298	Bridgman (1954)
67.1	26.7	45.8	0.255	–	298	Smith et al. (1957)
~74.3	–	–	–	–	0	Belov et al. (1964)
66.9	26.3	44.8	0.272	–	300	Rosen (1968b)
74.4	29.8	46.0	0.248	194	0	Rosen (1968b)
64.8[b]	26.3[b]	40.2[b]	0.231[b]	–	300	Palmer and Lee (1972)
70.2[b]	28.8[b]	41.5[b]	0.218[b]	189.5[b]	0	Palmer and Lee (1972)
–	–	40.8	–	–	300	Salama et al. (1973)
–	–	41.6	–	–	300	Rosen et al. (1974)
–	–	41.2	–	191.5	0	Rosen et al. (1974)
–	–	40.1	–	–	298	Fisher et al. (1973)

[a]Converted from isothermal to adiabatic using Gschneidner's (1964) values for α, C_p and ω in eq. (8.5). [b]Computed from experimental single crystal constants.

9.14. *Erbium*

Erbium, because it undergoes at least three magnetic phase transitions at sub-ambient temperatures, exhibits the most complex elastic constant temperature dependence of all the rare earth metals. This complexity and the scientific motivation for sorting out the interconnection between the magnetic phases probably are the reasons several detailed studies of the elastic properties have been conducted in recent years. Fisher et al. (1973), Rosen et al. (1973), Palmer et al. (1974) and du Plessis (1976) have all published single crystal data covering, in general, the temperature range from ambient to 4.2 K. Although the room temperature and near-zero values of C_{ij}'s (especially C_{44}, C_{12} and C_{13}) exhibit some disparities among the investigations, the agreement is respectable. Two of the groups, Palmer et al. (1974) and du Plessis (1976), examined the effect of magnetic fields on the C_{ij}'s while Fisher et al. (1973) evaluated their pressure dependence. It is difficult to decide which set of results to consider best values. The most recent investigations, Palmer et al. (1974) and du Plessis (1976), obtained results which are particularly difficult to choose between. The writer elected to use the data of Palmer et al. because they were presented in tabular form; this enabled a more accurate re-presentation of the data and permitted a more accurate computation of bulk elastic properties from them. Temperature dependencies of the C_{ij}'s are illustrated in fig. 8.80 and bulk properties computed from them are presented in figs. 8.81 and 8.82. Ambient and near-zero bulk properties from several investigations are listed for comparison in table 8.20 and the bulk properties computed from the data of Palmer et al. (1974) are included in the summary provided in table 8.22.

Historically, Belov et al. (1964) were probably the first to show the magnetic transition anomalies in Young's modulus and, a few years later, Rosen (1968b) measured all the polycrystalline elastic properties from room temperature to 4.2 K. Rosen's data revealed the anomalies very clearly.

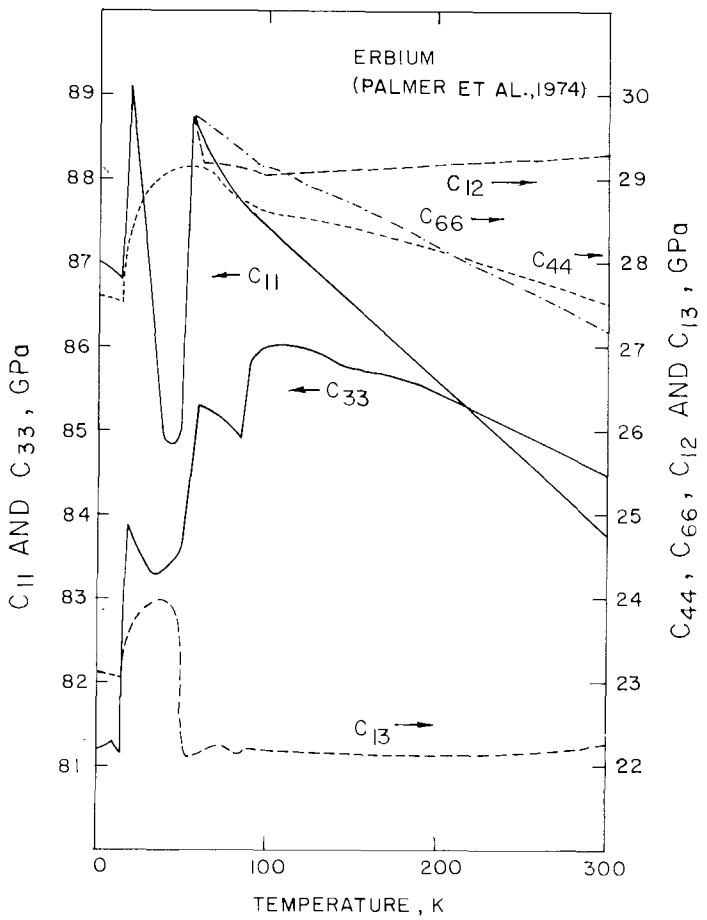

Fig. 8.80. Temperature dependence of the elastic stiffnesses of erbium. Palmer et al. (1974).

In fig. 8.80 the three magnetic transitions are readily identified by the precipitous softening of C_{33} near 80 K, 55 K and 20 K. Similar anomalies in C_{33} were noted by Fisher et al. (1973), Rosen et al. (1973) and du Plessis (1976). In the work of Rosen et al. (1973), the behavior of C_{33} following the sharp drop at 55 K is slightly different from the behavior observed by the other investigators. Rosen et al. found only a small dip whereas the other investigators observed a dip encompassing the range from 55 K to 20 K with a minimum at about 35 K. In contrast to C_{33}, C_{11} exhibits only an inflection at 80 K followed by rapid softening at 55 K and 20 K. The shear constant, C_{44}, has an inflection at 80 K followed by a wide maximum from 80 K to 20 K where it drops sharply. According to Palmer et al. (1974), C_{13} is virtually independent of temperature down to 80 K where it exhibits a small dip. At 55 K, their C_{13} shows only a small dip followed by a rise between 50 K and 20 K where it drops again. Both du

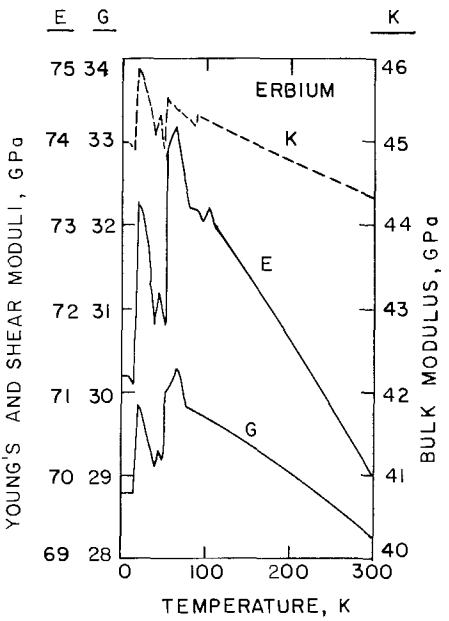

Fig. 8.81.

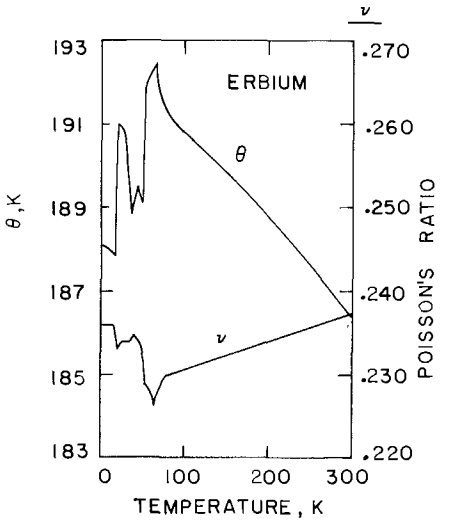

Fig. 8.82.

Fig. 8.81. Young's (E), shear (G), and bulk (K) moduli of erbium computed from the single crystal constants in fig. 8.80.

Fig. 8.82. Poisson's ratio (ν) and theta (θ) of erbium computed from the single crystal constants in fig. 8.80.

TABLE 8.20.
Adiabatic elastic properties of erbium.

E(GPa)	G(GPa)	K(GPa)	ν	θ_D(K)	T(K)	References
73.3	29.6	46.5	0.238	–	298	Smith et al. (1957)
–	–	39.6[a]	–	–	298	Bridgman (1954)
81.6	–	–	–	–	0	Belov et al. (1964)
72.9	29.6	45.7	0.231	–	300	Rosen (1968b)
74.9	30.3	47.8	0.236	193	0	Rosen (1968b)
69.9	28.3	44.3	0.237	–	300	Palmer et al. (1974)
71.2[b]	28.8[b]	45.0[b]	0.236[b]	188[b]	0	Palmer et al. (1974)
71.6[c]	28.9[c]	45.5[c]	0.238[c]	–	300	Fisher et al. (1973)
70.0[c]	28.4[c]	43.4[c]	0.231[c]	–	300	Rosen et al. (1973)
72.0[c]	29.6[c]	42.0[c]	0.215[c]	190[c]	0	Rosen et al. (1973)
68.9[c]	27.6[c]	45.3[c]	0.246[c]	–	300	du Plessis (1976)
70.3[c]	28.3[c]	45.4[c]	0.242[c]	187[c]	0	du Plessis (1976)
–	–	43.8[d]	–	–	295	Al'tshuler et al. (1968)

[a]Converted from the isothermal value using Gschneidner's (1964) values of α, ω and C_p in eq. (8.5). [b]Obtained by using data for C_{12} and C_{66} taken in a magnetic field of 2.5T below 55 K. [c]These bulk properties are Hill (1952) averages computed with the same density values used by Palmer et al. (1974). [d]Shock compression value for v_B in eq. (8.8).

Plessis (1976) and Rosen et al. (1973) observed a rather large dip in C_{13} at 55 K. Elastic constant C_{66} in fig. 8.80 rises normally with decreasing temperature until it displays a slight inflection near 80 K and continues to rise at a higher rate to 55 K where it decreases sharply. Rosen et al. (1973) and du Plessis (1976) show that the drop at 55 K is large and that C_{66} rises again but exhibits only a small dip at 20 K. C_{12} falls gradually with decreasing temperature to a shallow minimum at about 90 K and rises rapidly at about 60 K. Rosen et al. (1973) and du Plessis (1976) have more detailed results below 55 K for C_{12}. They show that the rise in C_{12} at about 60 K is substantial. They further indicate additional anomalies between the rise and the precipitous softening at 20 K.

Hill's (1952) averages of the single crystal elastic constants give the bulk properties and their temperature dependencies as shown in figs. 8.81 and 8.82. All the bulk properties reveal anomalous behaviors reflecting the magnetic transitions at 80 K, 55 K and 20 K and they are in qualitative agreement with the experimental results of Rosen (1968b).

9.15. *Thulium*

The only investigation of the elastic constants of thulium known to the writer is that of Rosen (1971) on polycrystalline samples using an ultrasonic pulse technique (10 MHz). Acoustical path lengths were corrected for temperature variations. The temperature dependence of the elastic moduli, compressibility and theta (θ) are shown in figs. 8.83 and 8.84. Theta (θ) and the moduli, E and G,

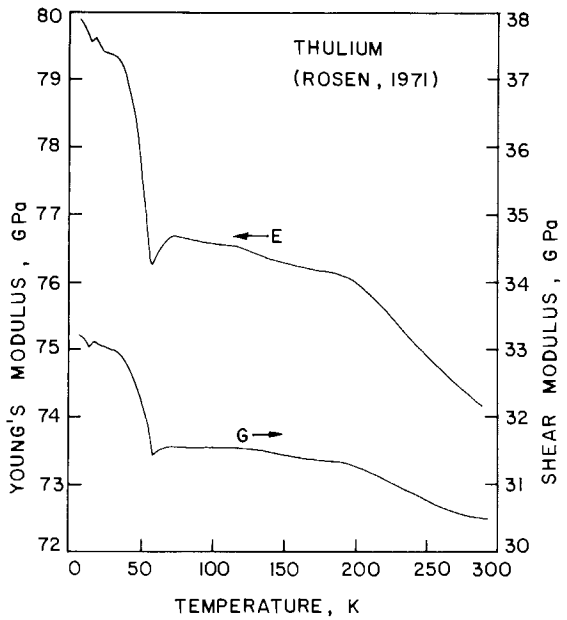

Fig. 8.83. Temperature dependence of Young's (E) and shear (G) moduli of polycrystalline thulium. Rosen (1971).

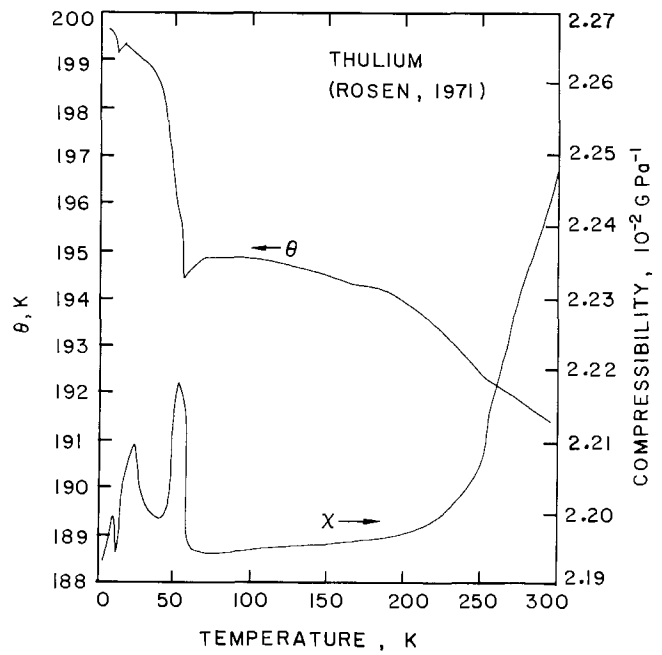

Fig. 8.84. Compressibility (χ_s) and theta (θ) of polycrystalline thulium. Rosen (1971).

increase normally with decreasing temperature down to about 200 K followed by a broad region of temperature independence down to about 70 K. At lower temperatures a slight cusped minimum followed by a sharp rise occurs near the Néel temperature of 55 K. Two additional small anomalies occur near 25 and 13 K. The adiabatic compressibility exhibits a sharp peak at 55 K, a smaller but broader maximum at 25 K, and a small peak at 13 K. The two lower temperature anomalies probably are associated with the transition to ferromagnetic behavior at the Curie point (~22 K).

Bridgman (1954) obtained a room temperature adiabatic bulk modulus of 38.2 GPa (coverted by the writer from the isothermal value using eq. (8.5) and Gschneidner's (1964) values for α, C_p and ω). This result is somewhat less than Rosen's value of 44.5 GPa. Rosen's results are presented in the summary, table 8.22.

9.16. *Ytterbium*

Rosen (1971) is the only investigator known by the writer to have measured the temperature dependence of the elastic properties of ytterbium. Using an ultrasonic pulse technique (10 MHz) to determine acoustic wave velocities in polycrystalline ytterbium Rosen obtained the results given in figs. 8.85 and 8.86. He corrected the acoustic wave path length for thermal expansion. The values of E, G and θ increase smoothly with decreasing temperature and approach the

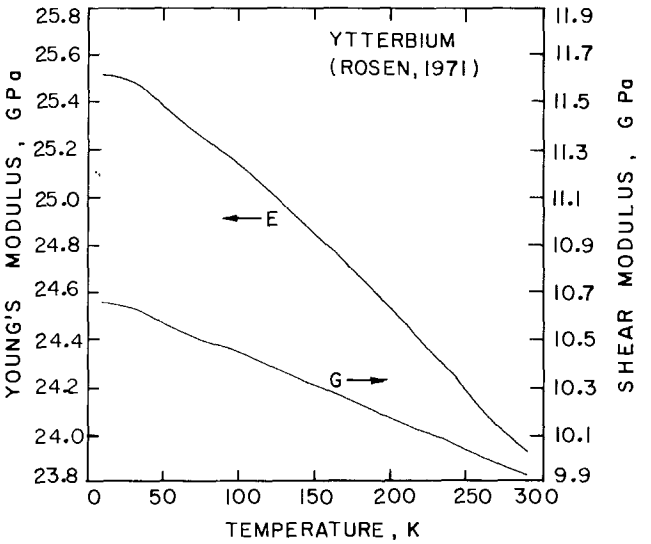

Fig. 8.85. Young's (E) and shear (G) moduli of polycrystalline ytterbium. Rosen (1971).

absolute zero value in accordance with thermodynamic requirements. On the other hand, the compressibility (reciprocal bulk modulus) exhibits a rather pronounced decrease between about 260 and 225 K followed by a slower decrease to a minimum near 75 K. The slight increase in compressibility below 75 K was not explained by Rosen (1971). It is somewhat surprising that E, G and

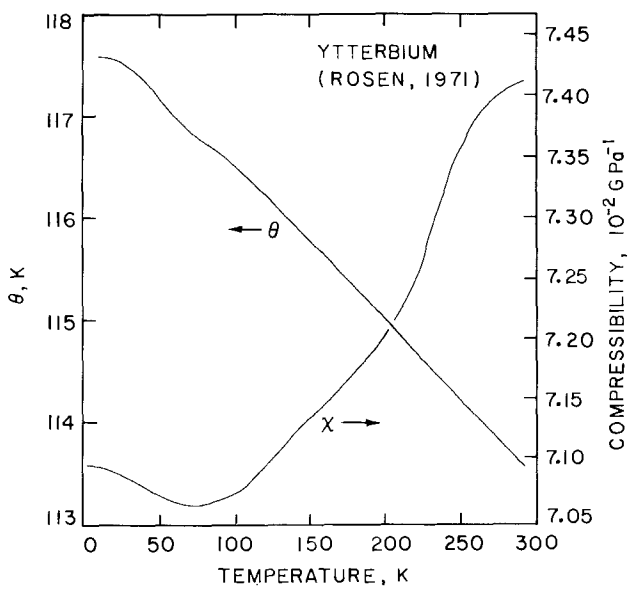

Fig. 8.86. Compressibility (χ_s) and theta (θ) of polycrystalline ytterbium. Rosen (1971).

TABLE 8.21.
Adiabatic elastic properties of ytterbium.

E(GPa)	G(GPa)	K(GPa)	ν	θ_D(K)	T(K)	Reference
18.8	7.3	15.0	0.290	–	298	Gust and Royce (1973)
17.8	7.0	13.8	0.284	–	298	Smith et al. (1957)
23.9	9.9	13.5	0.207	–	300	Rosen (1971)
25.5	10.7	14.1	0.196	117.6	0	Rosen (1971)
–	–	13.4*	–	–	298	Bridgman (1954)
–	–	15.3*	–	–	298	Stephens (1964)
–	–	17.7*	–	–	298	Hall (1963)

*Converted from an isothermal value using Gschneidner's (1964) values for α, C_p and ω in eq. (8.5).

θ, revealed no anomalies in the temperature region near 250 K since it is known that f.c.c. ytterbium transforms martensitically to a h.c.p. structure beginning at ~260 K (Kayser, 1970, 1971) or ~240 K (Owen and Scott, 1970). Normally martensitic transformations are accompanied by lattice softening which should appear as a decrease in the elastic moduli. Perhaps the temperature intervals used by Rosen (1971) were spaced too widely to detect the effect. This should be investigated further. Table 8.21 summarizes the available data for ytterbium. Although the values obtained by Smith et al. (1957) and Gust and Royce (1973) are lower than those of Rosen (1971), the latter's results are given as the best values in table 8.22 because the work included the temperature dependence.

9.17. *Lutetium*

Other than Bridgman's (1954) and Liu's (1975) ambient temperature measurements of the isothermal compressibility, the only elastic property data for lutetium were determined by Tonnies et al. (1971). They employed an ultrasonic pulse superposition technique and corrected the acoustic path length for thermal expansion. The temperature dependencies of their single crystal elastic constants are shown in fig. 8.87. In general the temperature dependencies are normal in that the elastic constants increase linearly, or almost linearly, with decreasing temperature until absolute zero is approached. The constants C_{12} and C_{13} are virtually temperature independent. Polycrystalline, or the so-called bulk property, data computed from the single crystal constants of Tonnies et al. (1971) are depicted in figs. 8.88 and 8.89 and included in the best value summary of table 8.22. The room temperature bulk modulus value of 47.6 GPa is within the estimated error of Liu's (1975) value of 46.2 ± 2 GPa and is about 11 percent larger than Bridgman's (1954) value of 42.9 GPa. The zero particle velocity from the shock compression studies of Al'tshuler et al. (1968) allows one to compute a bulk modulus of 47.1 GPa.

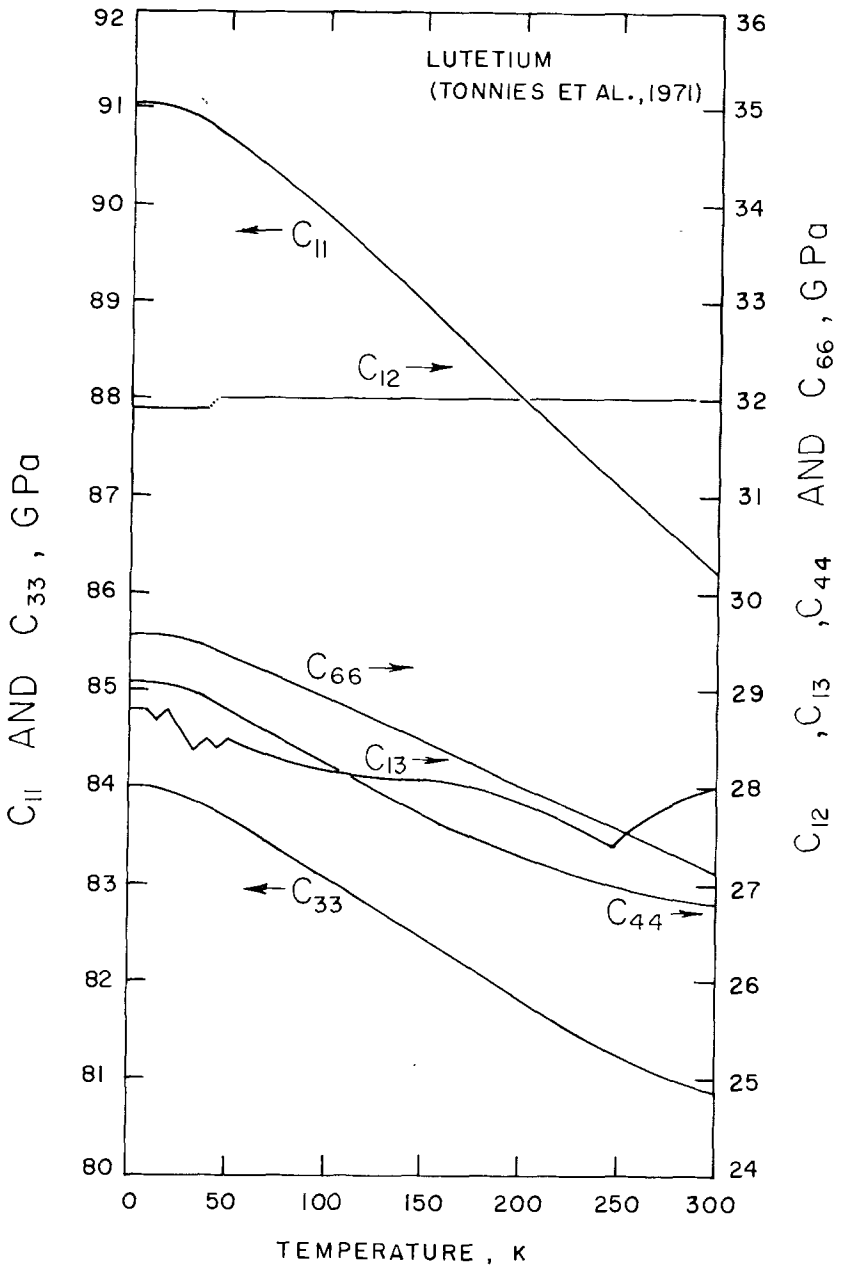

Fig. 8.87. Elastic stiffness constants of lutetium. Tonnies et al. (1971).

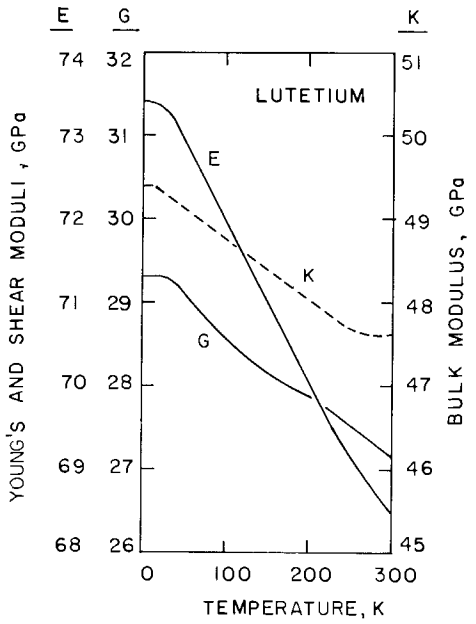

Fig. 8.88.

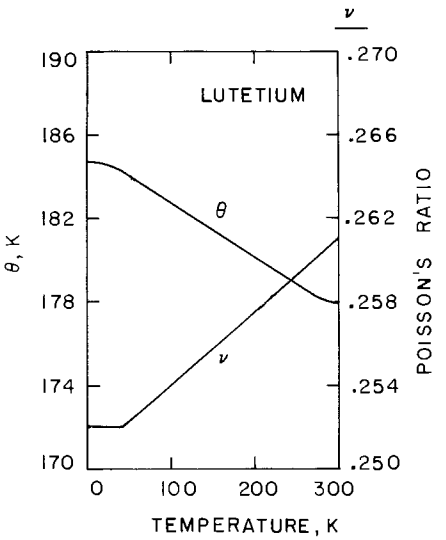

Fig. 8.89.

Fig. 8.88. Young's (E), shear (G), and bulk (K) moduli of lutetium computed from the single crystal data shown in fig. 8.87.
Fig. 8.89. Poisson's ratio (ν) and theta (θ) of lutetium computed from the single crystal data in fig. 8.87.

9.18. *Summary*

A general appreciation of the effect of electronic structure on the elastic properties of the rare earth metals can be realized by viewing figs. 8.90 and 8.91. These figures show the room temperature elastic properties as a function of atomic number. Room temperature values were chosen because they should not be affected by polymorphic and magnetic transitions. Both figs. 8.90 and 8.91 reveal a definite trend toward higher elastic constants with increasing atomic number, a fact that is well appreciated. They also indicate, as has long been recognized, that scandium and yttrium should be included with the heavy lanthanides. From praseodymium through dysprosium, the single crystal constants, fig. 8.90, increase smoothly, almost linearly, with increasing atomic number. At, or near, holmium, the C_{ij}'s tend to deviate from this trend. Bulk elastic properties, fig. 8.91, are more revealing in some respects. For example, except for some uncertainty in the trend of lanthanum and cerium, the bulk elastic properties increase linearly with atomic number from praseodymium through samarium. Another linear increase, but with a different slope, occurs from terbium through thulium. For gadolinium all the bulk properties shown are too low to fit the linear plot of the light rare earths and too high to fit the linear plot of the heavy rare earths. Whether this deviation is due to high impurity concentrations in the gadolinium metal used in the measurements or is explicable

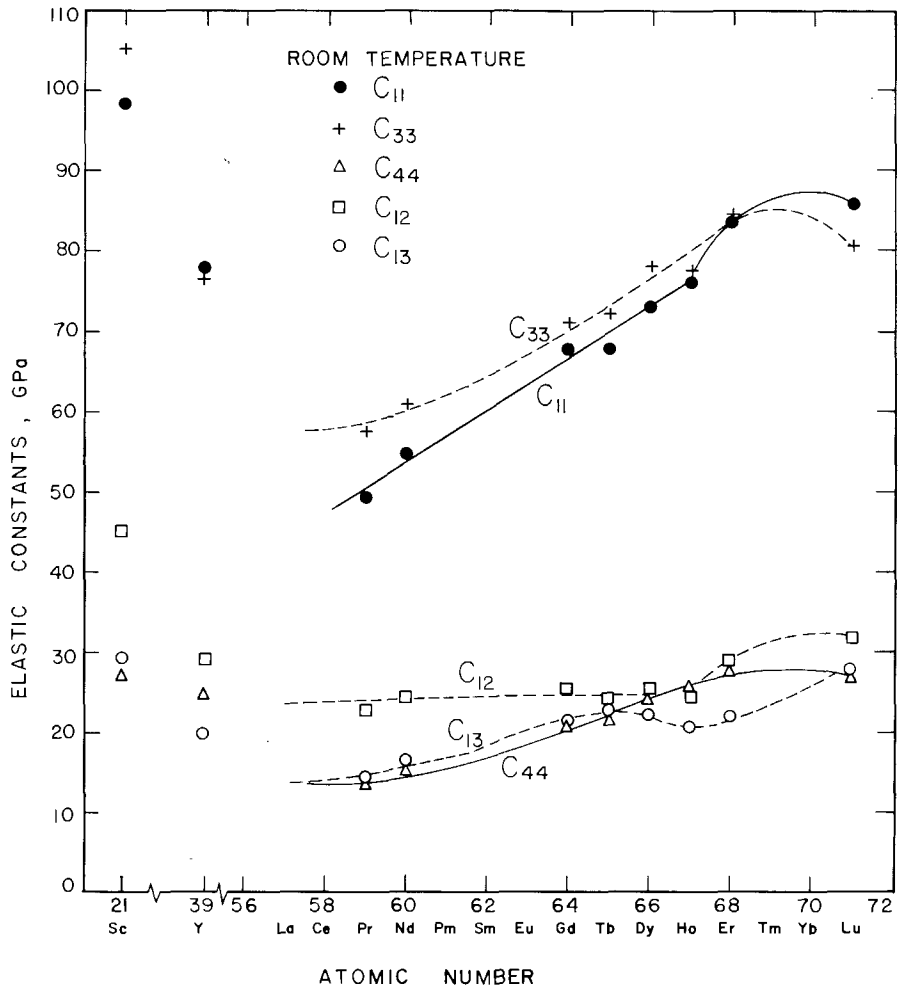

Fig. 8.90. A graphical summary of selected room temperature elastic stiffness constants of the rare earth metals.

on the basis of its electronic structure is unclear to the writer. If anything, effects of the magnetic transition near room temperature in gadolinium would be expected to cause an anomalously low value of the elastic properties. In addition to the low values observed for the cubic metals, europium and ytterbium, lutetium has lower values than an extrapolation of the line through the data for elements of lower atomic number would predict. No explanation for this fact can be offered. The uncertainties in the values for cerium and lanthanum might be a result of high impurity concentration (especially in lanthanum) or mixed-phase microstructures (γ and β in the case of cerium). No single crystal data were available for these metals.

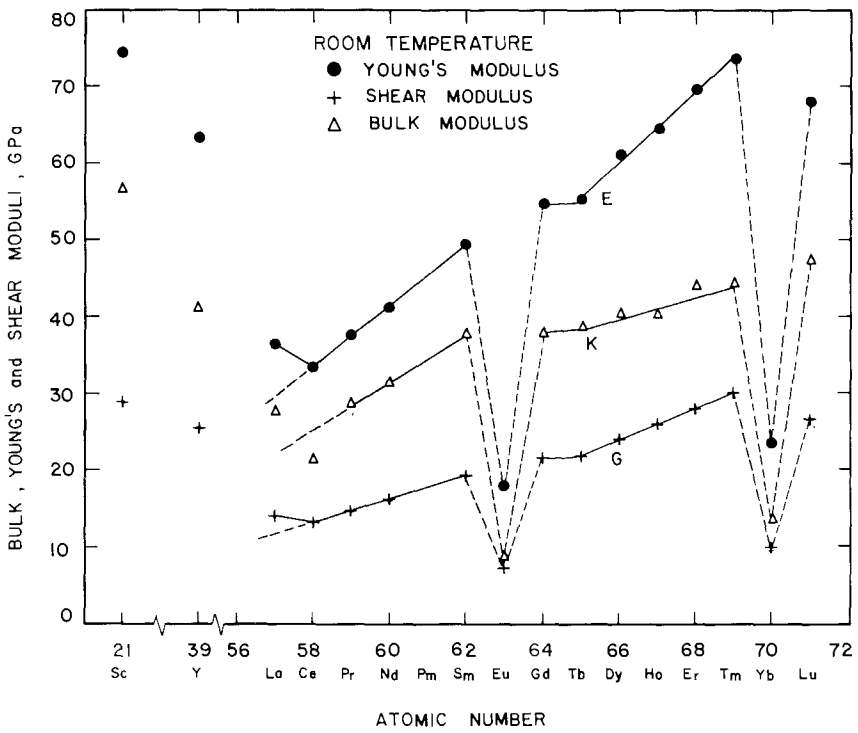

Fig. 8.91. A graphical summary of selected room temperature values for Young's modulus (E), bulk modulus (K), and shear modulus (G) of the rare earth metals.

A summary of the writer's choices for "best values" of the elastic properties of all the rare earth metals, except promethium, is given in table 8.22. No elastic property data for promethium are available and no absolute-zero data exist for lanthanum. No bulk property values are listed for scandium at absolute zero because C_{13} was not determined at that temperature; C_{13} is needed to compute the bulk properties from the C_{ij}'s.

It should be pointed out that temperatures of 300 K and 0 K are indicated in table 8.22 where the actual values were often 298 K and 4.2 K. Voigt, Reuss and Hill averages are given for the bulk modulus (K) and the shear modulus (G). Only Hill averages are given for Young's modulus (E) and for Poisson's ratio (ν) because they can be calculated from K and G values. Also included in table 8.22 are the three elastic anisotropy ratios (A^*, B^* and C^*) and the Debye temperatures (θ_D) at absolute zero. The room temperature density (ρ) values used in the computation of the elastic properties are listed.

TABLE 8.22. "BEST" ADIABATIC BULK ELASTIC PROPERTIES

PROPERTY / METAL		K_V[b] (GPa)	K_R (GPa)	K_H (GPa)	G_V[c] (GPa)	G_R (GPa)	G_H (GPa)	E_H[d] (GPa)	ν_H[e]	A*[f]	B*	C*	Θ_D[g] (K)	ρ[h] (kg/m^3)	Ref.[i]
Sc	300K	56.7	56.6	56.6	29.4	28.7	29.1	74.4	.279	1.026	1.071	1.541	-	2989	1
	0K	-	-	-	-	-	-	-	-	-	-	-	-	-	
Y	300K	41.2	41.1	41.2	25.7	25.5	25.6	63.5	.243	1.015	0.987	1.460	-	4472	2
	0K	42.1	41.8	41.9	28.3	28.1	28.2	69.1	.226	1.013	0.960	1.656	258	-	
La[a]	300K	-	-	27.9	-	-	14.3	36.6	.280				-	6130	3
	0K	-	-	-	-	-	-	-	-					-	
γ-Ce[a]	300K	-	-	21.5	-	-	13.5	33.6	.24				-	6758	4
α-Ce[a]	0K	-	-	19.8	-	-	13.4	32.7	-					-	
Pr	300K	28.8	28.8	28.8	15.1	14.5	14.8	37.3	.281	1.030	1.163	1.605	-	6772	5
	0K	29.5	29.5	29.5	15.4	15.0	15.2	38.4	.280	1.134	1.096	1.662	152	-	
Nd	300K	31.8	31.8	31.8	16.5	16.1	16.3	41.4	.281	0.995	1.110	1.483	-	7007	6
	0K	33.0	33.0	33.0	18.2	17.7	18.0	45.1	.269	0.947	1.108	1.517	163	-	
Sm[a]	300K	-	-	37.8	-	-	19.5	49.7	.274				-	7483	7
	0K	-	-	38.0	-	-	20.3	51.8	.276				169	-	
Eu[a]	300K	-	-	8.3	-	-	7.9	18.2	.152				-	5285	8
	0K	-	-	10.0	-	-	9.0	20.6	.144				118	-	
Gd	300K	37.9	37.9	37.9	21.9	21.7	21.8	54.8	.259	0.986	1.050	1.237	-	7895.4	9
	0K	41.3	41.2	41.3	24.9	24.5	24.7	61.8	.250	1.048	1.029	1.653	182.2	-	
Tb	300K	38.7	38.7	38.7	22.1	22.1	22.1	55.7	.261	0.983	1.064	1.058	-	8272	10
	0K	-	-	-	-	-	-	-	-	-	-	-	-	-	
Dy	300K	40.5	40.5	40.5	24.7	24.6	24.7	61.4	.247	1.004	1.068	1.135	-	8560	11
	0K	43.7	43.5	43.6	26.5	25.6	26.1	65.2	.251	1.235	1.062	1.973	182.6	-	
Ho	300K	40.2	40.2	40.2	26.3	26.3	26.3	64.8	.231	1.004	1.020	1.204	-	8800	11
	0K	41.5	41.4	41.5	28.8	28.8	28.8	70.2	.218	1.055	0.990	1.302	189.5	-	
Er	300K	44.4	44.3	44.4	28.3	28.2	28.3	69.9	.237	1.011	1.008	1.320	-	9042.7	12
	0K	45.7	44.9	45.0	28.8	28.8	28.8	71.2	.236	0.952	0.933	1.255	188.1	-	
Tm[a]	300K	-	-	44.5	-	-	30.5	74.0	.213				-	9208	13
	0K	-	-	45.7	-	-	33.2	80.0	.205				200	-	
Yb	300K	-	-	30.5	-	-	9.9	23.9	.207				-	6991	13
	0K	-	-	33.2	-	-	10.7	25.5	.196				117.6	-	
Lu	300K	47.7	47.6	47.6	27.2	27.1	27.2	68.6	.261	0.986	0.938	1.143	-	9846	14
	0K	49.5	49.3	49.4	29.3	29.3	29.3	73.4	.252	0.984	0.923	1.108	184.6	-	

[a] Experimental measurement with polycrystalline samples.

[b] K_V, K_R and K_H are Voigt, Reuss, and Hill averages of the bulk modulus computed from C_{ij} according to eqs. (8.13a), (8.14a) and (8.17) respectively.

[c] G_V, G_R and G_H are Voigt, Reuss, and Hill averages of the shear modulus computed from C_{ij} according to eqs. (8.13b), (8.14b) and (8.17) respectively.

[d] Hill average of Young's modulus computed according to eq. (8.16).

[e] Hill average of Poisson's ratio computed according to eq. (8.15).

[f] A*, B* and C* are anisotropy ratios computed from C_{ij}'s using eqs. (8.20).

[g] Debye temperature computed using Anderson's (1963) wave velocity averaging scheme for v_m, eq. (8.19), in eq. (8.18).

[h] Room temperature density used to calculate the constants listed.

[i] References appended to this table.

References and Comments for Table 8.22

1. Fisher, E.S. and D. Dever, 1968, Anomalous Effects of Temperature and Impurities on the Elastic Moduli of Scandium Single Crystals, presented at 7th Rare Earth Research Conference, Coronado, California. ANL-MS-1048, Argonne National Laboratory, Argonne, Illinois. Also reported by Gschneidner, K.A.: 1975, in *Scandium*, Horovitz, C.T., K.A. Gschneidner, G.A. Nelson, D.H. Youngblood and H.H. Schock, eds. (Academic Press, New York, 1975) pp. 76–110. No value of C_{13} was determined at 4.2 K. Therefore, bulk properties could not be computed for that temperature.
2. Smith, J.F. and J.A. Gjevre, 1960, J. Appl. Phys. **31**, 645.

3. Gust, W.H. and E.B. Royce, 1973, Phys. Rev. **B8**, 3595.
4. Rosen, M., 1969, Phys. Rev. **181**, 932. Data taken from graphs of experimental bulk properties versus temperature.
5. Greiner, J.D., R.J. Schiltz, J.J. Tonnies, F.H. Spedding and J.F. Smith, 1973, J. Appl. Phys. **44**, 3862.
6. Greiner, J.D., D.M. Schlader, O.D. McMasters, K.A. Gschneidner and J.F. Smith, 1976, J. Appl. Phys. **47**, 3427.
7. Rosen, M., 1969, Phys. Rev. **180**, 540. Data taken from graphs of experimental bulk properties versus temperature.
8. Rosen, M., 1968, Phys. Rev. **166**, 561. Data taken from graphs of experimental bulk properties versus temperature.
9. Palmer, S.B., E.W. Lee and M.N. Islam, 1974, Proc. Roy. Soc. Ser. **A338**, 341. Used C_{12} data taken in a 2.5 Tesla magnetic field applied parallel to the c-axis at temperatures below 235 K.
10. Salama, K., F.R. Brotzen and P.L. Donoho, 1972, J. Appl. Phys. **43**, 3254.
11. Palmer, S.B. and E.W. Lee, 1972, Proc. Roy. Soc. Ser. **A327**, 519.
12. Palmer, S.B., E.W. Lee and M.N. Islam, 1974, Proc. Roy. Soc. Ser. **A338**, 341. Used data for C_{12} and C_{66} taken in a 2.5 Tesla magnetic field at temperatures below 55 K.
13. Rosen, M., 1971, J. Phys. Chem. Solids **32**, 2351. Data taken from graphs of experimental bulk properties versus temperature.
14. Tonnies, J.J., K.A. Gschneidner and F.H. Spedding, 1971, J. Appl. Phys. **42**, 3275.

Acknowledgements

In an undertaking of the sort involved in the preparation of this chapter many people provide various forms of assistance and deserve the gratitude of the author. In this particular instance the following individuals deserve special thanks: C.V. Owen, my colleague in rare earth mechanical property research; L.K. Reed for a host of tasks performed for me; J.D. Greiner and D.M. Bailey for use of their computer program and advice on its use; J.F. Smith for helpful comments on elastic constants; K.A. Gschneidner for patience with the author for many delays and for stimulating discussions about rare earth metals; Carol Scott for proof-reading and editorial comments.

This work was supported by the U.S. Department of Energy, Division of Basic Energy Sciences.

References

Al'tshuler, L.V., A.A. Bakanova and I.P. Dudoladov, 1967, Zh. Eksp. Teor. Fiz. 53. Engl. Transl., 1968, Sov. Phys.-JETP **26**, 1115.

Anderson, O.L., 1963, J. Phys. Chem. Solids **24**, 909.

Andreeva, L.P., G.P. Zinov'eva and P.V. Gel'd, 1971, Fiz. Tverd. Tela **13**, 3435. Engl. Transl., 1972, Sov. Phys.-Solid State **13**, 2896.

Arajs, S. and R.V. Colvin, 1964, J. Appl. Phys. **35**, 1043.

Barson, F., S. Legvold and F.H. Spedding, 1957, Phys. Rev. **105**, 418.

Bartholin, H. and D. Block, 1969, Phys. Rev. **188**, 845.

Belov, K.P., R.Z. Levitin and S.A. Nikitin, 1961, Izv. Akad. Nauk SSSR, Ser. Fiz. **25**, 1382. Engl. Transl., 1961, Bull. Akad. Sci. USSR, Phys. Ser. **25**, 1394.

Belov, K.P., R.Z. Levitin, L.A. Malevskaya and V.I. Sokolov, 1964, Fiz. Metal. Metalloved. **17**, 617. Engl. Transl. 1964, Phys. Met. Metallogr. **17**, 137.

Belov, K.P., R.Z. Levitin, S.A. Nikitin and A.V. Ped'ko, 1961, Zh. Eksp. Teor. Fiz. **40**, 1562. Engl. Transl., 1961, Sov. Phys. JETP, **13**, 1096.

Bohlander, K.M., 1961, Mechanical Fabrication of Rare Earth Metals, in: Spedding, F.H. and A.H. Daane, eds., *The Rare Earths*, (John Wiley and Sons, New York) pp. 163–174.

Bol'shutkin, L.I., Yu.Ye. Krot and V.A. Moskalenko, 1965, Fiz. Metals Metalloved. **20**, 465. Engl. Transl., 1965, Phys. Met. Metallogr. **20**, 151.

Borisov, E.V. and G.A. Vedenyapin, 1971, Fiz. Khim. Mekhan. Mat. **7** [3], 96. Engl. Transl. 1973, Sov. Mater. Sci. **7**, 346.

Borisov, E.V., G.A. Vedenyapin, L.V. Smirnov and Yu.S. Suganeev, 1971, Fiz. Khim. Obrabot. Mat. [1], 75.

Bridgman, P.W., 1954, Proc. Amer. Acad. Arts Sci. **83**, 1.

Brown, H.L., P.E. Armstrong and C.P. Kempter, 1966, J. Less-Common Metals **11**, 135.

Burdett, C.F. and R.B. Layng, 1967a, Brit. J. Appl. Phys. **18**, 367.

Burdett, C.F. and R.B. Layng, 1967b, Brit. J. Appl. Phys. **18**, 1551.

Burdett, C.F. and R.B. Layng, 1968, Brit. J. Appl. Phys. **1**, 1005.

Burdett, C.F., 1968, Phil. Mag. **18**, 745.

Burdett, C.F., 1969, Phil. Mag. **19**, 555.

Burdett, C.F., 1970, Phil. Mag. **21**, 755.

Burkhanov, A.M., N.P. Grazhdankina and I.G. Fakidov, 1967, Fiz. Tverd, Tela **9**, 748. Engl. Trans. 1967, Sov. Phys.-Solid State **9**, 586.

Carlson, O.N., D.W. Bare, E.D. Gibson, and F.A. Schmidt, 1959, Survey of the Mechanical Properties of Yttrium and Yttrium Alloys, in: *Symposium on Newer Metals*, A.S.T.M. Spec. Tech. Pub. No. 272 (American Society for Testing Materials, Philadelphia) pp. 144–159.

Carnahan, T.G. and T.E. Scott, 1973, Met. Trans. **4**, 27.

Clinard, F.W., 1969, J. Appl. Phys. **40**, 3067.

Cline, C.F., H.L. Dunegan and G.W. Henderson, 1967, J. Appl. Phys. **38**, 1944.

Darnell, F.J., 1963, Phys. Rev. **132**, 128.

Dashkovskiy, A.I. and E.M. Savitskiy, 1961, Met. i Metall. Chistykh Metallov [3], Moscow, Gasatomizdat. Also discussed in Savitskiy et al. (1963).

du Plessis, P. deV., 1976, J. Phys. F: Metal Phys. **6**, 873.

Evdokimova, V.V. and Yu.S. Genshaft, 1965, Fiz. Tverd. Tela **6**, 2449. Engl. Transl., 1965, Sov. Phys.-Solid State, **6**, 1941.

Fisher, E.S. and L.C.R. Alfred, 1968, Trans. AIME **242**, 1575.

Fisher, E.S. and D. Dever, 1967, Trans. AIME **239**, 48.

Fisher, E.S. and D. Dever, 1968. Anomalous Effects of Temperature and Impurities on the Elastic Moduli of Scandium Single Crystals, presented at 7th Rare Earth Research Conference, Coronado, California. ANL-MS-1048, Argonne National Laboratory, Argonne, Illinois. ~~Also reported by Gschneidner, K.A., 1975, in *Scandium*,~~ Gschneidner, K.A., 1975, in *Scandium*, Horovitz, C.T., K.A. Gschneidner, G.A. Nelson, D.H. Youngblood and H.H. Schock, eds. (Academic Press, New York, 1975) pp. 76–110.

Fisher, E.S., M.H. Manghnani and R. Kikuta, 1973, J. Phys. Chem. Solids **34**, 687. Also appeared as: Fisher, E.S. and D.J. Dever, 1968, Proc. 6th Rare Earth Conf. Gatlinburg, Tenn. (1967), pp. 522–533.

Frolov, A.P., K.P. Rodionov and L.F. Vereshchagin, 1969, Fiz. Metal. Metalloved. **28**, 993. Engl. Transl., 1969, Phys. Met. Metallogr. **28**, 34.

Geiselman, D., 1962, J. Less-Common Metals **4**, 362.

Gladkikh, A.N., V.A. Skudnov and L.D. Sokolov, 1969a, Izv. Akad. Nauk SSSR, Metal. [3], 94. Engl. Transl., 1969, Russ. Met [3], 75.

Gladkikh, A.N. et al., 1969b, Fiz. Khim. Obrabotka Mater. [4], 151.

Gladkikh, A.N., 1970, Izv. Akad. Nauk Azerb. SSR, Ser. Fiz.-Tekh. Mat. Nauk [5], 115.

Gladkikh, A.N., 1975, Met. i Term. Obrabotka Metallov (MiTOM) [7], 12. Engl. Transl., 1975, Met. Sci. Heat Treat. **17**, 558.

Greiner, J.D., R.J. Schiltz, J.J. Tonnies, F.H. Spedding and J.F. Smith, 1973, J. Appl. Phys. **44**, 3862.

Greiner, J.D., D.M. Schlader, O.D. McMasters, K.A. Gschneidner and J.F. Smith, 1976, J. Appl. Phys. **47**, 3427.

Gschneidner, K.A., 1964, in *Solid State Physics*, Seitz, F. and D. Turnbull eds. (Academic Press, New York, 1964), vol. 16, p. 275.

Gust, W.H. and E.B. Royce, 1973, Phys. Rev. B **8**, 3595.

Hall, H.T. and L. Merrill, 1963, Inorg. Chem. **2**, 618.

Hill, R., 1952, Proc. Phys. Soc. **65**, 350.

Huntington, H.B., 1958, in *Solid State Physics*, Seitz, F. and D. Turnbull, eds. (Academic Press, New York, 1958), vol. 7, Chap. 3.

Kayser, F.X., 1970, Phys. Rev. Lettrs. **25**, 662.

Kayser, F.X., 1971, Phys. Status Solidi-A **8**, 233.

Klimker, H. and M. Rosen, 1973, Phys. Rev. B **7**, 2054.

Koepke, B.G., E.D. Gibson, and T.E. Scott, 1967, Trans. Quart. ASM **60**, 409.

Koskimaki, D.C., K.A. Gschneidner, Jr. and N.T. Panousis, 1974, J. Cryst. Growth **22**, 225.

Lenkkeri, J.T. and S.B. Palmer, 1977, J. Phys. F: Metal Phys. **7**, 15.

Levitin, R.Z. and S.A. Nikitin, 1961, Fiz. Metal. Metalloved. **11**, 948. Engl. Transl., 1961, Phys. Met. Metallogr. **11**, 121.

Liebermann, H.H. and C.D. Graham, Jr., 1977, Acta Met. **25**, 715.

Liu, L.G., 1975, J. Phys. Chem. Solids **36**, 31.

Long, M., A.R. Wazzan and R. Stern, 1969, Phys. Rev. **178**, 775.

Love, B., 1959, "Selection and Evaluation of Rare or Unusual Metals – Part II. The Metallurgy of Yttrium and the Rare Earth Metals," WADC-TR-57-666, Wright Air Development

Guinan; M.W. and D.J. Steinberg, 1974, J. Phys. Chem. Solids 35, 1501.

Center, U.S. Air Force, Wright-Patterson Air Force Base, Ohio (March 1959).
Love, B., 1960, "The Metallurgy of Yttrium and Rare Earth Metals – Part II. Mechanical Properties," WADD-TR-60-74 (Pt. 2), Wright Air Development Division, U.S. Air Force, Wright-Patterson Air Force Base, Ohio (June 1960).
Lüthi, B., M.E. Mullen and E. Bucher, 1973, Phys. Rev. Lett. **31**, 95.
Maeda, T., 1971, J. Phys. Soc. Japan **30**, 375.
McWhan, D.B., P.C. Souers and G. Jura, 1966, Phys. Rev. **143**, 385.
Milstein, F. and J.A. Baldwin, Jr., 1972, J. Inst. Metals **100**, 337.
Milstein, F., J.A. Baldwin, Jr. and T.W. James, 1973, J. Appl. Phys. **44**, 4824.
Monfort, C.E. and C.A. Swenson, 1965, J. Phys. Chem. Solids, **26**, 623.
Musgrave, M.J.P., 1954, Proc. Roy. Soc. **A226**, 339 and 356.
Nabutovskaya, O.A., 1969, Fiz. Tverd. Tela **11**, 1434. Engl. Transl., 1969, Sov. Phys.-Solid State **11**, 1172.
Naumkin, O.P., V.F. Terekhova, and E.M. Savitskiy, 1963, Fiz. Metal. Metalloved. **16** [5], 663. Engl. Transl., 1963, Phys. Met. Metallogr. **16**, 22.
Nye, J.F., 1957, Physical Properties of Crystals (Oxford University Press, London, 1957) p. 147.
Owen, C.V. and T.E. Scott, 1968, J. Less-Common Metals **16**, 447.
Owen, C.V. and T.E. Scott, 1970, J. Less-Common Metals **21**, 427.
Owen, C.V. and T.E. Scott, 1971, J. Less-Common Metals **25**, 161.
Owen, C.V. and T.E. Scott, 1974, J. Less-Common Metals **37**, 353.
Owen, C.V. and T.E. Scott, 1975, J. Less-Common Metals **41**, 303.
Owen, C.V. and T.E. Scott, 1976, J. Less-Common Metals **46**, 151.
Owen, C.V. and T.E. Scott, 1977, J. Less-Common Metals **51**, 117.
Palmer, S.B. and E.W. Lee, 1972, Proc. Roy. Soc. A**327**, 519.
Palmer, S.B., E.W. Lee and M.N. Islam, 1974, Proc. Roy. Soc. Ser. A **338**, 341.
Palmer, S.B., 1975, J. Phys. F: Metal Phys. **5**, 2370.
Rapperport, E.J. and C.S. Hartley, 1959, Trans. TMS-AIME **215**, 1071.
Reuss, A., 1929, Z. Angew. Math. Mech. **9**, 49.
Rhyne, J.J., and S. Legvold, 1965, Phys. Rev. A **138**, 507.
Rosen, M., 1967, Phys. Rev. Lettrs. **19**, 695.
Rosen, M., 1968a, Phys. Rev. **166**, 561.
Rosen, M., 1968b, Phys. Rev. **174**, 504.
Rosen, M., 1969a, Phys. Rev. **181**, 932.
Rosen, M., 1969b, Phys. Rev. **180**, 540.
Rosen, M., 1971, J. Phys. Chem. Solids **32**, 2351.
Rosen, M. and H. Klimker, 1970, Phys. Rev. **1**, 3748.
Rosen, M., D. Kalir and H. Klimker, 1974, J. Phys. Chem. Solids **35**, 1333.
Ross, I.N., 1967, J. Inst. Mets. **95**, 337.
Salama, K., F.R. Brotzen and P.L. Donoho, 1972, J. Appl. Phys. **43**, 3254.
Salama, K., F.R. Brotzen and P.L. Donoho, 1973, J. Appl. Phys. **44**, 180.
Savitskiy, E.M. and V.F. Terekhova, 1955, Izv. Sekt. Fiz. Khim. Anal. (Inst. Obshehei Neorg. Khim. Akad. Nauk SSSR), pp. 148–155.
Schaufelberger, Ph. and H. Merx, 1975, High Temp.-High Pressures **7**, 55.
Shibarov, V.V., D.I. Shetulov and L.D. Sokolov, 1971, Fiz. Khim. Mekhan. Mat. **7** [3], 29. Engl. Transl., 1973, Sov. Mater. Sci. **7**, 280.
Simmons, C.R., 1959, "The Mechanical Properties of Yttrium, Scandium and the Rare Earth Metals," AECU-4423, General Electric Co., Aircraft Nuclear Propulsion Dept., Cincinnati, Ohio.
Simmons, C.R., 1961, The Mechanical Properties of Yttrium, Scandium, and the Rare Earth Metals, in: Spedding, F.H. and A.H. Daane, eds., *The Rare Earths* (John Wiley and Sons, New York) pp. 428–452.
Skudnov, V.A., L.D. Sokolov and A.N. Gladkikh, 1969a, Izv. Akad. Nauk Arm. SSR, Ser. Tekh. Nauk **22**, 43.
Skudnov, V.A., L.D. Sokolov and A.N. Gladkikh, 1969b, Izv. Akad. Nauk BSSR, Ser. Fiz.-Tekh. Nauk [2], 114. Engl. Transl. available as Doc. No. AD-742-893 from National Technical Information Center, Springfield, VA, 22151.
Smith, J.F., C.E. Carlson and F.H. Spedding, 1957, J. Metals **9**, 1212.
Smith, J.F. and F.A. Gjevre, 1960, J. Appl. Phys. **31**, 645.
Sokaski, M., 1975, "Low Temperature Deformation Characteristics of Yttrium Single Crystals," Ph.D. Thesis, Oregon State University, Corvallis, Oregon.
Sokolov, L.D., A.N. Gladkikh, and V.A. Skudnov, 1969a, Izv. Akad. Nauk Arm. SSR, Ser. Tekh. Nauk **22**, 52.
Sokolov, L.D., V.A. Skudnov and A.N. Gladkikh, 1969b, Probl. Prochnosti [6], 104. Engl. Transl., 1969, Strength Mater. [6], 671.
Sokolov, L.D., V.M. Solenov, V.A. Skudnov, A.M. Shneyberg, and A.N. Gladkikh, 1970a, Izv. Akad. Nauk SSSR, Metal. [2], 181. Engl. Transl., 1970, Russ. Met. [2], 106.
Sokolov, L.D., V.M. Solenov, V.A. Skudnov and A.N. Gladkikh, 1970b, Fiz. Metal. Metalloved. **30**, 894. Engl. Transl., 1970, Phys, Met. Metallogr. **30**, 232.
Sokolov, L.D., V.M. Solenov, A.N. Gladkikh and V.A. Skudnov, 1971, Probl. Prochnosti [3], 67. Engl. Transl., 1971, Strength Mater. [3], 308.
Sokolov, L.D., 1972, Mekhanicheskie Svoistva Redkikh Metallov (Mechanical Properties of the Rare Metals) (Izdatel'stvo "Metallurgiya," Moscow), p. 103.
Solenov, V.M., L.D. Sokolov and A.N. Gladkikh, 1969, Fiz. Metal. Metalloved. **28** [5], 915. Engl. Transl., 1969, Phys. Met. Metallogr. **28** [5], 159.
Owen, C.V. and T.E. Scott, 1973, J. Less-Common Metals 30, 113.
Rosen, M., D. Kalir and H. Klimker, 1973, Phys. Rev. B 8, 4399.
Savitskiy, E.M., V.F. Terekhova, I.V. Burov, I.A. Markova and O.P. Naumkin, 1962, in Rare Earth Alloys (Publishing House of the Academy of Sciences USSR, Moscow; Engl. transl., U.S. Atomic Energy Commission Report AEC-tr-6150), pp. 45-48 (pp. 52-55 in Engl. transl.).

Solenov, V.M., L.D. Sokolov, V.A. Skudnov and A.N. Gladkikh, 1971, Met. i Term. Obrabotka Metallov (MiTOM) [6], 66. Engl. Transl., 1971, Met. Sci. Heat Treat. **13**, 519.
Spedding, F.H., D. Cress, and B.J. Beaudry, 1971, J. Less-Common Metals **23**, 263.
Spedding, F.H., J.J. Hanak and A.H. Daane, 1958, Trans. AIME **212**, 379.
Srivastava, O.N. and J. Kumar, 1968, Phys. Lett. **27 A**, 675.
Stephens, D.R., 1964, J. Phys. Chem. Solids **25**, 423.
Stephens, D.R. and Q. Johnson, 1969, J. Less-Common Metals **17**, 243.
Suganeyev, Yu.S., M.Kh. Shorshorov and M.V. Yakutovich, 1970, Izv. Akad. Nauk SSSR, Metally [3], 132. Engl. Transl., 1970, Russ. Met. [3], 95.
Syassen, K. and W.B. Holzapfel, 1975, Solid State Comm. **16**, 533.
Terekhova, V.F. and E.M. Savitskiy, 1967, *Yttrium* (Academy of Sciences U.S.S.R., A.A. Baikov Inst. Metallurgy, Moscow). Engl. Transl. available as AEC-tr-6980 from U.S. Dept. of Commerce (1970), pp. 47–61.
Tonnies, J.J., K.A. Gschneidner, Jr. and F.H. Spedding, 1971, J. Appl. Phys. **42**, 3275.
Vaidya, S.N. and G.C. Kennedy, 1970, J. Phys. Chem. Solids **31**, 2329.
Varanov, F.F., L.F. Vereshchagin and V.A. Goncharova, 1960, Dokl. Akad. Nauk SSSR **135**, 1104. Engl. Transl., 1960, Sov. Phys.-Doklady **135**, 1280.
Voigt, W., 1928, Lehrbuch der Kristallphysik (B.G. Teubner, Leipzig, 1928) p. 956.
Weertmann, J., 1955, J. Appl. Phys. **26**, 1213.
Weertmann, J., 1957, J. Appl. Phys. **28**, 362.
Westlake, D.G., 1967, Acta Met. **15**, 1407.
Wolcott, N.M., 1959, J. Chem. Phys. **31**, 536.

Handbook on the Physics and Chemistry of Rare Earths, edited by K.A. Gschneidner, Jr. and L. Eyring

Chapter 9

HIGH PRESSURE STUDIES: METALS, ALLOYS AND COMPOUNDS

A. JAYARAMAN
Bell Laboratories, Murray Hill, New Jersey 07974, USA

Contents

Symbols

A_i = exchange interaction
c_p = specific heat at constant pressure
D = density
E_F = Fermi energy
G = Gibbs' free energy
g = Landé's g factor
H = magnetic field
J = total angular momentum
K = compressibility
k_f = wave vector of cond. electron
L = latent heat
M = atomic mass
m = magnetic moment
m^* = effective mass of electron
n = molecular field coefficient
P = pressure
R = gas constant
S = entropy
$\bar{S}$ = spin quantum number
T = temperature
U = internal energy
U_p = particle velocity
U_s = shock velocity
V = volume
w_m = magnetic energy
α = linear coefficient of thermal expansion
β = volume coefficient of thermal expansion
Γ = coupling constant
μ_B = Bohr magneton
ρ = resistivity
σ = specific magnetization
σ_s = saturation magnetization
θ_c = ferrimagnetic Curie temperature
θ_{Fi} = ferrimagnetic Curie temperature
θ_N = Néel temperature
θ_p = paramagnetic Curie temperature

1. Introduction

From the point of view of high pressure studies, the rare earth metals, their alloys and compounds have been one of the most exciting systems. P.W. Bridgman was the earliest to study rare earth elements under pressure (Lawson, 1956). Bridgman measured the resistivity as well as the compressibility of the entire series up to about 100 kbar and noted anomalies in some of the elements. Bridgman was the first to discover the now well-known electronic transition in Ce at 7 kbar at room temperature. Since Bridgman's earlier measurements, the melting behavior and phase stability including magnetic transitions of almost all the rare earth elements have been quite extensively investigated. The resistivity and compressibility measurements have been extended to ultra-high pressure regions (several hundred kbar static pressure) and P-V relationships to the megabar range, using shock wave techniques. The introduction of many new techniques of study at high pressure, and the extension of the pressure range to ultra-high pressure regions have unraveled several unusual and new phenomena in rare earth systems. Very interesting pressure-induced structural transformation sequence, pressure-induced electronic transitions (valence state changes) and unusual melting behavior have come to light. In earlier general reviews on phase transformations in solids at high pressure (Klement and Jayaraman 1966, Pistorius 1976) phase changes in rare earths have been covered briefly. Also, in the present volume the behavior of Ce under pressure and the valence changes in compounds are especially covered in chs. 4 and 20, respectively. In this chapter we will be concerned with the effect of pressure on structure, fusion behavior, resistivity, $P-T$ diagrams of rare earth elements, compressibility and shockwave studies, magnetic transitions under pressure and synthesis of new phases involving rare earths at high pressure and temperature.

2. Pressure-induced structure change in metals

The rare earth metals crystallize in close packed structures (Gschneidner, Jr. 1961a, Gschneidner, Jr. 1961b) with the exception of Eu which has the body centered cubic (bcc) arrangement. Normally La, Pr, Nd and Pm have the double hexagonal close packed (dhcp), Sm a rhombohedral, Ce and Yb the face centered cubic (fcc) and Gd to Lu the hexagonal close packed (hcp) structure. These structures represent different stacking arrangements of the atomic layers; hcp-ABAB...(hhh), Sm-type ABABCBCAC,ABAB...(hhc, hhc), dhcp-ABACABAC (hchc...) and fcc:–ABC, ABC...(ccc). Further, most of the rare earth metals undergo a temperature induced transformation to the bcc structure at high temperatures, before melting. The range of stability of the allotropes of rare earth metals as a function of temperature and also the structures that occur in intrarare earth alloys have been particularly well covered in the reviews of Koch (1970) and Altstetter (1973). The latter reviews have also discussed the pressure-induced phase transformations in the rare earth metals and intrarare earth alloys.

Bridgman noted anomalies in resistivity as well as in compressibility in the case of Ce at about 7 kbar, in Yb ~ 40 kbar, in La ~ 25 kbar and in Gd ~ 25 kbar (see Lawson, 1956); the transformation is found to be rather sluggish in the latter two. Subsequent studies have shown that these anomalies are associated with crystal structure changes; in the case of Ce due to γ to α-Ce transition (see ch. 4), in Yb due to fcc→bcc transition (Hall et al. 1963), in La due to dhcp→fcc transition (McWhan and Bond, 1964) and in the case of Gd due to hcp→Sm-type rhombohedral structure change (Jayaraman and Sherwood, 1964a). Further, Sm has been found to transform to the dhcp structure near 30 kbar (Jayaraman and Sherwood, 1964b). The high pressure phases of Gd and Sm were made by pressurizing samples to 35 kbar at about 300°C and the transformed phases were found to be metastably retained at atmospheric pressure and room temperature; the Sm-type phase of Gd was however less stable compared to the dhcp phase of Sm. Based on these results, and from the structural pattern observed in the intrarare earth alloy systems involving a lighter and a heavier rare earth, Jayaraman and Sherwood (1964b) proposed, that there exists a pressure-induced transformation sequence in the rare earth elements, from hcp→Sm-type→dhcp→fcc, with increasing pressure, the same being true for the alloy systems Jayaraman and Sherwood (1964b) proposed that there exists a pressure-induced have been reported; in Pr and Nd from dhcp to fcc (Piermarini and Weir, 1964, King and Harris, 1970); in Tb, Dy and Ho, from hcp to Sm-type (McWhan and Stevens 1965 and Stephens and Johnson, 1969) and similar transformation (hcp→Sm-type) in Tm and Lu (Liu et al. 1973, and Liu 1975). Perez-Albuerne et al. (1966) reported a transformation from hcp to dhcp in Ho, Er and Tm (quoted pressures are 75, 90, and 110 kbar respectively) and this has been construed as a violation of the proposed sequence of transformation. However the recent work of Liu et al. (1973) and Liu (1975) has definitely shown that there is no violation of the sequence. It is possible that in the work of Perez-Albuerne et al. the pressures were in excess for the Sm-type phase to be stable and therefore the Sm-phase was missed. It is also likely that the additional Debye Scherrer lines that appear with the loss of cubicity could also be easily missed because of broadening and preferred orientation problems that are usually present in the anvil type high pressure cells.

The most remarkable change in the physical property associated with the transition in Gd is the disappearance of ferromagnetic ordering in the Sm-type structure; in the latter structure Gd shows antiferromagnetic ordering (Jayaraman and Sherwood, 1964a; McWhan and Stevens, 1965). This is also found to be true in the intrarare earth alloys of Gd, wherein ferromagnetic ordering exists only in the hcp phase (Jayaraman et al., 1966).

Several explanations have been advanced to rationalize the observed sequence of close-packed structures, namely, hcp→Sm-type→dhcp→fcc: (1) correlations with an averaged effective atomic number (Lundin, 1966; Harris and Raynor, 1969); (2) Influence of 4f electrons (McWhan and Stevens 1965, Gschneidner and Valletta 1968); (3) stability of close packed structures on the basis of a theory of interactions between pairs of close packed planes (Hodges, 1967), and (4) phase transitions at certain critical values of an atomic parameter f which can be

related to the pseudopotential (Johansson and Rosengren, 1975). The correlation proposed by Lundin is a size effect correlation while that of Harris and Raynor is a rationalization based on the c/a ratio, which falls into distinct regions as a function of atomic number or average atomic number for the intrarare earth alloys (see fig. 9.1). McWhan and Stevens (1965) suggested that the degree of delocalization of the 4f electron with pressure and hence the degree of participation of the 4f electron in the bonding might be responsible for the transformation sequence. Gschneidner and Valletta (1968) expanded on this idea of 4f electron contribution to the bonding and have attempted a semiquantitative correlation between the observed structure and the ratio R_m/R_{4f}; R_m being the metallic radius of the rare earth metal and R_{4f} the radius of the 4f electron. According to this, fcc is stable when $R_m/R_{4f} \leq 3.24$, dhcp $-3.28 \leq R_m/R_{4f} \leq 3.54$, Sm-type $-3.60 \leq R_m/R_{4f} \leq 3.65$ and hcp when $R_m/R_{4f} \geq 3.68$. In calculating the

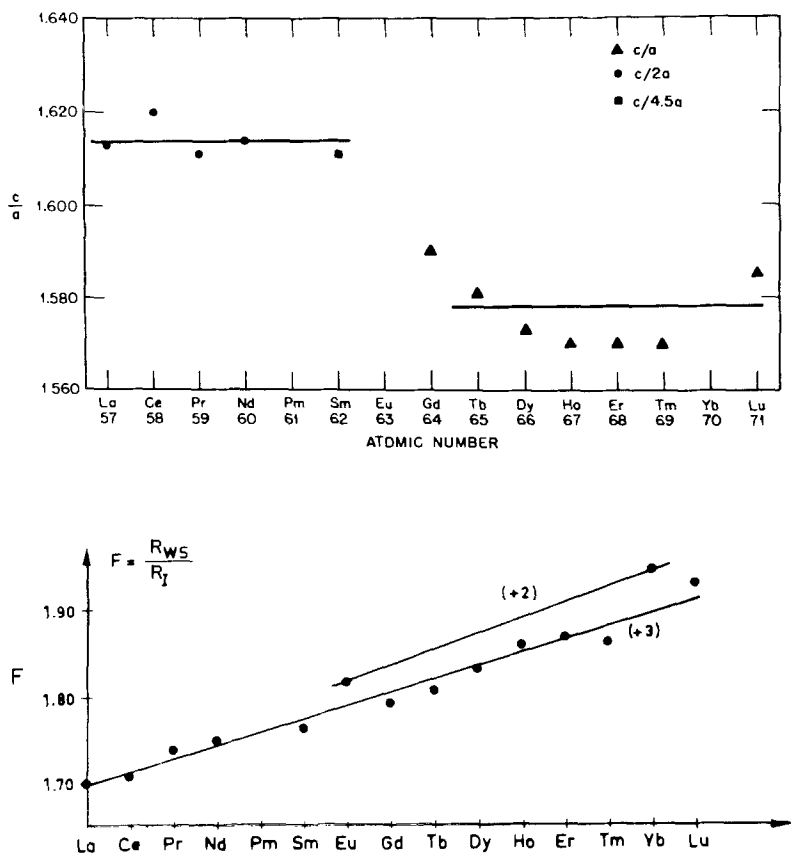

Fig. 9.1. c/a ratio (upper fig.) vs atomic number, the ratio of Wigner–Seitz radius (R_{WS}) to the ionic radius (R_I) (lower fig.) vs atomic number for the lanthanide metals (from Johansson and Rosengren, 1975).

ratio R_m/R_{4f} for the pressure induced polymorphs in the elements they assumed the 4f radius to be independent of pressure, and calculated the metallic radius from the known compressibility data. The agreement between the semiquantitative calculations and experimental data appears reasonable. The approach of Hodges (1967) is through establishing a connection of the interaction energy (stacking fault energy) between pairs of close-packed planes and the deviation from the ideal c/a ratio. Again, Hodges seems to have obtained good agreement for the rare earths. Although these correlations are interesting they are not free from objections. For instance pressure effect is in the opposite direction from the size effect. The influence of 4f bonding may also be questioned, since there are systems such as LaY where the influence of 4f electron may not exist. Johansson and Rosengren's (1975) approach although empirical appears to be free from most of the objections. As mentioned earlier, one of the puzzling facts about the pressure-induced transition sequence is, the more an element is compressed the more its structure tends to be "light element like". Johansson and Rosengren (1975) have argued that this difficulty disappears when one considers the ratio R_{WS}/R_I, where R_{WS} is the Wigner–Seitz radius and R_I is the ionic radius, as the factor determining the structural stability. They argue that when the volume decreases, R_{WS} decreases, but the ionic radius remains insensitive to pressure and this would cause the free electrons (which now have less volume available because of smaller R_{WS}), to act in a relative sense as if R_I has increased. Hence the greater the pressure the smaller will be the R_{WS}/R_I and the system will be forced to behave like the lower atomic number element (see fig. 9.1). The above arguments are similar to those of Gschneidner and Valletta, but do not involve the 4f electrons. In their paper Johansson and Rosengren (1975) have rationalized the observed crystal structures in the rare earths by using a characterizing parameter f: $f = r_s/r_c$, where r_s is the value which minimizes the total energy E ($E = E_{kin} + E_{HF} + E_{corr} + E_{pseud} + U_{bs} + U_{ew}$, where the various energy contributions are the kinetic, Hartree–Fock, correlation, pseudopotential and the U_{bs} and U_{ew} are associated with the first and second order pseudopotential and the ion–ion interaction energy respectively) for a given value of the pseudopotential core radius r_c (r_c is an atomic parameter, proportional to the radius of the outer orbital of the ion). The quantity f increases with the atomic number. Using the alloy data from the Gd–Pr system they calculate r_c and obtain $r_c = 0.381$ for the Pr concentration at which the structure changes from hcp to the Sm-type, a value corresponding to a "fictitious element" between Sm and Gd. For this "fictitious element" they calculate the corresponding equilibrium density, from which the critical value of f is obtained for hcp to Sm-type structure transformation as $f = 6.88$. According to Johansson and Rosengren (1975) the pressure of transition for a particular rare earth element can also be calculated by finding the volume at which the energy dependence on c/a for the element under consideration can be matched with that of the "fictitious element". Apparently this matching occurs only at a certain critical volume of the element. The compression required to obtain this critical volume represents the critical pressure for the transition. Adopting this

procedure the transition pressures for the hcp → Sm-type transition for the heavy rare earths from Gd to Lu have been calculated and the values are found to be in good agreement with the experimental values. Further, the onset of the transition occurs near the predicted f value of 6.88 (see table 9.1). For Sm-type to dhcp transition they obtain $f_{\text{critical}} = 6.64$ from the element Nd.

The above approach is very useful, in view of the inherent inability in carrying out precisely the cohesive energy calculations for different structures and showing which one would be favored under a given condition. The changes involved are subtle and must be connected with subtle changes occurring in the Fermi-surface Brillouin Zone interactions and hence must be traced to electronic instabilities in the system. To understand them fully, experimental work of a rather sophisticated nature, perhaps on single crystals needs to be done.

2.1. *The case of* Ce, Eu *and* Yb

Cerium metal is discussed in ch. 4 and only a brief mention of its high pressure behavior will be made here (for references see the list in ch. 4). Cerium can exist at atmospheric pressure in the fcc (γ) or dhcp (β) form and undergoes an isostructural transition near 100 K to another fcc-form referred to as α-Ce. The γ-α Ce transition occurs at 7 kbar at room temperature and this transition is accompanied by about 8% volume decrease. This is one of the most widely studied transitions as a function of pressure and temperature and is believed to involve a valence change from 3^+ towards a higher valence state (3.7^+). The γ to α transition line terminates at a critical point; the very first example in which a solid – solid transition was shown to exhibit a liquid–vapor-like critical point. A pressure-induced phase transition near 50 kbar, initially reported to be yet another isostructural transition has been shown to be from fcc (α-Ce) to an orthorhombic phase with the α-U structure. Stager and Drickamer (1964) have reported a pronounced resistance anomaly near 120 kbar indicative of a phase transition, but the nature of this transition is unknown. The fusion behavior of Ce is again unique in that it exhibits a minimum.

TABLE 9.1
Calculated and experimental values for hcp → Sm type structure transition (Johansson and Rosengren, 1975).

Element	Critical pressure (kbar)		Critical value of f
	Calculated	Experimental	
Gd	23	32	6.89
Tb	36	38	6.90
Dy	54	52	6.91
Ho	73	72	6.92
Er	92	99	6.93
Tm	117	119	6.94
Lu	167	~200	6.96

Both Eu and Yb are divalent in the metallic state and exhibit a striking resemblance to the alkaline earth metals Ba and Sr in their properties including the high pressure behavior. They are similar in their crystal structure at atmospheric pressure; Eu and Ba are both bcc, Yb and Sr are fcc. The existence of a hcp phase in very pure Yb has been established in recent low temperature studies (see Altstetter, 1973). Europium shows a sharp rise in resistivity at about 150 kbar (revised pressure scale) followed by a decrease (Stager and Drickamer, 1964). Johansson and Rosengren (1975) (also in Rosengren and Johansson 1976) have calculated the enthalpies for di- and trivalent Eu as a function of pressure and find a transition near 150 kbar. The static compression data of Eu in the low pressure region and the compression obtained from the shock wave data for the high pressure region have been presented in support of the occurrence of such a transition. Since Ba becomes hcp at the 55 kbar transition, a similar transition may be expected in Eu.

Ytterbium has been shown to undergo a structural transition from fcc to the bcc structure near 40 kbar at room temperature, by Hall et al. (1963). The latter have argued that this transition involves a change in the valence state from 2^+ to the 3^+ state but this has been shown to be untenable and the fcc – bcc transition is the same as the temperature induced fcc – bcc transition occurring at atmospheric pressure (see fig. 9.4 in the next section, Jayaraman, 1964). Strontium exhibits similar behavior and there can be no valence change in Sr (Jayaraman et al., 1963). Also subsequent high pressure studies on Yb (Katzman and Mydosh, 1972) have not given support to any valence transition in the 1 to 100 kbar region. From binding energy calculations, Johansson and Rosengren (1975) predict a valence change from 2^+ to the 3^+ state in Yb metal near 140 kbar and again present the static and shock compression data as a support.

Both Eu and Yb, whose divalent character is an anomaly among the rare earth metals, can be expected to become trivalent at high pressure. Even if the transition pressures are larger by a factor of two than the predicted values, it should be possible to verify its occurrence by a direct high pressure X-ray diffraction study.

3. Fusion behavior under pressure and P–T diagrams of RE metals

For a first-order transition the criterion for equilibrium between two phases is the equality of the Gibbs free energy G

$$G = U - TS + PV \tag{9.1}$$

of the phases. By equating infinitesimal variations in G along the transition line one obtains the well-known Clapeyron equation

$$\frac{\mathrm{d}T_{\mathrm{Tr}}}{\mathrm{d}P} = \frac{\Delta V}{\Delta S} = \frac{\Delta V}{L} T_{\mathrm{Tr}}, \tag{9.2}$$

where T_{Tr} is the transition temperature at standard pressure, ΔV is the volume

change, ΔS is the entropy change and L is the latent heat of transition. When dT/dP is determined for a transition ΔV or ΔS can be calculated via the Clapeyron equation, if one of the latter two quantities are known.

If the transition is second-order the Ehrenfest relation can be employed

$$\frac{dT_{Tr}}{dP} = VT_{Tr}\frac{\Delta\beta}{\Delta C_p} = \frac{\Delta K}{\Delta\beta} \tag{9.3}$$

if β is the volume coefficient of expansion, K the compressibility and C_p the specific heat at constant pressure of the two phases are known. For a λ-type second-order transition

$$\frac{dT_{Tr}}{dP} = VT_{Tr}\frac{\Delta\beta}{\Delta C_p} = 3\,V\,T_{Tr}\frac{(\Delta\alpha)}{\Delta C_p}, \tag{9.4}$$

where $\Delta\alpha$ is the difference in the linear thermal expansion coefficients between the two phases.

The fusion behavior of most of the rare earth metals has been investigated to moderate pressures, except those of the very high melting end members; in the latter only the initial slopes have been established (Jayaraman, 1964, 1965a, 1965b; Klement and Jayaraman, 1966 and Young, 1975). The P–T diagrams of the lanthanide elements are shown in fig. 9.2 and the thermodynamic data of interest obtained are presented in table 9.2. Using the published experimental data and adopting certain fitting procedures, Johansson and Rosengren (1975) have constructed a generalized phase diagram for the trivalent lanthanide (see fig. 9.3). The various solid–solid transitions and the melting curves are fused in the diagram. Not fitted into the general scheme are the anomalous cases; Ce, Eu and Yb. The phase diagram for Ce is shown in figs. 4.1 and 4.2 and a discussion is presented in ch. 4, section 2 about its anomalous features. In fig. 9.4 the P–T diagrams of Eu and Yb are presented. Europium exhibits a fusion curve maximum and possibly Yb has also a maximum. It is seen that the fcc–bcc transition encountered at 40 kbar for Yb at room temperature is due to the intersection of the fcc–bcc line coming down from the high temperature region. The P–T diagrams of Eu and Yb are strikingly similar to that of Ba and Sr respectively, at least in so far as the moderate pressure region goes. If the predicted valence change from 2^+ to the 3^+ state were to occur in Eu and Yb near 150 kbars, this region of the P–T diagram would be very interesting and quite anomalous.

Recently Carter et al. (1975) have extended the melting curves of the rare earth metals to the ultra high pressure region by calculation and have predicted melting curve maxima for almost all the rare earths. Some of these diagrams are presented in fig. 9.5.

A rather interesting plot (see fig. 9.6a) is the initial melting slope dT/dP of the rare earth elements versus atomic number. In this plot the divalent and trivalent lines are well established from the slopes of Eu and Yb and from La, Gd and Lu respectively. The quadrivalent line drawn parallel to these is perhaps not unreasonable. The deviations of the data points from the trivalent line, of Sm

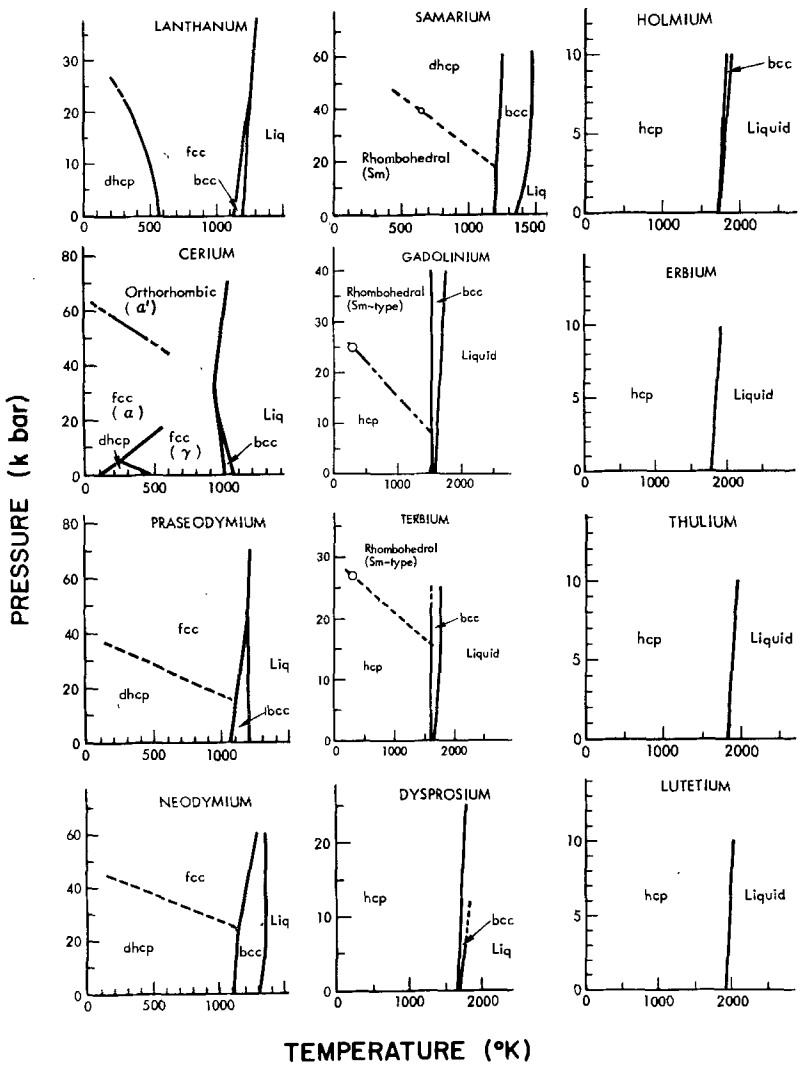

Fig. 9.2. P–T diagrams of the lanthanide metals, from Young's (1975) compilation of Jayaraman, 1965 and Stephens, 1965 data. Pure Ho at atmospheric pressure does not appear to have a bcc allotrope, but apparently the bcc phase field appears at high pressure.

and the heavier rare earths (Tb through Tm) were attributed to a partial change in the valence to the divalent state upon melting and to a partial change to the quadrivalent state in the case of Ce and Pr. In this connection it is interesting to compare the plot of the ionization energy I of the divalent rare earth ions against atomic number (fig. 9.6b) taken from the paper of Johansson and Rosengren (1975) with fig. 9.6a. The resemblance is striking. However there appears to be no evidence from high temperature enthalpy data (ΔH_{fus}) for any valence change upon melting.

TABLE 9.2.

Thermodynamic data for lanthanide metals S–S = transformation to bcc structure; S–L = melting. From Jayaraman (1965); Melting and transformation temperature from ch. 2, tables 2.15 and 2.14, respectively.

R.E. metal	MP (°C)	Transformation temperature to bcc (°C)	ΔS/mol. S–S e.u.	S–L	dT/dP°/kbar S–S	S–L	ΔV/mol. S–S cm^3	S–L
La	918	865	0.67	1.34	5	2.5	0.14	0.14
Ce	798	726	0.70	1.157	−1.4	−4.7	−0.04	−0.22
Pr	931	795	0.71	1.365	~2[a]	~0.1	0.06	0.005
Nd	1021	863	0.63	1.314	~2[a]	3.5	0.05	0.19
Sm	1074	922	0.625	1.53	~3[b]	11.5	0.08	0.72
Eu	822			2.23		15		1.39
Gd	1313	1235	0.607	1.53	~−1.5[c]	6.5	−0.04	0.41
Tb	1356	1289	0.80	1.56	~0.4[c]	9		0.61
Dy	1412	1381	...	2.04	~5.0[c]	~12		0.93
Ho	1474		...	2.25	~12[c,d]	~15		1.4
Er	1529			2.67		~15		1.66
Tm	1545			2.31		~12		1.25
Yb	819	795	0.396	1.64	−16	19	−0.26	1.26
Lu	1663			1.71	~8.5			0.64

[a]dhcp → bcc; [b]rhombohedral → bcc; [c]hcp → bcc; [d]The bcc phase in Ho apparently exists at high pressure.

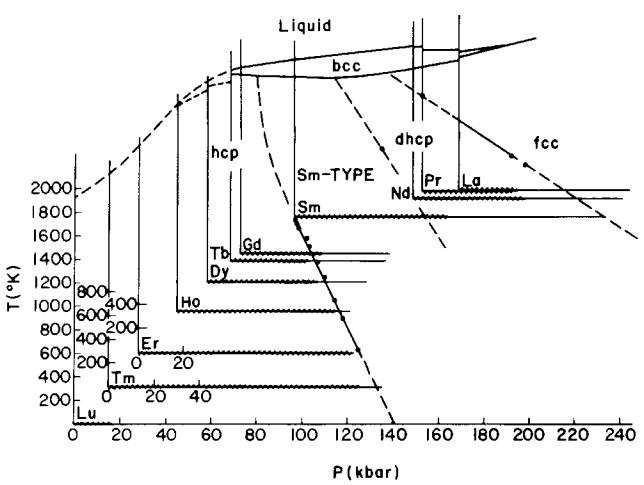

Fig. 9.3. Generalized P–T diagram of the lanthanide metals. The points are measured transitions. The wavy line on the P-axis denotes the highest pressure for which a known phase transition of the element was utilized for the construction of the diagram (from Johansson and Rosengren, 1975).

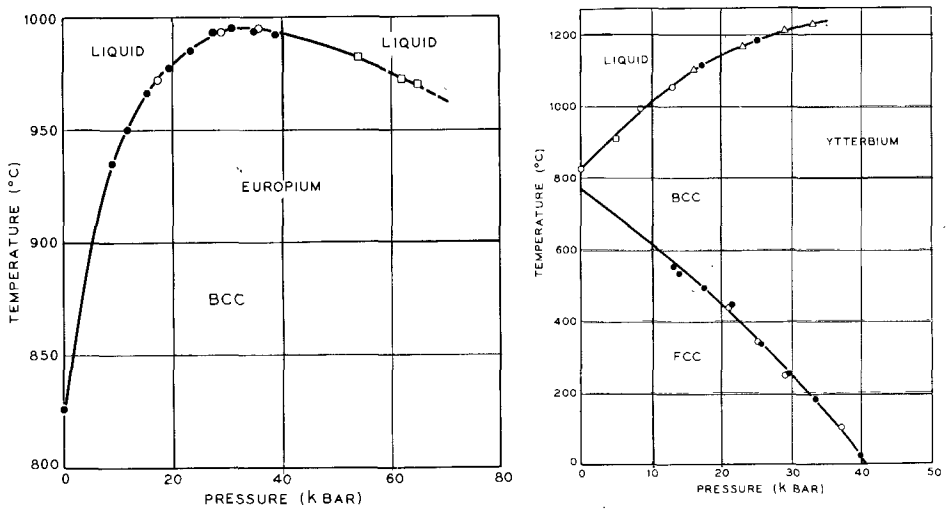

Fig. 9.4. P–T diagram of Eu and Yb (from Jayaraman, 1964).

4. Pressure effect on the resistivity of rare earth metals

The resistivity under pressure and in some cases Hall effect measurements under pressure on rare earth metals have been the subject of several studies. Bridgman's early resistivity measurements are summarized in the review by Lawson (1956). Stromberg and Stephens (1964) carried out resistivity measurements on a number of rare earth metals to about 150 kbar. Stager and Drickamer (1964) extended the resistivity measurements to several hundred kilobar pressure at 296 K, 197 K and 77 K. (See also Drickamer 1965.) Most of the elements exhibit one or several anomalies (see fig. 9.7); rather pronounced resistivity anomalies for Pr near 300 kbar, for Eu near 170 kbar, for Nd near 150 kbar, for Tb near 200 kbar are observed. For most of the rare earth metals there is some sort of anomaly below 100 kbar, which is evident even in the room temperature data. These are undoubtedly due to the structural transformations involving the stacking arrangements of the atomic layers discussed earlier. The origin of the resistance anomaly in the case of Ce near 120 kbar and the anomalies in Pr, Nd and Yb at high pressure are yet to be resolved. More recently resistivity and Hall effect measurements under hydrostatic pressure have been reported on single crystals of Dy and polycrystalline Gd and Tb by Vinokurova et al. (1973, 1972a, 1972b) and by Fujii et al. (1972) on heavy rare earth metals. The resistivity variations with pressure are in general difficult to interpret because they involve several contributing factors in materials like the rare earth metals; in the paramagnetic region there is the spin disorder contribution, contributions from the change in the exchange interaction with pressure and variations related to the change in the effective mass of the conduction electrons, all superimposed on the normal terms. In some cases $\partial\rho/\partial P$ can yield information on these, if the

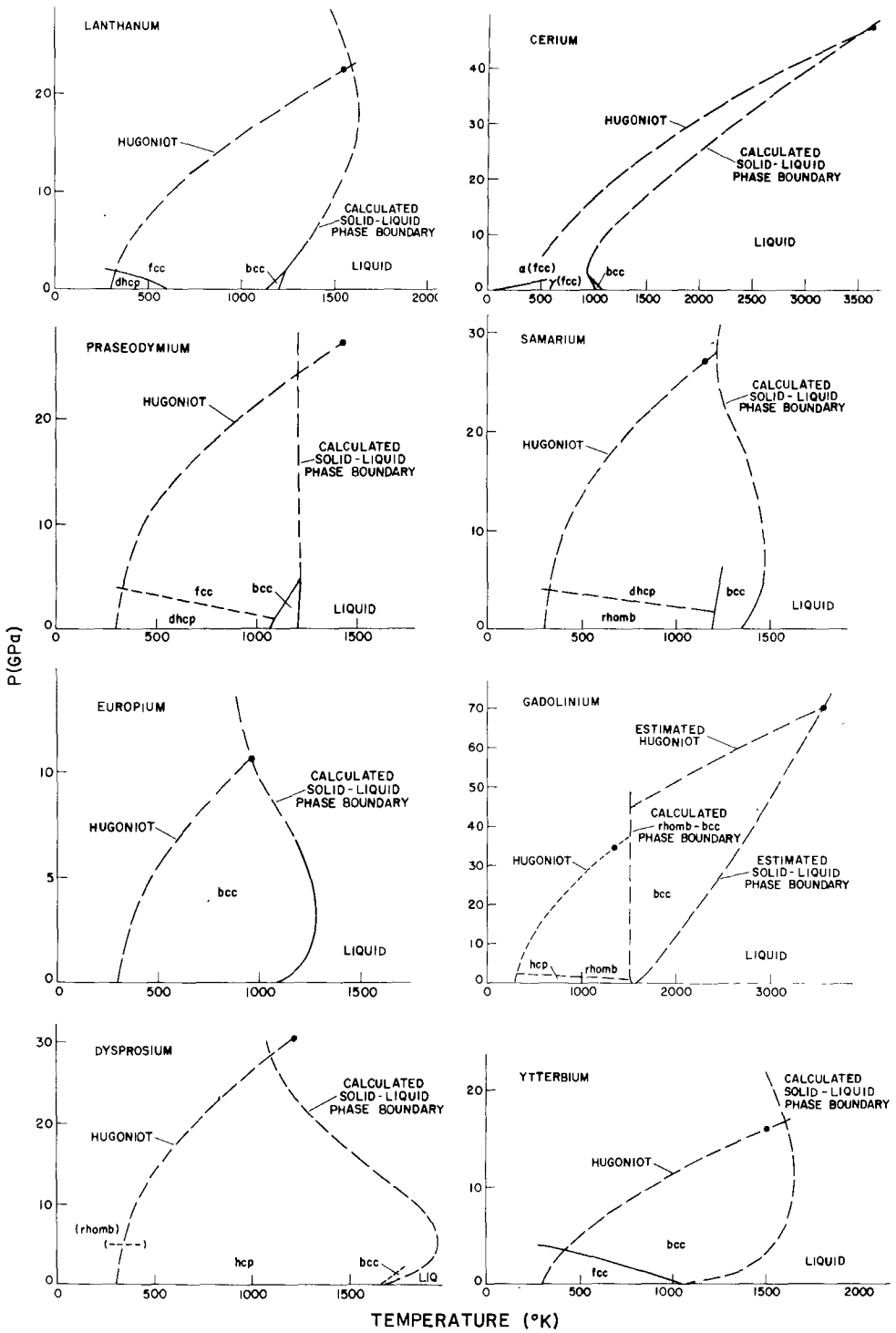
LANTHANUM
HUGONIOT
CALCULATED SOLID-LIQUID PHASE BOUNDARY
fcc
dhcp
bcc
LIQUID
CERIUM
HUGONIOT
CALCULATED SOLID-LIQUID PHASE BOUNDARY
LIQUID
α(fcc)
γ(fcc)
bcc
PRASEODYMIUM
HUGONIOT
CALCULATED SOLID-LIQUID PHASE BOUNDARY
fcc
bcc
dhcp
LIQUID
SAMARIUM
CALCULATED SOLID-LIQUID PHASE BOUNDARY
HUGONIOT
dhcp
bcc
rhomb
LIQUID
EUROPIUM
CALCULATED SOLID-LIQUID PHASE BOUNDARY
HUGONIOT
bcc
LIQUID
GADOLINIUM
ESTIMATED HUGONIOT
CALCULATED rhomb-bcc PHASE BOUNDARY
HUGONIOT
ESTIMATED SOLID-LIQUID PHASE BOUNDARY
bcc
LIQUID
hcp
rhomb
DYSPROSIUM
CALCULATED SOLID-LIQUID PHASE BOUNDARY
HUGONIOT
(rhomb)
hcp
bcc
LIQ
YTTERBIUM
CALCULATED SOLID-LIQUID PHASE BOUNDARY
HUGONIOT
bcc
LIQUID
fcc
P(GPa)
TEMPERATURE (°K)

Fig. 9.5.

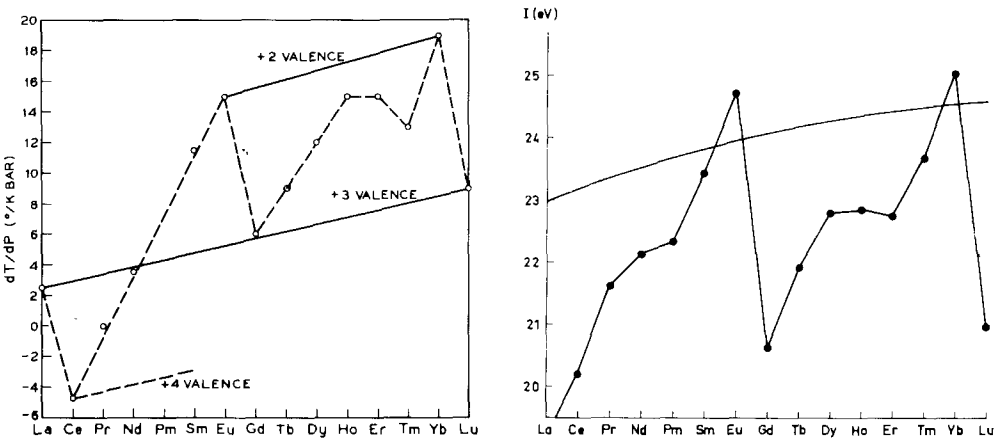

Fig. 9.6. Melting slope dT/dP and ionization energy I for divalent lanthanide ions against atomic number, from Jayaraman (1965) and Johansson and Rosengren (1975) respectively. To be noted is the remarkable resemblance of the two sets of data. The smooth curve is the interpolated binding energy difference between divalent and trivalent metallic states.

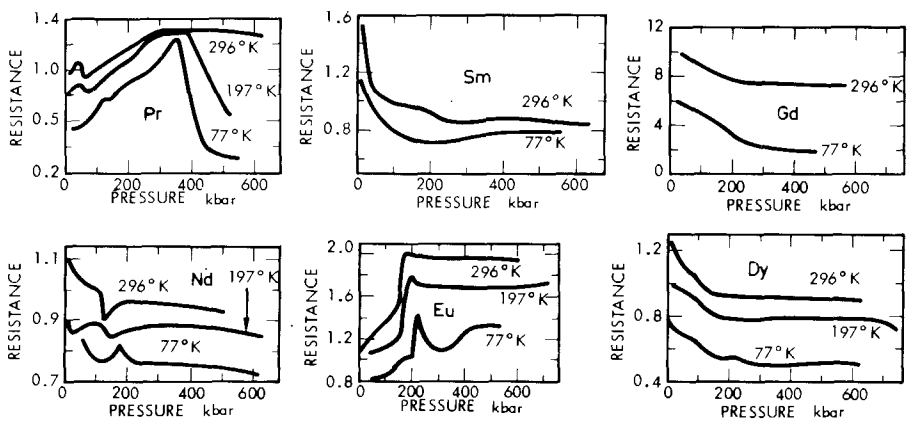

Fig. 9.7. Pressure versus resistance for some rare earth metals (from Drickamer, 1965). The pressures are now believed to be lower by about 30% according to revised calibration.

Fig. 9.5. Proposed P–T diagram for some rare earth metals. Pressure in GPa (1 GPa = 10 kbar). The solid lines are experimentally determined portions. The intersection of the Hugoniot with the calculated melting line, close to the experimental point is taken as strong evidence for melting under shock pressure. To be noted is also the increasing stability of the bcc phase in going from La to Eu (from Carter et al., 1975).

various contributions can be sorted out. Fujii et al. (1972) made some precision measurements on Gd, Tb, Dy, Ho and Er up to 10 kbar on samples of 99.9 purity, in the temperature range 150–400 K. From the data in the paramagnetic region the spin disorder contribution to ρ has been evaluated and from this $d \ln \Gamma / d \ln V$ has been obtained; Γ is the s–f exchange coupling constant (see section 6). Sawaoka and Tomizuka (1971) have also measured the resistivity of Gd under hydrostatic pressure.

4.1. *Ytterbium*

A rather special case is Yb in which the resistivity and Hall effect measurements under pressure have been made by several investigators at different temperatures (Bridgman, 1954; Souers and Jura, 1963; Stager and Drickamer, 1963; Jayaraman et al., 1963; Stromberg and Stephens, 1964; Jayaraman, 1964; McWhan et al., 1969; Holzapfel and Severin, 1971; Iida, 1972; Jullien and Jerome, 1971; Katzman and Mydosh, 1972). The resistivity of Yb rises by several orders of magnitude with pressure at low temperatures and then abruptly decreases at about 40 kbar. At room temperature the rise in resistivity is not as spectacular, but it is still quite striking. In fig. 9.8 this behavior is shown (from

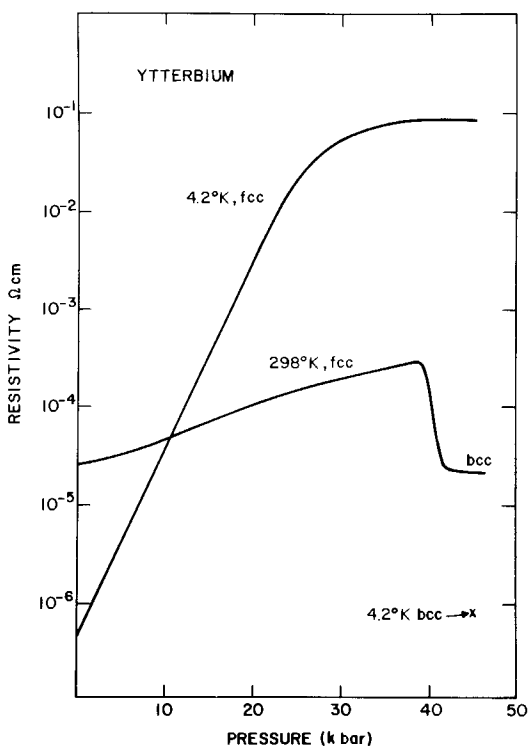

Fig. 9.8. Pressure versus resistance for Yb metal at 4.2 K and at R.T. The sharp decrease at about 40 kbar is due to fcc–bcc transition (from McWhan et al. 1969).

McWhan et al., 1969). The sharp drop in resistance near 40 kbar is due to the fcc–bcc transition (Hall et al., 1963). The rise in resistivity before this transition has been attributed to a gradual transition from the metallic to the semiconducting state in fcc Yb, due to the removal of the band overlap. Some of the other divalent fcc metals (Ca, and Sr) exhibit similar behavior and these pressure induced metal-semiconductor or metal-semimetal transitions (in Sr, see McWhan et al., 1969) have stimulated many theoretical studies, including band structure calculations on Yb (Johansen and Mackintosh, 1970; Jepsen and Anderson, 1971) and related materials (see Vasvari et al., 1967 and see McWhan et al., 1969). Although the calculations of Vasvari et al. do not involve Yb as such, it is believed that a similar picture would be valid for Yb; in the case of Yb the Fermi surface shrinks to the point that an energy gap opens up, making it a semiconductor. From the temperature dependence of resistivity of bcc–Yb in the temperature range 1.3 K to 100 K at pressures in the range 50 to about 160 kbar, Katzman et al. (1972) have concluded that bcc Yb is divalent.

Among the compounds the resistivity of many divalent rare earth monochalcogenides has been investigated under pressure and this will be discussed in ch. 20.

5. Static and shock compression measurements on rare earth metals

The compressibility of the rare earth metals was first investigated up to 40 kbar by Bridgman (see Lawson's review, 1956) for most of the members of the series, and in some cases to about 90 kbar. Since Bridgman's earlier measurements, Stephens (1964) has published compression data on Pr, Eu, Tb, Yb and Sc to 45 kbar and Perez-Albuerne et al. (1966) have reported on the compressibility of Ho, Er and Tm to about 200 kbar (see Drickamer et al., 1966). More recently Liu et al. (1973) and Liu (1975) have measured the compressibility of Tm and Lu respectively in a diamond anvil high pressure X-ray apparatus to several hundred kbar. Syassen and Holzapfel (1975) have reported on the compression of La to 120 kbar. Anomalies corresponding to the phase transitions discussed earlier were noted in some cases in these static compression measurements; at the γ to α-Ce transition near 7 kbar (ch. 4, section 2.1) and in La at the dhcp–fcc transition near 25 kbar (Bridgman, see Lawson's review, 1956), in Yb at the fcc–bcc transition near 40 kbar (Stephens, 1964) and in Lu from the hcp to Sm-type transition near 230 kbar (Liu, 1975). Bulk moduli evaluated from these data are plotted in fig. 9.11. For Gd, Dy, and Er single crystal elastic constant data and their pressure variation have been obtained (Fisher et al., 1973).

5.1. *Shock compression*

Compression studies of rare earth metals into the megabar range have been carried out using shock wave techniques by several investigators (Al'tshuler et

al., 1966a,b, 1968; Al'tshuler and Bakanova, 1969; Bakanova et al., 1970; Gust and Royce, 1973; Carter et al.. 1975). The shock wave techniques are quite well known (see Rice et al., 1958 and McQueen, 1963). When the shock velocity (U_s)-versus-particle velocity (U_p) relationship is linear, i.e., $U_s = C_0 + \Phi U_p$, the Hugoniot relations for pressure and volume can be expressed as

$$P = D_0 U_p (C_0 + \Phi U_p) \ldots,$$

$$V/V_0 = [C_0 + (\Phi - 1)U_p]/C_0 + \Phi U_p \ldots, \tag{9.6}$$

$$P = D_0 C_0^2 \eta/(1 - \Phi\eta)^2, \tag{9.7}$$

where

$$\eta = 1 - V/V_0, \qquad V/V_0 = D_0/D, \tag{9.8}$$

and the D's are the densities. The shock data can be presented conveniently by plotting U_s against U_p, since the relationship is usually linear ($U_s = C_0 + \Phi U_p$ where the Hugoniot intercept C_0 and the slope Φ are determined from the data by the method of least squares). If there are no phase changes the intercept C_0 should correspond to the bulk speed of sound at $P = 0$. Since the slope is linearly related to the pressure derivative of the adiabatic bulk modulus $(\partial B_s/\partial P)_s$ a linear $U_s - U_p$ Hugoniot reflects a nearly linear dependence of B_s on the pressure. If the linear $U_s - U_p$ relation holds, the Rankine–Hugoniot equations can be used to express the pressure and energy as a function of volume along the Hugoniot. Shock data for several rare earth elements are shown in figs. 9.9 and 9.10. Throughout the rare earth series kinks in the $U_s - U_p$ relationship are ubiquitous. In table 9.3 the numerical values of the data for the rare earths along with other parameters of interest are presented. Reynolds and Barker (1974) find from the data of Gust and Royce (1973), the compression of rare earth elements can be expressed in the form $\Delta V/V_0 = a_1 P + a_2 P^2 + a_3 P^3$ and have determined the coefficients. They find that the anharmonic contributions are evident and these are of considerable importance.

The shock data of the various investigators are in reasonable agreement; all of them show kinks in the $U_s - U_p$ curves but the interpretation of the data differ. The cusps and kinks are indicative of some kind of phase transition. (See Doran and Linde, 1966). In general the rare earth metals are much more compressible compared to a typical d-band metal such as Hf, Ta or W. While Al'tshuler et al. (1966, 1968) ascribe the high pressure stiffening of the Hugoniots to electronic transitions, Gust and Royce (1973) have argued that the stiffening of the Hugoniots is related to the onset of repulsive interaction between the noble-gas cores and regard that neither melting, nor structural or electronic transitions are the cause of the kinks in the $U_s - U_p$ plots. On the other hand Carter et al. (1975) have argued in favor of interpreting their data as due to melting. They calculate the temperature T and entropy S along the Hugoniot and then combine this with the known enthalpy to obtain the free energy ($G = H - TS$) along the Hugoniots of both phases. Once these are obtained the melting curve can be calculated, setting $\Delta G = 0$. The results are then extended to get the free energy in the region

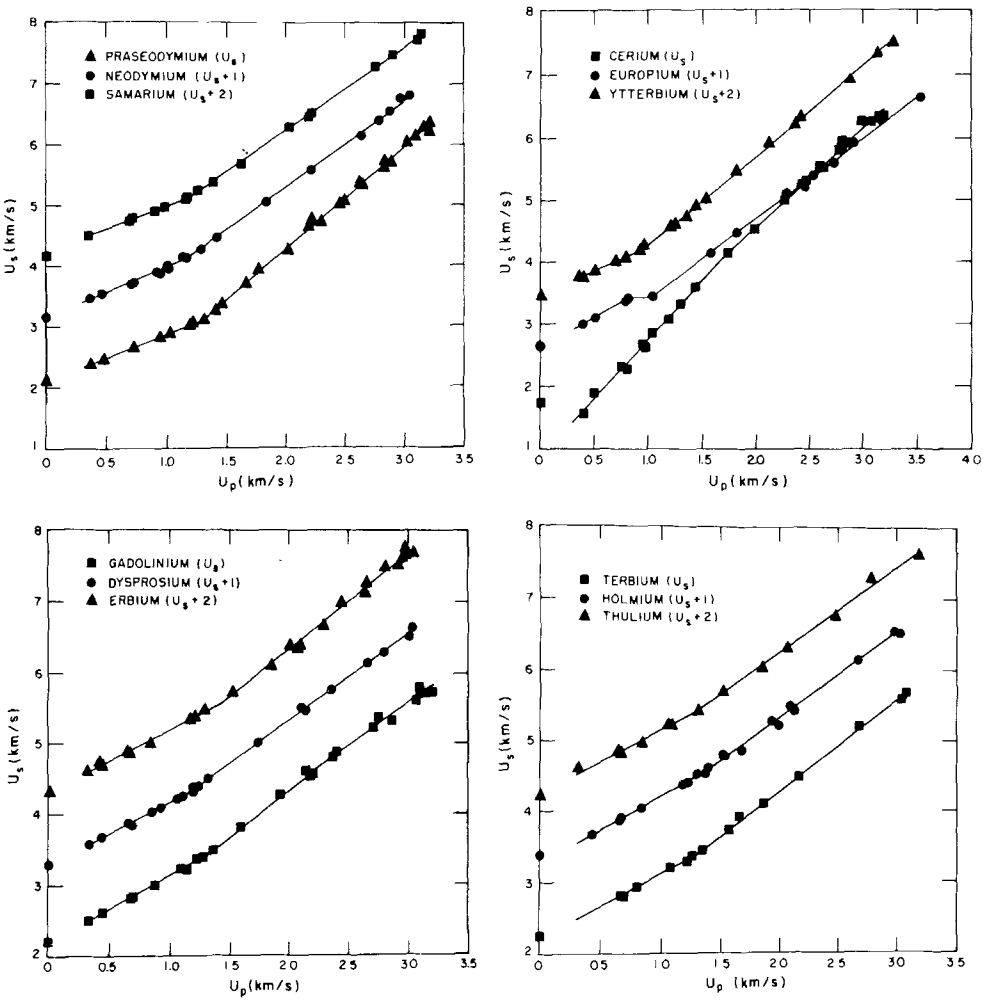

Fig. 9.9 Shock wave velocity U_s against particle velocity U_p for a number of rare earth metals. Kinks in the U_s–U_p relationship occur for most of the rare earth metals (from Carter et al., 1975).

of interest and from this the melting curve is extended to very high pressure regions. By this procedure Carter et al. (1975) have shown that the extrapolated experimental phase lines (Jayaraman, 1965a and 1965b) intersect the Hugoniots in the neighborhood of the observed transition point in all cases, which they consider as strong evidence for melting. Some of their proposed P–T diagrams are shown in fig. 9.5. Further they predict maxima in the fusion curve for all the rare earth elements and in this connection have suggested that a continuous electronic transition in the liquid phase may be occurring in all cases.

The interpretation of Carter et al. (1975) is not untenable and indeed is quite interesting. The proposed fusion curve maxima, in several cases, fall well within

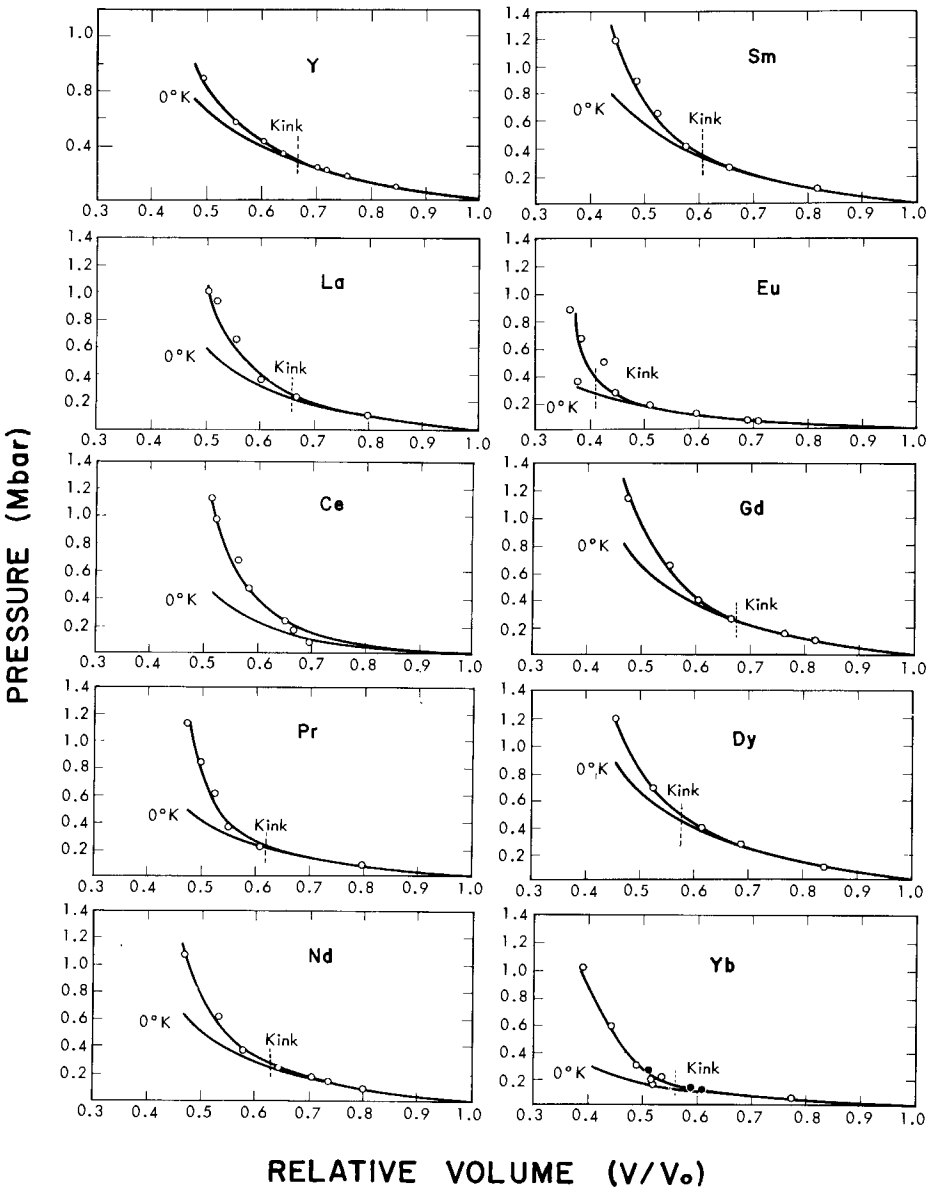

Fig. 9.10. Pressure-volume relationship for rare earth metals deduced from shock data. The position of the kinks in the $U_s - U_p$ relationship is indicated by an arrow. The 0 K isotherm is also shown (from Gust and Royce, 1973). Pressure in mega bar.

the capabilities of existing static apparatus and hence can be verified. Further, with new techniques developing such as the split sphere apparatus for generating super-high-pressures (megabar), with the capability of attaining high temperatures (Kawaii and Endo, 1970), or the laser heated diamond anvil apparatus

TABLE 9.3.
Shock compression data (from[a] Gust and Royce, 1972 and[b] Carter et al., 1975).

Element and atomic no. (Z)	Average initial density (g/cc)	Pressure (P) (kbar)	Relative volume (V/V_0)	Temperature on Hugoniot (10^3 K)
Y[a]	4.513	93	0.847	0.35
(39)		172	0.758	0.51
		217	0.721	0.66
		234	0.704	0.76
		329	0.638	1.4
		423	0.607	2.05
		562	0.555	4.03
		891	0.497	8.7
La[a]	6.134	85	0.798	0.51
(57)		225	0.667	1.59
		361	0.602	3.35
		653	0.556	6.5
		929	0.520	11.9
		1090	0.505	15.5
Ce[a]	6.759	74	0.696	1.26
(58)		164	0.666	1.79
		233	0.649	2.15
		469	0.583	5.40
		674	0.565	7.05
		969	0.522	14.5
		1170	0.506	...
Pr[a]	6.758	89	0.795	0.4
(59)		232	0.618	1.39
		374	0.549	3.3
		621	0.525	5.56
		849	0.497	11.5
		1140	0.472	...
Nd[a]	6.983	86	0.082	0.41
(60)		88	0.798	0.41
		139	0.737	0.59
		165	0.706	0.75
		241	0.643	1.37
		365	0.579	2.94
		613	0.533	5.5
		1070	0.469	14.6
Sm[a]	7.477	101	0.818	0.41
(62)		255	0.655	1.25
		414	0.577	2.88
		653	0.525	5.55
		890	0.488	9.4
		1190	0.488	16.8
Eu[a]	5.282	67	0.691	0.52
		65	0.711	0.47
		122	0.596	0.96
		185	0.515	1.85
		276	0.446	4.03
		363	0.378	22.5

TABLE 9.3 (*Cont.*)

Element and atomic no. (Z)	Average initial density (g/cc)	Pressure (P) (kbar)	Relative volume (V/V_0)	Temperature on Hugoniot (10^3 K)
		450	0.426	5.2
		669	0.385	19.0
		883	0.365	...
Gd[a]	7.912	99	0.821	0.41
(64)		152	0.764	0.55
		262	0.665	1.25
		403	0.605	2.43
		660	0.551	4.79
		1150	0.476	13.3
Tb[b]	8.27	150	0.764	
(65)		190	0.730	
		330	0.634	
		480	0.581	
		620	0.550	
		800	0.520	
		1400	0.460	
Dy[a]	8.559	91	0.839	0.39
(66)		262	0.686	1.03
		391	0.615	1.97
		682	0.524	4.95
		1200	0.456	12.2
Ho[b]	8.80	100	0.842	
(67)		220	0.729	
		400	0.634	
		500	0.602	
		720	0.551	
		1200	0.483	
Er[b]	9.05	100	0.853	
(68)		220	0.727	
		520	0.597	
		840	0.527	
		1100	0.515	
		1450	0.474	
Tm[b]	9.33	80	0.882	
(69)		230	0.725	
		520	0.595	
		830	0.528	
		1100	0.486	
		1600	0.436	
Yb[a]	6.966	61	0.744	0.35
		125	0.607	0.75
		163	0.516	2.35
		150	0.589	0.89
		197	0.515	2.35
		214	0.535	1.71
		270	0.511	2.28
		306	0.489	3.88
		593	0.441	11.2
		1020	0.389	...

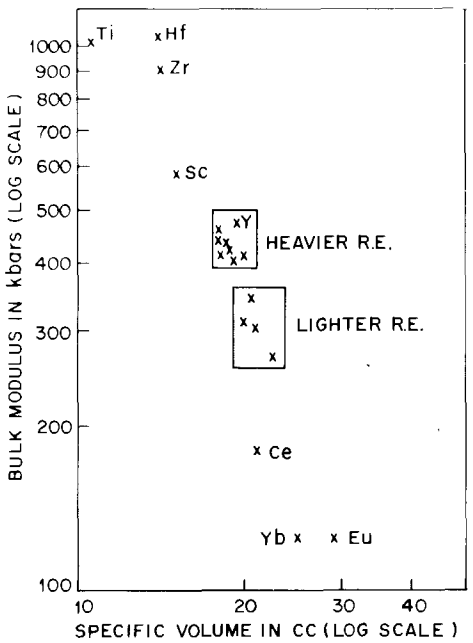

Fig. 9.11. A plot of the log of bulk modulus against log of specific volume for rare earth metals. The heavier and lighter rare earths fall into two groups and the ambivalent Ce, and the divalent cases Yb and Eu metals are distinct.

(Ming and Bassett, 1974), these predictions can be checked in almost all cases. Until a direct experimental check up confirms the proposed $P-T$ diagrams, the conclusions of Carter et al. (1975) have to be treated as good speculations.

In fig. 9.11 we present a rather interesting plot of the log of the bulk modulus versus log of the specific volume for the rare earth elements. It is seen that in this plot the divalent and trivalent cases fall in distinct groups, while Sc which is normally trivalent is quite outside these two groups.

5.2. *Compounds*

Among the compounds the compressibilities of divalent monochalcogenides and a few members of the monopnictides have been investigated. In several of the divalent monochalcogenides and CeP the occurrence of phase transition involving valence change has been established through their $P-V$ relationships. These will be discussed in chapter 20. In fig. 9.12a the compressibilities of EuTe, EuSe, EuS and EuO are shown. The first three do not show any evidence for a valence change in the range of pressure investigated, although in general they are found to be quite compressible. The discontinuities in them are due to a phase change from NaCl to the CsCl structure (Chatterjee et al., 1972 and Jayaraman et al., 1974). A useful plot of the bulk modulus data for related

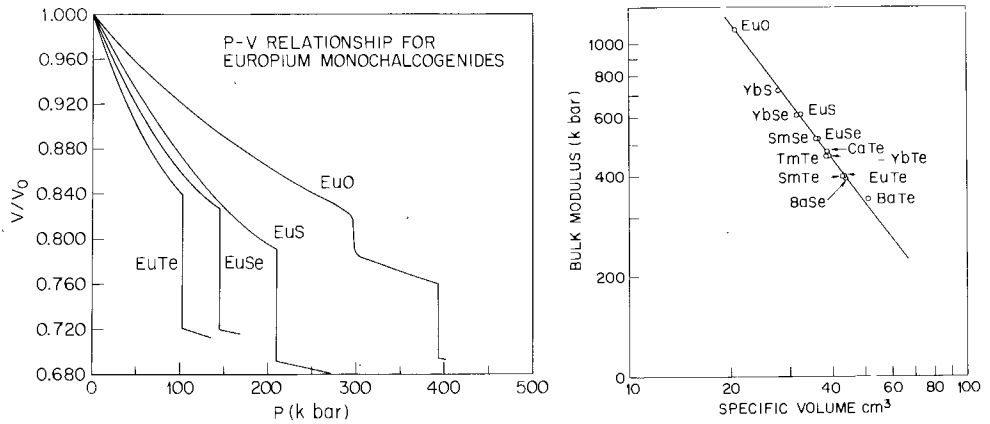

Fig. 9.12. Pressure-volume relationship for Eu monochalcogenides (left fig.) and a plot of the log of bulk modulus against log of specific volume for R.E. monochalcogenides showing the straight line relationship. In the $P-V$ relationship of Eu monochalcogenides the discontinuities are due to NaCl to CsCl transition. In EuO the first discontinuity is due to a valence transition in Eu (from Jayaraman et al., 1974).

compounds is the log of B_0 vs log of specific volume shown in fig. 9.12b for the divalent rare earth chalcogenides (Jayaraman et al., 1974). A straight line relationship holds and this can be taken advantage of to compute the bulk modulus of a substance belonging to this class, provided the cell dimension is known. In table 9.4 the data of interest for many of the compounds are presented.

In the case of pnictides the compression has been measured up to 200 kbar pressure for CeP (Jayaraman et al., 1976) and to about 80 kbar in the case of GdN (McWhan, 1965). The pressure-volume relationship (see fig. 9.13) of CeP shows anomalies due to a valence change (see ch. 20).

6. Magnetic transitions under pressure

High pressure studies on magnetic transitions in rare earth metals, intra-rare earth alloys and compounds (the monochalcogenides, ferrites, spinels (RFe_2O_4) and garnets ($R_3Fe_5O_{12}$ where R is a rare earth element)) have been numerous and all the work prior 1969 has been reviewed by Bloch and Pavlovic (1969). For the discussion on pressure studies of magnetic transition in this chapter, much material has been drawn from the above review.

For experimental details, high pressure apparatus and techniques, references to original articles can be found in the review by Bloch and Pavlovic (1969). Briefly, the most common methods used in following a magnetic transition are: change in the mutual inductance sensed through a set of coils placed around the specimen in a transformer-like set up, magnetic susceptibility, electrical resistivity and in some cases thermal dilation. To a limited extent more sophisticated

TABLE 9.4.
Lattice parameters and bulk moduli of divalent rare earth monochalcogenides (Jayaraman et al., 1974).

Substance	Lattice parameter a(Å)	Bulk modulus B_0(kbar)	M/ρ(cm^3)	Bulk modulus B_0(kbar) other work
EuTe	6.60	400 ± 50	43.3	400 ± 30[a] 360 ± 50*[b]
EuSe	6.19	520 ± 50	35.7	526 ± 100[a] 476 ± 50*[b]
EuS	5.97	610 ± 50	32.0	555 ± 55[a] 500 ± 75*[b]
EuO	5.14	1100 ± 50	20.45	900 ± 150[a] 900 ± 100*[b]
YbTe	6.36	460 ± 50	38.75	
YbSe	5.93	610 ± 50	31.42	610†
YbS	5.68	720 ± 50	27.55	740†
TmTe	6.34	460 ± 50	38.33	465†
SmTe	6.60	400 ± 50	43.2	400†
SmSe	6.22	400 ± 50	35.86	520†
SmS	5.97	151(?)	32.0	600† 476 ± 50[c][d]
GdS**	5.56	1200 ± 50	25.5	1200 ± 50
YS**	5.49		24.9	998[d]

*adiabatic values; **trivalent; †from fig. 9.12; [a]Levy and Wachter (1970); [b]Shapira and Reed (1972); [c]Kaldis and Wachter (1972), also Penney et al. (1972); [d]Penney (private communication).

techniques such as measuring the magnetization through NMR, Mössbauer and neutron scattering have been employed.

6.1. *Some useful thermodynamic equations*

With a magnetic material the usual Gibbs function describing the thermodynamic state of the material is

$$G = U - TS + PV - Hm \tag{9.9}$$

where H is the magnetic field and m is the total magnetic moment; the other terms are well-known.

For a reversible process the change in the Gibbs' function becomes

$$\mathrm{d}G = -S\,\mathrm{d}T + V\,\mathrm{d}P - m\,\mathrm{d}H \tag{9.10}$$

and since this must be an exact differential one immediately obtains

$$(\partial m/\partial P)_{H,T} = -(\partial V/\partial H)_{P,T} \tag{9.11}$$

or

$$D(\partial\sigma/\partial P)_{H,T} = -V^{-1}(\partial V/\partial H)_{P,T} = -(\partial\omega/\partial H)_{P,T}, \tag{9.12}$$

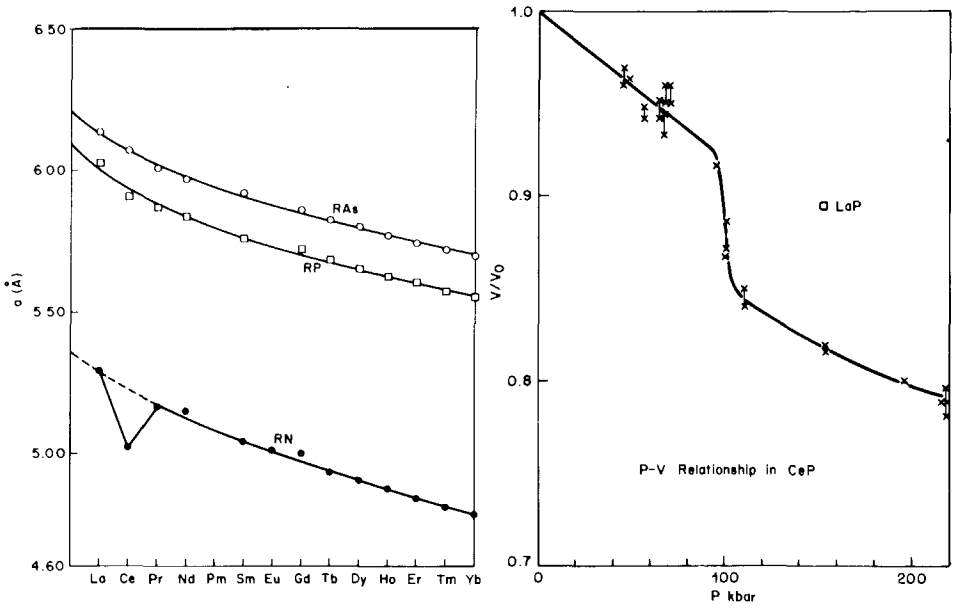

Fig. 9.13. Lattice parameter vs atomic number plot for R.E. pnictides. The deviation of a of CeN is due to the higher valence state of Ce. The right fig. is the $P-V$ relationship for CeP and the anomaly is due to a valence change in Ce towards the 4^+ state. The data point for LaP is shown for comparison (from Jayaraman et al., 1976).

where D is the density of the material, σ is the specific magnetization and $(\partial\omega/\partial H)_{P,T}$ the forced volume magnetostriction. The specific spontaneous magnetization σ_0 of a ferromagnetic material at temperature T can be written as

$$\sigma_s = \sigma_0 f(T/\theta_C) \tag{9.13}$$

where σ_0 is the specific spontaneous magnetization at $T = 0$ K and it is assumed that $f(T/\theta_C)$ varies with pressure only by virtue of its volume dependence of θ_C the Curie temperature. From this relation it can be shown (see Bloch and Pavlovic) that

$$\frac{1}{\sigma_s}\left(\frac{\partial\sigma_s}{\partial P}\right) = \frac{1}{\sigma_0}\left(\frac{\partial\sigma_0}{\partial P}\right) - \frac{T}{\sigma_s}\left(\frac{\partial\sigma_s}{\partial T}\right)\frac{1}{\theta_C}\left(\frac{\partial\theta_C}{\partial P}\right) \tag{9.14}$$

is a good approximation. In dealing with a ferromagnetic material one would like to measure both σ_s and (θ_C) as a function of pressure. The above expression can be used to compute $(1/\sigma_0)(\partial\sigma_0/\partial P)$ from experimental values of other quantities or $d\theta_C/dP$ when the assumption is made that $(1/\sigma_0)(\partial\sigma_0/\partial P) = 0$. More often it is the logarithmic volume dependence of these quantities

$$\left(\frac{\partial \log \theta_C}{\partial \log V}\right)_T \quad \text{and} \quad \left(\frac{\partial \log \sigma_0}{\partial \log V}\right)_T \tag{9.15}$$

that are wanted to extract information about the exchange interactions among

the magnetic ions. Therefore a knowledge of the compressibility of the material becomes a prerequisite for the analysis of the data.

In ferromagnetic materials there exists a volume anomaly ΔV_0 at absolute zero. For an isotropic substance the magnetic energy W_m is related through the equation

$$\Delta V_0/V_0 = -K(\partial W_m/\partial V)_0. \tag{9.16}$$

The volume anomaly ΔV_0 is the difference between the true volume and the volume which would exist in the absence of magneto-elastic interactions and can be obtained by extrapolation of the empirical volume temperature relation, from the high temperature phase.

6.2. *Molecular-field approximation*

The molecular field theory has been quite successful in describing the magnetic properties of many simple ferro-ferri- and antiferromagnetic spin arrangements in solids. According to this, the expression for the magnetic ordering temperature of various types of order and crystal structures is

$$\theta = \frac{2\bar{S}(\bar{S}+1)}{3k}\sum_i (\pm)A_1(i) + \sum_j (\pm)A_2(j) \tag{9.17}$$

where $\bar{S}$ is the total spin quantum number of the atom and k is Boltzmann's constant. The sums $\Sigma\,(\pm)A_1(i)$ and $\Sigma\,(\pm)A_2(j)$ are of the exchange interactions of the nearest and next nearest neighbor atoms respectively where $(\pm)$ is associated with parallel and antiparallel configurations. For an fcc lattice with 12 ferromagnetically coupled nearest-neighbor atoms and six ferromagnetically coupled next nearest neighbor atoms

$$\theta_C = \frac{2\bar{S}(\bar{S}+1)}{3k}(12A_1 + 6A_2) \tag{9.18}$$

In several magnetic materials A_2 is negative and much larger than A_1, leading to an antiferromagnetic state with Néel temperature

$$\theta_N = -4\bar{S}(\bar{S}+1)A_2/k \tag{9.19}$$

One would obtain the same expression if among the 12 nearest neighbors six were ferromagnetically coupled and six were antiferromagnetically coupled with the central atom. In the above case with magnetic atoms in well defined S-states, the effect of pressure influences only the value of exchange interaction A_2 and then

$$\left(\frac{\partial \log \theta_N}{\partial \log V}\right)_{\theta_N} = \left(\frac{\partial \log |A_2|}{\partial \log V}\right)_{\theta_N} \tag{9.20}$$

where

$$\left(\frac{\partial \log \theta_N}{\partial \log V}\right)_{\theta_N} = \frac{-(1/K)(\partial \log \theta_N/\partial P)}{1-(3\alpha/K)(\partial\theta_N/\partial P)} \tag{9.21}$$

The term in parenthesis in the denominator arises because of temperature variation of θ_N due to the thermal expansion of the lattice. The magnetic energy of this lattice can be approximated

$$W_{m,0} = -\tfrac{3}{2}R\theta_{N,0} = -6RS^2\left|\frac{A_2}{k}\right|_0 \tag{9.22}$$

and its volume dependence is given by

$$\left(\frac{\partial \log W_m}{\partial \log V}\right)_0 = \left(\frac{\partial \log |A_2|}{\partial \log V}\right)_0 = \frac{V_0(\Delta V/V_0)}{K_0 W_{m,0}} \tag{9.23}$$

From these relations one can obtain an expression for the exchange interaction in terms of experimentally accessible quantities

$$\left|\frac{A_2}{k}\right| = -\frac{V_0\theta_N(\Delta V/V_0)}{6RS^2(\partial\theta_N/\partial P)} \tag{9.24}$$

The same approach has been applied to ferrimagnetic materials with two magnetic sublattices (see Bloch and Pavlovic, 1969). The volume dependence of θ_{Fi} can be related to that of the molecular field coefficients n by the relation

$$\left(\frac{\partial \log \theta_{Fi}}{\partial \log V}\right)_{\theta_{Fi}} = \left(\frac{\partial \log n}{\partial \log V}\right)_{\theta_{Fi}} \tag{9.25}$$

When applied to a ferromagnetic material the molecular field theory gives for the Curie temperature

$$\theta_C = (J+1)nM\sigma_0^2/3JR \tag{9.26}$$

where J is the total angular momentum, M the atomic mass of the material, σ_0 specific magnetization at absolute zero, R the gas constant. The volume dependence of the molecular field coefficient is the interesting quantity, since it is related to the exchange integral. For a constant J one has

$$\left(\frac{\partial \log n}{\partial \log V}\right)_T = \left(\frac{\partial \log \theta_C}{\partial \log V}\right)_T - 2\left(\frac{\partial \log \sigma_0}{\partial \log V}\right)_T \tag{9.27}$$

In this case one has to know the volume dependence of the Curie temperature as well as the specific magnetization σ_0 at absolute zero.

6.3. *Indirect exchange*

Although the molecular field approximation, which rests on the direct exchange mechanism, seems to have wide applicability including to magnetic rare earth systems, it is well accepted now that the indirect exchange mechanisms mediated via the conduction electrons are the dominant interactions for rare earth metallic systems. For nonmetallic systems this indirect exchange is often mediated by the electrons of the anion (superexchange); oxygens in ferrites and garnets, etc. The indirect coupling mechanisms involve the so-called Ruderman–Kittel-function

and the expression for the magnetic ordering temperature is

$$\theta = \frac{3\pi Z_i^2}{4k} \frac{\Gamma^2}{V^2 E_F} (g-1)^2 J(J+1) \sum F(2k_F R_{mn}) \tag{9.28}$$

where Z_i is the ionic charge, Γ the coupling constant between the spin of a 4f electron and a conduction electron, E_F the Fermi energy k_F the wave vector of the conduction electron, V the atomic volume, g Landé's factor of the ions, R_{mn} the distance between the ions m and n and $F(P)$ is the oscillatory Ruderman–Kittel function: The magnetization ΔM of the polarized conduction electrons is given by

$$\Delta M = (g-1) J \frac{3 Z_i \Gamma}{4 E_F} \mu_B \tag{9.29}$$

and the magnetic resistivity

$$\rho_m = \frac{3\pi}{8} \frac{m^*}{he^2} (g-1)^2 \frac{\Gamma^2}{V E_F} J(J+1), \tag{9.30}$$

where m^* is the effect mass of the electron.

The sum appearing in the expression for θ has been shown to be independent of volume. Therefore the pressure derivatives of θ, ΔM and ρ_m can easily be written in terms of the volume variation of the coupling constant Γ and m^*

$$-\frac{1}{K}\left(\frac{1}{\theta}\frac{\partial \theta}{\partial P}\right)_{H,T} = -\tfrac{4}{3} + 2\left(\frac{\partial \log \Gamma}{\partial \log V}\right)_{H,T} + \left(\frac{\partial \log m^*}{\partial \log V}\right)_{H,T} \tag{9.31}$$

$$-\frac{1}{K}\left(\frac{1}{\rho_m}\frac{\partial \rho_m}{\partial P}\right)_{H,T} = -\tfrac{1}{3} + 2\left(\frac{\partial \log \Gamma}{\partial \log V}\right)_{H,T} + 2\left(\frac{\partial \log m^*}{\partial \log V}\right)_{H,T} \tag{9.32}$$

$$-\frac{1}{K}\left(\frac{1}{\Delta M}\frac{\partial \Delta M}{\partial P}\right)_{H,T} = \tfrac{2}{3} + \left(\frac{\partial \log \Gamma}{\partial \log V}\right)_{H,T} + \left(\frac{\partial \log m^*}{\partial \log V}\right)_{H,T} \tag{9.33}$$

It is the coupling constant which is quite sensitive to volume. Another useful expression for metallic systems is

$$\frac{\partial \ln \theta_C}{\partial \ln V} = -2 + 2\frac{\partial \ln \Gamma_{sf}}{\partial \ln V}\frac{\partial \ln E_F}{\partial \ln V} \tag{9.34}$$

where Γ_{sf} is the sf exchange interaction and E_F is the Fermi energy.

6.4. *Pressure studies on metals and alloys*

The rare earth metals exhibit a variety of ordered states from ferromagnetic to complicated antiferromagnetic structures; collinear, spiral, helical, conical and fan structures, which can be altered by temperature, magnetic fields or by the application of pressure (Nikitin et al., 1972). These complicated arrangements of spins result from the balance in energy between magnetocrystalline anisotropy and exchange forces (Elliott, 1965). Much pressure work has been done on pure rare earth metals and alloys in the last decade especially, and measurements

cover the effect of pressure on the transition temperature, saturation magnetization and magnetocrystalline anisotropy. Bloch and Pavlovic (1969) have extensively covered in their article work on rare earth metals and alloys prior to 1968. In tables 9.5 and 9.6 the pressure data of interest are presented.

6.4.1. *Gadolinium*

Gd metal exhibits a transition directly from the paramagnetic to the ferromagnetic state at 291.8 K. It is found that pressure depresses the Curie temperature θ_C in Gd and the best value for $d\theta_C/dP$ based on hydrostatic measurement (Bartholin and Bloch, 1967, 1968) yields a slope of -1.48 ± 0.02 K/kbar.

TABLE 9.5.
Pressure data for the magnetic transitions in rare earth metals.

Rare earth element	θ_N or θ_C (K)	$d\theta/dP$ (K/kbar)	$\frac{\partial \ln \theta}{\partial \ln V}$	$\sigma_s^{-1}\partial\sigma_s/\partial P$ ($\times 10^3$ kbar)
Eu	(θ_N) 91	~ 0[f]	~ 0[f]	
		0.22[g]		
Gd	(θ_C) 290.1	-1.63 ± 0.02[a]	2.2	-1.1 ± 0.3[c]
Tb	(θ_N) 227 ± 1	-1.07 ± 0.03[a]	1.8	
		-0.82 ± 0.1[b]		-3.8 ± 0.4(77 K)[b]
Dy	(θ_N) 179 ± 2	-0.66 ± 0.04[a]	1.4	
		-0.6 ± 0.1[b]		-0.15 ± 0.2(77 K)[b]
	(θ_F^{AF}) 84.7	-1.24 ± 0.1[e]		
Ho	(θ_N) 118	-0.45 ± 0.15[b]		-8.4 ± 0.5[d]
		-0.48 ± 0.01[a]	1.4	
Er	(θ_N) 85	-0.26 ± 0.01[e]		
	(θ_F^{AF}) ~ 20	-0.8 ± 0.2[e]		-11.73 ± 0.78[d]

[a]McWhan and Stevens (1965); [b]Bloch and Pauthenet (1965); [c]Bartholin and Bloch (1967); [d]Vinokurova and Kondorskii (1964); [e]Milton and Scott (1967); [f]McWhan et al. (1966); [g]Menyuk et al. (1971).

TABLE 9.6.
Pressure and volume variations of some physical quantities for Gd, Tb, Dy, Ho

Element	$\left(\frac{\partial \log \Gamma}{\partial \log V}\right)_{H,T}$	$\left(\frac{\partial \log m^*}{\partial \log V}\right)_{H,T}$	$\left(\frac{1}{\Delta M}\frac{\partial \Delta M}{\partial p}\right)_{H,T}$
Gd	2.6	-1.7	-4.1
	1.6[a]	-0.2[a]	
Tb	1.2	0.3	-4.1
Dy	1.9	-1.1	-3.9
	2.0[a]	-1.4[a]	
Ho	2.3	-1.2	-4.6

[a]From Austin and Mishra (1967).

Measurements of various investigators fall between − 1.2 K/kbar and − 1.8 K/kbar. Among the values for $(1/\theta_s)(d\theta_s/dP)$ (Kondorskii and Vinokurova, 1965; Bloch and Pauthenet, 1965) the value of $-1.1 \pm 0.3 \times 10^{-3}$/kbar obtained by Bloch and Pauthenet appears to be consistent. The rate of change of Curie temperature with pressure for Gd was calculated from the experimentally determined $\partial\sigma_s/\partial T$ and $(1/\sigma_0)(\partial\sigma_0/\partial P)$ using equation 9.14 as $d\theta_C/dP = -1.63$ K/kbar, in good agreement with experiment. Also $(\partial \log \Gamma/\partial \log V)_{H,T}$, $(\partial \log m^*/\partial \log V)_{H,T}$ and $(1/\Delta M)(\partial \Delta M/\partial P)_{H,T}$ were calculated (see table 9.6). The results show that the coupling constant Γ is a rapidly varying function of volume. The investigations of Robinson et al. (1964) and McWhan and Stevens (1965) have shown that above 25 kbar two new peaks appear in the secondary voltage versus temperature data. This has been attributed to the hcp–Sm type transition reported by Jayaraman and Sherwood (1964a). The high pressure phase was found to be antiferromagnetic by McWhan and Stevens (1965) in accordance with the earlier observation of Jayaraman and Sherwood (1964a) on quenched material.

6.4.2. Tb, Dy, Ho *and* Er

The magnetic behavior of the above rare earth metals is much more complicated, since they undergo the complex type of antiferromagnetic spin arrangements, before ordering ferromagnetically. These metals have been studied and in fig. 9.14 are shown the data of McWhan and Stevens (1965) for Gd,

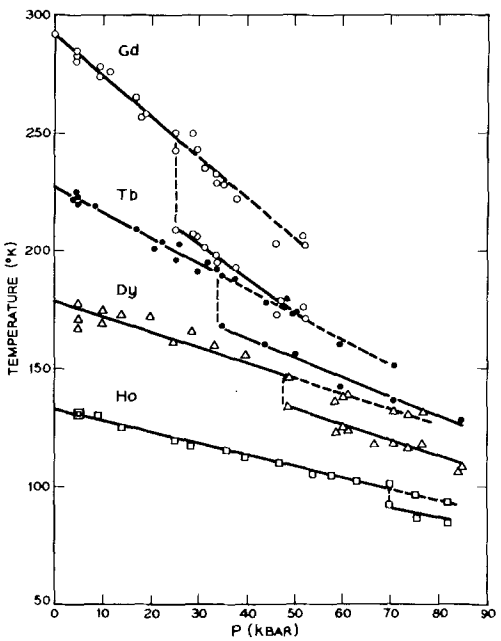

Fig. 9.14. Change in magnetic ordering temperature with pressure of Gd, Tb, Dy and Ho (from McWhan and Stevens, 1965). The break in the curve in each case is due to hcp to Sm-type transition.

Tb, Dy and Ho to 80 kbar pressure, the highest pressure at which the magnetic transitions in rare earth metals have been investigated. The plot shows the variation of θ_N with pressure. The abrupt changes are due to the hcp → Sm type phase transition in these materials. They have also been studied under strictly hydrostatic pressure to a maximum of 6 or 7 kbar; magnetization studies as well as $d\theta_N/dP$ determinations (Bloch and Pauthenet, 1965; Vinokurova and Kondorskii, 1965a,b; Bartholin and Bloch, 1968). In some studies, results have been obtained with single crystals; Wazzan et al. (1967) used an electrical resistivity technique, and Tatsumoto et al. (1968) used susceptibility measurements. Dysprosium undergoes a transition to an AF phase with helicoidal structure at 178 K and an AF to F transition at 85 K, at atmospheric pressure. Souers and Jura (1964) and Robinson et al. (1966) measured $d\theta_N/dP$ of Dy using the electrical resistivity anomaly, to rather high pressures. The AF transition in Ho was also studied by Kawaii et al. (1967) who used electrical resistivity and by Umebayashi et al. (1968) by neutron diffraction. In the latter study the pressure dependence of the helical turn angle ω was also measured. Erbium is much more complicated in its magnetic behavior, exhibiting three magnetic transitions. Only two pressure studies are on record on Er (Milton and Scott, 1967, on θ_N and Vinokurova and Kondorskii, 1964 on the magnetization). The magnetic susceptibility of Ho and Er under pressure was studied by Okamoto et al. (1968).

The magnetic properties of lighter rare earths under pressure have not been studied. Fisk and Matthias (1969) report that the magnetic susceptibility of Pr under pressure resembles that of Ce at normal pressure.

6.4.3. *Rare earth alloys*

Many pressure studies have been made on intrarare earth alloys, as well as on rare earth intermetallic compounds. In table 9.7 some selected data are presented. Among the intrarare earth alloys, systems involving Gd have evoked much

TABLE 9.7.
Pressure data for some rare earth alloys

System	θ_C or θ_N (1 bar)	$d\theta/dP$ K/kbar	Phase transition kbar
$Tb_{0.95}Y_{0.05}$[a]	219	−0.80	30
$Tb_{0.90}Y_{0.10}$[a]	211	−0.77	40
$Tb_{0.80}Y_{0.20}$[a]	196	−0.63	60
$Tb_{0.60}Y_{0.40}$[a]	169	−0.41	>70
$Tb_{0.30}Y_{0.70}$[a]	111	−0.28	>85
$Gd_{0.85}Y_{0.15}$[b]	268(θ_C)	−1.3	—
$Gd_{0.70}Y_{0.30}$[b]	220(θ_C)	−1.23	—
$Gd_{0.91}Lu_{0.09}$[b]	267(θ_C)	−1.46	—
$Gd_{0.80}Lu_{0.20}$[b]	259(θ_C)	−0.130	—
$Gd_{0.70}Lu_{0.30}$[b]	221(θ_C)	−1.25	—

[a]McWhan and Stevens (1967); [b]Austin and Mishra (1967).

interest; Gd–Dy alloys (Milstein and Robinson, 1967); Gd–Lu and GdY (Austin and Mishra, 1967); Gd–Y alloys (Jayaraman et al., 1966; McWhan and Stevens, 1967; Ito et al., 1972; Ito, 1973). The hcp alloys in the Gd system, involving Gd and a lighter rare earth viz, La, Nd, Pr, show ferromagnetic ordering and undergo the hcp–Sm type transition at high pressure. The Tb–Y system was

TABLE 9.8.
Curie temperatures, the initial pressure dependences and $d \ln T_C/d \ln V$ for rare earth intermetallic compounds. The last column may be called the magnetic Gruneisen parameter

Compound	T_CK	dT_C/dP K/kbar	$d \ln T_C/d \ln V$
Y_2Fe_{17}[f]	310	−9.8	33
Er_2Fe_{17}[g]	309	−4.1	18
YCo_3[c]	301	−3.8	12.8
Y_2Co_7[a]	639	−5.9	13.5
YCo_5[c]	977	−1.0	1.5
Y_2Co_{17}[b]	1167	−0.3	0.4
$PrCo_2$[b]	54	−0.75	15
$PrCo_3$[c]	349	−1.8	5.9
$NdCo_2$[b]	98	−0.8	9
Nd_2Co_{17}[c]	1150	+0.7	−1.0
$GdCo_2$[b]	395	−2.45	6
$GdCo_3$[a]	612	−9.5	19.6
Gd_2Co_7[a]	775	−3.5	6.4
$GdCo_5$[c]	1008	−0.8	1.1
Gd_2Co_{17}[c]	1209	+0.6	−0.8
$TbCo_2$[b]	228	−1.1	5
$TbCo_3$[a]	506	−5.7	14.5
$DyCo_2$[b]	135	−0.8	6
$HoCo_2$[b]	74	−0.65	9
$ErCo_2$[b]	33	−0.4	13
Er_2Co_{17}[c]	1186	+1.1	−1.6
$LuCo_3$[a]	362	−2.3	8.5
Y_2Ni_{17}[d]	151	−0.44	4.5
$GdNi_2$[b]	77	0	0
Dy_2Ni_{17}[d]	154	−0.44	4.3
Ho_2Ni_{17}[e]	152	−0.44	4.4
Er_2Ni_{17}[e]	140	−0.44	4.7
GdCu[h]	144	0.03	−0.09
GdAg[h]	~140	0.43	−1.6
$GdAl_2$[j]		0.71	
$TbAl_2$[j]		0.60	

[a]Bloch and Chaisse (1972); [b]Bloch et al. (1971); [c]Brouha and Buschow (1973); [d]Jaakkola et al. (1975); [e]Jaakkola and Parviainen (1974); [f]Givord et al. (1971); [g]Brouha and Buschow (1973); [h]Sekizawa et al. (1970); [j]Jaakkola (1974).

studied by McWhan et al. (1966b) in detail and other heavy rare earth alloys by Yagasaki et al. (1973).

Among the rare earth intermetallics the magnetic transitions, in RAl_2 compounds (Jaakkola, 1974), in R–Co and R–Fe intermetallics (Brouha et al., 1974); Brouha and Buschow 1973a, 1973b, Voiron and Bloch, 1971; Voiron et al., 1973 and Bloch and Chaisse, 1972), in R_2Ni_{17} (Jaakkola and Parviainen, 1974 and Jaakkola et al., 1975) have been studied. Some rare earth intermetallic compounds with CsCl structure have been investigated; $GdZn_{1-x}In_x$ by Hiraoka (1974) and Hiraoka and Fuchikami (1974), GdCu and GdAg by Sekizawa et al., (1970). In table 9.8 the pressure data of interest are presented.

6.5. *Rare earth compounds*

Among the chalcogenides by far the most extensively investigated compounds are the Eu monochalcogenides. Most recent pressure studies, not included by Bloch and Pavlovic (1969) are of Lara and Xavier (1974) on EuO and EuS, Hidaka (1970–71) and Schwob (1969). The pressure data of interest are summarized in table 9.9 which also shows the exchange interaction coefficients and the logarithmic volume derivatives.

The effect of pressure on the Curie temperature of some ferrimagnetic (θ_{Fi}) iron rare earth garnets are shown in fig. 9.15. The iron rare earth garnets have the general formula $R_3Fe_5O_{12}$ (R = rare earth element). The θ_{Fi} increases linearly with pressure at a rate of about 1–2 K/kbar in the pressure range of 10 kbar. However, in a more recent study Bocquillon et al. (1973a) have extended the measurement to 60 kbar pressure (see fig. 9.15). According to this study, the Curie temperature increases with pressure, following a parabolic law ($\theta_{Fi} = \theta_{Fi,0} + bP + cP^2$). The data are presented in table 9.10 in which the pressure and volume

TABLE 9.9.
Pressure data on the magnetic transition in Eu chalcogenides and GdN.

Substance	Ordering θ K	$\frac{d\theta}{dP}$ K/kbar	$\frac{\partial \ln A_1}{\partial \ln V}$ $\times 10^2$	$\frac{\partial \ln A_2}{\partial \ln V}$ $\times 10^2$
EuO	(θ_C) 69.3	0.4 ± 0.1[a]	-0.07[d]	—
EuS	(θ_C) 16.0	0.28[b]		
		0.20[c]		
		0.24[d]	-0.09[d]	—
EuSe	(θ_N) 4.6	~ 1[b]		
		0[d]	0.37	0.55
		0.16[c]		
EuTe	(θ_N) 9.64	0.10[d]	3.42	-0.10
GdN		0.08 ± 0.04[e]		

[a]Sokolova et al. (1966); [b]Schwob and Vogt (1967); [c]Srivastava and Stevenson (1968); [d]Hidaka (1971); [e]McWhan (1966).

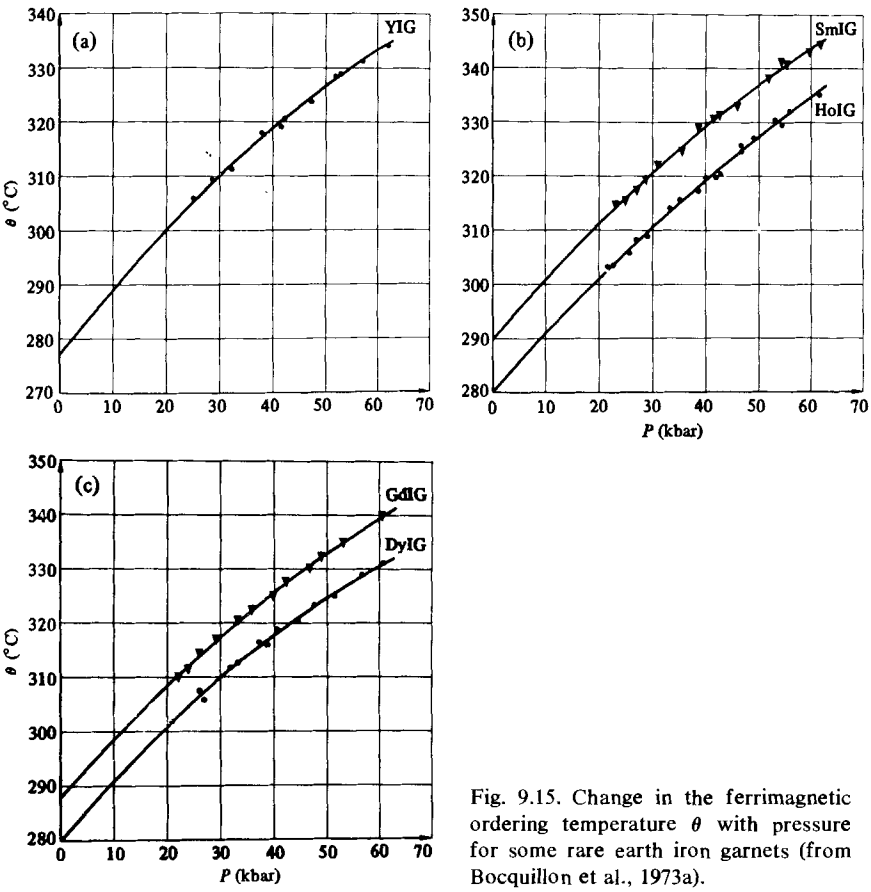

Fig. 9.15. Change in the ferrimagnetic ordering temperature θ with pressure for some rare earth iron garnets (from Bocquillon et al., 1973a).

TABLE 9.10.
Relative variations with volume of Curie θ_{Fi} and compensation temperatures θ_t of rare earth ion garnets. ($R_3Fe_5O_{12}$) (Bloch and Pavlovic).

Garnet	$d\theta_{Fi}/dP$ °K/kbar	$\frac{d \ln \theta}{d \ln V}$	$d\theta_t/dP$ °K/kbar	$\frac{d \ln \theta_t}{d \ln V}$
$Y_3Fe_5O_{12}$	1.25 ± 0.05	-3.40	0.95 ± 0.07	-4.8
$Gd_3Fe_5O_{12}$	1.28 ± 0.05	-3.48	0.77 ± 0.05	-4.5
$Tb_3Fe_5O_{12}$	1.23 ± 0.05	-3.45	0.40 ± 0.1	-2.7
$Dy_3Fe_5O_{12}$	1.15 ± 0.05	-3.22	0.38 ± 0.2	-4.2
$Ho_3Fe_5O_{12}$	1.28 ± 0.05	-3.55	—	—
$Er_3Fe_5O_{12}$	1.22 ± 0.05	-3.44	—	—
$Yb_3Fe_5O_{12}$	1.08 ± 0.05	-3.08	—	—

derivatives are summarized. Application of pressure produces a variation of the exchange interactions within each of the two sublattices, as well as between the two sublattices (see ch. 29, sections 3.2 and 3.5 for a detailed description of the sublattices involved in garnets). Apparently in these systems not only the variation in the interatomic distance affects the exchange interaction but also the angle change between the oxygen ion and the magnetic ions.

Another aspect that has been studied under pressure in garnets is the shift in the compensation point (see Bloch and Pavlovic, 1969). The logarithmic volume derivative for the compensation temperature is given by

$$\left(\frac{\partial \log \theta_{\text{comp}}}{\partial \log V}\right)_{\theta_{\text{comp}}} = \left(\frac{\partial \log n}{\partial \log V}\right)_{\theta_{\text{comp}}} \tag{9.35}$$

These data are also included in table 9.11. The effect of pressure on the anisotropy constants has also been investigated for some of the compounds (Timofeev et al., 1973a, 1973b).

6.6. *Theoretical aspects of the pressure studies on magnetic transition*

The pressure studies on magnetic properties of rare earth metals and alloys have led to several experimental interaction curves for the rare earth systems. The inadequacy of the Bethe–Slater interaction curve or the Néel interaction curve to account for the results on R.E. metals was first recognized by Robinson et al. (1964), and they proposed an interaction curve to fit Gd and Tb. In this curve θ_C and θ_p were plotted against the ratio of interatomic distance D to $2R$, R being the diameter of the unfilled 4f shell. McWhan and Stevens (1965) found that their results on Dy were not in agreement with the interaction curve proposed by Robinson et al. (1964) in that it predicted a positive $d\theta_C/dP$ for Dy while experimentally a negative $d\theta_C/dP$ is observed. Consequently McWhan and Stevens proposed a new interaction curve for the rare earth and intrarare earth alloys in which they plotted the ordering temperature T divided by the DeGenne's function $(g-1)^2J(J+1)$ versus R/r, the ratio of the interatomic distance R to the unfilled 4f shell radius r (see fig. 9.16). The data thus plotted fall into two curves representing the low and high pressure phases of the heavy rare earth metals and show that the exchange interaction increases smoothly in going from Gd to Ho with increasing R/r. Other experimental interaction curves have been proposed (see fig. 9.16), based on intrarare earth alloy data, in which the effective exchange interaction $J(Q)$ was plotted against $(r_{4f}^2)^{1/2}/V^{1/3}$ (McWhan and Stevens, 1967); θ_p divided by DeGenne's function plotted against c/a ratio (Milstein and Robinson, 1967), and $\theta_N/(g-1)^2J(J+1)$ vs c/a (Wazzan et al., 1967). While these experimental interaction curves are of some value in interpreting the behavior, they do not lead to a deeper understanding of the interaction mechanism. More recently the role played by the electronic band structure on the magnetic ordering in rare earth metals and alloys has been stressed. Since exchange interaction in rare earth metals is mediated via the conduction electron, the detailed features of the Fermi surface geometry has a

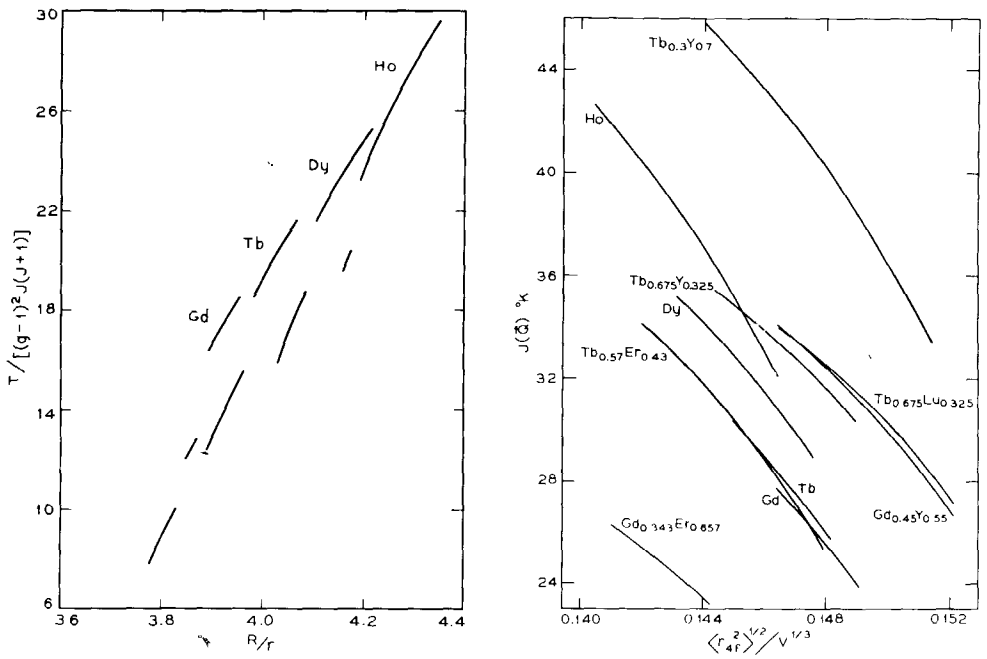

Fig. 9.16. Two of the proposed experimental interaction curves for rare earth metals and alloys. The two sets of curves in left fig. are for hcp (top set of 4) and for the high pressure phases (bottom set of 5) (from McWhan and Stevens, 1965 and 1967).

strong influence on the magnetic ordering (Keeton and Loucks, 1968; Evenson and Liu, 1968, 1969; Fleming and Liu, 1970). Kasuya (1966) has discussed s–d and s–f interactions in rare earth metals. The complex magnetic structures that occur in heavy rare earth metals lead to superzone boundaries and open up gaps in the Fermi surface and this situation appears to be not dissimilar to that of chromium. The lowering of electronic energy brought about by the existence of the spin wave structures would then be responsible for their stability, and a nesting of the hole and electron part of the Fermi surface apparently is involved (Keeton and Loucks, 1968). Since conduction electrons are involved in the indirect exchange model the Fermi surface variation with pressure is of much importance to a detailed understanding of the pressure effects. More experiments combined with calculations on the electronic band structure as a function of volume may be expected to lead to further progress in the field.

7. Mössbauer studies at high pressure on rare earth systems

Mössbauer studies under pressure in metals with ^{161}Dy, ^{170}Yb and ^{151}Eu have been reported (Holzapfel, 1975). The isomer shift measurements on Yb metal (Boehm, 1970) with pressure have not clearly indicated any changes in the valence

state or transfer of 4f electrons. The observed changes can be explained on the basis of the conduction electron contribution, as in the case of ^{115}Eu in Eu metal (see Holzapfel, 1975). Quite a few Eu compounds have been investigated (Wortmann et al., 1972; Klein et al., 1973, 1976). Eu^{2+} compounds in general show a stronger variation of the isomer shift, compared to Eu^{3+}. High pressure Mössbauer studies on EuO and EuS suggest that all seven 4f electrons remain well localized up to 100 kbar, in agreement with other pressure studies on Eu chalcogenides (see Jayaraman et al., 1974). In $Eu_2Ti_2O_7$ the change of the electric-field gradient has also been evaluated (Klein et al., 1973, and Klein et al., 1976). It was observed that the effect of pressure is stronger by about a factor of 4 than what one would expect from a simple point charge model. The conclusion is that the valence electron contribution dominates even in this $4f^6(^7F_0)$ configuration and that this contribution varies significantly more strongly than V^{-1}.

Some Mössbauer studies have been carried out on rare earth oxides (Boekema et al., 1975, and Halasa et al., 1974). The isomer shifts and hyperfine field changes have been measured. More recently, Mössbauer studies on Sm monochalcogenides have been made on SmS and in doped systems and these will be discussed in chapter 20. A complete coverage of Mössbauer studies under pressure can be found elsewhere (Drickamer and Frank, 1973).

8. Synthesis of new phases and compounds involving rare earths at high pressure and temperature

Ever since the successful synthesis of diamond under high pressure the high pressure-high temperature method has been tried for synthesizing new materials and in polymorphic forms in which they do not normally exist. Many new compounds and phases involving rare earths have been prepared in this manner. Some of these developments have been covered by Klement and Jayaraman (1966) and more recently by Pistorius (1976). One of the earliest systems in which pressure-induced transformations were found is the rare earth sesquioxide R_2O_3 (R = rare earth and Y). The rare earth sesquioxides involving Ho to Lu and Y were known only in the cubic forms, but application of 15 to 60 kbar and temperatures in the range 500 to 1500°C were found to convert them into the monoclinic-form (Hoekstra and Gingerich, 1964; Hoekstra, 1966). Marezio et al. (1966a) studied rare earth garnets under pressure and temperature and found that $Y_3Fe_5O_{12}$ broke down to $3YFeO_3 + Fe_2O_3$; the former with the perovskite-like structure and the latter with the corundum structure. This route was used to prepare many of the rare earth ortho ferrites, gallates and aluminates in the perovskite-like structure (Marezio et al., 1966b, 1968; Dernier and Maines, 1971; see also Goodenough et al., 1972). Shimada (1972) has claimed to have made denser modifications of R.E. garnets $Y_3Fe_5O_{12}$ and $Gd_3Fe_5O_{12}$ with a distorted perovskite-like structure, by treating them at pressures in the range 25–65 kbar at 1500°C. Other perovskite-like compounds that have been made under high

pressure and temperature conditions are $RInO_3$ (R = Eu, Gd and Dy) (Sawamoto, 1973); RMn_7O_{12} compounds with R = La, Nd (Bochu et al., 1974; Chenavas et al., 1974). Some of the other oxide compounds involving rare earths, which have been prepared under high pressure and temperature treatment are: $NaRGeO_4$ and $NaRSiO_4$, where R is a rare earth element or Y, in the tetragonal form (originally in the olivine structure, Chenavas et al., 1969); $Tm_2Si_2O_7$ in a new form as well as in the monoclinic gamma form (Bocquillon et al., 1973b; $Sm_2Ti_2O_7$ in the monoclinic form (Bocquillon et al., 1971; see also Queyroux et al., 1971); $LiRO_2$ compounds in the monoclinic form (Waintal and Gondrand, 1967).

Cannon et al. in a number of publications have recently reported pressure-induced transitions in several intermetallic compounds involving rare earth elements: transformation to the cubic structure in RAl_3 (Cannon and Hall, 1975); cubic $MgCu_2$ type to the hexagonal $MgZn_2$ type in RRu_2 and ROs_2 where R is a lanthanide (Cannon et al., 1972, 1973); synthesis of cubic Laves phases of $PrFe_2$, $NdFe_2$, $YbFe_2$ (Cannon et al., 1972); $LaCo_2$ (Robertson et al., 1972); RTe_{2-x} compounds with tetragonal structure and $LuTe_3$ with the orthorhombic structure at 100 kbar and 1200°C(Cannon and Hall, 1970).

The following compounds have also been studied under pressure and some synthesized: ROF compounds with R = La, Sm, Gd and Er by Pistorius (1973), phase transitions in ROF with R = La, Pr, Nd, Sm, Eu, Gd to the $PbCl_2$ structure* Gondrand et al., 1970); R_2C_3 compounds (with R = Y, La–Er) with Pu_2C_3 type structure (Krupka and Bowman, 1970 at 35 kbar and 1400°C; and $GdSb_2$ and $TbSb_2$ in $LaSb_2$ structure (Eatough and Hall, 1969), denser forms of $GdSb_2$ and $TbSb_2$ with orthorhombic structure (Johnson, 1971) and only in the denser form of RSb_2 with R = Y, Dy to Lu (Eatough and Hall, 1969). Rare earth polysulfides with tetragonal LaS_2 structure have been prepared for Tm, Yb and Lu and new polymorphs with the cubic LaS_2 structure for Gd to Lu and Y at high pressure (Webb and Hall, 1970a); sesquiselenides in Th_3P_4 cubic structure (Eatough and Hall, 1970); and polyselenides in the tetragonal $ErSe_2$ structure (Webb and Hall, 1970b); RSn_3 compounds with the fcc ($AuCu_3$) structure at 85 kbar for R = Tb to Er and Y (Miller and Hall, 1972, 1973) have also been made. A new pressure-induced form of DyF_3 which is metastable at atmospheric pressure was made by Vezzoli (1970).

Most of the pressure-induced phases were metastably retained at room temperature on release of pressure and in some cases their physical properties have been studied. Some of the studies were undertaken to check whether 4f bonding has any influence in determining the crystal structure in a particular series, or the size effects of the rare earth ions is the determining factor. A typical system in which such a study was done is the RAl_3 system (Cannon and Hall, 1975). However, the results obtained do not give a clear cut answer. The one definite result of the study on RAl_3 seems to be that application of high pressure tends to make the lower-atomic weight lanthanide behave more like those of higher atomic weight. Thus the pressure-induced phase changes in the RAl_3 system were in the direction of structures with increased cubic character.

*(Gondrand, 1970; Gondrand and Christensen, 1971;

Acknowledgments

I wish to thank R.G. Maines for helping in many ways during the preparation of the article and Mrs. Karen Miller for the painstaking effort in getting the manuscript typed. I would also like to thank Dr. B. Johansson, Dr. W.H. Gust, Dr. W.J. Carter and Dr. D.A. Young for supplying originals of figures, from which some of the figures for this article were composed and to Mr. H.H. Teitelbaum for his help in the literature survey.

References

Altshuler, L.V. and A.A. Bakanova, 1969, Sov. Phys. Usp., **11**, 678.
Altshuler, L.V., A.A. Bakanova and I.P. Dudoladov, 1966a, Zh. Eksp. Teor. Fiz. Pisma Red., **3**, 483.
Altshuler, L.V., A.A. Bakanova and I.P. Dudoladov, 1966b, JETP Lett. **3**, 315.
Altshuler, L.V., A.A. Bakanova and I.P. Dudoladov, 1968, Sov. Phys. JETP, **26**, 1115.
Altstetter, C.J., 1973, Met. Trans., **4**, 2723.
Austin, I.G. and P.K. Mishra, 1967, Phil. Mag., **15**, 529.
Bakanova, A.A., I.P. Dudoladov and Yu. N. Sutulov, 1970, Sov. Phys. Solid State, **11**, 1515.
Bartholin, H. and D. Bloch, 1967, C.R. Acad. Sci., Paris, **264**, 1135.
Bartholin, H. and D. Bloch, 1968, J. Phys. Chem. Solids, **29**, 1063.
Bloch, D. and F. Chaisse, 1972, C.R. Acad. Sci. Paris, Ser. B, **274**,221.
Bloch, D., F. Chaisse, F. Givord and J. Voiron, 1971, J. Phys. (Paris), **32**, C1–659.
Bloch, D. and R. Pauthenet, 1965, Study of the Magnetic Properties of the Rare Earth Elements Under Hydrostatic Pressure, in: Proceedings of the International Conference on Magnetism, Nottingham, 1964 (Institute of Physics, London) pp. 255–259.
Bloch, D. and A.S. Pavlovic, 1969, Magnetically Ordered Materials at High Pressure, in: Bradley, R.S., ed., Advances in High Pressure Research, 1969, Vol. 3 (Academic Press, New York and London) pp. 41–147.
Bochu, B., J. Chenavas, J.C. Joubert and M. Marezio, 1974, J. Solid State Chem., **11**, 88.
Bocquillon, G., C. Loriers–Susse, M. Dellalian and J. Loriers, 1973b, C.R. Acad. Sci., Paris, Ser. C, **276**, 543.
Bocquillon, G., C. Loriers–Susse and J. Loriers, 1973a, High Temp.–High Press., **5**, 161.
Bocquillon, G., F. Queyroux, C. Susse and R. Collongues, 1971, C.R. Acad. Sci., Paris, Ser. C, **272**, 572.
Boehm, H.G., 1970, Dissertation, Technische Universität, München.
Boekema, C., F. Van der Woude and G.A. Sawatzky, 1975, Phys. Rev. B, **11**, 2705.
Bridgman, P.W., 1954, Proc. Am. Acad. Arts Sci., **83**, 1.
Brouha, M. and K.H.J. Buschow, 1973a, J. Phys. F. (GB), **3**, 2218.
Brouha, M. and K.H.J. Buschow, 1973b, J. Appl. Phys. **44**, 1813.
Brouha, M., K.H.J. Buschow and A.R. Miedema, 1974, I.E.E.E. Trans. Magn. (USA), **10**, 182.
Cannon, J.F. and H.T. Hall, 1970, Inorg. Chem., **9**, 1639.
Cannon, J.F. and H.T. Hall, 1975, J. Less-Common Met., **40**, 313.
Cannon, J.F., D.L. Robertson and H.T. Hall, 1972, J. Less-Common Met., **29**, 141.
Cannon, J.F., D.L. Robertson, H.T. Hall and A.C. Lawson, 1973, J. Less-Common Met., **31**, 174.
Carter, W.J., J.N. Fritz, S.P. Marsh and R.G. McQueen, 1975, J. Phys. Chem. Solids, **36**, 741.
Chatterjee, A., A.K. Singh and A. Jayaraman, 1972, Phys. Rev. B, **6**, 2285.
Chenavas, J., J.C. Joubert and M. Marezio, 1974, High Pressure Synthesis and Crystal Structure of a New Series of Perovskite Compounds..., International Crystallography Conference on Diffraction of Real Atoms and Real Crystals, Melbourne, Australia, 1974, II J–3/221–2.
Chenavas, J., A. Waintal, J.J. Capponi and M. Gondrand, 1969, Mater. Res. Bull., **4**, 425.
Dernier, P.D. and R.G. Maines, 1971, Mater. Res. Bull., **6**, 433.
Doran, D.G. and R.K. Linde, 1966, Shock Effects in Solids, in: Seitz, F. and D. Turnbull, eds., Solid State Physics, 1966, Vol. **19** (Academic Press, New York and London) pp. 230–288.
Drickamer, H.G., 1965, Effect of High Pressure on the Electronic Structure of Solids, in: Seitz, F. and D. Turnbull, eds., Solid State Physics, 1965, Vol. **17** (Academic Press, New York and London) pp. 1–127.
Drickamer, H.G. and C.W. Frank, 1973, Electronic Transitions and The High Pressure Chemistry and Physics of Solids, (Chapman and Hall, London).
Drickamer, H.G., R.W. Lynch, R.L. Clendenen

and E.A. Perez-Albuerne, 1966, X-ray Diffraction Studies of the Lattice Parameters of Solids Under Very High Pressure, in: Seitz, F. and D. Turnbull, eds., Solid State Physics, 1966, Vol. **19** (Academic Press, New York and London) pp. 135–228.
Eatough. N.L. and H.T. Hall, 1969, Inorg. Chem., **8**, 1439.
Eatough, N.L. and H.T. Hall, 1970, Inorg. Chem., **9**, 417.
Elliott, R.J., 1965, Theory of Magnetism in the Rare Earth Metals, in: Rado, G.T. and H. Suhl, eds., Magnetism, Vol. II A (Academic Press, New York and London) pp. 385–424.
Evenson, W.E. and S.H. Liu, 1968, Phys. Rev. Lett., **21**, 432.
Evenson, W.E. and S.H. Liu, 1969, Phys. Rev., **178**, 783.
Fisher, E.S., M.H. Manghani and R. Kikuta, 1973, J. Phys. Chem. Solids, **34**, 687.
Fisk, Z. and B.T. Matthias, 1969, Science, **165**, 279.
Fleming, G.S. and S.H. Liu, 1970, Phys. Rev. B, **2**, 164.
Fujii, H., H. Tani, T. Okamoto and E. Tatsumoto, 1972, J. Phys. Soc. Jap. **33**, 855.
Givord, D., F. Givord and R. Lemaire, 1971, J. Phys (Paris), **32**, C1–668.
Gondrand, M., 1970, Bull. Soc. Fr. Mineral-Cristallogr., **93**, 421.
Gondrand, M. and A. N. Christensen, 1971, Mater. Res. Bull., **6**, 239.
Gondrand, M., J.C. Joubert, J. Chenavas, J.J. Capponi and M. Perroud, 1970, Mater. Res. Bull., **5**, 769.
Goodenough, J.B., J.A. Kafalas and J.M. Longo, 1972, High Pressure Synthesis, in : Hagenmuller, P., ed., Preparative Methods in Solid State Chemistry (Academic Press, New York and London) pp. 1–69.
Gschneidner, Jr., K.A., 1961a, Crystallography of the Rare-Earth Metals, in: Spedding, F.H. and A.H. Daane, eds., The Rare Earths (John Wiley and Sons, Inc., New York and London) pp. 190–215.
Gschneidner, Jr., K.A., 1961b, Rare Earth Alloys, (Van Nostrand, New York) pp. 1–65.
Gschneidner, Jr., K.A. and R.M. Valletta, 1968, Acta Met., **16**, 477.
Gust, W.H. and E.B. Royce, 1973, Phys. Rev. B, **8**, 3595.
Halasa, N.A., G. De Pasquali and H.G. Drickamer, 1974, Phys. Rev. B, **10**, 154.
Hall, H.T., J.D. Barnett and L. Merrill, 1963, Science, **139**, 111.
Harris, I.R. and G.V. Raynor, 1969, J. Less-Common Met., **17**, 336.
Hidaka, Y., 1970, J. Phys. Soc. Jap., **29**, 515.
Hidaka, Y., 1971, J. Sci. Hiroshima Univ. (Jap.), **35**, 93.
Hiraoka, T., 1974, J. Phys. Soc. Jap., **37**, 1238.
Hiraoka, T. and T. Fuchikami, 1974, J. Phys Soc. Jap., **36**, 1488.
Hodges, C.H., 1967, Acta Met., **15**, 1787.
Hoekstra, H.R., 1966, Inorg. Chem., **5**, 754.
Hoekstra, H.R. and K.A. Gingerich, 1964, Science, **146**, 1163.
Holzapfel, W.B., 1975, C.R.C. Critical Reviews in Solid State Sciences, **5**, 89–123.
Holzapfel, W.B. and D. Severin, 1971, Phys. Lett., **34A**, 371.
Iida, K. and G. Fujii, 1972, Res. Rep. Fac. Eng. Meiji Univ. (Jap.), **26**, 43.
Ito, T., 1973, J. Sci. Hiroshima Univ. (Jap.), **37**, 107.
Ito, T., H. Fujii, T. Okamoto and E. Tatsumoto, 1972, J. Phys. Soc. Jap., **33**, 854.
Jaakkola, S., 1974, Phys. Lett., **50A**, 35.
Jaakkola, S. and S. Parviainen, 1974, Phys. Status Solidi A, **21**, K53.
Jaakkola, S., S. Parviainen and H. Stenholm, 1975, Z. Phys. B, **20**, 109.
Jayaraman, A., 1964, Phys. Rev., **135**, A1056.
Jayaraman, A., 1965a, Phys. Rev., **139**, A690.
Jayaraman, A., 1965b, Phys. Rev., **137**, A179.
Jayaraman, A., W. Klement, Jr. and G.C. Kennedy, 1963, Phys. Rev., **132**, A1620.
Jayaraman, A., W. Lowe, L.D. Longinotti and E. Bucher, 1976, Phys. Rev. Lett., **36**, 366.
Jayaraman, A. and R.C. Sherwood, 1964a, Phys. Rev. Lett., **12**, 22.
Jayaraman, A. and R.C. Sherwood, 1964b, Phys. Rev., **134**, A691.
Jayaraman, A., R.C. Sherwood, H.J. Williams and E. Corenzwit, 1966, Phys. Rev., **148**, 502.
Jayaraman, A., A.K. Singh, A. Chatterjee and S. Usha Devi, 1974, Phys. Rev. B, **9**, 2513.
Jepsen, O. and O.K. Andersen, 1971, Solid State Comm., **9**, 1763.
Johansen, G. and A.R. Mackintosh, 1970, Solid State Comm. **8**, 121.
Johansson, B. and A. Rosengren, 1975, Phys. Rev. B, **11**, 2836.
Johnson, Q., 1971, Inorg. Chem., **10**, 2089.
Jullien, R. and D. Jerome, 1971, J. Phys. Chem. Solids, **32**, 257.
Kaldis, E. and P. Wachter, 1972, Solid State Commun., **11**, 907.
Kasuya, T., 1966, s-d and s-f Interactions and Rare Earth Metals, in: Rado, G.T. and H. Suhl, eds., Magnetism, Vol. II B (Academic Press, New York and London) pp. 215–291.
Katzman, H. and J.A. Mydosh, 1972, Z. Phys., **256**, 380.
Kawaii, N. and S. Endo, 1970, Rev. Sci. Instr., **41**, 1178.
Kawaii, N., M. Sakakihara, A. Marizumi and A. Sawaoka, 1967, J. Phys. Soc. Jap., **23**, 475.
Keeton, S.C. and T.L. Loucks, 1968, Phys. Rev., **168**, 672.
King, E., and I.R. Harris, 1970, J. Less-Common Met., **21**, 275.
Klein, U.F., G. Wortmann, G.M. Kalvius and W.B. Holzapfel, 1973, Verh. Dtsch. Phys. Ges. VI, **8**, 350.
Klein, U.F., G. Wortmann and G.M. Kalvius, 1976, J. Magn. and Magn. Mater. **3**, 50.
Klement Jr., W. and A. Jayaraman, 1966, Progress in Solid State Chemistry, Vol. 3 (Pergamon Press, Oxford and New York) pp. 289–376.
Koch, C.C., 1970, J. Less-Common Met., **22**, 149.
Kondorskii, E.I. and L.V. Vinokurova, 1965,

Effect of Hydrostatic Pressure on Magnetization of Some Rare Earth Metals, in: Proceedings of the International Conference on Magnetism, Nottingham, 1964, (Institute of Physics, London) pp. 260–265.
Krupka, M.C. and M.G. Bowman, 1970, Coll. Internatl. C.N.R.S., **188**, 409.
Lara, S. and R.M. Xavier, 1974, Notas Fis. (Brazil), **22**, 91.
Lawson, A.W., 1956, Prog. Met. Phys., **6**, 1.
Levy, F. and P. Wachter, 1970, Solid State Commun., **8**, 183.
Liu, L., 1975, J. Phys. Chem. Solids, **36**, 31.
Liu, L., W.A. Bassett and M.S. Liu, 1973, Science, **180**, 298.
Lundin, C.E., 1966, Denver Res. Inst. Rept. 2326, (Denver University, Denver, Colorado).
Marezio, M., J.P. Remeika and P. Dernier, 1966b, Mater. Res. Bull., **1**, 247.
Marezio, M., J.P. Remeika and P. Dernier, 1968, Inorg Chem., **7**, 1337.
Marezio, M., J.P. Remeika and A. Jayaraman, 1966a, J. Chem. Phys., **45**, 1821.
McQueen, R.G., 1963, Laboratory Techniques for Very High Pressures and The Behavior of Metals Under Dynamic Loading, in: Gschneidner, Jr., K.A., M.T. Hepworth and N.A.D. Parlee, eds., Metallurgy at High Pressures and Temperatures (Gordon and Breach, New York) pp. 44–132.
McWhan, D.B., 1966, J. Chem. Phys., **44**, 3528.
McWhan, D.B. and W.L. Bond, 1964, Rev. Sci. Instr., **35**, 626.
McWhan, D.B., E. Corenzwit and A.L. Stevens, 1966b, J. Appl. Phys., **37**, 1355.
McWhan, D.B., T.M. Rice and P.H. Schmidt, 1969, Phys. Rev., **177**, 1063.
McWhan, D.B., P.C. Souers and G. Jura, 1966a, Phys. Rev., **143**, 385.
McWhan, D.B. and A.L. Stevens, 1965, Phys. Rev., **139**, A682.
McWhan, D.B. and A.L. Stevens, 1967, Phys. Rev., **159**, 438.
Menyuk, N., K. Dwight and J.A. Kafalas, 1971, J. Appl. Phys., **42**, 1301.
Miller, K. and H.T. Hall, 1972, Inorg. Chem., **11**, 1188.
Miller, K. and H.T. Hall, 1973, J. Less-Common Met., **32**, 275.
Milstein, F. and L.B. Robinson, 1967, Phys. Rev., **159**, 466.
Milton, J.E. and T.A. Scott, 1967, Phys. Rev., **160**, 387.
Ming, L.C. and W.A. Bassett, 1974, Rev. Sci. Instr., **45**, 1115.
Nikitin, S.A., L.I. Solntseva and V.A. Suchkova, 1972, Izv. Akad. Nauk, SSSR. Ser. Fiz., **36**, 1449.
Okamoto, T., H. Fujii, T. Ito and E. Tatsumoto, 1968, J. Phys. Soc. Jap., **25**, 1729.
Penney, T. (private communication).
Perez-Albuerne, E.A., R.L. Clendenen, R.W. Lynch and H.G. Drickamer, 1966, Phys. Rev., **142**, 392.
Piermarini, G.J. and C.E. Weir, 1964, Science, **144**, 69.
Pistorius, C.W.F.T., 1973, J. Less-Common Met., **31**, 119.
Pistorius, C.W.F.T., 1976, Progress in Solid State Chemistry, Vol. II (Pergamon Press, Oxford and New York) pp. 1–120.
Queyroux, F., G. Bocquillon, C. Susse and R. Collongues, 1971, Some $Ln_2Ti_2O_7$ Compounds and Their Pressure Induced Transformation, in: Field, P.E., ed., Proceedings of the Ninth Rare Earth Research Conference, Blacksburg, Virginia, 1971, Vol. I (U.S. Department of Commerce, Springfield, Virginia) pp. 103–112.
Reynolds Jr., C.L. and R.E. Barker, Jr., 1974, J. Chem Phys., **61**, 2548.
Rice, M.H., R.G. McQueen and J.M. Walsh, 1958, Compression of Solids by Strong Shock Waves, in: Seitz, F. and D. Turnbull, eds., Solid State Physics, 1958, Vol. 6 (Academic Press, New York and London) pp. 1–63.
Robertson, D.L., J.F. Cannon and H.T. Hall, 1972, Mater. Res. Bull., **7**, 977.
Robinson, L.B., F. Milstein and A. Jayaraman, 1964, Phys. Rev., **134**, A187.
Robinson, L.B., S. Tan and K.F. Sterrett, 1966, Phys. Rev., **141**, 548.
Rosengren, A., and B. Johansson, 1976, Phys. Rev. B. **13**, 1468.
Sawamoto, H., 1973, J. Appl. Phys. Jap., **12**, 1432.
Sawaoka, A. and C.T. Tomizuka, 1971, Phys. Lett. **37A**, 211.
Schwob, P., 1969, Phys. Kondens. Materie, **10**, 186.
Schwob, P. and O. Vogt, 1967, Phys. Letters, **24A**, 242.
Sekizawa, K., H. Sekizawa and C.T. Tomizuka, 1970, J. Phys Chem. Solids, **31**, 215.
Shapira, Y. and T.B. Reed, 1972, Compressibilities and Debye Temperatures of the Europium Chalcogenides, in: AIP Conference Proceedings, No. 5, Part 2, pp. 837–839 (Seventeenth Annual Conference on Magnetism and Magnetic Materials, Chicago, 1971).
Shimada, M., 1972, Jap. J. Appl. Phys., **11**, 964.
Sokolova, G.K., K.M. Demchuk, K.P. Rodionov and A.A. Samokhvalov, 1966, Sov. Phys. JETP, **22**, 317.
Souers, P.C. and G. Jura, 1963, Science, **140**, 481.
Souers, P.C. and G. Jura, 1964, Science, **145**, 575.
Srivastava, V.C. and R. Stevenson, 1968, Can. J. Phys., **46**, 2703.
Stager, R.A. and H.G. Drickamer, 1963, Science, **139**, 1284.
Stager, R.A. and H.G. Drickamer, 1964, Phys. Rev., **133**, 830.
Stephens, D.R., 1964, J. Phys. Chem. Solids, **25**, 423.
Stephens, D.R., 1965, J. Phys. Chem. Solids, **26**, 943.
Stephens, D.R. and Q. Johnson, 1969, J. Less-Common Met., **17**, 243.

Stromberg, H.D. and D.R. Stephens, 1964, J. Phys. Chem. Solids, **25**, 1015.
Syassen, K. and W.B. Holzapfel, 1975, Solid State Commun., **16**, 533.
Tatsumoto, E., H. Fujiwara, H. Fujii, N. Iwaka and T. Okamoto, 1968, J. Appl. Phys., **39**, 894.
Timofeev, Yu. A., E.N. Yakovlev, A.N. Ageev and A.G. Gurevich, 1973a, Effect of High Pressure on Anisotropy and Relaxation in Rare Earth Doped Ferromagnetic Garnets, in: AIP Conference Proceedings, No. 10, Part 1, pp. 155–163 (Eighteenth Annual Conference on Magnetism and Magnetic Materials, Denver, 1972).
Timofeev, Yu.A., E.N. Yakovlev, A.G. Gurevich and A.N. Ageev, 1973b, Sov. Phys. Solid State, **14**, 2835.
Umebayashi, H., G. Shirane, B.C. Frazer and W.B. Daniels, 1968, Phys. Rev., **165**, 688.
Vasvari, B., A.O.E. Animalu and V. Heine, 1967, Phys. Rev., **154**, 535.
Vezzoli, G.C., 1970, Mater. Res. Bull., **5**, 213.
Vinokurova, L.I. and E.I. Kondorskii, 1964, Sov. Phys. JETP., **19**, 777.
Vinokurova, L.I. and E.I. Kondorskii, 1965a, Sov. Phys. JETP, **21**, 283.
Vinokurova, L.I. and E.I. Kondorskii, 1965b, Sov. Phys. JETP, **20**, 259.
Vinokurova, L.I., E.I. Kondorskii, V. Yu. Ivanov, V. M. Eva and K.H. Rakhimova, 1973, Sov. Phys. Solid State, **14**, 2981.
Vinokurova, L.I., E.I. Kondorskii, V.Yu. Ivanov, and K.H. Rakhimova, 1972a, Izv. Akad. Nauk. SSSR Ser. Fiz., **36**, 1419.
Vinokurova, L.I., E.I. Kondorskii, K.H. Rakhimova and V. Yu. Ivanov, 1972b, Sov. Phys. Solid State, **14**, 613.
Voiron, J., J. Beille, D. Bloch and C. Vettier, 1973, Solid State Commun., **13**, 201.
Voiron, J. and D. Bloch, 1971, J. Physique (Paris) **32**, 949.
Waintal, A. and M. Gondrand, 1967, Mater. Res. Bull., **2**, 889.
Wazzan, A.R., R.S. Vitt and L.B. Robinson, 1967, Phys. Rev. **159**, 400.
Webb, A.W. and H.T. Hall, 1970a, Inorg. Chem., **9**, 1084.
Webb, A.W. and H.T. Hall, 1970b, Inorg, Chem., **9**, 843.
Wortmann, G., U.F. Klein, G.M. Klavius and W.B. Holzapfel, 1972, Pressure Dependence of the Isomer Shifts and Quadrupole Splittings of Di- and Trivalent Europium Compounds, Presented at the International Conference on Applications of the Mössbauer Effect, Ayeleth Hashahar, Israel, 1973.
Yagasaki, K., H. Fujii and T. Okamoto, 1973, J. Phys. Soc. Jap., **34**, 832.
Young, D.A., 1975, Phase Diagrams of the Elements, U.C.R.L. Report No. 51902, Lawrence Livermore Laboratory, University of California (USA), September 1975.

Handbook on the Physics and Chemistry of Rare Earths, edited by K.A. Gschneidner, Jr. and L. Eyring

Chapter 10

SUPERCONDUCTIVITY: METALS, ALLOYS AND COMPOUNDS

C. PROBST and J. WITTIG
Institut für Festkörperforschung, Kernforschungsanlage Jülich, 5170 Jülich, Fed. Rep. Germany

Contents

Symbols

C_V = specific heat at constant volume
e/a = electron-per-atom ratio
$F(\omega)$ = phonon density of states
I = current
$\langle I^2 \rangle$ = average of the squared electron–phonon matrix element
k_B = Boltzmann's constant
M = atomic mass
$N(E_F)$ = density of states at the Fermi energy
$\langle n_{4f} \rangle$ = 4f shell occupation number
P = pressure
q = wave number
R = electrical resistance
R_{4K} = electrical resistance at 4 Kelvin
T = absolute temperature
T_c = superconducting transition temperature
T_0 = magnetic ordering temperature
V = volume; voltage; BCS-coupling parameter
$\alpha^2(\omega)$ = electron–phonon interaction
$\beta(T)$ = volume coefficient of thermal expansion
γ = electronic specific heat coefficient
γ_G = Grüneisen constant
$\Delta(0)$ = superconducting energy gap at $T = 0$ K
ΔT_c = width or shift of the superconducting transition
$\Delta V/V$ = relative volume change
Θ_D = Debye temperature
κ = compressibility
λ = electron phonon coupling parameter
μ^* = Coulomb pseudopotential
ω_i = mode frequency

$\langle\omega^2\rangle$ = average of the squared phonon frequencies

$\omega(q)$ = phonon frequency as a function of wave number

1. Introduction

Superconductivity is a rather common phenomenon in metals at low temperatures. In the rare earth group however, the only superconducting element at normal pressure is lanthanum. Most rare earth metals are magnetic due to their incomplete 4f shell. The magnetism inhibits the formation of Cooper pairs and thus inhibits superconductivity. Similarly, magnetism prevents superconductivity in the 3d-transition period beyond vanadium (cf. fig. 10.1).

The superconducting state becomes stable below an ordering temperature T_c. This superconducting transition temperature depends chiefly on the strength of the electron–phonon interaction. Although the basic theory of the superconducting state is now well understood, the question cannot simply be answered, why certain metals are "good" superconductors while others are not. For transition metals, including the rare earths, it is still impossible to predict theoretically the strength of the electron–phonon coupling from the physical properties in the normal state. The reason is that the necessary normal-state properties, e.g. the electronic energy bands near the Fermi energy or the phonon spectra, are not sufficiently well known for most superconductors to make a calculation of T_c worthwhile (McMillan, 1968).

The situation is perhaps quite well illustrated by the behavior of the rare earth metals scandium, yttrium, lanthanum and lutetium. In this family of nonmagnetic trivalent metals, Sc, Y and Lu are not superconducting down to temperatures in the millikelvin range, whereas La becomes superconducting with a $T_c \simeq 5$ K. Theory predicts that a high density of states at the Fermi energy should be favorable for a high T_c. An inspection of the low-T electronic specific heat coefficient (cf. section 3.3) reveals that all these rare earth metals have a similarly high density of states. Apparently, other parameters are more decisive in determining T_c for these metals. At present it is not possible to predict the T_c's of Sc, Y and Lu theoretically. Also, the different behavior of La cannot be explained theoretically from "first principles". Therefore, in this chapter we will follow McMillan's original suggestion that a great deal can be learned about the normal-state properties of a metal (e.g. the electronic band structure of La) from its measured superconducting properties.

It was found that the T_c of La, already fairly high at normal pressure, increases strongly if the metal is compressed by external pressure (Smith and Gardner, 1966). Subsequently, Y, Lu and Sc have also been studied for superconductivity. The experiments led to the discovery of pressure-induced superconductivity in Y and Lu. At the highest pressures reported below (150–200 kbar) the volume compression $\Delta V/V$ of La, Y and Lu is of the order of

30%. The interatomic spacings are hence reduced by about 10%. This is an appreciable effect in a metal and drastic changes of its physical properties may be anticipated.

The electronic structure of cerium undergoes fundamental changes with pressure, see ch. 4, Briefly, Ce has a paramagnetic moment corresponding to a $4f^1$ shell at low pressure (e.g. Schlapbach, 1974). At high pressure, no local magnetic moment exists on the 4f shell. The magnetism disappears so thoroughly that Ce even becomes a fairly "good" superconductor. The rare earth group therefore now contains 4 superconducting elements at high pressure.

Figure 10.1 shows the corresponding section of the periodic table. Pressure-induced superconductors are marked by a solid triangle. One may notice that instead of La the last rare earth metal Lu appears below Y in the third column. This is different from standard representations of the periodic system. The reason for this exchange will be given in section 3.3.

The purpose of this chapter is to review the superconductivity of the rare earth metals, alloys and compounds. We place emphasis upon the pure elements because of their principal importance for an understanding. In section 2 we present the existing data for the pressure dependence of T_c for La, Ce, Y and Lu. The data for Lu have not been published elsewhere (Probst, 1974). The resistivity of La shows highly anomalous features under pressure. The data are included, since they are probably related to the superconductivity of La. In addition, electron tunneling experiments have provided interesting information about the phonon spectrum of La and its changes under pressure.

In section 3 we discuss previous and new approaches toward an understanding of the superconductivity in the rare earth group. On a phenomenological level, fairly definite conclusions can be drawn as to the electronic band structure of La

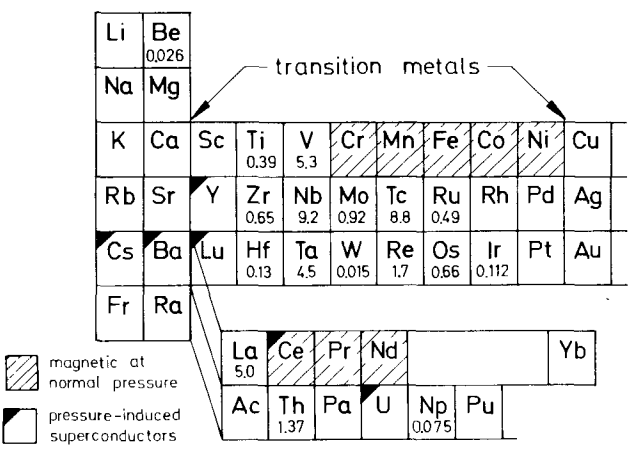

Fig. 10.1. Left side of the periodic table. Instead of La, Lu has been placed below Sc and Y (Hamilton, 1965). The values below the symbols of the elements are the superconducting transition temperatures in degrees K. Recently, pressure-induced superconductivity has also been observed in a new high pressure phase of scandium (cf. section 6).

and Ce. A hypothesis is briefly discussed that perhaps Ba and Cs also become genuine members of the 4f group at high pressure (cf. fig. 10.1). Although this is entirely hypothetical at the time of writing, it once more stresses the point that pressure is an indispensable variable for the understanding of the superconductivity in the rare earths.

Section 4 presents some selected topics on superconducting rare earth alloys and compounds. In this chapter we do not discuss the influence of paramagnetic rare earth impurities on the T_c of a superconducting host metal. There is an excellent recent review of this subject by Maple (1973). The chapters by Fulde and Maple will also cover this topic. Finally, section 5 summarizes our conclusions.

2. Experimental situation for the rare earth metals

2.1. *Pressure dependence of T_c for lanthanum*

Smith and Gardner (1966) discovered that the superconducting critical temperature, T_c, of La increases strongly under pressure. Figure 10.2 shows the pressure dependence of T_c up to 200 kbar as recently published by Balster and Wittig (1975). The horizontal width of the rectangles indicates the pressure inhomogeneity. The vertical width characterizes the spread of the superconducting transition. Also included are data by Maple et al. (1969) measured under hydrostatic pressure up to $\simeq$20 kbar (triangles). They are probably the most reliable values for the metastable fcc phase. The thermodynamically stable phase at low temperature and low pressure is the double-hexagonal close-packed (d–hcp) phase (cf. fig. 10.5). As seen from fig. 10.2, T_c also increases steeply with pressure in this phase, being roughly 1 K lower than in the metastable fcc phase.

At 200 kbar, $T_c(P)$ saturates. The maximum transition temperature is 13 K, several degrees higher than for all other elemental superconductors. Zarubina (1973) reported a saturation of $T_c(P)$ at approximately 11 K. The origin of the discrepancy is not clear at present.

Another remarkable feature of La is a sharp kink in $T_c(P)$ at $\simeq$53 kbar (see also insert). The only other element for which a similar kink has been previously found in $T_c(P)$ is the 5f-band metal uranium (Smith and Fisher, 1973). It has been suggested that in both metals *isostructural* phase transformations occur at liquid helium temperature at the pressures where the kinks occur (Smith and Fisher, 1973; Balster and Wittig, 1975; Wittig, 1975). Clearly, an isostructural phase change is a special kind of a lattice instability. Certain longitudinal phonons will tend to become soft near the transition. Such a phonon softening can lead to a kink in $T_c(P)$ as will be briefly outlined in the following paragraph.

According to McMillan (1968) the T_c of a superconductor is given by

$$T_c = \frac{\Theta_D}{1.45} \exp\left(-\frac{1.04(1+\lambda)}{\lambda - \mu^*(1+0.62\lambda)}\right). \tag{10.1}$$

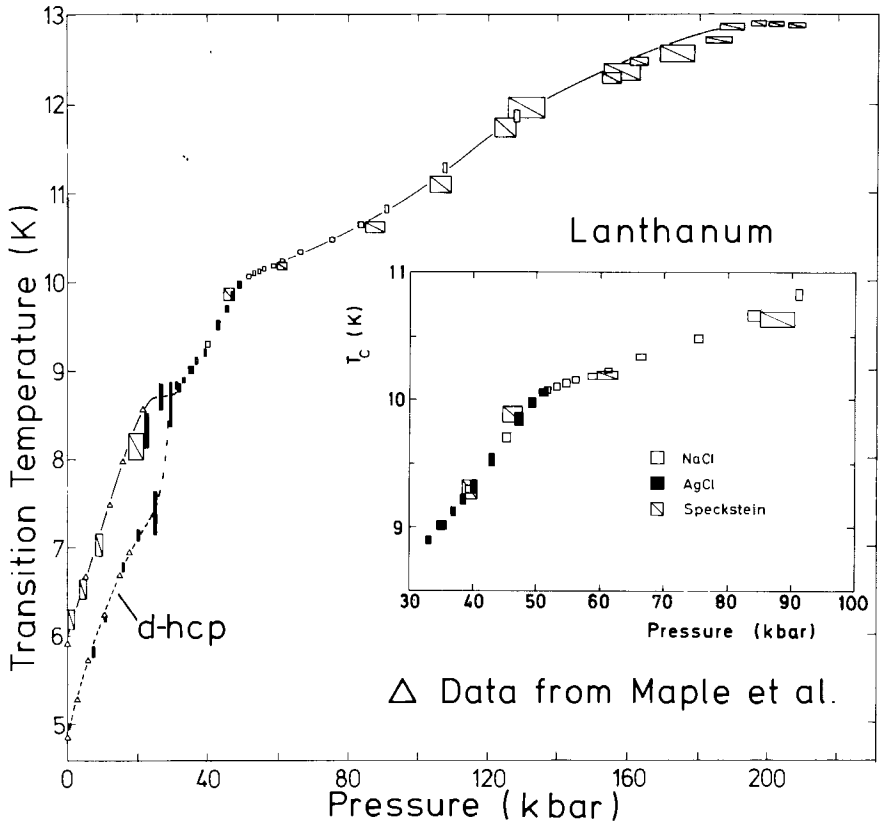

Fig. 10.2. T_c for fcc and d-hcp La as a function of pressure. A marked feature of the T_c–P dependence of fcc La are kinks at about 50 and 25 kbar (cf. insert and fig. 10.3).

Further below we consider the limit $\lambda \ll 1$. In this case the formula takes on the simplified form

$$T_c = \frac{\Theta_D}{1.45} \exp\left(-\frac{1.04}{\lambda - \mu^*}\right), \tag{10.2}$$

where Θ_D is the Debye temperature. The Coulomb pseudopotential μ^* describes the repulsive electron–electron interaction. Very little is known about this quantity in transition metals. It is normally taken to be constant $\simeq 0.13$. Usually, the electron–phonon coupling parameter λ regulates the magnitude of T_c for different metals and, also the dependence of T_c on pressure. According to McMillan, it can be written as

$$\lambda = \frac{N(E_F)\langle I^2\rangle}{M\langle\omega^2\rangle} \tag{10.3}$$

where $N(E_F)$ is the density of states at the Fermi energy, $\langle I^2\rangle$ is an average of a

squared electron–phonon matrix element. M stands for the atomic mass and $\langle\omega^2\rangle$ is an average of the squared phonon frequencies. A decrease of $\langle\omega^2\rangle$ thus leads to an increase of λ, if $N(E_F)$ and $\langle I^2\rangle$ stay constant. This, in turn, will lead to an increase of T_c, since the exponential factor dominates the prefactor Θ_D which simultaneously decreases. Therefore, an enhancement of T_c is expected, if a structural phase transition is accompanied by a softening of phonon modes.

The anticipated explanation for La is illustrated in fig. 10.3. The dashed curve shows a hypothetical smooth $T_c(P)$ dependence, assuming the 53 kbar structural transition does not occur. Due to the progressive phonon softening toward 53 kbar one observes a considerable enhancement of $T_c(P)$ on either side of the transition. If the volume discontinuity at the transition is sufficiently small, no discontinuity in T_c will be detectable. Hence, only a marked change of the slope dT_c/dP will occur at the transition point (Balster and Wittig, 1975).

An interesting alternative explanation for the kink at 53 kbar (fig. 10.2) has recently been advanced by Glötzel (1976). He has carried out band structure calculations for fcc La at various lattice parameters corresponding to pressures up to 120 kbar. A topological change of the Fermi surface occurs at 60 kbar. A hole opens up in the first band. According to Lifshitz (1960), a Van Hove singularity should pass through the Fermi level with strong consequences for the thermodynamic properties in the neighborhood of the critical pressure or critical volume. Glötzel has suggested that the low temperature 53 kbar transition in La may have such an electronic origin. A corresponding anomalous pressure dependence of the electronic density of states $N(E_F)$ may thus also lead to a kink in $T_c(P)$ without any phonon softening.

Presumably, the truth will be somewhere in between. If the "electronic" properties, $N(E_F)$ and $\langle I^2\rangle$, behave anomalously near 53 kbar, the "phononic" properties, i.e. $\langle\omega^2\rangle$, will also be anomalous and vice versa. In the case of

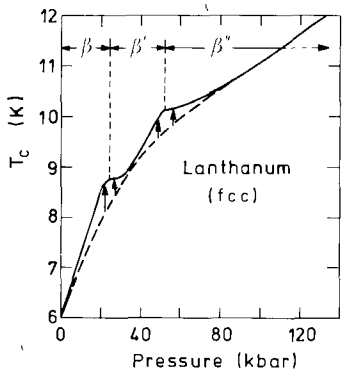

Fig. 10.3. Interpretation of the kinks in $T_c(P)$ for fcc La (Balster and Wittig, 1975). Solid curve: experimental data from fig. 10.2. Dashed curve: a hypothetical smooth T_c–P dependence *without* a special phase-boundary enhancement of T_c near *isostructural* transformations at about 50 and 25 kbar. The phases are labelled β, β' and β'' (cf. fig. 10.5).

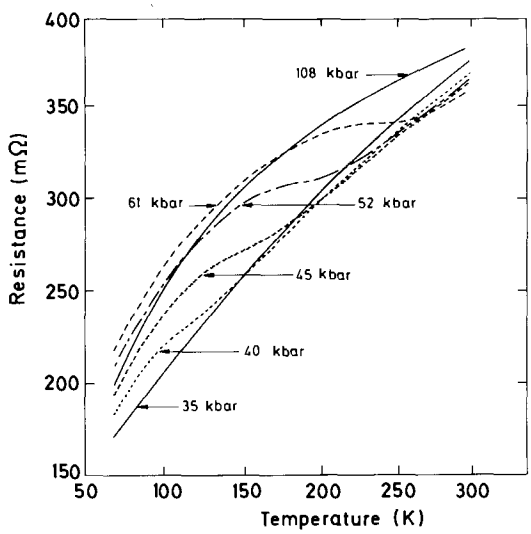

Fig. 10.4. Resistance vs. temperature for fcc La at various pressures above 35 kbar. A point of inflection is seen which shifts rapidly to higher temperatures with pressure. The phenomenon has been ascribed to a first-order fcc→fcc phase transition or a continuous transition (Balster and Wittig, 1975).

long-wavelength phonons ($q = 0$) the influence of $N(E_F)$ on $\omega(q)$ is known as the renormalization of the velocity of sound (e.g. Ziman, 1972).

Balster and Wittig (1975) detected another anomaly of La which is shown in fig. 10.4. A point of inflection occurs in the R–T characteristic of fcc La above 40 kbar. It readily shifts to higher temperatures with pressure. The positions of the points of inflection are shown by the circles in fig. 10.5 which is a hypothetical low-temperature phase diagram. The locus of the points of inflection passes through room-temperature around 70 kbar. This resistance anomaly is not associated with a change of crystal symmetry. Syassen and Holzapfel (1975) found that La has the fcc structure between 30 and 120 kbar at room-temperature. It was hence concluded that the points of inflection may indicate the existence of another isostructural phase change whose phase boundary runs into the pressure axis at $\simeq$25 kbar just where a second kink in $T_c(P)$ occurs for metastable fcc La (fig. 10.2).

It was suggested that both phenomena are caused by soft phonon modes. Soft phonon modes may profoundly influence the resistivity. Simultaneously, they may lead to the enhancement in $T_c(P)$ at 25 kbar just as at the 53 kbar anomaly (fig. 10.3). In summary, it is possible that three slightly different fcc phases exist in La at low temperatures. We have termed them β, β' and β'' in the order of increasing pressure (fig. 10.5).* The phase diagram should be considered as a

*The notation follows the conventional nomenclature for the crystallographic phases of La. Balster and Wittig (1975) proposed a notation analogous to that used for Ce since they suggested that there is a qualitative correspondence between the P–T diagrams of Ce and La.

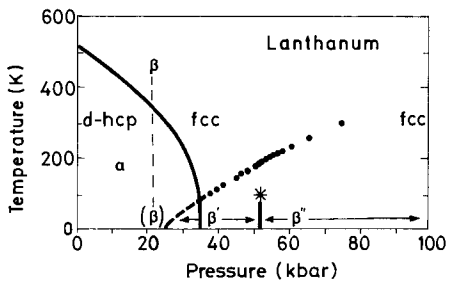

Fig. 10.5. Hypothetical low-temperature phase diagram for La (Balster and Wittig). Following the conventional notation, the d-hcp phase is called α. The high-temperature fcc β-phase can metastably exist at low temperatures in the d-hcp range (β). Solid circles show the T–P dependence of the points of inflection from fig. 10.4. The locus of the points of inflection was identified with the β/β' phase boundary. Another subtle phase transformation between two fcc phases (β' and β'') has been postulated at about 50 kbar. The phase boundary may terminate in a critical point at higher temperatures (asterisk).

working hypothesis which is compatible with the presently known facts (Balster and Wittig, 1975).

The $T_c(P)$ and $R(T)$ data for La have revealed interesting properties at high pressure. Other experiments are necessary to check the proposed phase diagram. It will be interesting to investigate the lattice parameter of La by X-ray diffraction under *hydrostatic* pressure between 50 and 100 kbar when the locus of the points of inflection passes through room temperature. The compressibility will probably be anomalous. Is there a volume discontinuity indicating a first order phase change? Or is the transition continuous, not being a phase transition in the strict sense? Such experiments should also be carried out at constant pressure down to liquid helium temperature, particularly around 53 kbar. Very small volume changes are expected at the phase transitions in La, as is well-established for the isostructural phase transitions in uranium at 23 K and 37 K (Steinitz et al., 1970). The latter transitions, fortunately, occur at normal pressure.

2.2. *Tunneling data for lanthanum*

The method of electron tunneling can give information about the phonon spectrum of a metal, provided it is a superconductor with strong electron–phonon coupling. The requirement normally means that the superconductor must have a fairly high T_c. One studies the current-voltage characteristic of a tunnel diode, usually consisting of two metal films evaporated on top of each other, but separated by a thin insulating oxide layer as the tunneling barrier. In the superconducting state, the derivative of the I–V curve reveals characteristic fine-structure from which the phonon spectrum can be calculated (McMillan and Rowell, 1969).

Lanthanum is one of the few transition metal superconductors for which such

experiments have been successfully carried out. The normal-pressure data of Shen (1972), Lou and Tomash (1972), and Wühl et al. (1973) are in reasonable overall agreement. In particular, all three investigations reveal a reduced gap $2\Delta(0)/k_B T_c = 3.7$–3.8 which is slightly larger than the value 3.52 required by the BCS theory for a weak-coupling superconductor (e.g. Rickayzen, 1969). The dotted line in fig. 10.6 shows the weighted phonon density-of-states for (supposedly) d-hcp La at normal pressure. A marked feature is the high density of states at low energy around 3–5 meV. These particular phonons are probably medium- or short-wavelength phonons which possess a higher density of states (because of the larger phase space) than the long-wavelength phonons. Low-lying modes, an anomalous property of La, are also reflected in the low Debye temperature (Johnson and Finnemore, 1967). For comparison, the phonon spectrum of yttrium reveals a very low density of states up to 6 meV (Sinha et al., 1970). Unfortunately, no such data seem to exist for Lu which would be the most appropriate element for a comparison (see section 3.3). The dashed line in fig. 10.6 shows the phonon spectrum at a pressure of 17.5 kbar. It is seen that the phonon peak at $\simeq 10$ meV shifts to higher frequencies, as is normally observed in other metals. However, the low-frequency flank of the phonon spectrum between 2 and 4 meV shifts to even lower energies, while the height of the peak at $\simeq 4.5$ meV diminishes. It appears as if some phonon density of states is transferred to lower energies.

A peak in the phonon density of states corresponds to a minimum in the second derivative d^2I/dV^2 of the tunneling current. Figure 10.7 shows the pressure dependence of the 4.5 meV peak, obtained by this method from the raw data, together with the results for two other characteristic phonon peaks. Average Grüneisen constants $\gamma_G = -d \ln \omega_i / d \ln V = \kappa^{-1} d \ln \omega_i / dP$ (κ = compressibility) were assigned and are listed in the figure. The negative γ_G for the 4.5 meV peak reflects the anticipated phonon softening. The behavior of the 9 meV phonons is also unusual, since the frequency does not increase at all under a pressure of 17.5 kbar.

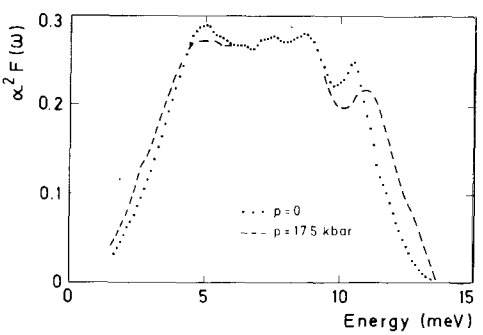

Fig. 10.6. Weighted phonon density-of-states for La at 1 K from electron tunneling data. The pressure-induced shift of the low-frequency flank to lower energies has been interpreted as a softening of short-wavelength phonons (Wühl et al., 1973).

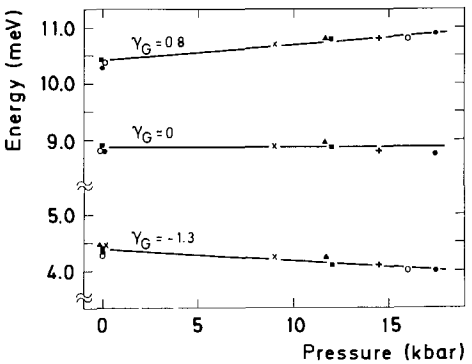

Fig. 10.7. Shift of three characteristic peaks of the phonon spectrum of La under pressure. The negative Grüneisen constant $\gamma_G = -1.3$ reflects the phonon softening (Wühl et al., 1973).

The tunneling experiment gives the weighted phonon density of states α^2F, where the weighting factor is the frequency dependent electron–phonon interaction $\alpha^2(\omega)$. An increase of this quantity with pressure in the range of the low frequency flank (fig. 10.6) could equally account for the data. Such a change of $\alpha^2(\omega)$ with pressure can not be ruled out at present. It is however not very likely that the shift of the peak (fig. 10.7) is caused by a strong frequency-dependence of $\alpha^2(\omega)$ with pressure.

The assumption that the shift of the low frequency flank is primarily caused by phonon softening is to a certain extent supported by the following evidence. From the Grüneisen relation

$$\gamma_G(T) = \beta(T)V/\kappa C_V$$

(β volume coefficient of thermal expansion, V volume, κ compressibility, C_V specific heat) one may expect that the thermal expansion $\beta(T)$ will become negative at sufficiently low temperatures when the modes with a negative Grüneisen constant are predominantly excited. Such a negative thermal expansion has been in fact observed by Andres (1968) for fcc La below 37 K. The tunneling data are, supposedly, for d–hcp La (see however the remark below). Strictly speaking, a comparison can therefore not be made. However, the physical properties of d–hcp and fcc La are so much alike (Johnson and Finnemore, 1967) that one strongly expects a negative thermal expansion for d–hcp La too. A thorough investigation of the low temperature thermal expansion of pure d–hcp La is necessary for progress on the subject.

Using inelastic neutron scattering Nücker (1976) has recently determined the phonon spectrum of fcc and d–hcp La. The spectrum of a sample containing 95% d–hcp phase shows an overall shift of $\simeq 0.8$ meV to higher energies in comparison to the tunneling data at normal pressure of fig. 10.6. On the other hand, a spectrum for a fcc sample agreed much better with the tunneling data. Hence it is questionable, whether the tunneling experiments have been carried out on d–hcp La. It is possible that the evaporated La films contained a large

number of stacking faults, so that the films were neither d-hcp nor pure fcc La.

We conclude that La has unusually soft phonons at short wavelengths. Some of them become softer under pressure. The existing tunneling data do not allow quantitative conclusions to be drawn as to the extent to which the rapid increase of T_c with pressure is caused by the phonon softening (Wühl et al., 1973). For the element uranium, the situation seems to be fairly analogous. A strong increase of T_c with pressure (Smith and Fisher, 1973) goes hand in hand with an anomalous thermal expansion at low temperatures (Barrett et al., 1963; Andres, 1968). No direct proof exists so far for pressure-induced phonon softening at short wavelengths in U (Wittig, 1975). Long-wavelength phonons, however, show marked softening near the isostructural phase changes at low temperatures (Fisher, 1974).

2.3. *Pressure dependence of T_c for cerium*

The superconductivity of cerium at high pressure was discovered by the present authors (Wittig, 1968; Probst and Wittig, 1975). Figure 10.8 shows the pressure dependence of T_c up to 200 kbar. In the low pressure α phase (cf. the phase diagram in fig. 10.9 as well as ch. 4.) Ce is a superconductor in the millikelvin range (fig. 10.8, insert). T_c increases from 20 mK at 20 kbar to 50 mK at 40 kbar. The straight-line fit of the data in fig. 10.8 extrapolates to $T = 0$ at $\simeq 10$ kbar.

It is however not impossible that α-Ce is a superconductor even at normal

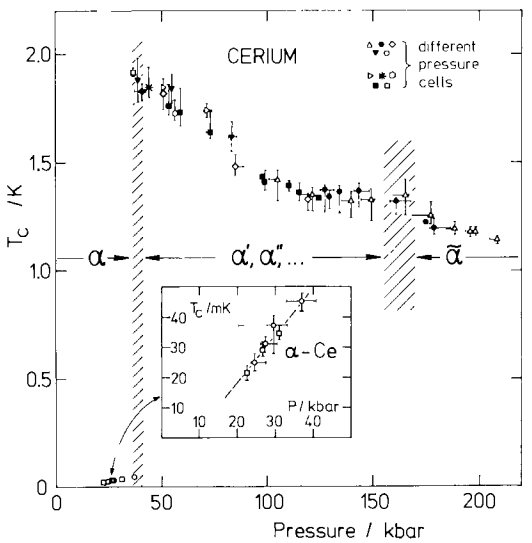

Fig. 10.8. Pressure dependence of T_c for Ce. In the α-phase, Ce is a superconductor in the millikelvin range (cf. insert). The notation α', α''... Ce accounts for the occurrence of coexisting phases between 40 and about 165 kbar. There is evidence for a subtle phase transition at $\simeq 165$ kbar to a phase called $\tilde{\alpha}$ (see text and Probst and Wittig, unpublished).

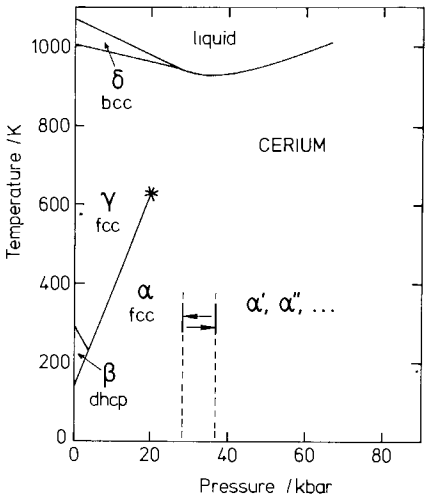

Fig. 10.9. Phase diagram of Ce after Beecroft and Swenson (1960), Gschneidner et al. (1962), Jayaraman (1965b) and Probst and Wittig (... unpublished). According to the latter work, the α phase may transform to the α', α''... regime at pressures as low as 37 kbar at room-temperature. This pressure is lower than those reported previously (e.g. King et al., 1970; Schaufelberger and Merx, 1975). As indicated, the hysteresis interval amounts to approximately 10 kbar. Other features of the P–T diagram are discussed in ch. 4, section 2.

pressure. Instead of a straight-line fit, it is reasonable to fit eq. (10.2) to the experimental data. In the absence of better knowledge, the overall coupling parameter $\lambda - \mu^*$ was assumed to be a linear function of pressure between 40 kbar and zero pressure. The (small) pressure dependence of the Debye temperature was neglected. Θ_D is reported to be $\simeq 180$ K at normal pressure (Koskimaki and Gschneidner, 1975). The fit revealed a convex T_c–P curve which is compatible with the present data and extrapolates to roughly 6 mK at zero pressure. Of course, the assumption of $\lambda - \mu^*$ varying linearly with pressure is rather arbitrary (Probst and Wittig, to be published).

Paramagnetic impurities lower the T_c of a superconductor (e.g. Maple, 1973). This can be a serious problem for the study of a superconductor in the millikelvin range. The investigated Ce sample contained magnetic rare earth impurities at the level of 100 at.ppm. If the depression of T_c in Ce is as large as in La (Matthias et al., 1958), one expects a reduction of T_c of the order of 20 mK. This means that the T_c–P curve for ideally pure Ce probably lies higher than the data in the insert of fig. 10.8.

In the measurements reported here, α-Ce undergoes a phase change at $\simeq 40$ kbar and room-temperature (fig. 10.9), evidenced by a sharp rise of the electrical resistance. The superconducting T_c jumps by a factor of 40 to $\simeq 1.9$ K (fig. 10.8). With further pressure, T_c decreases. After passing a plateau between 120 and 165 kbar, it again decreases for pressures up to 200 kbar.

As indicated by the vertical bars, most of the superconducting transitions are

fairly broad ($\Delta T_c \simeq 0.1$–0.2 K). From the pressure inhomogeneity ΔP and the rate of decrease dT_c/dP one would expect much narrower superconducting transitions according to the simple relation $\Delta T_c = dT_c/dP\,\Delta P$. ΔP is given by the size of the symbols or by the horizontal bars. Especially in the plateau, the transition width ΔT_c should be extremely narrow.

Ellinger and Zachariasen (1974) observed the coexistence of at least two high pressure phases above 51 kbar. One phase (α') has the orthorhombic α-U structure which is a distorted hcp lattice. A second phase (α'') has monoclinic symmetry. The structure is a slight distortion of a fcc lattice. In order to account for the simultaneous occurrence of different phases we denote in the following the corresponding range of the P–T diagram (fig. 10.9) with the symbol $\alpha', \alpha'' \ldots$ Ce. Schaufelberger and Merx (1975) also detected phase mixtures at pressures exceeding 51 kbar. According to their indexing Ce is a mixture of isodense hcp and fcc phases (also see ch. 4, section 2.2).

It is very likely that phase mixtures have been studied in the experiments of fig. 10.8 also. Slightly different T_c's for the phases may lead to a broadening of the superconducting transitions and also to the observed scatter of their mid-points. The assumption of very similar T_c's does not appear unreasonable in view of the fact that the α' and α'' phases have the same density (Ellinger and Zachariasen, 1974; Schaufelberger and Merx, 1975). If the interpretation is correct, such phase mixtures are apparently present even up to $\simeq 160$ kbar. Above that pressure, the transitions become sharper.

What is the significance of the plateau of $T_c(P)$ between 120 and 165 kbar? Scrutinizing the data of fig. 10.8, one realizes that a faint maximum was passed at 165 kbar in one series of measurements (open triangles). Among several possible explanations the following is favored. It is suggested that an isostructural phase transformation may occur in Ce at $\simeq 165$ kbar to a phase termed $\tilde{\alpha}$, similar to the transitions characterized by a kink in $T_c(P)$ for La and U (Probst and Wittig, unpublished). We refer to the discussion of fig. 10.3 in section 2.1. Following Glötzel's suggestion for La, one may alternatively think of a pressure-induced change in the topology of the Fermi surface. The 165 kbar anomaly in $T_c(P)$ is probably related to the drop of the room-temperature resistance as observed by Stager and Drickamer (1964) and Probst and Wittig (to be published). See also ch. 4, section 2.1.

Figure 10.10 shows the pressure dependence of T_c for Ce in comparison to thorium. Th is below Ce in the periodic table at the beginning of the 5f series. It is therefore the most reasonable element for a comparison. The pressure dependence of T_c for Th has been previously determined by Fertig et al. (1972). As seen from fig. 10.10, T_c steeply decreases up to 50 kbar. Around 75 kbar it passes a shallow minimum. Above 110 kbar Fertig et al. observed again a small decrease of T_c. The curve shown for Ce is a smooth fit of the data of fig. 10.8. We think there is a striking similarity to the T_c–P curve of Th. The peculiar shape of the curves deserves further study.

It is tempting to speculate that both metals obey, electronically, a law of corresponding states. Clearly, the dilemma is that Th has the fcc lattice structure

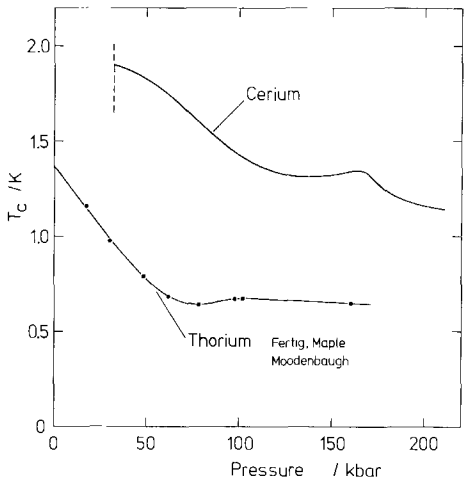

Fig. 10.10. T_c vs. pressure for Ce in the α', α''... phase range in comparison to Th. The curves are strikingly similar and thus point to very similar electronic properties of Ce and Th. Th is below Ce in the periodic table.

at normal pressure. Originally, Franceschi and Olcese (1969) reported α'-Ce to be fcc. However the recent indexing of high pressure X-ray data favor the orthorhombic or the hcp structure for the thermodynamically stable phase of Ce at high pressure (Ellinger and Zachariasen, 1974; Schaufelberger and Merx, 1975; Schaufelberger, 1976; also see ch. 4, section 2.2). Most recently, Zachariasen and Ellinger (1977) reported the observation of single-phase samples of α''-Ce at 90 kbar. The experiment shows that under certain conditions of pressure, temperature and/or perhaps inhomogeneous strain a slightly distorted *fcc* lattice can be the stable lattice at such high pressures. However nothing definite can be said at present as to a close similarity of Th and Ce.

2.4. *Pressure dependence of T_c for yttrium*

The superconductivity of Y was discovered at pressures above $\simeq 110$ kbar by Wittig (1970). The solid symbols in fig. 10.11 are the original data together with two additional data points. Different symbols refer to different pressure cells. The horizontal bars show the pressure inhomogeneity. The vertical bars denote the width of the superconducting transitions. The lowest accessible temperature was $\simeq 1.3$ K. No superconductivity was found to this temperature at various pressures below 110 kbar as indicated by arrows. Above 110 kbar, T_c steeply rises up to $\simeq 2.7$ K at pressures of the order of $\simeq 160$ kbar. The data can be fitted by a straight line with a slope $dT_c/dP = 3.5 \times 10^{-5}$ K/bar. This is a large effect in comparison to the variation of T_c with pressure in the other transition metal superconductors. It is however much smaller than for La which reveals an initial rate of increase $dT_c/dP \simeq 12 \times 10^{-5}$ K/bar (fig. 10.2). On the other side, a rough

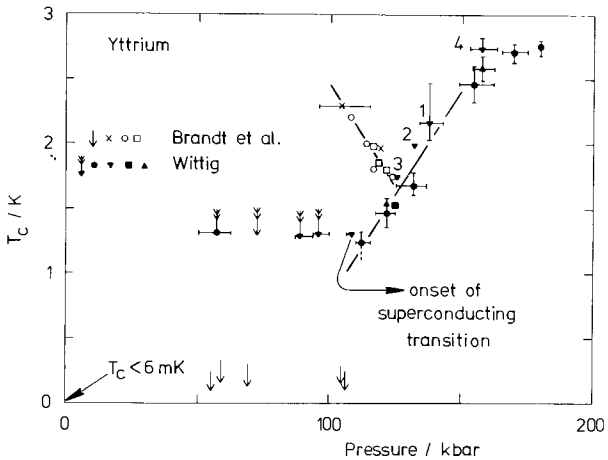

Fig. 10.11. T_c vs. pressure for yttrium. The data are from two different investigations. Arrows indicate that no superconductivity was detected down to this temperature in the particular experiment.

estimate shows that the compressibility of Y at 120 kbar is a factor of 3 smaller than for La at normal pressure. Therefore, dT_c/dV for La and for Y are quite close in value.

There were no indications of a structural phase change, except perhaps at the highest pressures (see below). For instance, the room-temperature resistance is a smooth and reversible function of pressure up to $\simeq 160$ kbar. It increases by 25–30% between normal pressure and 160 kbar. The residual resistance (R_{4K}) proved to be fairly independent of pressure, except in the two runs above 160 kbar where it was markedly higher. It is conceivable that a pressure-induced phase transformation may escape detection while one is monitoring the room-temperature resistance. However, one should expect that it will show up in an increase of R_{4K} due to extra disorder scattering in the transition region. Since such an increase was not observed, it was concluded that the normal-pressure hcp phase of Y is stable up to $\simeq 160$ kbar. At zero pressure, the same Y sample was not superconducting down to 6 mK. Between 110 and $\simeq 160$ kbar, the superconducting T_c depends reversibly on pressure. The numbered triangles in fig. 10.11 show an example. The data were taken in the indicated sequence (1 . . . 4), the pressure being changed at 4.2 K. Similar experiments, whose results are not included in fig. 10.11, were performed at lower pressure, particularly around 110 kbar. The strict reversibility of $T_c(P)$ shows fairly convincingly that a single-phase sample was studied in this pressure interval.

The T_c–P dependence has been recently confirmed by Brandt et al. (1974) for pressures exceeding 130 kbar. However, in the pressure range between 105 and 125 kbar they find a pressure dependence of T_c (fig. 10.11, open symbols) entirely different from the one described so far. $T_c(P)$ decreases at roughly the same rate as it increases according to Wittig's data. Brandt et al. did not detect super-

conductivity down to a lowest temperature of $\simeq 0.1$ K (fig. 10.11, arrows) at pressures up to 105 kbar. Hence they concluded that a crystallographic phase change occurs at this pressure from a non superconducting phase Y I($T_c < 0.1$ K) to a superconducting modification Y II with a T_c (105 kbar) $\simeq 2.3$ K. Another modification, Y III, is postulated to exist above 130 kbar, in order to account for the different sign of dT_c/dP in their data below and above this pressure. However, as outlined above, Wittig finds no evidence for such an event.

We have no explanation for the discrepancy between the T_c data below 130 kbar. Notice that the values of T_c for the two investigations differ by one degree K at $\simeq 105$ kbar. Obviously these two sets of data cannot be reconciled by invoking slightly different pressure scales. It appears that one of the measurements is incorrect.

A final remark pertains to the data at the highest pressure. Above 140 kbar Brandt et al. observed a marked increase of the critical magnetic field. In order to explain this finding they suggested that a further high pressure phase, Y IV, is formed. Indications for a phase transition are also present in Wittig's data. As mentioned above, the residual resistance R_{4K} was markedly higher above 160 kbar. Also, $T_c(P)$ does not increase at the same rate as at lower pressure (cf. fig. 10.11). A high-pressure X-ray investigation of the lattice structure of Y would be a very useful experiment to clarify the situation.

2.5. *Pressure dependence of T_c for lutetium*

Recently superconductivity was discovered in Lu at high pressure (Probst, 1974; Wittig et al., 1972). As indicated by arrows in fig. 10.12, no superconductivity was detected at 8 and 31 kbar down to a lowest temperature of 22 mK. At 45 kbar superconducting transitions are observed at $\simeq 20$ mK. T_c rises steeply and nonlinearly with pressure up to 300 mK at $\simeq 110$ kbar. The numbers in fig. 10.12 indicate the sequence of measurements on one particular sample. It is seen that T_c is a reversible function of pressure.

The smooth and reversible $T_c(P)$ curve gives no indication of a crystallographic phase change. Since the electrical resistance also varies smoothly with pressure up to 180 kbar at room-temperature as well as at liquid helium temperature, it was concluded that the normal-pressure hcp phase of Lu is stable up to 180 kbar. Recently, Liu (1975) has published a paper claiming from X-ray diffraction studies that the hcp phase of Lu is stable to above 200 kbar. As discussed in section 2.3 for α-Ce, paramagnetic impurities such as other rare earth metals will cause a depression of the transition temperature of the matrix by the process of Cooper pair breaking. A definite answer for the magnitude of the effect cannot be given for the two samples of fig. 10.12. A mass spectrographic analysis, claimed to be accurate within a factor of 3 (up and down), revealed nominally 200 at.ppm magnetic rare earth impurities in the sample whose T_c data are represented by triangles. Assuming that T_c is lowered at the same rate ($\simeq 0.5$ mK/1 at.ppm) as in the similar systems $La_{1-x}Gd_x$ or $(La_{1-x}Gd_x)Al_2$ (Matthias et al., 1958; Maple, 1968), one calculates a reduction $\Delta T_c \simeq$

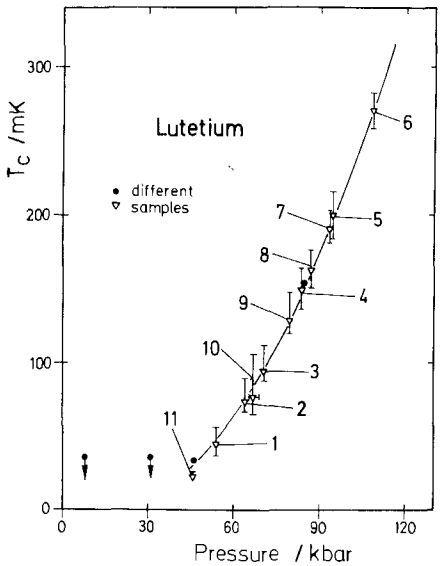

Fig. 10.12. T_c vs. pressure for lutetium. The numbers indicate the sequence of 11 measurements for one particular sample. As seen, T_c is a reversible function of pressure. Two arrows indicate that no superconductivity was detected at those pressures down to ≃20 mK. The curve is a smooth fit of the data (Probst, 1974).

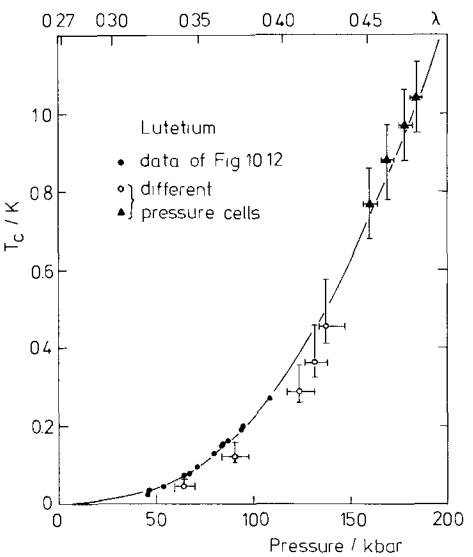

Fig. 10.13. T_c vs. pressure for Lu up to 200 kbar. Solid circles are the data of fig. 10.12. Open circles systematically deviate from the curve (see text). The curve is a fit of eq. (10.1) to the data assuming a linear pressure-dependence of the electron–phonon coupling parameter λ upon pressure. The upper scale shows the corresponding values of λ.

100 mK. However, the T_c's of a Lu sample from an independent source agreed within 10 mK at 46 and 85 kbar (solid circles in fig. 10.12). Since it seems unlikely that two samples of an entirely different origin will have almost the same large impurity effect, it was concluded (Probst, 1974) that the actual depression of T_c was probably much smaller than 100 mK. This is also suggested by the result of a second independent mass spectrographic analysis revealing only 16 at.ppm magnetic rare earth impurities. The possible influence of 3d impurities such as Fe cannot be estimated at present. For instance, it is not known whether single Fe impurities are magnetic in Lu. The solubility of Fe seems to be very small and possible clustering would preclude a strong influence on T_c (Spedding and Croat, 1973).

Figure 10.13 shows additional data (Probst, 1974) with the pressure range extended to 180 kbar. At this pressure T_c is ≃ 1 K and is thus a factor of 50 higher than at 45 kbar. Lu is the only superconductor for which such a large relative change of T_c has been observed in one crystallographic modification. The data marked by open circles are from consecutive runs with one sample. They lie systematically at lower temperatures than the data from fig. 10.12 measured under quasi-hydrostatic pressure. However, the same strong upward curvature can be noticed. Possible reasons for the deviation are a higher concentration of

paramagnetic impurities, effects of cold working due to the lower hydrostatic pressure or a pressure difference of $\simeq 10$ kbar between the Lu-sample and the pressure-sensing sample or a combination of these effects. The comparatively broad superconducting transitions between 160 and 180 kbar (solid triangles) are a consequence of the pressure inhomogeneity and the large $dT_c/dP \simeq 1.2 \times 10^{-5}$ K/bar.

The $T_c(P)$ dependence of Lu (fig. 10.13) has been discussed as follows (Probst, 1974). The strong curvature of $T_c(P)$ resembles strongly the dependence of T_c on the electron–phonon coupling parameter λ (for $\lambda \lesssim 0.5$) as shown in fig. 11 of McMillan's paper (McMillan, 1968). The pronounced curvature in the theoretical $T_c(\lambda)$ curve is a consequence of the exponential dependence of T_c on λ according to eq. (10.1). It was therefore tempting to fit eq. (10.1) to the T_c data in fig. 10.13. In the absence of better knowledge, a linear variation of λ with pressure was assumed ($\lambda = a + bP$). Changes of the Debye temperature $\Theta_D \simeq 210$ K with pressure were neglected. A constant value $\mu^* = 0.13$ was used. The curve shown in fig. 10.13 is a best fit by adjusting the two parameters a and b (Probst, 1974). The corresponding values for λ are shown on the upper scale, for instance $\lambda(P = 0) = 0.27$. This value compares favorably with estimates of 0.30 ± 0.05 (from specific heat data) for the column members Sc and Y (Knapp and Jones, 1972). The calculated T_c at zero pressure is 1 mK. A search for superconductivity in Lu at millikelvin temperatures at normal pressure is thus promising, provided samples of higher purity than the present ones become available. We briefly mention other investigations of Lu for superconductivity. Nikulin et al. (1973) reported a very broad superconducting transition at normal pressure below 0.5 K for a Lu sample of a nominal purity of 99.9%. Another sample containing large amounts of iron was not superconducting. They concluded that Lu is a superconductor with $T_c = 100 \pm 30$ mK, provided the sample is sufficiently pure. The above discussion showed that Lu is indeed fairly likely to be a superconductor at ambient pressure. However, a T_c as large as 100 mK does not appear to be acceptable. Jensen (1965) also observed broad superconducting transitions between 0.9 and 0.1 K. He attributed them to precipitations of tantalum which dissolves in Lu during the manufacturing process in Ta-crucibles. The T_c of such an inhomogeneous system is badly defined due to the superconducting proximity effect.

The strong increase of T_c with pressure is an interesting common property of Lu, Y and La. The neighboring elements Ti, Zr and Hf (cf. fig. 10.1) possess also a positive pressure coefficient of T_c. It is however much smaller. A slight decrease of T_c with pressure is observed for the superconductors in the second half of the d periods (see e.g. Smith, 1972). From the empirical data Hopfield (1971) noted that in $\lambda = N(E_F)\langle I^2\rangle/M\langle a\rangle^2$ the numerator increases at roughly the same rate for all transition metals, the logarithmic derivative being $d \ln[N(E_F)\langle I^2\rangle]/d \ln V \simeq -3.5$. This effect alone would lead to an increase of T_c under pressure. For most transition metals, the denominator increases more rapidly due to the overall phonon stiffening under pressure. The early transition metals are distinguished by unusually small Grüneisen constants $\gamma_G = -d \ln \Theta/d \ln V$ (Gschneidner, 1964). As a result, the numerator increases more rapidly than the

denominator. This explains the increase of λ or T_c with pressure. The microscopic origin of the increase of $N(E_F)\langle I^2\rangle$ with pressure is not understood at present. Also, it is not known why the Grüneisen constants are low at the beginning of the d-transition periods. Both effects contribute to the steep increase of T_c with pressure.

2.6. *Other rare earth elements*

Scandium has been investigated for superconductivity at high pressure by Probst and Wittig (1975). No superconductivity could be detected at $\simeq 164$ kbar and $\simeq 193$ kbar down to a lowest temperature of 20 mK. The sample contained $\simeq 40$ at.ppm magnetic rare earth impurities as determined mass spectrographically. The residual resistance ratio of the heavily cold-worked sample was 10. It would be interesting to study very pure Sc at even higher pressures. Physically it would be a very gratifying aspect, if all s^2d^1 metals would show pressure-induced superconductivity*.

Ytterbium was investigated for superconductivity in its normal-pressure low-temperature hcp phase (Bucher et al., 1970). No superconductivity was detected down to a temperature of 15 mK. Fcc Yb becomes a semiconductor under pressure. After a phase transformation to the bcc structure at $\simeq 40$ kbar it is again a metal. No superconductivity was found in bcc Yb between 50 and $\simeq 160$ kbar down to a lowest temperature of 1.3 K (Katzman and Mydosh, 1972). The physical properties of pure Yb are similar to the alkaline-earth metals Sr and Ca (but not Ba (Wittig, 1973)). The filled 4f shell is apparently not affected by pressure, similar to the case of Lu. Reale (1975) has recently published a letter claiming that quench-condensed thin films of Ce, Pr, Nd, Eu and Yb become superconducting with T_c's of several degrees K. For lanthanum, Reale finds a $T_c = 8$ K for a film thickness of 900 Å. This is in strong disagreement with other data reported in the literature. Schwidtal (1962) reports a $T_c = 4.7$ K for a quench-condensed film of 900 Å. Values very close to 4.7 K have been reproducibly found in this laboratory recently (Wühl, 1976). Reale's data show a strong thickness dependence of T_c in his La films up to a thickness of 2000 Å. Wühl (1976) never observed any thickness dependence for such thick La films. Löffler and Mydosh (1973) have studied quench-condensed films of Ce showing no superconductivity above 1.5 K. Reale's Ce films become superconducting between 6 and 3 K, T_c again strongly depending on thickness. We think these are probably all spurious results which do not represent the true behavior of the elements being studied.

3. Approaches to the superconductivity of the rare earths

3.1. *Early models for lanthanum*

Following the historical development, we review the attempts which have been made in order to understand the occurrence of superconductivity in the rare

**Note added in proof*: Superconductivity has indeed been recently discovered in scandium at high pressure (cf. section 6).

earth group. Hamilton and Jensen (1963) made the interesting suggestion that La should be removed from its hereditary place below Y and Sc in the periodic table and should be replaced by Lu as shown in fig. 10.1. In the free atom, Lu has the same outer electron configuration $6s^25d^1$ as La. La and Lu should therefore have very similar metallic properties, provided the "open 4f shell" plays no role in the electronic band structure of La. At that time, La was the only known superconductor among the s^2d^1 metals, since no high pressure data existed for Y and Lu. According to Matthias' rule (Matthias, 1957, 1969), the superconducting T_c varies very regularly in the d-transition metal periods. T_c has a deep minimum at an electron-per-atom ratio of $\simeq 6$ (cf. fig. 10.16). Maxima of T_c occur at $e/a \simeq 5$ and $\simeq 7$. T_c drops off toward the beginning and the end of the d periods. The replacement of La by Lu restored the systematic picture. The third column now contained three non-superconducting elements Sc, Y and Lu.

Hamilton and Jensen also emphasized that Lu has the same hcp crystal structure as Sc and Y. On the other hand, La crystallizes in the d–hcp structure which also occurs in Ce, Pr and Nd. As discussed in section 3.3, there is further evidence now that La has, from the structural point of view, much more in common with Ce, Pr and Nd than with Sc, Y and Lu.

Hamilton and Jensen pointed out that the melting temperature of La is unusually low. The anomaly is seen from fig. 10.14 which shows the melting temperatures of the d-transition metals and the neighboring elements. Subsequently, Matthias et al. (1967) made a general survey of the melting points in the periodic system. They noticed that many metals at the beginning of the 4f and 5f series have abnormally low melting points. They suggested that this may be caused by the presence of some f character in the hybridized wave functions

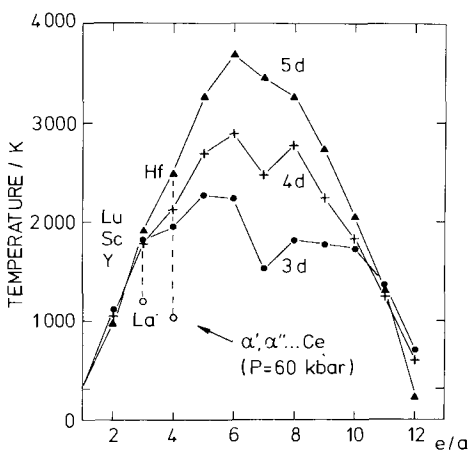

Fig. 10.14. Melting points of the d-period transition metals as a function of the electron-per-atom ratio. Neighboring elements on both sides of the d-periods are included. The melting point of La is relatively low in comparison to the other trivalent metals. The melting point of α', α''... Ce is catastrophically low in comparison to the other tetravalent metals.

of those elements. As far as the 4f metals are concerned, this was quite an unconventional picture, since one was accustomed to thinking in terms of highly localized 4f states together with an integer 4f shell occupation number $n = 0, 1, 2, \ldots$ in La, Ce, Pr, ... Matthias et al. and also Gschneidner (1971) made estimates for the number of 4f-band electrons in La, Ce ....

A remark is necessary in connection with fig. 10.14. Lu has a much smaller metallic radius (1.74 Å) than La (1.88 Å) at normal P (Zachariasen, 1973) due to the lanthanide contraction. For a proper comparison of the melting points one should therefore compress La by external pressure (a pressure of $\simeq 100$ kbar will suffice), so that its metallic radius equals that of Lu. An extrapolation of the melting curve of La (Jayaraman, 1965a) to 100 kbar shows that the melting point at that pressure is still $\simeq 400$ K lower than for Lu. Although the melting point anomaly of La becomes, after the above correction, a debatable effect, we believe that it is a significant effect as will become clear from the discussion of Ce (see section 3.2).

After the removal of La from the third column of the periodic table, the problem still remained to explain its anomalously high T_c. Hamilton and Jensen (1963) and Kuper et al. (1964) therefore proposed a new pairing mechanism for La (and also for U) different from the normal electron–phonon interaction in order to specifically account for the superconductivity. The model involved a sharp unoccupied 4f level just above the Fermi energy. The theoretical model predicted that the reduced gap $2\Delta/k_B T_c$ should deviate significantly from the value of the BCS theory. This prediction was not confirmed by specific heat measurements (Johnson and Finnemore, 1967) or the most recent tunneling experiments (see section 2.2). On the contrary, from the phonon-induced structure in the tunneling characteristic one can conclude that the electron–phonon interaction is responsible for the superconductivity of La.

At about the same time, Kondo (1963) showed in a model calculation that the superconducting T_c can be strongly enhanced in a metal by the presence of a sharp empty band close to the Fermi level. He advanced the idea that the comparatively high T_c of La may be a consequence of the presence of the 4f band close to the Fermi level.

An entirely opposite model was proposed by Coqblin and co-workers for the superconductivity of La and Ce (Coqblin, 1971; Ratto et al., 1969; Coqblin et al., 1972). In La, T_c increases strongly with pressure (fig. 10.2) in contrast to most elemental superconductors whose T_c is lowered by pressure. The primary aim of the model is to account for this unusually strong increase of T_c with pressure. It is assumed that a narrow 4f level lies close above the Fermi energy, so that it is partially occupied. The small fraction of an electron in this 4f virtual bound state on each atom leads to a depression of the superconducting T_c, due to the anticipated strong Coulomb repulsion in the narrow level. It is further postulated that the 4f level rises under pressure. This is in analogy to the "promotional model" developed for Ce, in order to account for the loss of magnetism under pressure (cf. section 3.2). A shift of the 4f level away from the Fermi energy would cause its depopulation, a smaller Coulomb repulsion and

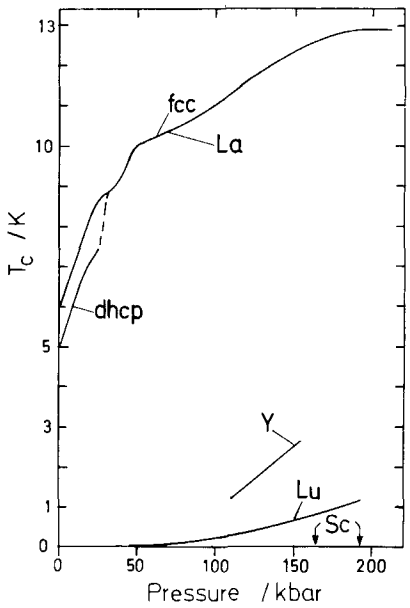

Fig. 10.15. T_c vs. pressure for the trivalent rare earths. In the case of Sc, two arrows indicate the absence of superconductivity at 20 mK. Recently, pressure-induced superconductivity has also been observed in Sc at approximately 200 kbar (cf. section 6).

hence an increase of $T_c(P)$. Eventually, at very high pressure, the 4f level is completely unoccupied and the "intrinsic" T_c of La without the detrimental influence of the 4f electrons is attained. Experimentally, a saturation of $T_c(P)$ is indeed observed at 200 kbar (fig. 10.2). A deficiency of the model is that it offers no explanation for the unusually high "intrinsic" $T_c = 13$ K of La.†

In the case of Ce, Coqblin suggests that the sharp 4f level is close to the Fermi energy in α-Ce. This may explain the low values of T_c in this phase (fig. 10.8, inset). After the phase transformation to the α', α'' ... range, Ce is a "good" superconductor with a $T_c \simeq 1.9$ K (fig. 10.8). According to Coqblin et al., the 4f level is now well above the Fermi surface and "Ce behaves as a normal tetravalent and superconducting metal". This is however a controversial point, as we will show in section 3.2.

The experimental situation changed considerably with the discovery of superconductivity in Y and Lu at high pressure. The pressure dependence of T_c is shown in fig. 10.15 for a comparison with La. It is seen that the T_c's of Y and Lu increase similarly and as strongly as in La at $\simeq 150$ kbar. Y and Lu certainly have no 4f states near the Fermi energy. Their conduction bands have purely sd character. The similar pressure dependence of T_c may therefore imply that La is also a true sd-band metal without any 4f character like Y and Lu. This was an

†More recently, Appel (1973) has argued that a phonon exchange between d and f electrons may be responsible for the particularly high T_c of La.

apparent trend of opinion at the 1971 Conference on Superconductivity in d- and f-Band Metals (Douglass, 1972). On this occasion Smith (1972) categorized La as a d-band metal. Garland and Bennemann (1972) claimed that they can calculate the T_c of La, totally neglecting the f-character. They do not explain, however, the decisive point, why the electron-phonon coupling parameter λ is at least a factor of 2 larger than for Lu (Bennemann and Garland, 1972). It is the present authors' opinion that our physical understanding of the solid state properties of, say, Y or La is in such a rudimentary stage that calculations of such a complex quantity as T_c can only fortuitously agree with the experimental value.

A different analysis of the superconductivity data for Y, Lu, La and Ce at high pressure was given by Wittig (1973, 1974) and Probst (1974) and is presented in section 3.2 and 3.3.

3.2. *Cerium*

The analysis begins with a discussion of the properties of the high pressure phase α', α''... Ce (cf. fig. 10.9). As shown below, this substance seems to be the clearest example of a nonmagnetic 4f-band metal (Probst and Wittig, 1972; Wittig, 1974). Having gained confidence in the existence of 4f-band metals, we thoroughly reinspect the properties of the neighboring element La in section 3.3. The recently discovered superconductivity of α-Ce is also briefly discussed at the end of this section.

In the promotional model for Ce the disappearance of magnetism under pressure is a consequence of the transfer of the (magnetic) 4f electron to the sd-conduction band. The various modifications of this model are treated in ch. 4 section 5 in connection with the γ/α transformation. According to this model, it is rather generally assumed that Ce has completely lost its energetically unstable 4f electron in the α', α''... phase (Wohlleben and Coles, 1973; Hirst, 1974; Maple and Wohlleben, 1974). Therefore, the conduction-band configuration should be $(6s5d)^4$, i.e. 4 electrons should reside in a hybridized 6s5d band, which is the same conduction-band configuration as in the transition metal hafnium.

The physical properties of the d-transition metals vary systematically with the electron-per-atom ratio and from one period to the other. Hence the superconducting T_c's of Hf and the *hypothetically* isoelectronic α', α''... Ce should be very similar. Figure 10.16 shows on a logarithmic scale the T_c's of the 4d and 5d transition metal superconductors. Also tentatively listed at $e/a = 4$ is the range over which the T_c of α', α''... Ce varies between 40 and 200 kbar (cf. fig. 10.8). It is seen that the T_c of Ce is an order of magnitude too high in comparison to the T_c of Hf. The weak pressure dependence of T_c for Hf was neglected (Probst and Wittig, 1972; Probst, 1974). Since the T_c's are different by an order of magnitude it was suggested that the 4f electron has not been completely "squeezed" out in α', α''... Ce. An unknown fraction of a 4f electron seems to survive as a 4f-band electron at high pressure. The 4f admixture to the conduction electron wave functions is believed to be the origin of the relatively

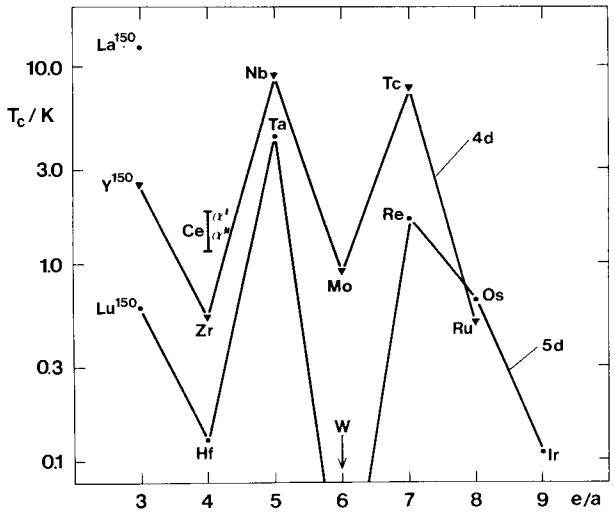

Fig. 10.16. The regular pattern of T_c vs. electron-per-atom ratio for the 4d and 5d-transition metal superconductors. Also included are the T_c's of La, Y and Lu at a pressure of 150 kbar (cf. fig. 10.15) and the range of the T_c's for α', α'' ... Ce (cf. fig. 10.8). The T_c of pure hafnium is 0.13 K (Probst, 1974).

high T_c of α', α'' ... Ce in comparison to Hf (Probst and Wittig, 1972; Wittig, 1973).

One may argue that the lattice structure of the high pressure phase of Ce is probably not hcp as for Hf (cf. section 2.3). Ellinger and Zachariasen (1974) detected an orthorhombic phase (α') co-existing with a monoclinic modification (α''). A comparison of the T_c's may therefore not seem very meaningful, since T_c depends on the lattice structure to some extent. Although we do not share this opinion, this brings up an important point. The lattice symmetry of the d-transition metals varies strictly regularly with the electron-per-atom ratio. The only exceptions from the rule are the magnetic 3d metals Mn, Fe and Co. Hence, why is Ce at high pressure probably not a hcp metal as Ti, Zr and Hf? Why does the complicated orthorhombic α-U structure occur in Ce under pressure? In line with the above conclusion from T_c, Ellinger and Zachariasen suggested the presence of some f character in the electronic band structure of α', α'' ... Ce.

The melting temperature is the only other physical property of α', α'' ... Ce which is accurately known at present apart from the superconducting T_c. Figure 10.14 shows the melting temperature of α', α''... Ce at a pressure of ~ 60 kbar. It is taken from Jayaraman's work (1965b) on the melting curve under pressure (cf. fig. 10.9). The melting temperature is 1000 K. As seen from fig. 10.14, it is almost 1500 K lower than the melting temperature for the regular 5d-period metal Hf. It has been concluded that this huge melting point depression provides unambiguous proof that the material α', α'' ... Ce cannot be a pure $(6s5d)^4$-band metal (Wittig, 1973, 1974). Since similarly low melting temperatures occur in the

actinide metals (Matthias et al., 1967) which undoubtedly have 5f hybridized conduction bands, it was inferred that α', α'' ... Ce is a $(6s5d4f)^4$-band metal with probably an appreciable 4f character. In other words, the promotional model for Ce, inasmuch as it requires the total depopulation of the 4f shell in the α', α'' ... phase, is apparently invalid. This was first suggested by Gempel et al. (1972) in order to interpret their positron annihilation experiments.

It is remarkable that the material α', α'' ... Ce is a "good" superconductor (by Hf-standards) in spite of its considerable 4f admixture in the conduction electron wave functions. There seems to be no detrimental effect on T_c which one might expect from the narrow-band character of the 4f electrons. On the contrary, T_c is apparently enhanced by an order of magnitude. We think this is an important result. It may indicate that the "4f level" can be well described in terms of the conventional one-electron band picture in α', α'' ... Ce. Previously, Coulomb correlation effects on the 4f shell were usually thought to be always so large that the band model was considered to be inappropriate for the 4f electrons (see e.g. Freeman 1972). Apparently this is not true for the substance α', α'' ... Ce. If intra-atomic Coulomb correlation effects were strong, we would not expect such a high T_c.

The melting point depression of α', α'' ... Ce is actually less than 1500 K. As for La, the melting temperature should be corrected because of the lanthanide contraction. The metallic radius of Hf is 1.58 Å at normal pressure (Zachariasen, 1973). α'-Ce and α''-Ce are reported to have a metallic radius of 1.63 Å at 56 kbar (Ellinger and Zachariasen, 1974). Some additional pressure is necessary to compress it by 3% to the metallic radius of Hf. From the known compressibility (Schaufelberger and Merx, 1975) one can estimate that the necessary 9% volume reduction will be achieved at $\simeq$110 kbar. A straight line extrapolation of the melting curve (fig. 10.9) to 110 kbar gives a melting temperature of less than 1200 K. The necessary correction of the melting point in fig. 10.14 is thus small indeed.

Hill and Kmetko (1975) carried out a more complicated analysis for the melting point of α'-Ce. Essentially, they come to the same result that the melting point is anomalously low. Their assignment of about two 4f-band electrons per atom for α'-Ce is a guess which should be taken with reservation. An APW band structure calculation for α'-Ce by Kmetko (1971) revealed 1.4 4f electrons. Recently, Glötzel (1976) carried out a band structure calculation for α-Ce. He determined 0.7 4f electrons per atom. Within the promotional model α-Ce should have more 4f electrons than α'-Ce. These large discrepancies imply that no quantitative conclusions can be drawn at present as to the number of 4f-band electrons in α', α'' ... Ce. Qualitatively, however, it seems to be now certain that some entirely nonmagnetic 4f-band electrons are present in α', α'' ... Ce. They decisively influence its physical properties as seen from the melting point depression and the relatively high superconducting T_c.

One may speculate that the low melting temperature and the relatively high T_c may both be mediated by a particularly soft phonon spectrum. According to the Lindemann formula, the melting temperature is proportional to $M\langle\omega^2\rangle$ (see e.g.

Ziman, 1972). From the low melting temperature one may infer that the average of the squared phonon frequencies $M\langle\omega^2\rangle$ is appreciably smaller for α', $\alpha''\ldots$Ce than for Hf. This, in turn, will favor a larger electron–phonon coupling parameter λ as seen from eq. (10.3).

We briefly turn to the superconductivity of α-Ce (fig. 10.8). Some tentative conclusions for the material α-Ce may be drawn. An interesting feature is the low superconducting T_c in α-Ce in comparison to α', $\alpha''\ldots$Ce. This may indicate a smaller electron–phonon coupling parameter $\lambda = N(E_F)\langle I^2\rangle/M\langle\omega^2\rangle$ than in the α', $\alpha''\ldots$phase. Another possibility, however, seems to be more likely. From the similar melting temperatures (cf. fig. 10.9) it may be inferred that $\langle\omega^2\rangle$ is roughly the same for both superconducting phases. The electronic specific heat coefficient is unusually large in the α-phase (Phillips et al., 1968; Koskimaki and Gschneidner, 1975). This points to a high density of states $N(E_F)$ which is a favorable condition for a large value of λ and a high T_c. The observed T_c is however low. As a remedy we would like to suggest that the effective coupling parameter $\lambda - \mu^*$ (see section 2.1) is markedly reduced in α-Ce because of an unusually strong Coulomb repulsion μ^* due to the narrow-band character of the 4f electrons. The quantity μ^* includes possible exchange effects as well as the normal Coulomb repulsion.

As seen from the jump in T_c (fig. 10.8), the effective coupling parameter $\lambda - \mu^*$ increases drastically at the $\alpha \rightarrow \alpha'$, $\alpha''\ldots$phase transformation. This may chiefly be caused by a decrease of μ^*. A decrease of μ^* is plausible, since the 4f-band width will presumably increase under pressure. Anyway, the unusually large change of the coupling parameter $\lambda - \mu^*$ makes it very likely that this phase transition goes hand in hand with radical electronic changes just as in the well-known γ/α transition.

The main result of this section is that Ce is not kicked out of the 4f series proper by pressure. The phases α', $\alpha''\ldots$Ce and also α-Ce are in our view clear-cut tetravalent 6s5d4f-band metals with an appreciable 4f admixture in both cases. In α', $\alpha''\ldots$Ce, the 4f component does not seem to be in any respect detrimental to superconductivity. On the other hand, α-Ce is probably a metal characterized by strong Coulomb correlations on the 4f shell and consequently a low transition temperature T_c (Coqblin, 1971; MacPherson, 1971; Koskimaki and Gschneidner, 1975).

Recently, superconductivity was discovered in the 5f-band metal neptunium at $\simeq$75 mK (Smith and Hill, 1976). It is possible that Np is a metal similar to α-Ce, both with fairly strong electron–phonon coupling yet with a low T_c due to unusually strong Coulomb repulsion in the narrow f band. We mention that this has also been suggested for uranium whose T_c is below 300 mK at normal pressure (Bader and Knapp, 1975; Bader et al., 1975).

3.3. *Lanthanum, lutetium and yttrium*

In this section we examine phenomenologically the properties of the trivalent rare earth metals, La, Lu and Y. It will become evident that La behaves in

several respects very differently from Y and Lu. We would like to recall that Lu is the proper element for a comparison, since it has in the free atom the same outer electron configuration $6s^2 5d^1$. Some of the arguments were presented in section 3.1 but will be more thoroughly discussed here.

Figure 10.15 shows the pressure dependence of the superconducting T_c's. The T_c of La is 13 K at 200 kbar and thus 4 K higher than for any other elemental superconductor. This outstandingly high T_c is one of the most unusual properties of La. In comparison the T_c of Lu is an order of magnitude smaller at this pressure. We believe this is incompatible with the stringent systematics of the superconductivity of the d-transition metals. One may argue that the $T_c(P)$ of La saturates at 200 kbar whereas the $T_c(P)$ of Lu still increases (fig. 10.15). So, perhaps at 1 Mbar, the T_c of Lu may also reach 13 K. We think this is not a good argument. Our concern here is not what may happen at 1 Mbar. A fair procedure is to compare properties at the same interatomic spacing. At $\simeq 100$ kbar, the metallic radius of La is equal to the metallic radius of Lu at normal pressure. As seen from fig. 10.15 the T_c of La is 11 K. However, the T_c of Lu at normal pressure, is probably in the millikelvin range (see section 2.5).

It is instructive to compare the transition temperatures of La, Lu and Y with the T_c's of the d-transition metals at normal pressure. In fig. 10.16 the T_c's of La, Lu and Y are shown for a pressure of 150 kbar. Such a comparison seems to be justified since the pressure dependence of T_c for the transition metals with $e/a \geq 4$ is very weak (e.g. Smith, 1972). It is seen that the T_c of the 5d-period metals is generally lower than the T_c for the corresponding member in the 4d period. The rule only breaks down toward the end of the 4d period at the element ruthenium.† Interestingly enough, the pair of pressure-induced superconductors, Lu and Y, obeys this rule, since the T_c of Lu is smaller than for Y. Hence Lu behaves as a real 5d-transition metal from a systematic point of view. On the other hand, the T_c of La is an order of magnitude too high to be a plain 5d-band metal.

One may raise the objection that the T_c's of La and Lu cannot be compared so naively. The crystal structure of La is fcc at high pressure, whereas Lu has a hcp lattice. This may influence T_c. There is rather clear evidence however that the influence of the crystal symmetry on the T_c of La is not excessively large. At low pressure La exists in the d–hcp structure. The $T_c(P)$ of the metastable fcc phase is also known (fig. 10.2). It is seen that both phases possess very similar T_c's and, moreover, the same strong pressure dependence. So, the structural argument is not persuasive and our comparison of the T_c's of La and Lu is probably justified.

We think it would be more appropriate to ask: why is the structure of La not hcp as for Sc, Y and particularly Lu? The d–hcp and fcc structure of La do not at all fit in the systematics of the d-transition metals. In fact, the structure of La

†The reason for the low T_c of Ru may be related to its being in the neighborhood of palladium and Rhodium in the periodic table. Long-lived spin fluctuations are believed to suppress superconductivity in Pd (e.g. Gladstone et al., 1969). Andres and Jensen (1968) have suggested that strong intra-atomic Coulomb interactions inhibit superconductivity in Rh.

is different not only just at normal pressure. From Syassen and Holzapfel's investigation (1975) it is known that the fcc phase (cf. fig. 10.5) is stable up to 120 kbar and, very likely, even to 200 kbar (Balster and Wittig, 1975). However Lu is hcp in the same wide pressure range (Liu, 1975). In addition, the P–T phase diagram of La resembles those of the 4f-group metals Pr and Nd (e.g. Cannon). We believe this gives a strong hint that the electronic structure of La is not that of a pure $(sd)^3$ metal as Lu or Y. This applies also to Pr and Nd as briefly outlined in section 5. In agreement with previous authors (Kondo, 1963; Hamilton and Jensen, 1963; Hamilton, 1965; Matthias et al., 1967; Gschneidner, 1971), we think it is most likely that La is a $(6s5d4f)^3$-band metal with the 4f component causing the various unusual properties.

The kinks in $T_c(P)$ for fcc La at 25 and 53 kbar (fig. 10.3) are another unusual property of La. The question of their origin is not yet settled (see section 2.1). For comparison, the T_c–P dependence of Lu does not exhibit such anomalies. Similar sharp kinks in $T_c(P)$ have only been observed in the 5f-band metal uranium. For the 4f-band metal α', α''... Ce a similar kink in T_c may occur at $\simeq 165$ kbar (see section 2.3). Further experiments are yet necessary to establish this. One may however already suspect that this anomaly is specifically connected to the presence of f character at the Fermi surface.

We would like to draw attention to another anomaly of La which is also not well understood at present. The temperature dependence of the electrical resistivity shows a strong negative curvature, particularly at high pressure (cf. the 108 kbar-isobar in fig. 10.4). On the other hand, the electrical resistivity of Lu increases linearly with T above $\simeq 200$ K at all pressures (Probst, 1974). La seems to be exceptional in this respect among the elemental d-band superconductors. The 5f-band metals U, Np and Pu possess similar R–T characteristics as La (Brodsky et al., 1974). Phenomenologically, this also points to a partially occupied 4f band in La even though the anomaly is not understood at present (Balster and Wittig, 1975).

Consider now the low melting temperature of La which is roughly 400 K lower than for Lu, after correction has been made for the lanthanide contraction (see section 3.1 and fig. 10.14). The huge melting point depression of the 4f-band metal α', α''... Ce strengthens appreciably our conviction that the melting point of La is conspicuously too low for it to be a plain $(sd)^3$-transition metal. It is possible that the extraordinarily high T_c (by Lu-standards) and the low melting point may be mediated by a particularly soft phonon spectrum. We have discussed this matter above for α', α''... Ce.

The Debye temperature of La is anomalously low, as first noticed by Kasuya (1966). Table 10.1 shows the Debye temperatures and electronic specific heat coefficients for La, Lu, Y and Sc. The Debye temperature of d–hcp La is 152 K in comparison to 205 K for Lu. Strictly speaking, the data cannot be compared so simply. The Debye temperature of La will increase under a pressure of 100 kbar, which should be applied in a Gedanken-experiment to correct for the lanthanide contraction. The corresponding volume compression is 24% (Syassen and Holzapfel, 1975). For an estimate of an upper bound we use the largest

TABLE 10.1.
Debye temperature $\Theta_D(0)$ and electronic specific heat coefficient γ for the trivalent rare earths Sc, Y, Lu and La. Error limits are those given in the original papers.

Element	$\Theta_D(0)$, K	γ, mJ $K^{-2}mole^{-1}$
Sc	346 ± 1[a]	10.34 ± 0.02[a]
Y	248 ± 3[b]	8.2 ± 0.1[b]
Lu	205 ± 3[b]	6.8 ± 0.1[b]
d-hcp La	152 ± 2[c]	9.4 ± 0.1[c]
fcc La	140 ± 2[c]	11.5 ± 0.3[c]

[a]Tsang et al. (1976); [b]Wells et al. (1976); [c]Johnson and Finnemore (1967).

mode-Grüneisen parameters $\gamma_i = -\mathrm{d} \ln \omega_i / \mathrm{d} \ln V = 0.8$ from the tunneling data (cf. section 2.2). It follows that the Debye frequency may increase by 19% to 181 K. For a realistic comparison with Lu, the value must be multiplied by $M_{La}^{1/2}/M_{Lu}^{1/2} = 0.89$. The corrected characteristic temperature of La is 161 K and is thus anomalously low indeed with respect to Lu.

As seen from table 10.1, the electronic specific heat of both phases of La is larger than that of Lu. However, no conclusion can be drawn as to a higher density of states in La. The electronic specific heat coefficient γ is proportional to the density of states times the electron–phonon enhancement factor

$$\gamma \propto N(E_F)(1+\lambda)$$

The electron–phonon coupling parameter λ in La is of the order of 0.8–0.9 at normal pressure (Wühl et al., 1973). The coupling parameter for Lu is expected to be small, possibly $\simeq 0.3$ (see section 2.5). The calculated values for the density of states are thus just equal for La and Lu. Apparently, the 4f character of La is not reflected in a particularly high density of states $N(E_F)$ as in α-Ce (section 3.2). One should however keep in mind that La is a complicated metal which also has strong d character. At present it is unknown to what extent the 5d and the 4f bands contribute to the density of states (see however Glötzel (1976)).

The notion of a partially occupied 4f band in La or of 4f-hybridized wave functions has physically the following meaning. The conduction electrons hop on the 4f orbit and leave it after a short while, so that the orbit is partially occupied in the time average. Figure 10.17 shows our view of a few La atoms as they look in La metal. The probability maximum of the 4f wave function for the free atom lies at a distance of roughly 0.4 Å from the nucleus (Herman and Skillman, 1963; Waber and Cromer, 1965). The haloes should indicate the share of 4f-band electrons. The 4f-charge cloud is the screening charge of a 4f virtual bound state on each site (Friedel, 1958; Hamilton, 1965). Not shown are the other wave functions.

We believe there is one experiment in which the existence of this faint virtual

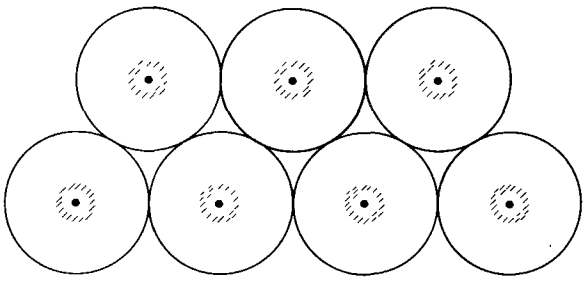

Fig. 10.17. Schematic picture of a metal with 4f-hybridized conduction-electron wave-functions. Haloes indicate the probability maximum of the radial part of the 4f function at a distance of roughly 0.4 Å from the nucleus. The picture probably applies to La metal and Ce at high pressure.

bound state has been experimentally verified. Sugawara (1965) has studied the residual resistivity of Y, doped with 1 at.% of the other rare earth metals. The results are shown in fig. 10.18. Randomly distributed Ce impurities are the strongest scatterers for the conduction electrons. We will not go into this interesting detail here. The weakest scatterers are trivalent Lu impurities. The reason is probably that the 5d-wave function of the Lu atom is fairly similar to the 4d–wave functions of the Y matrix. In other words, the conduction electrons "see" a very similar potential on a Lu site as elsewhere in the matrix. Hence they are weakly scattered. In the conventional picture, La has no 4f electrons (viz. no haloes in contrast to fig. 10.17) and roughly the same sd-wave functions as Lu. As noted by Sugawara, it is therefore all the more surprising that La atoms are much stronger scatterers than Lu atoms (fig. 10.18). Can this be a consequence of the different metallic radii of La (1.877 Å) and Lu (1.735 Å) and a corresponding mismatch of the d-wave functions? We think this is very unlikely. The radius of the Y host atoms (1.800 Å) (Zachariasen, 1973) is just intermediate. So, the deviations from the metallic radius of the matrix are about the same. It was therefore concluded (Wittig, 1973) that this experiment may have sensibly checked the additional scattering due to the 4f virtual bound state (or the

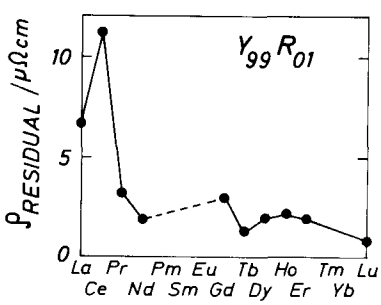

Fig. 10.18. Residual resistivity caused by 1 at.% R-metal dissolved in yttrium. La and Ce are much stronger scatterers than the other R-metals, particularly Lu. The background scattering of the undoped yttrium has been subtracted (Sugawara, 1965).

corresponding scattering potential) on the La atom which we expect it to carry into this dilute alloy. We suggest that further experiments in this direction should be made.

In summary, we think there is considerable evidence now, especially from the macroscopic properties of La metal, that it has occupied nonmagnetic 4f-band states. According to our analysis, this must be also true at very high pressure, at least up to 200 kbar. We now need experiments in order to check this concept on the microscopic level. The conduction band properties of Lu and Y are not affected by 4f electrons. They are pure d-transition metals. Following the original idea of Hamilton and Jensen (1963) (Hamilton, 1965), we have therefore placed Lu below Y in the periodic table (fig. 10.1).

A brief remark should be added concerning the existing band structure calculations for La. Fleming et al. (1968) and Myron and Liu (1970) have carried out relativistic APW calculations. The 4f bands have been artificially removed from the scene. Gschneidner (1971) therefore concluded that "these calculations have not been able to shed any light on the nature of the valence electrons in the lanthanide metals". Kmetko (1971) has published a few results of an APW calculation for fcc La. He finds considerable 4f character at the Fermi surface. Recently, Glötzel (1976) has performed band structure calculations for fcc La at different pressures using the cellular method. He finds about 0.3 4f electrons per atom. This value increases slightly to 0.4 at 120 kbar in contrast to Kmetko who observes a decrease of the 4f occupation number with pressure.

3.4. *Hypothetical* 4f *metals*

The absence of a local magnetic moment on the 4f shell in La has led to the traditional picture that it has no 4f electrons. The 4f group is believed to start abruptly at the element Ce with a magnetic $4f^1$ shell as found in γ-Ce and β-Ce. An "intermediate valence" is usually admitted for α-Ce. The term is used to indicate a partial occupation of the 4f shell. However, above $\simeq$40 kbar, α', α'' . . . Ce is usually thought to possess an empty 4f shell. In the last two sections it was concluded that the 4f series probably commences with two *nonmagnetic* (sd4f)-band metals. The commencement of the 4f series is therefore much more "gradual" and "smooth" according to our reasoning. Small and noninteger occupation numbers of the 4f shells are expected for both La and Ce. Hence it is tempting to look even further to the left of La in the periodic system in order to inspect the physical properties of barium and cesium.

We think there are indications that the properties of Ba and Cs are fairly anomalous, particularly at high pressure. Both metals are superconductors at high pressure (Wittig, 1970; Moodenbaugh and Wittig, 1973). In addition, the melting temperatures seem to be unusually low (see e.g. Cannon, 1974). There is no point in repeating the facts, arguments and counter-arguments here (Wittig, 1973, 1976a). As a possible reason for the anomalies, it was suggested that Ba and Cs may be also 4f-band metals at high pressure. Figure 10.19 illustrates the anticipated situation at a pressure of, say, 50 or 100 kbar. The occupation

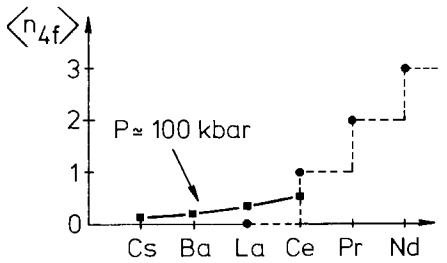

Fig. 10.19. Hypothetical occupation number of the 4f shell for the metals at the beginning of the 4f group at high pressure (squares). The 4f group commences very gradually with increasing atomic number (Wittig, 1973, 1976a). In the traditional view (circles) the 4f group is thought to begin abruptly at the element Ce (at normal temperature and pressure).

number $\langle n_{4f} \rangle$ of the 4f shell is thought to rise very gradually with increasing atomic number. A whole family of 4 *nonmagnetic* 4f-band metals may thus exist at high pressure. This is in contrast to the broken curve which shows the conventional picture. We sincerely hope that these remarks will stimulate a broader interest in this problem.

4. Superconducting alloys and compounds

The nonmagnetic rare earth metals form only a small number of alloys with other elements. Alloying with d-transition elements having $e/a > 3$ is hampered by the large metallic radius of the trivalent rare earth metals. Below we briefly discuss the superconductivity of solid solutions of La with the isoelectronic Y. Huber (1971) extensively studied the variation of T_c for Th-based alloys of Lu, Sc and Y. The superconductivity of alloys containing Ce is covered in ch. 11, sections 3.2 and 4.2. On the other hand, the rare earths form a variety of intermetallic compounds. The partners can be transition as well as nontransition elements. At least a hundred superconductors have been found among the compounds of Sc, Y, Lu and La. Compounds of Ce and Yb are, occasionally, also superconductors. It is not the purpose of this chapter to present the flood of data. Roberts' compilations (1964–1976) are most useful in retrieving information on a particular compound. The quoted T_c for a substance may considerably change from one printing to the next. For instance, the T_c of $CeRu_2$ has been revised from 4.9 K to 6.2 K in the course of time. One simple reason is that often T_c depends sensitively on the degree of metallurgical perfection (e.g. stoichiometry) of the compound. Improvements in sample preparation and a better knowledge of the metallurgy may thus lead to revisions in other cases too. In what follows we discuss a few selected topics.

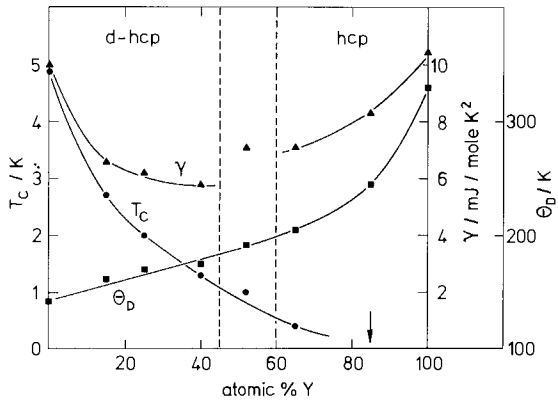

Fig. 10.20. T_c, electronic specific heat coefficient γ and Debye temperature Θ_D as a function of concentration x in the alloy system $La_{1-x}Y_x$ (Satoh and Ohtsuka, 1967).

4.1. *Superconductivity in* La–Y *alloys*

Satoh and Ohtsuka (1967) tackled the "lanthanum problem" very early. They investigated the question of what happens, if the "good" superconductor La is diluted with the nonsuperconductor Y. Figure 10.20 shows the data for the solid solutions which have the d–hcp structure on the La-rich side and the hcp structure on the Y side. T_c drops with increasing Y concentration (Anderson et al., 1958) and is <0.1 K at 85 at.%. The electronic specific heat coefficient passes a pronounced minimum. The rate of increase of the Debye temperature Θ_D is first small and becomes appreciably larger near pure Y. From the original BCS expression for T_c (Bardeen et al., 1957), $T_c = 1.14\ \Theta_D \exp(-1/N(E_F)V)$, they evaluated the effective coupling parameter V as a function of the Y concentration. They noted that the coupling parameter is markedly smaller in the Y-rich region. This finding agrees with our conclusions for Y and Lu in section 2.5. In the present terminology, Y is not a superconductor (at normal pressure and accessible temperatures) because the coupling parameter $\lambda = N(E_F)\langle I^2\rangle/M\langle\omega^2\rangle \simeq N(E_F)\ V$ is too small.

On the La-rich side, V turned out to be roughly constant. This correlates with the small variation of Θ_D upon addition of Y. Satoh and Ohtsuka suggested therefore that the specific influence which is responsible for the high T_c of La may be also related to the low Θ_D. This was a remarkable conclusion at that time, since according to the BCS formula, a low Θ_D seems to cause a low T_c. At present it is well known that V (or λ) itself depends on the phonon frequencies, i.e. Θ_D. As outlined in section 2.1, this works in the opposite direction and overcompensates the influence of Θ_D as a prefactor of the exponential term. It is worth mentioning that Satoh and Kumagai (1973) have suggested that the relatively low Θ_D of thorium may have the same origin as the low Θ_D of La, namely the presence of vacant f levels above the Fermi surface.

4.2. *Cerium compounds*

The cubic Laves phase compounds $CeRu_2$ and $CeCo_2$ are the only known superconductors among the Ce intermetallics.† Their T_c's are indicated in fig. 10.21 by solid circles. Following Hill (1970), the Ce–Ce interatomic spacing was used as the display parameter. The triangles show the magnetic ordering temperatures (T_0) for β-Ce and some magnetic Ce compounds. Apparently, if the Ce–Ce spacing is smaller than $\simeq 3.3$ Å, the compounds are superconductors, just as pure Ce is in the α-phase and in the α', α''... phase. For larger Ce–Ce spacings, magnetism appears on the Ce atom as in β-Ce or, equivalently, in the γ-phase. Hill has suggested that the 4f band broadens with decreasing Ce–Ce spacing so strongly that magnetism on the 4f shell breaks down.

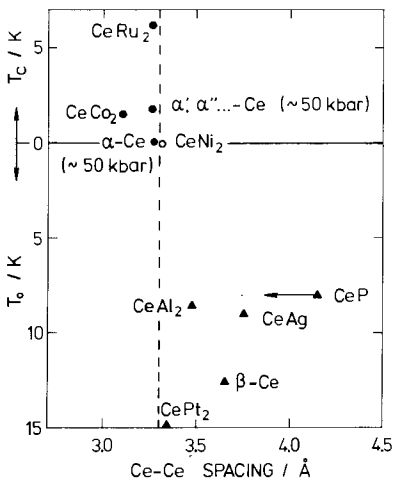

Fig. 10.21. Superconducting T_c or magnetic ordering temperature T_0 vs. interatomic Ce–Ce spacing in the phases of Ce and for several Ce-intermetallics. The dashed line at 3.3 Å appears to be a dividing line between superconductivity and magnetism. $CeNi_2$ is neither superconducting down to 0.015 K nor magnetic (Smith and Harris, 1967). For $CeRu_2$ see Wilhelm and Hillenbrand (1970). $CeCo_2$: Luo et al. (1968). $CePt_2$: Smith and Harris (1967). $CeAl_2$: Williams et al. (1962). CeAg: Walline and Wallace (1965). CeP: Busch and Vogt (1966). β-Ce: Wilkinson et al. (1961). The values of T_0 are not accurately known in some cases (see section 6: Recent developments).

Recently, Jayaraman et al. (1976) have discovered a volume collapse in cerium phosphide under a pressure of 100 kbar resembling the γ/α transition of pure Ce. They suggest that CeP may therefore be a superconductor at high pressure. The arrow in fig. 10.21 shows the reduced Ce–Ce spacing at their maximum pressure of 200 kbar. It is still appreciably larger than the apparent "critical distance" of $\simeq 3.3$ Å for the appearance of superconductivity. In this light, it does not seem

†Superconductivity was also reported for $CeIr_3$ and $CeIr_5$ by Geballe et al. (1965) but no structural data exist.

likely that CeP will be a superconductor at 200 kbar. Besides the Ce–Ce interatomic distance, other parameters will be however equally important, e.g. the metallic radius of Ce and its coordination number. This will certainly modify the "critical distance" for compounds with different lattice structures. At any rate, from fig. 10.21 it does not seem impossible that the compound $CeAl_2$, which is at normal pressure close to the critical distance, may become a superconductor in the pressure range up to 200 kbar. The compound $CeNi_2$, just on the border line, is not superconducting down to 0.015 K. Perhaps it is also a good candidate for a high pressure experiment.

4.3. *Dialuminides and* Ag *compounds*

The cubic Laves phase compounds RAl_2 (R = La, Lu, Y, Sc) represent an interesting family in which the La compound is distinguished by a relatively high T_c. This may be closely related to the "lanthanum problem" (cf. section 3.3). Table 10.2 shows the available information. $LuAl_2$ has been investigated for superconductivity to a lowest temperature of 0.05 K. $LaAl_2$ becomes superconducting at 3.26 K. Its T_c is thus at least a factor of 60 higher than for $LuAl_2$. Also shown are data for the electronic specific heat coefficient. For $LaAl_2$ it is almost twice as large as for the other two compounds. This probably indicates a higher density of states at the Fermi surface. As first noticed by Hungsberg and Gschneidner (1972), the Debye temperature of $LaAl_2$ is anomalously low (table 10.2) (as is Θ_D of pure La). The next column shows calculated values $\Theta_{D,calc}$ for $LaAl_2$ and $LuAl_2$. $\Theta_{D,calc}$ was evaluated from the formula $\Theta_{D,calc}/\Theta_{D,Y} = (M_Y/M_R)^{1/2}$, where M_R is the mass per unit formula, if yttrium is replaced by the "oscillators" La and Lu. From the close agreement of Θ_D and $\Theta_{D,calc}$ for $LuAl_2$ it follows that the elastic binding forces are nearly the same as in YAl_2. However for $LaAl_2$ they are markedly lower. In order to account for the unique behavior of $LaAl_2$ it was suggested (Hungsberg and Gschneidner, 1972; Silbernagel et al., 1973; Wittig, 1973) that some 4f admixture exists at the Fermi surface. Switendick (1973) has carried out an APW energy band calculation for RAl_2 (R = La,

TABLE 10.2.
Low temperature properties of the nonmagnetic R-dialuminides.

C–15 compound	T_c, K	γ, mJ K^{-2}mole^{-1}	Θ_D, K	$\Theta_{D,calc}$, K
$ScAl_2$	< 1.02[a]	—	—	—
YAl_2	< 0.35[a]	1.81[d]	473[d]	(473)
$LaAl_2$	3.26[b]	3.45[e]	366[e]	407
$LuAl_2$	< 0.05[c]	1.9[d]	384[d]	374

[a]Smith and Luo (1967); [b]Riblet and Winzer (1971); [c]Havinga et al. (1973); [d]Hungsberg and Gschneidner (1972); [e]Steglich (1976).

Lu, Y). He concludes "that there is considerable f-electron character mixed into the conduction band states near the Fermi energy in $LaAl_2$".

Among the CsCl-compounds LaAg, YAg and LuAg, only LaAg is superconducting with $T_c = 0.94$ K (Chao et al., 1966). The compounds with Y and Lu are not superconducting above 0.33 K (Smith and Luo, 1967). It would be interesting to investigate them at even lower temperatures, in order to explore how exceptional the behavior of the La-compound is. Experiments at high pressure may also be instructive, since the strong increase of the T_c with pressure in the pure elements Y and Lu (cf. section 2.4–2.5) may occur in the corresponding "diluted" Ag compounds too. It would be also interesting to have precise specific heat data, in order to see whether the La compound is distinguished by a comparatively large γ and a low Θ_D as in the dialuminides. We think the relatively high T_c of LaAg may reflect the presence of 4f character at the Fermi surface as in pure La. Hasegawa et al. (1975) have recently published an APW band structure calculation for LaAg. A sharp peak in the density of states lies right above the Fermi surface. However, they ascribe it to electrons with d character.

There are many other La-intermetallics exhibiting fairly high T_c's (Roberts, 1964–1976). However we could not find other suitable systems for a comparison. Often, the corresponding Lu compound has not been studied or does not metallurgically form. Among the hexagonal Laves phases ROs_2, $LaOs_2$ has again the highest T_c (Lawson, 1973). However, the other compounds (R = Sc, Y, Lu) have T_c's of similar magnitude (Compton and Matthias, 1959). One must therefore doubt that the higher T_c of $LaOs_2$ is a significant effect. Clearly, in many compounds the expected presence of a subtle 4f resonance on the La atom may be completely obscured by other effects.

4.4. $AuCu_3$-*type compounds*

The R metals La, Y, Lu and Yb form various superconducting $AuCu_3$-type compounds RX_3 with X = Pb, Sn, Tl, In, Al, ... Havinga et al. (1970) discovered that the superconducting T_c has an interesting oscillatory dependence on the average number of valence electrons in such compounds as $La\ Sn_{3-x}Tl_x$ or $Y\ Pb_{3-x}In_x$ $(0 < x < 3)$. The effect has been ascribed to a Fermi surface-Brillouin zone interplay. The oscillatory dependence of T_c on the electron-per-atom ratio is accompanied by oscillatory variations of the electronic specific heat, the magnetic susceptibility and the thermoelectric power. An exhaustive review has appeared recently (Havinga and Van Maaren, 1974).

In contrast to the nearly free electron model used by Havinga et al., another group of authors (Toxen et al., 1973) have emphasized the transition-metal character of such compounds as e.g. $LaSn_3$. The magnetic properties of the superconductor $LaSn_3$ ($T_c \simeq 6$ K) are most interesting. At high temperatures, the susceptibility follows a Curie–Weiss law with a large Curie constant corresponding to a magnetic moment of $\simeq 1$ Bohr magneton per La atom. Below $\simeq 100$ K the susceptibility becomes temperature-independent. Initially, there was

the fascinating idea (from the present authors' point of view) that a localized magnetic moment exists on the 4f shell of the La atom due to a partial occupation of the 4f level (Toxen and Gambino, 1968). However, in a subsequent paper it was suggested that the dominant contribution to the susceptibility results from the La d-orbital motion (Toxen et al., 1973).

The La-rich compounds La_3In and La_3Tl also crystallize in the Cu_3Au structure. They are superconductors with fairly high T_c's of 9.5 and 8.9 K (e.g. Heiniger et al., 1973). The La–La nearest neighbor distance is smaller in these compounds than in pure fcc La, due to the small metallic radii of In and Tl. In view of the strong increase of T_c with pressure for fcc La (section 2.1) it has been suggested that these compounds may be considered as a "diluted" fcc La in a state of natural compression. Various superconducting properties are reported by Heiniger et al.

Two ytterbium compounds, $YbPb_3$ and $YbAl_3$, have been thus far found to be superconducting (Havinga et al., 1970). They also crystallize in the $AuCu_3$ structure. Havinga et al. (1973) report anomalous properties for the compound $YbAl_3$ ($T_c \simeq 0.9$ K). It appears as if the Yb ion is close to trivalent and yet nonmagnetic at low temperatures. Another anomalous property is a huge electronic specific heat coefficient of 45 mJ mole^{-1} K^{-2}.

4.5. *Rare earth sesquicarbides*

Giorgi and co-workers discovered that the sesquicarbides Y_2C_3 and La_2C_3 are both superconductors with T_c's as high as about 11 K (Giorgi et al., 1969, 1972). The T_c depends strongly on the conditions of sample preparation which is not unusual for carbides. La_2C_3 crystallizes in the body-centered cubic Pu_2C_3-type structure. Y_2C_3 can also be prepared in this structure by the application of high pressure at high temperatures (Krupka et al., 1969). After quenching to ambient temperatures, it can metastably exist at normal pressure. By partially substituting thorium for La and Y, Giorgi and co-workers succeeded in raising the T_c to 14 K in the $La_{1-x}Th_xC_{1.5}$ system (Giorgi et al., 1972) and to even 17 K in the $Y_{1-x}Th_xC_{1.5}$ ternary system (Krupka et al., 1969). These high transition temperatures are quite remarkable, since all other known superconducting materials with $T_c > 15$ K involve the presence of the transition metals Nb, V or Mo.

4.6. *Rare earth chalcogenides*

Many R-chalcogenides (R = Sc, Y, Lu, La) are superconductors. They crystallize in the rocksalt structure. Table 10.3 shows some examples for recently reported T_c's, or the ranges of temperature, where superconducting transitions were observed. The Sc, Y and Lu monochalcogenides are known to be defect structures which can exist with an appreciable anion or cation deficiency (Hulli ger and Hull, 1970; Moodenbaugh et al., 1974). The T_c's depend strongly on composition and are therefore not well-defined.

Bozorth et al. (1965) discovered superconductivity in La_3S_4 and La_3Se_4. The

TABLE 10.3.
Superconducting transition temperatures for some R-chalcogenides.

NaCl-type compound	ScS	YS	LuS	YTe	LuSe	LaS	LaSe	LaTe
T_c, K	4.5[a]	1.3[b]–2.9[c]	0.8[b]–1.6[c]	1.5–2.0[b]	0.5[b]	0.84[d]	1.02[d]	1.48[d]

Th_3P_4–type compound	La_3S_4	La_3Se_4	La_3Te_4
T_c, K	8.06[d], 8.12[e]	7.80[d], 7.63[e]	5.30[d], 4.61[e]

[a]Moodenbaugh et al. (1974); [b]Hullinger and Hull (1970); [c]Moodenbaugh (1975); [d]Bucher et al. (1975); [e]Shelton et al. (1975).

compounds crystallize in the cubic Th_3P_4-type structure. For the nearly stoichiometric compounds fairly high T_c's are reported (table 10.3). These compounds are also defect structures which can exist with a large concentration of vacancies at the cation sites. Accordingly, T_c varies strongly with composition. An exhaustive review of the properties of these compounds was published by Bucher et al. (1975). Recently, Dernier et al. (1975) discovered that La_3S_4 and La_3Se_4 undergo a cubic-to-tetragonal lattice distortion at low temperatures. Shelton et al. (1975) investigated the pressure dependence of T_c. They detected a dramatic increase of T_c for La_3S_4 up to 11.5 K at $\simeq$20 kbar. It would be worthwhile to extend these experiments to higher pressures and to investigate in detail how the pressure dependence of T_c is related to the low-T lattice instability.

4.7. *Ternary molybdenum chalcogenides*

This new class of compounds has the general formula XMo_6S_8 or XMo_6Se_8, where X = Pb, Sn, Cu, ... and also R. They were first described by Chevrel et al. (1971). Subsequently, Matthias et al. (1972) discovered superconductivity in many of these compounds. At present the compound $PbMo_6S_8$ is known to have the highest $T_c \simeq 14$ K. Fischer and co-workers detected that this substance stays superconducting up to extremely high critical magnetic fields $H_{c2} > 50$ Tesla at $T = 0$ K (Odermatt et al., 1974). Recent investigations showed unusual effects when magnetic rare earth ions are substituted for X.

Figure 10.22 shows the structure. Eight S(Se) atoms at the corners of a cube enclose an octahedron formed by Mo atoms. These units are arranged as indicated. The third element X is normally surrounded by 8 such cubes. The Pb atoms can be substitutionally replaced by rare earth atoms. Figure 10.22 shows T_c as a function of concentration for R = La, Lu and Gd in the series $Pb_{1-x}R_xMo_6S_8$. The interesting point is that the compound $GdMo_6S_8$ is a super-

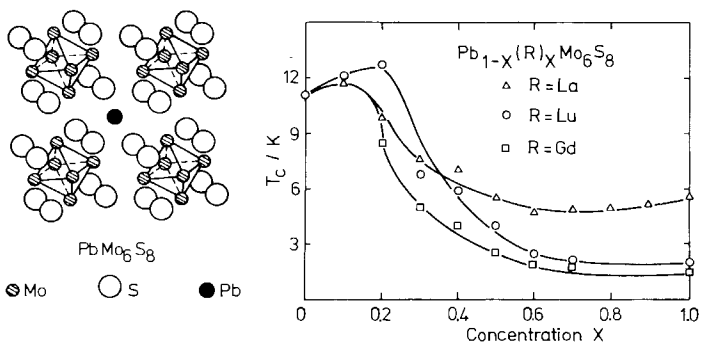

Fig. 10.22. Structure of the ternary molybdenum chalcogenides (left side). The plot on the right side shows the variation of T_c with concentration x, if Pb is substitutionally replaced by R-atoms (Fisher, 1975).

conductor with $T_c \simeq 1.4$ K in spite of the fact that it contains $\simeq 7$ at.% magnetic Gd ions (Fisher et al., 1975). The classical experiment by Matthias et al. (1958) in this field showed that superconductivity of La metal is entirely quenched by the addition of $\simeq 1$ at.% Gd due to the exchange scattering by the magnetic Gd ions. Very recently it was reported that the corresponding selenide compound $Gd_{1.2}Mo_6Se_8$ has an even higher $T_c \simeq 5.4$ K. Similar high T_c's were reported for most RMo_6Se_8 compounds (Shelton et al., 1976). The question arises why are magnetic rare earths so inefficient in lowering the T_c in this class of compounds. It has been suggested that the superconducting electrons are mainly the Mo d-electrons (Fisher, 1975). These electrons have little overlap with the 4f wave function of the rare earth atom due to the relatively large Mo–R distance. Hence the exchange scattering is weak. In other words, the peculiar lattice structure of these compounds restricts the superconducting electrons mainly to regions of the crystal well away from the magnetic rare earth ions.

5. Concluding remarks

This chapter deals extensively with the experimental data on the superconductivity of the rare earth metals at high pressure. The results are discussed from a phenomenological point of view emphasizing systematics. This seems appropriate at the present stage of understanding. The analysis results in rather clear-cut conclusions for the electronic structure of cerium and lanthanum. It is hoped that they will serve as a useful guide-line for future experimental and theoretical work. We would like to summarize the following results and problems.

1. Cerium is not "squeezed" out of the 4f group by the application of high pressure. The Pauling–Zachariasen hypothesis (cf. ch. 4, section 5.1) that the 4f electron is "promoted" to the sd-conduction band by pressure is not the full truth. From the discussion given in section 3.2, Ce remains in the 4f group proper as a tetravalent sd4f-band metal with an appreciable share of nonmagnetic 4f-band electrons at pressures up to at least 200 kbar. We think this is physically a gratifying result. It means that the potential-well in the interior of the Ce atom, which is capable of attracting one 4f electron in γ or β-Ce, cannot be so drastically changed by a modest pressure of, say, 50 or 200 kbar that it looses the capability of binding at least a certain fraction of a 4f electron in the time-average. Figure 10.17 is a schematic picture of the partially occupied 4f orbit in real space for the analogous case of La. Apparently, the 4f admixture of the conduction electrons can be, with respect to superconductivity, either "moderately detrimental" (as in α-Ce with T_c in the millikelvin range) or even entirely nondetrimental (as in $\alpha', \alpha'' \ldots$ Ce).

2. There is considerable evidence now that Ce's left-hand neighbor lanthanum, is not a "plain" sd-transition metal like the other trivalent metals Lu, Y and Sc. As discussed in section 3.3, we think it is at present a well-founded concept that La is, at normal pressure as well as at 200 kbar, a 4f-band metal

similar to Ce in the α', α''... range (Wittig, 1973, 1974; see however Stern, 1975). It is probably reasonable to assume that the 4f-occupation number in La is smaller than in α', α''... Ce as suggested by fig. 10.19. This should be considered as a guess of course. No quantitative conclusions can be drawn at present for the occupation of the 4f shell in La. The nonmagnetic 4f-band electrons are (in an unknown way) responsible for the many unusual properties, including, e.g., the sharp kinks in $T_c(P)$ at 25 and 53 kbar which occur in connection with subtle low-temperature lattice-instabilities (cf. fig. 10.3 and section 2.1). Without doubt, the major portion of the 4f band lies above the Fermi energy E_F. However, the frequently used phrase "La has no 4f electrons" appears to be incorrect, since the physical properties of La and certain La-intermetallics appear to be decisively influenced by the small 4f share in the conduction electron wave functions.

3. It again turns out that Y and Lu (and also Sc) are rare earth metals by convention only. Strictly speaking, they are trivalent d-transition metals, in contrast to La which belongs to the 4f group proper. Y and Lu are however very interesting d-transition metals. Their T_c's increase by orders of magnitude between normal pressure and 200 kbar. There is no fundamental understanding of this effect at present. Following Hamilton's suggestion, the element below Y should be Lu instead of La (see fig. 10.1) in a periodic table fashioned for the practical needs of a solid-state physicist.

4. The phenomenological approach has lead to the hypothesis that barium and even the alkali metal cesium are perhaps, at high pressure, also 4f-band metals of a similar kind as La and Ce (Wittig, 1973, 1976a). The future must show whether this prognosis is correct or not, thereby showing the usefulness or, one of the pitfalls of a phenomenological approach. Several theoretical investigations of the highly interesting properties of Cs under pressure do not reveal 4f electrons (Sternheimer, 1950; see e.g. Louie and Cohen, 1974). Although we see at the time of writing no point of making more than a brief remark in section 3.4, we strongly hope that it helps to draw attention to an interesting current problem in solid state physics. One can put it in the following simple form: allowing for moderate pressures (of the order of 50–100 kbar), which element, in the periodic table, is the first genuine member of the 4f group?

5. A remark should be added concerning the electronic structure of the other light lanthanides Pr, Nd,.... Matthias et al. (1967) and Gschneidner (1971) first pointed out that Pr, Nd,... possess similarly low melting points as La. They noted that this is incompatible with the usual picture of a pure $(sd)^3$-conduction band (see e.g. Freeman, 1972). They proposed therefore that the conduction band should have some 4f character. It may be a $(sd4f)^3$ hybridized conduction band as for La (cf. section 3.3). In addition, Pr, Nd,... are thought to possess the magnetic configuration $4f^n$ ($n = 2, 3, \ldots$). Recently, points of inflection were discovered in the R–T characteristic of fcc Pr and Nd at high pressure just as for La (fig. 10.4) (Wittig, 1976b). This common anomaly points indeed to extremely similar conduction bands in La, Pr and Nd. Since the anomaly is very likely related to the 4f-band character of La, its occurrence in Pr and Nd

strongly points to 4f-band character in these elements too, in support of the conclusions made from the low melting point data.

6. The f-band metals (Ce, La, U, ...) seem to be characterized by unusually soft phonons both at long and at short wavelengths (Balster and Wittig, 1975; Wittig, 1975). This leads to relatively low Debye-temperatures, low melting points and, apparently, rather frequently to lattice instabilities (see section 2.1 and 2.3). Often (but not always) the soft phonons are reflected in a relatively high superconducting T_c (La, α', α'' ... Ce, $LaAl_2$, ...). We hope that the problem of soft phonons in f-band substances will attract theorists.

7. The properties of the 4f-band metals Ce and La depend sensitively on pressure. It is surprising that *pressure* is a powerful variable which can induce strong effects in 4f-band substances. Traditionally, the 4f-wave function is thought to be an *inner* wave function with negligible overlap between neighboring atoms. It should not be strongly affected by pressure. Because of the strong dependence of the effects on interatomic distance one may therefore suspect that the 4f–4f overlap in the metals has been so far underestimated (cf. Kasuya, 1966) and increases appreciably under pressure. It is therefore quite possible that experiments at high pressure will play a key-role in understanding f-electron metals.

6. Recent developments

Duthie and Pettifor (1977) have published a paper showing that La's anomalous d-hcp and fcc structures are the consequence of La's having approximately 0.6 5d-band electrons more than hcp Lu at normal pressure. At the same time Glötzel and Fritsche (1977) find a *4f-band* occupation of $\simeq 0.3$ electrons per atom in their band structure calculation for fcc-La. A self-consistent calculation did not lead to a substantial change for this value (Glötzel, 1977). In view of these discrepancies on the theoretical side, the phenomenological approach of the present chapter appears to be once more justified.

X-ray photoemission spectra (XPS) have been studied for La, Ce, Pr, ... in recent years (Baer and Busch, 1974; Steiner et al., 1977; Höchst et al., 1977). Unfortunately the XPS data so far do not render any information on the anticipated 4f contribution to the conduction band of these rare earth metals.

Endo et al. (1977) have reported the observation of a body-centered tetragonal lattice in Ce at pressures between 121 and 175 kbar. This is probably the same phase which was labelled $\tilde{\alpha}$ in section 2.3 (cf. fig. 10.8). Note that the finding is in strong contrast to our suggested isostructural character of the transformation.

Probst and Wittig (1977) have observed superconductivity above 37 kbar in the bcc phase of Ba (cf. section 3.4). T_c increases steeply with pressure whereas the melting temperature *decreases*. This has been ascribed to a considerable 4f hybridization of the conduction electron wave function in the neighborhood of the Fermi level as previously suggested for the high pressure phases of Ba (Wittig, 1973).

There is a striking similarity between the P–T phase diagrams of La and Pr (Heinrichs and Wittig, to be published). One may therefore suspect that the electron–phonon coupling strength in Pr increases with pressure similarly strongly as for La (cf. the T_c–P dependence of La in fig. 10.2). A sample of rather pure Pr ($R_{300\,K}/R_{4.2\,K} \simeq 100$) has been investigated for superconductivity at 140 kbar down to a lowest temperature of 42 mK, however with negative result.

In connection with sections 4.2 and 4.3 some new experimental data are now available. Probst and Wittig (1978) have investigated the electrical resistivity of $CeAl_2$ at high pressure and as a function of temperature. Rather clear evidence has been found that the compound undergoes a magnetic-to-nonmagnetic transition in the pressure range between 50 and 100 kbar. No superconductivity has been observed down to a lowest temperature of 15 mK at $\simeq$ 140 kbar contrary to what may be expected from fig. 10.21 upon crossing the dashed line (Probst and Wittig, 1978). One should however keep in mind that pure Ce is first an extremely low-T_c-superconductor after its collapse to the α-phase (cf. fig. 10.8). This may also be the case with $CeAl_2$. A systematic study of other Ce compounds under pressure is now desirable. Matthias et al. (1976) have published interesting data which demonstrate the comparatively "good" superconducting properties ($T_c = 0.94$ K) of LaAg; no sign of superconductivity was detected in RAg (R = Sc, Y and Lu) down to the lowest temperature of 40 mK. It has been pointed out to us by D. Wohlleben that the low $T_c = 0.12$ K of the compound LaB_6 (Arko et al., 1975) as compared to the high $T_c \simeq 7$ K for YB_6 (e.g. Roberts, 1976) is just opposite to the trend for the T_c's in RAl_2 and RAg in which the La compound has by far the highest T_c. We think however, it is not too surprising that the properties of the individual R-metals are not reflected anymore in such a border-like metal crystal as RB_6.

The magnetic ordering temperature T_0 of $CePt_2$ (cf. fig. 10.21) has been redetermined by Joseph et al. (1972). According to this work $CePt_2$ orders antiferromagnetically at $T_0 = 1.6$ K. The magnetic ordering temperature of CeAg is possibly a little lower than shown in fig. 10.21. Ihrig and Lohmann (1977) have published a paper discussing the low-T properties of CeAg. The paper lists references to other recent work. The ordering temperature of $CeAl_2$ is probably 4–5 K rather than 8 K as shown in fig. 10.21 (see e.g. Walker et al., 1973).

Note added in proof

Recently, superconductivity has been observed in a new high pressure phase of scandium (J. Wittig, C. Probst, F.A. Schmidt and K.A. Gschneidner, Jr., to be published in 1978). At a pressure of approximately 200 kbar, Sc undergoes a crystallographic phase transition as inferred from a dramatic resistance increase by a factor of four at room temperature. This new high pressure phase is superconducting. T_c increases with pressure from below 50 mK to 0.3 K at the highest pressure so far studied, There are indications that the low pressure hcp phase of Sc is *also* a superconductor (at millikelvin temperatures) just before the transformation to the new high pressure phase. If this should turn out to be correct there would be a beautiful similarity between the superconducting properties of Sc, Y

and Lu (Fig. 10.15). Will the element yttrium, being below Sc in the Periodic System, show an analogous phase transformation? For lutetium, a crystallographic phase transition has been reported to occur at 230 kbar (Liu, 1975). It is thus possible that the latter transformation is the direct counterpart of the new phase transition in Sc. The study of the crystallographic and superconducting properties of Sc, Y, Lu and La up to the highest possible pressures will therefore continue to be an interesting research topic.

References

Anderson, G.S., S. Legvold and F.H. Spedding, 1958, Phys. Rev. **109**, 243.

Andres, K., 1968, Phys. Rev. **168**, 708.

Andres, K. and M.A. Jensen, 1968, Phys. Rev. **165**, 533.

Appel, J., 1973, Phys. Rev. B **8**, 1079.

Bader, S.D., N.E. Phillips and E.S. Fisher, 1975, Phys. Rev. B **12**, 4929.

Bader, S.D. and G.S. Knapp, 1975, Phys. Rev. B **11**, 3348.

Balster, H. and J. Wittig, 1975, J. Low Temp. Phys. **21**, 377.

Bardeen, J., L.N. Cooper, and J.R. Schrieffer, 1957, Phys. Rev. **108**, 1175.

Barrett, C.S., M.H. Mueller, and R.L. Hitterman, 1963, Phys. Rev. **129**, 625.

Beecroft, R.I. and C.A. Swenson, 1960, J. Phys. Chem. Solids **15**, 234.

Bennemann, K.H. and J.W. Garland, 1972, Theory for Superconductivity in d-Band Metals, in: Douglass, D.H., ed., Superconductivity in d-and f-Band Metals, AIP Conf. Proc. No. 4 (American Inst. of Physics, New York 1972) p. 103.

Bozorth, R.M., F. Holtzberg, and S. Methfessel, 1965, Phys. Rev. Lett. **14**, 952.

Brandt, N.B., J.V. Berman and Yu.P. Kurkin, 1974, Zh. Eksp. Teor. Fiz. Pis'ma **20**, 20; Sov. Phys. JETP Lett. **20**, 8.

Brodsky, M.B., A.J. Arko and A.R. Harvey, 1974, Transport Properties, in: Freeman, A.J. and J.B. Darby, Jr., eds., The Actinides – Electronic Structure and Related Properties, Vol. II (Academic Press, New York 1974) p. 185.

Bucher, E., K. Andres, F.J. di Salvo, J.P. Maita, A.C. Gossard, A.S. Cooper, and G.W. Hull, Jr., 1975, Phys. Rev. B **11**, 500.

Bucher, E., P.H. Schmidt, A. Jayaraman, K. Andres, J.P. Maita, K. Nassau and P.D. Dernier, 1970, Phys. Rev. B **2**, 3911.

Busch, G. and O. Vogt, 1966, Phys. Lett. **20**, 152.

Cannon, J.F., 1974, J. Phys. Chem. Ref. Data **3**, 781.

Chao, C.C., H.L. Luo and T.F. Smith, 1966, J. Phys. Chem. Solids **27**, 1555.

Chevrel, R., M. Sergent and J. Pringent, 1971, J. Solid State Chem. **3**, 515.

Compton, V.B. and B.T. Matthias, 1959, Acta Cryst. **12**, 651.

Coqblin, B., 1971, J. Phys. Suppl. **32**, C1, 599.

Coqblin, B., E. Galleani d'Agliano and R. Jullien, 1972, Superconductivity of Rare Earths and Actinides, in: Douglass, D.H., ed., Superconductivity in d- and f-Band Metals, AIP Conf. Proc. No. 4 (American Inst. of Physics – New York, 1972) p. 154.

Dernier, P.D., E. Bucher and L.D. Longinotti, 1975, J. Solid State Chem. **15**, 203.

Douglass, D.H., 1972, Superconductivity in d- and f-Band Metals, AIP Conf. Proc. No. 4 (American Inst. of Physics – New York 1972).

Ellinger, F.H. and W.H. Zachariasen, 1974, Phys. Rev. Lett. **32**, 773.

Fertig, W.A., A.R. Moodenbaugh and M.B. Maple, 1972, Phys. Lett. **38A**, 517.

Fischer, Ø., A. Treyvaud, R. Chevrel and M. Sergent, 1975, Solid State Commun. **17**, 721.

Fischer, Ø., 1975, Higher critical field superconductors, in: Krusius, M. and M. Vuorio, eds., Proc. 14th International Conf. on Low Temp. Phys., Otaniemi, Vol. V (North-Holland Publishing Comp., Amsterdam) p. 172.

Fisher, E.S., 1974, Ultrasonic Waves in Actinide Metals and Compounds, in: Freeman, A.J. and J.B. Darby, Jr., eds., The Actinides – Electronic Structure and Related Properties, Vol. II (Academic Press, New York 1974) p. 289.

Fleming, G.S., S.H. Liu and T.L. Loucks, 1968, Phys. Rev. Lett. **21**, 1524.

Franceschi, E. and G.L. Olcese, 1969, Phys. Rev. Lett. **22**, 1299.

Freeman, A.J., 1972, Energy Band Structure, Indirect Exchange Interactions and Magnetic Ordering, in: Elliott, R.J., ed., Magnetic Properties of Rare Earth Metals (Plenum Press, London and New York, 1972) p. 245.

Friedel, J. 1958, Nuovo Cimento Suppl. **7**, 287.

Garland, J.W. and K.H. Bennemann, 1972, Theory for the Pressure Dependence of T_c for Narrow-Band Superconductors, in: Douglass, D.H., ed., Superconductivity in d- and f-Band Metals, AIP Conf. Proc. No. 4 (American Inst. of Physics – New York 1972) p. 255.

Geballe, T.H., B.T. Matthias, V.B. Compton, E. Corenzwit, G.W. Hull, Jr., and L.D. Longinotti, 1965, Phys. Rev. **137**, A 119.

Baer, Y. and G. Busch, 1974, J. Electron Spectrosc. 5, 611.

Duthie, J.C. and D.G. Pettifor, 1977, Phys. Rev. Lett. 38, 564.

Gempel, R.F., D.R. Gustafson and J.D. Willenberg, 1972, Phys. Rev. B **5**, 2082.
Giorgi, A.L., E.G. Szklarz and M.C. Krupka, 1972, Superconductivity of Various Ternary Thorium Compounds, in: Douglass, D.H., ed., Superconductivity in d- and f-Band Metals, AIP Conf. Proc. No. 4 (American Inst. of Physics – New York 1972) p. 147.
Giorgi, A.L., E.G. Szklarz, M.C. Krupka and N.H. Krikorian, 1969, J. Less-Common Metals **17**, 121.
Gladstone, G., M.A. Jensen and J.R. Schrieffer, 1969, Superconductivity in the Transition Metals: Theory and Experiment, in: Parks, R.D., ed., Superconductivity, Vol. 2 (Marcel Dekker, Inc., New York) p. 665.
Glötzel, D., 1976, Untersuchung der elektronischen Struktur von Lanthan und Cer, Thesis, Technische Universität Clausthal.
Gschneidner, K.A., Jr., R.O. Elliott and R.R. MacDonald, 1962, J. Phys. Chem. Solids **23**, 555.
Gschneidner, K.A., Jr., 1964, Physical Properties and Interrelationships of Metallic and Semimetallic Elements, in: Seitz, F. and D. Turnbull, eds., Solid State Physics, Vol. 16 (Academic Press, New York 1964) p. 275.
Gschneidner, K.A., Jr., 1971, J. Less-Common Metals **25**, 405.
Hamilton, D.C., 1965, Am. J. Phys. **33**, 637.
Hamilton, D.C. and M.A. Jensen, 1963, Phys. Rev. Lett. **11**, 205.
Hasegawa, A., B. Bremicker and J. Kübler, 1975, Z. Phys. B **22**, 231.
Havinga, E.E., H. Damsma and M.H. van Maaren, 1970, J. Phys. Chem. Solids **31**, 2653.
Havinga, E.E., K.H.J. Buschow and H.J. van Daal, 1973, Solid State Commun. **13**, 621.
Havinga, E.E. and M.H. van Maaren, 1974, Physics Reports **10**, 107.
Heiniger, F., E. Bucher, J.P. Maita and P. Descouts, 1973, Phys. Rev. B **8**, 3194.
Herman, F. and S. Skillman, 1963, Atomic Structure Calculations (Prentice-Hall, Inc., Englewood Cliffs, New Jersey, 1963).
Hill, H.H., 1970, in Miner, W.N., ed., Plutonium 1970 and Other Actinides (New York: AIME) p. 2.
Hill, H.H. and E.A. Kmetko, 1975, J. Phys. F: Metal Phys. **5**, 1119.
Hirst, L.L., 1974, J. Phys. Chem. Solids **35**, 1285.
Hopfield, J.J., 1971, Physica **55**, 41.
Huber, J.G., 1971, Nonmagnetic Impurities with Partially Filled d- or f-Electron Shells in Superconducting Hosts. Ph.D. Thesis, University of California, San Diego, 1971.
Hullinger, F. and G.W. Hull, Jr., 1970, Solid State Commun. **8**, 1379.
Hungsberg, R.E. and K.A. Gschneidner, Jr., 1972, J. Phys. Chem. Solids **33**, 401.
Jayaraman, A., 1965a, Phys. Rev. **139**, A 690.
Jayaraman, A., 1965b, Phys. Rev. **137**, A 179.
Jayaraman, A., W. Lowe, L.D. Longinotti and E. Bucher, 1976, Phys. Rev. Lett. **36**, 366.
Jensen, M.A., 1965, Superconductivity in the Transition Metals at very Low Temperatures, Ph.D. Thesis, University of California, San Diego.
Johnson, D.L. and D.K. Finnemore, 1967, Phys. Rev. **158**, 376.
Kasuya, T., 1966, S – d and s – f Interaction and Rare Earth Metals, in: Rado, G.T. and H. Suhl, eds., Magnetism, Vol. II B (Academic Press, New York and London 1966) p. 215.
Katzman, H. and J.A. Mydosh, 1972, Z. Phys. **256**, 380.
King, E., J.A. Lee, I.R. Harris and T.F. Smith 1970, Phys. Rev. B **1**, 1380.
Kmetko, E.A., 1971, in: Bennett, L.H., ed., Electronic Density of States (Nat. Bur. Stand., US, Spec. Publ. 323) p. 67.
Knapp, G.S. and R.W. Jones, 1972, Phys. Rev. B **6**, 1761.
Kondo, J., 1963, Progr. Theor. Phys. (Kyoto) **29**, 1.
Koskimaki, D.C. and K.A. Gschneidner, Jr., 1975, Phys. Rev. B **11**, 4463.
Krupka, M.C., A.L. Giorgi, N.H. Krikorian and E.G. Szklarz, 1969, J. Less-Common Metals **19**, 113.
Kuper, C.G., M.A. Jensen and D.C. Hamilton, 1964, Phys. Rev. **134**, A 15.
Lawson, A.C., 1973, J. Less-Common Metals **32**, 173.
Lifshitz, I.M., 1960, Zh. Eksper. Teor. Fiz. **38**, 1569; Sov. Phys. JETP **11**, 1130.
Liu, L., 1975, J. Phys. Chem. Solids **36**, 31.
Löffler, E. and J.A. Mydosh, 1973, Solid State Commun. **13**, 615.
Lou, L.F. and W.J. Tomasch, 1972, Phys. Rev. Lett. **29**, 858.
Louie, S.G. and M.L. Cohen, 1974, Phys. Rev. B **10**, 3237.
Luo, H.L., M.B. Maple, I.R. Harris and T.F. Smith, 1968, Phys. Lett. **27A**, 519.
MacPherson, M.R., G.E. Everett, D. Wohlleben and M.B. Maple, 1971, Phys. Rev. Lett. **26**, 20.
Maple, M.B., 1968, Phys. Lett. **26A**, 513.
Maple, M.B., J. Wittig and K.S. Kim, 1969, Phys. Rev. Lett. **23**, 1375.
Maple, M.B., 1973, Paramagnetic Impurities in Superconductors, in: Suhl, H., ed., Magnetism, Vol. V (Academic Press, New York and London 1973) p. 289.
Maple, M.B. and D. Wohlleben, 1974, Demagnetization of Rare Earth Ions in Metals due to Valence Fluctuations, in: Graham, C.D., Jr., and J.J. Rhyne, eds., Magnetism and Magnetic Materials – 1973, Boston, AIP Conf. Proc. No. 18, Part 1 (American Inst. of Physics – New York 1974) p. 447.
Matthias, B.T., 1957, Superconductivity in the Periodic System, in: Gorter, C.J., ed., Progress in Low Temperature Physics, Vol. II, (North-Holland Publ. Comp. – Amsterdam 1957) p. 138.
Matthias, B.T., H. Suhl and E. Corenzwit, 1958, Phys. Rev. Lett. **1**, 92.
Matthias, B.T., W.H. Zachariasen, G.W. Webb and J.J. Engelhardt, 1967, Phys. Rev. Lett. **18**, 781.

Matthias, B.T., 1969, Systematics of Superconductivity, in: Wallace, P.R., ed., Superconductivity, Vol. 1 (Gordon and Breach, Science Publishers – New York 1969) p. 227.
Matthias, B.T., M. Marezio, E., Corenzwit, A.S. Cooper and H.E. Barz, 1972, Science **175**, 1465.
McMillan, W.L., 1968, Phys. Rev. **167**, 331.
McMillan, W.L. and J.M. Rowell, 1969, Tunneling and Strong-Coupling Superconductivity, in: Parks, R.D., ed., Superconductivity, Vol. 1 (Marcel Dekker, Inc., New York 1969) p. 561.
Moodenbaugh, A.R. and J. Wittig, 1973, J. Low Temp. Phys. **10**, 203.
Moodenbaugh, A.R., D.C. Johnston and R. Viswanathan, 1974, Mat. Res. Bull. **9**. 1671.
Moodenbaugh, A.R., 1975, Superconductivity of Some NaCl Structure Sulfides, Selenides and Phosphides. Ph.D. Thesis, University of California, San Diego.
Myron, H.W. and S.H. Liu, 1970, Phys. Rev. B **1**, 2414.
Nikulin, E.I., N.V. Volkenshtein and V.E. Startsev, 1973, Zh. Eksp. Teor. Fiz. Pis'ma **17**, 470; Sov. Phys. JETP Lett. **17**, 337.
Nücker, N., 1976, Verhandlungen der Deutschen Physikalischen Gesellschaft VI, **11**, 740, private communication and to be published.
Odermatt, R., Ø. Fischer, H. Jones and G. Bongi, 1974, J. Phys. C: Solid State Phys. **7**, L13.
Phillips, N.E., J.C. Ho and T.F. Smith, 1968, Phys. Lett. **27A**, 49.
Probst, C. and J. Wittig, 1972, in: Timmerhaus, K.D., W.J. O'Sullivan and E.F. Hammel, eds., Low Temperature Physics – LT13, Boulder, Vol. 3 (Plenum Publish. Corp., New York) p. 495.
Probst, C., 1974, Die Supraleitung der Elemente Lutetium und Hafnium, Thesis, Technische Universität München, 1974.
Probst, C. and J. Wittig, 1975, unpublished data.
Probst, C. and J. Wittig, 1975, in: Krusius, M. and M. Vuorio, eds., Proc. 14th Internat. Conf. on Low Temp. Phys., Otaniemi, 1975, Vol. 5 (North-Holland Publ. Comp. – Amsterdam) p. 453.
Ratto, C.F., B. Coqblin and E. Galleani d'Agliano, 1969, Advan. in Phys. **18**, 489.
Reale, C., 1975, Thin Solid Films 28, L29.
Riblet, G. and K. Winzer, 1971, Solid State Commun. **9**, 1663.
Rickayzen, G., 1969, The Theory of Bardeen, Cooper, and Schrieffer, in: Parks, R.D., ed., Superconductivity, Vol. 1 (Marcel Dekker, Inc., New York 1969) p. 51.
Roberts, B.W., 1964–1976, Superconducting Materials and Some of their Properties, in: Mendelssohn, K., ed., Progress in Cryogenics, Vol. 4 (Temple Press Books, London 1964) p. 159, and Survey of Superconducting Materials and Critical Evaluation of Selected Properties, J. Phys. Chem. Ref. Data **5**, 581 (1976).
Satoh, T and T. Ohtsuka, 1967, J. Phys. Soc. Japan **23**, 9.
Satoh, T. and K. Kumagai, 1973, J. Phys. Soc. Japan **34**, 391.
Schaufelberger, Ph. and H. Merx, 1975, High Temperatures – High Pressures **7**, 55.
Schaufelberger, Ph., 1976, J. Appl. Phys. **47**, 2364.
Schlapbach, L., 1974, Phys. cond. Matter **18**, 189.
Schwidtal, K., 1962, Z. Phys. **169**, 564.
Shelton, R.N., A.R. Moodenbaugh, P.D. Dernier and B.T. Matthias, 1975, Mat. Res. Bull. **10**, 1111.
Shelton, R.N., R.W. McCallum and H. Adrian, 1976, Phys. Lett. **56A**, 213.
Shen, L.Y.L., 1972, Superconductivity of Tantalum, Niobium and Lanthanum Studied by Electron Tunneling: Problems of Surface Contamination, in: Douglass, D.H., ed., Superconductivity in d- and f-Band Metals, AIP Conf. Proc. No. 4 (American Inst. of Physics – New York 1972) p. 31.
Silbernagel, B.G. and J.H. Wernick, 1973, Phys. Rev. B 7, 4787.
Sinha, S.K., T.O. Brun, L.D. Muhlestein and J. Sakurai, 1970, Phys. Rev. B **1**, 2430.
Smith, J.L. and H.H. Hill, 1976, Bulletin of the American Physical Society, Series II, **21**, p. 383.
Smith, T.F. and W.E. Gardner, 1966, Phys. Rev. **146**, 291.
Smith, T.F. and I.R. Harris, 1967, J. Phys. Chem. Solids **28**, 1846.
Smith, T.F. and H.L. Luo, 1967, J. Phys. Chem. Solids **28**, 569.
Smith, T.F., 1972, Determination of Pressure Dependence of T_c for d- and f-Band Superconductors, in: Douglass, D.H., ed., Superconductivity in d- and f-Band Metals, AIP Conf. Proc. No. 4 (American Inst. of Physics – New York) p. 293.
Smith, T.F. and E.S. Fisher, 1973, J. Low Temp. Phys. **12**, 631.
Spedding, F.H. and J.J. Croat, 1973, J. Chem. Phys. **59**, 2451.
Stager, R.A. and H.G. Drickamer, 1964, Phys. Rev **133A**, 830.
Steglich, F., 1976, Z. Phys. B **23**, 331.
Steinitz, M.O., C.E. Burleson and J.A. Marcus, 1970, J. Appl. Phys. **41**, 5057.
Stern, H., 1975, Phys. Rev. B **12**, 951.
Sternheimer, R.L., 1950, Phys. Rev. **78**, 235.
Sugawara, T., 1965, J. Phys. Soc. Japan **20**, 2252.
Switendick, A.C., 1973, in: Proc. 10th Rare Earth Research Conf., Arizona, Vol. I, Kevane, C.J. and T. Moeller, eds. (USAEC Technical Information Center, Oak Ridge, 1973) p. 235.
Syassen, K. and W.B. Holzapfel, 1975, Solid State Commun. **16**, 533.
Toxen, A.M. and R.J. Gambino, 1968, Phys. Lett. **A28**, 214.
Toxen, A.M. and R.J. Gambino and L.B. Welsh, 1973, Phys. Rev. B **8**, 90.
Tsang, T.W.E., K.A. Gschneidner, Jr. and F.A. Schmidt, 1976, Solid State Comm. **20**, 737.

Probst, C. and J. Wittig, 1977, Phys. Rev. Lett. 39, 1161.

Waber, J.T. and D.T. Cromer, 1965, J. Chem. Phys. **42**, 4116.
Walline, R.E. and W.E. Wallace, 1964, J. Chem. Phys. **41**, 3285.
Wells, P., P.C. Lanchester, D.W. Jones and R.G. Jordan, 1976, J. Phys. F: Metal Phys. **6**, 11.
Wilhelm, M. and B. Hillenbrand, 1970, J. Phys. Chem. Solids **31**, 559.
Wilkinson, M.K., H.R. Child, C.J. McHargue, W.C. Koehler and E.O. Wollan, 1961, Phys. Rev. **122**, 1409.
Williams, H.J., J.H. Wernick, E.A. Nesbitt and R.C. Sherwood, 1962, J. Phys. Soc. Japan **17**, Suppl. B **1**, 91.
Wittig, J., 1968, Phys. Rev. Lett. **21**, 1250.
Wittig, J., 1970, Phys. Rev. Lett. **24**, 812.
Wittig, J., C. Probst and W. Wiedemann, 1972, in: Timmerhaus, K.D., W.J. O'Sullivan and E.F. Hammel, eds., Low Temp. Physics – LT13, Boulder, Vol. 3 (Plenum Publishing Corp., New York) p. 490.
Wittig, J., 1973, The Pressure Variable in Solid State Physics: What about 4f-Band Superconductors? in: Queisser, H.J., ed., Festkörperprobleme – Advances in Solid State Physics, Vol. XIII (Vieweg, Braunschweig) p. 375.
Wittig, J., 1974, Comments Solid State Phys. VI, 13.
Wittig, J., 1975, Z. Phys. B **22**, 139.
Wittig, J., 1976a, Proc. 12th Rare Earth Research Conf., July 18–22, 1976, Vail, Colorado, C.E. Lundin, ed. Vol. 2, p. 866.
Wittig, J., 1976b, Proc. 12th Rare Earth Research Conf., July 18–22, 1976, Vail, Colorado, C.E. Lundin, ed. Vol. 2, p. 873.
Wohlleben, D.K. and B.R. Coles, 1973, Formation of Local Magnetic Moments in Metals: Experimental Results and Phenomenology, in: Suhl, H., ed., Magnetism, Vol. V (Academic Press, New York and London 1973) p. 3.
Wühl, H., A. Eichler and J. Wittig, 1973, Phys. Rev. Lett. **31**, 1393.
Wühl, H., 1976, private communications.
Zachariasen, W.H., 1973, J. inorg. nucl. Chem **35**, 3487.
Zachariasen, W.H. and F.H. Ellinger, 1977, Acta Cryst. A**33**, 155.
Zarubina, O.A., 1973, Fiz. Tverdogo Tela **14**, 2890; Sov. Phys. – Solid State **14**, 2497.
Ziman, J.M., 1972, Principles of the Theory of Solids, 2nd ed. (Cambridge at the University Press 1972).

References to section 6

Arko, A.J., G. Crabtree, J.B. Ketterson, F.M. Mueller, P.F. Walch, L.R. Windmiller, Z. Fisk, R.F. Hoyt, A.C. Mota, R. Viswanathan, D.E. Ellis, A.J. Freeman and J. Rath, 1975, Int. J. Quantum Chem. Symp. No. 9, p. 569.
Baer Y., and G. Busch, 1974, J. Electron Spectrosc. Relat. Phenom. **5**, 611.
Duthie, J.C. and D.G. Pettifor, 1977, Phys. Rev. Lett. **38**, 564.
Endo, S., H. Sasaki and T. Mitsui, 1977, J. Phys. Soc. Japan **42**, 882.
Glötzel, D., 1977, private communication.
Glötzel, D. and L. Fritsche, 1977, Phys. Stat. Sol. (b) **79**, 85.
Höchst H., P. Steiner and S. Hüfner, 1977, J. Magn. Magn. Mater. **6**, 159.
Ihrig, H. and W. Lohmann, 1977, J. Phys. F: Metal Phys. **7**, 1957.
Joseph, R.R., K.A. Gschneidner, Jr. and R.E. Hungsberg, 1972, Phys. Rev. B5, 1878.
Matthias, B.T., E. Corenzwit, J.M. Vandenberg, H. Barz, M.B. Maple and R.N. Shelton, 1976, J. Less-Common Metals, **46**, 339.
Probst, C. and J. Wittig, 1977, Phys. Rev. Lett. **39**, 1161.
Probst, C. and J. Wittig, 1978, to be published in Proc. Int. Conf. Low Temp. High Pressure Physics (Cleveland 1977).
Steiner, P., H. Höchst and S. Hüfner, 1977, J. Phys. F: Metal Phys. **7**, L 145.
Walker E., H.-G. Purwins, M. Landolt and F. Hulliger, 1973, J. Less-Common Metals **33**, 203.

Handbook on the Physics and Chemistry of Rare Earths, edited by K.A. Gschneidner, Jr. and L. Eyring

Chapter 11

KONDO EFFECT: ALLOYS AND COMPOUNDS*

M. Brian MAPLE, Lance E. DeLONG and Brian C. SALES
Institute for Pure and Applied Physical Sciences, University of California, San Diego, La Jolla, California 92093, USA

Contents

Symbols

C = specific heat
ΔC = specific heat jump at the superconducting transition
E_{exc} = excitation energy between lanthanide electron configurations $4f^n$ and $4f^{n-1}$
E_F = Fermi energy
E_ℓ = energy separating centroid of localized state and Fermi level
E_n = energy of lanthanide electron shell configuration $4f^n$
g = Landé's g-factor
h = Planck's constant
H = magnetic field
H_c = critical magnetic field
$\mathscr{H}$ = exchange hamiltonian
$\mathscr{H}_R$ = exchange hamiltonian for lanthanides
$\mathscr{J}$ = exchange interaction parameter
$\boldsymbol{J}$ = total angular momentum operator
k_B = Boltzmann's constant
$\boldsymbol{L}$ = orbital angular momentum operator
n = impurity concentration
$N(E_F)$ = conduction electron density of states at the Fermi level
$\boldsymbol{S}$ = spin angular momentum operator
s = conduction electron spin density
T = temperature
T_c = superconducting transition temperature
T_K = Kondo temperature
T_F = Fermi temperature
T_0 = magnetic moment fluctuation temperature
T_{sf} = magnetic moment fluctuation temperature
T_{RKKY} = characteristic temperature of RKKY interaction
$\mathscr{U}$ = intra-atomic Coulomb repulsion parameter
V_{kl} = conduction electron – localized electron state admixture matrix element
γ = electronic specific heat coefficient

*Supported by the U.S. Energy Research and Development Administration under Contract No. ERDA E (04-3)-34 PA227.

Δ = half width in energy of localized state
δ = crystal field splitting
$\epsilon(n)$ = fraction of time 4f shell has configuration $4f^n$
χ = magnetic susceptibility
μ_B = Bohr magneton
μ_{eff} = effective magnetic moment
ν_0 = valence fluctuation frequency
ρ = electrical resistivity
θ = Curie–Weiss temperature
τ_{sf} = magnetic moment lifetime
τ_0 = valence or interconfiguration fluctuation lifetime

1. Introduction

The interaction between impurity ions with partially filled d or f electron shells and the conduction electrons of a metallic host can lead to variations in certain physical properties with temperature and magnetic field which have come to be associated with the "Kondo effect". In zero magnetic field, these temperature-dependent anomalies in the physical properties scale with a characteristic temperature T_K, the so-called Kondo temperature, above which the matrix-impurity system behaves *magnetically* and below which the matrix-impurity system behaves *nonmagnetically*. The physical properties which exhibit anomalies attributable to the Kondo effect include the electrical resistivity, magnetic susceptibility, thermoelectric power, specific heat; and, in systems where appropriate, superconducting properties such as the critical temperature T_c and the jump in specific heat which occurs at T_c.

With respect to the electrical resistivity, the Kondo temperature roughly separates a high temperature region ($T \gg T_K$) where the resistivity varies linearly with the logarithm of the temperature, and a low temperature region ($T \ll T_K$) where the resistivity saturates to the so-called "unitary limit" as $T \to 0$. For temperatures well above T_K, the magnetic susceptibility resembles a Curie–Weiss law with a Curie–Weiss temperature which is of the order of several times T_K, whereas for temperatures well below T_K, the susceptibility exhibits at most a weak temperature dependence and approaches a finite value as $T \to 0$. The specific heat and thermoelectric power exhibit broad maxima as a function of temperature which peak in the vicinity of T_K.

In matrix-impurity systems in which the matrix is a superconductor and T_K is sufficiently low compared to T_{c_0}, the critical temperature of the pure host, the temperature dependent scattering of conduction electrons by impurity spins may even lead to the striking phenomenon of *re-entrant superconductivity* (where alloys within a certain impurity concentration range exhibit a transition to the superconducting state at a critical temperature T_{c_1} which is followed by a return to the normal state at a second lower critical temperature T_{c_2}) as well as pronounced deviations of the specific heat jump from the BCS law of corresponding states.

Historically, the types of normal state "Kondo anomalies" described above were first studied in *dilute* alloys of 3d (Fe-group) transition metals dissolved in "simple" metal hosts such as the noble metals Cu, Ag and Au. However, in 1965,

Sugawara observed the first resistance minimum phenomenon due to a lanthanide solute in the dilute alloy system YCe. Following this discovery of the Kondo effect in the YCe system, numerous dilute and concentrated lanthanide metallic systems have been investigated over the past decade. Of the thirteen lanthanide ions with partially-filled 4f shells, Kondo-like behavior has been observed for Ce, Pr, Sm, Eu, Tm and Yb.

The Kondo-like anomalies in the normal state physical properties of concentrated lanthanide systems closely resemble those of dilute lanthanide systems. This is true for two reasons. First, the spatial extent of the 4f wave functions of the lanthanide ions is only of the order of one-tenth of an interatomic spacing (substantially smaller than the spatial extent of the 3d wave functions of transition metal ions) so that direct exchange coupling via overlap of the neighboring 4f wavefunctions is virtually negligible. Second, the magnitude of the exchange interaction between the 4f and conduction electrons is only of the order of 0.1 eV so that indirect RKKY exchange (Ruderman and Kittel, 1954; Kasuya, 1956; Yosida, 1957) is relatively weak. In view of the similarity in their physical properties, we consider in this review concentrated as well as dilute assemblages of lanthanide ions with partially-filled 4f electron shells immersed in a sea of conduction electrons. In these systems, the magnetic character of the lanthanide ions can span the entire range between magnetism and nonmagnetism, and with a particular system there can be associated a characteristic temperature above which the lanthanide ions behave magnetically and below which they behave nonmagnetically.

It should be noted that when the characteristic temperature is low, it is invariably referred to as the Kondo temperature T_K, whereas when it is high, it is often identified with a magnetic moment fluctuation temperature which is usually denoted by T_{sf} or T_0 [recent experimental evidence from studies on concentrated lanthanide metallic systems suggests that these magnetic moment fluctuations may be due to temporal fluctuations of the lanthanide ions between two ionic configurations whose occupation number differs by one electron (see section 2)]. These correspondences are, however, based on two distinct microscopic models. One of the models appears to be valid in the magnetic (low T_K) limit; the other seems to be valid in the weakly magnetic or nonmagnetic (high T_{sf} or T_0) limit. To date, no successful unified theory has been developed to connect these two limits in a continuous fashion. This is in spite of the substantial body of experimental data which documents in detail the continuous demagnetization of a lanthanide ion with a partially-filled 4f shell in a metallic environment. Therefore, *we emphasize that there is generally a continuum of types of magnetic behavior between the extreme magnetic and nonmagnetic limits.* (Of course, a dense array of lanthanide ions in a metallic system may undergo a discontinuous cooperative phase transition between two distinct magnetic states upon alloying with another element or the application of an external pressure.) Moreover the physical properties in each magnetic state of this continuum are similar when the temperature is scaled with the appropriate characteristic temperature – hence *it seems highly probable that there is a single physical mechanism that is respon-*

sible for the entire spectrum of magnetic behavior exhibited by numerous metallic lanthanide systems which incorporates the Kondo and spin fluctuation models as limiting cases.

Because of the wide range of magnetic character displayed by the lanthanide metallic systems reviewed herein, they provide a rich testing ground for the concepts and theories which have been advanced to account for Kondo-like anomalies in the physical properties of these systems. However, before reviewing the Kondo-like behavior of dilute and concentrated lanthanide metallic alloys and compounds in sections 3 and 4 of this article, respectively, we briefly discuss a number of models in the following section which have been proposed to describe the systems which exhibit Kondo-like behavior in their physical properties. The article is concluded in section 5.

2. Concepts and models for Kondo-like systems

In the traditional view, the interaction which is believed to be responsible for the Kondo effect proceeds via the conduction electron-impurity spin exchange interaction. The hamiltonian for this interaction (the so-called s–d or s–f hamiltonian) is

$$\mathcal{H} = -2\mathcal{J}\boldsymbol{S}\cdot\boldsymbol{s}, \tag{11.1}$$

where $\mathcal{J}$ is a parameter that characterizes the sign and magnitude of the interaction, $\boldsymbol{S}$ is the spin on the impurity ion, and $\boldsymbol{s}$ is the conduction electron spin density at the impurity site. The strong spin–orbit coupling found in lanthanide ions suggests that a more appropriate interaction hamiltonian (deGennes, 1962a) is

$$\mathcal{H}_R = -2\mathcal{J}(g-1)\boldsymbol{J}\cdot\boldsymbol{s} \tag{11.2}$$

which is obtained by replacing $\boldsymbol{S}$ by its projection onto the total angular momentum vector $\boldsymbol{J} = \boldsymbol{L} + \boldsymbol{S}$ of the Hund's rule multiplet, i.e.,

$$\boldsymbol{S} \rightarrow [\langle \boldsymbol{S}\cdot\boldsymbol{J}\rangle / J(J+1)]\boldsymbol{J} = (g-1)\boldsymbol{J}, \tag{11.3}$$

where g is the Landé g-factor for the appropriate Hund's rule ground state.

Calculations based on the conduction electron-impurity spin exchange hamiltonian [eq. (11.1)] yield the characteristic anomalies in the physical properties which are associated with the Kondo effect when $\mathcal{J}$ is negative. This was first demonstrated by Kondo in 1964 when he explained the "resistance minimum phenomenon" first observed for 3d transition element impurities in noble metal hosts. Kondo's theory consisted of a perturbation calculation of the scattering of conduction electrons by the impurity spins to third order in the exchange coupling parameter $\mathcal{J}$. His calculation of the electrical resistivity yielded a logarithmic temperature dependence in agreement with experiment, but exhibited a divergence at a characteristic temperature, T_K, given by

$$T_K \sim T_F \exp[-1/N(E_F)|\mathcal{J}|] \tag{11.4}$$

which has since come to be known as the Kondo temperature. Here, T_F is the Fermi temperature and $N(E_F)$ is the host density of states at the Fermi level.

Since Kondo's original calculation, a great deal of effort has been put forth by theorists to calculate the various physical properties of matrix-impurity systems for temperatures both above and below T_K (see, for example, Suhl, 1973; Grüner and Zawadowski, 1964). This has lead to a physical interpretation of the Kondo temperature as the characteristic temperature for the formation of a "quasi-bound" state in which the conduction electron spins tend to antiferromagnetically compensate the spins of the impurities with the degree of compensation increasing gradually as the temperature is lowered through T_K. At temperatures well below T_K the many-body electron-impurity spin system behaves non-magnetically (i.e., the magnetic susceptibility approaches a constant value as $T \to 0$) whereas at temperatures well above T_K, it behaves magnetically, giving rise to a Curie–Weiss temperature dependence of the magnetic susceptibility and the temperature-dependent anomalies in the electrical resistivity, specific heat and thermoelectric power noted in the introduction.

The reader is cautioned to observe, however, that existing theories for the various physical properties of Kondo systems do not provide a self-consistent definition for the characteristic temperature as defined by the temperatures of the typically broad anomalies in the thermoelectric power, electrical resistivity, heat capacity and magnetic susceptibility. Thus the values of the characteristic temperature inferred from different measurements may differ by as much as an order of magnitude.

Many of the earlier theories gave satisfactory results for temperatures above and around T_K, but were inadequate at temperatures below T_K. Recently, new theoretical techniques, pioneered by Wilson (see, for example, Wilson, 1975; Nozieres, 1975), have been successfully applied to the Kondo problem and allow one to pass continuously through T_K from the weak coupling ($T \gg T_K$) to the strong coupling ($T \ll T_K$) limit. The interested reader is referred to a brief critical discussion of these theoretical developments in a recent article in Physics Today (July, 1976, p. 17).

The antiferromagnetic conduction electron-impurity spin exchange interaction ($\mathcal{J} < 0$) which is responsible for the temperature-dependent Kondo anomalies originates from hybridization (mixing) between the conduction electron states and the localized impurity states (Anderson and Clogston, 1961; Kondo, 1962; deGennes, 1962b). Schrieffer and Wolf (1966) showed that when hybridization is included, the exchange hamiltonian can be written with an effective *negative* conduction electron-impurity spin exchange interaction parameter of the following form

$$\mathcal{J} \sim \frac{\langle V_{kl}^2 \rangle \mathcal{U}}{E_\ell (E_\ell + \mathcal{U})}, \qquad (\Delta \ll \mathcal{U}) \tag{11.5}$$

if the hybridization between conduction electron and localized electron states is *not too strong*. Here, V_{kl} is the matrix element of the interaction which admixes conduction electron and localized electron states, $\mathcal{U}$ is the intra-atomic Coulomb

repulsion parameter which scales the splitting of spin-up and spin-down states in the Friedel–Anderson model (Friedel, 1958; Anderson, 1961), E_ℓ is the energy separating the centroid of the localized impurity state and the Fermi level E_F, and Δ is the half-width in energy of the localized state. The "Schrieffer–Wolf transformation" [eq. (11.5)] has been generalized to include orbital contributions for the lanthanides and applied to Ce and its "4f-hole" counterpart Yb by Coqblin and Schrieffer (1969). This negative contribution competes with the positive Heisenberg contribution to the exchange interaction, and if the hybridization is strong enough, the net conduction electron-impurity spin exchange interaction can be negative. Here it is assumed that the amount of hybridization is strong enough to generate a negative exchange interaction, but not so strong as to threaten the long-lived status of the impurity moment and hence to make the exchange interaction hamiltonian inappropriate as a model describing the interaction between the conduction electrons and the impurity ions.

The term "long-lived" signifies that the lifetime τ_{sf} of the impurity moment is large compared to thermal fluctuation lifetimes in the temperature or magnetic field range of interest. In other, so-called "localized spin fluctuation" models (consult Mills et al., 1975; and references cited therein), the local moment on the impurity site is alleged to fluctuate with a frequency τ_{sf}^{-1}. The magnetic moment lifetime decreases as the amount of hybridization between conduction electron and impurity electron states increases. This implies an increase in V_{kl} or a decrease in $|E_\ell|$ [cf. eq. (11.5)]. Thus it is apparent that only a moderate admixture of conduction electron and impurity electron states is admissible for the exchange hamiltonian to remain a reasonable starting point for a theoretical description of Kondo systems. That is to say, the very same increase in hybridization (increase in V_{kl} or decrease in $|E_\ell|$) which leads to an increase in the Kondo temperature T_K, results in a decrease of the localized spin fluctuation lifetime, which, in turn, ultimately jeopardizes the validity of the exchange hamiltonian as a description of systems with arbitrarily large characteristic temperatures.

In the event that the amount of hybridization is too strong for the exchange hamiltonian to be an adequate starting point for a theoretical description of the Kondo-like anomalies in the physical properties, the characteristic temperature is often identified with a spin fluctuation temperature T_{sf} which has the obvious definition $T_{sf} \equiv h/k_B\tau_{sf}$. In this view, T_{sf}, rather than T_K, is a boundary which separates high temperature (compared to T_{sf}) magnetic behavior from low temperature nonmagnetic behavior.

At temperatures much higher than T_{sf}, the temporal fluctuations of the magnetic moment are slow compared to thermal fluctuations, and the susceptibility is expected to be strongly temperature dependent, behaving like a Curie–Weiss law with a Curie–Weiss temperature of the order of T_{sf}. At temperatures much lower than T_{sf}, the intrinsic magnetic moment fluctuations are rapid compared to thermal fluctuations, and the resultant dynamical magnetic moment averages to zero over the timescale of interest so that the susceptibility approaches a constant value in the limit $T \to 0$. In this model, anomalies in other

physical properties are expected such as a peak in the thermoelectric power near T_{sf}. Low temperature resistivity minima are anticipated with solute contributions which vary as $1-(T/T_{sf})^2$ for $T \ll T_{sf}$ as well as large enhancements of the electronic specific heat coefficient γ.

Although the basic mechanism involved in spin fluctuation models is quite different from models based on the exchange interaction, the general behavior of the physical properties as a function of temperature and magnetic field are quite similar; and, in practice, it is difficult to distinguish a matrix-impurity system with a high Kondo temperature from one which exhibits localized spin fluctuations. For this reason we consider systems which have been associated with both models in this article, realizing that the Kondo effect, when approached from the point of view of the exchange model, is simply one regime in a continuous spectrum corresponding to differing degrees of hybridization of conduction electron and localized electron states.

It is also appropriate to mention recent experimental work on *concentrated* metallic lanthanide alloys and compounds which exhibit Kondo-like anomalies in their physical properties. This work indicates that lanthanide ions which behave "nonmagnetically" below a characteristic temperature T_0 (as evidenced by a magnetic susceptibility which, below T_0, approaches a finite value as $T \to 0$) can be quite generally pictured to have a time-averaged 4f shell occupation which is nonintegral. The nonintegral 4f shell occupation (or nonintegral valence) can actually be observed by means of measurements of the lattice constant, Mössbauer isomer shift, soft X-ray absorption and X-ray photoemission spectroscopy (XPS).

A physical interpretation for the correlated existence of the "nonmagnetic" susceptibility at low temperatures ($T \ll T_0$) and the intermediate 4f shell occupation number has recently been advanced by Maple and Wohlleben (1971, 1974) using a model proposed by Hirst (1970). They propose that the 4f shell of a lanthanide ion in these intermediate valence systems undergoes temporal valence or interconfigurational fluctuations (ICF) between the configurations $4f^n$ and $4f^{n-1}$ accompanied by the emission and absorption of a conduction electron. The lifetime τ_0 associated with the fluctuations between the states $4f^n$ and $4f^{n-1}$ is believed to be of the order of 10^2 K for several compounds which is roughly the temperature below which the magnetic susceptibility saturates to a constant value as $T \to 0$. This idea is consistent with "slow" Mössbauer measurements as well as "fast" XPS measurements. Mössbauer measurements cannot resolve the isomer shift for the two configurations $4f^n$ and $4f^{n-1}$, but rather yield an isomer shift which is intermediate between that expected for the two configurations. The characteristic measuring time appropriate for this experiment is of the order of 10^{-9}–10^{-7} sec which gives a lower limit $\sim 10^7$–10^9 cps for the ICF frequency τ_0^{-1}. On the other hand, the "fast" XPS measurements are able to resolve f-hole excitation spectra which correspond to the simultaneous presence of both configurations $4f^n$ and $4f^{n-1}$. The characteristic time for XPS is of the order of 10^{-17} sec which provides an upper limit $\sim 10^{17}$ cps for τ_0^{-1}.

These interconfiguration fluctuations are believed to occur when the energies

E_n and E_{n-1} of the configurations $4f^n$ and $4f^{n-1}5d^1$ are approximately degenerate in energy within the width $\Delta \simeq \pi\langle V_{kl}^2\rangle N(E_F)$. The energy broadening Δ of the 4f states again is supposed to arise from hybridization of the localized 4f states and the extended states of the conduction band. Thus at temperatures well below T_0, the physical properties of lanthanide ICF systems are expected to, and indeed do, resemble those of a metal with a narrow band of width Δ which overlaps the Fermi level. In such cases one expects to observe large linear specific heat coefficients γ which can be as high as $\sim 10^2$ states/eV atom (compared to a few states/eV-atom for normal nonmagnetic metals) and the characteristic saturation (absence of a divergence in susceptibility or magnetic order) of the magnetic susceptibility in the limit $T \to 0$ (reminiscent of exchange enhanced paramagnets such as Pd). Although no microscopic theory for ICF systems has been developed, it is significant to note that Kondo-like anomalies are often observed such as a pronounced peak in the specific heat and thermoelectric power near the characteristic temperature T_0 and an electrical resistivity minimum followed by an increase in resistivity with decreasing temperature.

In contrast, in systems where the excitation energy between the two configurations, $E_{exc} = E_n - E_{n-1}$ is much larger than Δ, interconfiguration fluctuations are "blocked" by energy considerations, and the simple ionic limit ($\tau_0 \to \infty$), which typifies the behavior of most lanthanide ions in a metallic environment, is recovered. Here, the lanthanide ions carry well-defined magnetic moments which are consistent with Hund's rules, giving rise to Curie–Weiss behavior of the magnetic susceptibility as a function of temperature with crystal-field and Van Vleck modifications, magnetic order, and so on.

Finally, it is interesting to note that the criterion for the formation of a local moment in the ICF model is roughly given by the relation

$$\Delta/E_{exc} \lesssim 1 \tag{11.6}$$

which can be compared to the Hartree–Fock criterion which is given by

$$\Delta/\mathcal{U} \lesssim 1 \tag{11.7}$$

where $\mathcal{U}$ is the previously mentioned intra-atomic Coulomb repulsion which splits spin-up and spin-down states in the Friedel–Anderson model. Thus in the ICF model, one can retain the strong correlations between electrons within the 4f shell, which have a characteristic energy $\mathcal{U} \sim 5$–10 eV, and still describe nonmagnetic situations even though Δ is only of the order of 10^{-2} eV, as long as $E_{exc} < \Delta$. Physically, the nonmagnetic behavior can be visualized as arising from the "randomizing" influence of the interconfiguration fluctuations on the orientation of the magnetic moment for either of the correlated Hund's rule $4f^n$ and $4f^{n-1}$ configurations in an applied magnetic field. In magnetic fields which are small compared to T_0, the magnetic moment cannot survive an appreciable fraction of the period of its Zeeman precession in the magnetic field before the 4f shell spontaneously emits or absorbs an electron during the passage to any of the Zeeman levels of the complementary configuration. Phenomenologically, this leads to the following form for the magnetic susceptibility (Maple and

Wohlleben, 1974; Sales and Wohlleben, 1975)

$$\chi(T) = \frac{\epsilon(n)[\mu_{\text{eff}}(n)]^2 + [1 - \epsilon(n)][\mu_{\text{eff}}(n-1)]^2}{3k_B(T + T_0)} \tag{11.8}$$

where $\epsilon(n)$ is the fraction of the time that the 4f shell has the configuration $4f^n$ and T_0 represents the randomizing influence of the interconfiguration fluctuations.

For more detailed reviews of various theoretical aspects concerning mixed-valence rare earth alloys and compounds, the reader is referred to articles by Hirst (1975), Mott (1974), Varma (1976), Goncalves da Silva and Falicov (1975), Rosengren and Johansson (1976), Khomskii and Kocharjan (1976), Anderson and Chui (1974), Stevens (1976), Wohlleben and Coles (1973), and references cited therein, (also see ch. 20, section 6).

3. Kondo-like behavior in dilute lanthanide impurity systems

3.1. *Introduction*

Dilute magnetic impurity systems are interesting with respect to the problem of the physical behavior of a localized magnetic moment in a metallic environment because they approximate the simplest possible system: one in which the conduction electrons of the host interact with a single *isolated* impurity. The various theoretical models treating this interaction are generally restricted to the dilute impurity limit to avoid the additional complications introduced when the magnetic impurities are allowed to interact with each other via the indirect RKKY exchange interaction.

Early work on dilute lanthanide systems was motivated by the vast experimental and theoretical effort that had been expended on understanding dilute magnetic 3d impurities in noble metal hosts. In 1965, Sugawara discovered a resistance minimum in the YCe system, providing the first evidence of Kondo behavior for a lanthanide solute. This led to the discovery of numerous lanthanide Kondo systems which exhibited anomalies in their physical properties qualitatively identical to those found in 3d Kondo systems.

Working with lanthanide systems offers two major advantages over their 3d counterparts. First, with lanthanide systems, one can deal with relatively concentrated alloys and yet preserve the isolated impurity limit to a good approximation. As we noted in the Introduction (section 1), this is due to the small spatial extent of the 4f wavefunctions (of the order of one-tenth of an interatomic spacing) which implies little direct interaction between neighboring lanthanide ions, and the relatively small magnitude of the exchange interaction parameter ($|\mathcal{J}| \sim 0.1$ eV). The concentrated systems are discussed in the next section; however, it should be emphasized that the anomalies observed in the physical properties of both concentrated and dilute lanthanide systems are qualitatively identical. Hence, one frequently can perform measurements on a

concentrated system, where the measurement is simpler due to the larger impurity-host signal ratio, and then extrapolate to the dilute impurity limit. This is a very powerful technique since the variety of experiments possible is greatly increased.

Second, it was noticed by Matthias and coworkers (Matthias et al., 1958) that the superconducting transition temperature of La was strongly depressed by the addition of magnetic lanthanide impurities (particularly Ce). This led to considerable experimental and theoretical research on the effects of magnetic impurities on the superconducting properties of the host. The subsequent agreement between experiment and theory is quite striking as evidenced, for example, by the early success of the Abrikosov–Gor'kov (AG) theory (Abrikosov and Gor'kov, 1961) and the prediction by Müller–Hartmann and Zittartz (1971) of re-entrant superconductivity which was subsequently observed in several matrix-Ce impurity systems. Because of the close correspondence between experiment and theory for matrix-impurity systems, it has been possible to use magnetic impurities to investigate the superconductivity of a host, or the effects of impurities on the superconductivity of a host to probe the magnetic state of the solute ions (see, for example, several reviews by Maple, 1972, 1973, 1976).

In this section, we discuss examples of dilute lanthanide systems which exhibit Kondo-like anomalies in both their normal and superconducting state physical properties.

3.2. *Cerium impurity systems*

The system LaCe is one of the first and the most extensively studied of the dilute lanthanide systems in which the Kondo effect has been observed. Measurements of the low temperature electrical resistivity by Sugawara and Eguchi (1966) revealed a resistivity minimum near 6 K in LaCe similar to that first observed in the noble metal based −3d (Fe group) impurity systems (Heeger, 1969 and references therein). Measurements on this system to lower temperatures have revealed that the Ce incremental resistivity varies as $(-\log T)$ between 0.4 and 6 K for sufficiently dilute Ce concentrations (Sugawara and Eguchi, 1969) and that there is a concentration dependent maximum which extrapolates to $T_m = 0.17$ K as $n \to 0$ where n is the Ce impurity concentration (Wollan and Finnemore, 1970). These features suggest that T_K is low, probably of the order of 0.2 K, since the resistivity is expected to saturate to the unitarity limit for $T \leqslant T_K$. This value is close to other estimates of the Kondo temperature for LaCe which range from ~0.1 to ~0.6 K (Sugawara and Eguchi, 1969; Kim and Maple, 1970; Gey and Umlauf, 1971; Flouquet, 1971). The absence of a peak in the thermoelectric power above 7 K is consistent with a low Kondo temperature for this system (Sugawara and Eguchi, 1969).

Sugawara and Eguchi (1966) also reported on the behavior of the magnetic susceptibility of LaCe alloys which they interpreted in terms of a splitting of the

Ce J = $\frac{5}{2}$ multiplet into a Γ_7 doublet and a Γ_8 quartet in the cubic crystal field of the fcc La matrix. They also reported on the superconducting properties (Sugawara and Eguchi, 1966, 1967) such as the anomalously large depression of the superconducting transition temperature T_c of La by Ce additions (compared to other R additions) first reported by Matthias et al. (1958) and on the behavior of T_c as a function of Ce concentration as well as the temperature dependence of the critical magnetic field H_c. From this work, they inferred that the Kondo temperature T_K was ~0.1 K.

Following the pioneering work of Sugawara and Eguchi, measurements of the magnetic susceptibility of LaCe alloys were reported in two publications by Edelstein (1968) and Edelstein et al. (1971). From these measurements, they inferred values of T_K of the order of 20 K. However, these analyses did not take into account crystal field effects. Recent calculations of the magnetic susceptibility of matrix-impurity systems which simultaneously exhibit crystal-field effects and the Kondo effect have been carried out by DeGennaro and Borchi (1973, 1974). Their analysis of Edelstein's magnetic susceptibility data for the LaCe system gave reasonable values for the Γ_7 ground state–Γ_8 excited state splitting of 110–130 K and low values ~0.4–0.8 K for T_K. Nuclear orientation measurements on the LaCe system reported by Flouquet (1971) yield a value of ~0.1 K for T_K. Specific heat measurements on the LaCe system by Culbert and Edelstein (1974) show a broad Kondo anomaly with a peak near 1.2 K which is not inconsistent with a low Kondo temperature. We note that Hall effect measurements on the LaCe system have been reported by Fert and Jaoul (1972).

A number of measurements on the LaCe system have been made under pressure. Smith (1966) reported that the depression of T_c of La by Ce impurities increases markedly with pressure in the range 0–10 kbar, whereas the depression of the T_c of La by other R impurities shows only a small decrease with pressure in this range. A subsequent study by Maple et al. (1969) to pressures as high as 140 kbar revealed that the depression of T_c actually exhibits a pronounced maximum near 15 kbar which is followed by a decrease to a relatively small depression which is nearly constant above ~100 kbar. These results were interpreted as due to a pressure-induced continuous demagnetization of the Ce impurities due to the increased mixing of the Ce localized 4f states with conduction electron states as the pressure was increased. Kim and Maple (1970) studied the change in the logarithmic slope of the Ce incremental resistivity, $d(\Delta\rho)/d(\log T)$, associated with the Kondo effect in the LaCe system under pressure to ~20 kbar. They found that $|d(\Delta\rho)/d(\log T)|$ also exhibited a maximum near 15 kbar as a function of pressure. Similar results for the behavior of the depression of T_c and $|d(\Delta\rho)/d(\log T)|$ for LaCe as a function of pressure were obtained by Gey and Umlauf (1971), although their interpretation of the data differed somewhat from that of Maple et al. (1969) and Kim and Maple (1970). The reader is referred to several review articles for a detailed description of these pressure experiments on LaCe and their interpretation (Maple, 1972, 1973, 1976). Nuclear orientation measurements under pressure to ~10 kbar were recently reported by Benoit et al. (1974a), who inferred that T_K increases initially with

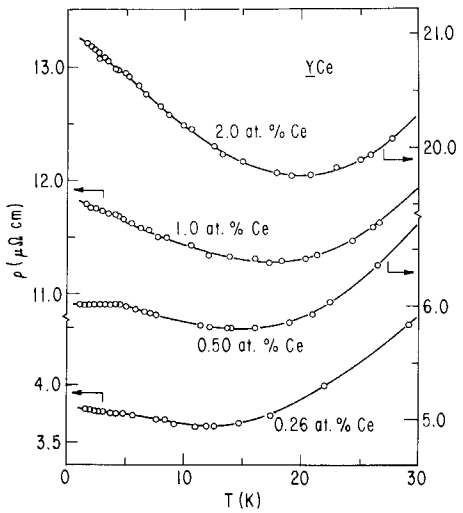

Fig. 11.1. Electrical resistivity of YCe alloys vs temperature. The break in slope near 4.3 K is due to superconductivity of Ta impurities in the Y starting material [after Sugawara (1965)].

pressure, which is consistent with an increased amount of itinerant-local electron mixing with increasing pressure.

Prior to the studies on the LaCe system, Sugawara (1965) had found that Ce impurities dissolved in an Y host give rise to the resistance minimum phenomenon. Sugawara's original data are shown in fig. 11.1. From these and additional low temperature data, Sugawara and Yoshida (1968) extracted the temperature dependence of the incremental resistivity $\Delta\rho$ contributed by the Ce impurity ions; i.e., $\Delta\rho(T) = \rho_{YCe}(T) - \rho_Y(T)$. These data are shown in fig. 11.2. The incremental resistivity was found to have the following characteristic form below 5 K –

$$\Delta\rho = \rho_0[1 - (T/\Theta)^2] \tag{11.9}$$

where $\Theta = 42$ K. For this type of variation of $\Delta\rho$ with temperature which is appropriate for the temperature range $T \ll T_K$, T_K is expected to be of the order of Θ, or 40 K. This is consistent with a previous estimate of T_K for the YCe system of 20–40 K by Nagasawa et al. (1968), which was based on magnetic susceptibility and thermoelectric power measurements. The magnetic susceptibility conformed to a Curie–Weiss temperature dependence between ~20 and 200 K with an effective moment of $\sim 2.3\,\mu_B$ and a Curie–Weiss temperature of ~ -40 K, while the thermoelectric power exhibited a peak near 20 K. Again, splitting of the Ce^{3+} $J = \frac{5}{2}$ multiplet into three doublets in the hexagonal crystalline electric field of the Y matrix was not taken into account in this work. Crystal field effects were considered, however, in a later investigation of single crystal YCe samples in which magnetic susceptibility, electrical resistivity and specific heat measurements were made (Sugawara and Yoshida, 1971). Borchi and

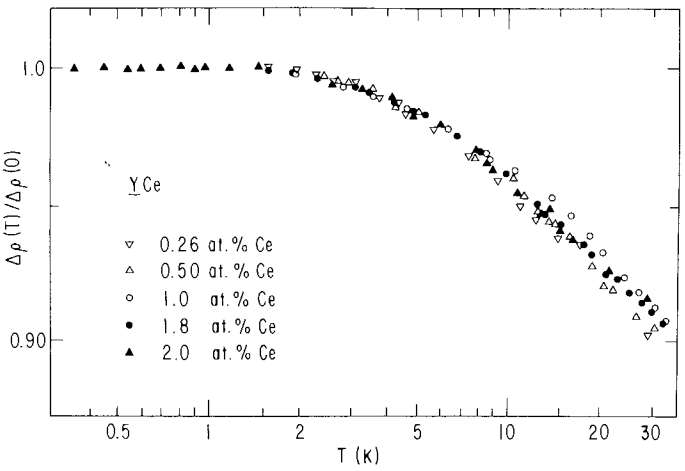

Fig. 11.2. Cerium solute contribution to the electrical resistivity of YCe alloys, normalized to its value at 0 K, vs temperature. The Ce contribution at 0 K is equal to 12.0 ± 1.5 $\mu\Omega$ cm/at.% Ce [after Sugawara and Yoshida (1968)].

DeGennaro (1974) calculated the magnetic susceptibility for single crystal YCe alloys, including crystal field and Kondo effects simultaneously, as they did for LaCe, and obtained good agreement with experiment for the case where the external magnetic field was parallel to the c-axis of the crystal. The technique of nuclear magnetic resonance has also been applied to YCe alloys (polycrystalline) by Silhouette (1970).

Like the LaCe system, the YCe system has been studied under pressure. The electrical resistivity has been measured as a function of pressure to ~ 140 kbar by Maple and Wittig (1971) and to 40 kbar by Dietrich et al. (1972). The results are consistent with a pressure-induced demagnetization of the Ce impurity ions, and an initial increase of T_K with pressure.

Several other binary matrix-Ce impurity systems have been studied in connection with the Kondo effect. Delfs et al. (1975) measured the depression of T_c as a function of Ce concentration and the normal state electrical resistivity anomaly associated with the Kondo effect in quench-condensed films of PbCe and InCe. Their analysis of the results indicated that $T_K \sim 1$ K for PbCe and $T_K \lesssim 0.1$ K for InCe. Nuclear orientation measurements have been made on AuCe alloys by Flouquet and Marsh (1970) and on AgCe alloys by Flouquet (1971). The results of both studies indicate that the Ce magnetic moments are long-lived in Au and Ag hosts, but there is probably no Kondo effect (i.e., $\mathcal{J} > 0$). This is in contrast to the thermoelectric power measurements of Gainon et al. (1967) which indicated unusually large room temperature values for AuCe and AgCe. Hedgcock and Petrie (1970) performed magnetic susceptibility and electrical resistivity measurements on MgCe alloys. From these results they inferred that Ce was magnetic, but that there was no Kondo effect. Burr and Pirich (1975)

interpreted their magnetic susceptibility measurements on monocrystalline MgCe alloys in terms of a crystal field splitting of the Ce^{3+} $J = \frac{5}{2}$ multiplet.

A continuous demagnetization of Ce impurities which proceeds with increasing Th composition in the (La, Th)Ce system appears to be an analog of the pressure-induced demagnetization of Ce impurities in the LaCe system. This was first inferred from a recent study of superconductivity in the (La, Th)Ce system which showed that the initial depression of T_c with Ce concentration, $(-dT_c/dn)_{n=0}$, exhibits a pronounced maximum as a function of Th composition similar to that which occurs as a function of pressure in the LaCe system (Ortega et al., 1974). Following this initial work, detailed measurements were made of T_c/T_{c_0} vs Ce impurity concentration (Huber et al., 1974) and $\Delta C/\Delta C_0$ vs T_c/T_{c_0} for various La, Th host compositions (Luengo et al., 1974; Luengo et al., 1975). The resultant T_c/T_{c_0} vs n curves displayed in the three dimensional plot in fig. 11.3, show the various types of behavior which are found across the continuum from LaCe to ThCe; the pronounced maximum in the initial depression of T_c vs n, the smooth sweep from negative to positive curvature, and the appearance of re-entrant superconductivity, similar to that

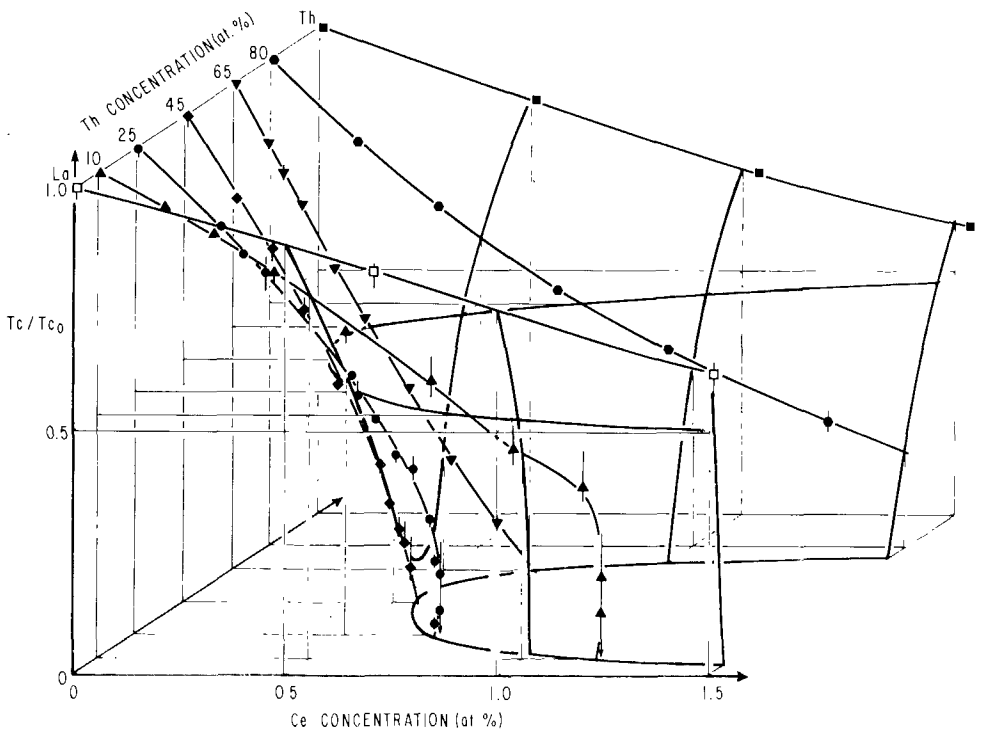

Fig. 11.3. Normalized transition temperature T_c/T_{c_0} vs. Ce concentration and Th concentration for (La, Th)Ce. The curves of T_c/T_{c_0} vs Ce concentration for the ($La_{0.90}Th_{0.10}$)Ce and the ($La_{0.75}Th_{0.25}$)Ce systems are re-entrant [after Huber et al. (1974)].

observed first in the (LaCe)Al_2 system (Riblet and Winzer, 1971; Maple et al., 1972) to be discussed below. Like the initial depression of T_c with n which exhibits a maximum at a La, Th host composition of ~45 at.% Th, the initial depression of $\Delta C/\Delta C_0$ with T_c/T_{c_0} sweeps through a maximum at a La, Th composition of ~15 at.% Th. These characteristic resonant variations of the initial depression of T_c/T_{c_0} with n and $\Delta C/\Delta C_0$ with T_c/T_{c_0} in the (La, Th)Ce system have been interpreted as due to the continuous passage of the Ce impurity magnetic moments from long-lived in La-rich La, Th matrices to short-lived in Th-rich La, Th matrices.

Indeed, an earlier investigation of the ThCe system revealed that the depression of T_c/T_{c_0} with n followed a modified exponential relation of the form $T_c/T_{c_0} = \exp[-An/(1-Dn)]$, while the depression of $\Delta C/\Delta C_0$ with T_c/T_{c_0} conformed to the linear BCS law of corresponding states (Huber and Maple, 1970). The modified exponential relation for T_c/T_{c_0} vs n was derived theoretically by Kaiser (1970) for matrix-impurity systems in which the impurities contribute localized d or f states which are nonmagnetic in the sense of the Friedel–Anderson model (i.e., $\pi\Delta/U > 1$); A and D can be related to the Friedel–Anderson parameters $N_l(E_F)$ and U which characterize the localized d or f state. On the basis of thermoelectric power measurements, Cooper and Rizzuto (1973) have suggested that the characteristic spin fluctuation temperature of the ThCe system is of the order of 10^3 K. Measurements of the lattice constant as a function of relative Th–Ce composition indicate that the valence of Ce is ~3.25 in the ThCe system up to ~20 at.% Ce (Harris and Raynor, 1964).

The data for the initial depression of T_c/T_{c_0} with n and $\Delta C/\Delta C_0$ with T_c/T_{c_0} for the (La, Th)Ce system have been analyzed in terms of the theory of Müller–Hartmann and Zittartz (1970; 1972) for superconducting-Kondo systems and found to be consistent with an increase of T_K with increasing Th content over an appreciable range of La, Th host compositions. However, it was found that the theory failed to describe the specific heat data for Th-rich (La, Th)Ce alloys. This discrepancy between theory and experiment was attributed to the inappropriateness of the conduction electron-impurity spin exchange hamiltonian for situations in which the solute moments are short-lived. The studies of the superconducting properties of the (La, Th)Ce system also include measurements of the upper critical field for a series of $La_{0.80}Th_{0.20}Ce$ alloys which exhibit re-entrant superconductivity (Fertig, 1976). In addition to the aforementioned superconducting properties, the normal state electrical resistivity (Peña and Meunier, 1974) and magnetic susceptibility (Huber et al., 1975) of the (La, Th)Ce system have been measured as a function of La, Th composition. The slope of the Ce solute resistivity which is linear in log T exhibits an initial increase and then falls off smoothly to zero at ~50 at.% Th as the Th concentration is increased. The magnetic susceptibility measurements are especially interesting since they document the Ce impurity demagnetization directly. The diminution of the Ce magnetic moment with increasing Th concentration is evident in the inverse susceptibility vs temperature plots for various (La, Th)Ce alloys which are reproduced in fig. 11.4.

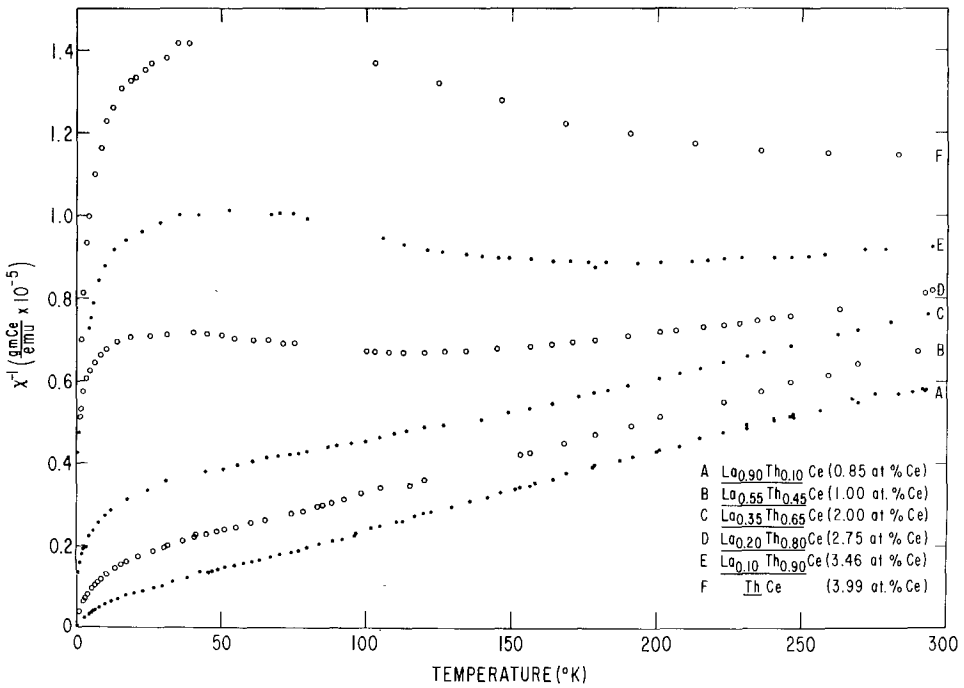

Fig. 11.4. Inverse magnetic susceptibility vs temperature for (La, Th)Ce alloys with La, Th matrix compositions of 10, 45, 65, 80, 90 and 100 at.% Th [after Huber et al. (1975)].

There have been a number of other experiments in which the composition of a binary alloy solvent has been varied to induce changes in the magnetic character of Ce solutes which yield results similar to those discussed above for the (La, Th)Ce system. The (Y, Th)Ce and (Sc, Th)Ce systems have been studied through measurements of T_c/T_{c_0} vs n by Huber and Maple (1972) and $\Delta C/\Delta C_0$ vs T_c/T_{c_0} by Sereni et al. (1975). The results show that Ce impurities become more magnetic as Y is alloyed with Th and less magnetic when Sc is alloyed with Th with respect to their magnetic behavior in the pure Th host. Masuda and coworkers (Aio et al., 1974; Takeuchi et al., 1975) have studied the (La, Y)Ce system through measurements of the depressions of T_c/T_{c_0} with n and $\Delta C/\Delta C_0$ with T_c/T_{c_0} and of the variation of the upper critical field with temperature. Here, the effect of adding Y to La is similar to that of adding Th to La in that it results in an increase of T_K. Peterson et al. (1976) have studied the Ce solute resistivity in the (La, Y)Ce and (Lu, Y)Ce systems for a fixed Ce concentration of 2 at.% They find that the slope $|d(\Delta\rho)/d(\log T)|$ varies markedly with the average atomic volume of the alloy host and shows a sharp maximum for the host composition $La_{0.95}Y_{0.05}$. These authors discuss the analogy of their experiments with the pressure experiments on LaCe and YCe described previously.

The Kondo effect in a matrix-lanthanide impurity system in which the metallic matrix is a compound, rather than an element, was first discovered for the

system (LaCe)Al_2 by Maple and Fisk (1968; Maple, 1969). Since then, many other matrix-impurity systems in which the matrix is a compound that exhibits Kondo-like anomalies have been discovered and studied. These include (LaCe)B_6 (Winzer and Samwer, 1975), (YCe)B_6 (Maple and Fisk, 1968), (LaCe)$_3$Al (Aoi and Masuda, 1974), (LaCe)$_3$In (Maple and Kim, 1969; Jones et al., 1972), (LaCe)In_3 (van Maaren and van Haeringen, 1975), (LaCe)Pd_3 (Rao et al., 1971) and (YCe)Al_2 (Purwins et al., 1972). Of all these, the system (LaCe)Al_2 has been by far the most extensively investigated, and we therefore discuss the properties of this exemplary matrix-impurity Kondo system in some detail. Moreover, the (LaCe)Al_2 system offers the desirable features that single-phase alloys may be readily prepared and that Ce interimpurity interactions are relatively weak in contrast to the case of LaCe alloys.

The first indication of the existence of a Kondo effect in the (LaCe)Al_2 system was provided by measurements of the initial depression of T_c, $(-dT_c/dn)_{n=0}$, of $LaAl_2$ by R impurities (Maple and Fisk, 1968; Maple, 1969). The results of these measurements, which are shown in fig. 11.5, revealed that $(-dT_c/dn)_{n=0}$ is anomalously large for Ce impurities. This is similar to the behavior previously observed in the LaCe system (Matthias et al., 1958), also displayed in fig. 11.5, and suggests by analogy that the conduction electron-impurity spin exchange coupling in the (LaCe)Al_2 system is large and antiferromagnetic. These measurements were followed by measurements (Maple and Fisk, 1968; Maple, 1969) of the low temperature electrical resistivity and the magnetic suscep-

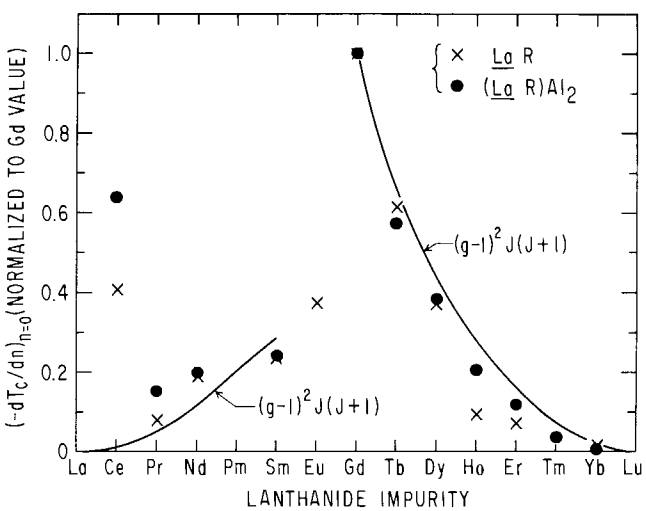

Fig. 11.5. Initial rate of depression of the superconducting transition temperature of LaR alloys (Matthias et al., 1958) and (LaR)Al_2 alloys (Maple, 1970) vs R impurity (normalized to the Gd value). The solid line is the deGennes factor $(g-1)^2J(J+1)$, normalized to the Gd value. The values of $-(d/T_c/dn)_{n=0}$ for Gd impurities are 5.3 and 3.79 K/at.% Gd substitution in La for LaR and (LaR)Al_2, respectively [after Maple (1973)].

tibility. The electrical resistivity revealed a resistivity minimum and a Ce impurity contribution which varied logarithmically with temperature, thus corroborating the existence of a Kondo effect in the (LaCe)Al_2 system. The magnetic susceptibility measurements indicated that the Ce^{3+} $J = \frac{5}{2}$ Hund's rule multiplet is split by the cubic crystalline field of the $LaAl_2$ matrix into a ground state doublet and an excited state quartet with a splitting $\delta \sim 10^2$ K. However, the behavior of the susceptibility could not be described in terms of crystal field effects alone as illustrated in fig. 11.6(a). Here χT vs T data for several

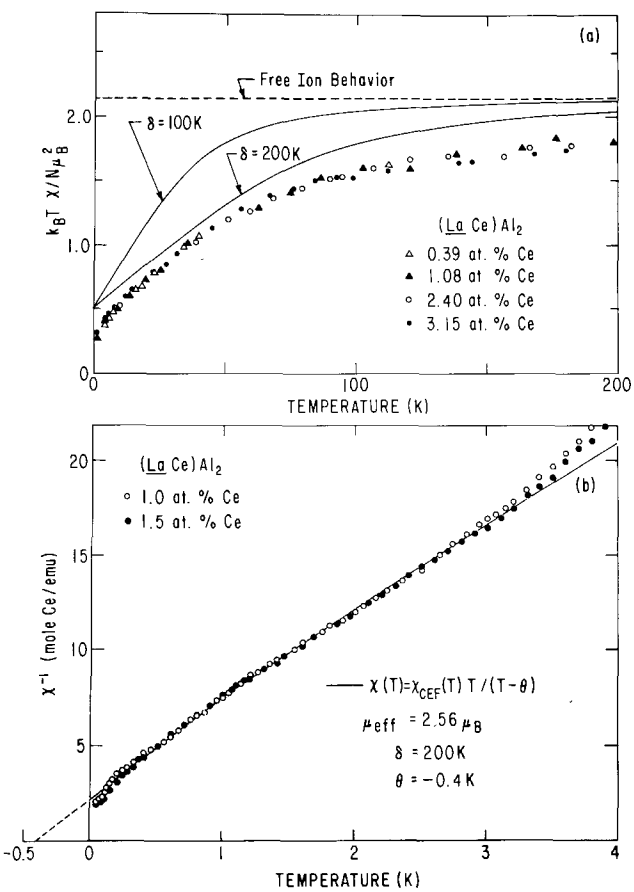

Fig. 11.6. (a) χT vs T plot of the magnetic susceptibility (corrected for the susceptibility of $LaAl_2$) of (LaCe)Al_2 alloys. The dashed line gives the value for free Ce^{3+} ions for which $k_B T\chi/N\mu_B^2 = g^2J(J+1)/3 = 2.14$. The solid curves represent the susceptibility appropriate to a cubic crystal field which splits the Ce^{3+} $J = \frac{5}{2}$ multiplet into a Γ_8 quartet and a ground state Γ_7 doublet [after Maple (1969); Maple and Fisk (1968)]. (b) Inverse magnetic susceptibility (corrected for the susceptibility of $LaAl_2$) vs temperature for two (LaCe)Al_2 alloys below 4 K. The solid line represents a modified Curie-Weiss law with a temperature-dependent Curie constant $C(T) = \chi_{CEF}(T)T$ where $\chi_{CEF}(T)$ is the susceptibility for a Γ_7–Γ_8 splitting δ of 200 K in the cubic crystalline electric field [after Felsch et al. (1975)].

(LaCe)Al_2 alloys are compared with the expected ionic behavior for a Ce^{3+} Γ_7 ground state doublet and a Γ_8 excited state quartet with either a splitting of 100 or 200 K.

Borchi and DeGennaro (1975) calculated the magnetic susceptibility for the (LaCe)Al_2 system, again taking into account the simultaneous existence of a Kondo effect and crystal field splitting of the Ce^{3+} $J = \frac{5}{2}$ multiplet. They find that the temperature dependence of the magnetic susceptibility can be well described by theory for a Γ_7–Γ_8 splitting $\delta = 200$ K and $N(E_F)(g-1)\mathcal{J} = 0.035$. Magnetic susceptibility measurements on the (LaCe)Al_2 system to lower temperatures, which are shown in fig. 11.6(b), have recently been carried out by Felsch et al. (1975). The magnetic susceptibility, which is dominated by the Γ_7 doublet ground state at these lower temperatures, resembles a Curie–Weiss law with a Curie–Weiss temperature θ of -0.4 K. This suggests that T_K is of the order of 0.1 K, in analogy with other matrix-impurity Kondo systems for which $|\theta|$ is generally 3 to 4 times larger than T_K.

Heat capacity measurements on the (LaCe)Al_2 system in zero and high magnetic fields were carried out by Bader et al. (1975). Typical results for a (LaCe)Al_2 alloy with 0.64 at.% Ce are shown in fig. 11.7. There is a pronounced Kondo heat capacity anomaly in zero field with a peak near 0.140 K which is well described by the Bloomfield–Hamann theory (Bloomfield and Hamann, 1967) for $S = \frac{1}{2}$ and $T_K \cong 0.42$ K. In the Bloomfield–Hamann theory, $T_K \sim 3\,T_{max}$

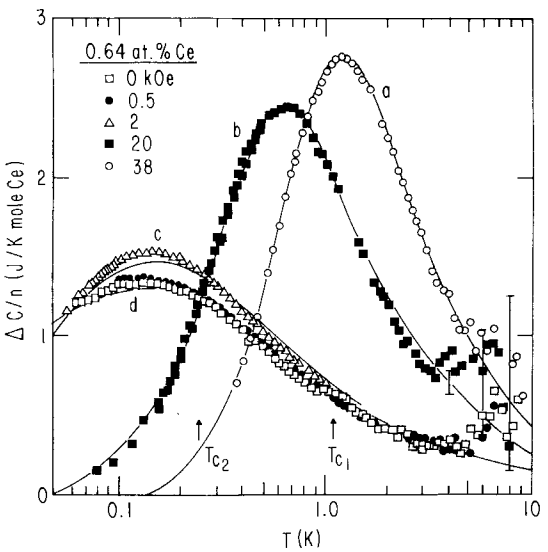

Fig. 11.7. Heat capacity per mole Ce of a (LaCe)Al_2 alloy of composition 0.64 at.% Ce vs temperature in various magnetic fields up to 38 kOe. Curves a–c, which have been drawn to fit more accurate data (not shown) for a (LaCe)Al_2 alloy with 0.906 at.% Ce, correspond to an entropy of $k_B \ln 2$ per Ce ion, showing that the Ce^{3+} ground state is a doublet. Curve d is based upon calculations of Bloomfield and Hamann (1967) for $S = \frac{1}{2}$ and $T_K = 0.42$ K. The zero field superconducting transition temperatures are indicated [after Bader et al. (1975)].

where T_{max} is the temperature at which the magnetic heat capacity attains its maximum value. In high fields (up to 38 kOe), the anomaly becomes more pronounced and the peak moves to higher temperatures. This allows an assessment of the magnetic entropy associated with the anomaly which is found to be equal to k_B ln 2 per Ce impurity ion, confirming that the Ce^{3+} ground state is indeed a Γ_7 doublet. The thermoelectric power of a series of (LaCe)Al_2 alloys has recently been measured (Moeser et al., 1974) and the results are shown in fig. 11.8. There is a characteristic peak in the thermoelectric power near 1 K which is in accord with a low value for T_K. Nuclear orientation measurements on the (LaCe)Al_2 system yield a value for T_K of 0.1 K (Benoit et al., 1973). A large negative magnetoresistivity for the (LaCe)Al_2 system has been reported by Felsch and Winzer (1973). Large Kondo anomalies in the thermal conductivity and Lorentz ratio of (LaCe)Al_2 have been observed by Moeser and Steglich (1975).

Perhaps the most striking manifestations of the Kondo effect are those which occur in the superconducting state for the case when the matrix is a superconductor and $T_K \ll T_{c_0}$ (T_{c_0} is the superconducting transition temperature of the matrix). The literature concerning the Kondo effect in superconducting matrix-impurity systems is extensive, and the interested reader is referred to several review articles (Maple, 1972, 1973, 1976) for detailed discussions of the subject and citations of the original literature. In this article, we will only refer to a few of the more unusual superconductive properties that are manifestations of the anomalous conduction electron-impurity spin exchange scattering associated with the Kondo effect which are exemplified by the (LaCe)Al_2 system.

The condition $T_K \ll T_{c_0}$ is satisfied in the (LaCe)Al_2 system ($T_{c_0} = 3.3$ K), and it exhibits a most unusual phenomenon referred to as re-entrant superconductivity wherein alloys with Ce impurity concentrations within a certain range exhibit two critical temperatures. As an alloy within this Ce concentration range is

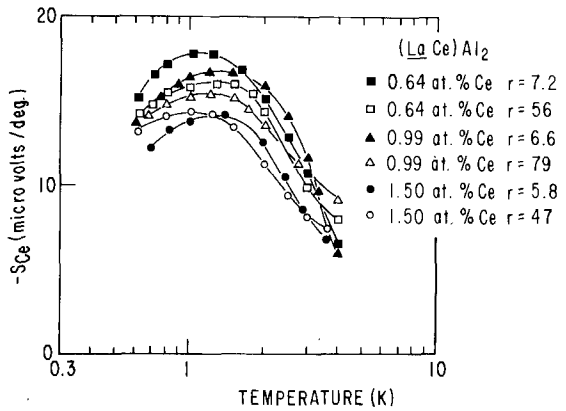

Fig. 11.8. Negative thermoelectric power contributed by Ce impurities in various (LaCe)Al_2 alloys as determined from the Gorter–Nordheim relation. The symbol r denotes the resistance ratio R(300 K)/R(12 K) of each sample [after Moeser et al. (1974)].

cooled to low temperatures, it first enters the superconductivity state at a critical temperature T_{c_1} and then remains superconducting to a lower critical temperature T_{c_2} at which it then returns to the normal state for all temperatures $T < T_{c_2}$. Re-entrant superconductive behavior was first predicted on theoretical grounds by Müller-Hartmann and Zittartz (1971) and by Ludwig and Zuckermann (1971) and observed by Riblet and Winzer (1971). According to these theories, there should actually be a third transition temperature T_{c_3}, in addition

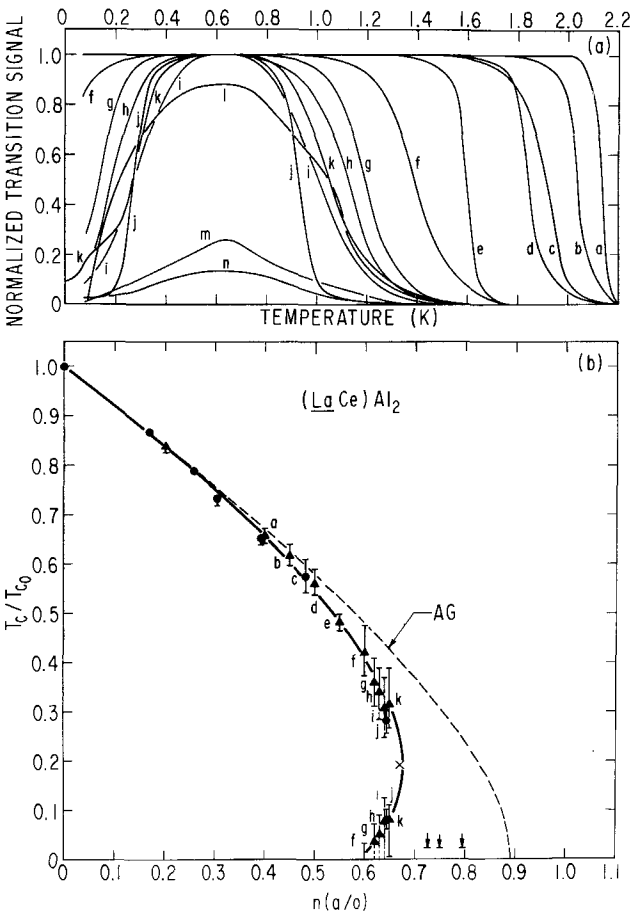

Fig. 11.9. (a) Normalized transition signal vs temperature for several (LaCe)Al_2 alloys. The superconducting state corresponds to a transition signal of unity. The sequence of letters a–n identifies the transition curves in the order of increasing Ce impurity concentration. (b) Reduced transition temperature T_c/T_{c_0} vs impurity concentration n for the (LaCe)Al_2 system. Transition temperatures corresponding to the transition curves in (a) are identified. The symbol (×) denotes the estimated turning point of the T_c/T_{c_0} vs n curve, while the solid circles and triangles distinguish two separately prepared sets of alloys. The Abrikosov–Gor'kov (1961) curve (dashed) is shown for comparison [after Maple et al. (1972)].

to and below T_{c_2}, at which an alloy with the appropriate magnetic impurity concentration again becomes superconducting for all temperatures $T < T_{c_3}$. No evidence for the existence of the third transition temperature T_{c_3} has been found experimentally, and several refinements of the theory have recently appeared which cast doubt on the existence of T_{c_3} (Schlottmann, 1975a, 1975b; Matsuura and Nagaoka, 1976; Müller-Hartmann et al., 1976).

Examples of transition curves (ac susceptibility) which undergo a return to the normal state at a lower critical temperature and the corresponding re-entrant reduced transition temperature vs Ce concentration curve for the (LaCe)Al_2 system are shown in figs. 11.9(a) and (b) (Maple et al., 1972). The data are also compared with the predictions of the Abrikosov–Gor'kov (AG) theory (Abrikosov and Gor'kov, 1961) (dashed line) which hold for superconducting matrix-impurity systems for which there is no Kondo effect ($\mathcal{J} > 0$) and for which the degeneracy of the Hund's rule impurity ion multiplet is not lifted by a crystalline electric field.

In addition to the remarkable re-entrant behavior of the T_c/T_{c_0} vs n curve, the depression of the specific heat jump ΔC at T_c as a function of T_c (Armbrüster et al., 1974; Luengo et al., 1972; Bader et al., 1975) also displays some interesting features which are shown in fig. 11.10. Here, it can be seen that the curve of reduced specific heat jump $\Delta C/\Delta C_0$ vs reduced transition temperature T_c/T_{c_0} shows a pronounced downward deviation from both the BCS law of corresponding states and, as well, the AG theory. It is worth noting that recent specific heat measurements (Bader et al., 1975) on a re-entrant (LaCe)Al_2 specimen (0.64 at.% Ce) to temperatures lower than T_{c_2} indicate that the tran-

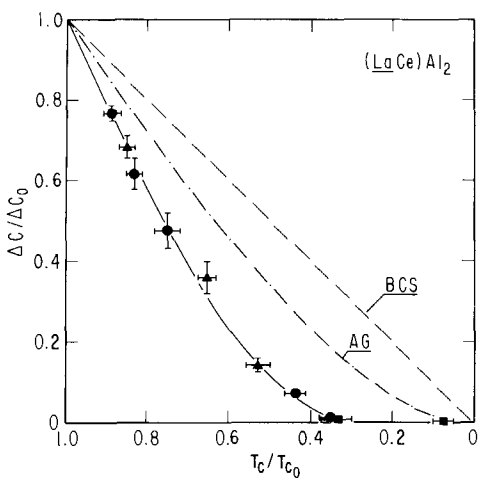

Fig. 11.10. Reduced specific heat jump $\Delta C/\Delta C_0$ vs. reduced transition temperature T_c/T_{c_0} for the (LaCe)Al_2 system. The solid triangles, circles and squares represent data from Luengo et al. (1972), Armbrüster et al. (1974), and Bader et al. (1975), respectively. The dashed line represents the BCS law of corresponding states, the dot-dashed line indicates the AG result, and the solid line is a smooth curve drawn through the data [after Maple (1976)].

sition at T_{c_2} is second order as it is at T_{c_1}. The two reduced specific heat jumps for this specimen are indicated in fig. 11.10 by the solid squares.

Figures 11.9 and 11.10 exemplify the behavior of T_c/T_{c_0} vs n and $\Delta C/\Delta C_0$ vs T_c/T_{c_0} for matrix-impurity systems which exhibit a Kondo effect ($\mathscr{J} < 0$) with $T_K \ll T_{c_0}$.

3.3. *Praseodymium impurity systems*

The first observation of anomalous behavior in a dilute alloy containing Pr impurities was made by Fisk and Matthias (1969) in the system (ZrPr)B_{12}. They observed an extremely large initial depression of the superconducting transition temperature of ZrB_{12} with the addition of Pr impurities. This value of $(-dT_c/dn)_{n=0} \approx 13$ K/at.% Pr was approximately an order of magnitude larger than the initial depressions of T_c due to the addition of any other lanthanide to ZrB_{12}.

These authors also performed resistivity measurements on several (ZrPr)B_{12} compositions and found a resistance minimum at about 35 K in each of the samples studied (Pr concentrations smaller than 3 at.%). Their measurements of magnetic susceptibility revealed a simple Curie law for (ZrPr)B_{12} with an effective magnetic moment of approximately 3.6 μ_B for the Pr^{3+} impurities.

Fisk and Matthias explained their experimental results by assuming that the effective lattice pressure exerted on the Pr impurities by the ZrB_{12} host environment was about 200 kbar, thus giving rise to a virtual bound 4f level close to the Fermi level.

Hillenbrand and Wilhelm (1972) observed a large initial depression of the superconducting transition temperature in the (LaPr)Ru_2 system. This value of $(-dT_c/dn)_{n=0} = 1.1$ K/at.% Pr was much larger than their value of $(-dT_c/dn)_{n=0} = 0.45$ K/at.% Gd in the analogous (LaGd)Ru_2 system. Their susceptibility measurements revealed an effective magnetic moment of 3.84 μ_B in contrast to the Hund's rule value of 3.58 μ_B for Pr^{3+}. They suggested that this discrepancy might be evidence for a magnetic polarization cloud associated with conduction electrons in the vicinity of the Pr local moments.

Recalling the above-mentioned work of Fisk and Matthias on (ZrPr)B_{12}, they pointed out that while there should be almost no lattice pressure effect in (LaPr)Ru_2, Ce impurities were known (Hillenbrand and Wilhelm, 1970) to be nonmagnetic in (LaCe)Ru_2, and thus the possibility of a virtual bound 4f state in (LaPr)Ru_2 could not be ruled out.

Recent experiments on (LaPr)Sn_3 alloys have rekindled interest in the possibility of a Kondo effect in a Pr impurity system. The early observation by Bucher et al. (1968) of a large depression of the superconducting transition temperature T_c of $LaSn_3$ by Pr impurities (relative to other R impurities) is shown in fig. 11.11. This initial observation stimulated McCallum et al. (1975a) to perform more detailed measurements of the depression of T_c with Pr concentration, the superconducting and normal state heat capacity, and the normal state magnetic susceptibility of (LaPr)Sn_3 alloys. Calculated values of the ther-

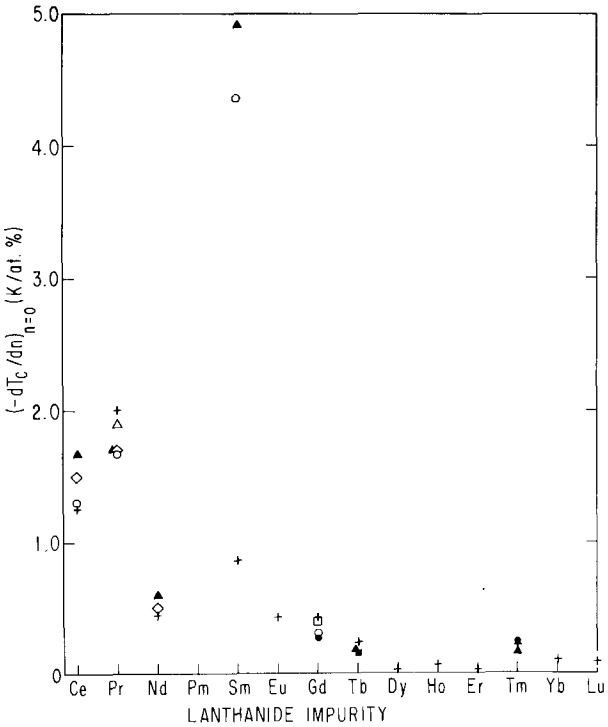

Fig. 11.11. Initial rate of depression of the superconducting transition temperature of (La R)Sn_3 alloys vs R impurity. The data are taken from: Schmid and Umlauf (1976) – crosses; McCallum et al. (1975a) and DeLong et al. (1975, 1976) – open circles; Abou Aly et al. (1976) – solid triangles; van Maaren and van Haeringen (1975) – open diamonds; Lethuillier (1975) – open triangles; Toxen et al. (1968) – open squares; Guertin et al. (1973) and Bucher et al. (1968) – solid circles; Hoenig et al. (1975) – solid squares.

modynamic critical fields of (LaPr)Sn_3 alloys have also been reported by McCallum et al. (1975b) using the specific heat results of McCallum et al. (1975a).

The strong positive curvature of the T_c vs Pr concentration data for (LaPr)Sn_3 is good evidence for the nonmagnetic nature of the crystal field ground state of Pr^{3+} in $LaSn_3$. A pronounced Schottky anomaly in the normal state heat capacity and the Van Vleck contribution to the magnetic susceptibility are consistent with a unique energy level scheme for the Pr^{3+} ion in the $LaSn_3$ crystalline electric field (CEF) in which the ground state is a Γ_1 singlet.

However, the most remarkable results of the measurements of McCallum et al. (1975a) were the large, positive deviations of the reduced specific heat jump $\Delta C/\Delta C_0$ from the predictions of the BCS theory as shown in fig. 11.12. This was the first time such a positive deviation has been observed for any superconductor. It is most important to point out that *all* of the above phenomena in (LaPr)Sn_3 can be adequately described by the theories of Fulde and coworkers

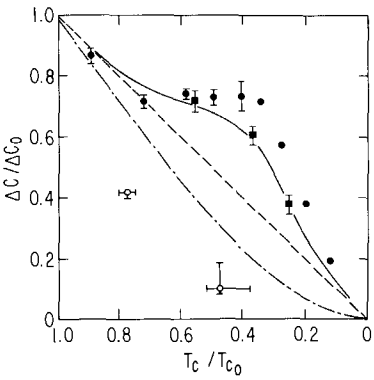

Fig. 11.12. Reduced specific heat jump $\Delta C/\Delta C_0$ vs reduced transition temperature T_c/T_{c_0} for (LaPr)Sn_3 alloys (solid circles and solid squares; McCallum et al., 1975a) and (LaSm)Sn_3 alloys (open circles; DeLong et al., 1976). The solid line is derived from numerical calculations based on the theory of Keller and Fulde (1973) for crystal field-split lanthanide impurities in a superconductor. The BCS law of corresponding states behavior (dashed curve) and the AG behavior (dot-dashed curve) are shown for comparison. The negative deviations of the $\Delta C/\Delta C_0$ vs T_c/T_{c_0} data from the AG curve are consistent with Kondo behavior (see fig. 11.10) for (LaSm)Sn_3 alloys.

(Keller and Fulde, 1973; Fulde and Peschel, 1972) for magnetic impurities with CEF-split ground states in superconductors without the introduction of Kondo mechanisms (McCallum et al., 1975a).

However, subsequent measurements of the electrical resistivity (Haen and Lethuillier, 1975; Abou Aly et al., 1975; Lethuillier and Haen, 1975) and the pressure dependence of T_c (DeLong et al., 1975) were performed which may prove difficult to reconcile with a simple ionic behavior for Pr impurities in $LaSn_3$. The electrical resistivity measurements show weak minima in the vicinity of 10–20 K at a Pr concentration of greater than, or the order of, 10 at.%. The resistivities also exhibit a local maximum around 7.5 K for Pr concentrations less than 80 at.%, which is the lowest Pr concentration where the resistivity maximum and the Néel temperature (as determined by static susceptibility measurements) coincide. For Pr concentrations well below 80 at.%, the resistivity maximum and the rapid decrease in the resistivity below 7.5 K have been associated with a thermal depopulation of the CEF excited states of Pr.

Attempts (Haen and Lethuillier, 1975; Abou Aly et al., 1975; Lethuillier and Haen, 1975) to apply the theory of Rao and Wallace (1970) for the resistivity introduced by magnetic scattering from a CEF-split ionic configuration have only been marginally successful in that the minimum in the (LaPr)Sn_3 resistivity cannot be accounted for if one includes all of the known Pr CEF levels in the calculation.

DeLong et al. (1975) have measured the pressure dependence of T_c in the (LaPr)Sn_3 system and found an anomalously large decrease in T_c with pressure when compared to their results for (LaGd)Sn_3, a system which is free from CEF effects. An examination of the Pr^{3+} energy level scheme of McCallum et al.

(1975a) and the predictions of a simple point charge model forced them to conclude that either the overall splittings of the Pr^{3+} energy level scheme were decreasing under pressure, contrary to the point charge model, or the magnitude of the conduction electron-impurity exchange interaction parameter $\mathcal{J}$ was increasing more rapidly than would be predicted from the (LaGd)Sn_3 data. They pointed out that such large pressure dependences of $\mathcal{J}$ are frequently found in Kondo systems.

In spite of the large amount of data in existence for the (LaPr)Sn_3 system, the evidence for a Kondo effect in these alloys is still ambiguous. In particular, the expected negative deviations (Maple, 1976, and references therein) from the BCS law of corresponding states for $\Delta C/\Delta C_0$ vs T_c/T_{c_0} accompanying the Kondo effect have not been observed in the (LaPr)Sn_3 system (compare the (LaPr)Sn_3 data to those for (LaCe)Al_2 in fig. 11.10 and (LaSm)Sn_3 in fig. 11.12). In addition, there has been a lack of any serious theoretical discussion of the results of the resistivity and pressure experiments which might include more general treatments of this problem (including the effects of anisotropic exchange scattering, for example); nor have a sufficient number of experiments been performed on other (LaR)Sn_3 systems to ascertain the details of the impurity-conduction electron interactions in these host-impurity systems.

3.4. *Samarium impurity systems*

Although several concentrated alloys and compounds of Sm (notably the Sm monochalcogenides and SmB_6) have been studied in connection with valence fluctuation phenomena, there is only one *dilute* alloy system reported to date containing Sm impurities which exhibits Kondo-like behavior.

The existence of an unusually large depression of the superconducting transition temperature of $LaSn_3$ by Sm impurities has been reported by Schmid and Umlauf (1976) and Abou Aly et al. (1976). The data of fig. 11.11 show that the value of $(-dT_c/dn)_{n=0}$ for Sm impurities in $LaSn_3$ is much greater than the initial depressions for all other lanthanides dissolved in $LaSn_3$.

Recently, DeLong et al. (1976) reported measurements of the depression of T_c, the magnetic susceptibility, specific heat and pressure dependence of T_c for (LaSm)Sn_3 alloys. The extremely large value of the initial depression of T_c was confirmed by ac susceptibility and specific heat measurements in the superconducting state.

Measurements of the normal state specific heat of (LaSm)Sn_3 alloys revealed an enhancement of the $LaSn_3$ host density of states by Sm impurities which is the largest (207 states/eV-atom-spin direction) observed to date for a dilute alloy system. The superconducting state specific heat data for $\Delta C/\Delta C_0$ are plotted vs T_c/T_{c_0} in fig. 11.12, and show strong negative deviations from both the BCS law of corresponding states and the predictions of the AG theory. These data are similar to the corresponding specific heat jump measurements for the Kondo systems (LaCe)Al_2 (fig. 11.10) and (La, Th)Ce mentioned in section 3.2, and strongly support the existence of a Kondo effect in the (LaSm)Sn_3 system.

Measurements of the temperature dependence of the magnetic susceptibility of a 1.1 at.% (LaSm)Sn_3 sample yielded a temperature independent Sm impurity contribution of about 1.3×10^{-3} cm^3/mole Sm from 300 K down to around 50 K. Below 50 K a small "tail" appeared in the impurity susceptibility, but no divergence in the susceptibility was observed to a lowest temperature of 1.4 K, indicating a nonmagnetic impurity state for the Sm ions at low temperatures. Although Sm is known to be trivalent in $SmSn_3$ (Malik, 1970 and references therein), the combined effects of the CEF and J-mixing can lead to very unusual behavior for the magnetic susceptibility in Sm systems, making a unique theoretical description of experimental data difficult (de Wijn et al., 1975). The low temperature susceptibility data, therefore, do not necessarily imply either purely divalent (nonmagnetic, $J = 0$) Sm or a nonmagnetic ICF state for Sm in $LaSn_3$.

The recent measurements of the temperature dependence of the electrical restivity of (LaSm)Sn_3 alloys by Bakanowski et al. (1977) indicate the presence of resistivity minima in the samples studied (all of which were for Sm concentrations of less than 20 at.%). These observations would favor a more nearly trivalent state for Sm in $LaSn_3$ and clearly support the presence of a Kondo effect in (LaSm)Sn_3 alloys. However, the situation is incomplete at the time of this writing; further data may reveal an entirely new class of behavior represented by this interesting system.

3.5. *Europium impurity systems*

Gainon et al. (1967) observed a "giant" thermoelectric power in AgEu and AuEu alloys. Their magnetic susceptibility measurements for temperatures greater than 40 K indicated paramagnetic behavior in these alloys with Curie–Weiss temperatures of 11 ± 3 K for AuEu and 15 ± 3 K for AgEu. The effective moments were $7.6 \pm 0.2\ \mu_B$ and $7.7 \pm 0.2\ \mu_B$, respectively, for AuEu and AgAu suggesting a divalent state for Eu in both alloys. Annealing of the samples caused expected variable behavior for the thermoelectric power since the concentrations of Eu employed were close to the believed solubility limit for Eu in noble metals. Thus these measurements should be treated with caution; however, they do suggest that further work on these alloys might prove rewarding.

3.6. *Ytterbium impurity systems*

The evidence for the Kondo effect in dilute alloys containing Yb lacks the numerous cases of model behavior as have been found for dilute alloys containing Ce impurities, and (Ag, Au)Yb remains to date the only extensively-documented example of anomalous behavior for Yb impurities in a dilute alloy. Unfortunately, this system is also a classic example of the severe limitations that metallurgical effects can place on the clarity of the interpretation of even the most carefully performed experiments. The crux of the problem lies in the rather poorly understood levels of solubility of the lanthanides in Ag and Au.

Early studies of the solubilities of various lanthanides in Au (Rider et al., 1965) and Ag (Bijvoet et al., 1966) suggested that Yb was slightly less than trivalent in Au and divalent in Ag. The low temperature thermoelectric power and magnetic susceptibility of Yb in both Ag and Au were reported by Gainon et al. (1967), Hirst et al. (1968) and Williams and Hirst (1969). The magnetic susceptibility of AuYb showed that for temperatures of about 100 K or higher the susceptibility was well described by a Curie–Weiss law with an effective moment of 4.3 μ_B (close to the trivalent Hund's rule value of 4.54 μ_B). Large deviations of the susceptibility from free ion behavior below 50 K were ascribed to crystal field effects resulting in a Γ_7 ground state with a Γ_8 first excited state at 79 K and a Γ_6 second excited state at 83 K. A weakly temperature dependent susceptibility was found for AgYb confirming the presence of divalent Yb.

Hirst and coworkers also performed EPR measurements (Hirst et al., 1968; Williams and Hirst, 1969) on AuYb and AgYb. No resonance was found in AgYb, but the resonance discovered in AuYb corresponded to a g value of 3.30 ± 0.10, consistent with a Γ_7 ground state for Yb in Au, and a value of $|\mathcal{J}| = 0.22$ eV. Tao et al. (1971) confirmed the results of Hirst et al. by performing their own EPR measurements on AuYb. They determined a value* of $\mathcal{J} = -0.43$ eV which they asserted was indicative of a large (negative) covalent mixing contribution to $\mathcal{J}$ due to the proximity of the $4f^{13}$ and $4f^{14}$ levels of Yb to the Fermi level of Au.

Indeed, the resistivity studies of AuYb by Murani (1970, 1973) demonstrated that resistance minima did exist in AuYb alloys. Using the theory of Kondo (1964), Murani found a value of $\mathcal{J} = (-0.14 \pm 0.01)$ eV, which he discussed in terms of Hirst's ideas (1970) concerning ICF phenomena.

Mössbauer experiments have also been performed on AuYb and extensively analyzed by Stöhr and coworkers (Stöhr, 1975; Shenoy et al., 1974), and Gonzalez-Jimenez and coworkers (Gonzalez-Jimenez and Imbert, 1972, 1973; Gonzalez-Jimenez et al., 1974a, 1974b, 1974c, 1975; Hartmann-Boutron, 1974). Some of these experimental results (Gonzalez-Jimenez and Imbert, 1972, 1973; Gonzalez-Jimenez et al., 1974a, 1974b, 1974c, 1975; Hartmann-Boutron, 1974) indicate $T \ln T$ behavior in the temperature dependence of the Mössbauer relaxation rate for $T < 10$ K. A recent theoretical analysis by Bhattacharjee and Coqblin (1976) found that the AuYb Mössbauer data are consistent with a very low Kondo temperature and an effective value of $\mathcal{J} \approx -0.38$ eV.

Benoit et al. (1974b; Flouquet and Brewer, 1975) have made nuclear orientation measurements on AuYb alloys and determined that $T_K \ll 10$ mK. Unfortunately, the detailed analysis of these experiments is greatly complicated by interaction effects (at very low temperatures), lattice defects and the possible presence of Yb intermetallic compounds.

Some of the more recent results on AuYb have more accurately determined limits for the magnitude of T_K. Cornut and Coqblin (1975) measured the

*This value has been corrected for a difference of a factor of 2 in the hamiltonian of these authors and that used by most other authors cited in this review.

magnetization of very dilute unannealed alloys (Yb concentrations less than 0.3 at.%) of AuYb as a function of magnetic field up to 90 kOe and in the temperature range 0.07 K to 50 K and performed electrical resistivity measurements between 1.1 K and 300 K. They determined that AuYb was well described by single impurity ionic behavior (reflecting a very low T_K) when the combined effects of Kondo scattering and the Au CEF were considered. This interpretation was supported by the elegant measurements of the electronuclear susceptibility of unannealed AuYb alloys by Frossati et al. (1975, 1976) using SQUID magnetometry to a lowest temperature of 7 mK. They were able to show that the T_K of AuYb is much less than 1 mK.

There have also been more refined attempts to uncover magnetic behavior in AgYb alloys. The resistivity measurements of Murani (1974a) on AgYb alloys revealed weak resistance minima around 5 K. Murani explained his results on the basis of an ICF state for Yb in Ag which is also consistent with the small temperature dependence of the susceptibility of AgYb (Gainon et al., 1967).

Murani's interpretation of his work on AgYb has been challenged by Bekker and van Duren (1974), whose measurements of the thermoelectric power in AgYb revealed a strong dependence of their experimental results on annealing procedure. They asserted that this constituted evidence for the presence of an additional scattering mechanism in their alloys which they analyzed theoretically in terms of the presence of Fe impurities. However, these authors did not attempt to analyze their data in terms of the clustering of Yb impurities or the possible formation of regions containing Ag–Yb intermetallic compounds within their samples.

The experimental results just discussed for AgYb and AuYb strongly suggest that it should be possible to study the gradual valence change of Yb from a divalent state to a trivalent state as the host composition is varied from pure Ag to pure Au in *perfectly random* alloys of the type (Ag, Au)Yb. The (Ag, Au)Yb system might then be thought of as a nearly exact analog of the (La, Th)Ce system discussed earlier in this article with AuYb constituting the f-hole analog of LaCe.

The first study of (Ag, Au)Yb alloys was done by Boes et al. (1968), who observed that for Yb concentrations of less than 0.15 at.% in a Ag, Au host a Kondo minimum in the temperature dependence of the electrical resistivity was found in annealed alloys for Au concentrations between 10 and 40 at.%. However, the resistive behavior was also found to depend markedly on the details of the alloy heat treatment.

Allali and coworkers (1969, 1970) performed susceptibility and thermoelectric power measurements on (Ag, Au)Yb alloys. They found that for Au concentrations ≥ 5 at.% a Curie–Weiss fit to the magnetic susceptibility yielded an effective moment of around 4.3 μ_B, as shown in fig. 11.13. For Au concentrations <5 at.% the effective moment μ_{eff} rapidly goes to zero. For Au concentrations ≥ 30 at.% the Curie–Weiss temperature θ is approximately constant and equal to -10 K due to CEF effects. A small composition-dependent anomaly in the Curie–Weiss temperature occurs for Au concentrations between 5 and 30 at.%

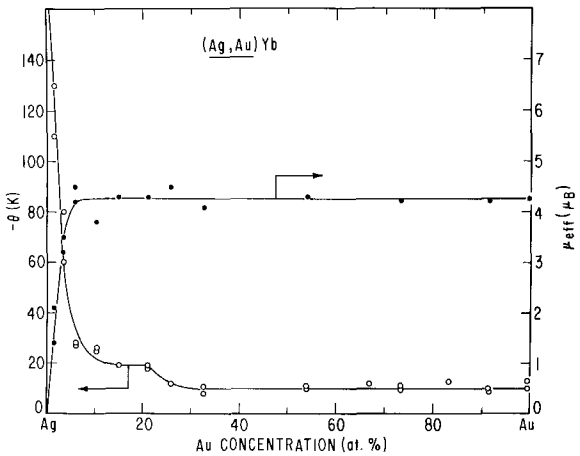

Fig. 11.13. Curie–Weiss temperature θ and effective magnetic moment μ_{eff} for (Ag, Au)Yb alloys vs. Au composition of the Ag, Au matrix from magnetic data of Allali et al. (1970).

which these authors attributed to the presence of a Kondo effect. The Curie–Weiss temperature rapidly increases in magnitude as the Au concentration goes to zero (for Au concentration <5 at.%). All of these observations reflect the absence of a divergent susceptibility as T goes to zero for Au concentrations $\leq$10 at.%. In addition, magnetization curves taken at 1.5 K exhibited marked saturation for Au concentration >10 at.%, and no such effect for Au concentrations <10 at.%. Measurements of the thermoelectric power contribution due to Yb impurities showed a sharp "edge" at a Au concentration of 7.5 at.% and a negative "peak" for Au concentrations between 10 and 30 at.%.

The more recent EPR measurements of Nagel et al. (1973) on (Ag, Au)Yb alloys were analyzed for the temperature dependence of the resonance linewidth where a resonance was observed. No resonance signal was detected for Au concentrations <70 at.%, but in varying the Au concentration from 100 to 70 at.%, $|\mathcal{J}|$ can be inferred to double while the g factor changes continuously from 3.34 to 3.22.

All of the work on (Ag, Au) Yb mentioned above has been discussed (Boes et al., 1968; Allali et al., 1969, 1970; Nagel et al., 1973) in terms of Kondo phenomena for Au concentrations between 10 and 30 at.%. However, the previously mentioned evidence for Kondo behavior in both AuYb and AgYb are consistent with a smooth dependence of T_K on Au concentration as occurs in the (La, Th)Ce system discussed earlier in this article, thus making a restricted concentration "regime" for the presence of Kondo behavior in (Ag, Au)Yb unlikely. Particularly interesting is that only a 1 at.% addition of Au to a pure Ag host results in an approximately five-fold increase in the magnitude of the resistivity contribution of Yb in Ag (Murani, 1974a). However, solubility problems for Yb in Ag make these data difficult to interpret. Measurements of the thermoelectric power (Bekker and van Duren, 1975) of a $Ag_{0.8}Au_{0.2}Yb$ alloy place $T_K \approx 1$ K, a value which is certainly reasonable compared to inferred values of T_K for AuYb or AgYb.

Murani (1974b) has subsequently performed measurements of electrical resistivity on (Ag, Pd)Yb and found that the maximum Kondo slope in the resistivity of (Ag, Pd)Yb alloys was one-third the maximum slope in (Ag, Au)Yb, but this could be due to the severe Yb solubility problems encountered in this system.

The recent work of Talmor and Sierro (1975) on the electrical resistivity of (Ag, Au)Yb alloys is directly addressed to the problem of sample characterization. They found that the values of $\mathscr{J}$ obtained from their data varied by as much as a factor of three depending on the sample heat treatment. Talmor and Sierro also showed (fig. 11.14) that there is a sharp peaking of the depth of the Kondo resistance minimum $\Delta\rho_{\min}$ and of the logarithmic slope of the resistivity $|\mathrm{d}(\Delta\rho)/\mathrm{d}(\log T)|$ at Au concentrations ≈ 25 at.% This suggests a region favorable to the formation of additional metallurgical phases. X-ray results for a $Ag_{0.70}Au_{0.30}Yb$ sample indicated the presence of Au_3Yb and a microprobe analysis detected a precipitated phase in the alloy.

Attempts to prepare single phase AuYb and Au_3Yb compounds for resistivity studies resulted only in mixed phase Au_3Yb–Au_4Yb and AuYb–Au_2Yb samples. However, Talmor and Sierro found relatively enormous resistance minima in both types of composite samples followed by steep drop-offs at lower temperatures due to magnetic ordering.

Thus the present state of understanding of the Kondo effect in (Ag, Au)Yb alloys is complicated by solubility problems and the presence of additional phases of Yb intermetallic compounds which are known to produce resistance minima.

Fisk et al. (1969) have measured the resistivity of a sample of approximate composition $(Sc_{0.95}Yb_{0.05})B_{12}$ and found a very pronounced minimum near 45 K. No additional measurements have been performed, but this system is of interest

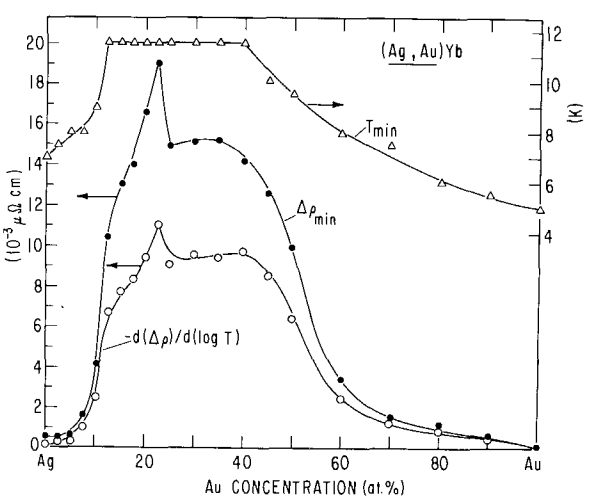

Fig. 11.14. Temperature of the Kondo resistance minimum $T_{\min}$, depth of the resistance minimum $\Delta\rho_{\min}$, and logarithmic slope of the solute incremental resistivity $-\mathrm{d}(\Delta\rho)/\mathrm{d}(\log T)$ for (Ag, Au)Yb alloys vs Au composition of the Ag, Au matrix from resistivity data of Talmor and Sierro (1975).

since it is the only other dilute alloy containing Yb impurities [other than (Ag, Au)Yb] which exhibits a resistance minimum.

4. Kondo-like behavior in concentrated lanthanide alloys and compounds

4.1 *Introduction*

The greatest advantage of studying single impurity effects in metallic lanthanide systems is that one can work with concentrated alloys and even compounds. The extreme local nature of the 4f wavefunction (typically about 0.1 lattice spacing) means that there is virtually no direct overlap of nearest neighbor 4f wavefunctions. This is in contrast to the 3d metals where one must work with ppm concentrations of 3d impurities in a nonmagnetic metallic host to insure no direct 3d interactions, and must then try to extract the impurity signal from a relatively large host background. One can perform a much wider variety of measurements on concentrated lanthanide systems since the 4f contribution to a physical property is a much larger fraction of the total measured quantity. This provides not only a broader variety of possible experiments but allows one to better characterize the sample.

However, concentrated lanthanide systems have two major disadvantages. First, in concentrated *alloys* one can have several different local environments for the rare earth ions. The local environment of an A atom in an AB alloy can vary depending on how many nearest neighbor B atoms it has. The lanthanide ions may therefore exhibit a characteristic temperature T_0 for *each* local environment, which makes the interpretation of the experimental data more difficult. Second, in concentrated alloys and compounds there are interaction effects between the lanthanide ions. The interaction is indirect and is mediated through the conduction electrons (RKKY interaction). In some concentrated systems this interaction can be neglected ($T_{RKKY} \ll T_0$), while in others, particularly compounds, it is dominant ($T_{RKKY} \gg T_0$) and magnetic ordering results.

As mentioned in the Introduction (section 1), the electrical resistivity, specific heat, magnetic susceptibility and thermoelectric power anomalies of concentrated lanthanide Kondo systems are qualitatively similar to those found in the dilute lanthanide systems discussed previously. *However the importance of the concentrated systems is that they provide a totally new view of Kondo-like phenomena.* Lattice constant, X-ray photoemission (XPS) and Mössbauer isomer shift measurements indicate a strong correlation between systems that exhibit Kondo-like anomalies and systems in which the lanthanide ion has a mixed or intermediate valence. By mixed valence we mean that there are two 4f electron configurations accessible to *each* rare earth ion (e.g., Ce^{3+}–Ce^{4+}, Eu^{2+}–Eu^{3+}, Yb^{2+}–Yb^{3+}). Phenomenologically the traditional Kondo anomalies are qualitatively consistent with the mixed valence picture, although at present there is no "first principles" theory based on the mixed

valence concept. These ideas will be discussed in more detail in this section with respect to specific systems.

4.2. *Cerium systems*

As is the case in dilute lanthanide systems, Kondo anomalies in concentrated alloys and compounds are most frequently found in Ce systems. Kondo anomalies in a concentrated system were first observed in the electrical resistivity of $CeAl_2$ by Buschow and van Daal (1969). Although $CeAl_2$ orders antiferromagnetically at 3.4 K (Barbara et al., 1975; Hill and Machado da Silva, 1969; Swift and Wallace, 1968; Maple, 1969), above this temperature a minimum in the resistivity was observed suggesting a Kondo effect. This conclusion was supported by the high temperature heat capacity work of Deenadas et al. (1971). In $CeAl_2$ the Ce^{3+} $J = 5/2$ multiplet is split into a doublet groundstate and quartet excited state (splitting about 100 K) by the cubic crystalline electric field. The high temperature heat capacity showed a Schottky type anomaly due to the splitting but the anomaly was much broader than expected from two sharp levels – a feature characteristic of a Kondo anomaly.

The compound $CeAl_3$ and its associated alloys is one of the most thoroughly studied concentrated lanthanide systems. Above 25 K the magnetic susceptibility of $CeAl_3$ follows a Curie–Weiss law with a Curie–Weiss temperature of -46 K and an effective moment of 2.63 μ_B (Buschow and Fast, 1966; Mader and Swift, 1968). Below 25 K the curvature in χ^{-1} was attributed to the effects of a hexagonal crystal field. The ground state of the Ce^{3+} ion must at least be a doublet due to Kramer's theorem; however, the susceptibility exhibits neither magnetic order nor diverges as $T \to 0$. The lack of magnetic order above 2 K has also been verified by neutron diffraction measurements (Mahoney et al., 1973; Edelstein et al., 1976). The electrical resistivity of $CeAl_3$ (a metal) is unusual as it increases upon cooling below 300 K suggesting a minimum in the resistivity above room temperature (van Daal and Buschow, 1970; Buschow et al., 1971; Edelstein et al., 1974). At 40 K the resistivity reaches a maximum followed by a rapid decrease upon further cooling. We also note that Percheron et al. (1973) have studied the effects of pressure on the resistivity of $CeAl_3$.

The "Kondo side-band" explanation of the electrical resistivity of $CeAl_3$ (and other transport properties) was first given by Maranzana (1970; Maranzana and Bianchessi, 1971) using the s–f exchange hamiltonian. He showed that in the presence of crystal fields, the conduction electron scattering rate diverges not at the Fermi energy, as calculated by Kondo without consideration of crystal fields, but at energies displaced from the Fermi energy by the crystal field splitting δ. This leads to a maximum in the resistivity at $T = \delta/3k_B$ and to a resistivity curve qualitatively similar to the resistivity of $CeAl_3$. A more detailed calculation of the side-band model based on an Anderson-like hamiltonian including orbital quantization has been given by Cornut and Coqblin (1972).

The thermoelectric power of the (La, Ce)Al_3 system has been investigated by van Aken et al. (1974). The thermoelectric power of $CeAl_3$ has a large peak of

40 μV/K at about 60 K (roughly the same temperature as the maximum in the resistivity). The low and high temperature heat capacity of $CeAl_3$ exhibits several Schottky type anomalies at 25 K, 6 K and 4 K; however, these anomalies as well as the total measured entropy are not explainable in terms of crystal field effects alone (van Maaren et al., 1971; Mahoney et al., 1973). Recent measurements by Andres et al. (1975) showed that at very low temperatures (T = 10–200 mK) the specific heat of $CeAl_3$ follows a γT law with γ = 1620 mJ/mole-K^2 and the electrical resistivity a T^2 law.

Another interpretation of the $CeAl_3$ data in terms of a fluctuating Ce valence was given by Sales (1974). The series of rare earth compounds $CeAl_3$ through $GdAl_3$ crystallize in the hexagonal Ni_3Sn structure. The lattice constants (van Vucht and Buschow, 1965) of $CeAl_3$ deviate from the trend established by the other RAl_3 compounds suggesting a valence of about 3.1 for Ce in $CeAl_3$. In addition, the magnetic susceptibility and electrical resistivity of $CeAl_3$ are qualitatively identical to those of $CeCu_2Si_2$ (Sales and Viswanathan, 1976). For the $CeCu_2Si_2$ compound it has been shown that one can quantitatively interpret the data in terms of a phenomenological model based on the fluctuating valence idea. This interpretation has recently been supported by neutron diffraction measurements on $CeAl_3$ by Edelstein et al. (1976). They found a Ce valence between 3.0 and 3.1 and no evidence of a spin compensating conduction electron cloud at low temperatures.

Several Ce compounds of the form CeX_3 (X = Pb, In, Pd, Sn) exhibit one or more anomalies associated with the Kondo effect. All these compounds crystallize in the cubic Cu_3Au structure.

$CeIn_3$ is similar to $CeAl_2$ in that although it orders antiferromagnetically at 10.4 K (van Diepen et al., 1971), above this temperature there is a broad minimum in the electrical resistivity at about 170 K (van Daal and Buschow, 1970). The high

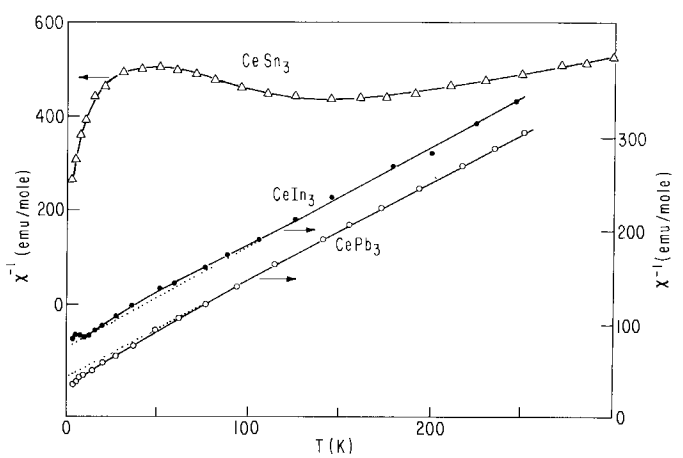

Fig. 11.15. Inverse magnetic susceptibility vs temperature for $CeSn_3$ (open triangles), $CeIn_3$ (solid circles) and $CePb_3$ (open circles). Measurements were made in a magnetic field of 19 kOe [after Tsuchida and Wallace (1965)].

temperature magnetic susceptibility (fig. 11.15) follows a Curie–Weiss law with $\theta = -62$ K and $\mu_{eff} = 2.7\,\mu_B$ (Tsuchida and Wallace, 1965). The thermoelectric power of $CeIn_3$ (Gambino et al., 1973) has a maximum of 40 μV/K at 75 K.

For the three compounds $CeSn_3$, $CePb_3$ (fig. 11.15) and $CePd_3$ there is no evidence of magnetic order (Tsuchida and Wallace, 1965; Shenoy et al., 1970; Malik and Vijayaraghavan, 1973; Cooper et al., 1971; Gardner et al., 1971, 1972; Hutchens et al., 1971; Harris et al., 1972), the electronic specific heat coefficients are very large (53,200 and 37 mJ/mole-K^2 respectively) (Malik and Vijayaraghavan, 1973; Cooper et al., 1971; Hutchens et al., 1972) and there are large peaks in the respective thermoelectric powers. $CeSn_3$ has a very broad thermoelectric power maximum of 33 μV/K from 100–300 K (Cooper et al., 1971) while $CePd_3$ (Gambino et al., 1973) and $CePb_3$ (Cooper et al., 1971) have sharper thermoelectric power maxima of 120 μV/K and 40 μV/K at 125 K and 40 K respectively.

Using lattice constant measurements Gardner et al. (1972) have determined that the Ce ion valence in $CePd_3$ is about 3.45 when the expansion of the Pd lattice is taken into account. The electrical resistivity of $CePd_3$ (Hutchens et al., 1971; Rao et al., 1971) is qualitatively similar to that of $CeAl_3$ and $CeCu_2Si_2$ discussed previously. Upon cooling the resistance increases from room temperature to 80 K exhibiting a local maximum at about 120 K. At 80 K there is a sharp drop in the resistivity with decreasing temperature. The magnitude of the resistance is large – more than a factor of 10 larger than the resistance of $LaPd_3$.

Harris and Raynor (1965) found the lattice constant of $CeSn_3$ to be strongly temperature dependent suggesting a temperature dependent Ce valence. The electrical resistivity of $CeSn_3$ is relatively normal although the increase of resistance with temperature at room temperature is slower than T^1 (van Daal and Buschow, 1970). Misawa (1974) analyzed $CeSn_3$ in terms of the Fermi liquid approach and was able to account for the broad maximum in the magnetic susceptibility at about 150 K and the finite susceptibility at $T = 0$.

The compound $CeBe_{13}$ crystallizes in the cubic $NaZn_{13}$ structure and has a lattice constant which suggests an intermediate Ce valence (Shoemaker et al., 1952). The magnetic susceptibility of $CeBe_{13}$ (Cooper et al., 1971; Bucher et al., 1975a; Borsa and Olcese, 1973) shows no evidence of magnetic order and is very similar to the susceptibility of $CeSn_3$. The electronic specific heat coefficient (Cooper et al., 1971) is 115 mJ/mole-K and there is a large peak in the thermoelectric power of 60 μV/K at 120 K. The electrical resistivity of $CeBe_{13}$ has no sharp anomalies but at room temperature the resistance rise is slower than T^1. Borsa and Olcese (1973) measured the nuclear magnetic resonance and relaxation rate of the Be nucleus in $CeBe_{13}$. They interpreted their data in terms of a variable Ce valence with Ce^{3+}–Ce^{4+} resonance lifetime of order 10^{-13} sec.

Several other Ce compounds (such as CeAs, CeN, CeB_4, CeP) (Tsuchida et al., 1970; Sales, 1974; Fisk et al., 1972; Weaver and Schirber, 1976) exhibit one or more Kondo-like anomalies; however, none of these compounds have been extensively studied.

Elliott et al. (1969) have studied the resistive and magnetic properties of

concentrated Ce–La and Ce–Y alloys. They observed resistance minima in all Ce–Y alloys with 2–75 at.% Ce and in Ce–La alloys with 14–18 at.% La.

Lawrence et al. (1975) have studied the electronic properties of the Ce, Th system in some detail. While there are definite "Kondo anomalies" in this system, the main thrust of this work is concerned with the thermodynamic behavior near valence instabilities, particularly near the critical point. A detailed discussion of the work is beyond the scope of this article and we refer the reader to the following references: Parks and Lawrence (1976) and Varma (1976 and references therein).

The element cerium is known to exhibit several anomalies in its physical properties which have been attributed to the Kondo effect; however, the body of literature on the various phases of cerium metal is vast, and we refer the reader to ch. 4 by Koskenmaki and Gschneidner which is devoted to this fascinating element, especially see section 4.3.2.

4.3. *Samarium systems*

It was remarked earlier that there is a strong correlation between systems which exhibit a mixed or fluctuating valence and systems which show Kondo-like anomalies. This connection was particularly clear in the Ce systems considered previously. A wide variety of experimental measurements has shown that in SmB_6 and "collapsed" SmS, the Sm ions have a mixed valence (Sm^{2+}–Sm^{3+}). We consider these systems not because they are classic Kondo systems (they are not), but because they provide considerable insight into the nature of the mixed valence state. These systems are also interesting with respect to the study of metal-insulator transitions, but this aspect will be discussed in ch. 20 by Jayaraman.

SmB_6 crystallizes in the cubic CsCl structure with only one type of site for the Sm ion. If the Sm ion is divalent ($4f^6$) the compound should be a semiconductor, while if the Sm ion is trivalent ($4f^5$) the compound should be a metal. The size of the Sm^{2+} ion is much larger than the Sm^{3+} ion. From lattice constant measurements as a function of temperature, Nickerson et al. (1971) showed that the Sm ion has a temperature independent valence of about 2.7. The electrical resistivity (Menth et al., 1969; Nickerson et al., 1971; Sturgeon et al., 1974) of SmB_6 is relatively constant from 300–70 K but increases two orders of magnitude from 70–8 K at which point it saturates. The Hall coefficient and Hall mobility (Nickerson et al., 1971) change sign twice between 1 and 300 K and exhibit sharp minima at 15 K. The thermoelectric power data of Paderno et al. (1969) is similar to the Hall mobility in shape and sign changes, and exhibits a large negative maximum of 350 μV/K at about 15 K.

At high temperatures the magnetic susceptibility (Menth et al., 1969; Nickerson et al., 1971) of SmB_6 (fig. 20.10) falls between the susceptibilities of the Sm^{2+} and Sm^{3+} configurations. At low temperatures the susceptibility saturates with no evidence of magnetic order down to 0.35 K. The electronic contribution to the SmB_6 heat capacity (Nickerson et al., 1971) is large

(determined by comparison to the isostructural compound LaB_6) but complicated, possibly due to interband transitions between closely adjacent valence and conduction bands. Soft X-ray absorption measurements by Vainshtein et al. (1965) and X-ray photoelectron spectroscopy results of Aono et al. (1975) indicate the presence of both valence configurations ($4f^6$ and $4f^5\ 5d^{0.8}\ 6s^{0.2}$) at room temperature. Mössbauer isomer shift measurements on the Sm nucleus by Cohen et al. (1970) showed *one* temperature independent absorption line centered between the positions characteristic of Sm^{2+} and Sm^{3+} ions.

The transport properties of SmB_6 were explained by Nickerson et al. (1971) using a semiconductor band model with two valence bands: a normal parabolic "s type" band and a very narrow "d or f like" band situated at a slightly higher energy. Using this model they found that the total change in carrier concentration (valence) accompanying the electrical resistivity change below 65 K is relatively small. This is consistent with the Mössbauer and lattice constant measurements which indicate no appreciable valence change as a function of temperature. Chui (1976) explained the resistance of SmB_6 in terms of the coulomb interaction between the d and f electrons producing excitonic effects. This leads to an increase in the resistance upon cooling without a change of valence.

The results for "collapsed" SmS are similar to those for SmB_6. At zero pressure SmS is a narrow gap semiconductor and the Sm ion is divalent. Jayaraman et al. (1970a), however, showed that at 6 kbar there was a pressure-induced semiconductor-metal transition without a change of crystal structure.

The SmS semiconductor to metal transition was later verified by the direct observation of a discontinuous change in the optical reflectivity at 6 kbar (Kirk et al., 1972). This is consistent with a first order magnetic phase transition which was directly verified by magnetic susceptibility measurements under pressure by Maple and Wohlleben (1971). In the collapsed phase the susceptibility of SmS showed no magnetic order down to 0.35 K and was almost identical to the susceptibility of SmB_6 (see fig. 20.10 of volume 2). Bader et al. (1973) measured the heat capacity (fig. 11.16) and electrical resistivity (fig. 11.17) of SmS under pressure. They found a large electronic contribution to the heat capacity ($\gamma = 145$ mJ/mole-K^2) and a resistivity reminiscent of SmB_6. Mössbauer isomer shift measurements of SmS under pressure by Coey et al. (1976) reveal the transition from a Sm^{2+} isomer shift at zero pressure to an intermediate value at pressures above 6 kbar (fig. 11.18). The isomer shift of SmS above 6 kbar was found to be about the same as the isomer shifts for "chemically collapsed" $Sm_{0.77}Y_{0.23}S$ and SmB_6 at zero pressure.

Jayaraman et al. (1973) demonstrated that one could chemically collapse the Sm ion in SmS by alloying with Gd [(Sm, Gd)S]. Chemically collapsing the Sm ions in SmS through alloying is extremely useful since one can then study the mixed valence state at atmospheric pressure by varying the alloy composition. Subsequent X-ray photoemission spectroscopy studies on this and similar alloys [(Sm, Th)S, (Sm, As)S] by Campagna et al. (1974a), Freeouf et al. (1974) and

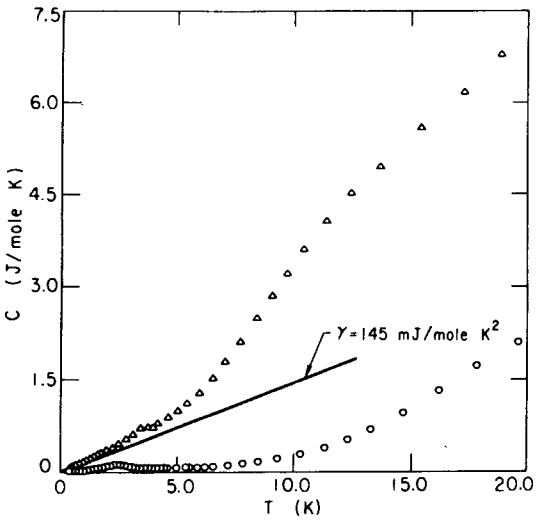

Fig. 11.16. Heat capacity C vs. temperature of SmS at approximately 15 kbar (triangles) and at zero pressure (circles). A plot of C/T vs. T^2 shows that the limiting coefficient γ of the linear term in the heat capacity of the collapsed metallic phase is $\gamma \cong 145$ mJ/mole K^2 [after Bader et al. (1973)].

Pollak et al. (1974), showed the presence of both Sm^{2+} and Sm^{3+} configurations (see fig. 11.19)

We note that electrical resistivity, Hall coefficient, optical measurements and Raman scattering measurements have been reported on the (Sm, Y)S system (Penney and Holtzberg, 1975; Guntherodt and Holtzberg, 1976; Tsang, 1976).

The Mössbauer, magnetic susceptibility, X-ray absorption and X-ray photoemission results for SmB_6 and SmS can be qualitatively understood in terms of the fluctuating valence notion proposed by Maple and Wohlleben (1971; see section 2). They envisioned the Sm ion as fluctuating in time between the two configurations, Sm^{2+} and Sm^{3+}, with a frequency $\nu_0 = \tau_0^{-1}$. This frequency is related to the strength of the interaction of the 4f shell with the conduction electrons and the energy separation between the two configurations. For SmS and SmB_6 they determined $T_0 = h\nu_0/k_B \approx 100$ K, which is consistent with the narrow d or f like bandwidth of 100 K found by Nickerson et al. (1971) for SmB_6.

If measurements are made on a time scale large compared to $\tau_0 = 10^{-12}$ sec, then one will "see" a time average of the two configurations. Magnetic susceptibility and Mössbauer isomer shift experiments are "slow" measurements (measuring times of order 10^{-10} sec and 10^{-8} sec, respectively) on such a time scale. At high temperatures ($T \gg T_0$) the susceptibility is the weighted average of the susceptibilities of the two configurations, but at low temperatures ($T \ll T_0$) saturates to a constant value. The Mössbauer isomer shift experiment should show only one absorption line at a position intermediate between that associated with either Sm^{2+} or Sm^{3+}. Soft X-ray absorption and X-ray photoemission, however, are relatively fast measurements ($\sim 10^{-17}$ sec) and hence will "see"

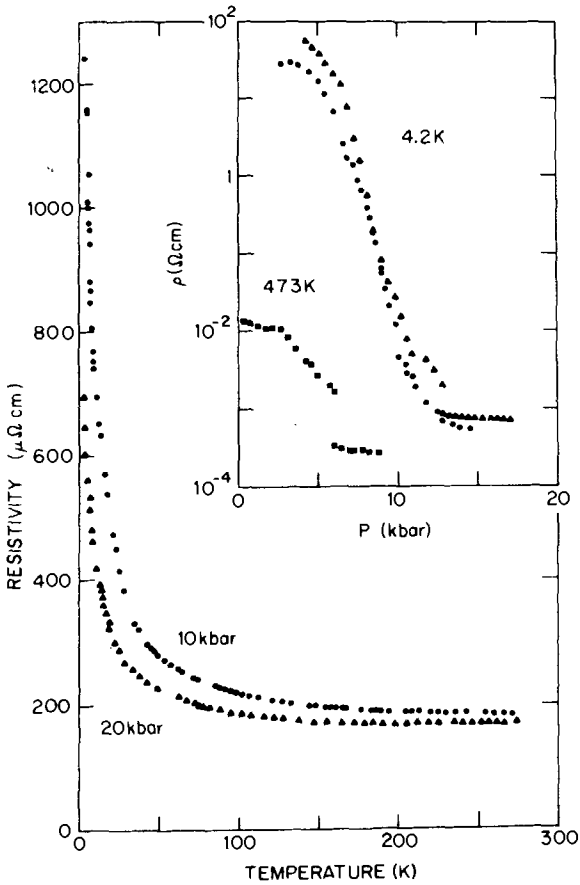

Fig. 11.17. Electrical resistivity ρ vs temperature of SmS at 10 and 20 kbar. The inset compares the insulator-metal transition as a function of pressure at 4.2 and 473 K. The pressure transmitting medium was AgCl (circles), frozen (triangles) or liquid (squares) n-pentane isoamyl alcohol [after Bader et al. (1973)].

either one configuration or the other over the period of a measurement. This results in effects due to the presence of both configurations appearing in the final spectra.

4.4. *Europium systems*

Two concentrated Eu systems have been found to exhibit "Kondo-like" anomalies: $EuCu_2Si_2$ and (Eu, La)Rh_2. Mössbauer experiments on both systems have been performed by Bauminger et al. (1973). For the $EuCu_2Si_2$ system, which has only one site for the Eu ion, they found one temperature dependent absorption line situated between the two regions corresponding to either Eu^{2+} or Eu^{3+}. Previously no Eu compound had exhibited an isomer shift in this

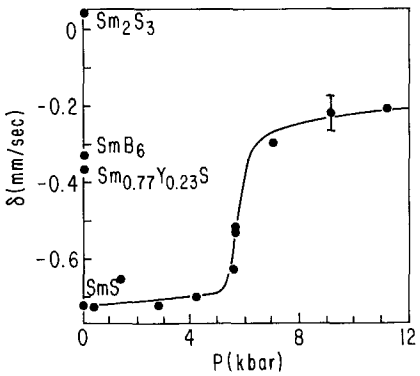

Fig. 11.18. Mössbauer isomer shift of ^{149}Sm in SmS vs pressure at room temperature. The isomer shifts are relative to a source of ^{149}Eu in EuF_3. At zero pressure the isomer shifts of $Sm_2S_3(Sm^{3+})$, SmB_6 and $Sm_{0.77}Y_{0.23}S$ (mixed valence) are shown for comparison [after Coey et al. (1976)].

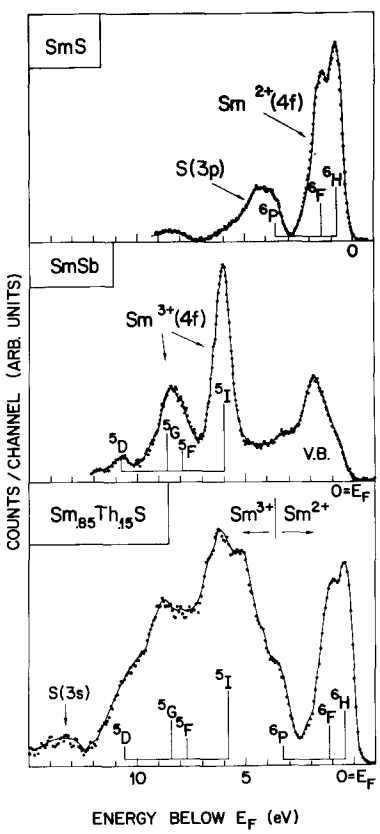

Fig. 11.19. Comparison of the X-ray photoemission spectra of 4f electrons in SmS (zero pressure, divalent Sm), SmSb (trivalent Sm) and the mixed valence $(Sm_{0.85}Th_{0.15})S$ alloy. The vertical bars indicate the calculated multiplet intensities using the method of fractional parentage [after Campagna et al. (1976)].

intermediate region. The data were interpreted in terms of a fluctuating valence ($4f^6$–$4f^7$) and a lower limit of 3×10^{10} cps was placed on the fluctuation frequency. Similar results were obtained for the (Eu, La)Rh_2 system (Bauminger et al., 1974), but in this alloy there are five different environments for the Eu atoms depending on the number of nearest neighbor La atoms. This results in a complicated absorption spectrum with each different Eu environment having a different characteristic fluctuation frequency.

Mössbauer measurements on $Eu_{0.25}La_{0.75}Rh_2$ under pressure have been made by Wortmann et al. (1976). They found a strong pressure induced shift of the resonance lines which they explained by an increase in the energy separation between the Eu^{2+} and Eu^{3+} valence states. We note that Bauminger et al. (1976) have recently reported Mössbauer measurements on the Eu(A, $B)_2$ (A = Rh, Ir, B = Pt, Al) systems.

The magnetic susceptibility, electrical resistivity, thermoelectric power and heat capacity of $EuCu_2Si_2$ have been measured by Sales and Viswanathan (1976). The susceptibility shows no evidence of magnetic order down to 0.4 K, and has a value intermediate between that of Eu^{2+} and Eu^{3+} over the temperature range 0.4–300 K. At room temperature the susceptibility is strongly pressure dependent with $d\chi/dP = -1.6 \times 10^{-4}$ emu/mole·kbar. The resistivity has no sharp features but follows a T_3 law at low temperatures and exhibits pronounced negative curvature near room temperature. The thermoelectric power shows a very broad maximum of 9 μV/K from 20–200 K-similar in shape to that of $CeSn_3$ which also has a strongly temperature dependent valence (see section 4.2). The electronic contribution to the heat capacity is large with $\gamma = 67.5$ mJ/mole·K^2. Sales and Viswanathan (1976) interpreted their data in terms of a fluctuating Eu valence with a fluctuation frequency of 2×10^{12} cps (50 K).

4.5. *Thulium systems*

TmTe and TmSe have been investigated with respect to valence fluctuations. The lattice constants of the R-tellurides and R-selenides were reported by Iandelli (1961) and from these data it appears that TmTe is divalent and TmSe has an intermediate valence at room temperature. All of these compounds crystallize in the rock salt structure.

Jayaraman et al. (1970b) found a very strong pressure induced decrease in the lattice parameter and electrical resistivity of TmTe. Wohlleben et al. (1972) have investigated the magnetic susceptibility of TmTe over the temperature range from 0.4–300 K and at pressures from 0–50 kbar. They found no clear evidence of magnetic order, although the magnetization curves at low temperatures are highly nonlinear. Three different electronic regimes were found as a function of pressure and explained as different temporal mixtures of Tm^{2+} and Tm^{3+} configurations. X-ray photoemission measurements on TmTe by Campagna et al. (1974b) (at atmospheric pressure and room temperature) indicated the presence of both Tm^{2+} and Tm^{3+} configurations. They interpreted their results in terms of valence fluctuations. However, recent optical absorption and ultraviolet photo-

emission measurements by Suryanarayanan et al. (1975) on thin films of TmTe indicated that the Tm was essentially divalent. They found that a small ultraviolet photoemission spectroscopy (UPS) signal corresponding to Tm^{3+} was obtained but that this signal was strongly dependent on the surface condition. This conclusion is supported by the reflectivity measurements on TmTe by Batlogg et al. (1976) and Ward et al. (1975). It should be noted, however, that the lattice constants of the various TmTe samples studied differed appreciably and that there may be problems related to variations in stoichiometry and vacancies. (See Bucher et al., 1975a and Batlogg et al., 1976.)

The TmSe lattice constant, resistivity and magnetic susceptibility were investigated by Bucher et al. (1975b). From these data as well as XPS measurements by Campagna et al. (1974b), it was concluded that TmSe had a nonintegral valence and underwent temporal fluctuations between Tm^{2+} and Tm^{3+} configurations. However, low temperature specific heat and magnetization measurements by Bucher et al. (1970) revealed that TmSe ordered at 3 K although there was no evidence of long range magnetic order or crystal fields in neutron diffraction experiments performed at 1 K (Cox et al., unpublished). Ott et al. (1975) have investigated in detail the nature of the ordered state of TmSe by means of thermal expansion, magnetostriction and a.c. susceptibility measurements in different magnetic fields. They found that the ordering is antiferromagnetic in nature but that there appear to be at least three different phases below the Néel temperature. The reflectivity measurements of Batlogg et al. (1976) and Ward et al. (1975) are in disagreement with respect to the presence of valence fluctuations in TmSe. As is the case with the TmTe samples there may also be problems (related to stoichiometry and vacancies) with the TmSe samples. Further investigation of this interesting system is needed.

4.6. *Ytterbium systems*

With the exception of Ce systems, lanthanide compounds and alloys made with Yb most frequently exhibit Kondo anomalies. Two of the most thoroughly studied Yb systems are $YbAl_2$ and $YbAl_3$. The phase diagram for the Yb–Al system has been reported by Palenzona (1972). $YbAl_2$ crystallizes in the cubic $MgCu_2$ Laves phase while $YbAl_3$ forms in the cubic Cu_3Au structure. Iandelli and Palenzona (1972) measured the lattice constants of both compounds from 80–800 K.

For $YbAl_3$ the Yb ion appears to have a temperature independent valence of about 2.9, while in $YbAl_2$ the Yb valence is about 2.5 at 800 K, but is almost completely divalent at 80 K (Iandelli and Palenzona, 1972). The magnetic susceptibility of $YbAl_3$ (van Vucht and Buschow, 1965; Iandelli and Palenzona, 1972; Sales and Wohlleben, 1975; Havinga et al., 1973) (fig. 11.20) follows a Curie–Weiss law at high temperatures with a Curie–Weiss temperature $\theta = -143$ K and an effective moment $\mu_{eff} = 3.89\ \mu_B$. At about 120 K there is a broad maximum in the susceptibility and there is subsequently no evidence of magnetic order down to 0.4 K. At room temperature there was no effect of pressure

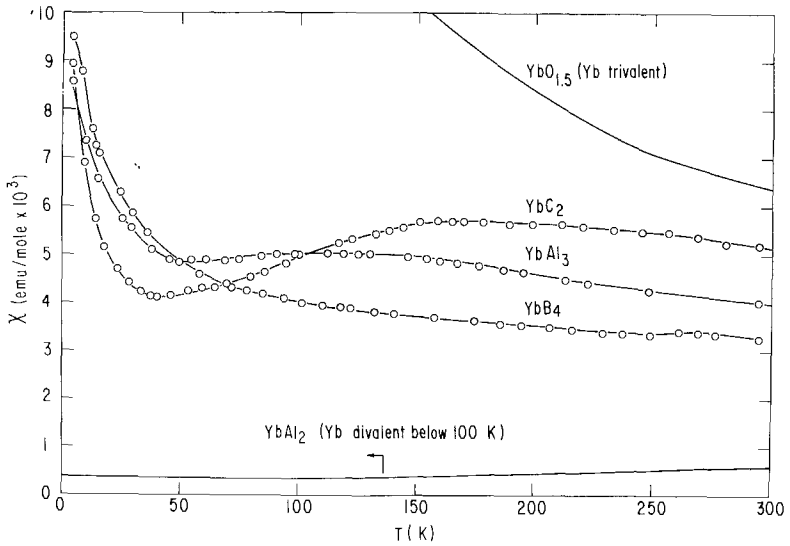

Fig. 11.20. Magnetic susceptibility vs temperature for several nonmagnetic Yb compounds with nonintegral valence. The rapid increase below 50 K is attributed to less than 1% of Yb_2O_3 impurity. For comparison, the magnetic susceptibility of Yb_2O_3 (Yb^{3+}) and $YbAl_2$ (Yb^{2+}) are also shown [after Sales (1974); Maple and Wohlleben (1974)].

($P < 15$ kbar) on the $YbAl_3$ susceptibility ($d\chi/dP < 1.5 \times 10^{-6}$ emu/gm-kbar) Sales, 1974). The magnetic susceptibility of $YbAl_2$ is temperature independent at low temperatures (0.6×10^{-6} emu/mole), but increases with increasing temperatures reaching a maximum of 5.5×10^{-6} emu/gm at 850 K (Klasse et al., 1973). At room temperature the susceptibility of $YbAl_2$ is strongly pressure dependent with $d\chi/dP = 2 \times 10^{-5}$ emu/mole·kbar (Sales, 1974).

The electrical resistivities of both compounds $YbAl_2$ and $YbAl_3$ have no sharp anomalies. The electronic specific heat coefficients are $\gamma = 16.8$ mJ/mole·K^2 and $\gamma = 45$ mJ/mole·K^2 for $YbAl_2$ and $YbAl_3$, respectively (Havinga et al., 1973) as compared to $\gamma = 5.7$ mJ/mole·K^2 for $LuAl_2$ (Hungsberg and Gschneidner, 1972). The magnitude of the thermoelectric power of $YbAl_3$ (van Daal, 1974) has a maximum of $-90\ \mu$V/K at 250 K – a factor of 30 higher than the thermopower of $LuAl_3$ at the same temperature. Havinga et al. (1973) interpret the $YbAl_3$ and $YbAl_2$ data at low temperatures in terms of a virtual bound 4f state just below the Fermi level, while at high temperatures a two level model is employed with an Yb^{2+} ground state and an Yb^{3+} excited state.

$YbCu_2Si_2$ crystallizes in the tetragonal $ThCr_2Si_2$ structure (Rieger and Parthe, 1969). At room temperature the lattice constant suggests an Yb valence of about 2.8. The high temperature magnetic susceptibility (Sales and Viswanathan, 1976) follows a Curie–Weiss law with $\mu_{\text{eff}} = 4.19\,\mu_B$ and $\theta = -160$ K for $H \| a$ and $\theta = -42$ K for $H \| c$. Below 75 K the susceptibility flattens out in both directions with no evidence of magnetic order down to 0.4 K. At room temperature there was no effect of pressure on the susceptibility ($d\chi/dP < 1.5 \times$

10^{-6} emu/mole·kbar). The electrical resistivity is a monotonic function of temperature but at room temperatures the increase is much slower than T^1. The thermoelectric power has a maximum of $40\,\mu$V/K at 60 K, as compared to $5\,\mu$V/K for YCu_2Si_2 at the same temperature. The electronic specific heat coefficient is large with $\gamma = 135$ mJ/mole·K^2. Sales and Viswanathan (1976) interpreted their data in terms of a fluctuating Yb valence with an intrinsic lifetime of the Yb^{3+} configuration of 0.3×10^{-12} sec (75 K).

The compounds YbC_2, YbB_4, $YbIn_3$, and $YbCu_2$ (Gschneidner, 1961; Klaasse et al., 1973; Fisk et al., 1972; Sales, 1974) exhibit one or more anomalies associated with the Kondo effect. However, with the exception of a minimum at 40 K in the electrical resistivity of YbC_2 (Sales, 1974), the three compounds discussed previously typify the anomalies found in Yb systems.

5. Concluding remarks

In this chapter, we have shown that both dilute and concentrated assemblages of lanthanide ions with partially-filled 4f electron shells in a metallic environment exhibit a continuum of magnetic behaviors which span the entire range between magnetism and nonmagnetism. We have emphasized that with each magnetic state of a lanthanide ion in this continuum there can be associated a phenomenological characteristic temperature above which the metallic lanthanide system behaves *magnetically* and below which the system behaves *nonmagnetically*. The characteristic temperature increases with the amount of hybridization or admixture of the localized 4f electron states of the lanthanide ions with the extended states of the conduction band. Thus within a given temperature range, increasing hybridization tends to drive the metallic lanthanide system towards nonmagnetic behavior. This 4f-conduction electron hybridization is also responsible for the striking temperature-dependent Kondo-like anomalies which occur in a growing number of dilute and concentrated metallic lanthanide systems. Among the thirteen lanthanide ions with partially-filled 4f electron shells, Ce, Pr, Sm, Eu, Tm and Yb have been observed to exhibit Kondo-like behavior in numerous metallic alloys and compounds.

An important point we have stressed in this chapter is that the magnetic state of lanthanide ions can often be profoundly varied through the application of external pressure or by alloying with another element. This has made it possible to follow the evolution of the physical properties throughout the entire range of magnetic character of the lanthanide ion in a number of dilute and concentrated lanthanide systems. In the (La, Th)Ce system, the superconducting and normal state physical properties have been documented in detail throughout the continuous demagnetization of the Ce solute ions which proceeds as the La, Th matrix composition is varied from pure La to pure Th. This, and similar studies, have made it possible to study the response of the superconducting electron gas to the presence of localized states of solutes whose magnetic character spans the entire range from magnetism to nonmagnetism. These studies have also revealed

that a strong correlation exists between the behavior of the superconducting properties and the magnetic state of a solute ion. This, in turn, has provided a means whereby the magnetic state of a solute dissolved in a superconducting metallic matrix may be determined by studying the modification of the superconducting properties of the matrix caused by the introduction of the impurity ion.

We have also emphasized that in metals interactions between lanthanide ions are relatively weak compared to interactions between their transition metal ion counterparts. This is perhaps the most significant advantage afforded by lanthanide ions in the study of Kondo-like behavior in both dilute and concentrated lanthanide systems. The weak Ce inter-impurity interactions in the (LaCe)Al_2 system have permitted the classic single impurity Kondo anomalies in both the superconducting and normal state of this exemplary system to be documented in great detail as a function of temperature and magnetic field. The extensive data which have been accumulated for (LaCe)Al_2 have provided strong tests of several theories which have been developed to account for the striking temperature dependent Kondo effects in both the superconducting and normal state.

The relatively weak interactions between lanthanide ions in concentrated lanthanide systems often allow Kondo-like anomalies (which are qualitatively identical to those which occur in dilute lanthanide systems) to be investigated without the additional complications which are introduced by the occurrence of magnetic order. The Kondo anomalies in the physical properties of concentrated lanthanide systems are large and generally dominate over the ordinary lattice and conduction electron contributions. This minimizes the ambiguities often encountered in the study of Kondo phenomena in dilute impurity systems (particularly those which involve 3d transition metal impurity ions) where the variation of the normal state properties with temperature and magnetic field can only be obtained after the large background of the matrix has been subtracted.

Studies on concentrated lanthanide metallic systems have also made it possible to establish a correlation between nonintegral valence (observable in *concentrated* lanthanide systems through lattice constant, Mössbauer isomer shift, soft X-ray absorption and X-ray photoemission spectroscopy measurements) and *nonmagnetic* behavior of a lanthanide ion below the characteristic temperature. This has led to the concept of valence fluctuations (or interconfiguration fluctuations) which has stimulated the current intense activity among theorists and experimentalists alike.

SmS, Ce metal and $CeAl_3$ are three of the most thoroughly studied concentrated systems which exhibit Kondo-like anomalies. In analogy with the dilute (La, Th)Ce system, the magnetic state of the lanthanide ions in these concentrated materials has also been varied by applying external pressure or by alloying with other elements.

From this review, it is apparent that lanthanide metallic systems exhibit many varied and striking types of superconducting and normal state behavior in their physical properties, and that they provide a rich testing ground for concepts and models describing Kondo-like anomalies. We have made an effort to point out

that the field is still in the developing stage. A unified "first principles" theoretical description for the formation of a localized magnetic moment in a metal and the attendant Kondo-like anomalies in the physical properties has yet to emerge, despite the considerable amount of experimental data which have been accumulated and the intense theoretical effort which has been expended over the past decade. Thus our understanding of lanthanide systems which exhibit Kondo-like behavior is far from complete, and there is a large amount of room for future contributions from both theorists and experimentalists. Undoubtedly, new effects and types of behavior await to be discovered, studied and explained as our knowledge of this fascinating class of materials advances.

References

Abou Aly, A.I., S. Bakanowski, N.F. Berk, J.E. Crow and T. Mihalisin, 1975, Phys. Rev. Lett. **35**, 1387.

Abou Aly, A.I., S. Bakanowski, N.F. Berk, J.E. Crow and T. Mihalisin, 1976, in: Proceedings of the Twenty-first Annual Conference on Magnetism and Magnetic Materials, Philadelphia, 1975 (AIP Conf. Proc. No. 29), pp. 358–360.

Abrikosov, A.A. and L.P. Gor'kov, 1961, Sov. Phys. JETP **12**, 1243.

Allali, V., P. Donzé and A. Treyvaud, 1969, Solid State Commun. **7**, 1241.

Allali, V., P. Donzé, D. Gainon and J. Sierro, 1970, J. Appl. Phys. **41**, 1154.

Anderson, P.W. and A.M. Clogston, 1961, Bull. Am. Phys. Soc. **6**, 124.

Anderson, P.W., 1961, Phys. Rev. **124**, 41.

Anderson, P.W. and S.T. Chui, 1974, Phys. Rev. B**9**, 3229.

Andres, K., J.E. Graebner and H.R. Ott, 1975, Phys. Rev. Lett. **35**, 1779.

Aoi, T., J. Takeuchi and Y. Masuda, 1974, J. Phys. Soc. Japan **36**, 1485.

Aoi, T. and Y. Masuda, 1974, J. Phys. Soc. Japan **37**, 673.

Aono, M., S. Kawai, S. Kono, M. Okusawa, T. Sagawa and Y. Takehana, 1975, Solid State Commun. **16**, 13.

Armbrüster, H., H.V. Lohneysen, G. Riblet and F. Steglich, 1974, Solid State Commun. **14**, 55.

Bader, S.D., N.E. Phillips and D.B. McWhan, 1973, Phys. Rev. B**7**, 4686.

Bader, S.D., N.E. Phillips, M.B. Maple and C.A. Luengo, 1975, Solid State Commun. **16**, 1263.

Bakanowski, S., J.E. Crow and T. Mihalisin, 1977 Solid State Commun. **22**, 241.

Barbara, B., M.F. Rossignol, H.G. Purwins and E. Walker, 1975, Solid State Commun. **17**, 1525.

Batlogg, B., E. Kaldis, A. Schelegel and P. Wachter, 1976, Phys. Lett. **56**A, 122.

Bauminger, E.R., D. Froindlich, I. Nowik, S. Ofer, I. Felner and I. Mayer, 1973, Phys. Rev. Lett. **30**, 1053.

Bauminger, E.R., I. Felner, D. Levron, I. Nowik and S. Ofer, 1974, Phys. Rev. Lett. **33**, 890.

Bauminger, E.R., I. Felner, D. Levron, I. Nowik and S. Ofer, 1976, Solid State Commun. **18**, 1073.

Bekker, F.F. and C.J.A. van Duren, 1974, Physica **77**, 609.

Bekker, F.F. and C.J.A. van Duren, 1975, in: Krusius, M. and M. Vuorio, eds., Proceedings of the Fourteenth International Conference on Low Temperature Physics, Otaniemi, Finland, 1975, vol. 3 (North Holland, Amsterdam), pp. 406–409.

Benoit, A., J. Flouquet and J. Sanchez, 1973, Solid State Commun. **13**, 1581.

Benoit, A., R. Delaplace and J. Flouquet, 1974a, Phys. Rev. Lett. **32**, 222.

Benoit, A., J. Flouquet and J. Sanchez, 1974b, Phys. Rev. B**9**, 1092.

Bhattacharjee, A.K. and B. Coqblin, 1976, Solid State Commun. **18**, 1587.

Bijvoet, J., A.J. van Dam and Flora van Beek, 1966, Solid State Commun. **4**, 455.

Bloomfield, P.E. and D.R. Hamann, 1967, Phys. Rev. **164**, 856.

Boes, J., A.J. van Dam and J. Bijvoet, 1968, Phys. Lett. **28**A, 101.

Borchi, E. and S. DeGennaro, 1974, Phys. Rev. B**9**, 209.

Borchi, E. and S. DeGennaro, 1975, Phys. Lett. **54**A, 159.

Borsa, F. and G. Olcese, 1973, Phys. Stat. Sol. a **17**, 631.

Bucher, E., K. Andres, J.P. Maita and G.W. Hull, Jr., 1968, Helv. Phys. Acta **41**, 723.

Bucher, E., A.C. Gossard, K. Andres, J.P. Maita and A.S. Cooper, 1970, in: Henrie, T.A. and R.F. Lindstrom, eds., Proceedings of the Eighth Rare Earth Conference (USGPO), Washington, D.C., 1970, pp. 74–89.

Bucher, E., J.P. Maita, G.W. Hull, R.C. Fulton and A.S. Cooper, 1975a, Phys. Rev. B**11**, 440.

Bucher, E., K. Andres, F.J. DiSalvo, J.P. Maita, A.C. Gossard, A.S. Cooper and G.W. Hull, 1975b, Phys. Rev. B**11**, 500.

Burr, C.R. and R.G. Pirich, 1975, J. Phys. Chem. Solids **36**, 1223.

Buschow, K.H.J. and J.F. Fast, 1966, Z. Phys. Chem. **50**, 1.

Buschow, K.H.J. and H.J. van Daal, 1969, Phys. Rev. Lett. **23**, 408.

Buschow, K.H.J., H.J. van Daal, F.E. Maranzana and P.B. van Aken, 1971, Phys. Rev. B**3**, 1662.
Campagna, M., E. Bucher, G.K. Wertheim and L.D. Longinotti, 1974a, Phys. Rev. Lett. **33**, 165.
Campagna, M., E. Bucher, G.K. Wertheim, D.N.E. Buchanan and L.D. Longinotti, 1974b, Phys. Rev. Lett. **32**, 885.
Campagna, M., G.K. Wertheim and E. Bucher, 1976, Structure and Bonding **35**, 125 (to be published).
Chui, S.T., 1976, Phys. Rev. B**13**, 2066.
Coey, J.M.D., S.K. Ghatak, M. Avignon and F. Holtzberg, 1976, Phys. Rev. B **14**, 3744.
Cohen, R.L., M. Eibschutz and K.W. West, 1970, Phys. Rev. Lett. **24**, 383.
Cooper, J.R., C. Rizzuto and G.L. Olcese, 1971, J. Physique Suppl. **32**, C1-1136.
Cooper, J.R. and C. Rizzuto, 1973, J. Low Temp. Phys. **10**, 207.
Coqblin, B. and J.R. Schrieffer, 1969, Phys. Rev. **185**, 847.
Cornut, B. and B. Coqblin, 1972, Phys. Rev. B**5**, 4541.
Cornut, B. and B. Coqblin, 1975, in: Krusius, M. and M. Vuorio, eds., Proceedings of the Fourteenth International Conference on Low Temperature Physics, Otaniemi, Finland, 1975, vol. 3 (North Holland, Amsterdam), pp. 410–413.
Cox, D.E., R.J. Passel R. Birgeneau, E. Bucher, H.A. Mook and H.C. Davis, unpublished.
Culbert, H.V. and A.S. Edelstein, 1974, Solid State Commun. **15**, 1633.
Deenadas, C., A.W. Thompson, R.S. Craig and W.E. Wallace, 1971, J. Phys. Chem. Solids **32**, 1853.
DeGennaro, S. and E. Borchi, 1973, Phys. Rev. Lett. **30**, 377.
DeGennaro, S. and E. Borchi, 1974, Phys. Rev. B**9**, 4985.
deGennes, P.G., 1962a, J. Phys. Rad. **23**, 510.
deGennes, P.G., 1962b, J. Physique **23**, 630.
Delfs, R.J., B.J. Beaudry and D.K. Finnemore, 1975, Phys. Rev. B**11**, 4212.
DeLong, L.E., R.W. McCallum and M.B. Maple, 1975, in: Krusius, M. and M. Vuorio, eds., Proceedings of the Fourteenth International Conference on Low Temperature Physics, Otaniemi, Finland, 1975, vol. 2 (North Holland, Amsterdam), pp. 541–544.
DeLong, L.E., R.W. McCallum, M.B. Maple and J.G. Huber, 1976, Bull. Am. Phys. Soc. **21**, 383.
deWijn, H.W., A.M. van Diepen and K.H.J. Buschow, 1975, in: Devine, R.A.B., ed., Proceedings of the First Conference on Crystalline Electric Field Effects in Metals and Alloys, Montreal, 1974 (unpublished), pp. 401–453.
Dietrich, M., W. Gey and E. Umlauf, 1972, Solid State Commun. **11**, 655.
Edelstein, A.S., 1968, Phys. Rev. Lett. **20**, 1348.
Edelstein, A.S., L.R. Windmiller, J.B. Ketterson, G.W. Crabtree and S.P. Bowen, 1971, Phys. Rev. Lett. **26**, 516.
Edelstein, A.S., C.J. Tranchita, O.D. McMasters and K.A. Gschneidner, Jr., 1974, Solid State Commun. **15**, 81.
Edelstein, A.S., H.R. Child and C. Tranchita, 1976, Phys. Rev. Lett. **36**, 1332.
Elliott, R.O., H.H. Hill and W.N. Miner, 1969, Phys. Stat. Sol. **32**, 609.
Felsch, W. and K. Winzer, 1973, Solid State Commun. **13**, 569.
Felsch, W., K. Winzer and G. v. Minnigerode, 1975, Z. Phys. **21**B, 151.
Fert, A. and O. Jaoul, 1972, Solid State Commun. **11**, 759.
Fertig, W.A., 1976, Ph.D. Thesis, University of California, San Diego, La Jolla, California (unpublished).
Fisk, Z. and B.T. Matthias, 1969, Science **165**, 279.
Fisk, Z., B.T. Matthias and E. Corenzwit, 1969, Proc. Nat. Acad. Sci. **64**, 1151.
Fisk, Z., A.S. Cooper, P.H. Schmidt and R.N. Castellano, 1972, Mat. Res. Bull. **7**, 285.
Flouquet, J. and D. Marsh, 1970, Phys. Lett. **32**A, 501.
Flouquet, J., 1971, Phys. Rev. Lett. **27**, 515.
Floquet, J. and W.D. Brewer, 1975, Phys. Scripta **11**, 199.
Freeouf, J.L., D.E. Eastman, W.D. Grobman, F. Holtzberg and J.B. Torrance, 1974, Phys. Rev. Lett. **33**, 161.
Friedel, J., 1958, Nuovo Cimen. Suppl. **12**, 1861.
Frossati, G., J.M. Mignot, D. Thoulouze and R. Tournier, 1975, in: Krusius, M. and M. Vuorio, eds., Proceedings of the Fourteenth International Conference on Low Temperature Physics, Otaniemi, Finland, 1975, vol. 3 (North Holland, Amsterdam), pp. 402–405.
Frossati, G., J.M. Mignot, D. Thoulouze and R. Tournier, 1976, Phys. Rev. Lett. **36**, 203.
Fulde, P. and I. Peschel, 1972, Adv. Phys. **21**, 1.
Gainon, D., P. Donzé and J. Sierro, 1967, Solid State Commun. **5**, 151.
Gambino, R.J., W.D. Grobman and A.M. Toxen, 1973, Appl. Phys. Lett. **22**, 506.
Gardner, W.E., J. Penfold and I.R. Harris, 1971, J. Physique Suppl. **32**, C1139.
Gardner, W.E., J. Penfold, T.F. Smith and I.R. Harris, 1972, J. Phys. F **2**, 133.
Gey, W. and E. Umlauf, 1971, Z. Phys. **242**, 241.
Goncalves da Silva, C.E.T. and L.M. Falicov, 1975, Solid State Commun. **17**, 1521.
Gonzalez-Jimenez, F. and P. Imbert, 1972, Solid State Commun. **11**, 861.
Gonzalez-Jimenez, F. and P. Imbert, 1973, Solid State Commun, **13**, 85.
Gonzalez-Jimenez, F., F. Hartmann-Boutron, P. Imbert, B. Cornut and B. Coqblin, 1974a, J. Physique Colloq. **35**, C6-420.
Gonzalez-Jimenez, F., P. Imbert and F. Hartmann–Boutron, 1974b, Phys. Rev. B**9**, 95.
Gonzalez-Jimenez, F., F. Hartmann-Boutron and P. Imbert, 1974c, Phys. Rev. B**10**, 2122.
Gonzalez-Jimenez, F., B. Cornut and B. Coqblin, 1975, Phys. Rev. B**11**, 4674.

Grüner, G. and A. Zawadowski, 1974, Reports on Prog. in Phys. **37**, 1497.
Gschneidner, K.A., Jr., 1961, Rare Earth Alloys (D. Van Nostrand, Princeton).
Guertin, R.P., J.E. Crow, A.R. Sweedler and S. Foner, 1973, Solid State Commun. **13**, 25.
Guntherodt, G. and F. Holtzberg, 1976, Solid State Commun. **18**, 181.
Haen, P. and P. Lethuillier, 1975, in: Krusius, M. and M. Vuorio, eds., Proceedings of the Fourteenth International Conference on Low Temperature Physics, Otaniemi, Finland, 1975, vol. 3 (North Holland, Amsterdam), pp. 418–421.
Harris, I.R. and G.V. Raynor, 1964, J. Less-Common Met. **6**, 70.
Harris, I.R. and G.V. Raynor, 1965, J. Less-Common Met. **9**, 7.
Harris, I.R., M. Norman and W.E. Gardner, 1972, J. Less-Common Met. **29**, 299.
Hartmann-Boutron, F., 1974, Phys. Rev. B**10**, 2113.
Havinga, E.E., K.H.J. Buschow and H.J. van Daal, 1973, Solid State Commun. **13**, 621.
Hedgcock, F.T. and B. Petrie, 1970, Can. J. Phys. **48**, 1283.
Heeger, A.J., 1969, in: Seitz, F. and D. Turnbull, eds., Solid State Physics, vol. 23, 1969 (Academic Press, New York), pp. 283–411.
Hill, R.W. and J.M. Machado da Silva, 1969, Phys. Lett. **30**A, 13.
Hillenbrand, B. and M. Wilhelm, 1970, Phys. Lett. **33**A, 61.
Hillenbrand, B. and M. Wilhelm, 1972, Phys. Lett. **40**A, 387.
Hirst, L.L., Gwyn Williams, D. Griffiths and B.R. Coles, 1968, J. Appl. Phys. **39**, 844.
Hirst, L.L., 1970, Phys. Kondens. Mat. **11**, 255.
Hirst, L.L., 1975, in: Graham, Jr., C.D., G.H. Lander, J.J. Rhyne, eds., Magnetism and Magnetic Materials – 1974, San Francisco, 1974 (AIP Conf. Proc. No. 24), pp. 11–15.
Hoenig, H.E., H. Happel, H.K. Njoo and H. Seim, 1975, in: Devine, R.A.B., ed., Proceedings of the First Conference on Crystalline Electric Field Effects in Metals and Alloys, Montreal, 1974, (unpublished), pp. 298–322.
Huber, J.G. and M.B. Maple, 1970, J. Low Temp. Phys. **3**, 537.
Huber, J.G. and M.B. Maple, 1972, in: Timmerhaus, K.D., W.J. O'Sullivan and E.F. Hammel, eds., Proceedings of the Thirteenth International Conference on Low Temperature Physics, Boulder, 1972, vol. 2 (Plenum Press, New York). pp. 579–584.
Huber, J.G., W.A. Fertig and M.B. Maple, 1974, Solid State Commun. **15**. 453.
Huber, J.G., J. Brooks, D. Wohlleben and M.B. Maple, 1975, in: Graham, Jr., C.D., G.H. Lander and J.J. Rhyne, eds., Magnetism and Magnetic Materials – 1974, San Francisco, 1974 (AIP Conf. Proc. No. 24), pp. 475–476.
Hungsberg, R.E. and K.A. Gschneidner, Jr., 1972, J. Phys. Chem. Solids **33**, 401.
Hutchens, R.D., V.U.S. Rao, J.E. Greedan, W.E. Wallace and R.S. Craig, 1971, J. Appl. Phys. **42**, 1293.
Hutchens, R.D., 1972, J. Phys. Soc. Japan **32**, 451.
Iandelli, A., 1961, in: Kleber, E.V., ed., Rare Earth Research (McMillan, New York), p. 135.
Iandelli, A. and A. Palenzona, 1972, J. Less-Common Met. **29**, 293.
Jayaraman, A., V. Narayanamurti, E. Bucher and R.G. Maines, 1970a, Phys. Rev. Lett. **25**, 1430.
Jayaraman, A., E. Bucher and D.B. McWhan, 1970b, in: Henrie, T.A. and R.E. Lindstrom, eds., Proceedings of the Eighth Rare Earth Conference (USGPO), Washington, D.C., 1970, pp. 333–344.
Jayaraman, A., E. Bucher, P.D. Dernier and L.D. Longinotti, 1973, Phys. Rev. Lett. **31**, 700.
Jones, H., Ø. Fischer, G. Bongi and A. Treyvaud, 1972, Solid State Commun. **10**, 927.
Kaiser, A.B., 1970, J. Phys. C**3**, 409.
Kasuya, T., 1956, Progr. Theoret. Phys. (Kyoto) **16**, 45.
Keller, J. and P. Fulde, 1973, J. Low Temp. Phys. **12**, 63.
Khomskii, D.I. and A.N. Kocharjan, 1976, Solid State Commun. **18**, 985.
Kim, K.S. and M.B. Maple, 1970, Phys. Rev. B**2**, 4696.
Kirk, J.L., K. Vedam, V. Narayanamurti, A. Jayaraman and E. Bucher, 1972, Phys. Rev. B**6**, 3023.
Klaasse, J.C.P., J.W.E. Sterkenburg, A.H.M. Bleyendaal and F.R. deBoer, 1973, Solid State Commun. **12**, 561.
Kondo, J., 1962, Prog. Theo. Phys. (Kyoto) **28**, 846.
Kondo, J., 1964, Prog. Theo. Phys. (Kyoto) **32**, 37.
Lawrence, J.M., M.C. Croft and R.D. Parks, 1975, Phys. Rev. Lett. **35**, 289.
Lethuillier, P., 1975, Phys. Rev. **12**B, 4836.
Lethuillier, P. and P. Haen, 1975, Phys. Rev. Lett. **35**, 1391.
Ludwig, A. and M.J. Zuckermann, 1971, J. Phys. F **1**, 516.
Luengo, C.A., M.B. Maple and W.A. Fertig, 1972, Solid State Commun. **11**, 1445.
Luengo, C.A., J.G. Huber, M.B. Maple and M. Roth, 1974, Phys. Rev. Lett. **32**, 54.
Luengo, C.A., J.G. Huber, M.B. Maple and M. Roth, 1975, J. Low Temp. Phys. **21**, 129.
McCallum, R.W., W.A. Fertig, C.A. Luengo, M.B. Maple, E. Bucher, J.P. Maita, A.R. Sweedler, L. Mattix, P. Fulde and J. Keller, 1975a, Phys. Rev. Lett. **34**, 1620.
McCallum, R.W., C.A. Luengo and M.B. Maple, 1975b, in: Krusius, M. and M. Vuorio, eds., Proceedings of the Fourteenth International Conference on Low Temperature Physics, Otaniemi, Finland, 1975, vol. 2 (North Holland, Amsterdam), pp. 537–540.
Mader, K.H. and W.M. Swift, 1968, J. Phys. Chem. Solids **29**, 1759.
Mahoney, J.V., V.U.S. Rao, W.E. Wallace, R.S. Craig and N.G. Nereson, 1973, Phys. Rev. B**9**, 154.
Malik, S.K., 1970, Phys. Lett. **31**A, 33.
Malik, S.K. and R. Vijayaraghavan, 1973, in: Proceedings of the International Conference on Magnetism, Moscow, 1973.
Maple, M.B. and Z. Fisk, 1968, in: Allen, J.F.,

D.M. Findlayson and D.M. McCall, eds., Proceedings of the Eleventh International Conference on Low Temperature Physics, St Andrews, Scotland, 1968, vol. 2 (St. Andrews), pp. 1288–1292.
Maple, M.B., J. Wittig and K.S. Kim, 1969, Phys. Rev. Lett. **23**, 1375.
Maple, M.B., 1969, Ph.D. Thesis, University of California, San Diego La Jolla, California (unpublished).
Maple, M.B. and K.S. Kim, 1969, Phys. Rev. Lett. **23**, 118.
Maple, M.B., 1970, Solid State Commun. **8**, 1915.
Maple, M.B. and D. Wohlleben, 1971, Phys. Rev. Lett. **27**, 511.
Maple, M.B. and J. Wittig, 1971, Solid State Commun. **9**, 1611.
Maple, M.B., 1972, in: Douglass, D.H., eds., Superconductivity in d- and f-Band Metals, Rochester, 1971 (AIP Conf. Proc. No. 4), pp. 175–203.
Maple, M.B., W.A. Fertig, A.C. Mota, L.E. DeLong, D. Wohlleben and R. Fitzgerald, 1972, Solid State Commun. **11**, 829.
Maple, M.B., 1973, in: Suhl, H., ed., Magnetism, vol. V (Academic Press, New York), chapter 10.
Maple, M.B. and D. Wohlleben, 1974, in: Graham, Jr., C.D. and J.J. Rhyne, eds., Magnetism and Magnetic Materials – 1973, Boston, 1973 (AIP Conf. Proc. No. 18), pp. 447–462.
Maple, M.B., 1976, Appl. Phys. **9**, 179.
Maranzana, F.E., 1970, Phys. Rev. Lett. **25**, 239.
Maranzana, F.E. and P. Bianchessi, 1971, Phys. Stat. Sol. b **43**, 601.
Matsuura, T. and Y. Nagaoka, 1976, Solid State Commun. **18**, 1583.
Matthias, B.T., H. Suhl and E. Corenzwit, 1958, Phys. Rev. Lett. **1**, 92.
Menth, A., E. Buehler and T.H. Geballe, 1969, Phys. Rev. Lett. **22**, 295.
Mills, D.L., M.T. Béal-Monod, P. Lederer, 1975, in: Suhl, H., ed., Magnetism, vol. V (Academic Press, New York), pp. 89–117.
Misawa, S., 1974, Solid State Commun. **15**, 507.
Moeser, J.H., F. Steglich and G. v. Minnigerode, 1974, J. Low Temp. Phys. **15**, 91.
Moeser, J.H. and F. Steglich, 1975, Z. Phys. B **21**, 165.
Mott, N.F., 1974, Phil. Mag. **30**, 403.
Müller-Hartmann, E., B. Schuh and J. Zittartz, 1976, Solid State Commun. **19**, 439.
Müller-Hartmann, E. and J. Zittartz, 1970, Z. Phys. **234**, 58.
Müller-Hartmann, E. and J. Zittartz, 1971, Phys. Rev. Lett. **26**, 428.
Müller-Hartmann, E. and J. Zittartz, 1972, Solid State Commun. **11**, 401.
Murani, A. P., 1970, J. Phys. C: Metal Phys. Suppl., S153.
Murani, A.P., 1973, Solid State Commun. **12**, 295.
Murani, A.P., 1974a, Solid State Commun. **14**, 199.
Murani, A.P., 1974b, Solid State Commun. **15**, 987.
Nagasawa, H., S. Yoshida and T. Sugawara, 1968, Phys. Lett. **26**A, 561.
Nagel, J., S. Hüfner and M. Grünig, 1973, Solid State Commun. **13**, 1279.
Nickerson, J.C., R.M. White, K.N. Lee, R. Bachmann, T.H. Geballe and G.W. Hull, Jr., 1971, Phys. Rev. B**3**, 2030.
Nozieres, P., 1975, in: Krusius, M. and M. Vuorio, eds., Proceedings of the Fourteenth International Conference on Low Temperature Physics, Otaniemi, Finland, 1975, vol. 5 (North Holland, Amsterdam), pp. 339–374.
Ortega, S., M. Roth, C. Rizzuto and M.B. Maple, 1974, Solid State Commun. **15**, 453.
Ott, H.R., K. Andres and E. Bucher, 1975, in: Graham, Jr., C.D., G.H. Lander and J.J. Rhyne, eds., Magnetism and Magnetic Materials – 1974, San Francisco, 1974 (AIP Conf. Proc. No. 24), pp. 40–41.
Paderno, Yu. B., V.I. Novikov and E.S. Garf, 1969, J. Powder Met. (USSR) **83**, 70.
Palenzona, A., 1972, J. Less-Common Met. **29**, 289.
Parks, R.D. and J.M. Lawrence, 1976, in: Proceedings of the Twenty-First Annual Conference on Magnetism and Magnetic Materials, Philadelphia, 1975 (AIP Conf. Proc. No. 29), pp. 479–483.
Peña, O. and F. Meunier, 1974, Solid State Commun. **14**, 1087.
Penny, T. and F. Holtzberg, 1975, Phys. Rev. Lett. **34**, 322.
Percheron, A., J.C. Archard, O. Gorochov, B. Cornut, D. Jerome and B. Coqblin, 1973, Solid State Commun. **12**, 1289.
Peterson, T.S., S. Legvold and P. Burgardt, 1976, in: Proceedings of the Twenty-First Annual Conference on Magnetism and Magnetic Materials, Philadelphia, 1975 (AIP Conf. Proc. No. 29), pp. 366–367.
Pollak, R.A., F. Holtzberg, J.L. Freeouf and D.E. Eastman, 1974, Phys. Rev. Lett. **33**, 820.
Purwins, H.G., P. Donzé, C.P. Susz and A. Treyvaud, 1972, Phys. Lett. **40**A, 217.
Rao, V.U.S. and W.E. Wallace, 1970, Phys. Rev. B**2**, 4613.
Rao, V.U.S., R.D. Hutchens and J.E. Greedan, 1971, J. Phys. Chem. Solids **32**, 2755.
Riblet, G. and K. Winzer, 1971, Solid State Commun. **9**, 1663.
Rider, P.E., K.A. Gschneidner, Jr. and O.D. McMasters, 1965, Trans. Met. Soc. AIME **233**, 1488.
Rieger, W. and E. Parthe, 1969, Monatshefte für Chemie **100**, 444.
Rosengren, A. and B. Johansson, 1976, Phys. Rev. B**13**, 1468.
Ruderman, M.A. and C. Kittel, 1954, Phys. Rev. **96**, 99.
Sales, B.C., 1974, Ph.D. Thesis, University of California, San Diego, La Jolla, California (unpublished).
Sales, B.C. and D.K. Wohlleben, 1975, Phys. Rev. Lett. **35**, 1240.
Sales, B.C. and R. Viswanathan, 1976, J. Low Temp. Phys. **23**, 449.
Schlottmann, P., 1975a, Solid State Commun. **16**, 1297.
Schlottmann, P., 1975b, J. Low Temp. Phys.

20, 123.
Schmid, W. and E. Umlauf, 1976, Commun. Phys. **1**, 67.
Schrieffer, J.R. and P.A. Wolf, 1966, Phys. Rev. **149**, 491.
Sereni, J.G., J.G. Huber, C.A. Luengo and M.B. Maple, 1975, Solid State Commun. **17**, 1581.
Shenoy, G.K., B.D. Dunlap, G.M. Kalvius, A.M. Toxen and R.J. Gambino, 1970, J. Appl. Phys. **41**, 1317.
Shenoy, G.K., J. Stöhr, W. Wagner, G.M. Kalvius and B.D. Dunlap, 1974, Solid State Commun. **15**, 1485.
Shoemaker, D.P., R.E. Marsh, F.J. Ewig and L. Pauling, 1952, Acta Cryst. **5**, 637.
Silhouette, D., 1970, Solid State Commun. **8**, 467.
Smith, T.F., 1966, Phys. Rev. Lett. **17**, 386.
Stevens, K.W.H., 1976, J. Phys. C**9**, 1417.
Stöhr, J., 1975, Phys. Rev. B**11**, 3559.
Sturgeon, G.D., J.P. Mercurio, J. Etourneau and P. Hagenmuller, 1974, Mat. Res. Bull. **9**, 117.
Sugawara, T., 1965, J. Phys. Soc. Japan **20**, 2252.
Sugawara, T. and H. Eguchi, 1966, J. Phys. Soc. Japan **21**, 725.
Sugawara, T. and H. Eguchi, 1967, J. Phys. Soc. Japan **23**, 965.
Sugawara, T. and S. Yoshida, 1968, J. Phys. Soc. Japan **24**, 1399.
Sugawara, T. and H. Eguchi, 1969, J. Phys. Soc. Japan **26**, 1322.
Sugawara, T. and S. Yoshida, 1971, J. Low Temp. Phys. **4**, 657.
Suhl, H., 1973, ed., Magnetism, vol. V (Academic Press, New York).
Suryanarayanan, R., G. Guntherodt, J.L. Freeouf and F. Holtzberg, 1975, Phys. Rev. B**12**, 4215.
Swift, W.M. and W.E. Wallace, 1968, J. Phys. Chem. Solids **29**, 2053.
Takeuchi, J., T. Aoi and Y. Masuda, 1975, J. Phys. Soc. Japan **38**, 1210.
Talmor, Y. and J. Sierro, 1975, Phys. Rev. B**11**, 300.
Tao, L.J., D. Davidov, R. Orbach and E.P. Chock, 1971, Phys. Rev. B**4**, 5.
Toxen, A.M., P.C. Kwok and R.J. Gambino, 1968, Phys. Rev. Lett. **21**, 792.
Tsang, J.C., 1976, Solid State Commun. **18**, 57.
Tsuchida, T. and W.E. Wallace, 1965, J. Chem. Phys. **43**, 3811.
Tsuchida, T., M. Kawai and Y. Nakamura, 1970, J. Phys. Soc. Japan **28**, 528.
Vainshtein, E.E., S.M. Blokhin and Yu. B. Paderno, 1965, Sov. Phys.: Solid State **6**, 2318.
van Aken, P.B., H.J. van Daal and K.H.J. Buschow, 1974, Phys. Lett. **49**A, 201.
van Daal, H.J. and K.H.J. Buschow, 1970, Phys. Stat. Sol. a **3**, 853.
van Daal, H.J., P.B. van Aken and K.H.J. Buschow, 1974, Phys. Lett. **49**A, 246.
van Diepen, A.M., R.S. Craig and W.E. Wallace, 1971, J. Phys. Chem. Solids **32**, 1867.
van Maaren, M.H., K.H.J. Buschow and H.J. van Daal, 1971, Solid State Commun. **9**, 1981.
van Maaren, M.H. and M. van Haeringen, 1975, in: Krusius, M. and M. Vuorio, eds., Proceedings of the Fourteenth International Conference on Low Temperature Physics, Otaniemi, Finland, 1975, vol. 2 (North Holland, Amsterdam), pp. 533–536.
van Vucht, J.H.N. and K.H.J. Buschow, 1965. J. Less-Common Met. **10**, 98.
Varma, C.M., 1976, Rev. Mod. Phys. **48**, 219.
Ward, R.W., B.P. Clayman and T.M. Rice, 1975, Solid State Commun. **17**, 1297.
Weaver, H.T. and J.E. Schirber, 1976, Phys. Rev: B**13**, 1363.
Williams, Gwyn and L.L. Hirst, 1969, Phys. Rev. **185**, 407.
Wilson, K.G., 1975, Rev. Mod. Phys. **47**, 773.
Winzer, K. and K. Samwer, 1975, in: Krusius, M. and M. Vuorio, eds., Proceedings of the Fourteenth International Conference on Low Temperature Physics, Otaniemi, Finland, 1975, vol. 3 (North Holland, Amsterdam), pp. 430–433.
Wohlleben, D., J.G. Huber and M.B. Maple, 1972, in: Graham, Jr., C.D. and J.J. Rhyne, eds., Magnetism and Magnetic Materials – 1971, Chicago, 1971, Part 2 (AIP Conf. Proc. No. 5), pp. 1478–1482.
Wohlleben, D.K. and B.R. Coles, 1973, in: Suhl, H., ed., Magnetism, vol. V (Academic Press, New York), chapter 1.
Wollan, J.J. and D.K. Finnemore, 1970, Phys. Lett. **33**A, 299.
Wortmann, G., J. Moser and U.F. Klein, 1976, Phys. Lett. **55**A, 486.
Yosida, K., 1957, Phys. Rev. **106**, 893.

References added in proof

There have been a number of developments in this subject since this article was concluded during the summer of 1976. Most of these developments were reported in the following conference proceedings:

(1) Proc. Int. Conf. on Valence Instabilities and Related Narrow Band Phenomena, Rochester, New York, 1976, R.D. Parks, ed., (Plenum, New York, 1977).
(2) Proc. Int. Conf. on Magnetism, Amsterdam, The Netherlands, 1976 (North-Holland, Amsterdam, 1977).
(3) Proc. Twenty-Third Annual Conf. on Magnetism and Magnetic Materials, Minneapolis, Minnesota, 1977.

Handbook on the Physics and Chemistry of Rare Earths, edited by K.A. Gschneidner, Jr. and L. Eyring

Chapter 12

DIFFUSION IN RARE EARTH METALS

Moshe P. DARIEL†
Materials and Molecular Research Division, Lawrence Berkeley Laboratory, Berkeley, California, USA

Contents

Symbols

a_0 = lattice parameter
C_i = concentration of solutes in interstitial sites
C_s = concentration of solutes in substitutional sites
D = diffusion coefficient
D_A^B = solute diffusivity of B in A
D_A^A = self-diffusion coefficient of A
D_0 = pre-exponential term in the expression for the temperature dependence of the diffusion coefficient
D_i = diffusivity of solutes in interstitial sites
D_s = diffusivity of solutes in substitutional sites
D_A = intrinsic diffusivity of component A
f = correlation factor
H = enthalpy
ΔH_f = enthalpy of formation of defects
ΔH_m = enthalpy of migration of defects
K_A^B = ratio of solute (B) diffusivity in A to the self-diffusion coefficient in A
L_m = latent heat of melting
N_A = molar fraction of component A
Q = activation energy
r_A = Goldschmidt radius of element A
S = entropy
ΔS_f^v = entropy of formation of a vacancy
ΔS_m^v = entropy of migration of a vacancy
T_m = melting temperature
V = volume
ΔV_f^d = activation volume of formation of a defect
v_k = rate of displacement of inert markers

†On leave from the Department of Materials Engineering, Ben-Gurion University of the Negev and the Nuclear Research Center-Negev, Beer-Sheba, Israel from September 1974 to August 1976. Address all correspondence to: Dept. of Materials Engineering, Ben-Gurion University of the Negev, Beer-Sheba, Israel.

Γ = Eshelby factor
γ = geometrical factor in the expression for the diffusion coefficient
γ_A = activity coefficient of component A
χ_T = isothermal compressibility
μ = shear modulus
ν = Poisson ratio
ν = characteristic vibration frequency

1. Introduction

Since the beginning of this century, the various aspects of diffusion in metallic systems have been extensively investigated. The considerable practical importance of diffusion-controlled processes in many fields of modern technology resulted in a large number of phenomenological studies. Investigations of mass transport in metallic lattices yield valuable information concerning the basic properties which determine the mobilities of atoms. Mass transport is affected to a large extent by the concentration and nature of the defects present in a metal. Diffusion studies offer an insight into the interaction between the atoms in a metal with various defects such as vacancies, interstitials and dislocations.

Contrary to the huge amount of experimental data available for many of the common metals, there is a relative paucity of information concerning the rare earth metals. This situation is the result of several factors. The rare earth metals or rare earth rich alloys have found, up to quite recently, only limited use in technologically important processes. There was, therefore, no practical incentive to carry out diffusion studies in these materials. As for the more basic type of research, the destructive nature of the experimental techniques and the relative scarceness of high purity single crystals, coupled with the usually high reactivity of the rare earth metals at elevated temperatures were sufficient to discourage researchers from undertaking studies in these materials.

On the other hand, the rare earth elements constitute about one fourth of all existing metals. They form a group of elements closely related in their chemical, physical and metallurgical properties. In particular, most rare earth metals possess a similar electronic structure while other relevant properties often vary in a gradual, systematic manner. Thus, it appears that the rare earth metals constitute, potentially at least, favorable systems for the study of some of the basic factors which determine diffusion mechanisms in metallic systems.

In retrospect, after several years of diffusion studies in rare earth metals, these expectations seem to have been fulfilled. Several of the currently most interesting subjects related to diffusion in metals have been encountered in the course of these studies. Diffusion in rare earth metals is an area far from being exhausted and further fruitful activity in this field of research can be expected.

2. Experimental techniques

Experimental techniques using radioactive tracer methods are considered as being the most reliable and accurate for the determination of self or solute

diffusion coefficients in metals (Tomizuka, 1959). The great majority of the diffusion studies in rare earth metals has, indeed, been carried out using the thin layer sectioning or grinding of samples which had previously been coated by a surface layer of radioactive tracers. The details of this method and its variants, such as the residual activity measurement, have been described in many details (Adda and Philibert, 1966). In the following, mention will be made only of those points which are specific to diffusion studies involving the rare earth metals. More detailed descriptions of the experimental details can be found in the original theses devoted to diffusion studies in rare earth metals (Dariel, 1968; Languille, 1973; Zanghi, 1975; Fromont, 1975).

Purity of samples. Most authors report a purity of 99.9 w% for the rare earth metals used. It is believed that too often this figure represents an over optimistic estimate, in particular, when rare earth metals of commercial stock were employed. The light elements represent the bulk of impurities found in the rare earth metals. These impurities, often hard to assess, are present at concentrations at least one order of magnitude higher than the non rare earth metallic impurities. The solubility of the light elements in the rare earth metals is, in general, very restricted and lower than their usual concentration. The light impurities react with the rare earth matrix and form compounds which appear as inclusions under metallographic examination. No information on the effect these impurities have on diffusion processes in rare earth metals is available, even though it is known (e.g. see Lichtenberg et al., 1974 and Beaudry and Spedding, 1975) that in some instances their solubility increases significantly at elevated temperatures.

Single crystal versus polycrystalline samples. In accurate diffusion experiments, the use of single crystals is highly recommended in order: 1. to eliminate the presence of short circuiting grain boundaries and, 2. to reveal any anisotropy effects in non-cubic crystals. Actually most of the available, highly reliable diffusion data on diffusion in most common metals has been derived from the studies of single crystal specimens. Unfortunately, even though single crystals are by now available for almost any of the rare earth metals (see ch. 2, section 5), they are expensive and for some metals still difficult to grow. Considering the destructive nature of diffusion experiments, it is not surprising that few results in rare earth metals have been obtained using single crystal samples.

Chemical reactivity. Most rare earth metals oxidize readily and react with container materials at elevated temperatures (also see ch. 2, section 3.6). Also, the often employed method of depositing the thin radioactive tracer layer by electrolytic coating from aqueous solution is unpracticable since it results in the formation of a surface oxide barrier layer. Usually vacuum evaporation of metallic tracers or electrolytic coating from non-aqueous organic solutions have been employed. Diffusion anneals at high temperatures require protection of the samples from exposure to reactive gases or container materials. This was achieved by wrapping the samples in thin tantalum foils and sealing them in evacuated or inert gas containing capsules. A protective atmosphere was also required in some instances during the sectioning stage of the samples in order to

prevent oxidation or even ignition of the thin chips. Additional details concerning the annealing and handling of rare earth metals are noted in ch. 2, section 3.

Electrotransport, solid state electrolysis or, in other words, the migration of impurities under the influence of an electrical field, has been studied in the rare earth metals mainly for the purpose of finding a suitable method of purification. The common approach in these studies is to start with an initially homogeneous distribution of a particular impurity in the sample and pass a relatively high d.c. current through it. Under the influence of the electric field and as a result of momentum transfer between the charge carriers and the impurities, a concentration gradient of these impurities is set up. If the experiment is carried out for a sufficiently long time, steady state conditions are achieved. It can be shown (Verhoeven, 1966) that by analyzing the concentration profile of the impurities, relatively reliable diffusion coefficients can be deduced. Since a lengthy anneal at high temperature is required for setting up the steady state distribution, problems of contamination from the surrounding atmosphere and the current carrying electrodes usually arise. Methods of overcoming these difficulties have been discussed by Jordon and Jones (1973) and Carlson et al. (1975). Electrotransport has been used mainly for the purification of the rare earth metals from light, non-metallic impurities, also see ch. 2, section 2.3.

3. Self-diffusion in rare earth metals

3.1. *Self-diffusion in close-packed structures*

Most studies of self-diffusion in rare earth elements have been motivated by the desire to clarify the problems involved in identifying basic diffusion mechanisms in metals. It is useful therefore, to begin this section by recalling the main features which are believed to be characteristic of a normal diffusion mechanism. These features can be summarized by several semi-empirical rules which have evolved as a result of studies in metals in which diffusion takes place by a vacancy mechanism. This is the reason for the present tendency to identify normal diffusion with a vacancy mechanism, in contrast to anomalous diffusion to be discussed later. The semi-empirical rules have been listed by Le Claire (1965) as follows:

1. The temperature dependence of the self-diffusion coefficients follows an Arrhenius-type relationship, i.e. $D = D_0 \exp(-Q/RT)$ where D_0, the pre-exponential term, and Q, the activation energy, are temperature independent.

2. The activation energy correlates to the melting temperature (T_m) or the latent heat of melting (L_m) within 20%, $Q = 34\ T_m$ or $Q = 16.5\ L_m$.

3. The pre-exponential term D_0 is equal to unity within one order of magnitude

$$10^{-1} < D_0 < 10 \quad \text{cm}^2/\text{sec}$$

According to the Wert–Zener formulation, $D_0 = \gamma a_0^2 f \nu \exp(-\Delta S^v/R)$, where γ is a geometrical factor, f the correlation factor, a_0 the lattice parameter, ν a characteristic vibration frequency usually the Debye frequency and $\Delta S^v =$

$\Delta S_f^v + S_m^v$ is the entropy associated with the formation and migration of the vacancy.

Theoretical calculations which have been borne out by the experimentally observed values of D_0 in regular fcc metals show that ΔS_f^v is positive for a vacancy controlled diffusion mechanism. The formation of a vacancy results in the lowering of the vibrational frequency in its neighborhood, implying a positive value for ΔS_f^v. The motion of the atom through the saddle point configuration between lattice sites causes an increase of the local vibration frequency. This effect, however, is more than offset by the lowering of the overall frequency due to relaxation at the free surface (Vineyard, 1957). Thus, the entropy of migration for a vacancy ΔS_m^v is also positive and usually small. Positive values of ΔS^v account for the observed range of D_0 values associated with the vacancy mechanism. Recent accurate experimental work has shown that the first of the above-mentioned criteria is not being rigorously followed in fcc metals such as Ni or Au. The rather minor deviations from a linear Arrhenius-type behavior have been ascribed to the contribution of bi-vacancies to self-diffusion in the temperature range $T > 0.8\ T_m$ (Seeger, 1972).

A variety of close-packed structures are observed in the rare earth elements. Actually all rare earth metals, with the exception of Eu, appear in at least one close-packed allotropic structure. Self-diffusion coefficients have been determined, however, in only a small fraction of the existing close-packed structures. The results are summarized in table 12.1. Two widely divergent sets of results have been obtained in fcc β-La and hcp α-Y. In β-La, the early results of Zamir and Schreiber (1964) were determined using an N.M.R. technique. The self-diffusion coefficients in β-La were later remeasured by Dariel et al. (1969b) who employed the more direct radioactive tracer method. Dariel et al. also pointed out the possible source of the discrepancy between the two sets of results. In Y, the more recent measurements of Gornyy and Al'tovsky (1970), who used single crystals, seem more reliable than the older results by Maskalets et al. (1967). Considering only the more recent results in these two metals, it appears that in

TABLE 12.1
Diffusion parameters in close-packed structures of rare earth metals

Element	Structure	D_0 cm^2/sec	Q kcal/mole	Q/T_m	Temperature interval (K)	Ref.
$Y_{\parallel}$[a]	hcp	0.82	60.3	33.8	1173–1173	[b]
$Y_{\perp}$[a]	hcp	5.2	67.1	37.6	1173–1573	[b]
La	fcc	1.5	45.1	37.9	937–1110	[c]
Ce	fcc	0.6	36.6	34.3	800–970	[d]
$Er_{\parallel}$	hcp	3.7	72.05	40.4	1475–1685	[e]
$Er_{\perp}$	hcp	4.5	72.27	40.5	1475–1685	[e]
Yb	hcp	3.4×10^{-2}	35.06	32.1	800–990	[f]

[a]$\parallel$ and $\perp$ represent directions parallel and perpendicular to the c-axis; [b]Gornyy and Al'tovskiy (1970); [c]Dariel et al. (1969b); [d]Dariel et al. (1971); [e]Spedding and Shiba (1972); [f]Fromont et al. (1974).

the close packed structures the pre-exponential terms and activation energies conform rather well to the semi-empirical rules mentioned above. Thus, since self-diffusion in the close packed rare earth structures seems to follow in a satisfactory manner the criteria associated with a vacancy mechanism, there appears little reason to believe that it proceeds by a different mechanism. Further evidence for a vacancy controlled diffusion mechanism is based on some chemical diffusion experiments performed in the La–Ce system (Dariel, 1968). These results will be discussed in more detail in section 6.1. Briefly, a Kirkendall shift of inert markers placed at the initial interface of La–Ce diffusion couples and a pronounced porosity on the Ce side were observed. These effects can be accounted for on the basis of an indirect type of diffusion mechanism (vacancies or interstitialcies) and seem to eliminate direct interchange or pure interstitial as possible alternatives.

Akimov and Kraftmakher (1970), using heat capacity measurements, determined the enthalpy of formation ΔH_f (23 kcal/mole) of thermally activated defects in β-La. This value represents one-half of the experimentally measured activation energy for self-diffusion (Dariel et al., 1969b). Since $Q = \Delta H_f + \Delta H_m$ (with ΔH_m the enthalpy of migration of the defects) and since it is well established that $\Delta H_f \cong \Delta H_m$ for vacancies as diffusion determining defects in fcc metals, the heat capacity results seem to constitute further evidence for a vacancy dominated self-diffusion mechanism in the close-packed structures.

Obviously, this evidence in favor of a vacancy mechanism for self-diffusion in rare earth metals is indirect and fragmentary at best. It will be shown in the next sections that serious consideration is given to other than a vacancy mechanism for self-diffusion in the bcc and some solute diffusion in both the bcc and the close-packed phases. Furthermore, preliminary results (Marbach, 1975) concerning the pressure dependence of the self-diffusion coefficients in fcc γ-Ce indicate a negative activation volume, $\Delta V/V = -0.17$ (V = atomic volume of Ce). Negative volumes have also been reported in the bcc phases of some rare earth metals (see section 3.2) and constitute important arguments against the vacancy mechanism. If indeed, the presence of a negative activation volume is a real feature of self-diffusion in γ-Ce, it would then appear that the situation in this metal in particular, and perhaps in other close-packed rare earth metal phases as well, is not as clear and simple as we would like to believe. It seems, therefore, imperative that further work be done to confirm definitively the vacancy mechanism as the self-diffusion controlling mechanism in the close-packed structures. With the increased purity of the available rare earth metals and the possibility of growing or obtaining single crystals, critical experiments such as the Simmons–Baluffi, isotope effect, positron annihilation and more detailed and careful Kirkendall effect measurements may become realizable.

Gornyy and Al'tovsky (1970), Spedding and Shiba (1972) determined the anisotropy of self-diffusion in single crystals of Y and Er, respectively. Self-diffusion in Y seems to be strongly anisotropic to contrast to the results in Er (table 12.1). Further work, particularly in the hcp phases of the heavy rare earth metals, should elucidate this problem.

3.2. *Self-diffusion in bcc rare earth metals*

The experimental data concerning self-diffusion in the bcc structure of the rare earth metals is given in table 12.2. This table includes the values of the activation volumes deduced from measurements of the pressure dependence of the self-diffusion coefficients. The values measured for self-diffusion in ϵ-Pu, an actinide metal, have been added since they form, together with results of δ-Ce, the basis of the activated interstitial model (section 3.3). Values of the ratio Q/T_m (T_m = melting temperature) are also shown as a criterion of the normality of self-diffusion in that particular phase. The inverse temperature dependence of the logarithm of the self-diffusion coefficients of several rare earth metals is shown in fig. 12.1. In 4 of these metals, measurements have been carried out both in the close-packed and in the bcc phases. A common feature repeating itself is the discontinuous increase of the self-diffusion coefficients by about 2 orders of magnitude at the temperature of the phase transformation. This point is of importance because, as shown in section 4, the diffusivities of many solutes in the same matrices follow a different behavior. This discontinuous increase of the self-diffusion coefficients has been also observed in non rare earth metals which undergo a close-packed to bcc phase transformation (Fe, Ti, Zr, Tl).

TABLE 12.2
Diffusion parameters in body-centered cubic rare earth metals

Element	D_0 cm^2/sec	Q kcal/mole	Q/T_m	Temperature interval (K)	ΔV cm^3/mole	$\Delta V/V_0$ (V_0 = mol. vol)
La	1.3×10^{-2}	24.5	20.5	1140–1173[a]		
	0.11	29.9	24.3	1143–1183[b]	2.20[c]	0.1
Ce	1.2×10^{-2}	21.5	20.0	1000–1073[d]		
	7×10^{-3}	20.5	19.0	1000–1073[e]	−2.1[f]	−0.1
Pr	8.7×10^{-2}	29.4	24.3	1050–1200[g]	0[c]	~0
Gd	8.5×10^{-3}	32.2	20.3	1538–1585[h]		
Eu	1	34.5	31.4	773–1073[h]		
Yb	0.12	28.9	26.3	1003–1073[i]	15.7[j]	0.59
Pu*	3×10^{-3}	15.7	17.2	773–885[k]	−4.9[l]	−0.34

*Non rare earth metal; [a]Dariel (1973); [b]Languille et al. (1974b); [c]Boidron (1975); [d]Dariel et al. (1971); [e]Languille et al. (1973); [f]Languille et al. (1974a); [g]Dariel et al. (1969a); [h]Fromont (1975a); [i]Fromont et al. (1974); [j]Fromont (1975b); [k]Dupuy and Calais (1968); [l]Cornet (1971).

The initial motivation for the study of self-diffusion in the bcc phases of the rare earth elements is connected to the problem of so-called anomalous diffusion in bcc metals. Any discussion of self-diffusion in the bcc rare earth metals must be viewed against the background of this anomalous diffusion. This subject has received extensive coverage and has been summarized by Le Claire (1965), Lazarus (1965), Peterson (1968) and Seeger (1972).

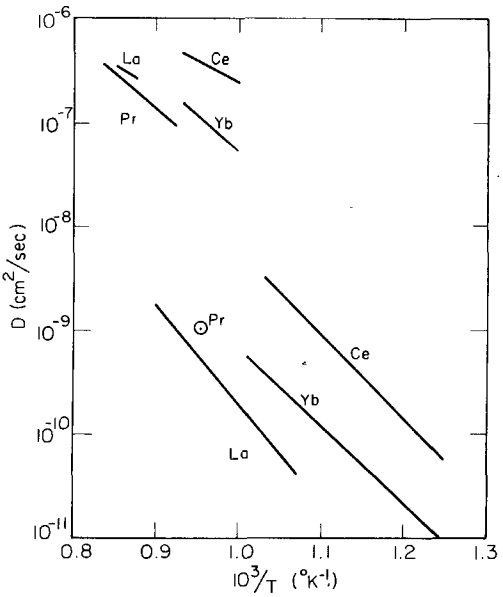

Fig. 12.1. Self-diffusion coefficients of La, Ce, Pr and Yb as function of the inverse temperature.

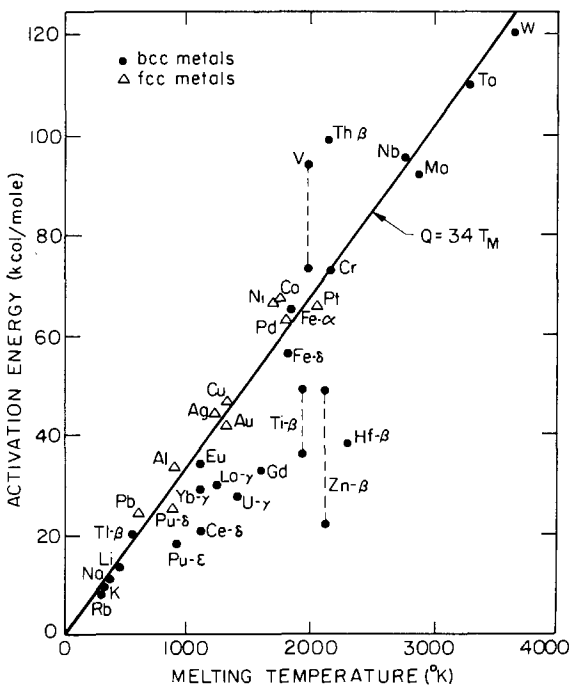

Fig. 12.2. The activation energy for self-diffusion as function of the melting temperature of bcc and fcc metals.

Anomalous diffusion was first observed in β-Zr, β-Ti, β-Hf and γ-U. The main anomalous features which seem to characterize self-diffusion (and some solute diffusion) in these metals can be summed up as follows.

1. A pronounced curvature of the Arrhenius plot is apparent whenever the temperature interval over which the measurements were made was wide enough to allow its detection.

2. The activation energy for the diffusion process (in the low temperature range for curved Arrhenius plots) is significantly lower than predicted on the basis of melting point or other semi-empirical correlations (fig. 12.2).

3. The pre-exponential term has values usually much lower than the 10^{-1}–$10\ cm^2/sec$ range, leading actually to negative entropies of activation if a vacancy mechanism is assumed.

A survey in table 12.2 of the activation energies and the pre-exponential terms suggests that the bcc rare earth elements, with the exception of Eu, are

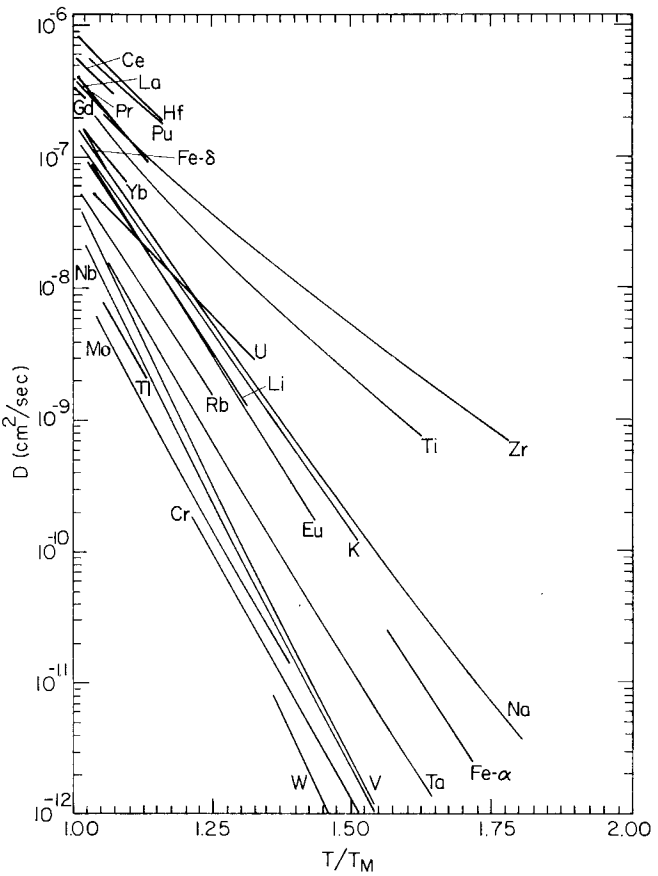

Fig. 12.3. Self-diffusion of bcc metals as function of relative temperature.

anomalous with respect to self-diffusion. Curved Arrhenius plots, even if present, could hardly be detected in view of the limited extension of the temperature interval over which the bcc phases exist. The anomaly appears to be of a variable degree, very pronounced for δ-Ce and β-Gd, less so for β-Pr and γ-Yb. The low values of the activation energies, even though coupled with low pre-exponential factors, lead to very high self-diffusion coefficients as shown in fig. 12.3. These self-diffusion coefficients are among the highest observed in metals.

In the course of the past decade several explanations have been put forward to account for the anomalous diffusion in bcc metals. The different models based on the presence of extrinsic vacancies (Kidson, 1963), on the temperature dependence of elastic constants (Aaronson and Shewmon, 1967), on dislocation enhanced diffusion (Peart and Askill, 1967) or on vacancy anharmonicity (Gilder and Lazarus, 1975) have been thoroughly discussed in the original and in the various review papers. Two additional models, the activated interstitial and, more recently, the ω-embryo model, have been proposed as alternative explanations for anomalous bcc diffusion. These two models and their possible common interpretation on the basis of the Engel–Brewer electron correlation theory will be discussed in the next sub-section.

3.3. *The activated interstitial model*

The activated interstitial model has been put forward on the basis of self-diffusion measurements as functions of temperature and pressure in bcc ϵ-Pu and δ-Ce. These two metals possess certain unusual properties which set them apart from the other metals. Both Ce and Pu transform upon heating from the fcc to a bcc structure which subsists up to the melting point. In both metals, the melting is accompanied by an increase of density. This negative volume change is related through the Clapeyron relation, $\mathrm{d}T/\mathrm{d}p = \Delta V/\Delta S$, to the negative slope of the liquidus in the respective p–T diagrams. Jayaraman (1965) suggested that the passage from bcc to liquid cerium involves a $4f \rightarrow 5d$ electron promotion and consequently a collapse of the atom to a smaller size. It is indeed well established from the study of lattice parameter relationships and magnetic properties that the energy level of the single 4f electron in Ce is close to the conduction band. This rather simple picture of Ce, based on the size consideration has not been borne out by magnetic susceptibility measurement in the bcc and liquid phases (Burr and Ehar, 1966). The large scale promotion of electrons at the bcc-liquid transition was not confirmed and the slight decrease of the magnetic susceptibility could be accounted for by crystal field induced changes of the Pauli susceptibility. However, these experiments do not rule out altogether the possibility of electron promotion taking place in a small fraction of the Ce atoms. It also seems that in order to account for the negative volume change at melting in Ce, some kind of electronic transition which leads to the

reduction of the ionic radius must be considered. The electronic structure of Pu is more complex than that of Ce, with several close-lying alternative electronic configurations, as witnessed by the numerous phase transitions occurring over a relatively narrow temperature interval.

Cornet (1971) having observed the negative activation volume in ϵ-Pu put forward the activated interstitial model, later extended by Languille et al. (1973) to Ce. According to this model a promotion of electrons takes place from the 5f to the 6d band in ϵ-Pu (4f and 5d in δ-Ce) on roughly 1% of the atoms. The atomic size of those atoms in which promotion takes place is reduced since, with the decreased screening by the f electrons, the outer d and s like electrons are drawn in by the nuclear change. The energy required for the formation of such a collapsed self-interstitial in an octahedral site is much lower than for an atom having undergone no electron promotion and could account for the low activation energies of self-diffusion. Furthermore, the formation volume of the activated interstitial, calculated using the elastic theory, is negative and compatible with the experimentally observed values. Even though the negative activation volume does not rule out a vacancy mechanism, it does require for Pu a very large relaxation volume ($\Delta V/V \approx 0.67$).

Languille et al. (1974) tried to confirm the activated interstitial model by measuring self-diffusion coefficients in bcc γ-La, the first element in the lanthanide series. Simultaneous measurements were carried out by Dariel (1973) who also determined the solute diffusivity of La in bcc δ-Ce. Both sets of measurements indicate that the general characteristics of self-diffusion in bcc γ-La are similar to those in bcc δ-Ce (and ϵ-Pu) with low activation energies and high diffusion coefficients (table 12.2). Languille et al. (1974) chose to interpret these results as confirming the 4f character in La metal, suggested on the basis of results concerning the pressure dependence of T_c (superconductivity transition temperature, see ch. 10, sections 3.1 and 3.3), the compressibility at high pressures and the magnetic structure in some La–R alloys at low temperatures. However, even assuming that the 4f character of La persists in the high temperature, normal pressure bcc phase, Languille et al. realized that the La matrix would still consist of a majority of atoms having a 2.7–2.8 valence and a minority undergoing electron promotion to valence +3, with a correspondingly small decrease of the atomic radius. The activated interstitial model in its initial form did not appear, therefore, to be applicable to La and had to be modified. This was done as will be discussed below by Zanghi (1975).

Dariel (1973), on the basis of similar results, argued that it seemed highly implausible that the activated interstitial model should yield similar results in bcc γ-La, δ-Ce and β-Pr considering that the model depended so critically upon the number of 4f electrons of the migrating atom and the possibility of their promotion to the conduction band. According to Dariel, the common diffusion behavior ensues from the particular properties of the bcc structure of the rare earth elements rather than from the electronic structure of the various diffusing species.

In order to achieve a better understanding of anomalous bcc diffusion behavior, Zanghi (1975) carried out a series of self-diffusion measurements as function of pressure of Pu in stabilized bcc Pu–Zr alloys. Zanghi also determined the solute diffusivities of Am in these alloys as a function of temperature and pressure. The results indicated that the activation volume of Pu increased from its negative value in pure ϵ-Pu (table 12.2) to +0.2 atomic volume at 40 at.% Zr. With respect to the diffusivities of Am, a quasi-similarity was observed between the self-diffusion behavior of Pu on one hand and the solute diffusivity of Am on the other. It thus appeared, following the same arguments as those put forward by Dariel (1973), that diffusion in these systems takes place by means of defects having a volume and an energy of formation which do not depend critically on the diffusing species.

On the basis of these results, Zanghi (1975) modified the activated interstitial model by suggesting that the elementary defect (initially a simple interstitial) was actually a many-body defect with a self-interstitial at its core. Within the volume of this many-body defect, compressive stresses are set up due to the presence of the interstitial. These stresses, causing a reduction of the interatomic distances, favor an increased d–f hybridization in the solvent atoms (Pu or Ce) through an enhanced overlap of their respective wave functions. Jullien et al. (1973) have shown that d–f hybridization plays an important role in determining both the properties and the structure of the various Pu allotropes. The elastic energy involved in the formation of self-interstitials is high enough to prevent the formation of such defects under ordinary circumstances. In Pu, however, and, by extension, possibly in Ce, the elastic stresses can be alleviated by the possibility of some of the neighboring atoms to an interstitial reducing their interatomic distances, by undergoing an electronic transition through increased d–f hybridization. Thus, the elastic energy should be reduced, making the presence of a self-interstitial at the core of the many-body defect plausible.

With respect to the negative activation volumes (table 12.2), Zanghi used the elastic theory formula for the defect volume of formation ΔV_f^d:

$$\Delta V_f^d = \Delta v \frac{\Gamma}{\Gamma_d} \pm V_{at}$$

where Δv is the difference between the volume of the defect and the volume of the site in which the defect settles, and Γ and Γ_d are the Eshelby factors for the matrix and defect, respectively, with

$$\Gamma = 1 + \tfrac{4}{3}\mu\chi_T = 3\frac{1-\nu}{1+\nu}$$

μ, the shear modulus, χ_T, the isothermal compressibility and ν, Poisson's ratio.

The sign of V_{at}, the atomic volume, depends on the nature of the defect, (+) for a vacancy, (−) for an interstitial. For the defect centered on the interstitial $\Delta V > 0$, but $\Delta v\Gamma/\Gamma_d < V_{at}$ will lead to negative values of V_f^d. Thus, even if the activation volume is negative, an interstitial causes an expansion of the lattice in its immediate neighborhood ($\Delta v > 0$), favorable to the above mentioned d–f hybridization.

The modified activated interstitial model seems to account, qualitatively at least, for the low activation energies, negative volumes of activation and solute diffusion behavior in bcc ϵ-Pu and possibly δ-Ce. It also offers, again qualitatively only, an explanation for the low values of the pre-exponential terms which have been observed not only for ϵ-Pu and δ-Ce, but that are associated with all the anomalous bcc metals. It was shown in section 3.1, that a vacancy mechanism through positive values of ΔS, the entropy associated with the diffusion process, accounts for the observed values of D_0 in normal metals. According to the modified activated interstitial model, the defect involved in the diffusion process comprises the interstitial and one or several surrounding shells of neighboring atoms. In the course of the formation of this defect with the interstitial at its core, compressive stresses are set up which increase the vibrational lattice frequency and result in negative entropies of formation. The motion of a many-body defect might also be highly correlated, with low values of the correlation factor f, leading to a further lowering of D_0.

3.4. *The ω-embryo model and the Engel–Brewer correlation theory*

The activated interstitial model which hinges on the relative ease of some f electron promotion in its initial form or on the possibility of d–f hydridization in its modified form seems to account for the main anomalous features observed in connection with self-diffusion in bcc ϵ-Pu, δ-Ce and possibly γ-La and γ-Yb. Beside these metals, however, anomalous diffusion has also been observed in β-Ti, β-Zr, β-Hf, γ-U and the rare earth metals β-Pr, β-Nd and β-Gd. The normal behavior of Eu (table 12.2), which among this latter group of metals is the only one having the bcc structure as its only allotropic form, stands out in marked contrast to the other bcc rare earth metals. It strongly supports Seeger's (1972) suggestion that anomalous diffusion in bcc metals is in some way connected to the phase transformation which precedes the bcc phase.

Recently Sanchez and de Fontaine (1975) suggested a new model in order to account for anomalous self-diffusion in Group IV-A metals, Ti, Zr and Hf. In these metals, beside the normal bcc to hcp transition, an alternative phase transformation takes place upon alloying or under pressure from the bcc to the metastable hexagonal ω phase. The structure of this phase which is not a close packed hexagonal one is closely related to that of the bcc structure. As a result of the interrelationship between the two structures, there are four equivalent orientations of ω relative to the bcc matrix of β-Ti or β-Zr. (Doherty and Gibbons, 1971). Sanchez and de Fontaine pointed out that in bcc metals the activated complex in the elementary diffusion process, that is the configuration with an atom in between two regular lattice sites, is actually identical with an ω-phase embryo. In the neighborhood of the transition temperature from the bcc to the ω phase, the free energy of formation of ω will be small and, therefore, the formation of activated complexes will be greatly increased as compared to that in normal bcc metals. With increasing temperature, the thermal vibrations will tend to destroy the ω embryos and diffusion will revert to a normal

behavior. The presence of ω embryos in the bcc phase has been confirmed by electron and neutron diffraction. A noteworthy feature of the ω structure is the presence of two inequivalent lattice sites which differ markedly in the coordination number and nearest neighbor distance. A detailed study of this structure led Doherty and Gibbons (1971) to postulate the simultaneous presence in the ω structure of a pure IV-A element of two species of atoms with different electronic configurations. Thus, the ω structure is stabilized by an electronic transition taking place in part of the atoms of the matrix. This picture is highly reminiscent of that postulated in the activated interstitial model, except that there are no f electrons involved.

Actually both models, the activated interstitial and the ω embryo, can be viewed as special cases of a general diffusion behavior put forward by Engel (1965) on the basis of the Engel–Brewer correlation theory of metals. According to Engel, the presence of a phase transformation, whether to the ω or to a close packed phase, indicates that two (or possibly more) electron configurations have similar bonding energy (within terms of the order of $T\Delta S$). Thus, when the difference in bonding energies corresponding to the two configurations is sufficiently small, atoms having both electron configurations co-exist simultaneously. In other words, in a predominantly bcc matrix (d^2s configuration according to the Engel–Brewer theory, Brewer, 1967), small clusters of atoms may momentarily possess an electron configuration and a spatial arrangement corresponding to a close-packed structure (sp^2 or dsp). In some special cases, the transition from one configuration to another may also involve a change in the number of f electrons, possibly accompanied by a change of the atomic radii. Such cases correspond to those considered in connection with the activated interstitial model. On the other hand, changes of electron configuration may, in principle, take place with no change in the number of f electrons whenever there are none available (Ti, Zr) or when they are very stable (Hf, Pr, Nd and Gd). For these metals, the change of electron configuration would involve only a change in the relative number of s, p or d electrons. An estimate for the energy differences between the alternative electron configurations in non rare earth metals was given by Engel (1965). Using the spectroscopic data reported by Brewer (1971), one can estimate the difference in bonding energies between the bcc and the hcp configuration in solid β-Pr and β-Gd to be of the order of 2 kcal/mole. The distribution of the atoms in the 2 configurations and, therefore, the concentration of activated complexes will be temperature dependent. This would lead to the curved Arrhenius plots observed in some of the anomalous bcc metals. Furthermore, the presence of clusters having a higher local density of atoms will certainly disturb severely the vibration spectrum of the matrix. It is not unlikely that it might actually increase the local vibration frequency leading to negative entropies of defect formation and, hence, to the low values observed for the pre-exponential factors.

The nature of the defect involved in the diffusion process is not specified at this stage. It would appear, however, that it is an extended, many-body defect. It might be a vacancy adjacent to an ω embryo, a strongly relaxed vacancy with

reaccommodated nearest and next to nearest neighbors or a cluster of atoms with an interstitial at its core. The common feature of these extended defects would be, according to the Engel theory, their formation as a result of the availability of suitable, alternative electronic configurations for the matrix atoms.

4. Metallic solute diffusion in rare earth metals

This section is concerned with diffusion studies of metallic solutes at infinite dilution in rare earth metals. Many such studies have been carried out in the more common metals, providing important insight into the fundamental details of the diffusion processes. About one decade ago the vacancy mechanism seemed firmly established as the dominant diffusion mechanism for self-diffusion and for diffusion of substitutional solutes in metals. In a number of specific metal matrices (noble and some bivalent metals), successful quantitative models were developed to account for the relative values of solute diffusivities in a particular solvent. An electrostatic Coulomb interaction was assumed to determine the binding between the excess charge on the solute and the vacancies. Since the excess charge is generally well screened by the conduction electrons, the solute-vacancy binding energies are small with respect to the vacancy formation energy. This conclusion is especially valid for polyvalent solvent metals (e.g. the rare earth matrices) where computations (March and Murray, 1961) have shown that the electron density surrounding an impurity charge is so high that the charge is screened at distances less than an atomic radius. It is not surprising, therefore, that the diffusivities of metallic solutes were observed to lie within one order of magnitude of the self-diffusion coefficients of the solvent matrices. Alternative diffusion mechanisms to the vacancy mechanism and, in particular, the interstitial one were not seriously considered because they implied the momentary occupancy, at least, of interstitial sites by metallic solutes. Since the ratio r_A/r_B of the Goldschmidt radii of the components in metallic systems significantly exceeds the Hägg (1929, 1930) limit for interstitial solubility, ($r_A/r_B = 0.59$), such solutions seemed precluded on the basis of size considerations.

In the course of the past years, a growing body of evidence has shown that, with respect to the solute diffusion of metallic solutes, the situation is more complex than it would appear from the foregoing discussion. This conclusion is mainly based on the increasingly numerous metallic systems in which the solute diffusivities were observed to exceed by several orders of magnitude the self-diffusion coefficients of the solvent metals. This behavior, called fast or ultra-fast diffusion, was first observed in Group IV-B (Si, Ge, Sn, Pb) and Group III-B (In, Tl) solvent metals. At present it is well established that fast diffusion also occurs in the alkali metals (Li, Na, K), the Group IV-A metals (Ti, Zr), the rare earth metals and some actinides. Fast diffusion solutes are the noble metals (Cu, Ag, Au) and some transition metals (Fe, Co, Ni) and to a lesser extent Zn and Cd. Fast diffusion and its characteristic features have been reviewed by Anthony (1970) and Warburton and Turnbull (1975). At present, fast diffusion is interpreted as taking place by a mechanism different from the vacancy

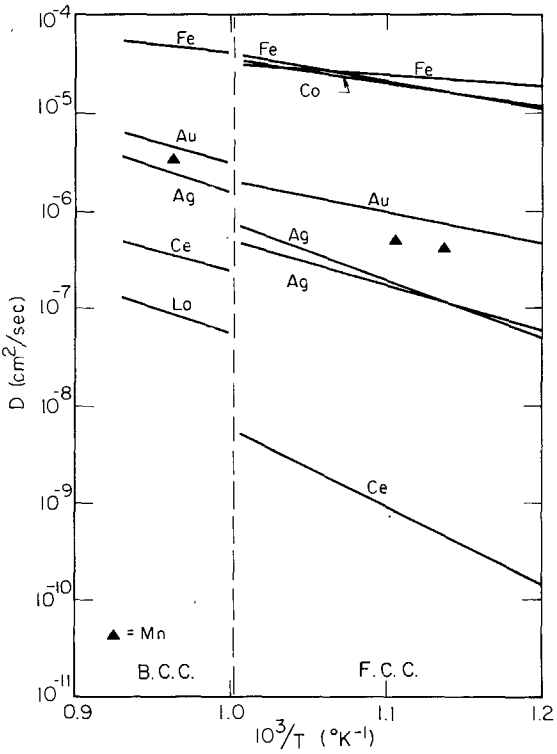

Fig. 12.4. The diffusivities of various solutes in fcc and bcc Ce as function of the inverse temperature.

mechanism which determines self-diffusion in metals (except possibly some bcc phases). This mechanism, as will be discussed below, implies the partial solubility of the fast diffusing solutes in interstitial sites of the solvent matrices. Since the great majority of the experimental results on solute diffusion in rare earth metals reflects the fast diffusion behavior, the rest of this section will be mainly devoted to this subject.

The results of metallic solute diffusion studies in rare earth metals are shown in table 12.3. Also included in this table are values of the ratio $K_A^B = D_A^B/D_A^A$ (where D_A^B is the solute diffusivity of B in A and D_A^A is the self-diffusion coefficient of A), at the highest temperature at which it could be determined in each phase. Most solute diffusion measurements have been carried out in Ce and Pr. The temperature dependence of the solute diffusivities in these two metals is shown in figs. 12.4 and 12.5.

As mentioned above, high values of K_A^B are characteristic of the new interstitial-like diffusion of metallic solutes. Table 12.3 shows that these values of K_A^B vary in a quasi continuous manner from $K_A^B < 1$ to $K_A^B = 2 \times 10^4$. Such an extended, continuous range for K_A^B has also been observed in other metals such

TABLE 12.3
Metallic solute diffusion in rare earth metals

Solvent matrix	Solute	D_0 cm²/sec	Q kcal/mol	$K = \frac{D_{solute}\dagger}{D_{self}}$	Diffusivity*	Ref.
Y-α, hcp	Zr	4×10^{-3}	38	12	?	a
	^{59}Fe	1.8×10^{-2}	20	2×10^{4}	F	b
	^{110}Ag	5.4×10^{-3}	18	10^{4}	F	b
La-β, fcc	^{198}Au	2.2×10^{-2}	18.1	3.5×10^{3}	F	c
La-γ, bcc	^{141}Ce	1.8×10^{-2}	25	1.2	N	d
Ce-γ, fcc	^{110}Ag	2.5×10^{-2}	21.1	1.2×10^{2}	F	e
	^{198}Au	4.4×10^{-3}	14.9	5×10^{2}	F	e
	^{110}Ag	1.4	28	2×10^{2}	F	f
	^{60}Co	1×10^{-2}	11	2.7×10^{4}	F	f
	^{59}Fe	3.3×10^{-4}	46	2.6×10^{4}	F	f
	^{59}Fe	1.7×10^{-2}	11.9	10^{4}	F	g
Ce-δ, bcc	^{110}Ag	1.2×10^{-1}	22.2	16	F	e
	^{198}Au	9.5×10^{-2}	20.5	10	F	e
	^{59}Fe	2×10^{-3}	7.7	17	F	g
	^{140}La	1.3×10^{-2}	24.5	0.75	N	h
Pr-α, dhcp	^{64}Cu	8.4×10^{-2}	18.1	8×10^{3}	F	i
	^{110}Ag	1.4×10^{-1}	25.4	3.5×10^{2}	F	j
	^{198}Au	4.3×10^{-2}	19.7	1.8×10^{3}	F	j
	^{60}Co	4.7×10^{-2}	16.4	10^{4}	F	j
	^{59}Fe	2.1×10^{-3}	9.4	1.1×10^{4}	F	g
	^{65}Zn	1.8×10^{-1}	24.8	5×10^{2}	F	k
Pr-β, bcc	^{64}Cu	5.7×10^{-2}	17.8	10^{2}	F	i
	^{110}Ag	3.2×10^{-2}	21.5	8	F	j
	^{198}Au	3.3×10^{-2}	20.1	16	F	j
	^{65}Zn	6.3×10^{-1}	27.0	15	F	k
Pr-β, bcc	^{59}Fe	4×10^{-3}	10.4	10^{2}	F	g
	^{140}La	1.8×10^{-2}	25.7	1	N	l
	^{166}Ho	9.5×10^{-3}	26.3	0.3	N	l
	^{114}In	9.6×10^{-2}	28.9	1.1	N	l
Nd-α, dhcp	^{59}Fe	4.6×10^{-3}	12.2		F	g
Nd-β, bcc	^{59}Fe	1.0×10^{-2}	13.6		F	g

†Ratio of solute diffusivity to self-diffusion in the solvent matrix at the highest measured temperature. *N stands for normal diffusion, presumably the same mechanism for solute and self-diffusion; F stands for fast-diffusion with a partly interstitial component for solute diffusion. [a]Rogozin et al. (1968); [b]Murphy et al. (1975); [c]Dariel et al. (1969b); [d]Fromont (1975); [e]Dariel et al. (1972); [f]Cathey et al. (1973); [g]Dariel (1975); [h]Dariel (1973); [i]Dariel (1971); [j]Dariel et al. (1969c); [k]Dariel (1970); [l]Dariel et al. (1969a).

as Ti, U or Pb. Solutes having values of $K_A^B > 10^2$ seem to be fast solutes, diffusing by a mechanism different from that for self-diffusion. On the other hand, solutes with $K_A^B < 10$, probably diffuse by a mechanism similar to that for self-diffusion. This last group includes the rare earth solutes and possibly non-transition metal polyvalent solutes (e.g. In).

The light rare earth metals undergo a high temperature phase transformation

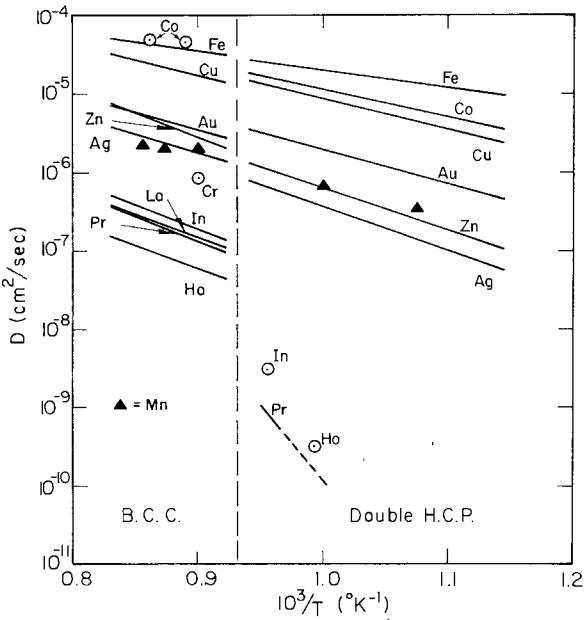

Fig. 12.5. The diffusivities of various solutes in double-hcp and bcc Pr as function of the inverse temperature.

from a close packed to the bcc structure. The self-diffusion coefficients increase by approximately two orders of magnitude upon change of the crystal structure (fig. 12.1). The slow diffusing solutes behave in a similar manner, strengthening the assumption of identical mechanisms in both cases. The effect of the phase transformation on the solute diffusivities provides the means of determining whether the solutes with $10 < K_A^B < 10^2$ are real interstitial fast diffusers or substitutional solutes diffusing by a vacancy mechanism at unusually high rates.

Anthony (1970) and Dariel et al. (1968) have pointed out that one of the characteristic and yet unexplained features of fast diffusion is the small, sometimes barely discernible effect exerted by the phase transformation taking place in the solvent matrix on the solute diffusivities. Such a behavior is in marked contrast to the discontinuous increase of the self and, presumably substitutional, solute diffusivities. Thus, using the effect of the phase transformation as a criterion, it appears that the noble metals, the transition metals (Mn, Fe, Co) and Zn behave as fast diffusers in the rare earth metals.

Diffusion theory in metals, at its present state of art, is not able to provide a quantitative or even qualitative account for the relative values of the solute diffusivities in rare earth metals. The electrostatic interaction theory, which achieved notable success is accounting for the relative diffusivities of various solutes in the noble metals is not applicable to the polyvalent rare earth solvents (Dariel, 1968). Size effects are probably important in determining relative solute

diffusivities. The available experimental data (Dariel et al., 1969a; Dariel, 1973; Fromont, 1975) does not yield, however, a consistent picture and more work is required on these systems.

With respect to the fast diffusing noble metal solutes, the trend $D_{Cu} > D_{Au} > D_{Ag}$ is similar to that observed in other matrices (Li, In, Tl, Sn, Pb). Noteworthy are the diffusivities of the transition metal solutes (Fe, Co) in the bcc phases of Ce, Pr and Nd (figs. 12.4 and 12.5). The measured values 3×10^{-5} cm^2/sec are the highest measured for metallic solutes in crystalline matrices and are of the same order as the diffusivities in liquid metals. Indeed, the highest diffusivities in metals seem to be associated with fast solutes in anomalous bcc solvent metals. The giant diffusivities of transition metal solutes, higher than those of the noble metals, seem to be a feature common to Group III-A (rare earth) and IV-A (Ti, Zr) metals, contrary to III-B and IV-B solvents in which noble metals have the highest diffusivities.

In a recent review, Warburton and Turnbull (1975) discussed the mechanism by means of which the fast diffusion of metallic solutes is assumed to take place. There seems to be general agreement that part or all of the fast diffusing solutes enter into interstitial sites during the diffusion process. Several independent experimental techniques, beside diffusivity measurements, have indeed confirmed that interstitial solubility, to a variable extent, occurs in these systems. Initially, Frank and Turnbull (1956) put forward the dissociative mechanism, according to which the measured diffusivity D_m can be expressed by

$$D_m \equiv \frac{C_i}{C_i + C_s} D_i + \frac{C_s}{C_i + C_s} D_s,$$

where D_i and D_s are the diffusivities, C_i and C_s the concentrations of the solute in interstitial and substitutional positions, respectively. Postulating, for reasons at that time not yet clear, that C_i is significantly larger than in the usual metallic solid solutions and assuming that the barriers for interstitial solute motion are not too high, a qualitative explanation for the high values of D_m can be found. Variations of the values of C_i, C_s, D_i and D_s in the different crystalline structures can account for any, including the slight positive or negative, solute diffusivity discontinuities observed at the temperature of the phase transformations of the solvent metals. However, the dissociative mechanism, assuming a simple interstitial defect, is not consistent with the results of isotope effect, solvent diffusion enhancement, solute diffusion dehancement and internal friction results. More complex defects such as associated interstitial-vacancy pairs, solute–solute or solute–solvent split interstitials have been proposed.

It is likely indeed, considering the great variety of metallic systems in which fast diffusion has been observed, as well as the extended range for K_A^B, that several kinds of defects (ranging from a pure interstitial to a simple vacancy) are involved in the solute diffusion processes in the various systems.

The exceedingly high diffusivity of some metallic solutes in the rare earth elements suggests that a significant fraction of these solutes is able to dissolve as interstitials. This is related to the "open" structure of the rare earth host atoms

which possess a relatively large ratio of the Goldschmidt to ionic radius. This feature, coupled with the relatively small Goldschmidt radii of the solutes, is a necessary (albeit not sufficient) condition for the occurrence of fast diffusion.

The ratio of the Goldschmidt radii of the solute to that of the solvent atoms ranges from 0.7 to 0.9 in the fast diffusing solutes systems. These values greatly exceed the well-known Hägg limits for interstitial solid solution formation. The presence of a significant fraction of the solutes apparently violating these rules offers intriguing implications concerning the validity of the established laws for alloy formation. Size effects are undoubtedly important, but in a more subtle manner than previously believed. Turnbull (1974) pointed out that many binary metallic systems in which fast diffusion of one of the components was observed also show a tendency towards amorphous alloy formation when cooled from the liquid phase. This feature is well apparent in rare earth metal solvent systems. Both rare earth noble metal systems (Johnson et al., 1975) and rare earth transition metal systems (Rhyne et al., 1972; Heiman and Lee, 1974) have a tendency for extensive amorphous solution formation and for fast diffusion (table 12.3). Turnbull associates both features with the presence of a pair potential ϕ_{AB} (A-solvent, B-solute) which has an abnormally soft repulsive branch. This accounts for these systems being relatively insensitive to the solute–solvent interatomic distance. As a result, solutes are able to approach solvent atoms without great expanditure of energy to within distances significantly smaller than the sum of the atomic radii of the pure elements. This model is supported both by theoretical calculations in alkali metals (Schober et al., 1975) and by experimental evidence reviewed by Turnbull (1974).

Undoubtedly the rare earth metals, with the continuous change of size within the series, offer a highly promising field of study for these new, partly interstitial solid solutions. Examples of the variety of defect structures that can be obtained are the Y(Cu) and the Gd(Cu, Fe) systems. In the former, splat quenching (Giessen et al., 1971) yielded a purely interstitial solid solution; in the latter, (Ray, et al., 1972) the solutes were in the form of bi-substitutionals i.e. associated solute pair at one lattice site.

Solute diffusion measurements have so far been restricted to Y and light lanthanide solvent metals; it seems highly desirable to extend such measurements to heavy lanthanide matrices. In particular, with the increasing availability of single crystals, efforts should be made to determine the anisotropy of solute diffusion in the hexagonal close-packed phases. Similar experiments (Dyson et al., 1967) provided useful evidence concerning the nature of fast diffusion.

In general the solubility of the fast solutes is severely limited in the solvent metals. By studying the solute concentration dependence of the solvent and the solute diffusivities, Miller (1969a, 1969b) and Warburton (1973), respectively, were able to draw important conclusions concerning the mechanism of fast diffusion. No such studies have yet been carried out in the rare earth metals, even though in some instances (Pr(Au), Griffin and Gschneidner, 1971) the solubility of the fast diffusing solutes seems surprisingly large.

The amorphous solid solutions of the fast diffusing solutes in rare earth metals

possess some very interesting (superconductive, magnetic) properties. This should provide a strong motivation for intensive studies of these systems. It is hoped that the increasing understanding of the structure and properties of amorphous solutions will yield additional insight into the nature of fast diffusion.

5. Electrotransport in rare earth metals

The presence of an external electric field induces an effect of mass transport in solids. If the temperature is sufficiently high, the atoms migrate either toward the anode or the cathode. The study of this effect, which has been alternatively called electromigration, electrotransport or electrorefining, has interesting aspects, both practical and theoretical. The main practical importance of electromigration lies in it being a potential method of purification. The electric field currents cause the impurities to be driven toward one of the electrodes. Their accumulation at the edges leaves the sample with a decreased impurity content over most of its length. From the basic science point of view, electromigration experiments yield insight into the interaction between the migrating ion with the electric field and the charge carriers. The results of such experiments can be used to analyze solute diffusion kinetics and to deduce information on various vacancy jump frequencies. The experimental and theoretical aspects of electromigration and electrorefining have been reviewed extensively, the most recent reviews are those of Huntington (1975a, 1975b).

The highly reactive rare earth metals show a strong affinity toward the non-metallic interstitial solutes i.e. carbon, nitrogen and oxygen. The concentration of these impurities is, therefore, usually high even in carefully prepared materials. Early experiments by Williams and Huffine (1961) and Marchant et al. (1961) had shown electrotransport to be a promising method of purification of the rare earth metals, not only from non-metallic, but from some metallic impurities as well. These results provided the motivation of the overwhelming majority of electrotransport experiments which have been carried out in the rare earth metals. The avowed objective of these experiments has been to study and optimize the parameters involved in electrorefining the various rare earth metals. The experimental aspects of these studies in metals have been discussed by Peterson (1971), the use of this method for purification has been reviewed by Carlson et al. (1975) and is also treated in ch. 2 section 2.3. As a by-product of the electrotransport studies, valuable information concerning basic diffusion behavior in rare earth metals could be deduced.

A variety of solutes in the rare earth metals present a partly or total interstitial character. These solutes include beside the metalloid classical interstitials also some metallic elements, the so-called fast-diffusers, discussed in section 4. In general the study of electromigration of interstitials offers two advantages as compared to that of substitutional solutes. From the experimental point of view, the relatively high mobilities of the interstitial solutes increases the electrotransport effects often allowing to achieve steady state conditions within

reasonable periods of time. From the theoretical side, the effects associated with interstitial diffusion are more readily interpretable. The defect structure of an interstitial is simpler than that of a vacancy and its scattering power stays constant during the diffusion process. Considering the relative variety of interstitials encountered in rare earth metals, electrotransport studies present certain advantages which are, however, counterbalanced by having to work with high reactivity metals possessing complex band structures.

The main qualitative result of the electrotransport studies in rare earth metals, namely the direction in which the various solutes are driven by the electric field

TABLE 12.4
Compilation of the direction of electrotransport of various solutes in rare earth metals

Solvent rare earth	Solute	Sign of* Z_{eff}	Ref.	Solvent rare earth	Solute	Sign of* Z_{eff}	Ref.
La	Fe	–	[a]	Gd	O	–	[e]
	Al, Cu, Mn	+	[a]		O	–	[f]
					Si	+	[g]
Ce	Mn, Fe, Co, Ni, Cu	–	[b]		C, N, O	–**	[g]
	Mo	+	[b]				
	O, Mn, Fe	–	[a]	Tb	N, O	–	[h]
	Cu, Mo	+	[a]				
	Fe, Co	–**	[c]	Lu	C, N, O	–**	[i]
	Ag	+**	[c]				
				Y	N, O	–	[j]
Pr	Fe	–	[a]		Mn, Fe, Co, Ni	–	[j]
	Cu	+	[a]		H, C, N, O	–**	[k]
	Ag	–	[d]		Fe	–**	[l]
					Ag	+**	[l]

*(–) stands for anode directed and (+) for cathode directed solutes. **Quantitative results. [a]Marchant et al. (1971); [b]Moore et al. (1965); [c]Cathey et al. (1973); [d]Tessler and Dariel (1971); [e]Graham (1967); [f]Jordan and Jones (1973); [g]Peterson and Schmidt (1972); [h]Jordan et al. (1975); [i]Peterson and Schmidt (1969); [j]Williams and Huffine (1961); [k]Carlson et al. (1966); [l]Murphy et al. (1975).

TABLE 12.5
Mobilities, diffusion coefficients and purification factor of metalloid solutes at 0.9 T_m

	Solvent matrices†									
	$U(10^{-5}\,cm^2/sec\cdot V)$			$D(10^{-5}\,cm^2/sec)$				$U/D(V^{-1})$		
Solutes	α-Gd	Lu	α-Y	α-Gd	Lu	α-Y	γ-Ce*	α-Gd	Lu	α-Y
C	3.4	4.2	15.0	0.18	0.16	2.00	0.28	18.8	26.2	7.0
N	5.1	14.0	14.0	0.22	0.59	0.53	3.2	23.0	23.8	18.8
O	19.0	39.0	39.0	0.75	2.00	1.10	1.3	25.4	19.5	18.3

†The results for Gd, Lu and Y have been compiled by Carlson et al. (1975). *Results of internal friction studies in the 20–300 C temperature range extrapolated to 0.9 T_m of Ce (Borisov et al., 1971).

and current, is shown in table 12.4. Quantitative results such as solute mobilities and diffusivities which in some instances could be deduced from the electrotransport data are shown in table 12.5. This table also includes some results deduced from internal friction studies of C, N and O in Y.

A survey of table 12.4 allows to draw certain general conclusions. The interstitial non-metallic solutes, C, N and O migrate in all instances toward the anode. In that respect, the rare earth metal matrices are similar to Group IV-A (Ti, Zr) metals and different from the other transition metal solvents. The fast diffusing metallic solutes, discussed in section 4 can be divided in two groups. The first group includes the ferrous transition metals Mn, Fe, Co and Ni. These solutes, like the metalloids, possess extremely high mobilities and diffuse toward the anode. The second group of fast diffusing solutes, the noble metals (Cu and Ag) migrate toward the cathode. Whether this implies that Au would behave similarly, is not clear. In Pb (another matrix for fast diffusion), Ag diffuses toward the cathode while Au diffuses toward the anode (Herzig and Stracke, 1975).

According to all current electrotransport theories the force on a migrating ion in the electrotransport process consists of two parts. The first one represents the direct electrostatic interaction of the applied electric field with the migrating ion. The second force arises from the momentum transfer from the charge carriers scattered by the ion. This latter force will be anode directed in an electron conduction type metal and cathode-directed in hole conduction. The negative effective charge of the anode directed metalloids in Group III-A and IV-A metal matrices has been interpreted as indicating that the dominant electrotransport-determining effect is the momentum transfer term. In the elements lying to the right of Group VI-A, the reversal of the sign of the effective charge is then attributed to the influence of holes which become the charge carriers in the nearly filled high density bands. Unfortunately, this rather simplistic picture breaks down considering that the ferrous interstitial solutes behave like the metalloids but the noble metal interstitials show an opposite behavior. Undoubtedly the situation is more complex in the rare earth metals which have several overlapping bands. The results indicate that the sign of the effective charge depends both on the nature of the migrating solute ion and that of the solvent matrix. Murphy et al. (1975) remarked that average properties such as the Hall effect have only limited value in predicting the direction of electrotransport, as shown by the fact that Fe and Ag behave in a similar manner in Y and Ce, yet the Hall coefficient of Y is negative and that of γ-Ce positive.

Almost no results concerning the electrotransport of substitutional solutes in rare earth metals have been reported. Even for interstitial solutes the results are fragmentary and mostly qualitative. Much is therefore to be yet done in order to achieve a coherent picture of electrotransport phenomena in rare earth metals. The double challenge being offered by the practical applicability of such studies on one hand, and their importance towards furthering the understanding of basic diffusion phenomena in metals on the other, should provide the necessary motivation for additional research in this area.

6. Various diffusion related subjects

6.1. *Chemical diffusion studies*

The previous sections were concerned with self-diffusion or solute diffusion studies in which the environment of the migrating atoms did not change either as a function of time or the spatial coordinates. In solute diffusion or electrotransport experiments these conditions were fulfilled as a result of the extremely low concentration of the diffusing species. Even if the distribution of the solutes changed as a consequence of the diffusion process, it did not affect in any significant manner the overall local composition of the sample.

In chemical diffusion experiments, on the other hand, steep concentration gradients are set up which vary appreciably both as a function of time and distance. As a result of the continuously varying environment in the diffusion zone, the interpretation of the results is much more complex. Chemical diffusion studies present, however, a practical interest since in many cases situations arise which involve the initial presence of concentration gradients.

The study of diffusion in systems with a concentration gradient allows the determination of $\tilde{D}$, the chemical diffusion coefficient, which in a binary system can be expressed as

$$\tilde{D} = (D_A^* N_B + D_B^* N_A)\,(1 + \partial \ln \gamma_A / \partial \ln N_A),$$

where D_A^*, D_B^* are composition dependent intrinsic diffusivities, N_A, N_B are the mole fractions of components A and B and γ_A, the activity coefficient of A. The second right hand term takes account of the deviations of the system from an ideal solution. A second equation relates the rate of displacement v_k of inert markers placed at the initial interface of the diffusion couple to the intrinsic diffusivities.

$$v_k = (D_A - D_B)\,\partial N_A / \partial x \qquad \text{with} \qquad D_A = D_A^*(1 + \partial \ln \gamma_A / \partial \ln N_A)$$

The displacement of the inert markers and the micrographic aspect of the diffusion zone allow one to draw some conclusions concerning the nature of the diffusion mechanism.

Dariel (1968) and Languille (1973) carried out chemical diffusion studies in La–Ce, Pr–Nd and La–Pr diffusion couples. The components of these systems are closely related in their properties, departures from an ideal behavior are therefore expected to be slight, as indeed was established in the Pr–Nd system (Lundin et al., 1965).

A significant shift of the inert markers and the formation of porosity were observed only in the La–Ce couples. The lack of inert markers shift in the other systems was attributed to the essentially similar intrinsic diffusivities of the two components. The concentration dependence of the intrinsic diffusivities (at constant temperature) seemed to correlate with the temperature of the solidus in the binary system. In all instances precipitates containing a ternary component, most likely oxygen, appeared in the diffusion zone, their presence was attributed

to the difference in the solubility of oxygen in the two components of the diffusion couple.

Chemical diffusion-like studies were carried out in Pu–Ce δ stabilized bcc alloys (Harvey et al., 1968). The similarity between Pu and Ce was mentioned in section 3.3. It is not surprising therefore that Ce dissolves in and stabilizes δ-Pu.

6.2. *Diffusion of rare earth solutes in other metals*

Several investigations of the diffusion of rare earth metal solutes in non rare earth metals have been reported in literature (table 12.6). The main objective of these experiments has been the study of the diffusion behavior in a common solvent metal of a closely related group of solutes in which properties varied in a gradual and systematic manner. In particular, the results were expected to provide information concerning the validity of Swalin's (1957) treatment of solute diffusion in metals according to which mechanical properties such as size and deformability determine relative solute diffusivities.

In general, the studies showed a highly anomalous, structure sensitive diffusion behavior of the rare earth tracers. Non-Gaussian penetration plots which usually consisted of an initial steep slope followed by a gradual decrease of the tracer activity were observed. These results were attributed to the overall low solubility of the rare earth solutes in the metals (Al, Cu, Ni, Ag and Pb) examined, to the contribution of short circuiting diffusion paths or to the presence of surface oxide barriers. Efforts were made to analyze the penetration plots in terms of contributions from several overlapping thermally activated mechanisms. As a consequence of the experimental difficulties and the ambiguity of the results, no conclusions could be reached concerning the validity of Swalin's theory.

The solute diffusivity of Y in single crystals on several refractory metals was studied by Gornyy and Al'tovskiy (1971). A normal diffusion behavior has been reported with the activation energy of the solute diffusivity low as compared to that of the self-diffusion of the host metal.

A general conclusion of these investigations seems to be that the study of diffusion of rare earth solutes in different metals has been less fruitful than diffusion studies carried out in rare earth matrices.

TABLE 12.6
Diffusion studies of rare earth solutes in various metals

Solvent metal	Solute	Ref.
Ag, Pb	Ce, Nd, Pm	Williams and Slifkin (1963)
Al	La, Ce, Pr, Nd, Sm	Murarka and Agarwala (1968)
Zr	Ce	Paul et al. (1968)
Cu	Ce, Pm, Eu, Tb, Tm, Lu	Badrinarayanan and Mathur (1970)
Ni	Ce, Nd	Paul and Agarwala (1971)
Mo, W, Nb, Ta	Y	Gornyy and Al'tovskiy (1971)

6.3. *Diffusion in rare earth containing compounds*

This last sub-section summarizes some diffusion related effects in compounds and especially in the $SmCo_5$-type compounds, which are probably the best known rare earth containing intermetallics. These materials owe their usefulness to their outstanding magnetic properties and, in particular, to their exceedingly high magnetic energy product. $SmCo_5$-based permanent magnets have reached the stage of commercial production for a variety of applications. The properties and details of the preparation methods have been fully described in the literature and are discussed in ch. 14 section 6.

$SmCo_5$-type magnets are prepared by a sequence of arc-melting, milling, magnetic aligning, compression and sintering steps. The relevant magnetic properties depend critically on the various stages. The mechanism of sintering and its relation to the intrinsic coercive force has been studied by Benz and Martin (1972) who observed a $\frac{1}{2}$ power dependence of the volume shrinkage of $SmCo_5$ pressings on the sintering time. These findings were later confirmed by Jorgensen and Bartlett (1975) and were interpreted, according to the prevalent theories of sintering, as suggesting grain boundary diffusion as the rate limiting step for the sintering process. Benz and Martin also studied the concentration dependence of the rate of shrinkage in the homogeneity range of the $SmCo_5$ phase. The highest rate of shrinkage was observed for hyperstoichiometric (Sm-rich) $SmCo_5$ compounds and attributed to the presence of structural Co vacancies on the Co sublattice. On the basis of these results Benz and Martin proposed a sintering model which includes a Co vacancy flow from the curved surface of the pores toward the relatively planar grain boundaries which act as vacancy sinks. There is a net counterflow of Co and Sm atoms to the vacancy flux. The Co atoms are assumed to diffuse by direct interchange with the Co vacancies i.e. vacancies on the Co sub-lattice, whilst Sm atoms diffuse by a Sm atom-Co vacancy cluster interchange. The net flux of vacancies from the pore area and the counterflux of atoms result in the shrinkage and final annihilation of the pores. The rate-limiting step in this model is the diffusion of Sm atoms from the grain-boundary regions towards the pore surfaces.

The model, just described, depends on the observed concentration dependence of the rate of shrinkage with its maximum at high Sm-concentrations. These results have not been confirmed by Jorgensen and Bartlett (1975), who suggest the presence of more than one (unspecified) transport mechanisms taking place most likely, along grain boundaries.

The mechanism of sintering in Sm–Co alloys has also been studied over a wide (23 to 42 w% Sm) composition range by Gessinger and de Lamotte (1973). These authors observed that the stoichiometric compounds Sm_2Co_7, $SmCo_5$ and Sm_2Co_{17} are characterized by a relatively slow sintering behavior, while non-stoichiometric $SmCo_5$ shows maximum densification at the limits of its homogeneity range. These results were interpreted as being due to the effect of structural vacancies on the Sm and Co sub-lattices in the non-stoichiometric compound.

Beside their obvious contribution to sintering, diffusion processes are also important in determining the thermal stability of $SmCo_5$ type materials. The thermal stability and its influence upon magnetic properties is affected by: 1. The eutectoid decomposition which takes place at elevated temperatures (Den Broeder and Buschow, 1972, Buschow and Den Broeder 1973); 2. the presence of oxygen. The eutectoid transformation is clearly a diffusion controlled process and its kinetics determine the stability of the $SmCo_5$-phases at low temperatures. Its presence in RCo_5 compounds has been definitively established by means of diffusion couple techniques in the Sm–Co (Martin and Smeggil, 1974) and the Ce–Co (Martin et al., 1975) systems. The microstructural changes caused by the presence of oxygen and its diffusion during the sinter-annealing and the thermal aging stages have been studied by Bartlett and Jorgensen (1974). The selective oxidation of samarium sets up samarium activity gradients which may result in the apparition of samarium depleted phases. The mobility of oxygen may be beneficial since it allows the removal of oxide inclusions which coalesce in a few coarse grains.

All these processes may affect in a significant manner the magnetic properties (Searle and Garret, 1974) and, therefore, deserve further detailed studies.

Acknowledgements

Thanks are due to Dr. D. Calais for providing me, in advance of publication, with his group's most recent results, to Dr. L. Brewer and Dr. J. Wang for fruitful discussions and to Dr. N. Cannon and Mr. A. Levy for helpful suggestions. I also wish to extend my deep gratitude to Dr. M.R. Pickus for his support and encouragement.

This work was supported by the U.S. Energy Research and Development Administration.

References

Aaronson, H.I. and P.G. Shewmon, 1967, Acta Met. **15**, 385.

Adda, Y. and J. Philibert, 1966, La Diffusion dans les Metaux, (Presses Universitaires de France, Paris) ch. 3.

Akimov, A.I. and Ya. A. Kraftmakher, 1970, Phys. Status Solidi **42**, K41.

Anthony, T.R., 1970, Interstitial Metal Impurity Diffusion in Metals, in: Seeger, A., D. Schumacher, W. Schilling and J. Diehl, eds., Vacancies and Interstitials in Metals (North Holland, Amsterdam) p. 935.

Badrinarayanan, S. and H.B. Mathur, 1970, Indian J. Pure Appl. Phys. **8**, 324.

Bartlett, R.W. and P.J. Jorgensen, 1974, J. Less-Common Metals **37**, 21.

Beaudry, B.J. and F.H. Spedding, 1975, Met. Trans. **6B**, 419.

Benz, M.G. and D.L. Martin, 1972, J. Appl. Phys. **43**, 3165.

Boidron, M., 1975, quoted in Fromont (1975), table X.

Borisov, E.V., G.A. Vedenyapin, Yu. S. Suganeev and L.V. Smirnov, 1971, Fiz. Khim. Obrab. Mater. **1**, 75.

Brewer, L., 1967, Viewpoints of Stability of Metallic Structures in: Rudman, P. T. Stringer and R.I. Taffee, eds., Phase Stability in Metals and Alloys (McGraw-Hill, New York) p. 39.

Brewer, L., 1971, J. Opt. Soc. Amer. **61**, 1101.

Burr, C.R. and S. Ehara, 1966, Phys. Rev. **149**, 551.

Buschow, K.H.J. and F.J.A. Den Broeder, 1973, J. Less-Common Metals **33**, 191.

Carlson, O.N., F.A. Schmidt and D.T. Peterson, 1966, J. Less-Common Metals **10**, 1.
Carlson, O.N., F.A. Schmidt and D.T. Peterson, 1975, J. Less-Common Metals **39**, 277.
Cathey, W.N., J.E. Murphy and J.R. Woodyard Jr., 1973, Met. Trans. **4**, 1463.
Cornet, J.A., 1971, J. Phys. Chem. Solids **32**, 1489.
Dariel, M.P., 1968, Ph.D. Thesis, Weizmann Institute of Science, Rehovoth, Israel.
Dariel, M.P., 1970, Phil. Mag. **22**, 563.
Dariel, M.P., 1971, J. Appl. Phys. **42**, 2251.
Dariel, M.P., 1973, Phil. Mag. **28**, 915.
Dariel, M.P., 1975, Acta Met. **23**, 473.
Dariel, M.P., G. Erez and G.M.J. Schmidt, 1968, Proceedings of the International Conference on Vacancies and Interstitials in Metals, Vol. 1, (Kernforschungsanlage Jülich, Germany) p. 91.
Dariel, M.P., G. Erez and G.M.J. Schmidt, 1969a, Phil. Mag. **19**, 1045.
Dariel, M.P., G. Erez and G.M.J. Schmidt, 1969b, Phil. Mag. **19**, 1053.
Dariel, M.P., G. Erez and G.M.J. Schmidt, 1969c, J. Appl. Phys. **40**, 2746.
Dariel, M.P., D. Dayan and A. Languille, 1971, Phys. Rev. **B4**, 4348.
Dariel, M.P., D. Dayan and D. Calais, 1972, Phys. Status Solidi (a) **10**, 113.
Den Broeder, F.J.A. and K.H.J. Buschow, 1972, J. Less-Common Metals **29**, 65.
Doherty, J.E. and D.F. Gibbons, 1971, Acta Met. **19**, 275.
Dupuy, M. and D. Calais, 1968, Trans. Met. Soc AIME **242**, 1679.
Dyson, B.F., T.R. Anthony and D. Turnbull, 1967, J. Appl. Phys. **38**, 3408.
Engel, N., 1965, The Electron Concentration Concept and Diffusion. in: Diffusion in Body-Centered Cubic Metals (American Society for Metals, Metals Park, Ohio) p. 87.
Frank, F.C. and D. Turnbull, 1956, Phys. Rev. **104**, 617.
Fromont, M., 1975a, Thèse, Université de Paris-Sud, Orsay, France.
Fromont, M., 1975b, J. Phys. Chem. Solids **36**, 1397.
Fromont, M., A. Languille and D. Calais, 1974, J. Phys. Chem. Solids **35**, 1367.
Giessen, B.C., R. Ray and S. Hahn, 1971, Phys. Rev. Lett. **26**, 509.
Gessinger, G.H. and E. de Lamotte, 1973, Z. Metallk. **64**, 771.
Gilder, H.M. and D. Lazarus, 1975, Phys. Rev. B **11**, 4916.
Gornyy, D.S. and R.M. Al'tovskiy, 1970, Fiz. Metal. Metalloved. **30**, 85.
Gornyy, D.S. and R.M. Al'tovskiy, 1971, Fiz. Metal Metalloved. **31**, 108.
Graham, C.D., 1967, Solid State Electrolysis of Gadolinium, in: 5th Rare Earth Research Conference, Vol. 5, Iowa State University, p. 89.
Griffin, R.B. and K.A. Gschneidner, Jr., 1971, Met. Trans. **2**, 2517.
Hägg, G., 1929, Z. Phys. Chem. **6B**, 221.
Hägg, G., 1930, Z. Phys. Chem. **7B**, 339.
Harvey, M.R., A.L. Rafalski and D.H. Riefenberg, 1968, ASM Trans. Quart. **60**, 629.
Heiman, N. and K. Lee, 1974, Phys. Rev. Lett. **33**, 778.
Herzig, C. and E. Stracke, 1975, Phys. Status Solidi (a) **27**, 75.
Huntington, H.B., 1975a, Thin Solid Films **25**, 265.
Huntington, H.B., 1975b, Electromigration in Metals, in Nowick, A.S. and J.J. Burton, eds., Diffusion in Solids – Recent Developments (Academic Press, New York) ch. 6.
Jayaraman, A., 1965, Phys. Rev. **137**, A179.
Johnson, W.L., S.J. Poon and P. Duwez, 1975, Phys. Rev. B **11**, 150.
Jordan, R.G. and D.W. Jones, 1973, J. Less-Common Metals **31**, 125.
Jordan, R.G., D.W. Jones and V.J. Helms, 1975, J. Less-Common Metals **42**, 101.
Jorgensen, P.J. and R.W. Bartlett, 1974, J. Less-Common Metals **37**, 205.
Jullien, R., E. Galleani d'Agliano and B. Coqblin, 1973, J. Low Temp. Phys. **10**, 685.
Kidson, G.V., 1963, Can. J. Phys. **41**, 1563.
Languille, A., 1973, Thèse, Université Paris-Sud, Orsay, France.
Languille, A., M.P. Dariel, D. Calais and B. Coqblin, 1973, Mem. Sci. Rev. Met. **70**, 241.
Languille, A., D. Calais and M. Fromont, 1974a, J. Phys. Chem. Solids **35**, 1373.
Languille, A., D. Calais and B. Coqblin, 1974b, J. Phys. Chem. Solids **35**, 1461.
Lazarus, D., 1965, Diffusion in Body-Centered Cubic Transition Metals – A Theoretical Critique in: Diffusion in Body-Centered Cubic Metals (American Society for Metals, Metals Park, Ohio) p. 155.
Le Claire, A.D., 1965, Application of Diffusion Theory to the Body-Centered Cubic Structures in: Diffusion in Body-Centered Cubic Metals (American Society for Metals, Metals Park, Ohio) p. 3.
Lichtenberg, R.R., J.C. Warner and O.N. Carlson, 1974, J. Less-Common Metals **35**, 275.
Lundin, C.E., J.F. Nachman and A.S. Yamamoto, 1969, Investigations of the Praseodymium–Neodymium System in: Vorres, K.S., ed., Rare Earth Research II, Proceedings of the Third Conference on Rare Earth Research, Apr. 1963 (Gordon and Breach, New York) p. 315.
Marbach, G., M. Fromont and D. Calais, 1975, quoted in Fromont (1975).
March, N.G. and A.M. Murray, 1961, Proc. Roy. Soc., Ser. A **261**, 119.
Marchant, J.D., E.S. Shedd and T.A. Henrie, 1961, Solid-State Electrorefining of Rare Earth Metals in: Nachman, J.F. and C.E. Lundin, eds., Proceedings of the Second Conference on Rare Earth Research, 1961 (Gordon and Breach, New York) p. 143.
Marchant, J.D., E.S. Shedd, T.A. Henrie and M.M. Wong, 1971, Electrotransport of Impurities in Rare Earth Metals Using a Pulsed Current, U.S. Bureau of Mines Rep. RI-7480.

Martin, D.L. and J.G. Smeggil, 1974, IEEE Trans. Mag-10, 704.
Martin, D.L., J.G. Smeggil, W. Hatfield and R. Bolon, 1975, IEEE Trans. Mag-11, 1420.
Maskalets, V.N., E.A. Smirnov, D.M. Skorov and G.B. Fedorov, 1967, Met. Metalloved. Chist. Metallov, Atomizdat, Moscow, p. 189.
Miller, J.W., 1969a, Phys. Rev. **181**, 1095.
Miller, J.W., 1969b, Phys. Rev. **188**, 1074.
Moore, R.H., F.M. Smith and J.R. Morrey, 1965, Trans. Met. Soc. AIME **233**, 1259.
Murarka, S.P. and R.P. Agarwala, 1968, Diffusion of Rare Earth Elements in Al, Indian Atomic Energy Comm. Report, BARC-368.
Murphy, J.E., G.H. Adams and W.N. Cathey, 1975, Met. Trans. **6A**, 343.
Paul, A.R. and R.P. Agarwala, 1971, Met. Trans. **2**, 2691.
Paul, A.R., M.S. Anand, M.C. Naik and R.P. Agarwala, 1968, Proceedings International Conference on Vacancies and Interstitials in Metals, Vol. 1, Kerforschungsanlage, Jülich, Germany, p. 105.
Peart, R.F. and J. Askill, 1967, Phys. Status Solidi **23**, 263.
Peterson, N.L., 1968, Diffusion in Metals in: Seitz, D., D. Turnbull and H. Ehrenreich, eds., Solid State Physics, Vol. 22 (Academic Press, New York) p. 409.
Peterson, D.T., 1971, Experimental Factors in the Purification of Metals by Electrotransport in: Lodding, A. and T. Lagerwall, eds., Atomic Transport in Solids and Liquids (Verlag der Zeitschrift für Naturforschung, Tübingen) p. 104.
Peterson, D.T. and F.A. Schmidt, 1969, J. Less-Common Metals **18**, 111.
Peterson, D.T. and F.A. Schmidt, 1972, J. Less-Common Metals **29**, 321.
Ray, R., M. Segnini and B.C. Giessen, 1972, Sol. State Com. **10**, 1163.
Rhyne, J.J., S.J. Pickart and H.A. Alperin, 1972, Phys. Rev. Lett. **29**, 1962.
Rogozin, V.D., L.M. Gert and A.A. Babad-Zakhryapin, 1968, Izv. Akad. Nauk SSSR, Metal **3**, 228.
Sanchez, J.M. and D. de Fontaine, 1975, Phys. Rev. Lett. **35**, 227.
Schober, H., R. Taylor, M.J. Norgett and P.M. Stoneham, 1975, J. Phys. F, Metal Phys. **5**, 637.
Searle, C.W. and H.J. Garrett, 1974, J. Appl. Phys. **45**, 5037.
Seeger, A., 1972, J. Less-Common Metals **28**, 387.
Spedding, F.H. and K. Shiba, 1972, J. Chem. Phys. **57**, 612.
Swalin, R.A., 1957, Acta Met. **5**, 443.
Tessler, A. and M.P. Dariel, 1974, J. Less-Common Metals **35**, 235.
Tomizuka, C.T., 1959, Diffusion, in: Lark-Horowitz, K. and V.A. Johnson, eds., Methods of Experimental Physics, Vol. 6, Part A, Solid State Physics (Academic Press, New York) p. 364.
Turnbull, D., 1974, J. Physique **35** (Colloque No. 4) 1.
Verhoeven, J.D., 1966, J. of Metals **18**, 26.
Vineyard, G., 1957, J. Phys. Chem. Solids **3**, 121.
Warburton, W.K., 1973, Phys. Rev. B **7**, 1330.
Warburton, W.K. and D. Turnbull, 1975, Fast Diffusion in Metals, in: Nowick, A.S. and J.J. Burton, eds., Diffusion in Solids – Recent Developments (Academic Press, New York) p. 171.
Williams, J.M. and C.L. Huffine, 1961, Nucl. Sci. Eng. **9**, 500.
Williams, G.P., Jr. and L. Slifkin, 1963, Acta Met. **11**, 319.
Zamir, D. and D.S. Schreiber, 1964, Phys. Rev. **A136**, 1087.
Zanghi, J.P., 1975, Thèse, Université Paris-Sud, Orsay, France.

SUBJECT INDEX